19990430 048

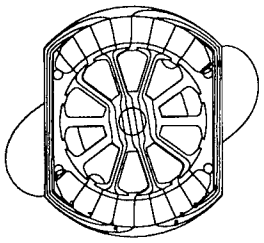

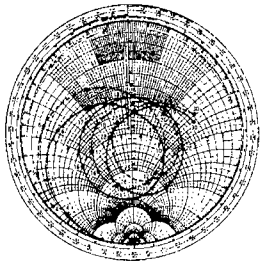

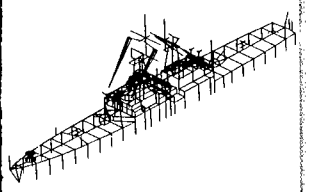

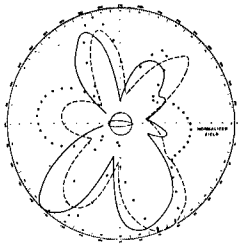

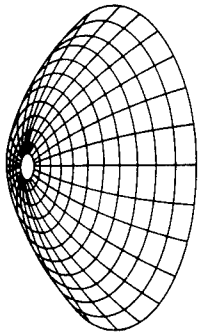

15th Annual Review of Progress in

APPLIED

COMPUTATIONAL

ELECTROMAGNETICS

at the

Naval Postgraduate School

Monterey, CA

March 15-20, 1999

CONFERENCE PROCEEDINGS

DISTRIBUTION STATEMENT A
Approved for Public Release
Distribution Unlimited

CONFERENCE PROCEEDINGS

15th Annual Review of Progress in

APPLIED

COMPUTATIONAL

ELECTROMAGNETICS

at the

Naval Postgraduate School

Monterey, CA

March 15-20, 1999

TECHNICAL PROGRAM CHAIRMAN

Randy Haupt

Sponsored by

The Applied Computational Electromagnetics Society,

Naval Postgraduate School, University of Nevada-Reno,

Brigham Young University and University of Kentucky

DTIC QUALITY INSPECTED 4

Table of Contents i

2000 Call for Papers ix

1999 Symposium Program Committee xi

Technical Program Chairman's Statement xii

ACES President's Statement xiii

ACES 99 Short Courses xiv

Agenda xv

PLENARY SESSION I

"Computational Electromagnetics in Spacecraft Design", Reinaldo Perez 2

SESSION 1: FDTD Chair: Atef Elsherbeni

"A Finite-Difference Time-Domain Algorithm Based on the Recursive Convolution Approach for Propagation of Electromagnetic Waves in Nonlinear Dispersive Media"
S.J. Yakura, J.T. MacGillivray and D. Dietz 4

"Method for Including Lumped Elements in FDTD Simulations"
I.Rumsey, J. Mix and M. Piket-May 12

"A Novel Subgridding Scheme for Refractive Index Adaptive FDTD"
T.O. Korner and W. Fichtner 16

"Characterizing Meander Line Antennas for RF and Wireless Communications Using the FDTD Technique"
C-Wen P. Huang, J-B. J. Chen, A.Z. Elsherbeni and C.E. Smith 24

"Impulse Response of Microwave Devices by FDTD and Moment Expansion"
G. Marrocco and F. Bardati 32

"The Cause of Oscillatory Dispersion Relation of Equivalent Circuit Parameters for Microstrip Components Using FDTD Method", L. Liou 38

"An Implicit Characteristic Based Finite Difference Method for Computational Electromagnetics", J.H. Beggs and W.R. Briley 45

SESSION 2: ANTENNAS Chair: Nathan Ida Co-Chair: Jacob Kim

"End Fed Antennas", R.P Haviland 54

"Investigation of a Multi-Resonant Antenna for Wideband Application"
P.L. Werner, N.V. Veremey, R. Mittra and D.H. Werner 69

"Computation of Clustered Phased Array EM Fields Using Particle Accelerator Codes"
R.A. Speciale 72

"Extended Ray-Optical Technique for Installed Performance of Large Airborne Antenna Systems"
J.J. Kim, K. Wu, S.W. Theis, and O.B. Kesler 86

"Antenna Imaging and Visualization"
J. Shaeffer and B. Cooper 93

"Are Fractals Naturally Frequency Invariant/Independent?"
N. Cohen 101

"The Ultimate Antenna Training Aid", A. Nott 107

SESSION 3: INTERACTIVE POSTER SESSION

"Extension of the Method of Lines for Planar 3D Structures", Y.O. Shlepnev 116

"Noise Issues in Submicron Design", R. Perez 122

"Numerical Calculations for the Back Scattering and Extinction Cross Sections of Plane Waves Incident Obliquely on an Eccentric Multilayered Cylinder"
H.A. Yousif and A.Z. Elsherbeni 130

"Using the Partial Element Equivalent Circuit (PEEC) Simulation Technique for EMC Applications", B. Archambeault 137

"Analytic Validation of a Low-Frequency Magnetic Induction Code with Nonuniform Sources", T.W. Dawson 143

"A Study of Finite Element and Cylindrical Perfectly Matched Layer Approach"
Y. Xiao and Y. Lu 150

"Conditioning of Biorthogonal Wavelet Transforms and Iterative Solvers for Electromagnetic Integral Equations", W.L. Golik 156

"Exact Implementation of Bayliss-Turkel Boundary Operators in 2D and 3D Scalar and Vector Wave Equation", O.M. Ramahi 163

"Formulae for Instantaneous Power and Time-Average Power Delivered to Charge-Current Distributions", R.M. Bevensee 171

SESSION 3: INTERACTIVE POSTER SESSION(cont)

"CEM for RCS Measurement Calibration: Some Parametric Observations"
K.C. Hill and W.D. Wood, Jr. 178

"Analytical Bistatic k Space Images Compared to Experimental Swept Frequency
ISAR Images", J. Shaeffer, B. Cooper and K. Hom 184

"A Hybrid Periodic Moment Method Formulation for Scattering from Large
2D Wire Arrays", P.J. Collins and J.P. Skinner 191

"Accuracy and Conditioning of the Method of Moments for the 2D Efie"
K.F. Warnick and W.C. Chew 198

"hp-Adaptive FE Modeling for Maxwell's Equations -- Evidence of Exponential
Convergence", W. Rachowicz, L. Demkowicz and L. Vardapetyan 205

PLENARY SESSION II

"Multimedia-and Computer-Based Engineering Education", Magdy Iskander 212

SESSION 4: FINITE ELEMENTS I Chair: Leo Kempel Co-Chair: Jianming Jin

"Electromagnetic Modeling of Microstrip Structures in Multilayer Media"
F. Ling, J-M. Jin, D-G. Fang and N. Feng 218

"Modeling Wideband Conformal Antennas Using Finite Element-Boundary Integral
Techniques", K.D. Trott and R.D. Guidry 226

"The Northrop-Grumman Duct RCS Prediction Code"
Y-C. Ma, S. Bindiganavale and M. Sancer 232

"Implementation of Various Hybrid Finite Element-Boundary Integral Methods:
Bricks, Prisms, and Tets", L.C. Kempel 242

"Fast Hybrid Finite Element Methods and their Applications for Conformal Antennas"
J.L.Volakis, L.S. Andersen, T.F. Eibert, K. Sertel, and Z. Li 250

"A Hybrid MoM/FEM Method for Scattering from a Complex BOR with Appendages"
A.D. Greenwood and J-M. Jin 258

"Frequency-Domain Complementary Operators for Finite Elements Simulations"
O.M. Ramahi 266

SESSION 5: MODEL-BASED PARAMETER ESTIMATION
Chair: Andreas Cangellaris Co-Chair: Edmund Miller

"Model-Based Frequency Extrapolation of Antenna Radiation Characteristics on Complex Platforms", T. Su, Y. Wang and H. Ling 272

"Developing Adaptive Models and Estimating the Uncertainty of Presampled Spectral Data" E.K. Miller 278

"Techniques for Model-Based Parameter Estimation of Antenna Radiation Patterns" R.J. Allard and D.H. Werner 286

"Full Wave Analysis of Generalized Microstrip Lines Using Model Order Reduction Techniques" K. Radhakrishnan and W.C. Chew 294

"Frequency and Angular Extrapolations in Hybrid Finite Element-Boundary Integral Systems" Y.E. Erdemli, A.D. Brown, and J.L. Volakis 302

"Reduced-Order Modeling of Three-Dimensional Electromagnetic Wave Fields" R.F. Remis and P.M. van den Berg 308

"Rapid Simulation of Electromagnetic Resonant Structures Using Model Order Reduction and Unstructured Finite Difference" L. Zhao and A.C. Cangellaris 316

SESSION 6: OPTIMIZATION Chair: John Volakis Co-Chair: Zachi Baharav

"Recent Results in Electromagnetic Optimization of Microwave Components Including Microstrip T-Junctions" J.W. Bandler, M.H. Bakr, N. Georgieva, M.A. Ismail, and D.G. Swanson, Jr. 326

"Extraction of Equivalent Circuits of Microwave Devices Using the Genetic Algorithm" P.L. Werner, R. Mittra and D.H. Werner 334

"A Comparison of Various Optimization Strategies for Yagi-Uda Antenna Design" E.A. Jones and W.T. Joines 342

"Broad-Banding Uniformly Excited Antenna Arrays Using a Genetic Algorithm" B.J. Barbisch and D.H. Werner 348

"Optimizing Genetic Algorithm Parameters for Adaptive Nulling" Y.C. Chung and R.L. Haupt 359

"Mutual Coupling Compensation for Circular Arrays Using a Genetic Algorithm" B-K. Yeo and Y. Lu 365

"Pareto Genetic Algorithm Based Optimization of Log-Periodic Monopole Arrays Mounted on Realistic Platforms" D.S. Weile, S.E. Fisher, E. Michielssen, and W. Woody 371

SESSION 6: OPTIMIZATION (cont)

"Optimum Design of Non-Uniform Luneburg Lens Antennas: Genetic Algorithms with Adaptive Cost Function", H. Mosallaei and Y. Rahmat-Samii 379

"On the Search for the Optimal Grouping of Basis Functions", Z. Baharav 387

"Genetic Algorithms and Their Practical Implementation Strategies for Design Optimization of Electrical Devices", O.A. Mohammed 394

SESSION 7: WIRE MODELS Chair: Keith Lysiak Co-Chair: Chris Trueman

"Extension of a Thin-Wire Algorithm for Wires Moved Laterally Within a Mesh" G.J. Burke and D.J. Steich 404

"A Practical Method for Increasing the Speed and Stability of the Matrix Solve in Moment Method Simulations Within a Frequency Band", H. MacMillan and J.M. Dunn 412

"Modeling the Bifilar Helix Antenna Using NEC 4.1", S.R. Best 420

"MMSNEC - Multiple Matrix Solver NEC", J.v. Hagen, R. Mittra and D. Werner 428

"Comparison and Results for Models of a Thick Bent-Wire Dipole Using NEC4 and WIPL" J. Stamm, M-W. Fenton, and J.K. Breakall 436

"MF Broadcast Antennas and Antenna Arrays: A Historic Branch of Antenna Engineering Revisited by Computer Simulationn and Measurement", J.S. Belrose 442

"The High Frequency Electromagnetic Environment of the U.S. Coast Guard 87-foot Coastal Patrol Boat", M.E. McKaughan, D. Melton, and K. Seals 449

"Extending a MoM/PO/UTD Hybrid Method by an Automatic Selection of the Computational Methods Based on Neural Networks" U. Jakobus, A. Buchau, and F.M. Landstorfer 455

"Umbrella Top Loaded Antennas: Base Fed, Folded, and with a Tuned Insulated Counterpoise", J.S. Belrose 463

PLENARY SESSION III

"Observations From the Computational Electromagnetics Revolution: A Personal Perspective" E.K. Miller 470

SESSION 8: CONFORMAL ANTENNAS Chair: Doug Werner Co-Chair: Ping Werner

"Mutual Coupling Between Microstrip Antennas on a Cylindrical Surface" K-L. Wong 472

"Simulating the Dielectric-Loaded Quadrifilar Helix Antenna Using a Brute-Force TLM Approach", O.P. Leisten, J.C. Vardaxoglou, and E. Agboraw 479

SESSION 8: CONFORMAL ANTENNAS (cont)

"Conformal Aperture Coupled Microstrip Patch Antennas on Cylindrical Surfaces for Radar and SDMA Applications", D. Loffler and W. Wiesbeck 484

"Absorbing Boundary Conditions for Convex Object-Conformable Boundaries" O.M. Ramahi 490

"Cylindrical and Conical FSS" J.C. Vardaxoglou, G. Loukos, M. Jayawardene, R. Seager, and J. Eade 496

"A MATLAB Code for Multi-Layered FSS-S with Generally Shaped Elements" A. Stjernman 500

"A Reciprocity Approach for Calculating Radiation Patterns of Arbitrarily Shaped Patch Antennas Mounted on Circularly-Cylindrical Platforms" D.H. Werner, G.D. Mouyis, R. Mittra, and J.S. Zmyslo 508

SESSION 9: FINITE ELEMENTS II Chair: David B. Davidson

"Hierarchal 2D and 3D Vector Finite Elements for Electromagnetic Wave Eigenvalue Problems", D.B. Davidson and R.H. Hansmann 518

"Local Error Estimation for High-Frequency Problems Using Hierarchical Tangential Vector Finite Elements", S. Savage 524

"Time-Domain Simulationof Nonlinear Transmission Lines: Interface of Finite Elements to Circuit Analysis", K.N. Wassef and A.F. Peterson 530

SESSION 10: ERRORS Chair: Edmund K. Miller

"A Comparison of Solution Accuracy Resulting from Factoring and Inverting Ill-Conditioned Matrices", E.K. Miller 542

"Benchmarks for Integral Equation Solutions of Wideband Scattering: The Spherical Cap Reflector" S.M. Booker, P.D. Smith, E.D. Vinogradova, and S.S. Vinogradov 547

"Propagation of Errors through Computer Codes Via Fuzzy Logic", R.M. Bevensee 555

"Scalable Algorithm for Solving Boundary Value Problems Arising in Electromagnetics Based on Implicit Operator Projection" M. Rewienski and M. Mrozowski 563

SESSION 11: TIME DOMAIN METHODS Chair: J. Dunn Co-Chair: Chris Holloway

"Large Scale FD-TD--A Billion Cells", U. Andersson and G. Ledfelt 572

"New High Order Time-Stepping Schemes for Finite Differences"
M. Aidam and P. Russer 578

"The Mismatch of Perfectly Matched Layers (PML) in Cylindrical and Spherical
Coordinate System", L. Zhao and A.C. Cangellaris 586

"The Effect of the Binding Material Permittivity on the Input Impedance of CTHAs"
K.M. ELSherbini, F.A. Pertl, R.P.M. Craven, and J.E. Smith 594

"Numerical Dispersion in Haar-Wavelet Based MRTD Scheme -- Comparison Between
Analytical and Numerical Results", M. Fujii and W.J.R. Hoefer 602

"Comparison Between Discontinuous Galerkin Method and a Finite Volume Time-Domain
Method in Solving Maxwell Equations, in Heteregeneous Media"
M. Remaki and L. Fezouli 608

"A Controllability Method for the Calculation of the time periodic Solutions of the
Vlasov-Maxwell System", M. Bostan 615

"Time-Domain Equivalent Edge Currents"
A. Altintas, S. Lindenmeier and P. Russer 622

"A Numerical Study on the Accuracy of TLM-SCN Formulations for the Solution of
Initial Value Problems", J. Rebel, M. Aidam, and P. Russer 628

SESSION 12: BIOELECTROMAGNETICS Chair: Cynthia Furse Co-Chair: Susan Hagness

"Computational Estimate of the Frequency Response of Metallic Implants in Biological Tissues Exposed to RF Fields", A.H.J. Fleming, V. Anderson, and J. Rowley 638

"Towards Computational Methods for Studying Cellular Effects Due to EM Fields" A.H.J. Fleming 644

"Comparison of Computer Simulated and Measured SAR Values in the Head of a Human Phantom Next to Mobile Phone", F.J.C. Meyer and U. Jakobus 652

"Validation of the FDTD Near Fields of a Portable Radio Handset and Simple Head" C.W. Trueman, S.J. Kubina, D. Cule, and W.R. Lauber 660

"FDTD for Bioelectromagnetics: Modeling MICS Implants in the Human Body" E. Villaseca 668

"Numerical Studies of an Ultrawideband Microwave Radar Technology for the Detection of Nonpalpable Breast Tumors", S.C. Hagness, A. Taflove, and J.E. Bridges 675

"Numerical Dosimetry for Human Occupational Exposure to Realistic 60-Hz Magnetic Fields", T.W. Dawson, K. Caputa, and M.A. Stuchly 682

"Characterization of Near Electromagnetic Fields from Hand-held Radio Antennas" M.J. Packer 689

"Application of Multigrid Method for Quick Simulation of SAR and Temperature Distribution During Hyperthermia Treatment of Cervical Malignancies" M.P. Debicki, M. Mrozowski, and P. Debicki 697

AUTHOR INDEX 705

THE APPLIED COMPUTATIONAL ELECTROMAGNETICS SOCIETY

CALL FOR PAPERS

The 16th Annual Review of Progress in Applied Computational Electromagnetics

March 20-25, 2000

Naval Postgraduate School, Monterey, California

"Share Your Knowledge and Expertise with Your Colleagues"

The Annual ACES Symposium is an ideal opportunity to participate in a large gathering of EM analysis enthusiasts. The purpose of the Symposium is to bring analysts together to share information and experience about the practical application of EM analysis using computational methods. The symposium offerings include technical presentations, demonstrations, vendor booths and short courses. All aspects of electromagnetic computational analysis are represented. Contact for details:

Technical Program Chairman
Doug H. Werner
EE Dept, Room 211, EEE
Penn State University
University Park, PA 16802
Phone: (814) 863-2946
Fax: (814) 863-8783
Email:dhw@psu.edu

Symposium Co-Chairman
Randy Haupt
EE Dept., 260
University Of Nevada
Reno, NV 89557-0153
Phone: (702) 784-6927
Fax: (702) 784-6627
Email:haupt@ee.unr.edu

Symposium Co-Chairman
PingJuan Werner
EE Dept.
Penn State Dubois Campus
Dubois, PA 15801
Phone: (814) 867-1452
Fax: (814) 863-8457
Email:plw@psu.edu

Vendor Chair
Leo C. Kempel
Michigan State Univ.
ECE Engr.
2120 Engineering Bldg.
E. Lansing, MI 48824-1126
Phone: (517) 353 9944
Fax: (517) 353-1980
Email:l.kempel@ieee.org

Symposium Administrator
Richard W. Adler
ECE Dept, Code EC/AB
Naval Postgraduate school
833 Dyer Road, Room 437
Monterey, CA 93943-5121
Phone: (831)646-1111
Fax: (831)649-0300
Email:rwa@ibm.net

The ACES Symposium is a highly influential outlet for promoting awareness of recent technical contributions to the advancement of computational electromagnetics. Attendance and professional program paper participation from non-ACES members and from outside North America are encouraged and welcome.

Early Registration Fees; (approximate*)	**ACES MEMBERS**	**$290**
	NON-MEMBER	**$340**
	STUDENT/RETIRED/UMEMPLOYED	**$130 (no proceedings)**
	STUDENT/RETIRED/UNEMPLOYED	**$165 (includes proceedings)**

*The exact fee will be announced later. Each conference registration is entitled to publish two papers in the proceedings free of charge. Excess pages over a paper limit of 8 will be charged $15/page.

2000 ACES Symposium
Sponsored by: ACES, NPS, U of NV, BYU, PSU
in cooperation with: The IEEE Antennas and Propagation Society, the IEEE Electromagnetic Compatibility Society and USNC/URSI

Visit ACES on line at: www.emclab.umr.edu/aces and http://aces.ee.olemiss.edu

THE APPLIED COMPUTATIONAL ELECTROMAGNETICS SOCIETY

CALL FOR PAPERS

The 16th Annual Review of Progress in Applied Computational Electromagnetics

March 20-25, 2000

Papers may address general issues in applied computational electromagnetics, or may focus on specific applications, techniques, codes, or computational issues of potential interest to the Applied Computational Electromagnetics Society membership. Area and topics include:

- Code validation
- Code performance analysis
- Computational studies of basic physics
- Examples of practical code application
- New codes, algorithms, code enhancements, and code fixes
- Computer Hardware Issues
- Partial list of applications:

antennas	wave propagation
radar imaging	radar cross section
shielding	bioelectromagnetics
EMP, EMI/EMC	visualization
dielectric & magnetic materials	inverse scattering
microwave components	MIMIC technology
fiberoptics	remote sensing & geophysics
communications systems	propagation through plasmas
eddy currents	non-destructive evaluation

- Partial list of techniques:

frequency-domain & time-domain techniques	
integral equation & differential equation techniques	
finite difference & finite element analysis	
diffraction theories	physical optics
modal expansions	perturbation methods
hybrid methods	moment methods

INSTRUCTIONS FOR AUTHORS AND TIMETABLE

November 20, 1999: Submission deadline. Submit four copies of a full-length, camera-ready paper to the Technical Program Chairman. Please supply the following data for the corresponding author: name, address, email address, FAX, and phone numbers. See below for instructions for the format of paper.

December 21, 1999: Authors notified of acceptance.

PAPER FORMATTING REQUIREMENTS

The recommended paper length is 6 pages, with 8 pages as a maximum, including figures. The paper should be camera-ready (good resolution, clearly readable when reduced to the final print of 6 x 9 inch paper). The paper should be printed on 8-1/2 x 11 inch papers with 13/16 side margins, 1-1/16 inch top margin, and 1 inch on the bottom. On the first page, place title 1-1/2 inches from top with author and affiliation beneath the title. Single spaced type using 10 or 12 point front size, entire text should be justified (flush left and flush right). No typed page numbers, but number your pages lightly in pencil on the back of each page.

SHORT COURSES/HANDS-ON-WORKSHOP

Short courses and Hands-on-Workshops will be offered in conjunction with the Symposium covering numerical techniques, computational methods, surveys of EM analysis and code usage instruction. It is anticipated that short courses will be conducted principally on Monday and Friday. Workshops will be held Monday, Friday, and Saturday. **Short Course Fees: Half-day course** $100; **Full-day course** $160. **Workshop Fees: Half-day workshop** $120; **Full-day workshop** $235. ***Fees are subject to change. Quoted fees apply only if booked before 1 March 2000.***

EXHIBITS

Vendor booths and demonstrations will feature commercial products, computer hardware and software demonstrations, and small company capabilities.

1999 Symposium Program Committee

for the

15th Annual Review of Progress
in
Applied Computational Electromagnetics

at the
Naval Postgraduate School
Monterey, CA

Technical Program Chairman
Randy Haupt
EE Dept, 260
University of Nevada
Reno, NV 89557-0153
Phone: (702) 784-6927
FAX: (702) 784-6627
Email: haupt@ee.unr.edu

Co-Chair
Indira Chatterjee
EE Dept., 260
University of Nevada
Reno, NV 89557-0153
Phone: (702) 784-1346
FAX: (702) 784-6627
Email:indira.ee.unr.edu

Co-Chair
James Henson
EE Dept, 260
University of Nevada
Reno, NV 89557-0153
Phone: (702) 784-6929
FAX: (702) 784-6627
Email:jmh@proton.ee.unr.edu

Short Course Chairman
Michael A. Jensen
ECE Dept. 349 CB
Brigham Young University
Provo, UT 84602
Phone: (801) 378-5736
FAX: (801) 378-6586
Email: jensen@ee.byu.edu

Vendor Chairman
Keith W. Whites
EE Dept. 453 Anderson Hall
University of Kentucky
Lexington, KY 40506-0046
Phone: (606) 257-1768
FAX: (606) 257-3092
Email: whites@engr.uky.edu

Symposium Administrator
Richard W. Adler
ECE Dept/Code EC/AB
Naval Postgraduate School
Monterey, CA 93943-5121
Phone: (831) 646-1111
FAX: (831) 649-0300
Email:rwa@ibm.net

Conference Secretary:
Mrs. Pat Adler
Email: pba@ibm.net

Advisory Committee:
Richard W. Adler, Naval Postgraduate School
Bruce Archambeault, IBM
Robert Bevensee, Boma Enterprises
John Brauer, Ansoft Corp.
Anthony Brown,
Andreas Cangellaris, University of Illinois
Adalbert Konrad, University of Toronto
Eric Michielssen, University of Illinois
Ray Perez, Jet Propulsion Lab.
Andrew Peterson, Georgia Institute of Technology
Norio Takahashi, Okayama University
W. Perry Wheless, Jr., University of Alabama

PREFACE

On behalf of the ACES Technical Program Committee, I welcome you to "The 15th Annual Review of Progress in Applied Computational Electromagnetics." The Symposium has been extended to six days this year beginning Monday, March 15 through Saturday, March 20, 1999, and takes place at the Naval Postgraduate School (NPS) in Monterey, California. The Symposium is sponsored by the Applied Computational Electromagnetics Society, NPS, and the University of Nevada Reno.

Monday, March 15, Friday, March 19, and Saturday, March 20 are devoted to short courses and workshops. Technical sessions take place Tuesday, March 16 through Thursday, March 18, with an Interactive Session and Vendor Exhibits scheduled for Tuesday afternoon. This year's Symposium features twelve technical sessions and three plenary speakers. Several students are also participating in the Student Paper Contest.

Many volunteers cooperated to make this symposium possible. Symposium Co-Chairs, Professor Indira Chatterjee and Professor James Henson helped review papers and organize sessions. Professor Michael Jensen organized short courses and Professor Keith Whites organized vendor exhibits. I am indebted to these professors for their efforts. Professor Richard Adler and his wife Pat spend many days making all the arrangements, getting the proceedings published, organizing registration, and training me. I'd like to thank Dr. Bob Bevensee, the ACES Conference Committee Chairman, for his support, and to Professor Atef Elsherbeni for collecting the abstracts for posting on the web site. Earlene Absher, Janel Fontana, and Erwin Coleman provided significant support here at the University of Nevada. Finally, a big thanks to the session organizers for putting together some excellent sessions and our plenary speakers.

Enjoy the 15th Annual Review and your stay in Monterey.

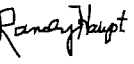

Randy Haupt
Technical Program Chair
1999 ACES Conference

ACES PRESIDENT'S STATEMENT

The ACES Annual Review of Progress in Applied Computational Electromagnetics has a tradition of excellence that guarantees a pleasant and educational experience. On the other hand, there is no guarantee that California will remain attached to the rest of the continent. So long as it does, however, good ACESians everywhere can look forward to a Monterey pilgrimage during the third week of March. The Naval Postgraduate School has been a gracious host and afforded this special and important event, and we again thank Dick and Pat Adler for their many hours devoted to local arrangements.

Randy Haupt and his capable conference team have put together an excellent technical program. You should know that ACES has intentionally reduced the number of accepted papers, both last year and continuing again this year, so that the annoyance of multiple parallel sessions might be substantially alleviated. Many registrants still remember, with some fondness, the earlier years with "1" parallel session. The opportunity for all to gather and hear the technical program in a single auditorium was a distinctive feature of the ACES conference for several years. Parallel sessions unavoidably fragment the audience and disrupt the personal encounters and exchanges that were hallmarks of our early conferences. As a practical matter, we probably cannot go back to the "single-session" format, but ACES is committed to holding the line at a maximum of three parallel sessions in the future, and we further aspire to generally achieve a format with only two parallel sessions. This is slightly short of ideal, but a good compromise and a heckuva lot better than you find at most conferences elsewhere.

Anyway, we recognize that conferences are more than just paper sessions, short courses, and award banquets, and ACES is actively striving to enhance your opportunities to spend some quality time with colleagues and friends, both old and new. If you see a way that we can further improve the conference, please do let us hear from you!

In addition to enjoying the ACES Annual Review, I hope you will similarly enjoy the availability of ACES Publications the next time you are ready to publish! The ACES Journal and ACES Newsletter are influential information outlets for the CEM community worldwide, and you are invited to make them your publishing vehicle of choice in the future.

Best wishes for a full and gratifying 15th Annual Review!

Perry Wheless
ACES President

ACES 1999 SHORT COURSES/WORKSHOPS

MONDAY 15 MARCH 1999

0830-1630 SHORT COURSE #1 (FULL-DAY)
"Model-Order Reduction as a Means of Increasing the Efficiency of Computational Electromagnetics"
Andreas Cangellaris, University of Illinois at Urbana-Champaign, Edmund K. Miller, Santa Fe, NM.

0830-1630 SHORT COURSE #2 (FULL-DAY)
"Finite-Difference Time Domain Method", Omar Ramahi, Compaq Computer Corp., Maynard, MA.

0830-1630 SHORT COURSE #3 (FULL-DAY)
"Finite Elements for Electromagnetics", Scott Savage, Ansoft Corporation, Pittsburgh, PA.

PLEASE NOTE THAT A 10% DISCOUNT IS IN EFFECT FOR ALL WORKSHOPS TAKEN AFTER ATTENDING AN INITIAL WORKSHOP. THIS APPLIES TO THE GROUP OF WORKSHOPS FOR MATLAB AND MATHCAD. IT ALSO APPLIES TO THE NEC WORKSHOPS. NOTE THAT MATLAB/MATCAD DISCOUNTS DO NOT APPLY TO THE NEC WORKSHOPS, AND VICE VERSA.

0830-1130 HANDS-ON-WORKSHOP #4 (HALF-DAY)
"Basic MATHCAD" (Introduction for Workshop #9)
Jovan Lebaric and Robert Vitale, Naval Postgraduate School, Monterey, CA.

1330-1630 HANDS-ON-WORKSHOP #5 (HALF-DAY)
"Basic MATLAB" (Introduction for Workshop #11)
Jovan Lebaric and Robert Vitale, Naval Postgraduate School, Monterey, CA.

FRIDAY 19 MARCH 1999

0830-1130 SHORT COURSE #6 (HALF-DAY)
"Verification and Validation of Computational Electromagnetics Software"
Edmund K. Miller, Santa Fe, NM

1330-1630 SHORT COURSE #7 (HALF-DAY)
"A Survey and Comparison of Computational Electromagnetics Options"
Edmund K. Miller, Santa Fe, NM

0830-1630 SHORT COURSE #8 (FULL-DAY)
"Genetic Algorithm Optimization"
Randy L. Haupt, and J. Michael Johnson, University of Nevada, Reno, NV

0830-1630 HANDS-ON-WORKSHOP #9 (FULL-DAY)
"Method of Moments (MoM) Using MATHCAD"
Jovan Lebaric and Robert Vitale, Naval Postgraduate School, Monterey, CA.

0830-1630 HANDS-ON-WORKSHOP #10 (FULL-DAY)
"Introduction to Using NEC under Windows"
J.K. Breakall, Penn State University, G.J. Burke, LLNL, R.W. Adler, Naval Postgraduate School, Monterey, CA.

SATURDAY 20 MARCH 1999

0830-1630 HANDS-ON-WORKSHOP #11 (FULL-DAY)
"Finite Difference (FD) Using MATLAB"
Jovan Lebaric and Robert Vitale, Naval Postgraduate School, Monterey, CA

0830-1630 HANDS-ON-WORKSHOP #12 (FULL-DAY)
"Advanced Applications using NEC4.1 under Windows"
J.K. Breakall, Penn State University, G.J. Burke, LLNL, R.W. Adler, Naval Postgraduate School, Monterey, CA.

AGENDA

The Fifteenth Annual Review of Progress in Applied Computational Electromagnetics

NAVAL POSTGRADUATE SCHOOL
15-20 March 1999

Randy Haupt, Technical Program Chairman

Indira Chatterjee, Symposium Co-Chairman

James Henson, Symposium Co-Chairman

Michael Jensen, Short Course Chairman

Keith Whites, Vendor Chairman

Richard W. Adler, Symposium Administrator

MONDAY MORNING 15 MARCH 1999

0700-0730	**CONTINENTAL BREAKFAST** *(For short course and hands-on-workshop attendees only)*	**Glasgow Courtyard**
0730-0820	**SHORT COURSE/HANDS-ON-WORKSHOP REGISTRATION**	**Glasgow 103**
0830-1630	**SHORT COURSE #1 (FULL-DAY)** "Model-Order Reduction as a Means of Increasing the Efficiency and Effectiveness of Computational Electromagnetics" Andreas Cangellaris, University of Illinois at Urbana-Champaign, and Edmund Miller, Santa Fe, NM.	
0830-1630	**SHORT COURSE #2 (FULL-DAY)** "Finite-Difference Time-Domain Method" Omar Ramahi, Compaq Computer Corporation, Maynard, MA	
0830-1630	**SHORT COURSE #3 (FULL-DAY)** "Finite Elements for Electromagnetics", Scott Savage, Ansoft Corporation, Pittsburgh, PA.	
0830-1130	**HANDS-ON-WORKSHOP #4 (HALF-DAY)** "Basic MATHCAD" (Introduction for Course 9) Jovan Lebaric and Robert Vitale, Naval Postgraduate School, Monterey, CA.	
0900-1200	**CONFERENCE REGISTRATION**	**Glasgow 103**
1130-1315	**BOD BUSINESS LUNCHEON**	**Del Monte Room**

MONDAY AFTERNOON

1330-1630	**HANDS-ON-WORKSHOP #5 (HALF-DAY)** "Basic MATLAB" (Introduction for Course #11) Jovan Lebaric and Robert Vitale, Naval Postgraduate School, Monterey, CA.	
1400-2000	**CONFERENCE REGISTRATION**	**Glasgow 103**

MONDAY EVENING

1900	**PUBLICATIONS DINNER**	

TUESDAY MORNING 16 MARCH 1999

0700-0745	**CONTINENTAL BREAKFAST**		**Glasgow Courtyard**
0745	**ACES BUSINESS MEETING**	**President Perry Wheless**	**Glasgow 102**
0800	**WELCOME**	**Randy Haupt**	**Glasgow 102**
0815	**PLENARY SPEAKER:** "Computational Electromagnetics in Spacecraft Design"	**Reinaldo Perez**, JPL	**Glasgow 102**

SESSION 1: **FDTD (Parallel with Session 2)**
Chair: Atef Elsherbeni

0920	"A Finite-Difference Time-Domain Algorithm Based on the Recursive Convolution Approach for Propagation of Electomagnetic Waves in Nonlinear Dispersive Media"	S.J. Yakura, J.T. MacGillivray, D. Dietz
0940	"Methods for Including Lumped Elements in FDTD Simulations"	Ian Rumsey, Jason Mix, Melinda Piket-May
1000	"A Novel Subgridding Scheme for Refractive Index Adaptive FDTD"	T.O. Korner, W. Fichtner
1020	**BREAK**	
1040	"Characterizing Meander Line Antennas for RF and Wireless Communications Using the FDTD Techniques"	Chun-Wen Paul Huang Jiang-Bin James Chen Atef Z. Elsherbeni Charles E. Smith
1100	"Impulse Response of Microwave Devices by FDTD and Moment Expansion"	Gaetano Marrocco Fernando Bardati
1120	"The Cause of Oscillatory Dispersion Relation of Equivalent Circuit Parameters for Microstrip Component Using FDTD Method"	Lee L. Liou
1140	"An Implicit Characteristic Based Finite Difference Method for Computational Electromagnetics"	John H. Beggs W. Roger Briley
1200-1300	**PUBLICATION COMMITTEE BUSINESS & LUNCHEON**	**Del Monte Room**
1200	**LUNCH**	

SESSION 2: **ANTENNAS (Parallel with Session 1)**
Chair: Nathan Cohen Co-Chair: Jacob Kim

0920	"End Fed Antennas"	R.P. Haviland
0940	"Investigation of a Multi-Resonant Antenna for Wideband Application"	P.L. Werner, N.V. Veremey, R. Mittra and D.H. Werner
1000	"Computation of Clustered Phased Array EM Fields Using Particle Accelerator Codes"	Ross A. Speciale
1020	**BREAK**	

TUESDAY MORNING 16 MARCH 1999

SESSION 2: ANTENNAS (cont)

1040	"Extended Ray-Optical Technique for Installed Performance of Large Airborne Antenna Systems"	Jacob J. Kim, Kuang Wu, Sidney W. Theis Oren B. Kesler
1100	"Antenna Imaging and Visualization"	John Shaeffer Brett Cooper
1120	"Are Fractals Naturally Frequency Invariant/Independent?"	Nathan Cohen
1140	"The Ultimate Antenna Training Aid"	Alan Nott
1200	**LUNCH**	

TUESDAY AFTERNOON

INTERACTIVE POSTER SESSION 1300-1530	**Ballroom, Herrmann Hall**
VENDOR EXHIBITS 1300-2000	**Ballroom, Herrmann Hall**
WINE AND CHEESE BUFFET 1500-1700	**Ballroom, Herrmann Hall**

SESSION 3 INTERACTIVE POSTER SESSION **Ballroom, Herrmann Hall**
1300-1530

"Extension of the Method of Lines for Planar 3D Structures"	Yuri Slepnev
"Noise Issues in Submicron Design"	Reinaldo Perez
"Numerical Calculations for the Back Scattering and Extinction Cross Sections of Plane Waves Incident Obliquely on an Eccentric Multi-layered Cylinder"	Hashim Yousif Atef Z. Elsherbeni
"Using the Partial Element Equivalent Circuit (PEEC) Simulation Technique for EMC Applications"	Bruce Archambeault
"Analytic Validation of a Low-Frequency Magnetic Induction Code with Nonuniform Sources"	Trevor W. Dawson
"A Study of Finite Element and Cylindrical Perfectly Matched Layer Approach"	Ying Xiao and Yilong Lu
"Conditioning of Bi-orthogonal Wavelet Transforms and Iterative Solvers for Electromagnetic Integral Equations"	Wojciech L. Golik
"Exact Implementation of Bayliss-Turkel Boundary Operators in 2D and 3D Scalar and Vector Wave Equations"	Omar M. Ramahi
"Formulae for Instantaneous Power and Time-Average Power Delivered to Charge-Current Distributions"	R.M. Bevensee
"CEM for RCS Measurement Calibration: Some Parametric Observations"	Kueichien C. Hill
"Analytical Bistatic K Space Images Compared to Experimental Swept Frequency ISAR Images"	John Shaeffer Kam Hom
"A Hybrid Periodic Moment Method Formulation for Scattering from Large 2-D Wire Arrays"	Peter J. Collins J. Paul Skinner
"Accuracy and Conditioning of the Method of Moments for the 2D EFIE"	Karl F. Warnick Weng Cho Chew
"hp-Adaptive FE Modeling for Maxwell's Equations- - Evidence of Exponential Convergence "	W. Rachowicz L. Demkowicz L. Vardapetyan

TUESDAY EVENING 16 MARCH 1999

1900	**BOD DINNER**	**Vitos Italian Restaurant**

WEDNESDAY MORNING 17 MARCH 99

0700-0800	**CONTINENTAL BREAKFAST**	**Glasgow Courtyard**
0815	**PLENARY SPEAKER:** **Magdy Iskander**, University of Utah "Multimedia – and Computer-Based Engineering Education"	
SESSION 4 :	**FINITE ELEMENTS I (Parallel with Session 5)** **Chair: Leo Kempel Co-Chair: Jianming Jin**	
0920	"Electromagnetic Modeling of Microstrip Structures in Multilayer Media"	Feng Ling Jianming Jin Da-Gang Fang Ningning Feng
0940	"Modeling Wideband Conformal Antennas Using Finite Element-Boundary Integral Techniques"	Keith D. Trott Rene D. Guidry
1000	"The Northrop-Grumman Duct RCS Prediction Code"	Yan-Chow Ma Sunil Bindiganavale Maurice Sancer
1020	**BREAK**	
1040	"Implementation of Various Hybrid Finite Element-Boundary Integral Methods: Bricks, Prisms, and Tets"	Leo C. Kempel
1100	"Fast Hybrid Finite Element Methods and Their Applications for Conformal Antennas"	John L. Volakis Lars S. Andersen Thomas F. Eibert Kubilay Sertel Zhifang Li
1120	"A Hybrid MoM/FEM Method for Scattering from a Complex BOR with Appendages"	Andrew Greenwood Jian-Ming Jin
1140	"Frequency-Domain Complementary Operators for Finite Elements Simulation"	Omar M. Ramahi
SESSION 5:	**MODEL-BASED PARAMETER ESTIMATION (Parallel with Session 4)** **Chair: Andreas Cangellaris Co-Chair: Edmund Miller**	
0920	"Model-Based Frequency Extrapolation of Antenna Radiation Characteristics on Complex Platforms"	Tao Su, Yuanxun Wang Hao Ling
0940	"Developing Adaptive Models and Estimating the Uncertainty of Presampled Spectral Data"	Edmund Miller
1000	"Techniques for Model-Based Parameter Estimation of Antenna Radiation Patterns"	R.J. Allard D.H. Werner
1020	**BREAK**	
1040	"Full Wave Analysis of Generalized Microstrip Lines Using Model Order Reduction Techniques"	Kaladhar Radhakrishnan Weng Cho Chew
1100	"Frequency and Angular Extrapolations in Hybrid Finite Element-Boundary Integral Systems"	Y.E. Erdemli A.D. Brown John L. Volakis
1120	"Reduced-Order Modeling of Three-Dimensional Electromagnetic Wave Fields"	R.F. Remis P.M. van den Berg
1140	"Rapid Simulation of Electromagnetic Resonant Structures Using Model Order Reduction and Unstructured Finite Difference"	Li Zhao Andreas Cangellaris
1200	**LUNCH**	

WEDNESDAY AFTERNOON 17 MARCH 1999

SESSION 6: OPTIMIZATION (Parallel with Session 7)
Chair: John Volakis Co-Chair: Zachi Baharav

1320	"Recent Results in Electromagnetic Optimization of Microwave Components Including Microstrip T-Junctions"	J.W. Bandler M.H. Bakr N. Georgieva M.A. Ismail D.G. Swanson, Jr.
1340	"Extraction of Equivalent Circuits of Microwave Devices Using The Genetic Algorithm"	P.L. Werner R. Mittra D.H. Werner
1400	"A Comparison of Various Optimization Strategies for Yagi-Uda Antenna Design"	Eric A. Jones William T. Joines
1420	"Broad-Banding Uniformly Excited Antenna Arrays Using a Genetic Algorithm"	Brian J. Barbisch D.H. Werner
1440	"Optimizing Genetic Algorithm Parameters for Adaptive Nulling"	You Chung Chung Randy Haupt
1500	**BREAK**	
1520	"Mutual Coupling Compensation for Circular Arrays Using a Genetic Algorithm"	Beng-Kiong Yeo Yilong Lu
1540	"Pareto Genetic Algorithm Based Optimization of Log-Periodic Monopole Arrays Mounted on Realistic Platforms"	D.S. Weile S.E. Fisher E. Michielssen W. Woody
1600	"Optimum Design of Non-Uniform Luneburg Lens Antennas: Genetic Algorithms with Adaptive Cost Function"	H. Mosallaei Y. Rahmat-Samii
1620	"On the Search for the Optimal Grouping of Basis Functions"	Zachi Baharav
1640	"Genetic Algorithms and their Practical Implementation Strategies for Design Optimization of Electrical Devices"	Osama A. Mohammed

SESSION 7: WIRE MODELS (Parallel with Session 6)
Chair: Keith Lysiak Co-Chair: Chris Trueman

1320	"Extension of a Thin-Wire Algorithm for Wires Moved Laterally within a Mesh"	Gerald J. Burke David J. Steich
1340	"A Practical Method for Increasing the Speed and Stability of the Matrix Solve in Moment Method Simulations within a Frequency Band"	Hugh MacMillan John M. Dunn
1400	"Modeling the Bifilar Helix Antenna Using NEC 4.1"	Steven R. Best
1420	"MMSNEC - Multiple Matrix Solver NEC"	J.V. Hagen R. Mittra D.H. Werner
1440	"Comparison and Results for Models of a Thick Bent-Wire Dipole Using NEC4 and WIPL"	James Stamm Mun-Won Fenton James K. Breakall
1500	**BREAK**	

WEDNESDAY AFTERNOON 17 MARCH 1999

SESSION 7: WIRE MODELS (cont)

1520	"MF Broadcast Antennas and Antenna Arrays: A Historic Branch of Antenna Engineering Revisited by Computer Simulation and Measurement"	John Belrose
1540	"The High Frequency Electromagnetic Environment of the U.S. Coast Guard 87-foot Coastal Patrol Boat"	Michael E. McKaughan David Melton, Kelly Seals
1600	"Extending a MoM/PO/UTD Hybrid Method by an Automatic Selection of the Computational Methods Based on Neural Networks"	U. Jakobus A. Buchau F.M. Landstorfer
1620	"Umbrella Top Loaded Antennas: Base Fed, Folded, and with a Tuned Insulated Counterpoise"	John Belrose

WEDNESDAY EVENING 17 MARCH 1999

1830	**NO HOST BAR**	**La Novia Terrace**
1930	**AWARDS BANQUET**	**La Novia Room**

THURSDAY MORNING 18 MARCH 1999

0710-0810	**CONTINENTAL BREAKFAST**	**Glasgow Courtyard**
0815	**PLENARY SPEAKER:** **Edmund K. Miller**, Santa Fe, NM "Observations from the Computational Electromagnetics Revolution: A Personal Perspective"	

SESSION 8: CONFORMAL ANTENNAS (Parallel with Session 9)
Chair: Doug Werner Co-Chair: Ping Werner

0920	"Mutual Coupling Between Microstrip Antennas on a Cylindrical Surface"	Kin-Lu Wong
0940	"Simulating the Dielectric-Loaded Quadrifilar Helix Antenna Using a Brute-Force TLM Approach"	O.P. Leisten J. C. Vardaxoglou E. Agboraw
1000	"Conformal Aperture Coupled Microstrip Patch Antennas on Cylindrical Surfaces for Radar and SDMA Applications"	D. Loffler and W. Wiesbeck
1020	**BREAK**	
1040	"Absorbing Boundary Conditions for Convex Object-Conformable Boundaries"	Omar M. Ramahi
1100	"Cylindrical and Conical FSS"	J.C. Vardaxoglou G. Loukos M. Jayawardene R. Seager and J. Eade
1120	"A MATLAB Code for Multi-Layered FSS:S with Generally Shaped Elements"	Anders Stjernman
1140	"A Riciprocity Approach for Calculating Radiation Patterns of Arbitrarily Shaped Patch Antennas Mounted on Circularly-Cylindrical Platforms"	Doug Werner, G.D. Mouyis R. Mittra and J.S. Zmyslo

SESSION 9: FINITE ELEMENTS II (Parallel with Session 8) Chair: David B. Davidson

0920	"Hierarchal 2d and 3d Vector Finite Elements for Electromagnetic Wave Eigenvalue Problems"	David B. Davidson Riana H. Hansmann
0940	"Local Error Estimation for High-Frequency Problems Using Hierarchical Tangential Vector Finite Elements"	Scott Savage John Manges
1000	"Time-Domain Simulation of Nonlinear Transmission Lines: Interface of Finite Elements to Circuit Analysis"	Karim N. Wassef Andrew F. Peterson

THURSDAY MORNING 18 MARCH 1999

1020 **BREAK**

SESSION 10: ERRORS (Parallel with Session 8) Chair: Edmund K. Miller

1040	"A Comparison of Solution Accuracy Resulting From Factoring and Inverting Ill-Conditioned Matrices"	Edmund K. Miller
1100	"Benchmarks for Integral Equation Solutions of Wideband Scattering: The Spherical Cap Reflector"	S.M. Booker P.D. Smith E.D. Vinogradova S.S. Vinogradov
1120	"Propagation of Errors through Computer Codes via Fuzzy Logic"	R.M. Bevensee
1140	"Scalable Algorithm for Solving Boundary Value Problems Arising in Electromagnetics Based on Implicit Operator Projection"	Michal Rewienski Michal Mrozowski

1200 **LUNCH**

SESSION 11: TIME DOMAIN METHODS (Parallel with Session 12)
Chair: John Dunn Co-Chair: Chris Holloway

1320	"Large Scale FD-TD--A Billion Cells"	Ulf Andersson Gunnar Ledfelt
1340	"New High Order Time-Stepping Schemes for Finite Differences"	Martin Aidam Peter Russer
1400	"The Mismatch of Perfectly Matched Layers (PML) in Cylindrical and Spherical Coordinate System"	Li Zhao Andreas Cangellaris
1420	"The Effect of the Binding Material Permittivity on the Input Impedance of CTHAs"	Khaled M. ELSherbini Franz A. Pertl Robert P.M. Craven James E. Smith
1440	"Numerical Dispersion in Haar-Wavelet Based MRTD Scheme--Comparison Between Analytical and Numerical Results"	Masafumi Fujii Wolfgang J.R. Hoefer

1500 **BREAK**

1520	"Comparison Between Discontinuous Galerkin Method and a Finite Volume Time-Domain Method in Solving Maxwell Equations, in Heteregeneous Media"	Malika Remaki L. Fezoui
1540	"A Controllability Method for the Calculation of the Time Periodic Solutions of the Vlasov-Maxwell System"	Mihai Bostan
1600	"Time-Domain Equivalent Edge Currents"	A. Altintas S. Lindenmeier Peter Russer
1620	"A Numerical Study on the Accuracy of TLM-SCN Formulations for the Solution of Initial Value Problems"	Jurgen N. Rebel Martin Aidam Peter Russer

THURSDAY AFTERNOON 18 MARCH 1999

SESSION 12: BIOELECTROMAGNETICS (Parallel with Session 11)
Chair: Cynthia Furse Co-Chair: Susan Hagness

1320	"Computational Estimate of the Frequency Response of Metallic Implants in Biological Tissues Exposed to RF Fields"	A.H.J. Fleming V. Anderson J. Rowley
1340	"Towards Computational Methods for Studying Cellular Effects Due to EM Fields"	A.H.J. Fleming
1400	"Comparison of Computer Simulated and Measured SAR Values in the Head of a Human Phantom Next to a Mobile Phone"	F.J.C Meyer U Jakobus
1420	"Validation of the FDTD Near Fields of a Portable Radio Handset and Simple Head"	C.W. Trueman S.J. Kubina D. Cule and W.R. Lauber
1440	"FDTD for Bioelectromagnetics: Modeling MICS Implants in the Human Body"	Eduardo H. Villaseca
1500	**BREAK**	
1520	"Numerical Studies of an Ultrawideband Microwave Radar Technology for the Detection of Nonpalpable Breast Tumors"	Susan C. Hagness Allen Taflove Jack E. Bridges
1540	"Numerical Dosimetry for Human Occupational Exposure to Realistic 60-Hz Magnetic Fields"	Trevor W. Dawson K. Caputa Maria A. Stuchly
1600	"Characterization of Near Electromagnetic Fields From Hand-Held Radio Antennas"	Malcolm Packer
1620	"Application of Multigrid Method for Quick Simulation of SAR and Temperature Distribution During Hyperthermia Treatment of Cervical Malignancies"	Michal P. Debicki Michal Mrozowski Piotr Debicki.

FRIDAY 19 MARCH 1999

0730-0830 **CONTINENTAL BREAKFAST**
(For short course and hands-on-workshop attendees only)

0830-1130 **SHORT COURSES #6 (HALF-DAY)**
"Verification and Validation of Computational Electromagnetics Software"
Edmund K. Miller, Santa Fe, NM

1330-1630 **SHORT COURSES #7 (HALF-DAY)**
"A Survey and Comparison of Computational Electromagnetics Options"
Edmund K. Miller, Santa Fe, NM

0830-1630 **SHORT COURSES #8 (FULL-DAY)**
"Genetic Algorithm Optimization"
Randy L. Haupt, and J. Michael Johnson, University of Nevada, Reno, NV

PLEASE NOTE THAT A 10% DISCOUNT IS IN EFFECT FOR ALL WORKSHOPS TAKEN AFTER ATTENDING AN INITIAL WORKSHOP. THIS APPLIES TO THE GROUP OF WORKSHOPS FOR MATLAB AND MATHCAD. IT ALSO APPLIES TO THE NEC WORKSHOPS. NOTE THAT MATLAB/MATCAD DISCOUNTS DO NOT APPLY TO THE NEC WORKSHOPS, AND VICE VERSA.

0830-1630 **HANDS-ON-WORKSHOP #9 (FULL-DAY)**
"Method of Moments (MoM) Using MATHCAD"
Jovan Lebaric and Robert Vitale, Naval Postgraduate School, Monterey, CA.

0830-1630 **HANDS-ON-WORKSHOP #10 (FULL-DAY)**
"Introduction to Using NEC under Windows"
J.K. Breakall, Penn State University, G.J. Burke, LLNL, and R.W. Adler, Naval Postgraduate School, Monterey, CA.

SATURDAY 20 MARCH 1999

0730-0830 **CONTINENTAL BREAKFAST**
(For short course and hands-on-workshop attendees only)

0830-1630 **HANDS-ON-WORKSHOP #11 (FULL-DAY**
"Finite Difference (FD) Using MATLAB"
Jovan Lebaric and Robert Vitale, Naval Postgraduate School, Monterey, CA

0830-1630 **HANDS-ON-WORKSHOP #12 (FULL-DAY**
"Advanced Applications using NEC4.1 under Windows"
J.K. Breakall, Penn State University, G.J. Burke, LLNL, and R.W. Adler, Naval Postgraduate School, Monterey, CA.

PLENARY SESSION 1

Reinaldo Perez

Computational Electromagnetics in Spacecraft Design

Reinaldo Perex
Jet Propulsion Laboratory
California Institute of Technology

The business of building satellites has been around for over 30 years. Over the last several years considerable improvements have been made in the design, development and manufacture of satellite subsystems in order to accommodate the increasing needs of wireless communications companies and the needs of purely scientific missions from NASA and other government agencies. We discuss in this work some of the advances done in spacecraft which are built for scientific missions; specifically small spacecraft designed for the exploration of outer planets and other celestial bodies. In this work we discuss the role played by computational electromagnetic in assisting in some of the design aspects.

SESSION 1

FDTD

Chair: Atef Elsherbeni

A Finite-Difference Time-Domain Algorithm Based on the Recursive Convolution Approach for Propagation of Electromagnetic Waves in Nonlinear Dispersive Media

S. J. Yakura, J. T. MacGillivray and D. Dietz
Air Force Research Laboratory, Directed Energy Directorate
Kirtland AFB, NM 87117-5776
Phone: (505) 846-0995; Fax: (505) 846-0566
E-mail: yakuras@plk.af.mil

Abstract

We present for the first time a successful formulation of a finite-difference time-domain algorithm that is based on the recursive convolution approach and is used to evaluate the propagation of electromagnetic waves in nonlinear dispersive media. We treat in particular the case where the nonlinear polarization term depends only on the product of the square of the electric field and the third-order electric susceptibility function. However, the approach is general and we can easily extend the formulation to the product of any power of the electric field with the nth-order electric field susceptibility function. We find that, in contrast to the usual formulation for linear dispersive materials which uses a simple linear relationship between the next-time-step electric field and the previous-time-step electric field, the formulation for nonlinear dispersive materials with a third-order susceptibility function results in an algebraic cubic equation which relates the next-time-step electric field to the previous-time-step electric field. Consequently, the algebraic cubic equation must be solved at each time step to advance the electric field.

I. INTRODUCTION

There has been considerable recent interest in understanding the transient behavior of an ultrafast laser pulse that interacts with a nonlinear dispersive material. In the last several years many experimentalists have made use of newly developed Kerr lens mode-locked titanium-sapphire lasers to perform well-controlled experiments to obtain accurate measurements of the transient behavior of ultrafast laser pulses in simple molecular liquids and solids which are known to exhibit nonlinear optical behavior [1]. To better understand the details of nonlinear processes that are observed in the experiments, numerical simulations have been used extensively to reproduce observed nonlinear effects. Until recently most computer simulation has been performed by solving an approximation to Maxwell's equations, known as the generalized nonlinear Schrödinger (GNLS) equation [2], to get information about the time evolution of the envelope of the propagating oscillating wave packet in order to obtain the overall shape of the propagating optical pulse. Because a GNLS equation-based computer simulation does not provide any information about the details of the oscillating waves inside the envelope of the optical pulse, there is a renewed interest in solving Maxwell's equations directly without having to rely on any approximations.

Happily, with the advent of present day computers which provide very fast execution times and great quantities of computer memory, we are at the point where we have enough computational power to solve Maxwell's equations directly for nonlinear dispersive materials. Among recently investigated numerical techniques that show great promise in achieving this goal is the well-known finite-difference time-domain (FDTD) method [3]. It is based on using a simple differencing scheme in both time and space to calculate the transient behavior of electromagnetic (EM) field quantities. Because of the usefulness of the FDTD method for many optical applications, recent researchers have focused their attention on the numerical evaluation of the linear and nonlinear polarization terms which appear in one of Maxwell's equations (Ampère's Law) as convolution integrals. An efficient evaluation of these terms allows us to model linear and nonlinear dispersive effects more effectively [4-9].

The designation of terms as linear and nonlinear depends upon the form of the integrand appearing in the convolution integral that relates the displacement field vector, $\underline{D}(t;\underline{x})$, to the electric field vector, $\underline{E}(t;\underline{x})$. For linear dispersive, isotropic materials, the relationship between $\underline{D}(t;\underline{x})$ and $\underline{E}(t;\underline{x})$ is usually expressed as

$$\underline{D}(t;\underline{x}) = \epsilon_o \epsilon_\infty \underline{E}(t;\underline{x}) + \epsilon_o \sum_{\rho=1}^{\rho_{max}} \int_{-\infty}^{\infty} \underline{E}(\tau;\underline{x}) X_\rho^{(1)}(t-\tau)\, d\tau , \tag{1.1}$$

where ϵ_o is the electric permittivity of free space, ϵ_∞ is the medium permittivity at infinite frequency, and $X_\rho^{(1)}(t-\tau)$ is the ρth term of the collection consisting of ρ_{max} time dependent, first-order electric susceptibility functions, where ρ_{max} is the maximum number of terms which we choose to consider for a particular formulation of Eq. (1.1). For isotropic materials that exhibit both linear and nonlinear polarization properties, specifically through the first-order

(linear) and third-order (nonlinear) electric susceptibility functions, $X_\rho^{(1)}(t-\tau)$ and $X_\rho^{(3)}(t,\tau,t_1,t_2)$, respectively, the relationship between $\underline{D}(t;\underline{x})$ and $\underline{E}(t;\underline{x})$ can be expressed as

$$\underline{D}(t;\underline{x}) = \epsilon_o\epsilon_\infty \underline{E}(t;\underline{x}) + \epsilon_o \sum_\rho \int_{-\infty}^{\infty} \underline{E}(\tau;\underline{x}) X_\rho^{(1)}(t-\tau)\, d\tau$$

$$+\epsilon_o \sum_\rho \int_{-\infty}^{\infty}\int_{-\infty}^{\infty}\int_{-\infty}^{\infty} \underline{E}(t_2;\underline{x})\left[\underline{E}(t_1;\underline{x})\bullet\underline{E}(\tau;\underline{x})\right] X_\rho^{(3)}(t,\tau,t_1,t_2)\, dt_2\, dt_1\, d\tau\,, \tag{1.2}$$

where $X_\rho^{(3)}(t,\tau,t_1,t_2)$ is the ρth term of the four-time dependent third-order susceptibility function which contributes to the nonlinear behavior of the material and $\bullet$ is the notation used for the dot product of vectors. When $X_\rho^{(3)}(t,\tau,t_1,t_2)$ is reduced to the single-time dependent susceptibility function, $\chi_\rho^{(3)}(t_1\text{-}t_2)$, by making use of the following Born-Oppenheimer approximation [10]:

$$X_\rho^{(3)}(t,\tau,t_1,t_2) = \delta(\tau-t_1)\,\delta(t-t_2)\left[\chi_\rho^{(3)}(t_2-t_1)+\delta(t_2-t)\,\alpha_{0\rho}^{(3)}\right], \tag{1.3}$$

where $\alpha_{o\rho}^{(3)}$ is a constant and $\delta(t)$ is the Dirac delta function, we can show that Eq. (1.2) reduces to an expression that consists of sums of convolution integrals of linear and nonlinear terms; namely,

$$\underline{D}(t;\underline{x}) = \epsilon_o\epsilon_\infty \underline{E}(t;\underline{x}) + \epsilon_o \sum_\rho \int_{-\infty}^{\infty} \underline{E}(\tau;\underline{x}) X_\rho^{(1)}(t-\tau)\, d\tau$$

$$+\epsilon_o\, \underline{E}(t;\underline{x}) \sum_\rho \int_{-\infty}^{\infty} \left[\underline{E}(\tau;\underline{x})\bullet\underline{E}(\tau;\underline{x})\right] \chi_\rho^{(3)}(t-\tau)\, d\tau + \epsilon_o\, \underline{E}(t;\underline{x})\left[\underline{E}(t;\underline{x})\bullet\underline{E}(t;\underline{x})\right] \sum_\rho \alpha_{o\rho}^{(3)}\,. \tag{1.4}$$

Based on the above expression, this paper provides a general formulation of the FDTD method, which we call the piecewise continuous recursive convolution (PCRC) approach, to evaluate the linear and nonlinear convolution integrals. We investigate in particular the case in which both the first-order and third-order electric susceptibility functions are expressed as complex functions that contain complex constant coefficients and exhibit exponential behavior in the time domain as follows:

$$X_\rho^{(1)}(t) = Re\left\{\alpha_\rho^L \exp(-\gamma_\rho^L t)\right\} U(t), \tag{1.5}$$

and

$$\chi_\rho^{(3)}(t) = Re\left\{\alpha_\rho^{NL} \exp(-\gamma_\rho^{NL} t)\right\} U(t), \tag{1.6}$$

where $Re\{\ \}$ is used to represent the real part of a complex function, $U(t)$ is the unit step function, and α_ρ^L, α_ρ^{NL}, γ_ρ^L and γ_ρ^{NL} are complex constant coefficients; superscripts L and NL are used to distinguish between linear and nonlinear coefficients. By making the proper choices of complex constant coefficients and performing Fourier transforms, we can readily obtain the familiar Debye and Lorentz forms of the complex permittivity in the frequency domain.

II. GOVERNING EQUATIONS AND GENERAL FORMULATION OF THE RECURSIVE CONVOLUTION APPROACH

In light of Eq. (1.4), Maxwell's equations inside the dispersive material can be written as

$$\underline{\nabla} \times \underline{E}(t;\underline{x}) = -\frac{\partial[\underline{\underline{\mu}}\, \underline{H}(t;\underline{x})]}{\partial t}, \tag{2.1}$$

$$\underline{\nabla} \times \underline{H}(t;\underline{x}) = \frac{\partial \underline{D}(t;\underline{x})}{\partial t} + \sigma\, \underline{E}(t;\underline{x}), \tag{2.2}$$

$$\underline{D}(t;\underline{x}) = \epsilon_o\epsilon_\infty \underline{E}(t;\underline{x}) + \epsilon_o \sum_\rho \underline{P}_\rho^L(t;\underline{x})$$

$$+\epsilon_o\, \underline{E}(t;\underline{x}) \sum_\rho P_\rho^{NL}(t;\underline{x}) + \epsilon_o\, \underline{E}(t;\underline{x})\left[\underline{E}(t;\underline{x})\bullet\underline{E}(t;\underline{x})\right] \sum_\rho \alpha_{0\rho}^{(3)}, \tag{2.3}$$

$$\underline{P}_{\rho}^{L}(t;\underline{x}) \equiv \int_{-\infty}^{\infty} \underline{E}(\tau;\underline{x})\, \chi_{\rho}^{(1)}(t-\tau)\, d\tau\,, \tag{2.4}$$

$$P_{\rho}^{NL}(t;\underline{x}) \equiv \int_{-\infty}^{\infty} \left[\, \underline{E}(\tau;\underline{x}) \bullet \underline{E}(\tau;\underline{x}) \right] \chi_{\rho}^{(3)}(t-\tau)\, d\tau\,, \tag{2.5}$$

where $\underline{H}(t;\underline{x})$ is the magnetic field vector, μ is the magnetic permeability, and $\underline{P}_{\rho}^{L}(t;\underline{x})$ and $[\underline{E}(t;\underline{x})P_{\rho}^{NL}(t;\underline{x})]$ are related to the ρth terms of linear and nonlinear polarization field vectors, respectively. Using an FDTD algorithm, the above equations can be solved numerically at each time step provided we can handle $\underline{P}_{\rho}^{L}(t;\underline{x})$ and $P_{\rho}^{NL}(t;\underline{x})$ numerically. Therefore, the whole solution rests on the question of how to carry out the numerical evaluation of $\underline{P}_{\rho}^{L}(t;\underline{x})$ and $P_{\rho}^{NL}(t;\underline{x})$ at each successive time step. For that reason, the rest of this section is devoted to the numerical formulation that treats $\underline{P}_{\rho}^{L}(t;\underline{x})$ and $P_{\rho}^{NL}(t;\underline{x})$ based on the recursive convolution approach.

To obtain second-order accuracy in time in evaluating the convolution integrals, $\underline{E}(t;\underline{x})$ is taken to be a piecewise continuous function over the entire temporal integration range so that $\underline{E}(t;\underline{x})$ changes linearly with respect to time over a given discrete time interval $[m\Delta t,\ (m+1)\Delta t]$, where $m=0,1,\ldots,n-1$, with $n\Delta t$ being the current time step [11]. Referring to Fig.1, we can express $\underline{E}(t;\underline{x})$ in the following form in terms of the electric field values, $\underline{E}_{ijk}^{\,m}$ and $\underline{E}_{ijk}^{\,m+1}$, which are, respectively, evaluated at discrete time steps $t=m\Delta t$ and $t=(m+1)\Delta t$ and at the same discrete spatial location $\underline{x} = (i\Delta x, j\Delta y, k\Delta z)$, with Δx, Δy and Δz being the spatial grid sizes in the x, y and z directions, respectively (we use a superscript to designate the discrete time step and a subscript for the discrete spatial location):

$$\underline{E}(t;\underline{x}) = \left\{ \underline{E}_{ijk}^{\,m} + \frac{(\underline{E}_{ijk}^{\,m+1} - \underline{E}_{ijk}^{\,m})}{\Delta t}(t - m\Delta t) \right\} \quad \text{for} \quad 0 \le m\Delta t \le t \le (m+1)\Delta t \le n\Delta t\,; \text{ and}$$

$$\underline{E}(t;\underline{x}) = 0 \qquad\qquad \text{for} \quad t \le 0\,. \tag{2.6}$$

When Eq. (2.6) is substituted into Eq. (2.4), we obtain after some manipulation the following expression for discrete values of $\underline{P}_{\rho}^{L}(t;\underline{x})$ at discrete time step $n\Delta t$ and discrete spatial location $(i\Delta x, j\Delta y, k\Delta z)$ [12]:

$$\underline{P}_{\rho}^{L}(n\Delta t; i\Delta x, j\Delta y, k\Delta z) \equiv (\underline{P}_{\rho}^{L})_{ijk}^{n} \equiv Re\left\{ (\underline{Q}_{\rho}^{L})_{ijk}^{n} \right\}, \tag{2.7}$$

where the discrete complex values, $(\underline{Q}_{\rho}^{L})_{ijk}^{n}$, are defined as

$$(\underline{Q}_{\rho}^{L})_{ijk}^{n} \equiv \sum_{m=0}^{n-1} \left\{ \underline{E}_{ijk}^{\,m} (\psi_{\rho,0}^{L})^{n,m} + (\underline{E}_{ijk}^{\,m+1} - \underline{E}_{ijk}^{\,m})(\psi_{\rho,1}^{L})^{n,m} \right\}, \tag{2.8}$$

with

$$(\psi_{\rho,0}^{L})^{n,m} \equiv \alpha_{\rho}^{L} \int_{(n-m-1)\Delta t}^{(n-m)\Delta t} exp(-\gamma_{\rho}^{L}\tau)\, d\tau\,, \tag{2.9}$$

$$(\psi_{\rho,1}^{L})^{n,m} \equiv \frac{\alpha_{\rho}^{L}}{\Delta t} \int_{(n-m-1)\Delta t}^{(n-m)\Delta t} [(n-m)\Delta t - \tau]\, exp(-\gamma_{\rho}^{L}\tau)\, d\tau\,. \tag{2.10}$$

Similarly, substituting Eq. (2.6) into Eq. (2.5), we obtain after some manipulation the following expression for discrete values of $P_{\rho}^{NL}(t;\underline{x})$ at discrete time step $n\Delta t$ and discrete spatial location $(i\Delta x, j\Delta y, k\Delta z)$ [12]:

$$P_{\rho}^{NL}(n\Delta t; i\Delta x, j\Delta y, k\Delta z) \equiv (P_{\rho}^{NL})_{ijk}^{n} \equiv Re\left\{ (Q_{\rho}^{NL})_{ijk}^{n} \right\}, \tag{2.11}$$

where the discrete complex values, $(Q_{\rho}^{NL})_{ijk}^{n}$, are defined as

$$\begin{aligned}(Q_{\rho}^{NL})_{ijk}^{n} \equiv \sum_{m=0}^{n-1} \Big\{ & \underline{E}_{ijk}^{\,m} \bullet \underline{E}_{ijk}^{\,m} (\psi_{\rho,0}^{NL})^{n,m} + 2\underline{E}_{ijk}^{\,m} \bullet (\underline{E}_{ijk}^{\,m+1} - \underline{E}_{ijk}^{\,m})(\psi_{\rho,1}^{NL})^{n,m} \\ & + (\underline{E}_{ijk}^{\,m+1} - \underline{E}_{ijk}^{\,m}) \bullet (\underline{E}_{ijk}^{\,m+1} - \underline{E}_{ijk}^{\,m})(\psi_{\rho,2}^{NL})^{n,m} \Big\}\,,\end{aligned} \tag{2.12}$$

with

$$(\psi_{\rho,0}^{NL})^{n,m} \equiv \alpha_{\rho}^{NL} \int_{(n-m-1)\Delta t}^{(n-m)\Delta t} exp(-\gamma_{\rho}^{NL}\tau)\, d\tau\,, \tag{2.13}$$

$$(\psi_{\rho,1}^{NL})^{n,m} \equiv \frac{\alpha_\rho^{NL}}{\Delta t}\int_{(n-m-1)\Delta t}^{(n-m)\Delta t}[(n-m)\Delta t-\tau]\exp(-\gamma_\rho^{NL}\tau)\,d\tau\,, \tag{2.14}$$

$$(\psi_{\rho,2}^{NL})^{n,m} \equiv \frac{\alpha_\rho^{NL}}{(\Delta t)^2}\int_{(n-m-1)\Delta t}^{(n-m)\Delta t}[(n-m)\Delta t-\tau]^2\exp(-\gamma_\rho^{NL}\tau)\,d\tau\,. \tag{2.15}$$

After some manipulation we can show that the ψ's defined in Eqs. (2.9), (2.10), (2.13), (2.14) and (2.15) satisfy the following recursive relationships relating the next time step, $(n+1)\Delta t$, to the current time step, $n\Delta t$:

$$(\psi_{\rho,0}^{L})^{n+1,m} = \exp(-\gamma_\rho^L\Delta t)(\psi_{\rho,0}^{L})^{n,m}\,, \tag{2.16}$$

$$(\psi_{\rho,1}^{L})^{n+1,m} = \exp(-\gamma_\rho^L\Delta t)(\psi_{\rho,1}^{L})^{n,m}\,, \tag{2.17}$$

$$(\psi_{\rho,0}^{NL})^{n+1,m} = \exp(-\gamma_\rho^{NL}\Delta t)(\psi_{\rho,0}^{NL})^{n,m}\,, \tag{2.18}$$

$$(\psi_{\rho,1}^{NL})^{n+1,m} = \exp(-\gamma_\rho^{NL}\Delta t)(\psi_{\rho,1}^{NL})^{n,m}\,, \tag{2.19}$$

$$(\psi_{\rho,2}^{NL})^{n+1,m} = \exp(-\gamma_\rho^{NL}\Delta t)(\psi_{\rho,2}^{NL})^{n,m}\,. \tag{2.20}$$

It is important to mention that we are able to obtain the above recursive relationships only because both the linear and nonlinear susceptibility functions are expressed in the exponential forms shown in Eqs. (1.5) and (1.6).

When Eqs. (2.16) through (2.20) are used in Eqs. (2.8) and (2.12), respectively, for the next discrete time step, we obtain the following expressions for $(\underline{P}_\rho^L)_{ijk}^{n+1}$ and $(P_\rho^{NL})_{ijk}^{n+1}$ based on the recursive relationships obtained for $(\underline{Q}_\rho^L)_{ijk}^{n+1}$ and $(Q_\rho^{NL})_{ijk}^{n+1}$ in terms of $\underline{E}_{ijk}^{n+1}$, $\underline{E}_{ijk}^{n}$, $(\underline{Q}_\rho^L)_{ijk}^{n}$ and $(Q_\rho^{NL})_{ijk}^{n}$ via Eqs. (2.16)-(2.20):

$$\begin{aligned}(\underline{P}_\rho^L)_{ijk}^{n+1} &\equiv Re\{(\underline{Q}_\rho^L)_{ijk}^{n+1}\} = Re\{\exp(-\gamma_\rho^L\Delta t)(\underline{Q}_\rho^L)_{ijk}^{n} + \underline{E}_{ijk}^{n}(\psi_{\rho,0}^{L})^{n+1,n} + (\underline{E}_{ijk}^{n+1}-\underline{E}_{ijk}^{n})(\psi_{\rho,1}^{L})^{n+1,n}\}\\ &= Re\{\exp(-\gamma_\rho^L\Delta t)(\underline{Q}_\rho^L)_{ijk}^{n} + \underline{E}_{ijk}^{n}(\psi_{\rho,0}^{L})^{1,0} + (\underline{E}_{ijk}^{n+1}-\underline{E}_{ijk}^{n})(\psi_{\rho,1}^{L})^{1,0}\}\,,\end{aligned} \tag{2.21}$$

and

$$\begin{aligned}(P_\rho^{NL})_{ijk}^{n+1} &\equiv Re\{(Q_\rho^{NL})_{ijk}^{n+1}\} = Re\{\exp(-\gamma_\rho^{NL}\Delta t)(Q_\rho^{NL})_{ijk}^{n} + \underline{E}_{ijk}^{n}\bullet\underline{E}_{ijk}^{n}(\psi_{\rho,0}^{NL})^{n+1,n}\\ &\quad + 2\,\underline{E}_{ijk}^{n}\bullet(\underline{E}_{ijk}^{n+1}-\underline{E}_{ijk}^{n})(\psi_{\rho,1}^{NL})^{n+1,n} + (\underline{E}_{ijk}^{n+1}-\underline{E}_{ijk}^{n})\bullet(\underline{E}_{ijk}^{n+1}-\underline{E}_{ijk}^{n})(\psi_{\rho,2}^{NL})^{n+1,n}\}\\ &= Re\{\exp(-\gamma_\rho^{NL}\Delta t)(Q_\rho^{NL})_{ijk}^{n} + \underline{E}_{ijk}^{n}\bullet\underline{E}_{ijk}^{n}(\psi_{\rho,0}^{NL})^{1,0}\\ &\quad + 2\,\underline{E}_{ijk}^{n}\bullet(\underline{E}_{ijk}^{n+1}-\underline{E}_{ijk}^{n})(\psi_{\rho,1}^{NL})^{1,0} + (\underline{E}_{ijk}^{n+1}-\underline{E}_{ijk}^{n})\bullet(\underline{E}_{ijk}^{n+1}-\underline{E}_{ijk}^{n})(\psi_{\rho,2}^{NL})^{1,0}\}\,.\end{aligned} \tag{2.22}$$

In the above expressions, $(\psi_{\rho,0}^{L})^{1,0}$, $(\psi_{\rho,1}^{L})^{1,0}$, $(\psi_{\rho,0}^{NL})^{1,0}$, $(\psi_{\rho,1}^{NL})^{1,0}$ and $(\psi_{\rho,2}^{NL})^{1,0}$ can be evaluated explicitly from Eqs. (2.9), (2.10), (2.13), (2.14) and (2.15) in terms of complex linear and nonlinear susceptibility coefficients α_ρ^L, α_ρ^{NL}, γ_ρ^L and γ_ρ^{NL} and Δt as follows:

$$(\psi_{\rho,0}^{L})^{1,0} \equiv \alpha_\rho^L\int_0^{\Delta t}\exp(-\gamma_\rho^L\tau)\,d\tau = \frac{\alpha_\rho^L}{\gamma_\rho^L}[1-\exp(-\gamma_\rho^L\Delta t)]\,, \tag{2.23}$$

$$(\psi_{\rho,1}^{L})^{1,0} \equiv \frac{\alpha_\rho^L}{\Delta t}\int_0^{\Delta t}(\Delta t-\tau)\exp(-\gamma_\rho^L\tau)\,d\tau = \frac{\alpha_\rho^L}{\gamma_\rho^L}\{1-\frac{1}{\gamma_\rho^L\Delta t}[1-\exp(-\gamma_\rho^L\Delta t)]\}\,, \tag{2.24}$$

$$(\psi_{\rho,0}^{NL})^{1,0} \equiv \alpha_\rho^{NL}\int_0^{\Delta t}\exp(-\gamma_\rho^{NL}\tau)\,d\tau = \frac{\alpha_\rho^{NL}}{\gamma_\rho^{NL}}[1-\exp(-\gamma_\rho^{NL}\Delta t)]\,, \tag{2.25}$$

$$(\psi_{\rho,1}^{NL})^{1,0} \equiv \frac{\alpha_\rho^{NL}}{\Delta t}\int_0^{\Delta t}(\Delta t-\tau)\exp(-\gamma_\rho^{NL}\tau)\,d\tau = \frac{\alpha_\rho^{NL}}{\gamma_\rho^{NL}}\{1-\frac{1}{\gamma_\rho^{NL}\Delta t}[1-\exp(-\gamma_\rho^{NL}\Delta t)]\}\,, \tag{2.26}$$

$$(\psi_{\rho,2}^{NL})^{1,0} \equiv \frac{\alpha_\rho^{NL}}{(\Delta t)^2}\int_0^{\Delta t}(\Delta t-\tau)^2\exp(-\gamma_\rho^{NL}\tau)\,d\tau = \frac{\alpha_\rho^{NL}}{\gamma_\rho^{nl}}\{1-\frac{2}{\gamma_\rho^{NL}\Delta t}[1-\frac{1}{\gamma_\rho^{NL}\Delta t}[1-\exp(-\gamma_\rho^{NL}\Delta t)]]\}\,. \tag{2.27}$$

To demonstrate how the above terms are used in the FDTD calculations, we consider the one-dimensional case where the propagating wave vector, $\underline{k}$, lies along a major axis in Cartesian coordinates. The analysis can be extended easily to two and three-dimensional cases, where the EM wave is propagating in any arbitrary direction, based on following the sample one-dimensional formulation presented below. For our one-dimensional case, we arbitrarily pick the $\underline{k}$ vector to lie in the x direction, D_y and E_y field vectors in the y direction and the H_z field vector in the z direction. When Eqs. (2.1) and (2.2) are differenced in both time and space using the usual Yee algorithm [3], we have

$$\left[\frac{(D_i^{n+1})_y-(D_i^n)_y}{\Delta t}\right]=-\left[\frac{(H_{i+\frac{1}{2}}^{n+\frac{1}{2}})_z-(H_{i-\frac{1}{2}}^{n+\frac{1}{2}})_z}{\Delta x}\right]-\sigma(E_i^n)_y, \tag{2.28}$$

$$\left[\frac{(\mu H_{i+\frac{1}{2}}^{n+\frac{1}{2}})_z-(\mu H_{i+\frac{1}{2}}^{n-\frac{1}{2}})_z}{\Delta t}\right]=-\left[\frac{(E_{i+1}^n)_y-(E_i^n)_y}{\Delta x}\right], \tag{2.29}$$

where subscripts y and z refer, respectively, to the y and z components of the field vectors. Based on expressions obtained in Eqs. (2.3), (2.21) and (2.22), the left-hand side of Eq. (2.28) can be expressed in terms of $(E_i^{n+1})_y$ and $(E_i^n)_y$ as

$$\begin{aligned}(D_i^{n+1})_y-(D_i^n)_y &= \epsilon_o\epsilon_\infty[(E_i^{n+1})_y-(E_i^n)_y]\\
&+\epsilon_o\sum_\rho Re\Big\{[\exp(-\gamma_\rho^L\Delta t)-1][(Q_\rho^L)_i^n]_y+(E_i^n)_y(\psi_{\rho,0}^L)^{1,0}+[(E_i^{n+1})_y-(E_i^n)_y](\psi_{\rho,1}^L)^{1,0}\Big\}\\
&+\epsilon_o\sum_\rho Re\Big\{[[(E_i^{n+1})_y]^3-[(E_i^n)_y]^3]\,\alpha_{0\rho}^{(3)}+[(E_i^{n+1})_y\exp(-\gamma_\rho^{NL}\Delta t)-(E_i^n)_y](Q_\rho^{NL})_i^n\\
&\quad+(E_i^{n+1})_y[(E_i^n)_y]^2(\psi_{\rho,0}^{NL})^{1,0}+2(E_i^{n+1})_y(E_i^n)_y[(E_i^{n+1})_y-(E_i^n)_y](\psi_{\rho,1}^{NL})^{1,0}\\
&\quad+(E_i^{n+1})_y[(E_i^{n+1})_y-(E_i^n)_y]^2(\psi_{\rho,2}^{NL})^{1,0}\Big\}.\end{aligned} \tag{2.30}$$

When Eq. (2.30) is substituted into Eq. (2.28), the following algebraic cubic equation results in which we need to solve for $(E_i^{n+1})_y$ in terms of known quantities a_0, a_1, a_2 and a_3 at $t=(n+1)\Delta t$:

$$a_0+a_1(E_i^{n+1})_y+a_2[(E_i^{n+1})_y]^2+a_3[(E_i^{n+1})_y]^3=0, \tag{2.31}$$

where a_0, a_1, a_2 and a_3 are given by

$$\begin{aligned}a_0 &\equiv \frac{\Delta t}{\Delta x}[(H_{i+\frac{1}{2}}^{n+\frac{1}{2}})_z-(H_{i-\frac{1}{2}}^{n+\frac{1}{2}})_z]+(E_i^n)_y\sigma\Delta t-(E_i^n)_y\epsilon_o\epsilon_\infty\\
&+\epsilon_o\sum_\rho Re\Big\{[\exp(-\gamma_\rho^L\Delta t)-1][(Q_\rho^L)_i^n]_y-[(E_i^n)_y]^3\,\alpha_{0\rho}^{(3)}-(E_i^n)_y(Q_\rho^{NL})_i^n\\
&\quad+(E_i^n)_y[(\psi_{\rho,0}^L)^{1,0}-(\psi_{\rho,1}^L)^{1,0}]\Big\},\end{aligned} \tag{2.32}$$

$$\begin{aligned}a_1 &\equiv \epsilon_o\epsilon_\infty+\epsilon_o\sum_\rho Re\Big\{\exp(-\gamma_\rho^{NL}\Delta t)(Q_\rho^{NL})_i^n+(\psi_{\rho,1}^L)^{1,0}\\
&\quad+[(E_i^n)_y]^2[(\psi_{\rho,0}^{NL})^{1,0}-2(\psi_{\rho,1}^{NL})^{1,0}+(\psi_{\rho,2}^{NL})^{1,0}]\Big\},\end{aligned} \tag{2.33}$$

$$a_2\equiv 2\epsilon_o\sum_\rho Re\Big\{(E_i^n)_y[(\psi_{\rho,1}^{NL})^{1,0}-(\psi_{\rho,2}^{NL})^{1,0}]\Big\}, \tag{2.34}$$

$$a_3\equiv\epsilon_o\sum_\rho Re\Big\{\alpha_{0\rho}^{(3)}+(\psi_{\rho,2}^{NL})^{1,0}\Big\}. \tag{2.35}$$

Eq. (2.31) can be solved for $(E_i^{n+1})_y$ by using any standard root-finding numerical technique. Hence, for complete computer simulation of the electric field response in nonlinear dispersive materials, we only need to consider updating Eqs. (2.21), (2.22), (2.29) and (2.31), respectively, for $[(Q_\rho^L)_i^{n+1}]_y$, $(Q_\rho^{NL})_i^{n+1}$, $(H_{i+\frac{1}{2}}^{n+\frac{1}{2}})_z$ and $(E_i^{n+1})_y$ at each time step.

For the purely linear dispersive case, a_2 and a_3, as well as some terms appearing in a_0 and a_1, turn out to be zero. In this case we can solve for $(E_i^{n+1})_y$ directly without having to rely on the numerical root finding technique; this case is discussed in the literature on computational schemes for linear dispersive materials [13-18].

III. EQUIVALNCE OF THE RECURSIVE CONVOLUTION APPROACH TO THE AUXILIARY DIFFERENTIAL EQUATION APPROACH

An alternative technique for solving the nonlinear dispersive problem is the so-called auxiliary differential equation approach. The auxiliary differential equation approach is in fact equivalent to the recursive convolution approach as we now show.

To begin, we first substitute Eq. (1.5) into Eq. (2.4) and Eq. (1.6) into Eq. (2.5) and then differentiate these integrals with respect to time to obtain the following first-order differential equations for complex functions $\underline{Q}_\rho^L(t;\underline{x})$ and $\underline{Q}_\rho^{NL}(t;\underline{x})$:

$$\frac{\partial \underline{Q}_\rho^L(t;\underline{x})}{\partial t} + \gamma_\rho^L \underline{Q}_\rho^L(t;\underline{x}) = \alpha_\rho^L \underline{E}(t;\underline{x}), \tag{3.1}$$

$$\frac{\partial Q_\rho^{NL}(t;\underline{x})}{\partial t} + \gamma_\rho^{NL} Q_\rho^{NL}(t;\underline{x}) = \alpha_\rho^{NL} [\underline{E}(t;\underline{x})]^2 . \tag{3.2}$$

From the above equations, the linear and nonlinear polarization vectors, $\underline{P}_\rho^L(t;\underline{x})$ and $[\underline{E}(t;\underline{x})P_\rho^{NL}(t;\underline{x})]$, can be obtained simply by taking the real parts of $\underline{Q}_\rho^L(t;\underline{x})$ and $[\underline{E}(t;\underline{x})Q_\rho^{NL}(t;\underline{x})]$, respectively. Now, solving these two equations *exactly* by using integrating factors $exp(\gamma_\rho^L t)$ and $exp(\gamma_\rho^{NL} t)$, respectively, and then integrating between $n\Delta t$ and $n\Delta t+\Delta t$, we have

$$\underline{Q}_\rho^L(n\Delta t+\Delta t;\underline{x}) = exp(-\gamma_\rho^L \Delta t)\underline{Q}_\rho^L(n\Delta t;\underline{x}) + \alpha_\rho^L exp(-\gamma_\rho^L \Delta t) \int_{n\Delta t}^{n\Delta t+\Delta t} \underline{E}(\tau;\underline{x})\, exp[-\gamma_\rho^L(n\Delta t-\tau)]d\tau , \tag{3.3}$$

and

$$Q_\rho^{NL}(n\Delta t+\Delta t;\underline{x}) = exp(-\gamma_\rho^{NL} \Delta t)Q_\rho^{NL}(n\Delta t;\underline{x}) + \alpha_\rho^{NL} exp(-\gamma_\rho^{NL} \Delta t) \int_{n\Delta t}^{n\Delta t+\Delta t} [\underline{E}(\tau;\underline{x})]^2 exp[-\gamma_\rho^{NL}(n\Delta t-\tau)]d\tau . \tag{3.4}$$

If $\underline{E}(t;\underline{x})$ is assumed to vary linearly in time between $n\Delta t$ and $n\Delta t+\Delta t$, as in the piecewise linear approximation of Eq. (2.6), we can substitute Eq. (2.6) into the right hand side (i.e., the inhomogeneous part) of Eqs. (3.3) and (3.4) so that we obtain the following expressions for $(\underline{Q}_\rho^L)^{n+1}$ and $(Q_\rho^{NL})^{n+1}$, respectively, at discrete time step $(n\Delta t+\Delta t)$ and discrete spatial location $(i\Delta x, j\Delta y, k\Delta z)$:

$$\underline{Q}_\rho^L(n\Delta t+\Delta t; i\Delta x, j\Delta y, k\Delta z) \equiv (\underline{Q}_\rho^L)_{ijk}^{n+1}$$
$$= exp(-\gamma_\rho^L \Delta t)(\underline{Q}_\rho^L)_{ijk}^{n} + \underline{E}_{ijk}^{n}(\psi_{\rho,0}^L)^{1,0} + (\underline{E}_{ijk}^{n+1} - \underline{E}_{ijk}^{n})(\psi_{\rho,1}^L)^{1,0} , \tag{3.5}$$

and

$$Q_\rho^{NL}(n\Delta t+\Delta t; i\Delta x, j\Delta y, k\Delta z) \equiv (Q_\rho^{NL})_{ijk}^{n+1}$$
$$= exp(-\gamma_\rho^{NL} \Delta t)(Q_\rho^{NL})_{ijk}^{n} + (\underline{E}_{ijk}^{n})^2(\psi_{\rho,0}^{NL})^{1,0}$$
$$+ 2\,\underline{E}_{ijk}^{n} \bullet (\underline{E}_{ijk}^{n+1} - \underline{E}_{ijk}^{n})(\psi_{\rho,1}^{NL})^{1,0} + (\underline{E}_{ijk}^{n+1} - \underline{E}_{ijk}^{n})^2(\psi_{\rho,2}^{NL})^{1,0} . \tag{3.6}$$

In the auxiliary differential equation approach, we first use Eq. (2.28) to update the displacement field vector, $\underline{D}_{ijk}^{n}$, to the next time step, $(n+1)\Delta t$. Then the electric field vector at time step $(n+1)\Delta t$, $\underline{E}_{ijk}^{n+1}$, is updated from Eq. (2.3) by setting $t=(n+1)\Delta t$:

$$\underline{D}_{ijk}^{n+1} = \epsilon_o \epsilon_\infty \underline{E}_{ijk}^{n+1} + \epsilon_o \sum_\rho Re\{(\underline{Q}_\rho^L)_{ijk}^{n+1}\} + \epsilon_o \underline{E}_{ijk}^{n+1} \sum_\rho Re\{(Q_\rho^{NL})_{ijk}^{n+1}\} + \epsilon_o \underline{E}_{ijk}^{n+1} [\underline{E}_{ijk}^{n+1} \bullet \underline{E}_{ijk}^{n+1}] \sum_\rho \alpha_{0\rho}^{(3)} . \tag{3.7}$$

Substituting Eqs. (3.5) and (3.6) into the above equation and considering the same one-dimensional case as we have treated in the previous section, we obtain the following algebraic cubic equation which we need to solve for $(E_i^{n+1})_y$ in terms of known quantities b_0, b_1, b_2 and b_3 at $t=(n+1)\Delta t$:

$$b_0 + b_1 (E_i^{n+1})_y + b_2 [(E_i^{n+1})_y]^2 + b_3 [(E_i^{n+1})_y]^3 = 0, \tag{3.8}$$

where b_0, b_1, b_2 and b_3 are given by

$$b_0 \equiv -(D_i^{n+1})_y + \epsilon_o \sum_\rho Re\left\{ exp(-\gamma_\rho^L \Delta t)[(Q_\rho^L)_i^n]_y + (E_i^n)_y [(\psi_{\rho,0}^L)^{1,0} - (\psi_{\rho,1}^L)^{1,0}] \right\}, \tag{3.9}$$

$$b_1 \equiv \epsilon_o \epsilon_\infty + \epsilon_o \sum_\rho Re\left\{ exp(-\gamma_\rho^{NL} \Delta t)(Q_\rho^{NL})_i^n + (\psi_{\rho,1}^L)^{1,0} + [(E_i^n)_y]^2 [(\psi_{\rho,0}^{NL})^{1,0} - 2(\psi_{\rho,1}^{NL})^{1,0} + (\psi_{\rho,2}^{NL})^{1,0}] \right\}, \tag{3.10}$$

$$b_2 \equiv 2\epsilon_o \sum_\rho Re\left\{ (E_i^n)_y [(\psi_{\rho,1}^{NL})^{1,0} - (\psi_{\rho,2}^{NL})^{1,0}] \right\}, \tag{3.11}$$

$$b_3 \equiv \epsilon_o \sum_\rho Re\left\{ \alpha_{0\rho}^{(3)} + (\psi_{\rho,2}^{NL})^{1,0} \right\}. \tag{3.12}$$

But we know that $(D_i^{n+1})_y$ is obtained from Eq. (2.28) and can be expressed as

$$(D_i^{n+1})_y = (D_i^n)_y - \frac{\Delta t}{\Delta x}[(H_{i+\frac{1}{2}}^{n+\frac{1}{2}})_z - (H_{i-\frac{1}{2}}^{n+\frac{1}{2}})_z] - (E_i^n)_y \sigma \Delta t, \tag{3.13}$$

and it follows from Eq. (2.3) that $(D_i^n)_y$ has the form

$$(D_i^n)_y = \epsilon_o \epsilon_\infty (E_i^n)_y + \epsilon_o \sum_\rho Re\left\{ [(Q_\rho^L)_i^n]_y \right\} + \epsilon_o (E_i^n)_y \sum_\rho Re\left\{ (Q_\rho^{NL})_i^n \right\} + \epsilon_o [(E_i^n)_y]^3 \sum_\rho \alpha_{0\rho}^{(3)}. \tag{3.14}$$

Now, substituting Eqs. (3.13) and (3.14) in Eq. (3.9), we can show that b_0 [Eq. (3.9)] is the same as a_0 [Eq. (2.32)]; likewise, we can see that $b_1=a_1$ [Eqs. (3.10) and (2.33)], $b_2=a_2$ [Eqs. (3.11) and (2.34)] and $b_3=a_3$ [Eqs. (3.12) and (2.35)]. Hence, we can conclude that the auxiliary differential equation approach is equivalent to the recursive convolution approach. The only difference is that the auxiliary differential equation approach requires additional memory to be allocated for the calculation of the displacement field vector, which is updated via Eq. (2.28), at each time step. Thus, in the auxiliary differential equation approach, we use Eqs. (2.28), (2.29), (3.5), (3.6) and (3.8) to update, respectively, for $(D_i^{n+1})_y$, $(H_{i+\frac{1}{2}}^{n+\frac{1}{2}})_z$, $[(Q_\rho^L)_i^{n+1}]_y$, $(Q_\rho^{NL})_i^{n+1}$ and $(E_i^{n+1})_y$ at each time step in order to perform a complete simulation of the electric field response in nonlinear dispersive materials.

IV. CONCLUSIONS

Based on the piecewise continuous recursive convolution (PCRC) approach presented in this paper, we can predict the formation of nonlinear solitary waves by solving Maxwell's equations directly for the propagation of electromagnetic waves in nonlinear dispersive media that exhibit both instantaneous Kerr and Raman scattering responses. The PCRC approach has been shown to be the same as the auxiliary differential equation approach provided that the auxiliary differential equations are solved analytically using integrating factors and the same piecewise linear approximation is used for $\underline{E}(t;\underline{x})$ to integrate the inhomogeneous part of auxiliary differential equations. Because of the piecewise linear approximation we used for the time dependent part of the electric field vector, the PCRC results in second-order accuracy in time. As a whole, the PCRC approach retains all the advantages of the usual first-order discrete recursive convolution approach, such as fast computational speed and efficient use of the computer memory; however, the PCRC approach provides second-order accuracy in time.

We pointed out that the exponential forms of the linear and nonlinear susceptibility functions were crucial in allowing us to implement the recursive feature in our algorithm. Also, we have shown that the FDTD formulation for nonlinear dispersive materials results in having to solve an algebraic cubic equation for electric field values at each time step as compared to just solving the linear equation in the case of linear dispersive materials.

We believe that the PCRC approach is robust: the FDTD algorithm can be extend to two and three-dimensional cases with ease by simply following the steps we have presented in this paper for the one-dimensional case.

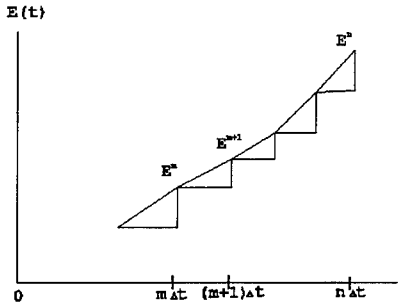

Fig. 1. Illustration of the Piecewise Linear Approximation for the Electric Field as a Function of Discrete Time Steps

REFERENCES:

[1] T-H. Huang, C-C. Hsu, T-H. Wei, S. Chang, S-M Yen, C-P. Tsai, R-T. Liu, C-T. Kuo, W-S. Tse and C. Chia, "The Transient Optical Kerr Effect of Simple Liquids Studied with an Ultrashort Laser with Variable Pulsewidth," IEEE Jour. of Selected Topics in Quantum Electronics, vol 2, pp. 756-775, 1996

[2] K. J. Blow and D. Wood, 'Theoretical Description of Transient Stimulated Raman Scattering in Optical Fibers," IEEE Jour. of Quantum Electronics, vol 25, pp. 2665-2673, 1989

[3] K. S. Yee, "Numerical Solution of Initial Boundary Value Problems Involving Maxwell's Equations in Isotropic Media," IEEE Trans. Antenna Propagat., vol AP-14, pp. 302-307, 1966

[4] P. M. Goorjian, A. Taflove, R. M. Joseph and S.C. Hagness, 'Computational Modeling of Femtosecond Optical Solitons from Maxwell's Equations," IEEE J. of Quantum Electronics, vol 28, pp. 2416-2422, 1992

[5] P. M. Goorjian, A. Taflove, "Direct Time Integration of Maxwell's Equations in Nonlinear Dispersive Media for Propagation of Femtosecond Electromagnetic Solitons," Opt. Lett., vol 17, pp. 180-182, 1992

[6] R. M. Joseph, P. M. Goorjian and A. Taflove, "Direct Time Integration of Maxwell's Equations in Two-Dimensional Dielectric Waveguides for Propagation and Scattering of Femtosecond Electromagnetic Solitons," Opt. Lett., vol 18, pp. 491-493, 1993

[7] R. M. Joseph and A. Taflove, "Spatial Soliton Deflection Mechanism Indicated by FD-TD Maxwell's Equations Modeling," IEEE Photonics Tech. Lett., vol 6, pp. 1251-1254, 1994

[8] R. W. Ziolkowski and J. B. Judkins, "Applications of the Nonlinear Finite Difference Time Domain (NL-FDTD) Method to Pulse Propagation in Nonlinear Media: Self Focusing and Linear Interfaces," Opt. Lett., vol 18, pp. 491-493, 1993

[9] R. W. Ziolkowski and J. B. Judkins, "Full-wave Vector Maxwell Modeling of the Self-focusing of Ultrashort Optical Pulses in a Nonlinear Kerr Medium Exhibiting a Finite Response Time," Jour. Opt. Soc. Am B., vol 10, pp. 186-198, 1993

[10] R. W. Hellworth, "Third-order Optical Susceptibility of Liquids and Solids," Prog. Quantum Electronics, vol 5, pp. 1-68, 1977

[11] D. F. Kelley and R. J. Luebbers, "Piecewise Linear Recursive Convolution for Dispersive Media Using FDTD," IEEE Trans. Antenna and Propagat., vol 44, pp. 792-797, 1996

[12] S. J. Yakura and J. MacGillivray, "Finite-Difference Time-Domain Calculations Based on Recursive Convolution Approach for Propagation of Electromagnetic Waves in Nonlinear Dispersive Media," Air Force Research Laboratory Report (PL-TR-97-1170) – Appendix, Oct 30, 1997.

[13] R. J. Luebbers, F. Hunsberger and K. S. Kunz, "A Frequency-dependent Finite Difference Time-Domain Formulation for Transient Propagation in Plasma," IEEE Trans. Antennas and Propagat., vol 39, pp. 29-34, 1991

[14] R. M. Joseph, S. C. Hagness and A. Taflove, "Direct Time Integration of Maxwell's Equations in Linear Dispersive Media with Absorption for Scattering and Propagation of Femtosecond Electromagnetic Pulses," Opt. Lett., vol 16, 1412-1414, 1991

[15] R. J. Luebbers and F. Hunsberger, "FDTD for Nth-order Dispersive Media," IEEE Trans. Antenna and Propagat., vol 40, pp. 1297-1301, 1992

[16] F. Hunsberger, R. Luebbers and K. Kunz, "Finite-Difference Time-Domain Analysis of Gyrotropic Media-I: Magnetic Plasma," IEEE Trans. Antennas and Propagat., vol 40, pp. 1489-1495, 1992

[17] R. Luebbers, D. Steich and K. Kunz, "FDTD Calculation of Scattering from Frequency-dependent Materials," IEEE Trans. Antennas and Propagat., pp. 1249-1257, 1993

[18] J. L. Young, "Propagation in Linear Dispersive Media: Finite Difference Time-Domain Methodologies," IEEE Trans. Antennas and Propagat., vol 43, pp. 411-430, 1995

Methods for including Lumped Elements in FDTD Simulations

Ian Rumsey, Jason Mix, Melinda Piket-May
University of Colorado at Boulder
Department of Electrical and Computer Engineering
Campus Box 425; Boulder, C0 80309
Phone: (303) 492-7891
Fax: (303) 492-5323
Email: rumsey@ucsub.colorado.edu
mix@spot.colorado.edu
mjp@colorado.edu

Abstract

As digital systems reach ever-increasing speeds and microwave circuits become more complex, it is necessary to include the effect of lumped circuit elements in full-wave electromagnetic simulation. Applications where lumped circuits become important include EMI/EMC of printed circuit boards, active antenna arrays, and integrated circuit packaging. This paper provides an overview of the methods available to include both passive and active devices in FDTD simulations.

Introduction

There are several methods for including lumped elements in the FDTD method. These methods are necessary as digital and microwave circuits increase in speed and complexity. The electromagnetic effects in these systems as well as the impact of passive and active circuits must be taken into account. The methods used to include lumped elements in FDTD simulations vary in complexity and robustness, and sometimes the best method to use is not obvious. This paper provides an overview of the methodology involved in each technique, and the accompanying presentation will provide examples of each method relevant to today's design problems. Recommendations for method choice in common applications will also be presented.

Extended FDTD Method

One of the basic techniques used to include lumped elements in the FDTD simulation space is the extended FDTD method [1]. This method utilizes the current density term (J_C) in Ampere's law to insert the current through a lumped device (J_L) into the full-wave FDTD solution. Ampere's Law with this term included is stated as:

$$\nabla \times \vec{H} = \varepsilon \frac{\partial}{\partial t} \vec{E} + \vec{J}_c + \vec{J}_L \qquad (1)$$

Where the current density through the device region can be related to the current through the lumped element by simply dividing the element current by the cross-sectional area of the FDTD grid cell. The voltage across one z-oriented FDTD cell is given by the product of Ez at that point and the cell height Δz. The remaining step is to write a finite-difference equation relating the current through the lumped

element and the voltage across it. Linear relations can be computed using a simple update equation, but nonlinear devices such as diodes and transistors require alternative methods to be used. As a simple example, consider a resistor. The current through this device is related to the voltage by V/R. Assuming that σ=0 in the cell where the device is located, an update equation for a resistor could be written as:

$$E_z\,|_{i,j,k}^{n+1} = E_z\,|_{i,j,k}^{n} + \frac{\Delta t}{\varepsilon}\nabla \times \vec{H}\,|_{ii,j,k}^{n+1/2} - \frac{\Delta t}{\varepsilon \Delta x \Delta y}\frac{\Delta z E_z\,|_{i,j,k}^{n}}{R} \tag{2}$$

This method has been extended into 3-D [2] and to allow elements to occupy multiple FDTD cells [3]. However, this method has been found to be numerically unstable [4], and a stable algorithm has been proposed which uses a time-averaged value for the device voltage.

Equivalent Source Method

The equivalent source method [5] is a technique which is concerned only with the relationship between current and voltage at the device terminals. Electric and magnetic fields in the device region are computed using a separate subroutine, so no alterations are made to the traditional update equations. In this method, the current flowing through the device region is found by integrating the magnetic field around a loop surrounding the port. This current is then substituted into an analytic expression for the device voltage as a function of the current. This voltage is then impressed in the device region by setting the electric field quantities along the port such that the device voltage is approximated by a uniformly distributed electric field across the port. The magnetic field is then updated using the standard update equations, and the process is repeated. Alternatively, the device voltage can be measured, and the magnetic fields around the port can be set to enforce the device current. Because this method does not involve directly manipulating the FDTD update equations, it is a more straight forward task to implement nonlinear and multi-port devices.

A derivative of the equivalent source method uses an external circuit solver such as SPICE to solve the I-V relationships of the lumped circuit. Because this method requires no knowledge of the circuit under test, including linear and nonlinear behavior, it is well-suited for implementation in a generalized software package. There are two dual techniques for interfacing the distributed FDTD, the current source [6] and voltage source [7] methods. These methods take into account the effects of the entire FDTD grid on the region where the lumped element resides (port) by manipulating Maxwell's equations in the region around the port.

The current source method is based on Ampere's law, which can be stated in integral form as:

$$\oint_C \vec{H} \bullet \vec{dl} = \int_S \vec{J} \bullet \vec{ds} + \int_S \frac{\partial}{\partial t}\varepsilon\, \vec{E} \bullet \vec{ds} \tag{3}$$

which can be written in terms of circuit quantities.

$$I = I(V) + C\,\frac{d}{dt}V \tag{4}$$

I is the total current flowing through the port, C is the space capacitance of the FDTD grid, V is the voltage across the device, and I(V) is the device current as a function of device voltage. This can be seen as an expression of Kirchoff's current law for the circuit shown in figure 1.

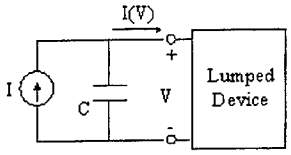

Figure 1. Norton Equivalent Circuit for SPICE Interface

The current source I is set from FDTD by performing a closed-loop integral of the magnetic field around the port, and the FDTD space capacitance C is found from the area of the port, the permittivity of the material in the port region, and the height of the port using the relation for a parallel-plate capacitor. The voltage across the terminals of the lumped device is then found from SPICE, and the electric field values in the port region are set such that the integral of E·dl across the port is equal to this voltage.

The voltage-source method is based on Faraday's law, which can be stated in integral form.

$$\oint_C \vec{E} \bullet \vec{dl} = -\frac{d}{dt}\int_S \mu \vec{H} \bullet \vec{ds} \tag{5}$$

As was done for the current-source method, this equation can be rewritten in terms of circuit quantities.

$$V_{tot} = L\frac{d}{dt}I + V_{dev} \tag{6}$$

Where V_{tot} is the voltage across the FDTD port region, L is the space-inductance of the FDTD grid, I is the current flowing through the port, and V_{dev} is the voltage across the lumped device. Similarly to the current-source method, this can be seen as an expression of Kirchoff's voltage law for the series circuit shown in figure 2.

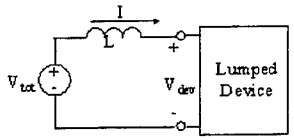

Figure 2. Thevenin Equivalent Circuit for SPICE Interface

For a port occupying a single FDTD electric field point, the relations for Vtot and L are given by [7,8].

S-Parameter Method

Another approach to lumped devices is to model them based on the scattering matrix representation of the circuit. This method would allow network-analyzer measurements of fabricated structures to be easily included in FDTD simulations, and will be very useful in microwave circuit design where device behavior is often given term of s-parameters. A similar technique [9] has been used to represent electromagnetic simulation results in lumped circuit simulators. This technique has been applied to transmission line termination in FDTD by specifying the reflection coefficient (S_{11})

presented by the termination. This method relates the voltage and current at the device terminals through the reflection coefficient in a manner similar to the equivalent source method. This relation is given by

$$V^{n+1/2} = S_{11}V^{n-1/2} + Z_{ref}(S_{11}+1)I^{n} \quad (7)$$

Where Z_{ref} is the characteristic impedance of the input transmission line. This method is currently limited to one-port devices with real, frequency-invariant reflection coefficients, but work is in progress to extend this method to include multi-port devices with complex s-parameters that can vary with frequency.

Conclusions

This paper provides an overview of the methodology involved in each technique for including lumped elements in FDTD simulations. The accompanying conference presentation will compare these methods with examples relevant to today's design problems. Common applications and recommendations for choosing a method for including lumped elements will also be discussed.

References

[1]W. Sui, D.A. Christensen, C.H. Durney, "Extending the Two-Dimensional FDTD Method to Hybrid Electromagnetic Systems with Active and Passive Lumped Elements", *IEEE Trans. on Microwave Theory and Techniques*, **vol. 40, no. 4,** April 1992, pp.724-730

[2]M. Piket-May, A. Taflove, and J. Baron, "FD-TD Modeling of Digital Signal Propagation in 3-D Circuits with Active and Passive Loads", *IEEE Trans. on Microwave Theory and Techniques,* **vol. 42, no.8,** August 1994, pp. 1514-1523

[3]C. Durney et.al., "A General Formulation for Connecting Sources and Passive Lumped-Circuit Elements Across Multiple 3-D FDTD Cells", *IEEE Microwave and Guided Wave Letters,* **vol. 6, no. 2**, Feb. 1996, pp. 85-87

[4]J. Xu et.al., "A stable Algorithm for Modeling Lumped Circuit Source Across Multiple FDTD Cells", *IEEE Microwave and Guided Wave Letters*, **vol. 7, no. 9**, Sept. 1997, pp 308-310

[5]J. Mix, M. Piket-May et.al., "Modeling Nonlinear Devices in FD-TD: The Equivalent Source Method," USNC/URSI National Radio Science Meeting; 1998 Digest; Atlanta, GA; pp.75

[6] M. Piket-May, V.Thomas, et.al., "The Use of SPICE Lumped Circuits as Sub-grid Models for FDTD Analysis", *IEEE Microwave and Guided Wave Letters*, **vol. 4, no. 5**, May 1994, pp. 141-143

[7] C.-N. Kuo, T. Itoh, et.al., "Modeling of microwave active devices using the FDTD analysis based on the voltage-source approach," *IEEE Microwave and Guided Wave Letters,* **vol. 6, no. 5,** May 196, pp. 199-201

[8]Allen Taflove, Advances in Computational Electrodynamics: The Finite Difference Time Domain Method, Artech House, Norwood, MA, 1998, chapter 8

[9] W.T. Beyene and J.E. Schutt-Ainé, "Integrating Data Obtained From Electromagnetic Field Analysis into Circuit Simulations," 1997 ACES Annual Review Conference Proceedings, pp. 156-163

A Novel Subgridding Scheme for Refractive Index Adaptive FDTD

T. O. Körner and W. Fichtner

Integrated Systems Laboratory, Swiss Federal Institute of Technology
ETH Zentrum, 8092 Zürich, Switzerland

Abstract

A new method for interfacing standard finite-difference time-domain grids with different node spacings at material boundaries is presented. This method greatly enhances the computational efficiency when modeling structures that contain homogeneous regions with large differences in refractive index. This situation is frequently encountered when modeling light sensitive semiconductor devices on which light is incident from vacuum. In addition to the superior computational performance, more accurate results can be obtained in comparison to standard FDTD due to decreased numerical dispersion. The stability of the method is discussed and demonstrated by means of test example problems.

1 Introduction

FDTD methods [1] play an ever increasing role in modeling all kinds of optical structures. In recent publications simulation results for light propagation in photonic crystals [2], waveguides [3], (VCSEL) laser cavities [4], integrated optics devices [5], liquid crystal displays [6], photodetectors [7], etc. have been presented.

One major drawback of standard FDTD is that it operates on a so called rectilinear tensor product grid (RTPG). By this we mean that the position of all the nodes is determined by a $1 \times n_i$-vector containing the node spacings for each of the orthogonal coordinate axes i (where $i \in \{1,2\}$ for 2D and $i \in \{1,2,3\}$ for 3D are corresponding to the x-, y- and z-directions respectively). In the following, we refer to a grid as being uniform if in each vector all the elements are equal. To get sufficiently accurate results from an FDTD simulation, the node spacing has to be chosen sufficiently small. The maximum allowable node spacing is determined by a couple of factors: Firstly, the grid spacing d within a homogeneous material region needs to be much smaller than the wavelength λ in this material. Generally, $d < \lambda/10$ is a minimum requirement for reliable results. For very large simulation domains (in wavelengths), finer grid spacing is necessary to keep the errors due to numerical dispersion below a tolerable limit. In addition, the grid spacing needs to

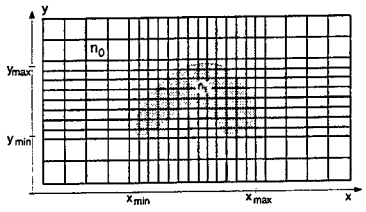

Figure 1: Nonuniform rectilinear tensor product grid for a region of high refractive index n_1 surrounded by lower refractive index $n_0 < n_1$.

be fine enough to resolve all geometrical features with sufficient accuracy. If a part of the simulation domain bounded by $[x_{\min}, x_{\max}]$, $[y_{\min}, y_{\max}]$ (and $[z_{\min}, z_{\max}]$ in 3D) is filled with a material of high refractive index or a structure containing fine geometrical detail, node spacing in all these intervals has to be set accordingly. In general, this results in fine node spacing in regions of the simulation domain where it would not be required according to the former criteria. This can lead to significant overheads in memory requirements. The situation is demonstrated in Fig. 1 for a nonuniform grid.

To overcome the problems arising a number of local subgridding schemes have recently been published in the electromagnetics literature [8, 9, 10, 11]. There, the need to use subgridding fre-

quently stems from the presence of fine geometrical detail. The algorithms dealing with this problem allow to mesh a subregion of the simulation domain with a local grid with finer node spacing than in the surrounding regions. Updating of this local grid is done at a smaller time step than the one used for the coarse grid. Interpolation between the fine and coarse grids is therefore done in both time and space.

When simulating light sensitive semiconductor devices, the standard situation is somewhat different. In this case, the required node spacing is often determined by the wavelength and the corresponding accuracy criterion mentioned above. Geometrical features are in many cases large enough to be sufficiently well represented using a grid spacing of $d < \lambda/10$, especially with nonuniform grids. Therefore, they impose no additional limits on the node spacing. However, large differences in refractive index normally impose strongly varying upper limits on the node spacing in the various regions. Since, on the other hand, the maximum time step which allows stable operation of the FDTD algorithm is governed by the "optically" smallest cell (where "optical size" is given by the product of dimension and refractive index), the fine resolution in the low refractive index inherent to standard FDTD on RTPGs leads to an unnecessarily small overall time step. These two effects considerably limit the size of structures that can be simulated within reasonable computation time for given memory resources.

In this article, we present an interpolation/integration scheme which interfaces FDTD grids with different node spacings along nonplanar material interfaces, thus allowing to adapt the node spacing in homogeneous domains to the corresponding refractive index. This way, the "optical" node spacing can be chosen constant throughout the entire simulation domain, leading to a common upper limit for the stable time step. Therefore, the same time step can be used for both grids, i.e. no temporal sub-sampling has to be carried out in the high resolution domain. The scheme presented is an extension of a formulation for grid interfacing at planar material boundaries [12].

2 Derivation and Implementation

In this section, we derive an algorithm for coupling two FDTD grids with different node spacing along a material interface in 2D.

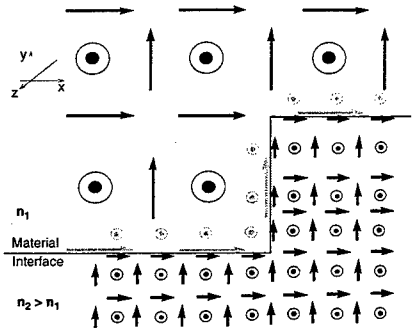

Figure 2: Non-planar FDTD grid interface.

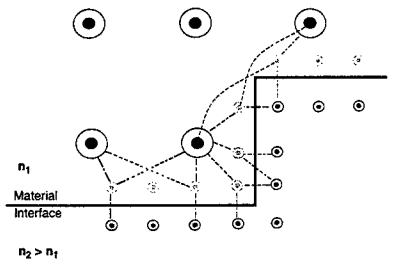

Figure 3: Interpolation of E_z field components

Throughout the rest of this article we assume that we have two homogeneous regions k ($k = 1, 2$) with refractive indices $n_1 < n_2$, whose common boundary can be represented by a staircase line. Both regions are supposed to have the same magnetic permeability μ. It is assumed that Region k is meshed by a rectilinear FDTD grid, Grid k. In what follows, superscript indices will be used to denote the grid the components and coordinates belong to. The grids have to be set up

in such a way that they have H-components (for TM polarization) along the material interface to be modeled. Node spacing may be nonuniform in both grids, so the latter requirement is not an overly strict limitation as long as minimum feature sizes are of the same order of magnitude as the wavelength of the excitation signal. Fig. 2 shows a detail of a non-planar interface region between two grids which contains all the possible interpolation scenarios that may appear in 2D and shows all the components that will be required for the interfacing process are. Note that the actual location of the vectors in the x-y-plane is in their centers, not at their feet points, for reasons of drawing. As indicated in the Figure, grids have to be truncated in such a way that for each H^2-component on the material boundary there is at least one adjacent E^2-component located within Region 1. All Grid 2 field components within Region 2 and all H^2-field components on the region boundary are updated by the standard Yee [13] algorithm, also all Grid 1 components within Region 1. We will refer to these components as regular grid components, they are drawn in black in Fig. 2. All the remaining field components will be referred to as irregular; the components depicted in grey in Fig. 2 are all irregular.

To explain our interpolation scheme, we shortly review the Yee scheme for time stepping in standard FDTD. Starting from Maxwell's equations in integral form

$$\frac{\partial}{\partial t}\int_S \boldsymbol{E} d\hat{\boldsymbol{S}} = \frac{1}{\epsilon}\oint_{\partial S} \boldsymbol{H} ds - \frac{1}{\epsilon}\int_S \boldsymbol{J} d\hat{\boldsymbol{S}} \quad (1)$$

$$\frac{\partial}{\partial t}\int_S \boldsymbol{H} d\hat{\boldsymbol{S}} = -\frac{1}{\mu}\oint_{\partial S} \boldsymbol{E} ds \quad (2)$$

one can derive the standard FDTD update equations for the electric field

$$E_z|_{i,j}^{n+1} = c_a E_z|_{i,j}^{n} + c_b\Big(H_y|_{i,j} - H_y|_{i-1,j} + H_x|_{i,j-1} - H_x|_{i,j}\Big)\Big|^{n+1/2} \quad (3)$$

with $c_a = [1 - \sigma_k\Delta t/(2\epsilon_k)][1 + \sigma_k\Delta t/(2\epsilon_k)]^{-1}$, $c_b = \Delta t/(\epsilon_k d_k)[1 + (1+\sigma_k\Delta t)/(2\epsilon_k)]^{-1}$ and for the magnetic field

$$H_x|_{i,j}^{n+1/2} = H_x|_{i,j}^{n-1/2} + \frac{\Delta t}{\mu d_k}\Big(E_z|_{i,j} - E_z|_{i,j+1}\Big)\Big|^{n}$$

$$H_y|_{i,j}^{n+1/2} = H_y|_{i,j}^{n-1/2} + \frac{\Delta t}{\mu d_k}\Big(E_z|_{i+1,j} - E_z|_{i,j}\Big)\Big|^{n} \quad (4)$$

where we assumed for simplicity of notation that we have uniform quadratic grids, i.e. equal node spacings in x- and y-directions. In addition, we restrict our attention to TM polarization, i.e. the electric field in z-direction and the magnetic field components in the x- and y-directions. Generalization to both TE polarization and nonuniform grids is straightforward; in fact, what follows is not influenced by whether the involved grids are uniform or not.

When updating the H^2-field components on the material boundary according to (4), appropriate values have to be found for the E_z^2-nodes in Region 1 (i.e the grayed ones in Fig. 3). To compute these values, three surrounding regular E_z^k-components from both grids are chosen for each node. Let $A(k,i,j)$ denote the rectangle containing all points (x,y) with $x_{i,j}^k \le x < x_{i+1,j}^k$ and $y_{i,j}^k \le y < y_{i,j+1}^k$, where $(x_{i,j}^k, y_{i,j}^k)$ is the coordinate of the Grid k node $E_z^k|_{i,j}$. The value for $E_z^2|_{i,j}$ is then determined as follows:

1. Find m,n so that $(x_{i,j}^2, y_{i,j}^2) \in A(1,m,n)$. Determine the regular components in $\{E_z^1|_{m,n}, E_z^1|_{m+1,n}, E_z^1|_{m,n+1}, E_z^1|_{m+1,n+1}\}$. If three such components are found, select the two diagonally opposing one another.
2. Find the regular components in $\{E_z^2|_{i-1,j}, E_z^2|_{i,j-1}, E_z^2|_{i+1,j}, E_z^2|_{i,j+1}\}$, i.e. the direct neighbors of $E_z^2|_{i,j}$.
3. If only one regular component in each grid was found in the above steps, proceed as follows: Find the regular direct members of the regular Grid 2 component. For each of these, form a triangle with the two components found in steps 1. and 2. Select the component which forms the triangle that contains $E_z^2|_{i,j}$.

The E_z-value at $(x_{i,j}^2, y_{i,j}^2)$ can now be computed by fitting an interpolation plane through the values at the three surrounding points and determining the value at the above position. For the scheme to work properly, one has to ensure that the E-field components in both grids have been updated

before the interpolation is carried out. Fig. 3 illustrates the situations that may appear. The values for the grayed E_z-components are computed by interpolating between the values of the components connected to them by the dashed lines (for reasons of clarity, the lines are only drawn for some representative fine grid components). Note that with the above algorithm problems in finding appropriate interpolation triangles may occur if cells with large aspect ratios are present at the boundary, especially if $d1/d2 \gg 3$. However, it shall be pointed out that the idea of the index adaptive gridding scheme presented is to have as uniform and quadratic grids as possible within homogeneous regions with appropriate interfaces between. This way, optimum efficiency is achieved (see below). If large aspect ratios can nevertheless not be avoided, the algorithm can easily be extended to cope with the problems arising.

To update the E^1-field nodes adjacent to H^1-field components located on the material boundary, the values for these latter components have to be determined by averaging the values of the appropriate H^2 components on the boundary. These components are found as follows: Starting from an E^1-field node which was required for the interpolation of some irregular E^2-field values, any H_ν^2-component on the boundary adjacent to one of these E^2-field values will be taken into account in the averaging process for any H_ν^1-component on the boundary adjacent to the E^1-field node started with, where either $\nu = x$ or $\nu = x$. In the averaging process, every H_ν^2-component will be weighted with exactly the weight the adjacent E^1-field node was weighted with when interpolating the values for the irregular E^2-field value. In numerical experiments carried out, it was noticed that this averaging procedure is crucial for guaranteeing the late-time stability of the interfacing scheme. If the averaging is carried out in such a way that each H_ν^2-component on the boundary contribute only to the value of its closest H_ν^1-component, instabilities are observed after a few 10000 time steps for standard examples.

For quadratic uniform grids, optimum performance is achieved when $d_1 = d_2 n_2/n_1$ is chosen, resulting in a common Courant limit for the stable time step Δt for both grids, since stability considerations require that

$$\Delta t_i \leq \frac{d_i}{\sqrt{2}c_0/n_i} \quad . \tag{5}$$

As was pointed out in [14], this time step results in the smallest numerical dispersion error possible within a homogeneous region with refractive index n_i and a resulting phase speed of $c = c_0/n_i$. As a result, the subgridding scheme presented above not only allows more efficient computation, but also higher modeling accuracy in the presence of large refractive index variations.

3 Numerical Results

3.1 Quasi-1D Test Example

Various tests were carried out to evaluate the accuracy of the formulation presented. First, we considered a quasi 1D test example of a Gaussian pulse plane wave incident onto a planar material interfaces. For this purpose, we used uniform quadratic $l_k \times m_k$ grids with $l_1 = 2$, $m_1 = 100$, $l_2 = 6$, $m_2 = 130$ and $d_2 = d_1/3$. Periodic boundary conditions were applied at $i = 0$ and $i = l_k$. A Gaussian pulse with a maximum frequency of about $f_{\max} = c_0/(10d_1)$ was used as excitation, giving a minimum wavelength of about $10d_1$ within Region 1. $n_1 = 1$ was assumed for Region 1, several calculations were done for Region 2 filled with materials having different refractive indices n_2. Time steps were $\Delta t = \min\left(d_2 n_2/(\sqrt{2}c_0), d_1/(\sqrt{2}c_0)\right)$. The reflected fields were computed by carrying out a reference simulation with no material and grid interface present. Frequency dependent reflection coefficients were then calculated by Fourier transform and compared to analytical results. Fig. 4 (left) shows the errors in numerically computed reflection coefficients $r_{\text{FDTD}} - r_{\text{analytical}}$ for various refractive indices n_2. The results show excellent agreement between analytical and numerical results when $n_2 = 3 = d_1/d_2 * n_1$. For refractive indices $n_2 \neq 3$, the errors increased with $n_2 - 3$. Computations were also carried out using a number of smaller time steps without any significant change in results. For comparison, we also examined reflection at a material interface using a uniform fine grid with node spacing $d = d_2$

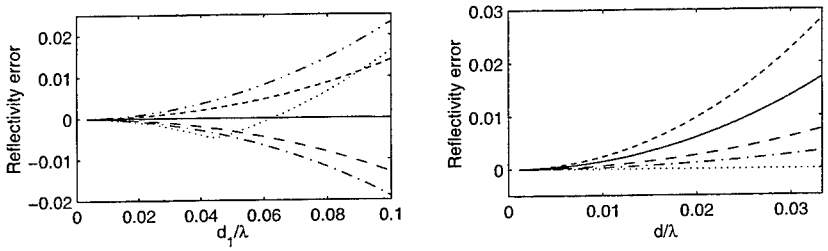

Figure 4: Errors in numerically computed reflection coefficients $r_{\mathrm{FDTD}} - r_{\mathrm{analytical}}$: $-\cdot\cdot$ $n_2 = 1$, $\cdots$ $n_2 = 1.0201$, $-\cdot$ $n_2 = 1.5$, $- -$ $n_2 = 2$, $—$ $n_2 = 3$, $- -$ $n_2 = 4$. **Left:** Material boundary at grid resolution interface. **Right:** Uniform grid with fine mesh. Note that $d = d_1/3$.

in both regions. Here, the time step used was $\Delta t = d_2/(\sqrt{2}c_0)$. The results are also shown in Fig. 4. In this case, there is obviously no conceivable error for $n_2 = 1$. With increasing difference in refractive index between the two regions, the error in the reflection coefficient increases. For the comparatively high maximum error of 0.03 for $n_2 = 4$, one has to be aware that at the corresponding wavelength λ_2 in Region 2, one has $\lambda_2/d = 7.5 < 10$, i.e. a value too small for obtaining high accuracy results.

Fig. 4 demonstrates that the most accurate results are found when the "optical" node spacing is equal in regions with different refractive index. The more unbalanced the "optical" node spacing, the bigger the errors that are obtained in the calculation. This can be thought of as an extension of results for simulation with nonuniform grids, where it was found that the spacings d_i between adjacent nodes need, as a rule of thumb, to obey $0.5d_i < d_{i+1} < 2d_i$ ($i \in \{1, l\}$ and equivalent in the other coordinate directions) to get sufficiently accurate results [1].

To assess the usefulness of the presented formulation for simulation of actual 2D problems, we first modeled the light propagation within a test structure on both a uniform grid and two adjacent grids with planar interfacing and compared the results. This time, we had $d_2 = d_1/4, l_1 = m_1 = 100, l_2 = 400, m_2 = 200$. Region 2 was assumed to be filled with a material with $n_2 = 4$, e.g. silicon. Part of Region 1 is filled with a structure consisting of a material with $n = 1.5$, e.g. silica, which extends 30 nodes in x-direction and 60 nodes in y-direction, throughout the rest of Region 1 we have $n_1 = 1$. Similar situations are often encountered in photodetector or sensor modelling, where some structure (e.g. a microlens or grating) is supposed to focus/guide light into a semiconductor substrate, which is responsible for the electronic part of light detection. Periodic boundary conditions were applied at $j = 0$ and $j = m_k$.Fig. 5 shows the intensity distribution for reflection/transmission of a Gaussian pulse plane wave with a maximum frequency of about $f_{\max} = c_0/(25d_1)$ incident on the structure/interface. For the graph on the left side, computation was carried out on a uniform mesh with $d = d_2$, for the graph on the right side, the algorithm presented was used. The results are in very good agreement.

To compare the computational effort required for the two different models, we assume that for the case with mesh interfacing, about three quarters of the computational domain are filled with the coarse grid. The total number of cells is therefore 7/16 of the total number of cells in the uniform fine grid case, resulting in a likewise decrease in memory requirements. The number of update steps necessary to reach a given state reduces to 1/4 of that for the uniform grid. Together, this results in a decrease in computation time by a factor of about 8.

3.2 2D Non-planar Interface

To assess the usefulness of the presented formulation for simulation of actual 2D problems, we modeled the light propagation within a test struc-

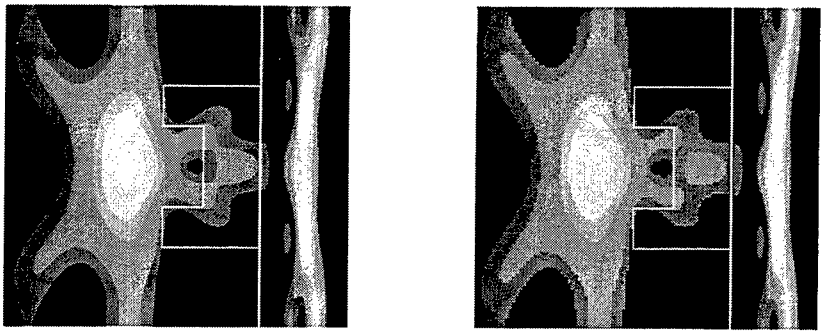

Figure 5: Planar grid interface: Intensity distribution for a Gaussian pulse plane incident on a structure on top of a planar material interface. The high refractive index region is to the right of the thick white line, the plane wave is incident from the left (i.e. traveling in $+x$-direction. Results for a uniform fine grid (left) are compared to results obtained by using a coarser grid in Region 1 (right). Contour lines are at the same intensity levels in both plots.

ture on both a uniform grid and two adjacent grids with interfacing and compared the results. For the refractive indices, it was assumed that $n_2 = 3n_1$. Uniform node spacing was chosen in both grids with $d_2 = d_1/3$. The time dependence of the incoming plane wave was of the form $\sin(\omega t)\exp(-t^2/a^2)$, with ω and a chosen in such a way that the maximum of the wavelength spectrum is at $\lambda = 20d_1$ and the minimum wavelength at $\lambda \sim 10d_1$ (both in Region 1). Periodic boundary conditions were applied at $j = 0$ and $j = m_k$. The structure to be considered consists of a wedge shaped non-planar interface. The wedge is $105d_2$ in x-direction and $59d_2$ in y-direction. Fig. 6 shows the intensity distribution for reflection/transmission of the incident wave at the interface. Fig. 7 shows a cut through the plots from Fig. 6 along the x-direction at y-nodes $j = 20$ and $j = 90$. All the results are in good agreement. As for the deviations conceivable, one has to bear in mind that in the quasi-1D example more accurate results were obtained when simulating with the interfaced grids.

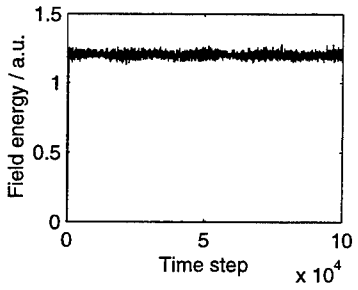

Figure 8: Demonstration of numerical stability: The field energy in a closed resonator with a subgrid region is shown for 100000 time steps. No instabilities can be observed. If instabilities were present, an increase of field energy with time would result.

3.3 Stability

As was mentioned above, an appropriate combination of interpolation and averaging is necessary to ensure the late-time stability of the method presented. In [11], conditions for the stability of subgridding schemes are given, which, however, are only sufficient but not necessary. A detailed eigenvalue analysis of the updating scheme presented would go beyond the scope of this article. We therefore restrict to demonstrating the numerical stability of the method by presenting simulation results for a suitable test structure. We used a resonator that is terminated by perfectly conducting

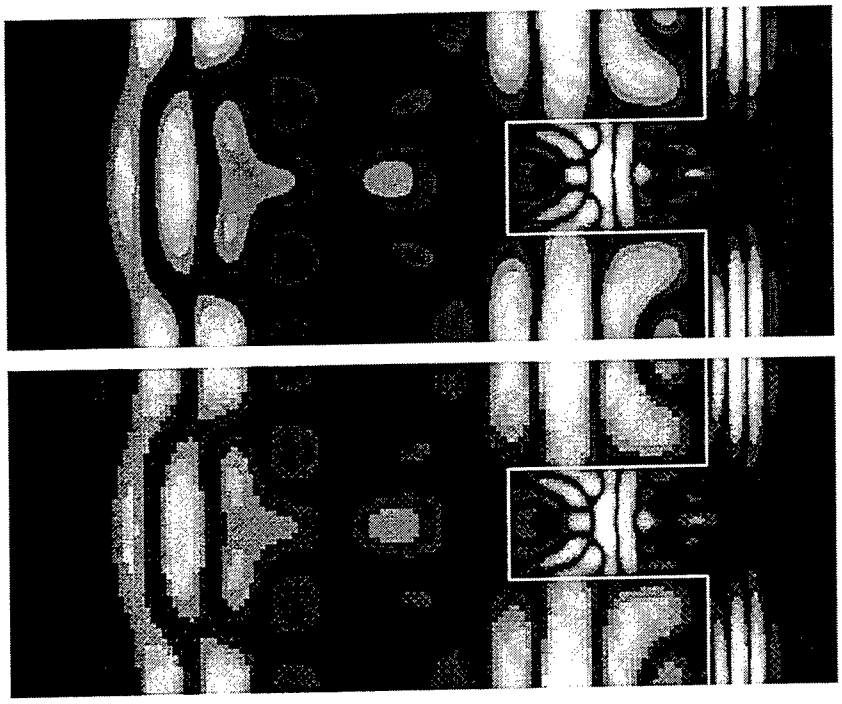

Figure 6: Non-planar grid interface: Electrical field for reflection/transmission of a plane wave at a non-planar region interface (white line), computed on a uniform fine mesh (top) and on two grids with different node spacing interfaced at the boundary. Contour lines are at equal levels in both plots.

walls on all four sides. The resonator is assumed to be filled with vacuum ($n_1 = 1$) and meshed by Grid 1 with dimensions $l_1 = m_1 = 60$. An 8×8-node region located at $i, j = (10, 10)$ contains a material with refractive index n_2 and is meshed by Grid 2 with $d_2 = d_1/n_2$. Simulations were carried out for $n_2 = 3$ and $n_2 = 5$. In both cases, the common Courant limit given by Eq. (5) was used to time advance both grids. The electromagnetic field was introduced by a dipole excitation, with the same time dependence as in the previous section, i.e. with a minimum wavelength of $\lambda \sim 10 d_1$ in Region 1. Fig. 8 shows the electromagnetic field energy in the resonator, obtained by numerically integrating the energy density $(\epsilon \boldsymbol{E}^2 + \mu \boldsymbol{H}^2)/2$ over both regions, for the $n_2 = 5$ case. No increase or decrease in the field energy can be observed. If stability were violated, this would result in an increase of field energy with time. The small oscillations are of numerical nature, they have also been observed for standard FDTD on a single grid. Equivalent results were found for the $n_2 = 3$ case.

4 Conclusions

A new algorithm for refractive index adaptive gridding in standard FDTD has been presented. This algorithm can greatly reduce the computa-

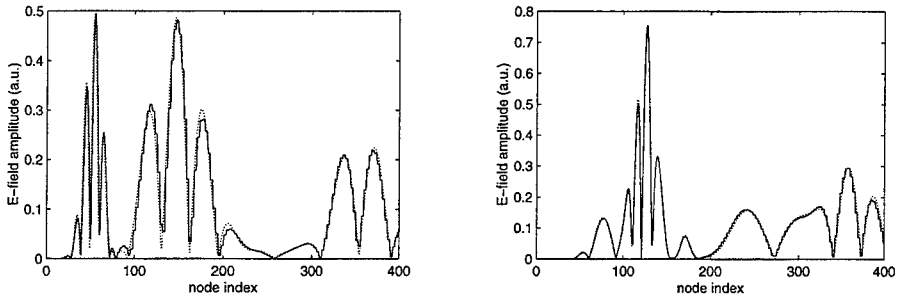

Figure 7: Cut through the plots from Fig. 6 along the x-direction at y-nodes $j = 20$ (left) and $j = 90$ (right). The solid line corresponds to the solution obtained using two interfaced grids with different node spacing. The dotted line was found by using a uniform grid with fine resolution.

tional effort when modelling structures with homogeneous regions with strongly differing refractive indices, which are frequently encountered when simulating light sensitive semiconductor devices. In addition, when choosing appropriate node spacing, the algorithm gives more accurate results for reflection at planar material interfaces than standard FDTD. This was found by comparison to analytical results. The numerical stability of the scheme presented has been demonstrated by means of test examples. The method has recently been extended to 3D, however, optimum implementation and stability issues are still under research.

5 Acknowledgments

This work was supported by the Swiss Commission for Technology and Innovation (KTI), project 3193.1.

References

[1] Allen Taflove. *Computational Electrodynamics — The Finite-Difference-Time-Domain Method.* Artech House, 1995.

[2] A. Mekis, J. C. Chen, I. Kurland, S. Fan, P. R. Villeneuve, and J. D. Joannopoulos. *Physical Review Letters*, 77:3787–3790, October 1996.

[3] J. Yamauchi, H. Kanbara, and H. Nakano. *IEEE Photonics Technology Letters*, 10:111–113, January 1998.

[4] L. Thode, G. Csanak, R. Hotchkiss, C. Snell, and M. Campbell. In *Proc. SPIE – Int. Soc. Opt. Eng*, volume 2399, pages 348–359, San Jose, CA, February 1995.

[5] T. Sterkenburgh, R. M. Michels, P. Dress, and H. Franke. *Applied Optics*, 36(6):1191–1197, 1997.

[6] B. Witzigmann, P. Regli, and W. Fichtner. *Journal of the Optical Society of America A*, 15:753–757, 1998.

[7] L. H. Bomholt, P. Regli, T. O. Körner, and W. Fichtner. In *Proceedings of the 4th European Conference on Radiations and their Effects on Circuits and Systems*, Cannes, France, 1997.

[8] M. J White and M. F. Iskander. *IEEE Trans. Antennas Propagat.*, 45(10):1512–1517, October 1997.

[9] M. W. Chevalier, R. J. Luebbers, and V. P. Cable. *IEEE Trans. Antennas Propagat.*, 45(3):411–421, March 1997.

[10] M. Okoniewski, E. Okoniewska, and M. A. Stuchly. *IEEE Trans. Antennas Propagat.*, 45(3):422–429, March 1997.

[11] P. Thoma and T. Weiland. *Int. J. Numerical Modelling*, 9(5):359–374, 1996.

[12] T. O. Körner and W. Fichtner. *Microwave and Optical Technology Letters*, 19(5):368–370, 1998.

[13] K. S. Yee. *IEEE Trans. Antennas Propagat.*, 14(3):302–307, March 1966.

[14] A. C. Cangellaris and R. Lee. *J. Electromagn. Waves Applicat.*, 6(12):1635–1653, 1992.

CHARACTERIZING MEANDER LINE ANTENNAS FOR RF AND WIRELESS COMMUNICATIONS USING THE FDTD TECHNIQUE

Chun-Wen Paul Huang, Jiang-Bin James Chen, Atef Z. Elsherbeni, and Charles E. Smith
Electrical Engineering Department, The University of Mississippi
University, MS 38677

Abstract

Printed small antennas are becoming the main subject of investigation for improved performance of personal wireless communication systems. In recent presentations a new type of printed meander line antenna is introduced. In this paper, the analysis of this type of antenna is performed using the finite difference time domain technique. Empirical design equations are obtained for the resonant (operating) frequency and the corresponding input impedance. Sample of the new designs provide antennas with good matching impedance to a 50 Ω system and a dual band operation.

Introduction

With the advancements of modern integrated circuit technologies, personal communication systems (PCS) are the fast growing sections of the present telecommunication industry. Modern designs of wireless personal communication systems are featured in light weigh, small size, high frequency operation, and high transmission efficiency. Mobile antenna design is one of the major tasks in PCS designs. In addition to the general features needed for PCS antennas for mobile personal communications, there is also a requirement that the antenna be easily integrated with the interior circuitry of the system. One of the most widely used wireless communications systems is the global system for mobile (GSM) communications, which operates at 890-915 MHz for uplink and 935-960 MHz for downlink. The new generation of personal communication systems, such as digital communication systems (DCS) 1800, operates at 1.710-1.785 GHz for uplink and 1.805-1.880 GHz for downlink. Therefore, antennas for current personal communication systems are required to operate at the frequency range form 0.9 GHz to 2.0 GHz. If the future use of higher frequency PCS and the possibility of applying PCS for military purposes are considered, then antenna designs for wireless personal communication systems should be expanded in scope to cover the frequency range from the current 0.9-2.0 GHz to 0.9-2.5 GHz range. In this paper, studies for the characteristics of a printed meander line antenna [1-5], using the finite difference time domain (FDTD) [6] techniques with

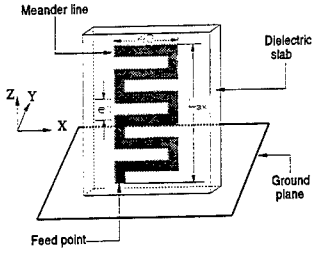

Figure 1 A meander line antenna on a small ground plane.

Berenger's perfectly matched layers (PML) [7] absorbing boundaries are presented. The presented designs of the antenna shown in Fig 1, feature small dimensions (77 x 11 x 3.17 mm^3), approximately 50 Ω input impedance, dual frequency band, and operate within the 0.9-2.5 GHz range on a comparably small ground plane (60 x 27 mm^2). One of the validations of the numerical code used in this investigation is made by computing the return loss of a rectangular printed patch antenna and comparing the numerical results with the computed and measured data reported in [8, 9]. Empirical design equations and the analysis for the input impedance and resonance frequencies of meander line antennas are also provided.

Analysis

The antenna considered in this investigation, as shown in Figure 1, is a meander line trace printed on a dielectric slab sitting on a perfectly conducting ground plane. The parameters e1 and e2 represent the lengths of the vertical and horizontal printed traces, respectively. In this study, e1 and e2 are chosen to be 3 mm, and the width of the printed trace is 1mm. The parameter L_{ax} is the vertical length of the meander line. The distance between the edge of the dielectric slab and the edge of the ending segment of the meander line is set equal to e1. The reason for modeling the meander line antenna on a small ground plane (60 x 27 mm^2) is to simulate its performance when this antenna is placed on top of a PCS handset. The main objective of this research is to design a meander line antenna with 50 Ω input impedance at dual operating frequencies within 0.9 to 2.5 GHz. Other important parameters are to minimize the size of the dielectric slab and the ground plane. The frequency range under study is extended form 0.9-2.5 GHz to 0.5 -3.0 GHz for clearer observations of the resonance behavior of the antenna.

The finite difference time domain (FDTD) technique is applied to model the antenna inside a 3 dimensional air chamber terminated with the artificial boundaries of Berenger's perfectly matched layers (PML) [7]. The PML is adopted to reduce the numerical reflection from the truncated boundaries of the finite problem space, which resembles the anechoic chamber for antenna measurements. An array of voltage sources with a Gaussian waveform are placed between the ground plane and the edge of the first vertical segment of the trace line for excitations.

To begin the meander line antenna design, the width (W_s) and thickness (t_s) of the dielectric slab are set to 3.17 mm and 11 mm, respectively. The changes in impedance and resonant frequency are observed by increasing the number of segments of the meaner line trace gradually until the design goal is achieved. The effects of dielectric constant, the width of the slab, and thickness of the slab are also studied. In this simulation, the values of the dielectric constant are 2.2, 3.1, 4.1, 7.1, and 10.2, while the thicknesses of dielectric slab are 0.794,1.588, 3.175, 4.763, and 6.35 mm. These values represent commonly used materials for radio frequency (RF) and microwave circuit boards. The width of the dielectric slab is varied from 11 to 41 mm which is an appropriate width to be incorporated with a PCS handset. From these numerical experiments, empirical equations are derived to facilitate the design procedure.

Numerical Results

The computation of the return loss of a rectangular patch antenna presented in [8] as shown in Figure 2 is reported here as a validation for the developed code. The FDTD cell discretization and the dimensions of this patch antenna can be found in [8]. In Figure 2, good agreement between the computed numerical results and the published computed and measured

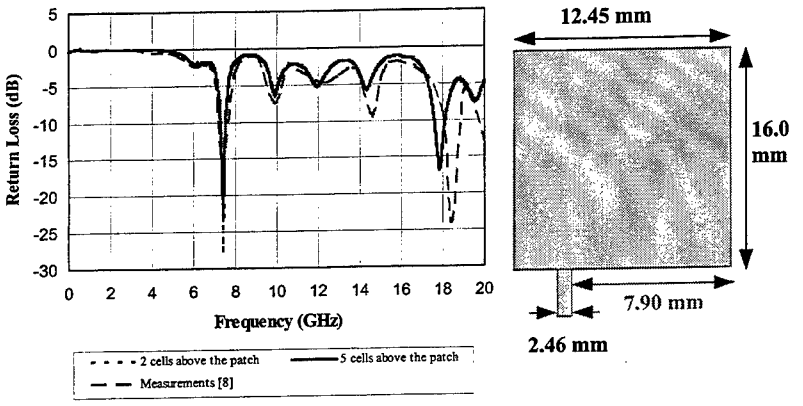

Figure 2 The Return loss of a rectangular patch antenna.

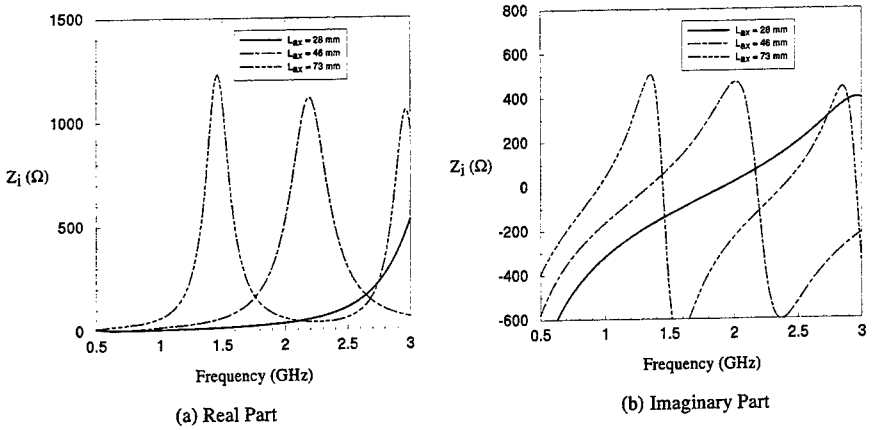

(a) Real Part

(b) Imaginary Part

Figure 3 The input impedance of a meander line antenna versus L_{ax}.

data are observed. The necessary number of layers of air buffer between the patch antenna and the PML is also illustrated in this example. Reference [9] presents results obtained by placing 10 cells of PML on top of 5 cells of air above the patch and 3 cells of air away from the edge of the patch. In this paper, the number of PML cells used in all numerical cases is 8. In Figure 2, negligible difference is observed due to the placement of the PML cells 2 and 5 cells away from the top surface of the patch. Therefore, the PML can be placed very close to the antenna under study as concluded in [7 and 9], which allows more computational resources for the problem space.

The input impedance of the initial design (t_s = 3.17 mm and W_s = 11 mm) of the meander line antenna for various numbers of segments are plotted in Figure 3. As shown in the Figure, the increase of L_{ax} decreases all the resonant frequencies but increases the resonance impedance. Additionally, an optimal case was found when using a length of 48 segments (73 mm for L_{ax}), where the input impedance at the first and third resonance frequency is 48.5 Ω and 44 Ω, respectively. This design shows that the antenna can operate at both 0.95 and 2.39 GHz and can adequately be matched to the traditional 50 Ω impedance of the front-end circuitry. This 50 Ω impedance characteristic should simplify the system components by removing the impedance matching network between the feed and the antenna. The return loss using different lengths of L_{ax} are plotted in Figure 4, which shows that the bandwidths of this case are 8 % and 4 %, respectively. The empirical equations for the first resonance frequency and impedance for various values of L_{ax} are derived from regression curve-fit of the data plotted in Figure 5 and 6, respectively. In Figure 5, the regression curve is also compared to the first resonant frequency computed by the empirical equation presented in [1, 3, 5], which define the length shortening ratio as

$$SR = \frac{\lambda/2 - 2L_{ax}}{\lambda/2} \tag{1}$$

Reference [5] suggests using a shortening ratio between 33% and 35% for computing the first resonant frequency of meander line antennas. From Figure 5, the resonant frequency computed by equation (1) departs from the currently presented regression curve as L_{ax} increases. The empirical equations for the first resonant frequency of meander line antennas using 1 mm trace, e1 = e3 = 3mm, t_s = 3.17 mm and W_s = 11 mm, on a 60 x 27 mm^2 ground plane is

$$f_o = 22.69 L_{ax}^{-0.7392} \tag{2}$$

and whose first resonant impedance as shown in Figure 6, can be modeled by

$$Z_o = 22.941 e^{0.0103 L_{ax}} \tag{3}$$

These new equations (1) and (2) can not only be used to solve for possible L_{ax} when a desired impedance is specified, but also to predict the first resonant frequency and impedance for a chosen L_{ax}.

In addition to changing L_{ax}, different values of the substrate dielectric constant are adopted to examine their influence on both resonant frequency and impedance in the optimal case. From Figures 7 and 8, both resonant frequency and impedance decrease with the increase of the dielectric constant. The effects on resonant frequenies are not as strong as that on the impedance.

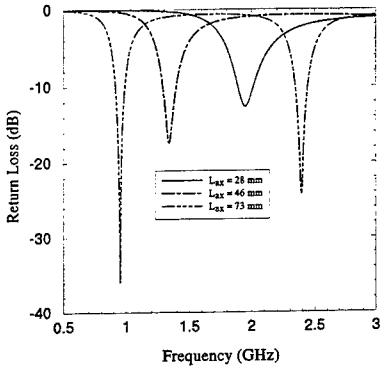

Figure 4 The return loss of a meander line antenna versus L_{ax}.

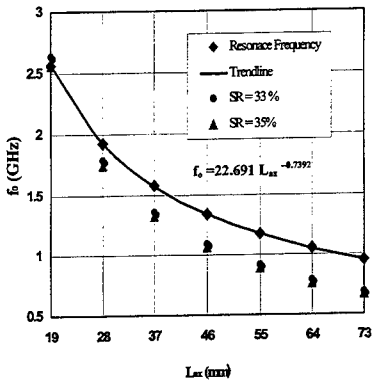

Figure 5 The first resonant frequency of a meander line antenna versus L_{ax}.

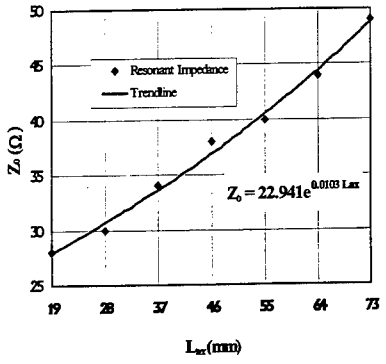

Figure 6 The first resonant impedance of a meander line antenna versus L_{ax}.

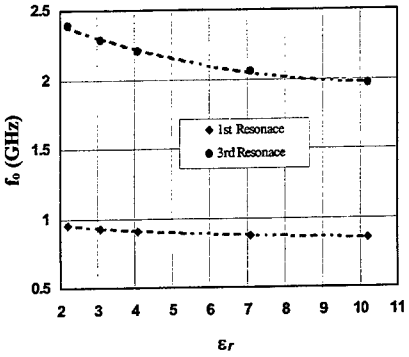

Figure 7 The first and third resonant frequencies of a meander line antenna versus the substrate dielectric constant.

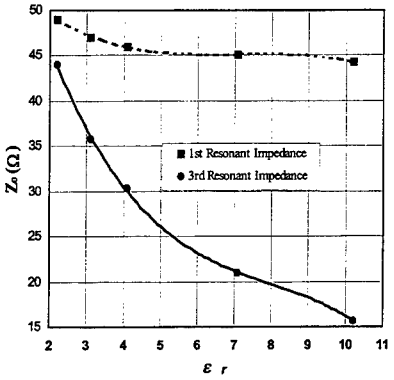

Figure 8 The first and third resonant impedance of a meander line antenna versus the substrate dielectric constant.

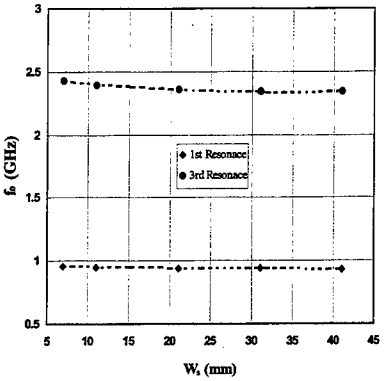

Figure 9 The first and third resonant frequencies of a meander line antenna versus the substrate width.

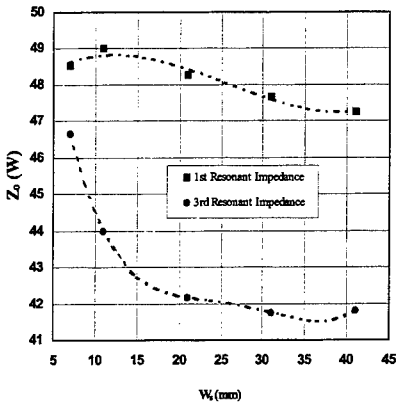

Figure 10 The first and third resonant impedance of a meander line antenna versus the substrate width.

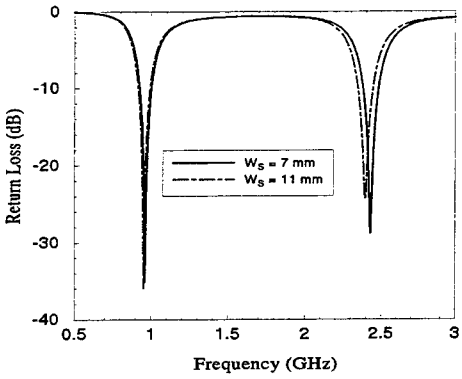

Figure 11 Dual band 50 Ω meander line antennas.

The effects of width of the dielectric slab are also investigated. From Figure 9, the variations of the first and third resonant frequencies due to the change of slab width are insignificant. However, the effects on the resonant impedance are clearly noticable. From Figure 10, the increase of the slab width casued the reduction of the resonant impedance. Furthermore, reducing the slab width from 11 mm to 7 mm results in another useful case with 48.53 and 46.66 Ω for the first and third resonances as shown in Figure 10. Transfering this impedance information into return loss, results in a return loss of 35.2 dB with 8% bandwith and 28 dB with 3% bandwidth for the first and third resonances, respectively as shown in Figure 11. In this design, the slab width is only 4 mm more than the width of the meander line trace. From these results, an appropriate method for fine-tuning the resonant impedance can be made by adjusting the slab width, which is also feasible in antenna realizations.

Finally, the effect of the dielectric slab thickness is also investigated. It is found that the thickness of the dielectric slab affects the resonant frequencies within 0.02 GHz for the first resonace and 0.1 GHz for the third resonace as shown in Figure 12. However, the resonant impedance of the first and third modes is changed over a range of 10 Ω as shown in Figure 13. Therefore, the variation in slab thickness does not apear to be an effictive procedure to fine-tune the meander line antenna.

Conclusions

A detailed investigation for optimizing the meander line antenna for personal wireless communication has been presented. Empirical equations are obtained and used to achieve a design in which an external matching network is not necessary. An additional fine tuning for the resonant frequency and impdeance can be achieved by varying the slab width. Future studies will be focused on the optimization of the radiation pattern parameters.

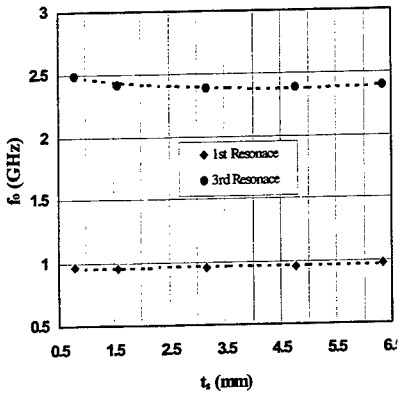

Figure 12 The first and third resonant frequencies versus the substrate thickness.

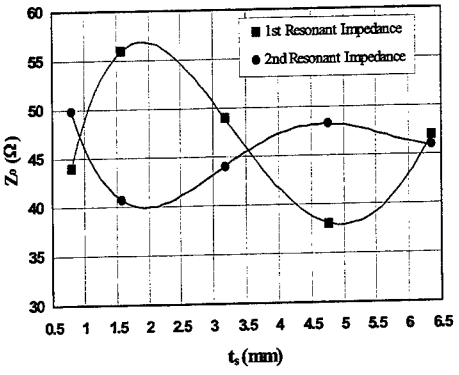

Figure 13 The first and third resonant impedance versus the substrate thickness.

References

[1] H. Nakano, H. Tagami, A. Yoshizawa, and J. Yamauchi, "Shortening ratio of modified dipole antennas," *IEEE Trans. Antennas Propagat.*, vol. AP-32, no. 4, pp. 385-386, April 1984.

[2] M. Ali, S. S. Stuchly, and K. Caputa, "A wide-band dual meander-sleeve antenna," *Journal of Electromagnetic Waves and Applications,* vol. 10, no. 9, pp. 1223-1236, 1996.

[3] K. Noguchi, M. Mizusawa, T. Yamaguchi, and Y. Okumura, "Numerical analysis of the radiation characteristics of the meander line antennas consisting of two strips," *IEEE AP-S Digest,* pp. 1598-1601, 1996.

[4] M. Ali, S. S. Stuchly, and M. Okoniewski, "Characterization of planar printed meander line antennas using the finite difference time domain technique," *IEEE AP-S Dig.,* pp. 1546-1549, 1997.

[5] A. Z. Elsherbeni, J. Chen, and C. E. Smith, "FDTD analysis of meander line antennas for personal communication applications," *PIER Meet. Dig.,* 1997.

[6] K. S. Yee, "Numerical solution of initial boundary value problems involving Maxwell's equations in isotropic media," *IEEE Trans. Antennas Propagat.,* vol. 14, pp. 202-307, 1966.

[7] J. P. Berenger, "A perfectly matched layer for the absorption of electromagnetic waves," *J. Computat. Phys.,* Oct. 1994.

[8] D. M. Sheen, S. M. Ali, M. D. Abouzahra, and J. A. Kong, "Applications of the three-dimensional finite difference time domain method to the analysis of planar microstrip circuits," *IEEE Trans. Microwave Theory Tech.,* vol. 38, no. 7, pp. 849-856, July 1990.

[9] S. D. Gedney, "An isotropic perfectly matched layer-absorbing medium for truncation of FDTD lattices," *IEEE Trans. Antennas Propagat.,* vol. 44, no.12, pp. 1630-1639, Dec.1996.

Impulse response of microwave devices by FDTD and moment expansion

Gaetano Marrocco Fernando Bardati
Dipartimento di Informatica Sistemi e Produzione, Università di Roma "Tor Vergata"
Via di Tor Vergata - 00133 Roma (ITALY)
e-mail marrocco@disp.uniroma2.it

Abstract: A simple deconvolution algorithm, based on a fourth-order moment-expansion, is presented to compute the impulse response of FDTD-modelled microwave devices. The algorithm is useful to characterize a structure by its impulse response matrix as needed by segmentation techniques, such as diakoptics, and to integrate data from electromagnetic field analysis into circuit simulations. The algorithm has been tested on microwave planar devices with satisfactory accuracy.

I. Introduction

The Finite Difference Time Domain method [1] proved to be an efficient and accurate tool for the modeling of microwave devices such as guiding and radiating structures. Moreover, by local modification of the standard algorithm, lumped linear and non-linear elements can be easily included in a model. However, finite computer resources limit the application of the algorithm to the analysis and optimization of small structures. Furthermore, instabilities and accuracy loss are experienced for large domains. Recently the method has been extended to larger systems by taking advantage of segmentation techniques such as the time-domain diakoptics [2,3]. In the last method a large structure is preliminary segmented into smaller modules, each one being simulated individually and then characterized with its impulse-response matrix. The whole structure is therefore analyzed as a module interconnection via interfaces performing convolutions between individual responses. Therefore, the accurate computation of the impulse response of a microwave device can play a very important role in the analysis of a composite structure. Moreover the knowledge of the impulse response allows the deembedding of equivalent lumped circuits [4,5] and therefore can be considered as a gate towards the integration into circuit simulations of data obtained from electromagnetic field analysis.

In this contribution the problem of the impulse-response computation by FDTD is investigated. Emphasis will be devoted to the selection of the input waveform with respect to FDTD accuracy and bandwidth. A simple deconvolution algorithm, based on a moment expansion, will be presented. This method performs a pure time-domain processing of the device time-response for suitable FDTD input waveforms while, ill-conditioned inverse Fourier transforms are avoided. Examples are given for a patch antenna and a planar low-pass filter.

II. Statement of the problem

Consider an N-port microwave device. At each input port (Fig. 1), which can be either a cable/microstrip transition or a waveguide connection, an input variable is an impressed voltage generator (voltage port) or an impressed current generator (current port) or an inward modal field distribution (modal port). At each output port, variables are physical currents or voltages, or outgoing mode amplitudes when the port is closed on a matched load.

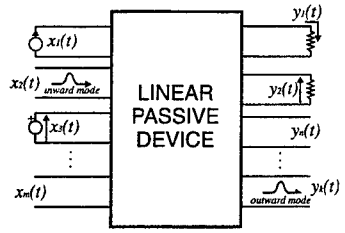

Fig. 1: *N-port microwave linear passive device. Input and output variables are time-domain signals*

Let $x_m(t)$ be a band-unlimited (time-dependent) excitation at the m-th port and $y_n(t)$ the output waveform at the n-th port. If the device is causal, passive and is governed by linear differential equations with constant coefficients, the following convolution integral holds:

$$(1) \qquad y_n(t) = \int_0^t x_m(\tau) h_{mn}(t-\tau) d\tau = x * h(t)$$

where $h_{mn}(t)$ is the impulse response between the m-th and n-th ports. $h_{mn}(t)$ can be formally defined as:

$$(2) \qquad h_{mn}(t) = \mathcal{F}^{-1}\left[\frac{Y_n(\omega)}{X_m(\omega)}\right]$$

where $\mathcal{F}^{-1}$ is the inverse Fourier transform, $X_m(\omega) = \mathcal{F}[x_m(t)]$ and $Y_n(\omega) = \mathcal{F}[y_n(t)]$. If FDTD is used, the Fourier transform of $y_n(t)$ is performed on data sampled at time $k\,\Delta t$, where Δt is the FDTD time-step.

The impulse response can be obtained directly in time domain by solving an integral equation (Eq.1) or by frequency-domain manipulations and Fourier processing (Eq.2). In either case, the accuracy of the impulse-response computation depends on both the input signal waveform and the FDTD accuracy. Numerical noise is mainly caused by numerical dispersion [6], boundary staircasing, approximation of numerical derivatives and imperfect grid termination.

Since the FDTD method performs a numerical finite approximation of an electromagnetic boundary value problem, the computation of $Y_n(\omega)$ is less accurate outside a frequency band $B_m = [f_{min}^{FDTD}, f_{max}^{FDTD}]$. The highest frequency depends on spatial discretization since, for a rectangular grid with largest cell size Δ, the shortest wavelength which can be accurately resolved is such that $\lambda_{min} \geq n\Delta$ with $n = (8 \div 10)$ and therefore $f_{max}^{FDTD} = c/n/\Delta$. A lower bound of FDTD bandwidth exists since, to accurately model slow field oscillations, the simulation should be carried on for a large number of iterations, but the numerical noise limits the simulation time-window. Though not directly quantifiable, f_{min}^{FDTD} is generally one or two order of magnitude lower than f_{max}^{FDTD}.

Therefore, the input waveform for FDTD computation, must be properly chosen in order to extract the maximum information in the band of the numerical algorithm. Moreover, the errors in $Y_n(\omega)$ are amplified by $1/X_m(\omega)$ depending on frequency, unless $x_m(t)$ is a Dirac pulse.

Generally, smooth, narrow pulses such as the Gaussian $x_G(t)$, the Modulated-Gaussian $x_{MG}(t)$ or the Derivated-Gaussian $x_{DG}(t)$ are appropriate FDTD excitations:

(3') $x_G(t) = e^{-\frac{(t-\tau)^2}{2T^2}}$

(3'') $x_{MG}(t) = sin(2\pi f_0 t) e^{-\frac{(t-\tau)^2}{2T^2}}$

(3''') $x_{DG}(t) = -\frac{t-\tau}{T} e^{-\frac{(t-\tau)^2}{2T^2}}$

It is possible to set up the desired time-domain and frequency-domain signal features by selecting the parameters T, τ and f_0. The Gaussian pulse (3'), though very short in the time domain, has a DC peak of spectral energy density. As a consequence, an important amount of energy excites those spectral components (of the electromagnetic structure response) which can not be accurately predicted by the finite band-width of the FDTD method. On the contrary, the modulated Gaussian pulse (3'') is well suited to perform high-frequency analysis and the excitation band can be properly tuned on the FDTD band-width. The drawback of this excitation is the high number of oscillations in the time domain which often cause a long settling time for the FDTD solution. An interesting compromise is the derivated Gaussian pulse (3''') which has a small low-frequency energy distribution and only two oscillations.

III. Deconvolution by moment expansion

Several stable algorithms are available [7,8] to solve general deconvolution problems with both discrete and continuous data without direct use of Eq.(2). However, if the input waveforms are those commonly used with FDTD method, the impulse response can be accurately approximated by a simple formula involving pure time domain quantities and operations. The Moment Expansion method can be applied in the form introduced by Papoulis [9] for image restoration and extended to the specific application. Papoulis' algorithm works properly when $x_m(t)$ takes significant values within an interval that is small compared with the variations of $y_n(t)$. This normally applies when a Gaussian or a Derivated-Gaussian waveform are used. The input-signal spectrum can be expressed, for any $t_o > 0$, by means of the following moment expansion:

(4) $$X_m(\omega) e^{j\omega t_0} = \sum_{k=0}^{+\infty} \frac{\mu_k}{k!} (-j\omega)^k$$

where the k-th moment of $x_m(t - t_0)$ is computed as:

(5) $$\mu_k = \int_{-\infty}^{+\infty} (t - t_0)^k x_m(t) dt = \sum_{p=0}^{k} \binom{k}{p} (-t_0)^{k-p} (j)^p \frac{d^p X_m(\omega)}{d\omega^p}_{|\omega=0}$$

A similar expansion holds for $[X_n(\omega) e^{j\omega t_0}]^{-1}$ with moments $\{a_\ell\}$ obtainable from $\{\mu_k\}$. A time domain formula for $h_{mn}(t - t_0)$ can be obtained from Eq.(2) as:

(6) $$h_{mn}(t - t_0) = \sum_{\ell=0}^{\infty} \frac{a_\ell}{\ell!} \mathcal{F}^{-1}\left[(-j\omega)^\ell Y_n(\omega)\right]$$

Finally, it easily shown that the impulse response can be written as the following series:

$$h_{mn}(t) = \begin{cases} \left[a_0 \int_0^{t+t_0} d\tau + a_2 \frac{1}{2!}\frac{d}{dt} + a_4 \frac{1}{4!}\frac{d^3}{dt^3} \cdots \right] y_n(t+t_0) \\ \left[a_0 - a_2 \frac{1}{2!}\frac{d^2}{dt^2} - a_3 \frac{1}{3!}\frac{d^3}{dt^3} + a_4 \frac{1}{4!}\frac{d^4}{dt^4} + \cdots \right] y_n(t+t_0) \end{cases} \quad (7)$$

when $x_m(t)$ has zero or non-zero mean, respectively.

The above series are rapidly convergent [9]. The numerical differentiation of discrete data is more and more inaccurate with the increase of the differentiation order. Therefore, only few terms are retained for reasonable accuracy. A second-order truncation of Eq.(7) was suggested in [9]. Instead, we found that a fourth-order truncation produced better results for FDTD analysis of microwave devices with Gaussian and Derivated-Gaussian excitation in Eq.(3). Accordingly, by choosing $t_0 = \tau$ the first non-zero moments are reported in TAB. I.

TAB. I: Moment Expansion coefficients

	Gaussian pulse	Derivated-Gaussian pulse
a_0	$\frac{1}{\sqrt{2\pi}T}$	$\frac{1}{\sqrt{2\pi}T^2 e^{1/2}}$
a_2	$-a_0 T^2$	$-a_0 T^2$
a_4	$3a_0 T^4$	$6a_0 T^4$

IV. Numerical Examples

Two numerical examples are reported. A multilayer patch antenna and a microstrip low-pass filter were modeled by an FDTD code [10] and impulse responses were computed at different ports of the structures.

Patch Antenna - A coaxially-fed stacked patch antenna (Fig. 2a) was FDTD modeled by means of a non-uniform grid with cell size $0.9mm \leq \Delta x, \Delta y \leq 1.8mm$ and $0.3mm \leq \Delta z \leq 1mm$. A simple model of the transition between coaxial cable and ground plane [11] was a real voltage generator with a series lumped resistor $R_0 = 50\,\Omega$ which is equivalent to the characteristic resistance of the cable. The grid was terminated by 6 cell PML absorbing boundary conditions. The time waveform, $v_0(t)$, of the voltage generator was a Derivated-Gaussian pulse with $\tau = 65ps$ and half-power bandwidth $[1.7GHz, 10GHz]$ which is wide enough to predict the first antenna resonances for standard working conditions ($2.4\ GHz$ to $3.4\,GHz$). This structure can be considered as a one-port device. The output variable is the current $i(t)$ at the source point. The current $i(t)$ is computed as the magnetic-field circulation around the excitation point. The impulse response $h(t)$ is defined as the inverse Fourier transform of the input admittance:

$$h(t) = \mathcal{F}^{-1}\left[\frac{I(\omega)}{V_0(\omega)}\right] \quad (8)$$

where $V_0(\omega) = \mathcal{F}[v_0(t)]$ and $I(\omega) = \mathcal{F}[i(t)]$.

To reduce the high-frequency numerical noise of the FDTD solution, $i(t)$ was low-pass filtered ($15GHz$ cut-off frequency) before numerical computation of second and fourth derivatives of $i(t)$ in Eq. 7. The computed impulse response evaluation is shown in Fig.2a. To appreciate the accuracy of the method, the convolution $v_0 * h(t) = \bar{i}(t)$ was evaluated and compared with $i(t)$ (Fig.2b). A good agreement can be observed and the relative *root mean square (r.m.s.)* error $\delta(i,\bar{i}) = \sqrt{\int |i(t) - \bar{i}(t)|^2 dt} / \sqrt{\int |i(t)|^2 dt}$ was less than 7%. The difference in the first transient is probably related to the source model which causes unphysical non-linear effects.

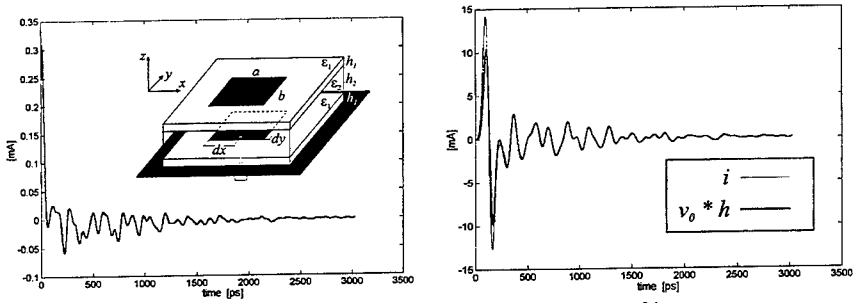

Fig. 2 *a) Current impulse response of a stacked patch antenna ($a = 41.8mm$, $b = 33.2\,mm$, $d_x = 20.9mm$, $d_y = 5mm$, $l_1 = 1.57mm$, $l_2 = 5.4mm$, $\varepsilon_1 = 2.2$, $\varepsilon_2 = 1$) at the coax/ground plane transition; b) comparison between the FDTD computed current and the convolution of the derivated Gaussian and the impulse response obtained by numerical deconvolution.*

Microstrip filter - A planar low-pass filter [12] on a $0.794\,mm$ substrate with 2.2 permittivity, was meshed on a non-uniform grid with cell sizes $0.3\,mm \le \Delta x, \Delta y \le 1\,mm$ and $0.1mm \le \Delta z \le 0.5mm$. The computation domain was truncated by 6-cell PML absorbing boundary conditions. The source was modeled as a Huygens-injector template [1] exciting a y^+-directed quasi-TEM mode (Gaussian stimulus with half-power bandwidth $[0, 15GHz]$ and $\tau = 65ps$). The input function was a voltage, $v_1(t)$, computed as the line integral of the incident electric field from the ground plane to the microstrip. The output was the voltage, $v_2(t)$, at port 2, defined in the same way. Therefore, the impulse response $h_{21}(t)$ was defined as $\mathcal{F}^{-1}[S_{21}]$ where S_{21} is the off-diagonal element of the scattering matrix.

Low-pass filtering ($20\,GHz$ cut-off frequency) is applied to $v_2(t)$ before evaluation of derivatives. The computed impulse response is shown in Fig.3a. The convolution $\bar{v}_2(t)$ of the impulse response (Fig.3a) and v_1(t) is plotted for comparison with $v_2(t)$ in Fig.3b. The diagrams are indistinguishable almost everywhere and the relative r.m.s error $\delta(v_2, \bar{v}_2)$ was less than 2%.

V. Conclusions

In this work, the time-domain characterization of a microwave device by its impulse response has been considered. With reference to the full-wave analysis of microwave devices by the FDTD method and Gaussian and Derivated-Gaussian input waveforms, a simple time-domain

deconvolution algorithm has been proposed to compute the impulse response from FDTD data. The deconvolution is based on a fourth-order moment expansion of the input spectrum. A numerical analysis has been carried out for two planar structures showing the practicability of the method.

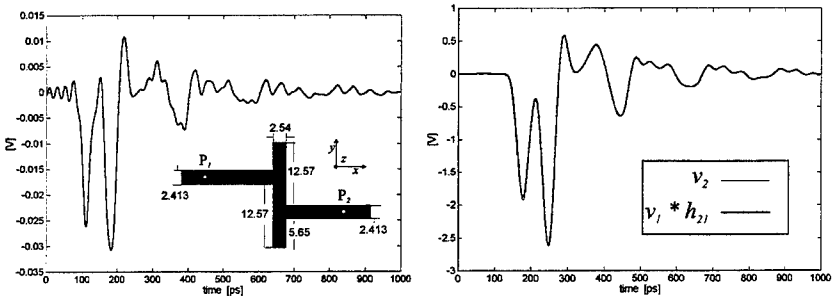

a) b)

Fig. 3 *a) Planar low-pass filter (size in mm) and its impulse response h_{21} vs. time by the FDTD/Moment Expansion method; b) v_2(FDTD computed) and $\bar{v}_2$(convolution of input and impulse response) vs. time for a Gaussian input v_1.*

References

1. A. TAFLOVE, *Advances in computational electromagnetics: The finite difference method*, Artech House, Norwood, MA, 1998
2. T.W. Huang, B. Housmand, T. Itoh, "The implementation of time-domain diakoptics in the FDTD method", *IEEE Trans. Microwave Theory Tech.*, MTT-43, no. 11, pp. 2149-2155
3. S. H. Hammadi, S. M. El-Ghazaly, "Extending FDTD/Convolution techniques to 3 D microwave structures", *IEEE APS Symposium 1994*, Digest, pp.2180-2183
4. C. E. Baum, "Toward an engineering theory of electromagnetic scattering: the singularity and eigenmode expansion methods", in *Electromagnetic Scattering*, edited by P. L. E. Uslenghi, Academic Press, New York, pp. 619-651, 1978
5. W. T. Beyene, J. E. Schutt-Ainè, "Integrating data obtained from electromagnetic field analysis into circuit simulations", *13th Annual Review of Progress in Applied Computational Ellectromagnetics*, Vol.1, pp.156-163, 1997
6. P. G. Petropoulos, "Phase Error Analysis Control for {FD-TD} Methods of Second and Fourth Order Accuracy", *IEEE Trans. Antennas Propagat.*, AP-42, pp.859-862, June 1994
7. A. J. Poggio, M. L. Van Blaricum, E. K. Miller, R. Mittra, "Evaluation of a processing technique for transient data", *IEEE Trans. Antennas Propagat.*, AP-26, pp. 165-173, 1978
8. J. Rahman, T. Sarkar, "Deconvolution and Total Lest Squares in finding the impulse response of an electromagnetic system from measured data", *IEEE Trans. Antennas Propagat.*, AP-43, pp. 416-421, April 1995
9. A. Papoulis, "Approximation of Point Spread for Deconvolution", *J. Optical Society of America*, VOL. 62, pp. 77-80, January 1972
10. G. Marrocco, F. Bardati, "Basic Electromagnetic Simulation Tool (BEST)", *European Space Agency (ESA) Report*, Contract number, NO. 11476/95/NL/NB, 1995
11. R. J. Luebbers, H. S. Langdon, "A simple feed model that reduces time steps needed for FDTD antenna and mocrostrip calculation",*IEEE Trans. Antennas Propagat.*, AP-44, pp. 1000-1005, 1996
12. D. Sheen, S. Ale, M. Abouzahra, J.A. Kong, "Application of the three dimensional finite difference time domain method to the analysis of planar microstrip circuits", *IEEE Trans. Microwave Theory and Techniques*, MTT-38, pp. 849-856, 1990

The Cause of Oscillatory Dispersion Relation of Equivalent Circuit Parameters for Microstrip Component Using FDTD Method

L. L. Liou
Sensor Directorate
Air Force Research Laboratory
Wright-Patterson AFB, OH. 45433-7322

Abstract

The finite difference in time domain (FDTD) method has been used to calculate the wave guiding parameters for microstrip components. The calculated characteristic impedance and the effective dielectric constant as a function of frequency commonly exhibit oscillatory behavior. The cause of this anomaly is analytically and numerically shown to be due to the imperfect absorption boundary condition (ABC). An equivalent circuit approach, by computing capacitance and inductance of a microstrip line, is shown to be useful in eliminating the oscillatory feature in dispersion relations.

I. Introduction

The finite difference in time domain (FDTD) method has been used to study the waveguiding properties of the devices in a MMIC [1-7]. Microstrip lines are the basic waveguiding structure in a MMIC. They are used to transfer microwave energy into and out of active devices in the integrated circuit . For a proper design of a matching circuit, one needs to know two important microwave parameters associated with microstrip lines. One is the characteristic impedance and the other is the effective dielectric constant. In FDTD analysis, the frequency dependence (dispersion relation) of these microwave parameters can be calculated in a straightforward manner. However, the results commonly exhibit oscillatory behavior. This behavior is not seen in the results obtained using a full wave analysis in the frequency domain and it is unique to the FDTD analysis. It is important to understand this behavior in order to improve the FDTD analysis and thus achieve useful information for a MMIC circuit design.

Several reasons have been speculated for this behavior. They are 1) imperfect absorbing boundary conditions (ABCs) that generate artificial reflection wave at the computational boundary; 2) the excitation source can contain mixed modes of propagation and evanescent waves; 3) the continuous radiation loss spectrum that was taken into account in FDTD, but failed to be implemented properly in the conventional method for the phase velocity determination; and 4) possible numerical errors due to the use of a numerical approximation of the fourier integration. Among these, the first is recognized to be the main cause. In this paper, we will show analytically and numerically that this is indeed the case.

With the FDTD results, the conventional way to calculate the phase velocity is to use the so called multiple-z method [1-5]. The multiple-z method uses multiple observation locations in the propagation direction to monitor the wave propagation at different frequencies. By comparing the phase for each frequency component at these locations, the propagation constant can be derived from the knowledge of the distance the wave travels between the monitoring locations. We have proposed an equivalent circuit approach to solve the oscillatory problem[7]. This approach needs only one observation point in the propagation direction to monitor the wave and to calculate the dispersion relation of the phase velocity; it is, therefore, also called the single-z method. The justification of the equivalent circuit approach will also be reported in this paper.

In the next section, a theory is presented to show the oscillatory behavior in the dispersion curve using FDTD results. Section III presents the numerical results and discussions and is followed by the conclusion.

II. Theory

In the waveguiding structure, the electric and magnetic waves propagate along the z-direction. The electric and magnetic fields as functions of x, y, z and t are given by:

$$E(x,y,z,t) = \sum_m \iint d\beta d\omega E_m(x,y,\beta,\omega) e^{i[\beta z - \omega_m(\beta)t]} \delta(w - w_m)$$

$$H(x,y,z,t) = \sum_m \iint d\beta d\omega H_m(x,y,\beta,\omega) e^{i[\beta z - \omega_m(\beta)t]} \delta(w - w_m)$$

where m stands for the mode number. Assuming only the fundamental modes are propagating, and the validity of linear circuit theory (i.e., TEM or TEM-like modes), the voltage and current waves can be given by:

$$V(z,t) = \int V_0(\omega) e^{i\frac{\omega}{v_0}z} e^{-i\omega t} d\omega$$

$$I(z,t) = \int I_0(\omega) e^{i\frac{\omega}{v_0}z} e^{-i\omega t} d\omega$$

where υ_0 is the phase velocity of the fundamental mode; V_0 is the line integral of the electric field of the fundamental mode between the microstrip line and the ground plane and I_0 is the line integral of the magnetic field of the fundamental mode around the microstrip metal. The fourier components of $V(z_0,t)$ and $I(z_0,t)$ at an angular frequency of ω are given by:

$$V(z_0,\omega) = V_0(\omega) e^{i\frac{\omega}{v_0}z_0}$$

$$I(z_0,\omega) = I_0(\omega) e^{i\frac{\omega}{v_0}z_0}$$

The time series obtained using FDTD contain artificial noise that is generated at the computation boundaries. The most significant component is from the end boundary of the propagation path, ie., $z=z_L$. This noise is superimposed on $V(z_0,\omega)$ and $I(z_0,\omega)$. They are now given by:

$$V(z_0,\omega) = V_0(\omega) e^{i\frac{\omega}{v_0}z_0} + V_n(\omega) e^{i\frac{\omega}{v_0}(2z_L - z_0)}$$

$$I(z_0,\omega) = I_0(\omega) e^{i\frac{\omega}{v_0}z_0} + I_n(\omega) e^{i\frac{\omega}{v_0}(2z_L - z_0)}$$

where V_n and I_n are the spectral noise (including possible phase reversal) generated at the computational boundary. One also notes that the noise term has a different phase factor due to a longer propagation length. The characteristic impedance is given by:

$$Z_0(z_0,\omega) = \frac{V(z_0,\omega)}{I(z_0,\omega)} = Z_0(\omega)[1 + (\frac{V_n}{V_0} - \frac{I_n}{I_0}) e^{i\Delta\vartheta}]$$

where $Z_0(z_0,\omega)$ is the position-dependent characteristic impedance and exhibits oscillatory behavior as a function of frequency, while $Z_0(\omega)$ is the true characteristic impedance and is independent of the monitor location, and

$$\Delta\vartheta = \frac{2\omega}{v_0}(z_L - z_0)$$

The cycle of this oscillation is about $\upsilon_0/(2(z_L - z_0)$. One also notes that the characteristic impedance at a low frequency ($\omega \rightarrow 0$) has a maximum deviation from the true value.

The oscillatory phenomenon in the frequency dependent phase velocity can be analyzed similarly. Following the conventional multiple-z method, the time series of voltage wave are observed at $z = z_1$ and z_2. The ratio of the frequency components of both series are given by:

$$\frac{V(z_2,\omega)}{V(z_1,\omega)} = e^{i\frac{\omega}{v_0}(z_2 - z_1)}[1 + \frac{V_n}{V_0}(e^{i\Delta\vartheta_2} - e^{i\Delta\vartheta_1})]$$

where $\Delta\vartheta_1 = 2\omega(z_L - z_1)/\upsilon_0$, and $\Delta\vartheta_2 = 2\omega(z_L - z_2)/\upsilon_0$. The noise term has both the magnitude and the phase dependent on z_1, z_2, z_L and frequency. The noise term adds a small quantity in the phase difference at the two observation points which are needed to determine the phase velocity. This small quantity causes the oscillation in the frequency dependence of the phase velocity. If the distance between the two observation points is small compared to the distance between the observation points and the boundary, then the period in frequency is about $\upsilon_0/\{2[z_L - (z_1+z_2)/2]\}$. With some formulations, it can be shown that as $\omega \rightarrow 0$,

$$v_0' = v_0(1 - \frac{V_n}{V_0})^{-1}$$

where υ_0' is the estimated phase velocity. Again, the phase velocity, at the low frequency, suffers the most deviation from the true value, as it does for the characteristic impedance case.

In the equivalent circuit approach, we calculate the equivalent circuit components of the inductance per unit length, L, and the capacitance per unit length, C. For detailed information on that approach refer to Reference 7. In the following, we shall show that this approach is immune to the oscillatory anomaly.

The magnetic flux per unit length, ψ, and the charge per unit length, Q are given by:

$$\psi(z_0,\omega) = \psi_0(\omega)e^{i\frac{\omega}{v_0}z_0} + \psi_n(\omega)e^{i\frac{\omega}{v_0}(2z_L - z_0)}$$

$$Q(z_0,\omega) = Q_0(\omega)e^{i\frac{\omega}{v_0}z_0} + Q_n(\omega)e^{i\frac{\omega}{v_0}(2z_L - z_0)}$$

where ψ_0 and ψ_n are the frequency components of the magnetic flux of the fundamental mode and the noise generated at the boundary. Q_0 and Q_n are the frequency components of the charge of the fundamental mode and the noise generated at the boundary. L and C are then given by:

$$L(z_0,\omega) = \frac{\psi(z_0,\omega)}{I(z_0,\omega)} = L_0(\omega)e^{i\frac{\omega}{v_0}z_0}[1+(\frac{\psi_n}{\psi_0}-\frac{I_n}{I_0})e^{i\Delta\vartheta}]$$

$$C(z_0,\omega) = \frac{Q(z_0,\omega)}{V(z_0,\omega)} = C_0(\omega)e^{i\frac{\omega}{v_0}z_0}[1+(\frac{Q_n}{Q_0}-\frac{V_n}{V_0})e^{i\Delta\vartheta}]$$

The characteristic impedance and the phase velocity are calculated by:

$$Z_0(z_0,\omega) = \{\frac{L(z_0,\omega)}{C(z_0,\omega)}\}^{1/2} = Z_0(\omega)\{1+[(\frac{\psi_n}{\psi_0}-\frac{I_n}{I_0})-(\frac{Q_n}{Q_0}-\frac{V_n}{V_0})]e^{i\Delta\vartheta}\}$$

$$v_0(z_0,\omega) = [L(z_0,\omega)C(z_0,\omega)]^{-1/2} = v_0(\omega)\{1+[(\frac{\psi_n}{\psi_0}-\frac{I_n}{I_0})+(\frac{Q_n}{Q_0}-\frac{V_n}{V_0})]e^{i\Delta\vartheta}\}$$

Since the noise components in both the magnetic flux and the current are determined by noise components in the magnetic field, the ratio terms in the inner parenthesis cancel each other. A similar situation applies to the noise terms for the charge and the voltage. Therefore, the noise terms have a very small effect on the characteristic impedance and the phase velocity in the equivalent circuit approach. As we shall see in the numerical verification, this is indeed the case.

III. Results and Discussion

In this study, the FDTD method is implemented with a dispersive boundary condition[5]. A simple source excitation scheme[6] is used in the present study. The microstrip line is on GaAs substrate (the dielectric constant ε is 12.9) with a thickness of 1000 μm. The width of the microstrip line is also 1000 μm. The computational domain contains N_x x N_y x N_z = 51 x 104 x 120 and the spatial interval is 100 μm. The source plane is located at z = 20 units. Fig. 1 shows the schematics of the microstrip line. Depending on the parameters used in the dispersive boundary condition, the noise generated at the computational boundary can be vastly different. Figs. 2 and 3 show the electric filed as functions of time at three observation locations. The parameters used in Fig. 2 corresponds to a good ABC with a small noise, while the ones used in Fig. 3 corresponds to a fair ABC with a large noise.

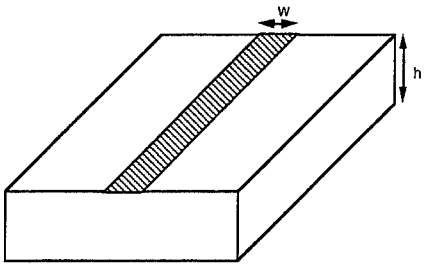

Fig. 1: Schematics of the microstrip line with linewidth of W and thickness of h.

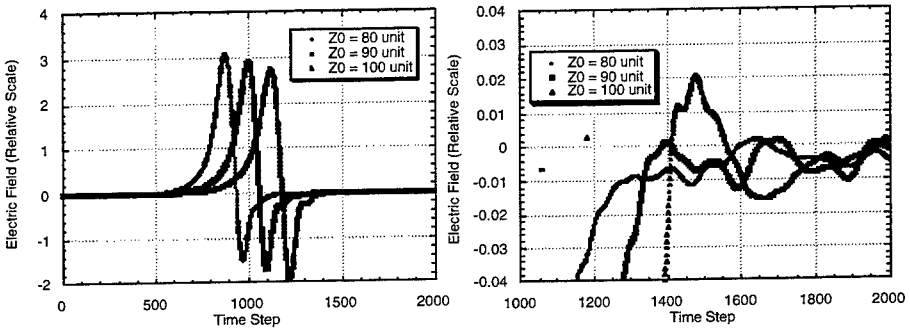

Fig. 2: (a) The time series of the electric field at three different z with a good ABC implemented. (b) the magnified time series of electric field showing the noise infested region.

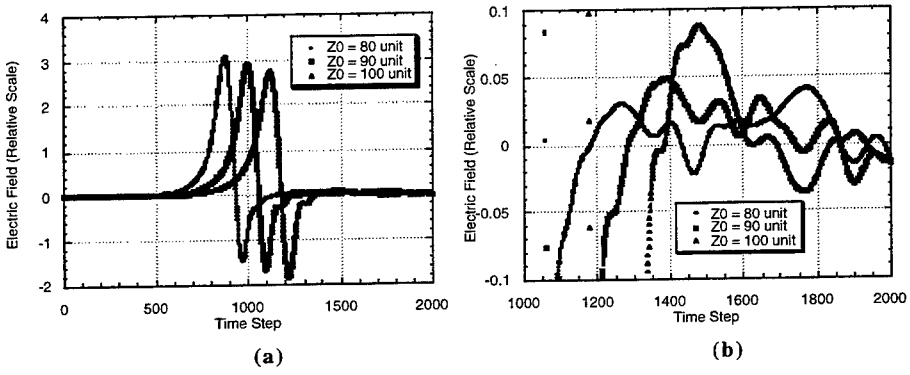

Fig. 3: (a) The time series of the electric field at three different z with a fair ABC implemented. (b) the magnified time series of electric field showing the noise infested region.

Using the fair ABC, Fig. 4 shows the characteristic impedance as a function of frequency between 0 and 60 GHz. The results of three cases of different z_L- z_0 values are shown. The results using the equivalent circuit approach are also shown. The period of the oscillation increases as (z_L- z_0) decreases. The periods are close to the estimated values which are 12.5, 16.7 and 25 GHz for (z_L- z_0) = 40, 30 and 20 units, respectively. The deviation from the true value at the low frequency is the maximum as expected. The equivalent circuit approach does not show the oscillatory behavior.

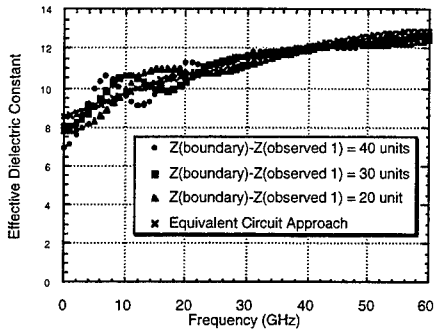

Fig. 4: The characteristic impedance as a function of frequency. The ABC is the same as in Fig. 2

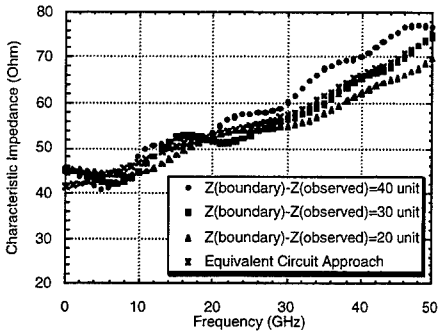

Fig. 5: The effective dielectric constant as a function of frequency. The ABC is the same as in Fig. 2.

Using the fair ABC, Fig. 5 shows the effective dielectric constant as a function of frequency between 0 and 60 GHz. The results of three cases of different z_L- z_0 values are shown. The results using the equivalent circuit approach are also shown. The multiple-z method shows oscillatory behavior. The period increases as z_L- $(z_0+z_2)/2$ increases. The deviation at the low frequency is maximum as expected. The equivalent circuit approach does not show the oscillatory behavior.

To summarize this study, there are several ways to reduce the effect of artificial noise on the microwave parameters. The first is to implement a good ABC to reduce the generated noise at the boundary. Fig. 6 and 7 show the results using a good ABC. The oscillatory anomaly is minimized. The second is to set up the model in a way that there is a long distance between the observation point and the boundary. This long distance reduces the influence of the noise. These two method can require a long computation time. The third is to implement the signal processing techniques [4] which eliminate the effects of the artificial noise. Lastly, the equivalent circuit approach has been shown to be effective in minimizing the effect of the noise due to an imperfect ABC.

IV. Conclusion

For microstrip line component analysis , the traditional FDTD method to determine phase velocity is based on multiple-z values. The traditional method to determine characteristic impedance is to compute the ratio between the voltage and current components. The results, usually, show an oscillatory feature in the dispersion relations. This phenomenon was analyzed. It was shown to be caused by the noise generated at the boundary due to an imperfect ABC. The equivalent approach using FDTD results evaluates the capacitance and the inductance at a single monitor location in the direction of propagation. The dispersion relation of the phase velocity and the characteristic impedance show little oscillatory anomaly. This is because the noise terms are canceled from each other in the capacitance and inductance evaluation.

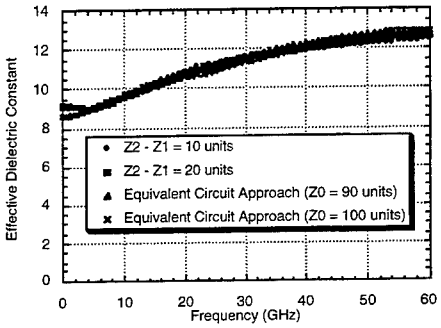

Fig. 6: The characteristic impedance as a function of frequency. The ABC is the same as in Fig. 3.

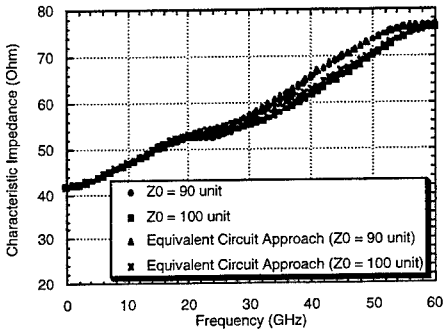

Fig. 7: The effective dielectric constant as a function of frequency. The ABC is the same as in Fig. 3.

REFERENCES

1. X. Zhang, J. Fang, K. K. Mei and Y. Liu, "Calculations of the Dispersive Characteristics of Microstrips by the Time-Domain Finite Difference Method," IEEE Tran. Microwave Theory Tech., vol. 36, no. 2, pp. 263-267, February 1988.

2. J. Fang, "Absorbing Boundary Conditions Applied to Model Wave Propagation in Microwave Integrated-Circuits," IEEE Trans. Microwave Theory Tech., vol. 42, no. 8, pp. 1506-1513, August 1994.

3. M. A. Schamberger, S. Kosanovich and R, Mittra, "Parameter Extraction and Correction for Transmission Lines and Discontinuities Using the Finite-Difference Time-Domain Method," IEEE Trans. Microwave Theory Tech., vol. 44, pp. 919-925, 1996.

4. K. Naishadham and X. P. Lin, "Application of Spectral Domain Prony's Method to the FDTD Analysis of Planar Microstrip Circuits," IEEE Trans. Microwave Theory Tech., vol. 42, no. 12, pp. 2391-2398, December 1994.

5. Z. Bi, K. Wu, C. Wu and J. Litva, "A Dispersive Boundary Condition for Microstrip Component Analysis Using The FD-TD Method," IEEE Trans. Microwave Theory Tech., vol. 40, no. 4, pp. 774-777, April 1992.

6. A. P. Zhao, A. V. Raisanen and S. R. Cvetkovic,"A Fast and Efficient FDTD Algorithm for the Analysis of Planar Microstrip Discontinuities by Using a Simple Source Excitation Scheme," IEEE Microwave and Guided Wave Letters, vol. 5, no. 10, pp. 341-343, October 1995.

7. L. L. Liou, M. Y. Mah and J. Cook, "An Equivalent Circuit Approach for Microstrip Component Analysis Using the FDTD Method," IEEE Microwave and Guided Wave Letters, December, 1998.

An Implicit Characteristic Based Finite Difference Method for Computational Electromagnetics

by
John H. Beggs [1] and W. Roger Briley [2]
Mississippi State University
MSU/NSF Engineering Research Center for Computational Field Simulation
Box 9627
Mississippi State, MS 39762

Abstract

The overall objective of this study is examine an implicit characteristic-based approach for numerical solution of Maxwell's time-dependent curl equations in flux conservative form. The present method combines a characteristic based finite difference spatial approximation with an implicit lower-upper approximate factorization (LU/AF) time integration scheme. This approach is advantageous for three-dimensional applications because the characteristic differencing enables a two-factor approximate factorization that retains its unconditional stability in three space dimensions, and it does not require solution of tridiagonal systems. Results are given for a a one-dimensional model problem involving propagation and scattering for free space and dielectric materials using both uniform and nonuniform grids. The model problem is designed to provide quantitative insight into both accuracy and efficiency. The explicit FDTD algorithm is used as a convenient reference algorithm for comparison. The one-dimensional results indicate that for low frequency problems on a highly resolved uniform or nonuniform grid, this LU/AF algorithm can produce accurate solutions at Courant numbers significantly greater than one, with a corresponding improvement in efficiency for simulating a given period of time.

1 Introduction

1.1 Background

In the regime of finite-difference solutions for Maxwell's time dependent curl equations, explicit methods such as the Finite-Difference Time-Domain (FDTD) method [1]–[4], the Transmission Line Method (TLM), or (more recently) Finite-Volume Time-Domain (FVTD) methods have been standard techniques for the past 20-30 years. These methods are relatively simple and efficient, and have proven very robust and adequate for many types of problems.

Since these explicit methods are conditionally stable, their maximum time step is limited by a stability constraint that depends on the local grid spacing. The conditional stability restriction can increase the cost of analyzing electromagnetic (EM) problems, especially when nonuniform grids are needed, because a small local grid structure can require a time step smaller than would otherwise be required to accurately resolve the physical wave propagation. On the other hand, implicit algorithms can provide unconditional stability which allows the time step to be selected for accuracy and resolution of the frequency content of the excitation sources, without a stability restriction.

Implicit algorithms were first proposed for electromagnetics by Holland [5]. They have not received widespread use in electromagnetics, however, perhaps due to increased complexity and in some cases the need to solve a linear system of equations. For example, centered spatial difference approximations in conjunction with alternating direction implicit (ADI) schemes require the solution of (for example) tridiagonal systems for each coordinate

[1]This work was sponsored in part by the Southeastern Center for Electrical Engineering Education under Grant # SCEEE-97-004 and by NSF under Grant # EEC-8907070

[2]WRB is also with Mississippi State University, Department of Mechanical Engineering, Box 9552, Mississippi State, MS 39762

direction. Furthermore, although this type of scheme is unconditionally stable for the first-order wave equation in two dimensions, it is known to be unconditionally unstable in three dimensions [6]. The usual Fourier stability analysis does not account for nonperiodic boundary conditions, however, and it has been shown using a matrix stability analysis that this three dimensional centered difference algorithm is conditionally stable when used with upwind boundary conditions [7].

There has been recent work in developing characteristic based explicit and implicit algorithms for CEM that are related to some solution algorithms from computational fluid dynamics. These methods have been developed for curvilinear three dimensional grids, using both finite difference and finite volume approximations. Shankar et al. [8], [9] developed explicit characteristic-based finite-volume methods, using both flux-vector and flux-difference splittings for electromagnetics. Shang, et. al. [10]–[17] have developed both implicit and explicit characteristic based methods. Shang [10]–[11] developed an implicit characteristic based ADI method that leads to simple bidiagonal systems that are easily solved, rather than tridiagonal or pentadiagonal systems. This characteristic-based scheme is unconditionally stable in two dimensions and conditionally stable in three dimensions [11]. Shang and Fithen [16] also developed characteristic based finite difference and finite volume schemes using Runge-Kutta time integration, in curvilinear coordinates. Gaitonde and Shang [18] and Turkel [4] have recently explored high order accurate compact differencing schemes that require tridiagonal solutions for spatial approximations, whether implicit or explicit time integration is used. Turkel [4] has suggested a two dimensional implicit version based on an ADI scheme.

1.2 Present Study

A characteristic-based approach to spatial differencing has advantages in constructing implicit algorithms, as well as in utilizing the natural method of incorporating boundary conditions for hyperbolic systems. The ability of characteristic based methods to provide accurate nonreflecting solutions at outer boundaries is well known and is discussed for electromagnetics by Shang [10]–[11] and others.

The present method combines a characteristic based approach to spatial differencing with an implicit lower-upper approximate factorization (LU/AF) time integration scheme that can be developed as a two-factor scheme that retains its unconditional stability in three space dimensions, unlike three-factor ADI schemes. The LU/AF scheme also avoids the need to solve tridiagonal implicit systems. A two-factor approximate factorization for three dimensions was first suggested by Jameson and Turkel [19]. This type of factorization (two implicit passes in three dimensions) has been combined with characteristic based differencing by Belk and Whitfield [20]. This general approach has been further developed for CFD and is discussed, for example, in [21].

Complex practical applications often involve nonperiodic solutions in finite regions with complex geometry and nonuniform grids. Grid nonuniformity is an important consideration because conditional stability criteria typically link the maximum permissible time step to the local grid spacing rather than to the underlying physical time and space "sampling" requirements of the solution. Stable implicit methods can benefit from choosing the time step to satisfy an accuracy requirement rather than a stability constraint, with the consequence that fewer time steps are needed for a fixed simulation time. Accordingly, a one-dimensional model problem with nonuniform grid is developed to explore the influence of grid nonuniformity on solution accuracy and efficiency. The explicit FDTD algorithm is used as a convenient reference algorithm for comparison.

2 One-Dimensional LU/AF Algorithm

This section details the theoretical background for development of a second-order accurate LU/AF algorithm. This algorithm is used in all comparisons with the FDTD method, and a first order algorithm is used at points adjacent to the outer boundaries of the computational grid.

Maxwell's equations for linear, homogeneous and lossless media in the one-dimensional case (taking $\partial/\partial y = \partial/\partial z = 0$) are

$$\frac{\partial(\epsilon E_z)}{\partial t} - \frac{\partial H_y}{\partial x} = 0, \quad \frac{\partial(\mu H_y)}{\partial t} - \frac{\partial E_z}{\partial x} = 0 \tag{1}$$

These equations can be rewritten in flux conservative form as

$$\frac{\partial \bar{q}}{\partial t} + \frac{\partial \bar{f}}{\partial x} = 0 \tag{2}$$

where $\bar{q} = [\epsilon E_z\ ,\ \mu H_y]^T$, $\bar{f} = [-H_y\ ,\ -E_z]^T$ and T denotes transpose. To develop the $O\left(\Delta t^2, \Delta x^2\right)$ LU/AF algorithm, the flux conservative form of (**??**) is rewritten to include the electric and magnetic conduction currents as

$$\frac{\partial \bar{q}}{\partial t} + \bar{A}\frac{\partial \bar{q}}{\partial x} = -\bar{P}\,\bar{q} \tag{3}$$

where $\bar{A}$ and $\bar{P}$ are given by

$$\bar{A} = \begin{bmatrix} 0 & -1/\mu \\ -1/\epsilon & 0 \end{bmatrix}, \quad \bar{P} = \begin{bmatrix} \sigma/\epsilon & 0 \\ 0 & \sigma^*/\mu \end{bmatrix} \tag{4}$$

The time derivative in (3) is approximated by a β-weighted, $O(\Delta t^2)$ difference equation given by

$$\frac{\partial \bar{q}}{\partial t} \approx \frac{(2\beta+1)q_i^{n+1} - 4\beta q_i^n + (2\beta-1)q_i^{n-1}}{2\Delta t} \tag{5}$$

The spatial derivative is replaced by a β-weighted average between time level $n+1$ and n. This can be rewritten using an operator notation as

$$\frac{\partial \bar{f}}{\partial x} \approx \beta\left(\Delta_{2i}^- \bar{f}_i^+ + \Delta_{2i}^+ \bar{f}_i^-\right)^{n+1} + (1-\beta)\left(\Delta_{2i}^- \bar{f}_i^+ + \Delta_{2i}^+ \bar{f}_i^-\right)^n \tag{6}$$

The $\Delta_{2i}^{\pm}$ operators are $O(\Delta x^2)$ difference operators to be defined shortly. The parameter β can be used to construct a series of explicit and implicit schemes. For example, if $\beta = 0$, this results in a leapfrog scheme; $\beta = 0.5$ results in a Crank-Nicolson scheme and $\beta = 1$ results in an Euler implicit scheme. Using (5) and (6), the finite-difference equation for (3) is

$$\frac{(2\beta+1)\Delta q_i^n - (2\beta-1)\Delta q_i^{n-1}}{2\Delta t} + \beta\left(\Delta_{2i}^- \bar{f}_i^+ + \Delta_{2i}^+ \bar{f}_i^-\right)^{n+1} + (1-\beta)\left(\Delta_{2i}^- \bar{f}_i^+ + \Delta_{2i}^+ \bar{f}_i^-\right)^n = -\beta\bar{P}\,\bar{q}_i^{n+1} - (1-\beta)\bar{P}\bar{q}_i^n \tag{7}$$

Using a flux vector splitting approach, this can be rearranged as

$$\left[\bar{I}/(2\Delta t) + \beta\theta\bar{P} + \beta\theta\left(\Delta_{2i}^- \bar{A}^+(\cdot) + \Delta_{2i}^+ \bar{A}^-(\cdot)\right)\right]\Delta\bar{q}_i^n = -\bar{R}_{2i}^n \tag{8}$$

The residual, $\bar{R}_{2i}^n$, is defined by

$$\bar{R}_{2i}^n \equiv \theta\left\{\bar{P}\bar{q}_i^n + \Delta_{2i}^- \bar{f}_i^{+,n} + \Delta_{2i}^+ \bar{f}_i^{-,n} + \frac{2\beta-1}{2\Delta t}\Delta\bar{q}_i^{n-1}\right\} \tag{9}$$

where $\theta \equiv 1/(2\beta+1)$. The difference operators in equation (9) are replaced by $O(\Delta x^2)$ backward and forward upwind difference operators on three-point one-sided stencils defined by

$$\Delta_{2i}^-(\cdot) = \left(3(\cdot)_i - 4(\cdot)_{i-1} + (\cdot)_{i-2}\right)/(2\Delta x), \quad \Delta_{2i}^+(\cdot) = \left(-3(\cdot)_i + 4(\cdot)_{i+1} - (\cdot)_{i+2}\right)/(2\Delta x) \tag{10}$$

Substituting $\left(\bar{f}^{\pm}\right)^n = \bar{A}^{\pm}\bar{q}_i^n$ into (9), the residual is given by

$$\bar{R}_{2i}^n = \theta\left\{\bar{P}\bar{q}_i^n + \Delta_{2i}^- \bar{A}^+\bar{q}_i^n + \Delta_{2i}^+ \bar{A}^-\bar{q}_i^n + \frac{2\beta-1}{2\Delta t}\Delta\bar{q}_i^{n-1}\right\} \tag{11}$$

Equation (8) is an $O(\Delta t^2, \Delta x^2)$, unfactored, upwind scheme for electromagnetics. The LU/AF scheme is defined by factoring the left side of (8) into two operators, each designed for a forward and backward grid sweep as in the first order implementation. The LU/AF scheme is then given by

$$\left[\bar{I}/(2\Delta t) + \beta\theta\bar{P} + \beta\theta\Delta_{2i}^- \bar{A}^+(\cdot)\right]\Delta\bar{q}_i^* = -\bar{R}_{2i}^n \tag{12}$$

$$\left[\bar{I}/(2\Delta t) + \beta\theta\bar{P} + \beta\theta\Delta_{2i}^+ \bar{A}^-(\cdot)\right]\Delta\bar{q}_i^n = \left[\bar{I}/(2\Delta t) + \beta\theta\bar{P}\right]\Delta\bar{q}_i^* \tag{13}$$

3 Fourier Analysis

A Fourier analysis shows that the second-order upwind LU/AF algorithm is unconditionally stable for $\beta > 1/2$, and that it contains both numerical dissipation and dispersion. The dissipation is present due to even order spatial derivatives in the truncation error which are a result of the upwind approximation. These schemes are consistent approximations with $O(\Delta t^2, \Delta x^2)$ truncation error for the second-order algorithm. A complete Fourier analysis is omitted here for the sake of brevity, but is shown in [22].

4 Boundary Conditions

The characteristic based LU/AF method requires no extraneous boundary condition such as the Liao absorbing boundary condition [23] or the PML [24]. The FDTD method uses a spatial central difference operator, which for a wave propagating from left to right, eventually requires a grid point *outside* the domain. This requirement introduces an additional equation (i.e. boundary condition) to solve the system and introduces information into the solution that is not required by Maxwell's equations. Using an upwind characteristic based approach, the interior point algorithm calculates the left-going characteristic at the left boundary (i.e. at $i = 0$) and the right-going characteristic at the right boundary (i.e. at $i = imax$). Therefore, the only additional information required is information about waves that are *entering* the domain. Waves exiting the domain are naturally handled by the interior point algorithm. Therefore, the characteristic boundary conditions are implemented as follows: at grid point $i = 0$, a first-order version of (13) is used along with a specification of the incoming, right-going flux, f_0^+. At grid point $i = imax$, a first-order version of (12) is used along with a specification of the incoming, left-going flux, f_{imax}^-. Therefore, the only additional information introduced at the boundary is nothing more than what is required by the physical system. In multidimensional problems, the local coordinates at the outer boundaries are rotated to align with the direction of wave propagation defined by $\bar{E} \times \bar{H}$. The characteristic equations are developed along this direction and are appropriately applied at the boundaries. This procedure was discussed and outlined by Shang [11].

5 Model Problem Results

The model problem results presented in this section demonstrate that the one-dimensional implicit characteristic-based LU/AF algorithm can produce accurate results on a nonuniform grid for time steps significantly larger than the maximum permissible for a typical conditionally stable scheme. Although the operation count for the implicit scheme is higher, as the mesh variation is increased, fewer time steps are needed for an accurate solution over a fixed simulation time, and this savings more than offsets the additional operations (beyond a certain mesh variation).

The second-order LU/AF algorithm was tested by implementing equations (12) and (13) for interior grid points away from absorbing boundaries and first-order equations at grid points next to the absorbing boundaries. Characteristic-based boundary conditions were used to terminate the computational domain and the incoming flux (f_{imax}^-) at the right boundary was set to zero. The code was initialized by writing a time snapshot of a propagating pulse in the grid. Several different types of problems were analyzed with the LU/AF algorithm and compared with the FDTD method in an attempt to assess the characteristics of the LU/AF algorithm as applied to a one-dimensional problem with a non-uniform grid. These are outlined in the following sections.

5.1 Propagation

To assess the dispersion and dissipation characteristics of the LU/AF algorithm, several propagation problems were analyzed using free space and dielectric materials and were compared with FDTD. A Gaussian pulse of the form

$$E_{yi} = e^{-\left(\frac{t-t_0}{\tau}\right)^2} \tag{14}$$

was used as an excitation source for both propagation and scattering problems. For propagation, the code was changed to use periodic boundary conditions to enable simulation of propagation over large distances compared to the shortest wavelength contained in the frequency spectrum of the pulse. To illustrate the potential benefit of the LU/AF algorithm over conventional explicit schemes, the main parameters of interest are the time resolution (i.e. number of time steps/period) and the grid resolution (i.e. number of cells/wavelength) of the highest frequency of interest in any given problem. These parameters will be designated as N_t and N_x, respectively. The other parameter of interest is the mesh stretch ratio, M_s. The highest frequency of interest, f_{max}, is calculated based upon N_x and the largest cell size, and the time step for the implicit scheme is calculated based upon f_{max} and the desired time resolution, N_t. For the FDTD method, the time step was calculated based upon the Courant stability condition using the smallest grid size.

5.1.1 Uniform Grid

The first propagation problem involves propagation in free space on a uniform mesh. The time and grid resolutions are $N_t = 30$ and $N_x = 30$, the cell size was 1 cm, the time step was 33.3 ps and $\nu = 1$. The maximum frequency of interest was 1 GHz and the problem space was 2000 cells. The pulse was allowed to propagate a distance equal to 100 wavelengths of the minimum wavelength, which corresponds to a distance of about 30 meters. Figure 1 shows the electric field versus distance obtained after 3000 time steps computed using the exact solution, FDTD and the LU/AF algorithm.

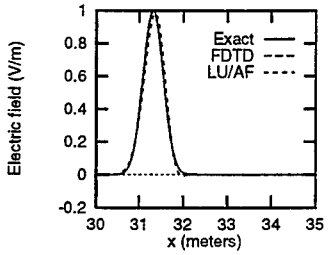

Figure 1:

Note the LU/AF scheme has slightly less accurate results due to the larger dispersion error; but the general shape of the pulse is still acceptable.

5.1.2 Nonuniform Grid

To demonstrate the LU/AF scheme on nonuniform meshes, the same problem outlined above was simulated using mesh stretch ratios of M_s=10:1 and M_s=100:1 and the mesh was periodic every 10 cells. Figure 2 illustrates an expanded section of the nonuniform mesh for a mesh stretch ratio of M_s =10:1. The smallest grid cells force the FDTD algorithm to take a time step 1/10th of the previous case, and it must run 10 times as many time steps to propagate the pulse the same distance. However, the LU/AF algorithm can take the same time step as before, because the time resolution, $N_t = 30$, has been preserved and the time step is set solely upon accuracy requirements, not on the Courant stability condition. The maximum cell size remains constant, and since N_x is also the same, the maximum frequency of interest remains constant at 1 GHz. The maximum grid coordinate changes from 20.0 in the uniform mesh case to 8.17 for the 10:1 nonuniform mesh. The Courant numbers in the grid for FDTD are in the range $0.1 \leq \nu \leq 1$ and the Courant numbers for the LU/AF algorithm are in the range $1 \leq \nu \leq 10$. Figure 3 shows the electric field versus distance obtained with the exact solution and after 30,000 time steps computed using FDTD and after 3,000 time steps using the LU/AF algorithm.

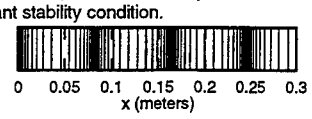

Figure 2:

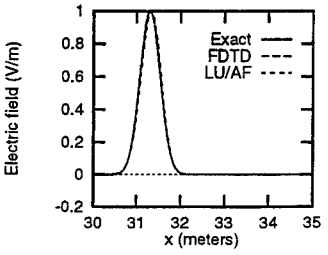

Figure 3:

Note the agreement is very good for both methods in this case. In fact, Figure 4 shows the error in electric field versus distance for both methods and the errors are almost equal in magnitude. The LU/AF method required about 52 seconds and 504×10^6 operations, but the FDTD method required about 66 seconds and 480×10^6 operations. Note, however, the improved performance of the LU/AF algorithm away from the area of the main pulse. Since the mesh stretch ratio was 10 for this problem, the FDTD method is forced by the Courant stability condition to take 10 times the number of time steps to simulate the same amount of physical time.

5.2 Lossy Dielectric Material

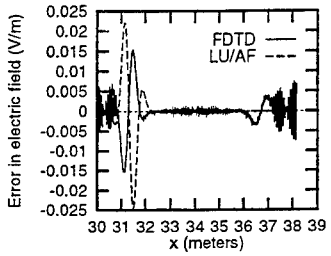

Figure 4:

To illustrate propagation in dielectric materials, the problem space was filled with a lossy dielectric material with parameters $\epsilon = 4\epsilon_0$, $\mu = \mu_0$ and $\sigma = 0.02$. The pulse was allowed to propagate on a uniform mesh for approximately 35 wavelengths at the minimum wavelength. Figure 5 shows the results of FDTD versus LU/AF with very good agreement between the two methods.

A similar level of agreement is found with the same problem on a nonuniform grid. The difference in these results is most likely attributed to the nonzero factorization error which occurs when the conduction current term is included.

6 Conclusions

This paper has explored the benefits of using implicit finite-difference methods for computational electromagnetics. An implicit, second-order accurate, LU/AF, characteristic based algorithm for electromagnetics has been implemented and tested on one-dimensional model problems for uniform and nonuniform grids. The one-dimensional model problem results for the characteristic based implicit scheme demonstrate that:

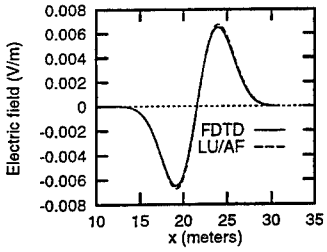

Figure 5:

1. Accurate solutions for wave propagation can be obtained using Courant number significantly greater than one on nonuniform grids.
2. Stability of the implicit scheme allows a given amount of time to be covered in fewer time steps than a conditionally stable scheme, and this can significantly improve efficiency when nonuniform grids are needed. This is also extremely beneficial for low frequency excitation sources where geometric details may force a highly oversampled mesh (uniform or nonuniform) in certain regions.

This approach appears promising for development of stable, accurate and efficient implicit LU/AF schemes for complex two and three dimensional applications.

References

[1] K. S. Yee, "Numerical solution of initial boundary value problems involving Maxwell's equations in isotropic media", *IEEE Trans. Antennas Propagat.*, vol. 14, no. 3, pp. 302–307, 1966.

[2] K. S. Kunz and R. J. Luebbers, *The Finite Difference Time Domain Method for Electromagnetics*, CRC Press, Boca Raton, FL, 1993.

[3] A. Taflove, *Computational Electrodynamics: The Finite-Difference Time-Domain Method*, Artech House, Boston, MA, 1995.

[4] Allen Taflove, editor, *Advances in Computational Electrodynamics: The Finite-Difference Time-Domain Method*, Artech House, New York, 1998.

[5] R. Holland, L. Simpson, and K. Kunz, "Finite-difference analysis of EMP coupling to lossy dielectric structures", *IEEE Trans. Electromagn. Compat.*, vol. EMC-22, no. 3, pp. 203–209, 1980.

[6] R. F. Warming and R. M. Beam, "An extension of a-stability to alternating direction implicit methods", *BIT*, vol. 19, pp. 395–??, 1979.

[7] R. C. Buggeln W. R. Briley and H. McDonald, "Solution of the three-dimensional navier stokes equations for a steady laminar horseshoe vortex flow", in *Proc. 7th Computational Fluid Dynamics Conference*, Cincinnati, OH, July 1985, AIAA Paper 85-1520-CP.

[8] V. Shankar, W. F. Hall, and A. Mohammadian, "A time-domain differential solver for electromagnetic scattering problems", *Proc. IEEE*, vol. 77, no. 5, pp. 709–721, 1989.

[9] W. F. Hall V. Shankar and A. H. Mohammadian, "A time-domain, finite-volume treatment for the Maxwell equations", *Electromagnetics*, vol. 10, pp. 127, 1990.

[10] J. S. Shang, "Characteristic based methods for the time-domain Maxwell equations", in *AIAA 29th Aerospace Sciences Meeting & Exhibit*, Reno, NV, Jan. 1991, vol. AIAA 91-0606.

[11] J. S. Shang, "A characteristic-based algorithm for solving 3-d time-domain Maxwell equations", in *AIAA 30th Aerospace Sciences Meeting & Exhibit*, Reno, NV, Jan. 1992, vol. AIAA 92-0452.

[12] J. S. Shang, "A fractional-step method for solving 3-d time-domain Maxwell equations", in *AIAA 31st Aerospace Sciences Meeting & Exhibit*, Reno, NV, Jan. 1993, vol. AIAA 93-0461.

[13] J. S. Shang and R. M. Fithen, "A comparative study of numerical algorithms for computational electromagnetics", in *AIAA 25th Plasmadynamics & Lasers Conference*, Colorado Springs, CO, June 1994, vol. AIAA 94-2410.

[14] J. S. Shang and D. Gaitonde, "Characteristic-based, time-dependent Maxwell equation solvers on a general curvilinear frame", *AIAA Journal*, vol. 33, no. 3, pp. 491–498, March 1995.

[15] J. S. Shang, "A fractional-step method for solving 3d, time-domain Maxwell equations", *Journal of Comp. Phys.*, vol. 118, pp. 109–119, 1995.

[16] J. S. Shang and R. M. Fithen, "A comparative study of characteristic-based algorithms for the Maxwell equations", *Journal of Comp. Phys.*, vol. 125, pp. 378–394, 1996.

[17] D. C. Blake and J. S. Shang, "A procedure for rapid prediction of electromagnetic scattering from complex objects", in *AIAA 29th Plasmadynamics & Lasers Conference*, Albuquerque, NM, June 1998, vol. AIAA 98-2925.

[18] D. Gaitonde and J. S. Shang, "High-order finite-volume schemes in wave propagation phenomena", in *AIAA 27th Plasmadynamics & Lasers Conference*, New Orleans, LA, June 1996, vol. AIAA 96-2335.

[19] A. Jameson and E. Turkel, "Implicit schemes and approximate factorizations", *Math. Comp.*, vol. 37, pp. 385–397, 1981.

[20] D. M. Belk and D. L. Whitfield, "Unsteady three-dimesional euler solutions on blocked grids using an implicit two-pass algorithm", January 1987, vol. AIAA Paper No. 87-0450.

[21] W. R. Briley, S. S. Neerarambam, and D. L. Whitfield, "Implicit Lower-Upper/Approximate-Factorization algorithms for incompressible flows", *Journal of Comp. Phys.*, vol. 128, pp. 32–42, 1996.

[22] J. H. Beggs and W. R. Briley, "An implicit characteristic based method for electromagnetics", *Applied Computational Electromagnetics Society Journal*, submitted.

[23] Z. P. Liao, H. L. Wong, B.-P. Yang, and Y.-F. Yuan, "A transmitting boundary for transient wave analysis", *Sci. Sin., Ser. A*, vol. 27, no. 10, pp. 1063–1076, 1984.

[24] J.-P. Berenger, "A perfectly matched layer for the absorption of electromagnetic waves", *J. Comput. Phys.*, vol. 114, no. 1, pp. 185–200, 1994.

SESSION 2

ANTENNAS

Chairs: Nathan Ida and Jacob Kim

END FED ANTENNAS

R.P. Haviland, W4MB
1035 Green Acres Circle, N.
Daytona Beach, FL 32119

In the early days of radio, a large percentage of antennas, amateur and commercial, were fed at the end, rather than at the center as is now more common. The major factors in the change-over appear to be:

- The move to higher frequencies
- Development of flexible solid-insulated transmission lines
- Development of the Yagi-Uda array, with simplified feed.

A result of the change-over is that standard references have very little information on end fed antennas. There is usually a mention of the type, and perhaps some examples of practical types, but no real analysis. At most there will be a general discussion. Kraus, for example, has no title or index entry. The ARRL Antenna Book has several entries and some discussion of general principles and some practical examples, but no references to theory. Schelkunoff and Friis mention that such antennas may be fed against the capacitance of the generator (to the rest of the world), or by connection to one side of an open wire transmission line. To these should be added feed against another antenna section, or against a ground or counterpoise.

This paper considers some aspects of end feeds, the primary purpose being to determine if the available practical design information needs extension.

END-POINT DRIVE IMPEDANCE

If first-order antenna theory is followed, it is not possible to end feed an antenna, since the current is zero and drive impedance is infinite: no power can be transferred. However, the theory neglects the possibility of the antenna being coupled to another conductor, and in any event the current does not go to zero until atomic distances are reached.

Current moment analysis methods do not provide for end feeds. It appears that the common practice for determining the drive impedance at the antenna end is to determine the center impedance of an antenna of twice the length, and use half of this as the drive impedance. An alternate is to feed the antenna against ground, and use the drive impedance directly. With a frequency sweep, these give a visualization of end feed drive characteristics.

For example, Fig. 1 shows a computer generated plot of center impedance of a 0.5 meter dipole of 1 mm diameter, over the range of 150 to 1400 MHz, as calculated by NEC-2 (EzNEC version). The step value was 50 MHz, sufficient to give good resolution for the series resonance points. However, the rate of change of reactance is very large around the parallel resonant points, as shown by the Vee-shapes of the point-to-point plot. The added arc is a better estimate of these impedances. See Kraus and Schelkunoff and Friis for theoretical and approximate methods of deriving these plots. This figure indicates that the drive resistance at the first two parallel resonant points is 600 and 1000 ohms, very closely.

A partially independent calculation of the drive impedance is possible by noting the drive impedance at the first segment of the moment method, and moving this segment closer to the antenna end by increasing the number of segments. The resulting curve should approach the drive impedance. Such a plot is shown in Fig. 2. for the range of 11 segments to 251. The initial increase in drive resistance as the number of segments increases appears to reflect an increase in calculation accuracy (MiniNEC shows the same pattern). The indicated increase in drive point reactance was not expected. It appears to arise from the continued decrease in the capacity of the segment between the drive point and the antenna end as segment length decreases: the indicated reactance is the sum of this plus that of the longer part of the antenna, which changes slowly with segment size. The estimated first parallel resonant end drive resistance is about 500 ohms by this method.

THE ZEPP ANTENNA

The classical Zepp antenna is a half wave dipole fed at the end by connection to one side of an open-wire one-quarter wave transmission line. Fig. 3 shows a view of the antenna in free space, with the calculated segment currents. The antenna current is very nearly sinusoidal, with a small current at the driven end. The currents on the line wires are essentially mirror-images except for the 10% closest to the antenna. Calculated drive impedance is 37+j46 ohms with the wire size and line spacing used, 1mm wire and a spacing of 1cm. Fig. 4 shows the SWR curve for 50 ohm feed to the transmission line short, indicating resonance at 294 MHz. The unbalance on the transmission line indicates that it is radiating. This shows in the free-space azimuth pattern plot of Fig. 5 (It also shows in the elevation plot).

With a wide range "antenna tuner", the Zepp is a good multi-wave antenna. For example, Fig. 6 shows the current pattern at the second harmonic, where the feed point impedance is 1850+j3050 ohms. The feedline- antenna interaction pattern is the same. The azimuth antenna pattern becomes more nearly a circle, the result of the four lobes of the antenna plus feed

radiation.

ZEPP VARIATIONS

A simple variation of the Zepp is to eliminate the unconnected transmission wire, feeding the other wire against ground, the antenna sometimes called the Marconi. The resulting currents at first resonance are shown in Fig. 7, the drive impedance being 94+j1 ohms. For these dimensions the pattern has a large vertical lobe, shown in Fig. 8. If the height is selected to give a half-wave transmission line, the currents are as shown in Fig. 9, with a drive impedance against ground of 2235+j215 ohms. Patterns are shown in Fig. 10. Another variation adds a grounded vertical section at the far end of the Marconi, sometimes called the half-square beam. Drive impedance is 124-j50 ohms, with currents as shown in Fig. 11. Patterns are shown in Fig. 12.

No attempt to optimize these Zepp variations for a particular characteristic is attempted here. While this can be done, a wide-range antenna tuner will compensate for most characteristics encountered.

THE J-POLE ANTENNA

There is a family of line-fed antennas, with the Zepp half-wave radiator at right angles to the feeders, and the "J-Pole" with it continuing the line of one feeder. The J-pole arrangement and calculated current distribution is shown in Fig. 13. Drive impedance at the center of the bottom short is 40+j8 ohms; match to coax is customarily secured by tapping up on the open wire line a short distance. The pattern is affected by the unbalanced transmission line currents, as shown in Fig. 14. However, the distortion is rarely noticed in use since it is small.

Some of the practical design in the literature depart from the 1/4 and 1/2 wave dimensions by a small amount, apparently to secure better SWR bandwidth. A few checks indicate that some improvement can be secured, but the possibilities have not been explored in detail.

CONCLUSIONS

While this study has shown some interesting detail about the operation and performance of end-fed antennas, the major conclusion is that the handbook concepts and design data are adequate for their intended purpose. There is indication that some optimization for a particular characteristic is possible, and that this can be done with the available moment-method programs.

References

Antenna Theory and Practice, Sergei A. Schelkunoff and Harald T. Friis, Wiley, New York, 1952

Antennas, 2nd ed., John D. Kraus, McGraw-Hill, New York, 1988

The ARRL Antenna Book, 17 ed., R. Dean Straw, ed, ARRL, Newington, 1994. Older editions are also useful.

Fig. 1. Center reactance-resistance plot for A 0.5 meter dipole of 1 mm diameter, from 150 to 1200 MHz, step 50 MHz. See text.

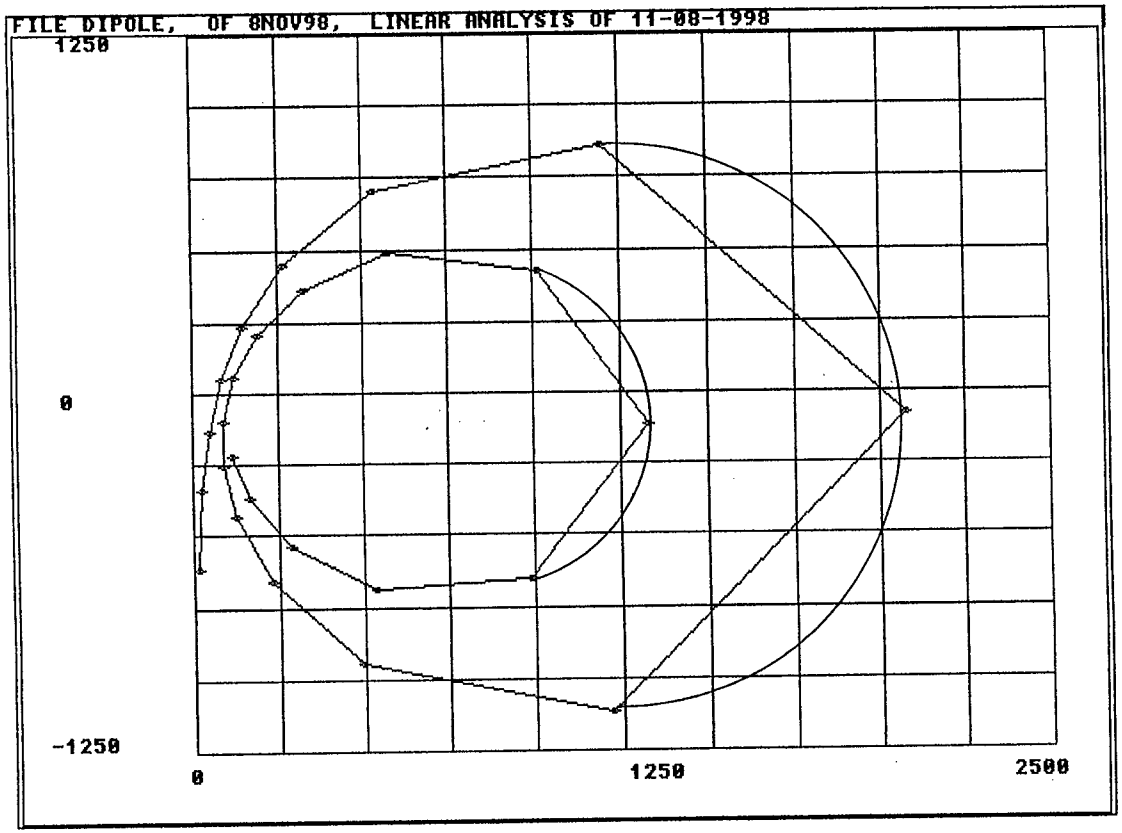

Fig. 2. Resistance and reactance at the first segment of the 0.5 meter antenna, as a function of the number of segments used in NEC calculation. See Text.

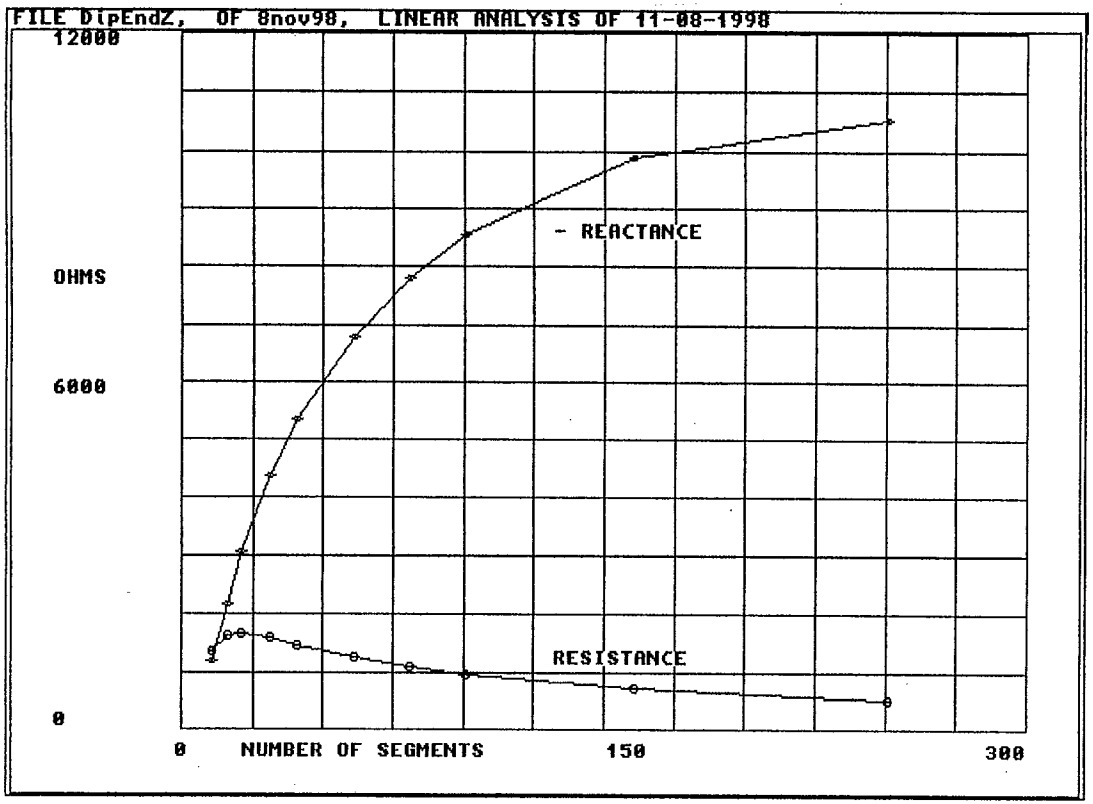

Fig. 3. Current distribution plot for a 0.5 meter 1 mm diameter Zepp antenna at 300 MHz, fed from the bottom center of a 0.25 meter open wire line spaced 1 cm.

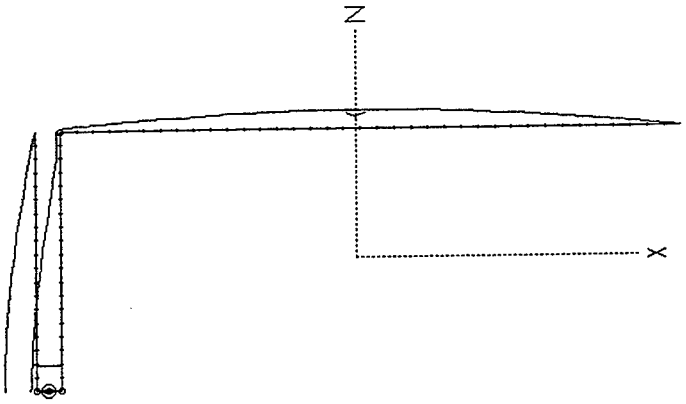

Fig. 4. SWR for the Zepp antenna fed with 50 ohm coax.

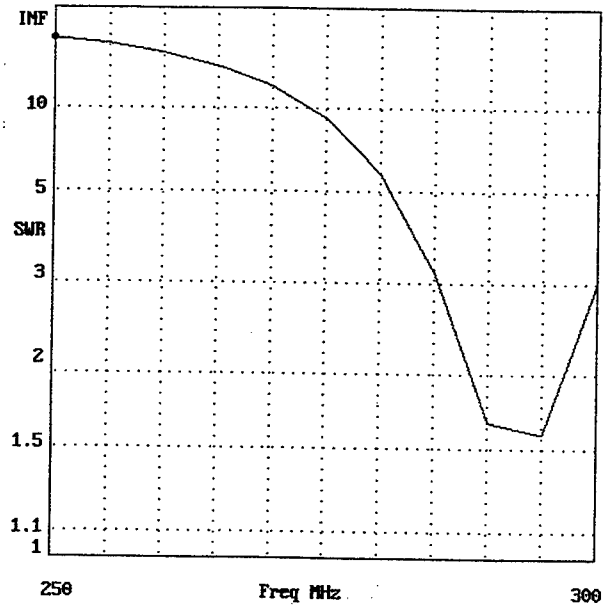

Fig. 5. Free space azimuth plot for the Zepp antenna at 300 MHz.Both antenna radiation and line leakage are present.

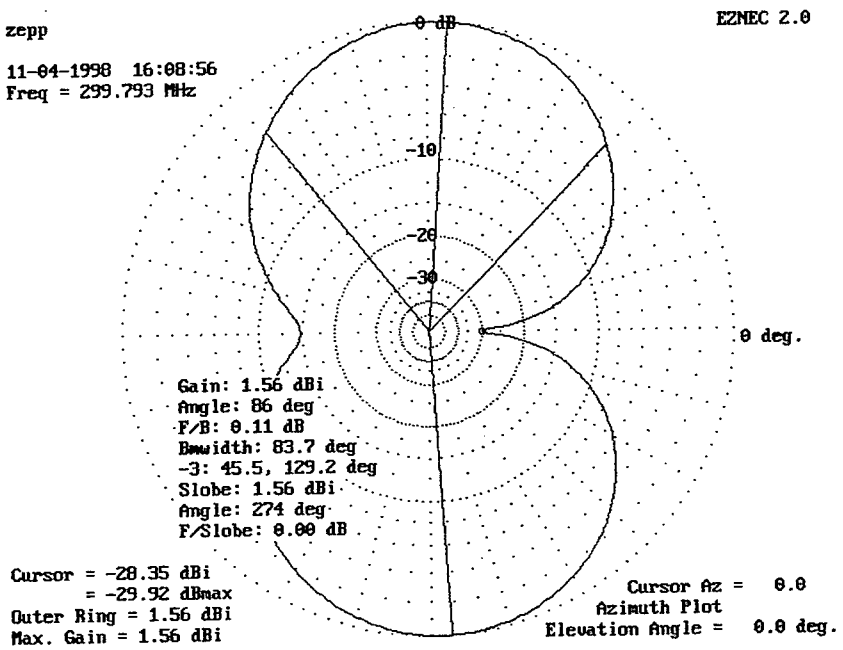

Fig. 6. Current distribution for the zepp antenna at 600 MHz. Note the similarity of feed line current to that of Fig. 1.

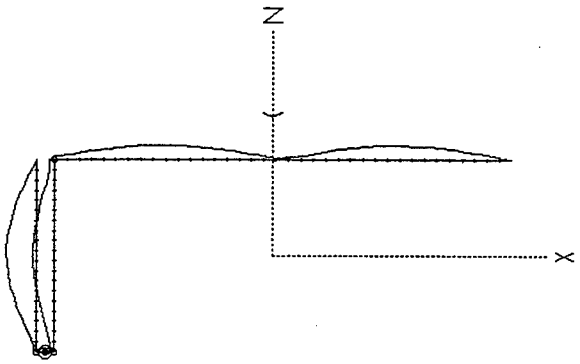

Fig. 7. Current distribution on an E11 or Marconi antenna, essentially a Zepp with one side of the transmission line removed and the other fed against ground. Height is 1/4 wave.

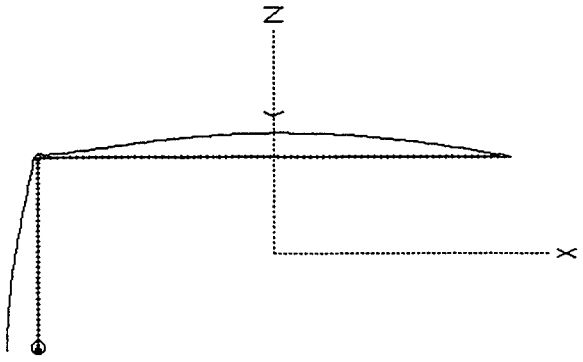

Fig. 8. Radiation pattern of the E11 antenna. The antenna lobe is directed upward, with the single wire feed acting as a vertical radiator.

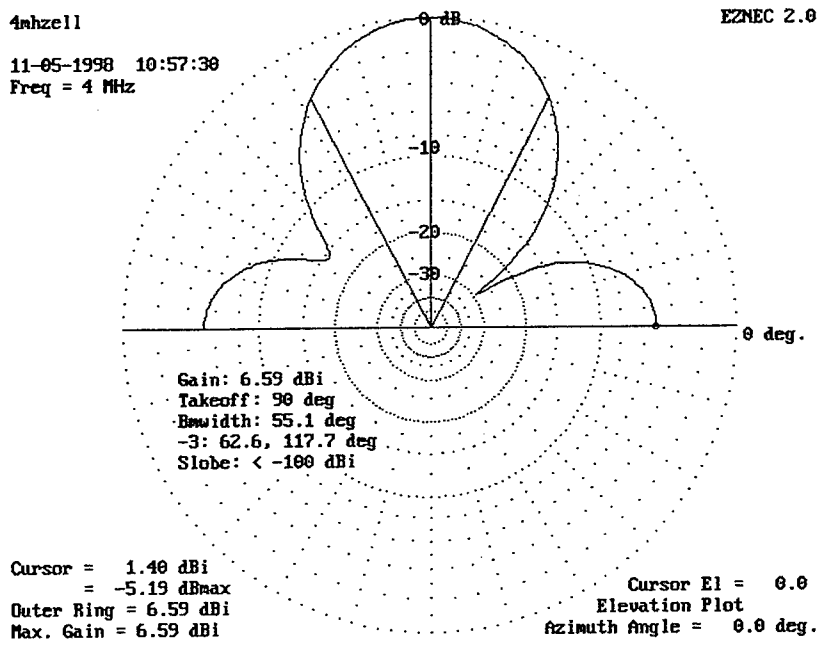

Fig. 9. Current distribution with the Ell raised to 1/2 wave and the transmission line extended.

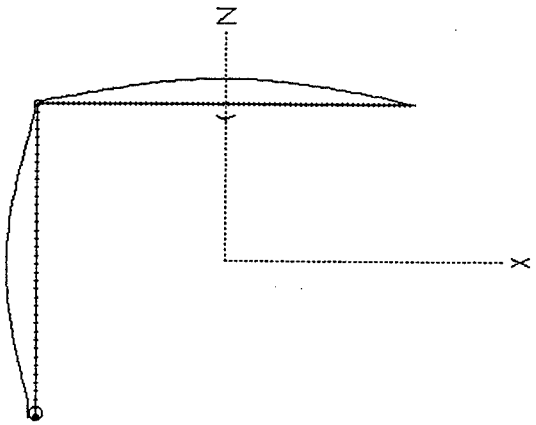

Fig. 10. Azimuth and elevation pattern plots for antenna of Fig. 9.

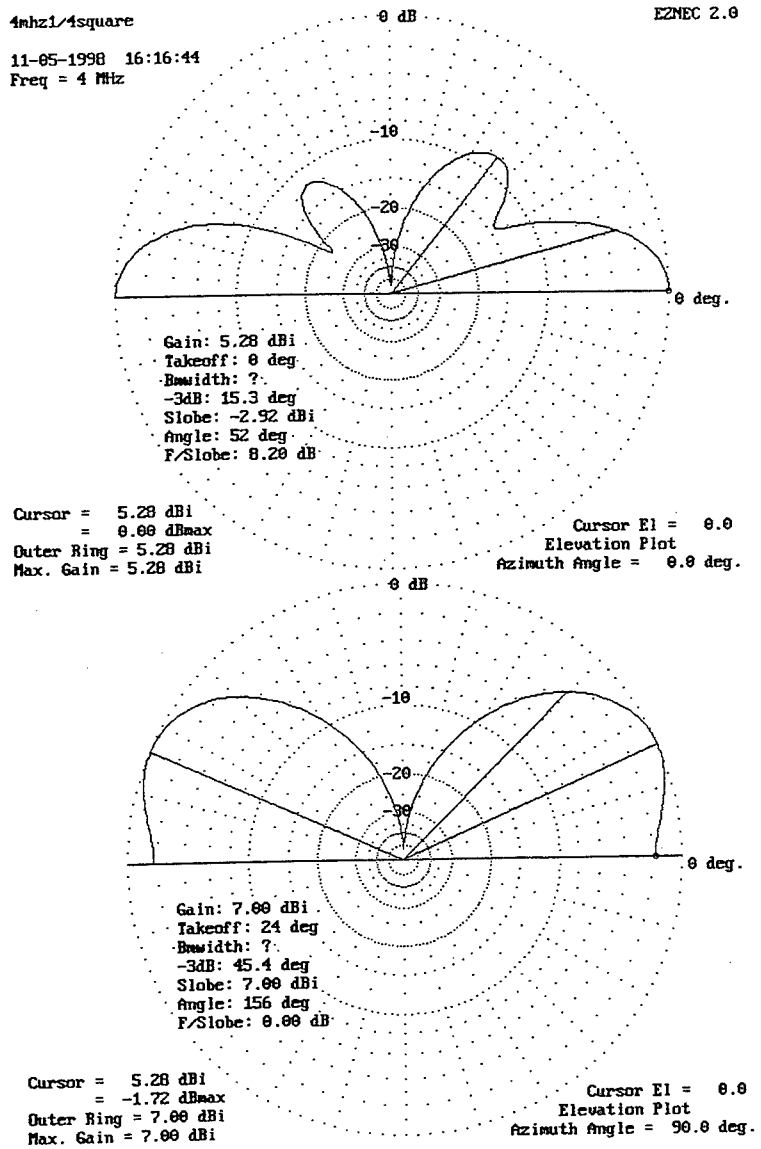

Fig. 11. Current distribution for a half-wave vertical fed with a collinear 1/4 wave open transmission line, the J-Pole antenna. Compare the current distribution with Fig. 1.

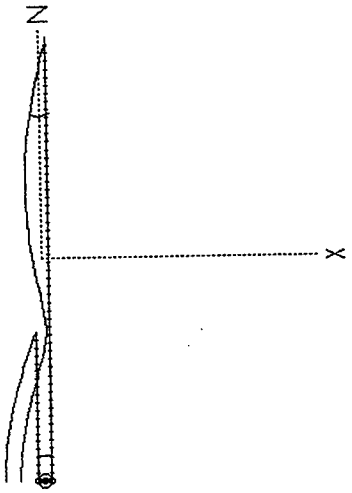

Fig. 12. Radiation pattern of the J-Pole in free space.

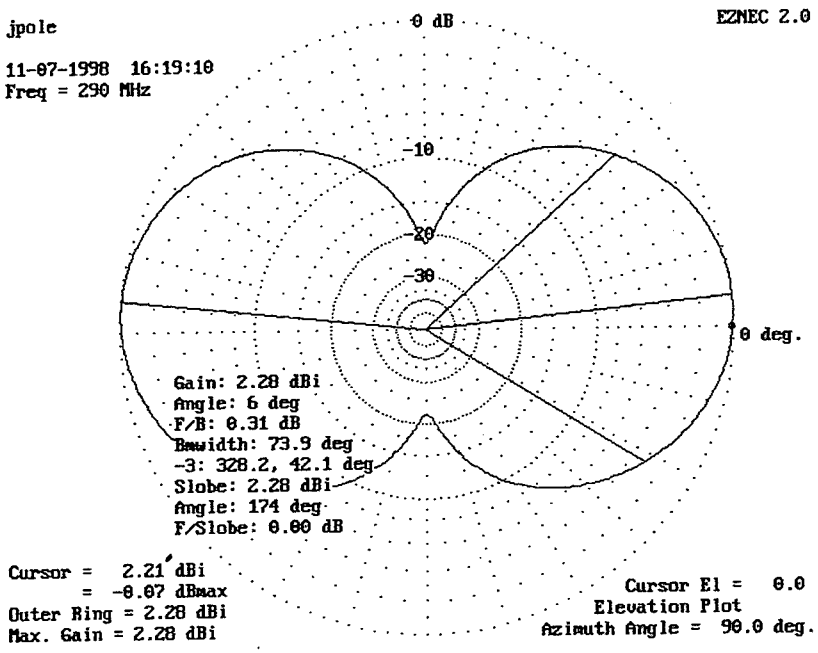

Investigation of A Multi-Resonant Antenna for Wideband Application

P.L. Werner*, N.V. Veremey , R. Mittra and D.H. Werner
Pennsylvania State University
Department of Electrical Engineering
University Park, PA 16802
E-mail address: plw7&psu.edu
Ph: (814) 865-6339, Fax: (814) 375-4724

Abstract- In this paper we present the results of our investigation of a multi-element antenna design, which was inspired by Laufer and Ono [1]. The objective of this effort is to evaluate the suitability of this type of antenna for VHF (30-88 MHz) applications. The Numerical Electromagnetics Code (NEC4) is utilized to analyze the characteristics of the antenna system. Three different excitation methods were studied to seek improvement in overall performance. Some representative numerical results are presented in the paper and conclusions based on these results are included.

1. Introduction

Broadband wire antennas have received a great deal of attention in recent years because they have found widespread applications in communication systems. Numerous design techniques have been proposed during the last few years [2,3] to improve the performance of wire antennas that are inherently narrowband in nature. The approach described in this paper to broadbanding the antenna is to employ multiple wire elements with a single feed, such that the elements resonate at different frequencies to cover the desired frequency range. We investigated this type of antenna design with a view to evaluating its broadband characteristics and suitability for a mobile communication unit. Three variants of the multiresonant antenna system have been studied in this effort. All of these have an identical upper portion comprising 9 parallel vertical wires of varying lengths. Both the directive Gain and VSWR characteristics have been examined, and the possibility of matching the antenna to bring the VSWR level down to 3.5:1 or better has been investigated.

2. The Antenna Analysis and the Results

The geometries of the three antennas modeled in this paper are shown in Fig. 1. All of them have an identical upper section, which consists of a set of nine parallel vertical wires (see Fig. 1). The lengths of the wires are 85cm, 92cm, 106cm, 120cm, 134cm, 148cm, 162cm, 176cm and 182cm, respectively. They are ranging from about one-quarter of the longest wavelength to one-quarter of the shortest wavelength in the 30-88 MHz frequency band.

As mentioned above, to look for an appropriated performance, three structures with different feeding at the lower part of the antenna (see Figs. 1a though 1c) were investigated. The first structure has a wire loop of radius r = 5cm (Fig. 1a), which supports the 9 vertical wires that are placed equidistantly around its periphery and fed through one wire. The lower part of the second configuration studied has a system of radial spokes r = 5cm that are, in turn, connected to the vertical wires as shown in Fig. 1b. Finally, the third geometry modeled consists of a system of inclined wire segments and radials that form a truncated cone-like structure, as shown in Fig. 1c. The radius of the upper and lower periphery of the truncated cone are R=5cm and r = 3cm,

respectively. All of these three antenna structures were analyzed via the NEC4 code. Some of the performance characteristics of the antennas, including the input impedance, input power, directive power gain, radiation pattern and VSWR, are presented.

Figures 2 and 3 depict the gain and VSWR performances of the three antenna structures. It is evident from these figures that the antennas suffer from the presence of multiple resonances in the frequency range of interest. An attempt to improve the VSWR of the antenna via the use of a matching network proved futile due to the presence of a large number of extreme peaks and valleys in the real and imaginary parts of the impedance. It was determined that the impedance was not matchable without paying a significant penalty in terms of the system gain performance. Therefore we conclude that the antennas shown in Fig.1, based on our analysis, are not suitable for a wideband communication system.

REFERENCE:

1. S. Laufer and K. Ono, U.S. Patent 4,302,760, Nov. 1981.
2. M. Bahr, Boag, E. Michielssen and Raj Mittra, "Design of Electrically Loaded Wire Antennas Using Genetic Algorithm," *IEEE AP-S Trans.* Vol. 44, No.5, pp. 687-695, 1996.
3. P. L. Werner, Z. Atlman, R. Mittra, D. H. Werner and A. J. Ferraro, "Genetic Algorithm Optimization of Stacked Vertical Dipoles Above A Ground Plane," *Proceedings of IEEE AP-S International Symposium* 1997, pp. 1976-1979.

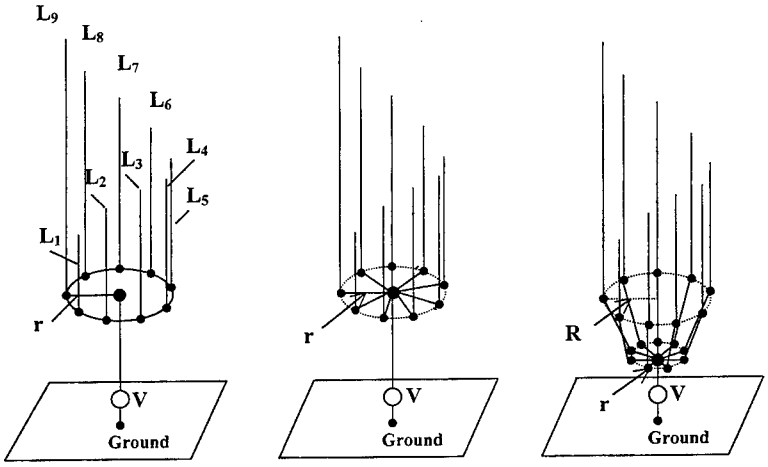

a) b) c)

Fig.1. Modeled antenna geometries.

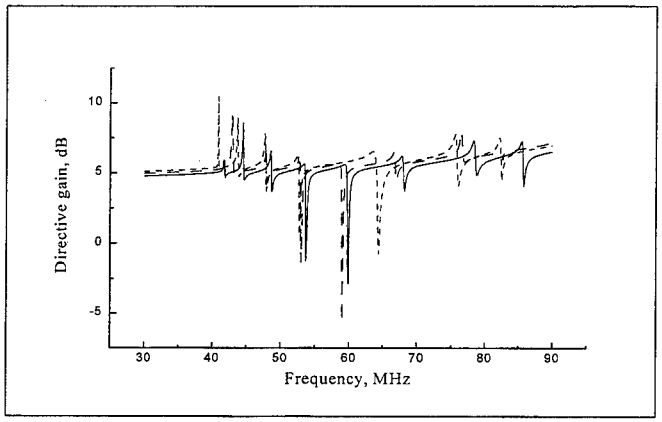

Fig.2. Gain performances of three antennas. Solid line corresponds to the antenna geometry in Fig. 1a; dashed – antenna in Fig. 1b; short dashed - antenna in Fig. 1c. Observation point : θ=89.957°.

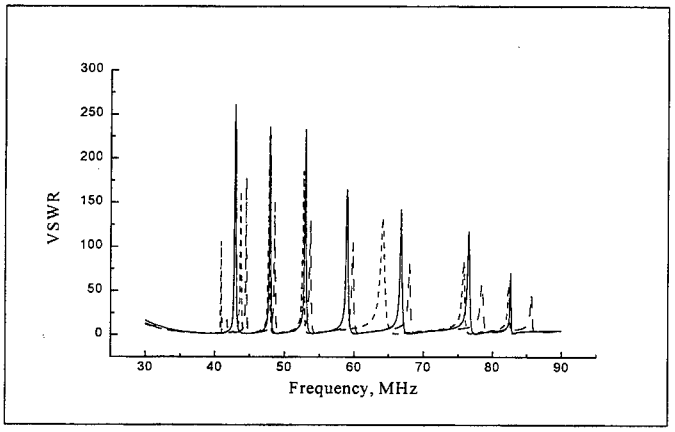

Fig.3. VSWR performances of three antennas. Solid line corresponds to the antenna in Fig. 1a; dashed – antenna in Fig. 1b; short dashed – antenna in Fig. 1c.

COMPUTATION OF CLUSTERED PHASED ARRAY EM FIELDS USING PARTICLE ACCELERATOR CODES

Ross A. Speciale

polytope@msn.com

ABSTRACT

Powerful *EM* codes, originally developed for the computation and visualization of electromagnetic fields in charged-particle accelerators, are currently being used to map the excitation fields of *Clustered Phased Arrays*.

The *2D* codes currently being used, were originally developed for large-scale main-frames, but have recently been ported to high-end PC-Workstations, and run under the Windows *95* or under the Windows *NT 4.0* operating systems. Other (much larger) *3D EM* accelerator codes are currently being ported from the original *Cray* or *Unix* Workstation environments.

These codes have been found to be ideally suited to the computation and graphic visualization of the internal excitation fields of *Clustered Phased Arrays*. These excitation fields are generated by the linear superposition of multiple traveling-waves that simultaneously propagate in all directions through a two-dimensional slow-wave guiding structure that extends in a plane located behind and parallel to the whole array aperture, thereby feeding all the array elements with signals of proper amplitudes and phases.

1 - FUNDAMENTAL OBJECTIVES.

The new *Clustered Phased Array* concept was conceived and is being developed for applications to high-directivity, electronically-steered microwave antenna systems, as a remarkably *affordable* alternative to the notoriously very expensive active apertures.

Clearly, very substantial reductions in array complexity and cost can be attained by using a feed-network configuration that requires a much smaller number of beam-steering controls, in particular much smaller than the very large number of radiating array elements [1-8].

Such complexity and cost reductions are actually possible because of the intrinsically very large redundancy of beam-steering degrees of freedom exhibited by active apertures. Indeed, in active aperture arrays, the use of numerous element-level active modules obviously provides the quite superfluous capability of synthesizing large numbers of totally *useless* aperture *distributions*, that do not generate any practical radiation pattern.

Remarkably smaller numbers of beam-steering controls become sufficient provided that :

a) the array feed-network used achieves a *pervasive synergism* of all beam-steering controls, where *each* control affects *all* radiating elements and *each element* is affected by *all controls*

b) only the *required* aperture distributions are generated, and . . .

c) the elementary aperture distributions, generated by all the beam-steering controls used, are linearly independent, or better yet mutually *orthogonal*. Ideally, these elementary aperture distributions should form a *complete set* of orthogonal *2D-Eigenfunctions*, spanning the vector-space of all the distributions required by the specified beam steering coverage.

A continuing theoretical and experimental research effort is currently being aimed at determining the applicability of two-dimensional wave-guiding structures, in the form of clusters of strongly coupled multiport cavity resonators, as the excitation-field distribution-circuits of steered phased-array feed-networks.

The current use of some particle-accelerator *EM* codes, for the computation and visualization of the internal fields of the cavity-cluster, is here intended to complement the results of previous extensive network-theoretical analyses [6-8], and experimental measurements [5], by providing a direct computer-simulated characterization of both single multiport cavity resonators as well as of a number of increasingly larger clusters of unit-cell resonators (See figures 1-3).

2 - CAPABILITIES OF THE *2D* LOS ALAMOS LABORATORY ACCELERATOR CODES.

The set of *2D EM* field-analysis codes, known as the *POISSON/SUPERFISH* group of codes, has been developed and progressively evolved by the Los Alamos Laboratory Accelerator Codes Group (*LAACG*), and is primarily intended for application to particle accelerator design [9-10].

Various components of the set are nevertheless sufficiently general to be applicable in the analysis of communication antennas and phased arrays.

All the numerous *FORTRAN 77* programs in the set have already been ported, from their original *UNIX* and/or *CRAY* environment, to high-end PC-Work Stations running Windows *95* or Windows *NT*.

Most remarkably, the *POISSON/SUPERFISH* group of codes is available *free of charge*, upon request, from the Los Alamos Laboratory Accelerator Codes Group (*LAACG*).

The group continuously improves the code functionality, and recurrently updates the related, very detailed documentation [9]. The following is a very short description of only those electromagnetic field-analysis capabilities, that are conveniently applicable to communication antenna and phased array problems.

2.1 - The Mesh Generator.

The *AUTOMESH* program, is the most fundamental component of the *POISSON/SUPERFISH* group of codes, and has advanced capabilities for generating and optimizing discrete triangular meshes with selectively controllable resolution across any given two-dimensional *EM* field-domain.

The *RF* structure to be analyzed and the *EM* field-domain can be geometrically outlined in either a *2D* Planar-Cartesian or a circularly-symmetric Cylindrical reference frame (in which case an implied C_∞ circular symmetry of both the structure and the *EM* fields is assumed).

The maximum total number of internal mesh-nodes is only limited by the size of *RAM* and *Virtual Memory* available in the system used. Further, different regions of the total field-domain can be geometrically outlined, and selectively meshed with the most appropriate resolutions for a faithful display of the expected field distributions.

The generated mesh is automatically optimized, by a process of successive over-relaxations that repetitively reshapes the mesh, aiming at one composed of quasi-equilateral triangles, and at the same time prevents the generation of triangles with large aspect ratios.

Also the input data, defining the geometry of the *RF* structure to be analyzed, are automatically checked for physical consistency.

The final configuration of the mesh is saved in a binary file, for subsequent graphic display and further use in the electromagnetic field solver programs *FISH* and *CFISH*.

2.2 - The Electromagnetic Field Solvers.

The mesh generated by the *AUTOMESH* program can be visualized by means of the *2D* graphic program *VGAPLOT*, and is further used in either of the two *RF* field solver programs *FISH* and *CFISH*. These *RF* field solvers compute the electromagnetic field values at the given mesh nodes, by numerically solving Maxwell's equations.

While the *FISH* code only computes the local field *amplitudes*, and is mainly used for searching for and identifying resonant structure modes, the *CFISH* code actually computes the local *real* and *imaginary* components of the fields, and can therefore map traveling-wave propagation processes in non-resonant systems.

The *RF* field solver *FISH* accepts, as inputs, Cartesian X and Y coordinates specifying the location of a single point-source. The *RF* field solver *CFISH*, however, can even accept the locations, amplitude- and phase-settings of multiple *RF* sources ($n \leq 5$), that can either be point-sources or line-sources.

In particular, the *CFISH* program can analyze the complex *EM* fields generated, at any specified fixed frequency, by multiple *RF* line-sources ($n \leq 5$), each line-source having different amplitude- and phase-settings. The *CFISH* program provides thus the capability of simulating the *simultaneous* propagation of *multiple* sets of traveling waves, in all possible directions, through *two-dimensional* wave-guiding structures.

Further, using the *CFISH* program, different regions of the field-domain can be geometrically outlined and electrically specified by selectively assigning the local values of the real and imaginary parts of the permittivity ε' and ε'', and those of the permeability μ' and μ'', thus simulating complex media and absorbing boundaries.

Either Dirichlet or Neuman boundary conditions can be assigned to selected external or internal field-interfaces, in both the *FISH* and *CFISH EM* field solver programs.

The *RF* field solver programs *FISH* and *CFISH* append the array of computed field values, in binary form, to the *AUTOMESH* output file. That binary file is used as both a repository of the output data sets generated by the various programs, and as a communication link between the different programs being run in any given simulation.

2.3 - Using the *E* and *H* Fields in Complementary Roles.

In the analysis of some *EM* problems in Cartesian geometry, where the X-Y reference plane is coincident with the *H*-plane of the field (with an implied $H_Z = 0$ component), the physical roles of the electric and magnetic fields *E* and *H* may be mutually exchanged, by actually solving the *dual EM* problem.

The *dual EM* problem is then defined by switching the type of boundary condition used along the external boundaries of the field-domain, from either Dirichlet to Neuman or from Neuman to Dirichlet.

This expedient circumvents the intrinsic inability of both the *FISH* and *CFISH EM* field solver programs to handle problems, set in a Cartesian reference frame, that are *a-priori* known to lead to a field solution having zero H_Z component. A typical, fundamental example is given by the propagation of *TE*-modes in a rectangular waveguide that has its broadside walls parallel to the X-Y reference plane. The *dual EM* problem is then defined by imposing a Neuman, rather than a Dirichlet, boundary condition along the traces of the waveguide short-walls on the X-Y reference plane, thus implying these to behave as *magnetic* rather than *electric* walls.

2.4 - Field Visualization.

The *2D* graphic program *VGAPLOT* can be used to visualize either the triangular mesh generated by the *AUTOMESH* program, or to generate contour plots of the fields. The contour lines generated from the resonant-mode analyses performed by the *FISH* code represent constant field *amplitudes*, while two-color contour plots of the real and imaginary field components are generated from the complex-field analyses performed by the *CFISH* code.

In a Cartesian reference frame, the VGAPLOT graphic program displays contours of either the H_Z, E_X, or the E_Y component, while in a circularly-symmetric Cylindrical reference frame the program displays contours of either the E_Z, H_φ, or the H_R component.

The values of all the computed field components can be interpolated along arbitrary lines cutting through any given region of the *EM*-field domain.

2.5 - Post-processing Capabilities.

The graphic display program *VGAPLOT* interpolates the computed mesh-node field-values in the selected two-dimensional reference frame, to generate smoother contour-lines of the real-field amplitudes computed by the

program *FISH*, or of the real and imaginary parts of the complex fields computed by the program *CFISH*. The contour-lines of the real and imaginary parts are displayed in different colors.

Further, the post-processing program *SF7* can be used to interpolate the computed mesh-node field-values along straight segments, arcs of circle, user-defined curves, and even on arbitrarily-sized rectangular regions, with a user-selected resolution along the lines, or along the *X*- and *Y*-dimensions of the rectangular regions. The interpolator routine uses the field values computed on the network nodes, including the first- and second-nearest nodes to the given interpolation path. Attempts at interpolating with high-resolution on a coarse mesh, however, will obviously generate jagged results.

Most remarkably, the post-processing program *SFO* can be used to *integrate* the local field gradient, along the same types of lines used for *SF7* interpolation. The performed line-integration computes thus the corresponding total potential change between the line end-points. This capability makes the computation of *equivalent* total *voltages* and *currents* possible, in particular along the interface lines that define the physical locations of the *ports* of a multi-port device. These interface lines should be carefully selected to coincide with appropriate *phase contour-lines*, that can be identified by generating *phase-contour* displays. None of the *POISSON/SUPERFISH EM*-solvers and post-processors has the capability of generating such phase-contours, but these can be easily obtained by exporting the solution data as described here below. Specially-defined *transit-time-integrals* can also be computed, for the complex fields generated by the program *CFISH*, thus taking into account possible *phase-differences* between the various points along the integration path. The *transit-time-integrals* were included in the *SFO* post-processor to compute the amounts of energy gained by charged particles being accelerated by the field, and for this purpose apply a given *relativistic velocity factor* $\beta = v / c < 1$. For purely electromagnetic computations, however, aiming at obtaining the values of *equivalent impedances*, and of the *active* or *reactive power* exchanged though a given interface line, as well as for the computation of *scattering* parameters, the value of β should be set equal to the *relative phase-velocity* of the propagating wave $v_{\varphi r} = v_{\varphi} / c$.

The results of the field interpolations, generated by the post-processing program *SF7* on rectangular regions, are written to an output ASCII file that may include all the interpolated values of the amplitudes, the real and the imaginary parts of the Cartesian components of the *E* and *H* fields, and those of the corresponding total fields. The tabulations sections of such *ASCII* files have lines of *constant record-length*, that can be extracted with any *ASCII*-file editor, saved as *flat ASCII* files, and loaded into *MATLAB*. The imported field-values can then be used as initial data in very extensive, and more specialized post-processing computations. Further the obtained results can be easily displayed in various *2D*- and *3D*-formats, by using the powerful built-in graphic capability of the *MATLAB* program. Most remarkably, *3D*-displays and contour-line plots of the field *phases* can be used to visualize, and quantitatively identify the shapes and locations of the *phase-fronts* of relevant propagating modes. Ultimately, advanced post-processing may enable the computation of the complex coefficients of modal-expansions, appropriately selected to match the fundamental symmetries of the fields and of the outer boundaries.

The post-processing program *SF7* can also be used to compute the total absorbed *active power* in any given rectangular region, including conductor losses if any and the power absorbed in regions filled with materials having complex permittivity and/or permeability. Most remarkably, the active power dissipated in simulated *absorbing boundaries* can be computed by confining the complex media, used in such simulation, to regions delimited by *lossless* outer walls. This capability provides yet another way of computing the amounts of active power propagated, through multi-port microwave devices, by traveling guided waves.

2.6 - Required Processing environment.

The already ported Fortran programs of the *POISSON/SUPERFISH* group of codes can not be strictly considered Windows 95 or Windows NT programs, but can nevertheless be run under control of either Windows 95 or Windows NT. The preferred environment is a *DOS Window* of either operating system, where the benefits of enhanced *DOS* support is provided by either of the two Windows Operating Systems to all the programs that do not directly access the system hardware. New versions of these programs, that run under Windows 95 with GUI control are being developed by the *LAACG*, and are actually already available as *Beta* releases.

While in the *DOS Window*, all these programs run in *character-mode*, and are basically *command-line controlled*, accepting (in an admittedly rather *old-fashioned* way) typed commands from the keyboard (only occasionally) or (mostly) from *control files*. The control files completely automate the numerical solution of any given electromagnetic problem, by executing the required programs in their logical order, and in the most appropriate *mode* for the given problem. The fundamental control file is the *SUPERFISH* initialization file *SF.INI*, that globally sets *almost all* the control parameters for the various programs of any given run. *Additional control files*, however, are also used to fine-tune, modify and/or override the global default settings for any specific program in a given run. The synergism of the fundamental *initialization* file *SF.INI*, and of the *additional control* files indeed provides great flexibility, almost comparable to that of modern *point-and-click* menus, but this flexibility can however only be exploited by manually *editing* the control files beforehand, and by carefully understanding the *mutual interactions* between the various controls.

The graphic programs of the set, that directly access the video display of the system, are the only ones that must be run in real *DOS-MODE*, with no *GUI* support.

Essentially all the Fortran programs of the *POISSON/SUPERFISH* group of codes use as much of the available system Extended Memory and Virtual Memory as needed, with *DOS* Protected Mode Interface (*DPMI*) support. This capabilities make possible the numerical simulation of very large *EM* problems, where the total extent of the mesh can even include hundreds of thousands of mesh-nodes.

The auxiliary graphic display programs that must run in real *DOS-Mode*, use a *VCPI DOS-Extender* (*PharLap.386*) to access the available Extended Memory of the computer system.

The intermediate results, generated by the various programs in an automated *control-file-driven* run, are passed to the next program in line by progressively *appending* them to a common *binary solution file*. The binary file is used both as the output file of a program and as the input file for the next program in the given running-order.

The installation procedure provided with the Fortran programs in the *POISSON/SUPERFISH* group of codes only extracts executable files from a compressed archive, and stores them in a newly-created folder, without affecting any of the Windows System files. The *PATH* environmental variable must therefore be manually modified, by editing the *AUTOEXEC.BAT* file, if one such file exists. Alternatively, the *Property* Settings of the individual programs may be appropriately edited, or *ad-hoc* path-statements may be inserted as a first line in the **.bat* file used to run any given simulation.

The *Property* Settings of each individual program are accessed by highlighting the file icon in the Windows Explorer, by then *right-clicking*, and by selecting the *Properties* entry of the right-click *pop-up* menu.

All the executable program files must be kept in the same folder (normally the newly-created *default* folder), because of undocumented functional *interdependence* between programs.

3 - THE SINGLE-CAVITY RESONATOR MODEL.

Figure 1 shows the geometry of a single, six-port cylindrical cavity resonator, intended to be the *unit-cell* of a large hexagonal *cluster* of mutually-identical, directly-coupled resonators. The model is here represented in a Cartesian reference frame, where the *X*/*Y*-plane is orthogonal to the cavity axis and is also coincident with the *H*-plane of six rectangular waveguides. The waveguides extend radially at 60° in azimuth from each other around the cavity axis. The shape of the outer boundaries, and the internal electromagnetic field pattern, generated by any given excitation, must be assumed uniform in the direction of the *Z*-axis. This assumption is obviously required by the restriction of the presently available *POISSON/SUPERFISH EM*-analysis programs to two dimensional EM-field simulations. The *Z*-axis is coincident with the cavity axis. The cavity is assumed to be air-filled, while the six rectangular waveguides are filled with a lossless dielectric. The permittivity value of the waveguide dielectric is sufficiently high to make the TE_{10} cut-off frequency of the waveguides sufficiently lower than the TM_{010} resonant frequency F_0 of the cavity resonator, so that the TE_{10} waveguide mode is *propagating* (above cut-off) at the resonant frequency F_0 of the cavity, while its *H*-plane is orthogonal to the cavity axis, and coincident with the *H*-plane of the TM_{010} resonant cavity mode. Because of the assumed uniformity of the fields in the direction of the *Z*-axis, the

simulated cavity mode actually is a TM_{01} mode, at cut-off with respect to propagation along the cavity axis. The six waveguides are closed on wedge-shaped matched loads, simulated by triangular regions filled with high-loss dielectric material having a wave-impedance equal to that of the TE_{10} fundamental waveguide mode. A single line-source is located in the arbitrarily-selected waveguide *No. 1* , at sufficient distance from both the *No. 1* waveguide-load, and from the arc of circle that represent the input interface of the resonator. The simulation model shown in Figure 1 represents only an *equatorial cross-section* of the actual shape selected for the unit-cell of the phased-array cavity-cluster. The full three dimensional geometry of the actual unit-cell is shown in Figure 3. The six ports of the resonator are there six *H-shaped irises*, as dictated by the two simultaneous requirements that: a) the irises be resonant on the TM_{010} resonant frequency F_0 of the resonator, and b) that the azimuth span of the coupling irises be sufficiently smaller than 60° , so that six irises may *fit* around the mid-section of the resonator, with adjacent irises having *negligible* direct mutual *coupling*.

In the Cartesian reference frame used, the complex-field electromagnetic solver *CFISH* always computes on the mesh nodes the values of the H_Z field component oriented along the Z-axis. In the given physical situation, however, the H_Z field component is identically zero, so that here the mentioned expedient of exchanging the roles of the E and H fields must be used to obtain a practical solution. As already described, the expedient of using the E and H fields in mutually complementary roles consists actually in posing and solving the *dual* of the actual physical problem. This means that the propagating waveguide mode must be assumed to be the TM_{10} mode, that has a *non-zero* H_Z field component and its E-plane coincident with the X/Y-plane of the simulation. In this *dual* representation of the actual physical situation, contour-lines of the H_Z component are shaped as those of the E_Z component in the actual physical model. The dual representation is simply obtained by replacing the external *electric-walls* of the cavity resonator, and of the waveguides, with fictitious *magnetic-walls*. This means setting the boundary condition along the wall of the cavity resonator and along those of the waveguides as *Dirichlet* (representing a *magnetic* wall) rather than *Neumann* (representing an *electric* wall). The obtained field solutions must obviously be *re-interpreted* in terms of the *physical* problem, after performing the computations. This means converting from Ampere/meter values, of the *computed* H_Z component, to Volt/meter values of the *physical* E_Z component.

Simulated excitation of the single-cavity model of Figure 1 is easily obtained by defining a magnetic-field line-source, of uniform intensity and phase, located across the *No. 1* waveguide at a sufficient electrical distance from the matched load on one side and from the cavity resonator port on the other. Both the *amplitude* in Ampere/meter and the *phase* in degrees can be specified, with the source-phase used as a common reference for the position-dependent phases of the electromagnetic field everywhere else within the cavity and its waveguides. Further, the post-processing program *SFO* can be used to *normalize* the local values of the fields, everywhere within the cavity and the waveguides, to any reference value arbitrarily assigned to the line-integral of the field, computed along the X/Y-plane trace of the port *No. 1* interface. The normalization applies then a *complex scale factor* to the local field values, that makes them consistent with the selection of port 1 as the zero-phase reference-location.

The *active* power absorbed by each of the six simulated matched loads (or *perfectly absorbing layers: PML*) can be computed by geometrically defining rectangular interpolation region, that fully cover each of the waveguide end-sections. The post-processing program *SFO* can then be used to *integrate* the active power absorbed within each rectangular region, which equals the total power absorbed by each of the simulated matched loads if the waveguide walls are defaulted to being *lossless*. Further, the *input* active power at port *No. 1* can also be computed as the real part of the complex product of the E- and H-field line-integrals, along the arc of circle that represents the X/Y-plane trace of the port *No. 1* interface. The five ratios of the active powers absorbed by each of the simulated matched-loads *No. 2* through *No. 6*, to the input active power at port *No. 1 must* all be mutually equal, because of representing the square of the magnitude of the *common value* of all the cross-term $S_{ij} = S_{ji}$ of the resonator scattering matrix. Indeed, as a consequence of the C_{6V} *rotation*-and-*reflection symmetries* of the six-port unit-cell resonator, its 6×6 scattering matrix is *a-priori* known to be simultaneously *symmetric* about its main diagonal, and *circulant*, so that: a) the six elements of its first row are the only different element of the whole matrix, and b) the elements symmetrically located about the main diagonal are mutually equal. The combination of the *geometric* and *reciprocity* symmetries

reduces the total number of different scattering matrix elements from $6^2 = 36$ to only two, the two being S_{ii} and S_{ij}. The *a-priori* knowledge implied by this symmetries provides a rigorous theoretical basis for enhancing the accuracy of the results of numerical field simulations by way of least-squares-fitting.

4 - THE HEXAFOLIUM : A FIRST 18-PORT RESONATOR CLUSTER.

Figure 2 shows the geometry of the simplest model of cavity-resonator cluster, that includes only seven mutually-identical six-port cylindrical cavity resonators. The seven resonators are the *unit-cells* of the *smallest* coupled-resonator cluster that can be considered as a *two-dimensional* wave-propagation medium. Two concentric tiers of *unit-cells* can be identified, the first consisting of the single *central* resonator, and the second composed of the outer ring of six resonators. The seven-resonator cluster of Figure 2 exhibits the same hexagonal C_{6V} *rotation*-and-*reflection symmetries* of each of its six-port unit-cells, and represent the simplest prototype of an *hexagonal cluster.* In the illustration of Figure 2, the model is represented in a Cartesian reference frame, where the *X/Y*-plane is orthogonal to the axes of the seven cavities and is also coincident with the *H*-plane of the cavity TM_{01} mode, of the TE_{10} mode of the *18* external waveguides and that of the *six* resonant irises of the central cavity. The simulated *18* radial waveguides and the *six* irises are filled with lossless dielectric, as in the single-resonator model of Figure 1. As a consequence of the C_{6V} *rotation*-and-*reflection symmetries* of the cluster its *18* × *18* scattering matrix is simultaneously *symmetric* about its main diagonal, and *block-circulant* with *circulant blocks*, so that: a) the *18* elements of its first row are the only different element of the whole matrix, b) the 3×3 matrix blocks that are symmetrically located about the main diagonal are the transpose of each other, and c) the four different 3×3 matrix blocks are all *circulant.* The combination of the *geometric* and *reciprocity* symmetries reduces the total number of different scattering matrix elements from $18^2 = 324$ to only *five*, the five being S_{11} , S_{12} , S_{14} , S_{17} , and $S_{1,10}$ [6]. Again, the *a-priori* knowledge implied by this symmetries provides a rigorous theoretical basis for vastly enhancing the accuracy of the results in numerical field simulations by way of least-squares-fitting.

Equivalent voltages and currents at the *18* external ports can be obtained from the post-processing program *SFO*, by computing the line-integrals of the local field gradients along the *18* arcs of circle that represent the *X/Y*-plane traces of the input-port interfaces to the external waveguides. Similarly, the equivalent voltages and currents at the *six* internal ports of the central resonator can be obtained by computing the line-integrals of the local field gradients along six straight segments, drawn halfway through the finite thickness of the irises of the central resonator. The segments represent the *X/Y*-plane traces of the interfaces between the inner and outer tier of resonators.

The post-processing program *SFO* can also be used to compute the total active power dissipated on the walls of the seven cavity resonator, by assuming the walls to have a finite value of surface resistivity. Particular attention must, however, be paid to the fact that, when solving complex-field electromagnetic problems with the *CFISH* program while at the same time using the *E* and *H* fields in *complementary* roles, by default *SFO* omits Dirichlet boundaries from power and local field calculations, unless it is specifically directed to *include* such boundaries. This can be easily done by setting the specific, logical control-variable *IncludeDirichletSegs* equal to *Yes*, in the *SUPERFISH* initialization file. The *SFO* program includes four different options for specifying the surface resistance of conductors, depending on whether these are normal conductors or superconductors, and whether the default values for copper or a user-specified resistivity value is to be used. Generally, the *E* and *H* fields are used in *complementary* roles to find the solution for a *TE* cavity mode, in which case, the roles of *E* and *H* are interchanged. The listed values of the *E*-field in the *SFO* output file actually correspond to the magnetic field *H* of the *TM* mode.

5 - SCATTERING PARAMETER EXTRACTION AND VALIDATION.

The complex, multi-dimensional scattering matrices *S* of multi-port single resonators, and that of resonator-clusters of relatively moderate extent can be directly computed from the complex field data generated by the *CFISH* program. This can be done by first interpolating and integrating the complex *E*- and *H*-fields along the input and

output interface-lines between the considered device and its external waveguides. Both the E- and H-field have there *constant phase* if the selected interface line is coincident with the *phase-fronts* of the traveling input- or output-wave at the considered port. The phase-front can easily be identified by generating phase-contour displays, as discussed above.

The obtained complex integrals represent the equivalent port-voltages and equivalent port-currents, so that the complex ratios of these integrals represent equivalent, local complex impedances. Further, the real parts of the voltage × current products represent the *active* input or output power at the given port, while the imaginary parts of the products represent the *reactive* power being exchanged at the given port between the device and the selected external waveguide. These results lead to the computation of the complex, equivalent, multi-dimensional *impedance* matrix Z of the considered device. The results obtained from field-simulation data can then be directly compared to those of previous experimental measurements, performed on physical models of single cavity resonators, and of resonator clusters of moderate extent [5].

An essentially infinite number of different multi-dimensional scattering matrices S of multi-port single resonators, or of a resonator-clusters can be computed from the obtained *unique* impedance matrix Z, depending on the selected *basis* of *impedance normalization*. The *basis* of the normalization could in principle be *any arbitrary* complex impedance matrix Z_0, of the *same size* as the impedance matrix Z, used as a parameter in the definition of the sets of in-going and out-going waves, to and from some given multi-port network. In common microwave engineering practice, however, only two choices have any useful physical significance: a) a *real diagonal* Z_0-matrix with all its main-diagonal elements equal to the wave-impedances Z_{0i} of the set of external waveguides used in the numerical field computation, and b) the *auto-normalization* matrix Z_{0I}, that is generally complex, and *block-diagonal* with as many *non-diagonal blocks* as there are separately-identified sets of network-ports, each set being considered as a *multi-port interface* [1-2]. The scattering matrix S_0 normalized to the matrix Z_0 includes the wave reflection coefficients S_{ii} and the wave transmission factors S_{ij} that characterize the response of the given multi-port network *when connected* to external waveguides having the Z_{0i} wave-impedances. Conversely, the scattering matrix S_I normalized to the matrix Z_{0I} is characterized by having *identically-zero* blocks along its main diagonal and off-diagonal elements S_{ij} that characterize the response of the given multi-port network *when connected* to a set of external *unconditionally-matched* load-networks. The scattering matrices S_0 normalized to the matrix Z_0 and the scattering matrix S_I normalized to the matrix Z_{0I} are mutually related by way of the scattering matrix re-normalization transform [30].

6 - NETWORK ANALYSIS OF LARGER CLUSTERS.

The mathematical problem of generating closed-form expressions of the characteristic Z, $ABCD$, S or T parameter-matrices of large two-dimensional clusters, using as inputs the scattering matrices of multi-port unit-cell networks, has been already solved, by applying advanced methods of multi-dimensional linear algebra [Ref. 5-8 and 16-20], and methodically exploiting the intrinsic geometric and electromagnetic *symmetries* of the clusters. Recursive solutions are readily available for clusters having *square* [17] or *hexagonal* [6] lattices, and for two-dimensional structures having two mutually-coupled layer, resembling *stacked-honeycombs* [8]. These *stacked-honeycomb*, two-dimensional structures include multiple *meandering* wave-paths, that alternate between the two cavity-resonator clusters of the top and bottom layer (Figure 4). Such structures are a two-dimensional generalization of the well-known, one-dimensional *side-coupled* cavity-resonator structure used in some high-current charged-particle linear accelerators. Extensive graphic visualizations of the field-simulation results obtained are to be presented in session.

7 - REFERENCES.

[1] Speciale R. A. ,"Advanced Design of Phased Array Beam-Forming Networks," IEEE Antenna and Propagation Magazine, Vol. 38 , No. 4 , August 1996, pp. 22-34.

[2] Speciale R. A. ,"Synthesis of Phased Array Aperture Distributions," Paper submitted on January 11, 1997 for publication in the IEEE Antenna and Propagation Magazine (an 85-page manuscript may be requested from the author, while the paper is being revised as suggested by reviewers).

[3] Speciale R. A. , US Patent No. 5,347,287 Awarded September 13, 1994 (Accessible at:
http://patent.womplex.ibm.com/details?patent_number=5347287, . . . and at:
http://patent.womplex.ibm.com/cgi-bin/db2www.cmd/v3/claims.d2w . . . →
→ . . . /report?patent_number=5347287).

[4] Speciale R. A. , US Patent No. 5,512,906 Awarded April 30, 1996 (Accessible at:
http://patent.womplex.ibm.com/details?patent_number=5512906, . . . and at:
http://patent.womplex.ibm.com/cgi-bin/db2www.cmd/v3/claims.d2w . . . →
→. . . /report?patent_number=5512906).

[5] Speciale R. A. ,"Mathematical Representation of Multiport Resonator Test Data," Proceedings of the 13th Annual Review of Progress in Applied Computational Electromagnetics, Monterey, California, March 17-21, 1997, Vol. 1, pages 516-532.

[6] Speciale R. A. ,"Wave Propagation on Two Dimensional Slow-Wave Structures with Hexagonal Lattice," Proceedings of the 13th Annual Review of Progress in Applied Computational Electromagnetics, Monterey, California, March 17-21, 1997, Vol. 2, pages 1015-1028.

[7] Speciale R. A. ,"Wave Propagation on Two Dimensional Slow-Wave Structures with Square Lattice," Proceedings of the 13th Annual Review of Progress in Applied Computational Electromagnetics, Monterey, California, March 17-21, 1997, Vol. 2, pages 1010-1014.

[8] Speciale R. A. ," Wave Propagation on Two-Level Twin-Stacked-Honeycomb Structures," Proceedings of the 13th Annual Review of Progress in Applied Computational Electromagnetics, Monterey, California, March 17-21, 1997, Vol. 2, pages 1029-1035.

[9] Billen J. H. and Young L. M. ,"POISSON/SUPERFISH," Software System Documentation, Report LA-UR-96-1834 (Revised August 28, 1997), Los Alamos National Laboratory, Los Alamos, New Mexico.

[10] Cooper R. K. et al. ,"Electromagnetic Design Codes Maintained on the MFE Network by the LAACG," Proceedings of the 5th Annual Review of Progress in Applied Computational Electromagnetics, Monterey, California, March 20-24, 1989, pages 9-21.

[11] Speciale R. A. ,"Advanced Design of Phased Array Beam-Forming Networks," Proceedings of the 12th Annual Review of Progress in Applied Computational Electromagnetics, Monterey, California, March 18-22, 1996, Vol. 2, pages 918-930.

[12] Speciale R. A. ,"Synthesis of Phased Array Aperture Distributions," Proceedings of the 12th Annual Review of Progress in Applied Computational Electromagnetics, Monterey, California, March 18-22, 1996, Vol. 2, pages 898-913.

[13] Speciale R. A. ,"New Results in the Synthesis of Aperture-Field Distributions for Ultra-High Gain Phased Arrays," Proceedings of the 12th Annual Review of Progress in Applied Computational Electromagnetics, Monterey, California, March 18-22, 1996, Vol. 2, pages 914-917.

[14] Speciale R. A. ,"Computation and Graphic Visualization of Plane-Wave K-Space Spectra and Far-Field Patterns with *MATLAB 4.0*," Proceedings of the 12th Annual Review of Progress in Applied Computational Electromagnetics, Monterey, California, March 18-22, 1996, Vol. 2, pages 1150-1157.

[15] Speciale R. A. ,"Computer Simulation of Isotropic, Two Dimensional Guided-Wave Propagation," Proceedings of the 11th Annual Review of Progress in Applied Computational Electromagnetics, Monterey, California, March 20-25, 1995, Vol. 2, pages 639-647.

[16] Speciale R. A. ,"Wave-Field Patterns on Electrically Large Networks," Proceedings of the 11th Annual Review of Progress in Applied Computational Electromagnetics, Monterey, California, March 20-25, 1995, Vol. 2, pages 656-663.

[17] Speciale R. A. ,"Symmetry Analysis of Large Two Dimensional Clusters of Coupled Cavity Resonators," Proceedings of the 9th Annual Review of Progress in Applied Computational Electromagnetics, Monterey, California, March 22-26, 1993, pages 281-288.

[18] Speciale R. A. ,"Sectored Cylindrical Cavity Resonators," Proceedings of the 8th Annual Review of Progress in Applied Computational Electromagnetics, Monterey, California, March 16-20, 1992, pages 274-281.

[19] Speciale R. A. ,"Guided Wave Propagation on Two Dimensional Clusters of Directly-Coupled Cavity Resonators," Proceedings of the 7th Annual Review of Progress in Applied Computational Electromagnetics, Monterey, California, March 18-22, 1991, pages 428-431.

[20] Speciale R. A. ,"Wave Propagation on Infinite, Two Dimensional Structures," Proceedings of the 5th Annual Review of Progress in Applied Computational Electromagnetics, Monterey, California, March 20-24, 1989, pages 200-244.

[21] Speciale R. A. ,"Computation and Graphic Visualization of Plane-Wave K-Space Spectra and Far-Field Patterns with MATLAB 4.0," Proceedings of the 1995 IEEE Antenna and Propagation Society International Symposium, Newport Beach, California, June 18-23, 1995, Vol. 2, page 1090.

[22] Speciale R. A. ,"Wave-Field Patterns on Electrically Large Networks," Proceedings of the 1995 USNC/URSI Radio Science Meeting, Newport Beach, California, June 18-23, 1995, page 8.

[23] Speciale R. A. ,"Computer Simulation of Isotropic, Two Dimensional Guided-Wave Propagation," Proceedings of the 1995 USNC/URSI Radio Science Meeting, Newport Beach, California, June 18-23, 1995, page 9.

[24] Speciale R. A. ,"Symmetry Analysis of Large Two Dimensional Clusters of Coupled Cavity Resonators," Proceedings of the 1993 IEEE Antenna and Propagation Society International Symposium, Ann Arbor, Michigan, June 28-July 2, 1993, Vol. 3, pages 1258-1261.

[25] Speciale R. A. ,"Symmetry Analysis of Large Two Dimensional Clusters of Coupled Cavity Resonators," Proceedings of the 1993 USNC/URSI Radio Science Meeting, Ann Arbor, Michigan, June 28-July 2, 1993, page 307.

[26] Speciale R. A. ,"Sectored Cylindrical Cavity Resonators," Proceedings of the 1992 USNC/URSI Radio Science Meeting, Chicago, Illinois, July 18-25, 1992, page 161.

[27] Speciale R. A. ,"Guided Wave Propagation on Two Dimensional Clusters of Directly-Coupled Cavity Resonators," Proceedings of the 1991 IEEE Antenna and Propagation Society International Symposium, London, Ontario, Canada, June 24-28, 1991, Vol. 2, pages 886-888.

[28] Speciale R. A. ,"The Experimental Determination of the Calibrated S-Parameters of a Single Resonant-Slot Array Element," Proceedings of the 1991 IEEE Antenna and Propagation Society International Symposium, London, Ontario, Canada, June 24-28, 1991, Vol. 2, pages 1272-1275.

[29] Speciale R. A. ,"Unusual Phased Array Architectures," Proceedings of the 1990 IEEE Antenna and Propagation Society International Symposium, Dallas, Texas, May 7-11, 1990, Vol. 4, pages 1421-1424.

[30] Speciale R. A. , "Derivation of the Generalized Scattering Parameter Re-normalization Transform," 1980 IEEE-ISCAS International Symposium on Circuits and Systems Digest of Technical Papers, Houston, Texas, April 28-30, 1980, pp. 166-169, IEEE Cat. No. 80CH1564-4.

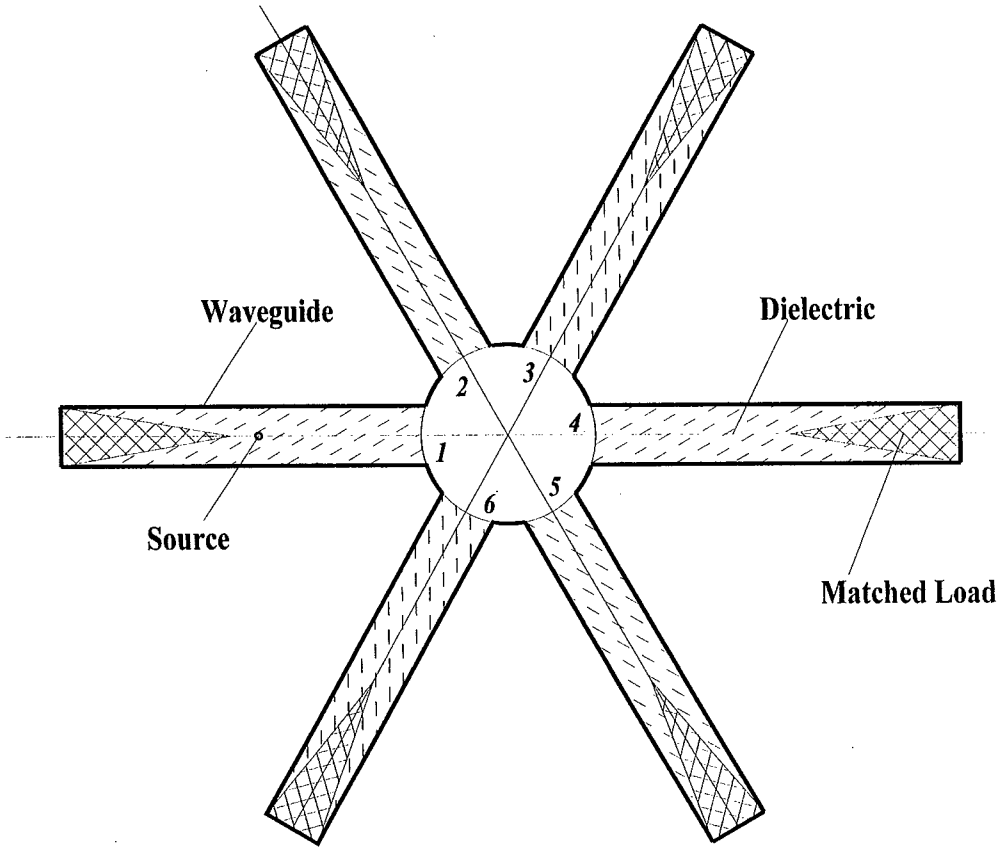

Figure 1 - Six-Port Cylindrical Cavity Resonator with C-6v Rotation/Reflection Symmetry.

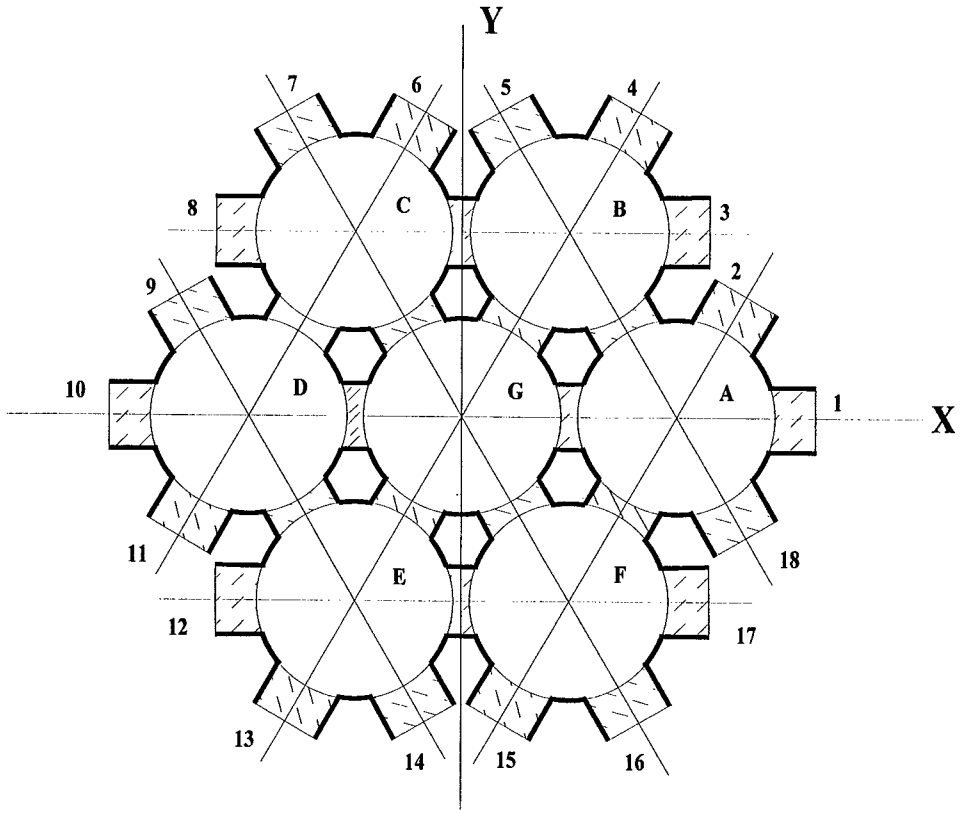

Figure 2 - Hexagonal Cluster of Resonant-Iris-Coupled Cylindrical Cavity Resonators.

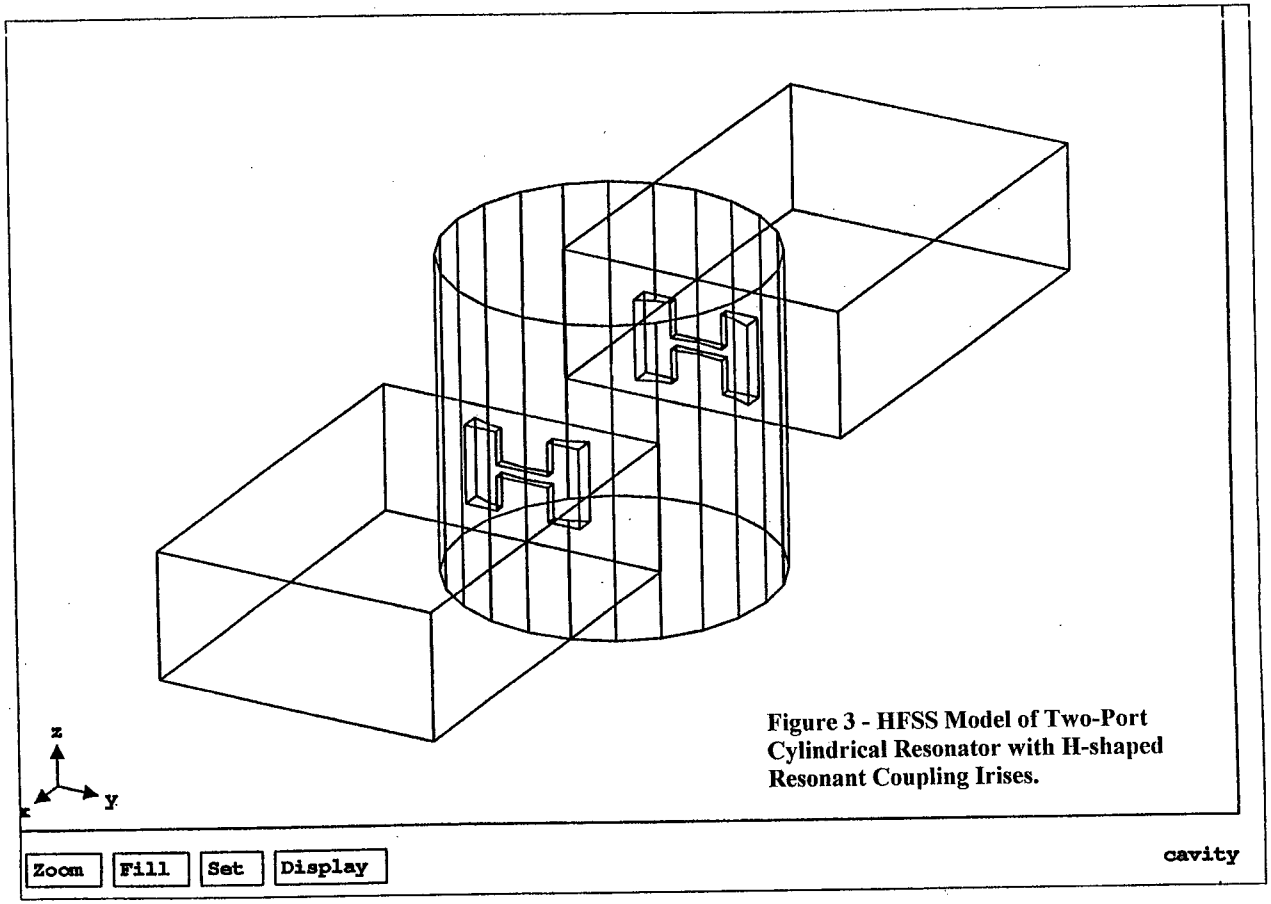

Figure 3 - HFSS Model of Two-Port Cylindrical Resonator with H-shaped Resonant Coupling Irises.

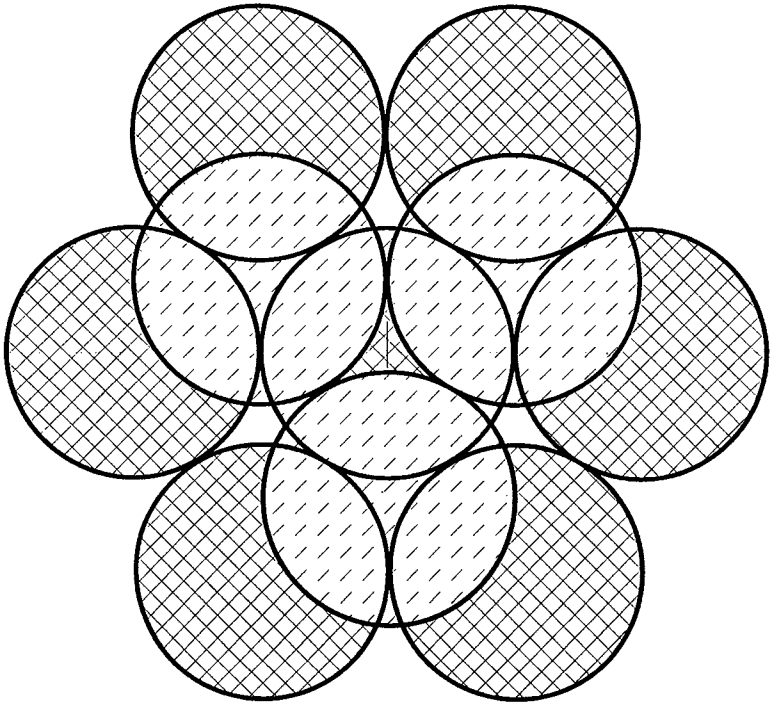

Figure 4 - Representative Geometry of a "Twin Stacked Honeycomb" Slow-Wave Structure. The Dashed Circles Represent here the Upper-Level Cylindrical Three-Port Resonators.

EXTENDED RAY-OPTICAL TECHNIQUE FOR INSTALLED PERFORMANCE OF LARGE AIRBORNE ANTENNA SYSTEMS

Jacob J. Kim, Kuang Wu, Sidney W. Theis, and Oren B. Kesler

Antenna/Nonmetallics Technology Center
Raytheon Systems Company
McKinney, Texas, U.S.A.

ABSTRACT

In recent years many electromagnetic (EM) analysis techniques and computer codes have been developed to predict radiation patterns of various antenna types in free space or radome effects. However, it is still a difficult task to predict total installed performance of large airborne antenna systems due to lack of efficient computer codes for both airframe interactions and radome effects. Thus, we developed an extended ray-optical technique, which could efficiently predict total installed performance of large airborne antenna systems, i.e., the near field scattering from aircraft structures and radome effects. The new analysis technique utilizes a ray-tracing method in the radome simulation and incorporates the radome effects into ray optical fields in the airframe scattering analysis code. Since the same ray technique is used on both airframe and radome simulations, the new analysis code can efficiently predict total installed performance of large airborne antenna systems with arbitrary shaped radomes.

1.0 INTRODUCTION

Until recently most airborne antenna systems were designed and tested in a free space environment without considering the near field scattering effects from host structures and radome effects. However, these higher order effects on airborne antenna systems are the matter of increasing concern with added performance demands in the ever increasing jammer and clutter interference environments. Typical effects of the near field scattering on airborne antenna systems are radiation pattern distortion, reduced gain, increased sidelobe levels, and increased clutter returns through multipath. Some of the radome effects are insertion loss, beam broadening, boresight error, sidelobe degradation, increased cross-pol levels, etc. These higher order effects associated with the aircraft and radome structures can significantly limit the capability of the modern airborne radar antenna systems in isolating and locating targets.

In the recent years many electromagnetic (EM) analysis techniques and computer codes have been developed to predict the radiation patterns of various airborne antennas or radome effects. However, there are still no efficient computer codes that can accurately predict total installed performance of large antenna systems mounted on a large aircraft. That is, some analysis codes can predict the airframe interactions of antenna systems but are lacking the radome effects. Other analysis codes can predict radome effects but are lacking airframe interactions. Some other codes have some limited capabilities to predict both airframe interactions and radome effects but do not provide the computational efficiency desired for practical airborne antenna designs. Thus, we

investigated the capabilities and limitations of currently available analysis techniques and computer codes for the installed performance of practical airborne antenna systems. Then we developed an extended ray-optical technique that bridges the gap between aircraft scattering analysis codes and radome analysis codes for the total installed performance (i.e., aircraft interactions and radome effects) of large airborne antenna systems.

This paper will show a brief description of high frequency EM analysis techniques used for installed performance, an extended ray-optical approach for both the radome and airframe scattering effects, and practical examples of an airborne antenna system on a large aircraft.

2.0 HIGH FREQUENCY EM ANALYSIS TECHNIQUES FOR INSTALLED PERFORMANCE

There are many high frequency EM analysis tools available in these days for the radiation prediction of antenna systems mounted on an aircraft. These simulation tools generally fall under the categories of Uniform Geometrical Theory of Diffraction (UTD) based analysis codes or Physical Theory of Diffraction (PTD) based analysis codes. The UTD based antenna analysis codes include NEC/Basic Scattering Code (BSC) [1] and Aircraft Code [2]. The PTD based antenna analysis codes includes the APATCH code [3] that also utilizes the Shooting and Bouncing Ray (SBR) technique. Most of radome analysis codes are based on either ray-tracing technique or Physical Optics (PO) technique. Each of these techniques has its advantages and limitations, depending on the particular application.

The UTD, which is used in this paper for airframe interactions, is a ray optical technique. Figure 1 shows various first order UTD terms incorporated into one of the UTD codes [2].

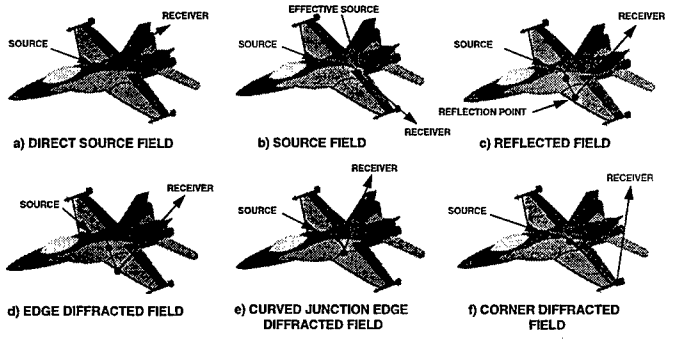

Figure 1. Various First Order UTD Terms For Aircraft Interactions

The total radiated field is the superposition of the following UTD field components: 1) direct field from the source; 2) curved surface diffracted fields from the fuselage (referred to as the source

field here); 3) reflected fields from wings or stabilizers; 4) diffracted fields from the leading or trailing edges of the wings or stabilizers, including diffraction from the curved junction edges formed by the intersection of the wings with the fuselage; 5) and vertex diffraction from each of the corners. In addition to the above first-order scattering from a structure, the rays reflected or diffracted from one structure tend to interact with other structures causing various higher order UTD terms such as double reflected, reflected-diffracted, diffracted-reflected, and double diffracted. Thus, the total radiated field of an antenna/array on an aircraft structure can be expressed as a summation of the above individual UTD terms. Note that separation of these terms based on path length might be important for accurately modeling the temporal dispersion caused by the aircraft interactions.

3.0 EXTENDED RAY-OPTICAL TECHNIQUE FOR TOTAL INSTALLED PERFORMANCE

We developed an extended ray-optical technique that combines the capabilities of both an airframe scattering analysis code and a radome analysis code for the total installed performance of large airborne antenna systems. The new technique can use either analytic surface or faceted surface for true radome geometry. Accurate modeling of the radome surface is very important in EM analysis since most radomes are in the proximity of the antenna aperture. It is note that the closer any scattering object is to the antenna aperture, the bigger its effects are on the resulting patterns. The new analysis technique utilizes a ray-tracing method in the radome simulation and incorporates the computed radome effects into ray optical fields in the airframe scattering analysis code. Since the same ray technique is used for both aircraft interactions and radome simulations, the analysis code is computationally very efficient.

Figure 2 shows more details on the extended ray-optical process. First the aircraft analysis code is used to determine the geodesic path between an antenna element and an observation point. Next the radome code is used to find an intersection point and corresponding reflection/transmission coefficients on the radome wall. Then the amplitude and phase of the transmitted ray from an antenna element are modified by radome transmission/reflection coefficients and the modified ray is used as an incident ray at the diffraction or reflection points on the aircraft structure.

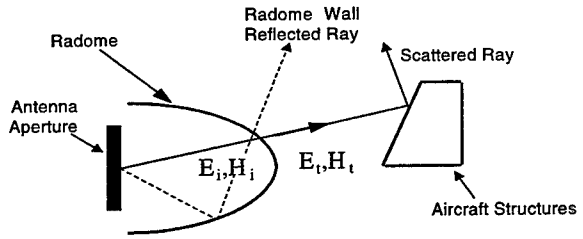

Figure 2. Extended Ray-Optical Technique For Installed Performance Of Airborne Antenna Systems w/ Radome

4.0 PRACTICAL EXAMPLES OF AN AIRBORNE ANTENNA SYSTEM

Figure 3 shows the configuration of a typical dorsal mounted airborne antenna system. We fully evaluated the total installed performance (i.e., airframe interactions and radome effects) of the airborne antenna system using the new analysis code based on the extended ray-optical technique. The airborne antenna system consists of an ellipsoid shaped radome and an aperture inside as shown in the figure.

First we evaluated the radome effects on the array patterns. Figure 4 shows a comparison of the elevation plane patterns of the array with and without radome surface. The comparison clearly shows the effects of radome such as insertion loss, mainbeam broadening, boresight error and cross polarization, etc. Note that the patterns shown in Figure 4 include only the direct transmission through the radome wall and do not include the reflection effects from the radome wall.

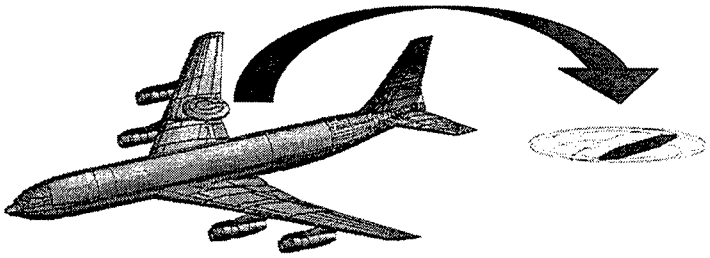

Figure 3. Computer Model for a Dosal Mounted Airborne Antenna System

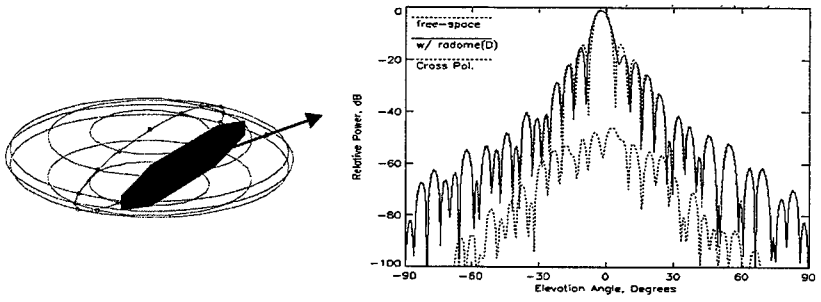

Figure 4. Elevation Patterns of the Array w/ and w/o Direct Transmission through Radome Surface.

Figure 5 shows a comparison of elevation patterns of the array with and without the radome effects including both direct transmission and wall reflection. The comparison indicates that the radome wall reflection effects are increased sidelobes between +45° to +70°angular section. It is noted that radome wall reflection depends on the radome shape and antenna scan angle. Since we used the -2° elevation scan angle of the array in this simulation, the radome wall effects in upper angular section appeared to be more severe than in the lower angular section. Figure 6 shows the boresight shift on main beam due to the radome surface. The boresight shift appears to be – 0.24° in this case.

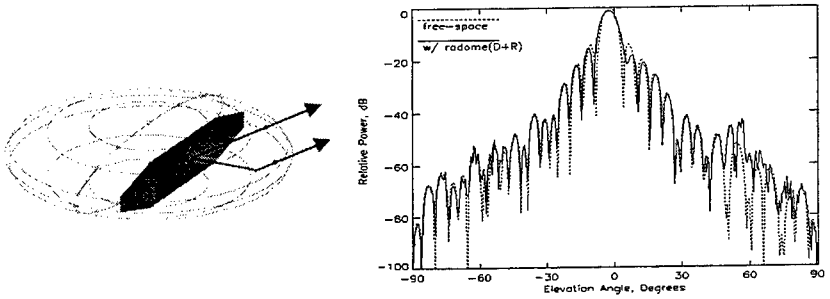

Figure 5. Elevation Patterns of the Array w/ and w/o total Radome Effects.

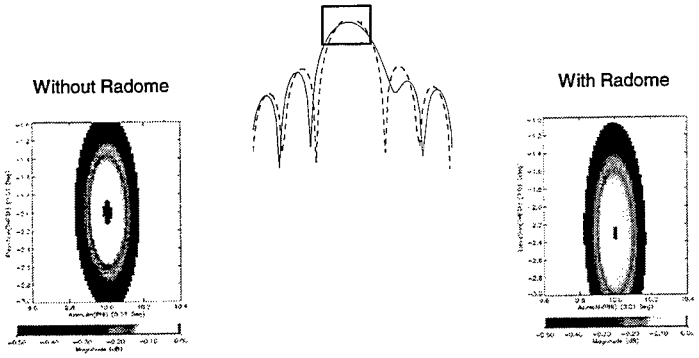

Figure 6. Sectional Volumetric Patterns in Main Beam Region with and without Radome

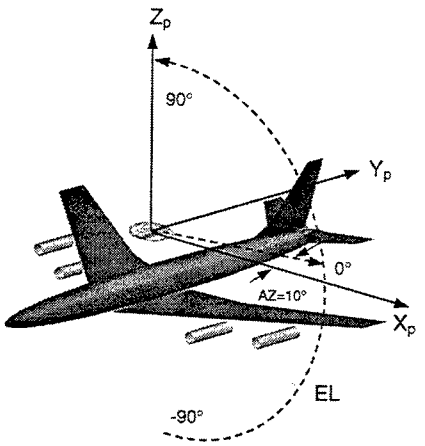

Figure 7 Computer Model of an Array with a Radome on an Aircraft.

Figure 7 shows the configuration of a computer model for an aperture inside a radome and an aircraft. First we evaluated the airframe interactions on the array radiation patterns without considering radome effects. Figure 8 shows an elevation pattern of the array on an airframe without a radome. It is noted that the elevation cut is a great circle cut through the mainbeam that is 10° squint in azimuth direction. The elevation plane pattern for an array on the airframe is also compared with that in free space to show the airframe interaction effects. The comparison clearly shows that the blockage effect by the wing appears in the -90° to +30°angular section and the sidelobe degradation due to the reflection off the wing appears in +30° to +90°angular section. The comparison shows that the main beam and a few sidelobes near the main beam are not affected by the aircraft interactions.

Next we evaluated the total installed performance of the array that includes both airframe interactions and radome effects. Figure 9 shows an elevation pattern of the array with a radome on an airframe. The elevation plane pattern for an array on the airframe is also compared with that in free space to show the airframe interactions and radome effects. The comparison clearly shows that the same blockage and reflection effects of the airframe in the ±90° to ±30° angular sections and radome effects around main beam region including insertion loss, mainbeam broadening, boresight shift, and sidelobe degradation. The computation time for the elevation patterns in Figures 8 and 9 was 1 hour and 3 minutes for the array with a radome and 1 hour for the array without a radome on a Sun workstation. It is noted that the array used in this calculation consists of 2432 radiating elements.

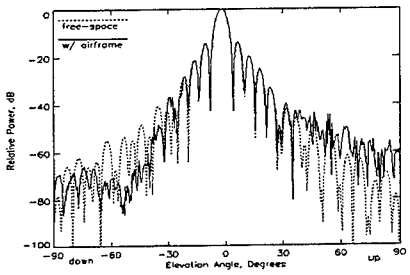

Figure 8. Elevation Pattern of the Array on an Aircraft without Radome.

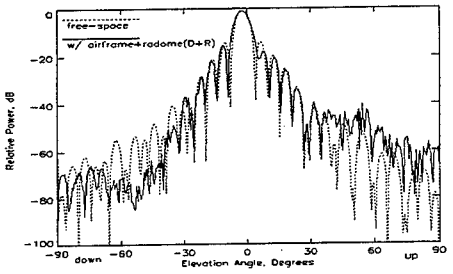

Figure 9. Elevation Pattern of an Array with a Radome on an Aircraft.

5.0 CONCLUSIONS

We developed an extended ray-optical technique that bridges the gap between the aircraft scattering analysis codes and the radome analysis codes for the total installed performance of practical airborne radar antenna systems. The new analysis technique uses the same ray technique on both airframe and radome simulations. Thus, it is computationally very efficient and can be used to analyze total installed performance of a large antenna system on a large airframe. The developed analysis code has been successfully used for the installed performance of a number of practical airborne surveillance radar systems and its accuracy has been fully verified with extensive range measurements. Typical computation time required for the radome analysis is only a small fraction (e.g., less than 5%) of the time required for the total installed performance analysis.

6.0 REFERENCES

1. R.J.Marhefka, J.W.Silvesto, "NEC/Basic Scattering Code User's Manual," The Ohio State University, March 1989.
2. W.D.Burnside, J.J.Kim, B.Grandchamp, R.G.Rojas, P.Law, "Airborne Antenna Radiation Pattern Code User's Manual," The Ohio State University, September 1985.
3. DEMACO, "APATCH v 2.1 User's Manual - Platform Radiation Code," July 1996.

Antenna Imaging and Visualization

John Shaeffer and **Brett Cooper**
Marietta Scientific, Inc.
376 Powder Springs St. 240A
Marietta, Georgia 30064
(770) 425-9760
msi@inetnow.net
www.inetnow.net/~msi

ABSTRACT: Three antennas are used as examples for demonstrating the utility antenna imaging and visualization for determining where on the structure radiation comes from. The image approach is bistatic k-space. This analytic technique uses a single excitation as computed from any frequency domain code such as MOM.

The three antennas are a Yagi, a long wire end fed traveling antenna, and a dipole fed parabolic dish. Visualization results include one and two-dimensional radiation images, near field distributions, far field radiation patterns, and current distributions. The electromagnetic performance was computed with a patch method of moments code.

The Yagi images show which of the elements are contributing energy to the far field. The long wire traveling wave antenna images show that radiation is produced along the entire length of the wire when the observer is located at the peak of the forward or reflected lobe. When the observer is located in the side lobe region perpendicular to the wire, the radiation sources appear at the end regions of the wire. The dipole fed parabolic dish antenna images show the relative levels of radiation contributed by the dipole feed and the reflector.

ANTENNA IMAGING: Radar cross section imaging has been in use since the late '70s. It has been instrumental in our understanding of scattering centers and the physical mechanisms contributing to radar cross section. Experimental imaging requires short pulse or wide bandwidth radiation. This is applicable for scattering but not for typical antenna applications due to their usually limited bandwidths. This has greatly reduced our ability to experimentally image antenna radiation center "hot spots" and to better understand the physical mechanisms contributing to main beam and side lobe radiation. Antenna imaging should improve our understanding not only of simple antennas, but more importantly, complex antenna environments on air vehicles, ships, and satellites where host body / antenna interaction affect performance.

The k-space image technique, however, is applicable to antennas *since no excitation frequency sweeps are required.* Bistatic k-space imaging uses the computed current distribution at a single frequency to obtain an image. The examples shown in this paper are among the first computational high resolution antenna images known.

VISUALIZATION IN COMPUTATIONAL ELECTROMAGNETICS: The ultimate goal of computational modeling is to predict measured or observed phenomena. For many years, computational scattering or antenna EM modeling output consisted of a backscatter or antenna radiation pattern that hopefully matched experimental results. In this mode, computational modeling did little to aid the identification and understanding of the physical mechanisms responsible for observed behavior. This limitation was unfortunate because computational EM codes should in principle be able to provide a rich insight to the scattering or radiation process if we just ask the proper questions and use the rapidly developing graphical display capabilities to illustrate the basic phenomena. Our EM visualization inspiration is similar to efforts in computational fluid dynamics; we are attempting to better understand the interaction of an EM wave or local excitation with a structure, the nature of body-body interactions, and the nature of the resultant radiation.

Visualization diagnostics for electromagnetics involve the display of body currents, near and far fields and radiation images. Each display tells us something different about the radiation process. Taken together, these diagnostics produce a more complete understanding.

Currents (or effective tangential magnetic or electric fields) are the fundamental quantities which produce far field radiation patterns and are often the computational goal, e.g., MOM codes. Knowledge of the current amplitude and phase distribution on a geometric structure is sufficient to compute the radiation pattern. Although a graphical display of currents

indicates the spatial amplitude distribution, it does not tell *how* the currents radiate in different directions in space, which is determined by the phase alone.

Displays of near field E and H indicate: how one part of a structure interacts with another part; how the surface currents and charges begin to form the eventual far-field radiation pattern; and how various surface current modes are formed, such as surface and edge traveling-wave mechanisms.

Imaging is yet another diagnostic tool for examining the scattering/radiation process. An image is not a picture of currents, but of the far field radiation produced by the currents. Images differ from a body current distribution in that an image shows *how* the currents radiate collectively. An image from a given angle tells us which *parts* of the current distribution are producing radiation in that direction.

The difference between images and far field radiation patterns is that the far field pattern is the phasor sum of signals from *all* radiation centers on the body which radiate in the observed direction. An image identifies each center as a separate entity. The utility of images results from the ability to separate and identify the individual radiation centers which have collectively summed to produce the net result. This enables us to understand the nature of each radiation center and also to modify it in ways which might be useful.

Several EM visualization computer codes are now beginning to appear. Hom [1] at NASA Langley has developed EM ANIMATE for use on Silicon Graphics workstations. Marietta Scientific, Inc. is developing EM VIZ [2], a PC / Windows based visualization program. EM VIZ input consists of points, triangles, and currents at the triangle vertices. This data can be generated by any frequency domain code such as the method of moments or physical optics. EM VIZ uses this current / geometry input information to display animated currents and computed near fields, bistatic k-space images, and far field radiation patterns. The results presented in this paper used EM VIZ.

The results presented here were computed using MOM3D, a surface patch method of moments code [3] whose output was formatted for input to EM VIZ.

Further background on the bistatic k-space image technique may be found in [4-5] and in [6-7] for other aspects of visualization.

BISTATIC VIEW REGION: Bistatic k-space images are obtained with one current distribution by computing the bistatically radiated field about an extended region centered on the view direction, Figure 1(a). This viewing region increases as the user specified resolution Δr becomes smaller. The k-space fractional bandwidth and resolution are related by the fundamental relation $\Delta r\, \Delta k = 2\pi$. As the resolution Δr becomes small, $\Delta k/k_0$ increases. This means that bistatic radiation over a wider angle is being sampled to form an image, Figure 1(b). Resolutions of $\Delta r = 0.5$ and $1.0\ \lambda$ have fractional bandwidths $\Delta k/k_0$ of $2k_0$ and $1\ k_0$ which correspond to view angle ranges of +/- 45° and 26° respectively on either side of the nominal receiver direction.

YAGI ANTENNA: The Yagi antenna example is a five-element array with one reflector element, one driven element, and three director elements. The frequency was 2 GHz and element lengths were 0.0850m, 0.0882m, and 0.0674m respectively. The antenna "wires" were modeled as flat narrow triangles. The patch geometry is shown as inserts in several of the results shown in Figure 2.

The E and H plane far field radiation patterns are shown in Figures 2 (a) and (b). The maximum gain is approximately 6.9 dBi and the front to back ratio is approximately 8 dB. The "time" snapshot H plane near fields, as computed from the current solution (and resulting surface divergence for electric charge) is shown in Figure 2(c). The forward peak radiated lobe is readily seen as well as the beginning formation of the upper and lower side lobes.

Images of electrically small antennas, i.e., those whose dimensions are near the image resolution limit, are difficult because the minimum resolution cell is not much smaller than the antenna itself. This Yagi antenna falls into this category. However, rectangular widowing, linear scales, and zero FFT padding can alleviate this situation somewhat.

Bistatic k-space images were computed with the receiver oriented on the main beam of the antenna. The specified resolution was $0.25\ \lambda$ so that the bistatic fractional bandwidth was $4k_0$ corresponding to a bistatic-viewing angle of +/-

180°. Images computations used a rectangular widow function to maximize resolution. The resulting FFT was zero padded for smoothing. The image amplitudes are shown on a linear scale rather than log scale to improve sensitivity of like scatterers. The 1D and 2D images clearly show maximum radiation is produced by the driven element, as one might expect. The next major contributor to the main beam are the currents on the middle director element.

We did not try to optimize this antenna for gain or front to back ratio. However, it is clear that the visualizations presented would considerably aid an engineer engaged in the optimization process by illustrating the physical results obtained by changes in configuration, feed points, and frequency.

FIVE LAMBDA TRAVELING WAVE ANTENNA: Our next sample antenna case is an electrically larger antenna. The well-known end fed long wire has its main radiation lobes near the axis for the forward and reflected traveling waves on the wire. Wire length and wavelength give the angular peak location of the end fire radiation, $\theta = 49\sqrt{\lambda / l} = 22°$ measured from grazing. The MOM antenna model was a thin triangular strip of width 0.01 λ.

The E plane axis symmetric radiation pattern is shown in Figure 3(a). The feed point is on the right side of the antenna insert. The main traveling wave lobe is approximately 10 dBi when looking into the feed point and 7 dBi when looking at the far end traveling wave reflection point.

The near electric field in the E plane is shown in Figure 3(b) where the four end fire lobes are clearly seen along with the interference pattern produced by the two oppositely directed traveling wave currents.

The bistatic image of this antenna was computed for a resolution of 0.5 λ that corresponds to a k-space fractional bandwidth of $2k_0$ and +/- 45° bistatic view angle. A rectangular FFT data window function was utilized to maximize resolution and a linear scale used to illustrate the resulting image. The FFT data was zero padded for smoothing.

The first 2D image, Figure 3(c), is centered on the main forward traveling wave lobe so that the feed point is toward the back end of the figure. The image suggests that radiation is produced along the entire length of the antenna with a peak near the rear feed point. At this angle, the radiation from all points on the traveling wave adds in phase along the antenna length. In this main beam direction, the path length phase and the phase of the traveling wave currents constructively phase add.

The second 2D image, Figure 3(d), is centered on the reflected traveling wave (TW) lobe. The far end of this figure is where the forward TW current reflects from the wire end. This image suggests that radiation is produced along the entire length of the reflected TW wire currents, with a peak at the rear termination. The radiation image amplitude decreases as the TW current loses energy due to the radiation process. A linear amplitude scale is the same for all three images so that the reader can estimate relative strengths.

The third 2D image, Figure 3(e), is centered perpendicular to the wire in the side lobe region. This radiation image strongly suggests that the contributions to the side lobe region are due to the end points of the antenna. The side lobes are caused by the phase addition and subtraction of the end point regions: peaks when the distances to each end phase add; nulls when the distances phase subtract.

PARABOLIC DISH WITH DIPOLE FEED: Our last sample antenna, Figure 4(a), is a five lambda diameter parabolic dish antenna with a focal point / diameter ratio, F/D, of 0.35. The dipole feed is placed at the focal point. The focal point was chosen to be an odd number of quarter wavelengths so that the dish reflected radiation would phase add with direct dipole radiation. No attempt was made to place a reflector behind the dipole to reduce its radiation in the main beam direction. The far field radiation pattern, Figure 4(b), shows a dipole like pattern with slightly higher gain on the reflector axis. We see that the reflector basically converts a fraction of the back dipole radiation to phase add with the front dipole radiation. A "time" snapshot of the reflector dish currents is shown in Figure 4(c) where axis symmetric rings of constant phase currents are seen. The E plane near fields, Figure 4(f), shows the formation of the main beam.

The 1D and 2D radiation images, Figure 4(d-e), with the observer on the parabolic axis, shows two major contributors to the far field radiation. The dipole feed is the main radiation source. The reflector dish contributes about 60% of the dipole front radiation. This suggests that the reflector dish intercepts about 60% of the rear dipole radiated energy for conversion

to the main beam. The resolution for these images is 0.5 λ with a +/- 45° bistatic view angle to either side of the image position. Note that the 1D image scale is linear while the 2D image scale is log.

SUMMARY: The utility of electromagnetic visualization for antenna problems has been illustrated. Visualization clearly aids in showing the physical processes by which radiation process occurs.

References

1. Kam Hom, "EM Animate: A Computer Program for Displaying and Animating Electromagnetic Near Field and Surface-Current Solutions", NASA Technical Memorandum 4539, May 1994.

2. "EM VIZ Users Guide", Marietta Scientific, Inc., January 1999.

3. John Shaeffer, "MOM3D Method of Moments Code Theory Manual," NASA CR 189594, Contract NAS1-18603, March 1992.

4. John Shaeffer, Kam Hom, Craig Baucke, Brett Cooper, and Noel Talcott, Jr., "Bistatic k-Space Imaging for Electromagnetic Prediction Codes for Scattering and Antennas", NASA Technical Paper 3569, July 1996

5. John Shaeffer, Kam Hom, Craig Baucke, Brett Cooper, and Noel Talcott, Jr., "A Review of Bistatic k-Space Imaging for Electromagnetic Prediction Codes for Scattering and Antennas", IEEE Antennas and Propagation Magazine, Feature Article, vol. 39, no. 5, October, 1997.

6. Kam Hom, Noel Talcott, Jr., and John Shaeffer, "Computational Diagnostic Techniques for Electromagnetic Scattering: Analytical Imaging, Near Fields, and Surface Currents", ACES, March 17-21, 1997.

7. Kam Hom and John Shaeffer, "Plate Scattering Visualization: Images, Near Fields, Currents, and Far Field Patterns", ACES, March 16-20, 1998.

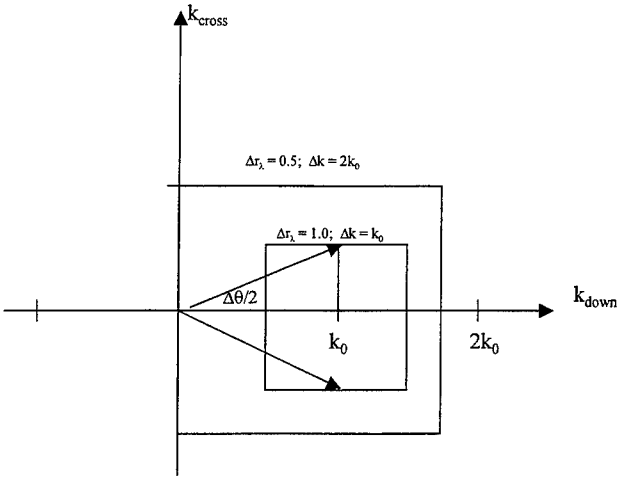

Figure 1a; Bistatic k space for computing radiation fields

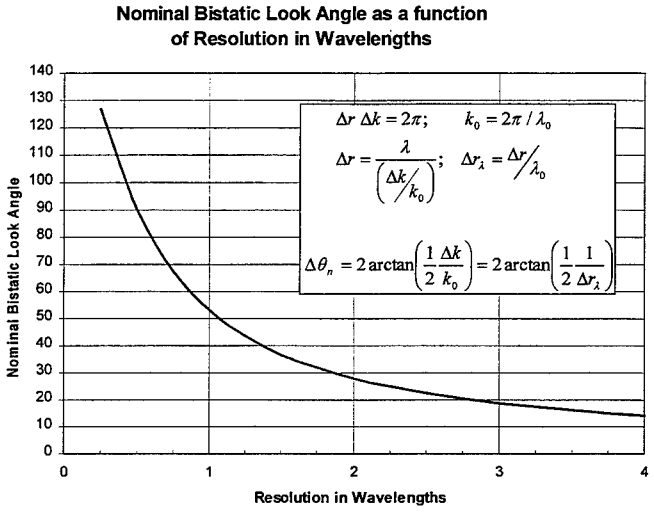

Figure 1b: Bistatic k-space look angle versus resolution

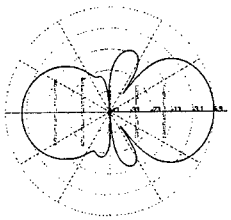

(a)

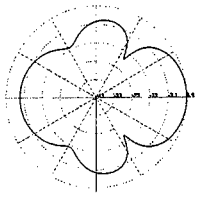

(b)

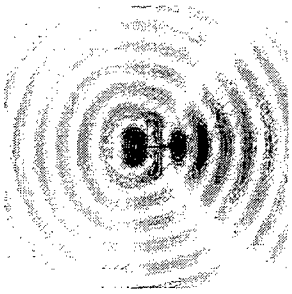

(c)

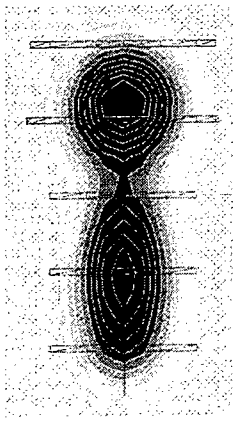

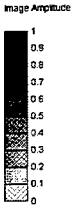

(d)

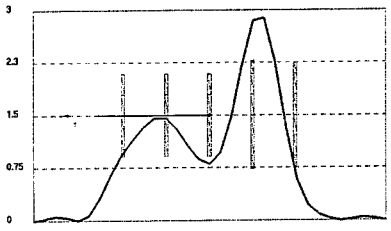

(e)

Figure 2: Yagi Antenna: a) Eplane pattern; b) H plane pattern;
c) Near Fields, H plane; d) 2D Image; e) 1D Image

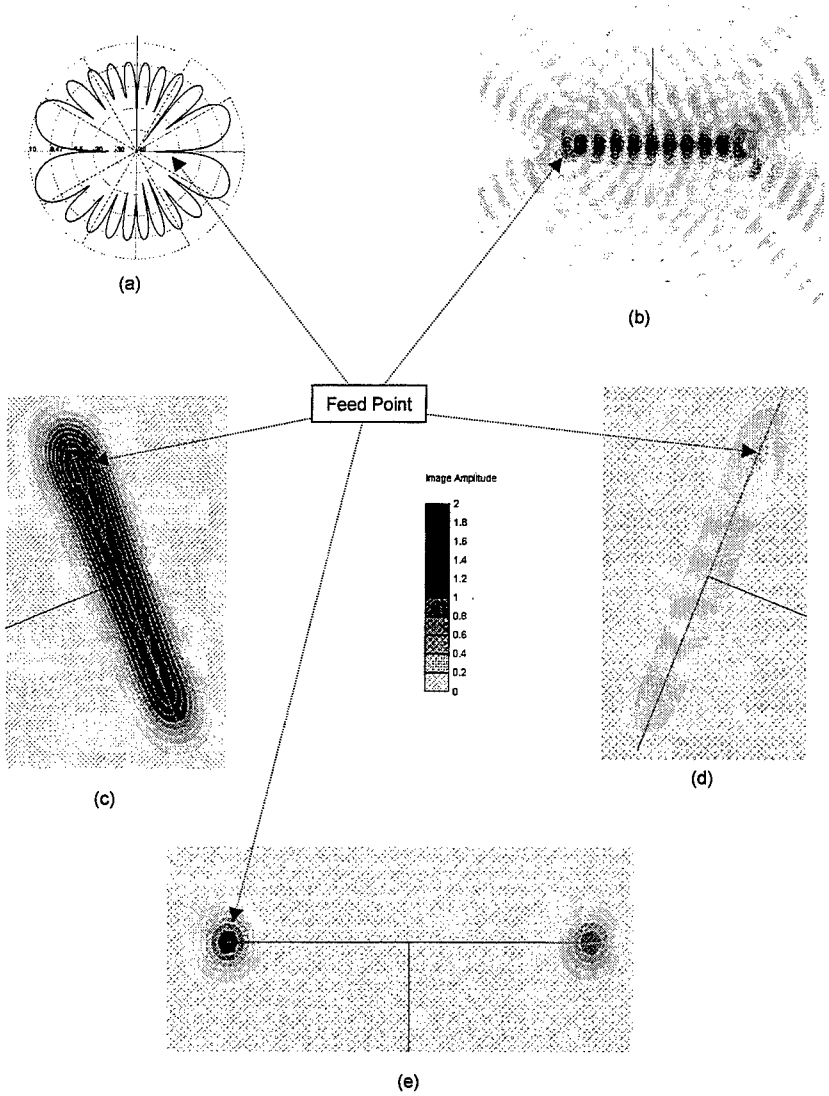

Figure 3: Five lambda traveling wave antenna: a) Far field pattern; b) Near fields; c) 2D image at forward lobe angle; d) 2D image at reflected lobe angle; e) 2D image at broadside. (Image scale is linear)

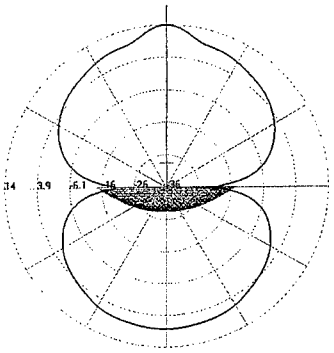

(a)

(b)

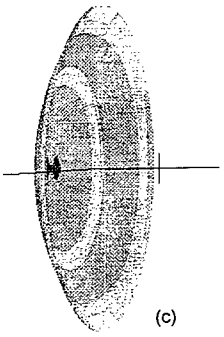

(c)

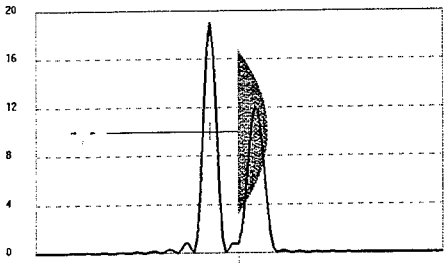

(d)

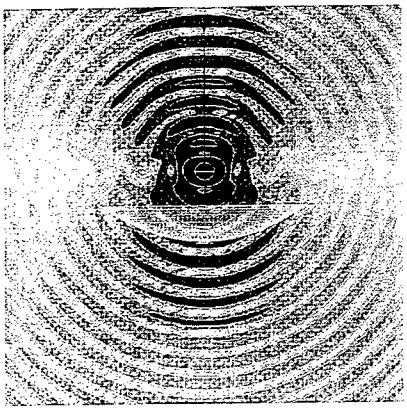

(f)

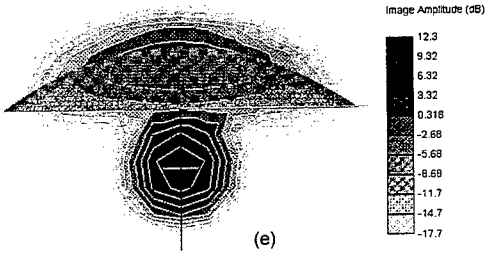

(e)

Figure 4: Parabolic dish antenna with dipole feed:
a) Geometry; b) Far field pattern, E plane;
c) Currents on dish; d) Down range image;
e) 2D image; f) Near fields, E plane.

Are Fractals Naturally Frequency Invariant/Independent?

Nathan Cohen

Fractal Antenna Systems., Inc.
2 Ledgewood Place
Belmont MA 02478

and

Science and Engineering Program
Boston University
Boston MA 02215

I. INTRODUCTION

Since their first published analysis (Cohen, 1995), fractals as antenna elements have stimulated considerable investigation (see, for example, Cohen, 1998; Puente et. al., 1996; Valdivia; 1996). As with all new investigations, this has met with some wrong turns and corrections (see, for example, Cohen, 1997). Although considerable progress on the behavior and use of fractal element antennae (FEA) has been realized, a long-standing misconception still persists regarding their ability to function as frequency invariant or frequency independent antennas. Here we present NEC4 simulations of simple fractal dipoles to demonstrate that while self- similarity brings very broad bandwidth, it ***does not*** produce a concomitant invariance with power pattern and gain.

II. MODEL AND SIMULATIONS

In Cohen (1998) the VSWR (and hence impedance) characteristics of a fractalized dipole were made evident by the application of a Koch triangle fractal generator over two successive iterations on the dipole. At wavelengths where the antenna was electrically large in its biggest dimension, the Koch dipole became extremely broad band, showing by example that a deterministic fractal is a naturally broad band antenna, even in a small number of iterations.

Iterations are a key issue with fractal antennae. There is no a priori reason to assume that invariance of one observable is emulated by other observables in the same iteration. Puente et al.(1997) have used analysis of fractal ***arrays*** to argue that FEA —when taken to many iterations—are also frequency independent or, alternatively, have discrete bands of invariance (that is, frequency invariance) for finite iterations (it should be noted that the fractal array analyses incorporate geometric symmetries in addition to fractal geometry.) This argument is used to explain the Sierpinski monopole's multiband/frequency invariant properties. (Puente et.al,1997).

Even with a perfect antenna, a large iteration number is unattainable. With large number of iterations, the width of wire, or, alternatively, etched connection width, becomes so small that ohmic losses dominate the impedance and gain observables. Hence we chose to model the Koch dipole to a 4^{th} iteration, where ohmic losses were still minimal and, like the 4^{th} iteration Sierpinski monopole (Puente et al, 1997) the finite but non-trivial iteration number may be expected to manifest some invariance properties—should they be a property of fractals.

The model is shown in **Figure 1**. The length in the X dimension is ½ wave at 65 MHz. Number 12 copper wire was modeled in free space. The feed was placed at the center with a short, symmetric horizontal wire length and NEC4 was used to accomplish the analysis from 500-2000 MHz. Segment densities were approximately twice that of conservative limits at each frequency. A 450 MHz PC platform was employed.

Table 1

Frequency (MHz)	*Impedance(ohms)*	*VSWR (300 ohms)*	*Gain (dBi)*
500	311 + j4	1.04	5.4
750	329 - j115	1.45	0.6
1000	298 - j150	1.65	3.9
1250	374 - j174	1.74	5.2
1500	195 - j113	1.87	4.5
1750	594 - j55	1.88	4.2
2000	354 - j132	1.54	6.5

III. RESULTS

Figure 2 shows the stacked comparison of the current distribution amplitudes. As noted in Cohen (1998) for the 2nd iteration Koch dipole, the current distribution 'pulls in' with higher frequency, much as with the cells on a log periodic array. A priori, the truncation by iteration number would produce less fine structure in the wire bending for which these frequencies are exposed, and hence the biggest deviation in characteristics from the lower frequencies.

However, **Table 1** reveals that while the VSWR remains reasonably invariant across the range, the gains vary by 6 dB. There is no simple dependence with increasing frequency. The gain is not invariant with, or independent of, frequency.

Figure 3 shows two representative azimuthal power patterns across the frequency range. The patterns bare little resemblance to each other. Again, the pattern is not invariant with, or independent of, frequency.

IV. DISCUSSION

Since only one counterexample illustrates the lack of validity of a generalized statement, we must conclude that frequency invariant and independent properties are not inherent to fractals as antenna elements.

It thus seems salient to explore what ***additional*** geometric constraints are necessary to achieve the effect. Rumsey's Principle (Rumsey,1966) connotes both self-complementarity

and a constant size/spacing ratio, as with the case of log periodic antennae. Impedance invariance—or at least a slow change of impedance—is achievable from fractal designs, so this attribute of self-complementary structures need not be treated as unique. What else is needed for frequency invariance/independence?

The answer to the above question is by no means clear. However, some insight is obtained by investigating the properties of two Koch dipoles that have different symmetries. The first, **Figure 4 (a),** is a 3rd iteration Koch dipole (again ½ wave in X at 65 MHz) which is **origin** (feed)-**symmetric**, while **Figure 4(b)** is **X-axis symmetric** (see the figure for definition of axes).

Table 2 illustrates the frequency behavior for VSWR and gain for these antennae. Neither is truly frequency independent. However, the origin symmetric version has an excursion of only about 0.4 dB from about 1000-2000 MHz. This, in most practical circumstances, is a close approximation to frequency independence. The azimuthal pattern is not invariant but has a largest excursion of about 25 degrees for the main lobe across the frequency range. In contrast, the X-symmetric version has large gain excursions over the frequency range. Furthermore it experiences orthogonal reversals in the main lobe angle over the frequency range. It does not approximate frequency independent or frequency invariant properties.

It is important to state that the monopole Sierpinski fractal element studied by Puente et al. *is* origin symmetric with respect to its mirror image Thus it would appear that fractal design with origin symmetry may have some utility in describing and producing frequency invariant/independent antennae. It has yet to be shown that these two characteristics are uniquely acceptable for inclusion within Rumsey's principle or some new corollary of it.

Table 2

Origin Symmetric			**X-Axis Symmetric**		
Freq.(MHz)	*VSWR (300 ohms)*	*Gain (dBi)*	*Freq.(MHz)*	*VSWR (300 ohms)*	*Gain (dBi)*
500	2.0	3.6	500	1.8	3.8
750	2.2	5.9	750	1.6	6.3
1000	1.8	5.1	1000	1.9	5.6
1250	1.7	4.7	1250	1.9	3.6
1500	1.4	4.9	1500	1.2	3.2
1750	1.3	4.8	1750	1.2	4.5
2000	1.7	4.7	2000	1.6	3.8

V. CONCLUSION

FEA are known to have wideband impedance behavior when electrically large. However this characteristic, or multiband (that is impedance invariant) behavior, does not necessarily imply invariance of gain and power pattern. We have shown that frequency invariant/independent behavior is not uniquely attributable to a fractal design. Additional geometric constraints dictate this possibility. Origin symmetry may be used to produce some FEA which have useful frequency invariant or frequency independent characteristics.

VI. ACKNOWLEDGEMENTS

I am grateful to Carles Puente for his discussions and encouragement to resolve this problem. Robert Hohlfeld helped sharpen my approach to the geometry issues.

VI. REFERENCES

Cohen,N., 1995, "Fractal Antennas Part 1", Communications Quarterly, Summer, 7.

Cohen,N., 1997, "NEC2 Modeling of Fractal-Element Antennas (FEA)", Proceedings ACES #13, 297.

Cohen,N., 1998, "Exploring a Fractal Dipole", ACES Newsletter, 13, 2, 23.

Puente,C., et al., 1996, "Fractal Multiband Antenna based on the Sierpinski Gasket", IEE Electronics Letters, 32,1,1.

Puente,C., et al., 1997, "Multiband Fractal Antennas and Arrays", in FRACTALS IN ENGINEERING, Vehel, Lutton, and Tricot, (eds), Springer-Verlag, Berlin,222.

Rumsey, V., 1966, FREQUENCY INDEPENDENT ANTENNAS, Academic Press.

Valdivia, J.,1996, Ph.D. Thesis, University of Maryland.

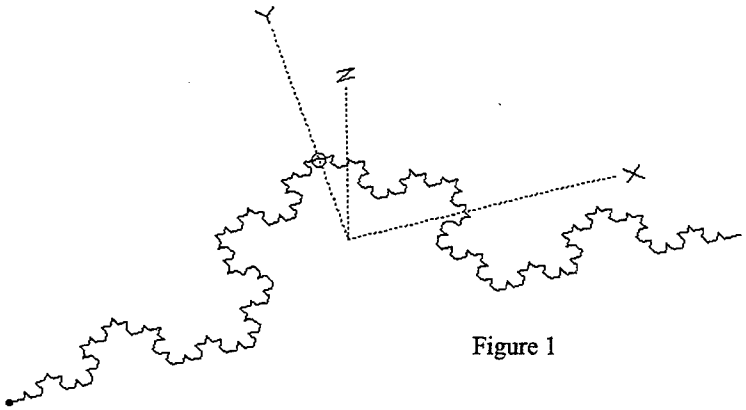

Figure 1

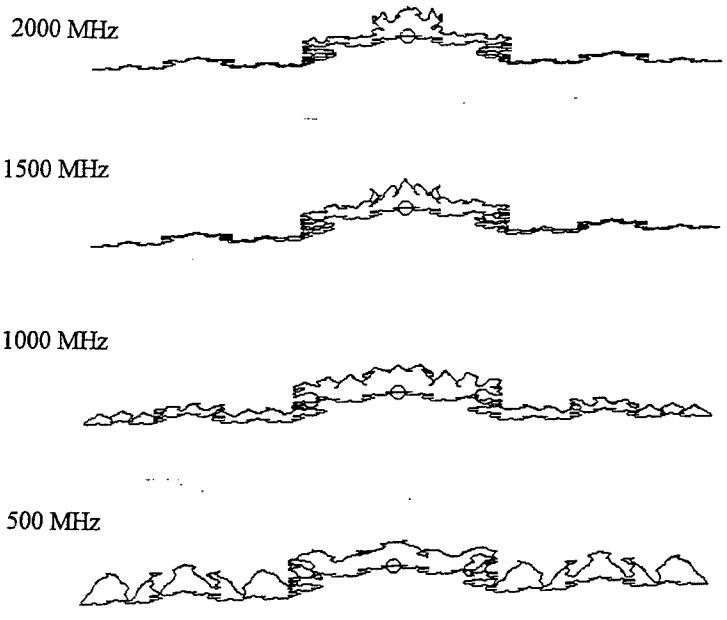

Figure 2

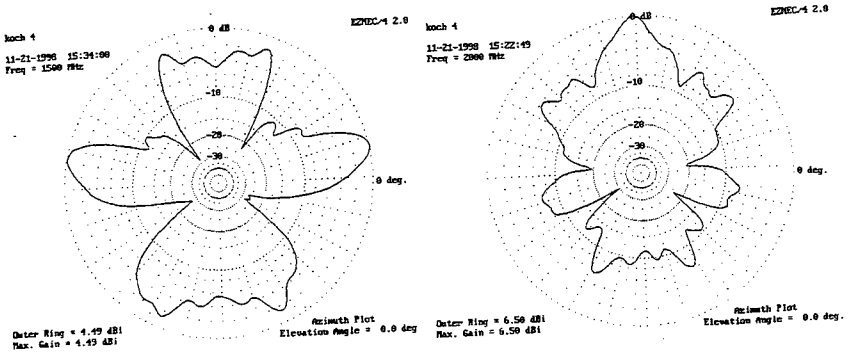

Figure 3

Figure 4(a)

ORIGIN SYMMETRIC

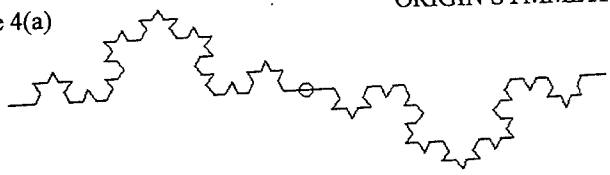

Figure 4(b)

X-AXIS SYMMETRIC

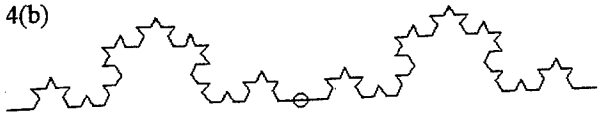

The Ultimate Antenna Training Aid.

Alan Nott, BEE, CEng, MIEE
Senior Electromagnetics and Software Engineer
Army Engineering Agency (AEA)
Department of Defence, Australia.
email: alan.nott@aea.sptcomd.defence.gov.au

Abstract:

This paper discusses the continuing development of antenna training aids at the Australian Army's Army Engineering Agency (AEA) for the Army's School of Signals, and the Navy's HMAS Cerberus Frequency Management School. The training aids rely heavily on the ability to produce high-quality rendered images of antenna radiation patterns using electromagnetic visualisation techniques developed at AEA. Data compression techniques developed for storage of antenna patterns permit the display of conventional radiation pattern graphs and together with a limited ionospheric modelling capability, of footprints of over-the-horizon communications parameters. Adjustment of parameters such as frequency, antenna height, slope, configuration, ground type and viewing angle control the selection and display of the appropriate antenna pattern image. Interactive operation coupled with the ability to view patterns either as a rendered 3D image, a graph, or a footprint provides excellent insight into the intricacies of antenna radiation patterns. This paper updates and consolidates a number of the author's previous papers on antenna training aids and related subjects.

Background:

Reliable communications depend on the best use of the available equipment, and effective exploitation of the communications medium. While this is true of any communications method, communication in the high frequency (HF) band, from 2 MHz to 30 MHz requires attention to matters considered by many to fall into the realm of 'the black arts'. Both the radio equipment and their antennas are generally required to operate over a wider range of frequencies (15:1) than equipment operating in other bands. As ionospheric conditions change during the day, corresponding frequency changes are required to maintain communications availability at an acceptable level.

For some antennas, particularly wide band antennas, the radiation pattern shape can vary significantly with frequency, and other parameters. While the radio equipment - the transmitter and receiver - may function well over the required band, and even match the antenna system, unless due attention is paid to the choice of antenna, its configuration, siting and orientation, the shape of the radiation pattern may make communications difficult, if not impossible. The use of low transmitter power to conserve battery life or for covert operation compounds the problem.

Proper antenna training will promote better understanding and exploitation of antenna radiation patterns, leading to improved communications availability and reliability. High performance personal computers, with high-capacity hard drives are becoming more readily available both in the training environment and in the field and can provide useful platforms for which visual antenna training aids can be developed.

Initial work at AEA:

In 1991, AEA obtained Version 2 of the Lawrence Livermore Laboratory's Numerical Electromagnetic Code (NEC)[1] for near field assessment. This was interfaced to AutoCAD® by procedures written in AutoLISP®, a programming language embedded in AutoCAD. These interfaces provided an environment for the creation and examination of NEC input files in a graphical context (Reference 1).

The interfaces were extended to plot contours and colour maps of near field data and to present far-field radiation pattern data as three dimensional meshes (figure 1). Using the SlideShow capability of AutoCAD, screen-dumps were saved as .SLD files, and by linking these images together with a script file, animations of field patterns were created. Although these ran fairly slowly, they showed considerable promise as a means of conveying an understanding of pattern characteristics. An upgrade to AutoCAD Version 12 allowed creation of rendered images of patterns (figure 2). The images were more 'realistic', and despite the minimal edge treatment of faces, further demonstrated the potential of these techniques.

[1] Distributed as part of NEEDS 2.0 through the Applied Computational Electromagnetics Society (ACES), CA, USA

®AutoCAD and AutoLISP are registered trademarks of AutoDesk Inc.

The rendering and animation package 3D Studio® Version 2 was obtained and interfaces written to directly read NEC output files. Using this capability 'photographic' quality images of 3D radiation patterns could be readily created either as still images or animation files. This work is discussed in References 2 and 3. Using the inherent capabilities of 3D Studio, animated frequency and other scales, backgrounds and other objects can be created to annotate the images. Careful attention to lighting, shadowing, camera positioning, the use of fog to suggest distance, choice of appropriate images, colour and textures for backgrounds, and for the representation of the earth and of the antenna pattern itself, can all provide subtle clues which greatly enhance the perception and comprehension of the pattern (see figures 3 and 4). Creation of good images is not a process to be taken lightly, but requires considerable practice to develop and maintain the appropriate skills.

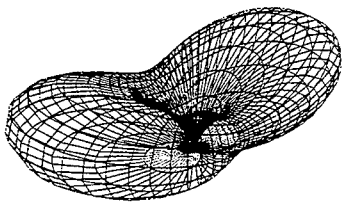

Figure 1: Mesh radiation pattern image (AutoCAD)

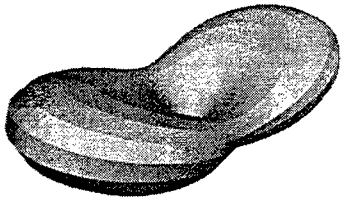

Figure 2: Rendered radiation pattern image (AutoCAD)

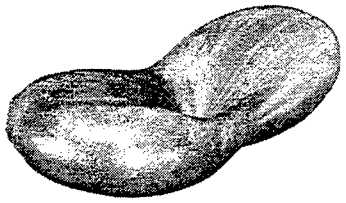

Figure 3: Rendered radiation pattern image (3D Studio)

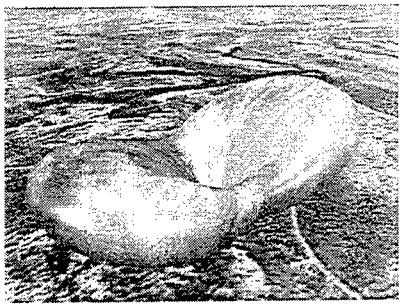

Figure 4: Rendered radiation pattern image in a scene (3D Studio)

Creation of an animation or a series of images in 3D Studio requires the assignment of keys to the objects to be animated. These modify the position, rotation shape, scale and other parameters of the objects, lights and cameras, thus creating the frame-by-frame changes for the animation. In 3D Studio Version 2, the keys were created by hand. In one instance over 11000 keys were created to produce an animation of a HF radiation pattern sweeping from 2 to 30 MHz, and viewed from 64 different viewpoints - a multi-dimensional set of radiation pattern images. Creation of the keys alone took just over three weeks but yielded an excellent result. Later work using 3D Studio Version 4 used programs written in the internal language 'Keyscript', reducing the key creation time to less than one minute (Reference 4).

® 3D Studio is a registered trademark of AutoDesk Inc.

The image output from 3D Studio can be saved as easily as an animation file, a series of still images or to videotape. The training aids use still images and the Joint Photographic Experts Group (.JPG) format easily gave the best image quality for a given file size, allowing almost 60000 images to be stored on a single compact disk (CD). By careful choice of compression parameters, image format and other options, this number could be extended to over 80000.

An antenna-specific viewer is written to display the image in response to selection of frequency, antenna geometry (height, angle, configuration etc), ground type, viewing angle and other parameters. The user can then display the appropriate image in terms of antenna parameters, rather than a file name. The viewers for different antennas are adapted from a generic viewer by the addition of controls which are specific to that antenna.

Considerable effort has recently been spent on reducing the manual effort needed to produce the large number of images needed for the training aids. To simplify multiple modelling runs, modifications have been made to NEC to allow passing of input and output filenames as command line arguments. In addition a program was written to read the NEC input file and directly create an input file for the NEC Sommerfeld/Norton ground modelling program SOMNEC. These changes considerably enhance batch mode running of NEC 2.

Image creation process:

Keeping track of the large number of files involved with the image creation process demands a structured approach to file names. File names used throughout the image creation process are generic, and are derived as follows:. The first two characters are a unique two-character designator **(BD)** referring to the antenna name (Bidirectional Delta in this case), The next two digits **(nn)** form a unique number assigned to each lowest level directory. The remaining two digits **(mm)** refer to the ordinal position of the file in the set. Other characters identify file types. Thus **BD01,I00** is the first NEC input file in directory 1 for a **B**idirectional **D**elta antenna.

The process commences with the creation of purpose-written program **(BDBUILD.EXE)** based on the antenna geometry and the range of variants. This program builds a directory structure based on the parameters to be user-adjustable in the final training aid. Typically, these would include ground type and the range of different antenna configurations. At the same time an Index File **(BD.NDX)** is written in the root directory. This lists generic file names and corresponding directory paths and is used to control much of the subsequent processing. For each directory NEC input files **(BDnn.Imm)** are written, together with a NEC batch file **(BDnn.BAT)** to control the running of NEC and SOMNEC within that directory. One input file is generally used for each frequency so that segmentation can be optimised. Finally, a Master batch file **(BD.BAT)** is written in the root directory to call individual NEC batch files and run the whole modelling process.

The production of a typical training aid can require the creation and running of up to 5000 separate NEC input files. Once the creation program is written, the processes of directory and file creation typically take less than ten minutes.

The Master batch file then calls SOMNEC and NEC for each of the input files in each directory to write corresponding output files **(BDnn.Omm)**. For simple wire antennas (typically up to about 20 wires), the 5000 modelling runs take about 3 hours using a 200 MHz Pentium-S CPU. More complex structures such as antennas on vehicles take correspondingly longer times.

Once all the modelling runs are completed, post-processing is initiated. NEC output files are read using the Index file for navigation, resulting in the creation of the following files for each directory:

- Three-dimensional Drawing eXchange Format **(BDnn.DXF)** files of radiation pattern shapes used to input the pattern data to 3D Studio,
- files containing data on the maximum envelopes of a sets of radiation pattern data used to calculate camera and lighting positions **(BDnn.ENV)**,
- **BDnn.VUE** files, used to control object, light and camera positioning during rendering by 3D Studio,

At the same time files containing pattern data in tabular form **(BDnn.ANT)**, files which contain summary data and any NEC error messages **(BDnn.SUM)**, and files of compressed antenna pattern data **(BDnn.DC3)** are automatically written to each lowest level directory.

The.DXF files are manually loaded into 3D Studio and merged with a previously created file **(BASIS.3DS)** containing common elements such as a dummy radiation pattern, earth, sky, lights and a camera. The resulting scene is then saved **(BD01.3DS)**. An Options file **(BDnn.OPT)** is also created to control various image parameters and a Rendering batch file **(BDREND.BAT)** is written in the root directory to create the images by 3D Studio rendering of the scenes.

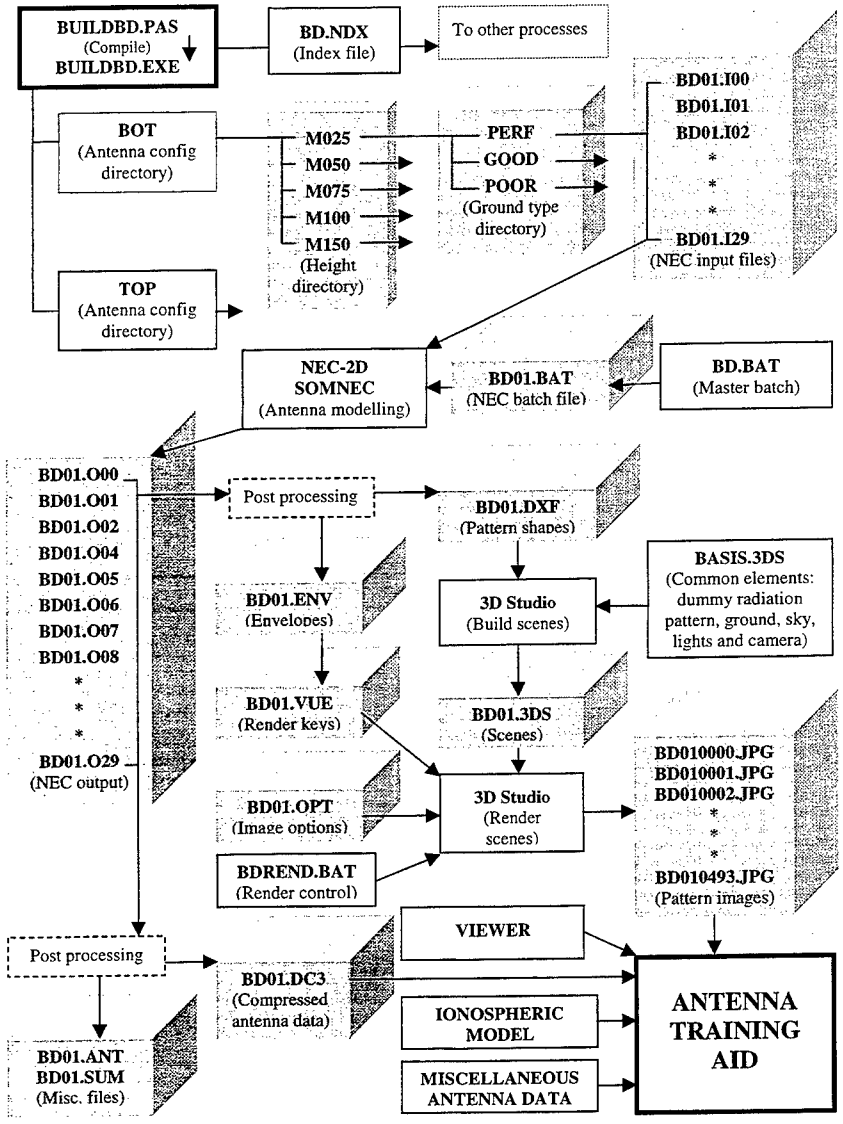

Figure 5: Training aid creation process for Bidirectional Delta antenna. 3D boxes indicate that the same structures that are repeated across multiple directories for different antenna configurations.

The Rendering bach file is then run to call 3D Studio and pass control to the appropriate .VUE and .OPT file to create the .JPG image files. For each rendering run within a directory 3D Studio automatically generates file names of the form **BDnnffff.JPG**, where **ffff** is the frame number in the series of images. For the Bidirectional Delta, 493 images were created per directory corresponding to 29 frequencies and 17 viewpoints. Once rendering is initiated it runs unattended for the whole suite of directories. The rendering time for each image varies with image content, but averages 23 seconds, a run of 50000 images taking some 13 days to complete.

In parallel with the image generation an antenna-specific viewer is written. This provides the means for the end user to navigate through the large number of rendered radiation pattern images in electromagnetic terms, rather than by using file names. In addition, it has interfaces to other methods of antenna pattern display, which are covered later in this paper.

The creation of training aids using rendered images of radiation patterns relies heavily on the ability to rapidly create and process large numbers of antenna models. The above processes of image generation could, in theory, be adapted to virtually any electromagnetic engine. However, without the ability to generate input files and process output files using external applications, the time needed to manually perform these operations would be excessive, and the process would not be viable. Such processing requires a detailed knowledge of the associated file formats, and reticence on the part of some software suppliers to release this information prevents their modelling engines from being used in this way. NEC has well-documented input and output file formats, and together with the modifications for batch mode operation, it is well suited to this application.

Antenna pattern compression:

Concurrent with the development of the image-based training aids, data compression methods for antenna patterns were being developed. Modelling of a number of in-service antennas indicated that to capture the structure of patterns, particularly for those antennas which were large or at significant heights above the ground, a minimum resolution of 5° in azimuth and elevation was required. This is the same resolution as used in the above image generation process. For the upper hemisphere of the pattern, this requires 1368 points per frequency. In many cases, for adequate frequency resolution across the HF band, 1 MHz steps have been found necessary, yielding pattern data files of about 160 kByte. The data compression methods of Reference 5 were developed in order to efficiently embed this amount of data in an application. Although the compression is lossy, the errors introduced during compression and decompression are restricted to the low gain areas (nulls) of the radiation pattern where they are of little importance to the intended application. Both full-hemisphere skywave as well as groundwave patterns are stored using the AEA developed algorithms which compress the total data to under 700 bytes per frequency. In addition the decompression process intrinsically provides interpolation between the original data points.

The pattern file also contains a header with a variety of antenna-related parameters. These include:

- the antenna name, plus 7 supplementary text fields,
- a unique antenna identifying number,
- the antenna model version,
- the boresite bearing of the antenna (usually 0°),
- a 'directional antenna' flag, and
- the antenna frequency limits.

Sufficient data to display a 3D drawing of the antenna is also stored, and this can accommodate up to 128 wires, 30 masts, 8 sources and 8 loads. The header information increases the file size by about 1.4 kByte, resulting in a final file size for an antenna specified at 1 MHz steps from 2 to 30 MHz of under 22kByte.

Using this compressed file format, displays of horizontal and conical cuts of the antenna pattern can readily be produced. The conical cut is taken at a user-specified takeoff angle, and is more appropriate in the context of skywave communications than the traditional horizontal cut.

If the pattern data is combined with an ionospheric modelling capability, antenna performance can be displayed as footprints of over-the-horizon parameters which are dependent on both the ionosphere and the antenna pattern. These include operational frequencies such as the maximum useable frequency (MUF), optimum working frequency (OWF) and lowest usable frequency (LUF). Other antenna-related useful parameters that can be displayed include are path length, number of hops, takeoff angle, to and from bearings, propagation mode, antenna gain, probability of intercept, and signal to noise ratio. The range of plots is limited only by the range of parameters available from the embedded ionospheric modelling techniques.

Current work:

Although the three methods of antenna pattern display described above were developed independently, work is proceeding on the creation of a single training aid, which embraces the three display types together with other antenna information as separate pages of a tabbed notebook. To summarise, the three display types are:

- Rendered images: These give an easily understood overall impression of the shape of the pattern. The ability to view the pattern from different viewpoints, and to observe the effects of changes of frequency, ground type and antenna configuration provide an environment where the shape of the pattern can be readily conceptualised.
- Graphical display: This displays the pattern data using traditional graphical methods and can also provide numerical data. A vertical cut and a conical cut at a user-selected takeoff angle are displayed.
- Map display: This shows the effects of the interaction between the antenna pattern and user-selected ionospheric conditions, displaying area coverage footprints of the antenna and other communications data.

Other pages provide additional antenna as follows:

- a photograph of the erected antenna,
- a line drawing based on data from the existing antenna handbook and showing antenna components and connections,
- textual information about the antenna components, related documentation, and operational parameters.

Figures 6 to 8 show screens show screens from the three pattern display capabilities which are to be embedded in a single training aid.

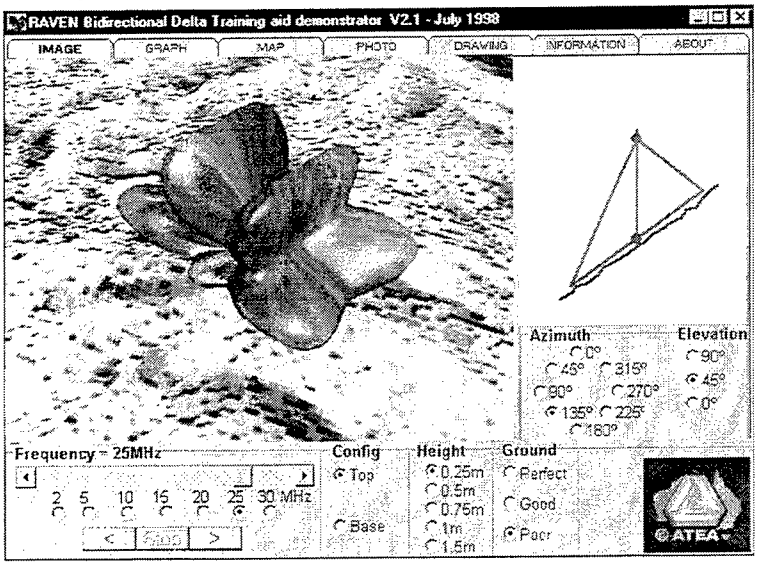

Figure 6: Radiation pattern rendered image display

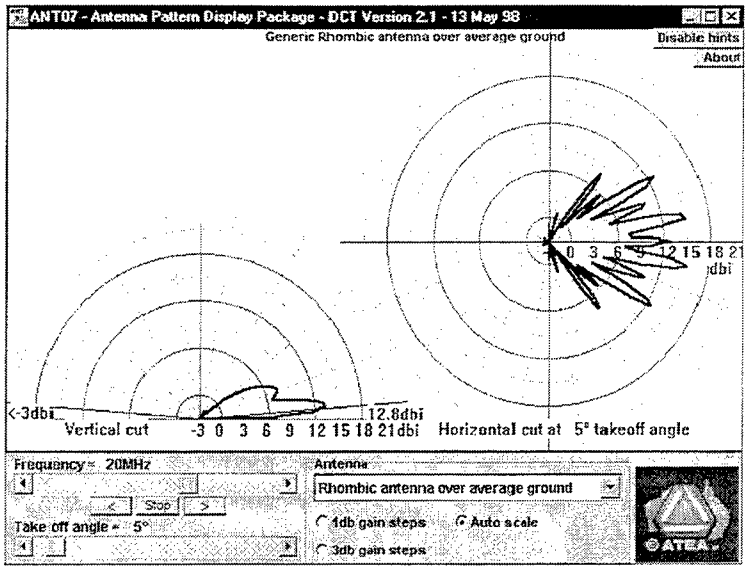

Figure 7: Antenna gain graphical display.

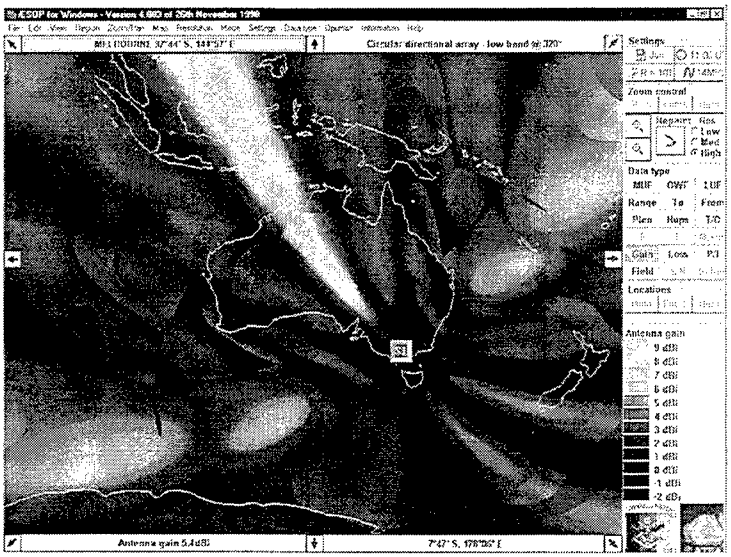

Figure 8: Antenna gain as an area coverage map.

Documentation:

AEA quality procedures require that software-based products for use outside the Agency be documented in accordance with an approved software specification, originally MIL-STD-498. Such documentation has been prepared for much of the training aid, and currently comprises the Software Development Plan (SDP), Software Design Description (SDD), Software Product Specification (SPS), System/Subsystem Specification (SSS), Software Test Plan (STP), Software Test Report (STR), and the Software User Manual (SUM), together with a 100 page work instruction on the image creation process and related issues. These documents were compiled during the development of the various stand-alone capabilities of the training aid for the RAVEN Bidirectional Delta antenna, and require to be merged into a coherent whole. However as the functionality of the training aids is different for different antennas, updating and extension will be required as additional training aids are produced.

Antenna data:

In order for the above training aids and related applications to embrace further antennas, accurate geometric data on antennas in use will be required to create the electromagnetic models from which the gain patterns are computed. In the case of fixed installations this is generally not a great problem, as the antenna geometry and that of the surroundings is fixed. However, in the case of field antennas, which are often expedient, obtaining adequate data on such antennas and their range of variants presents considerable difficulty. While antenna handbooks give broad-brush descriptions of antenna dimensions, in practice these are often not adhered to. Wisely applied, changing element slopes or adding a reflector or counterpoise can improve communications performance. In such a case the 'antenna intuition' which the training aids aim to develop, can be of considerable benefit. But in order to provide the maximum usefulness, geometric data on a wider range of antennas and variants needs to be captured so that they can be modelled and embedded in the applications. Previous experience suggests that attending Signals Unit exercises with a steel tape, theodolite camera and a keen eye might be the only way to obtain this urgently needed data.

Conclusions:

Aspects of the evolution of an antenna training aid capability developed by AEA for the Australian Army's School of Signals and HMAS Cerberus Frequency Management School has been presented. Strategies have been discussed for the efficient production of high-quality antenna radiation pattern images and of the compression of antenna pattern data based on antenna modelling using NEC. These techniques have been used to create to self-contained, CD-based antenna training aids which are easy to operate and provide excellent insight into the complexities of antenna radiation patterns. The best of all worlds is provided by the ability to view the same pattern as a rendered 3D image, graphically, or as footprints of pattern related data. To extend the usefulness of the applications, antenna geometric data covering the full range of antennas in use, particularly expedient antennas, needs to be captured so that the antennas can be modelled. The training aids find application not only in the classroom, but with the increasing availability of field computing, could extend into the tactical area, providing guidance in the field on antenna choice, configuration and siting. Properly applied, this will lead to an improvement in communications availability and the development of an 'antenna intuition' at a level previously obtained only after may years of field experience.

References:

[1] Alan Nott. "AutoNEC - A marriage of convenience". Proceedings of the 10th ACES Review of Progress, Monterey, CA, USA, March 21-26, 1994, Volume II, page 380.

[2] Alan Nott. "Electromagnetic Visualisation using Commercial Software". Proceedings of the 12th ACES Review of Progress, Monterey, CA, USA, March 18-22, 1996, Volume I, page 326.

[3] Alan Nott.and Deepak Singh. "An Antenna Training Aid using Electromagnetic Visualisation". Proceedings of the 13th ACES Review of Progress, Monterey, CA, USA, March 17-21, 1997, Volume I, page 41.

[4] Alan Nott. "Evolution of an Antenna Training Aid Using Electromagnetic Visualisation". Proceedings of the 14th ACES Review of Progress, Monterey, CA, USA, March 16-20, 1998, Volume I, page 560.

[5] Alan Nott. "A Data Compression Technique for Antenna Pattern Storage and Retrieval". Proceedings of the 13th ACES Review of Progress, Monterey, CA, USA, March 17-21, 1997, Volume I, page 56.

SESSION 3

INTERACTIVE POSTER SESSION

Extension of the Method of Lines for Planar 3D Structures.

Yuriy O. Shlepnev
Eagleware Corporation
4772 Stone Drive, Tucker, GA, 30084, USA
Tel. 770-939-0156, fax 770-939-0157
E-mail: yuriy@eagleware.com

Abstract. The Method of Lines (MoL) is extended for planar 3D structures with conductivity currents flowing across media layers. The extended MoL is applicable for the analysis of discontinuities in planar (M)MIC's lines with vias and other connectors between signal layers. It also makes it possible to analyze discontinuities taking into account metallization thickness. An admittance matrix of a layer with currents across it in a grid spectral domain is presented as the basic element of the algorithm. The extended MoL is illustrated by analysis of a via-hole grounded microstrip line.

Introduction. The method of partial discretization or method of lines is the well-established technique for the analysis of different microwave structures. It can be successfully used for the analysis of 2.5D (M)MIC discontinuities [1-4]. The one theoretical restriction of 2.5D technique is absence of conductivity currents inside a layered structure between signal layers. The signal or metallization layers are placed on the interfaces of the media layers and are supposed to have zero thickness. The MoL was recently extended for the analysis of some 4-port 3D MMIC structures [5], but applications of this expansion are still limited.

This paper proposes a technique to extend the 2.5D technique developed for the analysis of discontinuities in planar lines [1-4] on planar 3D structures. The technique keeps 2D discretization and spectral representation for homogeneous media layers as for usual 2.5D MoL and introduces a model of a media layer with constant conductivity currents across the layer. A combination of the signal layers with 2D currents, layers with the vertical currents, and the simple homogeneous media layers makes it possible to perform a kind of 3D discretization for some regions of a (M)MIC discontinuity. The classification planar 3D emphasizes the fact that vertical planes in those structures have infinitesimally small conductivity current components other then vertical. An analytical semi-discrete solution for homogeneous media layers as well as for the layers with the vertical currents transfers the advantages of the MoL on the planar 3D (M)MIC structures. The metallization thickness, vias, and different kinds of bridges can be simulated in this way.

The described technique is implemented for one signal layer in a program for electromagnetic simulation of (M)MIC, =EMPOWER=, developed at Eagleware Corporation (www.eagleware.com). Geometrical symmetry processing, the super-grid technique and the prime factor algorithm for the discrete Fourier transformation have been used in the program to expand capabilities and to accelerate the base MoL procedures. The generalized scattering parameters of a discontinuity are extracted by the method of simultaneous diagonalization [6,7]. A regular version 6.5A of the program is used to generate examples for this paper.

Problem Formulation. Let's consider a rectangular domain Ω in the Cartesian axes:

$$\Omega = \{(x, y, z) \mid 0 \le x \le a,\ 0 \le y \le b,\ d_0 \le z \le d_P\}$$

The domain has P media layers with the different or the same properties:

$$\varepsilon(x, y, z) = \varepsilon_p,\ \mu(x, y, z) = \mu_p,\ (x, y, z) \in \Omega^p,\ \Omega^p = \{(x, y, z) \mid 0 \le x \le a, 0 \le y \le b, d_{p-1} \le z \le d_p\}\ p = \overline{1,P}.$$

Here ε_p, μ_p are absolute dielectric permittivity and permeability of the layer p. The domain is bounded by the electric or magnetic walls. The media layers are homogeneous and can be lossy. A layer can have constant conductivity current across it with only one component j_z of the current volume density vector. The electric ($\vec{E}^p$) and magnetic ($\vec{H}^p$) fields are related by the Maxwell's equations inside a layer p for a harmonic signal with the radian frequency ω:

$$\left.\begin{aligned} &\mathrm{rot}\vec{H}^p = i\omega\varepsilon_p\vec{E}^p + j_z \\ &\mathrm{rot}\vec{E}^p = -i\omega\mu_p\vec{H}^p \\ &\mathrm{div}\vec{E}^p = 0,\ \mathrm{div}\vec{H}^p = 0 \end{aligned}\right\} (x,y,z) \in \Omega^p \qquad (1)$$

Conductivity currents with x and y components can exist only in signal layers $z = d_i$ parallel to the medium layer interfaces. If $\vec{\eta}_i$ is surface conductivity current density, the generalized boundary conditions for the signal layers are:

$$\left.\begin{aligned} &\vec{z}\times\left(\vec{H}^{p+1}(d_i) - \vec{H}^p(d_i)\right) = \vec{\eta}_i \\ &\vec{z}\times\left(\vec{E}^{p+1}(d_i) - \vec{E}^p(d_i)\right) = 0 \end{aligned}\right\} i = \overline{1, P-1} \qquad (2)$$

To complete the problem formulation for a (M)MIC structure, additional boundary conditions on perfect or lossy metal surfaces and in resistive film regions must be defined. To model external inputs of the structure and lumped element connections, auxiliary port regions are introduced into the problem domain. The desired solution of the electromagnetic problem is an immitance matrix relating the integral voltages and currents in all port regions. After connection of the lumped elements to the corresponding ports, the immitance matrix can be transformed into a generalized Y- or S-matrix using the simultaneous diagonalization method [7] or by other means.
Thus we have the problem formulation that is appropriate for a wide range of (M)MIC devices. Notice that the problem domain is not restricted by planar structures, because most of the three dimensional objects with negligible x- and y-directed currents on the mantle can be approximated by a set of the media layers with z-directed currents.

Mapping on Grid. To approximate the problem on a grid, let's define grid variables instead of continuous vector functions. It is convenient to define the grid analogues of electric and magnetic fields inside a layer p as elements of matrices:

$$\begin{aligned} &e_x^p(z) = \left(E_x^p\left((l-1/2)\Delta_x, m\Delta_y, z\right), l = \overline{1, L+1}, m = \overline{1, M}\right), \\ &e_y^p(z) = \left(E_y^p\left(l\Delta_x, (m-1/2)\Delta_y, z\right), l = \overline{1, L}, m = \overline{1, M+1}\right), \\ &e_z^p(z) = \left(E_z^p\left(l\Delta_x, m\Delta_y, z\right), l = \overline{1, L}, m = \overline{1, M}\right), \\ &h_x^p(z) = \left(H_x^p\left(l\Delta_x, (m-1/2)\Delta_y, z\right), l = \overline{1, L}, m = \overline{1, M+1}\right), \\ &h_y^p(z) = \left(H_y^p\left((l-1/2)\Delta_x, m\Delta_y, z\right), l = \overline{1, L+1}, m = \overline{1, M}\right), \\ &h_z^p(z) = \left(H_z^p\left((l-1/2)\Delta_x, (m-1/2)\Delta_y, z\right), l = \overline{1, L+1}, m = \overline{1, M+1}\right), \\ &z \in \Omega^p,\ \Delta_x = \frac{a}{L+1},\ \Delta_y = \frac{b}{M+1}. \end{aligned} \qquad (3)$$

Positions of the grid functions correspond to the x-y plane projection of the offset finite difference scheme [8]. Grid currents can be defined as integrals of the surface current components, and constant grid currents across a layer can be defined as surface integrals of the current volume density

j_z near the grid nodes:

$$J_x^i = \left(\int_{(m-1/2)\Delta y}^{(m+1/2)\Delta y} \eta_x\left((l-1/2)\Delta_x, y, d_i\right)dy, l = \overline{1, L+1}, m = \overline{1, M}\right), \; i = \overline{1, P-1}$$
$$J_y^i = \left(\int_{(l-1/2)\Delta x}^{(l+1/2)\Delta x} \eta_y\left(x, (m-1/2)\Delta_y, d_i\right)dx, l = \overline{1, L}, m = \overline{1, M+1}\right), \; i = \overline{1, P-1} \qquad (4)$$
$$J_z^p = \left(\int_{(m-1/2)\Delta y}^{(m+1/2)\Delta y}\int_{(l-1/2)\Delta x}^{(l+1/2)\Delta x} j_z\left(l\Delta_x, m\Delta_y, z\right)dx\,dy, l = \overline{1, L+1}, m = \overline{1, M}\right), \; d_{p-1} < z < d_p, p = \overline{1, P}$$

Having defined the grid equivalent of the problem functions, we can approximate Maxwell's equations (1) by a system of differential-difference equations in accordance with the x-y plane projection of the finite-difference scheme [8]. The continuity conditions (2) on the grid are approximated by the same conditions, but only on the grid nodes. The offset difference scheme approximates the initial system with the second order inside a layer. The global approximation order of a problem is usually lower because of possible singularities of the field and current components on the metal edges.

Grid Spectral Domain Solution. Let's define a Grid Green's Function (GGF) as a solution of the differential-difference analogue of the Maxwell's equations excited by a unit grid current (Jx,Jy or Jz). This response function is a discrete function in the x-y plane and continuous inside a layer along the z-axis. To solve the formulated problem we need a contraction of the GGF to the signal planes and to the regions with non-zero z-directed currents. This contraction is a matrix due to the discretization.

To find the GGF matrix, a spectral approach is used that is similar to the spectral domain technique. Instead of continuous TE and TM rectangular waveguide eigenwaves, their grid analogues are used as a basis to expand the electromagnetic fields inside a layer. The number of TE and TM waves is finite and their system is complete. This means that instead of summation of series, as in the spectral domain approach, we have finite sums, that in combination with the grid propagation constants of the eigenwaves provides monotonic convergence of the algorithm. So, transformation of the grid functions (3,4) to the grid TE and TM wave basis gives us new variables:

$$\begin{aligned}
\left(\tilde{e}_x / \tilde{h}_y / \tilde{J}_x\right) &= F_{x2}^t \cdot \left(e_x / h_y / J_x\right) \cdot F_{y1} \\
\left(\tilde{e}_y / \tilde{h}_x / \tilde{J}_y\right) &= F_{x1} \cdot \left(e_y / h_x / J_y\right) \cdot F_{y2}^t, \\
\left(\tilde{e}_z / \tilde{J}_z\right) &= F_{x1}^t \cdot \left(e_z / J_z\right) \cdot F_{y1} \\
\left(\tilde{h}_z\right) &= F_{x2}^t \cdot \left(h_z\right) \cdot F_{y2}
\end{aligned} \qquad (5)$$

and converts the differential-difference system of equations to a set of systems of ordinary differential equations. $F_{x1,2}$ and $F_{y1,2}$ in (5) are transformation matrices. Symbol ^{t} is a matrix transposition symbol. A solution of the system for a layer number p with z-directed currents and with undefined conditions at the layer boundaries $z = d_p$ and $z = d_{p-1}$ can be written as admittance matrices for each pair of the grid TE and TM eigenwaves:

$$\begin{bmatrix} \Delta_y \tilde{h}^p_{yl,m-1}(d_p) \\ -\Delta_x \tilde{h}^p_{xl-1,m}(d_p) \\ \tilde{J}^p_{zl-1,m-1} \\ -\Delta_y \tilde{h}^p_{yl,m-1}(d_{p-1}) \\ \Delta_x \tilde{h}^p_{xl-1,m}(d_{p-1}) \end{bmatrix} = Y^p_{l-1,m-1} \cdot \begin{bmatrix} \Delta_x \tilde{e}^p_{xl,m-1}(d_p) \\ \Delta_y \tilde{e}^p_{yl-1,m}(d_p) \\ \tilde{U}^p_{zl-1,m-1} \\ \Delta_x \tilde{e}^p_{xl,m-1}(d_{p-1}) \\ \Delta_y \tilde{e}^p_{yl-1,m}(d_{p-1}) \end{bmatrix}, \; Y^p_{l,m} = \begin{pmatrix} Y^p_{xxl,m} & Y^p_{xyl,m} & \frac{\Delta_y \gamma_{xl}}{i\omega\mu_p t_p} & Y^{pl}_{xxl,m} & Y^{pl}_{xyl,m} \\ Y^p_{xyl,m} & Y^p_{yyl,m} & \frac{\Delta_x \gamma_{ym}}{i\omega\mu_p t_p} & Y^{pl}_{xyl,m} & Y^{pl}_{yyl,m} \\ \frac{\Delta_y \gamma_{xl}}{i\omega\mu_p t_p} & \frac{\Delta_x \gamma_{ym}}{i\omega\mu_p t_p} & \Delta_x\Delta_y \frac{\left(\Gamma^p_{l,m}\right)^2}{i\omega\mu_p t_p} & -\frac{\Delta_y \gamma_{xl}}{i\omega\mu_p t_p} & -\frac{\Delta_x \gamma_{ym}}{i\omega\mu_p t_p} \\ Y^{pl}_{xxl,m} & Y^{pl}_{xyl,m} & -\frac{\Delta_y \gamma_{xl}}{i\omega\mu_p t_p} & Y^p_{xxl,m} & Y^p_{xyl,m} \\ Y^{pl}_{ixy,m} & Y^{pl}_{yyl,m} & -\frac{\Delta_x \gamma_{ym}}{i\omega\mu_p t_p} & Y^p_{xyl,m} & Y^p_{yyl,m} \end{pmatrix} \qquad (6)$$

Here $l = \overline{1, L+1}$, $m = \overline{1, M+1}$, and $\tilde{U}_z$ are voltages across the layer in the transformed domain. In the

initial domain it can be defined as $U_z^p = \int_{dp-1}^{dp} e_z^p(z)dz$. Equations for the Y-matrix elements are given by:

$$Y^p_{xxl,m} = \frac{\Delta_y \cot\left(\Gamma^p_{l,m}t_p\right)}{\Delta_x\chi^2_{l,m}}\left(\frac{\gamma^2_{ym}}{W^{Hp}_{l,m}} - \frac{\gamma^2_{xl}}{W^{Ep}_{l,m}}\right) + \frac{\Delta_y\gamma^2_{xl}}{i\omega\mu_p t_p \Delta_x\left(\Gamma^p_{l,m}\right)^2},$$

$$Y^p_{yyl,m} = \frac{\Delta_x \cot\left(\Gamma^p_{l,m}t_p\right)}{\Delta_y\chi^2_{l,m}}\left(\frac{\gamma^2_{xl}}{W^{Hp}_{l,m}} - \frac{\gamma^2_{ym}}{W^{Ep}_{l,m}}\right) + \frac{\Delta_x\gamma^2_{ym}}{i\omega\mu_p t_p \Delta_y\left(\Gamma^p_{l,m}\right)^2},$$

$$Y^p_{xyl,m} = -\frac{\gamma_{xl}\gamma_{ym}\cot\left(\Gamma^p_{l,m}t_p\right)}{\chi^2_{l,m}}\left(\frac{1}{W^{Hp}_{l,m}} + \frac{1}{W^{Ep}_{l,m}}\right) + \frac{\gamma_{xl}\gamma_{ym}}{i\omega\mu_p t_p\left(\Gamma^p_{l,m}\right)^2},$$

$$Y^{pl}_{xxl,m} = \frac{\Delta_y}{\Delta_x\chi^2_{l,m}\sin\left(\Gamma^p_{l,m}t_p\right)}\left(\frac{\gamma^2_{xl}}{W^{Ep}_{l,m}} - \frac{\gamma^2_{ym}}{W^{Hp}_{l,m}}\right) - \frac{\Delta_y\gamma^2_{xl}}{i\omega\mu_p t_p\Delta_x\left(\Gamma^p_{l,m}\right)^2},$$

$$Y^{pl}_{yyl,m} = \frac{\Delta_x}{\chi^2_{l,m}\Delta_y\sin\left(\Gamma^p_{l,m}t_p\right)}\left(\frac{\gamma^2_{ym}}{W^{Ep}_{l,m}} - \frac{\gamma^2_{xl}}{W^{Hp}_{l,m}}\right) - \frac{\Delta_x\gamma^2_{ym}}{i\omega\mu_p t_p\Delta_y\left(\Gamma^p_{l,m}\right)^2},$$

$$Y^{pl}_{xyl,m} = \frac{\gamma_{xl}\gamma_{ym}}{\chi^2_{l,m}\sin\left(\Gamma^p_{l,m}t_p\right)}\left(\frac{1}{W^{Ep}_{l,m}} + \frac{1}{W^{Hp}_{l,m}}\right) - \frac{\gamma_{xl}\gamma_{ym}}{i\omega\mu_p t_p\left(\Gamma^p_{l,m}\right)^2}, \qquad (7)$$

where:

$$\left(\Gamma^p_{l,m}\right)^2 = k_p^2 - \chi^2_{l,m},\ k_p^2 = \omega^2\varepsilon_p\mu_p,\ \chi^2_{l,m} = \gamma^2_{xl} + \gamma^2_{ym},$$

$$\gamma^2_{xl} = \frac{4}{\Delta_x^2}\sin^2\left(\frac{l\pi}{2(L+1)}\right),\ \gamma^2_{ym} = \frac{4}{\Delta_y^2}\sin^2\left(\frac{m\pi}{2(M+1)}\right),$$

$$W^{Hp}_{l,m} = -\frac{i\omega\mu_p}{\Gamma^p_{l,m}},\ W^{Ep}_{l,m} = -\frac{\Gamma^p_{l,m}}{i\omega\varepsilon_p},\ t_p = d_p - d_{p-1}.$$

Y-matrices for media layers without z-directed currents can be deduced from (6) by eliminating the row and column corresponding to the z-directed components, and eliminating the last summand in the equations for the matrix elements (7). So, we have (L+1)(M+1)-1 five-diagonal symmetrical Y-matrices (6) for each media layer that can be used to superimpose the boundary conditions at the interfaces (2) in the transformed domain. To find the GGF matrix, a unit current in the spectral domain can be defined. A reply on the current excitation is tangential local voltages at some layer interfaces and voltages across layers with z-directed currents in the transformed domain. The replies can be found independently for each pair of the grid TE and TM waves by simple connection of Y-matrices (6). To formalize this procedure, a conceptual multi-port corresponding to the system (6) can be introduced. An aggregate of these solutions for each possible excitation is the grid spectral domain solution of the problem.

Transforming the grid spectral domain solution back to the spatial domain, we get the GGF matrix. Finally, expressions for each element of the matrix look like double sums. These sums can be reduced to sums of four elements of an auxiliary vector with dimension 6*(L+1)*(M+1) per one signal layer. The vector elements depend only on the structure of the package and grid cell size. Its elements are calculated via discrete Fourier transforms. Before filling, the rank of the GGF matrix can be decreased by means of a super-grid technique and by implementing the geometrical symmetry of the problem. The super-grid technique gives a pseudo-non-equidistant grid over the regular grid that is finer near metallization edges and corners and coarser inside solid regions. It overcomes the restrictions of the MoL with a regular grid while keeping the main advantages of the equidistant grid. The composed GGF matrix are to be transformed to an immitance matrix (Y- or Z-

matrix) relating the grid currents and voltages in the input source regions. It can be done by direct inversion, factorization or by an iterative procedure.

Numerical Example. As a test example, we consider the analysis of a circular via-hole grounded microstrip structure described in [5] and shown in Fig 1. The analyzed structure has the following parameters: t1 = 0.794 mm, $\varepsilon 1 = 2.32$, t2 = 23 mm, $\varepsilon 2 = 1$, a = 5.175mm, b = 6.9mm, w=2.3 mm, d=0.6 mm. The circular cross-section of the via-hole is approximated on the grid by a staircase boundary, and the mantle of the via-hole cylinder is simulated by a set of z-directed currents. A regular version 6.5A of the =EMPOWER= program and a Pentium 200 MHz computer with 64 MB were used to simulate the via-hole. Fig. 2 shows the calculated magnitude of the transmission coefficient. It took about 2 minutes per frequency point and 9 MB of computer memory to solve the problem on the grid with cell size 0.0575 mm by 0.0575 mm. The result obtained by the hybrid finite-difference and finite-element time-domain method in [9] is also depicted in the Fig. 2 for comparison. A small constant bias in the results can be explained by differences in S-parameter extraction techniques.

Conclusion. This paper presents the base elements for the extension of the MoL on planar structures with vertical or z-directed currents. The admittance matrix, relating the grid analogues of the tangential electric and magnetic field components at the opposite surfaces of a layer, z-directed current, and integral of z-directed electric field inside the layer in the transformed domain, is given as the kernel element of the algorithm. Other parts of the numerical procedure are given schematically, because they are in compliance with the planar version of the MoL and the spectral domain technique. To author's knowledge, the MoL was not developed in this way, despite the fact that the similar integral equations techniques were extended for the structures with the vertical connections [10-12].

References.

1. Worm, S.B., Pregla, R. // *IEEE Trans.*, v. MTT-32, 1984, N2, p. 191.
2. Pregla, R., Pascher W. "The method of lines", in *Numerical techniques for microwave and millimeter-wave passive structures*, Edited by T. Itoh, J. Willey Publ., New York, 1989, p. 381-446.
3. Worm, S.B. //IEEE Trans., v. MTT-38, 1990, N10, p. 1510-1514.
4. Shlepnev Yu.O. Method of lines in mathematical modeling of MIC's planar elements (*in Russian*). - Thesis of Candidate of Science. - Novosibirsk, NTSU, 1990.
5. Vietzorreck, L., Pregla, R. // 1998 IEEE MTT-S International Microwave Symposium Digest, Baltimore, June 1998, p. 1547-1550.
6. Shlepnev, Yu.O., Sestroretzkiy B.V., Kustov V.Yu. // *Journal of Communication Technology and Electronics*. v.42, 1997, N1, p. 13-16.
7. Shlepnev, Yu.O. // in *Proceedings of the 14th Annual Review of Progress in Applied Computational Electromagnetics*, Monterey, CA, 1998, v. II, p. 664-671.
8. Yee, K.S. // *IEEE Trans.*, v. AP-14, 1966, N3, p.302-307.
9. Koh, D., Lee, H., Itoh T. // *IEEE Trans.*, v. MTT-45, 1997, N 12, p. 2217-2223.
10. Becks, T., Wolff, I., // *IEEE Trans.*, v. MTT-40, 1992, N 12, p. 2219-2227.
11. Tsai M.-J., Chen, C., Alexopoulos, N.G., Horng T.-S., // *IEEE Trans.*, v. MTT-44, 1996, N 12, p. 2504-2511.
12. Kinayman, N., Aksun, M.I., // *IEEE Trans.*, v. MTT-45, 1997, N 5, p. 593-603.

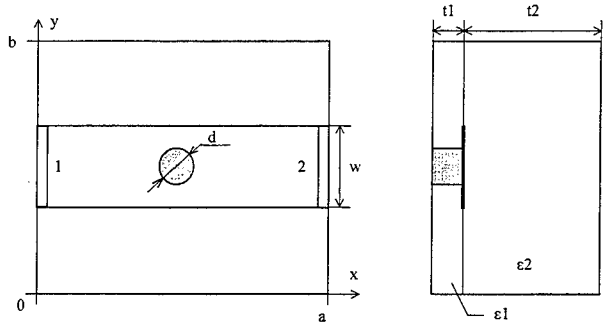

Fig. 1 A circular via-hole grounded microstrip line in a shielding box. Hatched areas near the sidewalls are regions of auxiliary ports to simulate inputs of the structure.

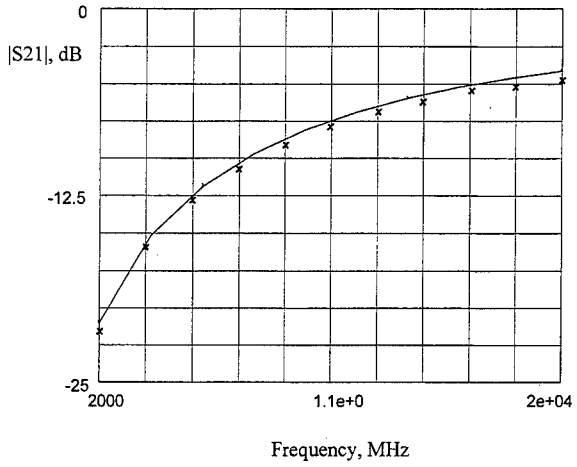

Fig. 2 Magnitude of the transmission coefficient of the via-hole grounded microstrip with the following parameters: t1 = 0.794 mm, ε1 = 2.32, t2 = 23 mm, ε2 = 1, a = 5.175mm, b = 6.9mm, w=2.3 mm, d=0.6 mm. Solid line – this method, x – results from [9].

Noise Issues in Submicron Design

Reinaldo Perez
Jet Propulsion Laboratory
California Institute of Technology

Abstract

Often in Electromagnetic Compatibility the main concern rest on the effects of noise current at the system, subsystem, and even circuit level. However, with the increasing trend of even more smaller devices, the issue of noise is becoming also of importance at the component level. The main issues concerning noise at the component level are addressed. A review of tools that could help address noise problem at the device level are also address.

Introduction.

It has been well known for many years that analog circuits are very susceptible to noise problems and interference in general. Noise current as small as a few mA (and even micro-amps) can cause significant degradation in analog circuits. For a while digital designers did not have to concern themselves with interference and noise at the digital circuit levels because digital circuits were highly regarded as immune to noise problems. That understanding started to change as mix-mode design came into the picture (i.e mixed design of analog and digital circuits in electronic boards). The art of electromagnetic compatibility experience a tremendous boost in the 1980's and early 1990's as the proper design of mix-mode printed circuit boards to avoid or mitigate interference problems became a prevalent issue. The use of new design techniques, modeling tools, signal integrity tools became common in the language of the PCB industry and a hot topic in conference, journal papers, and short courses.

Though interference and noise problems are still a important issue in electronic design at the subsystem and circuit levels, noise is also starting to become an issue at the submicron design of components. Noise has become a problem because as design rules reach the 0.25 μm level and below, interconnect becomes an increasing dominant factor in the design. Technology scaling is causing coupling capacitance between on-chip signals to become a larger portion of the total capacitance within the IC. At the same time because transistor cross-sections are shrinking and the number of interconnects is increasing, the quantity of interconnect related capacitances is becoming a much larger portion of the total gate capacitances. The end result is within an IC certain voltages are going from high-to low, from Vdd to ground, from ground to Vdd in a "soup" of capacitive parasitic effects.

Noisy Component ICs.

With the new trends in technology scaling, the more aggressive use of higher clock speeds, the jamming together of interconnect wires, the decrease of threshold voltages, are all conspiring together such that the noise immunity of digital circuits is not longer sufficient to protect them against their own inherent noise. As circuit densities continue to increase, interconnect capacitance will continue to increase becoming an increasing fraction of the total capacitance of the device. The old problems related with interconnections between devices on a PCB (signal integrity issues) are now becoming also a problem in the IC themselves. The microscopic metallic slivers that interconnect the devices internally are now starting to behave as transmission lines themselves. There has been a dramatic change is aspect ratio (the shrinking width of interconnects with respect to height). Furthermore, the lines are also much closer together, often closer than the line thickness themselves an in many cases the separation is less than the separation between lines on different layers. Therefore, line-to-line capacitance on the same layer has become dominant [1-3].

In PCB the layer-to-layer interaction could be the dominant factor, signals would rarely interact in a way that reduce current into the metal line. However, as the line-to-line capacitance increases it is very common to find coupling problems between individual signals where one line acts as the noise source capable of inducing noise current on a susceptible line. One solution that has been bee tried in the past to decrease line-to-line coupling is to increase the spacing between lines. Capacitive effects between lines can also be reduced by re-routing the lines. The use of lower dielectric constant materials between troublesome lines could also be tried. Noise can also affect switching circuits by altering delays in the propagation paths and causing timing inaccuracy. If the noise source line induces a current into a susceptible circuit while the susceptible circuit is changing states, the extra current into a susceptible circuit can hinder the change. Noise coupled between metal lines on the interconnect can also move from a switching line to a static line, or even into the power supply. In Figure 1 the static voltage drop across package and chip resistance reduces the supply voltage available to the circuitry. The change in ground reference due to changes in ground current further reduces the voltage available to the circuit.

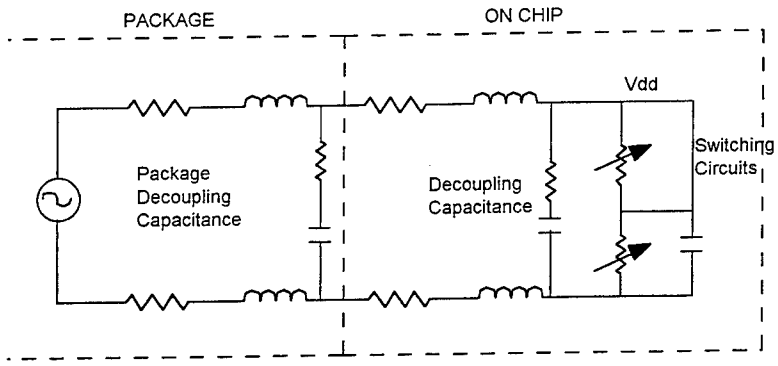

DC IR Drop: Variations in the DC power supply levels on-chip due to IR drops in the Power/Ground distribution

Ground Bounce: Simultaneous switching of off-chip drivers and internal circuits causes periodic variations in the supply and ground rails due to inductance on the chip and package supply and ground wires.

Figure 1.0 Illustration of Ground Bounce.

In the past in order to get more noise immunity under control "rule-based approaches" have been implemented. These rule-based approaches however, are constrained in that they don't apply to all cases; therefore, more rules need to be added all the time to incorporate ever more increasing complex cases. The second approach is a better established approach and is based on static noise analysis. Static noise analysis asks whether a design will work in the presence of noise. It calculates the noise appearing on every net and, in the worst case scenario, how much noise can appear on the net. Furthermore, static timing analysis evaluates the noise immunity of every net, flagging those where there are potential failures. Static analysis involves looking at the circuits interconnects and analyzes the entire design. High frequency effects need to be analyzed using tools that just go beyond static timing analysis. These effects include inductance and resistance in signal/signal return lines. In Figure 2 capacitive coupling and charge sharing can move a gate voltage beyond a threshold, causing that gate to make an unwanted transition.

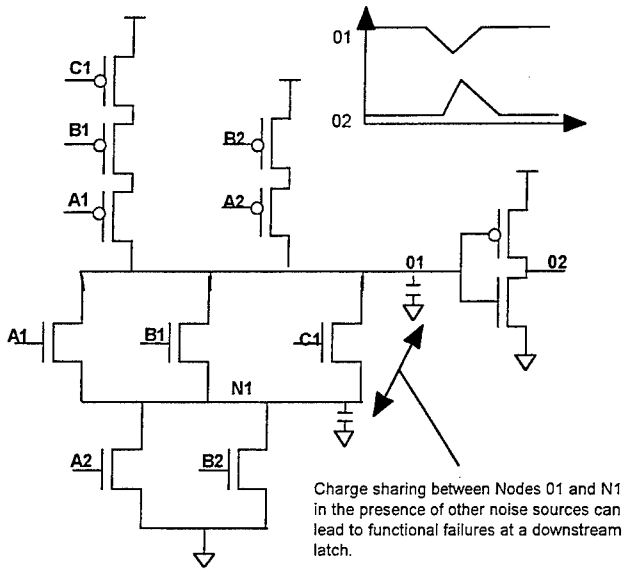
01
02
C1
B1
A1
B2
A2
01
02
A1
B1
C1
N1
A2
B2
Charge sharing between Nodes 01 and N1 in the presence of other noise sources can lead to functional failures at a downstream latch.

(2a)

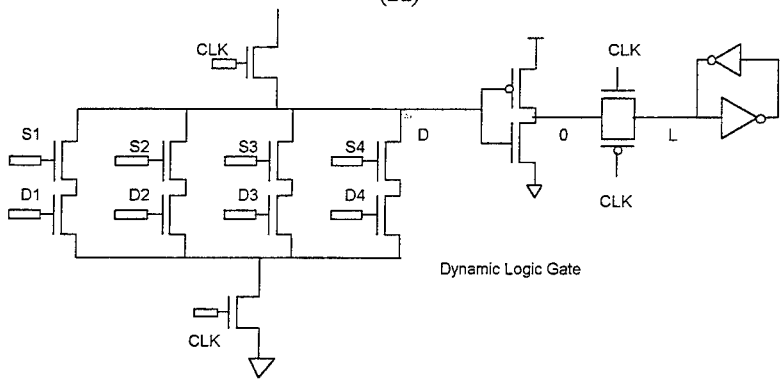
CLK
S1
S2
S3
S4
D
0
L
CLK
D1
D2
D3
D4
CLK
Dynamic Logic Gate
CLK

(2b)

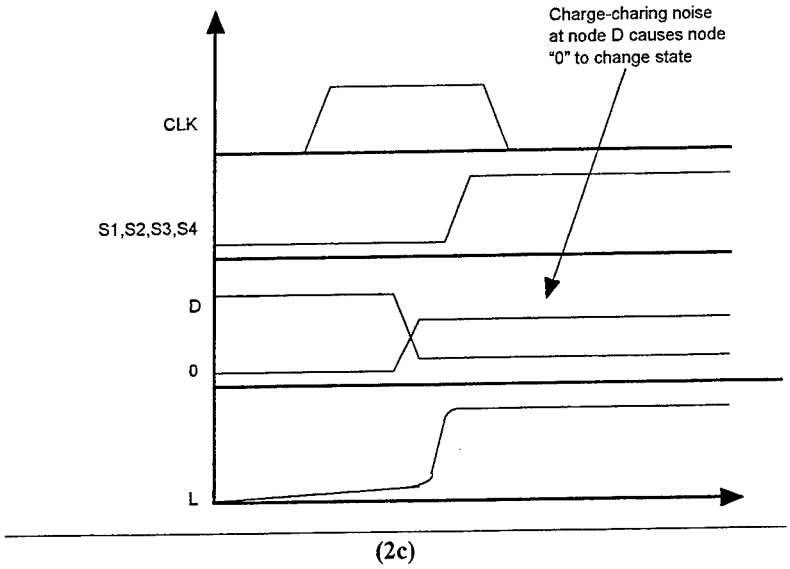

Figure 2. Illustration of Capacitive coupling, charge sharing, causing unwanted transitions.

Floorplanning Guides

In rule-based design approach for IC design, floorplanning a chip of moderate size is not a difficult task. The following recommendations are easy to implement and can help greatly

1) Develop a wiring plan, such that as the horizontal metal 1/vertical metal -2 scheme channel routers is used. Think about how best the layers can be exploited to make connections. Develop consistent schemes to assign layers to wires. Employing different layers for different wire directions or different types of nets will you the best approaches.

2) Include small components into larger ones. Many block diagrams include isolated gates or larger components. These small components increase the design complexities since they require extra effort for power and ground routing and can disrupt the flow of wiring across the chip. Either place them in an existing larger block or create a glue logic for all of these loose components.

3) Design simple wiring. Move first the blocks then the pin locations.

4) Design planar wiring as much as you can. The most important signals should have a planar routing and then we can add less critical signals later.

5) Make separate wiring plans for power and clock signals.

The effects of charge sharing can be reduced by changes in circuit topologies [2] as shown in Figure 3

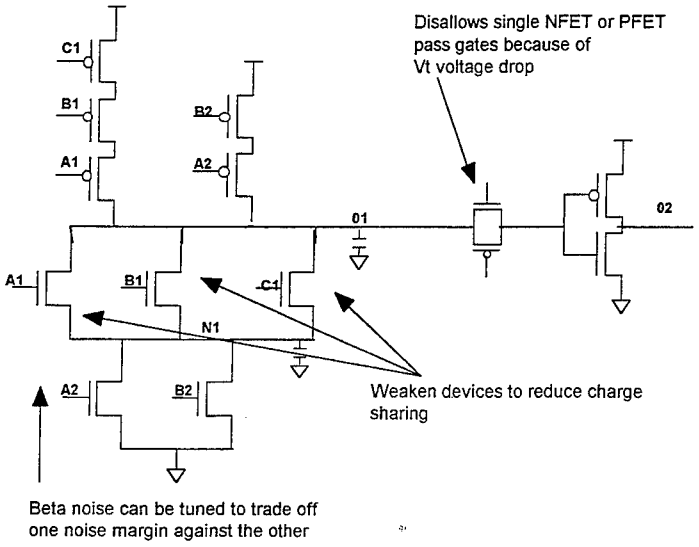

(3a)

DYNAMIC LOGIC GATE

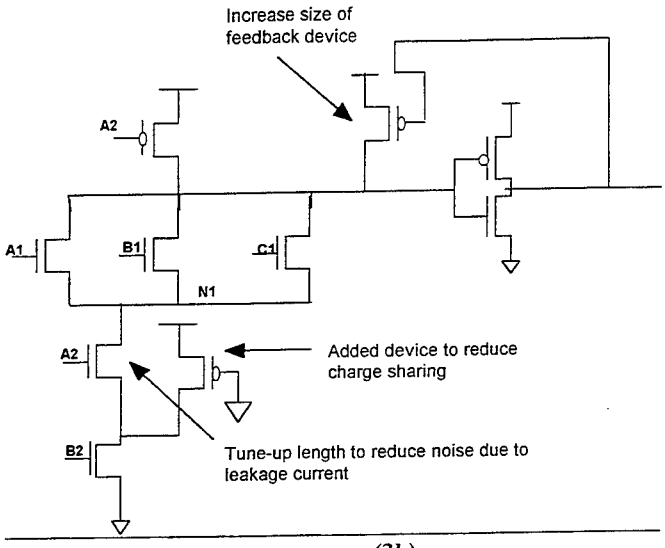

(3b)

Discussion on Tools:

The following table illustrate a list of tools (some are relevent to computational electromagnetics) which provide some help (and the help is described) in the analysis of submicron IC desing for assessing noise related problems. The conclusion from this table shows that in reality a variety of tools may need to be implemented to accomplish the desired results.

Type of Tool	Usefullness	How to use it	Evaluation
Integral Equations (e.g MOM)	Extremely limited	Capacitive effects only	Very intensive for very little advantages
Finite Difference & Finite Time Domain	Limited	Capacitive effects mainly	Very intensive for very little advantages
Transmission Line Methods	More suitable. Use widely by commercial signal integrity/EMI tools	As its name indicates, can easily model High Freq. Effects of transmission lines	Efficient in terms of computational time, memory, accuracy

Static/Quasi Static Methods	More suitable. The prefered method in CAD tools for PCB and IC design (parasitic extraction)	Can easily model all low frequency transmission line effects	Efficient in terms of computational time, memory. Limited accuracy at higher frequencies
Lumped Parameter Methods	Suitable. The prefered method in SPICE-like tools for circuit analysis	Suitable only at low frequencies	Efficient bu of limited accuracy
Charge Transport Methods	Very suitable. Under consideration for labor intensive jobs	Can easily and accurately model capacitive, resistive effects	Very computer intensive

Table 1. The role of several types of computational tools in modeling IC parasitic effects.

References.

[1] Montrose, M.I. 1991, "Overview of design techniques for printed circuit board layout used in high technology products." Proceedings of the IEEE Int. Symp. on Electromagnetic Compatibility, New York, IEEE.

[2] Dockey, R.W. and R.F German, 1993. New techniques for reducing printed circuit board common-mode radiation, " Proc. of the IEEE Int. Symp. on Electromagnetic Compatibility, New York, IEEE.

[3] Johnso,H and M.Graham,High Spped Digital Design, Prentice Hall, 1993.

[4] Robert Patton "The war on Noise," Electronic Journal, October 1998.

NUMERICAL CALCULATIONS FOR THE BACK SCATTERING AND EXTINCTION CROSS SECTIONS OF PLANE WAVES INCIDENT OBLIQUELY ON AN ECCENTRIC MULTILAYERED CYLINDER

Hashim A. Yousif
The University of Pittsburgh
300 Campus Drive
Bradford, Pennsylvania 16701
yousif@vms.cis.pitt.edu

Atef Z. Elsherbeni
Electrical Engineering Department
University of Mississippi
University, MS 38677
atef@olemiss.edu

Abstract

In this paper, a numerical solution of the scattering of electromagnetic plane waves from a multi-layered eccentric cylinder at oblique incidence is discussed briefly. The cylinders are infinitely long, penetrable, and of circular cross sections. Numerical data for the back-scattering and extinction cross sections are presented and discussed for two independent polarizations of the incident plane wave (TM and TE). The results indicate that the scattered fields by an eccentric cylinder are sensitive to the eccentricity parameters, cylinder's material, and the tilt angle of the incident plane wave.

1. Introduction

The scattering of electromagnetic plane waves from an eccentric multi-layered cylinder at oblique incidence was investigated analytically. The analytical solution was obtained by solving the wave equation in different spatial regions after expressing the field components in cylindrical wave functions and applying the boundary conditions at the boundaries [1]. Since the cylinders were eccentric, the translational addition theorem of Bessel functions was used to represent the field components in terms of the local coordinates of each individual cylinder before applying the boundary condition on the surface of each cylinder. A system of coupled equations with unknown expansion coefficients resulted and has been solved numerically. In this study, we present various new numerical results showing the electromagnetic properties of the eccentric cylinders.

2. Geometry of the problem

Figure 1 shows M (M >2) eccentric cylinders of radii r_j (j=1,..,M). Each cylinder is defined by its own cylindrical coordinate system, i.e., (ρ_j, ϕ_j, z_j) and the axes of the cylinders are parallel to the z-axis and are separated by a distance d_j.

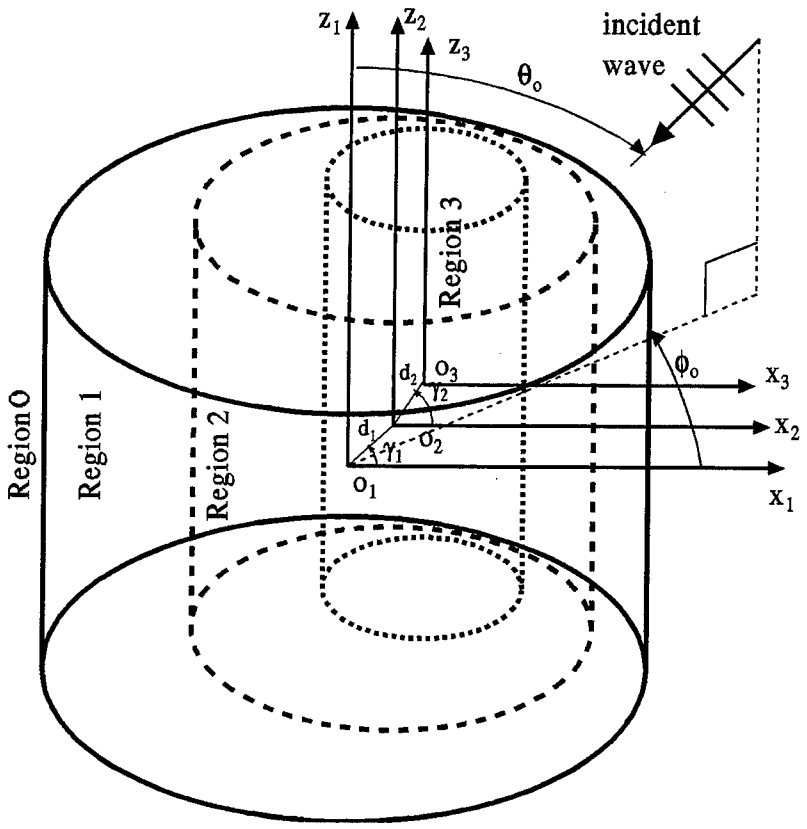

Figure 1. Eccentric cylinders of radii r_j (j=1,..,M). The incident plane wave makes an angle θ_0 with the negative z-axes and its projection on the x-y plane makes an angle ϕ_o with the negative x-axis.

The vector $\bar{d}_j$ is directed from the axis of cylinder j to the axis of cylinder j+1 and makes an angle γ_j with the positive x-axis. We will consider no-overlapping cylinders, i.e.; the cylinder of radius r_{j+1} is always inside that of radius r_j. Region 0 (j=0), the space outside the outer cylinder ($\rho_1 \geq r_1$), is a lossless dielectric with $\sigma_0 = 0$. Region1 (j=1) is the space occupied by the region between the outer cylinder and the next one to it. Region M (j=M) is the region occupied by the inner cylindrical core, $0 \leq \rho_M \leq r_M$. The permittivity, conductivity, and permeability of each region are denoted by ε_j, σ_j, and μ_j, respectively. The propagation vector of the incident wave makes an angle θ_0 with the negative z axes and its projection on the x-y plane makes an angle ϕ_o with the negative x axis. The cylinders are infinitely long with circular cross sections and with arbitrary materials.

3. Numerical solution

A computer program is written to calculate the projected back scattering and extinction cross sections from an eccentric multi-layered cylinder. The accuracy of the developed computer program is verified for different special cases. The single homogeneous cylinder calculations are obtained from our multi, eccentric cylinder computer program. In addition, we were able to duplicate the numerical calculations of two eccentric cylinders recently presented in [2]. Moreover, the extinction cross section is identical to the scattering cross section when the materials of the cylinders are not absorbing as expected.

4. Numerical calculations

Numerical calculations of the projected back scattering and extinction cross sections as a function of the angle of incidence ϕ_0 were generated. We define the projected back scattering cross section σ by $\sigma = Q \sin\theta_0$, where Q is the actual back scattering cross section. Figure 2 shows the projected back scattering and extinction cross sections for a three-layered eccentric cylinder as a function of ϕ_0. The radius of each layer is 1.0λ, 0.8λ, and 0.6λ, respectively, where λ is the incident wavelength. The plane wave is incident normally on the axis of the cylinder $\theta_0=\pi/2$. The eccentric parameters $d_1=0$ and $d_2=0.2\lambda$; the orientation angles $\gamma_1=\gamma_2=0$. The relative permittivites of outer and mid layer are 2, and 3, respectively. The solid, dashed, dotted solid, and chain dotted lines are for the inner layer's relative permittivity of 1, 2, 4, and 6.5, respectively. The effect of the material of the inner layer on the cross sections is quiet evidence from this figure. The figure shows that both the projected back scattering and extinction cross sections are very sensitive to the change of the material of the inner layer of the cylinder.

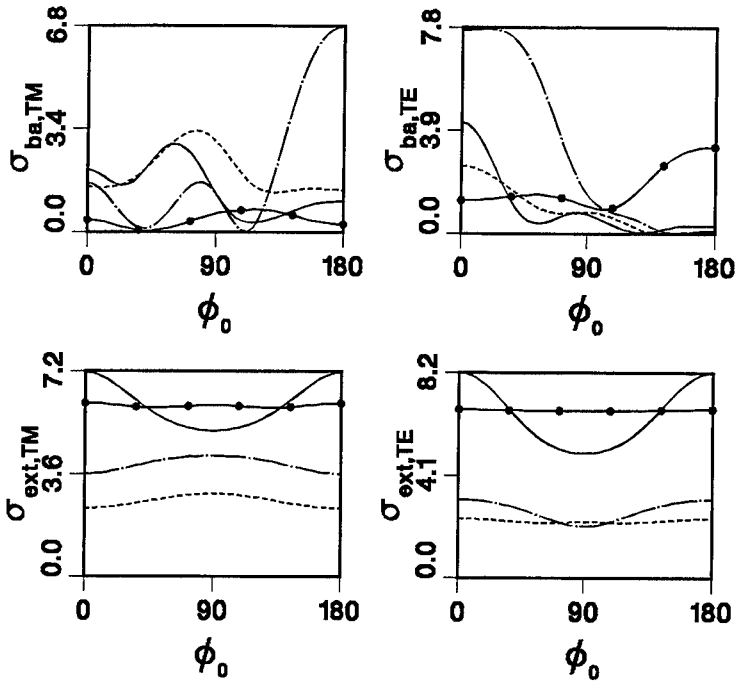

Figure 2. The projected back scattering and extinction cross sections as function ϕ_0 for a three-layered cylinder at normal incidence. The radius of each layer is 1.0λ, 0.8λ, and 0.6λ, respectively. d_1= 0, d_2=0.2λ, γ_1= 0, and γ_2= 0, relative permittivites of outer and mid layers are 2, and 3, respectively. The solid, dashed, dotted solid, and chain dotted lines are for relative permittivity of the inner layer of 1, 2, 4, and 6.5, respectively.

We have also investigated the effect of the tilt angle on the extinction and projected cross sections. Figure 3 shows these cross sections as functions of ϕ_0. The parameters of this figure are the same as those of figure 2 except that the tilt angle, θ_0, is $\pi/4$. Comparing the previous two figures shows a profound change in the scattering patterns. However, the projected back scattering cross section shows more sensitivity than the extinction cross section to this change.

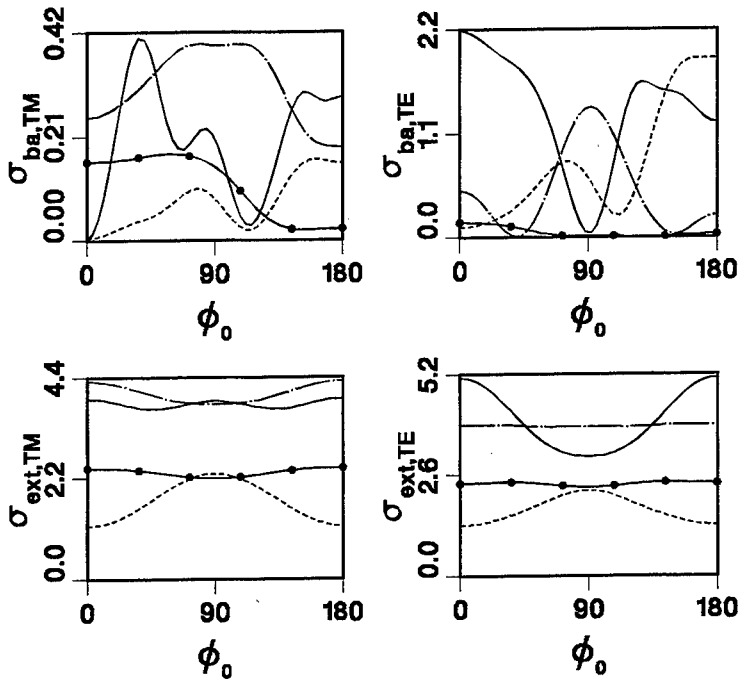

Figure 3. The projected back scattering and extinction cross sections as a function of ϕ_0. The parameters of this figure are the same as those of figure 2 except that the tilt angle, θ_0, is $\pi/4$.

We further considered the effect of the eccentricity parameters on the cross sections of a three-layered cylinder. Figure 4 shows the projected back scattering and extinction cross sections as a function of ϕ_0 for normal incidence with $d_1=\gamma_1=\gamma_2=0$. The radius of each layer of the cylinder is 1.0λ, 0.8λ, 0.6λ and the corresponding relative permittivity of each layer is 4, 3, and 2, respectively. The solid, dashed, dotted solid, and chain dotted lines are for d_2=0.2, 0.15, 0.1, and 0, respectively. The projected back scattering cross section shows a drastic response to the change in the eccentricity parameter.

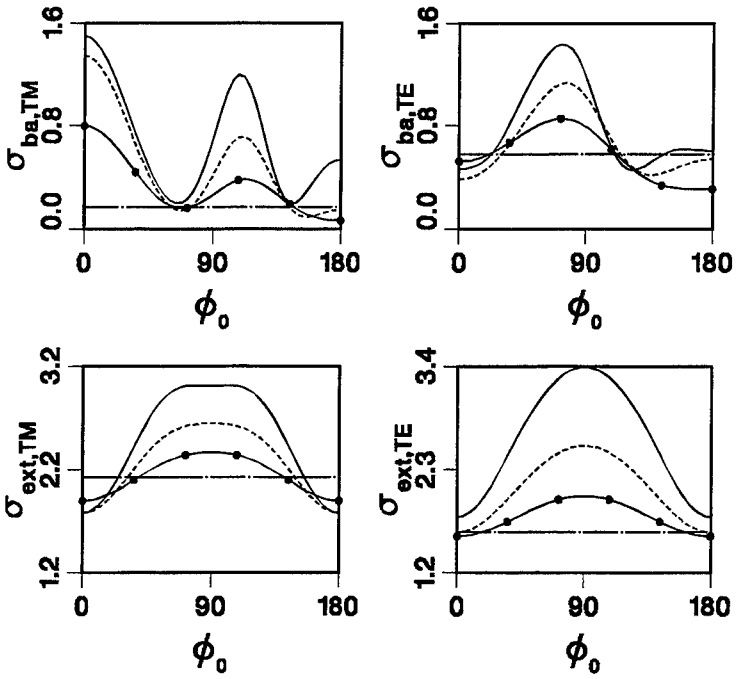

Figure 4. The projected back scattering and extinction cross sections as a function of ϕ_0 for $_\theta$ for a three-layered cylinder at normal incidence with $d_1=\gamma_1=\gamma_2=0$. The radius of each layer of the cylinder is 1.0λ, 0.8λ, 0.6λ and the corresponding relative permittivity of each layer is 4, 3, and 2, respectively. The solid, dashed, dotted solid, and chain dotted lines are for d_2=0.2, 0.15, 0.1, and 0, respectively.

Figure 5 shows the cross sections as a function ϕ_0. The parameters of this figure are the same as those of figure 4 except the tilt angle is 60°. The curves of the cross sections display smooth behaviors; this is especially true for the extinction cross section.

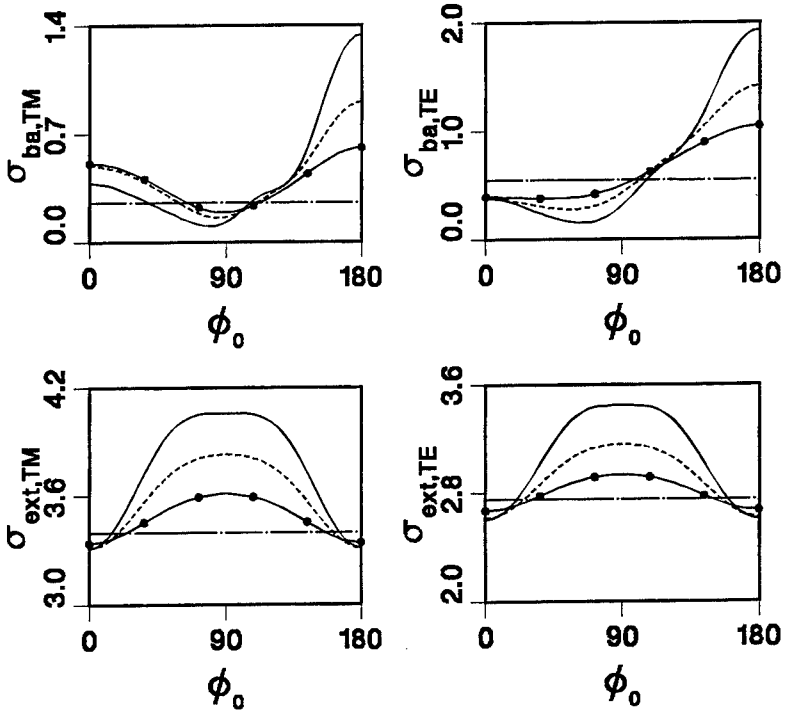

Figure 5. The projected back scattering and extinction cross sections as a function of ϕ_0. The parameters of this figure are the same as those of figure 4 except the tilt angle is 60°.

References

[1] H. A. Yousif, and A. Z. Elsherbeni, "Electromagnetic scattering from an eccentric multilayered cylinder at oblique incidence," J. of Electromagnetic waves and Applications, vol. 13, pp. 325-336, 1999.

[2] H. A. Yousif, and A. Z. Elsherbeni, "Oblique incidence scattering from two eccentric cylinders," J. of Electromagnetic waves and Applications, vol. 11, pp. 1273-1288, 1997.

Using the Partial Element Equivalent Circuit (PEEC) Simulation Technique for EMC Applications

Bruce Archambeault
IBM

Introduction

The Partial element Equivalent Circuit (PEEC) simulation technique was first introduced 25 years ago [1]. It has mostly been used for quasi-static partial inductance calculations until recently. New developments [2] have made PEEC a full-wave tool with time domain capabilities.

Modeling and simulation is not new to EMC applications. There have been many articles in the literature using the method of Moments (MoM), the Finite-Difference Time-Domain (FDTD) technique, the Transmission Line Method (TLM) or the Finite Element method (FEM). Each of these different techniques have areas where their individual strengths make them the best choice for a particular modeling problem, and each has areas where they are not appropriate. Therefore, a tool-box strategy is necessary, where the engineer has more than one modeling technique available, allowing the use of the proper technique for the given task.

PEEC has recently become a popular alternative to some of the more traditional modeling techniques. One of it's biggest advantages is the easy ability to add circuit elements into an electromagnetic simulator, making it a preferred choice for printed circuit board simulations which include lumped circuit elements, such as inductance, capacitance, and resistance. A number of examples of PEEC's usefulness in EMC modeling applications will be presented here.

Brief Description of PEEC

There are a number of technical articles describing the PEEC technique in detail, and those will not be repeated here. However, a very brief description will be presented.

PEEC is based on the integral equation formulation. All the structures to be modeled are divided into electrically small elements. The coupling between each element is described as an equivalent circuit shown in Figure 1. Once the matrix of equivalent circuits are developed, then a SPICE-like circuit solver is used to for the response of the system to the simulation applied to it.

Since the solution is a circuit based solution, then individual circuit elements, such as resistance, capacitance, and inductance can be easily added to any set of elements or nodes.

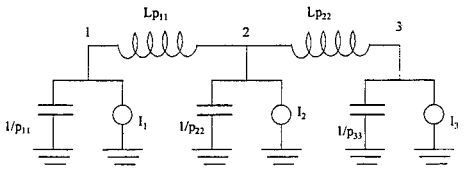

Figure 1 PEEC Model

EMC Applications

There are a variety of EMC applications for the PEEC technique. Since individual circuit elements can be added to the model easily, simulations involving printed circuit (PC) boards are straightforward to create.

Crosstalk Simulations

One of the most serious concerns of an EMC analysis of a PC board is the crosstalk between a critical net (such as a clock net) and an I/O net which could potentially provide a convenient path for the high frequency harmonics of the clock signal to escape the shielded enclosure. Figure 2 shows a diagram of an example.

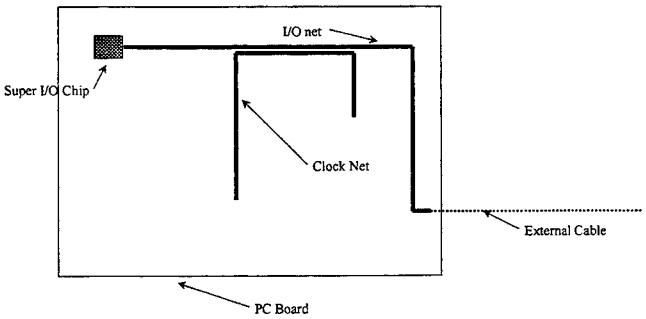

Figure 2 Crosstalk Example

The question about how much signal reduction is provided by additional distance between parallel traces is often debated. Also, the amount of benefit obtained by using a ground-guard trace on either side of a critical net vs. separation distance (without the ground-guard trace) is not clear.

A simple model was created (Figure 3) to illustrate how the undesired current coupled into the I/O net would be affected by increasing the separation between nets, or simply placing a ground-guard trace between the critical and I/O net.

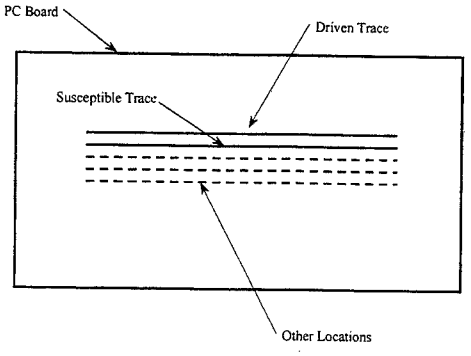

Figure 3 Crosstalk Model Configuration

Figure 4 shows the result of the PEEC model as the I/O net was moved further from the driving net. The PEEC time domain result has been transformed into the frequency domain using a FFT, and then normalized to the amount of crosstalk current present in the I/O trace when the I/O trace was as close as possible to the driving net. The change in the amount of crosstalk coupling is apparent as the separation between traces is increased. When the ground-guard trace is used, the crosstalk coupling is less than with the maximum separation.

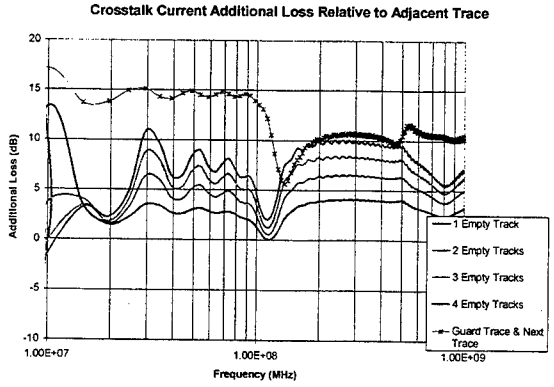

Figure 4 Crosstalk Current vs Separation

Cascade Crosstalk Simulations (Multi-level Crosstalk)
In addition to 'normal' crosstalk analysis as shown in the previous section, cascaded crosstalk, or multilevel crosstalk is also a consideration to EMC engineers. Figure 5 shows a diagram of a cascaded crosstalk configuration. As can be seen, the clock net is not close to the I/O net, but another net becomes a fortuitous conductor between them. This can allow some amount of clock-related signal voltage at the I/O connector, which then becomes a common-mode voltage (relative tot he outside of the shielded enclosure), and a potential EMI emissions problem.

Figure 6 shows the results of an example using PEEC to analyze the amount of unwanted signal level at the I/O connector due to cascaded crosstalk as the amount of parallel traces between the clock trace and fortuitous conductor is varied. The time domain waveforms from the PEEC analysis were converted to the frequency domain for convenient analysis.

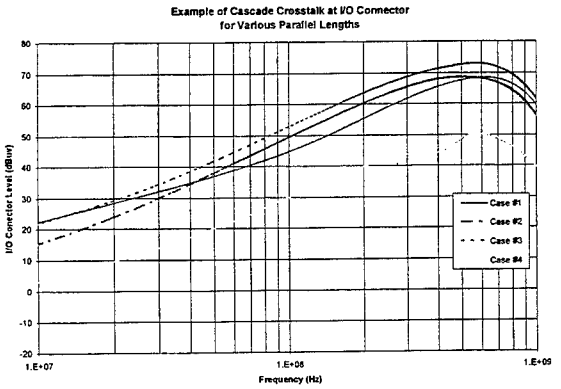

Figure 6 Cascade Crosstalk Output Example

Zig-Zag Trace Analysis
Another EMC application of PEEC modeling is given in the example of the analysis of zig-zag traces. In order to ensure clock signals arrive at all destination at the same instant in time, traces are often put through a zig-zag pattern to increase the trace length to match the longest clock trace. Once the traces are all the same length, then the clock signal will arrive at all destinations simultaneously.

There has been a considerable amount of debate concerning whether the length of the zig-zag makes a difference to EMC emissions from the traces, especially on four layer PC boards where the zig-zag pattern is exposed. Figure 7 shows examples of different zig-zag patterns which are commonly used. For this example, both zig-zag patterns have the

same overall trace length. In real-world designs, this pattern can be anything where the required length is achieved.

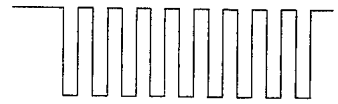

Zig-zag pattern #1

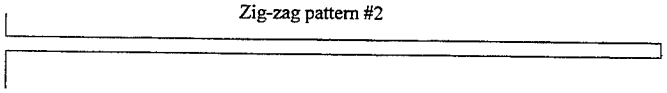

Zig-zag pattern #2

Figure 7 Zig-Zag Patterns

In addition to the EMC emissions concerns about the zig-zag pattern, there is also a signal integrity concern. PEEC was used to analyze the time domain waveshape on a number of different zig-zag patterns. In the first example, the trace is assumed to be perfectly terminated in its characteristic impedance. The difference in the waveshape arriving at the receiver is shown in Figure 8. One of the advantages of the PEEC technique is the easy ability to add or change circuit elements within an electromagnetic model. In the above example, the termination was changed from a resistor to a 10 pF capacitor (representative of the termination impedance of CMOS devices), and the net was terminated at the source with a series impedance.

Since the receive end of the net is not properly terminated, a reflection is expected. The source series termination is designed to match the net characteristic impedance as to inhibit any secondary reflection from the source end. Figure 9 shows the near-end time domain waveshape for the two zig-zag patterns. Clearly there is a significant difference between the cross-talk coupling effects between the two zig-zag patterns. This distortion of the initial pulse contributes additional (and unwanted) harmonic energy to the original signal. This additional harmonic energy will in turn contribute to additional direct emissions, as well as additional common mode emissions.

Summary

The need for a variety of modeling techniques for EMC applications has been well documented. Each of the various techniques has a different strength that the EMC engineer can use. PEEC has not been used for EMC applications until recently. One of the strong advantages of using PEEC is the convenience of including circuit based elements. A number of different examples were PEEC was used for EMC analysis were presented.

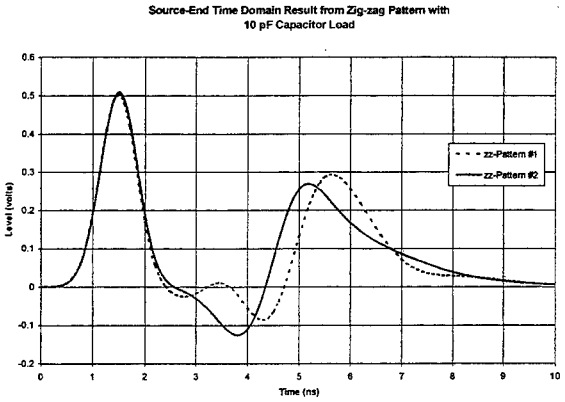

Figure 8 Zig-zag Pattern time Domain Result for Matched Load

References:

[1] A.E. Ruehli, "Equivalent Circuit Models for Three-Dimensional Multiconductor Systems," IEEE Trans. on Microwave Theory and Techniques, Vol. MTT-22, No. 3, March 1974

[2] J. Garrett, A.E. Ruehli, C.R. Paul, "Stability Improvement of Integral Equation Models," Proc. IEEE Antennas Prop. Society Symposium, Montreal, Canada, July 1997

Figure 9 Zig-zag Pattern time Domain Result for Unmatched Load

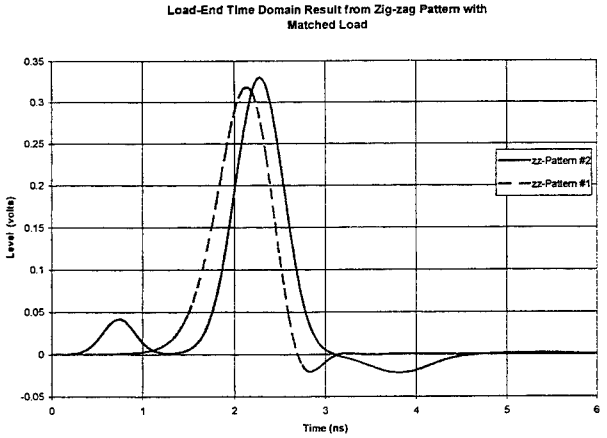

Analytic Validation of a Low-Frequency Magnetic Induction Code with Nonuniform Sources

Trevor W. Dawson
Dept. Elec. & Comp. Eng., University of Victoria
PO Box 3055 Stn CSC Victoria BC Canada V8W 3P6

Abstract

This paper considers the problem of extremely low-frequency induction in a homogeneous sphere by an external line-current source. The problem has an analytic closed-form solution that exhibits a fully three-dimensional electric field. The solution is particularly useful for testing more general-purpose numerical modeling codes. Earlier analytic solutions have provided tests for induction in homogeneous bodies by homogeneous magnetic fields, as well as induction in inhomogeneous spheres, also by uniform fields. These models exercise the basic implementation of the numerical implementation, as well as the handling of conductivity gradients. This new model provides an additional test of the source implementation. It has a particularly useful application in the validation of computer models for induction in humans by power transmission lines. In this paper, results computed using an established scalar-potential finite-difference code are compared with the analytic values. Excellent agreement is obtained, apart from surface field discrepancies associated with the staircasing approximation used for the sphere.

1 Introduction

When the source frequencies are sufficiently low, the induction in compact isolated conductors can be considered in terms of separate contributions due to electric and magnetic sources [*Olsen,* 1994]. The electric field inside the conductor may be represented in terms of an unknown scalar potential using Stevenson's method [*Van Bladel,* 1985]. The applied magnetic field manifests itself through a vector potential serving as an electric field source. The resulting mathematical equations can give rise to a variety of numerical schemes, including the Scalar Potential Finite Difference (SPFD) method [*Dawson et al.*, 1997]. It is desirable to validate any numerical solution, preferably by comparison with an analytical solution. Suitable analytic solutions are relatively rare, particularly for fully three-dimensional problems. The solution for uniform magnetic induction in a homogeneous sphere is elementary, but of restricted utility. There are recently published solutions for an uniform magnetic induction in an equatorially stratified sphere [*Dawson and Stuchly,* 1997; *Dawson,* 1997]. These serve to validate the handling of conductivity gradients in a numerical code, and were recently applied to a scalar potential finite difference code [*Dawson and Stuchly,* 1996]. This code is being extensively applied to the evaluation of 60-Hz induction in the human body [*Dawson and Stuchly,* 1998; *Dawson et al.*, 1997] by uniform magnetic fields. However, uniform magnetic excitation is not a suitable source model for occupational exposures faced by utility workers. Here, linear current elements, both finite and infinite in extent, are more suitable. It is desirable to ensure that such a source implementation in a numerical code is correct by comparison with an additional method, preferably analytical.

This paper presents such a validation for induction in a homogeneous conducting sphere by a line current source. The problem has a simple closed-form solution. The result is compared with data computed using the scalar potential finite difference code. It is shown that good agreement is obtained, thereby providing the requisite validation.

2 Model and Solution

Coordinates are defined with respect to a Cartesian coordinate system $\{x, y, z\}$. Coincident spherical $\{r, \theta, \varphi\}$ and cylindrical coordinates $\{\rho, \varphi, z\}$ will also be freely used. A notation such as $\hat{\boldsymbol{z}}$ defines a unit vector associated with the corresponding coordinate. The problem consists of an isolated homogeneous sphere of radius $a > 0$ and conductivity $\sigma_0 > 0$, centred at the coordinate origin. All fields are assumed time-harmonic with period T, frequency f, and radian frequency $\omega = 2\pi f$. A common time factor $e^{+j\omega t}$ is therefore assumed and suppressed throughout. Field vectors, denoted herein as uppercase bold quantities, therefore represent complex phasor amplitudes. A quasistatic approximation is assumed, so that the sphere is small compared both to the source wavelength and to the internal skin depth.

The problem is formulated using Stevenson's method [*Van Bladel,* 1985], which is based on an ordering of the fields in a power series ordered by source wavenumber $k_0 = \omega/c_0$, or equivalently, by frequency. Here c_0 denotes the speed of light in the vacuum surrounding the sphere. Thus the zeroth-order fields represent the static limit, first-order fields vanish linearly with frequency approaching zero, etc..

The sphere is under the influence of an applied line current density source, whose zeroth-order form near the plane $z = 0$, and in the neighborhood of the sphere, may be assumed to have the (static) form

$$\boldsymbol{J}_0^e(\boldsymbol{x}) = i_0 \delta(x - b)\, \delta(y)\, \hat{\boldsymbol{z}}, \tag{1}$$

where i_0 denotes the peak instantaneous current. Thus the line source lies parallel to the z-axis and intercepts the plane $z = 0$ at the point $x = b$, $y = 0$, with $b > a$. This last inequality ensures that the source is external to the sphere. The dimensionless parameter

$$0 < \kappa \equiv a/b < 1 \tag{2}$$

is used freely throughout the derivation.

This work considers only magnetic excitation, hence the zeroth-order external electric field is zero. Furthermore, it follows from the general results of Stevenson's method that the static limit of the electric field is zero within the conducting sphere. The zeroth-order electric field is therefore zero everywhere,

$$\boldsymbol{E}_0(\boldsymbol{x}) \equiv \boldsymbol{0}. \tag{3}$$

Similarly, the zeroth-order magnetic field is unperturbed by the presence of the conducting sphere, and satisfies the classical magnetostatic problem

$$\boldsymbol{\nabla} \times \boldsymbol{H}_0(\boldsymbol{x}) = \boldsymbol{J}_0^e(\boldsymbol{x}), \quad \boldsymbol{\nabla} \cdot \boldsymbol{H}_0(\boldsymbol{x}) = 0, \tag{4}$$

in the entire domain. The simple solution has the Cartesian representation

$$\boldsymbol{H}_0(\boldsymbol{x}) = \left(\frac{i_0}{2\pi}\right) \left[\frac{(x-b)\,\hat{\boldsymbol{y}} - y\hat{\boldsymbol{x}}}{(x-b)^2 + y^2}\right]. \tag{5}$$

This can be expressed in terms of a vector potential [*Stratton,* 1941]

$$\boldsymbol{H}_0(\boldsymbol{x}) = \boldsymbol{\nabla} \times \boldsymbol{A}_0(\boldsymbol{x}), \quad \text{where} \quad \boldsymbol{\nabla} \cdot \boldsymbol{A}_0(\boldsymbol{x}) = 0, \tag{6}$$

and it is readily verified that

$$\boldsymbol{A}_0(\boldsymbol{x}) \equiv \left(\frac{i_0}{2\pi}\right) L_b(x, y)\, \hat{\boldsymbol{z}}, \quad \text{where} \quad L_b(x, y) \equiv -\ln \sqrt{\frac{(x-b)^2 + y^2}{b^2}} = \sum_{n=1}^{\infty} \left(\frac{\rho}{b}\right)^n \frac{\cos n\varphi}{n}, \tag{7}$$

is an appropriate solution. The latter form for $L_b(x, y)$ follows from a Taylor expansion of the function $\ln(1 - \zeta)$ in the disk ($|\zeta| < 1$).

The first-order internal electric field satisfies the differential equations

$$\boldsymbol{\nabla} \times \boldsymbol{E}_1^i(\boldsymbol{x}) = -j\omega\mu_0 \boldsymbol{H}_0(\boldsymbol{x}) \quad \text{and} \quad \boldsymbol{\nabla} \cdot \left[\boldsymbol{E}_1^i(\boldsymbol{x})\right] = 0, \qquad (r < a). \tag{8}$$

subject to a boundary condition of tangential surface current flow,

$$\hat{\boldsymbol{r}}\cdot\boldsymbol{E}_1^i(\boldsymbol{x}) = 0, \quad (r = a)\,. \tag{9}$$

The second member of (8) arises from conservation of internal first-order current density, $\boldsymbol{\nabla}\cdot\left[\boldsymbol{J}_1^i(\boldsymbol{x})\right] = 0$, in the presence of a uniform conductivity. The internal electric field may be written in the form

$$\boldsymbol{E}_1^i(\boldsymbol{x}) = -j\left(\frac{\omega\mu_0}{2\pi}\right)\boldsymbol{\mathcal{E}}^i(\boldsymbol{x})\,, \qquad \text{where} \qquad \boldsymbol{\mathcal{E}}^i(\boldsymbol{x}) = \hat{\boldsymbol{z}}L_b\,(x,y) - b\boldsymbol{\nabla}\psi_1^i(\boldsymbol{x})\,, \tag{10}$$

involving a dimensionless electric field $\boldsymbol{E}_1^i(\boldsymbol{x})$ and scalar potential $\psi_1^i(\boldsymbol{x})$. The second member of (8) together with the boundary condition (9) shows the scalar potential to satisfy the boundary value problem

$$\nabla^2\psi_1^i(\boldsymbol{x}) = 0, \qquad (r < a)\,, \qquad \frac{\partial\psi_1^i(\boldsymbol{x})}{\partial r} = \cos\theta L_b\,(x,y)\,, \qquad (r = a)\,, \tag{11}$$

within the sphere. The boundary value problem can be solved using a simple two-dimensional method. Specifically, if a form

$$\psi_1^i(\boldsymbol{x}) = (z/b)\,Q_m\,(\rho,\varphi) \tag{12}$$

is assumed, then the latter function satisfies the two-dimensional boundary value problem

$$\nabla^2 Q_m\,(\rho,\varphi) = 0, \qquad \{1 + \rho\partial_\rho\}\,Q_m\,(\rho,\varphi) = L_b\,(x,y)\,, \qquad \{r = a\}\,. \tag{13}$$

The solution is readily obtained as follows. Separated solutions of (13a) regular at $\rho = 0$ and periodic are necessarily members of the set $\{\rho^m\cos(m\varphi), \rho^m\sin(m\varphi)\,|\,m = 0, 1, \ldots\}$. It is then straightforward to use the expansion (7b) and the boundary condition (13b) to verify that

$$Q_m\,(\rho,\varphi) \equiv \sum_{n=1}^{\infty}\left(\frac{\rho}{b}\right)^n\frac{\cos n\varphi}{n(n+1)}, \qquad (r < a)\,, \tag{14}$$

and hence that

$$\psi_1^i(\boldsymbol{x}) = \left(\frac{z}{b}\right)\sum_{n=1}^{\infty}\left(\frac{\rho}{b}\right)^n\frac{\cos n\varphi}{n(n+1)} = \left(\frac{z}{b}\right)\Re\left\{1 - \left(1 - \frac{1}{\zeta}\right)\ln(1-\zeta)\right\}, \qquad \left(\zeta \equiv \frac{x+jy}{b} = \frac{\rho e^{j\varphi}}{b}\right), \tag{15}$$

is a solution for the scalar potential. The series and closed-form expressions are both useful. Expressions for the electric field follow from an application of (10) in the appropriate coordinate system. In particular, the spherical coordinate radial component of the internal electric field is identically zero within the sphere.

The series solution leads to the analytic value

$$K\left(\kappa^2\right) \equiv \frac{1}{\mathcal{V}}\iiint_{\mathcal{V}}(\boldsymbol{\mathcal{E}}\cdot\boldsymbol{\mathcal{E}})\;d\mathcal{V} = \left(\frac{3}{2\kappa^3}\right)\left\{\frac{4}{3}\kappa + \frac{11}{9}\kappa^3 - \arcsin(\kappa)\left[\kappa\arcsin(\kappa) - \frac{2}{3}\left(2+\kappa^2\right)\sqrt{1-\kappa^2}\right]\right\} \tag{16}$$

for the mean-square dimensionless internal first-order electric field over the sphere. As indicated in the notation, the right-hand side depends only on the square of the source-sphere separation parameter κ. This quantity is required for computation of the physical values of the peak instantaneous volumetric mean-square internal electric field, mean-square internal current density, and average power deposition in the sphere.

3 Results

The particular model under consideration consist of a sphere of radius $a = 0.5$ m. The line source is located at $b = 1$ m, for a separation of 0.5 between the line and sphere surface. The dimensionless ratio is therefore $\kappa = 0.5$. The line source has frequency $f = 60$ Hz and carries a peak current $I_0 = 1$ A. The sphere conductivity does not enter into the electric field computation. For the homogeneous sphere under consideration, the current density is a simple multiple of the electric field.

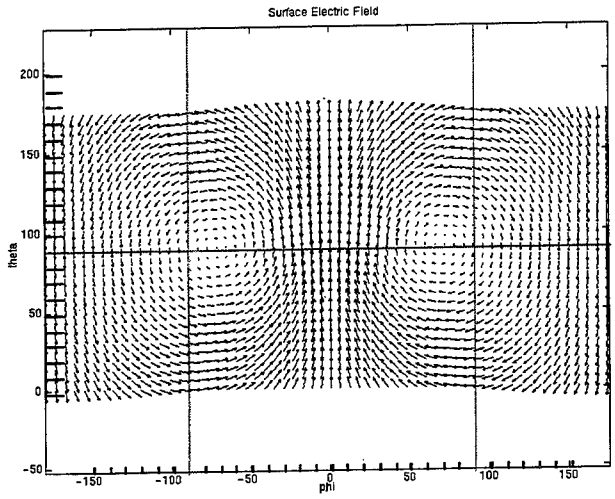

Figure 1: Depiction of the electric field (and hence current flow) on the surface of the sphere. Angular coordinates are in degrees.

The numerical calculations are based on a staircased sphere having cubic voxels with 1 cm edges, so that the sphere diameter is 100 voxel-widths. The SPFD code uses a conjugate gradient solver applied to a sparse symmetric matrix. The solution leads to electric field components defined on the staggered grid formed by the voxel edges. A four-point average is applied to each of the three sets of four parallel edge field components associated with each conducting voxel. This results in an electric field vector, defined in terms of its Cartesian components, at every point on the grid formed by the conducting voxel centers. For comparison purposes, a second set of Cartesian field vectors is computed on the identical three-dimensional array of points from the analytic solution. This allows a voxel-by-voxel comparison between the numerical and analytic data sets.

It may be recalled that the current pattern induced by a uniform field in a uniform sphere has circular current paths normal to the magnetic source vector, with field magnitude varying only in the transverse direction. The current pattern induced by the present line source is similar, being dominated by a vortex system whose axis is curved in the plane $z = 0$. The field pattern is given in Figure 1, which shows the surface current flow pattern for the test model using a pseudo-Cartesian representation. Angular coordinates are in degrees. The vector length is proportional to the local field magnitude (in arbitrary units) so that the higher field values near $\varphi = 0$ are clearly evident. The lighter lines in the figure lie at $\theta = \pi/2$ (corresponding to the equator of the sphere) and at $\varphi = \pm\pi/2$. Under induction by a uniform source directed along the y-axis, the core of the induced current vortex would intercept the surface of the sphere at the intersections of these lines. For the line source, the vortex-surface intercepts move closer to $\varphi = 0$.

To provide a preliminary demonstration of the agreement between the two computations, Table I presents three values of the volumetric root-mean-square of the induced electric field. Units are in microvolts per meter. The analytic value (first row) is computed from the exact solution (16). The numerical value in the second row is obtained using a discrete summation over the appropriate voxel-center electric fields magnitudes. The final entry in the table is computed using the same discrete summation method, but applied to the samples of the analytic solution. The difference between the values in the first two lines of the table is due to spatial mismatch between

Table I: Comparison of root mean square electric field within the sphere.

Analytic value	12.2074
Numerical value	12.2314
Discrete analytic	12.2280

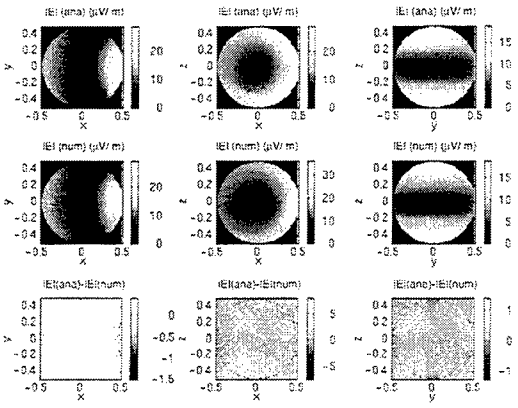

Figure 2: Comparison of the analytic (top row), numerical (middle row) and difference (bottom row) electric field magnitudes in the Cartesian planes $z = 0$ (left column), $y = 0$ (middle column) and $x = 0$ (right column). Units on the shading scale are microvolts per metre.

the analytic and voxel-based spheres, and the associated differences in surface current flow paths between the true and staircased spheres. That the discrepancy is due, in part, to the geometric differences between the models is further supported by the closer agreement between the last two rows of the table, where the differences arise in the third decimal place.

Figure 2 provides an additional visual indication of the induced field pattern, as well as a comparison between field values computed using the analytical and numerical solutions. The figure shows a shaded representation of the field magnitudes in the three principal Cartesian coordinate planes. The top and middle rows pertain to the analytic and numerical data sets, respectively. Field magnitudes are indicated in the associated color scales, with units being microvolts per meter. From left to right, the three columns pertain to the planes $z = 0$, $y = 0$ and $z = 0$, respectively. The line source is perpendicular to the plane of the first column, and is is one radius to the right of the sphere surface. The curvature of the current vortex system axis in the plane $z = 0$ is evident in the first column. The bottom row plots the voxel-wise difference fields. It is immediately evident that significant discrepancies are restricted to the sphere surface, where the staircasing errors are most pronounced.

Finally, Table II provides a numerical comparison between the two electric field solutions, in terms of the Cartesian components, as well as the field magnitude. The data comprise 5 spatial measures, including 2 local (minimum and maximum) and 3 global (average, standard deviation and average absolute value) quantities. The latter is only of interest when applied to the Cartesian components. Units are in microvolts per meter. These data are shown for the analytic (upper section) and numerical (second section) solutions, as well as for the voxel-wise difference fields (third section). The bottom row of the table indicates the full three-dimensional correlation coefficients between the two fields, taken over all conducting voxels. The table shows that pointwise discrepancies

Table II: Comparison of analytical and numerical computations.

		E_x	E_y	E_z	$\|E\|$
Analytic	Min.	−20.003	−3.366	−28.663	0.000
	Max.	20.003	3.366	14.189	28.909
	Avg.	0.000	0.000	0.000	5.530
	Std. Dev.	5.975	0.772	6.130	6.580
	Avg. Abs.	3.491	0.404	3.516	5.530
Numeric	Min.	−25.058	−5.048	−35.243	0.000
	Max.	25.058	5.048	17.632	35.947
	Avg.	0.000	0.000	0.000	5.520
	Std. Dev.	5.964	0.777	6.116	6.566
	Avg. Abs.	3.486	0.407	3.509	5.520
Ana - Num	Min.	−8.325	−3.641	−9.491	−7.856
	Max.	8.325	3.641	7.482	7.520
	Avg.	0.000	0.000	0.000	0.010
	Std. Dev.	0.209	0.112	0.218	0.233
	Avg. Abs.	0.034	0.020	0.035	0.038
Correlation		0.9994	0.9896	0.9994	0.9996

can be of the order 25%. However, as indicated in Figure 2, these are confined to the sphere surface. The global measures in the table confirm the good overall agreement between the two computations, and hence the correctness of the line current source implementation in the numerical code.

4 Closing Remarks

This paper has presented a comparison between numerical and analytical solutions to the problem of low-frequency induction in a uniform conducting sphere by a line current magnetic source. This problem is of relevance in the verification of computer models for the evaluation of low frequency induction in humans by power transmission lines. It is shown that the numerically computed results are in excellent agreement with the analytic values, apart from surface discrepancies related to the staircasing approximation used for the sphere.

Acknowledgment

This work was supported under the Natural Sciences and Engineering Research Council/BC Hydro/TransAlta Industrial Research Chair program.

References

[1] R. G. Olsen. Power-transmission electromagnetics. *IEEE. Antennas & Propagation Magazine*, **36**(6):7–16, December 1994.

[2] J. Van Bladel. *Electromagnetic Fields*. Hemisphere Publishing Corporation, Washington D.C., revised printing edition, 1985.

[3] T. W. Dawson, K. Caputa, and M. A. Stuchly. Influence of human model resolution on computed currents induced in organs by 60-Hz magnetic fields. *Bioelectromagnetics Journal*, 18(7):478–490, 1997.

[4] T. W. Dawson and M. A. Stuchly. An analytic solution for verification of computer models for low-frequency magnetic induction. *Radio Science*, 32(2):343–368, March-April 1997.

[5] T. W. Dawson. Analytic solution for low-frequency magnetic induction in an equatorially stratified sphere : Horizontal excitation. *Radio Science*, 32(5):1761–1776, September-October 1997.

[6] T. W. Dawson and M. A. Stuchly. Analytic validation of a three-dimensional scalar-potential finite-difference code for low-frequency magnetic induction. *Applied Computational Electromagnetics Society Journal*, 11(3):72–81, November 1996.

[7] T. W. Dawson and M. A. Stuchly. High resolution organ dosimetry for human exposure to low frequency magnetic fields. *IEEE Trans. Magn.*, 34(3):708–718, May 1998.

[8] J. A. Stratton. *Electromagnetic Theory*. McGraw-Hill Book Company, New York, 1941.

A Study of Finite Element and Cylindrical Perfectly Matched Layer Approach

Ying Xiao and Yilong Lu†
School of Electrical and Electronic Engineering
Nanyang Technological University
Singapore 639798
(† Corresponding author, eylu@ntu.edu.sg, http://www.ntu.edu.sg/home/eylu)

***Abstract*— In this study, a dual coordinate coupling method is proposed for implementation of finite element and cylindrical PML formulation. This method takes full advantages of the finite element method and the cylindrical PML method avoiding numerical integration normally required by the transformation of different coordinates. In this method, different coordinate systems are used in different regions, cylindrical based sectorial elements in PML region, and Cartesian coordinate based finite elements in scatterer and buffer regions. Compared with traditional coordinate transformation method, this method is more efficient and accurate.**

I. INTRODUCTION

In the past a few years, Perfectly Matched Layer (PML) techniques have attracted wide interest in truncating infinite space into finite space for effective solutions of electromagnetic scattering and radiation problems [1]-[3]. Finite Element Method (FEM) has proven to be a powerful tool in treating problems with complex geometry and material profile. The combination of FEM and PML takes the advantages of both techniques and is considered as a promising approach for solving radiation and scattering problems which involve objects with arbitrary geometry and material parameters.

An ideal PML comprises of an anisotropic medium, whose complex permittivity and permeability tensors $\overline{\overline{\epsilon}}$ and $\overline{\overline{\mu}}$ are chosen in such a way that it can absorb an arbitrary incident eletromagnetic wave without any reflection. PMLs were originally derived for Cartesian coordinates and planar interfaces, in which the plane wave of arbitrary frequency and angle is incident from half-free space upon the PML half-space. Recently, PMLs have been extended to cylindrical and spherical coordinates [4],[5] in order to solve curvilinear scattering problems more effectively. In these circumstances, a general curved vacuum-layer interface is more suitable than a planar interface. The use of cylindrical PML in these cases can reduce computational cost and increase result accuracy. Although the cylindrical PML has its advantage in solving unbounded problem, it encounters some implementation difficulties because the cylindrical PML is normally expressed in cylindrical coordinate, while the scatterer tends to be expressed in Cartesian coordinate.

In this paper, a dual-coordinate coupling element method is proposed to solve this problem. In this study, different kinds of elements are used in different regions. The sectorial elements are used to subdivide the PML region, and triangular or quadrilateral elements are used to subdivide the region enclosed by the PML. These two kinds of elements are coupled at their interfaces. In this study, the performance of this coupling element method is compared with the traditional method which transfers the different coordinates into one. Numerical results show that the coupling method is more effective than the traditional method in the implementation of cylindrical PML with Finite Element Method (FEM).

II. Implementation of Cylindrical PML

For a scatter with arbitrary shape and inhomogeneous material profile, we can use a hybrid FEM/PML approach. As shown in Fig. 1, the cylindrical PML is convenient for cylinder-like scatters. Using cylindrical PML can minimize the space between the PML layer and the scatterer, therefore reduce finite element region and the computational effort.

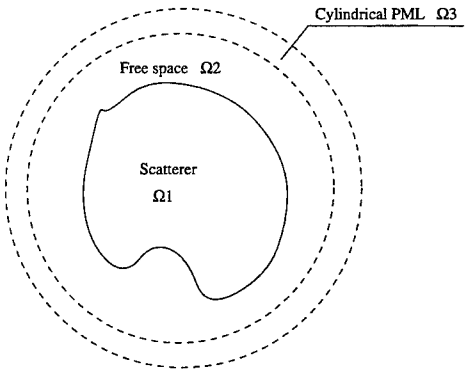

Fig. 1. Cylindrical PML.

Finite element meshes are normally expressed in in Cartesian coordinate while the cylindrical PMLs are best expressed in cylindrical coordinate. In the cylindrical PML, the material properties of the cylindrical PML is expressed as:

$$\frac{\bar{\bar{\mu}}}{\mu_0} = \frac{\bar{\bar{\epsilon}}}{\epsilon_0} = \begin{bmatrix} s_\phi s_z/s_\rho & 0 & 0 \\ 0 & s_\rho s_z/s_\phi & 0 \\ 0 & 0 & s_\rho s_\phi/s_z \end{bmatrix} \tag{1}$$

where $s_\rho = 1 - j\beta_\rho$, $s_z = 1 - j\beta_z$ and $s_\phi = (\rho_0 + \int_{\rho_0}^{\rho} s_\rho d\rho)/\rho$.

The traditional method transfers the cylindrical PML into Cartesian coordinate, so that the same coordinate system is used for both the FE and PML segmentations. The transformation from cylindrical coordinate to Cartesian coordinate is shown as follows.

Suppose the complex permittivity and permeablity tensors of PML medium are $\bar{\bar{\epsilon}} = \epsilon[A]$ and $\bar{\bar{\mu}} = \mu[A]$, where $[A]_{(\rho,\phi,z)}$=diag(a, b, c). It is necessary to calculate the representation of $[A]_{(x,y,z)}$ with respect to the canonical basis in (x, y, z) system, since the governing partial differential equations are given in terms of the variables (x, y, z).

The representation of $[A]_{(x,y,z)}$ in the (x, y, z) system is given by

$$[A]_{(x,y,z)} = J^T [A]_{(\rho,\phi,z)} J \tag{2}$$

where J is the transformation Jacobian.

The $\bar{\bar{\epsilon}}$ and $\bar{\bar{\mu}}$ at the point $P(\rho, \phi, z)$ are:

$$\frac{\bar{\bar{\epsilon}}}{\epsilon_0} = \frac{\bar{\bar{\mu}}}{\mu_0} = \begin{bmatrix} a\cos^2\phi + b\sin^2\phi & (a-b)\cos\phi\sin\phi & 0 \\ (a-b)\cos\phi\sin\phi & a\sin^2\phi + b\cos^2\phi & 0 \\ 0 & 0 & c \end{bmatrix} \tag{3}$$

In cylindrical PML, the parameters a, b and c in $[A]_{(\rho,\phi,z)}$ are different. Hence, the PML medium is inhomogeneous in (x, y, z) system, and numerical integrations are needed. Apparently, this method increases the computation cost and error, which counteracts the advantage of introducing and applying the cylindrical PML.

III. Coupling Element Method

To take the full advantage of the cylindrical PML, a simple and effective implementation of this method is proposed in this study. In this method, both of the Cartesian and cylindrical coordinate systems are used simultaneously, and the transformation is avoided. Finite elements based on the Cartesian coordinate system are used for the scatterer, and the cylindrical sectorial elements based on cylindrical coordinate system are used in the PML region. The two types of elements are coupled at the FE and PML interface.

According to the FEM theory, a basic requirement of the discretization is that there should be no overlaps and gaps between neighbor elements. Furthermore, the elements should be connected via their vertices, or in other words, a vertex of one element is also an vertex of the neighboring elements. In this coupling method, the connection of the elements at the interface is shown in Fig. 2.

Even though different kinds of elements are used, the neighbor elements are connected via their vertices. Although there exist small gaps between sectorial elements and finite elements, this error can be ignored when the element meshing is fine enough.

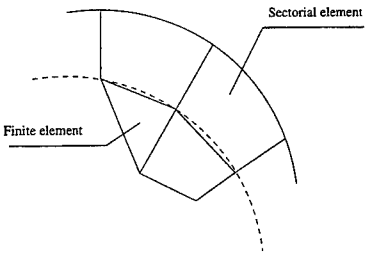

Fig. 2. Coupling mesh.

The coupling between the two formulations of these two kinds of elements should be assured by using suitable boundary conditions. In finite element method, the continuity of the tangential component of the field must be assured across the boundaries of the elements, so, it must be satisfied on the interfaces between the two different elements. Fortunately, at the interface between medium 1 and medium 2, we have the following boundary condition

$$\hat{n} \times (\vec{E}_1 - \vec{E}_2) = 0 \quad , \quad \hat{n} \times (\vec{H}_1 - \vec{H}_2) = 0 \tag{4}$$

Since the two different formulations are in different media, the connection of these two elements must be at the interface. According to (4), the tangential continuous condition of two element is satisfied between two kinds of elements, no matter whether the problem is TM or TE problem.

Taking 2-dimensional problem as example, in the region expressed by Cartesian coordinate system, triangular or quadrilateral elements are used. In the cylindrical PML region, as shown in Fig. 3, cylindrical sector elements are chosen.

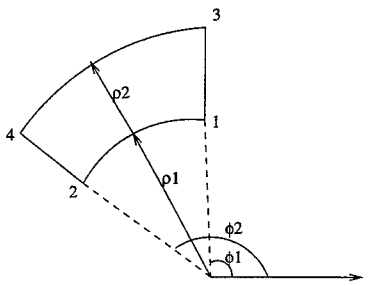

Fig. 3. sector element

The interpolation $N_j^e(\rho,\phi)$ for a sector element are:

$$\begin{aligned} N_1^e(\rho,\phi) &= (\rho-\rho_2)(\phi-\phi_2)/A, \quad & N_2^e(\rho,\phi) &= -(\rho-\rho_2)(\phi-\phi_1)/A \\ N_3^e(\rho,\phi) &= -(\rho-\rho_1)(\phi-\phi_2)/A, \quad & N_4^e(\rho,\phi) &= (\rho-\rho_1)(\phi-\phi_1)/A \end{aligned} \tag{5}$$

where $A=(\rho_1-\rho_2)(\phi_1-\phi_2)$

IV. FEM-PML Formulation

To solve a scattering problem, the open-region should be truncated by PML which is in turn covered by perfectly electrical conductor (PEC), as shown in Fig. 1.

In region Ω_3, only scattered field exists. In region Ω_1 and Ω_2, the field satisfies the double-curl equation:

$$\nabla\times[(\mu^{-1}(\nabla\times\vec{E})]-k_0^2\epsilon\vec{E}=0 \tag{6}$$

where $\vec{E}=\vec{E}^{(sc)}+\vec{E}^{(inc)}$, $\vec{E}^{(inc)}$ is the incident field, and $\vec{E}^{(sc)}$ is the scattered field.

In all regions (Ω_i, i =1, 2, and 3), the scattered field satisfies the following equations:

$$\nabla\times[\overline{\overline{\mu}}^{-1}\cdot(\nabla\times\vec{E}^{(sc)})]-k_0^2\bar{\bar{\epsilon}}\vec{E}^{(sc)}=\vec{F}^{(inc)} \tag{7}$$

$$\vec{F}^{(inc)}=\nabla\times[\mu^{-1}(\nabla\times\vec{E}^{(inc)})]-k_0^2\epsilon\vec{E}^{(inc)} \quad \text{in } \Omega_1 \text{ and } \Omega_2, \tag{8}$$

$$\vec{F}^{(inc)}=0 \quad in\ \Omega_3 \tag{9}$$

$$\hat{n}\times\vec{E}^{(sc)}=0 \quad on\ S_2 \tag{10}$$

where S_2 is the outer PEC boundary of PML.

This boundary value problem can be formulated by Ritz method:

$$\mathcal{F}(\vec{E}^{(sc)})=\int_V\left[(\overline{\overline{\mu}}^{-1}\cdot\nabla\times\vec{E}^{(sc)})\cdot(\nabla\times\vec{E}^{(sc)})-k_0^2\bar{\bar{\epsilon}}\vec{E}^{(sc)}\cdot\vec{E}^{(sc)}\right]dV-2\int_V\vec{E}^{(sc)}\cdot\vec{F}^{(inc)}dv \tag{11}$$

Equation (11) can be described by two different elements: the conventional triangular or quadrilateral elements in region 1 and 2, and the sectorial elements in region 3. In regions 1 and 2, the interpolation function is N_t, while, in region 3, the interpolation function is N_c. The electrical field is:

$$E_i = \sum_{i=1}^{3} E_i N_{ti}, \quad \text{if the element is in region 1 or 2} \tag{12}$$

$$E_i = \sum_{i=1}^{4} E_i N_{ci}, \quad \text{if the element is in region 3} \tag{13}$$

where E_i are the electrical field at the nodal points of each element.

The open region problem can be solved through equation (14)

$$[K^e][E] = [B] \tag{14}$$

where in regions 1 and 2:

$$[K^e] = \int_{V^{(e)}} \frac{1}{\mu_y}\{\frac{\partial N^e}{\partial y}\}\{\frac{\partial N^e}{\partial y}\}^T + \frac{1}{\mu_x}\{\frac{\partial N^e}{\partial x}\}\{\frac{\partial N^e}{\partial x}\}^T - k_0^2\epsilon_z\{N^e\}\{N^e\}^T dv \tag{15}$$

$$[B^e] = \int_{V^{(e)}} \{N^e\}F^{(inc)} dv \tag{16}$$

In region 3

$$[K^e] = \int_{\phi_1}^{\phi_2}\int_{\rho_1}^{\rho_2} \frac{1}{\mu_\rho}\frac{1}{\rho}\{\frac{\partial N_c^e}{\partial \phi}\}\{\frac{\partial N_c^e}{\partial \phi}\}^T + \frac{\rho}{\mu_\phi}\{\frac{\partial N_c^e}{\partial \rho}\}\{\frac{\partial N_c^e}{\partial \rho}\}^T - k_0^2\epsilon_z\rho\{N_c^e\}\{N_c^e\}^T d\rho d\phi \tag{17}$$

$$[B] = \int_{V^{(e)}} \{N^e\}F^{(inc)} dV \tag{18}$$

V. Implementation and Experiment

In this section, an example of 2D-TM incidence from a homogeneous cylinder of circular cross-section is studied by using cylindrical PML. The parameters of the PML material in a point (ρ, ϕ) are assumed as: $s_\rho = 1 - j\sigma_{\max} d^2/D^2$, and $s_\phi = 1 - j\sigma_{\max}\frac{d^3}{3\rho D^2}$, where $\sigma_{\max}$ denotes the maximal loss tangent, D the thickness of the PML, and d the distance between the point (ρ, ϕ) and the air-PML interface.

In this example, both implementations of cylindrical PML are compared. In the coupling element method, the triangular elements are used in scatterer and buffer region, and the sectorial elements are used in PML region. In the coordinate transformation method, only triangular elements are used, and one-point and three-point Gaussian numerical integrations are used, respectively. The numerical results of these two methods are shown in Fig. 4.

From Fig. 4, we can see clearly that the coupling element method achieves more accurate result than that of the transformation method. The accuracy of transformation method can be improved if the integral points are increased. But the increase of the number of integral points will also increase computational cost. The computational time that the two methods spend in forming the coefficient matrix is compared in Table I, it can seen that the coupling element method takes much less time than the transformation method. More time will be required in the transformation method if the number of integral points is further increased. This increase of the computation time may be formidable for 3D problems.

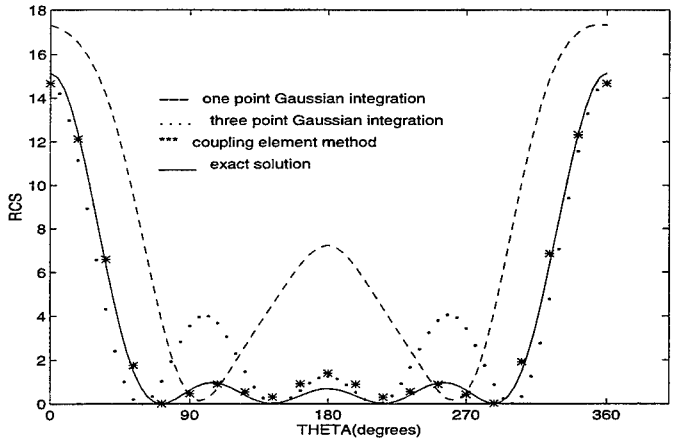

Fig. 4. RCS of a circular dielectric cylinder. The scatterer is a homogeneous cylinder, its radius is 0.3λ, $\epsilon = 4$, $\mu = 1$, TM plane wave incident in $-\hat{x}$ direction

TABLE I

Compare the coupling element and triangle element

	coupling method	1 point integral	3 point integral
matrix A	18.10 (sec)	28.08 (sec)	39.89 (sec)

VI. Conclusions

In this study, a coupling element method is proposed for cylindrical PML and FEM implementation. This method uses different coordinate systems in different regions, i.e., sectorial elements in PML region, and finite elements in scatterer and buffer regions. This method takes full advantage of the cylindrical PML method by avoiding the transformation of different coordinates. Numerical experiments show that this technique is more effective and accurate than traditional transformation method.

References

[1] J. Berenger, "A perfectly matched layer for the absorptin of electromagnetic waves," *J. comput. Phys.*, vol. 114, pp. 185-200, Oct. 1994.

[2] W. C. Chew and W. H. Weedon, "A 3D perfectly matched medium from modifiedd Maxwell's equations with stretched coordinate," *Microwave Opt. Technol. Lett.* no. 7, pp. 599-604, 1994

[3] Z. S. Sacks, D. M. Kingsland, R. Lee, and J. -F. Lee, "A perfectly matched anisotropic absorber for use as an absorbing boundary condition," *IEEE Trans. Antennas Propagat.* vol. 43, pp. 1460-14633, Dec. 1995

[4] B. Yang, D. Gollieb, and J. S. Hesthaven, "On the use of PML ABC's in spectral time-domain simulations of electromagnetic scattereing," *Proc. 13th Annu. Rev. of Prog. Appl. Comp. Electromag.*, Monterey, CA, Mar. 17-21, 1997, bol.2, pp. 926-9333

[5] M. Kuzuoglu, and R. Mittra, "Investigation of nonplanar perfectly matched absorbers for finite-element mesh truncation," *IEEE Trans. Antennas Propagat.* vol. 45, no. 3, Mar. 1997

[6] F. L. Teixeria and W. C. Chew, "Systematic cerivation of anisotropic PML absorbing media in cylindrical and spherical coordinate," *IEEE Microwave Guided Wave Lett.* vol. 7, no. 11, pp. 371-373, Nov. 1997

Conditioning of biorthogonal wavelet transforms and iterative solvers for electromagnetic integral equations

Wojciech L. Golik *
Department of Mathematics and Computer Science
University of Missouri-St. Louis
St. Louis, Missouri 63121
golik@arch.umsl.edu

Abstract

Wavelet transforms are often used to compress dense matrices arising in discretization of electromagnetic integral equations. The problem which kind of wavelets are best suited for this application is not yet settled. Recently some studies showed that the nonorthogonal wavelet transforms produce sparser matrices than those based on orthonormal wavelets. This paper studies the effect of B-spline biorthogonal wavelet transforms (BWTs) on conditioning and compression of impedance matrices. We demonstrate that large condition numbers produced by the BWTs cause corresponding increases in number of iterations needed to solve the sparsified systems. This tends to offset any gains from higher sparsity.

1 Introduction

Discretization of electromagnetic integral equations via the method of moments produces dense matrix equations. For electrically large objects the systems become so large that iterative solvers must be used. In such cases, an approximation to the solution is obtained in $O(pN^2)$ flops, where p is the number of iterations and N the size of the system, in contrast to $O(N^3)$ flops used by the direct solver. In order to further reduce the operation count various techniques have been used to sparsify the system matrices. Among such approaches the wavelet transforms continue to attract considerable interest [1, 2, 3, 4]. Information is still needed on what kind of wavelet transforms is more effective to solve the EM problems. Recently it has been demonstrated that the semi-orthogonal wavelet transforms, constructed by Chui and Wang [5], produce higher matrix sparsities than the orthonormal wavelet transforms at the same level of accuracy [6, 7]. This paper studies the effect of another B-spline based transform, the biorthogonal wavelet transforms (BWTs), proposed by Cohen,

*This research was supported by a grant from The Boeing Company.

Daubechies, and Feauveau [8], on conditioning and sparsification of impedance matrices. Although the BWTs have the attractive property of finite length filters for both primary and dual wavelets, we find that the BWTs lead to large condition numbers increasing the number of iterations needed to solve the matrix equations. Thus the cost of iterative solution of systems sparsified by the BWTs is larger than the corresponding cost for orthonormal wavelet transforms.

2 Matrix Sparsification

Consider the matrix equation $ZJ = E$ obtained by the method of moments from an electromagnetic integral equation. Here Z represents the dense (diagonalizable) impedance matrix of size $N \times N$, J is the surface current vector, and E is the excitation vector. To introduce sparsifying transformations we let T be the wavelet matrix and denote by $\tilde{T}^t$ its inverse. Consider the new system

$$(TZT^t)(\tilde{T}J) = (TE),$$

which can be written as $Z'J' = E'$. Various wavelet transforms T produce matrices Z' with many small elements which can be set to zero without adversely affecting the quality of the solution approximation. Matrix T is usually implemented by repeated application of low-pass and high-pass filters.

Popular candidates for such filters are based on Daubechies' compactly supported orthonormal wavelets [1, 2, 3] and B-spline biorthogonal wavelets of Cohen, Daubechies, and Feauveau [6]. In the case of orthonormal wavelets $\tilde{T} = T^t$, so that matrix Z' is orthogonally similar to matrix Z. Thus Z and Z' have the same eigenvalue spectrum and if X represents the matrix of N eigenvectors for matrix Z then TX is the matrix of eigenvectors for matrix Z'. This is important since the convergence of iterative solvers deteriorates with increase of condition number of the system matrix $\kappa(Z)$ (for the conjugate gradient on the normal equations (CGNE) solver) or with condition number of the matrix of eigenvectors $\kappa(X)$ (for the generalized minimal residual (GMRES) solver) [9]. If T is orthogonal, then $\kappa(Z) = \kappa(Z')$ and $\kappa(X) = \kappa(TX)$ so that iterative solvers will exhibit the same convergence history for both $ZJ = E$ and $Z'J' = E'$ systems.

The situation is quite different in the case of biorthogonal wavelets. In this case Z' is not similar to Z which implies different spectra and different condition numbers for matrices of corresponding eigenvectors. The next sections examine the dependence of these indicators on the size of Z and the wavelet as well as their impact on convergence properties of the CGNE solver.

3 Compactly supported orthonormal and biorthogonal wavelet transforms

Detailed descriptions of compactly supported orthonormal wavelet transforms and the B-spline biorthogonal wavelet transforms can be found in [10] and [8], respectively. This section introduces a specific notation needed to explain our results. We define the l-level wavelet transform T by the product of one level wavelet transforms W_k

$$T = W_{n-l+1} \cdots W_{n-1} W_n,$$

$$W_{n-j} = \begin{bmatrix} \begin{bmatrix} H_{n-j} \\ G_{n-j} \end{bmatrix} & \\ & I_{N-N/2^j} \end{bmatrix},$$

where H_{n-j}, G_{n-j} are low- and high-pass matrices defined by their filter coefficients $\{h_k, g_k\}$, which are highly related. Thus, in the case of the Daubechies orthonormal wavelets (OWT) with p vanishing moments, the high-pass coefficients g_k can be expressed in terms of low-pass coefficients h_k as $g_k = (-1)^k h_{2p-k+3}, \quad k = 1, \ldots, 2p+2$. In the case of biorthogonal wavelets coefficients g_k are given by $g_k = (-1)^k \tilde{h}_{2\tilde{p}-k+3}$, where $\{\tilde{h}_j\}$ denote the coefficients of the *dual* scaling function and, in general, $\tilde{p} \neq p$. For the family of $(m, K)-$ BWTs based on B-splines of order m, the filter coefficients h_k and $\tilde{h}_k$ are defined by the identities [8]

$$\begin{aligned} \textstyle\sum_0^{m+1} h_k z^k &= \sqrt{2}\left(\tfrac{1+z}{2}\right)^{m+1}, \\ \textstyle\sum \tilde{h}_k z^k &= \sqrt{2}\left(\tfrac{1+z}{2}\right)^{2K-m-1} \textstyle\sum_{j=0}^{K-1} \binom{K-1+j}{j} \left(\tfrac{1-z}{2i}\right)^{2j} z^{K-j}, \end{aligned} \tag{1}$$

where parameter K satisfies $K \geq (m+1)/2$. It follows that for a given parameter pair (m, K) there are $m+2$ and $4K-m-2$ nonzero coefficients h_k and $\tilde{h}_k$, respectively. The Haar wavelet is obtained by setting $m = 0, K = 1$. If, for example, $m = 2$ and $K = 3$, then

$$[h_0, h_1, \ldots, h_3] = [1, 3, 3, 1]\sqrt{2}/8,$$

$$[\tilde{h}_0, \ldots, \tilde{h}_7] = [3, -9, -7, 45, 45, -7, -9, 3]\sqrt{2}/64.$$

The number of vanishing moments for this type of wavelets is $2K - m - 2$. It is worth noting that the filter coefficients for the biorthogonal wavelets are rational numbers (except for the common factor $\sqrt{2}$). Both the scaling and wavelet functions have simple expressions and thus are well suited for direct method of moments computations as basis functions. This is not the case for the compactly supported orthonormal wavelets (except for the Haar wavelet). However, as we will see in the next sections, biorthogonal wavelets give rise to impedance matrices with large condition numbers.

4 Conditioning of B-spline biorthogonal wavelet transforms

Define the condition number of a given matrix T by $\kappa(T) = \|T\|_2 \|T^{-1}\|_2$, where $\|\cdot\|_2$ denotes the matrix 2-norm. It has recently been shown that the condition numbers of one-

level B-spline BWTs given by formula (1) increase with m at least as fast 2^m [11]. Table 1 illustrates the growth of $\kappa(T)$ as a function of m. Note that for fixed m, condition number $\kappa(T)$ quickly stabilizes at 2^m as K increases. Since the number of vanishing moments for this type of wavelet is $p = 2K - m - 2$ and the matrix sparsity is related to p, the best strategy to minimize $\kappa(T)$ and maximize p is to choose small m and large K.

Table 1: Condition numbers $\kappa(T)$ for one-level (m, K)BWT

K \ m	0	2	4	6	8
1	1.00				
3	1.42	4.00	16.0		
5	1.58	4.00	16.0	64.0	834.
7	1.68	4.00	16.0	64.0	259.
9	1.75	4.00	16.0	64.0	256.

Table 1 shows the condition numbers of just one level of wavelet transformation. Since, in practice, more than one level is used we study the condition number of a sample of BWTs as a function of number of levels l. Table 2 shows that $\kappa(T)$ increase fairly rapidly with l for BWTs with $m > 2$ and so the asymptotic bounds must turn out to be quite large. Asterisks denote cases where no transformation was possible due to the length of the filter. In addition, for each fixed level l, the condition numbers are larger for larger m. This tends to rule out the use of BWTs with large m. Interestingly, it has been shown recently that $\kappa(T)$ for each BWT is bounded as $l \to \infty$ (and thus the BWTs are *stable* in mathematical terms)[8, 12].

Table 2: Condition numbers $\kappa(T)$ for (m, K)BWT with l levels

l	1	2	3	4	5
(m,K)					
(0,2)	1.28	1.42	1.52	1.60	1.65
(0,3)	1.42	1.66	1.82	1.93	2.00
(0,4)	1.51	1.82	2.02	2.15	2.24
(0,5)	1.58	1.94	2.16	2.31	*
(2,2)	4.00	6.39	10.0	15.1	22.6
(2,3)	4.00	5.27	6.28	7.31	7.87
(4,5)	16.0	25.6	40.3	62.4	96.1
(6,7)	64.0	131.	415.	1221.	*
(8,9)	256.	876.	5995.	35980.	*

The condition numbers of system matrices are related by $\kappa(Z') \leq \kappa(Z)\kappa^2(T)$. Thus $\kappa(T)$ is only an indirect measure of conditioning of system matrix Z'. To provide a comparison, Table 3 lists the condition numbers of Z' for a system obtained from the point matching discretization of the combined field electric equation for a circular cylinder with 10 pulse functions per wavelength and $N = 256$. Note that the column with $l = 0$ corresponds to $\kappa(Z)$ (the original matrix). The results show that condition number of the transformed

matrix Z' grows rapidly with number of levels l (for fixed $m \geq 2$ and K) and with spline order m (for fixed level l). In addition, the comparison of Tables 2 and 3 shows that the bound $\kappa(Z)\kappa^2(T)$ is quite accurate.

Table 3: Condition numbers $\kappa(Z')$ for (m, K)BWT with l levels

l	0	1	2	3	4	5
(m,K)						
(0,2)	6.79	7.35	8.76	8.62	9.82	9.83
(0,3)	6.79	7.48	9.81	1.0e1	1.2e1	1.2e1
(0,4)	6.79	7.52	1.0e1	1.1e1	1.4e1	1.4e1
(0,5)	6.79	7.53	1.1e1	1.2e1	1.5e1	*
(2,2)	6.79	1.6e1	4.7e1	1.5e2	3.4e2	7.5e2
(2,3)	6.79	1.6e1	2.8e1	4.7e2	5.6e2	1.2e2
(4,5)	6.79	2.5e2	5.7e2	1.5e3	3.6e3	7.7e2
(6,7)	6.79	4.1e3	1.1e4	4.4e4	1.9e5	*
(8,9)	6.79	6.6e4	7.5e5	3.6e7	1.3e9	*

To illustrate the convergence of iterative solvers, the original and BWT-transformed systems described above with $N = 256$ were solved by the CGNE method with relative tolerance tol=1e-3. There was no preconditioning and the iterations started with the zero vector. The column with $l = 0$ shows iterations with the original impedance matrix Z. In addition, we performed iterations with matrix Z transformed with Daubechies orthonormal wavelets with vanishing moments $p = 1, \ldots, 7$ and levels $l = 1, \ldots, 5$. All such runs ended with the same number of 16 iterations. Note the considerable increase of iterations for the BWT-transformed systems with $m \geq 2$ and strong correlation between the size of $\kappa(T)$ (see Table 2) and the number of iterations. The growth of number of iterations for $m = 0$ is relatively mild. From these results we conclude that the only practical (m, K)BWTs are those with $m = 0$ (small condition numbers) and large K (large number of vanishing moments).

Table 4: CGNE iterations with tol=1e-3 for (m, K)BWT with l levels.

l	0	1	2	3	4	5
(m,K)						
(0,2)	16	18	22	20	22	22
(0,3)	16	18	23	24	26	26
(0,4)	16	18	25	23	30	30
(0,5)	16	18	26	25	33	*
(2,2)	16	35	60	71	55	60
(2,3)	16	36	55	60	76	72
(4,5)	16	99	122	73	85	93
(6,7)	16	193	124	84	87	*
(8,9)	16	256	104	133	152	*

In our last experiment we compare the compression rates (the number of non-zeros divided

by N^2) and the numbers of CGNE iterations for the circular cylinder problem described earlier. Only results for the $N = 256$ are given here. Note that for larger N more levels of BWT transforms will have to be used leading to higher condition numbers and thus more iterations. We use both (m, K)BWTs and the OWTs with various numbers of vanishing moments. The number of transformation levels varies with each method (depending on filter lengths). The sparsification of the matrix is via a thresholding technique designed to keep the relative errors within 1% of the actual solution. We included in Table 5 only the BWTs with $m = 0$ in view of the previous remarks. In fact, higher values of m give rise to denser matrices. The results suggest that the OWTs perform better than any of the BWTs.

Table 5: Compression rates and CGNE iterations with tol=1e-3 for (m, K)BWTs and OWTs

method	BWT	BWT	BWT	OWT	OWT
order	(0,3)	(0,4)	(0,5)	4	8
moments	4	6	8	4	8
compression	22%	21%	20%	15%	11%
iterations	26	30	28	16	16

5 Conclusions

Some nonorthogonal wavelet transforms have been shown to produce higher compression of matrices in computational electromagnetics than the orthonormal wavelet transforms. This paper studies the conditioning of B-spline biorthogonal wavelet transforms in the context of their application to computational electromagnetics. We found that the condition numbers of the transformed matrices increase considerably with the wavelet order m and the number of wavelet levels. Even for small number of vanishing moments m, for which the growth of condition numbers is not rapid, it directly affects iterative solvers. In addition, the compression rates obtained with the help of the BWTs were worse than those for the orthonormal wavelet transforms. We conclude that the biorthogonal wavelet transforms should not be recommended for matrix compression in computational electromagnetics.

A more detailed study of conditioning of other non-orthogonal wavelet transforms including optimal scaling of BWTs, semiorthogonal wavelet transforms, and wavelet packets will be presented elsewhere.

References

[1] H. Kim and H. Ling, "Wavelet analysis of radar echo from finite-size targets," *IEEE Trans. Antennas Propagat.*, vol. 41, no. 2, pp. 200–207, 1993.

[2] B.Z. Steinberg and Y. Leviatan, "On the useof wavelet expansions in the method of moments," *IEEE Trans. Antennas Propagat.*, vol. 41, no. 5, pp. 610–619, 1993.

[3] R.L. Wagner and W.C. Chew, "A study of wavelets for the solution of electromagnetic integral equations," *IEEE Trans. Antennas Propagat.*, vol. 43, no. 8, pp. 802–810, 1995.

[4] W.L. Golik, "Wavelet packets for fast solution of electromagnetic integral equations," *IEEE Trans. Antennas Propagat.*, vol. 46, pp. 618–625, 1998.

[5] C.K.Chui and J. Wang, "On compactly supported spline wavelets and a duality principle," *Trans. Amer. Math. Soc.*, vol. 330, pp. 903–915, 1990.

[6] Z. Xiang and Y. Lu, "An effective wavelet matrix transform approach for efficient solutions of electromagnetic integral equations," *J IEEE Trans. Antennas Propagat.*, vol. 45, no. 8, pp. 1205–1213, 1997.

[7] R.D. Nevels, J.C. Goswami, and H. Tehrani, "Semi-orthogonal versus orthogonal wavelet basis sets solving integral equations," *IEEE Trans. Antennas Propagat.*, vol. 45, no. 9, pp. 1332–1339, 1997.

[8] A. Cohen, I. Daubechies, and J.C. Feauveau, "Biorthogonal bases of compactly supported wavelets," *Comm. Pure Appl. Math.*, vol. 45, 1992.

[9] Y. Saad, *Iterative Methods for Sparse Linear Systems*, PWS Publishing Co., Boston, 1996.

[10] I. Daubechies, *Ten Lectures on Wavelets*, vol. 61 of *CBMS Lecture Notes*, SIAM, 1992.

[11] R. Turcajova, "Numerical condition of discrete wavelet transforms," *SIAM J. Matrix Anal. Appl.*, vol. 18, no. 4, pp. 981–999, 1997.

[12] F. Keinert, "Numerical stability of biorthogonal wavelet transforms," *J Adv. Comput. Math.*, vol. 4, pp. 1–26, 1995.

Exact Implementation of Bayliss-Turkel Boundary Operators in 2D and 3D Scalar and Vector Wave Equation

Omar M. Ramahi
Compaq Computer Corporation
Omar.Ramahi@digital.com

I. Abstract

This paper presents a simple, yet powerful scheme to incorporate Bayliss-Turkel Absorbing Boundary Conditions (ABCs) of *any* order into the finite element simulation of open-region radiation problems. The method is based on using finite-difference approximation of the normal derivatives in the original Bayliss-Turkel ABC formulation. This makes possible the implementation of BT operators of order three or higher, thus achieving levels of accuracy unrealized previously.

II. Introduction

The Bayliss-Turkel (BT) boundary operators theory states that spurious (non-physical) reflections arising from the mesh-truncation boundary can be made arbitrarily small by chosing an operator with the proper order (in three-dimensional space, the spherical mesh-truncation boundary can be located arbitrarily, whereas in two-dimensional space, the BT theory strictly applies to circular mesh-truncation boundaries located in the asymptotic region) [1]. However, despite this attractive feature, only first- and second-order operators were actually implemented in finite element codes. The reason for this had to do with the difficulty of representing normal derivatives in terms of tangential derivatives for boundary operators of order three or higher [2]. More explicitly, let us consider the homogeneous Helmholz equation in two-dimensional free space. Assuming scattering by a perfectly conducting object, Galerkin procedure leads to:

$$\int_{\Omega} \nabla v \cdot \nabla u - k^2 v u \, d\Omega = \int_{\Gamma_c} v \frac{\partial u}{\partial n} \, d\Gamma + \int_{\Gamma_o} v \frac{\partial u}{\partial n} \, d\Gamma \qquad (1)$$

where Ω is the solution space of the problem and Γ_c and Γ_o are the conductor boundary and the cylindrical mesh-termination (outer) boundary respectively. The unknown

field is represented by u and the testing function by v (for more details on the finite element derivation of (1), see [3]).

The normal derivative on the right-hand side of (1) is unavailable on the outer boundary of the finite element mesh and therefore, to complete the solution, this normal derivative must be exchanged with the field and its tangential derivatives on the boundary. Unfortunately, only the first- and second-order BT operators can be cast in the format that expresses the normal derivative in terms of tangential derivatives. BT operators of third or higher order contain mixed derivatives.

Despite this, however, one can find in the literature several ABC constructions based on the BT operators that extend beyond the second-order [2]. These constructions, however, are only approximations of higher-order operators where mixed derivatives are either assumed negligible or replaced by simple approximations that give results with varying degrees of accuracy. Unfortunately, such approximations, for the most part, are unsubstantiated analytically and often result in unsatisfactory levels of accuracy [2].

In this work, instead of interchanging the normal derivative with tangential derivatives, we maintain the original form of the operator and express (discretize) higher-order operators as a telescopic finite-difference expressions. The attractive features of this implementation are: 1) it does not require the use of higher-order finite elements, 2) it is remarkably simple to implement, while affecting the overall sparsity of the finite element matrix in a negligible way, and 3) it provides levels of accuracy unrealized before.

This paper presents the new formulation for the scalar two-dimensional wave equation. Numerical experiments will be given to demonstrate the levels of accuracy that can be achieved in comparison to previous implementations. Finally, we present the extension of the new formulation to the three-dimensional scalar and vector wave equation.

III. Formulation

The N^{th} order Bayliss-Turkel operator applied on a cylindrical outer boundary is expressed as [1]:

$$B\{u\} = \prod_{i=1}^{N} \left(\frac{\partial}{\partial \rho} + \frac{2i - 3/2}{\rho} + jk \right) u = 0 \tag{2}$$

where ρ is the radial variable and k is the wave number. When (2) is applied at an outer boundary located at a fixed radius ρ, the error in the solution is of the order $\frac{a}{\rho^{2N+1/2}}$, where the constant a depends on the proximity of the outer boundary to the scattering object and the wave number. (For two-dimensional cylindrical outer

boundaries, this accuracy measure is valid in the asymptotic region only.)

Next, we transform (2) into a discrete operator using the backward finite-difference approximation for the normal derivative, vis.,

$$\partial_\rho \rightarrow \frac{(I - S^{-1})}{\Delta\rho} \tag{3}$$

where I is the identity operator, S^{-1} is the space shift operator and $\Delta\rho$ is the space step in the radial direction. Substituting (3) into (2), we arrive at a finite-difference representation of the boundary operator in (2):

$$B^d\{u\} = \prod_{i=1}^{N} \left(\alpha_i I - \frac{S^{-1}}{\Delta\rho}\right) = 0 \tag{4}$$

where $\alpha_i = 1/\Delta\rho + jk + (2i - 3/2)/\rho$. In (5), B^d denotes a discrete operator. Notice that (4) is a backward finite-difference transformation of the operator in (2) (using nodes internal to the boundary). To enable the numerical implementation of (4), the finite elements that are adjacent to the outer boundary must be structured such that their nodes lie along mutually orthogonal curves as shown in Fig. 1. In light of the flexibility in creating the finite element mesh, such constraint does not pose any difficulty.

The transformation of the boundary operator into a telescoping finite difference expression as in (4) was successfully used by Higdon to implement the absorbing boundary operators that he developed for the finite-difference time-domain solution of the wave equation [4]. It is worth mentioning here that Higdon's operators are a special class of the BT operators (which can realized when $\rho \rightarrow \infty$ and completing the time-domain to frequency-domain transformation, i.e., $\partial_t \rightarrow k$).

IV. Implementation into Finite Element Simulation

The implementation of (4) into a finite element formulation is carried out at the numerical level by direct substitution into the finite element matrix. For brevity, we skip the finite element formulation and start with the matrix equation. Let us denote the boundary nodes that lie on the outermost boundary surface as $\mathbf{U}_o$, the nodes that are adjacent to the outermost surface and are involved in the description of the boundary operator as $\mathbf{U}_b$, and the remaining nodes as $\mathbf{U}_i$. Enforcing (4) at each of the outer boundary nodes gives the following algebraic equation:

$$\mathbf{U}_o = \mathbf{B}\mathbf{U}_b \tag{5}$$

The finite element matrix can be represented symbolically as

$$\begin{bmatrix} \mathbf{M}_{oo} & \mathbf{M}_{ob} & \\ \mathbf{M}_{bo} & \mathbf{M}_{bb} & \mathbf{M}_{bi} \\ & \mathbf{M}_{ib} & \mathbf{M}_{ii} \end{bmatrix} \begin{bmatrix} \mathbf{U}_o \\ \mathbf{U}_b \\ \mathbf{U}_i \end{bmatrix} = \begin{bmatrix} \mathbf{F}_o \\ \mathbf{F}_b \\ \mathbf{F}_i \end{bmatrix} \tag{6}$$

The vectors $\mathbf{F}_o$, $\mathbf{F}_b$ and $\mathbf{F}_i$ are related to the excitation and all boundary conditions. Finally, we substitute (5) into (6) to obtain the reduced system matrix:

$$\begin{bmatrix} \mathbf{M}_{bo}\mathbf{B} + \mathbf{M}_{bb} & \mathbf{M}_{bi} \\ \mathbf{M}_{ib} & \mathbf{M}_{ii} \end{bmatrix} \begin{bmatrix} \mathbf{U}_b \\ \mathbf{U}_i \end{bmatrix} = \begin{bmatrix} \mathbf{F}_b \\ \mathbf{F}_i \end{bmatrix} \tag{7}$$

We note that the fact that the Γ_o boundary integral was not implemented numerically does not introduce any deficiency in our new implementation. The matrix boundary condition substitution of (5) into (6) constitutes a constraint on the nodal fields such that they admit outgoing waves only. With such substitution, the finite element matrix system becomes well posed in the sense that a unique solution is admissible. This solution satisfies the wave equation in any unconstrained portion of the domain, satisfies any physical boundary conditions (as would be dictated, for instance, by perfectly conducting objects), and admits outgoing waves on the outer mesh boundary. For completeness, one can still assume that the boundary line integral in (1) is applied at a circular outer boundary that is positioned external to the boundary where (4) is applied. However, the application of (4) conceals any effect this line integral might have on the system matrix.

V. Numerical Experiment

To test the effectiveness of this new and highly simple scheme, we study the classical problem of plane wave scattering from perfectly conducting circular cylinder. We consider a cylinders of radius 8λ. The mesh for this problem consists of 500 uniformly spaced nodes in the angular direction and 6 uniformly spaced nodes in the radial direction with $\Delta\rho = 0.03\lambda$. Thus, the BT operators are applied at a distance of 0.15λ from the cylinder's surface. We present results for the H-polarized case only since it has been shown that this polarization is significantly more susciptible to ABCs than the E-polarized case [2].

We apply the second- and fourth-order BT operators using the new implementation. In Figs. 2 and 3, we show calculation of the surface current and Radar Cross Section (RCS). For this cylinder, there is a sizable number of harmonics containing evanescent energy and thus one expects the second-order BT operators to yield high errors as was previously confirmed in [2]. The results obtained using the fourth-order BT operator show a significant enhancement in accuracy careful observation of Fig. 3 reveals that the BT4 operator results in a maximum error in RCS of only 1.3 dB.

VI. Extension to the scalar and vector three-dimensional wave equation

The finite element solution of the vector Helmholtz equation is more difficult than that of the scalar one. Absorbing boundary conditions (ABCs) that were developed earlier for the vector wave equation were complex [2],[5],[6]. In fact, the numerical implementations of second-order ABCs were the only that were reported in the literature because ABCs of order three or higher were immensely difficult to implement in a finite element numerical code. Second-order operators were found to yield satisfactory solutions only when the outer boundary was positioned one or more wavelengths away from the scatterer, thus increasing the computational cost substantially. Absorptive material, on the other hand, such as the perfectly matched layer (PML), promises perfect matching in the analytic domain only, and the performance when incorporated into a discrete system might not be very satisfactory. The development of PML for three-dimensional spherical coordinates has recently been reported in [7]-[9].

Here, we develop a series of simple operators for the finite element solution of the three-dimensional vector wave equation. Unlike the methodologies adopted earlier, namely, that of developing operators by manipulating the vector field, and thus obtaining boundary conditions that involve the vector field itself, we develop operators that can be applied on the scalar field components of the vector field.

VII. Boundary Operators for Spherical Boundaries

According to the expansion theorem of Wilcox [10], a vector field $\mathbf{E}$ in three-dimensional space can be represented by a uniformly convergent series in powers of $1/r$:

$$\mathbf{E}(r,\theta,\phi) = \frac{e^{-jkr}}{r}\sum_{n=0}^{\infty}\frac{\mathbf{e}_n(\theta,\phi)}{r^n} \tag{8}$$

In (8) the vectors $\mathbf{e}_n$ are determined recursively (see [10] for a thorough exposition of the Wilcox expansion theorem and related corollaries). From (8), each of the scalar field components of the vector field can be expressed as:

$$E_\alpha(r,\theta,\phi) = \frac{e^{-jkr}}{r}\sum_{n=0}^{\infty}\frac{e_n(\theta,\phi)}{r^n} \tag{9}$$

where $\alpha = \phi,\theta,r$. The representation of the scalar field components as in (9) is significant because it shows that these scalar spherical components, despite the fact that they are not scalar radiation functions, can still be represented in a series of powers $1/r$. The fact that these series are strictly not a Wilcox expansion is inconsequential to our goal here of developing absorbing boundary operators.

The series in (9) possess all the convergence properties of the Wilcox expansion, and furthermore, these series can be differentiated term by term with respect to r. Therefore, we can conveniently use the procedure developed by Bayliss and Turkel [1] to show that E_α satisfies the N^{th} order operator

$$B = \prod_{i=1}^{N} (\partial_r + jk + \frac{2i-1}{r}) \tag{10}$$

up to a residual of $O(1/r^{2N+1})$.

For the numerical solution of an open-region finite element problem, only the tangential field components need to be evaluated on the boundary of the domain, therefore, as a boundary condition for the vector wave problem, we write

$$B \begin{pmatrix} E_\theta \\ E_\phi \end{pmatrix} = \prod_{i=1}^{N} (\partial_r + jk + \frac{2i-1}{r}) \begin{pmatrix} E_\theta \\ E_\phi \end{pmatrix} = 0 \tag{11}$$

The family of operators in (11) involve radial derivatives only, and since the series in (9) is uniformly convergent in θ, ϕ and r, for any fixed r, the operators in (11) can be implemented to yield any *arbitrary* accuracy desired (i.e., increased accuracy with increased order). (Of course, in numerical implementations, discretization artifacts put a limit on the accuracy that is predicted by theory.) Additionally, the well posedness of (5) is assured since it follows from the the Bayliss-Turkel theory [1],[11].

The numerical implementation of (8) and (9) is identical to the procedure outlined above for the two-dimensional wave equation, except for the analogous extension of two-dimensional cylindrical geometry to three-dimensional spherical geometry (for instance, the nodes of the finite elements adjacent to the spherical outer boundary must lie on mutually orthogonal planes.)

VIII. Summary

This paper presented an exact implementation of BT operators of *any order* in a finite element scheme. This makes possible the implementation of BT operators of order three or higher, thus achieving levels of accuracy unrealized previously. The numerical implementation of this scheme is simple requiring algebraic manipulations only. The resultant matrix equation's sparsity is reduced in a negligible manner. However, since the boundary nodes are eliminated from the system matrix, any incremental increase in computational cost due to the change in sparsity is offset by solving a smaller matrix.

References

[1] A. Bayliss and E. Turkel, "Radiation boundary conditions for wave-like equations, Comm. Pure Appl. Maths., 23, pp. 707-725, 1980.

[2] R. Mittra and O. M. Ramahi, "Absorbing boundary conditions for the direct solution of partial differential equations arising in electromagnetic scattering problems", in *Finite Element and Finite Difference Methods in Electromagnetic Scattering*, M. Morgan, ed., vol. II, New York, N.Y.: Elsevier Science, Inc., 1989.

[3] A. Peterson, S. Ray and R. Mittra, *Computational Methods for Electromagnetics*, IEEE Press, Piscataway, NJ, 1998.

[4] R. L. Higdon, "Radiation Boundary Conditions for Elastic Wave Propagation," *Siam J. Numer. Anal.*, vol. 27, no. 4, pp. 831-870, August 1990.

[5] A. F. Peterson, "Absorbing boundary conditions for the vector wave equation," *Microwave Opt. Technol. Lett.*, vol. 1, pp. 62-64, Apr. 1988.

[6] J. P. Webb aand V. N. Kanellopoulos, "Absorbing boundary conditions for the fin ite element solution of the vector wave equation," *Microwave Opt. Technol. Let t.*, vol. 2, pp. 370-372, Oct. 1989.

[7] M. Kuzuoglu and R. Mittra, "Investigation of nonplanar perfectly matched absorb ers for finite-element mesh truncation," *IEEE Trans. Antennas Propagat.*, vol. 45, pp. 474-486, March 1997.

[8] F. L. Teixeira and W. C. Chew, "Conformal Perfectly Matched Layer," in Proc. 14th Annual Review of Progress in Applied Computational Electromagnetic s, Monterey, California, pp. 507-514, March 16-20, 1998.

[9] B. Yang and D. Gottlieb, "Perfectly matched layer methods in spherical coordina tes," in Proc. 14th Annual Review of Progress in Applied Computational Electromagnetic s, Monterey, California, pp. 607-614, March 16-20, 1998.

[10] C. H. Wilcox, "An Expansion theorem for electromagnetic fields," *Comm. Pure Appl. Math.*, vol. 9, pp. 115-134, 1956.

[11] A. Bayliss, M. Gunzburger and E. Turkel, "Boundary conditions for the numerical solution of elliptic equations in exterior regions," *Siam J. Appl. Math.*, vol. 4 2, no. 2, pp. 430-451, April, 1982.

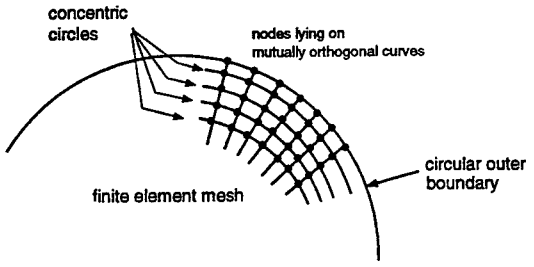

Fig. 1. Outer boundary finite element nodes lying along mutually orthogonal curves

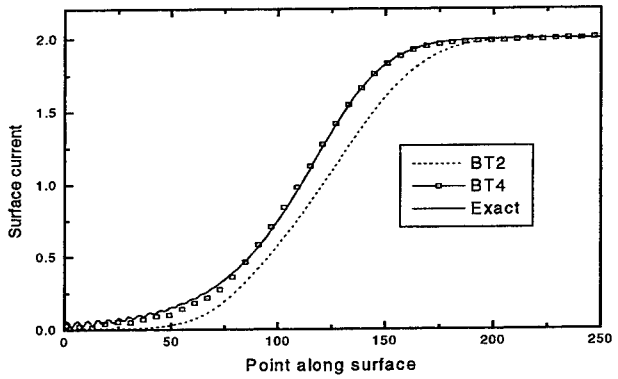

Fig. 2. Surface current (H-polarization) calculated using second-order BT (BT2), fourth-order BT (BT4) and the analytic (Exact) solution for an 8λ perfectly conducting cylinder.

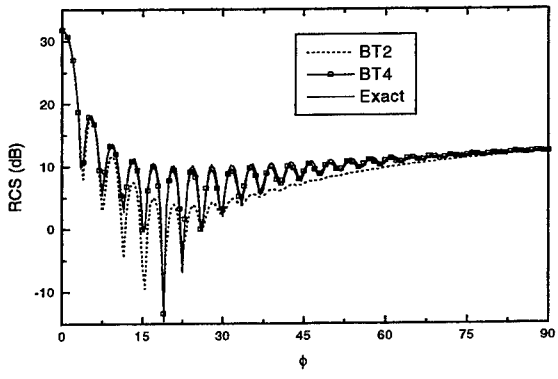

Fig. 3. RCS for the problem of H-polarized scattering from an 8λ perfectly conducting cylinder calculated using second-order BT (BT2), fourth-order BT (BT4) and the analytic (Exact) solution.

Formulae for *Instantaneous* Power and Time-average Power Delivered to Charge-Current Distributions

by
R. M. Bevensee

BOMA ENTERPRISES
P.O. Box 812 Alamo, CA, 94507-0812 USA

1. Summary

In a 1997 paper [1] the author presented formulas for total energy and time-average power radiated from charge-current distributions. The expression $W_{rad}(T)$, identified as total energy radiated during a time interval T, was actually the total energy which flowed in from the generator field, which was presumed to support the electric field induced by the flow (if not, the flow would change so its electric field as the sum of near-field and radiation-field components *would* match the generator electric field). It was implied that the flow was zero at the beginning and end of interval T.

The integrand of the time integral for $W_{rad}(T)$ could not directly be interpreted as instantaneous power flow; various time integrations by parts were necessary to identify the primary components of instantaneous power flow.

When the expression for $W_{rad}(T)$ was applied to an accelerating electron it was found to contain primary terms representing the increase in kinetic energy plus the radiated energy during T.

In the present paper the author presents a double spatial integral over charges and currents which *does* represent instantaneous power flow in from the generator field. Evaluation of its predominant terms for the accelerating electron of [1] yields the instantaneous time rate of increase of kinetic energy plus the power radiated. Because this expression, Eq. (11), includes the kinetic energy term it is labeled $P_{in}(t)$, the power *in from* the generator field and delivered to the charges and currents.

The time-average value of $P_{in}(t)$ at a single frequency agrees with that formula in [1].

2. Derivation of the Formula for Instantaneous Power flow.

This formula will be derived straightforwardly from the scalar and vector potentials ϕ and $\overline{A}$ from [1]. They are

$$4\pi\epsilon_0\phi_{ne}(\overline{r},t) = \oint_{S_a}\left(\frac{[q]}{R} + \frac{1}{c}\frac{[\overline{J}]\bullet\overline{R}}{R^2}\right)dS', \quad 4\pi\epsilon_0\phi_{ra}(\overline{r},t) = \frac{1}{c^2}\oint_{S_a}\frac{\dot{[\overline{J}]}\bullet\overline{R}}{R}dS' \tag{1}$$

$$4\pi\epsilon_0\overline{A}_{ne}(\overline{r},t) = \frac{1}{c}\oint_{S_a}\left(\frac{[q]\overline{R}}{R^2} + \frac{1}{c}\frac{[\overline{J}]\bullet\overline{R}\overline{R}}{R^3}\right)dS', \quad 4\pi\epsilon_0\overline{A}_{ra}(\overline{r},t) = \frac{1}{c^3}\oint_{S_a}\frac{\dot{[\overline{J}]}\bullet\overline{R}\overline{R}}{R^2}dS', \tag{2}$$

with the definitions

$$[\overline{J}] = \overline{J}(\overline{r}', t' = t - R/c), \quad [q] = q(\overline{r}', t'), \quad \dot{X} = \frac{\partial X}{\partial t}, \quad \overline{R} = (\overline{r} - \overline{r}'), \quad R = |\overline{R}| \tag{3}$$

One can verify directly that these yield the near fields (subscript "ne") and radiation fields ("ra") according to the prescriptions

$$\overline{E}_{ne} = -\nabla\phi_{ne} - \dot{\overline{A}}_{ne}, \qquad \overline{E}_{ra} = -\nabla\phi_{ra} - \dot{\overline{A}}_{ra} \tag{4}$$

$$\overline{H}_{ne} = \nabla\times\overline{A}_{ne}, \qquad \overline{H}_{ra} = \nabla\times\overline{A}_{ra}, \tag{5}$$

where the Panofsky-Phillips' expressions [2] for these field components, reproduced from [1], are

$$\overline{E}(\overline{r},t) = \overline{E}_{ne} + \overline{E}_{ra},$$

$$\overline{E}_{ne} = \frac{1}{4\pi\epsilon_0}\oint_{S_a}\frac{[q]\overline{R}}{R^3}dS' + \frac{1}{c}\oint_{S_a}\frac{[\dot{\overline{J}}]\bullet\overline{R}\overline{R} - \overline{R}\times([\overline{J}]\times\overline{R})}{R^4}dS' \tag{6}$$

$$\overline{E}_{ra} = \frac{1}{4\pi\epsilon_0 c^2}\oint_{S_a}\frac{([\dot{\overline{J}}]\times\overline{R})\times\overline{R}}{R^3}dS', \tag{7}$$

The associated magnetic field is

$$\overline{H}(\overline{r},t) = \overline{H}_{ne} + \overline{H}_{ra},$$

where

$$\overline{H}_{ne} = \frac{1}{4\pi}\oint_{S_a}\frac{[\overline{J}]\times\overline{R}}{R^3}dS', \qquad \overline{H}_{ra} = \frac{1}{4\pi c}\oint_{S_a}\frac{[\dot{\overline{J}}]\times\overline{R}}{R^2}dS' \tag{8}$$

The instantaneous power flowing into a charge-current distribution on surfaces from the generator field at time t is

$$P_{in}(t) = -\oint_{S_a}(\overline{E}_{ne} + \overline{E}_{ra})_t \bullet \overline{J}(t)dS \tag{9}$$

Substitution of (4) and integration of the $\nabla\phi\bullet\overline{J}$-terms by spatial parts yields

$$P_{in}(t) = \frac{1}{4\pi\epsilon}\oint_{S_a}(\phi_{ne}\dot{q} + \overline{J}\bullet\dot{\overline{A}}_{ne} + \phi_{ra}\dot{q} + \overline{J}\bullet\dot{\overline{A}}_{ra})dS \tag{10}$$

Now, upon sutstituting the potential expressions (1) and (2) we arrive at

$$P_{in}(t) = \frac{\mu_0}{4\pi}\oint_{S_a}dS\oint_{S_a}dS'\,\frac{1}{R}\Big\{\overline{J}(\overline{r},t)\bullet\frac{\partial}{\partial t}\overline{J}(\overline{r}',t'=t-\frac{R}{c}) + cq(\overline{r}',t')\frac{\partial}{\partial t}cq(\overline{r},t)$$
$$+\Big[\dot{q}(\overline{r},t)c\frac{\overline{J}(\overline{r}',t')\bullet\overline{R})}{R} + \frac{\overline{J}(\overline{r},t)\bullet\overline{R})}{R}\dot{q}(\overline{r}',t')c\Big]\Big\} \tag{11}$$

The bracketed expression in (11) evaluates to zero when integrated over either S_a or S'_a, (or over V or V' in the volume representation) as appropriate (See App. A).

For charges moving in one direction the terms for $t' \approx t$ agree with Miller's measure [3] of the instantaneous power leaving current and charge traveling on a straight-wire dipole as a *sum* of the time rate of change of a current energy $W_I(t) = \int I(s,t)^2 dS$ and a charge energy $W_Q(t) = \int Q(s,t)^2 dS$.

The remainder of this paper will evaluate (11) converted to volumetric form for the accelerating electron of [1], to derive the formula for instantaneous power radiated $\propto (\dot{v})^2$.

3. Evaluation of (11) for an Electron Accelerating in the z-direction.

For the electron moving in the z-direction, $\overline{\rho}$ designating a transverse position, we can write very generally

$$q(\overline{r},t) = g(\overline{\rho},z,t) = g\Big(\overline{\rho}, z - \int^t v(\tau)d\tau\Big), \qquad \int_V gdV = -e\,, \tag{12}$$

$$\overline{J}(\overline{r},t) = \overline{J}(\overline{\rho},z,t) = \overline{a}_z g v(t) \tag{13}$$

Note

$$\nabla \bullet \overline{J} = \frac{\partial J}{\partial z} = g'\, v(t) = -\dot{q}. \qquad ' = \frac{\partial}{\partial (arg)} \tag{14}$$

Now expand $q(\overline{r}', t' = t - R/c)$ about t:

$$q(\overline{r}', t' = t - R/c) = q(\overline{r}', t) - \frac{R}{c}\dot{q}(\overline{r}', t' = t) + \frac{1}{2}\left(\frac{R}{c}\right)^2 \ddot{q}(\overline{r}', t) - \frac{1}{6}\left(\frac{R}{c}\right)^3 \dddot{q}(\overline{r}', t) + \ldots \tag{15}$$

and similarly $\overline{J}(\overline{r}', t')$. Then P_{in} for volumetric charges and currents ($J(amp/m)dS \rightarrow J(amp/m^2)dV$, $q(coul/m^2)dS \rightarrow q(coul/m^3)dV$) reads

$$P_{in}(t) = \frac{\mu_0}{4\pi}\int dV \int dV' \frac{1}{R}\left\{\overline{a}_z J(\overline{r}, t) \bullet \overline{a}_z \left[\dot{J}(\overline{r}', t) - \frac{R}{c}\ddot{J}(\overline{r}', t) + \frac{1}{2}\left(\frac{R}{c}\right)^2 \dddot{J}(\overline{r}', t) - \ldots.\right]\right.$$

$$\left. + \dot{q}(\overline{r}, t)c^2 \left[q(\overline{r}', t) - \frac{R}{c}\dot{q}(\overline{r}', t) + \frac{1}{2}\left(\frac{R}{c}\right)^2 \ddot{q}(\overline{r}', t) - \frac{1}{6}\left(\frac{R}{c}\right)^3 \dddot{q}(\overline{r}', t) + \ldots.\right]\right\} \tag{16}$$

We have ignored the last bracket in (11) for the reason given earlier.

4. Evaluation of the $J\dot{J}$-terms in Eq. (16).

4.1 *the* $J(\overline{r}, t)\dot{J}(\overline{r}', t) - term.$

For an electron of uniform charge density this term evaluates [1] to

$$P_1 = \frac{\partial}{\partial t}\left(\frac{1}{2} m_{ke} v^2\right) = \dot{W}_{ke}, \tag{17}$$

the rate of change of kinetic energy. The kinetic mass evaluates to

$$m_{ke} = \frac{3}{10\pi}\frac{\mu_0 e^2}{r_0}, \qquad r_0 = electron\ radius, \tag{18}$$

which is double the classical mass m_{cl} obtained by equating the electrostatic energy required to build the electron to $m_{cl}c^2$

4.2 *The* $J(\overline{r}, t)\ddot{J}(\overline{r}', t) - term\ in\ Eq.\ (16)$

Expanding

$$\ddot{J}(\overline{r}', t) = \ddot{q}(\overline{r}', t)v(t) + 2\dot{q}\dot{v}(t) + q\ddot{v} \tag{19}$$

we have, for this term,

$$P_2 = -\frac{\mu_o}{4\pi c}\int dV \int dV' q(\overline{r}, t)v(t)\left[\ddot{q}(\overline{r}', t) + 2\dot{q}\dot{v} + q\ddot{v}\right] \tag{20}$$

The $\ddot{q}$- and $\dot{q}$-terms evaluate to zero when integrated over V'. Introducing $v\ddot{v} = \partial(v\dot{v})/\partial t - (\dot{v})^2$ we obtain

$$P_2 = -\frac{\mu_o e^2}{4\pi c}\frac{1}{2}\frac{\partial^2}{\partial t^2}(v^2) + \frac{\mu_o e^2}{4\pi c}(\dot{v})^2 \tag{21}$$

The first term in P_2 is proportional to a *second* time derivative of kinetic energy. Since this term integrates to zero over the total time of the flow we regard it as a *fluctuation* in the kinetic energy. The second term is 3/2 of the instantaneous power radiated by the electron.

4.3 *The* $J(\bar{r},t)\dddot{J}(\bar{r}',t)$ *– term in Eq.* (16)

If we add to this term the term with $\bar{r}$ and $\bar{r}'$ interchanged, divide by 2, and replace these two terms with the expansion of

$$\frac{\partial}{\partial t}\left[J(\bar{r},t)\ddot{J}(\bar{r}',t)+\dot{J}(\bar{r}',t)\dot{J}(\bar{r},t)\right]$$

we obtain for the $J(\bar{r},t)\dddot{J}(\bar{r}',t)$-term in (16),

$$T_3=\frac{\mu_o}{16\pi c}\int dV\int dV'\frac{R}{c}\left\{\frac{\partial}{\partial t}\left[J(\bar{r},t)\ddot{J}(\bar{r}',t)+\dot{J}(\bar{r}',t)\dot{J}(\bar{r},t)\right]-\frac{\partial}{\partial t}\left[\dot{J}(\bar{r},t)\dot{J}(\bar{r}',t)\right]\right\}.$$

The term within the first set of brackets evaluates to $\leq \frac{1}{4}\frac{r_0}{c}\frac{\partial}{\partial t}$ of P_2. Here $r_0/c\approx 10^{-23}sec.$ The last bracket yields terms small compared to $\dot{W}_{ke}$, $\ddot{W}_{ke}$ and the time derivative of the last or radiation term in (21).

5. Evaluation of the $q\dot{q}$-terms in Eq. (16).

5.1 *The* $\dot{q}(\bar{r},t)q(\bar{r}',t')$ *– term*

Addition to this term of the term with $\bar{r}$ and $\bar{r}'$ interchanged and division by 2 yields a double integral proportional to

$$\frac{\partial}{\partial t}\int dV\int dV'\frac{1}{R}q(\bar{r},t)q(\bar{r}',t). \tag{22}$$

The value of the double integral is independent of the position of the electron, hence its time derivative is zero.

5.2 *The* $\dot{q}(\bar{r},t)\dot{q}(\bar{r}',t)$ *– term in Eq.* (16)

Using (14) this double integral is of the form

$$P_3=\int dV\int dV'\frac{\partial J(\bar{r},t)}{\partial z}\frac{\partial J(\bar{r}',t)}{\partial z'} \tag{23}$$

We can integrate each J-derivative separately through the entire electron sphere and obtain zero for P_3.

5.3 *The* $\dot{q}(\bar{r},t)\ddot{q}(\bar{r}',t)$ *– term in* (16)

As in Sec. 5.1 we can interchange $\bar{r}$ and $\bar{r}'$ in the integrand, add it to the integrand above and divide by 2. The resultant integral is proportional to

$$P_4\sim\frac{\partial}{\partial t}\int dV\int dV' R\dot{q}(\bar{r},t)\dot{q}(\bar{r}',t)=0 \tag{24}$$

when we substitute (14) for each $\dot{q}$ and note the value of the double integral is independent of t.

5.4 *The* $\dot{q}(\bar{r},t)\dddot{q}(\bar{r}',t)$ *– term in Eq.* (16)

This term is

$$P_5=-\frac{\mu_0}{4\pi}\frac{1}{6c}\int dV\int dV' R^2\dot{q}(\bar{r},t)\dddot{q}(\bar{r}',t),\qquad R^2=|\bar{\rho}-\bar{\rho}'|^2+(z-z')^2 \tag{25}$$

With the identity

$$\frac{\partial}{\partial t}[\dot{q}(\bar{r},t)\dot{\bar{q}}(\bar{r}',t)] = \ddot{q}(\bar{r},t)\dot{\bar{q}}(\bar{r}',t) + \dot{\bar{q}}(\bar{r},t)\ddot{\bar{q}}(\bar{r}',t), \tag{26}$$

and introducing $J(\bar{r},t)$ and $\dot{J}(\bar{r}',t)$ via (14) we change P_5 to read

$$P_5 = -\frac{\mu_0}{4\pi}\frac{1}{6c}\int dV \int dV' R^2 \left\{ \frac{\partial}{\partial t}\left[\frac{\partial J(\bar{r},t)}{\partial z}\frac{\partial \dot{J}(\bar{r}',t)}{\partial z'}\right] - \frac{\partial \dot{J}(\bar{r},t)}{\partial z}\frac{\partial \dot{J}(\bar{r}',t)}{\partial z'}\right\}. \tag{27}$$

In [1, (25)-(28)] we evaluated the second term of P_5 as

$$-\frac{1}{3}\frac{\mu_0 e^2}{4\pi c}(\dot{v})^2 \tag{28}$$

(See App. B). By analogy, the first term of P_5 evaluates to

$$+\frac{\mu_0 e^2}{24\pi c}\frac{\partial^2}{\partial t^2}(v(t))^2 = +\frac{5}{18}\frac{r_0}{c}\dddot{W}_{ke} \tag{29}$$

6. Summary Evaluation of the Predominant Terms in $P_{in}(t)$ of (16)

The sum of terms P_1 through P_5 is

$$P_{in}(t) = \dot{W}_{ke}(t) - \frac{5}{9}\frac{r_0}{c}\ddot{W}_{ke}(t) + \frac{2}{3}\frac{\mu_0 e^2}{4\pi c}\dot{v}(t)^2 \tag{30}$$

The last term is the correct expression for instantaneous power radiated by the electron. The first term is the rate of increase in kinetic energy; the unexpected second term is regarded as a fluctuation in the kinetic energy since it integrates to zero over the duration of the flow , In words, (30) says

$$\begin{aligned} \textit{Power from generator field} &= P_{in}(t) \\ &= \textit{Rate of increase in kinetic energy, with a fluctuation term,} \\ &+ \textit{Power radiated.} \end{aligned} \tag{31}$$

7. The Sinusoidal Steady State, Time-average Power Radiated.

For sinusoidal steady state we integrate (11) without its last bracketed terms over time $T = 2\pi/\omega$, and substitute

$$\overline{J}(\bar{r},t) = \frac{1}{2}[\hat{J}(\bar{r})e^{j\omega t} + \textit{complex conjugate}] = \textit{Real}\,[\hat{J}(\bar{r})e^{j\omega t}] \qquad \textit{etc.} \tag{32}$$

into (11) for current flow on surfaces. There is no *time average* change in kinetic energy of the charged particles so we obtain, for this type of flow,

$$\begin{aligned} P_{in}(\omega) = P_{rad}(\omega) &= -\frac{1}{2}\textit{Real}\oint_{S_a} \hat{E}^*(\bar{r}) \bullet \hat{J}(\bar{r})\, dS \\ &= \frac{\mu_0}{8\pi}\textit{Real}\Big\{ j\omega \oint_{S_a}\oint_{S_a} dS dS' \Big[\hat{J}^*(\bar{r}) \bullet \hat{J}(\bar{r}') - c^2 \hat{q}^*(\bar{r})\hat{q}(\bar{r}')\Big]\frac{e^{-jkR}}{R}\Big\} \end{aligned} \tag{33}$$

This is the same expression quoted in [1, (31)], from which the correct radiation resistance was derived for a straight dipole with a triangular distribution of sinusoidal current and for a circular loop carrying a spatially uniform sinusoidally varying current.

7. Conclusions from These Results

The general Eq. (11) is the result of rigorous radiation *mathematics* but does not explain fully the radiation *physics*. Radiation is ordinarily ascribed to charge *acceleration*, but there is no acceleration term in $\dot{q}(\bar{r},t)q(\bar{r}',t')$. Eq. (11) only says that we can evaluate the power flowing into the charge-current distribution by integrating over space the "coupling" between current-current pairs and charge-charge pairs.

The physics of radiation are even more obscure in Eq. (33), where there is no obvious acceleration term. It merely says that we can evaluate the time-average power by integrating over current pairs and charge pairs, each pair multiplied by the Green function.

However, we can conclude–from the application of the volumetric form of (11) to the electron model–that $P_{in}(t)$ represents first-order rate of increase in kinetic energy of the charged particles plus radiated power. The first and second time derivatives of kinetic energy can be calculated from the kinematics of the charged particles themselves.

8.References

[1] R. M. Bevensee, *Formulae for Total Energy and Time-average Power Radiated from Charge-Current Distributions*, Proc. 13th Annual Review of Progress in Applied Computational Electromagnetics, Vol 1, Naval Postgraduate School, Monterey, CA, March 17-21, 1997. pp 248-255.

[2] W.K.H. Panofsky and M. Phillips,*Classical Electricity and Magnetism*, Addison- Wesley, 1962, pp. 246 et. seq.

[3] E. K. Miller, *Exploring Electromagnetic Physics Using Thin-Wire Time-Domain (TWTD) Modeling*, Proc. 14th Annual Review of Progress in Applied Computational Electromagnetics, Vol 1, Naval Postgraduate School, Monterey, CA, March 16-20, 1998. pp 583-588.

Appendix A. Proof that the Bracketed Expression in Eq. (11) is zero.

We label the two terms T1 and T2, respectively. Upon substituting $\nabla \bullet J = -\dot{q}$ for $\dot{q}(\bar{r},t)$ and similarly for $\dot{q}(\bar{r}',t)$ and neglecting the common c-factor, we write the identity

$$\nabla \bullet \left[\overline{J}(\bar{r},t)\frac{\overline{J}(\bar{r}',t')\bullet\overline{R}}{R^2}\right] = T1 + \overline{J}(\bar{r},t)\bullet\nabla\left[\frac{\overline{J}_x(\bar{r}',t')(x-x')+...+\overline{J}_z(\bar{r}',t')(z-z')}{R^2}\right] \qquad (A1)$$

We expand the last term in cartesian coordinates. Then we write the corresponding expansion for

$$\nabla' \bullet \left[\overline{J}(\bar{r}',t')\frac{\overline{J}(\bar{r},t)\bullet\overline{R}}{R^2}\right], \qquad (A2)$$

which equals T2 plus a term like the last $\overline{J}\bullet\nabla$-term in (A1).

Upon adding these two identities, (A1) and the corresponding one, we find that the expansion of the last term in (A1) cancels the corresponding expansion of the last term in (A2), and we obtain

$$\nabla \bullet \left[\overline{J}(\bar{r},t)\frac{\overline{J}(\bar{r}',t')\bullet\overline{R}}{R^2}\right] + \nabla' \bullet \left[\overline{J}(\bar{r}',t')\frac{\overline{J}(\bar{r},t)\bullet\overline{R}}{R^2}\right] = T1 + T2 \qquad (A3)$$

The divergent terms can be integrated over S_a or S_a', or over V or V', respectively, of the full charge-current distribution to yield zero.

Therefore the bracketed expression in (11), T1 + T2, is zero. QED.

Appendix B. Evaluation of the second term in (27).

$$T_5 = \frac{1}{6}\frac{\mu_0}{4\pi c}\int d\bar{\rho}\int d\bar{\rho}'\int dz\int dz'\frac{\partial\dot{\bar{J}}(\bar{r},t)}{\partial z}\left[|\bar{\rho}-\bar{\rho}'|^2+(z-z')^2\right]\frac{\partial\dot{\bar{J}}(\bar{r}',t)}{\partial z'} \qquad (B1)$$

The $|\overline{\rho} - \overline{\rho}'|^2$-term yields zero; only the $-2zz'$ within the brackets yields a finite answer. Integrating by spatial parts over z, z', we obtain

$$T_5 = -\frac{1}{3}\frac{\mu_0}{4\pi c}\int d\overline{\rho}\int d\overline{\rho}'\int dz\int dz'\dot{\vec{J}}(\overline{\rho},z,t)\dot{\vec{J}}(\overline{\rho}',z',t) \qquad (B2)$$

With

$$\dot{\vec{J}}(\overline{r},t) = \dot{\vec{q}}v + q\dot{\vec{v}} = -\frac{\partial J}{\partial z}v(t) + q(\overline{r},t)\dot{\vec{v}} \qquad (B3)$$

and similarly for $\dot{\vec{J}}(\overline{r}',t)$, we see the $\frac{\partial J}{\partial z}v$-term integrates over z to zero. The final result is (28).

CEM for RCS Measurement Calibration: Some Parametric Observations

Kueichien C. Hill and William D. Wood, Jr.
Air Force Research Laboratory
2591 K Street, Building 254
Wright-Patterson AFB OH 45433-7602

1.0 Abstract

This paper describes recent advances in the use of computational electromagnetics (CEM) for use by the radar cross section (RCS) measurement community to design improved calibration standards. We show how uncertainties in computed calibration data directly impact measured data. We present numerical examples for two calibration targets, a right circular cylinder and a corner reflector, demonstrating the sensitivity of the computations to several CEM parameters. We further show that these sensitivities are endemic to a wide class of integral equation-based CEM codes.

2.0 Introduction

Radar cross section (RCS) measurement ranges are complex systems used to measure the RCS of arbitrary targets. Recent advances in instrumentation radar technology have greatly improved the accuracy of measured RCS data, as well as the speed with which it is acquired. New sophisticated software tools transform broadband and/or wide-angle RCS data into various types of images, useful for analyzing target scattering characteristics. Various aircraft components have maximum RCS requirements levied upon them, so accurate RCS measurements are needed to verify compliance. This has resulted in an increased emphasis on quantifying sources of uncertainty in the RCS measurement process.

One aspect of the RCS measurement process which has received relatively little attention is the calibration process. Calibration is accomplished by measuring the electric field scattered by the target under test, $\hat{E}_{tgt}^{meas}$, and then repeating the measurement using a calibration standard, $\hat{E}_{cal}^{meas}$. The result is then correlated with the known scattered field of the calibration standard, $\hat{E}_{cal}^{exact}$, at the frequencies, polarizations, and aspect angles of interest, to compute the normalized scattered electric field of the target, $\hat{E}_{tgt}^{scat}$, according to

$$\hat{E}_{tgt}^{scat}(\omega, \theta) = \frac{\hat{E}_{tgt}^{meas}(\omega, \theta)}{\hat{E}_{cal}^{meas}(\omega, \theta)} \cdot \hat{E}_{cal}^{exact}(\omega, \theta) \qquad \text{(EQ 1)}$$

Equation 1 shows that uncertainties in the exact scattered field of the calibration standard establish an absolute lower bound for the uncertainty of the overall measurement.

Traditionally, a conducting sphere is the target which has been used most often for calibration, primarily because it is one of the few objects whose theoretical RCS can be computed exactly. Conversely, other targets have not been used for calibration purposes because of the lack of high-quality theoretical scattering data. The emergence of powerful new computational electromagnetics (CEM) tools can remove this barrier [1].

Modern CEM software provides a means to generate highly accurate theoretical scattering data for arbitrarily shaped objects, especially those based on the frequency-domain surface integral equation formulation. These codes discretize the scatterer surface and then solve the integral equation to estimate the electric current density on the discretized surface. Finally, the estimated currents radiate the far-zone scattered fields. Because of the numerical nature of the codes, the computed scattered fields are not exact, but rather approximations subject to uncertainties. The two primary areas in which uncertainties arise are the surface discretization and the integral equation solution.

Our research indicates that, far from being turn-key systems, modern CEM tools must be used carefully to generate *sufficiently* accurate scattering data from even simple shapes. Our accuracy requirements are driven by the measurement calibration process defined above, and is probably more stringent than many other requirements -- we typically require calculated data to be within 0.1-0.25 dB of the true value. Specifically, we have noticed considerable sensitivity to two factors: discretization density and the Combined Field Integral Equation (CFIE) parameter α. We demonstrate this for two cases: a right circular cylinder and a corner reflector.

3.0 "Squat" Cylinder

The Air Force Research Laboratory Advanced Compact Range (ACR) has adopted a family of "squat" cylinders as its primary calibration standard. The "squat" cylinder is oriented edge-on, so that its RCS is invariant with azimuth. Two mature body of revolution (BOR) codes have been used to generate theoretical data for the cylinders: JRMBOR [4] and CICERO [3]. Both of these codes are widely used throughout government and industry. Figure 1 shows the RCS as a function of frequency for the "450" cylinder (4.5 inches in diameter, 2.1 inches in height).

Several comments can be made regarding the results plotted in Figure 1. First, note the large (~0.2 dB) discontinuity in the CICERO results at 14 GHz, HH polarization. This is caused by using a single generating-arc discretization for frequencies 10-14 GHz, and another for 14-18 GHz. Both discretizations were intended to be sufficient for their respective frequency bands, but clearly there is a significant jump associated with transitioning between such discretizations. The JRMBOR generating-arc discretization was adaptively generated at each frequency, so no abrupt jumps in the JRMBOR results can be attributed to this cause. (Interestingly, an exponentially-tapered discretization was attempted in an effort to more finely sample the current density at the

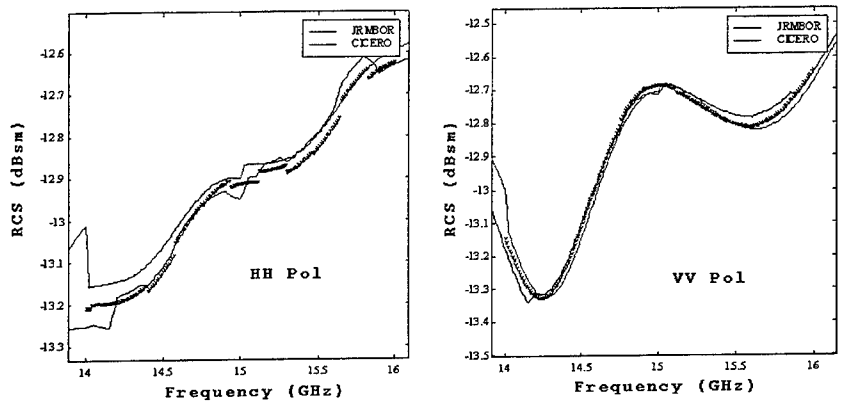

FIGURE 1. 450 "Squat" Cylinder Computed RCS vs. Frequency

corners of the cylinder; unfortunately, this approach led to numerical instabilities in the results, especially for electrically larger cylinders.)

Other, more subtle, discontinuities, are evident in the Figure 1 data, and these have been determined [2] to be caused by discontinuities in the number of Fourier modes included in the solution. Both BOR codes adaptively choose the number of Fourier modes based on the electrical girth of the target, so that at higher frequencies more Fourier modes are included in the solution. However, this causes jumps in the RCS data when each additional Fourier mode is included. When the number of Fourier modes is set to a predetermined number in the BOR code's input file, the discontinuities vanish.

4.0 Corner Reflector

The trihedral, or corner reflector, is another object that is used for RCS calibration purposes. Its advantages include ease of fabrication, large RCS relative to physical size, and broad monostatic scattering pattern at aspects near the maximum RCS orientation. The trihedral is shown in Figure 2. It's faces are each three inches square, and the plate thickness is 0.375 inch. The edges are beveled to 45 degrees. The trihedral is oriented such that it presents its maximum RCS along the positive x axis and one of its edges lies in the xz plane. In this orientation, the vertically and horizontally polarized RCS values are very nearly identical.

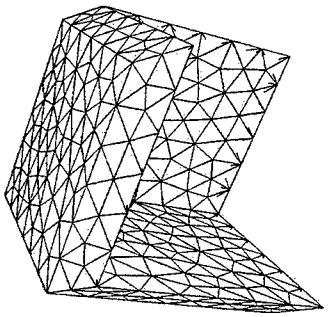

FIGURE 2. Discretized trihedral geometry

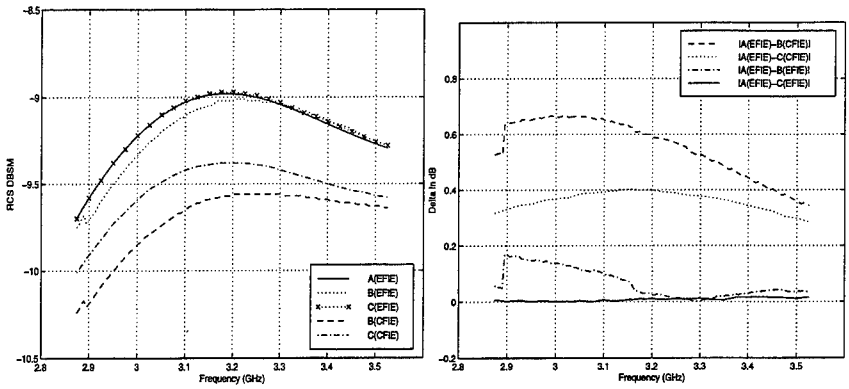

FIGURE 3. Calculated trihedral RCS results for Codes A, B, and C (horizontal polarization, maximum RCS aspect, 10 nodes per wavelength, $\alpha = 0.5$).

The trihedral is not a BOR, so it cannot be analyzed using the BOR codes discussed earlier. Instead, general purpose three-dimensional codes must be used. We have chosen three state-of-the-art integral equation codes, each with slightly different features. The first code uses an FFT-based method to iteratively solve a generalized form of surface integral equation. The second code uses the fast multipole method (FMM) to iteratively solve the combined field integral equation (CFIE). The third code solves the CFIE directly, using LU decomposition. We will denote these Codes A, B, and C, in no particular order. All three codes work from the same triangular facet model of the scatterer. (For the trihedral, the facet representation exactly captures the true geometry, but this is not true in general for curved surfaces.)

We expected Codes A, B, and C to provide nearly identical RCS results for the trihedral for the same input parameters, but instead initally generated results which varied by an amount greater than we were willing to accept. Figure 3 shows the calculated trihedral RCS, horizontal polarization, as a function of frequency. We see that Codes A and C (EFIE) agree very well, to within a few hundredths of a dB across the frequency band, but Code B (EFIE) differs from these two by as much as nearly 0.2 dB. Since we are interested in driving measurement uncertainty as low as possible, we adopt 0.1 dB as the uncertainty threshold for the computed trihedral RCS. We discard the results from Code B since its results are not consistent with those of the other two codes and thus we cannot consider it acceptable for our purposes (see Figure 3). In the course of running the computations, we discovered that the Code C results were very sensitive to the way in which the singular kernel of the MFIE was handled in the integrations. Failure to adequately extract this singularity produced results in error by several dB. Perhaps more noteworthy is the failure of the CFIE formulation to provide the correct results. The CFIE results for Codes B and C are erroneous by 0.3-0.7 dB across the frequency band. These results were generated using a CFIE alpha parameter of $\alpha = 0.5$, such that the EFIE and MFIE are weighted equally.

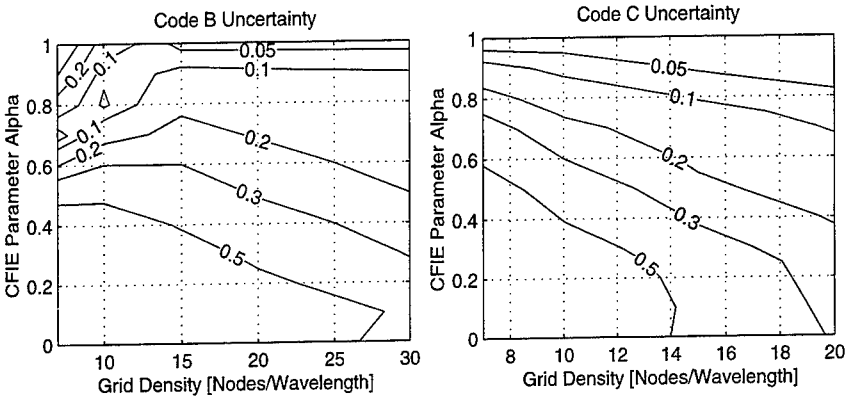

FIGURE 4. Computed trihedral RCS error for Codes B (left) and C (right). Results are for horizontal polarization, 3.2 GHz frequency, maximal RCS aspect.

A well-known "rule of thumb" for CFIE codes is to set $\alpha = 0.5$ and use a grid density of 10 to 15 nodes per wavelength. A parametric study was conducted to better understand the role of grid density and α in the CFIE results. The frequency was fixed at 3.2 GHz and aspect was fixed along the positive x axis. Code A is not based on the classical CFIE formulation, so variation with α was not applicable. However, Code A results varied only within 0.03 dB for grid densities from 7 to 30 nodes per wavelength. These results are shown in Figure 4. Code B was run for grid densities of 7, 10, 15, 20, and 30 nodes per wavelength, and for α varying from 0 (MFIE) to 1 (EFIE). Figure 4 shows that in order to drive the error below 0.1 dB, Code B's α must be greater than 0.9, with grid density greater than 14 nodes per wavelength. Code C was run identically (though a grid density of 30 nodes per wavelength was too large a problem for our computer) and the results are shown in Figure 4. This shows much the same trend as for Code B, albeit the error was more well-behaved as a function of grid density and α. The lesson to be learned is that a naive CFIE result may not be accurate, even for very fine grid densities.

An estimate of the uncertainty in the calculated trihedral RCS can be found by taking the maximal difference among multiple, independently computed results. Here, we assume each code is implemented correctly (*i.e.*, validated) and each individual result is as accurate as the code is capable of producing. Using Codes A and C, we estimate the computed RCS uncertainty to be 0.02 dB across the 2.875-3.525 GHz band. This uncertainty in the computed RCS of the trihedral provides a lower bound on the uncertainty of any RCS measurement calibrated by the trihedral.

5.0 Conclusions

We have discussed the RCS test process from the viewpoint of controlling measurement uncertainty using advanced CEM tools. We have shown that measurement uncertainty is fundamentally

limited by uncertainty in the theoretical RCS of the calibration standard. We have shown that careful application of first-principle based CEM scattering codes can reduce this lower bound to a few hundredths of a dB for the trihedral, but this comes at the cost of rigorous analysis of the code input parameters and scattered field results. Furthermore, we have shown that several well-known "rules of thumb" for moment-method codes may fail to achieve the necessary accuracy under certain circumstances.

6.0 Acknowledgments

The authors wish to thank Captain Brian Fischer(AFRL/XPN) and Mr. Alan Buterbaugh (Mission Research Corporation) for their help with the squat cylinder computations. The authors are further indebted to the High Performance Computing (HPC) Major Shared Resource Center (MSRC) at Wright-Patterson AFB Ohio for providing some of the computational resources used in this study.

7.0 References

1. Hill, K.C. and Wood, W.D., "On the Use of Computational Electromagnetics in the Radar Cross Section Measurement Calibration Process," *1998 ACES Proceedings*, March 1998.
2. Fischer, Brian E. *et. al.*, "Moment Method Inter-Code Comparison and Angular Sensitivity Studies for NIST Calibration (Squat) Cylinders," *1998 AMTA Proceedings*, November 1998.
3. Putnam, J.M., and Medgyeshi-Mitschang, L.N., "Combined Field Integral Equation Formulation for Axially Inhomogeneous Bodies of Revolution (Combined Field Formulation of CICERO)," Report MDCQA003, McDonnell Douglas Research Laboratory, St Louis MO, December 1987.
4. Rogers, J., "JRMBOR: Computation of Scattering from a General Body of Revolution," Vol. 1: Formulation and MoM Algorithm, Vol. 2: Test Cases, Vol. 3: Code Listing}, Technical Report JR-2, Atlantic Aerospace Corporation, Greenbelt MD, 1989.

Analytical Bistatic k Space Images Compared to Experimental Swept Frequency ISAR Images

John Shaeffer, Brett Cooper
Marietta Scientific, Inc.
376 Powder Springs St. 240A
Marietta, Georgia 30064
(770) 425-9760
msi@inetnow.net
www.inetnow.net/~msi

Kam Hom
NASA Langley Research Center
Hampton, Virginia 23665
(757) 864-5292
k.w.hom@larc.nasa.gov

ABSTRACT: A case study of flat plate scattering images obtained by the analytical bistatic k space and experimental swept frequency ISAR methods is presented. The key advantage of the bistatic k space image is that a single excitation is required, i.e., one frequency / one angle. This means that prediction approaches such as MOM only need to compute one solution at a single frequency. Bistatic image Fourier transform data are obtained by computing the scattered field at various bistatic positions about the body in k space. Experimental image Fourier transform data are obtained from the measured response to a bandwidth of frequencies over a target rotation range.

This paper compares both image approaches as applied to a flat plate. Full details are presented in [1].

Analytical and Experimental Images: Experimental images are the Fourier transform of the backscatter reflected field as a function of frequency and angle, $E(\omega,\theta)$. Analytical bistatic k space images [1] are the Fourier transform of the bistatic field computed from a current distribution **J** as a function of down and cross range wave number **k**, $E(\vec{k}_{down},\vec{k}_{cross})$. This quantity is computed from a single current distribution **J**(ω) from the generalized radiation integral

$$E_{pol}(\vec{k}_{down},\vec{k}_{cross}) = \iint \left(\hat{u}_{pol}\cdot J(\omega)\right) e^{j\vec{k}\cdot\vec{R}}\, dS \qquad (1)$$

where the wave vector **k** takes on down and cross range values in k space,

$$\vec{k} = (\Delta k + k_0)\,\hat{k}_{down} + \Delta k\,\hat{k}_{cross}.$$

where Δk is the k-space bandwidth in the down and cross range directions and $k_0 = 2\pi/\lambda$ is the nominal wave number corresponding to the excitation frequency ω. The resolution in each spatial direction is $\Delta r = 2\pi/\Delta k$ which can be recast in terms of fractional wave number space (similar to fractional frequency bandwidth), $\Delta r = \lambda/(\Delta k/k_0)$. Experimental resolution for comparison is $\Delta r = (\lambda/2)/(\Delta f/f_0)$ for downrange and $\Delta r = (\lambda/2)/(\Delta\theta)$ for cross range. The bistatic k-space bandwidth will be twice the experimental bandwidth for the same resolution Δr due to the bistatic one way path length change.

Table 1 compares various image issues between the experimental swept frequency ISAR approach and the analytical bistatic k-space approach.

Experimental and Bistatic k space image comparison: Due to space limitations, only 2-D cases are presented. The interested reader is directed to [1] for the 1-D cases. The target is a 6" (0.15 m) square plate viewed from three aspect angles: normal to the plate; edge on at 10° elevation; and at 45° azimuth along the diagonal at 10° elevation. The illumination frequency is 10 GHz with a wavelength of 1.18" (0.03 m). The normalized plate dimensions are $\ell/\lambda = 5.08$ and $A/\lambda^2 = 25.9$ for edge length and plate area respectively.

The analytical and experimental image comparisons each used a Hanning window function. The experimental data used a single resolution $\Delta r = 1.25\,\lambda$. The analytical images used three resolutions, which were 0.4, 0.8, and 1.2 times the Δr of the experimental value. This was done to demonstrate how resolution affects the resulting images.

The experimental resolution is 1.25 λ_c = 1.47" = 0.0375 m corresponding to a fractional bandwidth $\Delta f/f$ of 0.4 (8-12GHz) and an ISAR rotation angle of 20°. The bistatic k space image resolutions were 1.5, 1.0, and 0.5 λ corresponding to 0.015, 0.030, and 0.045 m respectively. This bracketed the experimental value. The nominal bistatic viewing angles were 38°, 57°, and 115° respectively.

The data scales between the experimental and computed images have been kept the same.

Computational Parameters: The square plate bistatic k space images were computed using MOM3D [3]. The mesh model had 5000 triangles resulting in 7400 unknowns. The geometry symmetry option was utilized so that the system matrix was decomposed into two smaller matrices of 3725 and 3675 unknowns each. The sample density was 286 unknowns / λ^2. The image extent was set to 0.5 m.

Image Comparisons: *View 1* is perpendicular to the plate, Figure 1, for horizontal polarization. The dominant scattering for this case is specular with a peak RCS of $\sigma_{specular} = 4\pi\frac{A^2}{\lambda^2} = 7.6\ \mathrm{m}^2 = 8.8\ \mathrm{dBsm}$. The 2-D images show backscattered radiation to be uniformly coming from the entire plate. Coarser resolutions distribute energy over the larger resolution cell.

The experimental image shows a lower level source emanating from behind the plate probably due to edge to edge diffraction sometimes called talking edges. This return is in the category of a multiple bounce and hence images later in time down range of the plate. This effect is not seen in the computed images. Residual signal processing side lobes are seen in the computed 2-D images.

View 2 is normal to the plate edges at an elevation angle of 10°. The dominant scattering is due to edge diffraction: leading edge for horizontal (parallel) polarization, Figure 2; and trailing edge, or alternately traveling wave reflection for vertical (perpendicular) polarization, Figure 3.

The H pol images show the leading edge as the dominant scattering mechanism along with two edge waves reflecting from the rear vertices. The leading edge return, from the 1-D images, is close to the theoretical knife edge value of $\sigma_{edge} = \ell^2/\pi = 0.0074\mathrm{m}^2 = -21.3\ \mathrm{dBsm}$. The experimental image also shows a scattering center behind the plate due to rear corner to corner diffraction that arrives later in time. The edge wave mechanism in the computed images shows a spatial distribution with a peak at the rear vertex. This corresponds to the interpretation that the edge wave, upon reflection, loses energy via radiation as it travels back towards the front corner. Thus we see in the image a decaying intensity. The coarser resolution computed images distribute the return over a larger spatial extent.

The V pol images show the trailing edge as the dominant scattering mechanism. The experimental image also shows a scattering center behind the plate due to a second bounce surface wave, i.e., from the rear edge to the front and a second reflection from the back edge. This arrives later in time and experimentally images behind the plate. This is not seen in the computed images.

The experimental V pol images suggest a scattering mechanism from the front edge of the plate which in not observed in the computed images. We believe this is due to the trailing edge reflected surface wave and that if the plate were electrically longer we would not see the leading edge. The computed images do not show a leading edge scattering center. The dominant mechanism for this viewing angle is the trailing edge traveling wave reflection. In the computed 1-D and 2-D images the peak occurs at the rear and decays towards the front of the plate. This corresponds to the interpretation that the traveling wave, upon reflection, loses energy via radiation as it travels back towards the front edge. Thus the image decays in intensity. This phenomenon is not observed in the experimental data because the swept frequency nature of the image causes the stationary phase locations to coincide with the edges of the plate. The leading edge return in the experimental images is interpreted as the trailing edge reflected surface wave that has not completely decayed by the time it reached the front. This happens because of the multiple bounce traveling wave arriving later in time. Because the traveling wave mechanism images differently for the computed and experimental approaches, the peak values do not correspond to each other.

View 3 is along the plate diagonal, azimuth angle of 45°, at an elevation angle of 10°, Figure 4 and 5 for H (parallel) and V (perpendicular) polarizations respectively. The dominant mechanisms are non-specular edge and traveling waves.

The H pol images show scattering from the four tips of the plate. The two dominant tips are the mid vertices which reflect the edge traveling wave. The 1.0 and 0.5 λ resolution images show these reflected edge waves on the two front illuminated edges with the peak amplitudes near the reflection point. The rear vertex scattering center is probably due to edge waves that "turned the first corner" and then reflected from the rear most vertex and / or possibly due to tip diffraction since the plate is viewed at an elevation of 10°. The front tip return has the lower magnitude and is due to tip diffraction.

The experimental images show the front vertex with a lower amplitude than the rear. The opposite occurs in the computed images. The reason for this is not clear. It is conjectured that the measured front tip image is the phasor sum of tip diffraction and the remainder of the reflected edge wave which are phase subtracting to produce a smaller return.

The V pol images show scattering from the rear vertex and is due to the reflected surface traveling wave. As before with traveling wave mechanisms, the experimental and computed image magnitudes differ. The computed results show a lower amplitude spatially distributed return while the experimental image shows a higher amplitude return localized to the rear vertex. The computed images show the maximum amplitude near the aft reflection point with the reflected traveling wave decreasing in intensity as is propagates toward the front. The 1-D measured image shows a small return from the front tip which may be the stationary phase residual of the reflected traveling wave.

The view angle in elevation is less than the angle for maximum surface wave reflection which would occur, using the plate diagonal length, at about 18°.

Image comparison summary:

- Scattering mechanisms that are localized image similarly. The experimental and computed images are similar in most respects for specular and leading edge scattering. For trailing edge diffraction we suspect similar images; however, we have not made this comparison for a large λ target.

- Multiple bounce scattering mechanisms image differently. The experimental images show multiple reflections further down range since this is a time delay mechanism. This agrees with our physical view. The bistatic k space approach images the current distribution that by definition exists only on the surface and thus can not be further down range since there is no time variation. The computed images show multiple bounce mechanisms as locations on the body where those current mechanisms exist, i.e., placement of radar absorbing material at these locations would reduce the scattering.

- Surface traveling and edge waves image differently. (And we suspect for creeping wave mechanisms, although we have not made that comparison) The computed images tend to show edge and traveling waves as distributed sources over the scattering surfaces/edges which corresponds to this physical mechanism. The swept frequency measured images show these mechanisms at the body fore and aft end point locations. In this case the bistatic images correspond closer to a physical view.

Summary: A bistatic k space imaging technique has been introduced which is applicable for many computational electromagnetic algorithms. Images are a useful diagnostic tool in that they provide a pictorial representation of those body currents which contribute to radiation in specified spatial directions. By knowing how the geometric current distribution radiates energy, it then becomes easier to modify the currents and/or geometry to produce user desired scattering or radiation results.

The bistatic k space image algorithm utilizes a computed body current distribution and a generalized k space radiation integral to compute the scattered field in k space. The Fourier transform of this data is then the image in one, two or three dimensions. This image technique can be applied to monostatic or bistatic scattering or to antennas since only one body excitation is required.

Bistatic k space images:

- *Bistatic k space images are not the same as experimental images.* Both methods produce similar results particularly for localized scattering mechanisms such as specular and edge diffraction. Experimental images show multiple bounce scattering centers delayed in time. Analytical k space images show the current distribution producing radiation. Surface traveling and edge waves image as distributed sources in the analytical k space method as compared to local end point regions in experimental images. Experimental images typically have two way path length changes while the bistatic k space images have a one way path length change.

- The method may be applied to any EM computational code that produces a current distribution, e.g., method of moments, physical optics, finite element frequency domain, etc. The computed current distribution must reside on the body, i.e., equivalent surface currents removed from the geometry will not image back to a physical source.

- The method is computationally cheap. It is equivalent to computing a bistatic or antenna radiation pattern from just one current excitation.

- Resolution is limited by the discreteness of the EM analysis and by user desired limits on the bistatic radiation angles.

- Image focusing and smearing is not a problem because the bistatic field is computed on a uniform grid in k space. Experimental data, in comparison, is usually on a circular arc region that must be projected to a uniform rectangular grid for input to an FFT.

- One, two or three-dimensional images may be obtained with a resolution limit of $\lambda/4$.

- The method may be used to produce images for antennas and for bistatic scattering or for monostatic scattering.

- Images may be made for arbitrary polarization, e.g., cross polarized images may be obtained.

References

1. John Shaeffer, Kam Hom, Craig Baucke, Brett Cooper, and Noel Talcott, Jr., "Bistatic k-Space Imaging for Electromagnetic Prediction Codes for Scattering and Antennas", NASA Technical Paper 3569, July 1996

2. John Shaeffer, Kam Hom, Craig Baucke, Brett Cooper, and Noel Talcott, Jr., "A Review of Bistatic k-Space Imaging for Electromagnetic Prediction Codes for Scattering and Antennas", IEEE Antennas and Propagation Magazine, Feature Article, vol. 39, no. 5, October, 1997.

3. John Shaeffer, "MOM3D Method of Moments Code Theory Manual," NASA CR 189594, Contract NAS1-18603, March 1992.

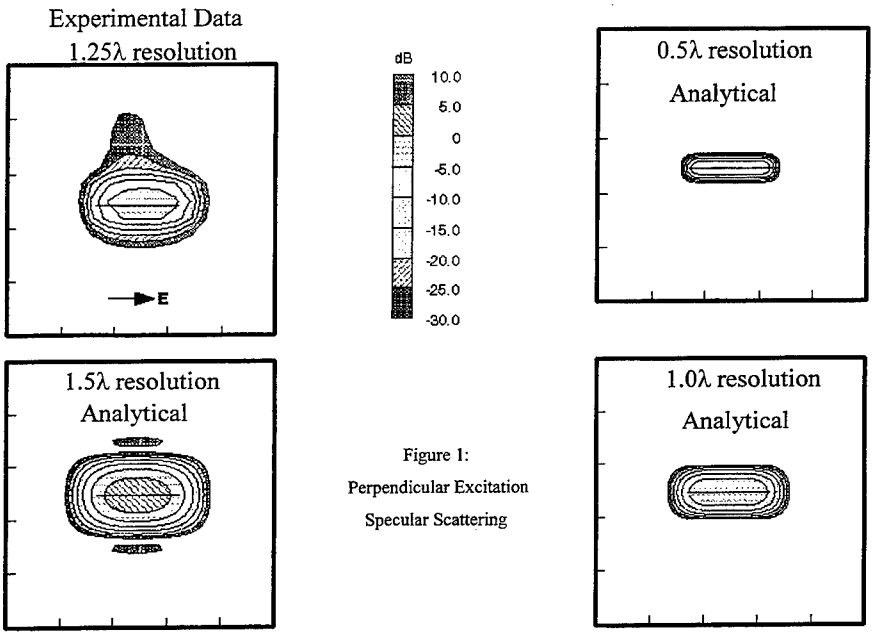

Figure 1:
Perpendicular Excitation
Specular Scattering

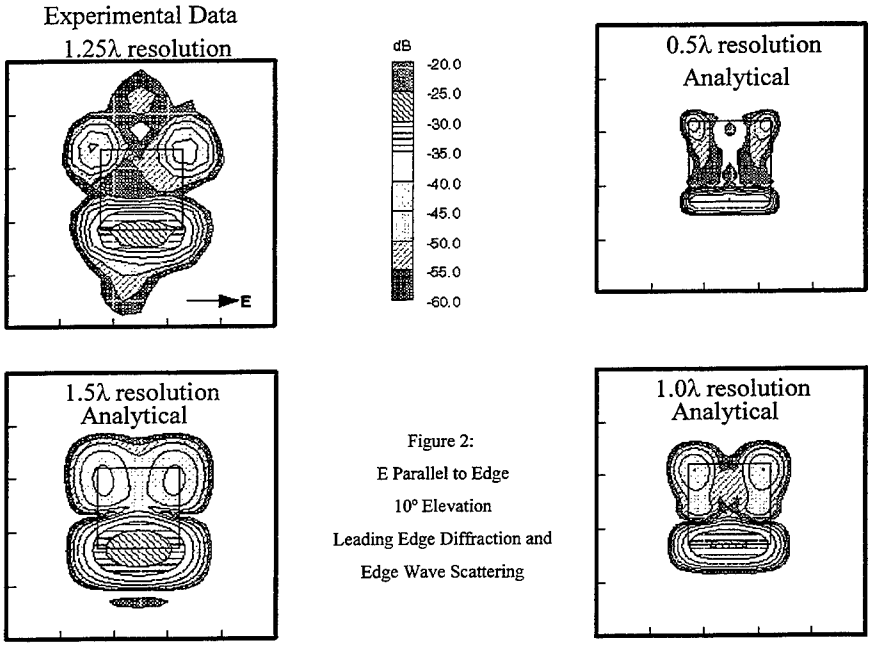

Figure 2:
E Parallel to Edge
10° Elevation
Leading Edge Diffraction and
Edge Wave Scattering

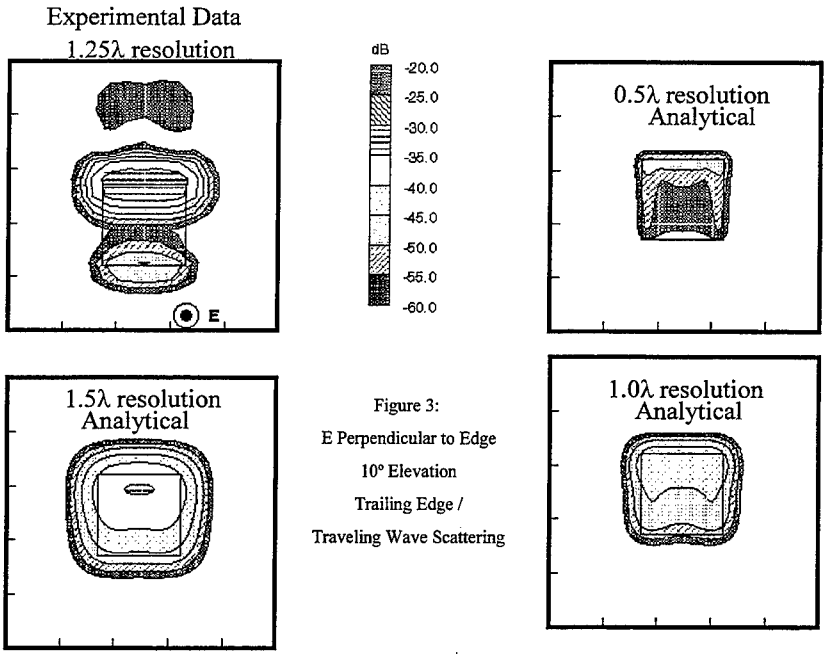

Figure 3:
E Perpendicular to Edge
10° Elevation
Trailing Edge /
Traveling Wave Scattering

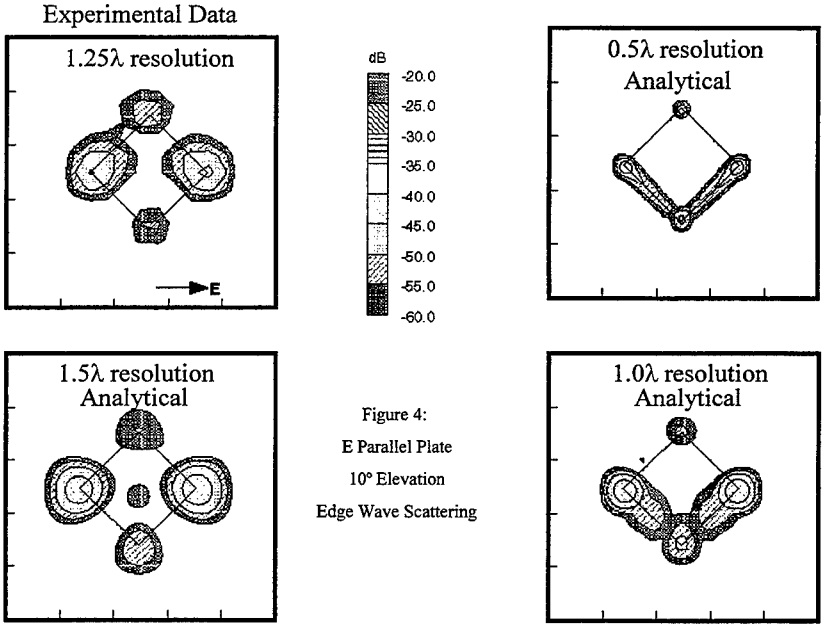

Figure 4:
E Parallel Plate
10° Elevation
Edge Wave Scattering

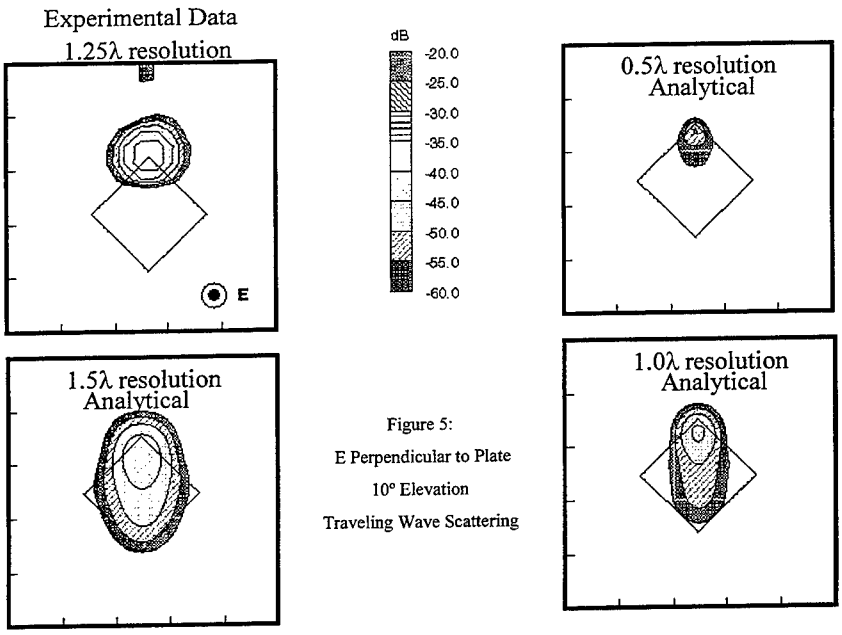

Figure 5:
E Perpendicular to Plate
10° Elevation
Traveling Wave Scattering

Issue	***Bistatic k Space Images***	***Experimental Images***
Origin of scattered field	Bistatic fields computed from generalized radiation integral	Measured backscatter fields
Transform Domain	Directly in k space	Frequency for down range Angle for cross range
Fourier Transform Variables	Wave number k and position r, kr	Frequency and time, ωt for down range and krθ for cross range
et Excitation Currents (What the image represents)	Only at frequency and illumination angle of excitation	Varies over the excitation frequency and illumination angle
Focus/Image Smear	None since image is computed directly in k space on an orthogonal grid of uniformly spaced points	Rotation angle limited to small angle without using focusing algorithms. Inherently a circular region in transform space
Resolution	≈λ/2, limited only by granularity of current representation, typically ≈λ/10, requires twice the experimental bandwidth	Set by available frequency bandwidth and small rotation angle approximation
Time delayed multiple bounce	Images currents which radiate in direction of image	Images downrange as time delay, hence see delayed in time
1-D Images 2-D Images 3-D Images	Down range (radial) in k space add cross range in k space add perpendicular direction in k space	Frequency Sweep add rotation angle add measurements over orthogonal plane
Fidelity for distributed current radiation (traveling waves)	Images the radiation as a distributed source	Because of frequency sweep, images the end points of distributed source
Antenna Images	Straight forward application	???
Image in direction other than excitation, i.e., bistatic images	Straight forward application	Very difficult, seldom done
Cross polarized image	Straight forward application	If separate transmit and receive feeds, rotate one feed

Table I Image Issues for Bistatic k-Space and Experimental

A Hybrid Periodic Moment Method Formulation for Scattering from Large 2-D Wire Arrays

Peter J. Collins and J. Paul Skinner
Air Force Institute of Technology

Abstract

We develop a hybrid method of moments numerical model for the electromagnetic scattering from large finite planar wire arrays The method incorporates the novel concept of a periodic physical basis function to dramatically reduce the required number of unknowns. The model can represent an arbitrary number of infinite length wires surrounded by a coplanar dielectric slab.

1 Introduction

Periodic screens have historically held great interest to the scientific and engineering communities. Often referred to as "frequency selective surfaces" for their frequency filtering properties, they find a wide range of application from optical spectroscopy to microwave antennas. Their practical usefulness has motivated a tremendous effort in developing numerical analysis methods for design purposes.

One common approach approximates the finite periodic structure with an infinite structure containing the same periodicity. An integral equation connecting the scattering currents to the incident field is reduced to a system of equations using the moment method. Floquet theory then reduces the infinite dimension problem to a finite one over a single reference element. Papers by Munk *et.al.* at the Ohio State University[1] and Mittra *et.al.* at the University of Illinois[2] are excellent examples of this approach, commonly called the periodic moment method.

While useful in many applications, the periodic moment method can not account for the edge effects present in all real geometries. In some applications, the edge effects play a critical role in the electromagnetic properties, motivating recent efforts in modeling finite arrays. The standard moment method, while capturing the edge effects, is often limited by current computer resources to small array geometries. This shortcoming has lead some authors to explore hybrid approaches.

In their 1988 article, Cwik and Mittra investigated truncated and curved strip arrays by approximating the induced current on each array element as if it were a member of an infinite array analogous to the physical optics approximation[3]. The authors then replace the edge element currents by those calculated for a much smaller array, combining the fields radiated by these currents through the standard radiation integral. Felsen and Carin have also investigated finite arrays using a novel ray field-Floquet mode approach which provides insight into the time domain scattering from truncated periodic structures[4][5]. Both of these techniques provide a reasonable first order approximation to the effects caused by truncating periodic structures. However, since neither technique accurately accounts for the coupling between the edge elements and those in the array interior, they provide poor results for cases where edge effects predominate.

In the following paragraphs, we present a new approach to modeling the coupling between the edge elements and the interior elements in a large array based on the concept of a "physical basis function." Although couched in different terms, the physical basis function concept was originally proposed by Morita[6], and later Tew and Tsai[7] in an effort to apply the moment method to infinite planar structures. Burnside, Yu, and Marhefka then applied it to the wedge diffraction problem, combining the geometrical theory of diffraction with the moment method[8]. To our knowledge, however, the current work represents the first application of the physical basis function concept to periodic structures.

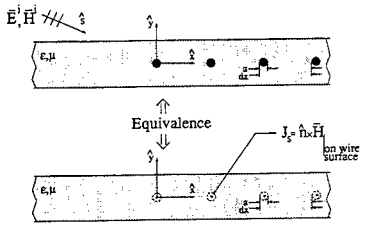

Figure 1: 2-D Wire Array Equivalent Geometry

2 Formulation

The core of the physical basis function concept involves a fairly straight-forward application of *a priori* knowledge of the induced current behavior to the moment method. Consider the currents impressed on a large planar array by a plane wave illumination (large implying many wavelengths). Starting from an edge and moving toward the center of the array, there will be some point where the current amplitudes become approximately constant over a large central section of the finite array. Over this portion one can use the periodic moment method to determine the representative admittance or impedance of these elements. This physical basis function can then be used along with the edge element basis functions to create a coupling matrix which relates the unknown current expansion coefficients to the known incident field. The coupling matrix explicitly incorporates the influence of the "infinite" portion of a large finite array into the small finite array analysis in a manner analogous to how the interconnection matrix of diakoptic theory combines the impedances of individual structural elements into a composite structure matrix[9]. This technique represents a departure from traditional hybrid methods characterized by the Cwik and Mittra "physical optics" approach.

To illustrate the method, consider the 2-D wire array geometry shown in Figure 1 illuminated by a TMz plane wave. Assuming the number of wires in the array, N, is large enough such that the two array edges are uncoupled, one can break the large finite array problem into two semi-infinite array problems. Once the induced currents are found for each semi-infinite problem, the first $\frac{N}{2}$ currents from each problem can be combined with the appropriate phase shift in the radiation integral to obtain the desired scattered fields. While the presence of the dielectric slab could be accounted for by a non-free space Green's function, we choose to develop expressions in the plane wave spectral domain where the planar boundaries are accounted for by simple Fresnel coefficients.

We start the analysis by considering the semi-infinite wire array in a homogeneous media with the material parameters of the dielectric slab. Using the surface equivalence theorem, we define a new geometry where impressed currents radiate into the homogeneous media. The equivalent problem contains an infinite number of unknown currents making a numerical solution via a traditional moment method approach impossible. In order to make the problem tractable, we assume the current amplitudes vary significantly only over the first B elements. The remaining elements have approximately equal amplitude currents which differ by a Floquet phasing factor dependent on the incident plane wave direction. This assumption reduces the problem to that of finding $(B+1)$ unknowns.

We next form an integral equation relating the unknown currents to the known incident field. As is common in these formulations, the total tangential electric field boundary condition is used to obtain an integral equation of the form

$$E_z^i(\overline{\rho}) = -\frac{\omega\mu}{4}\iint_{s_{wires}} J_z(\overline{\rho}')H_0^{(2)}(\beta\,|\overline{\rho}-\overline{\rho}'|)\,d\overline{\rho}', \qquad \overline{\rho}\in s_{wires} \tag{1}$$

where s_{wires} denotes the wire surfaces. We solve Equation (1) by expanding the unknown currents with appropriate known basis functions. In this case, B impulse basis functions and one physical basis function are required. These take the form

$$J_z(\overline{\rho}') \approx \left\{ \begin{array}{ll} J_0 \sum_{q=0}^{\infty} \delta\left(\overline{\rho}' - \overline{\rho}_q\right) e^{-j\beta\widehat{s}\cdot\overline{\rho}_q}, & b=0 \\ J_b \delta\left(\overline{\rho}' - \overline{\rho}_b\right), & b=1,2,\ldots B \end{array} \right\} \tag{2}$$

where $\overline{\rho}_q = q\,dx\,\widehat{x}$. Note that $\overline{\rho}_{q=0}$ locates the "edge" of the physical basis function and $\widehat{s}$ denotes the incident plane wave propagation direction. With this choice, we are effectively treating the edge wire basis functions as perturbations of the physical basis function. Inserting Equation (2) in Equation (1), we obtain the expression

$$E_z^i(\overline{\rho}) \approx -\frac{\omega\mu}{4}\left(J_0 \sum_{q=0}^{\infty} H_0^{(2)}(\beta\left|\overline{\rho} - \overline{\rho}_q\right|) e^{-j\beta\widehat{s}\cdot\overline{\rho}_q} + \sum_{b=1}^{B} J_b H_0^{(2)}(\beta\left|\overline{\rho} - \overline{\rho}_b\right|)\right), \qquad \overline{\rho} \in s_{wires} \tag{3}$$

Following Harrington's moment method formulation, we define an inner product and force a chosen set of $(B+1)$ testing functions to be orthogonal to the error function[10]. For the wire geometry, the filamentary current nature suggests a Dirac delta testing function. In order to avoid the Green's function singularity, we place the test location a wire radius away from the basis function. We also define the testing function associated with the physical basis function to be nonzero only over a chosen reference wire element to keep the coupling matrix elements bounded.

$$\theta_t = \delta\left(\overline{\rho} - \overline{\rho}_t\right), \qquad t = 0,1,\ldots B \tag{4}$$

where

$$\overline{\rho}_t = \left\{ \begin{array}{ll} \widehat{x}\,B\,dx + \widehat{y}\,a, & t=0 \\ \widehat{x}\,(t-1)\,dx + \widehat{y}\,a, & t=1,2,\ldots B \end{array} \right\}$$

Performing the inner product, we arrive at the following matrix equation

$$E_z^i(\overline{\rho}_t) \approx -\frac{\omega\mu}{4}\left(J_0 \sum_{q=0}^{\infty} H_0^{(2)}(\beta\left|\overline{\rho}_t - \overline{\rho}_q\right|) e^{-j\beta\widehat{s}\cdot\overline{\rho}_q} + \sum_{b=1}^{B} J_b H_0^{(2)}(\beta\left|\overline{\rho}_t - \overline{\rho}_b\right|)\right), \qquad t = 0,1,\ldots B \tag{5}$$

which can be solved for the unknown expansion coefficients, J_b. Once the currents are known for the two semi-infinite array problems, we can combine the first $\frac{N}{2}$ currents from each in the radiation integral to obtain the desired scattered fields.

In order to account for the dielectric slab, we need to convert the previous spatial domain expressions to the spectral domain. The spectral domain form also generally converges faster than the spatial domain summation. Consider the first term in Equation (5). This expresses the fields radiated by the physical basis function in terms of a collection of cylindrical waves. Using the one-sided Poisson sum formula described in our earlier paper[11], we transform the cylindrical wave expansion to a plane wave expansion of the form

$$E_z^{PBF}(\overline{\rho}_t) = -J_0 \frac{\omega\mu}{4\,dx\beta} \sum_{k=-\infty}^{\infty} \left\{ \frac{e^{-j\beta\overline{\rho}_t\cdot\widehat{\rho}}}{\rho_y} T\left(\overline{\rho}_t, \widehat{\rho}, k\right) + \frac{j}{\pi} \int_{-\infty}^{\infty} \frac{e^{-j\beta\overline{\rho}_t\cdot\widehat{\tau}}}{\tau_y\left(\tau_x - \rho_x\right)} T\left(\overline{\rho}_t, \widehat{\tau}, k\right) d\tau_x \right\} \tag{6}$$

where

$$\widehat{\rho} = \widehat{x}\left(s_x + \frac{k\lambda}{dx}\right) + \widehat{y}\sqrt{1 - \left(s_x + \frac{k\lambda}{dx}\right)^2}$$

The function denoted by T is the "T-factor" introduced by Munk which accounts for the multiple reflections of the plane wave radiated by the physical basis function. For a detailed description, see Munk's work on periodic surfaces in stratified media[12][1].

The remaining terms in Equation (5) express the fields radiated by the edge wires. To obtain a plane wave expansion, we use the "Array Scanning Method" first introduced by Munk and Burrell[13]. The basic ASM procedure starts with the spatial domain field from an edge element

$$E_{zb}^{wire}(\overline{\rho}_t) = -J_b \frac{\omega\mu}{4} H_0^{(2)}(\beta\,|\overline{\rho}_t - \overline{\rho}_b|) \tag{7}$$

We then create a "pseudo-array" around the edge element and express the fields in the spectral domain.

$$E_{zb}^{array}(\overline{\rho}_t) = -J_b \frac{\omega\mu}{2\widetilde{dx}\beta} \sum_{k=-\infty}^{\infty} \frac{e^{-j\beta[\overline{\rho}_t\cdot\widehat{\rho}^{asm} - \rho_x^{asm}(b-1)\widetilde{dx}]}}{\rho_y^{asm}} \tag{8}$$

where

$$\widehat{\rho}^{asm} = \widehat{x}\left(s_x^{asm} + \frac{k\lambda}{\widetilde{dx}}\right) + \widehat{y}\sqrt{1 - \left(s_x^{asm} + \frac{k\lambda}{\widetilde{dx}}\right)^2}$$

After multiplying by the "T-factor" to account for the dielectric slab, we recognize the resulting sum as a Fourier series whose central term is the fields radiated by the original edge element in the presence of the dielectric slab. We extract the central term using an appropriately defined inner product to obtain

$$E_{zb}^{wire}(\overline{\rho}_t) = -J_b \frac{\omega\mu}{4\pi} \sum_{k=-\infty}^{\infty} \int_{-1}^{1} \frac{e^{-j\beta[\overline{\rho}_t\cdot\widehat{\rho}^{asm} - \rho_x^{asm}(b-1)\widetilde{dx}]}}{\rho_y^{asm}} T(\overline{\rho}_t, \widehat{\rho}^{asm}, k)\, ds_x^{asm} \tag{9}$$

Combining Equations (6) and (9), we have a spectral domain equivalent to Equation (5) in the presence of the dielectric slab.

$$E_z^i(\overline{\rho}_t) \approx E_z^{PBF}(\overline{\rho}_t) + \sum_{b=1}^{B} E_{zb}^{wire}(\overline{\rho}_t), \qquad t = 0, 1, \ldots B \tag{10}$$

Equations (5) and (10) form the core of the wire array codes we use to generate the results in the next section.

3 Results

To demonstrate the accuracy of our formulation, we present the bistatic echowidth of a 50 wire array in free space illuminated 60° off-normal. The wires are placed 0.1λ apart. The plot in Figure 2 contains three traces; the standard moment method calculation containing 50 unknowns, the "physical optics" approximation where we've used 10 unknowns on each edge and one unknown for the center 30 wires, and the subject hybrid method using the same number of unknowns as the "physical optics" approach. Clearly the "physical optics" approach does not completely capture the scattering mechanisms. To see why, we examine the actual induced scattering currents calculated by each method.

Figure 3 contains the induced current magnitudes. According to the figure the "physical optics" currents next to the inner array wires are in error. The explanation lies in the fact these currents were computed in free space instead of next to an "infinite" wire array. Our hybrid method more accurately predicts the currents precisely because this coupling is inherently included in the coupling matrix.

As a final demonstration, we encapsulate the previous array in a 0.5λ thick dielectric slab with a relative permittivity of 2.0. Figure 4 shows the hybrid method's ability to include planar boundaries. The induced current magnitudes for a 20° off-normal incident angle are presented. While the hybrid method accurately predicts the edge current behavior, the slab increases the coupling between wires indicating more edge elements may be required.

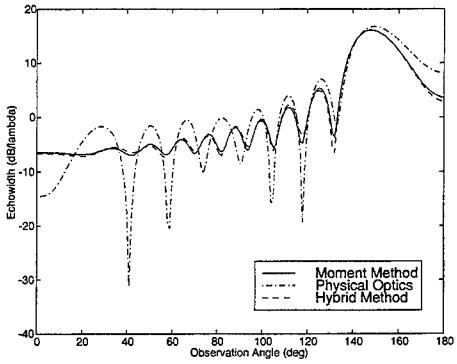

Figure 2: Bistatic Echowidth of a 50 Wire Array Illuminated at 60° Off-normal

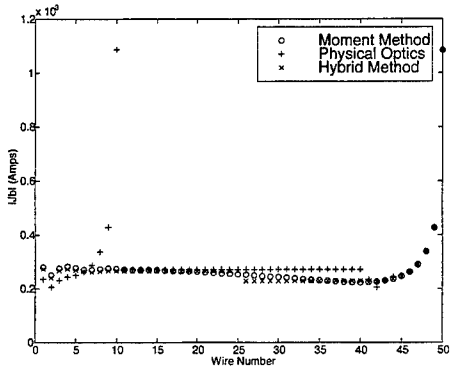

Figure 3: Induced Current Magnitude on Wire Array

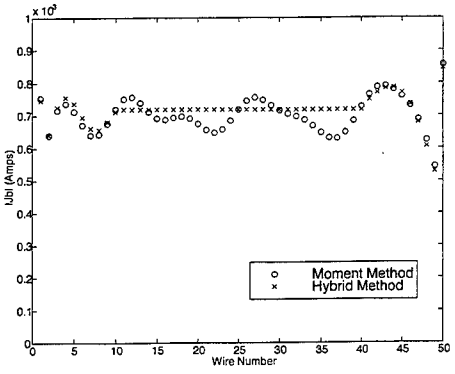

Figure 4: Induced Current Magnitudes on Wire Array in Dielectric Slab

4 Conclusion

In the previous paragraphs, we developed a hybrid periodic moment method solution for the electromagnetic scattering from large finite planar wire arrays. Based on the concept of a periodic physical basis function, the method explicitly incorporates the coupling between the edge wires and the central portion of the array in a moment method coupling matrix. In addition to providing a more accurate solution when compared to previous hybrid techniques, the method provides a computational advantage over standard moment method solutions by effectively removing the link between the array size and the required number of unknowns. This efficiency is demonstrated in a paper currently submitted to the IEEE transactions on Antennas and Propagation where we apply the method to more general slotted radome geometries.

References

[1] B. A. Munk, "A general theory of periodic surfaces in a stratified dielectric medium," Technical 715582-4, ElectroScience Laboratory, The Ohio State University, February 1986. Generated under contract F33615-83-C-1013 for Avionics Laboratory, Air Force Wright Aeronautical Laboratories, Wright-Patterson AFB, OH.

[2] R. Mittra, C. Chan, and T. Cwik, "Techniques For Analyzing Frequency Selective surfaces: a review," in *Proceedings of the IEEE*, vol. 76, pp. 1593–1615, December 1988.

[3] T. Cwik and R. Mittra, "The Effects of the Truncation And Curvature of Periodic Surfaces: a Strip Grating," *IEEE Transactions on Antennas and Propagation*, vol. 36, pp. 612–22, May 1988.

[4] L. B. Felsen and L. Carin, "Time harmonic and transient scattering by finite periodic flat strip arrays: Hybrid (ray)-(floquet mode)-(mom) algorithm," *IEEE Transactions on Antennas and Propagation*, vol. 41, pp. 412–21, April 1993.

[5] L. B. Felson and L. Carin, "Diffraction theory of frequency- and time-domain scattering by weakly aperiodic truncated thin-wire gratings," *Journal of the Optical Society of America*, vol. 11, pp. 1291–1306, April 1994.

[6] N. Morita, "Diffraction by arbitrary cross-sectional semi-infinite conductor," *IEEE Transactions on Antennas and Propagation*, vol. AP-19, pp. 358–65, May 1971.

[7] M. D. Tew and L. L. Tsai, "Use of *a priori* knowledge in moment method solutions," in *1972 GAP International Symposium*, (Williamsburg, VA), December 1972.

[8] W. D. Burnside and R. J. Marhefka, "A technique to combine the geometrical theory of diffraction and the moment method," *IEEE Transactions on Antennas and Propagation*, vol. AP-23, pp. 551–8, July 1975.

[9] G. Goubau, N. N. Puri, and F. K. Schwering, "Diakoptic theory for multielement antennas," *IEEE Transactions on Antennas and Propagation*, vol. AP-30, pp. 15–26, January 1982.

[10] R. F. Harrington, *Field Computation by Moment Methods.* Malabar, Florida: Robert E. Krieger Publishing Company, Inc., 1968.

[11] J. P. Skinner and P. J. Collins, "A one-sided version of the poisson sum formula for semi-infinite array green's functions," *IEEE Transactions on Antennas and Propagation*, vol. 45, pp. 601–7, April 1997.

[12] B. A. Munk, G. A. Burrell, and T. W. Kornbau, "A general theory of periodic surfaces in a stratified dielectric medium," Technical 784346-1, ElectroScience Laboratory, The Ohio State University, November 1977. Generated under contract F33615-76-C-1024 for Avionics Laboratory, Air Force Wright Aeronautical Laboratories, Wright-Patterson AFB, OH.

[13] B. A. Munk and G. A. Burrell, "Plane-wave Expansion for Arrays of Arbitrary Oriented Piecewise Linear Elements and Its Application in Determining the Impedance of a Single Linear Antenna," *IEEE Transactions on Antennas and Propagation*, vol. 27, pp. 331–43, May 1979.

Accuracy and Conditioning of the Method of Moments for the 2D EFIE

Karl F. Warnick and Weng Cho Chew
Center for Computational Electromagnetics
Department of Electrical and Computer Engineering, University of Illinois
1406 West Green St., Urbana, IL 61801-2991

1. Introduction

The accuracy of numerical methods for solution of scattering problems is in general poorly understood [1]. Codes are validated by comparison with test cases which are often much simpler than real–world scatterers. With any numerical method, the most important questions are "How long does it take to get a solution?" and "How accurate is that solution?" A theoretical understanding of the convergence of numerical scattering methods which answers these questions would be of great value to practitioners of computational electromagnetics.

A convergence theory consists of two parts: a bound on the solution error and an estimate of the condition number of the method, in terms of properties of the scatterer and the discretization scheme. Such a theory exists for the boundary element method applied to Laplace's equation [2]. This work has been extended to the dynamic case [3, 4] but the resulting bounds apply only asymptotically in the limit as the discretization length vanishes. For large scatterers, computational costs can be excessive even at the lowest possible discretization densities. Residual–based bounds are also available [5, 6], but in order to estimate discretization error, residuals must be computed using a finer discretization than that used to solve the problem. Global phenomena such as resonance also reduce the effectiveness of both of these types of bounds.

To overcome these difficulties, a convergence theory for computational electromagnetics must take into account not only the local nature of a problem but also global properties as well. For integral equation methods, this requires a knowledge of the spectrum of the operator. For separable geometries such as the cylinder and the sphere, the spectrum is known, but the spectrum is unavailable in closed form for more complex scatterers. In this paper, we give the approximate spectrum of the EFIE for an infinite conducting strip and a cavity, and use this to obtain the condition number of the EFIE for these scatterers. By comparing the continuous and discrete operators, we also obtain the spectral error introduced by the discretization.

2. TM Polarization

By transforming the EFIE for a TM–polarized field incident on a perfectly conducting strip to a spectral basis, the operator becomes diagonally dominant, and the spectrum of the EFIE is approximated by the self–interaction terms. The self–interaction of modes of the form $e^{ik_0\beta x}$ is

$$A_p \sim \frac{\eta}{2\sqrt{1-\beta^2}} - \frac{\eta}{2\pi^2(1-\beta^2)}\left[i + \frac{\beta}{\sqrt{1-\beta^2}}\ln\left(i\beta + \sqrt{1-\beta^2}\right)\right] L^{-1} + O(L^{-3/2}), \quad L \to \infty. \quad (1)$$

where $\beta = p/L$, $p = 0, \pm 1, \pm 2, \ldots$, and L is the length of the strip in wavelengths. The first term is the limiting value for an infinite plane, and higher order terms represent the effect of scattering by the edges of the strip. Equation (1) breaks down for $|\beta| = 1$, and is replaced by

$$A_{\pm L} \sim \frac{\sqrt{2}\eta}{3}(1-i)L^{1/2} + \frac{\eta}{8\sqrt{2\pi}}(1+i)L^{-1/2} - \frac{\eta}{6\pi^2}\left[i + \frac{7\sqrt{2}}{4}\right] L^{-1} + O(L^{-3/2}), \quad L \to \infty \quad (2)$$

for the self interaction of the surface wave. Figure 1 compares the spectrum of the impedance matrix for a strip of width $20\,\lambda$ to the values of A_p given by Eqs. (1) and (2).

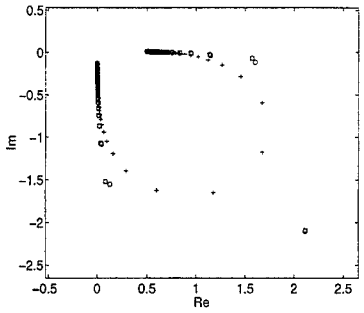

Figure 1: Spectrum of $\overline{\mathbf{Z}}$ for strip, $L = 20$, $n_\lambda = 10$. Pluses: computed. Circles: theoretical, Eqs. (1), (2), and (6). Squares: numerical evaluation of A_p.

Discretizing the EFIE with a finite basis leads to a cutoff of the spectrum near the accumulation point at the origin. The eigenvalue of the moment matrix $\overline{\mathbf{Z}}$ with the smallest magnitude is $\lambda_{\min} \simeq -i\eta/n_\lambda$ where $n_\lambda = \lambda/h$ is the discretization density or number of points per wavelength. The corresponding mode has the maximum spatial frequency representable in the finite basis, and its self–coupling is the most strongly localized. The largest eigenvalue is $\lambda_{\max} \simeq (\eta\sqrt{2}/3)(1-i)L^{1/2}$ and corresponds to the surface wave mode with a spatial frequency of k_0. Due to long range coupling by fields propagating parallel to the strip, the surface wave is antiresonant. A strong incident field is required to excite the mode, and its eigenvalue (which represents the energy stored by the mode for a unit surface current) grows with the strip length. The condition number of $\overline{\mathbf{Z}}$ can be approximated by the pseudo–condition number $|\lambda_{\max}|/|\lambda_{\min}|$, which is

$$\kappa(\overline{\mathbf{Z}}) \simeq (2/3)n_\lambda L^{1/2}. \tag{3}$$

If a near–neighbor preconditioner is employed, the growth in iteration count with n_λ can be mitigated, since the preconditioner accurately models the localized interaction between the high frequency eigenfunctions. Since the preconditioner does not capture the long range interactions which determine the largest eigenvalues, however, the condition number will still scale as $N^{1/2}$ as the size of the scatterer increases.

Discretization also shifts A_p by a small amount ΔA_p which approximates the discretization error in the spectrum of $\overline{\mathbf{Z}}$. Evaluating the interaction of the modes $e^{ik_0\beta x_n}$ using the moment matrix $\overline{\mathbf{Z}}$ and comparing to the continuous limit yields the relative spectral error $E_b(\beta, n_\lambda, \alpha) \equiv \Delta A_p/A_p$. b is the sum of the orders of the testing and expansion functions, where the delta function basis (point matching) is order 0, a piecewise constant basis (pulse function) is order 1, and a piecewise linear basis (triangle function) is order 2. The parameter α specifies the relative shift $\alpha h/2$ of the locations of the testing and expansion functions. There are two error components: (i) sampling error, due to aliasing of high frequency components of the singular kernel by the finite local basis, and (ii) smoothing error, caused by inaccurate interpolation of low frequency components.

We first assume exact integration of the moment matrix elements. For small β/n_λ, it can be shown that

$$E_0 \simeq 2i \ln\left[2\sin\left(\pi\alpha/2\right)\right] n_\lambda^{-1}; \quad E_1 \simeq -i\beta g(\alpha) n_\lambda^{-2} - (\pi^2\beta^2/6) n_\lambda^{-2}; \quad E_b \simeq -(\pi^2 b\beta^2/3) n_\lambda^{-2}, \;\; b > 1 \tag{4}$$

where $g(\alpha) = \mathrm{Li}_2(-e^{i\pi\alpha}) - \mathrm{Li}_2(-e^{-i\pi\alpha})$ and Li is the polylogarithm function. E_0 consists only of sampling error; the two terms of E_1 are sampling and smoothing errors, respectively; and smoothing error dominates for $b > 1$. The divergences of E_b correspond to point matching at locations where the derivative of the expansion function is undefined. E_0 has a minimum at $\alpha = 1/3$, where the leading spectral error term given in Eq. (4) vanishes. Figure 2 shows the relative spectral error over $0 \leq \beta \leq n_\lambda/2$ for $n_\lambda = 10$. For the $b = 0$ discretization, the expansion function is taken to be $\delta(x + h/6)/2 + \delta(x - h/6)/2$ and the testing function is $\delta(x)$, in which case the spectral error is $O(n_\lambda^{-2})$. Figure 3 compares the error of the numerical solution to the EFIE for a cylinder for various values of b. As predicted by the theory, the error for the $b = 0$ discretization is smallest, and increases with the order of the discretization. Since E_0 depends strongly on the value of α, this discretization scheme is more sensitive to irregular discretization than the higher order bases.

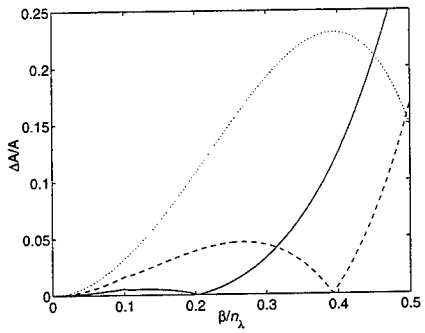

Figure 2: Relative spectral error, TM polarization, $n_\lambda = 10$. Solid line: b = 0 (point discretization, $\alpha = 1/3$). Dashed line: b = 1 (point matching, piecewise constant basis). Dotted line: b = 2 (point matching, piecewise linear basis).

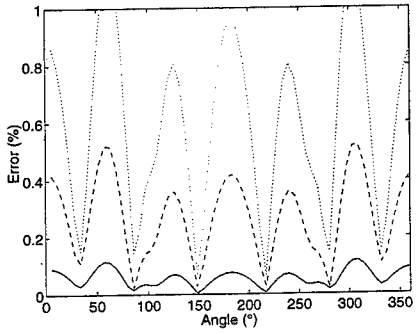

Figure 3: Relative current error for cylinder, $k_0 r = 2\pi$, TM plane wave incident at $\phi = 0$. Solid line: b = 0 (point discretization, $\alpha = 1/3$). Dashed line: b = 1 (point matching, piecewise constant basis). Dotted line: b = 2 (point matching, piecewise linear basis).

The use of numerical quadrature to evaluate moment matrix elements leads to an additional sampling error component. For the simplest M–point first order integration rule, the error is

$$E_{1,M} \simeq i2 \ln 2 \, (M n_\lambda)^{-1}. \tag{5}$$

Unless otherwise specified, the numerical results in this paper for the TM polarization employ a single point integration rule with analytical self term, for which the quadrature error is

$$E'_{1,1} \simeq i2 \ln (\pi/e) \, n_\lambda^{-1}. \tag{6}$$

For $b > 1$, the spectral error is of the same order as $E_{1,M}$. With any standard quadrature rule such as the trapezoidal rule and its generalizations or Gaussian quadrature with unity weight function, the order of the spectral error in Mn_λ is independent of the order of the quadrature rule. It is well known that in order to reduce error, the integration rule must take into account the form of the singularity of the kernel [7].

3. TE Polarization

The domain of the EFIE for the TE polarization is the Sobolev space $H^{1/2}$, which contains the square integrable functions vanishing at the edges of the strip [4]. Transforming the TE EFIE to a spectral basis for this space leads to

$$A_p \sim \frac{\eta\sqrt{1-\beta^2}}{2} - \frac{\eta}{2\pi^2}\left[i - \frac{\ln\left(i\beta+\sqrt{1-\beta^2}\right)}{\beta\sqrt{1-\beta^2}}\right] L^{-1} + O(L^{-2}), \quad L \to \infty \tag{7}$$

where $\beta = p/(2L)$ and $p = 1, 2, \ldots$. The self–interaction of the surface wave is

$$A_{2L} \sim [\eta\sqrt{2}/(2\pi)](1+i)L^{-1/2} - (i\eta/\pi^2)L^{-1} + O(L^{-3/2}), \quad L \to \infty. \tag{8}$$

Figure 4 compares the spectrum for a strip of length $10\,\lambda$ with A_p. In constrast to the TM case, the largest eigenvalue arises from the highest frequency mode, and the surface wave mode is resonant, so that its eigenvalue decreases as the strip length increases. From Eqs. (7) and (8), the condition number of $\overline{\mathbf{Z}}$ is

$$\kappa \simeq (\pi/4) n_\lambda L^{1/2} \tag{9}$$

which scales with the electrical size in the same way as in the TM case.

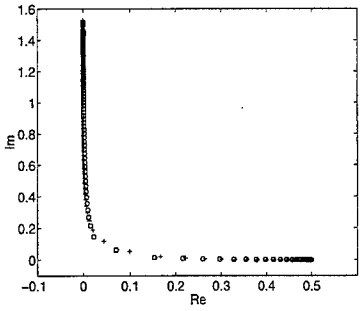

Figure 4: Spectrum of TE EFIE for strip, $L = 10$, $b = 1$ discretization, $n_\lambda = 10$. Pluses: computed. Circles: theoretical, Eqs. (7), (8) and (10). Squares: numerical computation of A_p.

For the first few values of b, the discretization error for the TE polarization is

$$E_0 \simeq -\frac{in_\lambda}{2}\csc^2(\pi\alpha/2), \quad E_1 \simeq \beta\tan(\pi\alpha/2) - \frac{\pi^2\beta^2}{6n_\lambda^2}, \quad E_2 \simeq -\frac{2i\beta^2}{n_\lambda}\ln\left[2\sin(\pi\alpha/2)\right] - \frac{\pi^2\beta^2}{3n_\lambda^2} \tag{10}$$

for small β/n_λ. Figure 5 shows the spectral error for several different discretizations. If $\alpha = 0$, the leading term of E_1 vanishes. In this case, the error is $O(n_\lambda^{-2})$, and is smaller than E_b for $b > 1$. Figure 6 compares the surface current for a plane wave incident on a cylinder of radius $k_0 r = 1/(2\pi)$ obtained using pulse basis functions and point matching ($b = 1$) with the exact solution. In the hypersingular term of the TE EFIE, the derivative of the pulse basis function leads to delta functions at the edges of the pulse. If these delta functions are located off the cylinder at the vertices of a polygon, the results of Peterson, *et al* [8] are recovered, and the point/pulse result is much poorer than pulse/triangle ($b = 3$). If the delta functions are moved

onto the cylinder, the current error norm decreases by a factor of 16, and the accuracy is roughly the same as the pulse/triangle discretization. For a strip, the $b = 1$ discretization is more accurate. Thus, the point/pulse discretization is not inherently less accurate than higher order schemes, but is more sensitive to geometrical modeling errors and irregular discretization.

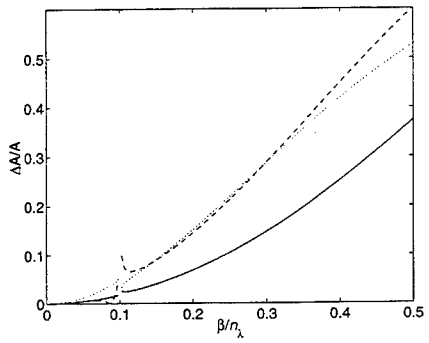

Figure 5: Relative spectral error, TE, $n_\lambda = 10$. Solid line: b = 1 (delta/pulse), $\alpha = 0$. Dashed line: b = 2 (delta/triangle), $\alpha = 1/3$. Dotted line: b = 3 (pulse/triangle), $\alpha = 0$.

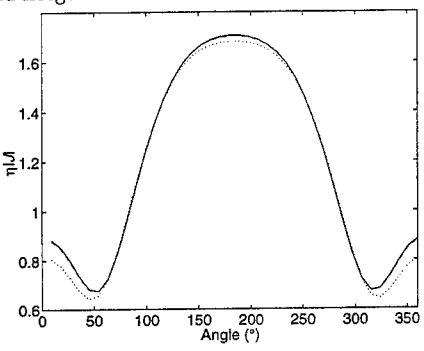

Figure 6: Surface current for cylinder, $k_0 r = 1/(2\pi)$, TE, plane wave incident at 0°. Solid line: Mie series. Dotted line: b = 1, delta functions off cylinder. Dashed line: b = 1, delta functions on cylinder.

For the $b = 0$ and $b = 1$ discretizations, the hypersingular term of the EFIE can be evaluated analytically, and the remaining term has the same kernel as the TM EFIE, so that the spectral error due to quadrature for the TE polarization is the same as Eq. (5). For $b > 1$, the singularity of the hypersingular kernel can be reduced by partial integration, and the quadrature error also becomes identical to the TM case.

4. Cavity

For two parallel strips separated by a distance of $W\,\lambda$, the spectrum of the EFIE consists of sums and differences of the self- and cross-coupling of modes on each strip. If $2W$ is an integer, the mode with the smallest difference eigenvalue is $\cos(\pi x/L)$. The eigenvalue is $\lambda_\tau \simeq i(\eta\pi/8)WL^{-2} + (\eta\sqrt{2}/16)W^{3/2}L^{-3}$. This leads to the condition number estimate

$$\kappa \simeq 1.6\frac{L^{5/2}}{W} \tag{11}$$

for the TM polarization. For the TE case, $\kappa \simeq 2n_\lambda L^2/(\pi W)$, so that the growth with L is not as fast, but discretization length continues to affect conditioning.

The spectral error ΔA_p makes an additional contribution to the resonant eigenvalue. If the basis is such that quadrature makes the only contribution to sampling error, the relative spectral error is

$$E_{b,M} \simeq 1.8\frac{L^2}{WMn_\lambda}. \tag{12}$$

The growth with L implies poor convergence of the numerical solution for the cavity, which has been observed experimentally [9]. For a cavity such that $L = 15$ and $W = 4$, Eq. (12) leads to the condition $Mn_\lambda \gg 101$, so that the usual ten points per wavelength discretization density

combined with a low order integration rule fails to model the resonant behavior of the cavity. Since smoothing error affects both the self– and cross–coupling of the resonant mode, its effect on the difference eigenvalue is less significant than that of sampling error. If sampling error is eliminated by the use of an accurate quadrature rule for the kernel of the EFIE, the relative spectral error becomes independent of the cavity size.

The EFIE also becomes ill–conditioned at non–resonant frequencies, for which $2W$ is not an integer. In this case, the mode with the smallest difference eigenvalue has spatial frequency $\beta = \sqrt{\alpha}/W$, where $\alpha = 2W - \lfloor 2W \rfloor$. The real part of the eigenvalue for this mode is $\mathrm{Re}\{\lambda_p\} \simeq \eta\sqrt{\alpha W}/(2L)$. The real part of λ_p approximates the magnitude of λ_p, so that for the TM polarization,

$$\kappa \simeq \frac{4}{3}\frac{L^{3/2}}{\sqrt{\alpha W}}. \tag{13}$$

For the TE polarization, $\kappa \simeq n_\lambda L/(2\sqrt{\alpha W})$. Figure 7 shows the condition number of $\overline{\mathbf{Z}}$ for $L = 10$ as a function of width W. The decrease in condition number as W increases is due to the tilting of the direction of propagation of the fields radiated by the mode closest to resonance. As the direction moves away from normal, radiation loss increases, the eigenvalue grows, and the condition number decreases.

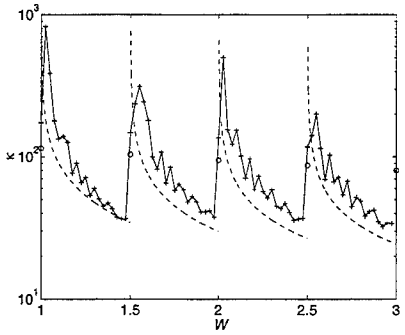

Figure 7: Condition number of $\overline{\mathbf{Z}}$ for parallel strips, $L = 10$. Pluses: computed value. Dashed line: theory, off–resonance, Eq. (13). Circles: theory, at resonance.

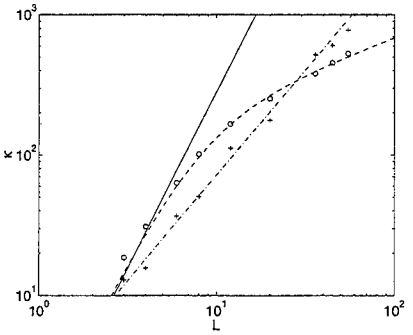

Figure 8: $\kappa(\overline{\mathbf{Z}})$, parallel strips. Circles: computed, at resonance ($W = 2$). Pluses: computed, off–resonance ($W = 2.2$). Solid line: theory, at resonance, $n_\lambda = \infty$. Dashed line: theory, at resonance, $n_\lambda = 10$. Dash-dot line: theory, off–resonance. (Predicted curves scaled by a factor of 1.5.)

Figure 8 shows the condition number as a function of L at resonance ($W = 2$) and off–resonance ($W = 2.2$). At resonance, the smallest eigenvalue approaches the origin along the imaginary axis. Since sampling error is imaginary, the resonant eigenvalue eventually stops moving towards the origin as the cavity size increases. Away from resonance, the smallest eigenvalues are closely spaced on a circle which approaches the origin along the real axis, so that sampling error does not keep them away from the origin. Thus, the condition number of the impedance matrix grows faster with problem size for a non–resonant frequency for large L than at resonance.

In addition to ill–conditioning, resonant modes also cause *a posteriori* residual–based error bounds [5, 6] to break down. These bounds rely on the closeness of fractional order Sobolev norms to the inverses of the TE and TM EFIEs. For resonance–regime structures, long range

coupling produces eigenvalues which depend on the scatterer size and cause these norms to differ significantly from the operator inverses, so that the Sobolev norm of the residual no longer provides a good estimate of the solution error. The effect is most severe for the cavity at resonance, but also occurs for the cavity away from resonance and for the strip as well. These eigenvalues also cause the residual itself to become a poorer indicator of solution convergence.

5. Conclusion

We have given the condition number scaling for a conducting strip and resonant cavity for the TM and TE polarizations, and identified three sources of ill–conditioning: increasing discretization density, surface wave self–coupling, and resonance. Changing to a second–kind integral equation eliminates the first two sources, but real (not internal) resonances still cause ill–conditioning. Near–neighbor preconditioners reduce the growth rate with discretization density, but do not eliminate the growth with scatterer size.

We have also determined the spectral error introduced by discretization for piecewise polynomial bases. The results show that error can be smaller for simpler discretization schemes, but there is a trade–off between the complexity of the discretization and the sensitivity to irregular discretization and geometrical modeling error. In addition, with a proper choice of basis and quadrature rule, the spectral error is independent of problem size for both the strip and the cavity.

References

[1] M. B. Gedera, L. N. Medgyesi–Mitschang, R. Pearlman, J. M. Putnam, and D. Wang, "Modeling accuracy of method of moments," ACES, pp. 1194–1201, 1995.

[2] N. Heuer, E. P. Stephan, and T. Tran, "Multilevel additive Schwarz method for the h-p version of the Galerkin boundary element method," *Math. of Comp.*, vol. 67, pp. 501–518, Apr. 1998.

[3] H. Holm, M. Maischak, and E. P. Stephan, "The hp–version of the boundary element method for Helmholtz screen problems," *Computing*, vol. 57, pp. 105–134, 1996.

[4] E. P. Stephan and T. Tran, "Domain decomposition algorithms for indefinite hypersingular integral equations: the h and p versions," *SIAM J. Sci. Comput.*, vol. 19, pp. 1139–1153, Jul. 1998.

[5] E. F. Kuester, "Computable error bounds for variational functionals of solutions of a convolution integral equations of the first kind," *Wave Motion*, vol. 22, pp. 171–185, 1995.

[6] M. Feistauer, G. C. Hsiao, and R. E. Kleinman, "Asymptotic and a posteriori error estimates for boundary element solutions of hypersingular integral equations," *SIAM J. Numer. Anal.*, vol. 33, pp. 666–685, Apr. 1996.

[7] S. Wandzura, "Accuracy in computation of matrix elements of singular kernels," ACES, pp. 1170–1176, 1995.

[8] A. F. Peterson, R. Mittra, and S. R. Ray, *Computational methods for electromagnetics.* IEEE Press, 1998.

[9] M. D. Pocock and S. P. Walker, "The complex bi–conjugate gradient solver applied to large electromagnetic scattering problems; computational costs, and cost scalings," *IEEE Trans. Ant. Propag.*, vol. 45, no. 1, pp. 140–146, 1997.

hp-ADAPTIVE FE MODELING FOR MAXWELL'S EQUATIONS
Evidence of exponential convergence

W. Rachowicz, L. Demkowicz, L.Vardapetyan

Texas Institute for
Computational and Applied Mathematics
The University of Texas at Austin

Abstract

The *hp*−edge finite elements for steady-state Maxwell's equations are studied. Numerical evidence of exponential convergence for certain *hp*-discretizations is presented.

The *hp*-FEM for Maxwell's equations. This note provides a brief update of our work on the *hp*-adaptive Finite Element Method for steady-state Maxwell's equations. In the *hp*-methods, we can vary *locally* element size h and order of approximation p. The discretization proposed in [4, 13] generalizes Nedelec's rectangular elements of the first type [9] and his triangular elements of the second type [10]. Our two-dimensional implementation of the *hp*-FEM with hierarchical shape functions, $2Dhp90_EM$, utilizes the idea of *constrained approximation* [11]. An example of an *hp*-mesh is given in Fig. 1. Elements vary in size and different shades correspond to different orders of approximation. The method developed in [4, 13] guarantees stability and convergence of the approximation [4, 8]. As an illustration, Fig. 2 presents the solution of the 'two cylinders' problem [7] on the *hp*-mesh of Fig. 1. The solution is oscillation-free in the entire range of frequencies ω, including $\omega \to 0$.

Figure 1: Example of an *hp*-mesh

Figure 2: Two cylinders problem: E_x component

There are at least two arguments in favor of using *hp*-discretizations for practical computations. The first argument stems from the work of Ihlenburg and Babuška [6] who studied

how order of approximation p affects pollution error (related to phase error) in FE simulations. The authors showed that as the order of approximation increases, the pollution error significantly decreases. This means that higher order elements not only lower the interpolation error of the numerical solution but also *stabilize* Galerkin discretization. Thus, if possible, the higher order elements should be preferred in computations. Obviously, high p leads to elements of large size. In order to adequately approximate fine scale geometry, smaller size elements of low order are often needed. It is for these problems the co-existence of small elements of low order with the large elements of high order in the same mesh becomes crucial.

The second and more frequently used argument relies on the ability of hp-methods to deliver *exponential rates of convergence.* In the actual computations, an *a-posteriori* error estimation [2] is used to produce the hp-mesh which minimizes the error for a prespecified number of degrees of freedom or, equivalently, minimizes the problem size within a prescribed error tolerance.

The superiority of the hp-adaptive discretizations over classical uniform meshes and h-adaptive or p-adaptive methods is usually demonstrated by showing that *only* an optimal distribution of p and h can guarantee the exponential convergence for a wide class of problems, including those with irregular and singular solutions [12]. In this note we would like to present two numerical examples illustrating the possibility of such a convergence.

Exponential convergence result for a regular solution: Oblique wave problem. We solve the steady-state Maxwell's equations in a square domain $\Omega = (0,1)^2$, with Dirichlet boundary conditions. The boundary data and the impressed current correspond to the exact solution:

$$E_x = -kn_2 \sin(k\boldsymbol{n} \cdot \boldsymbol{x}) \quad E_y = kn_1 \sin(k\boldsymbol{n} \cdot \boldsymbol{x})$$
$$k = \omega = 3.0, \quad \boldsymbol{n} = (n_1, n_2) = (0.6, 0.8)$$

The $\boldsymbol{n}$ vector intersects with computational meshes at an oblique angle. For regular solutions, the p-method alone should deliver exponential convergence. We discretize the domain with a mesh of 6×6 elements, using uniform p-refinements with $p = 1, 2, 3, 4$. The convergence results are summarized in Fig. 3 – 4.

The error is measured in L^2-norm and $H(curl)$-seminorm. The convergence rates for the p-refinements are compared with (algebraic) convergence rates corresponding to uniform h-refinements.

Exponential convergence result for a singular solution: Diffraction problem. We consider the diffraction of a plane wave on a semi-infinite conducting screen. The problem is set up in a square domain $\Omega = (-1,1)^2$ shown in Fig. 5, with Dirichlet boundary conditions that correspond to the exact solution of the diffraction problem in the entire plane.

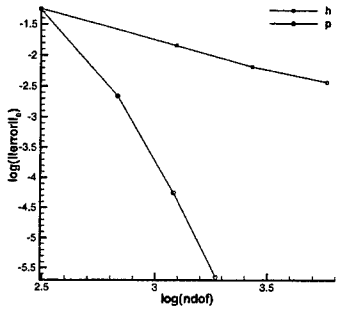

Figure 3: Smooth problem: exponential convergence in L^2-norm for the p-method

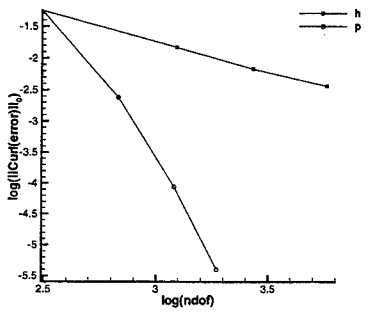

Figure 4: exponential convergence in $H(curl)$-seminorm for the p-method

$$H(r,\phi) = \frac{1}{\sqrt{\pi}} e^{\frac{\pi j}{4} - jkr} \left\{ F\left[(2kr)^{\frac{1}{2}} \sin\frac{1}{2}(\phi - \phi^{inc})\right] + F\left[(2kr)^{\frac{1}{2}} \sin\frac{1}{2}(\phi + \phi^{inc}\right]\right\}$$

$$\phi^{inc} = \frac{\pi}{2}$$

$$F(u) = \frac{1}{2}\sqrt{\pi} e^{ju^2} \left\{ e^{-\frac{\pi j}{4}} - \sqrt{2}\left[C\left(\sqrt{\frac{2}{\pi}}u\right) - iS\left(\sqrt{\frac{2}{\pi}}u\right)\right]\right\}$$

$$C(z) - jS(z) := \int_0^z e^{-\frac{1}{2}\pi j t^2}\, dt \text{ - Fresnel integrals}$$

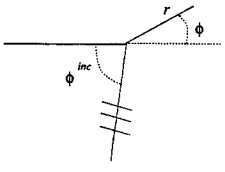

Figure 5: Diffraction problem

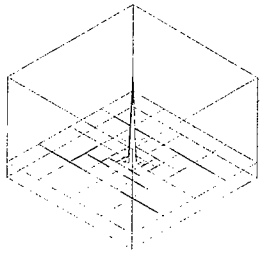

Figure 6: Error in the imaginary part of E_x near the singularity

Our initial uniform mesh consists of 8×8 linear elements. To reach exponential rates of convergence, we discretize the domain with geometrically graded meshes using a Babuška-type strategy. Away from the singularity, we conduct uniform p-refinements, whereas near it

we perform up to 9 levels of h-refinements. The details on the construction of adaptive meshes will be presented elsewhere. Fig. 7 and Fig. 8 demonstrate the evidence of exponential rate of convergence for our hp-adaptive meshes. For comparison, the error plots for h-adaptive meshes of linear elements are also presented. It is evident from the plots that the h-adaptivity may provide only algebraic rates of convergence.

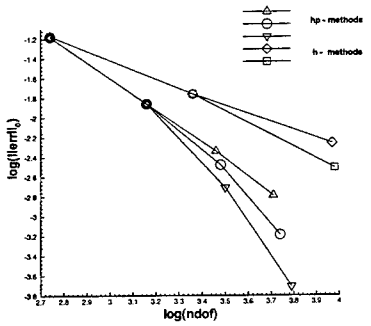

Figure 7: Screen problem: exponential convergence in L^2-norm for the hp-method

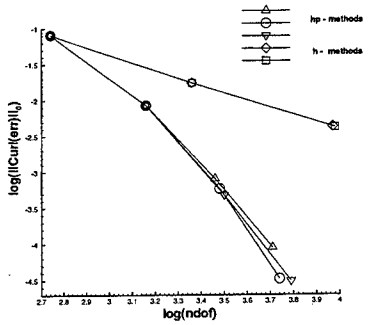

Figure 8: exponential convergence in $H(curl)$-seminorm for the hp-method

A sample solution on a representative intermediate mesh is presented in Fig. 9 – 12.

To conclude, we present in Fig. 6 the distribution of the point-wise error in the imaginary part of the E_x component. The plot shows the error in the vicinity within .0039 units from the origin. As expected, most of the error is localized right around the singular point.

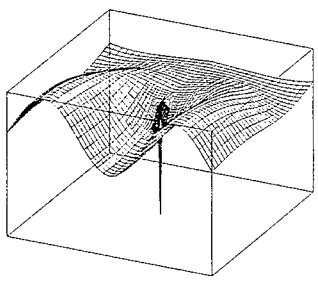

Figure 9: Screen problem: real part of E_x component

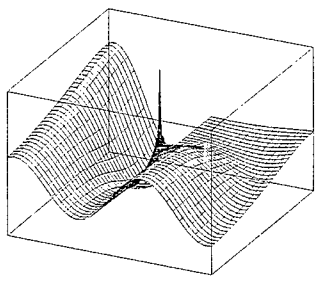

Figure 10: Imaginary part of E_x component

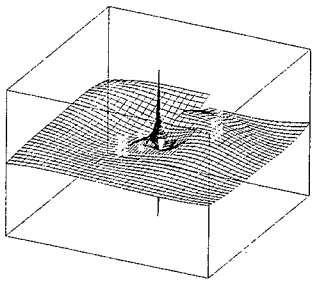

Figure 11: Screen problem: real part of E_y component

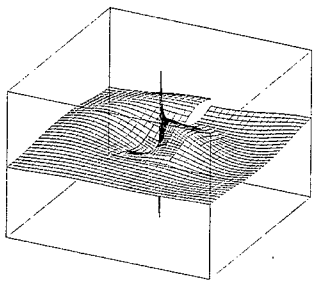

Figure 12: Imaginary part of E_y component

References

[1] W. Cecot, L. Demkowicz, and W. Rachowicz, "A Two-Dimensional Infinite Element for Maxwell's Equations", submitted to *Computer Methods in Applied Mechanics and Engineering.*

[2] L. Demkowicz, "A Posteriori Error Analysis for Steady-State Maxwell's Equations", in *Advances in Adaptive Computational Methods in Mechanics*, ed. P. Ladaveze and J.T. Oden, Elsevier, 1998.

[3] L. Demkowicz and M. Pal, "An Infinite Element for Maxwell's Equations", *Computers Methods in Applied Mechanics and Engineering*, in print.

[4] L. Demkowicz, L. Vardapetyan , "Modeling of Electromagnetic Absoption/Scattering Problems Using *hp*-Adaptive Finite Elements", *Computer Methods in Applied Mechanics and Engineering*, **152**, 1-2, 103-124, 1998.

[5] L. Demkowicz, T. Walsh, K. Gerdes, and A. Bajer, "2D hp-Adaptive Finite Element Package. Fortran 90 Implementation (2Dhp90)", *TICAM Report 98-14*, June 1998, The University of Texas at Austin, Austin, TX 78712.

[6] F. Ihlenburg and I. Babuška, "Finite Element Solution to the Helmholtz Equation with High Wave Number. Part I: The h-Version of the FEM", *Institute for Physical Science and Technology, Technical Note BN-1159*, November 1993.

[7] J. Jin, *The Finite Element Method in Electromagnetics*, John Wiley & Sons, Inc., New York 1993.

[8] P. Monk, L. Demkowicz, and L. Vardapetyan, "Discrete Compactness and the Approximation of Maxwell's Equations in $\mathbb{R}^3$", preprint, October 1998.

[9] J.C. Nedelec, "Mixed Finite Elements in $\mathbb{R}^3$", *Numerische Mathematik*, **35**, 315-341, 1980.

[10] J.C. Nedelec, "A New Family of Mixed Finite Elements in $\mathbb{R}^3$", *Numerische Mathematik*, **50**, 57-81, 1986.

[11] W. Rachowicz and L. Demkowicz, "A Two-Dimensional hp-Adaptive Finite Element Package for Electromagnetics", *TICAM Report 98-15*, July 1998, accepted to *Computer Methods in Applied Mechanics and Engineering.*

[12] W. Rachowicz, J.T. Oden, and L. Demkowicz, "Toward a Universal h-p Adaptive Finite Element Strategy: Part 3. Design of h-p Meshes", *Computer Methods in Applied Mechanics and Engineering*, **77**, 181-212, 1989.

[13] L. Vardapetyan and L. Demkowicz, "*hp*-Adaptive Finite Elements in Electromagnetics", *Computers Methods in Applied Mechanics and Engineering*, in print.

PLENARY SESSION 2

Magdy Iskander

Multimedia- and Computer-Based Engineering Education

Magdy F. Iskander
Electrical Engineering Department
University of Utah
Salt Lake City, Utah 84112

Abstract

Multimedia technology provides a valuable resource to boost interest in engineering education and enhance the ability to teach and to learn from engineering courses. The ability to combine visualization of complex mathematical and abstract subjects, gain experience with virtual laboratories, develop guided use of simulation software, and even experience virtual participation in practical applications are among the many advantages of technology-based education. In this paper we describe and demonstrate the main features of four multimedia CD-ROMs developed by the CAEME Center for Multimedia Education and Technology. This includes the *Physics Museum*, *Calculus Castle*, the Genetics CD-ROM, and the most recent CD-ROM on Engineering Electromagnetics. In addition to describing and demonstrating the features of the developed multimedia CD-ROMs, results from statistical studies showing benefits from multimedia and technology-based education will be discussed. Preliminary results from controlled educational experiments show that students learn by an average of 20% more when exposed to multimedia components in their learning and studying of their technical subject.

Introduction

The use of simulation software as part of engineering education is a common practice, and its advantages are well known. Simulation software allows students to experiment with phenomena and practice with designs which are too complex to calculate or expensive to reproduce in a laboratory. Furthermore, many simulation software packages are extensively used in industry and it is important that students practice and be familiarized with the use of software to simulate and design engineering problems.

The CAEME Center for Multimedia Education and Technology at the University of Utah has been developing software packages for engineering education with focus on "electromagnetics" since 1990. The first product from the Center was a compilation of 16 simulation software packages developed by engineering schools from universities across the USA [1]. The published book and associated software were well received, but many instructors reports limited use because of the extensive effort needed to integrate the software into established and traditional structures of academic courses. Instructors suggested that a stand-alone product which requires minimum intervention by teachers would be more effective in helping the integration of software in regular classroom teaching and would even be more useful to students in their individual studies.

In response to these suggestions, the CAEME Center included several tutorials in its second software book in electromagnetics [2, 3]. To date, the Center focuses its activities on the development of fully interactive multimedia products which include virtual laboratories, functional virtual instruments, animation and visualization of dynamic phenomena, and virtual experiences with practical applications in addition to the guided use of simulation software. It is important to note that the

development of multimedia products is expensive and time consuming. Therefore, it is necessary that focus be placed on the development of subject and concepts that can benefit most from the multimedia technology. Emphasis should be placed on enhancing interactivity to help students simulation, experiment, manipulate and use instruments, and even experience some aspects of practical applications. It is well known that these are the difficult-to-prepare multimedia components, but they are the elements known to enhance learning and increase benefits of multimedia- and technology-based education.

In the following sections, the procedure for implementing the interactive multimedia components in the CD-ROM products developed by the CAEME Center will be described in more detail.

Brief Description of the Developed Multimedia CD-ROMs

In addition to the two software books on electromagnetics, CAEME developed four interactive multimedia CD-ROMs in calculus, physics, genetics, and engineering electromagnetics. The following is a brief description of each of these CD-ROMs:

a. The *Calculus Castle*

This multimedia CD-ROM presents users with an animated three-dimensional castle housing eight complete calculus lessons. By selecting a topic in calculus from the main menu, users move through the castle into rooms which lead to lessons on the selected topics. Examples of topics include polar functions, limits, area under curves, rules of differentiation, particle motion, and definite integrals. In all, over eight hours of discussion are included with emphases placed on visualization, interactive Q&A sessions, and most importantly, experiences with applications of topics in calculus. Once inside the lessons, users learn by watching and interacting with animated graphics, listening to narration, running external software, and taking quizzes to evaluate their understanding.

b. The *Physics Museum*

The *Physics Museum* provides an environment of learning basic physics concepts by conducting experiments in virtual laboratories. As the user enters the museum, he faces three virtual elevators which lead to various laboratories in physics. The first elevator leads to lessons on vectors and coordinate systems, and mechanics. The second elevator leads to lessons on circuits, electrostatics, and principles of wave propagation; while the third elevator has topics on optics, acoustics, and the Frantic Physics action game. All lessons integrate two- and three-dimensional graphics, sound, video, and narration, and interactive multimedia virtual laboratories. Examples of the developed virtual labs include Coulomb's experimental apparatus, experimental verification of Snell's law, electric circuits laboratory, and several experiments illustrating acoustical concepts such as Doppler shift and interference of sound waves.

c. The Genetics CD-ROM

This multimedia CD-ROM focuses on the natural history of human genetics. Topics include the cell structure, Mandellian Genetics, DNA extraction experiments, Meioses and Mitoses, and an interactive criminal investigation demonstrating the application of DNA tests in criminal investigations.

d. Engineering Electromagnetics

The developed CD-ROM contains lessons that constitute a complete introductory course in electromagnetics. This includes electrostatics, magnetostatics, Maxwell's equations, electromagnetic waves, dielectric materials and their applications, transmission lines, antennas, and an extensive package of simulation software including 2D FDTD, MoM, transmission line solution on the Smith Chart, and a 2D Finite Element code written in LabVIEW. It is interesting to note that even in introducing a highly mathematical topic like Maxwell's equations, dependence on equations and text was minimized and instead users were taken back to the laboratory of the pioneers who experimentally developed these equations and were presented with virtual apparatus and allowed to conduct the same experiments which lead to the development of these equations. Every effort was made to describe and emphasize practical applications of electromagnetic fields not by listing and/or describing these applications but by allowing the user to experience these applications in virtual environments.

Enhanced Interactivity

As mentioned in earlier discussion, it is important to include as much student interaction with the multimedia application as possible to help maintain interest, increase effectiveness of learning, improve retention, and enhance exploration. It is believed that interactivity is the cornerstone for a good multimedia educational product and effective multimedia tutoring. In a multimedia product, interactivity may be enhanced by including the following:

- simulation software
- virtual laboratories
- use of intelligent virtual instruments such as those that may be developed using LabVIEW
- using gaming strategy
- by providing the student with the ability to navigate through the lesson and the freedom to tailor it to his needs.

It should be noted that these benefits do not come without cost. The more complex and detailed multimedia environments are, the more taxing on the underlying system. Applications that contain extensive video, narration, sound effects, graphics, and extensive navigation capabilities can become slow, choppy on less-capable computers, and present excessive demands on memory size and hardware capabilities. This does not mean that these elements should be avoided, but with proper planning and preparation, these concerns can be greatly alleviated.

Figures 1 and 2 show some results from simulation software packages included in the electromagnetics CD-ROM. The first demonstrates real-time results from the 2D FDTD code, while the other shows results from the Smith chart transmission line simulation software package.

Figures 3 and 4 show screen captures illustrating some of the developed virtual laboratories. Figure 3 shows the Biot-Savart experiment virtual laboratory, while Fig. 4 shows the transmission line impedance measurements virtual lab.

Figure 5 shows the Time Domain Reflectometer virtual instrument developed using LabVIEW, while Fig. 6 shows the navigation toolbar used in all the CAEME CD-ROMs. Figure 7 shows an

example of a virtual experience with a practical application, the microwave method for lung water measurements.

These, as well as other features of the interactive multimedia CD-ROM products developed by the CAEME Center, will be described and demonstrated in the presentation. In addition, comments will be made and statistical data will be presented regarding the effectiveness and the educational value of computer- and multimedia-based instruction.

References

1. M. F. Iskander, *et al.*, "NSF/IEEE CAEME Center: An Exciting Opportunity to Align Electromagnetics Education with the Nineties," *Comput. Appl. Eng. Educ.*, Vol. 1, No. 1, 1992/93, pp. 33-44.
2. M. F. Iskander, *et al.*, "Computer-Based Electromagnetic Education," *IEEE Trans. Microwave Theory Techniques*, Vol. 41, No. 6/7, 1993, pp. 920-931.
3. M. F. Iskander, *et al.*, "Interactive Multimedia CD-ROMs for Education," *Comput. Appl. Eng. Educ.*, Vol. 4, No. 1, 1996, pp. 51-60.

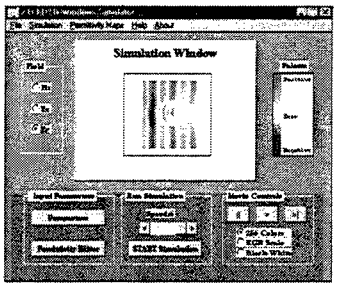

Figure 1. A screen caputured during a simulation performed with the 2D FDTD software package.

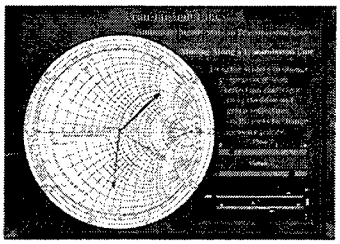

Figure 2. A screen from the Electronmagnetics CD-ROM illustrating the use of the Smith Chart.

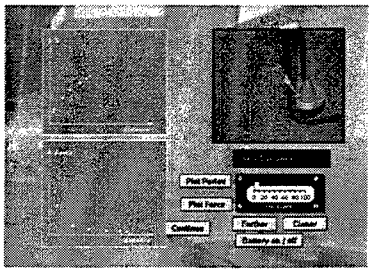

Figure 3. Biot-Savart experiment virtual laboratory.

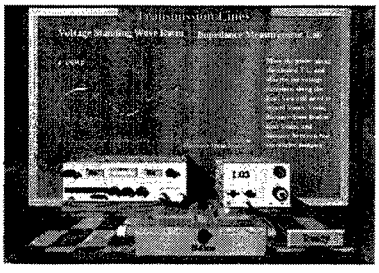

Figure 4. Transmission line impedance measurement virtual laboratory.

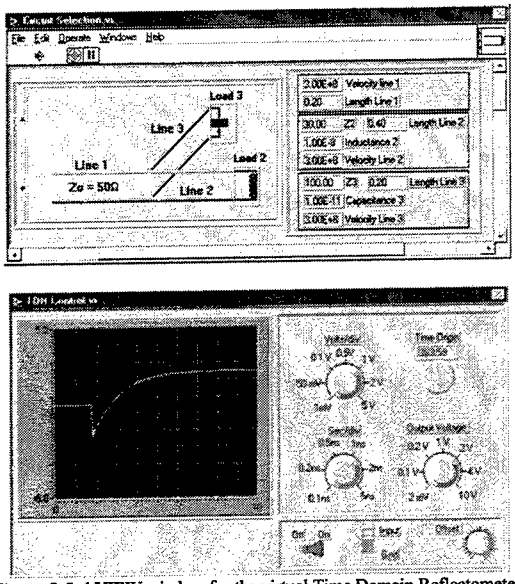

Figure 5. LabVIEW window for the virtual Time Domain Reflectometer.

Figure 6 . The toolbar used for navigation in all the CAEME CD-ROMS.

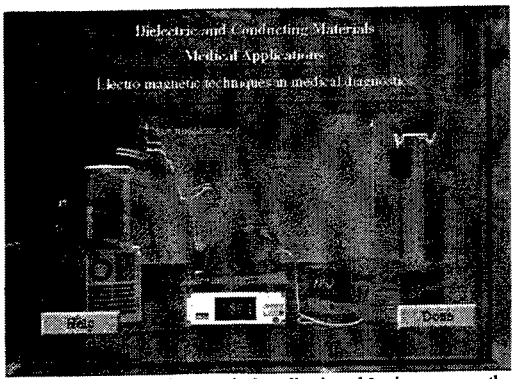

Figure 7. An example of a virtual experience with a practical application, the microwave method for measuring changes in lung water content.

SESSION 4

FINITE ELEMENTS I

Chairs: Leo Kempel and Jianming Jin

Electromagnetic Modeling of Microstrip Structures in Multilayer Media

Feng Ling[1], Jian-Ming Jin[1], Da-Gang Fang[2] and Ningning Feng[2]

[1]Center for Computational Electromagnetics
Department of Electrical and Computer Engineering
University of Illinois at Urbana-Champaign
Urbana, Illinois 61801-2991

[2]Millimeter Wave Techniques Laboratory
Department of Electrical Engineering
Nanjing University of Science and Technology
Nanjing 210094, China

1 Introduction

Electromagnetic modeling of microstrip structures, such as antennas, circuits and interconnects, becomes more and more essential comparing with the traditional quasi-static methods. For this purpose, a variety of methods have been developed. A review of them reveals that the method of moments (MoM) solution of the integral equation has received intense attention. In this method, the evaluation of Green's functions and the choice of basis functions are crucial to obtain an accurate and efficent solution. Therefore, many variations of this method have been implemented. Among them, the solution based on the mixed potential integral equation (MPIE) using the Rao-Wilton-Glisson (RWG) basis function [1] is an attractive approach [2]–[4], because the RWG basis function offers more flexibility to model arbitrarily shaped structures, and MPIE provides less singular kernel comparing with the electrical field integral equation (EFIE).

On the other hand, when microstrip structures become more and more complicated, multilayer media are employed to allow for more versatile designs [4], [5]. This fact necessitates the modeling to be capable of dealing with microstrip structures in multilayer media. To achieve this goal, the derivation of Green's functions for multilayer media is crucial. As we know, the spatial domain Green's function is the inverse Hankel transform of the spectral domain counterpart, which is commonly known as the Sommerfeld integral (SI). Generally speaking, the analytical solution of the SI is not available, and the numerical integration is time-consuming since the integrand is both highly oscillating and slowly decaying. Several efficient techniques have been developed to speed up this numerical integration, such as the method of averages [6] and the asymptotic extraction [7]. To further accelarate the computation, the scheme that precomputes the integrals and uses table lookup and interpolation techniques is popularly used [4]. Another approach to rapidly evaluate the SI is the discrete complex image method (DCIM) [8]–[11]. The basic idea of the DCIM is to approximate the spectral kernal by a sum of complex exponentials using the Prony method or the generalized pencil-of-function (GPOF) method [12]. Then,

the SI's can be evaluated in closed forms via the Sommerfeld identity. This method has been extensively employed to analyze microstrip structures. However, most of the work is confined to single-layered or double-layered structures because of the difficult treatment of surface-wave contribution for multilayer media.

This paper first presents the MPIE formulation for a general microstrip structure in multilayer media and the MoM solution to this equation. Then, we derive the spectral domain Green's functions for multilayer media. The DCIM is employed to efficiently evaluate the SI. It shows that the extraction of surface-wave contribution is not necessary, which makes the DCIM very suitable for multilayer media. Therefore, the spatial domain Green's functions can be represented in closed forms. Combination of the Green's functions and the RWG basis functions offers an accurate and efficient modeling of microstrip structures in multilayer media. Numerical results are presented and a good agreement with measured or published data is observed.

2 Formulations

Consider a general multilayer medium, as shown in Fig. 1. For layer i, the permittivity and permeability are denoted as ϵ_i and μ_i, respectively. In most cases, the bottom is backed by a ground plane and the top is open. The medium is assumed to be laterally infinite. In this section, the MPIE formulation for general microstrip structures is derived. To obtain the spatial domain Green's functions, we first derive analytically the Green's functions in the spectral domain. Then, the DCIM is employed to convert the spectral domain Green's functions into the spatial domain, which can be written as closed forms.

2.1 Mixed potential integral equation

The microstrip structures are assumed to be of infinitesimal conductor thickness and located in the ρ-plane. With excitation by an applied field $\mathbf{E}^a$, the induced current on the microstrips can be found by solving the following MPIE

$$j\omega\hat{z} \times \left[\mathbf{A}(\mathbf{r}) + \frac{1}{\omega^2}\nabla\Phi(\mathbf{r})\right] = \hat{z} \times \mathbf{E}^a(\mathbf{r}) \tag{1}$$

where the vector and scalar potentials can be expressed as

$$\mathbf{A}(\mathbf{r}) = \iint_S \bar{\mathbf{G}}_A(\mathbf{r},\mathbf{r}') \cdot \mathbf{J}(\mathbf{r}')ds' \tag{2}$$

$$\Phi(\mathbf{r}) = \iint_S G_q(\mathbf{r},\mathbf{r}')\nabla' \cdot \mathbf{J}(\mathbf{r}')ds' \tag{3}$$

in which $\bar{\mathbf{G}}_A$ and G_q denote the Green's functions for the vector and scalar potentials, respectively.

To solve the integral equation (1) by the MoM, we first divide the microstrips into triangular elements and then expand the current on the microstrips using the RWG basis function [1]. Applying Galerkin's method to (1) results in a matrix equation. The current on the microstrips can be obtained by solving the matrix equation.

The fast evaluation of the Green's functions is critical for an efficient analysis. However, the spatial domain Green's functions is represented by the SI

$$G_{a,q}(\mathbf{r},\mathbf{r}') = \frac{1}{4\pi}\int_{-\infty}^{\infty} \tilde{G}_{a,q}(k_\rho, z, z')H_0^{(2)}(k_\rho|\rho - \rho'|)k_\rho dk_\rho \tag{4}$$

where G_a is the xx-component of $\bar{\mathbf{G}}_A$ and $\tilde{G}_{a,q}(k_\rho, z, z')$ is the spectral domain counterparts of $G_{a,q}(\mathbf{r}, \mathbf{r}')$, which is time-consuming to evaluate. In the next two subsections, we will give the general form of spectral domain Green's functions and the efficient evaluation of SI's by the DCIM.

2.2 Spectral domain Green's functions

The basic principle to obtain the spectral domain Green's functions due to an arbitrary source embedded in a multilayer medium is to first decompose the fields into TE and TM waves. These TE and TM components are then expanded in terms of the plane waves and their propagations in multilayer media can be characterized by the generalized reflection and transmittion coefficient. For planar microstrip configurations, we consider a horizontal electric dipole (HED) embedded in layer m. The field point is located in layer n. The spectral domain Green's functions for scalar and vector potentials can be written as

$$\tilde{G}_a = \frac{\mu_m}{2jk_{mz}} F_n^{TE} \tag{5}$$

$$\tilde{G}_q = \frac{1}{2j\epsilon_n k_{mz} k_\rho^2} \left(\frac{\mu_m k_n^2}{\mu_n} F_n^{TE} - \frac{\partial}{\partial z_n} \frac{\partial}{\partial z_m} F_n^{TM} \right) \tag{6}$$

where F_n^{TE} and F_n^{TM} are the TE and TM components in layer n, respectively, which can be derived as in [13].

2.3 Discrete complex image method

Once the spectral domain Green's functions are obtained, the next step is to evaluate the SI, which is very time-consuming because of the highly oscillating and slowly decaying behavior of the integrand. Although some techniques have been proposed to fast evaluate the SI, the numerical integration is still the bottleneck to design a fast algorithm. The DCIM obviates numerical integration and represents the SI in a closed form. Initially, the DCIM first extracts the quasi-static and surface-wave contributions from the spectral domain kernel and then approximates the remainding kernel by a sum of complex exponentials and finally evaluates the integral via the Sommerfeld identity. Because the extraction of surface-wave contributions for multilayer media is quite cumbersome, it is difficult to extend the DCIM to multilayer media. The GPOF method has been applied to cast the Green's functions into closed forms, which is more robust and less noise sensitive compared to the original Prony method. The use of GPOF also shows that the extraction of surface-wave contributions is not necessary, which makes it easy to employ the DCIM for the multilayer media.

Rewrite the spectral domain Green's function in a simple form as

$$\tilde{G} = \frac{F}{2jk_{mz}} \tag{7}$$

As the first step of the DCIM, the quasi-static contributions, which dominate as $k_\rho \to \infty$, are extracted first, which makes the remaining kernel decay to zero for sufficently large k_ρ. Therefore, we can rewrite (7) as

$$\tilde{G} = \frac{F - F_0}{2jk_{mz}} + \frac{F_0}{2jk_{mz}} \tag{8}$$

where F_0 denotes the quasi-static term. With the aid of the Sommerfeld identity, the quasi-static contribution from the second term in (8) can be evaluated as

$$G_0 = F_0 \frac{e^{-jk_m\rho}}{4\pi\rho} \tag{9}$$

The first term in (8) can be approximated as a sum of complex exponentials using the GPOF method. The deformed integration path in the complex k_{mz} is chosen as $k_{mz} = k_m\left[(1 - t/T_0) - jt\right]$, where T_0 is determined such that $F - F_0$ becomes negligible beyond T_0. Uniformly sampling $F - F_0$ on $t \in [0, T_0]$ and applying the GPOF method, we can approximate $F - F_0$ as

$$F - F_0 = \sum_{i=1}^{N_c} a_i e^{-k_{mz}b_i} \tag{10}$$

Again using the Sommerfeld identity, we obtain

$$G = F_0 \frac{e^{-jk_m\rho}}{4\pi\rho} + \sum_{i=1}^{N_c} a_i \frac{e^{-jk_m r_i}}{4\pi r_i} \tag{11}$$

where $r_i = \sqrt{\rho^2 - b_i^2}$ is complex, which is the location of the complex image, and N_c is the number of complex images.

As mentioned in [10], when the source is in the bounded region of multilayer media, a modification of the DCIM is necessary. When the source is in the bounded layer, the exponentials are written in terms of the propagation coefficient of the unbounded layer instead of that of the source layer.

3 Numerical Results

First, we verify the spatial domain Green's functions obtained by the DCIM. Consider the three layer medium [11]. The first layer is the free space. The second layer is Teflon with relative permittivity $\epsilon_r = 2.1$ and thickness 0.7 mm. The third layer is GaAs with relative permittivity $\epsilon_r = 12.5$ and thickness 0.3 mm, which is backed by a ground plane. The frequency is 30 GHz. There are four types of Green's functions we seek. The HED can be at the interface of the first and the second layer $m = 1$ or the second and the third layer $m = 2$. The field point also has two choices, $n = 1$ or $n = 2$. The Green's functions of all these four types are given in Fig. 2 compared to those obtained by the numerical integration along the Sommerfeld integration path (SIP). A good agreement can be observed. The computation time for the DCIM is negligible compared to the numerical integration. In this calculation, we choose $T_0 = 20$ and $N_c = 5$.

After the validation of this technique, we incorporate the DCIM into the MoM solution of MPIE for microstrip structures in multilayer media. We first consider a proximity-coupled circular patch antenna. The two substrate layers have the same relative permittivity $\epsilon_r = 2.62$ and thickness 1.59 mm. The microstrip line is on the bottom layer and the patch is on the top layer. The radius of the patch is 17.5 mm and the width of the microstrip line is 4.372 mm. The overlapping length may be used to control the coupling. Here it is 17.5 mm. The input impedance with the reference plane 79.0 mm away from the patch center is given in Fig. 3, which agrees well with the measured data from [16].

We take a two-port asymmetric antenna as another example [17]. The two dipoles on the top layer have the different lengths so that the dual frequency operation is achieved. The two substrate layers have the same relative permittivity $\epsilon_r = 2.17$. The top layer has thickness 1.6 mm and the bottom layer has thickness 0.8 mm. On the top layer there are two orthogonally crossed dipoles. The transversal one has length 11.9 mm and the longitudinal one has length 10.2 mm. The width of them is 1.7 mm. On the bottom layer, the feeding line is 2.2 mm wide. The transversal one is located at a distance of 2.97 mm from the center of crossed dipoles and the longitudinal one is 3.4 mm away. Fed from the port on the left, the transversal dipole is excited at the resonant frequency 8.4 GHz. The current distribution can be seen from Fig. 4(a). Fed from the port on the bottom, the longitudinal dipole is excited at its resonant frequency 9.6 GHz. The current is shown in Fig. 4(b). At 11.2 GHz, both dipoles are resonant. The incident power is essentially transmitted from one port to the other port. The magnitude of S-parameters is given in Fig. 4(c). The measured data are available from [17]. The good agreement can be observed.

4 Conclusion

This paper gives an efficient MoM solution of the MPIE formulation for a general microstrip structure in multilayer media. In this method, the spectral domain Green's functions for multilayer media are derived and then converted to the spatial domain by the DCIM, which obviates the time-consuming numerical integration of the SI. The RWG basis functions are employed to provide more flexibility to model the arbitrary shapes. At last, some multilayer microstrip structures are analyzed. The agreements with measured or pulished data are observed.

Acknowledgment

This work was supported by a grant from AFOSR via the MURI Program under contract number F49620-96-1-0025, the Office of Naval Research under grant N00014-95-1-0848, and the National Science Foundation under grant NSF ECE 94-57735.

References

[1] S. M. Rao, D. R. Wilton, and A. W. Glisson, "Electromagnetic scattering by surface of arbitrary shape," *IEEE Trans. Antennas Propagat.*, vol. 30, pp. 409-418, May 1982.

[2] K. L. Wu, J. Litva, R. Fralich, and C. Wu, "Full-wave analysis of arbitrarily shaped line-fed microstrip antennas using triangular finite-element method," *IEE Proc.-H*, vol. 138, pp. 421-428, Oct. 1991.

[3] R. A. Kipp and C. H. Chan, "Triangular-domain basis functions for full-wave analysis of microstrip discontinuities," *IEEE Trans. Microwave Theory Tech.*, vol. 41, pp. 1187-1194, June/July 1993.

[4] M. J. Tsai, F. D. Flaviis, O. Fordham, and N. G. Alexopoulos, "Modeling planar arbitrarily shaped microstrip elements in multilayered media," *IEEE Trans. Microwave Theory Tech.*, vol. 45, pp. 330-337, Mar. 1997.

[5] E. K. L. Yeung, J. C. Beal, and Y. M. M. Antar, "Multilayer microstrip structure analysis with matched load simulation," *IEEE Trans. Microwave Theory Tech.*, vol. 43, pp. 143-149, Jan. 1995.

[6] J. R. Mosig and F. E. Gardiol, "A dynamical radiation model for microstrip structures," In *Advances in Electronics and Electron Physics*, vol. 59, pp. 139-237. New York: Academic Press, 1982.

[7] D. R. Jackson and N. G. Alexopoulos, "An asymptotic extraction technique for evaluating Sommerfeld-type integrals," *IEEE Trans. Antennas Propagat.*, vol. 34, pp. 1467-1470, 1986.

[8] D. G. Fang, J. J. Yang, and G. Y. Delisle, "Discrete image theory for horizontal electric dipole in a multilayer medium," *IEE Proc.-H*, vol. 135, pp. 297-303, Oct. 1988.

[9] Y. L. Chow, J. J. Yang, D. G. Fang, and G. E. Howard, "A closed-form spatial Green's function for the thick microstrip substrate," *IEEE Trans. Microwave Theory Tech.*, vol. 39, pp. 588-592, Mar. 1991.

[10] R. A. Kipp and C. H. Chan, "Complex image method for sources in bounded regions of multilayer structures," *IEEE Trans. Microwave Theory Tech.*, vol. 42, pp. 860-865, May 1994.

[11] M. I. Aksun, "A robust approach for the derivation of closed-form Green's functions," *IEEE Trans. Microwave Theory Tech.*, vol. 44, pp. 651-658, May 1996.

[12] Y. Hua and T. K. Sarkar, "Generalized pencil-of-function method for extracting poles of an EM system from its transient response," *IEEE Trans. Antennas Propagat.*, vol. 37, pp. 229-234, Feb. 1989.

[13] W. C. Chew, *Waves and Fields in Inhomogeneous Media*, Piscataway: IEEE Press, 1995.

[14] K. A. Michalski and J. R. Mosig, "Multilayered media Green's functions in integral equation formulations," *IEEE Trans. Antennas Propagat.*, vol. 45, pp. 508-519, Mar. 1997.

[15] Y. L. Chow, N. Hojjat, S. Safavi-Naeini, and R. Faraji-Dana, "Spectral Green's functions for multilayer media in a convenient computational form," *IEE Proc.-H*, vol. 145, pp. 85-91, Feb. 1998.

[16] M. Davidovitz and Y. T. Lo, "Rigorous analysis of a circular patch antenna excited by a microstrip transmission line," *IEEE Trans. Antennas Propagat.*, vol. 37, pp. 949-958, Aug. 1989.

[17] R. Gillard, J. Corre, M. Drissi and J. Citerne, "A general treatment of matched terminations using integral equations— modeling and application," *IEEE Trans. Microwave Theory Tech.*, vol. 42, pp. 2545-2553, Dec. 1994.

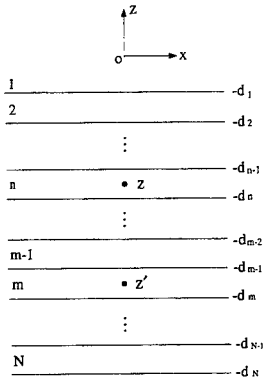

Figure 1: A multilayer medium with source and field points in layer m and layer n, respectively.

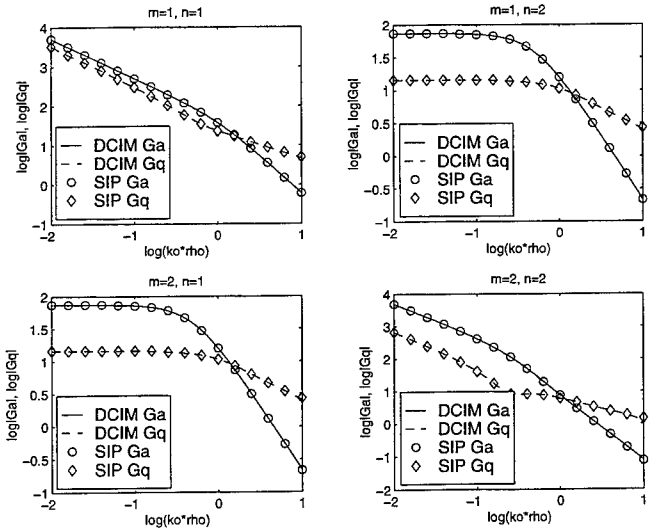

Figure 2: Green's functions of the scalar and vector potentials in three layer medium. The first layer is the free space. The second layer is Teflon with relative permittivity $\epsilon_r = 2.1$ and thickness 0.7 mm. The third layer is GaAs with relative permittivity $\epsilon_r = 12.5$ and thickness 0.3 mm, which is backed by a ground plane. The frequency is 30 GHz.

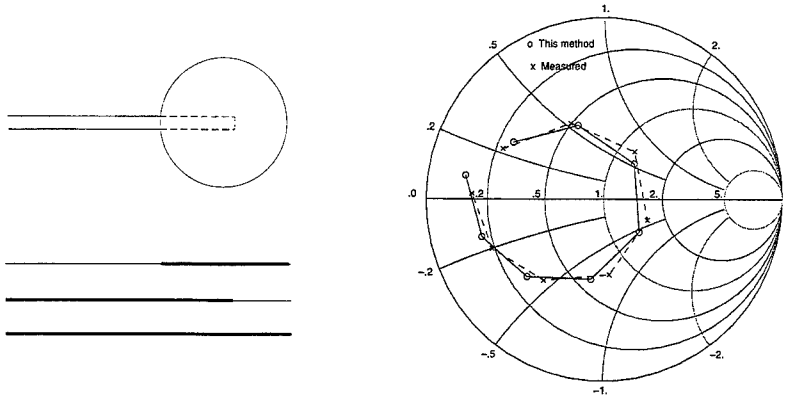

Figure 3: Input impedance for a proximity-coupled microstrip antenna. The frequency is from 2.80 GHz to 3.15 GHz with increment 0.05 GHz.

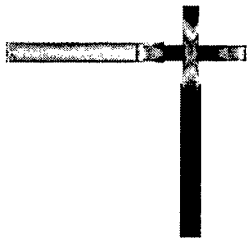

(a) f=8.4 GHz

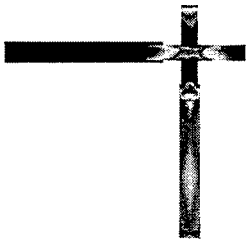

(b) f=9.6 GHz

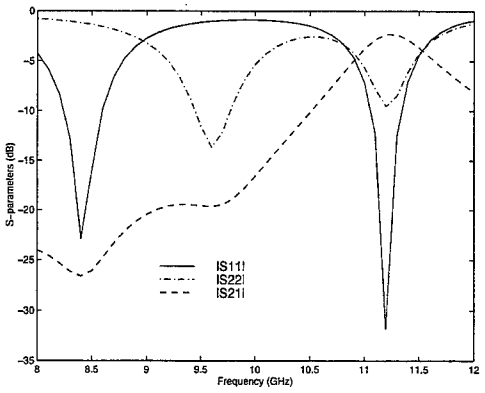

(c)

Figure 4: Current distributions and S-parameters for a two-port asymmetric antenna.

Modeling Wideband Conformal Antennas using Finite Element-Boundary Integral Techniques

Keith D. Trott and Rene D. Guidry
Mission Research Corp
147 John Sims Parkway
(850)729-0855 (voice)
trott@fwb.gulf.net

Abstract

Mission Research Corporation, in collaboration with Michigan State University (MSU), is applying unique, state-of-the-art computational electromagnetics (CEM) tools to investigate the performance parameters of wide bandwidth, multi-modal, conformal antennas. These antennas are used to determine angle-of-arrival (AoA) by means of multi-modal phase comparison. That is, the received phase difference between two simultaneous modes of a signal from a single aperture yields the AoA. We will discuss our efforts to develop finite element mesh generators for these types of antennas and the use of these special meshes with our FE-BI CEM tools to predict antenna performance parameters such as radiation pattern and impedance. Representative data will be discussed.

Introduction

The MRC Team's FE-BI CEM tools permit rapid analysis and design of conformal antennas, with particular emphasis on wide bandwidth, multi-modal antennas such as the ones used in angle of arrival (AoA) or direction finding (DF) applications. These antennas are cavity-backed and flush-mounted on planar, cylindrical, and even doubly-curved surfaces. Our CEM tools are based on the finite element-boundary integral (FE-BI) method. This CEM technology is uniquely capable of modeling complex geometrical and material properties. Below we present a brief summary of the FE-BI method.

Finite Element Boundary Integral (FE-BI) Method

Hybrid finite element methods (HFEM) have been explored for several years, most often being called either the finite element-boundary integral (FE-BI) or the finite element-integral equation (FE-IE) method. Both combine finite element and integral equation methods. Unfortunately, a general FE-IE method is not currently feasible due to heavy computational resource demand. In such a case, electric and magnetic currents are needed on the mesh boundary as well as the three components of the interior field. All IE formulations result in full matrices due to global coupling; hence, the two currents on the mesh boundary impose an excessive computational burden in terms of memory and compute cycles. Therefore, FE-IE formulations typically are restricted to specialized situations such as cavity-backed patches or slots recessed in an infinite metallic surface. In this case, the FE-IE method can be formulated such that it requires only one current (magnetic) over the apertures located within the ground plane or circular cylinder [1]. Accordingly, the memory and computational requirements associated with the mesh boundary is minimized. In addition, very large apertures can be efficiently modeled by exploiting Toeplitz symmetry, present in the IE sub-

matrix, provided these apertures lie in a metallic ground plane or circular cylinder and uniform sampling is used on the mesh boundary. Figure 1 illustrates the application of the FE-IE (or FE-BI) method.

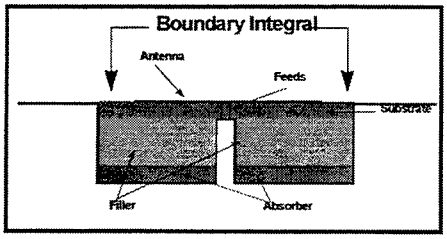

Figure 1: Application of FE-BI to a conformal antenna. Note computational volume.

Anisotropic Planar FE-BI Computer Code

MRC developed and delivered for GUI integration, a Fortran computer code, called PRISM, capable of modeling anisotropic antenna loading materials. This code also permits modeling R-card loads at the top of any layer of the mesh. PRISM uses right prism elements to discretize the volume as well as to expand the unknown electric field. The computer program has the following capabilities:

1. Plane wave incidence.
2. Filamentary feed models.
3. Radar cross section calculation.
4. Power gain calculation for radiation analysis.
5. Voltage at feed pins due to plane wave reception.
6. Input impedance calculation.
7. Anisotropic materials.
8. Resistive (R-card) treatments.

Anisotropic materials can be specified by fully populated symmetric or asymmetric permittivity or permeability tensors. Validation has been performed by comparison with XBRICK results for a patch antenna for both scattering and radiation.

The MRC Team has been a leading innovator in custom FE-BI solutions for antenna analysis. FE-BI is the only leading CEM technology capable of providing the geometric fidelity, efficiency, and accuracy required for demanding conformal antenna design and characterization.

Automatic Mesh Generators

We have developed a stand-alone C language code for each type of antenna we are modeling. These codes will be integrated with a graphical user interface (GUI) currently under design. The basis of the mesh generators is Carnegie-Mellon's (CMU's) TRIANGLE Planar Surface Mesher. It is written in C (source code is freely available), uses X-Windows

interface for mesh viewing, and we currently have it running on our SGI and other machines using Linux. We have created mesh generators for the log-periodic, the equiangular spiral, the Vivaldi notch, and the sinuous spiral. The associated polarization of the circular antennas is given below:

1. Circular log-periodic (linear polarization).
2. Spiral (circular polarization).
3. Sinuous Spiral (dual circular or linear polarization).

Log-Periodic Antenna Comparison:

AFRL/SNRP built a log-periodic antenna and measured it using their RASCAL facility. The antenna was then modeled using our FE-BI code and compared to the measurements. The results were very good and were presented at the 1998 URSI Radio Science Meeting [2] and are shown below in Figure 2.

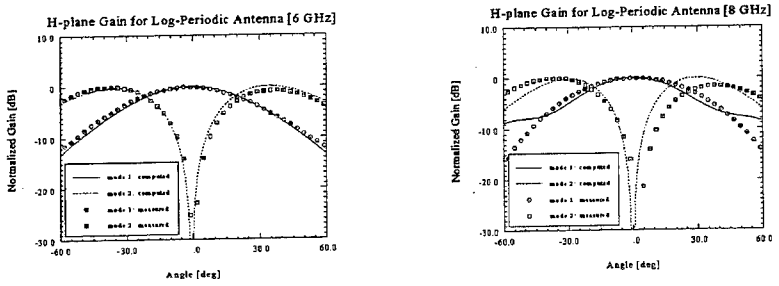

Figure 2: Comparison of measured and calculated data for 6 and 8 GHz

Spiral Mesh Generator

Mesh generators have been developed for both two-arm and four-arm equiangular spiral antennas (SPIRAL2 and SPIRAL4 respectively). The user can specify typical spiral antenna attributes such as the antenna flare rate, maximum amount of rotation of the spiral arms, and initial distance between the antenna arms. The codes, SPIRAL2 and SPIRAL4, are actually mesh generator interfaces used to create the input files used by TRIANGLE. TRIANGLE creates the triangular mesh, based on the input parameters specified by the user when SPIRAL2 or SPIRAL4 is run. SHOWME, also developed by CMU, is used to view the resulting mesh. Once the mesh files have been generated by TRIANGLE, an MRC developed code (INTERFACE) is used to create an input file for PRISM (our FE-BI code). PRISM is then used to calculate various electromagnetic parameters such as input impedance, radiation patterns, and far-field patterns. A relatively new feature of PRISM is the ability to calculate the electric surface fields. MRC developed codes, such as EDGER, provide an ability to decompose the surface field into components (x, y, total, rho, or phi). These fields may then be viewed in the MATLAB environment using MRC developed codes

such as FIELDVIEW or PHASEVIEW. Figure 3 provides an example of the spiral's surface fields. It should be noted that these plots are on two different scales.

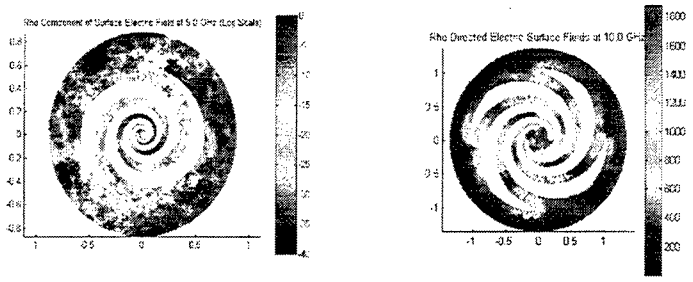

Figure 3: Surface fields for a 2-arm and 4-arm Spiral

Vivaldi Notch Antenna Mesh Generator:

The Vivaldi Notch program creates a data file containing the xy-coordinates of the antenna as calculated by the governing Vivaldi equation. This is an input file used by TRIANGLE to form the mesh and set attributes of the geometry. The meshed file is then used by PRISM to calculate the antenna parameters. As mentioned previously, the Vivaldi Notch antenna is a broadband antenna. Our main goal is to investigate the behavior of the surface fields as a function of frequency. We expected higher frequencies would have the maximum surface field boundary closer to the feed point, and the boundary would move outward from the feed as we decreased frequency. This is demonstrated in our plots. The geometry was modeled after that used by Eric Thiele and Allen Taflove [3]. Figure 4 shows examples for the surface fields in a Vivaldi notch.

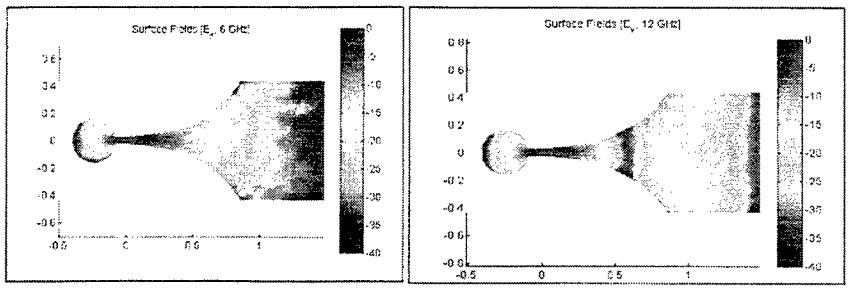

Figure 4: y-component of surface fields for a Vivaldi notch

Sinuous Spiral Antenna

The sinuous spiral antenna is the most difficult to model. This antenna is defined by angles and expansion ratios. Radii are related by the expression

$$R_p = \tau_{p-1} R_{p-1}, \tag{1}$$

where τ_p = ratio of inner-to-outer cell radii and α_p = angular width of cells. For example, $R_2 = \tau_1 R_1$. This ratio can be constant; hence, the inner-most radius would be equal to the outer-most radius by a power of the expansion ratio. A sinuous arm is formed rotating curve $\pm \delta$ about the origin yielding $\alpha_p \pm \delta$. The aperture design is self-complementary when α = 45° and δ = 22.5°. The polar coordinates, r and ϕ, of the sinuous curve are given by

$$\phi = (-1)^p \alpha_p \sin\left[\frac{180 \ln(r/R_p)}{\ln \tau_p}\right] \text{ for } R_{p+1} \le r \le R_p. \tag{2}$$

The details are shown in Figure 5. The angular rotation of a single arm through 360/N increments forms an N-arm structure. Typical four-arm structure develops dual linear and dual circular polarization. Orthogonal linear polarization formed by feeding the opposite arms 180° out of phase. This generates two rotationally symmetric beams linearly polarized with respect to each pair of arms. Dual circular polarization is formed by combining the linear beams with a ± 90° hybrid.

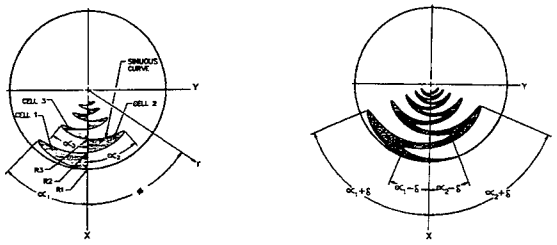

Figure 5: Sinuous spiral geometry

The active region of the antenna is where $2(\alpha_p + \delta)r \approx \lambda/2$. The low frequency is limited by R_1; hence, the low frequency limit is determined by $\lambda_L = 4R_1(\alpha_p + \delta)$. The high frequency limit is bounded by feed point design. The smallest segment should be somewhat smaller than $\lambda/4$; therefore, the upper frequency limit is defined by $\lambda_H = 8R_p(\alpha_p + \delta)$, with the active region moving inward with increasing frequency. An example of the mesh generated by TRIANGLE is shown in Figure 6.

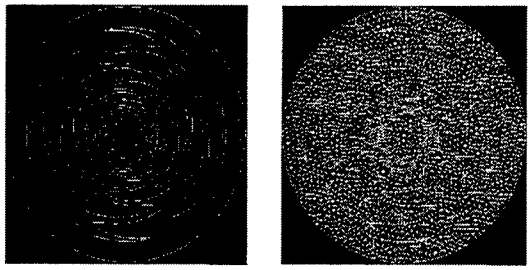

Figure 6: Sinuous mesh generated by TRIANGLE

The output using this mesh in our PRISM code is shown in Figure 7. Note the fields are somewhat aligned to the orthogonal components.

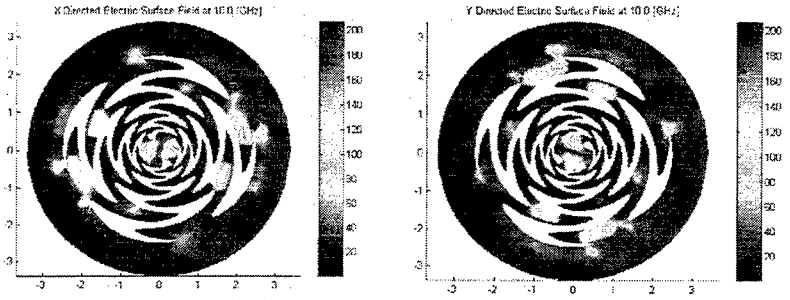

Figure 7: x and y-directed surface fields of sinuous spiral using PRISM code

Antenna Performance Prediction

We have discussed our efforts to develop mesh generators for wideband, multi-modal antennas. These meshes enable accurate and efficient modeling of the performance for these antennas using the FE-BI method. Research continues to determine design parameters that optimize performance of these antennas to solve real-world problems.

References

[1]. L.C. Kempel, J.L. Volakis, and R.J. Sliva, "Radiation by cavity-backed antennas on a circular cylinder," *IEE Proceedings, Pt. H*, 95.

[2]. L.C. Kempel & K.D. Trott, "Progress in modeling complex conformal antennas using the finite element-boundary integral method", URSI Radio Science Meeting, Atlanta, GA, June 98

[3]. E. Thiele & A. Taflove, "FD-TD Analysis of Vivaldi Flared Horn Antennas and Arrays," *IEEE Trans on Antennas and Propagat*, Vol. 42, No. 5, May 94.

The Northrop-Grumman Duct RCS Prediction Code

Yan-Chow Ma*, Sunil Bindiganavale and Maurice Sancer
Northrop Grumman Corporation
8900 E.Washington Blvd.
Pico Rivera
CA 90660
E-mail: ycma@world.northgrum.com
Phone: (562) 948-6700
FAX: (562) 948-6894

Abstract:

The Northrop-Grumman Duct RCS Prediction code is based on the curvilinear hybrid finite element-surface integral equation technique with several novel enhancements designed to cater to the special and formidable requirements of duct and engine inlet analysis. This paper focuses on the unique problems encountered while applying such a numerical technique to the analysis of ducts and the progress made in circumventing them. First, we discuss the formulation of a Computed Relationship (CR) which enables the de-coupling of the finite element and surface integral equation regions. Subsequently, we discuss the novel features of a banded matrix solver developed in-house, which yields considerable savings in execution time and storage in generating the CR from the finite element system. A dense linear system solver from ScaLAPACK is used to solve the surface integral system and its requirements are discussed in the context of our problem. Higher order basis functions to improve the accuracy of RCS predictions or equivalently reduce the number of discretization unknowns are implemented. Numerical results illustrating the code performance are generated on multiple processors of a high performance computing architecture – the SGI Origin 2000.

I. Introduction:

The basic Northrop-Grumman RCS prediction code is the SWITCH code which is based on a hybrid finite element-surface integral equation formulation of the electromagnetic scattering problem. Recently we have developed a special RCS code to predict scattering from ducts and engine inlets. This duct RCS code is based on the same analysis as the SWITCH code, however, it separates the finite element equation portion of SWITCH from its surface integral equation portion. The Northrop-Grumman duct RCS code consists of two codes – Sparse and Dense. Sparse is associated with the finite element equation and Dense is related to the surface integral equation of the discretized Maxwell equations.

The benefit of having two separate codes is that the coefficient matrix associated with Sparse is a symmetric, sparse and banded matrix. The unknowns in Sparse are the interior (N_{ei}) and the aperture (N_{es}) Electric (E) field coefficients and the aperture magnetic (H) field coefficients (N_{hs}). The total number of equations in sparse is N_e ($N_e = N_{ei}+N_{es}$) which is the total number of E-field unknown coefficients. Clearly there are more unknowns than equations in Sparse. Sparse is formulated such that the aperture H field coefficients are treated as the external excitations and we solve for the E field coefficients in terms of the H field coefficients. It has to be noted that for scattering problems we do not need the interior E field coefficients for far field computations. The necessary information at the end of execution of Sparse is a matrix relationship between the aperture E field and aperture H field unknown coefficients. We name this matrix the CR (for

Computed Relationship) matrix. The CR matrix with N_{es} rows and N_{hs} columns is not a square matrix. Also, for practical problems $N_{es} \approx N_{hs}$ and $N_e >> N_{es}$.

Section II describes a special direct solver developed at Northrop-Grumman, specifically for the banded matrices encountered in Sparse, called the Northrop Grumman Direct Sparse Solver (NGDSS). The NGDSS has two novel features – fast CR matrix generation and factored matrix storage reduction. To take advantage of the novel features of NGDSS, the E field unknown coefficients must be numbered in a prescribed manner and the Reverse Cuthill-McKee (RCM) scheme is employed for this numbering. The bandwidth of the sparse matrix is small as a result of using the RCM scheme.

The walls of the duct of interest are assumed metallic, hence the magnetic current vanishes on the walls. The surface integral equation over the duct exterior is comprised of the duct wall and the duct aperture opening with non-zero magnetic current. The aperture magnetic current in these regions is replaced, via CR matrix substitutions, by the aperture electric current. The coefficient matrix of Dense is dense and square of order N_h where N_h ($N_h = N_{hw} + N_{hs}$) is the total number of H field unknown coefficients which includes the aperture opening and the duct wall unknown J (electric current) coefficients.

The scattered far field is obtained by first executing Sparse to obtain the CR matrix, which then serves as the input for Dense. RCS of the duct is obtained at the end of execution of dense.

Section III describes the procedure for connection of the coefficient and right-hand side matrices of Dense to the ScaLAPACK [1] dense equation solver. ScaLAPACK has excellent scaling and portability characteristics on a wide variety of distributed memory and shared memory parallel computing platforms.

The basis and testing functions in Sparse and Dense are the linear roof top functions. A different duct code based on the quadratic, second order Lagrange interpolation polynomial basis functions has also been developed. For a given number of unknowns, the quadratic basis function code is more accurate than the linear roof top basis function code and will be discussed in Section IV.

Numerical results for sample duct geometries, obtained from computer codes utilizing the proposed analysis schemes, are given in Section V. These results were primarily generated on multiple processors of the SGI Origin 2000 shared memory parallel computer located at the Aeronautical Systems Center of the Major Shared Resources Center (ASC-MSRC), Wright-Patterson Air Force Base (Ohio). Sparse was parallelized using data-parallel directives and hence was based on a shared memory programming paradigm. Dense utilizes MPI (Message Passing Interface) thus simulating a distributed memory paradigm on the shared memory computer.

II. The Northrop-Grumman Direct Sparse Solver (NGDSS)

To apply NGDSS, the interior E field unknown coefficients must be numbered before any of the aperture E field unknown coefficients for reasons which will become obvious. The RCM scheme starts with the aperture E field unknown coefficients as the starting unknowns. Next, the unknowns that are the immediate (first level) neighbors of the starting unknowns are numbered. Second level neighbors, immediate neighbors of first level neighbors, are numbered after all first level neighbors. This process is continued until all the unknowns are numbered. At the end, the unknown numbers are reversed and the unknowns associated with the edges of the aperture opening have the highest numbers.

The system of equations (N_e) associated with Sparse can be expressed as

$$A\begin{bmatrix} E_i \\ E_s \end{bmatrix} = \begin{bmatrix} 0 \\ H_s \end{bmatrix} \begin{matrix} \uparrow N_{ei} \\ \downarrow N_{es} \end{matrix} \qquad (1)$$

In equation (1), A is a symmetric, sparse, square matrix of order N_e. There are N_{hs} right-hand sides where the first N_{ei} rows of the right-hand side matrix are zero elements. Since matrix A is symmetric, it can be factored using the LDL^T factorization algorithm

$$A = LDL^T \qquad (2)$$

In equation (2), L is a lower triangular matrix with unit values on the diagonal, D is a diagonal matrix and L^T is the transpose of L and is hence an upper triangular matrix.
After matrix A is factored, the solutions of (1) can be obtained as follows. Let

$$LX_k = b_k \qquad k = 1,2 \ldots N_{hs} \qquad (3)$$

where X_k is some intermediate solution vector, b_k is the k^{th} column of the right-hand side matrix. The intermediate solution vectors in (3) can be obtained by forward substitution. Let

$$DY_k = X_k \qquad k = 1,2 \ldots N_{hs} \qquad (4)$$

The new intermediate solution vectors Y_k can be found easily since D is a diagonal matrix. Let

$$L^T E_k = Y_k \qquad k = 1,2 \ldots N_{hs} \qquad (5)$$

E_k in (5) is the solution vector of (1) corresponding to the k^{th} column of the right-hand side matrix. E_k can be obtained by backward substitutions.
The CR matrix generation can be greatly simplified since the first N_{ei} rows of the right-hand side matrix are zeros. Let

$$X_k = \begin{bmatrix} 0 \\ \tilde{X}_k \end{bmatrix} \begin{matrix} \updownarrow N_{ei} \\ \updownarrow N_{es} \end{matrix} \quad Y_k = \begin{bmatrix} 0 \\ \tilde{Y}_k \end{bmatrix} \begin{matrix} \updownarrow N_{ei} \\ \updownarrow N_{es} \end{matrix} \quad b_k = \begin{bmatrix} 0 \\ H_{sk} \end{bmatrix} \begin{matrix} \updownarrow N_{ei} \\ \updownarrow N_{es} \end{matrix} \qquad (6)$$

The solution procedure given by equations (3)-(5) becomes

$$\tilde{L}\tilde{X}_k = H_{sk}$$

$$\tilde{D}\tilde{Y}_k = \tilde{X}_k \quad k = 1,2 \ldots N_{hs} \qquad (7)$$

$$\tilde{L}^T E_{sk} = \tilde{Y}_k$$

Matrix $\tilde{D}$ is a diagonal matrix of rank N_{es}. The diagonal elements of $\tilde{D}$ are the last N_{es} diagonal elements of the diagonal matrix D. Matrix $\tilde{L}$ is a lower triangular matrix with unit values on the diagonals and of rank N_{es}. It is comprised of the last N_{es} rows and columns of matrix L.

The procedure given by (7) explains the first novel feature of NGDSS, which is its speed in generating the CR matrix once A is factored. In essence it solves a greatly reduced system of equations. The reduction of CPU time by using (7) is of order (N_{es}^2/N_e^2) which is large for practical problems of interest.

The second novel feature of NGDSS can now be explained. It is clear from equation (7) that only the last N_{es} rows and columns of the lower triangular matrix L (i.e. $\tilde{L}$) and the last N_{es} diagonal elements of the diagonal matrix D (i.e. $\tilde{D}$) need to be stored for obtaining the CR matrix. The matrix A is factored one block at a time. In Figure 1 let *nc* be the number of columns per block and *nband* be the bandwidth of matrix A. The memory required to store a block of matrix elements is

*nc*nband* complex numbers. It is not required to store the factored matrix elements separately from the coefficient matrix A since the coefficient matrix elements are overwritten by the factored matrix elements. The factored matrix elements in the first block also partially factor the first *nband* columns of the next block. The total storage is therefore *(nc+nband)*nband* complex numbers for the lower triangular matrix L. In addition we need storage of *nc+nband* complex numbers for the diagonal matrix D.

The procedure to factor matrix A with storage reduction works in the manner described below. First the matrix elements of the first block of coefficient matrix A are computed. This block is factored column by column. Once a column is factored, the partial factorizations of subsequent columns due to this column are computed. The number of subsequent columns is *nband*. This process is continued until the last column (*nc*) is factored and the partial factorizations due to this last column have been computed. The first *nband* columns of the second block have already been partially factored even though the coefficient matrix elements of the second block have not been calculated. Next, the index for matrix elements are shifted. The first *nc* columns of factored matrix A (the first block) can be discarded. The last *nband* columns of the first block become the first *nband* columns of the second block. The original matrix elements of the second block can be computed and superimposed on the partially factored matrix elements. The second block is factored column by column similar to the procedure used for the first block. This process continues until the whole matrix is factored.

The memory requirement for the above procedure is *(nc+nband)*(nband+1)* complex numbers. The RCS of a duct of any size can be analyzed provided that *nband* is not large. Also, no matter how small *nc* is, for very large *nband* values, *(nc+nband)*(nband+1)* complex numbers cannot be stored in memory. For these cases an out-of-core NGDSS has been written but will not be discussed here.

III. Connection of Dense to ScaLAPACK dense solver:

The CR matrix from Sparse will be used to replace the aperture E field unknown coefficients by the aperture H field unknown coefficients. The problem size of Dense is the total number of exterior and aperture H field unknown coefficients.

ScaLAPACK is a library of computational routines, which utilize Message Passing Interface (MPI) for inter-processor communication. Dense was restructured to conform to MPI in order to connect it to ScaLAPACK. A two-dimensional block cyclic data distribution is employed by ScaLAPACK which yields an excellent compromise between load balancing and the ability to use level BLAS3 kernels for efficient computation on individual processors. Such a data distribution requires that the entries of the matrix be allocated to *abstract* processes along its rows and columns such that the product of these processes is equal to the total number of available *physical* processors. If *np* is the total number of available processors, it can be expressed as a product of processes along the matrix row (*nprow*) and column (*npcol*) as

$$np = nprow * npcol \qquad (8)$$

Ideal load balancing requires that *nprow* and *npcol* should be equal thereby necessitating that *np* be a perfect square. However, small deviations from square values for *np* does not deteriorate load balancing appreciably and, in general, the user specifies *nprow* and *npcol* based on processor availability. The coefficient and right hand side matrices are partitioned with two-dimensional blocks such that each processor computes and stores only a fraction of the total matrix. The two-dimensional blocks belonging to a particular processor are stored contiguously thus leading to a rectangular local array of dimensions *nrow* by *ncol*. Each matrix element is thus addressed by a

global index corresponding to the entire matrix and a local index corresponding to the local two-dimensional array of each processor. Integer arrays are used to connect the two sets of indices. It should be noted that the values of *nrow* and *ncol* might vary for each processor. The optimum two-dimensional block is square, with order 64, on most high-performance computing architectures.

The memory requirement for Dense is significant since each processor, requires, in addition to the coefficient and right hand side matrices, the CR matrix and the matrix coefficients associated with the aperture magnetic current. The memory requirement is alleviated, by partitioning the CR matrix, such that each processor stores only the elements required by it in order to perform CR substitutions. Partitioning yields *npcol* sub-matrices thus reducing the storage requirement of each processor by *1/npcol*. Processors with the same row number in the two-dimensional process array store the same elements of the CR matrix.

The memory requirement due to the aperture magnetic current is alleviated, by defining a one-dimensional complex array of size N_{es}. The testing function and associated two patches corresponding to a local or global row number are obtained. The coefficients associated with the aperture magnetic number for the same row number are computed and stored in the array. The CR matrix substitution for any global column number corresponding to the aperture electric current is performed. This complex array can be re-used for different row numbers thereby greatly reducing the memory requirement for the aperture magnetic current. This reduction is at the cost of matrix build time, which increases by approximately a factor of two.

IV. Higher Order Basis Functions for Duct Analysis

RCS prediction accuracy can be greatly improved by using higher order basis functions at the cost of longer matrix build times. However, the total build time continues to be insignificant due to the small number of non-zero elements in the system matrix of Sparse. Higher order basis functions increase the sparse matrix bandwidth and consequently the CPU time for factorization. The significant matrix build time of Dense is further increased by the application of higher order basis functions. Using linear roof top basis functions for testing alleviates this problem, with little deterioration in accuracy.

Second order Lagrange interpolation polynomials (quadratic) were the adopted higher order basis functions, leading to a sparse matrix with twice the bandwidth and consequentially quadrupling the factorization time for equal number of unknowns when compared with roof top basis. Quadratic basis functions can be explained with the aid of Figure 2 where a curved patch has been transformed into a unit square in the u-v plane. Four (2,5,8 and 11) of the twelve unknowns associated with the patch are interior unknowns and have their concomitant basis functions defined over the patch only. The rest (1,3,4,6,7,9,10,12) are boundary unknowns with their basis functions defined both over the patch in the figure and its neighbor sharing the boundary edge. The basis function associated with edge 1 is given by

$$f_1 = (1-u)(1-2v)(1-v) \qquad (9)$$

indicating a quadratic and linear variation in the transverse and longitudinal directions respectively. Higher order basis function definition in Sparse is similar to (9) resulting in 54 unknown coefficients per finite element.

V. Results and Conclusions

Figure 3 depicts the predicted RCS for a PEC duct with a square cross-section of side 3 wavelengths, length 10 wavelengths and gridded at 10 unknowns per wavelength. This geometry yields a problem size of 258100 for Sparse with a bandwidth of 2640 and a CR matrix of 1740 (N_{es})

by 1860 (N_{hs}). The system matrix was built, factored and the CR matrix computed in 50 minutes on a SGI Origin 2000 with 32 processors. The duct exterior was discretized at 7 and 10 unknowns per wavelength in the longitudinal and transverse direction respectively yielding 20400 unknowns for the electric current. Thus a completely dense system of order 20400 was built, factored and solved in 75 minutes on a SGI Origin 2000 with 32 processors. On 64 processors, the same system was solved in 40 minutes resulting in an excellent parallel efficiency of 93.75%.

Figure 4 depicts the predicted RCS for a similarly shaped duct with a cross-section of side 4 wavelengths and length 9 wavelengths. Problem size for Sparse was 417690 with a bandwidth of 4720, CR matrix was of size 3120 (N_{es}) by 3280 (N_{hs}), yielding a run-time of 7 hours. The corresponding fully populated dense system of order 26560 was solved in 2.5 hours.

The improved accuracy of higher order basis functions is demonstrated with reference to the EMCC duct which at 9.46 GHz, has a square cross-section with side 2 lambda and is 3 lambda long. RCS predictions with the moment method, applied by discretizing at a rate of 16 unknowns per wavelength resulting in 14272 unknowns, agree very well with measured data and will serve as the benchmark for comparisons. With higher order basis functions the discretization was 5 unknowns per wavelength in the transverse direction and 7 unknowns per wavelength in the longitudinal direction resulting in a total of 2000 unknowns for Dense and 3915 for Sparse. Figure 5 shows that RCS predictions with higher order basis functions for horizontal polarization agree almost exactly with the moment method. Figure 6 depicts RCS for the same number of unknowns while using sub-domain basis functions, clearly illustrating the higher accuracy of higher order basis. Figure 7 compares predictions with sub-domain basis employing 10 unknowns per wavelength (totals of 6400 for Dense and 33630 for Sparse) and the moment method predictions form Figure 5. Thus, Figures 5-7 illustrate that RCS computed with higher order basis functions with only 2000 unknowns is more accurate than that computed with sub-domain basis functions using 6400 unknowns.

A procedure to efficiently predict the RCS of ducts of arbitrary shape and material composition was discussed. The formulation of a computed relationship and its generation from the finite element system was given. A novel banded matrix solver was developed to rapidly generate the CR. The surface integral equation dense system was solved with a linear equation solver from ScaLAPACK. Higher order basis functions are implemented, which reduce the required discretization rate. Numerical results to validate the technique were presented. Future work includes improving the efficiency of the banded matrix solver and analysis of ducts of arbitrary shape and material composition.

Acknowledgement

The parallelized dense linear equation solver was obtained from the ScaLAPACK project (http://www.netlib.org). The Computer resources provided by the DoD High Performance Computing Major Shared Resource Center at the Aeronautical Systems Center, Wright Patterson Air Force Base are greatly appreciated. Interfacing of the ScaLAPACK solver to SWITCH was funded in part by the High Performance Computing/Common High Performance Computing Software Support Initiative (CHSSI) for Computational Electromagnetics and Acoustics under the lead of Dr. Bob Peterkin.

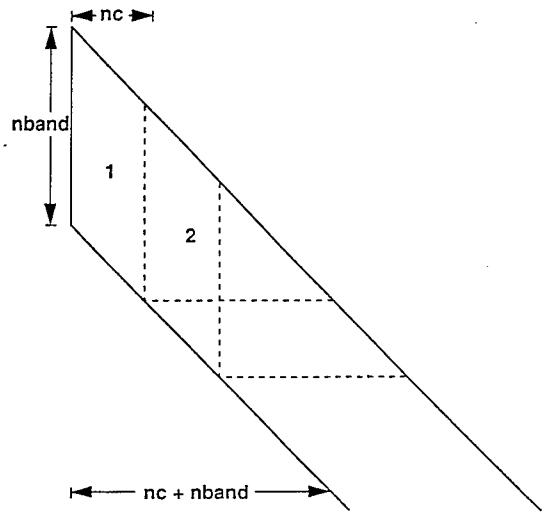

Figure 1: Banded matrix factorization

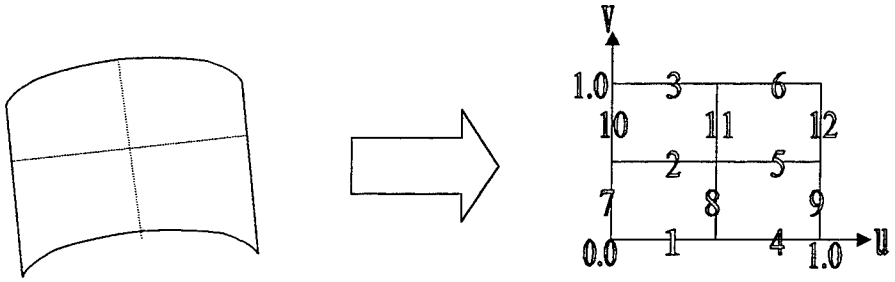

Figure 2: Quadratic basis functions over a patch in the u-v plane

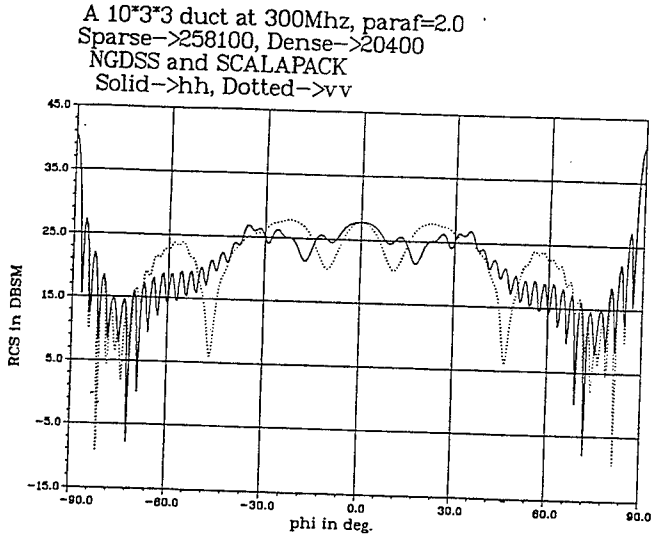

Figure 3: RCS of a square c-s duct of side 3λ and length 10λ

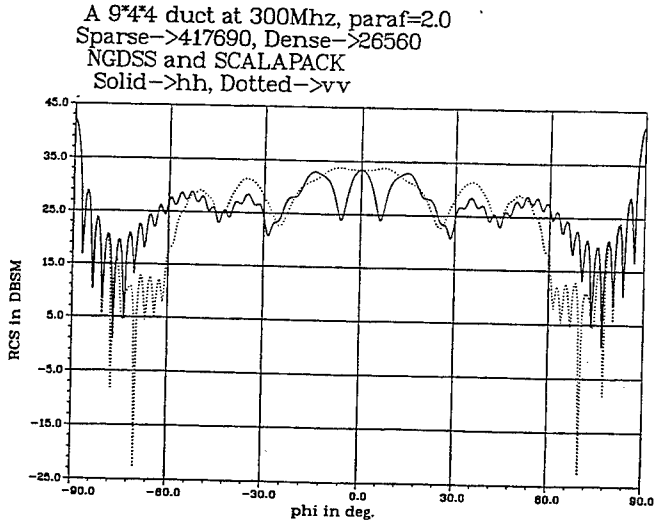

Figure 4: RCS of a square c-s duct of side 4λ and length 9λ

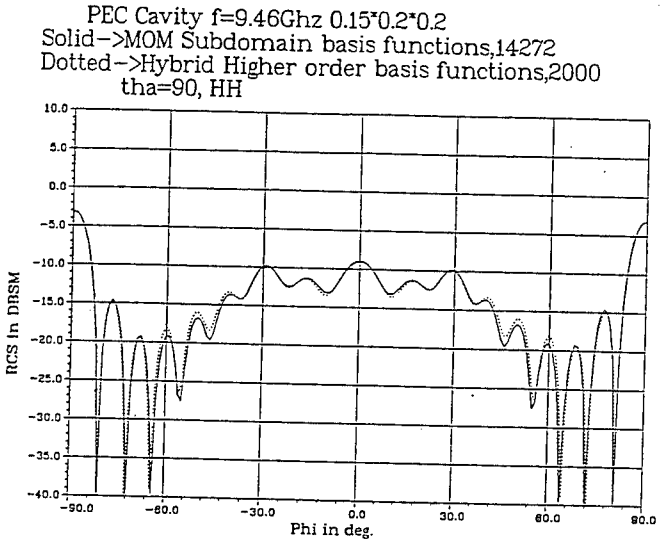

Figure 5: Reference RCS predictions compared with predictions from hybrid *higher order* basis functions using 2000 unknowns

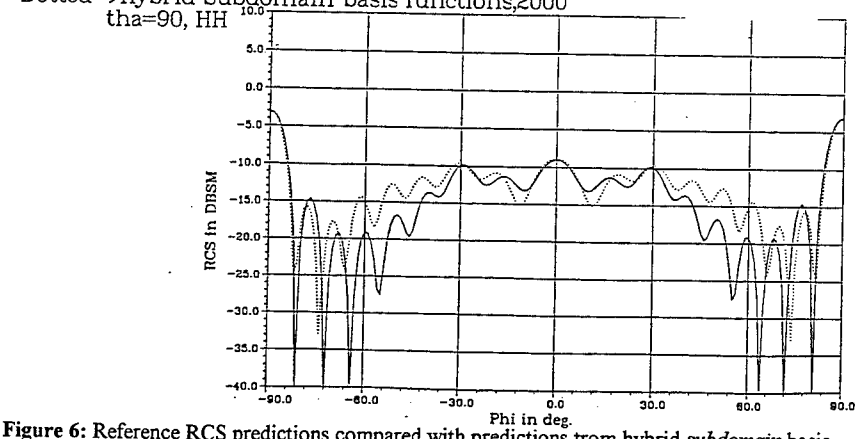

Figure 6: Reference RCS predictions compared with predictions from hybrid *subdomain* basis functions using 2000 unknowns

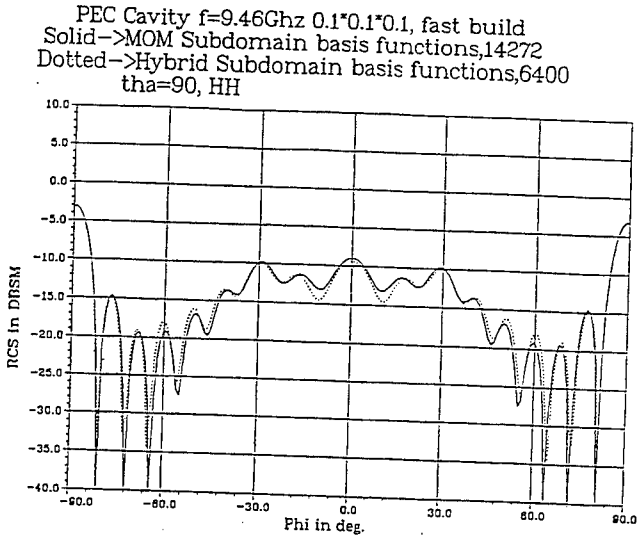

Figure 7: Reference RCS predictions compared with predictions from hybrid *subdomain* basis functions using 6400 unknowns

Reference

[1] L.S. Blackford et al., "ScaLAPACK Users' Guide", Society for Industrial and Applied Mathematics (SIAM), Philadelphia, 1997.

Implementation of Various Hybrid Finite Element-Boundary Integral Methods: Bricks, Prisms, and Tets

Leo C. Kempel
Department of Electrical and Computer Engineering
Michigan State University

Abstract

Although the methods and techniques associated with hybrid finite element-boundary integral method have been available in the literature for over ten years, practical advice involving the implementation of these techniques as efficient computer code is not generally available. The author has recently developed computer programs using three popular finite elements: bricks, right prisms, and tetrahedra.

In this paper, specific recommendations are made to potential finite element-boundary integral computer program developers. Topics discussed include: specific advantages and disadvantages of each element, suggested element expansion functions for use with anisotropic materials, issues involved in coupling the interior finite element formulation to the exterior boundary integral formulation, and comments on matrix solution techniques.

Introduction

The finite element-boundary integral method has been used in the electromagnetics analysis community for more than two decades, especially for electrostatics and magnetostatics analysis. Solution of dynamic problems, such as antenna characterization or radar cross section calculation, required the introduction of edge-based (also known as vector) finite elements. However, even with the use of vector finite elements, implementations of a hybrid finite element method were scarce and limited in their utility.

Hybrid finite element methods utilize a boundary integral to close the finite element mesh by providing the relationship between the tangential electric and magnetic fields on the surface of the mesh. The boundary integral explicitly couples each unknown (or edge) on the surface to all the other unknowns resulting in a fully-populated matrix. Hence, this hybrid finite element-boundary integral (FE-BI) method had limited utility in an era of Intel 386-based computers with upto 32 MB of RAM.

However, an important milestone was reached in the development of useful finite element-boundary integral computer programs when BRICK was released by Jian-Ming Jin and John Volakis [1]. These authors realized that if brick elements were utilized to mesh a rectangular volume recessed in a metallic groundplane, the resulting uniformly discretized surface aperture results in a boundary integral matrix that is block Toeplitz. Accordingly, there is tremendous redundancy in the boundary integral matrix so that only a small fraction of the fully populated matrix need be stored. In addition, if the matrix is stored in a convenient manner, iterative solutions of the matrix can be accelerated through the use of Fast Fourier Transforms. Such a solution made the hybrid FE-BI method attractive for use on commonly available computers. Indeed, even with contemporary computer resources, use of the AFRL's XBRICK computer program (see http://www.adinc.com) is as strong as ever.

As computer resources have improved (today, one can purchase a dual processor computer with 1 GB of RAM for less than $10,000), the limitations of BRICK have been alleviated by eschewing the memory and computational advantages of a Block Toeplitz boundary integral matrix. Specifically, computer program designers are utilizing triangular surface meshes and either right prism or tetrahedra meshes to solve rather complex antenna design problems. In doing so, these methods involve a fully-populated boundary integral sub-matrix and hence it is important to carefully design the computer program to avoid wasting resources. Although the use of "fast solvers" such as AIM or FMM is not within the scope of this paper, it should be noted that several research groups are now using AIM or FMM to accelerate hybrid FE-BI solutions while reducing memory consumption [2].

In the remainder of this paper, practical implementation tips are provided in the hope of saving valuable development time for those who wish to explore the capabilities of FE-BI methods. As a general rule, the methods described below assume the following:

1. planar aperture (e.g. antenna aperture in a ground plane),
2. total electric field as the unknown quantity,
3. anisotropic cavity fill, volume element extrusion from surface element specification,
4. and the use of similar basis functions (e.g. the volume basis function collapses to the surface basis function in the aperture).

We begin with general implementation comments that are relevant regardless of the element shape.

General Implementation Comments

Several comments may be made regardless of the finite element shape chosen for implementation. These comments are associated with common elements of the FE-BI method. The FE-BI equations for a total electric field formulation may be written as

$$\int_V \left[\nabla\times\mathbf{W}_i\cdot\overline{\overline{\mu}}_r^{-1}\cdot\nabla\times\mathbf{W}_j\right]dV - k_0^2\int_V\left[\mathbf{W}_i\cdot\overline{\overline{\varepsilon}}_r\cdot\mathbf{W}_j\right]dV + jk_0\int_{S_R}\left[\frac{\left(\hat{n}_R\times\mathbf{W}_i\right)\cdot\left(\hat{n}_R\times\mathbf{W}_j\right)}{R_e}\right]dS$$

$$-k_0^2\int_{S_a}\int_{S_a}\left[\mathbf{W}_i\cdot\hat{z}\times\overline{\overline{G}}_{e2}\times\hat{z}\cdot\mathbf{W}_j\right]dS'dS = f_i^{int} + f_i^{ext}$$

where the first term is associated with the curl of the basis function (the magnetic field), the second term is associated with the basis function itself (the electric field), the third term is necessary to account for an resistive transition conditions present, and the last term on the left-hand side is the boundary integral term (involving a second kind electric field dyadic Green's function). As shown, the placement of the material parameters $\left(\overline{\overline{\varepsilon}}_r,\overline{\overline{\mu}}_r\right)$ suggests that the basis functions $\left(\mathbf{W}_j\right)$ and test functions $\left(\mathbf{W}_i\right)$ should be chosen so that the dot products with the material tensors are accomplished readily. The basis functions presented herein were chosen to accomplish this goal.

An additional observation is that the boundary integral term does not involve the material parameters. Accordingly, since the basis functions and test functions are functionally identical (e.g. Galerkin's testing procedure was used) and the dyadic Green's function is symmetric, $G_{e2}^{xy} = G_{e2}^{yx}$ and $\overline{\overline{G}}_{e2}(\mathbf{r},\mathbf{r}') = \overline{\overline{G}}_{e2}(\mathbf{r}',\mathbf{r})$, then the boundary integral sub-matrix is symmetric. Therefore, it is not necessary to store either the lower or upper triangle of that matrix. Since the BI matrix is by far the

greatest consumer of RAM in the FE-BI method, this savings of roughly $\frac{1}{2}N_{ap}^2$ complex numbers is well worth the slightly more complex coding. Note that the exception to this rule is running the code on certain vector processors where the uneven vector length associated with such storage is inefficient. However, for the majority of the community who commonly run on workstations, symmetric BI storage should always be used since, if the problem does not fit on the machine, efficient execution is irrelevant.

On the other hand, since it is desirable to allow for the possibility of anisotropic materials within the computational volume, the sparse finite element matrix should be stored without symmetry considerations. Accordingly, it is recommended that the finite element and boundary integral matrices be stored separately and hence that an iterative solver (e.g. BiCG, CG, GMRES) be used. The most significant source of computational cost in an iterative solver is the matrix-vector multiply. This operation can be accomplished with separate matrix storage by realizing

$$\begin{bmatrix} A_{BB}+Y_{BB} & A_{BI} \\ A_{IB} & A_{II} \end{bmatrix}\begin{Bmatrix} E_B \\ E_I \end{Bmatrix} = \begin{bmatrix} A_{BB} & A_{BI} \\ A_{IB} & A_{II} \end{bmatrix}\begin{Bmatrix} E_B \\ E_I \end{Bmatrix} + \begin{bmatrix} Y_{BB} & 0 \\ 0 & 0 \end{bmatrix}\begin{Bmatrix} E_B \\ E_I \end{Bmatrix}$$

where "A" matrices denote finite element interactions and the "Y" matrix indicates the boundary integral matrix. The subscript "B" denotes a boundary edge while "I" indicates an interior edge. This decomposition of the finite element and boundary integral matrices allows the code designer to used optimized matrix storage and multiplication schemes for each portion.

Another common element to these hybrid finite element computer programs is the need for a volumetric mesh. If tetrahedra are used for the volume mesh, a commercial mesh generating package such as SDRC IDEAS may be used. However, for many applications, an extruded mesh will work perfectly well without the need for additional investment. Extrusion is accomplished by forming elements for each layer of the mesh by replicating the nodal distribution of the aperture for all lower layers of the mesh. Hence, to form the first layer of elements, the aperture nodes are replicated at the interface of the first and second layer. Elements are formed from those nodes (and the previous layer's "bottom" nodes) and edges are then formed based on the chosen finite element. Such meshes are fairly rigid and hence cannot represent the wide range of geometries that can be modeled using a free mesh (such as that produced by SDRC IDEAS).

For the remainder of the paper, idiosyncrasies of three typical finite element shapes are examined.

Brick Elements

Brick elements have minimal flexibility as a finite element (e.g. they are only geometrically suitable for rectangular volumes); however, they are rather simple to implement. Figure 1 illustrates the edge-based brick element consisting of eight nodes and twelve edges. Since the brick is defined in the usual Cartesian coordinate system, it is well defined for representing fields in a rectangular cavity that is filled with material with Cartesian defined anisotropic material.

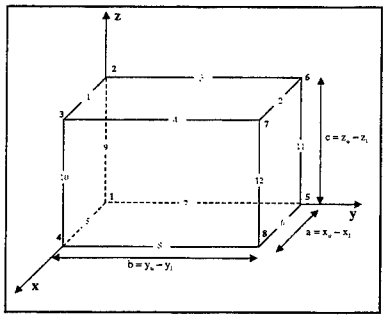

Figure 1. Brick edge-based finite element.

This brick element has twelve basis functions defined as:

$$W_1(x,y,z)=W_x(x,y,z;\cdot,y_u,z_l,-) \quad W_2(x,y,z)=W_x(x,y,z;\cdot,y_l,z_l,+)$$
$$W_5(x,y,z)=W_x(x,y,z;\cdot,y_u,z_u,+) \quad W_6(x,y,z)=W_x(x,y,z;\cdot,y_l,z_u,-)$$

$$W_3(x,y,z)=W_y(x,y,z;x_u,\cdot,z_l,-) \quad W_4(x,y,z)=W_y(x,y,z;x_l,\cdot,z_l,+)$$
$$W_7(x,y,z)=W_y(x,y,z;x_u,\cdot,z_u,+) \quad W_8(x,y,z)=W_y(x,y,z;x_l,\cdot,z_u,-)$$

$$W_9(x,y,z)=W_z(x,y,z;x_u,y_u,\cdot,+) \quad W_{10}(x,y,z)=W_z(x,y,z;x_l,y_u,\cdot,-)$$
$$W_{11}(x,y,z)=W_z(x,y,z;x_u,y_l,\cdot,-) \quad W_{12}(x,y,z)=W_z(x,y,z;x_l,y_l,\cdot,+)$$

where the three fundamental Cartesian basis functions are given by

$$W_x(x,y,z;\tilde{x},\tilde{y},\tilde{z},\tilde{s})=\frac{\tilde{s}}{bc}(y-\tilde{y})(z-\tilde{z})$$

$$W_y(x,y,z;\tilde{x},\tilde{y},\tilde{z},\tilde{s})=\frac{\tilde{s}}{ac}(x-\tilde{x})(z-\tilde{z})$$

$$W_z(x,y,z;\tilde{x},\tilde{y},\tilde{z},\tilde{s})=\frac{\tilde{s}}{ab}(x-\tilde{x})(y-\tilde{y})$$

Note that each basis function is associated with a sign that caused the sum of the two basis functions associated with each edge (across two adjoining bricks) to form a roof-top basis. These signs could be omitted by defining the local edges with the signs in place; however, this leads to additional programming for computation of element matrices.

Comments on Implementing Bricks

Bricks are rather easy to implement efficiently due to the inherent rigidity of the mesh. One a uniform discretization is chosen for the aperture (e.g. fixing a and b above), the only geometrical degree of freedom remaining is the cell thickness (c). Hence, the element matrix is identical for each layer of the mesh and accordingly, only two 12x12 element matrices need be computed stored for each layer regardless of the material distribution. In addition, since all the edges are either parallel or perpendicular to each other, the element matrices are simplified. The boundary integral, as mentioned

before if the edges in the aperture are all co-planar and uniformly spaced, results in a block Toeplitz matrix that can be manipulated using Fast Fourier Transforms. In addition to reduced computational complexity, the block Toeplitz matrix possesses sufficient symmetry and redundancy so that only one full row and one partial row of the matrix need be computed and stored.

Further details regarding the element matrices, boundary integral matrix storage, and use of Fast Fourier Transforms in computing matrix-vector products is given in [2]. Software, including a fully functional FE-BI computer program using bricks and the BiCG-FFT solver is available for download at: http://www.eecs.umich.edu/RADLAB/bookprograms.html

Right Prism Elements

The vector edge-based expansion functions used for right prisms are developed by multiplying the traditional Rao-Wilton-Glisson (RWG) basis function [3] with a function of the prism height for the transverse (e.g. x- and y-component) functions. The normal functions are simply the node-based simplex basis function (see for example [4]) multiplied by $\hat{z}$. Hence, the transverse basis functions for edges on the top of the prism are given by

$$\mathbf{W}_\chi = \left(\frac{z}{\Delta z}\right) S_k = \left(\frac{z}{\Delta z}\right) \frac{d_i}{2S^e} [(x - x_i)\hat{y} - (y - y_i)\hat{x}] \quad \chi = 1,2,3$$

where χ is the local edge number and i is the global edge number. Not that the local edge numbers are defined so that the edge is opposite the local node number as shown in Figure 2.

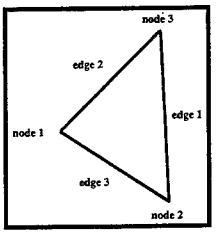

Figure 2. Illustration of local node and edge numbering for a triangle.

Transverse expansion functions on the bottom of the prism are given by:

$$\mathbf{M}_\chi = \left(\frac{\Delta z - z}{\Delta z}\right) S_k = \left(\frac{\Delta z - z}{\Delta z}\right) \frac{d_i}{2S^e} [(x - x_i)\hat{y} - (y - y_i)\hat{x}] \quad \chi = 4,5,6$$

Finally, the normal (z-directed) expansion functions are given by:

$$\mathbf{K}_\chi = \hat{z} \frac{(x_{k1} y_{k2} - x_{k2} y_{k1}) + (y_{k1} - y_{k2})x + (x_{k2} - x_{k1})y}{2S^e} \quad \chi = 7,8,9$$

where the indices k1 and k2 are given in the following table

χ	k1	k2
7	2	3
8	3	1
9	1	2

As stated previously, the choice of basis functions is dictated by the physical constraints of the geometry, the requirements for representation of a field, and convenience for implementation. The later consideration is understood by considering a version of the basis functions given in Chapter 5 of [2]. In that presentation, the basis functions are represented in a *local coordinate system* rather than the *global* treatment given above. Although the solutions are identical, inclusion of anisotropic materials is more difficult if the basis functions are expressed in local coordinates since a transformation back to global coordinates is required to perform the necessary dot products. Hence, the form of the basis functions given above is more convenient for implementation than the form given in [2].

Comments on Implementing Right Prisms

Right prisms are moderately difficult to implement since a surface mesh is required that may be rather complex. Various sources of surface meshes are available ranging from academic products (such as CMU's TRIANGLE code) to commercial products (such as SDRC IDEAS). However, once the surface mesh is provided, extrusion of prism elements is straightforward. Computation of element matrices is tedious, though functionally simple. Although the boundary integral matrix is fully populated, it is symmetric; thus only the upper (or lower) triangle need be computed and stored. The matrix-vector product requires more time than the case of a uniformly discretized brick code (since the latter can use FFTs).

Tetrahedral Elements

The third element shape investigated in this paper is the tetrahedra. Before presenting the basis functions, a discussion of creating the mesh is in order. A commercial mesh generator such as IDEAS can be used; however, tetrahedra can also be formed from prisms and bricks. For the case of bricks (or in general any hexahedral element), each hexahedra can be broken into five tetraheda. A good discussion of this process is available from the University of Missouri-Rolla via the World-Wide Web at: http://www.emclab.umr.edu/emap4/Meshing.html#mesh_gen. For the case of prisms, each prism can be divided into three different tetrahedra. Two different subdivision schemes are required for both the hexahedra and prisms. This is to allow diagonal edges on adjacent elements to align with each other so that on any face of the element, crossed edges do not occur. Figure 3 and Figure 4 illustrate the subdivision of two types of right prism into three tetrahedra.

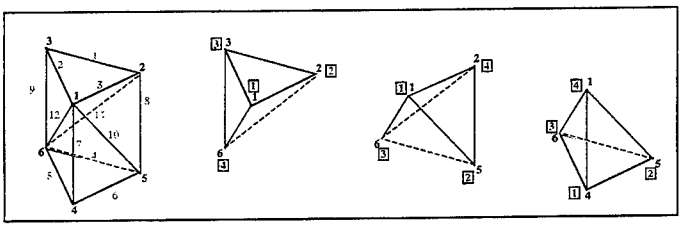

Figure 3. Subdivision of prism type 1 into three tetrahedra.

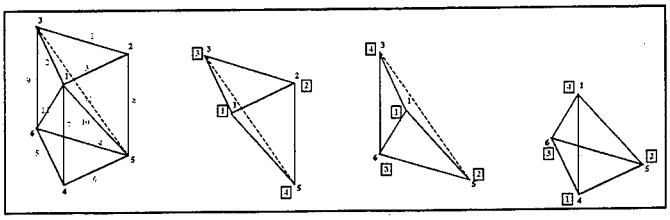

Figure 4. Subdivision of prism type 2 into three tetrahedra.

In these, local edge 11 has an opposite orientation in the two prism types and this allows the alignment of adjacent prism diagonal edges. Note that the user may need to rotate a prism to accomplish the required alignment.

Now that the tetrahedra have been created, it is necessary to expand the unknown fields within each element in terms of a suitable basis function. To simplify the implementation of anisotropic material, the form of these basis functions reported in [5] is recommended. The vector basis function is defined as

$$\mathbf{W}_j = \left(L_{j_1}\nabla L_{j_2} - L_{j_2}\nabla L_{j_1}\right)l_j$$

where the subscripts refer to the two *local* node numbers that define the edge (edge is directed from node j_1 to j_2), l_j is the length of the j^{th} edge, and the nodal basis functions are given by

$$L_j = \frac{1}{6V^e}\left(a_j^e + b_j^e x + c_j^e y + d_j^e z\right)$$

In this, V^e represents the volume of the tetrahedral element and the coefficients a,b,c,d, are determined based on the coordinates of the four local nodes that define the tetrahedral element. The utility of these element for implementing the FE-BI method for anisotropic materials lies in the fact that both the basis vector and its curl are readily expressed in terms of Cartesian quantities. For example, the curl of the basis vector is given by

$$\nabla\times\mathbf{W}_j = \frac{2l_j}{\left(6V^e\right)^2}\left[\hat{x}\left(c_{j_1}d_{j_2} - c_{j_2}d_{j_1}\right) + \hat{y}\left(d_{j_1}b_{j_2} - d_{j_2}b_{j_1}\right) + \hat{z}\left(b_{j_1}c_{j_2} - b_{j_2}c_{j_1}\right)\right]$$

Hence, the preferred basis function it one that satisfies all the requirements of a valid electromagnetic field and one convenient for implementing the required dot products.

Comments on Implementing Tetrahedra

Tetrahedra are no more difficult in principle to implement than are the right prisms. The only twist is that the source of meshes could be from a variety of sources. Consequently, the designer has less control over the mesh than in the case of extruded meshes. It is therefore important to assure that the local node numbering meets any conventions required in the code. For example, to compute the volume of the element, one might use the equation

$$V^e = \frac{1}{6}\begin{Bmatrix}(x_1 - x_4)[(y_2 - y_4)(z_3 - z_4) - (y_3 - y_4)(z_2 - z_4)] + \\ (y_1 - y_4)[(z_2 - z_4)(x_3 - x_4) - (z_3 - z_4)(x_2 - x_4)] + \\ (z_1 - z_4)[(x_2 - x_4)(y_3 - y_4) - (x_3 - x_4)(y_2 - y_4)]\end{Bmatrix}$$

This equation assumes a certain local ordering (e.g. sense) to the tetrahedral element. If the opposite sense is used, the computed volume is negative. To correct this, the user can swap local nodes 1 and 2.

Closing Remarks

In this paper, implementation details for three popular finite element shapes are discussed. Tips to the developer are given that will hopefully make the creation of a hybrid finite element-boundary integral computer program a little less daunting to the novice software designer. Basis functions that are particularly suitable for use in evaluating fields in anisotropic materials were presented. Key implementation hints will be given at the meeting.

References

[1] J.M. Jin and J.L. Volakis, "A hybrid finite element method for scattering and radiation by microstrip patch antennas and arrays residing in a cavity, *IEEE Trans. Antennas Propagat.*, 39, pp. 1598-1604, Nov. 1991.

[2] J.L. Volakis, A. Chatterjee, and L.C. Kempel, Finite Element Method for Electromagnetics, *New York: IEEE Press*, 1998.

[3] S.M. Rao, D.R. Wilton, and A.W. Glisson, "Electromagnetic scattering by surfaces of arbitrary shape," *IEEE Trans. Antennas Propagat.*, 30, pp. 409-418, May 1982.

[4] O.C. Zienkiewicz and R.L. Taylor, The Finite Element Method, 4th Ed., *New York: McGraw-Hill*, 1989.

[5]A.C. Polycarpou, Finite-Element Analysis of Microwave Passive Devices and Ferrite-Tuned Antennas, *Arizona State University Dissertation*, Tempe, AZ, 1998.

Fast hybrid finite element methods and their applications for conformal antennas

John L. Volakis, Lars S. Andersen, Thomas F. Eibert, Kubilay Sertel and Zhifang Li
Radiation Laboratory, EECS Department, University of Michigan
Ann Arbor, MI 48109-2122, USA
E-mail : {volakis, andersen, eibert, ksertel, zhifang}@umich.edu

Abstract

Hybrid finite element methods have been applied for accurate and efficient analysis of various conformal antennas. This paper presents a series of results that demonstrate the value of such methods for realistic applications. Furthermore, the potential of combining lowest and higher order field expansions selectively is demonstrated and an example of ferrite antenna design using sequential quadratic programming is given.

Introduction

Hybrid finite element / boundary integral (FE/BI) methods have been widely applied for analysis of conformal antennas and arrays [1, 2]. The requirements for high degrees of accuracy as well as modeling of volumetric materials and structural details associated with antenna geometries and their feeds can be addressed by the rigor and adaptability of the finite element method (FEM). Nevertheless, these attributes are often not sufficient for the practical characterization of complex antenna apertures and arrays due to the CPU and memory requirements associated with the BI portion of the hybrid FE/BI system. The BI subsystem dominates the CPU requirements with its $O(N_S^2)$ computations, where N_S refers to the number of unknowns on the antenna/array aperture. However, recent developments of fast integral methods [3, 4, 5] and adaptive higher order or multi-scale elements [6] have allowed us to circumvent some of these CPU bottlenecks and are permitting the analysis of large finite apertures and multilayered arrays. Most importantly, these speed-ups can lead to algorithms which can be used for design purposes.

This paper will consider the performance of three fast hybrid FE/BI methods in the context of various antenna and array analysis examples : (a) Hybrid FE/BI-AIM, where the adaptive integral method (AIM) [3] is used to speed up the BI matrix-vector products, (b) Hybrid FE/BI-FMM, where the fast multipole method (FMM) [4] is used to speed up the BI matrix-vector products and (c) Hybrid FE/BI-FSDA, where the fast spectral domain algorithm (FSDA) [5] is used to speed up the BI matrix-vector products. FSDA is a recent addition to the fast methods and draws its speed-up by working directly with the spectral form of the BI. As a result, it is particularly attractive for multilayered periodic array analysis since in that case the spectrum of the Green's function is discrete and of finite bandwidth. Another important difference between FSDA and AIM/FMM is that FSDA provides considerable speed-up even for small values of N_S. The performance of these hybrid methods will be demonstrated with their application to the characterization of various antenna problems. In addition, we will show the advantage of using hierarchical higher order tangential vector finite elements (TVFEs) [6] for accurate and efficient resonance frequency prediction. Finally, we will give an antenna design example where sequential quadratic programming (SQP - a gradient-based optimization algorithm) [7] is used for optimization.

Frequency selective surface of slot-coupled microstrip patches

Frequency selective surfaces (FSSs) are of practical relevance for construction of for instance polarizers, filters and radomes. In Fig. 1, the geometry of the unit cell of an FSS array consisting of slot-coupled microstrip patches is depicted. This infinite array was investigated in [8] and acts as a strongly resonant band-pass structure. The incidence angle ϑ_0 of the transverse electric (TE) polarized plane wave used to excite the structure varies with frequency according to the waveguide measurement setup in [8]. Fig. 2 compares the transmission coefficients obtained by FE/BI-AIM and FE/BI-FSDA solutions to measured data presented in [8]. The agreement between the three curves is good. We note that the FE/BI-FSDA results are closer to the measured data than those obtained by the FE/BI-AIM approach. With respect to complexity, the FE/BI-AIM solution used 98636 volume and 5308 BI unknowns on each of the top and bottom BI surfaces. Also, for the FE/BI-AIM approach, the BI was implemented as a conventional spatial domain formulation with Ewald acceleration of the Green's function modal series [9, 10] and AIM was employed to speed up the BI portion of the code. The required CPU time for the FE/BI-AIM implementation on a Pentium II PC/266 MHz was between 3 and 4 hours per frequency point. Using the FE/BI-FSDA, the CPU times were considerably decreased even though the number of unknowns was increased by putting additional air layers between the microstrip patches and the BI termination to reduce the number of Floquet modes needed. Specifically, the number of volume unknowns grew to a value of 137804 and the number of BI unknowns was increased to 14828 in each of the top and bottom BI surfaces. The required CPU time on the PC for FSDA 3+ (Floquet mode series indices ranging from -3 to +3) was about 50 minutes per frequency point.

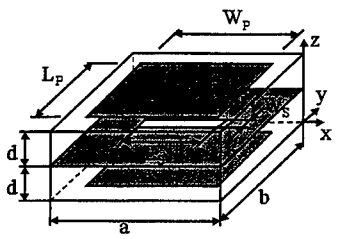

Figure 1: FSS unit cell of the aperture coupled microstrip patches as suggested in [8]. The parameters are $\varepsilon_r = 2.2$, $d = 1.6$ mm, $a = 36.07$ mm, $b = 34.04$ mm, $W_s = 2$ mm, $L_s = 8$ mm, $W_p = L_p = 28$ mm.

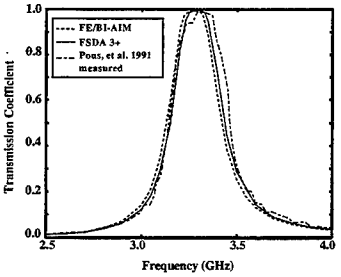

Figure 2: TE transmission coefficient of the FSS structure in Fig. 1 for different FE/BI models compared to measured results from [8]. $\varphi = 0°$, ϑ_0 varying from 57° to 32° for f varying from 2.5 GHz to 4.0 GHz, according to waveguide measurement setup in [8].

FE/BI-FMM analysis of cavity-backed antennas on curved platforms

In this section, we present an approximate FE/BI-FMM solution to problems involving antennas recessed in curved platforms. For cylindrical platforms, the closed form Green's function can be

used to formulate the problem [11]. The lack of a closed form Green's function for arbitrary doubly curved structures forces one to use an approximate Green's function. In this work, the half space Green's function is used as if the cavity resides in a flat ground plane. It is demonstrated that this approach is applicable for geometries which are not highly curved. The FMM [4] is used in the BI formulation to speed up the evaluation of matrix-vector products and lower the memory requirements.

5×1 patch antenna arrays on flat and curved platforms are examined. The effect of curvature on the radiation pattern and input impedance of the antenna will be predicted using the FE/BI-FMM approach. For the flat arrays, each antenna element is a square patch of size 3.5 cm $\times$ 2.625 cm. We consider the two different center-to-center spacings 6.125 cm and 5.250 cm. The flat arrays are backed by rectangular cavities of dimensions 33.25 cm $\times$ 6.125 cm $\times$ 0.3175 cm and 28.00 cm $\times$ 6.125 cm $\times$ 0.3175 cm, respectively, and recessed in an infinite metallic ground plane. The cavities are filled with a material of relative permittivity 2.32. Curved arrays are formed from the flat arrays by wrapping them onto metallic circular cylindrical platforms of radius 20 cm (spacing 6.125 cm) and 10 cm (spacing 5.250 cm). For all arrays, the five patches are fed in-phase by an offset vertical probe of constant current. The surface mesh (discretization into squares of dimensions 0.4375 cm $\times$ 0.4375 cm and subsequent division into triangles) is given in Fig. 3 for the curved array with spacing 6.125 cm.

The effects of curvature on the radiation pattern are demonstrated in Fig. 4 where for the spacing 6.125 cm the radiation patterns for flat and curved platforms are compared. The side lobes for the flat array are seen to be eliminated when the array is curved. Fig. 5-8 show the dependence on curvature of the input impedance of the first and second array element for flat and curved array geometries. This is shown for the two different element spacings 6.125 cm and 5.250 cm. The effect of coupling is observed for the input impedance of the second element when the spacing between the elements is 5.250 cm.

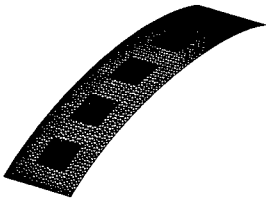

Figure 3: Illustration of 5×1 conformal array

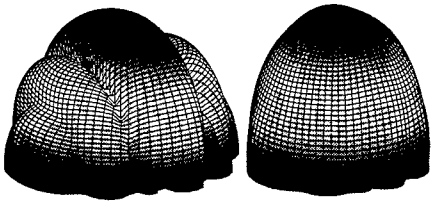

Figure 4: Radiation pattern of flat (left) and curved (right) array for spacing 6.125 cm.

Resonant frequency determination using selective field expansion

Consider a square metallic patch antenna backed by a rectangular cavity recessed in an infinite metallic ground plane, as illustrated in Fig. 9. The cavity-backed patch antenna is situated in free space characterized by the permittivity ε_0 and the permeability μ_0. The cavity is of dimensions 1.85 cm $\times$ 1.85 cm $\times$ 0.15 cm and filled with a dielectric material of permittivity $10\,\varepsilon_0$ and conductivity 0.0003 S/cm. The patch is of side length 0.925 cm and centered in the cavity aperture. It is fed

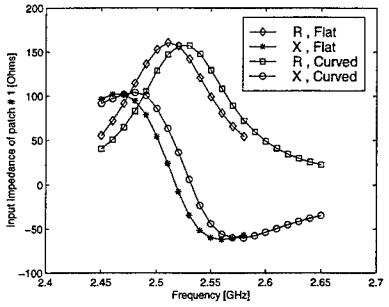

Figure 5: Input impedance of the 1st element of flat and curved (20 cm cylinder) array with spacing 6.125cm.

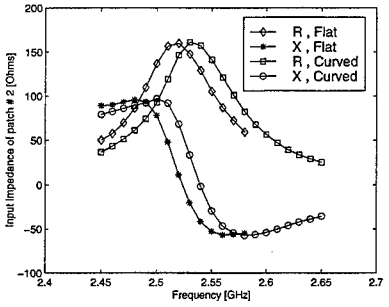

Figure 6: Input impedance of the 2nd element of flat and curved (20 cm cylinder) array with spacing 6.125cm.

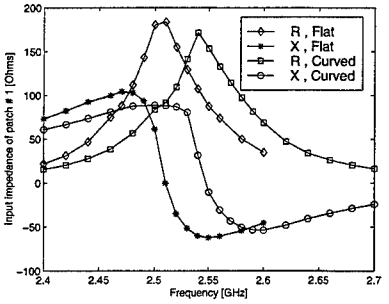

Figure 7: Input impedance of the 1st element of flat and curved (10 cm cylinder) array with spacing 5.250cm.

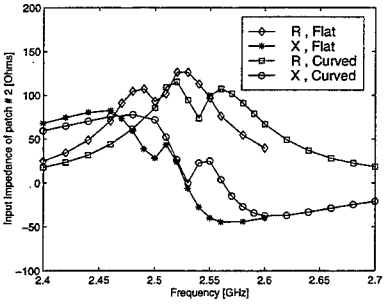

Figure 8: Input impedance of the 2nd element of flat and curved (10 cm cylinder) array with spacing 5.250cm.

by a vertical coaxial line whose outer conductor is attached to the ground plane and whose inner conductor is attached to the patch at the mid point of an edge, as illustrated in Fig. 9. The coaxial feed is modeled as a vertical probe of constant current.

An almost identical antenna was considered by Schuster and Luebbers [12]. In [12], the cavity walls and the ground plane were removed and a similar patch on a similar but finite grounded dielectric substrate was analyzed using the finite difference time domain method. In spite of these geometrical differences, the two antennas are expected to have nearly the same input impedance and, consequently, nearly the same resonant frequency since the dominant fields are confined to a volume under and in the near vicinity of the patch. The resonant frequency was estimated in [12] to be 4.43 GHz. The resistance at resonance was found to be 400 Ω while the reactance was in the range of 230 Ω to -170 Ω close to resonance. All results in [12] were found with a very fine discretization and can be considered accurate.

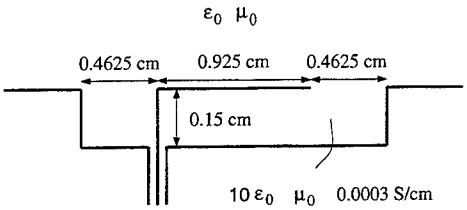

Figure 9: Square metallic patch antenna backed by a dielectric-filled rectangular cavity recessed in an infinite metallic ground plane.

Two different TVFE options are applied. The first TVFE option is to use the mixed-order TVFE of order 0.5 [6] throughout the mesh. For a mesh of average edge length 0.260 cm (Case 1), the input impedance is determined as a function of frequency and the resonant frequency of the patch is predicted. The coarse discretization of Case 1 means that this resonant frequency is most likely not accurate. For meshes of average edge lengths of 0.188 cm (Case 2), 0.153 cm (Case 3) and 0.133 cm (Case 4), more accurate resonant frequencies but also higher computational costs can be expected. The second TVFE option is to use the mixed-order TVFE of order 1.5 [6] close to the radiating edges and the mixed-order TVFE of order 0.5 elsewhere. For the meshes of average edge length 0.260 cm (Case 5) and 0.188 cm (Case 6), the input impedance is again determined and the resonant frequency is again predicted. The effectiveness of this approach (Case 5-6) in terms of accuracy / CPU time / memory requirements is compared to the previous one (Case 1-4). The six cases are summarized in Tab. 1.

Real and imaginary parts of the input impedance as a function frequency are given in Fig. 10 - 11 for Case 1-6 and corresponding resonant frequencies are provided in Tab. 1. For Case 1-4, a larger and larger resonant frequency is observed as the mesh becomes denser and denser. However, even for Case 4, the error as compared to the result obtained by Schuster and Luebbers is quite large (2.98 %) for resonant frequency computation. Use of selective field expansion (Case 5-6) leads to a significant accuracy improvement. Case 5 (error 2.42 %) gives a more accurate result than Case 1-4 and Case 6 (error 0.16 %) matches the result by Schuster and Luebbers almost exactly. The computational costs (number of unknowns, number of BI unknowns, number of non-zero matrix

Case	TVFE order(s)	Average edge length [cm]	Resonant frequency [GHz]	# of unknowns	# of BI unknowns	# of matrix entries	Time per frequency point [sec]
1	0.5	0.260	3.974	345	120	17119	7.52
2	0.5	0.188	4.147	817	288	89695	44.78
3	0.5	0.153	4.258	1489	528	291359	222.92
4	0.5	0.133	4.302	2361	840	725791	771.59
5	0.5/1.5	0.260	4.323	827	120	30675	17.33
6	0.5/1.5	0.188	4.437	1467	288	107963	77.28

Table 1: Computational costs for Case 1-6 for antenna in Fig. 9.

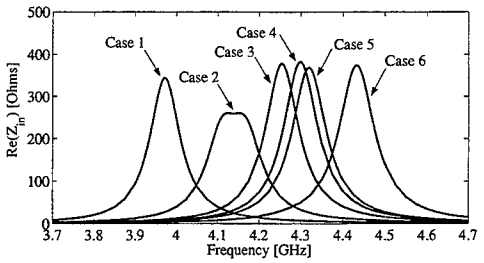

Figure 10: Real part of the input impedance of the antenna in Fig. 9 for Case 1-6.

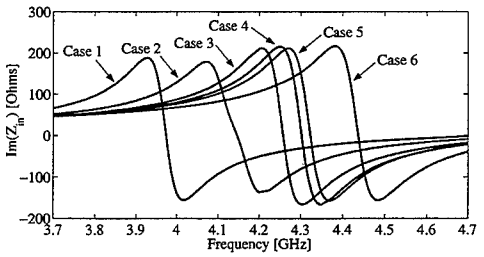

Figure 11: Imaginary part of the input impedance of the antenna in Fig. 9 for Case 1-6.

entries (memory usage) and CPU time per frequency point) to obtain these results are also given in Tab. 1. It is evident that the second TVFE option corresponding to Case 5-6 is significantly more attractive than the first TVFE option corresponding to Case 1-4. Case 5 gives a more accurate result than Case 4 but uses only 4.22 % of the memory and 2.15 % of the CPU time that Case 4 does. The accuracy of Case 6 is vastly superior to that of Case 4 and yet Case 6 uses only 14.88 % of the memory and 10.02 % of the CPU time that Case 4 does.

Resonant frequency tracking for ferrite antennas

Recently, the non-reciprocal properties of ferrites have been used to control printed circuits and antennas. The material properties of ferrites are mainly controlled by the direction and strength of an externally applied magnetic bias field, thus enabling control of various antenna radiation and scattering characteristics. These unique properties of ferrite materials provide many desirable features such as tunability, polarization diversity, beam steering and radar cross section control. Furthermore, because of the additional variables such as bias field strength, bias direction and saturation magnetization, optimization methods are very suitable for ferrite antennas.

Resonant frequency tracking and tuning are important for ferrite patch antennas. Instead of locating the resonance by frequency sweep, we apply SQP in conjunction with a FE/BI simulation

[7] to develop a set of design curves. The optimization problem can be formulated as follows:

$$\text{Find } f_* \text{ which minimizes } |\text{Imag}(Z_{in}(f))| \text{ subject to } f_L \leqslant f \leqslant f_U$$

where Z_{in} is the frequency-dependent input impedance and f_L and f_U are lower and upper bounds for the frequency. We use the definition that the antenna reaches resonancy when the imaginary part of the input impedance is zero.

As an example, we study an antenna similar to the one in [13], with $L = W = 0.61$ cm, $h = 0.127$ cm, and $\varepsilon_r = 15$. We place the antenna in a 1.22 cm $\times$ 1.22 cm cavity and a probe feed is located at the mid point of an edge. The geometry is illustrated in Fig. 12. For the isotropic case, the resonance should occur around 5.5 GHz. The antenna is biased parallel to one of the edges of the patch instead of normal to the patch as in [13]. We solve the optimization problem for various values of the bias field strength H_0 and saturation magnetization $4\pi M_s$. The results are plotted in Fig. 13-14 for x-bias (bias field perpendicular to the edge where the feed is located) and y-bias (bias field parallel to the edge where the feed is located), respectively. It is seen that the resonant frequency of the antenna shifts to a higher frequency as H_0 or $4\pi M_s$ increases. Also, the resonant frequencies for y-bias are higher than those for x-bias. This provides more tuning flexibility. Other ferrite parameters may also play a role in resonant frequency tuning.

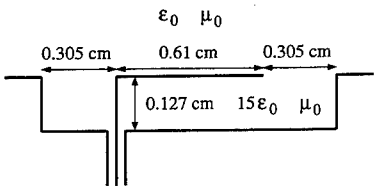

Figure 12: Illustration of cavity-backed patch antenna.

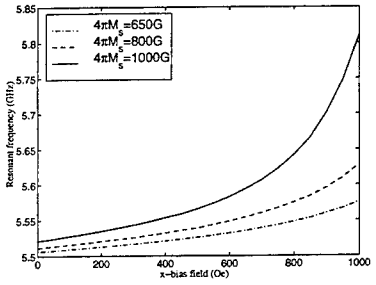

Figure 13: Resonant frequency for cavity-backed patch antenna in Fig. 12 as a function of the bias field and saturation magnetization (x-bias).

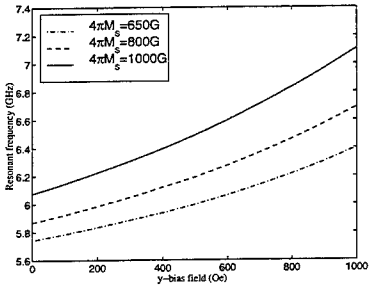

Figure 14: Resonant frequency for cavity-backed patch antenna in Fig. 12 as a function of the bias field and saturation magnetization (y-bias).

Conclusions

This paper presented a series of results that demonstrate the capabilities of fast hybrid FE/BI methods for accurate and efficient analysis of various conformal antennas. FE/BI-AIM, FE/BI-FMM as well as FE/BI-FSDA was considered. Furthermore, the potential of selective field expansion using hierarchical higher order TVFEs was demonstrated and an example of ferrite antenna design using SQP was provided.

References

[1] J.L. Volakis, T. Özdemir and J. Gong, "Hybrid finite element methodologies for antennas and scattering," *IEEE Trans. Antennas Propagat.*, vol. 45, pp. 493-507, March 1997.

[2] J.L. Volakis, A. Chatterjee and L.C. Kempel, *Finite Element Method for Electromagnetics*, IEEE Press, USA, 1998.

[3] E. Bleszynski, M. Bleszynski and T. Jaroszewicz, "AIM: Adaptive integral method compression algorithm for solving large-scale electromagnetic scattering and radiation problems," *Radio Science*, vol. 31, pp. 1225-1251, September-October 1996.

[4] W.C. Chew, C.C. Lu, E. Michielssen and J. M. Song, "Fast solution methods in electromagnetics," *IEEE Trans. Antennas Propagat.*, vol. 45, pp. 533-543, March 1997.

[5] T.F. Eibert and J.L. Volakis, "Fast spectral domain algorithm for rapid solution of integral equations," *Electronics Letters*, vol. 34, pp. 1297-1299, June 25, 1998.

[6] L.S. Andersen and J.L. Volakis, "Hierarchical tangential vector finite elements for tetrahedra," *IEEE Microwave and Guided Wave Letters*, vol. 8, pp. 127-129, March 1998.

[7] Z. Li, P.Y. Papalambros and J.L. Volakis, "Designing broad-band patch antennas using the sequential quadratic programming method," *IEEE Trans. Antennas Propagat.*, vol. 45, pp. 1689-1692, November 1997.

[8] R. Pous and D.M. Pozar, "A frequency-selective surface using aperture-coupled microstrip patches," *IEEE Trans. Antennas Propagat.*, vol. 39, pp. 1763-1769, December 1991.

[9] P.P. Ewald, "Die Berechnung optischer und elektrostatischer Gitterpotentiale," *Ann. Phys.*, vol. 64, pp. 253-287, 1921.

[10] K.E. Jordan, G.R. Richter and P. Sheng, "An efficient numerical evaluation of the Green's function for the Helmholtz operator on periodic structures," *J. Comp. Phys.*, vol. 63, pp. 222-235, 1986.

[11] L.C. Kempel, J.L. Volakis and R.J. Silva, "Radiation by cavity-backed antennas on a circular cylinder," *IEE Proc. Microw. Antennas Propagat.*, vol. 142, pp. 233-239, June 1995.

[12] J.W. Schuster and R. Luebbers, Private communication.

[13] D.M. Pozar, "Radiation and scattering characteristics of microstrip antennas on normally biased ferrite substrates," *IEEE Trans. Antennas Propagat.*, vol. 40, pp. 1084-1092, September 1992.

A Hybrid MoM/FEM Method for Scattering from a Complex BOR with Appendages

Andrew D. Greenwood
Air Force Research Laboratory
Directed Energy Directorate
Kirtland AFB, NM 87117

Jian-Ming Jin
ECE Department
University of Illinois
Urbana, Illinois 61801

1 Introduction

The symmetry present in body of revolution (BOR) electromagnetic scattering problems permits an efficient numerical solution using a two-dimensional (2-D) technique [1]–[5]. However, in many practical problems, the rotational symmetry is broken by the presence of small appendages (see Fig. 1). Thus, a three-dimensional (3-D) computational method is required to rigorously compute the electromagnetic scattering. Because of the increased computational complexity of a 3-D method, a hybrid method is developed which allows the scattering from small appendages to be approximately combined with the scattering from a large BOR in a similar manner to other hybrid techniques [6]–[9]. The rotational symmetry can then be exploited in the computation of the scattering from the large BOR. The hybrid method makes use of the finite element method (FEM) for BOR scattering as described in [1], and the method of moments (MoM) as described in [8]. The remainder of this paper discusses the hybridization of the two methods. The formulation is presented in Section 2, numerical results are given in Section 3, and concluding remarks are found in Section 4.

2 Formulation

The hybrid formulation is best understood by first considering the computation of the scattering from a BOR with appendages (see Fig. 1) entirely by the MoM. Assuming that the entire target consists of perfect conductors, the application of the MoM uses the integral equation

$$\mathbf{E}(\mathbf{r}) = \mathbf{E}^i(\mathbf{r}) - jk_0\eta_0 \iint_S \mathbf{G}_0(\mathbf{r},\mathbf{r}') \cdot \mathbf{J}(\mathbf{r}')dS' \tag{1}$$

where $k_0 = \omega\sqrt{\mu_0\epsilon_0}$ is the free-space wavenumber, $\eta_0 = \sqrt{\mu_0/\epsilon_0}$ is the impedance of free space, $\mathbf{G}_0$ is the free-space dyadic Green's function, $\mathbf{E}^i$ is a known incident electric field, $\mathbf{J}$ is the unknown current on the surface of the target, and S is the surface of the entire target. When using the MoM, $\mathbf{J}$ is found by discretizing the surface S and applying the appropriate boundary condition on the discretized surface.

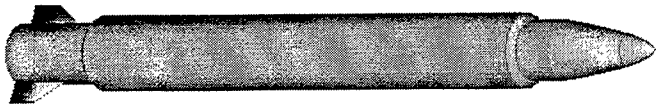

Figure 1: Example of a large BOR with small appendages.

The scattered field is then found from

$$\mathbf{E}^s(\mathbf{r}) = -jk_0\eta_0 \iint_S \mathbf{G}_0(\mathbf{r},\mathbf{r}') \cdot \mathbf{J}(\mathbf{r}')dS'. \tag{2}$$

This 3-D method generates a dense matrix equation; therefore, if the geometry is large, the method is very computationally intensive. Further, if the BOR contains inhomogeneous materials, the surface integral in Eq. (1) must be replaced with a volume integral, further increasing the computational complexity.

Because of the unfavorable computational complexity in solving Eq. (1) with the MoM, an alternate, hybrid method is sought. In the hybrid method, the MoM is applied to the small appendages only. Thus, Eq. (1) becomes

$$\mathbf{E}(\mathbf{r}) = \mathbf{E}^i_{\mathrm{BOR}}(\mathbf{r}) - jk_0\eta_0 \iint_{S_{\mathrm{App}}} \mathbf{G}_{\mathrm{BOR}}(\mathbf{r},\mathbf{r}') \cdot \mathbf{J}(\mathbf{r}')dS' \tag{3}$$

where $\mathbf{E}^i_{\mathrm{BOR}}$ represents the incident field on the appendages in the presence of the BOR, S_{App} represents the surface of the appendages, and $\mathbf{G}_{\mathrm{BOR}}$ represents the dyadic Green's function in the presence of the BOR. The solution of Eq. (3) requires the discretization of S_{App} rather than S and thus is much less computationally intensive. The incident field $\mathbf{E}^i_{\mathrm{BOR}}$ is calculated using the FEM [1], but difficulty is still encountered in solving Eq. (3) with the MoM because the Green's function $\mathbf{G}_{\mathrm{BOR}}$ is, in general, unknown. The unknown Green's function is needed not only for the solution of Eq. (3), but also to compute the scattered electric field from

$$\mathbf{E}^s(\mathbf{r}) = -jk_0\eta_0 \iint_{S_{\mathrm{App}}} \mathbf{G}_{\mathrm{BOR}}(\mathbf{r},\mathbf{r}') \cdot \mathbf{J}(\mathbf{r}')dS'. \tag{4}$$

The difficulty posed by the unknown Green's function $\mathbf{G}_{\mathrm{BOR}}$ is alleviated in two ways. An approximate Green's function is used for the solution of Eq. (3), and an alternate method based on the reciprocity theorem is used to compute $\mathbf{E}^s$.

There are four steps to using the hybrid method. First, the FEM described in [1] is used to compute scattering from the large BOR alone. Then, the result of the first step is used to compute $\mathbf{E}^i_{\mathrm{BOR}}$, the incident field on the appendages in the presence of the BOR. Next, the MoM with an approximate Green's function is used to solve Eq. (3) for $\mathbf{J}$, the current on the appendages. Finally, the scattered field generated by $\mathbf{J}$ is evaluated using reciprocity and added to the scattered field from the BOR, which is found in the first step. The result is an approximation to scattered field from the entire structure. In the remainder of this section, the construction of the approximate Green's function and the computation of the scattered field by reciprocity are each discussed in turn.

2.1 Approximate Green's function

The approximate Green's function used to solve Eq. (3) is developed by approximating the BOR on which the appendages reside as a long cylinder. The approximate Green's function must model the significant field interactions between points on the appendages but may neglect other, less significant interactions. The interactions are classified into four types. The first type of interaction is the direct path interaction between two points, and examples of this type of interaction are illustrated in Fig. 2a. The second type of interaction involves a reflection by the large BOR, and examples are illustrated in Fig. 2b. The third interaction type is the surface wave interaction which is illustrated in Fig. 2c. All other interactions

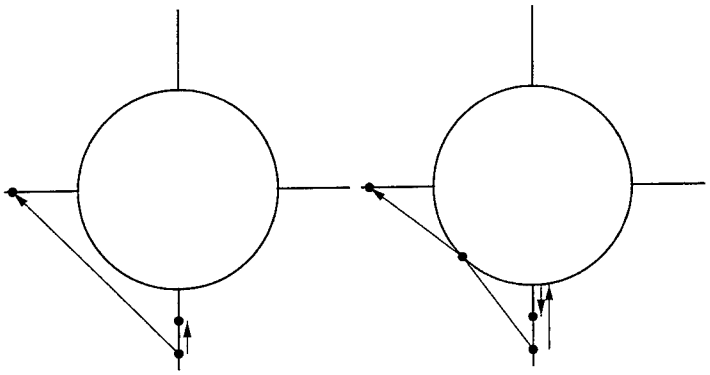

(a) Direct

(b) Reflected through base

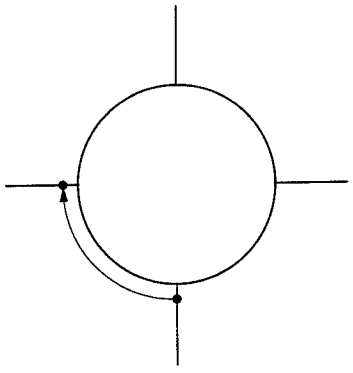

(c) Surface wave

Figure 2: Interactions between appendage points.

are classified as the fourth type. Most of these are complex interactions which are not modeled by the cylinder approximation to the BOR, and most are negligible.

If the line of sight between two points on the appendages is unobstructed by the cylinder approximation to the large BOR, the first two interaction types can be computed using the half-space Green's function. This is done by finding the reflection point on the cylinder and computing the tangent plane to the cylinder at that point. If the line of sight between the two appendage points is obstructed by the cylinder, both of the first two interactions are zero. For many problems, modeling the first two interactions produces acceptable results. If more accuracy is desired, the third type of interaction can be computed using the geometrical theory of diffraction (GTD) [10]. Also, if the appendages are near the end of the BOR, it may be necessary to compute an interaction based on edge diffraction from the nearby end. Note that the effect of neglecting some of the interactions is to neglect the corresponding field which is scattered by the appendages, reflected or diffracted back to the appendages, and scattered by the appendages again [6]–[9].

2.2 Computation of scattered field

While the use of the approximate Green's function allows Eq. (3) to be solved for $\mathbf{J}$, the approximation is not accurate when computing $\mathbf{E}^s$ from Eq. (4). Therefore, an alternate method of computing $\mathbf{E}^s$ is used. The alternate method is based on the reciprocity theorem. Consider a short dipole, located at point $\mathbf{r}$ and oriented in the $\hat{u}$ direction. From the reciprocity theorem,

$$\mathbf{E}^s(\mathbf{r}) \cdot \hat{u} = -jk_0\eta_0 \frac{e^{-jk_0 r}}{4\pi r} \iint_{S_{\text{App}}} \mathbf{E}^r_{\text{BOR}}(\mathbf{r}') \cdot \mathbf{J}(\mathbf{r}') dS' \tag{5}$$

where $\mathbf{E}^r_{\text{BOR}}$ is the field radiated by the dipole in the presence of the large BOR. Recall that this field can be computed by the FEM. In fact, when backscattering is being computed, $\mathbf{E}^r_{\text{BOR}}$ is the same as $\mathbf{E}^i_{\text{BOR}}$ that is used in Eq. (3). Thus, all components needed to compute $\mathbf{E}^s$ using Eq. (5) are known.

3 Numerical Results

Several numerical results are presented to show the validity and capability of the hybrid technique. In all of the results presented, the direct and reflected interactions are modeled by the approximate Green's function, and all other interactions are neglected.

First, the validity of the technique is tested by computing the scattering from metallic cylinders with one, two, or four wings. The scattering is compared with computations from the Fast Illinois Solver Code (FISC) [11], which is an MoM program that uses a multilevel fast multipole algorithm to speed up the matrix solution. The cylinders considered have a radius of 1.25λ and height of 5λ, where λ is the free-space electromagnetic wavelength. The attached wings are 1λ by 0.5λ by 0.025λ.

The monostatic RCS as a function of azimuth angle from the cylinder with one wing is shown in Fig. 3. The agreement between FISC and the hybrid method is very good. The scattering from the cylinder without the wing is flat as a function of azimuth angle, so it can be seen that the wing has added approximately 5 dB peak-to-peak swing to the RCS in the VV-polarized case and about 4 dB peak-to-peak swing in the HH-polarized case. Although adding a second wing presents the possibility of more complex interactions, the results shown in Fig. 4 continue to show good agreement between FISC and the hybrid method. The peak-to-peak variation in the RCS is about 4.5 dB in the VV-polarized case and almost 6 dB in the HH-polarized case when two wings are present. The scattering from the cylinder with four wings is shown in Fig. 5, where the agreement between FISC and the hybrid method

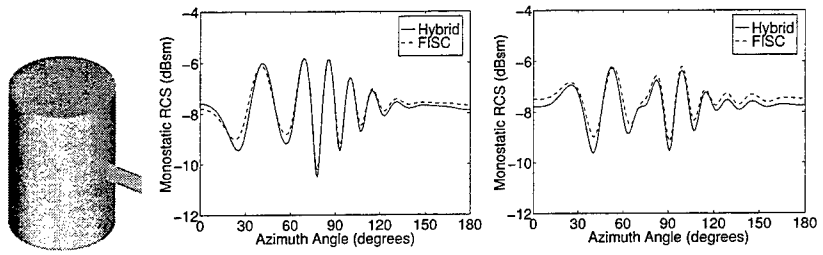

(a) VV-pol (b) HH-pol

Figure 3: RCS of a metallic cylinder with a wing. The cylinder has a radius of 1.25λ and height of 5λ, and the wing is 1λ by 0.5λ by 0.025λ.

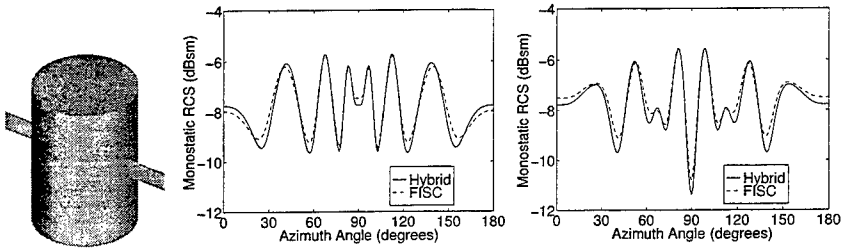

(a) VV-pol (b) HH-pol

Figure 4: RCS of a metallic cylinder with two wings. The cylinder has a radius of 1.25λ and height of 5λ, and the wings are 1λ by 0.5λ by 0.025λ.

remains very good. With four wings present, the peak-to-peak swing in the RCS is about 5 dB in the VV-polarized case and about 6 dB in the HH-polarized case.

To further illustrate the capability of the hybrid method, two more computed results are presented. Both of these results involve 1-GHz scattering from a missile with appendages. The missile is 12.5 m (41.7λ) long and has a radius of 0.625 m (2.1λ). For the first case, a 3-cm (0.1λ) by 3-cm (0.1λ) by 8.125-m (27.7λ) ridge is located on the missile at azimuth angle 0°, and computed results for an azimuth scan and for an elevation scan are presented in Fig. 6. Note that in the azimuth scan, the ridge causes the scattering to vary over a 3.5-dB range in the VV-polarized case and over a 3-dB range in the HH-polarized case while the missile alone, because of its rotational symmetry, has a constant RCS as a function of azimuth angle. In the second case, two 0.375-m (1.25λ) by 1-m (3.3λ) fins are located on the missile at azimuth angles 90° and −90°. The scattering is shown both for an azimuth cut and for an elevation cut in Fig. 7. In the azimuth cut, the scattering has changed from flat for the missile alone to a function with a 3 dB peak-to-peak variation in the VV-polarized case and a 2 dB peak-to-peak variation in the

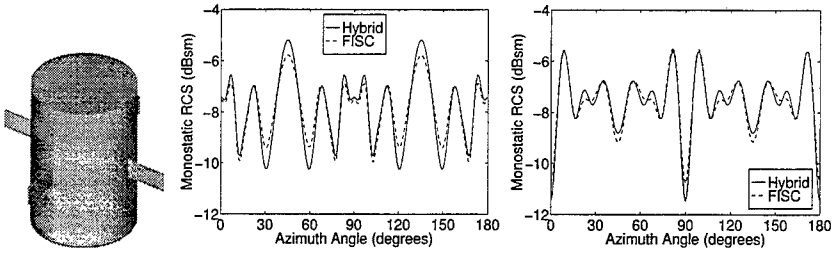

(a) VV-pol (b) HH-pol

Figure 5: RCS of a metallic cylinder with four wings. The cylinder has a radius of 1.25λ and height of 5λ, and the wings are 1λ by 0.5λ by 0.025λ.

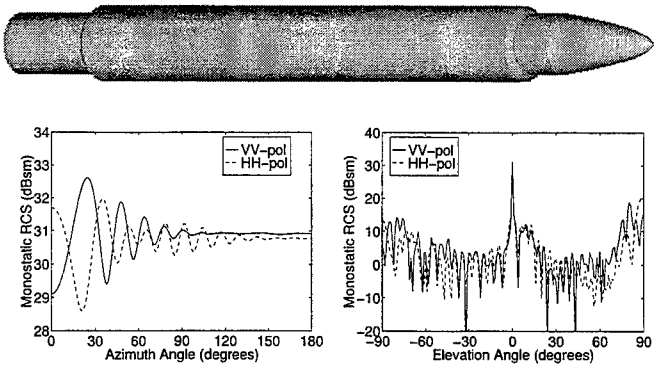

(a) Azimuth cut (b) Elevation cut

Figure 6: RCS of a missile with a ridge at 1 GHz. The missile is 12.5 m (41.7λ) long and has a radius of 0.625 m (2.1λ). The ridge is 3 cm (0.1λ) by 3 cm (0.1λ) by 8.125 m (27.7λ) and located at azimuth angle 0°.

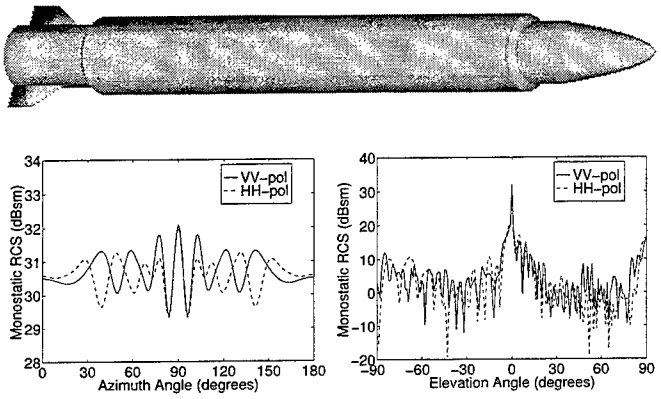

(a) Azimuth cut

(b) Elevation cut

Figure 7: RCS of a missile with two fins at 1 GHz. The missile is 12.5 m (41.7λ) long and has a radius of 0.625 m (2.1λ). The fins are 0.375 m (1.25λ) by 1 m (3.3λ) and located at azimuth angles 90° and −90°.

HH-polarized case.

4 Summary

The hybrid method is a useful extension of the FEM/BOR capability described in [1]. While rigorous computation of scattering from a BOR with appendages requires a 3-D computational method, the hybrid method separates the BOR part of the problem from the appendages. The rotational symmetry of the BOR part of the problem can then be exploited for computational efficiency while only the appendage part, which is typically much smaller than the BOR part, requires a 3-D method. Numerical results show the impact of the appendages on the scattering from the entire structure and verify the validity and capability of the hybrid method.

References

[1] A. D. Greenwood and J. M. Jin, "A novel, efficient algorithm for scattering from a complex BOR using mixed finite elements and cylindrical PML," *IEEE Trans. Antennas Propagat.*, 1998. accepted for publication.

[2] A. D. Greenwood and J. M. Jin, "Computation of the RCS of a complex BOR using FEM with coupled azimuth potentials and PML," *Electromagn.*, 1998. accepted for publication.

[3] M. G. Andreasen, "Scattering from bodies of revolution," *IEEE Trans. Antennas Propagat.*, vol. 13, pp. 303–310, 1965.

[4] J. R. Mautz and R. F. Harrington, "Electromagnetic scattering from a homogeneous material body of revolution," *Arch. Elektron. Uebertragungstech.*, vol. 33, pp. 71–80, 1979.

[5] L. N. Medgyesi-Mitschang and J. M. Putnam, "Electromagnetic scattering from axially inhomogeneous bodies of revolution," *IEEE Trans. Antennas Propagat.*, vol. 32, pp. 797–806, 1984.

[6] J. M. Jin, S. S. Ni, and S. W. Lee, "Hybridization of SBR and FEM for scattering by large bodies with cracks and cavities," *IEEE Trans. Antennas Propagat.*, vol. 43, pp. 1130–1139, 1995.

[7] A. D. Greenwood, S. S. Ni, and J. M. Jin, "Hybrid FEM/SBR method to compute the radiation pattern from a microstrip patch antenna in a complex geometry," *Microwave Opt. Tech. Lett.*, vol. 13, pp. 84–87, 1996.

[8] J. M. Jin, F. Ling, S. T. Carolan, J. M. Song, W. C. Gibson, W. C. Chew, C. C. Lu, and R. Kipp, "A hybrid SBR/MoM technique for analysis of scattering from small protrusions on a large conducting body," *IEEE Trans. Antennas Propagat.*, vol. 46, pp. 1349–1357, 1998.

[9] A. D. Greenwood and J. M. Jin, "Hybrid MoM/SBR method to compute the scattering from a slot array antenna in a complex geometry," *ACES Journal*, vol. 13, pp. 43–51, 1998.

[10] P. Munk, *A Uniform Geometrical Theory of Diffraction for the Radiation and Mutual Coupling Associated with Antennas on a Material Coated Convex Conducting Surface.* PhD thesis, The Ohio State University, Columbus, OH, 1996.

[11] J. M. Song, C. C. Lu, and W. C. Chew, "Multilevel fast multipole algorithm for electromagnetic scattering by large complex objects," *IEEE Trans. Antennas Propagat.*, vol. 45, pp. 1488–1493, 1997.

Frequency-Domain Complementary Operators for Finite Elements Simulation

Omar M. Ramahi
Compaq Computer Corporation
Omar.Ramahi@digital.com

I. Introduction

The Complementary Operators Method (COM) has been successfully used for open-region mesh truncation in the Finite-Difference Time-Domain (FDTD) solution of wave propagation problems [1]-[3]. The underlying mechanism of COM is two auxiliary differential operators, ∂_x and ∂_t. These operators are applied on an absorbing boundary condition (ABC) such as Higdon, Liao,...etc.. The purpose of these two auxiliary operators is to produce reflection coefficients that are 180° out of phase, not only in the analytic domain, but also in the discrete domain. By averaging the solutions obtained from the application of each of the two operators on an ABC, we arrive at a new solution that is devoid of first-order reflections.

In [1]-[3], the COM theory has been fully developed for time-domain simulation. In the frequency domain, a difficulty arises when obtaining the corresponding dual of the two auxiliary operators ∂_x and ∂_t. This difficulty becomes more apparent when performing the conversion $\partial_t \rightarrow j\omega$. In this work, we overcome this difficulty by introducing a new *averaging* operator which is analogous to ∂_t and achieves its objective in the time domain.

II. Frequency-Domain Complementary Operators

We consider the problem of wave propagation in two-dimensional space (the development here is equally applicable to the three-dimensional space). Let us consider a planar outer boundary parallel to the y-axis at $x = 0$. Let B deonte an ABC. Applying B on the field u, we have:

$$Bu = 0 \tag{1}$$

The first of the two complementary operators is constructed by applying ∂_x on B:

$$(\partial_x B)u = 0 \tag{2}$$

The corresponding reflection coefficient can be obtained by applying $\partial_x B$ on a plane wave $u = e^{-jk_x} + e^{jk_x}$, giving:

$$R(\partial_x B) = (-1)R(B) \tag{3}$$

In the discrete domain, however, the reflection coefficient due to $\partial_x B$ is affected by the discretization of the domain [2]. Therefore, to account for this discretization, we represent the field as

$$u = e^{-jk_x i\Delta x} + e^{jk_x i\Delta x} \tag{4}$$

where i is the space index in the x-direction. Approximating the partial derivative in (2) as a backward finite difference, we have

$$\partial_x \rightarrow D_x = \frac{(I - S^{-1})}{\Delta x} \tag{5}$$

where I is the identity operator and S^{-1} is the shift operator. Finally substituting (5) into (3) and applying the resulting operator on (4), we have

$$R(\partial_x B) \rightarrow R(D_x B) = (-1)e^{jk_x \Delta x} R^d(B) \tag{6}$$

where $R^d(B)$ denoted the discrete correspondence of $R(B)$.

For the complementary operation to be exact, we need a second complementary operator that gives a reflection coefficient of $(-1)R(D_x B)$. This can be accomplished by defining a new discrete-domain operator, which we denote by $\bar{D}_x$:

$$\bar{D}_x = \frac{I + S^{-1}}{\Delta x} \tag{7}$$

Finally, applying $\bar{D}_x$ on B, we have

$$R(\bar{D}_x B) = e^{jk_x \Delta x} R^d(B) \tag{8}$$

Equation (8) and (6) are precisely 180° out of phase; hence, full complementariness is achieved.

III. Numerical Experiment

The validity of the development above is demonstrated by a numerical experiment in which we study the problem of scattering by a $1.95\lambda \times 1.95\lambda$ perfectly conducting square cylinder. The outer boundary is positioned such that the separation between it and the conductor is 0.35λ as shown in Fig. 1. Figure 2 shows the magnitude of the electric field on the observation contour Γ (see Fig. 2) as calculated using the FEM solution. A total of 164 nodes span the observation contour. The numbering of the nodes starts at the lower left-hand corner and proceeds clockwise. Results are only shown for field values on the upper half of the contour due to the symmetry of the problem. For comparison, the Method of Moments (MoM) solution is also provided for this problem. The FEM solutions were obtained using Bayliss-Turkel second-order operator ($B = (\partial_n + jk)^2$), Bayliss-Turkel fourth-order operator ($B = (\partial_n + jk)^4$), and the fourth-order COM solution ($B = (\partial_n + jk)^3$); $n = x, y$. (The FEM implementation for the COM operators follows [4].) The numerical results show very strong agreement between the COM and MoM solutions.

IV. Conclusion

This paper presented the development of frequency-domain complementary operators. The application requires two independent solutions of the problem. Despite this, however, computer memory and execution time can be saved by positioning the outer mesh-truncating boundary closer to the conductor than what would be required when using other techniques.

References

[1] O. M. Ramahi, "Complementary operators: A method to annihilate artificial reflections arising from the truncation of the computational domain in the solution of partial differential equations," *IEEE Trans. Antennas Propagat.*, vol. AP-43, no. 7, pp. 697-704, July 1995.

[2] O. M. Ramahi, "Complementary boundary operators for wave propagation problems," *J. Computat. Phys.*, vol. 133, pp. 113-128, 1997.

[3] O. M. Ramahi, "The concurrent complementary operators method for FDTD mesh truncation," vol. 46, no. 10, pp. 1475-1482, Oct. 1998.

[4] O. M. Ramahi, "Exact Implementation of higher-order Bayliss-Turkel Absorbing Boundary Operators in 2D and 3D Scalar and Vector Wave Equation," submitted to The 15th Annual Review of Progress in Applied Computational Electromagnetics, March 15-20, 1999.

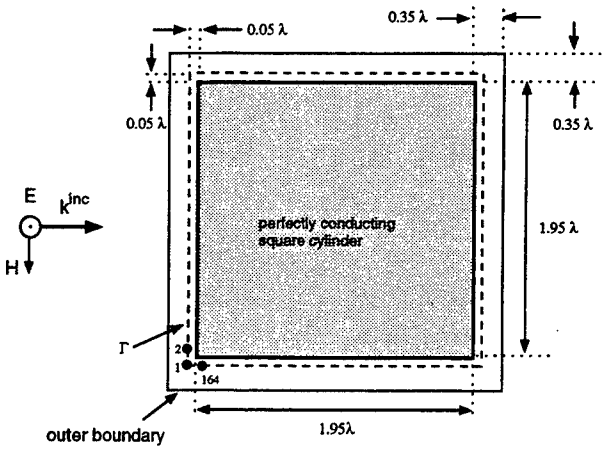

Fig. 2. Computational domain used for the problem of scattering by a perfectly conducting square cylinder.

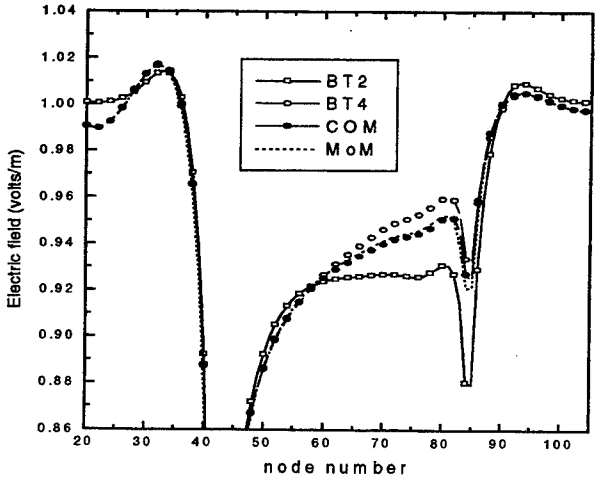

Fig. 2. Electric field for the problem of scattering by a perfectly conducting square cylinder shown in Fig. 1.

SESSION 5

MODEL-BASED PARAMETER ESTIMATION

Chairs: Andreas Cangellaris and Edmund Miller

Model-Based Frequency Extrapolation of Antenna Radiation Characteristics on Complex Platforms

Tao Su, Yuanxun Wang and Hao Ling
Department of Electrical and Computer Engineering
The University of Texas at Austin
Austin, TX 78712

I. Introduction

In antenna design and analysis, the mounting platform can have a significant effect on the antenna radiation characteristics. However, rigorous solution of the radiation problem over a complex platform is very time consuming, and the computation complexity increases dramatically as the frequency increases. In this paper, we present a model-based frequency extrapolation technique with which the radiated field over a broad band of frequencies can be obtained using the rigorously computed results at low frequencies.

Our approach entails three steps. First, the induced current on the platform surface is computed at low frequencies using the method of moments (MoM). Second, we apply the time-of-arrival model to the current on each basis element on the surface. The model coefficients are obtained using super-resolution algorithm ESPRIT [1]. Finally, the induced current at higher frequencies is computed using the model and the radiation characteristics are calculated. This approach is similar to that present in [2] and [3] for radar signature extrapolation. Our results show that when the frequencies and the discretization of the platform are properly chosen, the radiated field at higher frequencies can be extrapolated with only moderate computational cost.

II. Extrapolation Methodology

As the first step of the extrapolation process, the induced current on the target is computed at a small set of points at low frequencies. Once the current over the surface is computed at low frequencies, we apply the time-of-arrival model to each of the current element. In this model, we assume that the total current is induced by different scattering mechanisms, as shown in Fig. 1. Each of the incident mechanism has a distinct arrival time, so that the current can be written as

$$J(\omega) = \sum_{n=1}^{N} a_n e^{-j\omega t_n} \tag{1}$$

where ω is the angular frequency, N is the total number of incident mechanisms and t_n is the arrival time of the n^{th} incident mechanism.

Since the incident mechanisms correspond to scattering from different parts of the target, the maximum difference in t_n is related to the size of the target. Thus the sampling rate in the frequency domain should be high enough to distinguish these time events from all parts of the target. Based on this consideration, we approximately constraint the sampling rate in frequency to

$$\Delta f < c/D \tag{2}$$

where c is the speed of light and D is the maximum dimension of the target.

The model coefficients a_n and t_n are obtained using the superresolution algorithm ESPRIT, which is based on the model that the signal consists of a sum of exponential and additive white noise. Given a sequence with M samples, the algorithm can estimate the number of exponential N and determines the amplitude and period of each exponential term. The basic requirement in the number of samples is $M > 2N + 1$. Once the model parameters are found, the induced current at higher frequencies can be computed using (1). The radiated field is then easily obtained from the extrapolated current.

III. Results

As an example, we consider a 2-D structure as shown in Fig. 2 (a). We are interested in the radiation pattern over a frequency band from 0.15 to 0.45 GHz. To obtain the data for the extrapolation, we compute the induced current at 10 frequencies from 0.15 to 0.24 GHz. Then we use the ESPRIT algorithm to obtain the model coefficients for each current element and compute the radiated field based on the model. Fig. 2(a) shows the radiated field of a horizontally polarized line source as a function of frequency at an elevation angle of 40°. The dashed curve is obtained from the model-based extrapolation while the solid curve is the reference brute-force solution. We observe that the extrapolation algorithm correctly predicts the peaks and null positions in frequency, indicating a good estimate on the times-of-arrival. Fig. 2(b) is the time domain response obtained via an inverse Fourier transform of the frequency data. The first large peak corresponds to the specular scattering from the flat surface and the second large peak is due to the scattering from the step region.

We notice from Fig. 2(a) that the model-predicted field matches well with the reference field at the first 10 frequencies, but drops below the computed field as frequency goes higher. This is because the intensity of the field radiated by the line source is proportional to the square root of the frequency. We can overcome this by compensating this effect before doing the extrapolation. Thus the time-of-arrival model becomes

$$J(\omega) = \left(\sum_{n=1}^{N} a_n e^{-j\omega t_n} \right) \sqrt{\omega} \tag{3}$$

where $\sqrt{\omega}$ should be replaced by ω for 3-D situations. After the compensation, the extrapolation result is further improved, as shown by the frequency and time responses in Figs. 3(a) and 3(b).

Finally we look at the radiation problem of the 3-D platform in Fig. 4(a). The source is a horizontally polarized dipole. The solver used is FISC [4], which is a 3D MoM code based on the fast multipole method. Similar to the 2-D case, we use the computed current at 10 frequencies from 0.15 to 0.24 GHz to extrapolate the data to 0.45 GHz. The extrapolated radiation field as a function of frequency at the elevation angle of 40° is shown in Fig. 4(b) as the dashed curve. The reference brute-force solution is plotted as the solid curve. The major features of the radiated field are well characterized by the extrapolation algorithm.

IV. Conclusion and Discussion

As we have seen from the results, the frequency extrapolation technique is an efficient way of obtaining the radiation pattern over a broad band of frequencies. Computation time is reduced dramatically since the current is rigorously solved only at low frequencies. We improved the result by compensating the frequency factor of the source in the time-of-arrival model. This indicates that a wrong frequency dependence in the model may result in errors in the model coefficients. In addition to the frequency factor of the source, the frequency dependence of different scattering components of each current element could be different, due to different scattering physics. Further incorporation of these effects should further enhance the accuracy of the extrapolation.

Acknowledgments

This work is supported by the Office of Naval Research under Contract No. N00014-98-1-0178, and in part by the Air Force MURI Center for Computational Electromagnetics under Contract No. AFOSR F49620-96-1-0025.

References

[1] R. Roy, A. Paulraj and T. Kailath, "ESPRIT – a subspace rotation approach to estimation of parameters of cisoids in noise," *IEEE Trans. Acoust., Speech, Signal Processing*, vol. ASSP-34, pp. 1340-1342, Oct. 1986.

[2] Y. Wang, H. Ling J. Song and W. C. Chew, "A frequency extrapolation algorithm for FISC," *IEEE Trans. Antennas Propagat.*, vol. 45, pp. 1891-1893, Dec. 1997.

[3] Y.Wang and H. Ling, "Radar signature prediction using moment method codes via a frequency extrapolation technique," submitted to *IEEE Trans. Antennas Propagat.*, Feb. 1998.

[4] *User's Manual for FISC (Fast Illinois Solver Code),* Center of Computational Electromagnetics, Univ. of Illinois, Champaign, IL, and DEMACO, Inc., Champaign, IL, Jan. 1997.

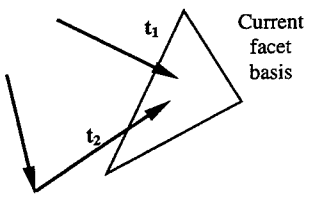

Fig. 1. Time-of-arrival model

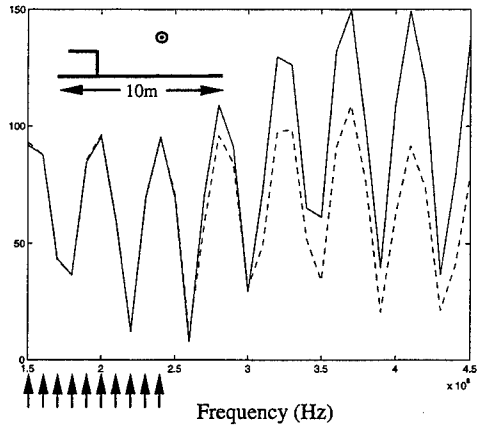

(a) Frequency response

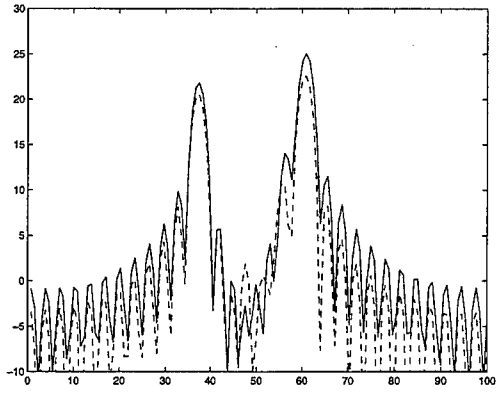

(b) Time domain response

Fig. 2. Frequency extrapolation for 2-D problem (H-Pol). ——— MoM, -------- 10 point MoM + extrapolation

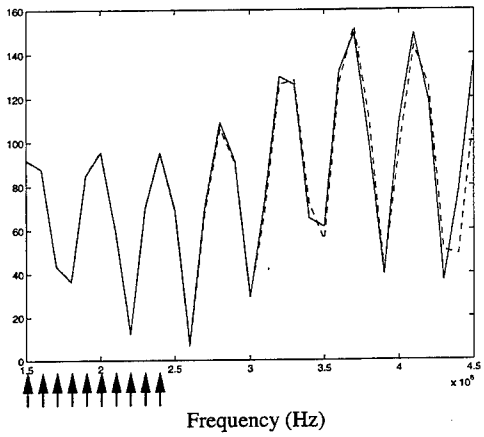

Frequency (Hz)

(a) Frequency response

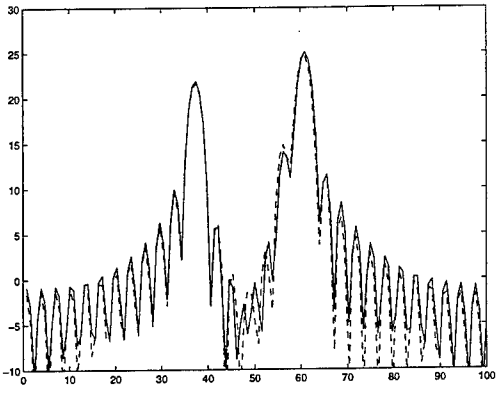

Time (ns)

(b) time domain response

Fig. 3. Frequency compensated extrapolation (H-pol). ——— MoM, -------- 10 point MoM + extrapolation

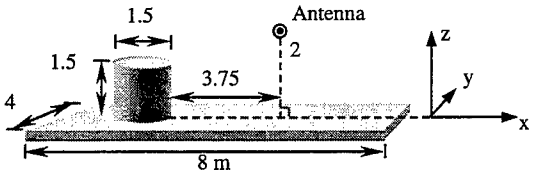

(a) Geometry of the 3-D platform

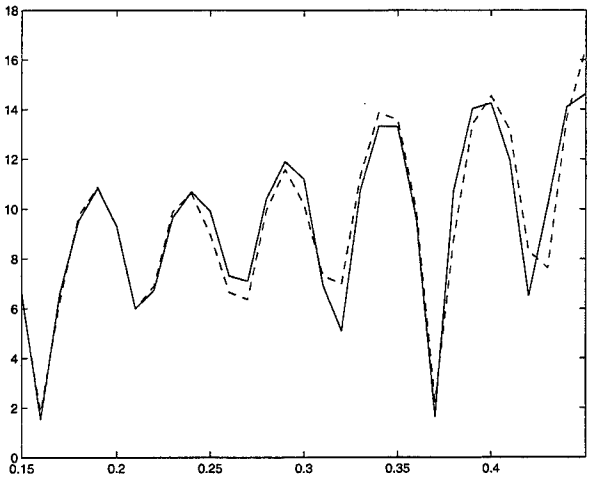

Frequency (GHz)

(b) Frequency response

Fig. 4. Frequency extrapolation for 3-D radiation. ——— FISC
-------- FISC at 10 point + extrapolation

DEVELOPING ADAPTIVE MODELS AND ESTIMATING THE UNCERTAINTY OF PRESAMPLED SPECTRAL DATA

Edmund K. Miller
3225 Calle Celestial, Santa Fe, NM 87501-9613
505-820-7371, emiller@esa.lanl.gov

0. ABSTRACT

Model-based parameter estimation (MBPE) provides a means of more efficiently describing observables such as frequency, or spectral, responses that are obtained from generating models (GM) like NEC through use of reduced-order fitting models (FM) derived from the problem physics. Besides decreasing the amount of data that is needed to develop a continuous, analytical representation of a response, these FMs can also be used to estimate the quantitative uncertainty of the GM samples themselves. These ideas, previously illustrated for sampling "on-the-fly", i.e., at the time the data samples are being computed, are extended here for application to presampled data.

1. INTRODUCTION

Use of MBPE has been previously described [Miller (1998)] as a way to adaptively sample frequency spectra, as a means of reducing the number of frequencies at which a GM computation is needed. This is made possible using a rational function (as a generalization of a pole series), reduced-order, FM to interpolate between the GM samples. Another use for such FMs is that of estimating the uncertainty of data that is sufficiently oversampled, either when being generated or only available in presampled form [Aly and Wong (1989)], in a fashion analogous to using linear regression for data described by a straight line of unknown slope and y-axis intercept. These two ideas are further developed, specifically for presampled data, in this discussion.

2. ADAPTIVE SAMPLING AND UNCERTAINTY ESTIMATION

2.1 Adaptive Sampling Based on FM Mismatch

Since the basic approach has been described elsewhere [Miller (1998)], the idea of achieving reduced-order EM-data descriptions using MBPE is only briefly outlined here. A mismatch error, or error measure

$$\Delta ME_{i,j}(y_k) \equiv \{[|M_i(y_k) - M_j(y_k)|]/[|M_i(y_k)| + |M_j(y_k)|]\} \quad (1)$$

is computed for each pair of overlapping, rational-function FMs M_i and M_j at sample locations y_k, $k = 1,. \ . \ .,Y$ to find the maximum mismatch error (MME) between FMs i and j, $ME_{ijL} = \max\{\Delta ME_{i,j}(y_k)\}$ at $y = y_L$. Location of the next GM sample is then chosen to maximize the added information it provides by adding it at y_L, where $\max\{ME_{IJL}\}$ is the overall maximum-mismatch error for all i,j,L comparisons. The true error of FM_i at y_L is also then becomes available as $\Delta GE_{i,L}$ before FM_i has been updated using GM_L. Sampling of the GM would be

concluded when the MME $\leq 10^{-C}$, where C is the convergence desired. In using this approach, the rank of an individual FM can also be maintained below some maximum value to circumvent possible ill conditioning (the effects of which can also be mitigated by singular-value decomposition). If the rank of a FM has increased to a specified threshold as a result of adding new GM samples in its window, it is divided into two, new overlapping FMs of lower order. This approach is illustrated conceptually in Fig. 1.

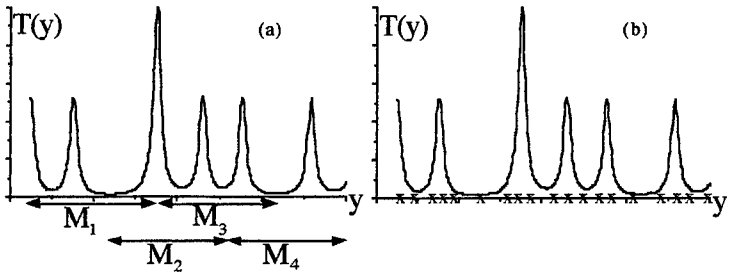

Figure 1. The possibility of developing a FM-representation of a transfer function over a wide frequency interval by employing a number of subinterval, overlapping, lower-order FMs, M_j, is illustrated conceptually here (a). Each additional GM sample used for the FM computation [the x's in (b)] is taken where the maximum FM-FM mismatch has been found, continuing until the overall mismatch falls below a specified estimation uncertainty. This results in a generally non-uniform placement of the GM samples. For presampled data the x's are restricted to the available sample locations.

2.2 Estimating Data Uncertainty

MBPE and reduced-order FMs can also be used to estimate the uncertainty of EM data, by which we mean the relative inconsistency of data obtained from a process that should satisfy Maxwell's equations. The procedure outlined here is intended to establish a bound on data uncertainty, for example to show that the data is uncertain to no more than one part in 10^4. As for the case of adaptive sampling, overlapping FMs may also be employed, with the major differences being that the GM data must be adequately oversampled and in how that data is used to quantify the FMs. At least three different approaches might be employed for estimating data uncertainty:

1) By varying the parameters [order of the numerator polynomial (n) and denominator polynomial (d), and window width (W)] of a single FM, a best-fit is sought between that FM and the unused GM data in that window.

2) Successive FMs are computed using fixed n, d and W values from GM data that has additive random noise of systematically reducing amplitude until no further change is found in the mismatch error between the FMs and unused GM data.

3) The data matrix, either square or over-determined, is solved using a pseudo-i verse solution from which a mismatch error between all of the GM data spanned by that FM representation is obtained.

The above approaches for adaptive sampling and uncertainty estimation of presampled GM data are illustrated below.

3. EXAMPLES OF ADAPTIVELY MODELING PRESAMPLED DATA

Previous examples of MBPE adaptive sampling were confined to perfect electric conductors (PEC) [Miller (1998)]. The reasonable question might arise about whether the approach works comparably well for dielectric and lossy objects, since a rationale' for the procedure is provided by SEM (Singularity Expansion Method) pole-based descriptions. The poles for a given PEC object and one of identical geometry but that is dielectric or lossy can possibly be quite different, e.g., branch cuts can be introduced [Aly and Wong (1989)]. As a matter of fact, I had been contacted [Cloete (1998)] about some apparent poor results resulting from attempting to model the frequency response of microstrip antennas on a lossy substrate. Therefore, it appeared timely to test the adaptive-sampling technique for the non-PEC application.

Not having a program to generate such results, I posted a request to NEC-LIST to see whether anyone might be able to provide me the needed data. [NEC-LIST is a BBS for exchanging EM information with a computational focus; it doesn't deal just with NEC-related issues. For information about, or to join NEC-LIST, contact Dave Michelson, davem@ee.ubc.ca]. This request generated several responses, and soon thereafter Michael Kluskens of the Naval Research Laboratory [Kluskens (1998)] sent me some data files via e-mail. It's that data that is modeled in Figs. 1-2.

The major difference between sampling a GM on the fly and handling pre-sampled GM data is, of course, that the data samples used to determine the mismatch between overlapping fitting models (FMs) cannot be arbitrarily located, but are limited to those frequencies at which GM samples are available. Thus, it's necessary that the GM data be sufficiently sampled that the FMs converge to the desired degree before exhausting the available data. In this case, the Kluskens-supplied data was sampled at 5-MHz increments from 5 to 495 MHz, for the backscattered field from an infinite, circular cylinder of radius a = 0.159 m, of relative permittivity 16 (Fig. 2) and 16 - j16 (Fig. 3), respectively. Five initial FMs and eight GM samples were used in each case, spanning samples 1-4, 1-5, 3-6, 4-8, 5-8. Additional GM samples, shown by the solid circles, were used from the pre-sampled set as needed until a maximum, normalized FM-FM mismatch of 0.01 was achieved. If adding a new GM samples to a given FM resulted in $n + d + 1 > 18$, it was divided into two new overlapping models, resulting in a total of 6 FMs for Fig. 2 where one new FM was divided and 5 for Fig 3, where this wasn't necessary. Generally speaking the added GM samples in both cases are located where the response is changing most rapidly, with the dielectric case requiring more points overall because of its greater complexity. The GM and FM results are generally graphically indistinguishable except in regions of rapid change where the average FM is sampled more finely than the precomputed GM data.

4. EXAMPLES OF ESTIMATING DATA UNCERTAINTY

Using a FM to estimate data uncertainty requires that "sufficient" GM data is available. For example, in using either approach (1) or (2) in Section 2.2, some of the GM data is used to quantify a FM whose match to the remaining GM data then provides the uncertainty test.

Approach (3) instead employs all of the available data, both to obtain a FM and to estimate the data uncertainty. Since the accuracy of the FM representation depends on both its parameters and the data being tested, it's advisable to vary the former and to observe the trends in the match between the FM predictions and GM data (called here the data fit). Based on computer experiments using various data, the best combination of FM parameters and GM data seems to be n = 7, d = 6 and a W that spans about two resonance peaks [Miller (1998)]. Some examples of various uncertainty tests follow.

4.1 Uncertainty Testing Using a Variable-Pamameter Fitting Model

Two examples of testing the uncertainty of presampled data using approach (1) of Section 2.2 are presented in Fig. 4a, the Kluskens data, and Fig. 4b, data provided by Cloete for the microstrip antenna. In both cases, a single FM is used having parameters n = 2,. . .,8 and d = 1,. . .,7 with W ≤ 42 so that at most only every other GM sample was used for the FM computation. It can be observed that in Fig. 4a the maximum average FM-GM match is about 6.5 digits whereas that in Fig. 4b is about 3.8 digits, indicating uncertainties of no worse than 3×10^{-7} and 1.6×10^{-4} respectively.

4.2 Uncertainty Testing Using Additive Noise

A further test of the Kluskens data is illustrated in Fig. 5 where four FMs are employed having n = 7 and d = 6 for models 1 and 4 and n = 7 and d = 7 for models 2 and 3, to ensure overlap of at least two FMs everywhere, and where alternate GM samples are reserved for testing the data fit. The average FM data fit is shown as a function of frequency with the parameter L denoting the level of the random noise of maximum value 10^{-L} added to the GM samples. For values of L up to 6, the individual data-fit values vary about an average of approximately L, but for L = 7 and 8 saturate at about 6.5, consistent with the results seen in Fig. 4.

4.3 Uncertainty Testing Using an Overdetermined System

The result in Fig. 6, using both the Kluskens and Cloete data, is for the case where 27 successive GM samples are used for the same four FMs as used for Fig. 5, but with each FM data matrix now overdetermined by 10 GM samples. It can be seen that the FM-GM match oscillates around an average of about 6.8, again consistent with previous results. The indication is that the Kluskens' data has a normalized uncertainty no worse than 2 to 3×10^{-7}. The corresponding value for the Cloete data from this test indicates an uncertainty of somewhat less than 10^{-4}, somewhat higher than implied by Fig. 4b.

4.4 Examples of Estimating the Uncertainty of Experimental-Data

Examples of using MBPE to estimate the uncertainty of experimental data are presented in Figs. 7-9 using results measured at the David Florida Laboratory [Mishra (1996)] for the field backscattered from a PEC cube . The actual data is comprised of 801 samples from 2 to 18 GHz. Initially, complex data was employed, yielding the results shown in the Fig. 7, where rather poor agreement is obtained between the FM (n = 7, d = 6) and the measured data.

Anticipating that the data might be known more accurately in magnitude than in phase

(which was used to obtain the real and imaginary components were), the FM was recomputed using only the magnitude data instead, with the outcome shown in Fig. 8. For simplicity, the computation continues to use a complex FM but since the input data is now pure real, the imaginary part of the FM is automatically zero. Graphically, it's clear that the match obtained between the FM and magnitude data is much better than when using the complex data.

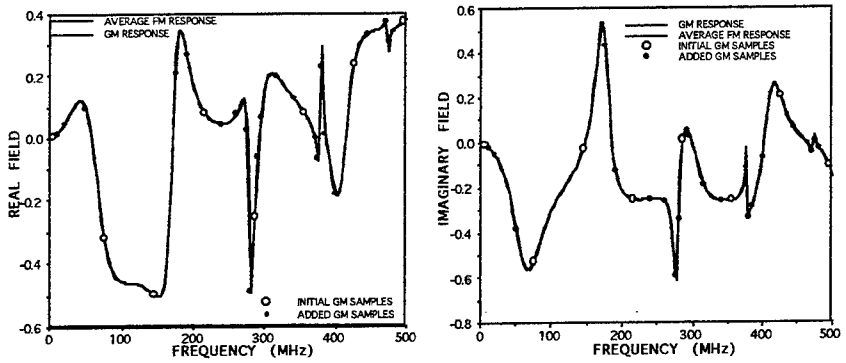

Figure 2. Adaptive sampling using precomputed data (from Kluskens) for the scattered field from an infinite, circular cylinder whose relative permittivity is 16 is illustrated here. The precomputed GM samples, spaced at 5-MHz intervals, are joined by a solid line while the average FM results are shown by the dotted line. The GM samples used for the original FM computation are shown by open circles while the samples added during the adaptation process are indicated by solid circles.

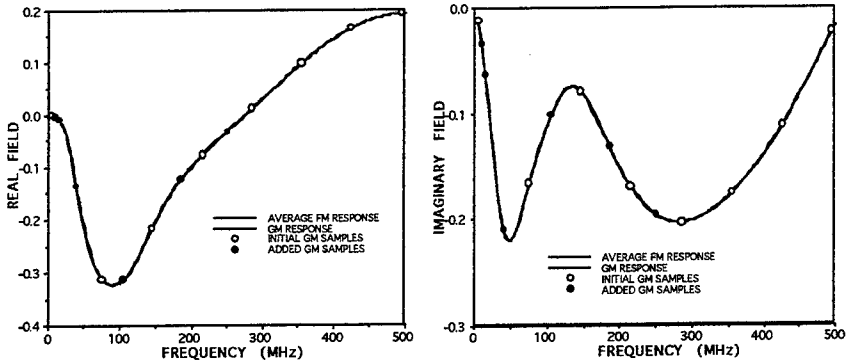

Figure 3. Adaptive sampling using precomputed data (from Kluskens) for the scattered field from an infinite, circular cylinder whose relative permittivity is 16 - j16 is illustrated here. The precomputed GM samples, spaced at 5-MHz intervals, are joined by a solid line while the average FM results are shown by the dotted line. The GM samples used for the original FM computation are shown by open circles while the samples added during the adaptation process are indicated by solid circles.

This is confirmed by the results of Fig. 9a, where the mismatch between the original data

and these two FMs is shown, indicating that the uncertainty of the measured magnitude data appears to be about 1 per cent on average. It appears reasonable to also conclude from these results that the error in the measured phase is substantially greater than that of the magnitude.

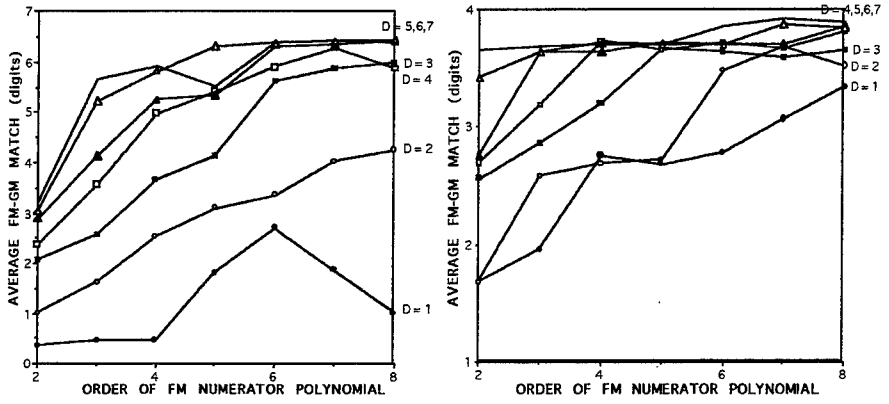

Figure 4. Average data fit between a FM of varying n and d and GM samples for the Kluskens data (a) and the Cloete data (b). These results indicate that for (a) the GM uncertainty is no worse than about 6.5 digits ($3x10^{-7}$) and for (b) about $2x10^{-4}$.

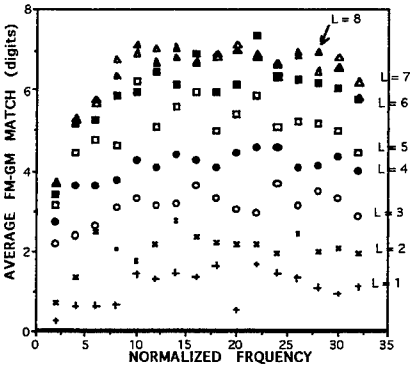

Figure 5. Data fit between average FM and GM samples as a function of normalized frequency for the Kluskens data with additive random noise of maximum value 10^{-L}. The data fit is seen to saturate at about 6.5 digits for L > 6.

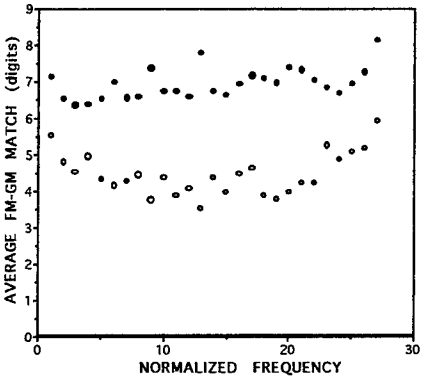

Figure 6. Data fit between the average FM and GM samples as a function of normalized frequency for the Kluskens data (solid symbols) and Cloete data (open symbols). Each computation employed four FMs and 10 extra GM samples with the over-determined data matrix solved using a pseudo inverse.

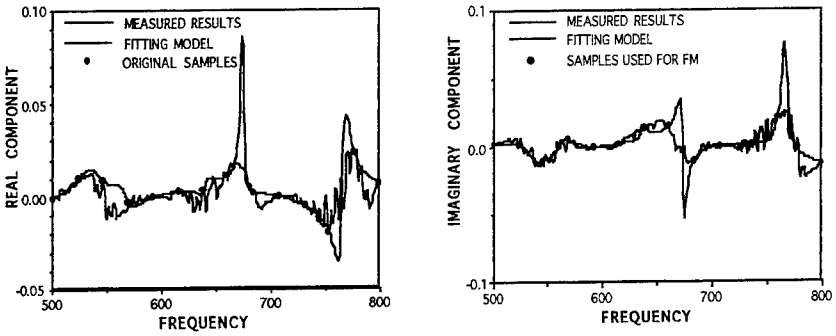

Figure 7. Results obtained from a 14-coefficient complex FM with n = 7 and d = 6 (the dark solid line) using data samples from a PEC cube (shown by the solid circles), with the narrow line showing the original data (from Mishra). Although the FM seems to average the oscillations seen in the experimental data, the overall agreement is poor.

Finally, the results of Fig. 9b demonstrate the relative insensitivity to the width of the FM frequency window, using in all cases a magnitude-only FM having n = 7 and d = 6. Despite varying the window width from 100 to 300, the uncertainty estimates in the frequency intervals where the different windows overlap are quite similar on average. Data points in both Figs. 8 and 9 that are near zero indicate that there is essentially no agreement between the FMs and the measured data.

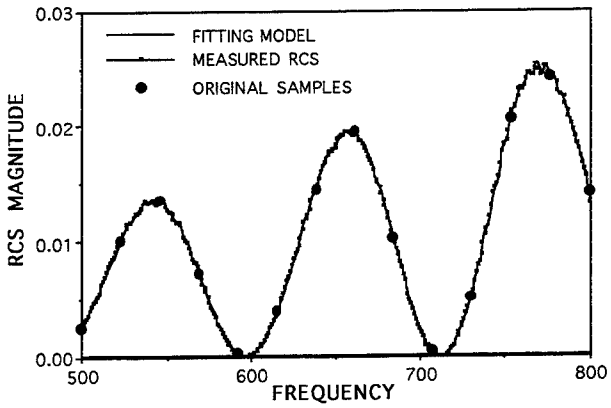

Figure 8. Repeat of Fig. 7 but using the magnitude of the measured data as the input. The data fit is much better here than when using complex input data.

5. CONCLUDING COMMENTS

The use of model-based parameter estimation (MBPE) to develop adaptive, windowed, rational-function fitting models for presampled electromagnetic data, and for estimating the uncertainty of such data has been outlined and illustrated here. For the former application, MBPE is advantageous in permitting a reduced-order, analytically continuous approximation to the discretely sampled data to be realized. For the latter, the MBPE procedure permits the uncertainty of the presampled data to be estimated in a manner analogous to linear regression when data is described by a straight line.

6. REFERENCES

M. S. Aly and T. T. Y Wong, "Root Nature of the Transverse Electric Characteristic Equation for a Dissipative Sphere, *IEEE AP-S Transactions*, 37(1), pp. 71-77, January 1989.

J. H. Cloete, Stellenbosch University, South Africa, private communication, 1998.

M. Kluskens, Naval Research Laboratory, Washington, DC, private communication, 1998.

E. K. Miller, "Model-Based Parameter Estimation in Electromagnetics: Part I. Background and Theoretical Development; Part II. Application to EM Observables; Part III. Application to EM Integral Equations," *IEEE AP-S Magazine*, February, pp. 42-52, April, pp. 51-64, and June, pp. 49-66, 1998.

Shantnu Mishra, David Florida Laboratory, Ottawa, Canada, private communication, 1996.

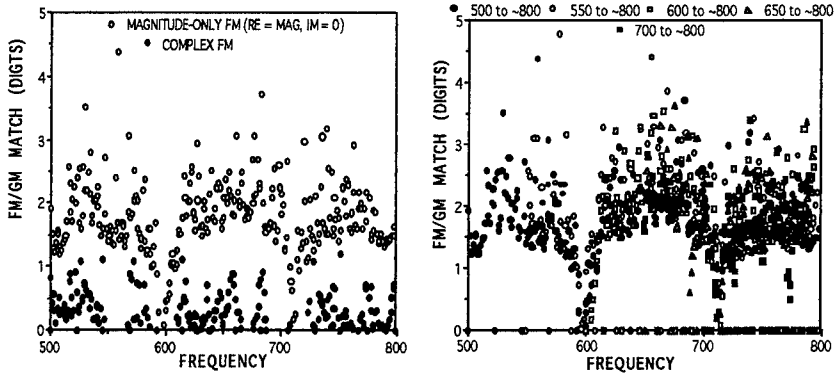

(a) (b)

Figure 9. The match in digits obtained using the complex FM (solid symbols) and magnitude-only FM (open symbols) (a) and match in digits obtained using a magnitude-only FM of various window widths (b) for the experimental field scattered from a PEC cube (from Mishra), in each case using n = 7 and d= 6. Average agreement for the magnitude-only FM in (a) is about 2 digits, with minima occurring in the vicinity of minima in the RCS. Window widths were used in (b)of 500-800 (solid circles), 550-800 (open circles), 600-800 (open squares), 650-800 (open triangles), and 700-800 (solid squares).

TECHNIQUES FOR MODEL-BASED PARAMETER ESTIMATION OF ANTENNA RADIATION PATTERNS

R.J. Allard and D.H. Werner
Applied Research Laboratory
The Pennsylvania State University
P.O. Box 30
State College, PA 16804-0030
rja5@psu.edu and dhw@psu.edu

ABSTRACT

A hybrid method for the simultaneous interpolation of antenna radiation patterns in the spatial and frequency domains is presented which combines the Padé rational function, a common MBPE fitting model, with a polynomial function to account for spatial variation. One of the most attractive features of this method is that a single set of previously determined interpolation coefficients can be used to reproduce an entire radiation pattern for a particular antenna at any frequency within its operational range, and with any desired angular resolution. Two methods for performing this hybrid interpolation will be presented and discussed in this paper. The first uses a generalized form of the Padé rational function and a multiple-domain sampling scheme to interpolate over the entire range of interest directly, and the second approach involves using a low-order (3-point) piece-wise interpolation scheme that only requires sampling in the spatial domain. The two methods are applied to a 0.5 meter dipole modeled from 150 to 950 MHz and from 0° to 90° in θ. This example is used to illustrate advantages and disadvantages in the use of both of these methods.

I. INTRODUCTION

The generation and storage of high-fidelity data for wideband antenna radiation patterns can place a significant burden on present-day computational platforms. For this reason, a technique which can quickly and efficiently interpolate, store, and reconstruct antenna radiation patterns, in both the spatial and frequency domains and with any desired fidelity, is highly desirable. An interpolation scheme based on Model-Based Parameter Estimation (MBPE) is well-suited for this problem because fitting equations that are model-based tend to greatly reduce the required order of the interpolation, and thus the amount of data that needs to be stored. A series of articles by Miller [1-3] describes in detail the principles behind MBPE, including a discussion of several model equations and their applications to a wide variety of EM problems. The model-based equation (fitting model) considered in this paper is the Padé rational function, which has been used successfully to interpolate antenna input impedance as a function of frequency [1-3], and also for the electric field frequency response of antennas [4-5]. The conventional form of this function containes no information about the position in space at which the data is being interpolated, so it cannot be used to predict how changes in spatial position affect the structure of the spectrum. A new hybrid MBPE technique was presented in [6] which included spatial dependence in the numerator and denominator coefficients of the Padé rational function. This enhancement allows the simultaneous interpolation of antenna radiation patterns in both the spatial and frequency domains such that only a single set of coefficients is required to reconstruct a radiation pattern at any desired frequency within the fitting model range. A procedure for using MBPE interpolated antenna input impedance as a function of frequency to transform the interpolated electric fields into corresponding gain patterns at any frequency was also introduced in [4-6].

The technique of simultaneous interpolation described in [6] was found to produce excellent results, with significant pattern compression ratios and only small errors in the interpolated gain patterns. Its only drawbacks involve the complexity of the matrix equations needed to perform the interpolations, and the amount of calculation time required to construct these matrices. This paper presents and discusses a modification to the procedure outlined in [6], which incorporates piece-wise spectral domain interpolation, with spatial dependence included, to model antenna radiation patterns over large bandwidths. This method only requires direct interpolation in the spatial domain, thereby using relatively small matrices and requiring much less computation time. It also allows the models used to incorporate spatial dependence to be interchanged quickly and efficiently without requiring that the entire problem be recalculated. Finally, this piece-wise procedure could be used in conjunction with the MBPE Windowed Adaptive Sampling procedure described by Miller [7-8] to determine optimum frequency sampling points for interpolating complex electric field spectra.

II. THEORY

The standard form of the Padé rational function is given by [1-3]

$$F(s)=\frac{N_0+N_1 s+N_2 s^2+\cdots+N_n s^n}{D_0+D_1 s+D_2 s^2+\cdots+D_{d-1}s^{d-1}+s^d} \tag{1}$$

which has a total of $n+d+1$ unknown numerator and denominator coefficients. For the interpolation of antenna radiation pattern frequency spectra, $F(s)$ is defined as the set of complex frequency-dependent MoM electric field data, and s is the complex-valued frequency, $j\omega$. However, this form of (1) is limited to interpolating frequency spectra at single points in space [4-5], and does not contain any information on the spatial variation of the spectrum. A more general form of the Padé rational function has been introduced in [6] which is given by

$$F(s,\theta)=\frac{N_0(\theta)+N_1(\theta)s+N_2(\theta)s^2+\cdots+N_n(\theta)s^n}{D_0(\theta)+D_1(\theta)s+D_2(\theta)s^2+\cdots+D_{d-1}(\theta)s^{d-1}+s^d} \tag{2}$$

where now the numerator and denominator coefficients are not only dependent on the complex frequency s but also on the spatial variable θ. This form of the Padé rational function is capable of interpolating an antenna radiation pattern simultaneously in both the spatial and frequency domains. The spatial dependence was modeled in [6] by assuming that each numerator and denominator coefficient could be represented by a polynomial expansion in θ of the form

$$\begin{aligned}
N_0(\theta)&=N_0^0+N_0^1\theta+N_0^2\theta^2+\cdots+N_0^k\theta^k\\
N_1(\theta)&=N_1^0+N_1^1\theta+N_1^2\theta^2+\cdots+N_1^k\theta^k\\
&\vdots\qquad\qquad\vdots\qquad\qquad\vdots\\
N_n(\theta)&=N_n^0+N_n^1\theta+N_n^2\theta^2+\cdots+N_n^k\theta^k\\
D_0(\theta)&=D_0^0+D_0^1\theta+D_0^2\theta^2+\cdots+D_0^k\theta^k\\
D_1(\theta)&=D_1^0+D_1^1\theta+D_1^2\theta^2+\cdots+D_1^k\theta^k\\
&\vdots\qquad\qquad\vdots\qquad\qquad\vdots\\
D_{d-1}(\theta)&=D_{d-1}^0+D_{d-1}^1\theta+D_{d-1}^2\theta^2+\cdots+D_{d-1}^k\theta^k
\end{aligned} \tag{3}$$

where k is the order of the polynomial. Under these conditions, (2) has $(n+d+1)\times(k+1)$ unknown complex coefficients. The procedure for determining these coefficients is to sample the MoM data set at $Nf\times N\theta$ points, write this sampled data in the form of a matrix equation using the Padé rational function, and invert the matrix equation to solve for the unknown parameters [6]. Here, $N\theta$ is the number of spatial sampling points taken at each of the Nf frequencies, and the dimensions of the resulting matrix that requires inversion is $[(n+d+1)\times(k+1)]$ by $(Nf\times N\theta)$. It should be noted that this procedure can be extended to included spatial dependence in two dimensions, for both θ and ϕ, by using a binomial spatial expansion for each numerator and denominator coefficient of the Padé rational function [6]. For the purpose of this paper, however, only one-dimensional spatial dependence will be considered.

A new technique for performing the same simultaneous interpolation described above is presented here which has several advantages over the generalized procedure. It involves using interpolation "windows", consisting of only three fitting frequencies, and incorporating a piece-wise scheme for interpolating over large frequency ranges. The Padé rational function of orders $n = 1$ and $d = 1$ with spatial dependence included is

$$F(s,\theta)=\frac{N_0(\theta)+N_1(\theta)s}{D_0(\theta)+s} \tag{4}$$

By evaluating (4) at three different sampling frequencies, we arrive at the following three equations which are dependent upon the spatial variable θ:

$$f_1(\theta)=\frac{N_0(\theta)+N_1(\theta)s_1}{D_0(\theta)+s_1} \qquad f_2(\theta)=\frac{N_0(\theta)+N_1(\theta)s_2}{D_0(\theta)+s_2} \qquad f_3(\theta)=\frac{N_0(\theta)+N_1(\theta)s_3}{D_0(\theta)+s_3} \tag{5}$$

where it is assumed that $f_i(\theta)$ exactly represents the spatial radiation pattern at the frequency s_i for $i = 1$, 2 and 3. The expressions in (5) may be rearranged and written in matrix form as

$$\begin{bmatrix} 1 & s_1 & -f_1(\theta) \\ 1 & s_2 & -f_2(\theta) \\ 1 & s_3 & -f_3(\theta) \end{bmatrix} \begin{bmatrix} N_0(\theta) \\ N_1(\theta) \\ D_0(\theta) \end{bmatrix} = \begin{bmatrix} f_1(\theta)s_1 \\ f_2(\theta)s_2 \\ f_3(\theta)s_3 \end{bmatrix} \tag{6}$$

Hence, since this only represents a 3-by-3 system, the vector of unknown coefficients may be solved for directly via Cramer's Rule [9], which yields the following expressions for the three Padé coefficients:

$$N_0(\theta)=\frac{f_1(\theta)f_2(\theta)[s_1s_3-s_2s_3]+f_2(\theta)f_3(\theta)[s_1s_2-s_1s_3]+f_1(\theta)f_3(\theta)[s_2s_3-s_1s_2]}{f_1(\theta)[s_2-s_3]+f_2(\theta)[s_3-s_1]+f_3(\theta)[s_1-s_2]}$$

$$N_1(\theta)=\frac{f_1(\theta)f_2(\theta)[s_2-s_1]+f_2(\theta)f_3(\theta)[s_3-s_2]+f_1(\theta)f_3(\theta)[s_1-s_3]}{f_1(\theta)[s_2-s_3]+f_2(\theta)[s_3-s_1]+f_3(\theta)[s_1-s_2]}$$

$$D_0(\theta)=\frac{f_1(\theta)[s_1s_3-s_1s_2]+f_2(\theta)[s_1s_2-s_2s_3]+f_3(\theta)[s_2s_3-s_1s_3]}{f_1(\theta)[s_2-s_3]+f_2(\theta)[s_3-s_1]+f_3(\theta)[s_1-s_2]} \tag{7}$$

To determine the coefficients given in (7), expressions for the three spatial radiation patterns at the frequencies s_1, s_2, and s_3 must be found using an interpolation scheme in the spatial domain. A similar polynomial expression to the one given in (3), also dependent on θ and with order k, has been shown previously to work well for interpolating one-dimensional spatial radiation patterns. Using this formulation, and incorporating a piece-wise scheme to interpolate large frequency ranges, three matrices of size $(k + 1)$ by $(k + 1)$ must be filled and inverted for each piece of the interpolation. A significant advantage occurs under these conditions since the resulting matrices, which are small compared to the one needed for the generalized procedure as described in [6], can collectively be filled and inverted in a relatively short period of time. A second advantage is that the expressions given in (7) allow the spatial dependence of the radiation pattern to be interpolated independently from the spectral variation, such that any function sufficient to accurately represent the spatial radiation pattern may be used for $f_1(\theta)$, $f_2(\theta)$, and $f_3(\theta)$. Using the generalized procedure, the entire sampling matrix would need to be recalculated and inverted in order to accomplish this same task. A third advantage of this new technique is that the reduced size and convenience of using much smaller interpolation ranges make it a suitable candidate for generalizing the MBPE Windowed Adaptive Sampling procedure, described in [7-8], for use in simultaneous interpolation. This would

allow optimal frequency sampling points to be chosen to increase the effectiveness of the simultaneous interpolations, and to eliminate trial-and-error as a means of choosing fitting points.

III. RESULTS

The generalized and piece-wise interpolation procedures were applied to the radiation pattern of a 0.5 meter dipole, modeled from 150 to 950 MHz, and for θ from 0° to 90°. For the generalized hybrid interpolation, seven fitting frequencies, 150, 300, 350, 600, 800, 900, and 950 MHz, and eight fitting angles, 2, 10, 20, 40, 60, 80, and 90°, were used to interpolate a Padé rational function of orders $n = 4$ and $d = 2$, and with polynomial spatial dependence order $k = 7$ [6]. This formulation resulted in a 56 by 56 matrix which required inversion to solve for the unknown parameters. The piece-wise hybrid MBPE technique was performed using 4 fitting windows, from 150 to 350 MHz (with fitting frequencies 200, 300, and 350 MHz), 350 to 550 MHz (with fitting frequencies 350, 425, and 550 MHz), 550 to 700 MHz (with fitting frequencies 550, 600, and 700 MHz), and 750 to 950 MHz (with fitting frequencies 750, 875, and 940 MHz). The spatial radiation patterns at the nine unique sampling frequencies were interpolated using $k = 7$ polynomials, and using the same fitting angles as in the generalized technique. This information was then used to determine explicit representations for the Padé coefficients given in (7). The difference in computation time required to perform these two operations was significant, with the piece-wise technique being much faster than the generalized hybrid interpolation. Figure 1 shows two sets of frequency spectra of electric field magnitude versus frequency for θ = 30, 70, and 90°. The left column shows results from the application of the piece-wise hybrid MBPE interpolation, and the right column the generalized technique, both are compared to the exact spectra generated via MoM. The two different interpolation procedures both show excellent agreement with the MoM data.

A more complete picture of the accuracy acheieved using these various interpolation procedures is found by examining the gain patterns which result from the estimated electric fields. To determine these patterns, a procedure which uses MBPE-estimated antenna input impedance as a function of frequency to transform from electric fields to gain patterns was introduced in [6]. This transformation was applied to three interpolations of the dipole case described above, the first two being the generalized and 4-window 3-point piece-wise interpolations, and the third being a 3-window 3-point piece-wise interpolation using just 7 fitting frequencies. The 3 fitting windows used in this interpolation were from 150 to 450 MHz (with fitting frequencies 200, 300, and 450 MHz), 450 to 650 MHz (with fitting frequencies 450, 550, and 650 MHz), and 650 to 950 MHz (with fitting frequencies 650, 875, and 940 MHz). Figure 2 shows gain pattern slices at 300 MHz and 720 MHz, with the left column presenting a comparison between the MoM, generalized, and 3-window gain patterns, and the right column showing the results from the MoM, generalized, and 4-window piece-wise interpolations. Figure 3 shows similar plots at 800 MHz and 933 MHz. The results in Figures 2 and 3 show that all three interpolated gain patterns agree very well with the MoM gain patterns at these four frequencies, with differences of a few dB apparent in both the 3- and 4-window piece-wise interpolations in the 720 and 800 MHz plots. An examination of the overall error in gain throughout the entire range of operation of the dipole antenna, from 150 to 950 MHz and over all points in space, shows that the generalized procedure does in fact produce the best results. The 3-window interpolation has a maximum gain error of 2.9 dB with an average error of about 1.0 dB, the 4-window interpolation has a maximum error of 1.79 dB with an average error at 0.7 dB, and the generalized procedure shows a maximum error of only 0.5 dB with an average gain error of less than 0.1 dB.

It is clear from these results that in order to obtain accuracies comparable to those achieved by solving the generalized Padé rational function [2], the piece-wise procedure requires a greater number of frequency sampling points. When interpolating the entire range from 150 to 950 MHz using a single model, information on the global structure of the spectrum, such as the locations of poles and zeros, improves the agreement between the actual and interpolated curves at all points in the model range. The smaller, isolated windows used in the piece-wise procedure possess information only on the local structure of the spectrum, and so more fitting frequencies are required to accurately model the data. One method for improving the ability of the piece-wise technique to model complex structures would be to employ 4-point windows, rather than the 3-point windows considered here, thus allowing a single window to capture more of the overall structure of the spectrum. The extension of this technique to 4-point windows is currently under investigation, as is research into other possible spatial domain fitting models, and the use of the adaptive windowed sampling procedure [7-8].

IV. CONCLUSIONS

By including spatial dependence in the numerator and denominator coefficients of the Padé rational function, antenna radiation patterns can be interpolated simultaneously in the spatial and frequency domains. This hybrid MBPE technique is performed by directly solving the generalized Padé rational function (2), or by using piece-wise interpolation with the spectral sampling constrained to only three frequencies per interpolation window. The piece-wise procedure allows for easy substitution of spatial-dependent fitting models without requiring that a large matrix equation be reevaluated. Another advantage of the method is that the small degree of the interpolations involved in the piece-wise procedure is amenable to the use of a Windowed Adaptive Sampling technique for the efficient determination of optimal sampling points. A comparison of the two techniques for performing simultaneous interpolation shows that both produce reconstructed models that are in excellent agreement with the original MoM data. While the piece-wise technique does require on average more sampling frequencies than the generalized interpolation approach, the additional flexibility and efficiency of the piece-wise interpolation procedure provides an attractive alternative.

ACKNOWLEDGEMENTS

The authors would like to gratefully acknowledge the assistance provided by Ed Miller in implementing Model-Based Parameter Estimation to antenna radiation patterns. His advice and guidance have been invaluable throughout the entire process.

REFERENCES

[1] E.K. Miller, "Model-Based Parameter Estimation in Electromagnetics: I --- Background and Theoretical Development," *Applied Computational Electromagnetics Society Newsletter,* Vol. 10, No. 3, pp. 40-63, 1995.

[2] E.K. Miller, "Model-Based Parameter Estimation in Electromagnetics: II --- Applications to EM Observables," *Applied Computational Electromagnetics Society Newsletter,* Vol. 11, No. 1, pp. 35-56, 1996.

[3] E.K. Miller, "Model-Based Parameter Estimation in Electromagnetics: III --- Applications to EM Integral Equations," *Applied Computational Electromagnetics Society Journal,* Vol. 10, No. 3, pp. 9-29, 1995.

[4] R.J. Allard, D.H. Werner, J.S. Zmyslo and P.L. Werner, "Spectral Domain Interpolation of Antenna Radiation Patterns Using Model-Based Parameter Estimation and Genetic Algorithms," *14th Annual Review of Progress in Applied Computational Electromagnetics,* Naval Postgraduate School, Monterey, CA, pp. 964-971, 1998.

[5] R.J. Allard, D.H. Werner, J.S. Zmyslo and P.L. Werner, "Model-Based Parameter Estimation of Antenna Radiation Pattern Frequency Spectra," *Proceedings of the IEEE Antennas and Propagation Society,* Atlanta, GA, Vol. 1, pp. 62-65, June 21-26, 1998.

[6] D.H. Werner and R.J. Allard, "The Simultaneous Interpolation of Antenna Radiation Patterns in Both the Spatial and Frequency Domains Using Model-Based Parameter Estimation," Submitted for publication in *IEEE Transactions on Antennas and Propagation,* 1998.

[7] E.K. Miller, "Minimizing the Number of Frequency Samples Needed to Represent a Transfer Function Using Adaptive Sampling," *12th Annual Review of Progress in Applied Computational Electromagnetics,* Naval Postgraduate School, Monterey, CA, pp. 1132-1139, 1996.

[8] E.K. Miller, "Using Windowed, Adaptive Sampling to Minimize the Number of Field Values Needed to Estimate Radiation and Scattering Patterns," *14th Annual Review of Progress in Applied Computational Electromagnetics,* Naval Postgraduate School, Monterey, CA, pp. 958-963, 1998.

[9] O. Schreier and E. Sperner, *Modern Algebra and Matrix Theory,* 378 pp., Chelsea Publishing Company, New York, 1951.

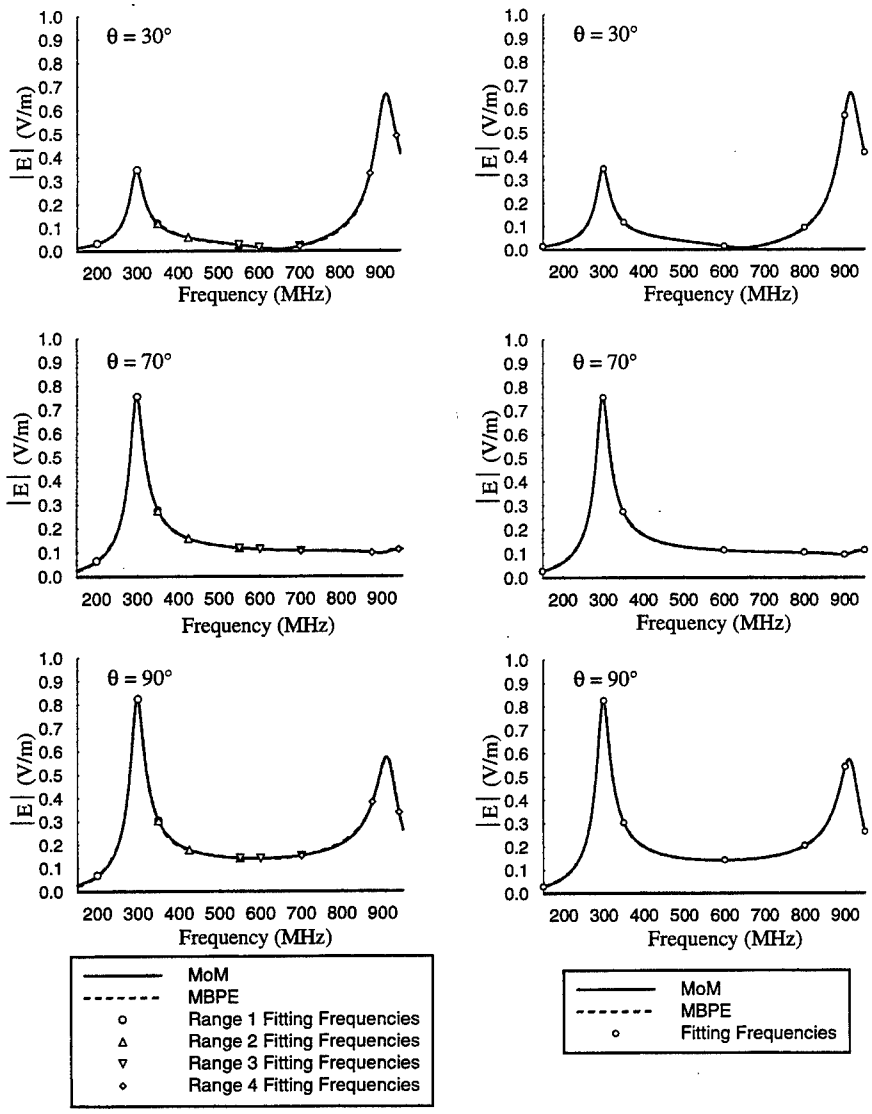

Figure 1: Plots of MBPE versus MoM electric field frequency spectra with 3-point fitting windows (left) and dual-domain sampling interpolation (right) methods. The fitting frequency windows are 150-350 MHz, 350-550 MHz, 550-700 MHz, and 700-950 MHz, with the fitting frequencies for each case defined by the symbols given. The MoM curves are indicated by solid lines and the MBPE determined curves are given by the dashed lines.

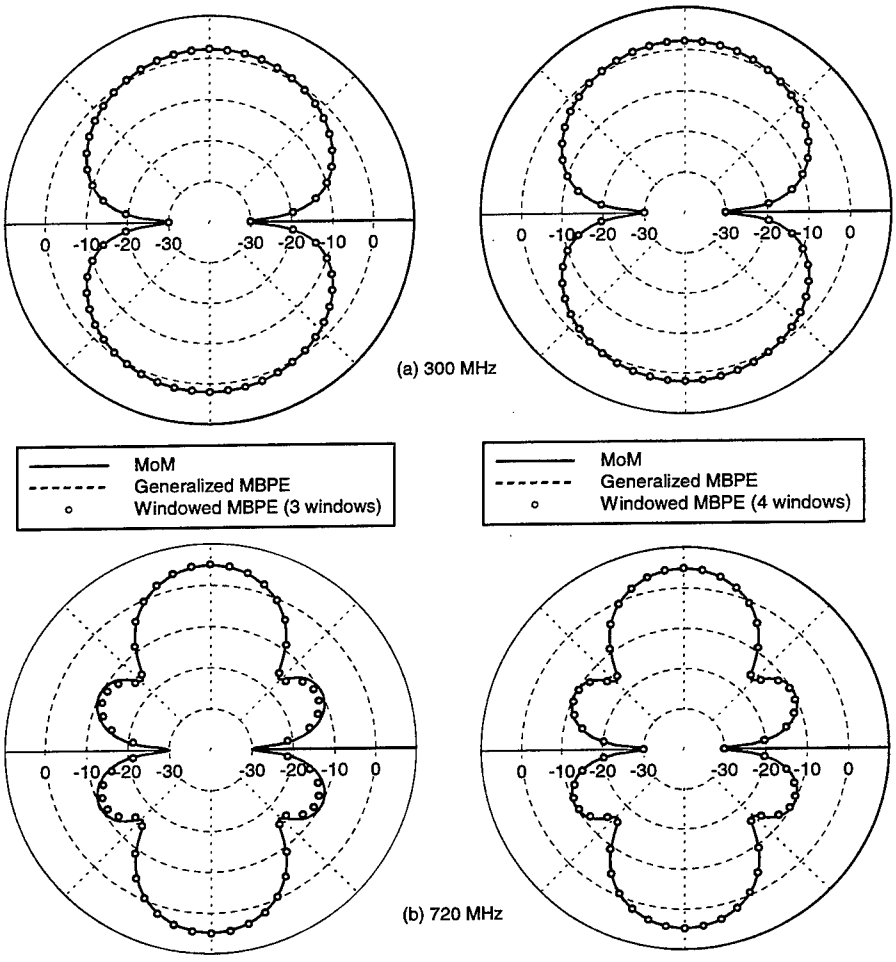

Figure 2: Comparison of MoM, generalzied MBPE, and windowed MBPE gain patterns at (a) 300 MHz and (b) 720 MHz. The left column shows results from using 3 windows (7 fitting frequencies) for the piece-wise interpolation procedure, while the right column shows results from the 4 window (9 fitting frequencies) piece-wise MBPE interpolation (as shown in the frequency spectra of Figure 1).

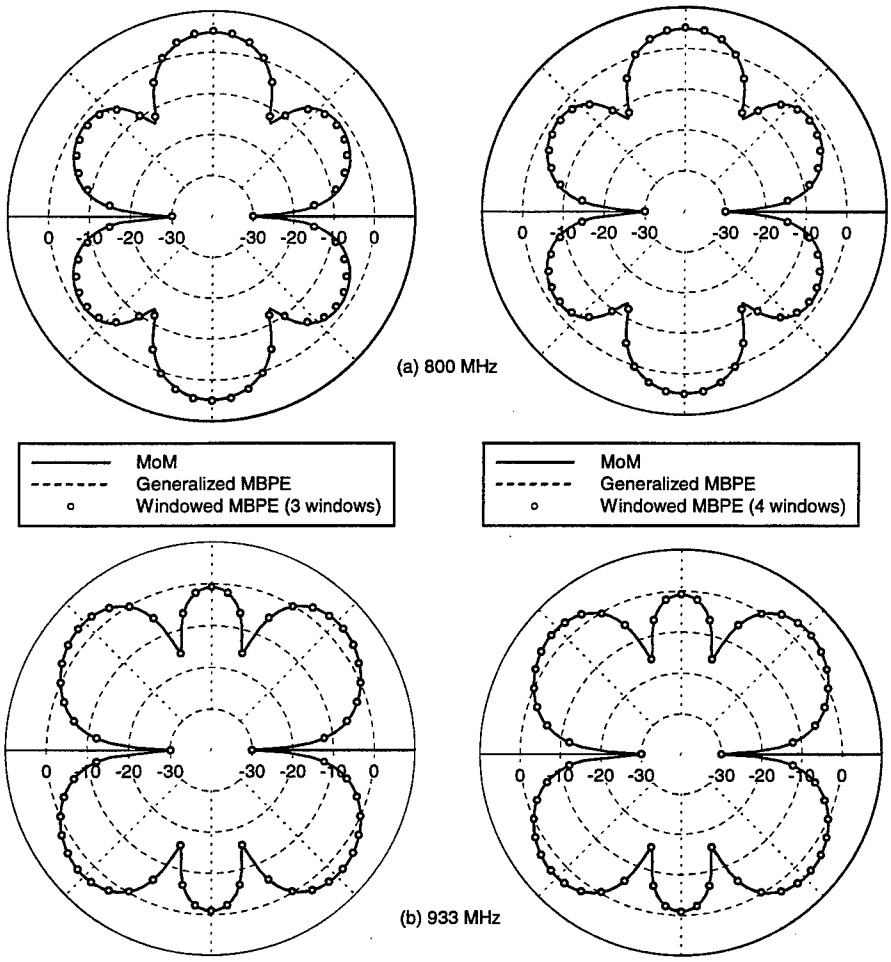

Figure 3: Comparison of MoM, generalzied MBPE, and windowed MBPE gain patterns at (a) 800 MHz and (b) 933 MHz. The left column shows results from using 3 windows (7 fitting frequencies) for the piece-wise interpolation procedure, while the right column shows results from the 4 window (9 fitting frequencies) piece-wise MBPE interpolation (as shown in the frequency spectra of Figure 1).

Full Wave Analysis of Generalized Microstrip Lines using Model Order Reduction Techniques †

KALADHAR RADHAKRISHNAN AND WENG CHO CHEW
CENTER FOR COMPUTATIONAL ELECTROMAGNETICS
DEPARTMENT OF ELECTRICAL AND COMPUTER ENGINEERING
UNIVERSITY OF ILLINOIS, URBANA, IL 61801
Email: kradhakr@uiuc.edu

Abstract

In this paper we have developed a numerical technique to carry out the full wave analysis of a generalized microstrip line on an inhomogeneous substrate. We use the finite difference method to express the problem in the form of a sparse matrix equation. A model order reduction technique is used to express the problem in terms of a smaller matrix. This is accomplished using the bi-Lanczos algorithm. The overall complexity of the algorithm is $O(N^{1.5})$. Storage requirements can be made to scale as $O(N)$ making it possible to analyze large problems on small computers. Very good agreement is seen between published results and the results obtained using this technique.

1. Introduction

Recent developments in microwave integrated circuits have led to complex waveguiding structures with multiple conductors on an inhomogeneous substrate. Several techniques are available for the analysis of microstrip lines [1]. More recently, these techniques have been extended to analyze complicated microstrip lines with multiple conductors on a multilayer substrate [2]-[7]. However, most of the work is limited to layered substrates whose permittivity is a piecewise constant function. In [7], a numerical technique was developed to analyze structures with continuous permittivity profiles along the lateral coordinate. This situation occurs when a substrate contains doping zones where the permittivity is different from that of the background. In [3], the vector finite element method is used to analyze the inhomogeneous multiconductor transmission line. However, their analysis is limited to quasi-TEM modes. To analyze the most general type of microstrip lines with an inhomogeneous substrate, one needs to use a numerical technique like the finite difference or the finite element method. This results in a sparse matrix equation with a large number of unknowns. By using a model order reduction technique like the bi-Lanczos method it is possible to solve such a sparse matrix equation efficiently.

In this paper, we have extended a numerical technique to analyze dielectric waveguides [8] to the analysis of microstrip lines on inhomogeneous substrates. The inhomogeneous vector wave equation is used as the governing equation. This allows us to model continuously varying permittivity profiles along both transverse directions. The transverse component of the wave equation is then discretized using the finite difference technique resulting in a sparse matrix equation. The eigenmodes of the sparse matrix equation correspond to the various modes of the microstrip line. Direct spectral decomposition of the matrix is expensive for complicated waveguiding structures with large matrices. However, by exploiting the sparsity of the matrices, it is possible to solve for the equation much more efficiently. This is accomplished using the bi-Lanczos algorithm.

2. Theory

The problem can be solved in terms of the transverse electric field components or the transverse magnetic field components. It has been shown [9] that both formulations are equivalent. The space-time dependence of the electromagnetic field is assumed to be $\exp[i(k_z z - \omega t)]$.

2.1. *Finite Difference Formulation*

The discretized vector wave equations can be derived from the source free Maxwell's equations and is given

† This work was supported by the MURI Program under grant F49620-96-1-0025, the National Science Foundation under grant NSF ECS 93-02145, and the Office of Naval Research under grant N00014-95-1-0872.

by [10]

$$\widehat{\nabla} \times \mu_{\mathbf{m}+\frac{1}{2}}^{-1} \widetilde{\nabla} \times \widetilde{\mathbf{E}}_{\mathbf{m}} - \Omega^2 \epsilon_{\mathbf{m}} \widetilde{\mathbf{E}}_{\mathbf{m}} = 0, \tag{1}$$

$$\widetilde{\nabla} \times \epsilon_{\mathbf{m}}^{-1} \widehat{\nabla} \times \widehat{\mathbf{H}}_{\mathbf{m}+\frac{1}{2}} - \Omega^2 \mu_{\mathbf{m}+\frac{1}{2}} \widehat{\mathbf{H}}_{\mathbf{m}+\frac{1}{2}} = 0. \tag{2}$$

In the above equation, $\widetilde{\nabla}\times$ is the curl operator using forward difference to approximate the derivatives while $\widehat{\nabla}\times$ represents the curl operator using backward difference to approximate the derivatives. Similarly, $\widetilde{\mathbf{E}}_{\mathbf{m}}$ is the fore-vector associated with the point (m, n) while $\widehat{\mathbf{H}}_{\mathbf{m}+\frac{1}{2}}$ is the back-vector associated with the point $(m+\frac{1}{2}, n+\frac{1}{2})$. This causes the electric and the magnetic field components to be defined over a staggered grid.

Matching the transverse field components of the vector wave equations and eliminating the z components, we get [9]

$$\mu_{\mathbf{m}} \widehat{\nabla}_s \times \mu_{\mathbf{m}+\frac{1}{2}}^{-1} \widetilde{\nabla}_s \times \widetilde{\mathbf{E}}_{\mathbf{m}}^s - \widetilde{\nabla}_s \epsilon_{\mathbf{m}}^{-1} \widehat{\nabla}_s \cdot \epsilon_{\mathbf{m}} \widetilde{\mathbf{E}}_{\mathbf{m}}^s - k^2 \widetilde{\mathbf{E}}_{\mathbf{m}}^s + k_z^2 \widetilde{\mathbf{E}}_{\mathbf{m}}^s = 0, \tag{3}$$

$$\epsilon_{\mathbf{m}+\frac{1}{2}} \widetilde{\nabla}_s \times \epsilon_{\mathbf{m}}^{-1} \widehat{\nabla}_s \times \widehat{\mathbf{H}}_{\mathbf{m}+\frac{1}{2}}^s - \widehat{\nabla}_s \mu_{\mathbf{m}+\frac{1}{2}}^{-1} \widetilde{\nabla}_s \cdot \mu_{\mathbf{m}+\frac{1}{2}} \widehat{\mathbf{H}}_{\mathbf{m}+\frac{1}{2}}^s - k^2 \widehat{\mathbf{H}}_{\mathbf{m}+\frac{1}{2}}^s + k_z^2 \widehat{\mathbf{H}}_{\mathbf{m}+\frac{1}{2}}^s = 0. \tag{4}$$

Here, the term $\widetilde{\mathbf{E}}_{\mathbf{m}}^s$ represents the transverse component of the electric field. Figure 1 describes the positioning of the transverse components of the electric field on the xy plane. The dielectric parameters, μ and ϵ, are defined at half grid points as well as the integer grid points to minimize the discretization error. The source term $\widetilde{\mathbf{J}}_{\mathbf{m}}^s$ is assumed to be localized on the $z = z'$ plane and represents the current element used to excite the modes in the microstrip line.

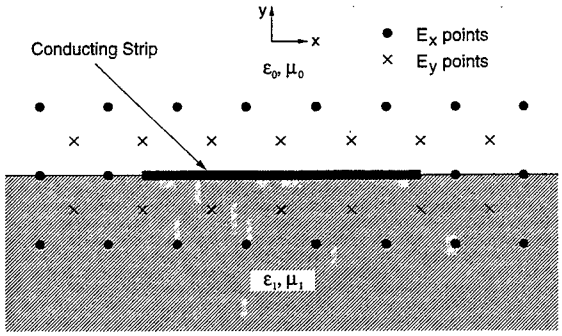

Figure 1. Location of the E_x and E_y points around the conducting strip.

Equations (3) and (4) can be expressed in the form of an eigenvalue problem

$$\overline{\mathcal{L}}_e \cdot \widetilde{\mathbf{E}}_s + k_z^2 \widetilde{\mathbf{E}}_s = 0, \tag{5}$$

$$\overline{\mathcal{L}}_h \cdot \widehat{\mathbf{H}}_s + k_z^2 \widehat{\mathbf{H}}_s = 0. \tag{6}$$

Both matrices, $\overline{\mathcal{L}}_e$ and $\overline{\mathcal{L}}_h$ are asymmetric and extremely sparse. Each eigenvector corresponds to the transverse field components for that mode while each eigenvalue represents k_z^2 for that particular mode. The bi-Lanczos algorithm is used to solve for the eigenpairs of the matrices. Each iteration in the bi-Lanczos algorithm requires two matrix vector multiplies. One computes $\overline{\mathcal{L}}_e \cdot \mathbf{v}$ while the other evaluates $\overline{\mathcal{L}}_e^T \cdot \mathbf{w}$. It is straightforward to compute the former since we know the exact definition for the operator $\overline{\mathcal{L}}_e$. In order to compute the latter without writing out the entire matrix, we seek a physical meaning to $\overline{\mathcal{L}}_e^T$. The fact that $\overline{\mathcal{L}}_e$ and $\overline{\mathcal{L}}_h$ share the same eigenvalues suggests that the latter might be related in some form to $\overline{\mathcal{L}}_e^T$. This is indeed the case and it can be shown that [8],

$$\overline{\mathcal{L}}_e^T = -\hat{z} \times \overline{\mathcal{L}}_h \cdot \hat{z} \times \tag{7}$$

2.2. Boundary Conditions

To model an open waveguide structure like the microstrip line on a finite computational domain, we need to surround the microstrip line with a metallic shielding. The boundary conditions satisfied by the transverse electric field components at the walls of a rectangular waveguide of width a and height b are

$$\left.\begin{aligned} E_x &= 0 \\ \frac{\partial E_y}{\partial y} &= 0 \end{aligned}\right\} x = 0, x = a \tag{8a}$$

$$\left.\begin{aligned} \frac{\partial E_x}{\partial x} &= 0 \\ E_y &= 0 \end{aligned}\right\} y = 0, y = b \tag{8b}$$

Since the formulation is valid for an inhomogeneous substrate, it is possible to model the conducting strip as a part of the substrate with high conductivity. However, this is not desirable since it leads to an ill-conditioned matrix with slow convergence in the bi-Lanczos method. The more efficient way is to model the conducting strip using boundary conditions. Figure 1 shows the location of the transverse field components around the conducting strip. The conducting strip should be defined on the plane where the E_x points are defined and should end at the midpoint between two adjacent E_x points. This corresponds to the location where the E_z component is defined. It has been shown [11] that the electric field component parallel to a conducting edge is always regular. By avoiding the computation of the E_x component at the edge of the conducting strip, we can keep the field finite throughout the computational domain.

In order to model the conducting strip using boundary conditions, we set the tangential electric field to be zero on the surface of the conducting strip. This implies that all E_x components which fall within the conducting strip will be set to zero. To impose the boundary conditions on the field points immediately surrounding the conducting strip, we make use of the condition that E_z should be zero on the conducting strip. Since the electric field satisfies the divergence free condition on the area just outside the conducting strip, the E_z component can be expressed in terms of the transverse field components as shown below.

$$ik_z \widetilde{\mathbf{E}}^z_{\mathbf{m}} = \epsilon^{-1}_{\mathbf{m}} \widehat{\nabla}_s \cdot \epsilon_{\mathbf{m}} \widetilde{\mathbf{E}}^s_{\mathbf{m}}. \tag{9}$$

While evaluating the field at the points immediately surrounding the conducting strip, the E_z term makes its presence felt through the second term in Eq. (3). The second term can be written in terms of E_z as shown below,

$$\widetilde{\nabla}_s \epsilon^{-1}_{\mathbf{m}} \widehat{\nabla}_s \cdot \epsilon_{\mathbf{m}} \widetilde{\mathbf{E}}^s_{\mathbf{m}} = ik_z \left[\hat{x} \left(\frac{E^z_{m+1,n} - E^z_{m,n}}{\Delta x} \right) + \hat{y} \left(\frac{E^z_{m,n+1} - E^z_{m,n}}{\Delta y} \right) \right]. \tag{10}$$

By setting the E_z components defined on the surface of the conducting strip to zero, it is possible to simulate the presence of the conducting strip. It is straightforward to extend the boundary conditions to model a conducting strip which is not infinitesimally thin. In that case, one needs to ensure that all four edges of the conducting strip end on E_z points.

2.3. Localized Current Source Response

In the presence of a localized current source, $\widetilde{\mathbf{J}}$ at $z = z'$, equations (5) and (6) become

$$\overline{\mathcal{L}}_e \cdot \widetilde{\mathbf{E}}_s + \frac{\partial^2}{\partial z^2} \widetilde{\mathbf{E}}_s = \widetilde{\mathbf{s}}_e \delta(z - z'), \tag{11}$$

$$\overline{\mathcal{L}}_h \cdot \widehat{\mathbf{H}}_s + \frac{\partial^2}{\partial z^2} \widehat{\mathbf{H}}_s = \frac{\partial}{\partial z} \widehat{\mathbf{s}}_h \delta(z - z'). \tag{12}$$

In the above equation, the z dependence of the fields has been supressed and $\mathbf{s}_e$ and $\mathbf{s}_h$ are defined as

$$\widetilde{\mathbf{s}}_e = i\Omega\mu_{\mathbf{m}} \widetilde{\mathbf{J}}^s_{\mathbf{m}} - \widetilde{\nabla}_s (i\Omega\epsilon_{\mathbf{m}})^{-1} \widehat{\nabla}_s \cdot \widetilde{\mathbf{J}}^s_{\mathbf{m}}, \tag{13}$$

$$\tilde{\mathbf{s}}_h = \hat{z} \times \epsilon_{\mathbf{m}}^{-1} \tilde{\mathbf{J}}_{\mathbf{m}}^s. \tag{14}$$

The generalized formal solution to the sparse matrix equations in terms of matrix functions is

$$\tilde{\mathbf{E}}_s = \frac{1}{2i} \overline{\mathcal{L}}_e^{-\frac{1}{2}} \cdot e^{i\overline{\mathcal{L}}_e^{\frac{1}{2}}|z-z'|} \cdot \tilde{\mathbf{s}}_e, \tag{15}$$

$$\hat{\mathbf{H}}_s = \pm \frac{1}{2} e^{i\overline{\mathcal{L}}_h^{\frac{1}{2}}|z-z'|} \cdot \hat{\mathbf{s}}_h. \tag{16}$$

To solve for the fields using equations (15) and (16), one needs to evaluate matrix functions of the form $f(\overline{\mathcal{L}}_e) \cdot \tilde{\mathbf{s}}_e$. A Krylov subspace based method is the ideal choice for solving such sparse matrix functions [12]. We use the bi-Lanczos algorithm [13] to solve the asymmetric matrix equation. The bi-Lanczos algorithm approximates the original matrix $\overline{\mathcal{L}}_e$ of size $N \times N$ with a smaller tri-diagonal matrix of size $M \times M$. Also generated during the bi-Lanczos algorithm are two sets of iteration vectors, $\overline{\mathbf{V}}$ and $\overline{\mathbf{W}}$, each of size $M \times N$. The relation between the iteration vectors and the matrices can be summarized as follows.

$$\overline{\mathcal{L}}_e \cdot \overline{\mathbf{V}} = \overline{\mathbf{V}} \cdot \overline{\mathbf{T}} \tag{17}$$

$$\overline{\mathcal{L}}_e^T \cdot \overline{\mathbf{W}} = \overline{\mathbf{W}} \cdot \overline{\mathbf{T}}^T \tag{18}$$

The iteration vectors, $\overline{\mathbf{V}}$ and $\overline{\mathbf{W}}$, in exact arithmetic are bi-orthogonal to each other. In practice, however they lose their orthogonality after a few iterations. Another alternative is to use the more robust Arnoldi method. The drawback with the Arnoldi method is that it becomes prohibitively expensive for large matrices since it performs explicit reorthogonalization at each iteration.

It can be shown that any matrix function of the form $f(\overline{\mathcal{L}}_e) \cdot \tilde{\mathbf{s}}_e$ can be evaluated as [8]

$$f(\overline{\mathcal{L}}_e) \cdot \mathbf{v}_1 = \overline{\mathbf{V}} \cdot \overline{\mathbf{Q}} \cdot f(\overline{\mathbf{\Lambda}}) \cdot \overline{\mathbf{Q}}^{-1} \cdot \mathbf{e}_1. \tag{19}$$

Here $\overline{\mathbf{Q}}$ represents the matrix containing the eigenvectors of the tridiagonal matrix, $\overline{\mathbf{T}}$ and $\overline{\mathbf{\Lambda}}$ is the diagonal matrix containing the eigenvalues of $\overline{\mathbf{T}}$. $\mathbf{e}_1$ is the first unit-M vector. The vector $\tilde{\mathbf{s}}_e$ is chosen as the starting vector, $\mathbf{v}_1$ in the bi-Lanczos iterations. Thus by carrying out the bi-Lanczos algorithm and the spectral decomposition of the resulting tridiagonal matrix, $\overline{\mathbf{T}}$, we can use Eq. (19) to solve the sparse matrix equation. The solution to Eq. (15) gives the field components at any given z plane for an arbitrary localized current source at $z = z'$. As a by-product of evaluating the current source response, it is also possible to solve for the propagating modes. The eigenvalues of the matrix $\overline{\mathbf{T}}$ are the same as the eigenvalues of the matrix $\overline{\mathcal{L}}_e$. Since these eigenvalues represent k_z^2 for that particular mode, it is possible to isolate the eigenpairs $(\lambda_i, \mathbf{q}_i)$ of the tridiagonal matrix $\overline{\mathbf{T}}$, which correspond to the propagating modes. From these eigenpairs, it is possible to obtain the eigenpairs of the $\overline{\mathcal{L}}_e$ matrix, $(\lambda_i, \overline{\mathbf{V}} \cdot \mathbf{q}_i)$. These eigenpairs contain all information that is required about the propagating modes.

2.4. Complexity and Storage Issues

The two main steps in the algorithm are the bi-Lanczos iterations and the spectral decomposition of the tri-diagonal matrix. Each bi-Lanczos iteration has two matrix-vector multiplies. Since the matrices are sparse, the matrix-vector multiply is an $O(N)$ operation. The number of bi-Lanczos iterations needed to propagate information transversely across the grid in the simulation domain is observed empirically to scale as $\sqrt{N}$. It should be noted that apart from the number of unknowns, the relative permittivity of the various substrates also play a role in determining the number of iterations required for convergence. This is because of the multiple-scattering that ensues and directly affects the condition number of the matrix. Another factor which might influence the convergence is the number of conducting strips. Since, each conducting strip has a singularity associated with its edges, the more the number of conducting strips, the higher the condition number of the matrix. The overall complexity of the bi-Lanczos algorithm is $O(N^{1.5})$. The complexity of the spectral decomposition procedure is $O(N^{1.5})$ since the size of the matrix $\overline{\mathbf{T}}$ scales as $\sqrt{N}$. If it is desired to solve for just the propagating modes, it

is possible to solve for just those eigenpairs instead of carrying out the whole spectral decomposition. This will make the algorithm faster but will not affect the overall complexity.

The iteration vectors, $\overline{\mathbf{V}}$ and $\overline{\mathbf{W}}$ are the primary bottleneck in limiting the storage requirement. Since the iteration vectors $\overline{\mathbf{W}}$ are not needed to compute the field, they can be discarded as they are generated. On the other hand, one needs to store $\overline{\mathbf{V}}$ in order to compute the current response or to compute the field distribution for the propagating modes. Hence the storage requirements scale as $O(N^{1.5})$ which is not desirable for solving large problems. Fortunately, it is possible to circumvent the storage bottleneck as discussed below.

In order to evaluate $f(\overline{\mathcal{L}}_e) \cdot \mathbf{v}_1$ or the eigenvector corresponding to the propagating modes, we need to evaluate a matrix equation of the form $\overline{\mathbf{V}} \cdot \mathbf{q}$, where $\mathbf{q}$ is a vector of size M. During the bi-Lanczos iterations, the vectors $\mathbf{v}_i$ are evaluated using the recursive relation,

$$\mathbf{v}_{i+1} = [\overline{\mathcal{L}}_e \cdot \mathbf{v}_i - \alpha(i)\mathbf{v}_i - \gamma(i-1)\mathbf{v}_{i-1}]/\beta(i). \tag{20}$$

In the above expression α, β and γ are the diagonal and sub-diagonal elements of the matrix $\overline{\mathbf{T}}$. If we store the starting vector, $\mathbf{v}_1$, it is possible to recursively obtain the subsequent iteration vectors using Eq. (20). As each vector $\mathbf{v}_i$ is computed, its contribution to the matrix-vector product $\overline{\mathbf{V}} \cdot \mathbf{q}$ is evaluated and then the vector is discarded. This process of regenerating the iteration vectors takes less than half the time required for the bi-Lanczos iterations because it needs only one matrix vector multiply and and the terms α, β and γ need not be recomputed. This increases the overall computational time of the algorithm by roughly 10% but reduces the storage to a small fraction of the original requirements. For small problems it is feasible to store the iteration vectors, but for larger problems it is imperative to discard and regenerate the iteration vectors.

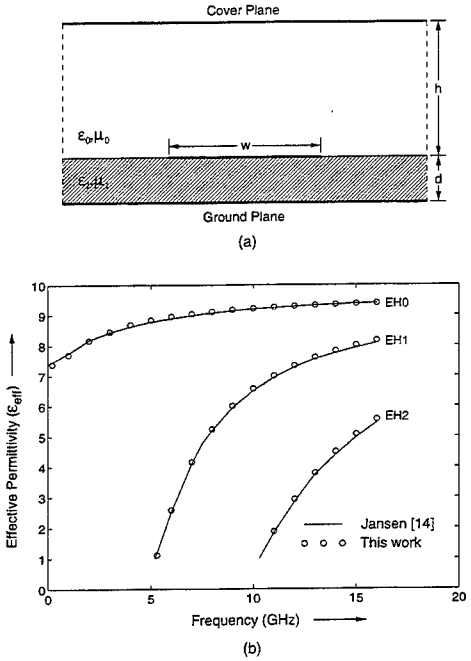

Figure 2. (a) Wide microstrip line structure, $\epsilon_1 = 9.7\epsilon_0$, w =9.15 mm, h =1.92 mm, d =0.64 mm. (b) Dispersion curves for the structure shown in Fig. 2(a).

3. Numerical Results

To study the performance of the numerical technique described in this paper, we consider three types of microstrip structures. The first structure analyzed is a simple wide microstrip line shown in Figure 2(a). Dispersion curves for the first three modes are shown in Figure 2(b). The results are compared with those published by Jansen [14]. These results were confirmed later using an analaytic technique in [15]. Very good agreement is seen between the two results.

The next example is that of a three conductor stripline structure shown in Figure 3(a). There are three distinct modes associated with this structure. Figure 3(b) plots the dispersion curves for these three modes. The results are compared with those published by Yang *et al* [4]. Once again, very good agreement is seen between the two results.

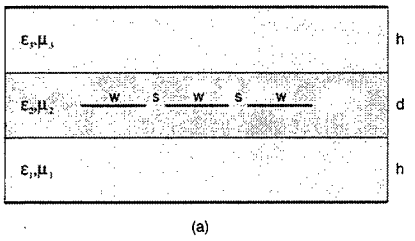

(a)

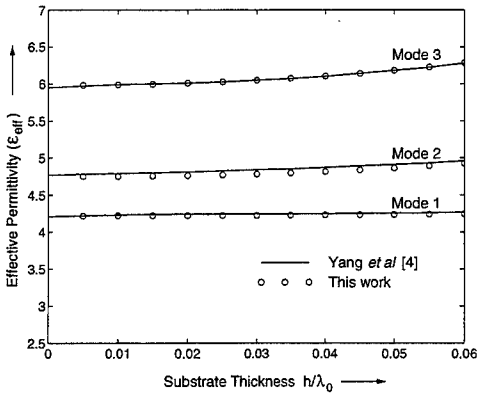

(b)

Figure 3. (a) Three conductor stripline structure, $\epsilon_1 = \epsilon_3 = 9.7\epsilon_0$, $\epsilon_2 = 4\epsilon_0$, $w/h = 1.0$, $s/h = 0.1$, $d = h$. (b) Dispersion curves for the structure shown in Fig. 3(a).

In our final example we consider a microstrip line on top of a laterally segmented substrate as shown in Figure 4(a). This example was chosen to show the ability of this technique to handle lateral inhomogeneities. Dispersion curves are plotted in Figure 4(b) for the fundamental mode at various values of b. The structure reduces to a simple homogeneous substrate for values of b =0 mm and b =2.5 mm. The results are compared with those published by Kiang [6]. Excellent agreement is seen between the two results.

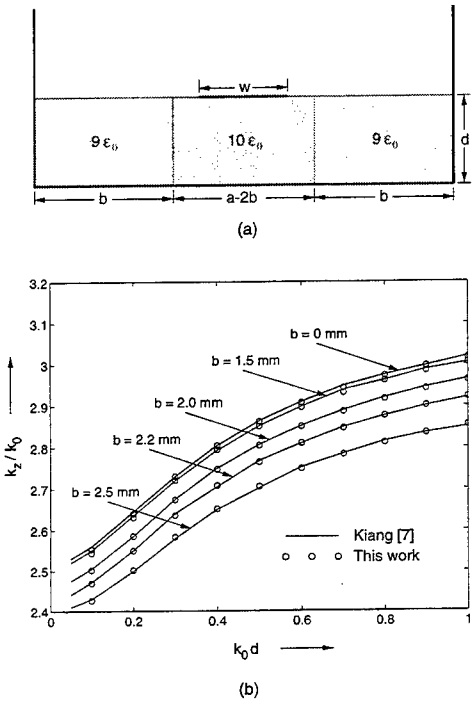

Figure 3. (a) Microstrip line on a segmented substrate, a =5 mm, w =1 mm, d =1 mm. (b) Dispersion curves for the structure shown in Fig. 4(a).

4. Conclusions

We have developed an efficient algorithm to solve the generalized microstrip line problem with multiple conductors on an inhomogeneous substrate. The strength of this technique is that the same algorithm can be used to analyze different microstrip structures by feeding in the permittivity profile of the substrate and the size and location of the conducting strips. This method can also be expanded to include anisotropic substrates as in [9]. The numerical results obtained using this technique agree well with previously published results. A possible area for future work is the use of PML to truncate the computational domain. This will help reduce the number of unknowns in open microstrip structures. Another way to accomplish this by using a subgridding technique which will also help model complex geometries accurately.

References

[1] T. Itoh, Ed., *Numerical Techniques for Microwave and Millimeter-wave Passive Structures,* New York: Wiley, 1989.

[2] C. Wei, R. F. Harrington, J. R. Mautz, and T. K. Sarkar, "Multiconductor transmission lines in multilayered media," *IEEE Trans. Microwave Theory Tech.*, vol. 32, pp. 437-449, Apr. 1984.

[3] G. W. Slade, and K. J. Webb, "Computation of characteristic impedance for multiple microstrip transmission

lines using a vector finite element method," *IEEE Trans. Microwave Theory Tech.*, vol. 40, pp. 34-40, Jan. 1992

[4] J. J. Yang, G. E. Howard, and Y. L. Chow, "A simple technique for calculating the propagation dispersion of multiconductor transmission lines in multilayer dielectric media," *IEEE Trans. Microwave Theory Tech.*, vol. 40, pp. 622-627, Apr. 1992

[5] K. Yasumoto, "Coupled-mode formulation of multilayered and multiconductor transmission lines," *IEEE Trans. Microwave Theory Tech.*, vol. 44, pp. 585-590, Apr. 1996.

[6] M. .S Alam, M. Koshiba, K. Hirayama, and Y. Hayashi, "Hybrid-mode analysis of multilayered and multiconductor transmission lines," *IEEE Trans. Microwave Theory Tech.*, vol. 45, pp. 205-211, Feb. 1997

[7] J. F. Kiang, "Microstrip lines on substrates with segmented or continuous permittivity profiles," *IEEE Trans. Microwave Theory Tech.*, vol. 45, pp. 229-235, Feb. 1997.

[8] K. Radhakrishnan, and W. C. Chew, "An efficient Krylov subspace based algorithm to solve the dielectric waveguide problem," submitted to *IEEE Trans. Microwave Theory Tech.*

[9] W. C. Chew, and M. Nasir, "A variational analysis of anisotropic, inhomogeneous dielectric waveguides," *IEEE Trans. Microwave Theory Tech.*, vol. 37, no. 4 pp. 661, 1989.

[10] W. C. Chew, "Electromagnetic theory on a lattice," *J. Appl. Phys.*, vol. 75, pp. 4843-4850, May 1994.

[11] J. Meixner, "The behavior of electromagnetic fields at edges," *IEEE Trans. Antennas Propagat.*, vol. 20, pp. 442-446, July 1992.

[12] V. Druskin, and L. Knizhnerman, "On application of Lanczos method to solution of some partial differential equations," Tech. rep. no. EMG-92-27, Schlumberger-Doll Research, April 1992.

[13] C. Lanczos, "An iteration method for the solution of the eigenvalue problem of linear differential and integral operators," *J. Res. Nat. Bur. Stand.*, vol. 45, pp. 255-282, 1950.

[14] R. H. Jansen, "High-speed computation of single and coupled microstrip parameters including dispersion, high-oeder modes, loss and finite strip thickness," *IEEE Trans. Microwave Theory Tech.*, vol 26, pp. 75-82, Feb. 1978.

[15] W. C. Chew, and J. A. Kong, "Asymptotic Eigenequations and analytic formulas for the dispersion characteristics of open wide microstrip lines," *IEEE Trans. Microwave Theory Tech.*, vol. 29, pp. 933-941, Sept. 1981.

Frequency and Angular Extrapolations in Hybrid Finite Element-Boundary Integral Systems

Yunus E. Erdemli, Arik D. Brown, and John L. Volakis
Radiation Laboratory
Department of Electrical Engineering and Computer Science
The University of Michigan
Ann Arbor, MI 48109-2122

Abstract

The hybrid finite element-boundary integral (FE-BI) method has been quite popular due to its adaptability in modeling arbitrarily shaped objects involving complex materials. However, being a frequency domain analysis, the FE-BI method may not be appealing for broadband frequency-dependent data generation. Also, it is unavoidable to resolve the hybrid system for each excitation (incidence angle) when an iterative solver is employed. Subsequently, monostatic radar cross section (RCS) calculations are computationally intensive, and therefore asymptotic waveform evaluation (AWE) as an extrapolation method becomes attractive for CPU time reduction. In this paper, we present frequency and angular extrapolation implementations in FE-BI systems. Scattering applications of the hybrid technique in conjunction with AWE will be presented to demonstrate the performance of these implementations in terms of accuracy and computational efficiency.

1 Introduction

Hybrid FE-BI methods have gained wide acceptance because they combine the rigor of the integral equation for truncating the mesh with the material generality and geometrical flexibility of the finite element method [1]. In these methods, a matrix system is formed and solved to obtain the desired parameters by using a direct or an iterative solver. For electrically large problems, however, the solution of the matrix system is computationally intensive and must be repeated at finer frequency increments. In addition, the solution must be independently carried out for each angle of incidence in case of an iterative solver. Hence, monostatic RCS calculations are computationally intensive; therefore AWE or other types of extrapolation methods become attractive for CPU time reduction.

The AWE method provides a reduced-order model of a linear system that has been successfully used in various electromagnetic and circuit applications [2]-[7]. It is worthy to note that every aspect of the method of model-based parameter estimation (MBPE), which is identical to AWE in nature, has recently been reviewed by Miller [8]-[10]. Furthermore, Miller introduced an MBPE based approach called windowed-adaptive-sampling pattern estimation (WASPE) to obtain radiation and scattering patterns [11]. In particular, the implementation of the AWE technique in conjunction with the method of moments (MoM) and the hybrid FE-BI method has also appeared in the recent literature [12]-[14]. These implementations dealt with accurate and efficient frequency-dependent data estimations. Also, a pattern fill implementation for MoM systems has been introduced in [14] as an application of angular extrapolation.

In this paper, we first present a brief review of formulation for frequency and angular extrapolations applied in FE-BI and MoM systems, respectively, given in [14]. We will then demonstrate the efficiency and accuracy afforded by these implementations for 3D scattering problems.

2 Frequency Extrapolation for FE-BI Systems

On the basis of AWE, a Taylor series expansion of the matrix system (MoM or FE-BI) is generated about a specific value of the system parameter (frequency or angle). The expansion coefficients or moments are then used to extract poles of the system, yielding a rational function (Padè approximation) of the system parameter. Padè representations have a larger circle of convergence and can therefore provide a broader extrapolation because they include not only zeros but also poles of the response. This representation results in an extension of the region of convergence (RoC) of the power series, thus increasing the accuracy of the analysis to a wider range. In this section, we will describe the implementation of AWE into FE-BI systems for frequency extrapolation.

In accordance with the FE-BI procedure [15], cavity-backed structures are formulated using the finite element method for the fields within the cavity and the boundary integral for mesh truncation across the aperture. With frequency f as the parameter of interest for extrapolation, discretization of the field equations using tetrahedron in the volume and triangles on the aperture [1] in conjunction with Galerkin's method yields the system

$$[A_{mn}(k)]\{e_n(k)\} = \{g_m(k)\} \tag{1}$$

where $[A_{mn}(k)]$ is a partly sparse, partly dense complex symmetric matrix, $\{g_m(k)\}$ is the excitation vector, $\{e_n(k)\}$ is the unknown electric field coefficient vector, and k is the free space wave number representing the frequency dependence of the system. For simple media, $[A_{mn}(k)]$ is a linear combination of matrices with k dependencies in the form of k^2 (due to FE-part), e^{-jk} and k^2e^{-jk} (due to BI-part) [14]. However, this dependence may become more complicated for frequency-dependent anisotropic media. For instance, depending on the direction of applied dc bias field, corresponding entries in permeability tensor of a ferrite material become rational functions in frequency. In addition, the k-dependence of $g_m(k)$ is determined by the type of excitation being applied. In case of a plane wave excitation, it takes the form of ke^{jk}. On the other hand, for a radiation problem, this form is specified by the type of the feed structure being used. For instance, $g(k)$ is a linear function of k for a probe-current feeding, whereas it is a function of ke^{jk} for a coaxial line feed structure [14].

To apply AWE to the system (1), we begin by expanding the unknown field vector $e(k)$ at a specific value of $k=k_0$ as

$$\{e_n(k)\} = \sum_{s=0}^{\infty}\{M_n^s\}(k-k_0)^s,\ \{M_n^0\} = \{e_n(k_0)\} \tag{2}$$

where the moments $\{M_n^s\}$ for $s>0$ given by

$$\{M_n^s\} = [A_{mn}(k_0)]^{-1}\left(\{g_m^{(s)}(k_0)\}/s! - \sum_{q=1}^{s}\left[A_{mn}^{(q)}(k_0)\right]\{M_n^{s-q}\}/q!\right) \tag{3}$$

Here $[A_{mn}(k_0)]^{-1}$ is the inverse of $[A_{mn}(k_0)]$ and $A_{mn}(k_0)$ is the q^{th} derivative of $A_{mn}(k)$ with respect to k evaluated at k_0. Similarly, $g_m^{(s)}(k_0)$ is the s^{th} derivative of $g_m(k)$ with respect to k evaluated at k_0. Once the AWE moments are obtained, the electric field coefficients at frequencies around the expansion frequency can be calculated via (2). However, the accuracy of (2) quickly deteriorates as k moves away from k_0. To extend the utility of the expansion, its Padè equivalent can in turn be used to obtain the frequency response [12]-[14].

The basic starting point for the Padè approximation is to obtain the Taylor series expansion of a given function about a reference point. Thus, each entry of the vector $\{e_n(k)\}$ in (2) is considered as a complex function of k and can be expanded as

$$e_n(k) = \sum_{s=0}^{\infty} M_n^s(k-k_0)^s \tag{4}$$

Using this notation, the Padè representation for each $e_n(k)$ is then given by

$$P_n(L/M) = \left(\sum_{l=0}^{L} a_n^l(k-k_0)^l\right)\Big/\left(1+\sum_{m=1}^{M} b_n^m(k-k_0)^m\right) \tag{5}$$

where the coefficients a_n^l and b_n^m are obtained by satisfying the equality

$$\sum_{s=0}^{\infty} M_n^s (k-k_0)^s = P_n(L/M) + O(k^{L+M+1}) \tag{6}$$

The integers L and M are the orders of the zero and pole expansions, respectively. The coefficients a_n^l and b_n^m are then found from

$$\sum_{j=1}^{l} M_n^{l-j} b_n^j = -M_n^l \ , \ L+1 \le l \le L+M \ , \ l > M : b_n^j = 0 \tag{7}$$

$$a_n^0 = M_n^0 \ , \ a_n^l = M_n^l + \sum_{j=1}^{\min(l,M)} M_n^{l-j} b_n^j \ , \ 1 \le l \le L \tag{8}$$

To demonstrate the frequency extrapolation implementation described above, we consider the scattering by a ferrite loaded cavity-backed aperture [16] as shown in Fig. 1. A y-directed dc biasing of H_0=800Oe is applied in the ferrite layers with a magnetization of $4\pi M_s$=445G. The discretization of the cavity volume resulted in 4182 unknowns of which 133 were on the aperture. In Fig. 1, the RCS response in the frequency band of 0.7-1 GHz is displayed for exact FE-BI and Padè approximations with L=M=2 for two different expansion points, f_0=0.8GHz and f_0=0.9GHz. As seen, both AWE results agree with the exact solution quite well. In particular, during the analysis of this problem, it was observed that the resonance frequency (f_r=0.85GHz) is captured by AWE

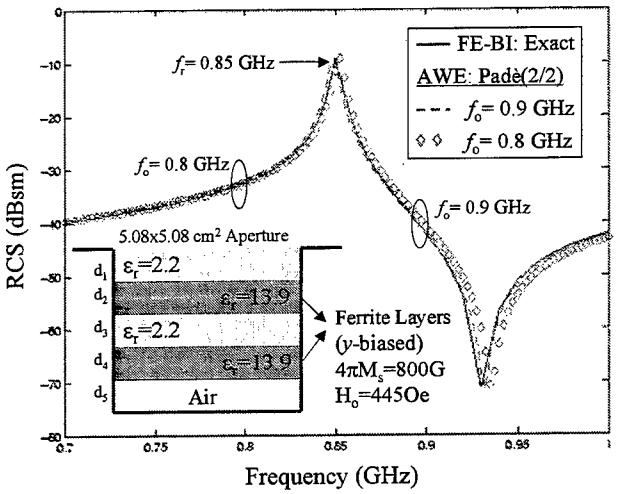

Figure 1. Monostatic RCS (normal incidence: θ_0=ϕ_0=0°) frequency response of a ferrite loaded cavity (d_1=0.726, d_2=1.790, d_3=0.737, d_4=0.762, d_5=1.065 in cm): FE-BI (exact) vs. AWE (approximate).

solutions with a reasonable accuracy regardless of the choice of expansion point. For CPU time comparisons, we used 31 frequency points for a reasonable approximation of the RCS response using the FE-BI. The corresponding CPU time was 1 hour 20 minutes. On the other hand, Padè (2/2) approximation was carried out in 30 minutes which is at least half of the CPU time consumed by the exact solution. Clearly, AWE provides a noticeable improvement in CPU time, as expected. It is important to note that the FE-BI solution was obtained using an iterative solver, but the AWE solutions were produced by employing a direct solver because of a need to use the inverse of the system matrix every time an AWE moment is generated (see Eqn. 3). When the FE-BI

solution is also obtained via a direct solver, the CPU time reduction with AWE becomes outstanding with a value of 95%.

3 Pattern Fill Implementation in MoM Systems

MoM has been a popular tool for accurate prediction of RCS calculations [17]. Its implementation in connection with the electric field integral equation (EFIE) involves a solution of the electric current surface density using a direct or some iterative solver. With incidence angle θ as the parameter of interest for extrapolation (at a fixed ϕ-cut and for a specific frequency), a usual form of the MoM system is given by

$$[Z_{mn}]\{I_n(\theta)\} = \{V_m(\theta)\} \tag{9}$$

where $[Z_{mn}]$ is a full complex matrix which is independent of incidence angle in nature, I_n refer to the unknown current density coefficients, and $\{V_m(\theta)\}$ is the excitation vector. It is apparent that only dependence on θ is due to the excitation, and for a plane wave incidence, $V_m(\theta)$ becomes a function of $e^{j(c_1 \sin\theta + c_2 \cos\theta)}$ in which c_1 and c_2 are constant terms with respect to θ.

For monostatic pattern evaluations using a direct solver it is necessary to carry out the matrix vector product $[Z_{mn}]^{-1}\{V_m(\theta)\}$ for each excitation. On the other hand, for iterative solvers, the entire solution must be repeated for each incidence angle. AWE can again be employed to eliminate repetition of the iterative solutions altogether except for a few pattern points used as the expansion points of the angular extrapolation.

To show how AWE can be applied, we assume that $\{I_n(\theta)\}$ has already been computed at a given direction (ϕ_0, θ_0). A Taylor series expansion on θ (with ϕ constant) is then given by

$$\{I_n(\theta)\} = \sum_{s=0}^{\infty} \{M_n^s\}(\theta - \theta_0)^s, \quad \{M_n^0\} = \{I_n(\theta_0)\} \tag{10}$$

$$\{M_n^s\} = [Z_{mn}]^{-1}\{V_m^{(s)}(\theta_0)\}/s! \tag{11}$$

where $V_m^{(s)}(\theta_0)$ is the s^{th} derivative of $V_m(\theta)$ with respect to θ evaluated at θ_0. For plane wave excitations, the moments $\{M_n^s\}$ can be trivially calculated, and one could therefore increase the order of the expansion as needed to extend the validity of the approximation. This is better achieved by casting (10)-(11) into a Padè rational function. In this case equations (4)-(6) are applicable provided e_n, k, and k_0 are replaced by I_n, θ and θ_0, respectively. We also note that the angular extrapolation described here is also applicable for FE-BI systems in a similar manner.

To demonstrate the proposed pattern fill procedure, we consider the scattering by a metallic plate (2λx2λ) with three circular holes as shown in Fig. 2. In this case, the resulting full matrix size was 649x649. The incident electric field is given by

$$\vec{E}_{inc}(\theta) = \hat{y}e^{jk_0(x\sin\theta - z\cos\theta)} \tag{12}$$

i.e. $\phi = 0°$. The monostatic RCS pattern was first computed at θ =14°, 38°, 58°, 75° using an iterative MoM code and these points were then used as expansion points to generate Padè approximations with L=3, M=1 and L=M=1. As seen in Fig. 2, each expansion best approximates the reference RCS pattern in the corresponding angular sector. In proving CPU time speed-ups, we used 91 MoM points as reference. The corresponding CPU time was 1 hour 37 minutes. On the other hand, the multi-point Padè approximation at 181 points was carried out in 25 minutes which is about a quarter of the CPU time used by the MoM. This comparison clearly shows how monostatic RCS patterns can be obtained much faster by means of AWE. Of course, as the number of angular (or frequency) points in the reference solution increases, AWE becomes more attractive in terms of CPU cost. As a result of a systematic study for AWE order vs. the angular band of the approximation, we observed

that a Padè expansion with L=1, M=1 or M=0 results in a sufficiently accurate approximation if one expansion point is chosen for every angular sector with a single lobe/null.

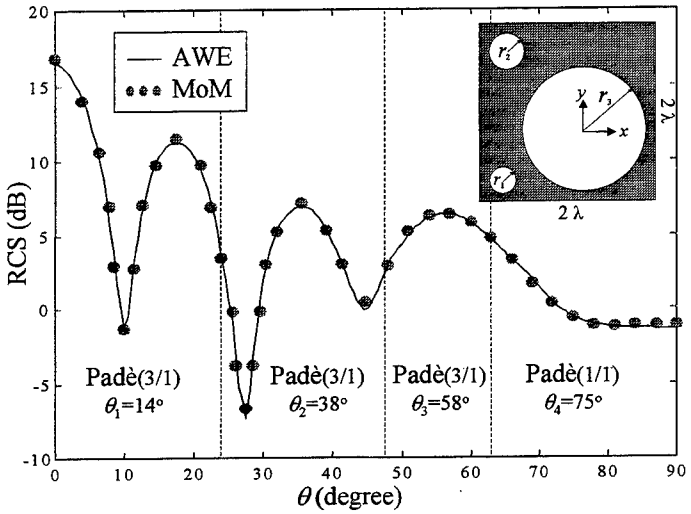

Figure 2. Monostatic RCS pattern of a square PEC plate with three circular holes (r_1=0.15λ, r_2=0.25λ, r_3=0.7λ): MoM (exact) vs. AWE (approximate).

4 Conclusion

In this paper, we presented frequency and angular extrapolation implementations in hybrid FE-BI systems for generating broadband RCS patterns using only a few points of the exact solution. Once again, it was demonstrated that AWE is a fast and accurate (within a bandwidth of the expansion point) model order reduction technique. We should point out that the accuracy and extrapolation range of the AWE implementation depend upon several factors such as pattern shape, location of the expansion points and the order of the Padè representation. If these design parameters are addressed properly, AWE proves to be an alternative method for the solution of scattering as well as radiation problems in frequency domain electromagnetics.

References

[1] J. L. Volakis, A. Chatterjee, and J. Gong, "A class of hybrid finite element methods for electromagnetics: A review," *J. Electromagn. Waves Applications*, vol. 8, no. 9/10, pp. 1095-1124, 1994.

[2] E. K. Miller and G. J. Burke, "Using model-based parameter estimation to increase the physical interpretability and numerical efficiency of computational electromagnetics," *Computer Phys. Commun.*, vol. 68, no. 1-3, pp. 43-75, Nov. 1991.

[3] S. Kumashiro, R. A. Rohrer, and A. J. Strojwas, "Asymptotic waveform evaluation for transient analysis of 3-D interconnect structures," *IEEE Trans. Computer-Aided Design*, vol. 12, no. 7, pp. 988-996, July 1993.

[4] E. Chiprout and M. Nakhla, *Asymptotic waveform evaluation and moment matching for interconnect analysis*. Norwell, MA: Kluwer, 1994.

[5] J. Gong and J. L. Volakis, "AWE implementation for electromagnetic FEM analysis," *Electron. Lett.*, vol. 32, no. 24, pp. 2216-2217, Nov. 1996.

[6] M. A. Kolbehdari, M. Srinivasan, M. S. Nakhla, Q.-J. Zhang, and R. Achar, "Simultaneous time and frequency domain solutions of EM problems using finite element and CFH techniques," *IEEE Trans. Microwave Theory Tech.*, vol. 44, no. 9, pp. 1526-1534, Sep. 1996.

[7] S. V. Polstyanko, R. Dyczij-Edlinger, and J.-F. Lee, "Fast frequency sweep technique for the efficient analysis of dielectric waveguides," *IEEE Trans. Microwave Theory Tech.*, vol. 45, no. 7, pp. 1118-1126, July 1997.

[8] E. K. Miller, "Model-based parameter estimation in electromagnetics: Part I. Background and theoretical development," *Antennas Propagat. Mag.*, vol. 40, no. 1, pp. 42-52, Feb. 1998.

[9] E. K. Miller, "Model-based parameter estimation in electromagnetics: Part II. Applications to EM observables," *Antennas Propagat. Mag.*, vol. 40, no. 2, pp. 51-65, Apr. 1998.

[10] E. K. Miller, "Model-based parameter estimation in electromagnetics: Part III. Applications to EM observables," *Antennas Propagat. Mag.*, vol. 40, no. 3, pp. 49-66, June 1998.

[11] E. K. Miller, "Computing radiation and scattering patterns using model-based parameter estimation," in *1998 IEEE AP-S Int. Antenna Symp. Dig.*, Atlanta, GA, June 1998, pp. 66-69.

[12] C. J. Reddy, M. D. Deshpande, C. R. Cockrell, and F. B. Beck, "Fast RCS computation over a frequency band using method of moments in conjunction with asymptotic waveform evaluation technique," *IEEE Trans. Antennas Propagat.*, vol. 46, no. 8, pp. 1229-1233, Aug. 1998.

[13] C. J. Reddy, M. D. Deshpande, C. R. Cockrell, and F. B. Beck, "Fast RCS computation over a frequency band using combined FEM/MoM technique in conjunction with asymptotic waveform evaluation (AWE)," *Electromagnetics*, vol. 18, pp. 613-630, 1998.

[14] Y. E. Erdemli, C. J. Reddy, and J. L. Volakis, "AWE technique in frequency domain electromagnetics," *J. Electromagn. Waves Applications*, vol. 13, pp. 359-377, 1999.

[15] J. L. Volakis, T. Ozdemir, and J. Gong, "Hybrid finite-element methodologies for antennas and scattering," *IEEE Trans. Antennas Propagat.*, vol. 45, no. 3, pp. 493-507, Mar. 1997.

[16] D. M. Kokotoff, "Full-wave analysis of ferrite-tuned cavity-backed antenna," Ph.D. dissertation, Arizona State Univ., 1995.

[17] E. K. Miller, L. Medgysi-Mitschang, and E. H. Newman (Eds), *Computational electromagnetics: Frequency domain method of moments*. New York: IEEE Press, 1992.

Reduced-Order Modeling of Three-Dimensional Electromagnetic Wave Fields

R.F. Remis and **P.M. van den Berg**
Laboratory of Electromagnetic Research, Faculty of Information Technology and Systems, Centre for Technical Geoscience, Delft University of Technology, P.O. Box 5031, 2600 GA Delft, The Netherlands

1. Introduction

In a previous paper [1] we presented a reduced-order modeling technique for the computation of two-dimensional transient electromagnetic wave fields in complex configurations. Here we extent the technique to the three-dimensional case. Maxwell's equations are taken as a starting point. These equations form a hyperbolic system of coupled first-order partial differential equations and are written in a particular matrix operator form. We then discretize these equations in space and in such a way that the structure of Maxwell's equations is preserved. The solution of the resulting algebraic matrix equation gives a numerical approximation of the electromagnetic field quantities and can be written in terms of a matrix exponential function operating on a source vector. The argument of the exponential function consists of a product of a large and sparse matrix and the continuous time coordinate. The problem with the expression for the solution vector is that standard decomposition techniques for evaluating the matrix exponential function cannot be applied since the order of the relevant matrix is simply too large. However, we do know that this matrix has certain symmetry properties because the structure of Maxwell's equations has been preserved. We make use of these symmetry properties in a modified Lanczos algorithm. This algorithm allows us to construct approximations to the solution vector without having to discretize the time variable. Computing such an approximation again requires the evaluation of a matrix exponential function, but this time we need to compute the exponential of a tridiagonal matrix. This matrix is generated by the Lanczos algorithm and its order is much smaller than the order of the matrices that result from discretizing Maxwell's equations directly. For this reason, we call the approximations reduced-order models. Numerical results, for three-dimensional configurations, illustrate the performance of the technique.

2. Maxwell's equations

Maxwell's equations, governing the pointwise behavior of the electromagnetic field present in an inhomogeneous, isotropic and lossy medium, can be written in the form

$$(\mathcal{D} + \mathcal{M}_1 + \mathcal{M}_2\partial_t)\mathcal{F} = \mathcal{Q}'. \tag{1}$$

In this equation, $\mathcal{F} = \mathcal{F}(\boldsymbol{x}, t)$ is the field vector consisting of the components of the electric field strength $\boldsymbol{E}$ and the magnetic field strength $\boldsymbol{H}$ as

$$\mathcal{F} = [E_1, E_2, E_3, H_1, H_2, H_3]^T, \tag{2}$$

and $\mathcal{Q}' = \mathcal{Q}'(\boldsymbol{x}, t)$ is the source vector composed of the components of the external electric-current sources $\boldsymbol{J}^{\mathrm{e}}$ and the external magnetic-current sources $\boldsymbol{K}^{\mathrm{e}}$ as

$$\mathcal{Q}' = -[J_1^{\mathrm{e}}, J_2^{\mathrm{e}}, J_3^{\mathrm{e}}, K_1^{\mathrm{e}}, K_2^{\mathrm{e}}, K_3^{\mathrm{e}}]^T. \tag{3}$$

The spatial differentiation operator matrix $\mathcal{D}$ is given by

$$\mathcal{D} = \begin{pmatrix} 0 & 0 & 0 & 0 & \partial_3 & -\partial_2 \\ 0 & 0 & 0 & -\partial_3 & 0 & \partial_1 \\ 0 & 0 & 0 & \partial_2 & -\partial_1 & 0 \\ 0 & -\partial_3 & \partial_2 & 0 & 0 & 0 \\ \partial_3 & 0 & -\partial_1 & 0 & 0 & 0 \\ -\partial_2 & \partial_1 & 0 & 0 & 0 & 0 \end{pmatrix} \tag{4}$$

and satisfies the anti-commutation relation

$$\mathcal{D}\delta^- = -\delta^-\mathcal{D}, \tag{5}$$

where we have introduced the signature matrix δ^- as

$$\delta^- = \mathrm{diag}(1, 1, 1, -1, -1, -1). \tag{6}$$

We also introduce the identity matrix δ^+ as

$$\delta^+ = \mathrm{diag}(1, 1, 1, 1, 1, 1), \tag{7}$$

and the matrices δ^{E} and δ^{H} as

$$\delta^{\mathrm{E}} = \frac{1}{2}(\delta^+ + \delta^-) = \mathrm{diag}(1, 1, 1, 0, 0, 0), \tag{8}$$

(9)

and

$$\delta^{\mathrm{H}} = \frac{1}{2}(\delta^+ - \delta^-) = \mathrm{diag}(0, 0, 0, 1, 1, 1). \tag{10}$$

The anti-commutation relation of Eq. (5) can then be rewritten in terms of the matrices δ^{E} and δ^{H} as

$$\mathcal{D}\delta^{\mathrm{E}} = \delta^{\mathrm{H}}\mathcal{D}, \tag{11}$$

or as

$$\mathcal{D}\delta^{\mathrm{H}} = \delta^{\mathrm{E}}\mathcal{D}. \tag{12}$$

Equations (11) and (12) show that if matrix $\mathcal{D}$ operates on a vector related to the electric field strength, a vector related to the magnetic field strength results and vice versa.

The time-independent matrices $\mathcal{M}_1$ and $\mathcal{M}_2$ are medium matrices given by

$$\mathcal{M}_1 = \mathrm{diag}(\sigma, \sigma, \sigma, 0, 0, 0), \tag{13}$$

and

$$\mathcal{M}_2 = \mathrm{diag}(\varepsilon, \varepsilon, \varepsilon, \mu, \mu, \mu). \tag{14}$$

Matrix $\mathcal{M}_1$ is positive semidefinite and matrix $\mathcal{M}_2$ is positive definite. These matrices satisfy the relations

$$\mathcal{M}_1\delta^- = \delta^-\mathcal{M}_1 = \mathcal{M}_1, \tag{15}$$

and

$$\mathcal{M}_2\delta^- = \delta^-\mathcal{M}_2. \tag{16}$$

In what follows, we consider source vectors of the form

$$\mathcal{Q}'(\boldsymbol{x}, t) = w(t)\mathcal{Q}(\boldsymbol{x}), \tag{17}$$

where $w(t)$ is the source wavelet that vanishes for $t<0$ and $\mathcal{Q} = \mathcal{Q}(\boldsymbol{x})$ is a time-independent vector. The source vector is said to be of the electric-current type if the vector $\mathcal{Q}$ satisfies $\mathcal{Q} = \delta^{\mathrm{E}}\mathcal{Q}$ and of the magnetic-current type if this vector satisfies $\mathcal{Q} = \delta^{\mathrm{H}}\mathcal{Q}$.

As a next step, we discretize Maxwell's equations in space and in such a way that Eqs. (5), (15), and (16), valid in the continuous context, have a counterpart after discretization. A simple discretization procedure that satisfies this requirement is the standard finite-difference technique of Yee [2]. We employ a homogeneous Dirichlet boundary condition to restrict the unbounded domain of computation to a bounded one. The discrete counterparts of $\mathcal{D}, \mathcal{M}_1, \mathcal{M}_2, \mathcal{F}$, and $\mathcal{Q}$ are given by D, M_1, M_2, F, and Q, respectively. The discrete counterparts of the matrices δ^-, δ^+,δ^{E}, and δ^{H} are denoted by the same symbols. After this discretization procedure we obtain the algebraic matrix equation

$$(D + M_1 + M_2\partial_t)F(t) = w(t)Q. \tag{18}$$

The matrices in this equation are all square; matrix D is real and anti-symmetric; and the medium matrices M_1 and M_2 are both diagonal, M_1 being positive semidefinite and M_2 being positive definite. Note that the order of the matrices is proportional to $6N^3$, where N is the number of sample points in each Cartesian direction.

Solving Eq. (18) for the field vector gives

$$F(t) = w(t) * \chi(t)\exp(-At)M_2^{-1}Q, \tag{19}$$

where the asterisk denotes convolution in time, where $\chi(t)$ is the Heaviside unit step function, and where matrix A is given by

$$A = M_2^{-1}(D + M_1). \tag{20}$$

Now let u be a vector such that the quantity

$$u^T F(t) = w(t) * \chi(t)u^T\exp(-At)M_2^{-1}Q \tag{21}$$

is a component of the electric or the magnetic field strength at a desired observation point. If a component of the electric field strength is selected, the vector u satisfies $u = \delta^{\mathrm{E}}u$, and if a

component of the magnetic field strength is selected the vector u satisfies $u = \delta^{\mathrm{H}} u$. For a source vector of the electric-current type ($Q = \delta^{\mathrm{E}} Q$), we then have the following reciprocity relations:

$$u^T \exp(-At) M_2^{-1} Q = Q^T \exp(-At) M_2^{-1} u, \tag{22}$$

for $u = \delta^{\mathrm{E}} u$, and

$$u^T \exp(-At) M_2^{-1} Q = -Q^T \exp(-At) M_2^{-1} u, \tag{23}$$

for $u = \delta^{\mathrm{H}} u$. The proof of these relations can be found in the Appendix. It is based on the observation that matrix A satisfies the relation

$$A^T M_2 \delta^- = M_2 \delta^- A. \tag{24}$$

For the sake of completeness we mention that similar reciprocity relations hold in case the source vector is of the magnetic-current type (see [3]).

The problem with the expression for the solution vector is that standard methods that use a full decomposition of matrix A for evaluating the matrix exponential function cannot be used because the order of this matrix is simply too large. To give an idea of its size, realistic three-dimensional configurations require a computational grid such that the order of matrix A can become as large as 10^7. Instead of computing a full decomposition, we propose to calculate a partial decomposition of matrix A by means of a modified Lanczos algorithm. Based on this decomposition, we can construct approximations to the solution vector without having to discretize the time variable.

3. Reduced-order models for the electromagnetic field quantities

Let $\langle \cdot, \cdot \rangle$ denote the standard inner product of two vectors from $\mathbb{R}^n$. By using the reciprocity relation of Eq. (24) it is easily verified that matrix A is symmetric with respect to the bilinear form $\langle M_2 \delta^- \cdot, \cdot \rangle$. This allows us to carry out the following modified Lanczos algorithm:

$$\left.\begin{aligned} \beta_1 v_1 &= M_2^{-1} Q \\ w_i &= A v_i - \beta_i v_{i-1} \\ \alpha_i &= \langle M_2 \delta^- v_i, w_i \rangle \\ \beta_{i+1} v_{i+1} &= w_i - \alpha_i v_i \end{aligned}\right\} \quad \text{for } i = 1, 2, ..., \tag{25}$$

with $v_0 = 0$. The algorithm produces coefficients α_i and β_i and Lanczos vectors v_i. The coefficients β_i are determined from the condition $\langle M_2 \delta^- v_i, v_i \rangle = 1$, for $i \geq 1$. After m steps of the above algorithm, the first m Lanczos vectors form a basis of the Krylov space $\mathcal{K}_m = \mathrm{span}\{M_2^{-1} Q, A M_2^{-1} Q, ..., A^{m-1} M_2^{-1} Q\}$, and the summarizing equation

$$A V_m = V_m T_m + \beta_{m+1} v_{m+1} e_m^T \tag{26}$$

holds. In this equation, matrix T_m is a complex, symmetric, and tridiagonal m-by-m matrix given by

$$T_m = \begin{pmatrix} \alpha_1 & \beta_2 & & & & \\ \beta_2 & \alpha_2 & \beta_3 & & & \\ & \beta_3 & \cdot & \cdot & & \\ & & \cdot & \cdot & \cdot & \\ & & & \cdot & \cdot & \beta_m \\ & & & & \beta_m & \alpha_m \end{pmatrix}, \tag{27}$$

and matrix V_m has the column partitioning $V_m = (v_1, v_2, ..., v_m)$. Note that complex arithmetic is introduced in the above algorithm. A way to avoid this is described in [3].

Based on Eq. (26), we can construct the reduced-order model (see [1])

$$F_m(t) = w(t) * \chi(t)\beta_1 V_m \exp(-T_m t)e_1. \tag{28}$$

It can be shown that the number of iterations needed to obtain an accurate result on the time interval $(0, t]$ is proportional to $\|A\|\, t$, where $\|A\|$ is the 2-norm of matrix A (see [3]).

4. Numerical results

We demonstrate the performance of the reduced-order modeling technique by two numerical examples. Consider a three-dimensional configuration in which the external magnetic-current sources vanish and where the external electric-current sources are given by

$$J_1^e(\boldsymbol{x}, t) = w(t)\delta(\boldsymbol{x} - \boldsymbol{x}^{\mathrm{src}}), \quad J_2^e(\boldsymbol{x}, t) = 0, \quad J_3^e(\boldsymbol{x}, t) = 0. \tag{29}$$

The source wavelet $w(t)$ is chosen to be a Ricker wavelet and is given by

$$w(t) = \chi(t)\sqrt{\frac{e}{2\theta}}\frac{\mathrm{d}}{\mathrm{d}t}\exp[-\theta(t - t_0)^2]. \tag{30}$$

With the parameter t_0 we can shift the non-zero part of this wavelet in time, and with the parameter θ we can vary its peak frequency. In all examples, we choose a peak frequency of 40 MHz. The spatial discretization is chosen such that we have about 31 points / λ, where λ is the free-space wavelength corresponding to the peak frequency of 40 MHz.

As a first example, we consider the electromagnetic field in vacuum generated by the electric-current source described above. For this simple configuration the electromagnetic field is known in closed-form (see, for example, [4]). In our finite-difference approximation, the delta function is approximated by a three-dimensional triangular distribution. The analytical solution is therefore weighted over this distribution. The resulting E_1 component of the electric field strength at an observation point located 5 m from the source is shown in Figure 1 (solid line). Reduced-order models for the E_1 component at the same observation point are also shown in this figure (dashed lines). The dashed line in Figure 1a shows the reduced-order model obtained after 100 iterations, in Figure 1b after 200 iterations, and in Figure 1c after 300 iterations. We observe that the interval in which the reduced-order model is correct increases with the number of iterations.

As a second example, consider the configuration of Figure 2. A cube is located 1 m below an air-earth interface. The source and the receiver are symmetrically located above this cube, 5 m apart. The solid line in Figure 3 shows the converged reduced-order model for the E_1 component of the electric field strength. The dashed line in Figure 3a shows the reduced-order model obtained after 100 iterations, in Figure 3b after 200 iterations, and in Figure 3c after 300 iterations. From these results we infer that the reduced-order models converge in a similar manner as in the previous example.

Appendix

We prove the reciprocity relations of Eqs. (22) and (23). From Eq. (24) it follows that

$$(A^T)^k M_2 \delta^- = M_2 \delta^- A^k \quad \text{for } k = 0, 1, \ldots. \tag{31}$$

Multiply this equation on the left and on the right by $\delta^{\mathrm{E}} M_2^{-1}$. We obtain

$$\delta^{\mathrm{E}} M_2^{-1} (A^T)^k \delta^{\mathrm{E}} = \delta^{\mathrm{E}} A^k M_2^{-1} \delta^{\mathrm{E}} \quad \text{for } k = 0, 1, ..., \tag{32}$$

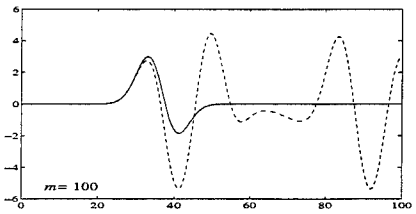

(a)

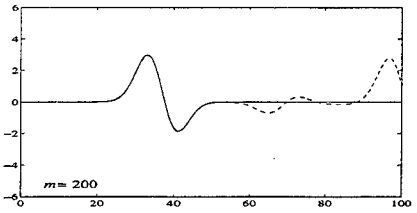

(b)

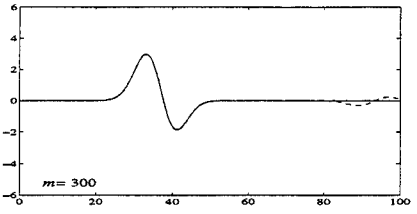

(c)

FIGURE 1. Electric field strength E_1 [V/m] as a function of time [ns]. The solid line signifies the exact result. The dashed line is the reduced-order model after (a) 100 iterations, (b) 200 iterations, and (c) 300 iterations.

since $\delta^{\mathrm{E}}\delta^{-} = \delta^{-}\delta^{\mathrm{E}} = \delta^{\mathrm{E}}$. If we multiply Eq. (31) on the left by $\delta^{\mathrm{E}}M_2^{-1}$ and on the right by $\delta^{\mathrm{H}}M_2^{-1}$, we get

$$\delta^{\mathrm{E}}M_2^{-1}(A^T)^k\delta^{\mathrm{H}} = -\delta^{\mathrm{E}}A^kM_2^{-1}\delta^{\mathrm{H}} \quad \text{for } k = 0, 1, ..., \tag{33}$$

since $\delta^{\mathrm{H}}\delta^{-} = \delta^{-}\delta^{\mathrm{H}} = -\delta^{\mathrm{H}}$. Now, since $u^T \exp(-At)M_2^{-1}Q$ is a scalar, we can write

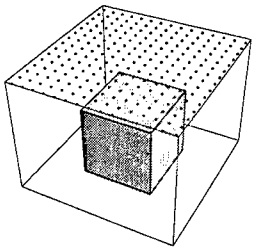

(a) A buried cube

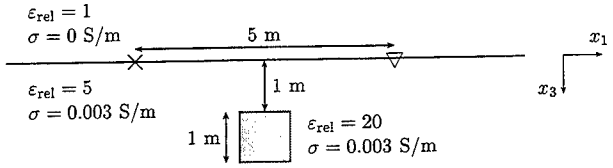

(b) Side view

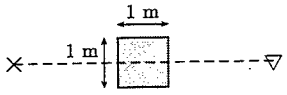

(c) View from above

FIGURE 2. An electric-current source J_1^e and a receiver symmetrically located above a buried cube. The permeability equals that of vacuum throughout the whole configuration.

$$\begin{aligned} u^T \exp(-At) M_2^{-1} Q &= Q^T M_2^{-1} \exp(-A^T t) u \\ &= Q^T M_2^{-1} \sum_{k=0}^{\infty} \frac{(-A^T t)^k}{k!} u, \end{aligned} \tag{34}$$

where we made use of the power series expansion of the exponential function. If the source vector is of the electric-current type and if the vector u satisfies $u = \delta^{\rm E} u$ we have

$$\begin{aligned} u^T \exp(-At) M_2^{-1} Q &= Q^T \delta^{\rm E} M_2^{-1} \sum_{k=0}^{\infty} \frac{(-A^T t)^k}{k!} \delta^{\rm E} u, \\ &= Q^T \delta^{\rm E} \sum_{k=0}^{\infty} \frac{(-At)^k}{k!} M_2^{-1} \delta^{\rm E} u \\ &= Q^T \exp(-At) M_2^{-1} u, \end{aligned} \tag{35}$$

where we have used Eq. (32). For an observation vector u that satisfies $u = \delta^{\rm H} u$ we use Eq. (33) instead of Eq. (32).

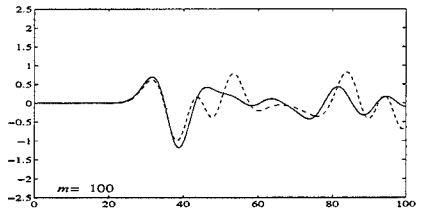

(a)

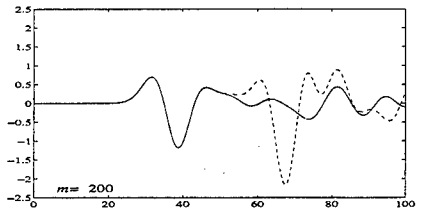

(b)

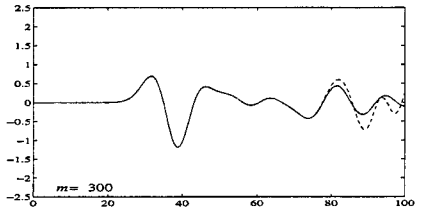

(c)

FIGURE 3. Electric field strength E_1 [V/m] as a function of time [ns]. The solid line shows the converged reduced-order model. The dashed line is the reduced-order model after (a) 100 iterations, (b) 200 iterations, and (c) 300 iterations.

References

[1] R.F. REMIS AND P.M. VAN DEN BERG, "A modified Lanczos algorithm for the computation of transient electromagnetic wavefields," *IEEE Transactions on Microwave Theory and Techniques*, vol. 45, no. 12, 1997, pp. 2139 -2149.
[2] K.S. YEE, "Numerical solution of initial boundary value problems involving Maxwell's equations in isotropic media," *IEEE Transactions on Antennas and Propagation*, vol. 14, no. 3, 1966, pp. 302-307.
[3] R.F. REMIS, "Reduced-Order Modeling of Transient Electromagnetic Fields," Ph.D. Thesis, Delft University Press, Delft, 1998.
[4] A.T. DE HOOP, "Handbook of Radiation and Scattering of Waves," Academic Press, London, 1995.

Rapid Simulation of Electromagnetic Resonant Structures Using Model Order Reduction and Unstructured Finite Difference

Li Zhao[1] and Andreas C. Cangellaris[2]

[1] ANSYS Inc.
Southpointe, 275 Technology Drive
Canonsburg, PA 15317
[2] Center for Computational Electromagnetics
Department of Electrical and Computer Engineering
University of Illinois at Urbana-Champaign
1406 West Green Street, Urbana, IL 61801

Abstract. In this paper, a model order reduction approach based on Krylov subspace iteration is used in conjunction with the Finite Difference method on unstructured grids for the rapid electromagnetic characterization of electromagnetic resonant structures. The proposed model order reduction algorithm is suitable for the non-symmetric matrices resulting from the finite difference approximation of the hyperbolic system of Maxwell's equations on unstructured, non-orthogonal grids. Numerical examples are used to validate the proposed algorithm and demonstrate its attributes.

1. Introduction

Over the past few years model order reduction techniques have been used to expedite the numerical simulation of electromagnetic systems [1]-[10]. The basic attribute of model order reduction methods is the generation of system response over a broad frequency range at the computational cost of the inversion (factorization) of the discrete system matrix only at one or a few frequencies. Such a *fast frequency sweep* is realized by generating a Padé approximation of the response of as high an order as necessary for acceptable accuracy over the desired bandwidth. Accurate, continuous Padé approximations of the response of electromagnetic systems are extremely useful for the design of high-Q electromagnetic components such as filters, impedance transformers, cavities, etc. The accurate prediction through simulation of the resonant behavior of such electromagnetic components often requires significant computational effort. For example, tens of thousands of time steps may be needed for the Finite-Difference Time-Domain (FDTD) method to capture the resonance of a high-Q system. Also, it is extremely time-consuming for traditional frequency-domain finite methods (finite difference, finite element) to obtain broadband responses for complex electromagnetic systems with discrete approximations involving tens or even hundreds of thousands of unknowns.

Preliminary efforts in the application of model order reduction practices focused on the Asymptotic Waveform Evaluation (AWE) method and its derivatives. However, the numerical instability of the Padé approximation generation process in the AWE process restricted its use to approximations of lower order. It is well known that continuous

electromagnetic systems are of infinite order. Thus, the number of the poles required for the exact presentation of their response is also infinite. Once a discrete method is used to approximate a continuous electromagnetic system the generated discrete electromagnetic system is of finite, yet very high order. More specifically, the order of the discrete system equals the number of state variables (unknowns) in the approximation. The objective of model order reduction is to generate a Padé approximation of the response of the discrete electromagnetic system maintaining only a limited number of poles which is much smaller than the order of the discrete system, yet high enough to model the response accurately over a broad frequency range.

With the success of Krylov subspace algorithms for model order reduction [11]-[14], the issue of stability of the generation of Padé approximations of high order has been addressed effectively. However, with the exception of the work by Remis and van de Berg [5] and Zunoubi et al [10], most model order reduction schemes based on Krylov subspace iteration effect Padé approximations by indirectly matching moments at a finite expansion frequency point. Even though there are many good reasons for doing so (e.g., finite frequency point expansions lead to accurate Padé approximations using only a few tens of poles), these approaches require the factorization of a sparse, yet very large matrix. This is highly undesirable when problems involving hundreds of thousands of unknowns need be modeled. Furthermore, the option of using an iterative process for the factorization becomes questionable when Padé approximations of fairly high order are needed. In view of the above concerns, we return to the use of the point at infinity as the expansion point for the generation of Padé approximations. Contrary to the aforementioned implementations of such an approach for the case of skew-symmetric [5], [9] or symmetric [10] matrix approximations to the electromagnetic equations, we examine the case of discrete approximations involving non-symmetric matrices. Such cases arise when finite difference or finite volume methods are used to approximate Maxwell's equations on unstructured grids. The paper begins with the mathematical description of the model order reduction methodology. Numerical examples from its application to the characterization of electromagnetic resonant structures are used to validate the method and demonstrate its attributes.

2. Semi-Discrete FORM of Maxwell's Equations

For the purposes of model order reduction, it is assumed that the media are linear, isotropic passive and time-independent. Thus, Maxwell's curl equations in the Laplace domain assume the form

$$\nabla \times \vec{E} = -s\mu\vec{H} - \vec{M}_s \tag{1a}$$

$$\nabla \times \vec{H} = s\epsilon\vec{E} + \sigma\vec{E} + \vec{J}_s \tag{1b}$$

where the permittivity ϵ, conductivity σ and permeability μ are assumed to be position-dependent. The semi-discrete form of Maxwell's equations (1) is obtained through the discretization of the curl operators by the unstructured finite difference method on an unstructured version of Yee's lattice

$$\begin{bmatrix} \mathbf{0} & \mathbf{C}_e \\ \mathbf{C}_h & \mathbf{D}_\sigma \end{bmatrix} \begin{bmatrix} \mathbf{H} \\ \mathbf{E} \end{bmatrix} + s \begin{bmatrix} \mathbf{D}_h & \mathbf{0} \\ \mathbf{0} & \mathbf{D}_e \end{bmatrix} \begin{bmatrix} \mathbf{H} \\ \mathbf{E} \end{bmatrix} = \begin{bmatrix} \mathbf{M}_s \\ \mathbf{J}_s \end{bmatrix} \tag{2}$$

In the above, the sparse matrices $\mathbf{C}_e$, $\mathbf{C}_h$ denote the discrete forms of the curl operators, while the matrices $\mathbf{D}_\sigma$, $\mathbf{D}_h$ and $\mathbf{D}_e$ are diagonal matrices that represent the discrete forms of the electric conductivity, magnetic permeability, and electric permittivity properties of the media, respectively. The vectors $\mathbf{E}$, $\mathbf{H}$ are the discrete forms of the unknown electric field and magnetic field components, while the vectors $\mathbf{M}_s$, $\mathbf{J}_s$ represent the discrete forms of spatial distributions of the electric and magnetic current sources, respectively. Because of the assumption of passivity of the media, the matrices $\mathbf{D}_h$, $\mathbf{D}_e$ are (symmetric) positive definite, and $\mathbf{D}_\sigma$ is (symmetric) non-negative definite. The resulting compact form of (2) is,

$$(\mathbf{G} + s\mathbf{C})\mathbf{X} = -\mathbf{B}\mathbf{U}(s) \tag{3}$$

where the vector $\mathbf{U}$ denotes the Laplace transforms of the current source waveforms, and the spatial dependence of the sources is described by the matrix $\mathbf{B}$. With the frequency shift $s = s_0 + s'$, (3) may be cast in the form

$$(\mathbf{I} - s'\mathbf{A})\mathbf{X} = \mathbf{R}\mathbf{U}(s') \tag{4}$$

where

$$\mathbf{A} = -(\mathbf{G} + s_0\mathbf{C})^{-1}, \quad \mathbf{R} = -(\mathbf{G} + s_0\mathbf{C})^{-1}\mathbf{B} \tag{5}$$

Defining a desired output vector as

$$\mathbf{Y}(s) = \mathbf{F}\mathbf{X}(s) \tag{6}$$

a transfer-function matrix can be defined for the system

$$\mathbf{H}(s') = \mathbf{F}(\mathbf{I} - s'\mathbf{A})^{-1}\mathbf{R} \tag{7}$$

The objective of model order reduction techniques is to generate rational function approximations (Padé approximations) to the elements of $\mathbf{H}(s')$ of order q much smaller than the number of state variables N. The most robust methodologies for the generation of high-order Padé approximations of dynamic systems are those based on Krylov subspace iteration using the Lanczos and Arnoldi algorithms.

3. The Process of Model Order Reduction

In order to illustrate how Krylov subspace iteration methods can be sued for model order reduction purposes, consider the change of variable

$$\mathbf{X} = \mathbf{V}\hat{\mathbf{X}} \tag{8}$$

where $\hat{\mathbf{X}}$ is the reduced state vector. Its length q is assumed to be much smaller than the length N of the original vector $\mathbf{X}$. The transformation matrix $\mathbf{V}$ is of dimension $N \times q$ and is assumed to be orthonormal, i.e. $\mathbf{V}^T\mathbf{V} = \mathbf{I}_q$, where $\mathbf{I}_q$ is the identity matrix of dimension q. Substitution of (8) into (3) and (6), followed by multiplication on the left of (3) by $\mathbf{V}^T$ yields

$$[(\mathbf{V}^T\mathbf{G}\mathbf{V}) + s(\mathbf{V}^T\mathbf{C}\mathbf{V})]\hat{\mathbf{X}} = -(\mathbf{V}^T\mathbf{B})\mathbf{U}(s) \tag{9}$$

$$\mathbf{Y} = (\mathbf{FV})\hat{\mathbf{X}} \tag{10}$$

Thus, a reduced-order system may be defined in terms of the matrices

$$\hat{\mathbf{G}} = \mathbf{V}^T\mathbf{G}\mathbf{V}, \quad \hat{\mathbf{C}} = \mathbf{V}^T\mathbf{C}\mathbf{V}, \quad \hat{\mathbf{B}} = \mathbf{V}^T\mathbf{B}, \quad \hat{\mathbf{F}} = \mathbf{F}\mathbf{V} \tag{11}$$

Because of the low order, the eigendecomposition of this system is very inexpensive, and provides for a fast calculation of the system response at any desirable frequency. From the above it is clear that the generation of the congruence transformation matrix $\mathbf{V}$ is the key to the successful implementation of such a model order reduction methodology. This can be achieved using, for example, the block Arnoldi algorithm to generate a Krylov subspace using the matrices $\mathbf{A}$ and $\mathbf{R}$ in (5) as described in [11]. From the point of view of CPU and memory requirements, the factorization of the matrix $(\mathbf{G} + s_0\mathbf{C})$, and the storing of the transformation matrix $\mathbf{V}$ are undesirable. Three-dimensional electromagnetic analysis of realistic problems using finite methods may lead to a semi-discrete system with hundreds of thousands, even millions, of unknowns. Thus, despite its sparsity, the factorization of $(\mathbf{G}+s_0\mathbf{C})$ may become prohibitive. A possible way of avoiding the factorization of the matrix is to use the Lanczos and Arnoldi algorithms for the generation of Padé approximations with expansion point at infinity ($s_0 \to \infty$). It will be shown that the implementation of such an algorithm is fairly straightforward when used in conjunction with FD-TD-based and Finite-Volume Time-Domain (FV-TD)-based field solvers.

The development of the algorithm begins by casting the state system of (3), (6) in the form

$$(s\mathbf{I} - \mathbf{A})\mathbf{X}(s) = \mathbf{R}\mathbf{U}(s) \tag{12}$$

$$\mathbf{Y}(s) = \mathbf{F}\mathbf{X}(s) \tag{13}$$

where

$$\mathbf{A} = -\mathbf{C}^{-1}\mathbf{G}, \quad \mathbf{R} = \mathbf{C}^{-1}\mathbf{B} \tag{14}$$

It is noted that that the inversion of $\mathbf{C}$ is trivial, since it is a diagonal matrix in the semi-discrete electromagnetic systems. Thus, the block Arnoldi algorithm may be cheaply used to generate the Krylov subspace needed for the passive reduction of the system. Furthermore, it should be apparent that the matrix-vector multiplication in each iteration of the block Arnoldi algorithm is computationally equivalent to one update for the electric and magnetic fields everywhere in the finite grids.

In the case of the memory shortage associated with the storage of the congruence transformation matrix $\mathbf{V}$, an alternative of the block Arnoldi algorithm, the block Lanczos algorithm [12], can be implemented for the generation of the reduced-order macromodel of electromagnetic systems. The block Lanczos algorithm reduces the system matrix $\mathbf{A}$ in (4) to a $q \times q$ block tridiagonal matrix, $\mathbf{T}_q$, such that

$$\mathbf{W}^T\mathbf{A}\mathbf{V} = \mathbf{D}\mathbf{T}_q, \quad \mathbf{W}^T\mathbf{V} = \mathbf{D} \tag{15}$$

where the $N \times q$ matrix $\mathbf{V}$ forms a basis for the Krylov subspace $Kr(\mathbf{A}, \mathbf{R})$, and the $N \times q$ matrix $\mathbf{W}$ forms a basis for the Krylov subspace $Kr(\mathbf{A}^T, \mathbf{R})$. The two matrices $\mathbf{V}$ and $\mathbf{W}$ are generated to be bi-orthogonal. Hence, the matrix $\mathbf{D}$ is a diagonal matrix. It should be

emphasized that the matrix $\mathbf{A}$ in (4) may be an arbitrary non-symmetric matrix. In such a case it is known that the block Lanczos algorithm may break down due to numerical round-off error. One of the remedies for such breakdown is to use the looked-ahead Lanczos algorithm. Alternatively, a modified Lanczos algorithm may be used for the generation of the Krylov subspace for the case of non-symmetric matrices such that

$$\mathbf{W}^T\mathbf{V} = \mathbf{I}_q \tag{16}$$

The details of the algorithm have been given in [13] and will not be repeated here. The model order reduction affected by the Lanczos algorithm may be illustrated by the change of variables

$$\mathbf{X} = \mathbf{V}\hat{\mathbf{X}} \tag{17}$$

Substituting (17) into (12) and multiplying on the left of (12) by $\mathbf{W}^T$ yield

$$(s\mathbf{I} - \mathbf{T}_q)\hat{\mathbf{X}} = \mathbf{W}^T\mathbf{R}\mathbf{U}(s) \tag{18}$$

Finally, the response of the reduced-order system is given by

$$\hat{\mathbf{Y}}(s) = \mathbf{F}\mathbf{V}(s\mathbf{I} - \mathbf{T}_q)^{-1}\mathbf{W}^T\mathbf{R}\mathbf{U}(s) \tag{19}$$

As already mentioned, the matrix-vector multiplications involving the matrices $\mathbf{A}$ and $\mathbf{A}^T$ are the curl operations based on the discretization of fields. More specifically, the matrix multiplication associated with the matrix $\mathbf{A}$ is identical to the curl operation done by the FD-TD or the FV-TD algorithm for one update of the fields. On the other hand, the multiplication involving the matrix $\mathbf{A}^T$ is a slightly different operation, which nevertheless can be affected also as a discrete curl operation. Thus, each iteration step of the block Lanczos algorithm is computationally equivalent to two FD-TD or FV-TD field updates.

Next, it is important to recognize the fact that the matrices $\mathbf{V}$ and $\mathbf{W}$ do not have to be stored, even though they seem to be needed for the generation of the reduced-order model in view of (19). As explained in [12], the matrices $\mathbf{V}$ and $\mathbf{W}$ are constructed in such a manner that it is

$$\mathbf{R} = \mathbf{V}\begin{bmatrix}\mathbf{a}_1\\ \mathbf{0}\end{bmatrix}, \qquad \mathbf{F} = [\mathbf{a}_2^T \quad \mathbf{0}]\mathbf{W}^T \tag{20}$$

where the matrices $\mathbf{a}_1$ and $\mathbf{a}_2$ are upper triangular matrices. Using the bi-orthogonality of $\mathbf{V}$ and $\mathbf{W}$, the response of the system may be cast in the form

$$\hat{\mathbf{Y}}(s) = [\mathbf{a}_2^T \quad \mathbf{0}](s\mathbf{I} - \mathbf{T}_q)^{-1}\begin{bmatrix}\mathbf{a}_1\\ \mathbf{0}\end{bmatrix}\mathbf{U}(s) \tag{21}$$

Clearly, all matrices in this final expression of the response are of dimension $q \times q$. These are the only arrays needed to be stored in the block Lanczos algorithm for model order reduction purposes. It should be mentioned that the Taylor expansions of the impulse response of the semi-discrete system of (12) around $t = 0$ agree with the reduced system of (21) up to the first q terms, where q is the order of the reduced system. The immediate consequence of this result is that the reduced system is expected to provide very good

accuracy for the early period of the transient response. An estimate of the time interval has been developed in [5] in terms of the order of the reduced model and a properly defined norm of the matrix **A**. According to this estimate, the higher the order of the reduced model, the longer the time interval over which the transient response can be captured by the reduced model. The rapid calculation of the electromagnetic response of resonant systems can be affected by directly extracting the response of the reduced-order model in the Laplace domain, instead of seeking the eigenvalues of the tridiagonal matrix $\mathbf{T}_q$ of the reduced-order system, if the excitation sources are assumed to be impulse functions in time. Clearly, the eigenvalues of the tridiagonal matrix $\mathbf{T}_q$ are only a subset of the eigenvalues of the original matrix **A**. In particular, for the case where the expansion point is the point at infinity, the generated Krylov subspaces are spanned by the eigenvectors corresponding to the highest eiegenvalues. Consequently, Padé approximations of very high order may be necessary if some of the lower eigenvalues of the sytem are needed. This is one of the major drawbacks of Padé approximations generated using the point at infinity as the expansion point.

4. Numerical Validation

The following examples are aimed at demonstrating the application of the proposed methodology to the rapid electromagnetic analysis of resonators. From the description of the methodology it should be clear that the eigen-analysis is affected through the impulsive excitation of the system and the subsequent generation of the reduced representation of its response using as basis eigenvectors in the generated Krylov subspace. We consider first a simple cylindrical resonant cavity for which closed-form solutions are available. The radius of the cavity is $1m$. The length of the cavity is equal to its radius. The semi-discrete form of Maxwell's equations (1) is obtained by the non-orthogonal discretization of the structure. The resulting system matrix is non-symmetric. Table I compares the resonant frequencies of the reduced order model, generated by the Lanczos algorithm with expansion frequency point at infinity, with the analytically obtained results. Also shown are the resonant frequencies obtained using the FD-TD algorithm on the non-orthogonal grid. Very good agreement is observed for the lowest four modes. The order of the reduced model is 250. As already explained in the previous section, the computational cost associated with the generation of the reduced model of order 250 is equivalent to 500 FD-TD updates. To achieve the resolution of $\Delta f = 1.5MHz$ for this problem, the non-orthogonal FD-TD algorithm requires 4096 time steps.

Table I. Resonant frequencies for an empty cylindrical cavity (MHz).

Mode	*Analytic*	*FDTD*	*MORe*
TM_{010}	114.7	113.6	113.8
TE_{111}	173.8	173.3	173.5
TM_{110}	183.0	181.8	181.0
TM_{011}	188.9	188.9	188.0

The second example concerns the eigenfrequency analysis of a cylindrical cavity loaded by a dielectric rod ($\epsilon_r = 37.6$). The radius and length of the cavity are 0.5in and $0.55in$,

respectively. The radius of the dielectric rod is $0.394in$. Table II compares the resonant frequencies produced by a reduced model of order 1000 with those obtained through a mode-matching solution, and a non-orthogonal FD-TD analysis of the problem. Once again, very good agreement is observed. Since the order of the reduced model is 1000, the computational cost of its generation is equivalent to 2000 FD-TD iterations. The non-orthogonal FD-TD algorithm requires about $16,800$ updates to achieve the resolution of $\Delta f = 0.05GHz$.

Table II. Resonant frequencies for a cylindrical cavity loaded by the dielectric rod (GHz).

$Mode$	$Mode-matching$	$FDTD$	$MORe$
–	1.50	1.47	1.49
–	2.44	2.41	2.42
HE_{11}	2.50	2.50	2.51
–	–	3.07	3.06
TM_{011}	3.38	3.31	3.32
HE_{211}	3.38	3.48	3.47

5. Conclusions

Model order reduction methodologies based on the Arnoldi and the Lanczos algorithms have been discussed in the paper. In order to overcome the major obstacle of the CPU and memory overhead associated with the use of these algorithms with finite frequency expansion points, the Lanczos algorithm with expansion point the point at infinity is an attractive alternative when discrete electromagnetic systems involving hundreds of thousands of unknowns need to be modeled.

For the three-dimensional electromagnetic resonators analyzed in this paper, the discrete electromagnetic model was generated using finite differences on an unstructured Yee's lattice. Such a discretization leads to a non-symmetric system matrix approximation of the coupled system of Maxwell's curl equations. Despite the potential of numerical breakdown of the Lanczos algorithm for such cases, no problems were encountered for the examples considered in this paper. In any case, remedies exist for avoiding such breakdowns; hence, this breakdown concern is by no means a prohibitive factor in the application of the Lanczos algorithm with non-symmetric discrete approximations of electromagnetic systems.

References

[1] A. Taflove, *Computational Electrodynamics: The Finite-Difference Time-Domain Method*, Artech House, Boston, 1995.

[2] X. Yuan and Z.J. Cendes "A fast method for computing the spectral response of microwave devices over a broad bandwidth," *1993 URSI Radio Science Meeting*, p. 196, Ann Arbor, MI, 1993.

[3] J. Gong and J.L. Volakis, "AWE implementation for electromagnetic FEM analysis," *Electron. Lett.*, vol. 32, no. 12, pp. 2216–2217, Nov. 1996.

[4] M. Celik and A.C. Cangellaris, "Simulation of multiconductor transmission lines using Krylov subspace order-reduction techniques," *IEEE Trans. Computer-Aided Design.*, vol. 16, pp. 485–496, May 1997.

[5] R.F. Remis and P.M. van den Berg, "A modified Lanczos algorithm for the computation of transient electromagnetic wavefields," *IEEE Trans. Microwave Theory Tech.*, vol. 45, no. 12, pp. 2139–2149, Dec. 1997.

[6] J.-P. Zhang and J.-M. Jin, "Preliminary study of AWE method for FEM analysis of scattering problems," *Microwave and Optical Tech. Lett.*, vol. 17, no. 1, pp. 7–12, Jan. 1998.

[7] L. Zhao and A.C. Cangellaris, "Reduced-order modeling of electromagnetic field interactions in unbounded domains truncated by perfectly matched layers," *Microwave and Optical Tech. Lett.*, vol. 17, no. 1, pp. 62–66, Jan. 1998.

[8] J.E. Bracken, d.-K. sun and Z.J. Cendes, "S-domain methods for simultaneous time and frequency characterization of electromagnetic devices," *IEEE Trans. Microwave Theory Tech.*, vol. 46, no. 9, pp. 1277–1290, Sept. 1998.

[9] A.C. Cangellaris and L. Zhao, "Passivity of discrete electromagnetic systems," *Proc. 14th Annual Review of Progress in Applied Computational Electromagnetics*, pp. 721–731, Monterey, California, March 1998.

[10] M.R. Zunoubi, K.C. Donepudi, J.-M. Jin and W.C. Chew, "Efficient time-domain and frequency-domain finite-element solution of Maxwell's equations using spectral Lanczos algorithm," *IEEE Trans. Microwave Theory Tech.*, vol. 46, no. 8, pp. 1141–1149, Aug. 1998.

[11] P. Feldmann and R.W. Freund, "Efficient linear circuit analysis by Padé approximation via the Lanczos process," *IEEE Trans. Computer-Aided Design*, vol. 14, pp. 639–649, 1995.

[12] P. Feldmann and R.W. Freund, "Reduced-order modeling of large linear subcircuits via a block Lanczos algorithm," *IEEE/ACM Proc. Design Automation Conference*, pp. 474–479, June 1995.

[13] K. Gallivan, E. Grimme and P. Van Dooren, "Padé approximation of large scale dynamic system with Lanczos method," *Proc. 33rd Conf. on Decision and Control*, pp. 443–448, Buena Vista, FL, Dec. 1994.

[14] A. Odabasioglu, M. Celik and L.T. Pileggi, "PRIMA: Passive reduced-order interconnect macromodeling algorithm," *IEEE Trans. Computer-Aided Design*, vol. 17, no. 8, pp. 645–653, Aug. 1998.

SESSION 6

OPTIMIZATION

Chairs: John Volakis and Zachi Baharav

RECENT RESULTS IN ELECTROMAGNETIC OPTIMIZATION OF MICROWAVE COMPONENTS INCLUDING MICROSTRIP T-JUNCTIONS

J.W. Bandler, M.H. Bakr, N. Georgieva, M.A. Ismail and D.G. Swanson, Jr.

Simulation Optimization Systems Research Laboratory
and Department of Electrical and Computer Engineering
McMaster University, Hamilton, Canada L8S 4K1

Tel 905 525 9140 Ext. 24818
Fax 905 523 4407

email: j.bandler@ieee.org

Abstract

This paper presents some recent advances in automated electromagnetic (EM) optimization of microwave components and circuits. We review the challenge of EM optimization and present illustrative examples, involving both direct optimization using commercial EM simulators and space mapping optimization. We review a robust new algorithm for EM optimization called TRASM (Trust Region Aggressive Space Mapping), which integrates a trust region methodology with the aggressive space mapping (ASM) technique. The trust region ensures that each iteration results in improved alignment between the coarse and fine models and recursive multi-point parameter extraction improves the conditioning of the extraction phase. We exploit Sonnet's *em*, MATLAB, OSA90, Datapipe, interpolation and database techniques and Geometry Capture. Examples include the EM optimization of microstrip T-junctions and an HTS filter.

INTRODUCTION

Future CAE systems for high-speed, wireless and microwave circuits and systems will not be regarded as complete without available powerful EM simulators integrated with optimization capabilities. Optimal design of active and passive devices, circuits and systems is expected to be physically and electromagnetically based, to include electrical, mechanical and thermal effects. Future developments in integrated CAE tools must concurrently link geometry, layout, physical, EM and process simulations, with performance, yield, cost, system specifications, manufacturability and testability in a manner transparent to the designer [1].

The significant features of EM simulators over empirical model/circuit-theory based simulators is their unsurpassed accuracy, extended validity ranges, and their capability of handling more arbitrary geometrical shapes. Increasingly more complex structures are being simulated accurately and quickly as computational techniques improve, making optimization more practical and attractive with tools such as HP HFSS [2]. As was discussed in the 1997 ACES Conference [3] EM simulators will not realize their full potential to the designer unless they are optimizer-driven to automatically adjust designable parameters [4,5,6].

J.W. Bandler is also with Bandler Corporation, P.O. Box 8083, Dundas, Ontario, Canada L9H 5E7.

D.G. Swanson, Jr., is with the M/A-COM Division of AMP, Inc., Central R&D Group, M/S L3, 100 Chelmsford Street, Lowell, MA 01853-3294.

This work was supported in part by the Natural Sciences and Engineering Research Council of Canada (NSERC) under Grants OGP0007239, STP0201832, TRIO, Com Dev, Nanowave Technologies and through the Micronet Network of Centres of Excellence. M.H. Bakr was supported under an Ontario Graduate Scholarship and N. Georgieva by a Postdoctorate Fellowship from NSERC.

This paper presents some recent advances in automated EM optimization of microwave components and circuits. We review the challenge of EM optimization and present illustrative examples, involving both direct optimization using commercial EM simulators and space mapping (SM) optimization [7,8]. SM optimization is not yet available in user-friendly form in a commercial package. The powerful SM concept uses a "coarse" model to carry out the bulk of computations in the optimization process. The coarse model can be an empirical model, an equivalent circuit model or an EM model with a coarse resolution. A "fine" or accurate EM model is used to align the coarse model and guide the optimization process.

We review what is claimed to be a robust new algorithm for EM optimization called Trust Region Aggressive Space Mapping (TRASM) [9], which integrates a trust region methodology with the aggressive space mapping (ASM) technique [8]. The trust region is to ensure that each iteration results in improved alignment between the coarse and fine models needed to execute ASM. A recursive multi-point parameter extraction process is proposed to improve the conditioning of the extraction phase.

We exploit Sonnet's ***em*** [10], MATLAB [11], OSA90 [12] and Empipe [12]. In addition we implement OSA's Datapipe technology, interpolation and database techniques, as well as Geometry Capture [12]. Examples include the direct EM optimization of microstrip T-junctions and the space mapping optimization of an HTS filter.

DIRECT OPTIMIZATION: DESIGN OF OPTIMAL MICROSTRIP T-JUNCTIONS

"Direct" optimization has been reported by Bandler *et al.* [4,5,13]. We describe here some new results. We compare four different configurations to compensate discontinuities in a microstrip T-junction by optimization over a broad frequency range. Three of them are taken from the literature, one is introduced here. The T-junctions are optimized to achieve the minimum possible mismatch at the three ports.

The T-junction configuration is symmetric and is connected to three 50 Ω microstrip lines. The first configuration shown in Fig. 1(a) was suggested by Chadha and Gupta [14]. The discontinuity is compensated by removing a triangle portion from the basic T-junction. The configuration of Fig. 1(b) was introduced in [15] but no optimization was performed. Here, the compensation is done by modifying the common arm and the two corners. The T-junction in Fig. 1(c) is introduced here: it is similar to that in Fig. 1(b). The one in Fig. 1(d) is suggested by Dydyk [16] but no optimization was applied. The T-junctions of Figs. 1(a) and 1(b) were compared by Swanson [17] without optimization. The optimization variable for Fig. 1(a) is the side length r at θ equal to 30°, 45° and 60°. For Figs. 1(b), 1(c) and 1(d) the optimization variables are x and y. These variables are adjusted to satisfy the theoretical simultaneous match condition which is 9.54 dB (20 log (1/3)) return loss at the three ports. The specifications are $|S_{11}| \leq 1/3, |S_{22}| \leq 1/3$ in the frequency range 2 GHz to 16 GHz. The width w, the height h and the relative dielectric constant ε_r are fixed during optimization. We use Sonnet's ***em*** [10] to compute the S parameters of the different T-junction configurations, the minimax optimizer in OSA90/hope [12] to perform optimization and Empipe [12] to parameterize the geometry of the T-junctions.

Optimization Results

The side length r of the triangle in Fig. 1(a) is optimized for θ equal to 30°, 45° and 60°. Table I shows the results. The T-junctions in Figs. 1(b), 1(c) and 1(d) are optimized here with respect to x and y, each from five starting points. Unique solutions are reached (Table II). Fig. 2 compares responses in the frequency range 2 GHz to 20 GHz for the optimized T-junctions in Fig. 1. It is clear that the T-junction in Fig. 1(a) with θ equal to 30° gives the worst results. The other T-junctions give satisfactory results with minor differences. Fig. 3 compares responses for the optimized T-junctions of Figs. 1(b), 1(c) and 1(d). The T-junction of Fig. 1(d) gives the best response. The response of the T-junction of Fig. 1(c) introduced here is slightly better than the T-junction of Fig. 1(b).

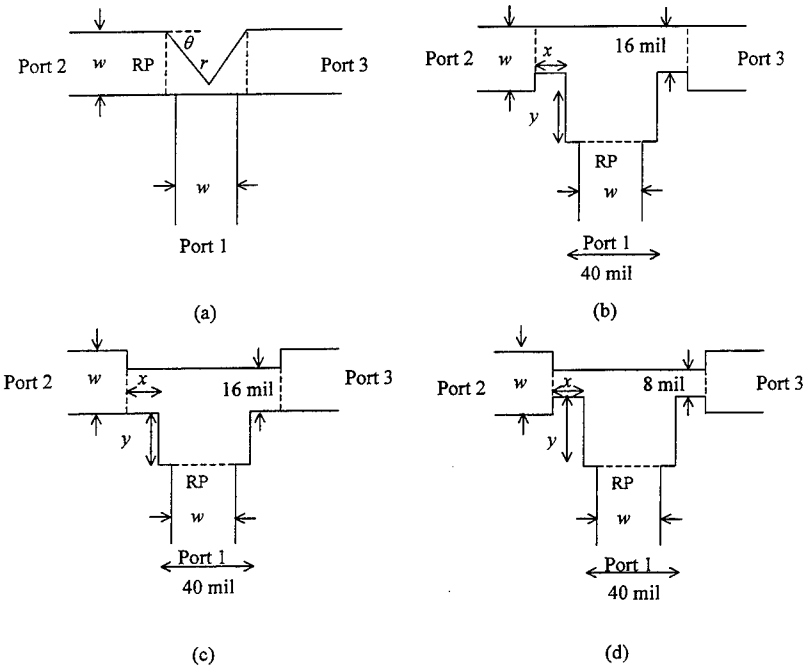

Fig. 1. Four different T-junctions with w= 24 mil, h=25 mil and ε_r=9.9.

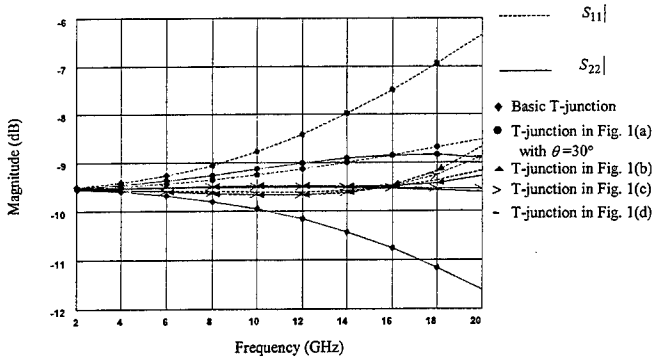

Fig. 2. $|S_{11}|$ and $|S_{22}|$ for the basic T-junction and the optimized T-junctions of Fig. 1.

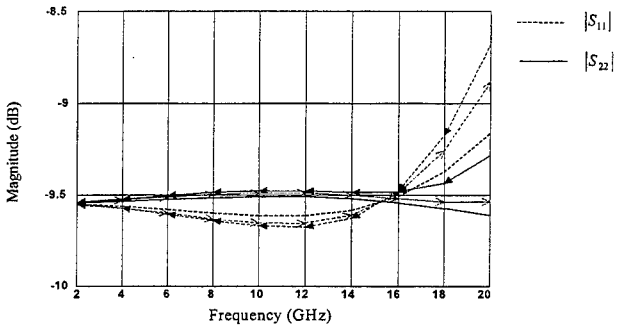

Fig. 3. $|S_{11}|$ and $|S_{22}|$ for the optimized T-junctions of Figs.1(b), 1(c) and 1(d). The range is expanded w.r.t. Fig. 2.

TABLE I
THE OPTIMAL VALUE OF r AT θ EQUAL TO 30°, 45° AND 60°
FOR THE T-JUNCTION IN FIG. 1(a)

θ	The optimal value of r
30°	1.556 w
45°	1.355 w
60°	1.158 w

TABLE II
THE OPTIMAL VALUES OF THE PARAMETERS x AND y FOR
THE T-JUNCTIONS IN FIGS. 1(b), 1(c) AND 1(d)

T-junction	Optimal value of x	Optimal value of y
Fig. 1(b)	0.9250 w	0.583 w
Fig. 1(c)	0.7271 w	0.7917 w
Fig. 1(d)	0.1 w	0.9167 w

OPTIMIZATION THROUGH SPACE MAPPING

Space mapping (SM) aims at aligning two different simulation models: the so-called "coarse" model, typically an empirical circuit simulation and a "fine" model, typically a full wave EM simulation [1, 7-9]. The concept is illustrated in Fig. 4, where the coarse model is called the "optimization" model and the fine model is identified as the "validation" model.

The technique combines the accuracy of the fine (validation) model with the speed of the coarse (optimization) model during the circuit optimization process. Parameter extraction is a crucial part of the technique. During this step the parameters of the coarse model whose response matches the fine model response are obtained. The extracted parameters may not be unique, causing the technique to fail to converge to the optimal design.

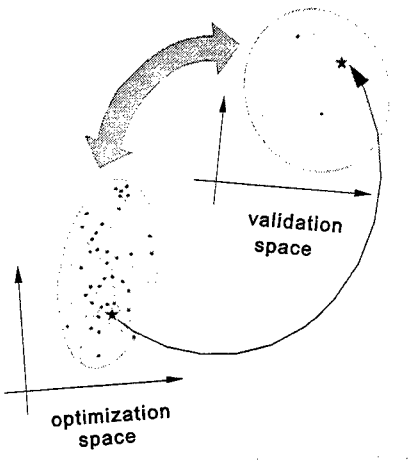

Fig. 4. Concept of aligning two spaces by the space mapping approach [8].

We briefly review aggressive space mapping (ASM) EM optimization. The vector of parameters of the fine model is referred to as x_{em}. The vector of parameters of the coarse model is referred to as x_{os}. The first step of the ASM technique is to obtain the optimal design of the coarse model $x_{os}^{\bullet}$. The technique aims at establishing a mapping P between the two spaces [8]

$$x_{os} = P(x_{em}) \tag{1}$$

such that

$$\left\| R_{em}(x_{em}) - R_{os}(x_{os}) \right\| \leq \varepsilon \tag{2}$$

where R_{em} is the vector of fine model responses, R_{os} is the vector of coarse mode responses and $\| \ \|$ is a suitable norm. The error function

$$f = P(x_{em}) - x_{os}^{\bullet} \tag{3}$$

is first defined. The final fine model design is obtained and the mapping is established if a solution for the system of nonlinear equations

$$f(x_{em}) = 0 \tag{4}$$

is found.

Let $x_{em}^{(i)}$ be the ith iterate in the solution of (4). The next iterate $x_{em}^{(i+1)}$ is found by a quasi-Newton iteration

$$x_{em}^{(i+1)} = x_{em}^{(i)} + h^{(i)} \tag{5}$$

where $h^{(i)}$ is obtained from

$$B^{(i)} h^{(i)} = -f(x_{em}^{(i)}) \tag{6}$$

and $B^{(i)}$ is an approximation to the Jacobian of the vector f with respect to x_{em} at the ith iteration. The matrix B is updated at each iteration using Broyden's update [18].

It is seen from (1)-(3) that the vector function f is obtained by evaluating $P(x_{em})$. This can be achieved through the process of parameter extraction. Parameter extraction involves solving a subsidiary optimization problem.

During parameter extraction the parameters of the coarse model whose response matches the fine model response are obtained. It can be formulated as

$$\underset{x_{os}}{minimize} \left\| R_{em}(x_{em}^{(i)}) - R_{os}(x_{os}) \right\|. \tag{7}$$

The extracted parameters may not be unique, causing the space mapping optimization technique to fail.

A TRUST REGION AGGRESSIVE SPACE MAPPING ALGORITHM FOR EM OPTIMIZATION

The TRASM algorithm [9] depicted in Fig. 5 integrates a trust region methodology [19] with ASM. The trust region is to ensure that each iteration results in improved alignment between the coarse and fine models needed to execute ASM. To improve the uniqueness of the extraction phase Bakr *et al.* [9] developed a recursive multi-point parameter extraction process, which exploits all available EM simulations already performed. TRASM automates the selection of fine model points used for the multi-point parameter extraction process. Also, the current approximation to the mapping between the two spaces is integrated into the parameter extraction step.

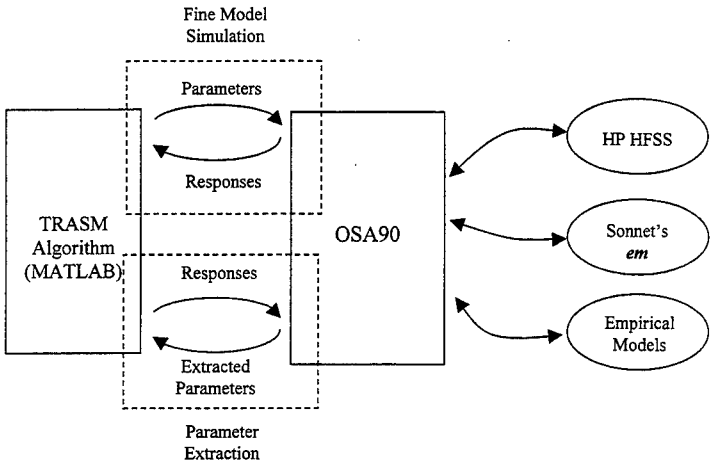

Fig. 5. The current implementation of the TRASM algorithm [9] using MATLAB [11].

HIGH-TEMPERATURE SUPERCONDUCTING FILTER EXAMPLE

We review optimization of a narrow band high-temperature superconducting (HTS) filter [20] (Fig. 6). The specifications are $|S_{21}| \geq 0.95$ in the passband and $|S_{21}| \leq 0.05$ in the stopband, where the stopband includes frequencies below 3.967 GHz and above 4.099 GHz and the passband lies in the range [4.008 GHz, 4.058 GHz]. The optimization variables are L_1, L_2, L_3, S_1, S_2 and S_3. We take $L_0 = 50$ mil and $W = 7$ mil. For complete details see [9] and [20]. The coarse model exploits the empirical microstrip line models, coupled lines and open stubs available in OSA90/hope. The fine model employs a fine-grid *em* simulation. The coarse model is first optimized using the OSA90/hope minimax optimizer. The corresponding fine model response is shown in Fig. 7. The final EM design was obtained in 5 iterations which required 8 fine

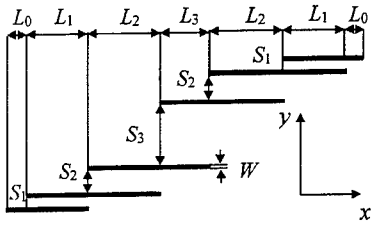

Fig. 6. The structure of the HTS filter [20].

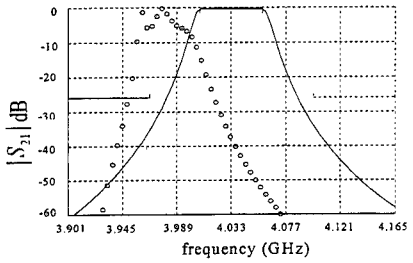

Fig. 7. The optimal coarse model response (—) and the fine model response (o) at the starting point for the HTS filter [9].

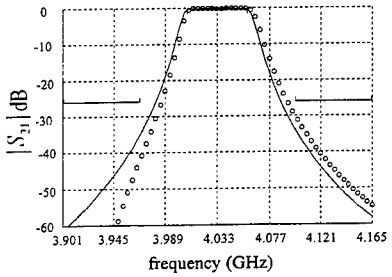

Fig. 8. The optimal coarse model response (—) and the optimal fine model response (o) for the HTS filter [9].

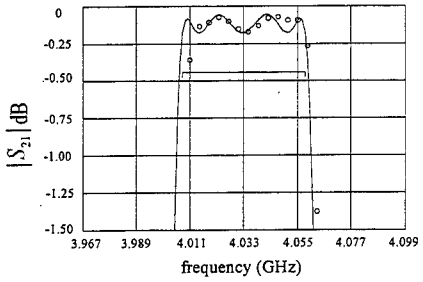

Fig. 9. The optimal coarse model response (—) and the optimal fine model response (o) for the HTS filter in the passband [9].

model simulations. The final fine model response at this design is shown in Fig. 8. The passband ripples are shown in Fig. 9.

ACKNOWLEDGEMENT

The authors thank Dr. James C. Rautio, President, Sonnet Software, Inc., Liverpool, NY, for continuing to make ***em*** available for this work. Use of software provided by Optimization Systems Associates Inc. (OSA) before acquisition by HP EEsof is also acknowledged.

CONCLUSIONS

Advances in computational electromagnetics and optimization technology allow direct exploitation of EM simulation techniques in circuit design optimization. In this paper we have reviewed recent advances in EM optimization of microwave components and circuits. We presented illustrative examples, involving both direct optimization using commercial EM simulators and space mapping optimization. The space mapping technique is a powerful approach to design optimization when extremely CPU intensive simulators are used, combining the speed of circuit-level optimization with the accuracy of EM simulations. We reviewed a new algorithm for EM optimization called TRASM.

Examples include the EM optimization of microstrip T-junctions and an HTS filter. In particular, we compared four different configurations to compensate discontinuities in a T-junction. A new configuration has been introduced here. The HTS filter is a particularly challenging optimization problem, characterized as it is by narrow bandwidth (about 1.24 %) and high dielectric constant (about 24) [20].

REFERENCES

[1] J.W. Bandler and Q.J. Zhang ,"Next generation optimization methodologies for wireless and microwave circuit design," *IEEE MTT-S Int. Topical Symp. On Technologies for Wireless Applications* (Vancouver, BC), Feb. 1999.

[2] *HP HFSS Designer*, HP EEsof Division, Hewlett-Packard Company, 1400 Fountaingrove Parkway, Santa Rosa, CA 95403-1799, 1998.

[3] J.W. Bandler, R.M. Biernacki and S.H. Chen, "Automated electromagnetic optimization of microwave circuits," *Proc. 13th Annual Review of Progress in Applied Computational Electromagnetics* (Monterey, CA), 1997, pp. 1358-1365.

[4] J.W. Bandler, R.M. Biernacki, S.H. Chen, P.A. Grobelny and S. Ye, "Yield-driven electromagnetic optimization via multilevel multidimensional models," *IEEE Trans. Microwave Theory Tech.*, vol. 41, 1993, pp. 2269-2278.

[5] J.W. Bandler, R.M. Biernacki, S.H. Chen, D.G. Swanson, Jr., and S. Ye, "Microstrip filter design using direct EM field simulation," *IEEE Trans. Microwave Theory Tech.*, vol. 42, 1994, pp. 1353-1359.

[6] Workshop WMFE, *Automated Circuit Design using Electromagnetic Simulators*. 1995 IEEE MTT-S Int. Microwave Symposium (Orlando, FL), 1995.

[7] J.W. Bandler, R.M. Biernacki, S.H. Chen, P.A. Grobelny and R.H. Hemmers, "Space mapping technique for electromagnetic optimization," *IEEE Trans. Microwave Theory Tech.*, vol. 42, 1994, pp. 2536-2544.

[8] J.W. Bandler, R.M. Biernacki, S.H. Chen, R.H. Hemmers and K. Madsen, "Electromagnetic optimization exploiting aggressive space mapping," *IEEE Trans. Microwave Theory Tech.*, vol. 43, 1995, pp. 2874-2882.

[9] M.H. Bakr, J.W. Bandler, R.M. Biernacki, S.H. Chen and K. Madsen, "A trust region aggressive space mapping algorithm for EM optimization," *IEEE Trans. Microwave Theory Tech.*, vol. 46, Dec. 1998.

[10] ***em***™ , Versions 3.0b, 4.0b and 5.1a, Sonnet Software, Inc., 1020 Seventh North Street, Suite 210, Liverpool, NY 13088, 1997 and 1998.

[11] MATLAB®, Version 5.0, The Math. Works, Inc., 24 Prime Park Way, Natick, MA 01760, 1997.

[12] *OSA90/hope*™ and *Empipe*™, Version 4.0, formerly Optimization Systems Associates Inc., P.O. Box 8083, Dundas, ON, Canada, L9H 5E7, 1997, now HP EEsof Division, Hewlett-Packard Company, 1400 Fountaingrove Parkway, Santa Rosa, CA 95403-1799.

[13] J.W. Bandler, R.M. Biernacki, S.H. Chen, L.W. Hendrick and D. Omeragić, "Electromagnetic optimization of 3D structures," *IEEE Trans. Microwave Theory Tech.*, vol. 45, 1997, pp. 770-779.

[14] R. Chadha and K.C. Gupta, "Compensation of discontinuities in planar transmission lines," *IEEE Trans. Microwave Theory Tech.*, vol. 30, 1982, pp. 2151-2156.

[15] S. Wu, H. Yang and N.G. Alexopoulos, "A rigorous dispersive characterization of microstrip cross and tee junctions," *IEEE MTT-S Int. Microwave Symp. Dig.* (Dallas, TX), 1990, pp. 1151-1154.

[16] M. Dydyk, "Master the T-junction and sharpen your MIC designs," *Microwaves*, vol. 16, May 1977, pp. 184-186.

[17] D.G. Swanson, Jr., "RF and wireless component design using electromagnetic simulation," lecture notes, Besser Associates Inc., Mountain View, CA 94040, 1998.

[18] C.G. Broyden, "A class of methods for solving nonlinear simultaneous equations," *Math. Comp.*, vol. 19, 1965, pp. 577-593.

[19] J.J. Moré and D.C. Sorenson, "Computing a trust region step," *SIAM J. Sci. Stat. Comp.*, vol. 4, 1983, pp. 553-572.

[20] J.W. Bandler, R.M. Biernacki, S.H. Chen, W.J. Gestinger, P.A. Grobelny, C. Moskowitz and S.H. Talisa, "Electromagnetic design of high-temperature superconducting filters," *Int. J. Microwave and Millimeter-Wave CAE*, vol. 5, 1995, pp. 331-343.

Extraction of Equivalent Circuits of Microwave Devices Using The Genetic Algorithm

P.L Werner, R. Mittra and D.H. Werner
Pennsylvania State University
Department of Electrical Engineering
University Park, PA 16802
plw7@psu.edu
Ph: 814 865-6339, Fax: 814 375-4724

Abstract – In this paper, the Genetic Algorithm (GA) [1,2,3,4] is employed as an efficient optimization tool to derive SPICE-type equivalent circuits of microwave components, and of discontinuities in coaxial lines, from their specified S-parameters. Nodal analysis and techniques are utilized in conjunction with the GA to extract these equivalent circuits, whose component values are the parameters optimized by the GA. Numerical examples, that demonstrate the fact that GA yields excellent results for the cases studied, are included in the paper.

1. Extraction of Equivalent Circuits Using the Genetic Algorithm (GA)

The GA is employed in this work to derive the equivalent circuit of microwave discontinuities and devices. This procedure considers each of the component values of the circuit as a parameter p_i to be optimized via the GA. Each of the parameters is assigned a lower and an upper limit, say p_i^{min} and p_i^{max}, and is represented in a discretized binary-coded form with N_i bits called a *gene*. The binary string of all the genes comprising the design is known as a *chromosome*.

The Objective function F for the optimization procedure is chosen to be

$$F = \sum_{n=1}^{N_f} \sum_{i=1}^{2} \sum_{j=1}^{2} | S_{ij}(f_n) - S_{ij}^{GA}(f_n) |^2 \qquad (1)$$

where N_f = Total number of frequencies of interest

S_{ij} = Specified S-parameters of the equivalent circuit

S_{ij}^{GA} = S-parameters calculated from the equivalent circuit selected by the GA

For a given set of specified S-parameters, the GA strives to minimize the objective function F by selecting the component values of the equivalent circuit. The GA starts with an initial population P_0 of N-bit chromosome binary strings. Each string is a candidate for the design. The GA then iteratively generates a new population P_{i+1}, derived from the previous one P_i, through the application of selection, crossover, and mutation, to evolve towards a better solution. In the process of applying the optimization procedure based on (1), we need to compute the S_{ij}^{GA}, the S-parameters of the circuit chosen by the GA, at each iteration step.

2. Derivation of S-Parameters from Nodal Equations

We introduce a technique that employs nodal analysis to derive the S-parameters of microwave components and discontinuities from their Spice-type description of the equivalent circuit. The nodal equations of a N-node circuit can be expressed in the following form,

$$\{ \mathbf{I} \}_{Nx1} = [Y]_{NxN} \{ V \}_{Nx1} \qquad (2)$$

where {I} and {V} are current and voltage vectors at the N nodes for the representative circuit and [Y] is the admittance matrix. Since only input port 1 and output port 2 contain the accessible nodes, and are of interest to us in defining the S-parameters of the two-port network, we can manipulate (2) into the convenient form

$$\boldsymbol{I}_1^R = \boldsymbol{Y}^R \boldsymbol{V}_1^R \tag{3}$$

where $$\boldsymbol{I}_1^R = \begin{bmatrix} I_1 \\ \\ I_2 \end{bmatrix}; \qquad \boldsymbol{V}_1^R = \begin{bmatrix} V_1 \\ \\ V_2 \end{bmatrix} \tag{4}$$

$$\boldsymbol{Y}^R = \begin{bmatrix} \boldsymbol{Y}_{11} & \boldsymbol{Y}_{12} \\ \\ \boldsymbol{Y}_{21} & \boldsymbol{Y}_{22} \end{bmatrix} = (\boldsymbol{A}_{11} - \boldsymbol{A}_{12}\boldsymbol{A}_{22}^{-1}\boldsymbol{A}_{21}) \tag{5}$$

$$\boldsymbol{A}_{11} = \begin{bmatrix} y_{11} & y_{12} \\ \\ y_{21} & y_{22} \end{bmatrix} \tag{6}$$

$$\boldsymbol{A}_{12} = \begin{bmatrix} y_{13} & y_{14} & \cdots & y_{1N} \\ y_{23} & y_{24} & \cdots & y_{2N} \end{bmatrix} \tag{7}$$

$$\boldsymbol{A}_{21} = \begin{bmatrix} y_{31} & y_{32} \\ y_{41} & y_{42} \\ \cdots & \\ \cdots & \\ y_{N1} & y_{N2} \end{bmatrix} \tag{8}$$

$$\boldsymbol{A}_{22} = \begin{bmatrix} y_{33} & y_{34} & \cdots & y_{3N} \\ y_{43} & y_{44} & \cdots & y_{4N} \\ \cdots & \cdots & & \\ \cdots & \cdots & & \\ y_{N3} & y_{N4} & \cdots & y_{NN} \end{bmatrix} \tag{9}$$

The S-parameter matrix of the circuit can now be calculated from

$$\boldsymbol{S} = [\boldsymbol{I} - \boldsymbol{Y}^R][\boldsymbol{I} + \boldsymbol{Y}^R]^{-1} \tag{10}$$

where $\boldsymbol{S}$ = S-parameter matrix of the circuit
$\boldsymbol{I}$ = Identity matrix

The above procedure for deriving S-parameters is used in the GA optimization process to choose the component values of the equivalent circuits.

3. Case Examples

3.1 Right-angled Bend

In the first example we consider a right-angled bend in a microstrip line. The geometry and the equivalent circuit of the discontinuity, derived from Gupta [5], are shown in Fig. 1. We begin with a set of S-parameters that was calculated for the right-angled bend by using a commercially-available software package called *Ensemble* [6]. The component values inserted between the nodes are the parameters to be optimized by the GA. The GA views the S-parameter information as the specifications, and searches for the component values of the equivalent circuit that meets these specifications. Figure 2 shows the results obtained from application of the technique. The component values derived from the GA are nearly identical to the ones given in Fig.1. As a consequence, the S-parameters computed from the GA-derived circuit duplicate the ones calculated by *Ensemble* almost exactly

3.2 Flat Spiral Inductor

Next, we study a flat spiral inductor model [7], whose physical configuration and the known equivalent circuit are given in Fig. 3. The parameters S_{11} and S_{21}, derived from component values shown in the first column of Table 1, were computed via *EESOF* [8], and were designated as the specified S-parameters. The GA views the specified S-parameters as the design objectives. The values of the components chosen by the GA are also listed in Table 1. Figure 4 shows a good agreement between the specified S-parameters and the ones derived from the GA.

3.3 Parallel Plate Capacitor

We then consider the problem of determining the component values for the equivalent circuit of a parallel plate capacitor, whose physical configuration and equivalent circuit (see [7]) are shown in Fig. 5. The component values of the circuit are listed in Table 2. Once again *EESOF* was utilized to compute the S-parameters that were viewed as the design objectives. The GA then chose the component values that are also shown in Table 2. Figure 6 plots the magnitude of the specified S-parameters and compares them with those computed from the GA-selected equivalent circuit.

3.4 Coaxial Discontinuity Problem

In this example, we deal with the problem of extracting the equivalent circuit of a coaxial transmission line with step discontinuities. The transmission line shown in Fig. 7 consists of three sections with different dielectric (ε_r) fillings. The effect of discontinuities can be expressed in terms of an equivalent T-circuit (Fig. 7b). The component values of the equivalent circuit are the parameters to be optimized by the GA to meet the S-parameter specifications. To derive the S-parameters for each selected values, it is convenient to employ an approach based on the cascading of T-matrices.

Each of the three sections of the coaxial line can be represented by a length of transmission line whose T-matrix can be represented by $\boldsymbol{T}_l$ (see [5]). The T-matrix of the T-circuit with series inductors and a shunt capacitor that represents the step discontinuity, can be expressed by $\boldsymbol{T}_C$ [5]. The composite T-matrix of the system can be obtained via a simple cascading procedure of matrix multiplication, and the S-matrix parameters can then be derived for the composite T-matrix.

To illustrate the above procedure we consider the coaxial configuration. The dielectric constants ε_r for the center line is chosen to be 1.5, and the length of the two air-filled and dielectric-filled lines are chosen to be 0.035m and 0.1m, respectively. The characteristic impedance is 50 ohms for each of the three lines. The series inductance is typically negligible for lower frequencies, so we simply use an estimated capacitance value of 0.01 pF for the step discontinuities, compute the S-parameters of the composite

structure, and feed these as inputs to the GA program. Fig. 8 plots the specified and computed S-parameters, and also shows the capacitance values. Once again, the GA has successfully selected the component values and has recovered the equivalent circuit of the coaxial line discontinuity. The method can be easily extended to coaxial lines containing three or more sections, without any difficulty.

4. Conclusions

In this paper, we have demonstrated a new technique for systematically extracting SPICE-type equivalent circuits of microwave components, and discontinuities in coaxial lines, from computed or measured S-parameters. The equivalent circuit has been derived by using a GA-based technique, which is a robust optimization tool.

References:

1. R.L. Haupt and S.E. Haupt, Practical Genetic Algorithms, NY: *John Wiley & Sons, Inc.,* 1997.
2. D.E. Goldberg, Genetic Algorithm in Serach, Optimization, and Machine Learning. Reading, MA: *Addison-Wesley,* 1989.
3. D.S. Weile and E. Michielssen, "Genetic Algorithm Optimization Applied to Electromagnetics : A Review," *IEEE Trans. Antennas Propagat.* Vol.45, No.3, pp.343-353, March 1997.
4. J. Michael Johnson and Yahya Rahmat-Samii, "Genetic Algorithms in Engineering Electromagnetics," *IEEE Antennas Propagat. Mag.,* Vol.39, pp.7-21, Aug. 1997.
5. K.C. Gupta, Ramesh Garg, and Rakesh Chadha, Computer-Aided Design of Microwave Circuits, MA: Artech House, Inc., 1981.
6. ENSEMBLE, Version 4.0, Boulder Microwave Technologies, Inc., 2336 Canyon Blvd., Suite 102, Boulder, CO 80302, U.S.A.
7. Karl-Heinz Drue, Jens Muller, and Leiko Thust, "RF Models of Passive LTCC-Components in the Lower Gigahertz-Range," *Advancing Microelectronics,* pp. 23-26, May/June, 1997.
8. Touchstone, Eesof Inc., U.S.A.

Table 1. Comparison of original and GA-derived component values for the planar inductor shown in Fig.4.

Component values of the equivalent circuit	Component values chosen by the GA
$L = 1.9790948\ nH$	$L = 1.953125\ nH$
$C = 0.7146493\ pF$	$C = 0.703125\ pF$
$R = 0.237845\ \Omega$	$R = 0.1367188\ \Omega$
$L_k = 2.190083\ nH$	$L_k = 2.402344\ nH$
$C_p = 0.265736\ pF$	$C_p = 0.2148438\ pF$

Table 2. Comparison of original and GA-derived component values for the parallel plate capacitor shown in Fig.6.

Component values of the equivalent circuit	Component values chosen by the GA
$C_{g1} = C_{g2} = 0.2798\ pF$	$C_{g1} = C_{g2} = 0.3770\ pF$
$L = 0.3847\ nH$	$L = 0.6387\ nH$
$R_p = 0.0189\ \Omega$	$R_p = 0.0195\ \Omega$
$R_d = 29288.8986\ \Omega$	$R_d = 29284.05\ \Omega$
$C_m = 10.8679\ pF$	$C_m = 10.8398\ pF$

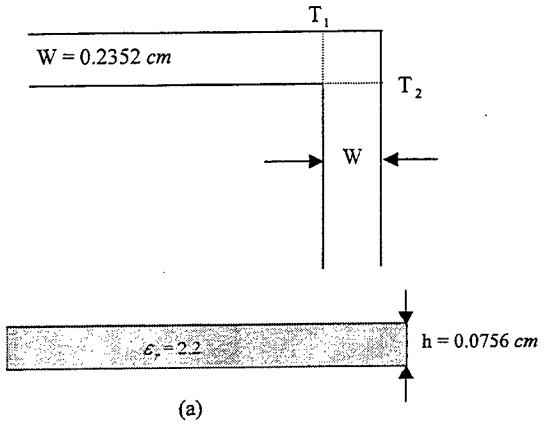

Specified	**GA**
$L = 0.1074\ nH$	$L = 0.1074219\ nH$
$C = 0.2047\ pF$	$C = 0.2041016\ pF$

Fig.1. Right-angled bend in microstrip line and its equivalent circuit

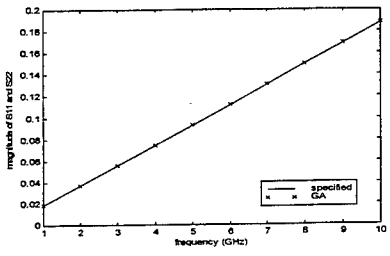

Fig.2. Magnitude of the specified S11 and S22 and those derived from the GA for a right-angled bend.

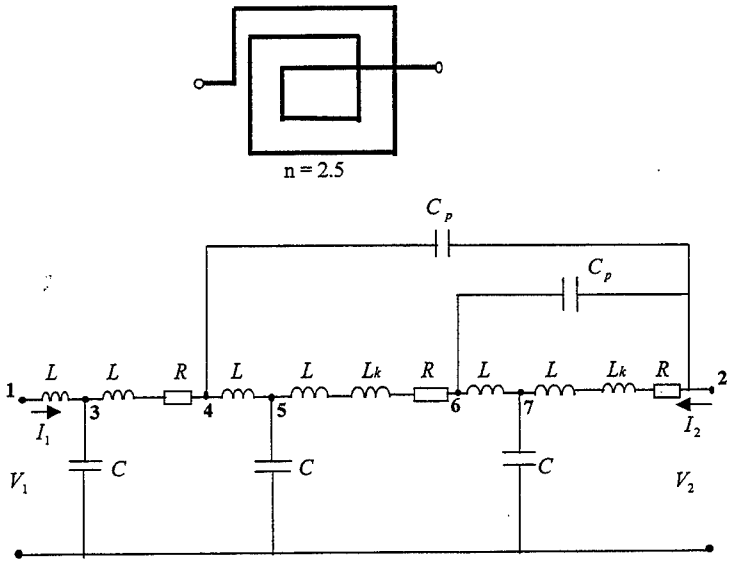

Fig. 3. Physical configuration of a 2.5 turn planar inductor and its equivalent circuit.

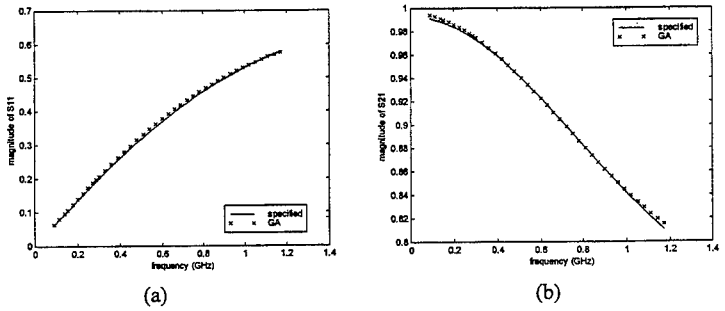

(a) (b)

Fig.4. Comparison of specified S_{11} and S_{21} of the planar inductor with that computed from the equivalent circuit selected by the GA.

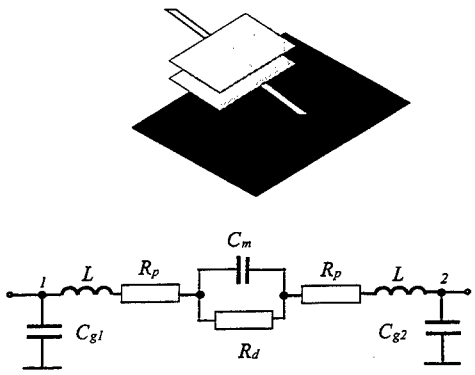

Fig.5. Physical configuration of a parallel plate capacitor and its equivalent circuit.

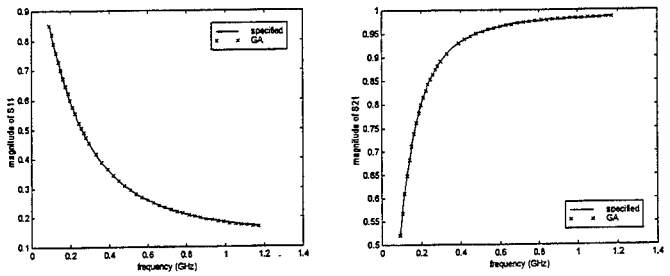

(a) (b)

Fig.6. Comparison of the specified S_{11} and S_{21} of the parallel plate capacitor with those computed from the equivalent circuit selected by the GA.

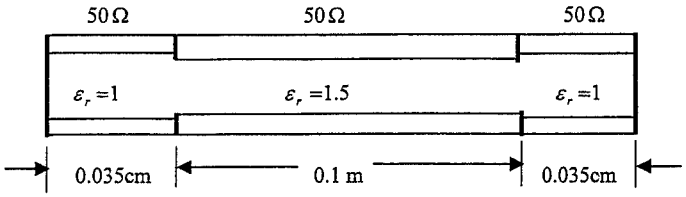

(a)

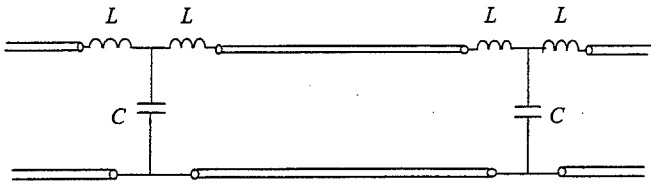

(b)

Fig.7. (a). A coaxial transmission line structure.
(b). The equivalent circuit of the coaxial line in (a).

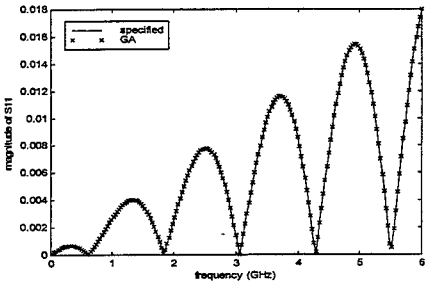

Specified
$C = 0.010000\,pF$

GA
$C = 0.0100098\,pF$

Fig.8. Comparison of the specified S_{11} of a coaxial line with that computed from the equivalent circuit selected by the GA.

A Comparison of Various Optimization Strategies for Yagi-Uda Antenna Design

Eric A. Jones and William T. Joines
Duke University
Durham, NC 27705

Abstract

This paper examines several optimization techniques as they are applied to Yagi-Uda antenna design. Most of the techniques discussed are various forms of genetic algorithms (GAs). A gradient method is also used both alone and in conjunction with GAs. Statistics are gathered as each method is run multiple times for the problem of a five element array optimized for gain, VSWR, and front-to-back ratio over a *5%* bandwidth. After comparing these statistics, the GA + Gradient method proved to be the most efficient of the methods examined. It also produced the best mean antenna fitness over *50* optimization runs.

Introduction

The most important two measures of an optimization technique are its efficiency and ability to consistently generate good results. As long as the first of these is reasonable, the latter is of much greater importance. Many modern optimization techniques, such as genetic algorithms and simulated annealing, are stochastic in nature. This makes it difficult if not impossible to guarantee the quality of their solution. Gradient methods, on the other hand, are efficient techniques which are well known to converge to a local optimum. Unfortunately this does not always result in a good design solution. In highly irregular search spaces with many local optima, the final results are dependent on the quality of the supplied initial guess. This short coming is somewhat ameliorated by running multiple optimizations from randomly chosen starting points at the expense of longer run times.

In this paper, we compare several variations of genetic algorithms and a gradient method by applying them to the design of a five element Yagi-Uda antenna optimized for gain, VSWR, and front-to-back ratio over a *5%* bandwidth. While the performance of optimization techniques is dependent on the problem being solved, this study provides some insight into how the various methods will perform in the domain of antenna design.

Genetic Algorithms

Genetic algorithms are an optimization technique modeled after the survival of the fittest paradigm found in nature. The theory and application of GAs to general problems is well described in the literature [1, 2]. Their use in electromagnetics have been explored in [3, 4] and others. Additionally, [5] provides a thorough description of how GAs apply to the design of Yagi-Uda antennas. A brief overview of the various GAs used in this paper follows.

GAs work with a population of potential design solutions. Individuals in the population are given a fitness score based on how well they solve the design problem. A probabilistic selection scheme then picks individuals out of the population with fitter individuals having a greater chance of being selected. Various genetic operators are then applied to the selected individuals to produce a new generation of designs. These operators can combine information from two designs to form a new individual, randomly mutate part of an individual design, or simply copy an individual into the new generation. This process of evaluation, selection, and then applying genetic operators is carried out for many generations until the population converges to a single solution or some other stopping criteria are met.

The abstract representation of a design solution in a GA population is called a chromosome. Chromosomes can have a variety of structures. For parametric optimization, it is common simply to concatenate the design parameters together into a string of numbers. The encoding of the Yagi-Uda antenna shown in Figure 1 is straight forward. The variable lengths and spacings of the array elements are concatenated together to form a string of numbers as shown below.

Antenna Chromosome Representation: $L_1L_2S_2L_3S_3L_4S_4L_5S_5$

The numeric values can either be represented as binary bit strings or as floating point numbers. While binary encodings are the traditional approach, floating point representations have grown in popularity. The choice of encodings does not affect most implementation issues for GAs, but it does affect mutation operators. In binary bit strings, a mutation is simply a random flipping of a bit. Floating point numbers are mutated by adding a noise term to their value. This noise term can be fabricated a variety of ways. Choosing from a Gaussian distribution centered around the current parameter value is a good choice.

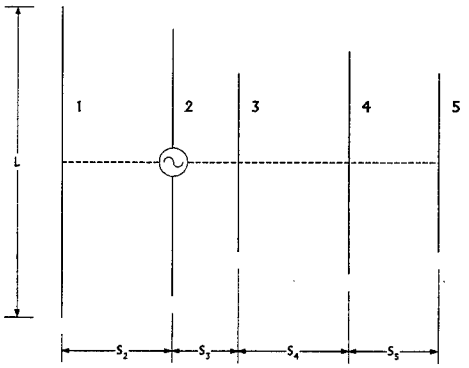

Figure 1: Diagram of a Yagi-Uda array with the length and spacing parameters labeled.

Traditional GAs have a single population that evolves as a group. A variation on the GA theme segments the population into small groups. These sub-populations evolve separately, but after each generation a few individuals from each population migrate to a neighboring population. Using sub-populations along with migration helps encourage population diversity while still allowing good designs to spread throughout the entire population.

The Gradient Method

Unlike genetic algorithms which work with a population of solutions, gradient methods start from a single point in the design space. The algorithm evaluates the current design point and multiple other points in a local region around the current point to determine the direction of steepest accent (or decent for minimization). The design point is then moved in this direction to a better design point. This process is carried out until a local maximum is found such that the gradient around the solution becomes zero.

Gradient methods usually converge to a solution very quickly. However, the quality of their final result is often dependent on the quality of the starting point. To insure a reasonable solution when the quality of the starting point is unknown, it is necessary to run the gradient search from multiple random starting locations scattered throughout the design space. For the Yagi-Uda antenna design problem, searches that start from a poor initial guess usually resulted in a poor final solution. In order to minimize the amount of time spent searching poor regions of the search space, the following algorithm was used:

1. Generate P random antennas with parameters between the limits L_{lower} and L_{upper}.
2. Pick the most fit antenna from *1* and use it as the starting point for a gradient search.
3. Put the result from *2* in a pool , B, that contains the final solution from all past gradient searches.
4. Narrow the search space by centering the parameter bounds, L_{lower} and L_{upper}, around the average of the members in B weighted by their score.

$$R = L_{upper} - L_{lower}$$

$$R_{new} = z * R, \quad z < 1$$

$$Center = \sum_i \frac{F(B_i)}{\sum_j F(B_j)} B_i$$

$$L_{lower} = Center - \frac{R_{new}}{2}$$

$$L_{upper} = L_{lower} + R_{new}$$

Here R is the parameter range, z is used to narrow the range by some percentage, and $F()$ is the antenna fitness function.

5. Return to *1* and repeat for N iterations.

Step *1* insures the gradient search starts at a reasonable location in the design space. Steps *3* and *4* use information from past evaluations to try and narrow future searches into a more promising region of the design space.

Gradient optimization can also be used in conjunction with genetic algorithms. When the two methods are combined, the genetic algorithm is run for a smaller than usual number of generations. The best design from the population is then used as the starting point for the gradient optimization. This approach capitalizes on the strengths of both methods. GAs excel at finding good regions in an irregular search space but are slow to converge to a final solution while gradient methods work well at searching a small region of the search space quickly.

Results

Five different search methods were applied to the problem of optimizing a five element Yagi-Uda antenna array. The different methods are:

1. The Gradient search algorithm described in previous section (GRAD),
2. A single population GA with binary encoding (GA-SB),
3. A single population GA with floating point encoding (GA-SF),
4. A multi-population GA with floating point encoding (GA-MF), and
5. A multi-population GA with floating point encoding + gradient optimization (GA-MFG).

For the gradient method, the parameters discussed in the previous section are as follows: $P=50$, $z=0.95$, and $N=10$.

The settings for each of the GAs is shown in Table 1. Crossover is the percentage of individuals chosen for combination each generation. Mutation is the percentage of bits in a binary encoding, or numbers in a floating point encoding chosen for mutation. Replacement is the percentage of the population that is overwritten with new individuals each generation. Migration is the number of individuals that move to a neighboring population after each generation. A Sigma Truncation Scaling scheme was used along with Stochastic Random Selection during the selection phase of the GA. These parameters and techniques are more fully discussed in [1].

All but the last GA were stopped either after *40* generations or when the standard deviation of the scores in a population was within *0.1%* of the average population score. The GA + Gradient method was stopped earlier when the standard deviation was within *0.3%* of the average fitness at which point the gradient method took over. These stopping criteria generally resulted in optimization runs that required between *3000* to *4000* function evaluations.

GA Type	Number of Pops.	Pop. Size	Crossover (%)	Mutation (%)	Replacement (%)	Migration	Convergence Stdev (%)
GA-SB	1	150	80	0.3	80	-	0.1
GA-SF	1	150	80	0.3	80	-	0.1
GA-MF	5	30	80	0.3	80	2	0.1
GA-MFG	5	30	80	0.3	80	2	0.3

Table 1: Optimization parameters for the various genetic algorithms.

The antenna was optimized for gain, VSWR, and front-to-back ratio over a *5%* bandwidth with a center frequency of *300 MHz*. The lengths of the antenna elements were allowed to vary between *0.3λ* and *0.7λ* and the spacings varied between *0.15λ* and *0.40λ*. The antennas were simulated at three equally spaced frequencies within the band using *NEC4*, a Method of Moments code.[6] The function used to evaluate the fitness of each design candidate is shown below:

$$Fitness = 20G_{\min} - 1.5VSWR_{\max}^{3} + 1.5FB_{\min}$$

Both the Gain, *G*, and the front-to-back ratio, *FB*, are specified in dB. The VSWR was calculated assuming a *50Ω* transmission line feed. The *FB* ratio was calculated by dividing the forward gain by the maximum gain found within *45°* of the backward direction. The subscripts min and max indicate the minimum or maximum value for a parameter over the frequency band. Therefore, this equation uses the worst points within the band for each characteristic to calculate the antenna fitness.

Each of the optimization methods was run *50* times. The results shown in Table 2 list the average number of antenna evaluations per run along with statistics on the final antenna scores. The ideal optimization algorithm would require few evaluations and produce a high average score with a small standard deviation. If the standard deviation is high, a larger number of optimization runs are necessary to guarantee good results.

For antenna optimization, the Method of Moments antenna simulations are by far the most computationally intensive part of the process. This is so much the case that comparing the number of antenna evaluations for the algorithms is a reliable indicator of their relative efficiency. To ease comparison, the speedup of each algorithm is calculated in the third column using GA-SF as the baseline method.

Method	Evals	Speedup	Mean Score	Std. Dev.	Min Score	Max Score
GRAD	3211	1.13	188.03	41.39	102.9	225.90
GA-SB	4950	0.73	225.71	3.11	216.8	230.22
GA-SF	3614	1.00	227.28	2.16	221.9	231.00
GA-MF	3972	0.91	227.78	2.41	220.2	231.11
GA-MFG	3244	1.11	228.25	1.66	225.2	230.94

Table 2: Statistics for the various optimization methods over the course of *50* runs.

Unfortunately, the enhancements to the gradient search described in the previous section did not reliably produce good antenna designs. Its mean score is far lower than those achieved by the GAs. Looking at the genetic algorithms, the single population GAs have similar mean scores; However, the floating point encoded GA converges to a solution much faster than the binary GA. If the binary GA is stopped after roughly *3500* iterations, its average score is around *218* – much lower than the floating point method for the same number of evaluations. Switching from the single population GA to a multi-population improves the mean slightly at the expense of more evaluations. The multi-population GA + Gradient (GA-MFG) provides both the best mean score and efficiency. The improved efficiency comes from stopping the GA sooner than normal and allowing the gradient method to quickly fine tune the solution. Table 3 lists the final lengths and spacings for an approximately average antenna, *score = 228.37*, and the best antenna, *score = 230.94*, found by the GA-MFG search over the *50* runs. Graphs of the VSWR, gain, and F/B ratio are shown for both antennas in Figure 2. While the best antenna has a better VSWR and F/B ratio, for applications where gain is the most important feature, the average antenna might be a better choice.

	Best		Average	
Element	Length (m)	Spacing (m)	Length (m)	Spacing (m)
1	0.4892	-	0.4911	-
2	0.4605	0.2449	0.4551	0.2039
3	0.4357	0.1917	0.4252	0.2468
4	0.4367	0.2336	0.4310	0.3023
5	0.4157	0.2454	0.4245	0.2380
$VSWR_{max}$	1.395		1.719	
$Gain_{min}$ (dB)	10.63		10.83	
F/B_{min} (dB)	14.55		12.88	

Table 3: The lengths and spacings for an approximately average and the best antenna design generated by the GA-MFG over the course of *50* runs. The minimum performance numbers across the band are also shown for gain, vswr, and front-to-back ratio.

Notice that all three floating point GAs produced similar maximum scores over the course of *50* runs. This suggests that any of these methods will produce excellent results given enough runs. For this five element problem, the average run time for a GA-MFG optimization was around seven minutes on a *300 MHz* Pentium II CPU. It is always a good idea to make several optimization runs when using GAs, however *5-10* runs are probably more reasonable than *50* runs -- especially for larger arrays that are more computationally intensive to simulate. The large number of runs used for this paper was necessary to obtain accurate statistics.

Conclusion

This study has examined several optimization techniques for the design of a five element Yagi-Uda antenna array. The GAs proved to be more effective at producing good results than the gradient method used. Of the GAs, floating point encodings faired better than binary encodings and multi-population techniques were arguably better than single population techniques. Finally, the multi-population GA + Gradient method proved to be the best approach both in terms of efficiency and consistent production of good antenna designs.

Acknowledgments: The Genetic algorithm code used in this paper is derived in part from Matthew Wall's GALib.[7] The gradient method was authored by Andre Tits et al. and is available from the authors as a package named CFSQP.[8]

1 D. E. Goldberg, *Genetic Algorithms*. New York: Addison-Wesley, 1989.
2 Z. Michalewicz, *Genetic Algorithms + Data Structures = Evolutionary Programs*. Berlin: Springer-Verlag, 1992.
3 R. L. Haupt, "Thinned Arrays using genetic algorithms, " *IEEE Trans. Antennas Papagat.*, vol 42. pp. 993-999, July 1994.
4 A. Boag, E. Michielssen, and R. Mittra, "Design of electrically loaded wire antennas using genetic algorithms," *IEEE Trans. on Antennas Propagat.*, vol. 44, pp. 687-695, May 1996.
5 E. A. Jones, W. T. Joines, "Design of Yagi-Uda antennas using genetic algorithms," *IEEE Trans. on Antennas Propagat.*, vol. 45, no. 9, pp. 1386-92, Sept 1997.
6 G. J. Burke and A. J. Poggio, "Numerical electromagnetics code (NEC) – Method of Moments," Rep. UCID18834, Lawrence Livermore Lab, CA, Jan. 1981.
7 M. Wall, "GaLib: A C++ genetic algorithms library," MIT, http://lancet.mit.edu/ga/, 1996.
8 C. Lawrence, J. Zhou, A. Tits, *User's Guide for CFSQP Version 2.5*, Institute for Systems Research TR-94-16r1, University of Maryland, College Park, MD.

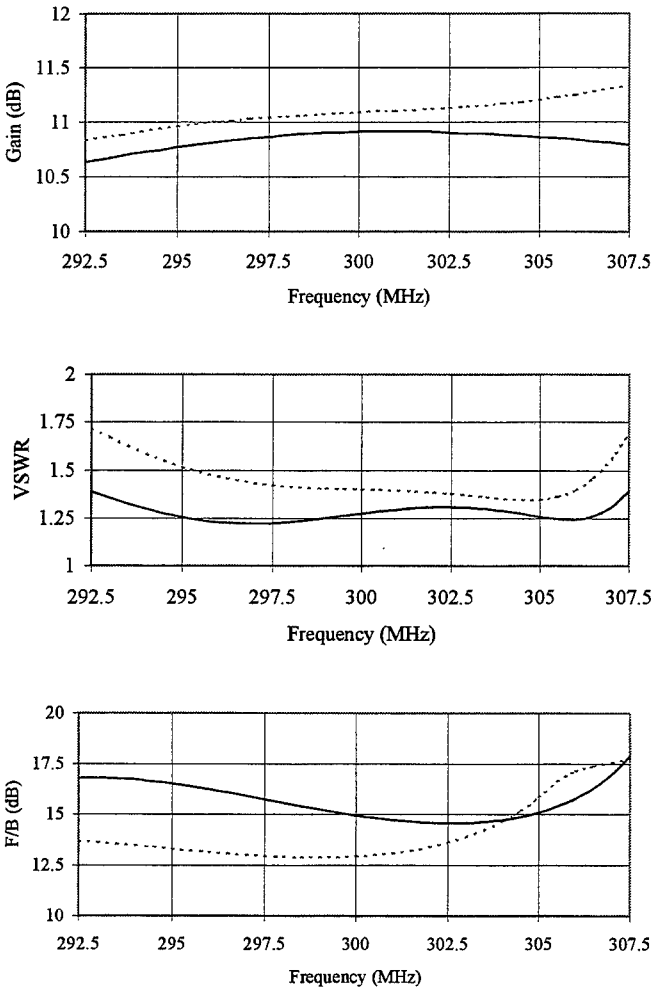

Figure 2: These three graphs gain, VSWR, and front-to-back ratio performance an average antenna (dashed) and the best antenna (solid) generated from *50* runs of the GA-MFB optimization method across the frequency band.

Broad-Banding Uniformly Excited Antenna Arrays Using a Genetic Algorithm

Brian J. Barbisch and D.H. Werner
The Pennsylvania State University
Applied Research Laboratory
P.O. Box 30
State College, PA 16804-0030
dhw@psu.edu

Abstract

A systematic approach for designing broadband low-sidelobe linear and planar antenna arrays by varying interelement spacings has not been available. Both the large number of possible spacing combinations along with theoretical limitations of the problem have made it difficult to formulate robust broadband design techniques. The genetic algorithm (GA) has recently proven to be a very effective design tool for nonuniformly spaced low sidelobe antenna arrays with uniform excitation intended for operation at a single frequency [5]. This paper deals with a generalization of previous GA techniques to include the design of low sidelobe arrays that are operable over a band of frequencies. It will be shown that the GA objective function is no more complicated to evaluate for broad-banding purposes than it is in the single frequency case. Several examples of GA-designed broadband low sidelobe arrays will be presented and discussed.

1. Introduction

In recent years, genetic algorithms have found a fairly strong presence in electromagentics optimization problems involving antenna design. The difficulty in solving many antenna design problems is that very often there are many parameters and no practical analytical methods available to optimally determine them. Such difficulties make efficient search strategies, like genetic algorithms, very important. The main advantages of using the GA over other search strategies are: 1) the GA can search from any number of random points to find a solution, 2) the GA works with a coding of the parameters and not the actual parameters, 3) GA's use random, not deterministic, transition rules, and 4) the GA does not require the evaluation of derivatives [1]. Among the first applications of genetic algorithms in antenna design was the thinning of large arrays [1]. Some other varieties of antenna arrays to which the GA has been applied include planar arrays [1,2], multiple beam arrays [3], and Yagi-Uda arrays [4]. There have also been several excellent review articles written about GA's and their application to solving complex engineering electromagnetics problems [5-7].

The capability of GA's to produce optimal low sidelobe designs for linear arrays of uniformly excited isotropic sources (at a single frequency) by allowing only the interelement spacings to vary was first demonstrated in [5]. Interelement spacings were decided by using a 3 bit parameter such that they could vary in increments of $\lambda/8$ with a minimum interelement spacing of $\lambda/4$. In this paper, we will demonstrate that GA's are also an extremely useful tool for broad-banding of uniformly excited, unequally spaced antenna arrays. There are two major advantages of the technique employed in this paper when compared to previously published methods, such as those described in [5]. These advantages are that 1) a much finer discretization ($\approx \pm 0.01\,\lambda$) will be used, and 2) the GA-designed arrays will have minimal sidelobes over a band of frequencies instead of at just one frequency. The steady-state genetic algorithm with uniform crossover [8] was chosen for use in optimizing

the array designs discussed in this paper.

Although many traditional analytical techniques exist for placing elements in unequally spaced arrays for broad-banding purposes, *viz.* [9-11], none of these methods are capable of producing significantly low sidelobe levels over the entire band. The focus of many of these methods is to place elements in an array such that the minimum separation between elements is greater than or even much greater than a wavelength. The advantage of such large interelement spacings is that a larger bandwidth can be achieved because a lower minimum frequency is possible. The disadvantage, however, is that a theoretical lower bound exists on the sidelobe level when average interelement separations exceed a wavelength [12]. This theoretical minimum is usually not low enough for practical applications. Keeping in mind this theoretical limitation, a design optimization technique will be introduced in this paper which attempts to place elements such that the average interelement spacing in the array is always less than a wavelength.

Another important consideration in the design of antenna arrays is their steerability. Broad-band arrays have the property that they may exhibit perfect steerability at lower frequencies of operation, but steerability is reduced when moving to higher frequencies. The fact that steerability changes with frequency can be quantified by the bandwidth-steerability product of the array [12].

A useful conversion factor will be introduced in Section 2 that permits design tradeoffs to be made between bandwidth and (minimum) element separation. Steerability issues will also be briefly discussed in Section 2. Sections 3 and 4 present and discuss four examples of genetic algorithm produced broadband low sidelobe array designs – two linear arrays (Section 3) and two planar arrays (Section 4). In addition, the GA objective function used to produce each design is given in the respective sections. All array designs considered in this paper were specified to have a maximum possible bandwidth with a minimum element separation of $\lambda/4$ and the lowest possible sidelobe level throughout the band.

2. Some Considerations for Broad-Banding Arrays

In designing a broadband array for low sidelobe performance, it is sufficient to design for the highest desired frequency of operation f_2. Having done this, the frequency may then be varied from f_2 to any f_1, provided $f_1 \le f_2$, without the appearance of any higher sidelobes. The bandwidth for such an array is defined to be $B = f_2 / f_1$. Furthermore, we note that if a minimum separation between two elements exists at the lowest design frequency f_1 that is considered too small for practical purposes, then that spacing can be made larger at the expense of a smaller bandwidth $B' < B$ (i.e., $f_2' < f_2$). This property is best illustrated by the following transformation:

$$s' = \left(\frac{f_2}{f_2'}\right) s = \left(\frac{B}{B'}\right) s \qquad (1)$$

where

$$B' = f_2' / f_1$$

s = the set of original element locations $\{s_n = d_n\lambda_1 : n = 1,2,...,N\}$

s' = the set of new element locations $\{s'_n = d'_n\lambda_1 : n = 1,2,...,N\}$

Hence, the array configuration need only be optimized for a desired maximum bandwidth B, subject to some specified tolerance on the minimum element separation. Once this optimal array design has been found using the GA then, if desired, the transformation given in (1) may be employed to find modified designs which tradeoff larger element separations for smaller operating bandwidths.

Another notable characteristic of broadband arrays is how steerability is affected with increasing bandwidth. It can be shown that the bandwith and steerability of a linear array are related by the following formula, which is known as the bandwidth-steerability product [11]:

$$B(1+\cos\theta_0) = \frac{2w_0}{d_{ave}/d_{\min}} \tag{2}$$

where

B = bandwidth

θ_0 = steering angle

w_0 = the maximum value of $(d_{ave}/\lambda)\cos\theta$ that can be used before a sidelobe will exceed the desired sidelobe level

d_{ave} = average interelement separation in the array

$d_{\min}$ = smallest interelement separation in the array

The right-hand side of this equation is a constant, and is characteristic of the individual array. Note that at a 1:1 bandwidth, the right-hand side of the equation must be at least two to guarantee perfect steerability. When a bandwidth of larger than 1:1 is desired, the left-hand side of this equation limits steerability at some of the higher frequencies in the band. Thus, while a broadband array may exhibit perfect steerability at lower frequencies of operation, steerability may become limited at higher frequencies of operation. In addition, arrays designed to operate at only one frequency when interelement spacings are small may not exhibit any steerability.

3. Linear Broadband Array Designs

The array factor expression for the far-field radiation pattern of a linear array of isotropic sources can be written in the following form:

$$AF(\theta) = 2\sum_{n=1}^{N} I_n \cos[2\pi(f/f_1)d_n \cos\theta + \alpha_n] \quad (3)$$

where

$$\alpha_n = -2\pi(f/f_1)d_n \cos\theta_0 \quad (4)$$

and

$2N$ = the total number of elements in the array

I_n = excitation current amplitude of the nth element in the array

α_n = excitation current phase of the nth element in the array

$s_n = d_n \lambda_1$ = total distance of the nth element from the axis

θ = angle measured from the line passing through antenna elements

θ_0 = steering angle

f_1 = base (minimum) frequency of operation

f = desired frequency of operation

The objective function used by the GA in this paper is based on the array factor expression given in (3), where the desired goal is to minimize the maximum sidelobe level of the array over some prescribed bandwidth. The form of this objective function is

$$F(\theta) = \max\left|2\sum_{n=1}^{N} I_n \frac{\cos[2\pi B d_n \cos\theta]}{AF_{\max}(\theta)}\right| \quad (5)$$

where

$AF_{\max}(\theta)$ = peak of the main beam (for normalization)

$B = f_2/f_1$ = desired bandwidth of the array ($f_2 \geq f_1$)

The parameters d_n were selected by the GA to minimize the maximum sidelobe level with I_n set to unity for

all values of n. The discretization of d_n was made relatively fine, such that it could be varied in increments of approximately ±0.01 between zero and some maximum selected value. The use of any finer discretization was found to yield little improvement in the overall results. It was also found that, in the case of broadband array optimization ($B>1$), the GA objective function need not be any more complicated to evaluate than it is for optimization of array performance at a single frequency ($B=1$). This is one of the attractive features of the technique presented here, since it means that the overall design optimization time required by the GA will be essentially the same regardless of whether single-frequency or broadband array configurations are being considered.

The first broadband design that will be considered is a uniformly excited 40 element array with a minimum element separation requirement of a quarter-wavelength at the lowest design frequency $f = f_1$, i.e., $\Delta_n = (d_{n+1} - d_n) \geq 0.25 \;\; \forall \, n = 1,2,...,N-1$. In this case, the GA was able to optimize interelement spacings in the 40 element array so that a bandwidth of B = 3.5 was possible for broadside operation with a maximum sidelobe level of -19.41dB throughout the entire band (see Table 1). Figures 1a–1c show plots of the array factor at the low-band ($f = f_1$), mid-band ($f = (f_1 + f_2)/2$), and high-band ($f = f_2$) design frequencies. Furthermore, Figures 2a-2c show the optimized 40 element array with the main-beam steered to 60^0 for the same three frequencies considered in Figures 1a-1c. These figures demonstrate that, for the low-band ($f = f_1$) and mid-band ($f = 2.25 f_1$) frequencies, it is possible to steer the main-beam to 60^0 without any increase in the synthesized sidelobe level. However, for the high-band frequency ($f = 3.5 f_1$), we see that the synthesized sidelobe level can no longer be maintained when the beam is steered to 60^0. Further investigation reveals that the steerability of this array at $f = f_2 = 3.5 f_1$ is, as predicted by (2), almost negligible. It was found that the maximum frequency at which this array exhibits perfect steerability is $f = 1.75 f_1$.

Larger sized arrays were found to be capable of producing wider bandwidths. For example, using $\lambda_1 / 4$ as the minimum interelement separation for a 100 element array, it was possible to optimize the array configuration using the GA to yield a bandwidth of $B = 3.97$ and a maximum sidelobe level of -20.32 dB (see Figure 3 and Table 1). The maximum frequency at which this array is steerable to 60^0 is at $f=2.64f_1$, and the maximum frequency at which this array exhibits perfect steerability is at $f = 1.98f_1$ (see Figure 5). If larger interelement spacings are desired, then (1) may be used to determine the corresponding reduction in bandwidth that would result. For instance, increasing the $\lambda_1 / 4$ minimum interelement separation to $0.49625\,\lambda_1$ reduces the bandwidth from 3.97 down to 2. On the other hand, the bandwidth of the array can be doubled to $B = 7.94$ by allowing the minimum element separations to be as small as $\lambda_1 / 8$. Reducing the minimum element separation to $\lambda_1 / 8$ also doubles the bandwidth over which the array is steerable – i.e., in this case the above array would be perfectly steerable over a bandwidth of $B = 3.96$ with a maximum sidelobe level of –20.32 dB.

4. Planar Broadband Array Designs

The GA optimization procedure described in the previous section for broadbanding linear arrays will be

generalized in this section to include planar array configurations. In particular, the GA design approach will be developed for rectangular arrays as well as for concentric circular arrays with variable element spacings. The array factor for a non-uniformly spaced rectangular array of isotropic sources may be represented in the following form:

$$AF(\theta,\phi) = 4\sum_{n=1}^{N}\sum_{m=1}^{M} I_{mn}\cos\left[2\pi d_{xn}(f/f_1)\sin\theta\sin\phi\right]\cos\left[2\pi d_{ym}(f/f_1)\sin\theta\cos\phi\right] \qquad (6)$$

where

$2M$ = total number of elements in the y-direction

$2N$ = total number of elements in the x-direction

$s_{xn} = d_{xn}\lambda_1$ = element locations in the x-direction

$s_{ym} = d_{ym}\lambda_1$ = element locations in the y-direction

The corresponding objective function in this case is given by

$$F(\theta,\phi) = \max\left|4\sum_{n=1}^{N}\sum_{m=1}^{M} I_{mn}\frac{\cos[2\pi d_{xn}B\sin\theta\sin\phi]\cos[2\pi d_{ym}B\sin\theta\cos\phi]}{AF_{\max}(\theta,\phi)}\right| \qquad (7)$$

The GA uses (7) to determine the set of parameters d_{xn} and d_{ym} that yields the lowest possible sidelobe level over a specified bandwidth B, assuming that the array is uniformly excited (i.e., $I_{mn} = 1$ for all values of m and n). In order to accomplish this, a spacing scheme was designed such that rows and columns were treated the same. For example, the GA selects a set of spacings $s = \{d_1, d_2, d_3, \ldots, d_n\}$, where n is the number of rows and columns in the array (i.e., $N = M = n$ where N and M are from (6)). The number d_i, $1 \le i \le n$, then represents the interelement spacing between elements (i,j) and $(i-1,j)$ and the elements (j,i) and $(j,i-1)$ $\forall j \ni 1 \le j \le n$, where the indices $(0,j)$ and $(j,0)$ are the y and x axes respectively. This scheme makes the objective function very simple to evaluate because the maximum sidelobe level will always be located in the $\phi = 0^0$ and $\phi = 90^0$ planes. Figure 4a and Figure 4b show radiation pattern cuts at $\phi = 0^0$ and $\phi = 45^0$, respectively, for a 4,096 element array which was designed to produced a bandwidth of $B = 3.5$ and a maximum sidelobe level of –19.41dB with a minimum specified element separation of $\lambda_1 / 4$.

Next we will consider an alternative design optimization approach based on concentric circular arrays which results in a more spatially uniform distribution of sidelobes. The objective function in this case was chosen to be

$$F(\theta,\phi) = \max \left| \frac{\sum_{m=1}^{M}\sum_{n=1}^{N_m} I_{mn} \exp\left[j2\pi B a_m \sin\theta\cos(\phi-\phi_{mn}) + j\alpha_{mn}\right]}{AF_{\max}(\theta,\phi)} \right| \quad (8)$$

where

$$AF(\theta,\phi) = \sum_{m=1}^{M}\sum_{n=1}^{N_m} I_{mn} \exp\left[j2\pi(f/f_1)a_m \sin\theta\cos(\phi-\phi_{mn}) + j\alpha_{mn}\right] \quad (9)$$

$$\alpha_{mn} = -2\pi(f/f_1)\sin\theta_0\cos(\phi_0-\phi_{mn}) \quad (10)$$

and

$r_m = a_m\lambda_1 =$ radius of the m*th* ring array

M = total number of concentric ring arrays

N_m = total number of elements in the m*th* ring

The spacing scheme was designed such that elements were placed on arcs spaced $\lambda_1/4$ apart, where λ_1 corresponds to the wavelength at the lowest design frequency f_1. In addition to this, the elements in each quadrant were assumed to be arranged symmetrically about their respective diagonal axis (e.g., the elements in the first quadrant are symmetric with respect to the $\phi = 45^0$ axis). Figure 5 shows one quadrant of a concentric circular array in the equally spaced case that could be constructed using this spacing scheme. For this example, the minimum arc length between any two consecutive array elements was set to $\lambda_1/4$. Figure 6 shows the radiation pattern produced over the $\phi = 45^0$ cut by a 308 element concentric circular array with element spacings optimized to yield a bandwidth of B = 3.5 with a maximum sidelobe level of –21.91dB throughout the band.

5. Conclusions

Uniformly excited array broad-banding has been achieved using a genetic algorithm optimization procedure with bandwidths as large as B = 3.97 for linear arrays and B = 3.5 for planar arrays with minimum element separation of $\lambda/4$. Minimum element separation can easily be made larger to avoid mutual coupling effects, or it can be made smaller to increase bandwidth by using the convenient conversion factor given in (1). Array steerability issues have also been addressed in this paper. Steerability varies with operation frequency as predicted by (2) – it is greater at lower frequencies of operation and lesser at higher frequencies of operation.

In addition, the bandwidth over which the array is steerable improves proportionally as (1) is used to increase bandwidth.

References

[1] R. L. Haupt, "Thinned Arrays Using Genetic Algorithms," *IEEE Trans. Antennas Propagat.*, Vol. 42, No. 7, pp. 993-999, July 1994.

[2] D. Marcano and A. Nieto, "Genetic Algorithms for the Synthesis of Planar Arrays, " *USNC/URSI Radio Science Meeting Abstracts*, Baltimore, MD, USA, July 21-26, 1996, Vol. 1, pp. 584-587.

[3] D. Marcano, F. Durán, and O. Chang, " Synthesis of Multiple Beam Linear Antenna Arrays Using Genetic Algorithms," *1995 IEEE Antennas and Propagation Society International Symposium Digest*, Newport Beach, CA, June 1995, pp. 938-941.

[4] E. A. Jones and W. T. Joines, "Design of Yagi-Uda Antennas Using Genetic Algorithms," *IEEE Trans. Antennas Propagat.*, Vol. 45, No. 9, pp. 1386-91, September 1997.

[5] R. L. Haupt, "An Introduction to Genetic Algorithms for Electromagnetics," *IEEE Antennas and Prop. Magazine*, Vol. 37, No. 2, pp. 7-14, April 1995.

[6] M. J. Johnson and Y. Rahmat-Samii, "Genetic Algorithms in Engineering Electromagnetics," *IEEE Antennas and Propagation Magazine*, Vol. 39, No. 4, pp. 7-25, August 1997.

[7] E. Michielssen, D. Treyer and D. S. Weile, "The Application of Novel Genetic Algorithms to Electromagnetic Problems," Proceedings of the 13th Annual Review of Progress in Applied Computational Electromagnetics (ACES), Vol. 2, Monterey, CA, March 1997, pp.1382-1386.

[8] G. Syswerda, "Uniform Crossover in Genetic Algorithms," *Proceedings of the Fifth International Conference on Genetic Algorithms,* pp. 2-9, 1988.

[9] D. D. King, R. F. Packard and R. K. Thomas, "Unequally-Spaced, Broad-Band Antenna Arrays," *IRE Trans. on Antennas Propagat.*, Vol. AP-8, No. 4, pp. 382-384, July 1960.

[10] A. Ishimaru and Y. S. Chen, "Thinning and Broadbanding Antenna Arrays by Unequal Spacings," *IEEE Trans. Antennas Propagat.*, Vol. AP-13, pp. 34-42, Jan. 1965.

[11] J. H. Doles III and F. D. Benedict, "Broad-Band Array Design Using the Asymptotic Theory of Unequally Spaced Arrays," *IEEE Trans. Antennas Propagat.*, Vol. 36, No. 1, January 1988.

[12] M. G. Andreasen, "Linear Arrays with Variable Interelement Spacings," *IRE Trans. Antennas Propagat.*, Vol. AP-10, pp. 137-143, March 1962.

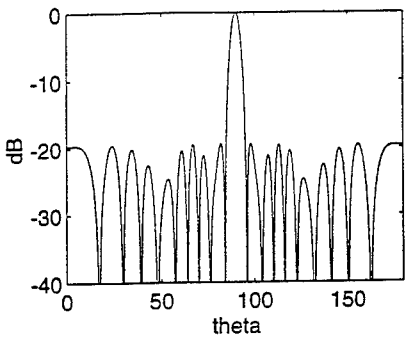

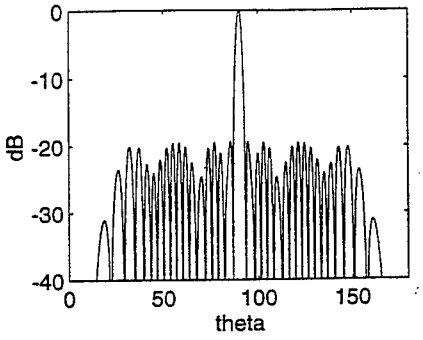

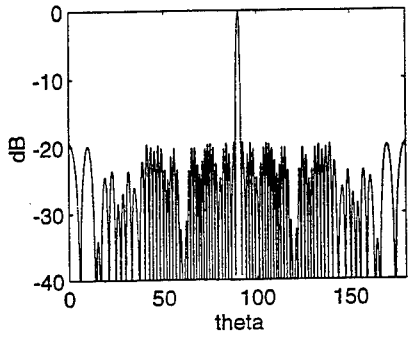

Figures 1a-1c. Uniformly excited, 80 element, isotropic, linear array factor plotted at broadside: 1(a) f/f_1 = 1, 1(b) f/f_1 = 2.25, and 1(c) f/f_1 = 3.5. Maximum bandwidth is f_2/f_1 = 3.5.

Element Number (n)	Element Separation (d_n/λ_1)	Element Number (n)	Element Separation (d_n/λ_1)	Element Number (n)	Element Separation (d_n/λ_1)	Element Number (n)	Element Separation (d_n/λ_1)
1	0.125	6	0.25	11	0.25	16	0.26
2	0.25	7	0.25	12	0.26	17	0.26
3	0.25	8	0.25	13	0.25	18	0.26
4	0.25	9	0.25	14	0.30	19	1.15
5	0.25	10	0.25	15	0.26	20	0.86

Table 1. Element separations at f_1 for the array depicted in Figures 1a-1c.

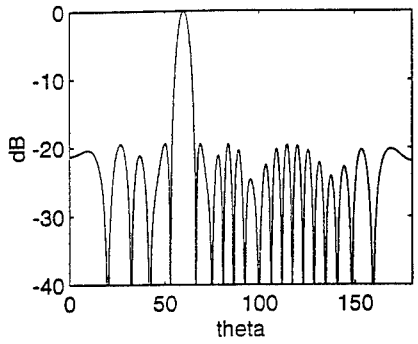

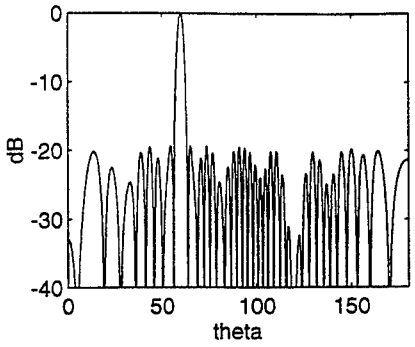

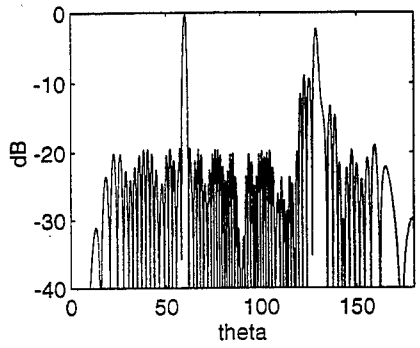

Figures 2a-2c. The 80 element arrays from Figures 1a-1c steered to 60^0. 2(a) $f/f_1 = 1$, 2(b) $f/f_1 = 2.25$, and 2(c) $f/f_1 = 3.5$.

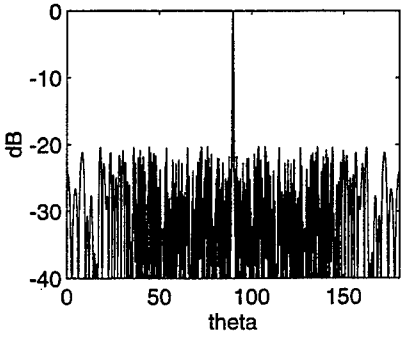

Figure 3. Uniformly excited, 100 element, isotropic, linear array plotted at $f/f_1 = 3.97$.

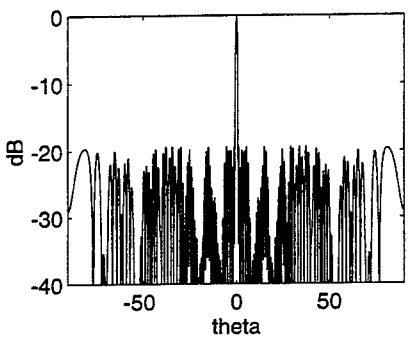

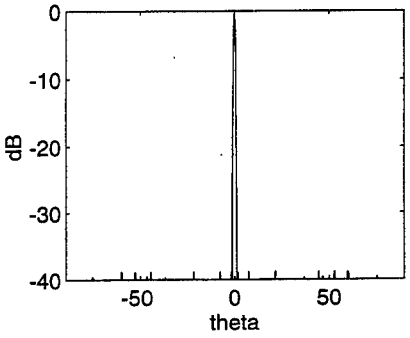

Figures 4a-4b. Radiation pattern cuts at $\phi = 0°$ (Figure 4a) and $\phi = 45°$ (Figure 4b) of a 4,096 element square planar array. $f/f_1 = 3.5$

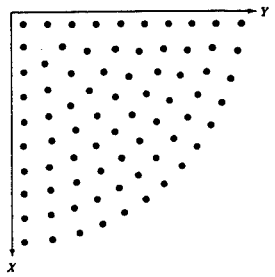

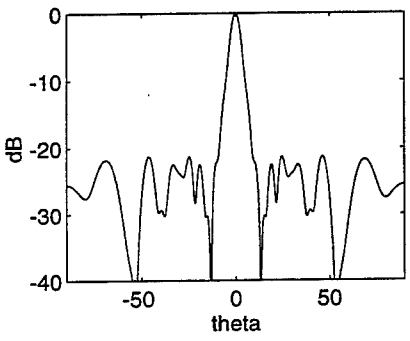

Figure 5. One quadrant of an equally spaced concentric circular arc array that is arranged symmetrically about its diagonal axis.

Figure 6. Broad-band concentric circular arc array cut at $\phi = 45°$. $f/f_1 = 3.5$

Optimizing Genetic Algorithm Parameters for Adaptive Nulling.

You Chung Chung
youchung@unr.edu
Electrical Eng. Dept.
University of Nevada
Reno, NV 89557

Randy L. Haupt
haupt@ee.unr.edu
Electrical Eng. Dept.
University of Nevada
Reno, NV 89557

Abstract

The best size of the population and percentage of mutation of phase-only adaptive nulling and amplitude & phase adaptive nulling with a genetic algorithm (GA) are found based on the null depths of transient and steady state responds of adaptive nulling since the convergence speed of a GA and the final solution of a GA depend on the size of population, percentage of mutation and the other parameters in genetic algorithms. The null depths of phase-only and amplitude & phase adaptive 32 elements half wavelength spaced linear arrays with a GA are compared when single interference incidents on an array. All simulation results are averaged over 30 runs after 25 generations.

1. Introduction

The genetic algorithm (GA) parameters: size of population, discard rate and percentage of mutation have been researched to optimize the GA performance [1 - 10]. Increasing the number of mutations increases the GA's ability to search outside of current convergence area. In addition, a large population generates more offspring to search a wider area. Therefore, the performance of a GA depends on the size of population, percentage of mutation, and the other parameters in genetic algorithms within a certain generation. Adaptive nulling with a GA requires generating multiple deep nulls very quickly so that the best or proper mutation rate and population size are required to optimize the adaptive nulling with a GA. One author has suggested a mutation rate of 1/L where L is number of bits in a chromosome [8].

The best population size and percentage of mutation will be found for 3 bit phase-only adaptive nulling and 5 bit amplitude & 3 bit phase adaptive nulling with a GA in terms of the null depths of transient and steady state responds of adaptive nulling. The 3 bit phase-only adaptive nulling with a GA outperforms any other bit setup phase-only with a GA, and 5 bit amplitude and 3 bit phase adaptive nulling with a GA outperforms any other phase-only and amplitude & phase adaptive nulling with a GA [11]. Multiple interference sources can be non-symmetric, symmetric or closely spaces in angle. In this paper, only results for a single interference at 109 degrees, that is larger than 10000 times of desired signal, are shown. The population size (chromosomes) is half of initial population when the discard rate is fixed as 0.5. The population is varied from 10 to 42, and mutation rate is varied from 0.1% to 5% since a population of 42 is good enough to place nulls, and lager than 5% and smaller than 0.1% mutation rate give worse results than 0.1 ~ 5% mutation rate for single interference case. All the

results of different population size and mutation rates are averaged over 30 runs after 25 generations.

2. Linear Array Elements and Interference

A linear array using amplitude and phase adaptive nulling with a GA is shown in Figure 1. The GA controls the least significant bits of the phase shifter bits and amplitude weight bits, and minimizes output power while it maintains the main beam direction and gain [10, 11]. The array pattern of half wavelength spaced 32 linear elements array with initial –30dB Chebyshev amplitude taper and single possible interference are shown in Figure 2.

The linear array pattern is given by

$$AF(\theta) = 2\sum_{n=1}^{N} a_n \cos[(n-1)\Psi + \Delta_n + \delta_n]. \quad (1)$$

a_n array weight at element n; $\Psi = kdu$;

$k = 2\pi / \lambda$; $\lambda =$ wavelength;

d = spacing between elements; $\theta =$ angle in degree;

δ_n = nulling phase; Δ_n = beam-steering phase;

$\phi =$ angle of incidence of electromagnetic plane wave;

The amplitudes are even symmetric, and the phase is odd symmetric [2, 10, 11].

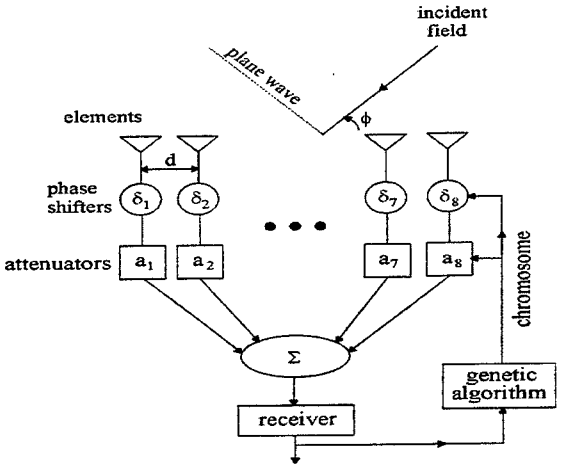

Fig. 1. Diagram of an amplitude and phase adaptive linear array.

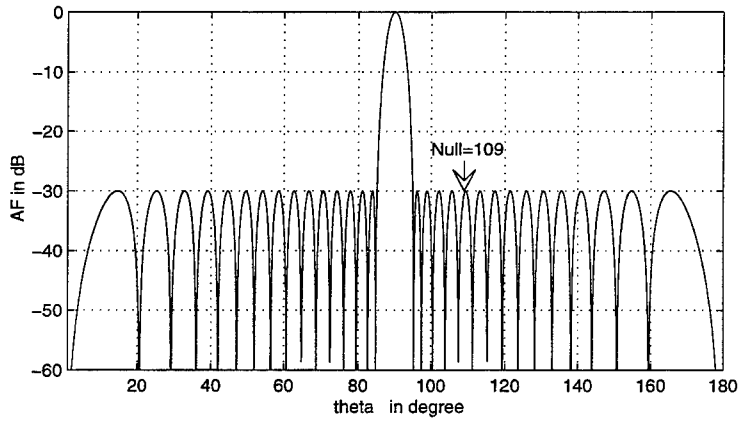

Fig. 2. Initial array pattern with single interference location, 109 degree.

3. Results

The results of phase-only and amplitude & phase adaptive nulling for an interference at 109 degrees with a GA based on different size of population and mutation rate are shown in Figures 3 to 8. All the results are averaged over 30 runs after 25 generation on each population and mutation rate.

The null depth in dB of phase-only and amplitude & phase adaptive nulling with a GA based on population and mutation rate are shown in Figures 3 and 4, respectively. Figures 3 and 4 show that null depth of amplitude & phase is deeper than null depth of phase-only after 25 generations. The best mutation rate of phase-only adaptive nulling is from 2% to 5% with 42 chromosomes in the population, and the range of the best mutation becomes smaller when population size is reduced. Figure 4, amplitude & phase, shows from 1% to 3% mutation with 42 population gives the best null depth after 25 generations. When the population size is reduced to 20, the best mutation rate range is reduced to 1 ~ 2.2% (figure 4). The proper mutation rate of amplitude & phase adaptive nulling is smaller than that of phase-only since the recommended mutation rate is 1/L where $L_{\text{amplitude \& phase}} = 128$ and $L_{\text{phase-only}} = 48$.

Figures 5 and 6 show transient responds of phase-only and amplitude & phase adaptive nulling with a GA. Figures 5 and 6 show that phase-only and amplitude & phase adaptive nulling produce almost the same null depth up to –70dB even though the mutation rate is changed. In addition, the amplitude & phase nulling generates deeper nulls quickly and the null depth is improved constantly while the null depth by phase-only are not improved after –70dB. Both Figures 5 and 6 indicate that below 0.8% and above 5% mutation rates are not recommended since the results of both range of mutation rates do not give good transient and steady state responds.

Figures 7 and 8 show transient null depth in dB is based on different population with the best mutation rate. The amplitude & phase adaptive nulling with a larger population, 42, gives better transient and steady state responds than any others. The phase-only and amplitude &

phase adaptive nulling with a genetic algorithm generate deep –60dB nulls in 5 generations except phase-only with 10 and 14 chromosome in the population. Generally, the –50dB nulls are achieved at the first generation with more than 14 chromosome in the population in both phase-only and amplitude and phase adaptive nulling with a GA.

4. Conclusion

The best values for the proper size of population and mutation rate of phase-only and amplitude & phase adaptive nulling with a genetic algorithm are found when a single interference is incident on a 32 element half wavelength spaced linear array. The null depths of each population size and mutation rate are averaged over 30 independent runs after 25 generations.

The population should be over 14 chromosome to generate –50dB nulls at the first generation, and phase-only adaptive nulling with a GA requires higher mutation rate than amplitude & phase adaptive nulling with a GA since the number of bits in a chromosome of phase-only is less than that of amplitude & phase. The best mutation rate should be larger than 0.8% and smaller than 5%, and the best mutation rate should be chosen based on the population size.

Generally, the phase-only and amplitude & phase adaptive nulling with a genetic algorithm generate deep nulls quickly, and amplitude & phase adaptive nulling generates deeper null than phase-only adaptive nulling with a GA.

References.

[1]. David E.Goldberg, *Genetic Algorithm.* NY: Addison-Wesley, 1989.

[2]. R. L. Haupt and S. E. Haupt, *Practical Genetic Algorithms*, John Wiley & Sons Inc., New York, NY, 1998.

[3]. J. J. Grefenstette, "Optimization on Control parameters for genetic algorithms," *IEEE Trans. Systems, Man, and Cybernetics.* SMC 16, p.128.

[4]. T. C. Forgarty, "Varying the probability of mutation in the genetic algorithm," *Proceedings of the third International Conference on Genetic Algorithm*, pp. 104-109, Morgan Kaufmann , San Mateo, CA, 1989.

[5]. P. Jog, J. Y. Suh and D. V. Gucht, "The effects of population size, heuristic crossover and local improvement on a genetic algorithm for the traveling salesman problem," *Proceedings of the third International Conference on Genetic Algorithm*, pp. 110-115, Morgan Kaufmann , San Mateo, CA, 1989.

[6]. D. E. Goldberg, "Sizing population for serial and parallel genetic algorithm," *Proceedings of the third International Conference on Genetic Algorithm*, pp. 70-79, Morgan Kaufmann , San Mateo, CA, 1989.

[7]. L. Davis, "Adapting operator probabilities in genetic algorithm," *Proceedings of the third International Conference on Genetic Algorithm*, pp. 61-69, Morgan Kaufmann , San Mateo, CA, 1989.

[8]. T. Back, "Optimal mutation rates in genetic search," *Proceedings of the fifth International Conference on Genetic Algorithm*, pp. 2-8, Morgan Kaufmann , San Mateo, CA, 1993.

[9]. D. M. Tate and A. E. Smith, "Expected allele coverage and role of mutation in genetic algorithm," *Proceedings of the fifth International Conference on Genetic Algorithm*, pp. 31-37, Morgan Kaufmann , San Mateo, CA, 1993.

[10]. R. L. Haupt, "Phase-only adaptive nulling with a genetic algorithm," *IEEE Trans. Antenna Propagat.*, vol. AP-45, pp. 1009-1015, June 1997.

[11]. Y. C. Chung, "Amplitude and phase adaptive nulling with a genetic algorithm," in *USNC/URSI Radio Science Meeting 1998 digest.*, pp. 225, June 1998, Atlanta, GA..

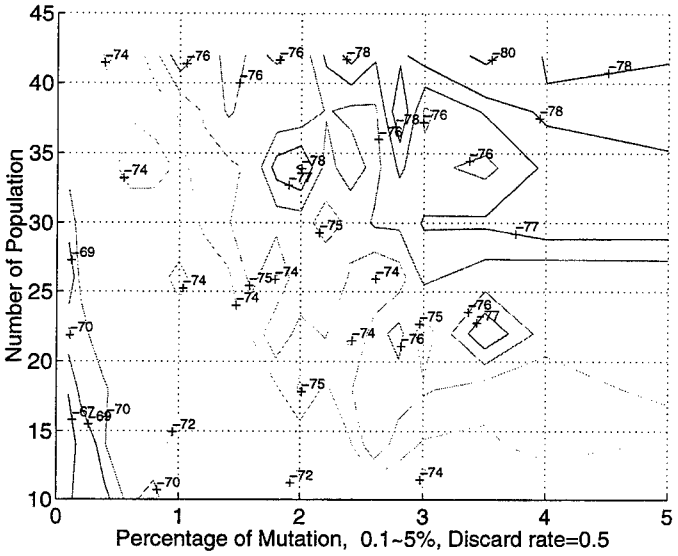

Fig. 3. Null dB vs. population and mutation by phase-only adaptive nulling with a GA.

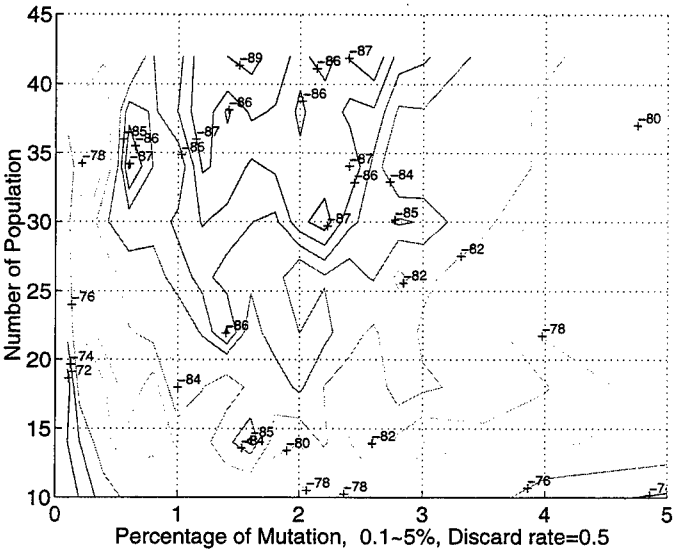

Fig. 4. Null dB vs. population and mutation by amplitude and phase adaptive nulling with a GA.

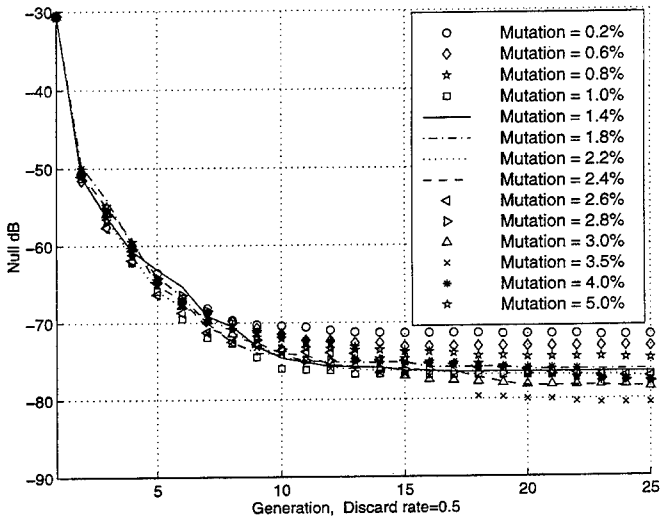

Fig. 5. Phase-only null dB vs. mutation rate at 42 population.

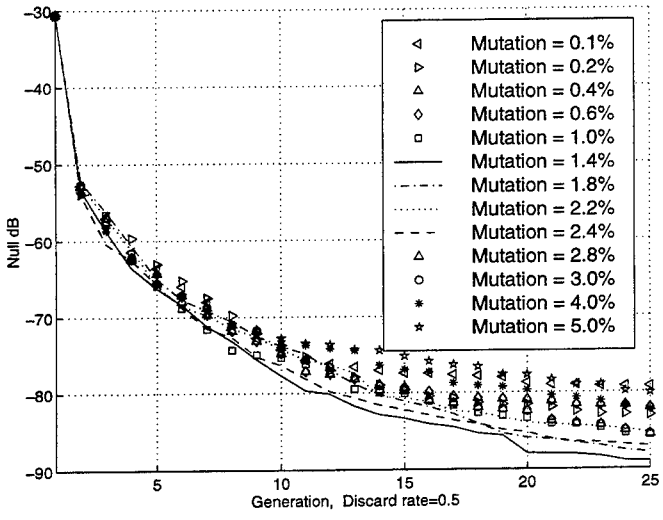

Fig. 6. Amplitude & phase null dB vs. mutation rate with 42 population.

Mutual Coupling Compensation for Circular Arrays using a Genetic Algorithm

Beng-Kiong Yeo and Yilong Lu†
School of Electrical and Electronic Engineering
Nanyang Technological University
Singapore 639798
(† Corresponding author, eylu@ntu.edu.sg, http://www.ntu.edu.sg/home/eylu)

***Abstract*— Mutual coupling among array elements would invariably distort the desired pattern shape of an array designed with ideal elements. A genetic algorithm (GA) is proposed to compensate for the mutual coupling effects in array antenna design. In this study, the Numerical Electromagnetic Code (NEC) is worked together with the GA optimizer that employs no binary coding and decoding. Near-solutions from other analytic or heuristic techniques may be injected into the initial population to speed up convergence. Numerical examples of circular arrays are presented to show the effectiveness of the approach.**

I. Introduction

The gain of an array is inextricably related to the gain of its individual elements [1]. However, the gain of an isolated element may be very different from that of the same element in the presence of the rest of the array. In addition, the element patterns and gain vary across the array with the elements near the edge behaving quite unlike those near the center. This behavior is due to the electromagnetic coupling among elements. It can result in more or less element gain in the array environment than when isolated.

Many iterative algorithms exist to combat the mutual coupling effects and numerous studies have been conducted to understand its effects [2]-[6]. In any finite array, the designated currents and fields differ from element to element in magnitude, phase and distribution. These differences vary as a function of frequency and array beam scanning angle. In practice, this complex interaction can be evaluated by writing the radiated field from all elements as generalized integrals that include current distributions over the surface of radiating elements and nearby diffracting bodies, such as through the use of Numerical Electromagnetic Code (NEC).

The NEC program is embedded, as part of the GA loop, within the fitness evaluation function which provides it with the relevant NEC codes to simulate the realistic impedance and pattern formation. From the NEC output, the evaluation function may then proceed to determine the fitness level of a candidate pattern. In the following sections, the results for mutual coupling compensation (MCC) using the EMS-GA [7] are elaborated.

II. Problem Formulation

For an arbitrary array, its array factor, AF, can be expressed by

$$AF = \mathbf{w}^T \mathbf{S}(\phi, \phi_m) \tag{1}$$

where

$$\mathbf{w} = \{w_1, w_2, \ldots, w_N\}^T, w_n \in C^n, \tag{2}$$

is the weighting vector, $\mathbf{S}$ is the steering vector, ϕ and ϕ_m are the direction variable and main beam direction, respectively. C^n is the set or a subset of all complex numbers.

Take for example, a circular array of N identical elements, the steering vector is

$$\mathbf{S}(\phi, \phi_m) = \exp\{jka * [\cos(\phi - \phi_n) - \cos(\phi_m - \phi_n)]\}, \tag{3}$$

where a is the radius of the circular array, $\phi_n = 2\pi n/N$, ϕ_m is the main beam pointing direction, and ϕ is the azimuth angle, provided the elevation is fixed at 90°. The same set of optimum weights for the main beam at a particular direction can be used for other directions, if the above $\mathbf{S}$ vector is recalculated for the new beam pointing direction. Thereafter any near-solution can be planted into the initial population, and the EMS-GA is applied to correct the sidelobe level (SLL) and main beam shape of the pattern, while taking mutual coupling into consideration.

III. The Genetic Algorithm

Based on natural evolution [8], genetic algorithms capitalize on tools that work well in nature. A mathematical treatment on GA's foundations is provided in [9], while numerous contemporary GA applications can be found in [10]. Living beings are encoded by chromosomes, one may encodes the possible solutions in the form of data structures with GAs.

A. Chromosome Structure

Most GAs use binary coding and binary genetic operations [11]. The proposed approach however applies floating-point genetic operations on complex array weighting vectors. Hence, each chromosome is a vector of complex numbers and the dimension of the vector is equivalent to the number of array elements.

B. Initial Population

An initial population of at least 100 random chromosomes is generated. The constrained adaptive algorithm in [12] is employed to produce a near-solution, $w^{(C)}$, with the elevation angle set to 90°, to replace the weakest individual among the initial population. Its insertion helps to improve the rate of convergence.

C. Reproduction

Rank-based fitness assignment sorts the individuals in a descending order of fitness for the k^{th} generation, G_k population of P individuals. Linear crossover is performed, where two parents produce two children. The selection method uses *Emperor-Selective* (EMS), where the best individual in G_k gets to mate with every other even sample in the population. It allows the fittest individual to procreate freely with practically the rest of the population.

D. Survival Selection

EMS works on G_k to produce $cPop$, which is the child population after mating and crossover. Concurrently, a non-uniform multi-modal mutation operator is applied to a population $mPop1$ which comprises of $X(X \leq P)$ copies of the fittest individual prior to the mating operation above. The Gaussian distribution parameter S, which is inversely proportional to the size of mutational changes introduced, is adaptively increased once stagnated growth due to premature convergence is detected. The same mutation operator is performed across a copy of the original population G_k, giving $mPop2$, the mutated child population based on P_m, the mutation probability which is usually greater than 0.04.

Unlike [7], only the best $Y(Y \leq P)$ individuals from $mPop1$ and $mPop2$ are selected to produce $tPop$, the population of best individuals produced through unary transformation.

Finally, the new set of P individuals that forms the next generation, G_{k+1}, are those from the best of $cPop$ and $tPop$.

E. Fitness Evaluation

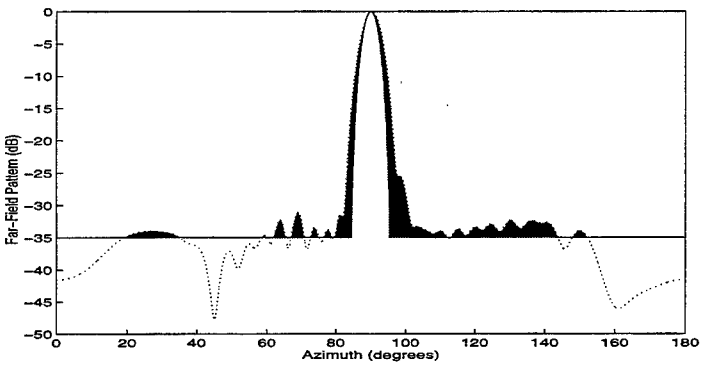

Fig. 1. Template cast over each decoded pattern to evaluate its fitness.

A template, formed by the shape of the main lobe and the specified SLL, is casted over the array pattern produced by each candidate, as shown in Fig. 1, to compute their cumulative difference as a form of fitness measure. Thus, the ideal array pattern is one that conforms to the original main beam shape with the specified SLL, as depicted in Fig. 1.

F. Termination Criteria

The maximum number of generations must be defined together with the desired fitness level. By satisfying either one of the above criteria, the GA will terminate.

IV. Simulation Results

A. Circular Array of 16 Vertical Dipoles

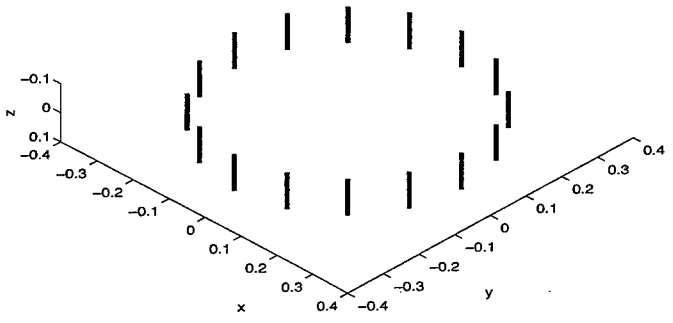

Fig. 2. A circular array of 16 vertical dipoles.

For ideal array pattern synthesis, the solution for the excitation coefficients can be obtained by the constrained adaptive algorithm [12]. An array beam obtained is shown by the dashed line in Fig. 3, with the elevation angle set to 90°.

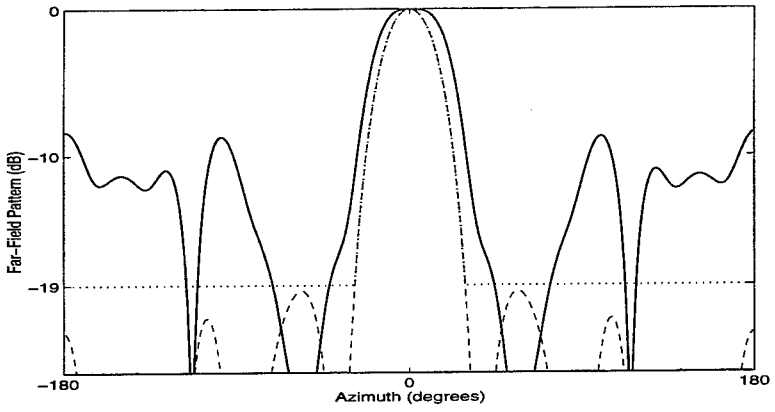

Fig. 3. Similarly, the original pattern (dashed line) becomes deformed (solid line) when mutual coupling is taken into consideration.

Once mutual coupling is considered after running the NEC simulation, the pattern designed with ideal weights is severely deformed as depicted by the solid line in Fig. 3. In this example, SLL changed from the original -19.38

dB to −8.3 dB. The template (dotted line) is set to produce a corrected pattern of −19 dB SLL. The normalized excitation coefficients are tabulated in Table I as shown below, while the fitness progress is plotted in Fig. 4.

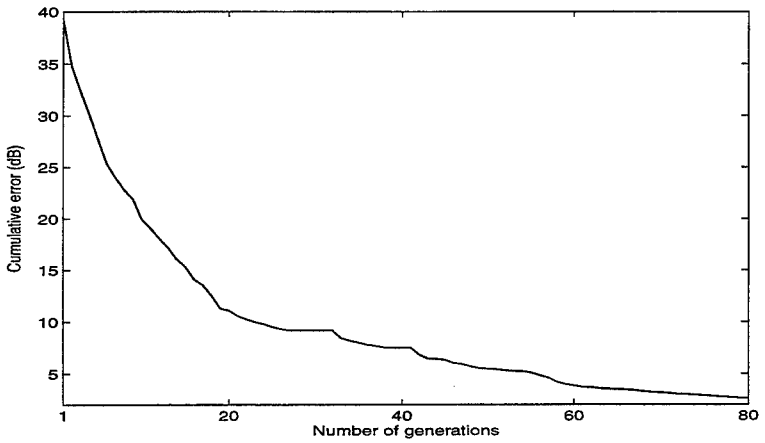

Fig. 4. Fitness progress chart obtained after averaging the results from 30 runs.

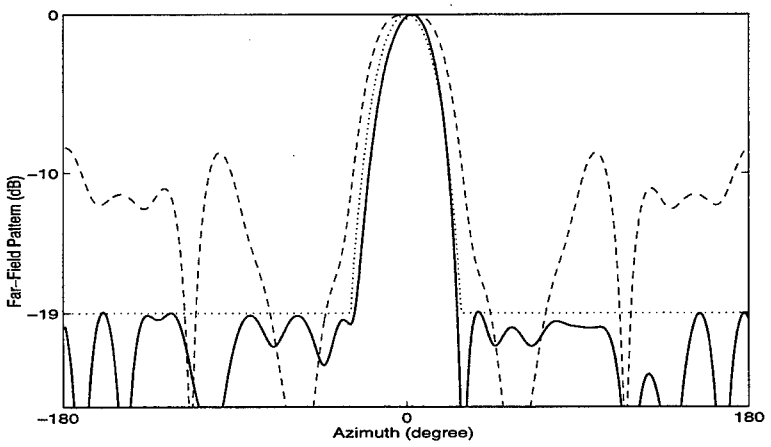

Fig. 5. The deformed pattern (dashed line) and the corrected pattern (solid line).

After an average of 73 generations, the corrected pattern is obtained. Fig. 5 shows the deformed pattern (dashed line) and the corrected pattern and (solid line). The SLL is recovered to −19 dB.

TABLE I
Normalised circular array excitation coefficients for compensated power pattern by the GA

Element Number	Original Weights Without Considering Mutual Coupling	Compensated Weights Considering Mutual Coupling
1.	0.01581695 +0.01154566j	0.00210863 +0.01281295j
2.	0.01806623 +0.01385511j	0.01026920 +0.00972533j
3.	0.01823458 -0.01058734j	0.02178864 -0.00621535j
4.	0.00555620 +0.00417207j	-0.00267502 -0.00622833j
5.	-0.01672706 +0.00000000j	-0.01049456 +0.01226553j
6.	0.00555620 -0.00417207j	-0.00628700 -0.01480830j
7.	0.01823458 +0.01058734j	0.01766233 +0.01615022j
8.	0.01806623 -0.01385511j	0.03292289 -0.00831566j
9.	0.01581695 -0.01154566j	0.00850921 -0.02939043j
10.	0.01806623 -0.01385511j	0.02530808 -0.00313775j
11.	0.01823458 +0.01058734j	0.01971566 +0.00929316j
12.	0.00555620 -0.00417207j	-0.00585220 -0.01205474j
13.	-0.01672706 +0.00000000j	-0.00787380 +0.00133553j
14.	0.00555620 +0.00417207j	-0.01053157+ 0.00263694j
15.	0.01823458 -0.01058734j	0.01740513 -0.00225400j
16.	0.01806623 +0.01385511j	0.00983548 +0.00177143j

V. Conclusions

The proposed mutual coupling compensation approach can be applied to any other array, since its operation is independent of the array configuration. However by using this approach, the algorithm can reduce the SLL, and at the same time, reshape the beam to any desired pattern by simply altering the shape of the ideal template.

References

[1] R. S. Elliot, *Antenna Theory and Design*, Prentice-Hall, 1981.

[2] A. J. Weiss and B. Friedlander, "Mutual coupling effects on phase-only direction finding," *IEEE Trans. Antennas Propag.*, vol.40, pp.535-541 May 1992.

[3] S. Basu and A. Chakraborty, "Study of mutual coupling effect in array of dipole radiators generating different beam shapes," *Proc. 1991 IEEE AP-S International Symposium*, pp.1736-1739, 1991.

[4] G. P. Junker, A. W. Glisson and A. A. Kishk, "Mutual coupling effects and radiation characteristics of a linear array of dielectric resonator elements fed by coaxial probes," *Proc. 1995 IEEE AP-S International Symposium*, pp.1998-2001, 1995.

[5] K. C. Lee and T. Chu, "Circuit model for antenna array mutual coupling effects," *Proc. 1995 IEEE AP-S International Symposium*, pp.946-949, 1995.

[6] L. J. du Toit, "Using a small array to optimize dipole match in the presence of mutual coupling," *Proc. 1995 IEEE AP-S International Symposium*, pp.926-929, 1995.

[7] B. K. Yeo and Y. Lu, "Array failure correction with a genetic algorithm", *Proc. 14th Annual Review of Progress in Applied Computational Electromagnetics Symposium*, pp.1087-1094, 1998.

[8] J. H. Holland, *Adaptation in Natural and Artificial Systems*, The University of Michigan Press, 1975.

[9] D. Whitley, *Foundations of Genetic Algorithms II*, Morgan Kaufmann Publishers, 1993.

[10] L. Chambers, *Practical Handbook of Genetic Algorithms: Applications*, CRC Press, vol.1, pp45-46, 1995.

[11] L. Davis (Ed), *Handbook of Genetic Algorithms* Van Nostrand Reinhold, 1991.

[12] K. K. Yan, *Study and Design of Circular Phased Array Antenna for Surveillance Radar* M.Eng Thesis, Nanyang Technological University, Singapore, 1996.

Pareto Genetic Algorithm Based Optimization of Log-Periodic Monopole Arrays Mounted on Realistic Platforms

D. S. Weile[†*], S. E. Fisher[†], E. Michielssen[†], and W. Woody[††]
[†]Department of Electrical and Computer Engineering
Center for Computational Electromagnetics
University of Illinois at Urbana-Champaign
Urbana, IL 61801

[††] Lockheed Martin TDS
1300 S. Litchfield Rd.
Goodyear, AZ 85338

Abstract

A three-objective Pareto genetic algorithm is applied to the design of practical impedance modulated feeds for log-periodic monopole arrays. Specifically, the arrays are designed to have a given radiation pattern while at the same time minimizing both the feed reflection coefficient and the amount of energy coupled into the array that does not get radiated. The use of a Pareto GA allows for a study of the tradeoffs between these three goals, and results in a database of designs representing optimal combinations among them. Numerical results illustrating the design of an array mounted on an airplane wing illustrate the optimization process. These results are compared to designs resulting from more traditional optimization methods (a simple genetic algorithm and the simplex method) and are shown superior in all respects.

1 Introduction

Since their invention in the 1960's, the log-periodic monopole array (LPMA) has become a popular antenna because it is easy to construct and has nearly frequency-independent radiation characteristics. LPMAs are usually mounted on very large ground planes so that they may be designed using image theory and log-periodic dipole array (LPDA) synthesis techniques [1, 2]. The assumption of a large ground plane thus makes standard LPMA design methods inapplicable to the design of arrays mounted on more complex structures, such as the airplane wing model shown in Figure 1. Mounting an LPMA on a complex, finite platform can degrade the antenna's performance in three ways:

- The array pattern can be altered due to the presence of the platform.
- The arbitrary structure of the platform may result in highly reflective feeds.
- The truncation of the array may lead to excessive power consumption in the terminating load of the feed.

This study will demonstrate that a redesign of the classical, impedance modulated LPMA feed [3] suffices to ameliorate these problems. This redesign is accomplished using a Pareto genetic

algorithm (PGA) designed to contemporaneously minimize the three above-listed deleterious effects of mounting the LPMA on a finite platform. In so doing, the work presented here illustrates not only the power of the PGA applied to electromagnetic design problems, but also that the design of an operating LPMA mounted on a less than ideal platform can be accomplished through the redesign of the feed alone.

Like the simple genetic algorithm (SGA), the PGA is an optimization algorithm based on the principles of natural selection discovered by Charles Darwin. Because it is derived from the SGA, the PGA retains the multifarious appealing properties of evolutionary optimization (e.g. robustness in avoidance of local optima, simplicity of coding, ability to work without gradient information, etc.). Unlike the SGA, however, the PGA does not converge to a single (supposedly) global optimum, but to a set of optima representing tradeoffs between the various design goals. Moreover, since such a result implies a more thorough search of the design space, the PGA often results in better designs for any single goal than an SGA provides for the same goal.

2 Formulation

In this section, the design of an LPMA feed using a Pareto GA is described. Section 2.1 discusses the optimization problem in general by describing the feed topology, optimization parameters, and analysis method. Section 2.2 then describes Pareto optimization and the PGA.

2.1 Log-Periodic Monopole Arrays

Because of its self-similar nature, a standard LPMA (Figure 2) consisting of N monopoles can be described fully with only three parameters. If the length of the n^{th} monopole in the array is denoted by l_n^e, the constant parameter τ describes the ratio between the lengths of adjacent elements as

$$\tau = \frac{l_{n+1}^e}{l_n^e}. \tag{1}$$

Similarly, the spacing between elements n and n+1 is related to l_n^e by a constant parameter

$$4\sigma = \frac{d_n}{l_n^e}. \tag{2}$$

Coupling these parameters with the length of one of the elements is sufficient for a complete description of the radiating structure of the LPMA. Because this study seeks to illustrate that no redesign of LPMA itself is required to ensure its proper operation, the geometric progression of element lengths and interelement spacing is given by equations (1) and (2) exactly.

The description of the impedance-modulated feed (Figure 3) is considerably more complicated. The feed network is connected to a source with impedance Z_{SRC} near the smallest monopole, and is terminated in a load impedance Z_L near the largest monopole. Surrounding each monopole n are two sections of transmission line of impedance Z_M^n and length l_n^M referred to as modulated lines. Between these modulated pieces of line (and before and after the first and last modulated lines) are transmission lines of impedance Z_0 and length l_n^0. (Because there are N+1 of

these non-modulated lines, l_n^0 is the length of line before monopole n+1, with l_{N+1}^0 denoting the length of line between the last modulated line and before the load impedance.) The PGA described in the next section will design the feed by fixing all of these values. Specifically, the impedance values are chosen from a database of readily available components, but the lengths of line allowed are allowed to vary continuously.

Like all optimization algorithms, the PGA requires some rating of the worth of a given design to operate. Unlike more standard algorithms, however, the PGA can simultaneously optimize many several functions of the feed parameters to determine optimal tradeoffs between them. In the case of LPMA design, the minimization of three quantities is sought: a weighted mean-square difference between the field provided by a given feed and an ideal feed (Δ), the maximum feed reflection coefficient over the band of operation (Γ), and the percentage of energy coupled into antenna that is dissipated by the load (Ξ). Thus, Pareto optimization can be seen as a vector optimization criterion, operating on the "goal vector" $[\Delta,\Gamma,\Xi]$.

Because the external radiating structure (i.e. the monopoles themselves and their platform) does not change during the course of the optimization, the analysis can be done in two steps. Before the optimization begins, the structure is analyzed using the method of Moments (MoM). Specifically, for several test frequencies ω_k $(k=1,\ldots,N_f)$ in the band of interest, the MoM is used to extract the $N\times N$ admittance matrix $\mathbf{Y}_k^{ant}$ of the N element array. Furthermore, the far field $\mathbf{F}_{k,n}(\theta_i,\phi_i)$ radiated by unit excitation of monopole n in the direction (θ_i,ϕ_i), $i=1,\ldots,N_{angle}$, and frequency k, of interest can be stored so that superposition can be used to find the field radiated by the element excitations established by an arbitrary feed.

Given this information, the evaluation of the feed network can be accomplished very simply. Using standard transmission-line theory, $\mathbf{Y}_k^{feed}$, the $(N+1)\times(N+1)$ admittance matrix of the feed describing the interaction of the single source port with the N antenna ports can be extracted. Denoting the voltage and current vectors for the N antenna ports by $\mathbf{V}_k^{ant}$ and $\mathbf{I}_k^{ant}$, and the current and voltage at the source port by V_k^s and I_k^s, the current and voltage at each of the ports can be related by the equations

$$\mathbf{I}_k^{ant}=\mathbf{Y}_k^{ant}\mathbf{V}_k^{ant}$$

$$\begin{bmatrix} I_k^s \\ -\mathbf{I}_k^{ant} \end{bmatrix}=\left[\begin{array}{c|c} Y_{k,ss}^{feed} & \mathbf{Y}_{k,sa}^{feed} \\ \hline \mathbf{Y}_{k,as}^{feed} & \mathbf{Y}_{k,aa}^{feed} \end{array}\right]\begin{bmatrix} V_k^s \\ \mathbf{V}_k^{ant} \end{bmatrix} \tag{3}$$

as the feed network is directly connected to the antennas. (The matrix in (3) has been partitioned to separate out the source interaction.) These partitioned matrix equations may be solved for the input admittance

$$Y_{k,in}=Y_{k,ss}^{feed}-\mathbf{Y}_{k,sa}^{feed}\left(\mathbf{Y}_k^{ant}+\mathbf{Y}_{k,aa}^{feed}\right)^{-1}\mathbf{Y}_{k,as}^{feed} \tag{4}$$

and the voltage at each antenna terminal

$$\mathbf{V}_k^{ant} = \begin{bmatrix} V_{k,1} \\ \vdots \\ V_{k,N} \end{bmatrix} = -\left(\mathbf{Y}_k^{ant} + \mathbf{Y}_{k,aa}^{feed}\right)^{-1} \mathbf{Y}_{k,as}^{feed}. \tag{5}$$

The field strength $F_k(\theta_i,\phi_i)$ computed at frequency k and angle (θ_i,ϕ_i) for a given feed is then given by

$$F_k(\theta_i,\phi_i) = 20\log\left\|\sum_{m=1}^{N} V_{k,m}\mathbf{F}_{k,m}(\theta_i,\phi_i)\right\|. \tag{6}$$

Then, Δ is defined by

$$\Delta = \sum_{k=1}^{N_{freq}}\sum_{i=1}^{N_{angles}}\left|F_k(\theta_i,\phi_i) - F_k^{ideal}(\theta_i,\phi_i)\right| W_k(\theta_i,\phi_i), \tag{7}$$

where $F_k^{ideal}(\theta_i,\phi_i)$ and $W_k(\theta_i,\phi_i)$ are the desired far-field amplitude and the weight assigned to the i^{th} angular direction at the k^{th} frequency, respectively. The weights $W_k(\theta_i,\phi_i)$ can be chosen so that the resulting values of Δ range between 0 and 1. Additionally, the reflection coefficient magnitude and inefficiency at frequency k are given by

$$\Gamma_k = \left|\frac{1 - Z_{SRC}Y_{k,in}}{1 + Z_{SRC}Y_{k,in}}\right| \tag{8}$$

and

$$\Xi_k = 1 - \frac{\mathrm{Re}\left\{\left(\mathbf{Y}_{k,as}^{feed}\right)^*\left[\left(\mathbf{Y}_k^{ant} + \mathbf{Y}_{k,as}^{feed}\right)^{-1}\right]^*\left(\mathbf{Y}_k^{ant}\right)^*\left(\mathbf{Y}_k^{ant} + \mathbf{Y}_{k,as}^{feed}\right)^{-1}\mathbf{Y}_{k,as}^{feed}\right\}}{\mathrm{Re}\left\{Y_{k,in}\right\}}, \tag{9}$$

where the asterisk denotes the complex conjugate transpose operation. Finally, the feed reflection coefficient magnitude and feed inefficiency are given by

$$\begin{aligned} \Gamma &= \max_{1\le k\le N_{freq}}\left(\Gamma_k\right) \\ \Xi &= \max_{1\le k\le N_{freq}}\left(\Xi_k\right). \end{aligned} \tag{10}$$

Derivation of these expressions can be found in [4].

2.2 The Pareto Genetic Algorithm

In the previous section, three minimization goals were discussed in the context of LPMA design. The PGA is an algorithm that searches for all optimal combinations of these goals. Before describing the PGA, therefore, a definition of optimality with respect to more than one goal is needed. Such a definition is embodied in the concept of *Pareto optimality*, which is described next.

Consider two LPMA designs a and b with goal vectors given by $[\Delta_a,\Gamma_a,\Xi_a]$ and $[\Delta_b,\Gamma_b,\Xi_b]$, respectively. Design a is said to *dominate* design b if $\Delta_a \le \Delta_b$, $\Gamma_a \le \Gamma_b$, and $\Xi_a \le \Xi_b$ with strict inequality holding in at least one of the three inequalities. A design is called *Pareto optimal* if it is not dominated by any other design in the search space, and the set of all such designs is called the *Pareto front*.

Despite their multiobjective optimization abilities, PGAs are very similar to SGAs. The two algorithms differ only in the implementation of the selection operator. For this reason, only the selection operator is described in detail here.

Like the SGA, the PGA begins with a random initialization of a population of N_P chromosomes. Each chromosome is composed of a string of bits that may be decoded to give all of the design parameters described in the previous section (see, for example, [5] for the decoding procedure). Once the population is initialized, the goal vector of each population is evaluated as described above.

After the population is evaluated, the selection operator is applied. The Pareto criterion poses two challenges to the PGA: To return the entire Pareto front, designs must be compared on the basis of their relative Pareto optimality, and at the same time the population's tendency to converge to a single design must be counteracted to produce an algorithm which returns a complete, diverse front.

To meet the first challenge, the Pareto ranking scheme of Fonseca and Fleming is used. Each population member is assigned a rank equal to the number of designs in the population that dominate it, plus one. Thus, all nondominated members of the population are assigned a rank of one, with the rest of the population having a higher rank.

To ensure populational diversity, the sharing operator is employed. Besides a Pareto rank, each member i of the population is assigned a *niche count* ρ_i which measures the number of similar designs surrounding it. Specifically, the distance d_i^j between chromosomes i and j is simply the Euclidean distance between their goal vectors considered as position vectors in 3-space. The niche count for chromosome i is then calculated as

$$\rho_i = \sum_{j=1}^{N_P} S\left(d_i^j\right) \tag{11}$$

where the sharing function S is defined as

$$S(d) = \max\left[1 - \left(\frac{d}{\sigma}\right)^E, 0\right] \tag{12}$$

where $\sigma > 0$ and E are user-defined parameters that determine the shape of the sharing function.

After niche counts and Pareto ranks are computed, each population member is assigned an objective function value as follows. Members of the first rank are given an arbitrary, identical, "pre-sharing" fitness value. To compute the fitness of a certain member i in the first rank, this value is then divided by ρ_i. The members of the second rank are then assigned a "pre-sharing" value equal to the lowest "post-sharing" value of the first rank members. The process then continues in this fashion until all members have been assigned a value.

Once the objective function values of the entire population are computed, the PGA continues as an SGA. Roulette-wheel selection, one-point crossover, and the usual mutation operator are used. The process is terminated after the Pareto front ceases to change.

3 Numerical Results

Using the PGA technique detailed above, an LPMA was designed for the wing model of Figure 1 with a band of operation ranging from 25 to 88 MHz. The LPMA structure consisted of eight monopoles, with $\tau = 0.850$, $\sigma = 0.096$, and $l_1^e = 3.125\,\mathrm{m}$. An ideal pattern was supplied in which most of the radiation was directed outboard from the wing at -30° elevation. The remaining PGA parameters were taken as $N_P = 10{,}000$, $\sigma = 0.08$, $E = 1.75$ and $N_f = 8$ with a crossover rate of 85% and a mutation rate of 0.5%. The specific frequencies used for optimization were 25.0, 30.0, 35.0, 45.0, 55.0, 65.0, 75.0, and 88.0 MHz. The PGA ran for 36 generations before converging.

In addition to optimizing the feed with the PGA, both the SGA and simplex methods were also used. Because neither of these methods is specifically tailored to Pareto optimization, both were run several times with objective functions corresponding to different linear combinations of the three goals. To ensure a fair comparison, both the SGA and the simplex method were allotted in total more than ten times the 36,000 function evaluations given the PGA. The Pareto fronts generated by the PGA and the SGA are shown in Figure 4. Notice that the front returned by the PGA dominates that returned by the SGA. The simplex method front was so completely dominated by the other two fronts that it does not even fit on the same graph.

As a further demonstration of the superiority of the PGA method, Figure 5 compares the voltage standing wave ratios (VSWRs) of designs selected from the front returned by each of the three methods. The designs compared in Figure 5 are the lowest reflection designs from the fronts returned by the SGA and the simplex method, and a design chosen from the PGA curve which dominates these designs. Figure 6 shows the patterns of the three designs at 55 MHz. Note that the PGA design has the lowest backlobe. More data will be presented at the talk to further compare the three methods.

4 Conclusions

A PGA-based method for the design of feeding networks for LPMAs mounted on arbitrary bodies was outlined. Given the LPMA geometry and the parameters of the body on which the LPMA was mounted, the presented method returns a good approximation to the Pareto front consisting of optimal tradeoffs between pattern shape, reflection coefficient and feed efficiency. The algorithm was greatly accelerated by the precomputation of the LPMA admittance matrix, and the field radiated by each monopole excited by a unit voltage. Results of the application of the PGA technique were compared to results returned by an SGA and the simplex method that demonstrated the PGA to be a more accurate and faster method of Pareto optimization.

5 References

[1] E. Huddock, "Near-field investigation of uniformly periodic monopole arrays," . Urbana-Champaign, IL: University of Illinois, 1963.

[2] P. E. Mayes, G. A. Deschamps, and W. T. Patton, "Backward wave radiation from periodic structures and application to the design of frequency independent antennas," *Proceedings of the IRE*, vol. 49, pp. 962-963, 1961.

[3] P. G. Ingerson and P. E. Mayes, "Log-periodic antennas with modulated impedance," *IEEE Transactions on Antennas and Propagation*, vol. 16, pp. 633-642, 1968.

[4] S. E. Fisher, D. S. Weile, E. Michielssen, and W. Woody, "Pareto genetic algorithm based optimization of log-periodic monopole arrays mounted on realistic platforms," *Journal of Electromagnetic Waves and Applications*, vol. (submitted), 1998.

[5] D. S. Weile and E. Michielssen, "Genetic algorithm optimization applied to electromagnetics: A review," *IEEE Transactions on Antennas and Propagation*, vol. 45, pp. 343-353, 1997.

Figures

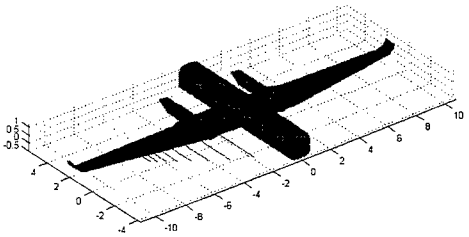

Figure 1. Log-periodic monopole array mounted on a wing.

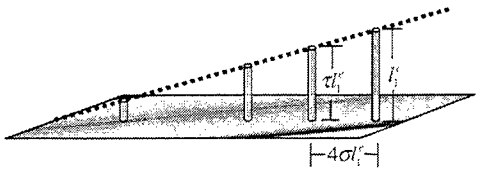

Figure 2. Standard LPMA mounted on an infinite ground plane, illustrating geometric parameters.

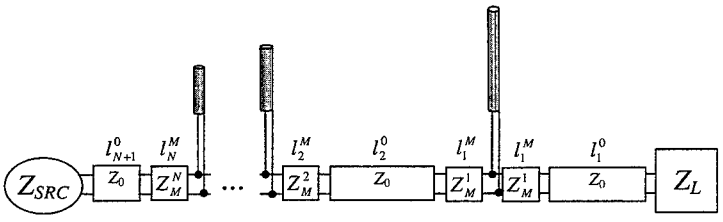

Figure 3. Impedance-modulated feed for an LPMA

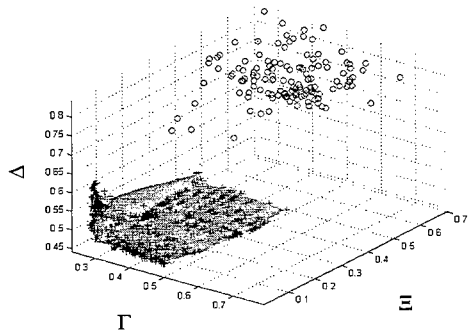

Figure 4. The PGA front (shown with crosses and interpolated surface) and the dominated iterated front(shown with circles).

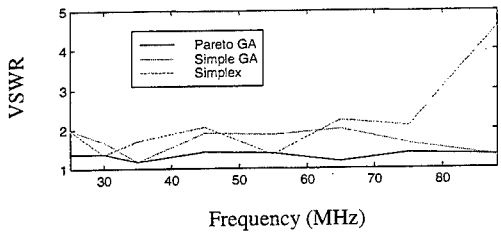

Figure 5. Comparison of the reflection performance of three feeds designed by the PGA, the SGA and the simplex methods.

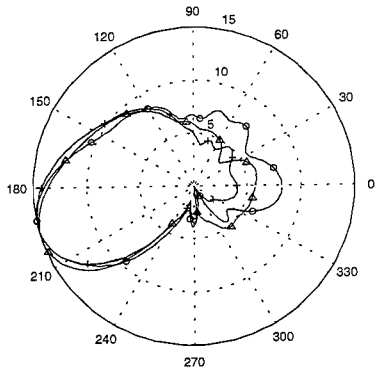

Figure 6. Comparison of the patterns of the three feeds at 55 MHz. The simplex feed is illustrated with circles, the SGA feed with triangles and the PGA feed with crosses.

Optimum Design of Non-Uniform Luneburg Lens Antennas: Genetic Algorithms with Adaptive Cost Function

H. Mosallaei and Y. Rahmat-Samii
Department of Electrical Engineering
University of California, Los Angeles
Los Angeles, CA 90095-1594
E-mail: rahmat@ee.ucla.edu

Abstract

In this paper, a novel optimization procedure for designing Luneburg lens antennas is presented. One of the important engineering objectives of designing an optimal Luneburg lens antennas is to use as small number of shells as possible while maintaining an acceptable gain and sidelobe performance. In a typical uniform design, by reducing the number of shells, the gain is decreased and the grating lobes are increased. This deficiency in the radiation performance of the uniform lens antenna can be overcomed by designing the non-uniform lens antenna. This necessitates the optimum selection of each layers thickness and permitivity. A Genetic Algorithm (GA) optimizer with adaptive cost function is implemented to obtain the optimal design. In this manner the GA optimizer simultaneously determines the optimal material and its thickness for each shell by controlling the gain and sidelobe envelope of the radiation pattern. The results have been satisfactory and demonstrate the utility of the GA/adaptive-cost-function algorithm. In this work, various lens geometries are analyzed by using the dyadic Green's function of the multi-layered dielectric sphere.

I. Introduction

For beam scanning at millimeter wave frequencies in mobile and satellite communication systems, there has been some interest in using radially symmetric lenses [1]. These types of lenses transform the feed's spherical radiation pattern to a plane wave [2]. Among various lenses, the Luneburg lens has received much attention. Since the mathematical design principal of lens antennas is based on the geometrical optics concept, a lens antenna can typically operate in a broad frequency band. On the other hand, spherical symmetry of the lens allows for multi-beam scanning usage by placing an array of feeds around it. While both radially symmetric lenses and phased array antennas can be used for beam scanning, the latter has narrower frequency bandwidth.

An ideal Luneburg lens consists of a dielectric sphere with varying permitivity ranging from 2 at the center to 1 at the surface. In practice, the Luneburg lens antenna is constructed as a multi-layered symmetrical lens that focuses the feed energy efficiently. However, to achieve the required high performance characteristics, a large number of shells may be required. By decreasing the number of shells, the directivity is decreased and substantially high levels of unwanted grating lobes are generated. This deficiency in the radiation performance of the lens can be improved by designing a non-uniform lens to overcome the grating lobe generations. The main question is as how to choose the optimum width and dielectric constant for a lens with reduced number of shell layers.

This paper focuses on the optimum synthesis of Luneburg lens antennas using the genetic algorithm (GA) optimizer. Since it is desired to simultaneously control the achievable gain with reduced grating lobe level structure, an adaptive cost function is used in the process of GA optimization. To determine the scattered field of the lens antenna, an analytic technique [3] is used based on the dyadic Green's function of the multi-layered spherical shell. The main features of this paper in designing the non-uniform lens antenna are summarized in the following:

- Applying the construction of the spherical vector wave solution
- Integrating the genetic algorithm optimizer with the vector wave solution processes
- Defining a suitable adaptive cost function based on both the gain and sidelobe envelop
- Presenting representative non-uniform Luneburg designs
- Discussing some of the engineering aspects and features of the results obtained

In the following section, the formulation of the underlying electromagnetic problem is presented. In Section III, some unique characteristics of the uniform Luneburg lens antenna are described. In Section IV, a non-uniform lens antenna is optimized using the GA/adaptive-cost-function technique and some key aspects of this implementation are discussed.

II. Computation and Optimization Methodologies

A. Computation Technique

Solution of Maxwell's equation in a concentric dielectric sphere, as shown in Fig. 1, is determined by using the dyadic Green's function of a multi-layered dielectric sphere and the mode matching technique.

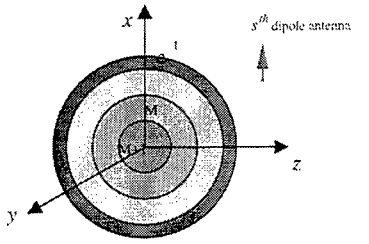

Fig. 1. Concentric dielectric sphere.

The total electric field in the presence of dielectric sphere can be written as

$$\mathbf{E}(\mathbf{r}) = \mathbf{E}^i(\mathbf{r}) + \mathbf{E}^s(\mathbf{r}) = \int_V \overline{\mathbf{G}}_e(\mathbf{r},\mathbf{r}') \cdot [-j\omega\mu_1 \mathbf{J}(\mathbf{r}')] dv' \qquad (1)$$

where $\overline{\mathbf{G}}_e(\mathbf{r},\mathbf{r}')$ is the dyadic Green's function responding to an infinitesimal dipole, $\mathbf{J}$ is the current density of the source, μ_1 is the permitivity of region 1 containing the current source, and $\mathbf{E}^i$ and $\mathbf{E}^s$ are the incident and scattered fields, respectively.

The scattered electric field $\mathbf{E}^s$ due to the arbitrary located infinitesimal dipole $Il\hat{p}$, in the i^{th} region is expressed as

$$\mathbf{E}^{s}_{(i)}(\mathbf{r}) = -\left(\frac{\omega\mu_1 Il}{4\pi}\cdot k_1\right)\sum_{n=1}^{\infty}\sum_{m=0}^{n}(2-\delta_{m0})\frac{(2n+1)(n-m)!}{n(n+1)(n+m)!}\cdot \tag{2}$$
$$\left\{\begin{aligned}&\left(A_{ni}\mathbf{M}^{(4)}_{e_o mn}(k_i)+C_{ni}\mathbf{M}^{(1)}_{e_o mn}(k_i)\right)\cdot\left(\mathbf{M}^{(4)'}_{e_o mn}(k_1)\cdot\hat{p}\right)\\+&\left(B_{ni}\mathbf{N}^{(4)}_{e_o mn}(k_i)+\mathbf{D}_{ni}\mathbf{N}^{(1)}_{e_o mn}(k_i)\right)\cdot\left(\mathbf{N}^{(4)'}_{e_o mn}(k_1)\cdot\hat{p}\right)\end{aligned}\right\}$$

where $\mathbf{M}$ and $\mathbf{N}$ are the spherical vector wave functions, and k_i and k_1 are the complex propagation constants in regions ith and 1, respectively. The unknown coefficients A_{ni}, B_{ni}, C_{ni}, and D_{ni} are determined by applying the boundary conditions at the dielectric interfaces. Based on this formulation and by using an accurate computer code developed in [3], the electromagnetic fields in all regions can be determined.

B. Implementation of the Genetic Algorithm with an Adaptive Cost Function

The genetic algorithms are iterative optimization procedures that start with a randomly selected population of potential solution, and gradually evolve toward better solution through the application of genetic operators that are selection, crossover, and mutation. GA methods are global optimizers and have some unique distinctions with respect to the local techniques such as conjugate-gradient and quasi-Newton methods. The local techniques are typically highly dependent on the starting point or initial guess, while global methods are largely independent of the initial starting point. Generally speaking, local techniques tend to be tightly coupled to the solution domain, resulting in relatively fast convergence to a local maximum. However, this tight solution-space coupling also places some constraints on the solution domain, such as differentiability and/or discontinuity that can be hard or even impossible to deal with in practice. The global techniques, on the other hand, are largely independent of the solution domain. Consequently, the GA method, being a global optimizer, could be an efficient technique for optimizing the new electromagnetic problems having discontinuities, constrained parameters, and a large number of dimensions with many local optima [4].

In the context of optimizing the radiation performance of the lens antenna with m spherical shells, the objective or fitness function F is defined by

$$F(\varepsilon_{r1}, t_1, \varepsilon_{r2}, t_2, ..., \varepsilon_{rm}, t_m) = \alpha\cdot G_0 + \beta\cdot Min[f(\theta) - G(\theta)]\big|_{sidelobe\ region} \tag{3}$$

where ε_{ri} and t_i represent the material choice for each shell and its thickness, respectively. $G(\theta)$ is the gain pattern of the lens antenna and G_0 is its maximum value. The cost function F attains the maximum gain with low sidelobe levels, for an optimum configuration. By a proper setting of parameters α, β, and the sidelobe envelop function $f(\theta)$, the gain and sidelobe levels can be controlled effectively.

In order to apply the GA method to the lens structure, material and thickness of each shell are represented in a binary code as

$$L_j = M_j T_j = \left[m_j^1 m_j^2 ... m_j^{N_{mb}}\right]\left[t_j^1 t_j^2 ... t_j^{N_{tb}}\right]. \tag{4}$$

The entire structure is subsequently represented by the sequence $G = L_1 L_2 ... L_m$. In the cases studied in this paper, $N_{mb} = N_{tb} = 10$ and a population with size $N_{pop} = 100$ is selected. For each case, EM fields and the cost function F are computed accurately. In the process of our GA implementation, crossover with $0.6 \le p_{cross} \le 0.9$ and mutation with $0.01 \le p_{mut} \le 0.1$ are used [5]-[7]. Additionally, in this design tournament selection and elitism are also employed.

III. Characteristics of Uniform Luneburg Lens Antennas

A Luneburg lens antenna transforms the point source radiation into the plane wave and vice versa. An ideal Luneburg lens consists of a spherically symmetric dielectric sphere with continuous varying permitivity from 2 at the center of inner core to the 1 at the outer edge, i.e., $\varepsilon_r = 2 - (r/a)^2$, where a is the radius of the sphere. In practice, however, the Luneburg lens is constructed by a finite number of spherical shells, retaining reasonable performance. Table. 1 shows the material and thickness for a 5-shell 30λ diameter uniform lens. In practice feed horns or open ended waveguides are used to illuminate the lens. In this paper, in order to model the radiation pattern of a typical horn antenna, an end-fire antenna consisting of four infinitesimal dipoles is used as shown in Fig. 2.

Table 1. 5-shell 30λ diameter Luneburg lens antenna. (Uniform Design)

Shell	ε_r	t/λ
1	1.18	3
2	1.50	3
3	1.74	3
4	1.90	3
5	1.98	3

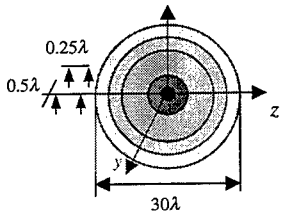

Fig. 2: 5-shell 30λ diameter Luneburg lens antenna.

For a Luneburg lens antenna with fixed diameter, the radiation performance is improved by increasing the number of shells, but the performance becomes saturated with $\approx 1\lambda$ thickness for each shell. Radiation pattern of a 10-shell 30λ diameter lens is shown in Fig. 3. As seen the gain is about 37.73 dB. Note that due to the existence of the periodic-like uniform shells, there are some grating lobes in the pattern occurring around $\theta \approx 30^\circ$. By decreasing the number of shells the thickness of each shell is increased and so the grating lobes are moved closer to the main beam, as seen for a 5-shell lens (see Fig. 3). In this case the gain of the lens is decreased to $36.46 dB$ and the grating lobes are occurred closer to the main beam, around $\theta = 17^\circ$.

From these plots, it is observed that a 10-shell 30λ lens antenna has superior performance. From the practical point of view, a 5-shell lens antenna has less number of shells and so its construction is easier. However, as mentioned earlier, due to the larger thickness of each shell, the grating lobes are occurred nearer to the main beam. The radiation performance of the 5-shell uniform Luneburg lens antenna can be improved by designing a non-uniform lens using the GA optimization method, as described in the next section.

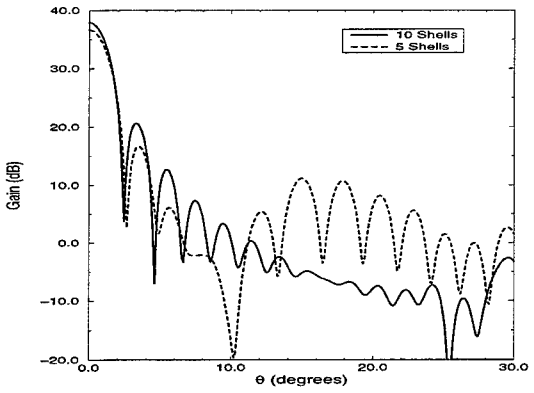

Fig. 3: Gain pattern of the 30λ Luneburg lens antenna in the $x-z$ plane. Note the appearance of the unwanted grating lobes.

IV. Design of Non-Uniform Lens

This section focuses on the key design aspects of a non-uniform Luneburg lens antenna using the genetic algorithm (GA). The goal is to determine the permitivity and thickness of each spherical shell for a 5-shell 30λ diameter lens antenna such that the maximum gain is achieved. However, besides maximizing the gain, the level of sidelobes should remain low. The problem then is to investigate the tradeoffs between these conflicting objectives.

In this study, the number of shells is $m=5$, and ε_{ri} is allowed to change between 1.0 to 2.0. For achieving the maximum directivity the parameters α and β are chosen 1 and 0, respectively. Fig. 4 shows a typical convergence curve for the GA method applying it to a 5-shell 30λ diameter non-uniform Luneburg lens antenna. The cost function F is the antenna gain G_0. As seen the GA method determines the optimum material and thickness for each spherical shell rapidly. Table 2 shows the optimum material and thickness for the lens antenna. Gain of the lens has been plotted in Fig. 5. It is observed that the gain is increased to $G_0 = 37.47\,dB$ and the grating lobe is decreased about $6.5\,dB$ with respect to the uniform design. However, the level of grating lobe is noticeably higher than the grating lobe level in a 10-shell uniform design. This grating lobe level can be further reduced by using the parameter β and function $f(\theta)$. As noted, the 10-shell 30λ lens has had a monotonically decaying sidelobes. Therefore, the function f is taken as the envelope of these sidelobes in the following form

$$f(\theta) = 12 - 38Log\left(\theta^{\circ}/5.8^{\circ}\right)(dB). \tag{5}$$

In this case a useful design is obtained by choosing $\alpha = 1, \beta = 0.5$. The goal is achieving the maximum gain while the level of sidelobes is also low, similar to a 10-shell lens. In order to create an adaptive cost function in the process of the GA optimization, in the first 20 generations the cost function F is taken as the antenna gain (i.e., $\beta = 0$). Next the effect of both gain and sidelobe level

together are used in the process of the optimization. This helps the optimization method to keep the antenna gain high while decreasing the sidelobe levels. The results are presented in Table 3 and Fig. 6. Note that the function f was chosen to control the sidelobe levels in the angular range $2.5^{\circ} \leq \theta \leq 25^{\circ}$ at 50 points. Fig. 6 shows that the gain is about $35.94\,dB$ and the grating lobes are decreased about $12\,dB$ with respect to the uniform design. The effectiveness of this adaptive optimization technique is shown in Fig. 7 by varying α and β in Eq. (3). It is observed that simultaneous application of α and β in the cost function provides the best result.

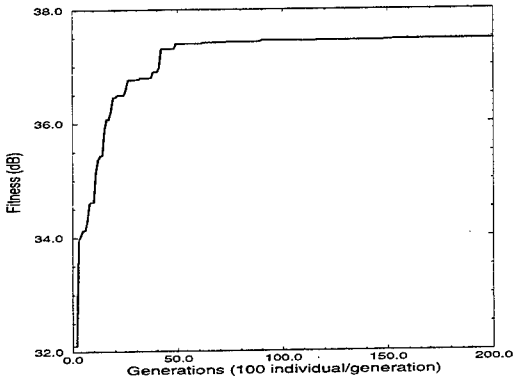

Fig. 4: Convergence curve of the GA method applied to the 5-shell 30λ diameter non-uniform lens. ($F = G_0$)

Table 2. Characteristics of a 5-shell 30λ diameter non-uniform Luneburg lens antenna. ($F = G_0$)

Shell	ε_r	t/λ
1	1.217	3.451
2	1.476	2.129
3	1.670	2.523
4	1.824	2.577
5	1.933	4.320

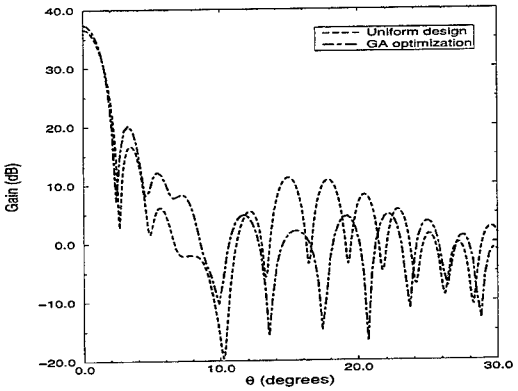

Fig. 5: Gain pattern of the 5-shell 30λ diameter non-uniform Luneburg lens antenna in the $x-z$ plane.

Table 3. Characteristics of a 5-shell 30λ diameter non-uniform Luneburg lens antenna.
$(F = G_0 + 0.5 \cdot Min[f(\theta) - G(\theta)]\big|_{sidelobe\ region})$

Shell	ε_r	t/λ
1	1.075	1.819
2	1.191	1.232
3	1.725	3.710
4	1.815	1.615
5	1.948	6.624

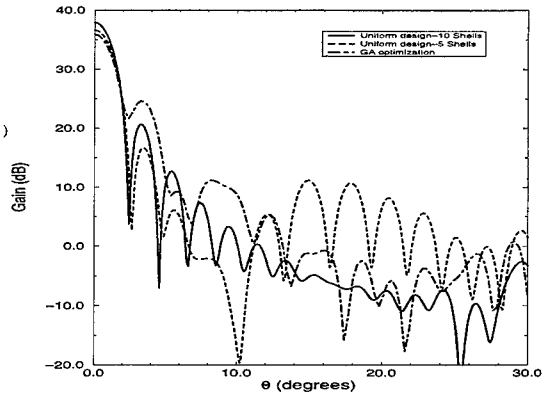

Fig. 6: Comparison between 10-shell and 5-shell uniform design with the 5-shell non-uniform optimized lens in the $x-z$ plane.
$(F = G_0 + 0.5 \cdot Min[f(\theta) - G(\theta)]\big|_{sidelobe\ region})$

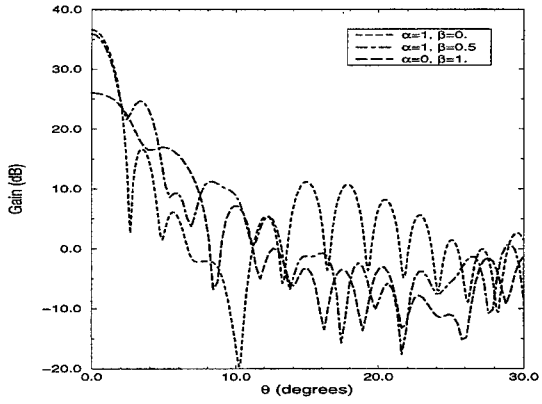

Fig. 7: Radiation performance of the 5-shell non-uniform optimized lens using various α and β in Eq. 3.

VI. Conclusions

In this paper, non-uniform Luneburg lens antennas are designed using the genetic algorithm optimization method. The multi-layered lens antenna is analyzed accurately using the dyadic Green's function and the mode matching technique. Since the genetic algorithm produces the global solution without requiring much information about the solution domain, it has been found to be a very efficient method for obtaining the optimum material and thickness for each spherical shell of the lens antenna. The radiation performance of the non-uniform lens was improved with respect to the uniform design efficiently. By choosing an appropriate cost function, the gain of the 5-shell 30λ lens was increased about $1dB$, and also its grating lobes decreased $6.5dB$ with respect to the uniform design. By optimizing the lens for both directivity and sidelobe level, the grating lobes decreased about $12dB$ with respect to the uniform design.

Although this paper described an optimization over a continuous parameter set, GA method is capable of optimizing the discrete structural parameters. This means that by using the GA method, the best material and thickness for the lens can be picked up among a finite set of materials in a database. By choosing the appropriate cost function, one can optimize the lens antenna based on the nature of the desired application. In addition, a Pareto GA's [8] may be used to further refine the design by creating a set of optimized solutions. In summary, the methodologies developed in this paper will allow efficient design of multi-layered lens antennas.

VII. References

[1] H. Shrank and J. R. Sanford, "A Luneburg Lens Update," *IEEE Antennas Propag. Magazine,* vol. 37, No.1, February 1995.

[2] R. K. Luneburg, *Mathematical Theory of Optics*, pp. 189-213, Brown University, Providence, Rhode Island, 1944; or pp. 182-187, University of California Press, Berkeley, 1964.

[3] K. W. Kim and Y. Rahmat-Samii, "Spherical Luneburg Lens Antennas: Engineering Characterizations including Air Gap Effects," *in Proc. IEEE-APS URSI Meet.*, Atlanta, 1998, pp. 2062-2065.

[4] Y. Rahmat-Samii and E. Michielssen, *Electromagnetic Optimization by Genetic Algorithms*, to published by John Wiley and Sons, 1999.

[5] J. M. Johnson and Y. Rahmat-Samii, "Genetic Algorithms in Engineering Electromagnetics," *IEEE Antennas and Propagation Magazine*, vol. 39, No. 4, pp. 7-21, Aug. 1997.

[6] R. L. Haupt, "Thinned Arrays using Genetic Algorithms," *IEEE Transactions on Antennas and Propagation*, Ap-42, 7, July 1994, pp. 993-999.

[7] D. L. Carroll, "Fortran Genetic Algorithm Driver," *University of Illinois at Urbana-Champaign*, 1997.

[8] D. S. Weile, and E. Michielssen, " Genetic Algorithm Optimization Applied to Electromagnetics: A Review," *IEEE Trans. Antennas Propag.*, vol. 45, No. 3, pp. 343-353, March. 1997.

On the Search for the Optimal Grouping of Basis Functions

Z. Baharav
Hewlett-Packard Labs.
1501 Page Mill Rd. , MS: 1U-14
Palo Alto, CA 94304
E-mail: zachi@hpl.hp.com

Abstract

When using the Method of Moments (MoM) to solve scattering problems, one of the crucial factors is the appropriate choice of basis functions. A judicious choice of the basis functions can lead to a sparse impedance matrix, or to a sparse solution vector, both of which will reduce the computational burden. However, pulse basis functions are usually used, both due to their simple description, and because there are already many software tools written to this aim. Therefore, some efforts had been recently invested in transforming a formulation that is the result of using pulse basis functions, to one using preferred basis functions. This transform produces grouping of the pulse functions into a new, more appropriate, set of basis functions. This paper discusses the search for an optimal grouping, in terms of the sparseness of the resulting solution vector. Various options are demonstrated and discussed, and numerical examples are given.

1 Introduction

The Method of Moments (MoM) is widely used for the solution of scattering problems, but one of its greatest limitations is the resulting large and dense impedance matrix. This imposes constraints both in terms of storage and solution-complexity of the impedance matrix. Most of the methods to relieve these constraints are concerned with rendering the matrix sparse, or otherwise exploit its structure.

A common approach to reduce solution complexity is to divide the matrix into regions (sub-matrices) which describe close interactions (sources and testing points are near), and far interactions (sources and test-points are far apart) [1, 2, 3, 4]. A different approach is that of using special basis functions such that the resulting impedance matrix will have only small number of dominant terms. Thus, thresholding the matrix will lead to a sparse matrix, with yet almost no degradation in the result. An example is the use of wavelets as basis functions [5]. In the

general category of selecting special basis functions also falls the Impedance Matrix Localization (IML) method of Canning [6, 7]. In this method one performs a basis-transformation in order to transform the impedance matrix into one with only a few dominant terms, and then performs a threshold operation to arrive at a sparse matrix.

A different point of view was recently suggested in the Impedance Matrix Compression (IMC) method [8, 9]. In the IMC one seeks to use basis functions such that the resulting solution vector is sparse. This, in turn, enables the use of a much smaller (in dimensions) impedance matrix, which is much easier to solve then the original impedance matrix. This is to be contrasted with the previously mentioned methods which sought a sparse matrix. The matrix and vectors used in the IMC are transformations of their counterparts for the existing pulse-basis function formulation.

In this paper we will look into what kind of basis functions should be used for the IMC, in order to have the most possible sparse solution vector. We will start by formulating more precisely the problem at hand, and will then proceed to description of possible solutions. Numerical examples will then be presented, followed by summary and conclusions.

2 Problem formulation

To make the following discussion more lucid, let us limit ourselves to a simple scattering scenario, as described in Fig. 1(a). The figure describes an incident EM wave with known components

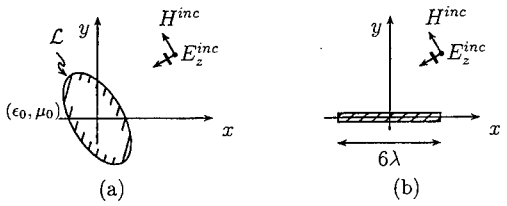

Figure 1: (a) General problem scenario. (b) Plate scenario.

$(\mathbf{E}^{inc}, \mathbf{H}^{inc})$. (In the following, bold-face font ($\mathbf{E}$) will denote spatial vectors, namely vectors with three coordinates corresponding to some Cartesian system, whereas the usual notation ($\vec{I}$) will be used to denote any other vector). The incident wave is a TM_z (Transverse Magnetic to $\hat{z}$) EM wave, for which we can write $\mathbf{E}^{inc} = \mathbf{E}_z^{inc}\hat{z}$, and $\mathbf{H}^{inc} = \mathbf{H}_x^{inc}\hat{x} + \mathbf{H}_y^{inc}\hat{y}$. The scatterer is an infinite cylinder lying with its axis along the $\hat{z}$ axis, and it is assumed to be a perfect electric conductor, with a known (yet arbitrary) cross section. The perimeter-line of the cylinder is denoted by $\mathcal{L}$, and the length parameter along this line is denoted by $l \in [0, l_{max}]$. On the perimeter of the scatterer there exists an induced electric current $\mathbf{J} = \mathbf{J}_z\hat{z}$, which is the unknown to be solved for. As can be seen in the above formulation, both the orientation of the impinging wave, and the specific cross-section of the scatterer, were left unspecified. The set of scattering problems, obtained by specifying these quantities, will be denoted as $\mathcal{S}$.

The scattering problem is then reduced to a matrix equation, using the MoM. In what follows, we will assume that pulse basis functions are used in conjunction with the Galerkin method, where

the pulse basis functions are defined as:

$$P_k(l) = \begin{cases} 1 & \text{if } l \in R_k \\ 0 & \text{otherwise} \end{cases} \qquad R_k = [\frac{k-1}{M} l_{max}, \frac{k}{M} l_{max}] \qquad k = 1, 2, \cdots, M \quad . \tag{1}$$

The resulting matrix equation is

$$[Z]\vec{I} = \vec{V} \quad , \tag{2}$$

where $[Z]$ is the impedance matrix, $\vec{I}$ is the vector of unknown coefficients, and $\vec{V}$ is the excitation vector. In line with the idea of basis transformation, or grouping, we introduce the transformation matrix $[W]$, which is real and unitary, and the following notations:

$$[\mathcal{Z}] = [Z][W]^T \quad , \text{(where } [W]^T \text{ stands for the transpose of } [W]\text{)} \tag{3}$$

$$\vec{\mathcal{I}} = [W]\vec{I} \quad . \tag{4}$$

Writing the impedance matrix equation in terms of the transformed quantities, we get

$$[\mathcal{Z}]\vec{\mathcal{I}} = \vec{V} \quad . \tag{5}$$

It is important to note that the two terms, "transformation-matrix" and "grouping-of basis functions", are synonymous. The latter however is a more explicit way of describing the meaning of the transformation matrix, as applied to the electromagnetic formulation. We will later see that this understanding of the electromagnetic characteristic features embedded in the problem, enables us to come with a feasible solutions.

Thus, following the above notations and explanations, our goal can be stated as follows:

Find a set of basis functions $[W]$ which will enable a sparse representation of the currents encountered in the set of scattering problems $\mathcal{S}$.

However, an immediate problem is the fact we do not know ahead what the currents are. One possible remedy is to assume a certain probability distribution over the possible currents, and try and choose the best basis-functions accordingly. This option requires decision over a model for the current. Another option, which does not explicitly assumes a certain model of the currents, uses a large sample of 'typical currents', which hopefully will serve as a good representatives of the currents one will encounter in practical problems. This option will be used here. The difficulty using this method is the question of how to choose these 'typical currents'. This is exactly the point where our physical understanding of the problem at hand gives us an edge over some abstract formulations, and it will be addressed later on in Sec. 4. At this stage we will assume we have a set of N ($M < N$) such 'typical vectors',$\{\vec{\mathcal{J}}_i\}_{i=1}^N$, and we order them columnwise in a matrix form to get a matrix $[\mathcal{J}]_{M\times N}$.

Our goal can now be stated as follows:

Find a set of basis-functions, described by a real unitary matrix $[W]$, such that

$$[W] = \arg\min_{[W]} \left[\sum_{i=1:N} \text{Spar}([W]\vec{\mathcal{J}}_i) \right] \quad , \tag{6}$$

where $\text{Spar}(\vec{x})$ is a sparseness-measuring function which evaluates the sparseness of $\vec{x}$ (the lower the value is, the more sparse the vector).

The sparseness-measuring function is of course crucial to the determination of $[W]$ and the whole optimization process. A few possible choices for the sparseness function are indicated in [10]. We will use a function such that the function value is the number of elements in $\vec{x}$ which convey 90% of its energy (the l_2 norm of $\vec{x}$). As we will see, this is a practical measure, but not that comfortable analytically.

In the next section we will describe various options for selecting $[W]$, and discuss their merits.

3 Various possible groupings

Rather than performing the optimization in (6) directly, we will, in this paper, resort to examining a few of the possible solutions. This will give us a valuable insight into the possible solution.

3.1 Karhunen-Loeve (KL)

The KL transform is actually a Singular Value Decomposition (SVD) analysis, when applied to probabilistic sources [11]. Given a matrix $[\mathcal{J}]_{M\times N}$ (where $M < N$), let us denote its SVD by the triplet $[U]_{M\times N}, [S]_{N\times N}, [V]_{N\times N}$, where $[U]$ and $[V]$ are unitary, and $[S]$ is diagonal. We will further assume that the (M non-zero) singular-values are arranged in a descending order on the diagonal of $[S]$. Thus, we can write

$$[\mathcal{J}] = [U][S][V]^T \quad . \tag{7}$$

It is also possible to express the matrix $[\mathcal{J}]$ as a weighted sum of the columns of $[U]$ and rows of $[V]^T$, namely

$$[\mathcal{J}]_{i,j} = \sum_{k=1:M} s_k [U]_{i,k} [V]_{jk} \quad . \tag{8}$$

Thus, one can see that according to the last equation, if we were to choose the best Q vectors which, on the average, will yield the best l_2 approximation of the currents represented in $[\mathcal{J}]$, then these vectors are the first Q column-vectors of $[U]$. However, this was not our goal as stated in (6). Though this might be viewed as some kind of sparseness requirement, it over looks the fact that in our formulation of the goal, the Q vectors chosen to describe best a signal could be drawn from a pool of M vectors, and thus they do not have to be the same Q vectors for all the set of N vectors.

3.2 Wavelets

Wavelets are a set of basis functions, which have some very useful properties for the sparse representation of natural signals, and have also been used for the description of currents [5, 12]. They are localized both in terms of their spatial-support area, and in terms of their spatial-frequency content. There are also fast transform methods, which are based on the hierarchical structure of the basis functions. For the above reasons, we choose to examine their suitability to the problem at hand. Various types of wavelets will be used (Haar, Daubechies, and Coifmans) in the sequel.

Wavepackets are variants of the wavelets, and when taken to the extreme, they can be viewed as Fourier basis functions on an interval. Namely, their spatial-support is very wide (relative to

wavelets), while their spatial-frequency support is narrow. We will not probe into their specific usage here, because, as will turn out, the KL basis-functions which results in our case are very similar to the wavepackets.

3.3 Optimal solution

A much more comprehensive optimization technique, which will be described in the talk and in a forthcoming paper, goes along the lines of [13]. To this aim, one defines a smoother cost function (than (6)), and then uses its analytic derivative to enable a gradient-descent type of optimization algorithm.

4 Numerical example

The first issue to address is the choice of the 'typical currents', namely the building of the matrix $[\mathcal{J}]$. As we mentioned earlier in Sec. 2, we are dealing with a set of scattering problems $\mathcal{S}$. For our purpose, we choose as a typical scatterer a plate, as described in Fig. 1(b). Note that this scatterer contains the two extreme cases of curvature: an edge (curvature= 0) and a straight segment (curvature= ∞). The resulting currents were computed for 31 various angles of incidence ($0:3:90$ degrees). To keep the description in what follows simple, we took only the first and last $N = 16$ samples of each of the resulting currents in this case (doubling the number of vectors to 62). Furthermore, we split them to real and imaginary parts (another double), and included all circular rotations (16 possible), which amounts to a total of 1984 ($= 31 * 2 * 2 * 16$) representing functions. Four of the resulting columns of the matrix $[\mathcal{J}]$ are depicted for example in Fig. 2.

The SVD decomposition of the this matrix was then computed, and the 16 eigen-vectors, as described by the columns of $[U]$, are depicted in Fig. 3. Note that these are in essence (apart from numerical errors) cosine/sine basis functions. The reason for that is that the SVD of a circulant matrix yields cosine/sine basis functions, and in the above case $[\mathcal{J}]$ is a concatenation of circulant matrices.

The performance of the conventional pulse basis, the basis which resulted from the SVD analysis, and the wavelet basis, are described in Fig. 4. In the plot only the results for the first 64 vectors of $[\mathcal{J}]$ are described, rather then the whole 1984 vectors, just in order to make it readable. In this figure the number of basis functions needed to describe each of the currents adequately (to within 90% of its energy) is described. We see that the conventional pulse basis functions performs the poorest, then comes the KL, and much better performs the wavelet basis functions. It is interesting to note that the use of various types of wavelets (Haar, Daubechie, Coifman) did have a significant impact on the results. For example, let us compare the avarage number of coefficients needed to describe the vectors in $[\mathcal{J}]$ well enough: For the case of pulse basis functions, an average of 11.7 coefficients were needed (out of a total of 164 coefficients); using the SVD basis functions resulted an average of 10.96; using the Haar wavelets led to an average of 9.5, whereas using the Daubechie-3 wavelets led to an average of 7.95. Other wavelets were tried out, but the results were similar to that of the Db3 wavelets.

In Figs. 5-6 the application of the above bases to two scattering problems are described: One is scattering from a circular cylinder, of radius 1λ, and the other is scattering from a square cylinder, with side-length of 1.5λ. The scattering problems were solved for 31 different angles of incidence

$(0:3:90)$. In both cases, the wavelet basis functions show better performance then the KL basis and the pulse basis functions.

5 Summary and Conclusions

This paper presented a methodology for finding the best basis functions to be used in a set of scattering problems. The basic idea is to use 'typical currents' to the problem at hand, and then find the appropriate basis functions for these 'typical currents'. It was shown that a conventional KL (SVD) approach is not appropriate, and that wavelets performs much better. An optimization problem was formulated, the solution of which will yield the best basis. The solution of this optimization problem is now under way, and the application of these methods to three-dimensional problems, where the initial basis functions are either triangular patches or square patches, will be done.

References

[1] N. Engheta, W. D. Murphy, V. Rokhlin, and M. S. Vassilliou, "The fast multipole method (FMM) for electromagnetic scattering problems", *IEEE Trans. on Antennas and Propagation*, vol. 40, no. 6, pp. 634–661, June 1992.

[2] R. L. Wagner and W. C. Chew, "A ray-propagation fast multipole algorithm", *Microwave Opt. Technol. Lett.*, vol. 7, no. 10, pp. 435–438, July 1994.

[3] C. C. Lu and W. C. Chew, "Fast far-field approximation for calculating the RCS of large objects", *Microwave Opt. Technol. Lett.*, vol. 8, no. 5, pp. 238–241, April 1995.

[4] E. Michielssen and A. Boag, "A multilevel matrix decomposition algorithm for analyzing scattering from large structures", *IEEE Trans. on Antennas and Propagation*, vol. 44, no. 8, pp. 1086–1093, August 1996.

[5] B. Z. Steinberg and Y. Leviatan, "On the use of wavelet expansions in the method of moments", *IEEE Trans. on Antennas and Propagation*, vol. 41, no. 5, pp. 610–619, May 1993.

[6] F. X. Canning, "The impedance matrix localization (IML) method for moment-method calculations", *IEEE Antennas and Propagation Soci. Mag.*, vol. 32, no. 5, pp. 18–30, October 1990.

[7] F. X. Canning, "Improved impedance matrix localization method", *IEEE Trans. on Antennas and Propagation*, vol. 41, no. 5, pp. 659–667, May 1993.

[8] Z. Baharav and Y. Leviatan, "Impedance matrix compression using adaptively constructed basis functions", *IEEE Trans. on Antennas and Propagation*, vol. 44, no. 9, pp. 1231–1238, September 1996.

[9] Z. Baharav and Y. Leviatan, "Impedance matrix compression (IMC) using iteratively selected wavelet-basis", *IEEE Trans. on Antennas and Propagation*, vol. 46, no. 2, pp. 226–233, February 1998.

[10] C. Taswell, "Top-down and bottom-up tree search for selecting bases in wavelet packet transforms", in *Wavelets and Statistics*, A. Antoniadis and G. Oppenheim, Eds., Lecture Notes in Statistics. Springer Verlag, 1995.

[11] G. H. Golub and C. F. Van Loan, *Matrix Computations, 2nd edition*, The Johns Hopkins University Press, Baltimore, Maryland, 1989.

[12] G. Strang and T. Nguyen, *Wavelets and filter banks*, Wellesley Cambridge Press, Ma., 1996.

[13] M. Lewicki and B. Olshausen, "A probabilistic framework for the adaptation and comparison of image codes", available through 'http://redwood.ucdavis.edu/bruno/papers.html', submitted to JOSA A, 1998.

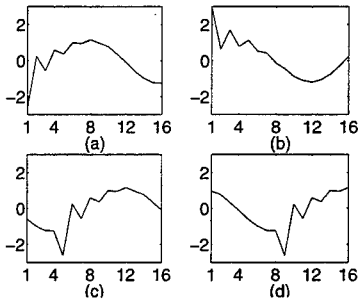

Figure 2: Four of the resulting columns of the matrix $[\mathcal{J}]$. (a-b) The real and imaginary parts of the current at an angle of 45 deg. (c-d) Two circulant rotations of the currents in (a).

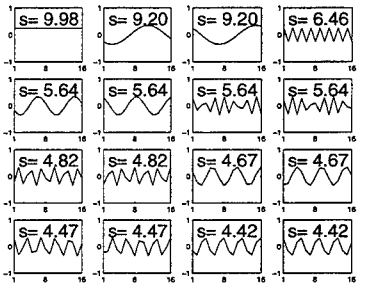

Figure 3: The 16 eigen-vectors, as described by the columns of $[U]$. In each subplot the appropriate singular-value is given.

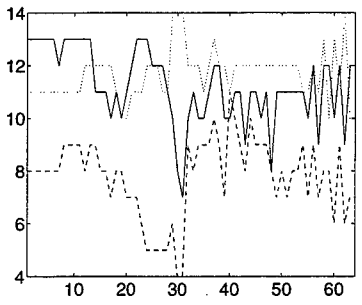

Figure 4: Sparseness of the columns of $[\mathcal{J}]$ in the three case: No basis transformation applied (dotted line) ; basis transformation which resulted from the SVD analysis (solid line); and wavelet (Daubeschie-3) basis transformation (dashed line).

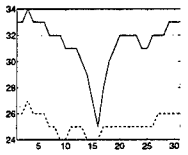

Figure 5: Scattering from a circular cylinder. The performance in the three case: No basis transformation applied (dotted line) - average cost of 32.0 (out of 64 coefficients) ; basis transformation which resulted from the SVD analysis (solid line) (Avg. 31.3); and wavelet (Daubeschie3) basis transformation (dashed line) (Avg. 25.2).

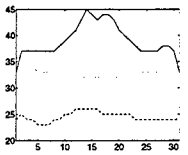

Figure 6: Scattering from a square cylinder. The performance in the three case: No basis transformation applied (dotted line) - average cost of 32.7 (out of 64 coefficients); basis transformation which resulted from the SVD analysis (solid line) (Avg. 38.9); and wavelet (Daubeschie-3) basis transformation (dashed line) (Avg. 24.5).

GENETIC ALGORITHMS AND THEIR PRACTICAL IMPLEMENTATION STRATEGIES FOR DESIGN OPTIMIZATION OF ELECTRICAL DEVICES

Osama A. Mohammed
Department of Electrical and Computer Engineering
Florida International University
Miami, Florida, USA

ABSTRACT: GAs provides a high level of robustness by simulating nature's capability of adapting to many different environments. Through the application of GAs to design optimization problems, the performance characteristics of the GAs are shown to be powerful in solving optimization problems with high dimensional objective functions containing several local minima. As they use only the fitness values, GAs does not require derivatives or any other additional information about the objective function. The performance of GAs can be improved significantly by applying selective pressure and adequately providing a shape modeling technique to control the range of variation for the shape to be optimized.

1. INTRODUCTION

The need to solve electromagnetic problems accurately and efficiently for large-scale complex problems has caused the emergence of computational electromagnetics. The methods developed, such as the finite difference method, the method of moments, the finite element method, and the boundary element method, have become increasingly sophisticated with ever increasing computational power. These numerical techniques are used by researchers as indispensable tools to compute the field parameters and predict the performance of devices in all areas of electromagnetics. These applications range from two-dimensional electrostatics to nonlinear eddy current calculations in three dimensions and to high frequency applications. The tremendous advancements in computer technology make it possible to enhance these analysis tools with state of the art modeling and post-processing capabilities to offer the researcher or the engineer everything that is necessary to analyze an electromagnetic problem in a user-friendly package.

Many researchers and engineers, however, seldom need to perform analyses alone. Their major task is to come up with the best solution for a problem. In other words, engineers need a tool that can help them synthesize the best solution for the problem in their hands. The place of an analysis package in this task description is to provide the solution and the performance measure of the current design, which help the researcher navigate in search of the optimum. With the definition of this new need, computational electromagnetics adopts another field, design optimization. Using the already perfected analysis modules in coordination with a search method, design optimization in computational electromagnetics seeks the optimum solution for a specified problem. This problem has an objective function and constraints. Design optimization's task is to maximize (minimize) the objective function while not violating the constraints. The objective function $f(x_i)$, is a function of the design variables, x_i. The number of design variables defines the dimension of the search space. There is a set of constraints that govern the domain of the design variables. Each constraint can be written as an inequality $p_j(x_i) \leq 0$. The optimization is formulated as:

$$\text{Maximize } f(x_i) \text{ (objective function)}$$
$$\text{Subject to } p_j(x_i) \leq 0 \text{ (constraints)}$$

Problems dealing with the optimization of parameters are seen in every field. Mathematical optimization can be dated back as early as the mid 1700s when Euler developed the calculus of variations. Many other mathematical

optimization techniques are derived from the calculus of variations. In the last 20-30 years, progress has been made in solving inverse problems largely due to the mathematical regularization theory developed by Soviet scientists [1].

In electromagnetics, numerical techniques combined with the available computing capability raise the opportunity for incorporating the analysis methods with a search scheme to locate the optimum in the search space. This very promising environment results in the addition of new techniques to the arsenal of numerical optimization methods. Stochastic search techniques, such as simulated annealing, evolution strategies, and genetic algorithms, along with artificial intelligence based methods, such as neural networks, have been introduced in the last ten years. Optimization schemes that combine one or a hybrid of several of these methods with computational electromagnetics' analysis tools are reported to have successful applications to design optimization problems of various kinds. Genetic algorithms (GAs), developed by John Holland in the 1970s, attracted the interest of more and more researchers due to their robustness and efficiency in handling search problems. In computational electromagnetics, design optimization can benefit from the use of this highly successful method. The finite element method joined with GAs to form a design optimization environment for electromagnetic devices.

One of the most difficult aspects of design optimization is the shape optimization problem. The optimization technique described here is not limited to shape optimization. Other design parameters, such as excitation and material characteristics as well as device terminal parameters may also be a part of the optimization's goal. Thus, a multidimensional search space is under consideration. The optimization method must be able to perform an effective search in a multidimensional parameter space. As a shape optimization problem may require a high number of control points to be adjusted, the number of design parameters can be quite large. This should not pose a major difficulty for the optimization scheme. In other words, the developed scheme must possess the flexibility to adapt easily to different design needs.

The multiparameter objective function for a simple design optimization problem in magnetostatics can be non-convex (local extremes), non-differentiable, and stiff [2-3]. The optimization algorithm must be able to deal with these difficulties. It is known that a search method based on deterministic methods tends to fail when the objective function is discontinuous. The local extremes also present a significant danger to the success of the search because the gradient based algorithm can be easily trapped in such a local extrema. Finally, the search process is rated by its speed of finding a solution and the accuracy of the solution, its closeness to the global optimum.

Besides the search algorithm, an analysis scheme is also needed. The analysis module's task is to provide field solutions for the different designs suggested by the search tool. Modeling the problem is one of the responsibilities of the analysis module. Especially in shape optimization, accurate modeling of the suggested design is very critical. The analysis section of the optimization environment, therefore, must be able to model the problem accurately and efficiently, and it must provide accurate solutions for the field parameters. The search relies on the analysis done on its suggestion.

2. APPLICATION OF GAs TO DESIGN OPTIMIZATION

There are two fundamental functional bodies in a design optimization process: the analysis tool and the search algorithm. They continuously interact, as for every new set of design parameters the search algorithm suggests the analysis tool, solves the governing equations and determines the value of a new point in the search space. The genetic algorithm performs the search operation and the finite element method carries out the analysis. A schematic diagram of the procedure is given in Figure (1). The GA comprises all the blocks on the left side of the figure. The analysis is shown as a single block, which contains all of the processes of FEM.

A GA starts the search from an initial population of a certain number of members. This population is randomly created within the domain of the search space. The members of the population are finite length string structures called chromosomes. Coding the design parameters using a finite length alphabet forms these structures. Generally a low cardinality alphabet is used, such as the binary system. The coding of the parameters is entirely application dependent and it is one of the critical aspect of the performance of a GA. For the binary alphabet, two of the well-known ones are binary and gray coding. The bits in the strings are called genes. As every chromosome in the population represents another design, it is necessary to determine how well fitted each design is. The FEM creates a mesh for that particular design, solves the governing equations, and informs the GA about the performance of the designed device by returning the necessary values such as magnetic flux densities at critical points.

From the results of the analysis, the GA calculates the objective function value for each chromosome. This value is called the fitness of the chromosome and plays a significant role in the further steps of the search. Also, an average fitness is calculated representing the fitness of the entire population. The decision on the convergence of the search is made based on the average fitness as indicated in Figure (1). If the search has to continue, the GA creates a new generation from the old one. There are three operators, which exclusively characterize the GAs: reproduction, crossover, and mutation.

Based on the fitness of a chromosome and the average fitness of the population, the reproduction operator determines, rather randomly, whether that particular chromosome will have copies in the next generation, and how many. There are many ways of designing this operator, however, the underlying idea is to give the chromosome with a higher fitness more *chance* to be represented in the next generation but leave the actual decision to a random variable. Once the reproduction is complete, the new generation is made of copies of the previous generations' members. Nevertheless, there is no new information. It is time for the chromosomes to exchange information through the crossover operator. At this point the number of chromosomes in the population has not changed.

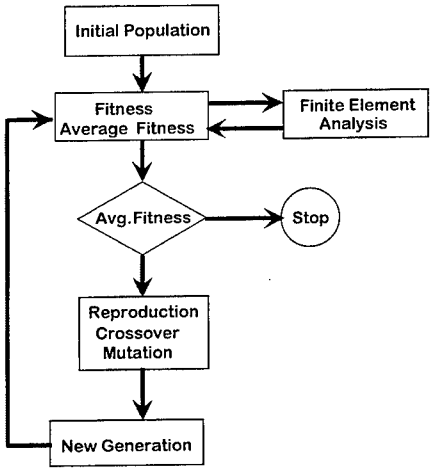

Figure (1) Genetic Algorithms in Design Optimization

The crossover operator forms pairs from the new generation mating chromosomes randomly. For each pair all bits from a randomly selected position on the string to the end of the string are swapped.

The third fundamental operator of GAs is the mutation operator. It occasionally changes the value of a gene acting as a protector against the complete loss of some important genetic information [4]. Both crossover and mutation operators have occurrence probabilities. Compared to crossover, mutation happens much less frequently.

After all these operators perform their functions, the new generation is made of members who have gained new information through the exchange between pairs. The better traits of the "parent" chromosomes are carried along to the future generations.

Several practical issues that need a special attention in implementing GAs to optimization problems will now be examined. These will contribute to achieving improvements in the convergence characteristics of GAs. There are three areas were improvements could be achieved. These include the representation scheme as well as the reproduction and crossover operators.

2.1 Representation scheme

The representation scheme is the method of coding the design variables into finite-length character strings. Generally, a binary alphabet is used as explained earlier. Although the trivial binary coding yields acceptable results, it is reported that the unit-distance Gray coding performs better [5]. Assume the binary number 01111111 represent a point in a one dimensional search space. The nearest point that can be mapped with this representation scheme using binary coding is 100000000. This small step in the search space, however, requires all 8 bits of the chromosomes to change. Gray code is a unit distance coding system. When the number the code represents changes by one unit, the change in the code is also only one bit. This characteristic of the Gray code prevents the search from getting trapped in cases like the above example.

2.2 Reproduction

Working on the entire population, the reproduction operator creates a new generation from the old generation. Reproduction in GAs is probabilistic. Based on the fitness measure of an individual and the average fitness of the population, the reproduction operator determines the number of copies that particular individual will have in the next generation. The underlying idea in designing the reproduction operator is to give the individual with higher fitness more chance to be represented in the next generation but leave the decision to a random variable.

2.3 Crossover

Through crossover, chromosomes exchange genetic information. The crossover operator simulates the recombination process of natural evolution. Both methods summarized below are derived from one-point crossover [6].

1) Two-point crossover: As the name suggests, there are two randomly selected crossover sites. Only the genes located between these two sites are swapped. This can be best demonstrated with an example. Suppose the coding is binary with an alphabet A = {0,1}. Assume that before crossover two strings, a_1 and a_2, are mated and are represented as:

$$a_1 = 110|010110|110100$$
$$a_2 = 100|110001|100010$$

also assume that the two randomly selected crossover sites for this pair are 3 and 9, as indicated above with the symbol |. After crossover the offspring become:

$$a'_1 = 110|110001|110100$$
$$a'_2 = 100|010110|100010$$

This technique can be generalized to implement n-point crossover algorithms. The bits between every other crossover site pair are then swapped.

2) Uniform crossover: Uniform crossover eliminates the positional bias inherent in one and two-point crossover methods. There are two main steps to perform a uniform crossover. The first step is to randomly determine how many bits are to be swapped. Assume the outcome is k. Of course k must be smaller than the chromosome length, l. In the second step, k locations on the chromosome are randomly selected, and the bits at these k locations are swapped. The genetic information exchange is still effective, and there is no bias regarding the position.

3. PROBLEM MODELING FOR SHAPE OPTIMIZATION

The technique used for the field solution of the electromagnetic problem is the finite element method. The geometric modeling of the problem establishes an interface that joins the search and the solution algorithms.

Therefore the efficiency of this interface is crucial to the performance of the optimization. In shape optimization problems, each member of the GAs populations describes the geometrical characteristics of a specific design that is translated into a finite element model and then solved to obtain the fitness for this particular individual. It is a significant task to determine the optimal set of design parameters. These parameters are used to form the outlines of different regions of the modeled device. Curve fitting techniques as well as an increase in the number of points that control the shape would enhance the problem modeling for shape optimization.

4. THE PREMATURE CONVERGENCE PROBLEM

A significant problem faced in the application of GAs, to some problems, is premature convergence. Relative to the other members in the population, if some of the average individuals have extraordinary fitness, the mechanics of GAs may lead the iterations to a premature convergence, which is defined as a convergence to a *sub-optimal* point. There are two main factors directly leading to this undesired problem in the implementation of GAs. The selective pressure applied by the selection operator is the first factor. The second factor is in the way the recombination or crossover is implemented. If the identical parents and their identical offspring represent a sub-optimal point, the convergence is premature. Luckily, there is another operator that quietly helps resolve this situation. The mutation operator randomly alters genetic information of the chromosomes by toggling some genes. The occurrence rate of a mutation, however, is significantly low. Therefore it is not always a cure for the causes of premature convergence.

In some applications of GAs, the parents are paired strictly based on their fitness to enhance the rate of convergence. Better individuals always mate with better partners. This strategy increases the possibility of having identical parents, and identical parents can only reproduce offspring genetically equal to them. Genetic diversity, which is one of the essentials driving forces of natural evolution, is severed. A safer approach is to leave the selection to a random variable while still giving the better individuals a higher chance of paring with each other. The problem of premature convergence is demonstrated in the following example.

5. HYBRID IMPLEMENTATION OF GAs

As the only search technique in an optimization process, GAs have been applied to a variety of design optimization problems in electromagnetics [4, 7-9]. Combining GAs with a deterministic gradient search method [10-12] creates a hybrid technique. Specific strengths of each algorithm are used at different stages of the search in the hybrid method.

GAs "explore and exploit" the search space to locate the global optimum without being attracted to local optima. They work with the value of the objective function and do not require derivatives. These characteristics become significant in optimization problems with non-convex objective functions, encountered in magnetostatic problems. The GA is used here to find the area of the search space which contain the global optimum where the objective function is assumed convex.

Deterministic methods, on the other hand, fail for these types of problems. Either the search becomes impossible due to the non-differentiability of the objective function, or it gets trapped in a local optimum.

The hybrid technique employs the two algorithms at different stages of the search. GAs initiate the search and locate the "zone" of the global optimum. Once in this zone, the gradient technique takes over [10]. Starting from this improved initial point, the search quickly converges. It is assumed that in the vicinity of the global optimum, the objective function is differentiable and is free from local optima.

6. THE GENERALIZED OPTIMIZATION ENVIRONMENT

When optimizing designs for practical electromagnetic problems, the number of design constraints and variables is increased drastically. The construction and step-by-step creation of an electrical system, in practice, is a trial and error process. The design may lead to a sub-optimal solution since the success of a design depends on the experience of the designer. It is therefore necessary to simulate the physical behavior of the electrical system by numerical methods in a generalized fashion. To obtain an automated optimum design, numerical optimization is

necessary to achieve a well-defined optimum. Optimization requires that all design goals, of a device, be connected into a single objective function with all independent variables and constraints. In applications to practical problems, effective pre-processing and post processing of data are necessary in addition to high performance computing capabilities. To achieve this process, a generalized optimization environment is suggested in Figure (2).

The system architecture for this optimization can be utilized for the computational creation of an electrical device or a system. It is intended to be a design and development toolbox system for practical applications in an industrial environment. As shown in Figure (2), the generalized optimization environment involves four main interacting blocks. These represent 1) the computing platform, 2) the analysis toolbox, 3) an optimization chest, and 4) the design engineer's observation and decision making path. The optimization *chest* is a black box of various optimization techniques. The choice of an optimization procedure versus another is based on the expectation that the selected method will work faster or give best answers to a particular problem rather than the heuristic choice of a method that is application specific. The interaction between the modules is described in a shared open system computational environment which will make use of available computing facilities and utilize the experiences and tools gained from previous application.

6.1 The Computing Platform

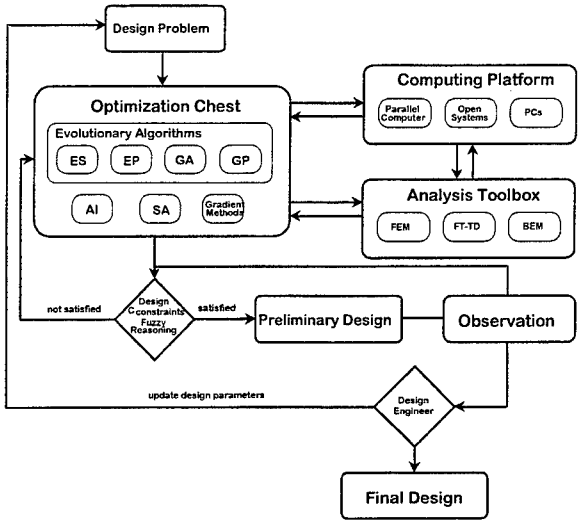

Figure (2) Generalized Optimization Architecture for Practical Design of Electrical Devices

The current improvements and increase in capabilities of desktop computing facilities will enable the designer to utilize vast computing resources that are available in the design environment. The computing platform block in Figure (2) represents the computing facilities that may be available in the design environment.

In this platform, parallel computing machines, clustered workstations and personal computers could be utilized to provide super-computing capabilities at low cost. Workstation farms connected to data switches and data communication networks could provide automated access to clusters of workstations that could be shared at distant locations or at the work place.

6.2 The Analysis Toolbox

This toolbox includes a collection of modeling tools and analysis techniques. Software packages for FEM, BEM, FDTD as well as other techniques will be accessed concurrently by the Optimization Chest to determine the objective function values, and by the design engineer to observe the performance and check the design parameters interactively. The analysis toolbox also include information about the various methods and their formulation, facilities for pre- and post processing of input and output data, mesh generation, mesh density information, adaptive meshing and additional interfacing software to access the various blocks in the overall system.

6.3 The Optimization Chest

This block includes a collection of design methods. Each is treated as a black box with an interface that accepts the appropriate problem specification. The techniques in this box include evolutionary algorithms such as evolution strategies, evolutionary programming, genetic algorithms and genetic programming. It also includes artificial intelligence algorithms such as neural networks, simulated annealing, expert systems, fuzzy reasoning and adaptive learning. In addition to these emerging methodologies standard search algorithms ranging from gradient methods, random search, hill climbing and biased random walk will be also included in the optimization chest. As practical applications require many objectives that may not be met by one of the methods, combinations and generalizations of these algorithms have proved to be powerful. Design sensitivity techniques are also included in the optimization chest.

6.4 Parametric Design in the Optimization Chest

The optimization chest described above is a stochastic blackbox approach to design optimization. To check its performance in a practical environment, each box representing a technique should be based on the same assumptions. These may include; 1) the values for each parameter must be found, 2) each parameter has finite number of possible values, 3) combinations of parameter values may be unacceptable, 4) there is a function to give a measure for each set of parameters, and 5) the objective function is to produce an optimal set of design parameter values for an acceptable scoring measure. The choice of an optimization method should be based on which method can work faster or give best answers to the problem rather than if the method will work at all for the given application. Approximating continuous parameters with discrete values will work for most applications but may increase the problem dimensionally. Combination methods are used to reduce the size.

6.5 Problem Specification

Applying any or all of the design methods to a given problem can be successful with proper problem specification. Some suggested methods to enable the user specify the problem are discussed here. These methods could be coded in software that will execute before invoking the design process. The creation of a design policy, in the form of a rule-generating function that produces a feasible set of rules, may be developed. Each use of this function may produce a different set of rules for every application. For this reason, the feasibility of the generated rules must be checked. Formulating a function that will be used to determine the feasibility of the generated rules is an important task in specifying the problem. Such a function will take any generated set of input and determines if the values satisfy all users imposed constraints. The next step in specifying the problem is a scoring function that takes the rules as input, evaluates it and returns a measure of merit. In order to evaluate several methods, the same scoring function must be used. The performance of any method in the optimization chest could be determined based on the number of objective function evaluations, or on the time it takes to return a feasible solution or a combination of these ideas. The final item in the problem specification process is an output function, which will display the input to the optimization chest. Here, other user inputs such as relating the parameters to those in a database or empirical data from previous design or adding explanations and additional restrictions on the parameters may be added. This process can be used at the end of the search process for determining if a good design is reached. This process can also be used during the search as a checking mechanism to interrupt to see the search result at some point.

6.6 Observations and Decision Making

This part of the optimization environment includes information access in the form of query search database in an industrial or a research environment. This may include interactive features to access information on field and experience data, design aids and rules, empirical data, knowledge base, cost tables and parts list for off-the-shelf design optimization.

7. CONCLUDING REMARKS

GAs provides a high level of robustness by simulating nature's capability of adapting to many different environments. Through the application of GAs to design optimization problems, the performance characteristics of the GAs are shown to be powerful in solving optimization problems with high dimensional objective functions containing several local minima. As they use only the fitness values, GAs does not require derivatives or any other additional information about the objective function. The performance of GAs can be improved significantly by applying selective pressure and adequately providing a shape modeling technique to control the range of variation for the shape to be optimized.

The generalized optimization environment is valuable for current and future activities in computational electromagnetics for analysis and design of practical applications. This environment involve interacting blocks and adds the input of the design engineer to the process and giving him the final decision making on the achievement of an optimal design. The interactions between the various blocks of the system can be implemented in an industrial or a research environment.

8. REFERENCES

[1] V. B. Glasko, Inverse problems of mathematical physics, New York, New York: American Institute of Physics, Translation Series, 1988.

[2] A. Gottvald, K. Preis, C. Magele, O. Biro, and A. Savini, "Global optimization methods for computational electromagnetics," IEEE Transactions on Magnetics, vol. 28, no. 2, pp., 1537-1540, March 1992.

[3] K. Preis, O. Biro, M. Friedrich, A. Gottvald, and C. Magele, "Comparison of different optimization strategies in the design of electromagnetic devices," IEEE Transaction on Magnetics, Vol. 27, No. 5, pp. 4154-4157, September 1991.

[4] D. E. Goldberg, *Genetic Algorithms in Search, Optimization & Machine Learning*, Reading, Massachusetts: Addison-Wesley Publishing Company, Inc., 1989.

[5] Mohammed, O. A. and Üler, F. G., "Ancillary Techniques for the Practical Implementation of GAs to the Optimal Design of Electromagnetic Devices," IEEE Transactions on Magnetics, Vol. 32, No. 3, pp. 1194-1197, May 1996.

[6] L. J. Eshelman, R. A. Caruana, and J. D. Schaffer, "Biases in the crossover landscape", in *Proceedings of the Third International Conference on Genetic Algorithms*, San Mateo, CA, 1989, pp. 10-19, Morgan Kaufmann Publishers, Inc.

[7] T. Back and H. P. Schwefel, "An overview of Evolutionary Algorithms for Parameter Optimization," MIT, Evolutionary Computation 1(1): 1 -23, 1993.

[8] F. G. Üler, O. A. Mohammed, and C. S. Koh, "Utilizing Genetic Algorithms for the Optimal Design of Electromagnetic Devices," *IEEE Trans. on Magnetics*, vol. 30, no. 6, pp. 4296-4298, Nov. 1994.

[9] G. F. Üler, O. A. Mohammed, and C. S. Koh, "Design Optimization of Electrical Machines Using Genetic Algorithms," *IEEE Transactions. on Magnetics*, vol. 31, no. 3, pp. 2008-2011, May 1995.

[10] K. Weeber, S. Hoole, "Geometric parameterization and constrained optimization techniques in the design of salient pole synchronous machines," *IEEE Trans. on Magnetics,* vol. 28, no. 4, pp. 1949, July 1992.

[11] I.-H Park, B.-T Lee and S.-Y Hahn, "Design sensitivity analysis for nonlinear magnetostatic problems using finite element method", *IEEE-Transactions on Magnetics*, Vol. 28, No. 5, 1992.

[12] J. Simkin and C. W. Trowbridge, "Optimizing electromagnetic devices combining direct search methods with simulated annealing," *IEEE Transactions on Magnetics*, Vol. 28, No. 2, pp. 1545-1548, March, 1992.

SESSION 7

WIRE MODELS

Chairs: Keith Lysiak and Chris Trueman

Extension of a Thin-Wire Algorithm for Wires Moved Laterally Within a Mesh

Gerald J. Burke and David J. Steich
Lawrence Livermore National Laboratory
Livermore, CA 94550

Introduction

While FDTD methods, such as that of Yee [1], are very versatile and have found widespread use in electromagnetics, modeling thin wires in such algorithms can present special problems. The wires are usually much thinner than the desired cell size, and reducing the cell size would require also reducing the time increment. Several methods have been used to treat thin wires in FDTD. Merewether and Fisher [2] and Umashankar *et al.* [3] used contour integration incorporating the $1/\rho$ field behavior. Parks *et al.* [4] and Holland [5] coupled the transmission line equations for the wire current to the FDTD mesh equations. Riley [6] and Mittra [7] solved integral equations for the wire current coupled to the mesh fields. These methods usually are best suited to wires that lie along edges for the electric or magnetic field in the mesh. When the wire can be moved, it often results in reduced accuracy. Requiring wires to lie on cell edges restricts the wire geometry when cells are orthogonal, and even with more general meshes it requires generation of a new mesh when a wire must be moved. This limitation may be a major reason that FDTD methods still are not nearly as popular as frequency domain integral equation and finite element techniques for modeling wire structures.

It would be very valuable to be able to locate wires independently of the mesh. This paper presents some efforts in that direction, considering the lateral movement of wires parallel to cell edges and also adjustment of the wire length with respect to the cell boundaries. The transmission line method used for the wire is similar to that described by Holland [5], but the averaging to couple the transmission line fields to the mesh fields is done in a way that can be generalized to wires moved with respect to cell edges. The treatment of wires passing through electric field edges is considered first, and then is generalized to wires moved from the edges. The accuracy when the wire is moved is demonstrated by comparisons with NEC [8].

Treatment of Wires on Cell Edges

In the method considered here the transmission line equations for current and voltage along the wire are coupled with the FDTD equations of the standard Yee algorithm [1]. The transmission line equations for the wire current are derived from the ϕ component of Maxwell's $\nabla \times \mathbf{E}$ equation and the ρ component of the $\nabla \times \mathbf{H}$ equation

$$\mu \frac{\partial H_\phi}{\partial t} = \frac{\partial E_z}{\partial \rho} - \frac{\partial E_\rho}{\partial z} \tag{1}$$

$$\epsilon \frac{\partial E_\rho}{\partial t} = \frac{1}{\rho}\frac{\partial H_z}{\partial \phi} - \frac{\partial H_\phi}{\partial z}. \tag{2}$$

For current I and charge Q on a wire on the z axis, the E_ρ and H_ϕ components for small ρ

can be approximated as

$$E_\rho = \frac{Q}{2\pi\epsilon\rho} \quad \text{and} \quad H_\phi = \frac{I}{2\pi\rho}.$$

Substituting for E_ρ and H_ϕ in equation (1) and integrating over ρ from the wire radius a to the transmission line radius r_t, with boundary condition $E_z(a) = 0$, yields

$$\frac{\mu \ln(r_t/a)}{2\pi}\frac{\partial I}{\partial t} = E_z(r_t) - \frac{\ln(r_t/a)}{2\pi\epsilon}\frac{\partial Q}{\partial z}$$

or, defining inductance $L_w = (\mu/2\pi)\ln(r_t/a)$,

$$\frac{\partial I}{\partial t} = \frac{1}{L_w}E_z(r_t) - \frac{1}{\mu\epsilon}\frac{\partial Q}{\partial z}. \tag{3}$$

At this point the transmission line radius r_t is an arbitrary distance to the outer shell of the transmission line that couples to the mesh fields. It will be found to drop out in the treatments that follow. Substituting for E_ρ and H_ϕ in equation (2), and averaging over ϕ to eliminate the $\partial H_z/\partial\phi$ term yields the continuity equation

$$\frac{\partial Q}{\partial t} = -\frac{\partial I}{\partial z}. \tag{4}$$

To reduce equations (3) and (4) to discrete form, the current and charge will be sampled at points spaced by Δz along the wire with time step Δt. Then I_k^n and Q_k^n represent the current and charge at sample point k and time step n, with charge points displaced from current by $\Delta x/2$. With a central difference approximation of the derivatives, and introducing an applied voltage V^{inc}, equations (3) and (4) become

$$I_k^{n+1/2} = I_k^{n-1/2} - \frac{\Delta t}{\Delta z \mu\epsilon}\left(Q_k^n - Q_{k-1}^n\right) + \frac{\Delta t}{\Delta z L_w}\left(E_{zk}^n \Delta z - V_k^{\text{inc}}\right) \tag{5}$$

$$Q_k^{n+1} = Q_k^n - \frac{\Delta t}{\Delta z}\left(I_{k+1}^{n+1/2} - I_k^{n+1/2}\right). \tag{6}$$

These can be written in terms of a voltage by defining capacitance $C_w = \mu\epsilon/L_w$ as

$$I_k^{n+1/2} = I_k^{n-1/2} - \frac{\Delta t}{\Delta z L_w}\left(V_k^n - V_{k-1}^n - E_{zk}^n \Delta z + V_k^{\text{inc}}\right) \tag{7}$$

$$V_k^{n+1} = V_k^n - \frac{\Delta t}{\Delta z C_w}\left(I_{k+1}^{n+1/2} - I_k^{n+1/2}\right). \tag{8}$$

The simplest situation for solving the transmission line equations coupled to the FDTD mesh is when the wire lies along the E_z edges. The transmission line current drives the mesh through the E_z update equation, and E_z from the mesh drives the transmission line through the E_{zk}^n term in equation (5). E_{zk}^n in equation (5) is interpreted as the mesh field averaged around the outer shell of the transmission line at radius r_t. However, the E_z value available from the mesh equations is the field averaged over a cell face. Holland [5] deals with this difference by averaging the equations (5) and (6), so that E_{zk}^n in equation (5) becomes the average field over the face, which is available, and L_w is averaged for ρ from a to $r_t = \sqrt{\Delta x \Delta y/\pi}$. The average inductance can be approximated as

$$\bar{L}_w = \frac{\mu}{2\pi}\frac{\int_a^{r_t}\ln(r/a) r\, dr}{\int_0^{r_t} r\, dr} = \frac{\mu}{2\pi}\left(\ln(r_t/a) - \frac{1}{2} + \frac{a^2}{2r_t^2}\right). \tag{9}$$

Holland also averages over a rectangular cell face and applies an empirical correction factor. This approach gives accurate results, but it is not clear how to generalize this averaging for a wire moved off of the E_z edge.

Another way that was found to work well for coupling the transmission line equations to the mesh fields with the wire on E_z edges is to use the exact inductance for $r_t = \Delta x/2$, and drive equation (5) with an average of the E_z mesh fields

$$E^n_{zk} = \tfrac{1}{2}\Big(E^n_{i_w,j_w,k} + \tfrac{1}{4}(E^n_{i_w-1,j_w,k} + E^n_{i_w+1,j_w,k} + E^n_{i_w,j_w-1,k} + E^n_{i_w,j_w+1,k})\Big) \tag{10}$$

for a wire at mesh coordinates (i_w, j_w, k). In comparisons with NEC, equation (10) seemed to give slightly better accuracy than Holland's average inductance with correction factor, and remained stable to larger wire $a/\Delta x$. Another method used by Riley [6] is to locate the wire on the H_z edges and let the transmission line radius pass through the surrounding E_z points. Actually Riley had an unstructured mesh and r_t was the average distance to E_z samples. For cubical cells, $r_t = \Delta x/\sqrt{2}$, and E^n_{zk} in equation (5) is the average of the E_z mesh fields

$$E^n_{zk} = \tfrac{1}{4}(E^n_{i_w,j_w,k} + E^n_{i_w+1,j_w,k} + E^n_{i_w,j_w+1,k} + E^n_{i_w+1,j_w+1,k}) \tag{11}$$

for the wire at $(i_w+1/2, j_w+1/2, k)$. It is not obvious how to generalize any of these averages for a wire at an arbitrary location in the x-y plane while maintaining the same accuracy. We also tried bi-quadratic interpolation on the 3×3 edges surrounding the wire on an E_z edge, and bi-cubic interpolation on the 4×4 E_z edges surrounding a wire on a H_z edge, but the results were not satisfactory.

Wires Displaced from Cell Edges

To generalize the wire location, we looked at the behavior of the fields in the mesh due to the wire excitation. The field component E_z at a distance 0, Δx and $2\Delta x$ from a wire located on the E_z edges is shown in Figure 1 for varying wire radius, with the computed fields connected by straight lines. The wire length was 1.4 m with a cell size of $\Delta x = 0.035$ m, and the center three segments of the wire were excited with 1/3 volts each, so that results could be compared for a cell size three times larger without changing the source gap size. The fields in Figure 1 were obtained using the average field of equation (10) to drive the transmission line. Similar results were obtained using Holland's average for a square cell with correction term [5, eq. 53] but that solution became unstable for radii of 0.01 and 0.014 m. The fields in Figure 1 represent the the peak values adjacent to the center of the wire due to a Gaussian pulse excitation with full-width-half-max (t_{fwhm}) of 2 ns. For all solutions in Figure 1 the wire current was in good agreement with the NEC model.

Examination of Figure 1 shows that E_z varies with x approximately as the average of $\ln(x/a)$ with the function going negative for $x < a$. This differs from the average in equation (9), where the field is assumed zero inside the wire. The transmission line equations, in effect, put a boundary condition $E_z(a) = 0$ on the fields that the mesh is averaging, but the field goes negative inside the wire as if it were produced by a filament of current on the wire axis. A simple model for comparison with the mesh fields is obtained by averaging $\log(\rho/a)$ over an annular region extending from $\rho = \max(0, r_0 - \Delta/2)$ to $r_0 + \Delta/2$. This yields

$$F_a(r_0, \Delta, a) = \begin{cases} -\frac{1}{2} + \frac{r_1^2 \ln(r_1/a) - r_2^2 \ln(r_2/a)}{r_1^2 - r_2^2} & \text{if } r_0 > \Delta/2 \\ -\frac{1}{2} + \ln(r_2/a) & \text{if } 0 \le r_0 \le \Delta/2 \end{cases} \tag{12}$$

Table. 1. Relations of average E_z from the mesh and corresponding average of $\log(r/a)$ for a distance of 0 and Δx from a wire of radius a (E_0, E_1 and A_0, A_1, respectively).

Wire rad. (m)	E_0/E_1	A_0/A_1	$(E_0+E_1)/(2E_0)$	$\log(\frac{\Delta}{2a})/A_0$
0.014	–0.557	–0.551	–0.411	–0.425
0.01	–0.169	–0.143	–2.48	–2.963
0.003	0.380	0.411	1.806	1.737
0.001	0.486	0.592	1.380	1.354
10^{-5}	0.826	0.821	1.112	1.111
10^{-7}	0.885	0.886	1.065	1.066

where $r_1 = r_0 - \Delta/2$ and $r_2 = r_0 + \Delta/2$. The average could be computed over cell faces, but in either case it was found that a fudge factor was needed on the region size for best agreement with the observed fields and best agreement of the currents with NEC. For a mesh of cubical cells with size Δx. it was found that the mesh fields near the wire were matched best by $F_a(\rho, f_c\Delta x. a)$ with f_c approximately 0.78. This seems to work reasonably well over a wide range of wire radii and cell sizes. When averaging over a square cell face. rather than an annular region. the factor was approximately $0.70\Delta x$ to shrink the side length. Holland arrived at a similar correction by subtracting a constant from his average inductance to make it cross zero at an $a/\Delta x$ that matched a moment method solution for the wire. The factor of 0.78 for the annular average was chosen for best agreement of the dipole input impedance with NEC, although 0.80 would work about as well. Any significance of this factor is not understood at this point. However, it was noted that $f_c = 0.802188$ is the solution of the equation

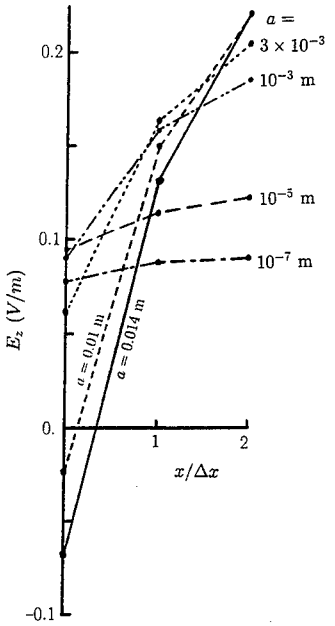

Fig. 1. E_z in the mesh at distances 0, Δx and $2\Delta x$ from a wire with radius a for Δx = 0.035 m.

$$[F_a(0, f_c\Delta x, a) + F_a(\Delta x, f_c\Delta x, a)]/2 = \log(\Delta x/2a) \tag{13}$$

independent of Δx and a. That is, the average of the two averages is equal to $\log(\rho/a)$ at $\rho = \Delta x/2$.

The ratios of E_0/E_1 and A_0/A_1 are compared in Table 1, where E_0 and E_1 are the mesh fields E_z at the wire and one Δx away, and A_0 and A_1 represent $F_a(\rho, f_c\Delta x, a)$ at $\rho = 0$ and Δx. The correspondence shows that $F_a(\rho, f_c\Delta x, a)$ tracks the field well over the range of wire radii. For the case of Figure 1, where $\Delta x = 0.035$ m and $t_{\text{fwhm}} = 17\Delta x/c$ the function $F_a(\rho, f_c\Delta x, a)$ tracks the mesh fields reasonably well out to several Δx from the wire, while for the same wire with $\Delta x = 0.1$ m and $t_{\text{fwhm}} = 6\Delta x/c$ the average tracks the mesh fields from 0 to one Δx. In the last two columns of Table 1, the average of the mesh fields $(E_0 + E_1)/2$ and $\log(\Delta x/2a)$ are compared, both normalized by their average about the wire. The correspondence is expected, since the average of equation (10) works well in driving the transmission line equations.

Using $F_a(\rho, f_c\Delta x, a)$ as a model for the averaged mesh fields, the local E_z at a distance

ρ from the wire can be related to the mesh field at the wire location as

$$E^n_{zk}(\rho) = E^n_z(i_w, j_w, k)\ln(\rho/a)/F_a(0, f_c\Delta x, a). \tag{14}$$

Equation (14) can be used with $\rho = r_t$ to obtain E^n_{zk} driving the transmission line in equation (5). However, equation (14) applies only to the E_z field due to a current on the wire. When the wire is excited with a voltage source, changing the boundary condition on $E_z(a)$, a field component due to the derivative of charge is introduced that is more slowly varying than the form of equation (14). Hence the applied voltage should be removed from the E_z mesh field before applying the correction, and the source term in equation (5) becomes

$$\begin{aligned}(E^n_{zk}\Delta x - V^{\text{inc}}_k) \rightarrow\ & \left[(E^n_{zk}\Delta x - V^{\text{inc}}_k)\ln(r_t/a)/F_a(0, f_c\Delta x, a) + V^{\text{inc}}_k\right] - V^{\text{inc}}_k \\ =&(E^n_{zk}\Delta x - V^{\text{inc}}_k)\ln(r_t/a)/F_a(0, f_c\Delta x, a).\end{aligned}$$

Equation (5) for the transmission line current then becomes

$$\begin{aligned}I^{n+1/2}_k =& I^{n-1/2}_k - \frac{\Delta t}{\Delta x\mu\epsilon}\left[Q^n_k - Q^n_{k-1}\right] \\ &+ \frac{\Delta t}{\Delta x L_w}\left[\Delta x E^n_z(i_w, j_w, k) - V^{\text{inc}}_k\right]\ln(r_t/a)/F_a(0, f_c\Delta x. a)\Big].\end{aligned}$$

Since $L_w = \frac{\mu}{2\pi}\ln(r_t/a)$, the $\ln(r_t/a)$ factors cancel to yield

$$I^{n+1/2}_k = I^{n-1/2}_k - \frac{\Delta t}{\Delta x\mu\epsilon}\left[Q^n_k - Q^n_{k-1}\right] + \frac{2\pi\Delta t}{\Delta x\mu F_a(0, f_c\Delta x, a)}\left[\Delta x E^n_z(i_w, j_w, k) - V^{\text{inc}}_k\right] \tag{15}$$

so that r_t is eliminated. Equation (15) is essentially the same as that obtained by Holland by averaging the equation, although the correction of the average is done in a different way.

When the wire is moved away from the E_z edge, Holland [5] suggested splitting the current by linear proportionality between the surrounding E_z edges. Thus for wire current I^n_k

$$J^n_z(i, j, k) = I^n_k(i + 1 - i_w)(j + 1 - j_w)/\Delta x\Delta y \tag{16a}$$
$$J^n_z(i + 1, j, k) = I^n_k(i_w - i)(j + 1 - j_w)/\Delta x\Delta y \tag{16b}$$
$$J^n_z(i, j + 1, k) = I^n_k(i + 1 - i_w)(j_w - j)/\Delta x\Delta y \tag{16c}$$
$$J^n_z(i + 1, j + 1, k) = I^n_k(i_w - i)(j_w - j)/\Delta x\Delta y \tag{16d}$$

are the current densities in the E_z update equations for the wire located at $i \le i_w < i + 1$ and $j \le j_w < j + 1$. Holland suggests using the same factors to interpolate the E_z fields from the mesh to drive equation (5). This approach gave reasonable agreement in the peaks of admittance, but poor agreement in peaks of impedance as the wire was moved within a cell.

The field average in equation (11) gave good agreement with NEC for a wire located on an H_z edge, where the current is split equally on to the four surrounding E_z edges. Examining the mesh fields from this solution showed that they do not behave as an average of a $\ln(\rho/a)$ function from the wire location, but rather behave as a sum of averaged $\ln(\rho/a)$ functions from the driven E_z edges. Generalizing to unequal edge excitations, the field averaged about a point $\mathbf{r}$ due to excited edges at $\mathbf{r}_i$ would be expected to have the form

$$\bar{E}_z(\mathbf{r}) = \sum_{i=1}^{4} c_i F_a(|\mathbf{r} - \mathbf{r}_i|, f_c\Delta x, a) \tag{17}$$

where the c_i represent excitation strengths. Assuming that the edge fields are excited in proportion to the currents driving them. the c_i will be in the ratio of the split currents. Then defining the factors

$$\begin{aligned} x_1 &= x_{1,1} = (i+1-i_w)(j+1-j_w) \\ x_2 &= x_{2,1} = (i_w-i)(j+1-j_w) \\ x_3 &= x_{1,2} = (i+1-i_w)(j_w-j) \\ x_4 &= x_{2,2} = (i_w-i)(j_w-j) \end{aligned}$$

equation (17) becomes

$$\bar{E}_z(\mathbf{r}) = C\sum_{i=1}^{4} x_i F_a(|\mathbf{r}-\mathbf{r}_i|, f_c\Delta x, a).$$

This leaves one unknown constant C that can be determined from the known average field at a mesh edge. Since we are assuming four excited edges, C can be evaluated as a weighted average as

$$C = \sum_{j=1}^{4} \alpha_j \bar{E}_z(\mathbf{r}_j) \qquad \text{where} \qquad \alpha_j = x_j \Big/ \sum_{i=1}^{4} x_i F_a(|\mathbf{r}_j-\mathbf{r}_i|, f_c\Delta x, a)$$

and $\sum x_j = 1$. The local field at a point $\mathbf{r}$ can then be evaluated as

$$E_z(\mathbf{r}) = C\sum_{i=1}^{4} x_i \ln(|\mathbf{r}-\mathbf{r}_i|/a).$$

The field driving the transmission line is this local field averaged over the outer shell of the transmission line. Assuming a transmission line with radius r_t located a distance r_d from an excited edge, the average of the log function is evaluated as

$$\begin{aligned} \bar{E}_t &= \frac{1}{2\pi}\int_0^{2\pi} \ln\left[(r_t^2 + r_d^2 - 2r_t r_d\cos(\phi))/a\right)\, d\phi \\ &= \ln(r_{\max}/a) \end{aligned}$$

where $r_{\max} = \max(r_t, r_d)$. Hence, if r_t is made large enough to enclose all driven edges, the average field for use in equation (5) in the k plane becomes

$$\begin{aligned} E_{zk}^n =& C\ln(r_t/a) = \ln(r_t/a)\sum_{j=1}^{4}\alpha_j E_{zk}(\mathbf{r_j}) \\ =& \ln(r_t/a)\Big[\alpha_1 E_z^n(i_w, j_w, k) + \alpha_2 E_z^n(i_w+1, j_w, k) \\ &+ \alpha_3 E_z^n(i_w, j_w+1, k) + \alpha_4 E_z^n(i_w+1, j_w+1, k)\Big]. \end{aligned} \tag{18}$$

Using (18) in equation (5), and subtracting the applied field from E_z results in the update equation

$$\begin{aligned} I_k^{n+1/2} = I_k^{n-1/2} - \frac{\Delta t}{\Delta x\mu\epsilon}\left(Q_k^n - Q_{k-1}^n\right) + \frac{2\pi\Delta t}{\Delta x\mu}\Big[\Delta x\Big(\alpha_1 E_z^n(i_w, j_w, k) + \alpha_2 E_z^n(i_w+1, j_w, k) \\ + \alpha_3 E_z^n(i_w, j_w+1, k) + \alpha_4 E_z^n(i_w+1, j_w+1, k)\Big) - \alpha_{\text{sum}} V_k^{\text{inc}}\Big] \end{aligned} \tag{19}$$

where $\alpha_{\text{sum}} = \sum_{i=1}^{4} \alpha_i$. The transmission line radius r_t is eliminated in the averaging. However, it would still occur in the equations involving voltage, since the transmission line voltage depends on the characteristic impedance of the line.

The input impedance of a a 1.4 m dipole modeled with cell size of 0.035 m is shown in Figure 2 as the wire is moved within a cell. The excitation was a voltage source spread over the center three segments (current nodes). The results in Figure 2a, using equation 19, show good agreement with NEC and independence of wire position. Similar results were obtained for the imaginary part of impedance and with other wire radii. Results in Figure 2b were obtained by splitting the wire current among the cell edges according to equation 16, as done for Figure 1a, but the electric field driving the transmission line equations was obtained as a weighted average of the surrounding mesh fields, using the average inductance of [5, eq. 53]. Much more variation is seen in the peaks of impedance as the wire is moved. However, when the results of Figure 1b are plotted as admittance, there is only a few percent variation in the admittance peaks as the wire is moved, similar to Holland's results.

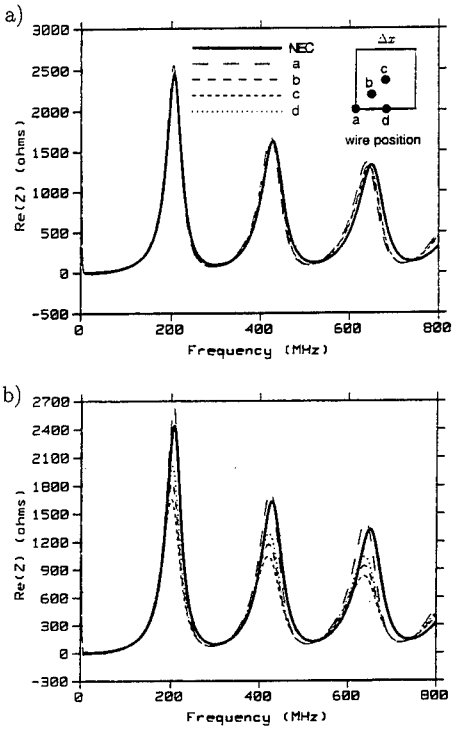

Fig. 2. Real part of input impedance as a 1.4 m dipole is moved within the mesh; a) result of equation (19), b) result using average cell inductance and linearly weighted average of mesh fields.

Adjustment of wire length

When equations (5) or (19) are solved with N charge (or voltage) nodes and fixed node spacing of Δz, the effective length of the wire is $N\Delta z$. The solution will include $N+1$ current nodes, including I_1 and I_{N+1} which have zero current and are located at $\Delta z/2$ before Q_1 and after Q_N, respectively. The length of the wire can be adjusted if the central difference for the derivate of current is replaced by a second-order approximation with arbitrary location of the zero current nodes. If the points where the current goes to zero are extended by δ from their normal positions on either ends of the wire, the derivatives are

$$\left.\frac{dI(z)}{dz}\right|_{z \text{ at } Q_1} = I_2 \frac{\Delta z - \delta}{\Delta z(\delta + \Delta z)} + I_3 \frac{\delta}{\Delta z(\delta + 2\Delta z)}$$

$$\left.\frac{dI(z)}{dz}\right|_{z \text{ at } Q_N} = -I_N \frac{\Delta z - \delta}{\Delta z(\delta + \Delta z)} - I_{N-1} \frac{\delta}{\Delta z(\delta + 2\Delta z)}$$

Results of adjusting the end locations by $\pm\Delta z/2$ from their normal positions on either end are shown in Figure 3, and are in good agreement with NEC. These results used $\Delta z = 0.1$

m, so the agreement with NEC is not as good as in Figure 2.

Conclusion

It was shown that the accuracy of results for wires moved laterally from mesh edges can be greatly improved by taking account of the behavior of the field in the vicinity of the wire. Also, the distance to the end of the wire can be adjusted within a cell by using a general second-order difference form for the derivative. Making the wire location completely independent of the mesh would require the additional ability to tilt the wire with respect to the edges. This seems to be a considerably more difficult problem than moving the wires laterally, since the component of the mesh field parallel to the wire gets mixed with the larger radial electric field due to charge on the wire. Simply averaging the mesh fields did not seem to work well, except in the case where the wire was tilted in one coordinate plane, and the mesh fields above and below the plane of the wire, on edges orthogonal to the wire normal, could be averaged. Further study is needed to develop a more general capability to tilt a wire with respect to the mesh.

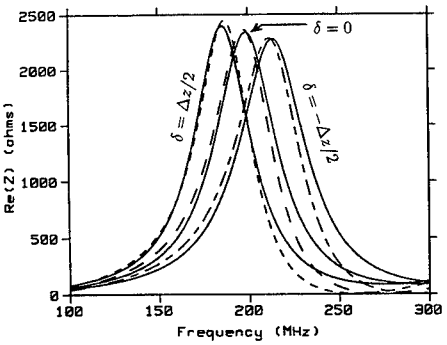

Fig. 3. Real impedance of a dipole antenna with radius 0.001 m, modeled with 14 charge nodes and Δz = 0.1 m, comparing NEC (solid) and FDTD (dashed). FDTD end points are extended by δ for effective lengths of 1.3, 1.4 and 1.5 m.

References

[1] K. S. Yee, "Numerical solution of initial boundary value problems involving Maxwell's equations in isotropic media," *IEEE Trans. Antennas Propagat.*, v. AP-14, pp. 302-307, May 1966.

[2] D. E. Merewether and R. Fisher, "Finite Difference Solutions of Maxwell's Equation for EMP Applications," Final Report on Contract DNA001-78-C-0231, April 22, 1980.

[3] K. R. Umashankar, R. A. Taflove and B. Beker, "Calculation and Experimental Validation of Induced Currents on Coupled Wires in an Arbitrary Shaped Cavity," *IEEE Trans. Antennas and Propagation*, v. 35, pp. 1248-1257, 1987.

[4] D. E. Parks, J. L. Gilbert and I. Katz, "A Technique for Treating Small Current-Carrying Struts in Electromagnetic Particle Codes," *Syst. Sci. Software*, SSS-R-76-2847, Jan. 1976.

[5] R. Holland, "Finite-Difference Analysis of EMP Coupling to Thin Struts and Wires," *IEEE Trans. Electromagnetic Compatibility*, v. EMC-23, no. 2, May 1981.

[6] D. J. Riley and C. D. Turner, "The *VOLMAX* Transient Electromagnetic Modeling System, Including Sub-Cell Slots and Wires on Random Non-Orthogonal Cells," *Proceedings of the 14th Annual Review of Progress in Applied Computational Electromagnetics*, Monterey, CA, March 1998.

[7] A. R. Bretones, R. Mittra and R. G. Martin, "A Hybrid Technique Combining the Method of Moments in the Time-Domain and FDTD," *IEEE Microwave and Guided Wave Letters*, v. 8, no. 8, pp. 281-283, Aug. 1998.

[8] G. J. Burke and A. J. Poggio, Numerical Electromagnetics Code (NEC) – Method of Moments, UCID-18834, Lawrence Livermore National Laboratory, CA, January 1981.

A Practical Method for Increasing the Speed and Stability of the Matrix Solve in Moment Method Simulations Within a Frequency Band

Hugh MacMillan and John M. Dunn

University of Colorado
Department of Electrical and Computer Engineering
Campus Box 425, Boulder, CO, 80309-0425

A method is investigated to speed up the solve time of matrix problems which arise in moment method numerical methods for electromagnetic field simulations using the mixed potential form of the EFIE [1, 2]. The method hinges on transforming the matrix to a curl-free (TM) and divergence-free (TE) basis. A singular value decomposition is then separately performed on the two respective diagonal blocks of the matrix. The result is a natural basis and testing space that separates the contributions of the TE and TM currents. For simulations over a band of frequencies, there is great potential for improvement of both speed and stability. Generating the above full domain boundary elements by performing the SVD on the matrix at a central frequency in the band, and by extracting this matrix from those at the surrounding bands, the knowledge of the singular values leads to an effective preconditioner over the matrices in the band. This is effectively applying the regularization developed by Vecchi et al. to non-static, yet non-resonant, regimes [3, 4]. Indeed at resonance, the ill-conditioning of the EFIE is more fundamental. It is found that only the dominant (smallest) singular values of the TM block need to be retained in order to express the solution, the current on the planar conductor. As such, a full SVD on the TM block is not necessary, only the first several singular values and their corresponding eigenfunctions need to be calculated. These are the currents that result in slowly varying (in space) charge. Unfortunately, the contribution to the solution from the TE part of the new basis is more complicated. In addition to the large singular value slowly varying TE current, many more rapidly varying TE eigenfunctions contribute to the solution in order to satisfy boundary conditions at the ports and edges of the planar conductors. Nevertheless, by preconditioning the matrices within the band and only using several TM basis functions, the new matrices to be solved are roughly half in size with conditioning that admits faster iterative techniques in place of the standard LU direct solvers.

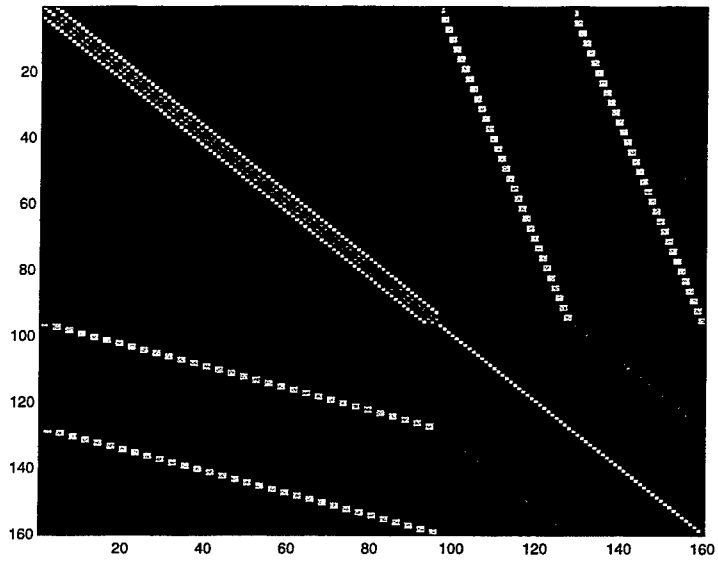

Figure 1: The original banded MoM matrix using a 2−dimensional rooftop basis for a 16mm long, .3mm wide 1−port line suspended above an hypothetical air substrate of height .5mm. The diagonal elements are largest and subbanding is due to typical numbering scheme. Here, the strip is discretized into $3X32$ cells, resulting in a $160X160$ matrix.

References

[1] A.W. Glisson and D.R Wilton, *Simple and efficient numerical methods for problems of electromagnetic radiation and scattering of surfaces*, IEEE Trans. on Antennas and Propagation **AP-28** (1980), 593–604.

[2] Juan R. Mosig and Fred E. Gardiol, *A dynamical radiation model for microstrip structures*, Advances in Electronics and Physics **59** (1982), 139–237.

[3] Giuseppe Vecchi et al., *A numerical regularizatoin of the efie for three-dimensional planar structures*, Int. J Microwave Millimeter-Wave CAE **7** (1997), 1–22.

[4] ———, *Analysis of cavity modes for the efie*, IEEE Trans. on Antennas and Propagation **AP-44** (1998), 234–239.

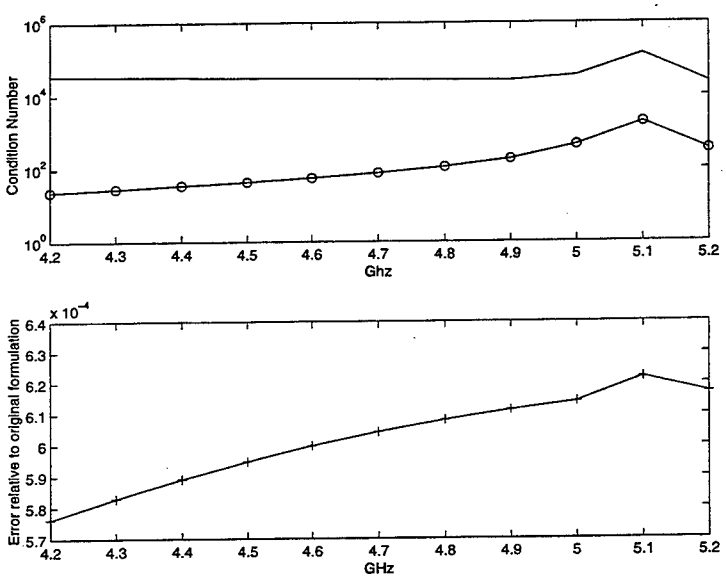

Figure 2: The top figure shows the condition number before and after the preconditioning. The bottom figure shows that by transforming to the SVD basis functions and inverting the singular values to precondition the matrix, sufficiently small error relative to the original formulation is maintained. The original solution is solved to machine accuracy using Matlab's LU direct solve.

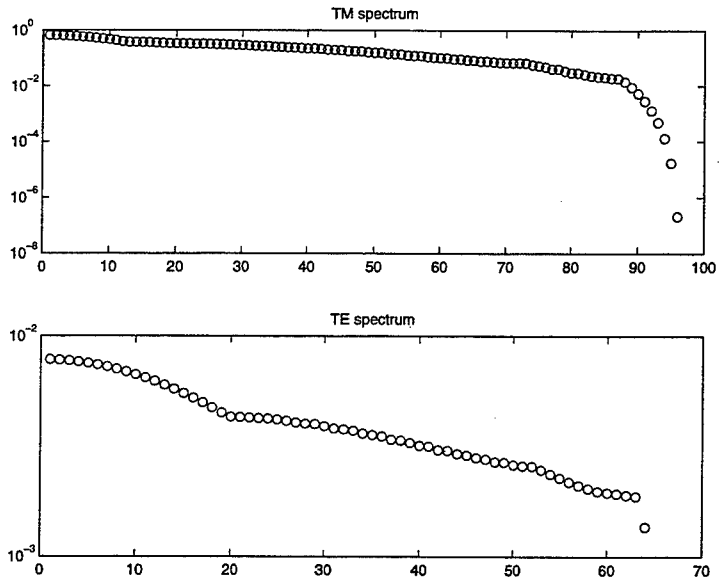

Figure 3: The TE part is purely an integral operator and has rapidly varying currents corresponding to its lowest singular values. On the other hand, lowest singular values of the integro-differential TM operator corresponds to slowly varying charge.

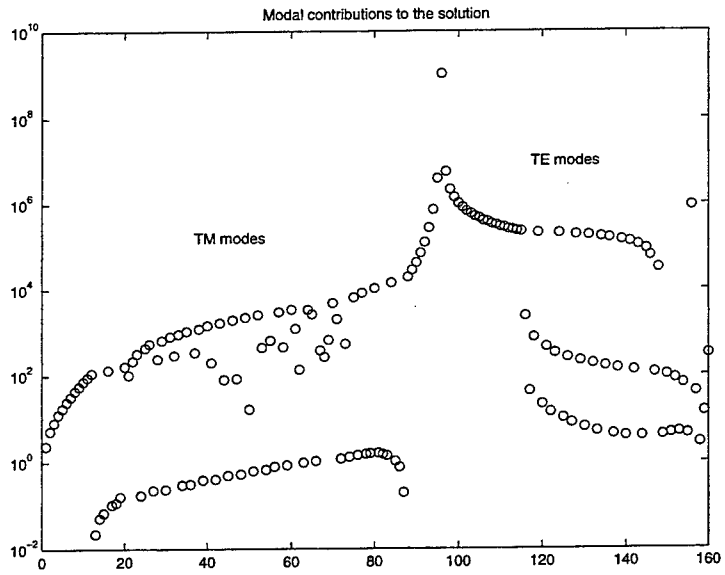

Figure 4: The solution's make-up in terms of the spectrum. The central spike corresponds to slowly varying TE and TM components contributing to the solution current.

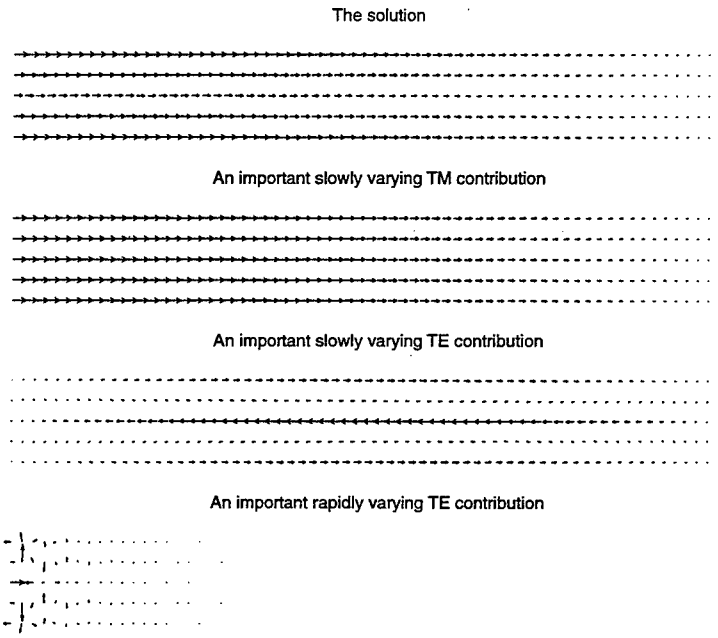

Figure 5: The solution, and the dominant TM and TE contributions. Where as only the slowly varying TM modes have a significant contribution, the solution calls on TE modes scattered about the TE spectrum

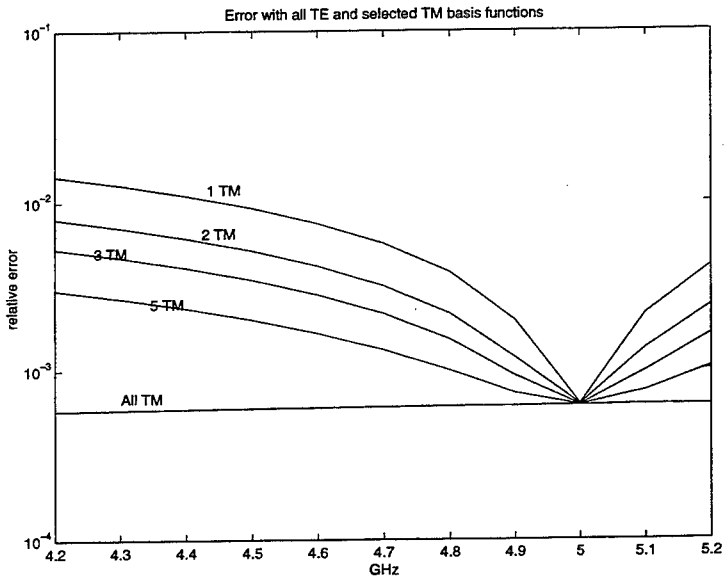

Figure 6: The effect of reducing the representation in TM modes, while maintaining all of the TE contributions. Again, the error is relative to the original MoM formulation.

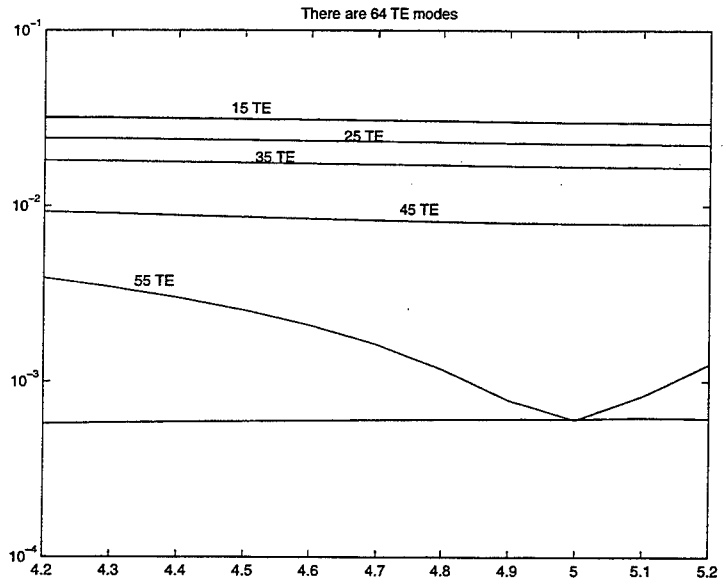

Figure 7: The effect of reducing the respresentation in TE modes while using only the first five lowest TM modes.

Modeling the Bifilar Helix Antenna using NEC 4.1

Steven R. Best
Cushcraft Corporation
48 Perimeter Road
Manchester, NH 03103

Abstract: The Numerical Electromagnetics Code (NEC 4.1) is used to model the radiation characteristics of a bifilar helix antenna. The performance parameters of interest are the antenna's boresight directivity and front-to-back ratio. While using NEC 4.1 to model the antenna's boresight directivity as a function of frequency, it was discovered that NEC 4.1 would not converge to a unique solution as a function of the segment wire radius chosen in the model. Numerical results are presented for a bifilar helix antenna with the number of wire segments in the antenna and the segment wire radius as variables. It is demonstrated that NEC 4.1 does not converge to a unique solution for any chosen value of segment wire radius.

Introduction: The bifilar helix antenna can be designed to provide moderately high directivity with good circular polarization axial ratio. The antenna is simple to construct, having only two helical arms and a single feed point. Additionally, directive radiation can be obtained without the use of a ground plane or reflective structure. In many applications, the bifilar helix is an attractive alternative to a monofilar or a quadrifilar helix antenna.

The initial objective of this work was to model the performance of the bifilar helix antenna as a function of the antenna's pitch ratio (axial length per turn/diameter) and the number of helical turns. Particular emphasis was to be placed on the fact that the antenna could be operated in a bi-directional end fire mode or a unidirectional end fire mode.

To provide a comprehensive analysis of this antenna, it is necessary to describe the antenna's boresight directivity and front-to-back ratio over some predetermined range of frequencies. When attempting to model the antenna's performance over a wide frequency range, it was discovered that NEC 4.1[1] would not converge to a unique solution as a function of the antenna's wire radius.

This paper will present the results of a brief numerical study of the bifilar helix antenna's boresight directivity performance as a function of frequency. Front-to-back ratio information is not presented. The modeling parameters varied were the number of segments used to describe the antenna and the wire radius (a).

Antenna Description: The antenna that was modeled in this study was a 2-turn bifilar helix as shown in Figure 1. The antenna has a diameter of 6.706 centimeters and an axial length of 13.411 centimeters.

To initially model the bifilar helix using NEC 4.1, the antenna structure was broken into wire segments with the antenna's helical arms being subdivided into 12 segments per helical turn and the antenna's straight wire sections being subdivided into 5 segments. This resulted in a wire segment length of 1.823 centimeters along the helical structure.

For numerical comparison, the antenna's helical arms were also subdivided into 36 and 72 segments per helical turn, resulting in a segment length of 0.613 centimeters and 0.307 centimeters, respectively. The antenna's straight sections were subdivided into 11 and 23 segments for the 36 and 72 segments per helical turn configurations, respectively.

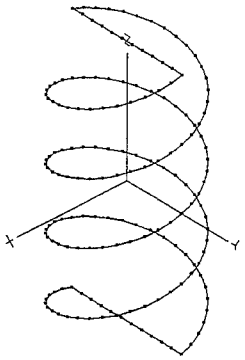

Figure 1. 3-dimensional View of the Bifilar Helix Antenna.

Numerical Results – Directivity Analysis: To evaluate the performance of the bifilar helix antenna, the first parameters of interest were the antenna's boresight directivity and front-to-back ratio as a function of frequency. The frequency range of interest was 500 to 3000 MHz. For the numerical analysis, the boresight directivity was calculated every 10 MHz, resulting in 251 frequency sample points. Front-to-back ratio information is not presented.

To determine the suitability of the wire segment model, the wire segment length and overall structure dimensions were compared to the operating wavelengths across the frequency band. Table 1 illustrates the dimensional comparison of the antenna relative to the operating wavelength.

Table 1. Antenna Structure Dimensions Compared to Operating Wavelength

	500 MHz	**1750 MHz**	**3000 MHz**
Wavelength	59.96 cm	17.13 cm	9.99 cm
Antenna Length	0.2237 λ	0.7829 λ	1.3425 λ
Antenna Diameter	0.1118 λ	0.3915 λ	0.6712 λ
Segment Length (12 segments)	0.0304 λ	0.1064 λ	0.1824 λ
Segment Length (36 segments)	0.0102 λ	0.0358 λ	0.0613 λ
Segment Length (72 segments)	0.0051 λ	0.0179 λ	0.0307 λ

The NEC documentation recommends that the wire segment length be less than 0.10 λ and no smaller than 0.001 λ. With the exception of the configuration with 12 segments per helical turn, this condition is satisfied across the entire frequency band of interest.

The wire radius (a) selected in the numerical model ranged from 4.0×10^{-4} meters to 1.0×10^{-20} meters. The NEC documentation recommends that the wire segment length to wire radius ratio be greater than 8 and that $2\pi a/\lambda$ be less than 1. Table 2 illustrates the segment length to wire radius ratio values and a calculation of $2\pi a/\lambda$ for the different wire radii used in the analysis of the bifilar helix antenna.

Table 2. Segment to Wire Radius Ratio (R) and a Calculation of $2\pi a/\lambda$.

Radius (a)	$2\pi a/\lambda$	R (12 segments)	R (36 segments)	R (72 segments)
4×10^{-4}	0.0147	45.58	15.33	7.68
2×10^{-4}	0.00734	91.15	30.65	15.35
1×10^{-4}	0.00367	182.3	61.3	30.7
5×10^{-5}	0.00183	364.6	122.6	61.4
5.96×10^{-6}	0.00022	3059	1029	515
1×10^{-6}	3.67×10^{-5}	18230	6130	3070
1×10^{-10}	3.67×10^{-9}	0.18×10^{9}	N/A	N/A
1×10^{-12}	3.67×10^{-11}	1.8×10^{10}	N/A	N/A
1×10^{-14}	3.67×10^{-13}	1.8×10^{12}	N/A	N/A
1×10^{-20}	3.67×10^{-19}	1.8×10^{18}	N/A	N/A

Note: $2\pi a/\lambda$ is calculated at 1750 MHz

With the exception the largest wire radius and the 72 segment per helical turn configuration, all of the wire radii chosen meet the NEC documentation requirements.

The first bifilar helix antenna modeled was the 12 segment per turn configuration. The boresight directivity was initially calculated for a wire radius of 0.0004 meters over the entire frequency band of 500 to 3000 MHz. In an attempt to gain confidence in the numerical model, the wire radius was adjusted and the directivity versus frequency was recalculated. At this point, it was evident that the NEC 4.1 calculations had not converged to a unique solution and the radius was adjusted again. No evidence of converge was obtained for any value of radius selected. Figures 2 and 3 present the boresight directivity of the bifilar helix versus frequency for the various radii of Table 2.

As evident in Figures 2 and 3, there is only a very small region of frequency where the directivity appears to converge as a function of wire radius. As the wire radius becomes very small, less than 1×10^{-10}, there appears to be more consistent results in the lower half of the frequency band but this does not hold at the upper frequencies.

The next step in the analysis process was to increase the number of segments per turn in the helical arms from 12 to 36 and then from 36 to 72. This significantly reduces the segment length relative to the operating wavelength. The values of the segment length to wire radius ratios are well within the requirements as specified in the NEC documentation. Figures 4 and 5 present the bifilar helix directivity as a function of frequency and wire radius for the 36 segment and 72 segment per helical turn antennas, respectively. The wire radius is only varied from 0.0004 meters to 0.000001 meters. As evident from Figures 4 and 5, converge is not reached within this range of radii values for either configuration. Apparent numerical convergence occurs only at the low end and extreme upper end of the frequency band. At 1650 MHz, there is a spread of over 7 dB in calculated boresight directivity over the range of radii.

To understand how the number of segments, or rather how the segment length affects numerical convergence, the directivity of each configuration was compared at fixed radius values. Figures 6, 7 and 8 present directivity versus frequency calculated for each antenna configuration with wire radius values of 0.0004m, 0.00005 m and 0.000001 m, respectively. From these figures, it is evident that the 36 and 72 segment per helical turn configurations are in very good

agreement. The 12 segment per helical turn configuration is consistent with the other configurations but it obvious that it may not provide sufficient structural accuracy. From these curves, it is apparent that consistent results can be obtained with a different number of segments per helical turn at a given wire radius. However, it is interesting to note that this condition is not valid for a given value of segment length to wire radius ratio.

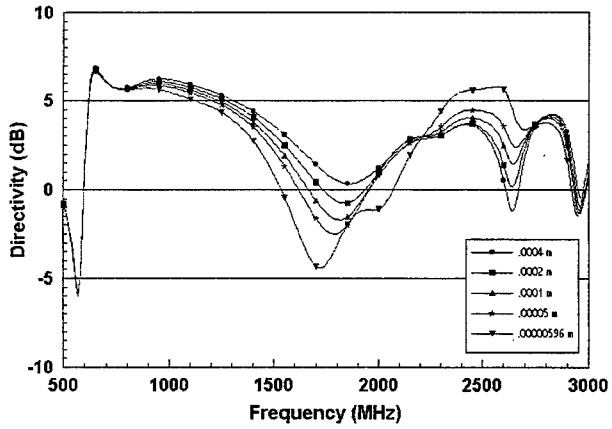

Figure 2. Directivity versus Frequency as a Function of Wire Radius. Bifilar Helix with 12 Segment per Turn.

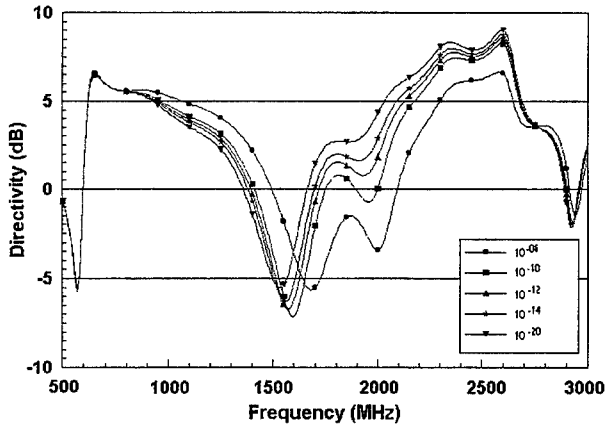

Figure 3. Directivity versus Frequency as a Function of Wire Radius. Bifilar Helix with 12 Segment per Turn.

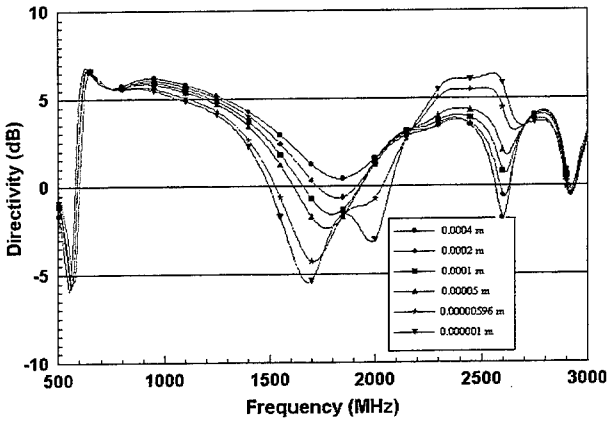

Figure 4. Directivity versus Frequency as a Function of Wire Radius. Bifilar Helix with 36 Segment per Turn.

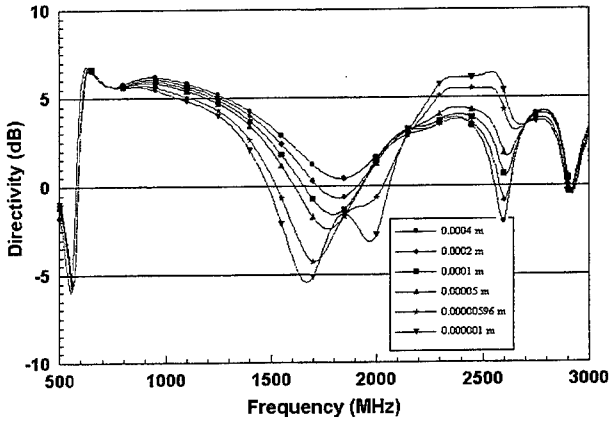

Figure 5. Directivity versus Frequency as a Function of Wire Radius. Bifilar Helix with 72 Segment per Turn.

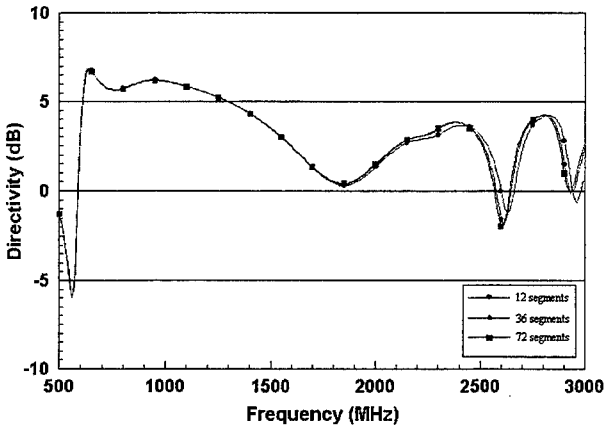

Figure 6. Directivity versus Frequency as a Function of the Number of Segments per Helical Turn. The Wire Radius is 0.0004 m.

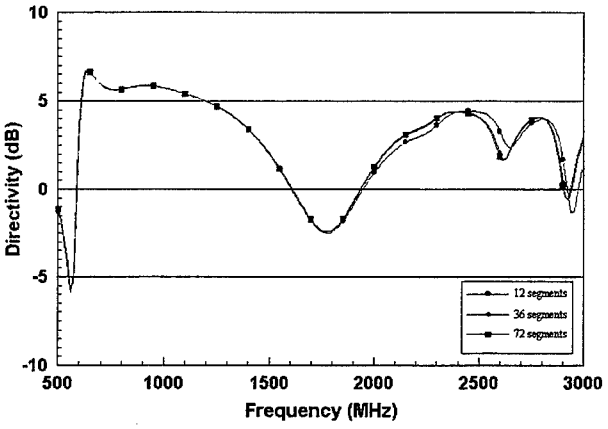

Figure 7. Directivity versus Frequency as a Function of the Number of Segments per Helical Turn. The Wire Radius is 0.00005 m.

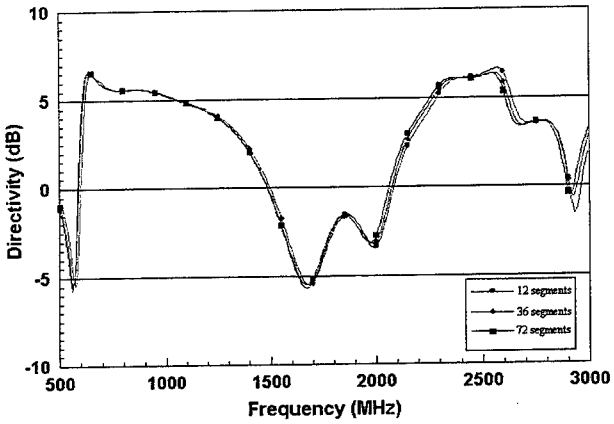

Figure 8. Directivity versus Frequency as a Function of the Number of Segments per Helical Turn. The Wire Radius is 0.000001 m.

Numerical Results - Pattern Analysis: In addition to the evaluation of boresight directivity as a function of frequency, it was important to evaluate the computed radiation pattern of the bifilar helix as the wire radius was varied. The radiation patterns for the antenna were computed at 650 MHz and 1650 MHz for the configuration with 72 segments per helical turn. These frequencies were selected because it appeared that numerical convergence occurred at 650 MHz but it did not occur at 1650 MHz. Radiation patterns were calculated for wire radii of 1×10^{-4} m, 1×10^{-5} m and 1×10^{-6} m. Radiation patterns are presented in Figures 9 and 10 for 650 and 1650 MHz, respectively.

From these radiation patterns, it is obvious that good numerical convergence does exist at 650 MHz but not at 1650 MHz. Although the radiation patterns at 1650 MHz for the different wire radii have almost identical maximum directivity, the variation between the calculated patterns is significant.

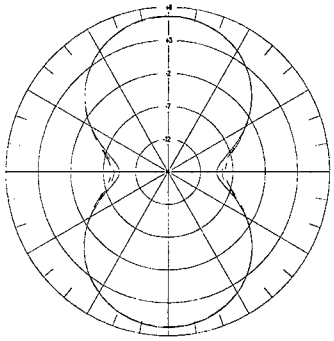

Figure 9. Radiation Pattern of the 72 Segment per Turn Configuration at 650 MHz. Wire Radius Varied.

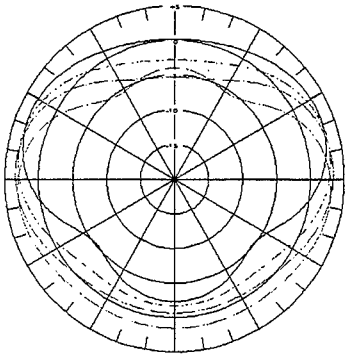

Figure 10. Radiation Pattern of the 72 Segment per Turn Configuration at 1650 MHz. Wire Radius Varied.

Conclusion and Future Work: A numerical analysis of the bifilar helix antenna has been presented. It was demonstrated that with a reasonable structure size, segment length and wire radius, numerical convergence could not be achieved with NEC 4.1 over the entire desired range of frequency bandwidth. As the wire radius was varied, as much as 7 dB variation in computed boresight directivity occurred. Future work should include additional analysis of the same antenna with an increased number of segments. Additionally, a similar analysis should be performed with other commercially available Method of Moments codes.

References: [1] Gerald Burke. Numerical Electromagnetics Code – NEC 4. Method of Moments. January 1992.

MMSNEC - Multiple Matrix Solver NEC

J. v. Hagen[1] R. Mittra[1] D. Werner[2]

[1]Electromagnetic Communication Research Laboratory
[2]Electrical Engineering Department
The Pennsylvania State University
224 EE East
University Park, PA 16802-2706

1 Introduction

Efficient solution of dense linear systems of equations arising in the Method of Moment (MoM) formulation is of considerable interest. While the time needed to fill the moment matrix is proportional to the square of the number of unknowns n, the solution of the system

$$Z\,I = V \tag{1}$$

(Z is the impedance matrix, I is the unknown current vector, V is the excitation vector) using a standard Gauss LU factorization scheme requires $\mathcal{O}(n^3)$ operations. For small problems, the fill time of the matrix is usually higher than the time it takes one to factorize it; however, for large n, the reverse is true and factorization time dominates the fill time, and, techniques to reduce the factorization time are highly sought after. In many situations, the user prefers to use a legacy MoM and speed up its solution, rather than rewriting the entire code using the Fast Multipole or other similar approaches to reduce the CPU time. The principal advantage of this approach is that only a small part of an existing program needs to be modified. To test different solution algorithms and to demonstrate their ease of implementation, we have chosen to add functionality to the NEC 4 code. Modifications of NEC 2 are equally possible as both codes differ only slightly in their solver subroutines. Beside the original LU decomposition in the NEC and LAPACK's LU decomposition, three different iterative algorithms and four different preconditioning techniques have been implemented to-date.

In Sec. 2 of this paper, we describe the different algorithms and identify both their strong and weak points. New cards that use the added functionality are presented in Sec. 3. A test case involving a wiregrid patch array with 1944 unknowns is discussed in Sec. 4.

2 Solver Algorithms and Preconditioners

2.1 *LU* Factorization

The preferred algorithm for solving general, complex, unstructured linear systems is the Gauss elimination or LU factorization. As a first step, the matrix Z is factorized to yield lower and a upper triangular matrices L and U, respectively. The unknowns I are then solved for in two steps, *viz.*, forward and back substitution. Mathematical libraries, e.g., the free LAPACK library, provide good and reliable routines using advanced techniques such as blocking. For comparison purposes, we have included the LAPACK routines ZGETRF/ZGETRS into this version of NEC and have

found that, in general, they improve the factorization and solve times. This is even more so when the matrix-matrix multiplication subroutines ZGEMM are tuned for the appropriate processor, or when vendor-provided BLAS libraries are used (cf. Acknowledgements).

2.2 Iterative Solver

For sparse matrices, i.e., matrices where only a few elements are non-zero, iterative methods that only require matrix-vector multiplications involving the original, unchanged matrix and some vectors, are found to decrease significantly the computation times. For full, diagonally-dominant matrices, the iterative solvers can reduce the computation time to solve (1) quite considerably.

A number of iterative algorithms have been published in the literature. It has been demonstrated that the quasi-minimal residual methods and their transpose-free variants have been shown to converge more smoothly [1] than the well-known (bi-)conjugate gradient methods. Fortran subroutines for various iterative solvers are available on the internet (`http://www.netlib.org/linalg/qmr`). In modifying the NECsolver, we have incorporated three different iterative algorithms: the Transpose–Free Quasi–Minimal Residual (TFQMR), the Quasi-Minimal Residual (QMR) and the Biconjugate Gradient (BCG-from-QMR) algorithms. All of these algorithms are based on the Lanczos methods without look-ahead, so that the additional memory requirements, over and above those for the original matrix and the right-hand-side vector, are quite minimal. The various matrix-vector multiplications are carried out by using the BLAS routines.

For the problems tested, the TFQMR method only used vector-matrix multiplications with the untransposed matrix. Furthermore, the solution vector always converged to the required limit faster than when the other two algorithms are used.

2.3 Preconditioner

Preconditioning techniques modify the original matrix Z, so that the system involving the resulting matrix Z' is easier and faster to solve. The solution I of the preconditioned system

$$Z' I = V \tag{2}$$

for the excitation V is an estimate for the exact solution I_e of (1). Obviously, Z' must represent the original matrix Z at least partially, so that I is close enough to I_e. In the following we propose several schemes on how to chose Z' for a given Z.

Since the preconditioning of (2) introduces some error when approximating the matrix Z, I will not be the exact solution I_e that satisfies (1). To improve the accuracy of I, one employs an iterative refinement procedure, which uses the original matrix Z as well as the preconditioned and factorized matrix Z'. The algorithm obtains a series I_k for the estimate I by solving for the error or (residual) $V_{k-1} - ZI_{k-1}$ from the equation

$$Z' I_k = V_{k-1} - ZI_{k-1} = V_k \tag{3}$$

The starting point for the first estimate is

$$Z' I_0 = V_0 = V \tag{4}$$

and the final solution I is derived from

$$I = I_0 + I_1 + \cdots + I_n \tag{5}$$

If the preconditioned matrix Z' is factorized, each iteration necessitates only one forward and one back substitution to obtain I_k. Also, V_{k+1} is obtained by one matrix-vector multiplication and one vector-vector subtraction. The iteration procedure is terminated when either $V_k - ZI_k$ or I_k is sufficiently small. Clearly, both the matrix Z and the factorized Z' must be stored in this procedure. We therefore use preconditioners that require only small additional storage for Z'. Since the cost for one iteration described in (3) is only $\mathcal{O}(n^2)$, the iterative algorithm provides an accurate solution much more rapidly than a direct solution if the factorization of Z' is much less expensive than the one of Z.

Physically, the different matrix elements Z_{ij} express the fields sampled by the weighting function i generated by the basis function j. For a local discretization scheme for straight wires, this is the sampled field on the segment i at the position $\vec{r}$, radiated by the current element located on segment j at the position $\vec{r}'$. The interaction between the segments that are separated by a large distance $\vec{R} = \vec{r} - \vec{r}'$ is relatively weak, since the free-space Green's function decays as $1/|\vec{R}|$. The interaction between two segments can be so weak that the corresponding elements of Z_{ij} only have a very slight influence on the solution I. There are two possible schemes for neglecting the influence of these elements, *viz.*, the block diagonal and band preconditioning. An alternative is to employ for the preconditioned matrix of Z' the factorized matrix of Z obtained previously at another frequency. It is expected that this would yield good estimates for frequencies f close to f'; however, the procedure may need many iterations when f and f' are far apart. Finally, the last technique is to reduce the matrix size and, hence, reduce the factorization time, by assuming a constant relationship for the different elements of I.

For multiple excitations V, the iteration described in (3) must be carried out for each V. For many situations, the total time for a preconditioned solver can become higher than for a complete LU factorization. The choice to apply a preconditioner must thus be made by the user, who must decide if it is advantageous for him to do so.

2.3.1 Block Diagonal Solver

For scatterers comprising multiple objects, the matrix Z can be partitioned into several blocks. Each diagonal block relates the currents on only one scatterer, while the off-diagonal blocks express the coupling between different scatterers. In [2], the authors have presented a method to compress the off diagonal blocks by incomplete QR and to include them into the solution step. In this paper we propose to neglect them altogether in the factorization step.

For S identical scatterers with m unknowns, the complete factorization cost is $\mathcal{O}\left((Sm)^3\right)$. Using the diagonal blocks reduces this to only $S\mathcal{O}(m^3)$. For example, for 81 scatterers with 24 unknowns each, the blocked factorization is 6561 times less expensive than the complete factorization.

2.3.2 Band Solver

In this approach we neglect the interaction of segments farther apart than a certain threshold distance. If the matrix Z is ordered such that for each element Z_{ij} the distance $i-j$ corresponds also to the physical distance between the elements i and j, we can easily accomplish this by choosing only a band matrix Z', which can then be stored and solved by appropriate banded matrix algorithms such as ZGBTRF/ZGBTRS in LAPACK.

The cost for one band factorization for a banded matrix with k_l sub- and k_u super-diagonals is $2nk_lk_u$ flops. With $k_l, k_u = 0.1n$, the cost for a factorization is only 0.03 or 3% of the complete solution, with an operational count of $2n^3/3$.

This technique is particularly suited for scatterer geometries for which one can assume that, at some distance, the coupling between two segments is negligible.

2.3.3 Modified Iterative Refinement MIR

To implement the modified iterative refinement algorithm, the factorized matrix of a previous solution at frequency f' is used for the preconditioned matrix Z' [3]. However, the storage requirements are doubled in this case, which might be prohibitive for systems with a large number of unknowns.

2.3.4 Pattern Solver

Local basis and testing functions in the Method of Moments are able to model arbitrary surfaces. This is not only true for general 3-D shapes, but also for arbitrary wire type structures. Therefore, often local basis and testing functions are typically utilized in the MoM formulation even though this leads to a very large matrix. However, the global functions, that can help reduce the matrix size considerably, can be used to model specific geometries very closely, though they are less suited for general structures. We propose a solver algorithm that combines the advantages of both of these discretization schemes, *viz.*, the ability to model arbitrary shapes with local basis and testing functions, and the fast solution of a small linear system.

In many cases, the spatial distribution of the current on the scatterer can be predicted and only the amplitude or the weight coefficient may be regarded as the unknonwn. In those cases, several localized functions can be grouped together by taking advantage of the known shape and applying it to the vectors I and V in (1). The resulting equation is a smaller system generated by two matrix-matrix multiplications with the pattern matrix P_p:

$$P_p^T Z P_p \, I = P_p^T V \tag{6}$$

The resulting matrix $P_p^T Z P_p$ is much smaller than the original matrix Z, and, consequently the solution time is much smaller as well. Usually the multiplications in $P_p^T Z P_p$ are not carried out explicitly, because P_p is sparse.

Without iterative refinements, the errors in the individual current distributions can be high. Errors for the near and far field quantities are usually much lower ($\ll 10$ %), as these are derived by integration from the currents, a process that tends to cancel out the individual errors.

2.4 Condition Number

A measure of linear system sensitivity is the condition number

$$\kappa(Z) = ||Z||\ ||Z^{-1}|| \tag{7}$$

defined for a square matrix Z. Several different condition numbers, that are based on the use of different norms, may be used for this purpose, though the most frequently-used are 1, 2 or ∞ norms. The condition number as defined in (7), is a norm-dependent quantity; however, all condition numbers are somewhat equivalent, and a system which is ill-conditioned in one norm, i.e., has a high κ, is also going to be ill-conditioned in another norm [4].

The determination of the condition number in (7) involves the computation of the norm of the inverse of the original matrix; however, this step is usually not performed. Computing the κ_∞ condition number is exactly three times as expensive as solving the corresponding system. To check if the system in (1) is ill-conditioned, the condition number can be estimated by using the LU factorization that involves only $\mathcal{O}(n^2)$ operations. The LAPACK library includes a subroutine to estimate the condition number ZGECON. Since this routine is based on the LU factorization, it rarely underestimates the actual condition number.

3 New Cards

The first card, the MS card allows the user to choose the appropriate algorithm and to provide necessary input parameters. Additional input parameters for some of these solvers are provided by the MC card. The condition number of Z in (1) can be estimated by using the LAPACK subroutines [5], that are selected by the third card, the MN card. The format of these three new cards is shown below.

3.1 MS

Purpose: Select the algorithm to solve the linear system $Z\ I = V$

Command:

MS	MSOLVER	MSNLIM	MSNBLKS	MSUNIT	EPS	REFEPS	BWRATE	R4
	I1	I2	I3	I4	F1	F2	F3	F4

Parameters:

I1 – 0 – original LU factorization (default)
- 1 – LAPACK's LU factorization
- 2 – TFQMR iterative solver
- 3 – QMR iterative solver
- 4 – block diagonal solver
- 5 – band solver
- 6 – pattern solver
- 7 – MIR solver
- 8 – QMR from BCG solver

3.2 MC

Purpose: Provide more data for solver algorithm.

Command:
MC I1 I2 I3 I4 F1 F2 F3 F4

Parameters:
I1, I2, I3, I4 – integer data for solver algorithm
F1, F2, F3, F4 – floating point data for solver algorithm
This card is presently only used for the block diagonal solver where I1, ..., I4 are block sizes.

3.3 MN

Purpose: Estimate the condition number of the moment matrix.

Command:
MN ICOMPCN

Parameters:
ICOMPCN – 0 – don't estimate condition number (default)
– 1 – estimate condition number. This also selects the LAPACK *LU* factorization

4 Numerical Examples

As an illustrative example, we consider a 9 by 9 array of wiregrid patches of size 0.3 m by 0.3 m, with a center-to-center distance of 1.0 m. Each patch is modeled with 24 unknowns, which leads to a total of 1944 unknowns. The associated moment matrix occupies 58 MB. We compute the currents on the patches, for a normally-incident plane wave, and for frequencies of $f = 299.8$ MHz and $f = 500$ MHz. All examples are run on a single 332 MHz PPC node of an IBM SP system. The fill time for all of the examples considered is approximately 39 s. The different run times aggregate of factorization and solution times achieved for this numerical experiment are displayed in Table 1.

It was found that substantial improvements in run times can be achieved on the IBM as well as on a Dec Alpha system by using LAPACK routines, in conjunction with the tuned GEMM routines and/or the vendor-provided BLAS routines in the ESSL library.

The results for the QMR and the BCG iterative solver are omitted as these two algorithms yield slower runtimes than did the TFQMR algorithm. For low frequencies (below the patch resonances) the matrix is diagonally dominant; hence the iterative solver converges and the total solution time is 4.4 times faster than it is for the original, complete *LU* factorization. In addition, the additional storage for the work vectors is negligible. However, for $f = 500$ MHz, the patches exhibit resonance, and the interaction between different patches becomes important. The matrix is no longer diagonally dominant when this happens, and the algorithm fails to converge.

The band preconditioner retains a sufficient number of off-diagonal elements in both cases to achieve convergence during the refinement steps. With this preconditioner, the total solution time is 17 times less than it is for a complete factorization, and the corresponding figure is 3.3 for

LAPACK. The total memory needed to store the two matrices is 75 MB – 58 MB for the original matrix, and 17 MB for the factorized banded matrix.

At $f = 500$ MHz, close coupling between the individual patches becomes apparent in the process of using the block preconditioner. If we choose 81 blocks for the matrix, one for each patch, the algorithm fails to converge. However, if we include some interaction between the patches by increasing the block size to 72, 216, or 648, we can again achieve convergence. The fastest solution time is achieved with 27 blocks comprising 72 unknowns each, and this is 26 (5.2 for LAPACK) times faster than it is for complete *LU* factorization. The storage for the different block matrices ranges from 2.1 MB for 27 blocks to 6.4 MB for 3 blocks, for a total that ranges between 61 MB to 65 MB.

To compute the pattern when using this algorithm one needs some information about the current distribution, e.g., that obtainable from a previous solution. In our numerical experiments we used the current distribution from a previous run at a frequency which is lower by 50 MHz. The pattern used for the central three rows were derived by averaging the currents on the elements of the corresponding row, and this enabled us to reduce the number of unknowns from 1944 to 1438 (74%). The errors in the current distributions can be relatively high if no iterative refinements are carried out; nevertheless near and far field quantities only exhibit a maximum error of 2% and 5.6% for the non-resonant and resonant cases, respectively. Additional storage needed for the reduced matrix is 32 MB, with the total being 89 MB.

The MIR algorithm [3] is the most memory-demanding of all among the ones we have investigated, and since it requires that both the complete factorized matrix, as well as the new matrix, be held in memory, the total memory requirement is twice that needed for complete *LU* factorization. For the present problem this total is 119 MB, which is rather large. Additionally, the largest frequency step for the two frequencies of interest was 10 MHz, which is relatively small. Other techniques for broad band computation, such as the MBPE [6], appear to be more efficient for handling this case.

5 Conclusions

We have presented a number of different techniques for speeding up the solution of linear systems of equations arising in the application of the NEC code. These techniques either handle the full matrix by using different algorithms, or precondition it to speed up the solution. They are not general-purpose, however, and the choice of the algorithm is left to the user who selects the appropriate algorithm via new input NEC cards.

The use of publicly-available subroutines obtainable from the internet, enables one to easily enhance the performance of legacy codes with relatively minor changes.

Acknowledgements

The use of matrix-matrix multiplication kernels (GEMM) tuned for RISC processors by Michel Dayde, Iain Duff et al. is acknowledged. The package was obtained from `http://www.enseeiht.fr/Recherche/Info/apo/Numeriq.html`.

Table 1: Run times for a 9 by 9 array of wiregrid patches

algorithm	$f = 299.8$ MHz factor in s	solution in s	total in s	$f = 500.0$ MHz factor in s	solution in s	total in s
original *LU*	378.19	1.10	379.29	376.79	1.13	377.92
LAPACK *LU*	72.76	0.44	73.20	75.47	0.45	75.92
TFQMR	0.00	85.76	85.76	no convergence		
band with 10 % bandwith	2.60	19.53	22.13	4.68	13.16	17.84
block diagonal (3 blocks)	10.02	7.66	17.68	9.84	6.60	16.44
block diagonal (9 blocks)	1.06	10.94	12.00	1.08	13.01	14.09
block diagonal (27 blocks)	0.15	9.74	9.89	0.19	14.29	14.48
block diagonal (81 blocks)	0.04	13.24	13.28	no convergence		
pattern	33.23	0.70	33.93	34.67	0.71	35.38
MIR	0.00	0.00	44.75	no convergence		

Note: Performance improvements between the original *LU* factorization and LAPACK's factorization vary with CPU, problem size, and impact of the tuned ZGEMM subroutines. Improvements on different platforms can be less spectacular.

References

[1] R. W. Freund, "A Transpose-Free Quasi-Minimal Residual algorithm for non-Hermitian linear systems," *SIAM Journal on Scientific Computing*, vol. 13, pp. 470–482, Mar. 1993.

[2] J.-R. Poirier, P. Borderies, R. Mittra, and V. Varadarajan, "Numerically efficient solution of dense linear system of equations arising in a class of electromagnetic scattering problems," *IEEE Trans. on Ant. and Prop.*, vol. 46, pp. 1169–1175, Aug. 1998.

[3] P. S. Simon, C. S. Kenney, K. McInturff, R. W. Jobsky, and T. A. Bryan, "A modified iterative refinement algorithm for efficient solution of parameter-dependent sets of linear equations," *IEEE Ant. and Prop. Symp. Digest*, Atlanta, GA, USA, pp. 1510–1513, July 1998.

[4] G. H. Golub and C. F. van Loan, *Matrix Computations.* Baltimore and London: The Johns Hopkins University Press, 1996.

[5] E. Anderson, Z. Bai, C. Bischof, J. Demmel, J. Dongarra, J. D. Corz, A. Greenbaum, S. Hammarling, A. McKenney, S. Ostrouchov, and D. Sorensen, *LAPACK Users' Guide.* Philadelphia, PA, USA: SIAM, 1992.

[6] E. K. Miller, "Model-based parameter estimation in electromagnetics: I – background and theoretical development," *ACES Newsletter*, vol. 10, pp. 40–63, Nov. 1995.

COMPARISON AND RESULTS FOR MODELS OF A THICK BENT-WIRE DIPOLE USING NEC4 AND WIPL

James Stamm and Mun-Won Fenton
RF Sensors Branch
48110 Shaw Road
Naval Air Warfare Center–Aircraft Division
Patuxent River, MD 20670

James K. Breakall
Department of Electrical Engineering
The Pennsylvania State University
University Park, PA 16802

ABSTRACT

Modeling of moderately thick wires can often involve feedpoint effects, which may or may not be handled properly when compared to actual physical construction and experimental measurements. In this paper, it is shown that attaching the two feedpoint wires on one side of a hollow cylindrical tube in the form of a dipole will introduce a frequency shift in the impedance or VSWR from what NEC4 would compute. A code such as WIPL, which uses a combination of plates and wires in an EFIE approach, is shown to produce results which are correlated well with experimental measurements of the physical dipole. Finally, this paper shows that a correction factor in length can be implemented to produce equivalence with NEC4 results even for bent stubs at the end of the dipole. This has implications in using codes such as NEC4 for optimization in arrays and construction of physical antenna elements.

1. INTRODUCTION

This paper will describe the modeling and measurements of a thick bent-wire dipole that is used as a driven element in a Yagi that forms one of the elements of a large circular array. This array is called the UHF Electronically Scanned Array (UESA) and is being proposed as a replacement for the current mechanically rotated array which is attached on top of an aircraft for Navy radar applications similar to the AWACS airborne radar array. It was desired to know two effects in the construction of such a dipole element: a bend in the dipole at the ends of the wire to allow its space usage without overlap of nearby neighbors, and the attachment of the feedline to the center feedpoint of the dipole. The NEC4 computer antenna modeling program has been used exclusively to optimize the Yagi array as a whole in a package called NECOPT [1]. The authors recently received another modeling package called WIPL [2]. This WIPL program allows the user to interactively define the geometry of any metallic structure as a combination of wires and plates and uses the EFIE formulation for solution of the currents, impedance, patterns, etc. The user can further check his data by using a built-in 3-D drawing capability of the structure. The program also provides the user with a variety of list and graphic output

capabilities, including 2-D and 3-D graphics. The authors only had the reduced version of the WIPL program which has the unknowns limited to 100 which was satisfactory for the modeling described in this paper using symmetry. The GNEC package was used for all NEC4 modeling in this paper and has extensive pre and post-processing under Windows for model input and display of results [3].

2. DIPOLE ANTENNA DESCRIPTION

The dipole in this paper is a moderately thick and hollow conductor being ¾ inches in diameter and having a half-length of 7.43 inches in both the straight and bent configurations. It is designed for operation around 400 MHz and it was found experimentally that the resonant frequency could be altered simply by changing the feedpoint attachment. Also, the dipole ends must to be bent to accommodate its fitting into the array without overlapping with its nearest neighbors on each side, since it is being used in a circularly symmetric array. This bend also cause a slight change in the resonant frequency of the isolated dipole element.

The feedpoint can either be attached with some form of screw connection on one side of the hollow cylindrical tube (in this case copper tubing) or at several attachment points. The NEC applied E-field voltage source model assumes that the electrical field is completely uniform in the gap region, which is very similar to what would occur in a capacitor between the plates. Since the optimization used NEC4, it was required to use another code and/or measurement that could give the same impedance as computed by NEC4 after an adjustment was made to the actual dipole's length. It was found that this equivalent NEC4 dipole could be achieved in practice with a bent stub length of 2.125 inches instead of 2.75 inches as was used in NEC4.

The WIPL code can actually model the cylindrical wire with plates and then connect a wire between the hollow tubes, much like that in the actual physical dipole connection. This is shown in Figure 1 for both the straight and bent configurations with only half of the dipole shown in each case. Symmetry is employed in this code to model the other half. The wire can also be seen connected to one side of the hollow tube. Only half of the dipole is modeled in the other plane as well to conserve unknowns in the version of this code that was provided to the authors. Three total types of feed arrangements were tried for this model and are shown in Figure 2. The Type 1 feed is as already described and the Type 2 feed uses 2 wires and the Type 3 feed uses 4 wires (the two additional feeds provided by a PMC boundary in the XOY plane) as shown to produce a more uniform field distribution which should be more similar to NEC4.

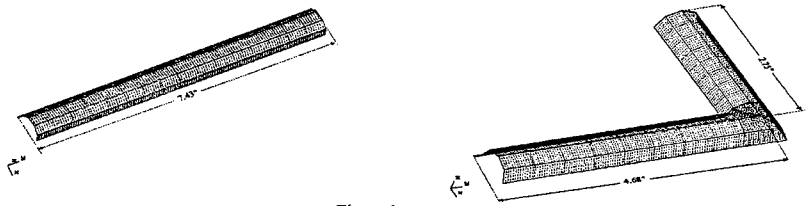

Figure 1

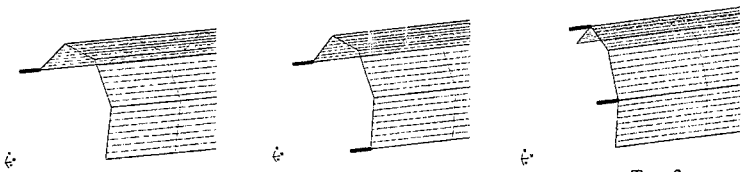

Figure 2

3. RESULTS

Results are shown in the form of both VSWR and input impedance for several different implementations of the basic configurations described above. WIPL results for a straight-wire model are shown in Figure 3 for the three different feed types, respectively. Similarly, WIPL results for the bent stub case of 2.75 inches are shown in Figure 4 for the same three different feed types, respectively. It was found that the bent stub length could be adjusted to give an impedance essentially the same as NEC using its applied E-Field source. The stub length for this condition was found to be 2.125 inches instead of the 2.75 inches as used in the NEC4 optimization. These results are shown in Figure 5 for WIPL and Figure 6 for NEC4. This WIPL result for the shorter bent stub is only done for the type 1 feed case since this is the case actually used in practice. A measurement was taken for the bent short stub case which was built and tested in the lab for a stub length of 2.125 inches instead of 2.75 inches and the resulting VSWR is shown in Figure 7.

4. CONCLUSIONS

It has been shown that the WIPL code using the EFIE formulation can accurately model the case of a dipole fed by connecting a feedline to one side of a hollow cylindrical conductor. Furthermore, it has been also shown that actual physical and WIPL impedance results can be made to be equivalent to that of a NEC4 model by simply shortening the total length of the dipole (in this case a bent stub) to form an equivalent dipole which can be used in optimization studies based on NEC4. Agreement between experimental measurements and both independent codes can then be obtained.

REFERENCES

1. J. K. Breakall, J. S. Young, R. J. Bauerle, A. I. McDowell and T. A. Erdley, "Numerical Electromagnetics Code Optimization Design Software (NECOPT)," 10th Annual Review of Progress in Applied Computational Electromagnetics, Naval Postgraduate School, Monterey, CA, 1994.

2. Branko M. Kolundzija, Jovan S. Ognjanovic, Tapan K. Sarkar, Roger F. Harrington, " WIPL: Electromagnetic Modeling of Composite Wire and Plate Structures," Artech House, 1995.

3. J. Finnerty, "GNEC, A Graphical User Interface (GUI) for NEC4," Nittany Scientific, 1997.

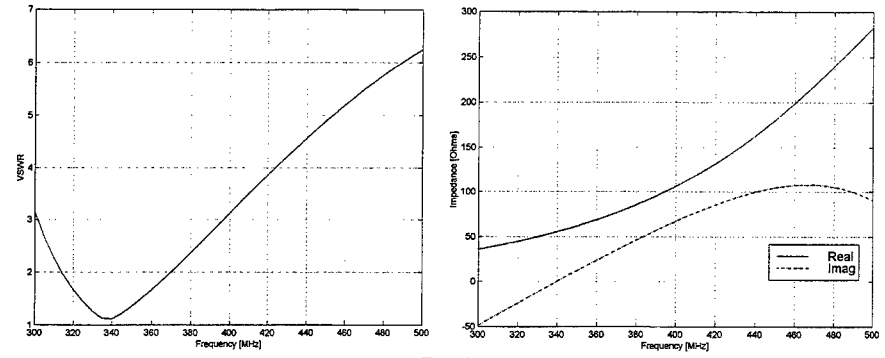

Type 1

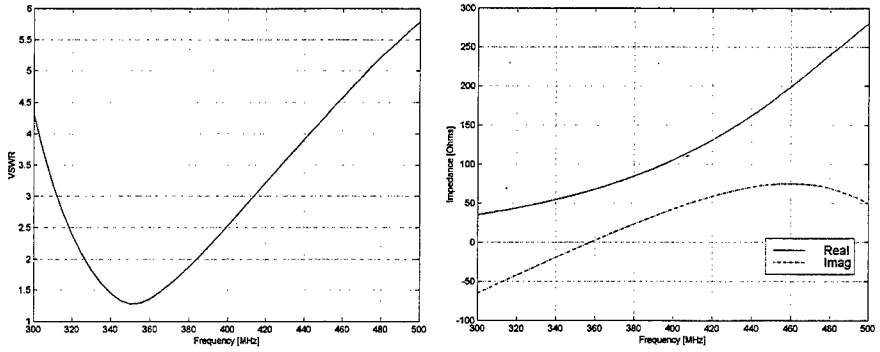

Type 2

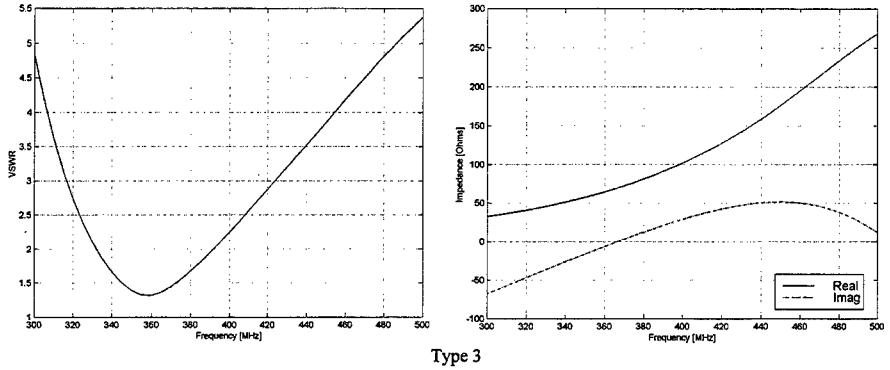

Type 3

Figure 3. WIPL Straight Wire Results

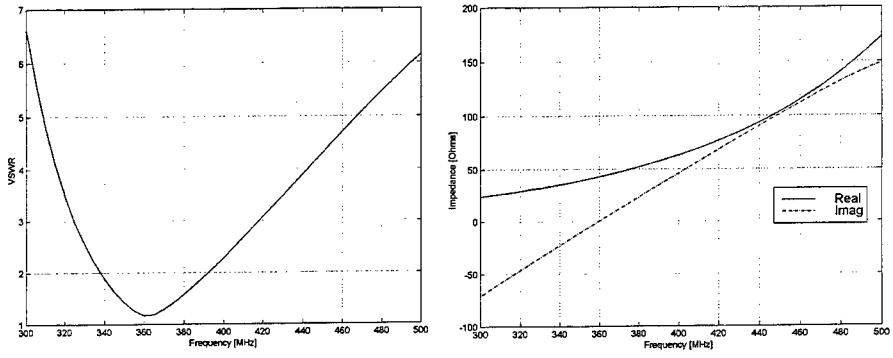

Type 1

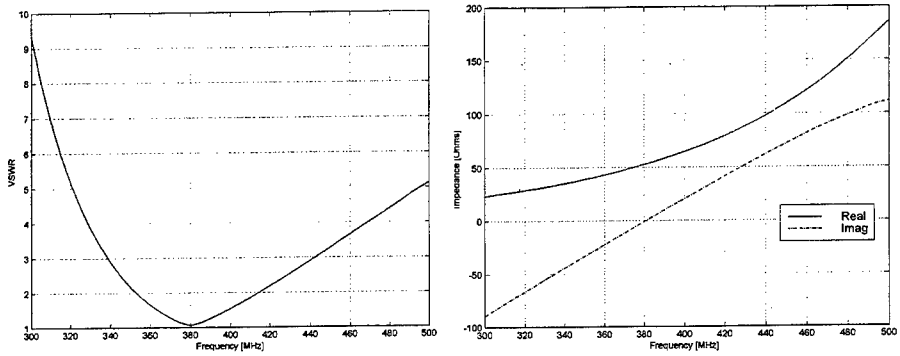

Type 2

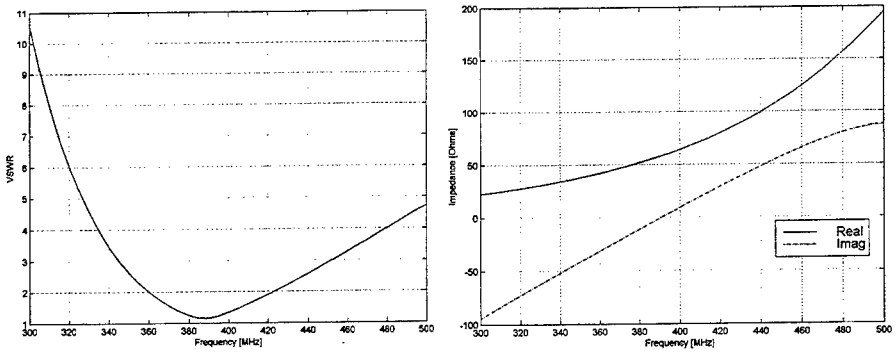

Type 3

Figure 4. WIPL Bent Stub Dipole Results

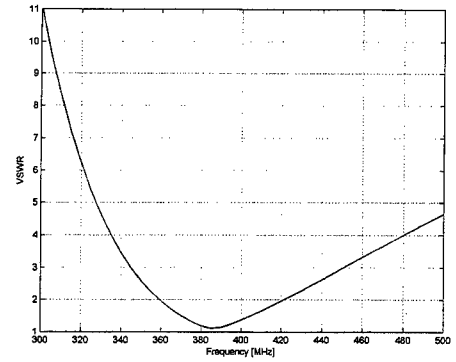

Figure 5: WIPL Results for Bent Dipole (2 $^{1}/_{8}$" Stub)

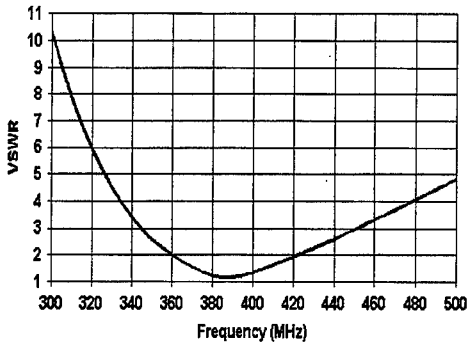

Figure 6. NEC4 Results for Bent Dipole (2 $^{3}/_{4}$" Stub)

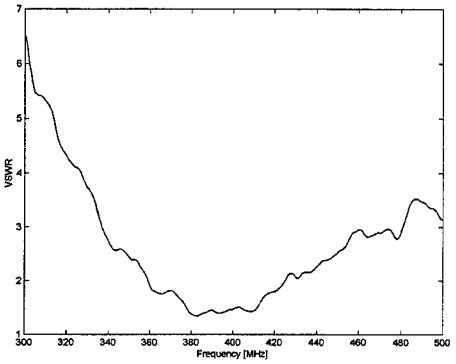

Figure 7. Measured Results of Bent Dipole with 2 $^{1}/_{8}$" Stub

MF Broadcast Antennas and Antenna Arrays: A historic branch of antenna engineering revisited by computer simulation and measurement

John S. Belrose, VE2CV
Radio Science Branch
Communications Research Centre
OTTAWA ON CANADA

Introduction

In the early eighties when I was preparing an overview [1] on VLF, LF and MF antennas I wrote that "the present day availability of microcomputers, combined with sophisticated antenna modelling codes (method of moments), provides the tools needed to more rigorously determine the characteristics of MF broadcast antennas. And, in the case of multi-element broadcast arrays, the calculated currents in amplitude and phase, which result in the desired pattern, should compare more exactly to those measured, thus facilitating initial set-up and reducing the time required to achieve the desired pattern by field measurement".

But my first attempt at numerically modelling MF broadcast antennas was not very satisfactory. The tools I had were MININEC and NEC-2. While NEC-2 does account for a Summerfeld-Norton ground beneath the antenna, the wire model must not touch the ground. I devised a trick to simulate "ground connection", viz. using elevated resonant radials. This launched me into a detailed study of elevated radials [2,3,4]. More recently, since now I am now licensed to use NEC-4 (I use EZNEC pro 4D), I can model antennas with buried radial ground systems. However, my initial studies seemed only to result in new problems to be concerned about.

Why am I concerned with modelling MF broadcast antennas? One reason is a current interest in near fields. This prompted a correspondence exchange with Valentin Trainotti, LU1ACM, since Tino measured near fields for two types of MF broadcast antenna systems [5]. While I agreed in principle with his views, I disagreed with some of his statements, and with some of the conclusions reached [6]. Also, since I am a subscriber to the NEC Listserver <dave@ee.ubc.ca>, this put me in touch recently with three MF broadcast engineers, Sylvio Damiani, Brazil, Alberto Fassio, Italy, and Grant Bingeman, KM5KG, with Continental Electronics, Dallas, TX. The stations in Brazil and Italy employ folded-unipole radiators, an antenna type not used in North America. And, the station in Brazil employs elevated radials, at quite a low height, and a high transmitter power (100 kW), which raises a concern about the magnitude of the near fields beneath the elevated radials --- but that is a subject for follow on studies. Finally, in December 1997, I received a request for advice and help in resolving a number of MF antenna problems in Australia and New Zealand [Stephen White, private communications, 1997].

This paper is a progress report, which summarizes some of my recent work. "Progress", since at the time of writing, preparations are underway to conduct experiments in Taupo, on the North Island, New Zealand, which will compare performance, for the same MF tower, at the same site, contrasting six elevated radials with 120 - 0.75 wavelength (0.75 λ) buried radials.

Antenna Systems without a Buried Radial Wire Ground System

A dipole-type vertical radiator can be used as a MF broadcast antenna system, without the 120 buried-radial-wire ground system. Trainotti [5] uses such an antenna system (see **Fig. 1**), which he calls an asymmetric vertical half wave dipole. I have, in previous publications, referred to such an antenna as a ground-plane type antenna with drooping radials. In the arrangement used practically, the top 70 metre (m) section of a 130 m high tower is fed against four sloping radial wires, each about a quarter wavelength long (70 m for a frequency of 1 MHz). The angle between the sloping radials and the tower is 45^{o}. Since the tower is not broken he uses a cage feed, arranged as a folded unipole, with four drop wires, for the top section. The tower is sitting on the ground, "grounded" for lightning purposes by a ring of ground rods. We have assumed that the tower itself, for purposes of modelling, is sunk into the ground to a depth of 5 m.

I have numerically modelled this antenna system (using NEC 4D) to compute ground wave field strength and impedance. I compute the field strength at 1 km E(1 km) = 127.7 dBμV/m, for a transmitter power of 50 kW; and Z_a = 148 + j 9 ohms. The measured FS was 128 dBμV/m, and the antenna's impedance is said to be between 150-200 ohms. The broadcast station site has very good ground conductivity (σ = 40 mS/m, ε = 30).

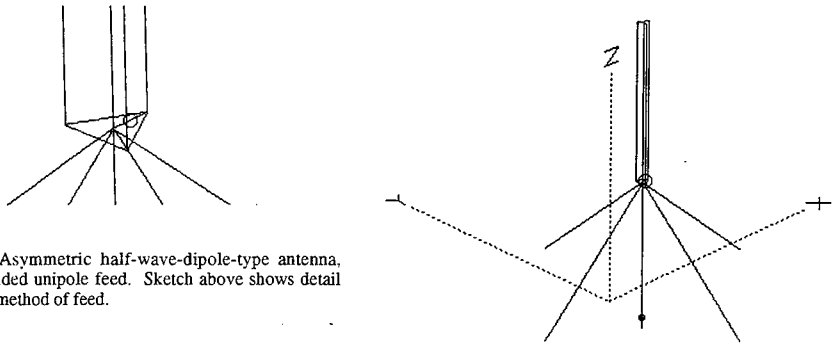

Fig. 1 Asymmetric half-wave-dipole-type antenna, with folded unipole feed. Sketch above shows detail on this method of feed.

Conventional Buried Radial Wire Ground Systems

The ground systems used by MF broadcasters are based on the results of the (classical) experimental studies of Brown et.al. [7]. I have modelled and re-modelled (making changes to the model) the pipe monopole system used by Brown and his colleagues, frequency 3 MHz, in an attempt to obtain an agreement with measure results. But I have to report that I did not find much agreement. I have computed impedance vs. tower height and vs. length and number of radials; and field strength in the same way as FS was measured (Brown et.al. measured FS at 0.3 miles and assumed a 1/distance (1/d) rate of change to 1 mile, the field strengths plotted). I have also looked at the decrease in current along a radial, but the agreement was not good.

These authors mention that the ground conductivity at the field site was 2 mS/m, I suspect (judging from the photographs shown) that the conductivity was much higher, but computing results for different conductivities did not help. We have to conclude, if we believe in NEC 4, and in Maxwell's equations, that their measurements were too crude to expect to find agreement. However the trends are right.

Most MF broadcast stations (based on the results of Brown et. al.) typically employ 120 radials of length 0.25 λ to 0.4 λ. Broadcast towers in Australia and New Zealand (which we discuss below) employ radials of length 150 m to 200 m, buried to a depth of 0.2 m.

Before we present any results from our files of numerical modelling, let me describe the model we use. Clearly if one looks at a real antenna, we do not put a source on a thick tower, we connect a wire to a thick tower and the source is on that wire. A source on a wire, connecting to the multi-wire radial ground system seemed to be a better method to model the buried ground screen. That is the connection to the ground system is a heavy gage wire. The lower end of this wire touches the ground. Next we connect a wire, having the same segment length as this wire on which we placed the source, which slopes downward at 45^{o}, and connects to the buried horizontal radial, see **Fig. 2**. The first segment on the horizontal radial has the same segment length as this sloping wire, and we use a segment taper option (available with EZNEC pro 4D), for the horizontal radial.

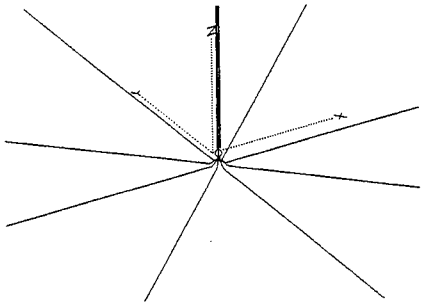

Fig. 2 Sketch illustrates a method of modelling a buried radial wire ground system connecting to a thick tower.

I have modelled towers without guys, and towers with guys, fed against a PEC ground; and towers without guys fed against 120-200 m long radials buried 0.2 m, average ground. Before presenting results which show in detail impedance vs. frequency (or tower height in wavelengths), let us look (for reference) at the differences for the case of a single frequency, between these models. Consider a 120 m high tower. diameter 1.58 m (I have measured data for such a tower, for two installations, Fairview and Highcliff. NZ, see below). The antenna's impedance at 625 kHz ($h/\lambda = 0.25$) for this tower without guys (PEC ground) $Z_a = 57 + j\ 38$ ohms, $E_u = 263$ mV/m; with guys (PEC ground). see **Fig. 4**, $Z_a = 65 + j\ 85$ ohms, $E_u = 269$ mV/m --- and with 120-200 m long radials buried to a depth of 0.2 m $Za = 65 + j\ 40$ ohms, $E_u = 254$ mV/m. The unattenuated field strength at 1 km, for 1 kW, has been calculated from the FS at 300 m, assuming a 1/d rate of change.

In what follows (**Figs. 3 and 5**) we assume a PEC ground. Previous work has shown differences, when comparing various curves of impedance versus frequency, or physical height H in electrical degrees. Since the differences between the curves, measured for different installations, or measured data compared with early prediction methods, could apparently be brought into better agreement by shifting one of the curves by an amount dependent on height, it was speculated that the differences are probably due to stray effects, such as base insulator capacitance, capacitance of guy insulators, lighting transformer, and etc. [1].

Stephen White has provided me with many tables of impedance measurements for a number of towers of different heights and tower diameters. We will consider here measurements for two towers, Fairview and Highcliff, NZ. One tower is quite a bit taller compared with the other, but the height/diameter ratios are about the same (H/D = 76). These towers were mounted over an extensive radial ground system, described above.

In **Fig. 3** we compare calculated base impedance for a tower with no guys, with measurement. The continuous curve is our computed result. The data points for R_a are plotted as circles; squares for X_a. Open circles and squares, and closed circles and squares refer to data for the two installations. The agreement between measurement and computer simulation is not very good.

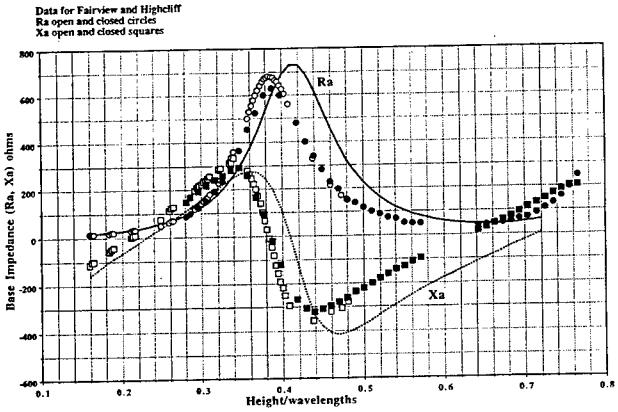

Fig. 3 Simulation impedance versus tower height in wavelengths for a tower with no guys, compared with measurements at two locations, Fairview and Highcliff, New Zealand.

If we include guys in the model, broken by insulators, see **Fig. 4** (30 pF capacitors for the break-up insulators, and 26 pF capacitors for the high voltage insulators where the guy wires connect to the tower), we obtain pretty good agreement, see **Fig. 5**. While the differences between the curves computed versus measured is greatest near the half-wave resonant height, it should be noted that there is also a difference between the measured data for this tower height.

Elevated Resonant Radials

To illustrate some of the pertinent factors and expectations if elevated radials are used, and to validate NEC 4D we consider here a two tower array, MF broadcast station KGGN, operating on 890 kHz, located near Gladstone, MO. We are fortunate

to have the detailed proof of performance report for this station. I have already published some results of this study [4], but ACES provides a different forum, and many of you will not have seen my Communications Quarterly article.

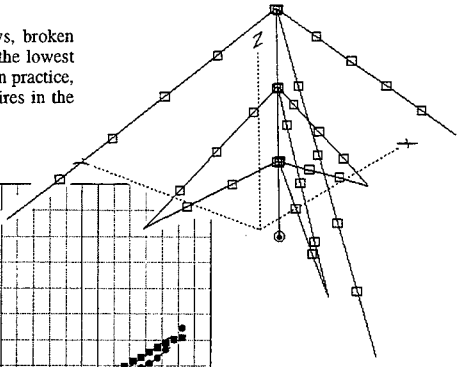

Fig. 4 Sketch shows the tower with guys, broken up by insulators. The guy section below the lowest insulator is connected to the PEC ground (in practice, connection is made to one of the radial wires in the ground system).

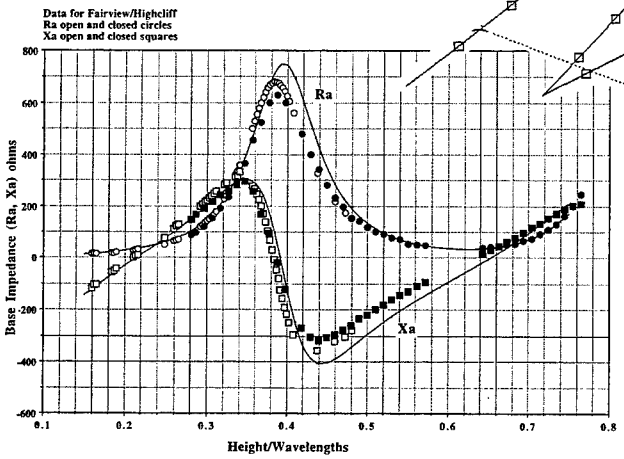

Fig. 5 Simulation impedance versus tower height in wavelengths for a tower with guys, compared with measurements at two locations, Fairview and Highcliff, New Zealand.

KGGN employs two vertical radiators of 60 m height (physical height 64 electrical degrees), 69.3 m (74 electrical degrees) apart, on a bearing of N 69^{o} E True. The towers are guyed, uniform triangular cross section, face width 0.457 m. The ground system consists, for each antenna, of six counterpoise wires arranged at 60^{o} intervals for symmetry, 86 m long. The radial wires are elevated 5 m above ground until the radials come to a point 5 m from each tower base. At this point, they slope downward at an approximately 45^{o} angle, terminating in insulators which are attached to the concrete base pier. The base height of the towers is 1 m above ground. Note: the radials are too long to be resonant, resonant length for radials at a height of 5 m over average ground is 80.86 m. The two counterpoises are not connected to each other (and cannot accidentally touch) except at the base of each tower, where a copper strap runs along the tower line and through the transmitter building. The copper strap is for lightning protection, tying the phasor, transmitter, collection rings of each counterpoise, mains breaker panel, and telephone gas protectors to a common earth. For our model we have assumed that the connection to earth is by means of a 10 m ground rod --- our modelled antenna array is sketched in **Fig. 6.** Tower 1, the tower on the left, carries a current of 1.0 $\angle 0^{o}$ amperes; and for Tower 2 the current is 0.92 $\angle 107.5^{o}$ amperes.

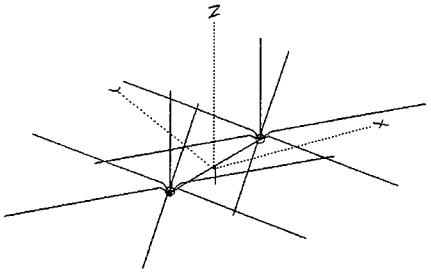

Fig. 6 The model used to numerically simulate performance for MF broadcast station KGGN 890 kHz, Gladstone, MO, which uses an elevated radial wire system.

The proof of performance documents field strengths for the nondirectional (ND) tower, measurements made at many locations in eight azimuthal directions, in the distance range 0.3 to 40 kilometers; and in the azimuthal direction of maximum gain, the field strengths for the ND tower and directional array were measured at the same locations, in the distance range 3 to 40 km.

Gladstone is NNE of Kansas City, MO. Notice, see **Fig. 7**, that excepting for 80.5° T and 138° T, the radial paths are all over rather rough terrain. Some of these radial paths pass through residential and urban areas. Clearly this should result in a scatter in the field strengths measured. And indeed there is a scatter, not shown here, which is too great to validate a comparison with computed field strengths.

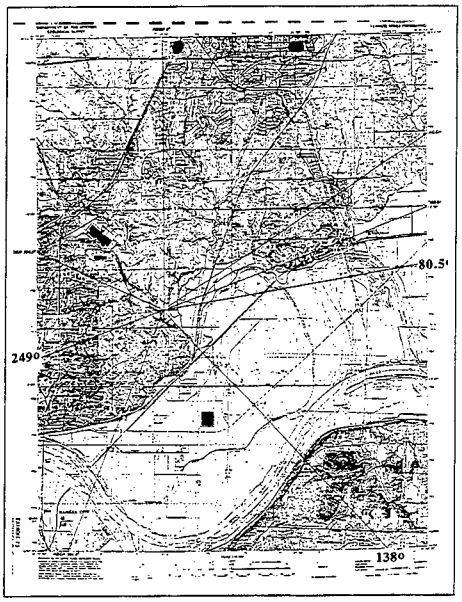

Fig. 7 Map showing terrain features surrounding the MF broadcasting station KGGN 890 kHz, Gladstone, MO, highlighting three azimuthal directions pertinent to our analysis for comparison with the measured data.

In **Fig. 8** I show a plot of FS for the ND tower with elevated radials vs. distance for the two azimuthal directions, 80.5° T and 138° T, which are the only two paths that lie over rural fairly open and level land (see **Fig. 7**). In retrospect we should have plotted only the data for the 80.5° T azimuth. The computed curve (the continuous line) has been calculated for average land (σ = 5 mS/m, ε = 13), a conductivity which is consistent with the measurements. I have not fitted a curve to the measured data. Notice that the measured data points cluster quite well about the theoretical curve. I conclude that indeed NEC-4D accurately predicts the ground wave field strength.

Now let us look at measured field strengths along the azimuthal direction corresponding to the main beam direction (249° T) for the directional array. In **Fig. 9** I show the results for the ND tower in this direction --- again the continuous curve is the theoretical curve (the same curve in **Fig. 8**), and the filled in circles the measured data. Notice, we will make reference to this below, the sudden break in the agreement between measured and predicted field strengths in the distance range 4-10 km. This is considered to be due to the rough terrain over which the wave passes to reach the measurement locations.

In this same figure we compare the theoretical field strength curve for the directional pattern (the continuous line) with the measured data (the open circle data points). Again, notice that the data points in the range 4-10 km lie below the theoretical

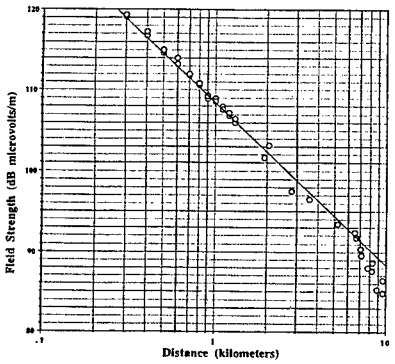

Fig. 8 Measured ND field strengths versus distance (open circles) for KGGN, for the two best azimuthal directions (80.5 degrees T and 138 degrees T) --- see map in **Fig. 7**. The continuous curve is the theoretical field strength.

curve. In fact the only data point that lies close to the theoretical curve is that measured at 3.3 km; which fortunately is the location where the field strength for the ND tower is rather close to the theoretical curve.

You may consider that this is not very satisfactory agreement between measurement and numerical modelling. So let us compare measurement with theory in another way. The array gain, gain over the ND tower, can be quite accurately determined from the ratio of measured field strengths (since ND and directional field strengths were measured at the same locations) in the distance range 3-12 km (nine values), see **Fig. 9**. The median value for the measured array gain is 3.8 dB. Our predicted array gain, is 4 dB. We can also compare the front/back ratio for the array, predicted vs. measured, 28.9 dB compared with 28.8 dB.

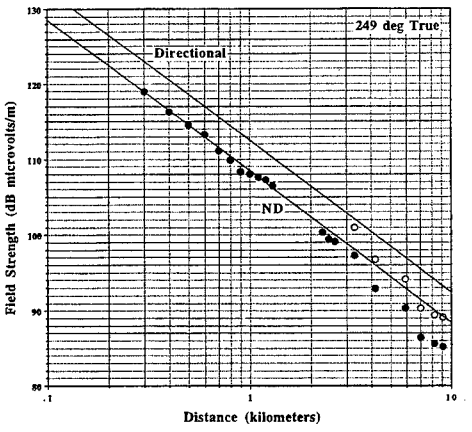

Fig. 9 Measured ND field strength versus distance (closed circles) for KGGN for the azimuth of maximum gain (249 degrees T); and field strength for the 2-tower directional array (open circles). The continuous curves are the theoretical field strengths.

Effect of Ground Conductivity

Certainly ground conductivity has a dominating effect on antenna performance and on propagation. I have calculated (using EZNEC pro 4D) parameters for a 1000 kHz quarter wave monopole with 4 resonant radials, for two radial heights 3m and 5m; and for 120 quarter wavelength buried radials (depth -0.2m) --- for two conductivities, good ground (σ = 5mS/m, ε = 13); and very poor ground (σ = 0.5 mS/m, ε = 3); see **Table 1**. The gain G is the space wave gain. The field strength at 1 km E (1 km) is the predicted ground wave field strength at that distance, for a measurement height of 1.5m, and a transmitter power of 1000 watts.

For the very poor conductivity case, be careful how you interpret the field strength at 1 km. In the distance range 200m to 1000m, the field strength falls off on a linear curve on a log-log plot, but faster than 1/distance. If I take the field strength at 200m as an unattenuated value, and assume that the field strength falls off as 1/d (unattenuated value), the unattenuated field strengths at 1 km for radial heights 5m, 3m and -0.2m (120 radials) are 254 mV/m, 249 mV/m and 263 mV/m. Clearly propagation effects dominate, even at distances < 1 km. But proof of performance measurements do not always show measurements so close in to the antenna --- and for a multi-tower antenna array this distance range is too close in --- the beam is not formed.

Conclusions

In conclusion, if we wish to seek a comparison between measurement and simulation for a monopole over sparse radial wire ground systems, we will need to conduct this experiment in an open field site, using modern measurement equipment.. And, the ground conductivity must be measured. Field strength is strongly influenced by the local environment, such as power lines and fences. The measurements clearly reveal the difficulty in determining an accurate field strength vs. distance curve with little scatter, needed for comparison with numerical modelling, which assumes a flat smooth earth. Only if sufficient detail is given in the proof of performance to sort the data and establish that indeed there can be a rather good agreement between measured and predicted field strengths are the measured data useful for validating computer simulation.

References

1. Belrose, J.S., "VLF, MF and HF antennas", in The Handbook of Antenna Design, Vol. 2 (editors Rudge, Milne, Olver and Knight), Ch. 15, Peter Peregrinus on behalf of the IEE, 1983, pp. 553-662.
2. Belrose, J.S., "Ground-Plane Type Antennas with Elevated Radial Systems", 12 Annual Review of Progress in Applied Computational Electromagnetics, Naval Post Graduate School, Monterey, CA, 18-22 March, 1996, pp. 2-11.
3. Belrose, J.S. "Elevated Radial Wire Systems for Vertically Polarized Ground-Plane Type Antennas - Part 1 - Monopoles", Communications Quarterly, Winter 1998, pp. 29-40.
4. Ibid., "Part 2 - Phased Arrays", Spring 1998, pp. 45-61.
5. Trainotti, V., "MF AM Asymmetric Vertical-Dipole Measurements", IEEE Antennas and Propagation Magazine, **38**, December 1996, pp. 75-82.
6. Belrose, J.S., "Comment on MF AM Asymmetric Vertical-Dipole-Antenna Measurements", IEEE Antennas & Propagation Magazine, August 1997, pp. 69-72.
7. Brown, G.H., R.F. Lewis and J. Epstein, "Ground Systems as a factor in Antenna Efficiency", Proc. IRE, **25**, June 1937, pp. 753-787.

Table 1
Effect of ground conductivity, see text for details.

Height (number) of radials		Ground Conductivity	
		Good	**Very Poor**
5m	Z_a	38.5 - j 1.7	37.6 - j 11
(4 radials)	Gain	1.89 dBi	-1.85 dBi
	E (1 km)	293.5 mV/m	181 mV/m
3m	Z_a	40.2	40.1 - j 10.4
4 radials)	Gain	1.8 dBi	-1.99 dBi
	E (1 km)	288.5 mV/m	176.4 mV/m
-0.2m	Z_a	37.7 + j 9.4	36.5 + j 5.6
(120 radials)	Gain	1.9 dBi	-1.4 dBi
	E (1 km)	292.7 mV/m	188.8 mV/m

The High Frequency Electromagnetic Environment of the U. S. Coast Guard 87-foot Coastal Patrol Boat

By

Michael E. McKaughan, PhD
Cadet First Class David Melton
Department of Engineering, U. S. Coast Guard Academy, New London, CT.

Ensign Kelly Seals
U. S. Coast Guard Cutter Polar Sea, Seattle, WA.

ABSTRACT

For successful mission operations, the U. S. Coast Guard's new 87-foot coastal patrol boat relies on effective radio communications systems. The Department of Engineering at the U. S. Coast Guard Academy has been tasked to assess the high frequency (H. F.) communications system on these patrol boats. Radiation patterns are predicted using Numerical Electromagnetic Code (NEC). Personnel radiation hazard potential is evaluated through on-site measurements, and verified using computer modeling with NEC near-field calculations. Results of these measurements are presented, which indicate that exposure levels are below current I.E.E.E. standards. Antenna placement is also evaluated using NEC.

1.0 INTRODUCTION

During the summer of 1998, the United States Coast Guard began accepting delivery of a new class of coastal patrol boats. The new cutters are 87 feet long, and will be used as replacements for the aging fleet of 82-ft, 95-ft, and 110-ft patrol boats. When the construction project is completed, some 50 new cutters will have entered the fleet of high utility search and rescue, environmental enforcement, and marine safety cutters. Because of the diverse missions for which these cutters are used, it is imperative that the communications suite performs optimally. The Antennas group of the Coast Guard Academy was tasked with generating an electromagnetic model of the new 87-ft coastal patrol boat. Once the model was created, we were asked to predict the H. F. performance of the cutter. While performing this analysis, personnel radiation hazards were assessed. During June 1998, data were collected aboard the cutter BARRACUDA in Eureka, CA. to validate the computer simulations. During the fall of 1998, modifications to the ship design were implemented on the second patrol boat to strengthen the ship's mast, and to change the location of some of the VHF and UHF antennas. These changes are presently being evaluated using a modified wire grid on the computer model. Computer predictions will be verified by physical measurements on one of the cutters.

2.0 DEVELOPING THE MODEL

To develop the electromagnetic model of the Coastal Patrol boat, we generated a two-foot grid from drawings of the ship. This grid spacing was chosen to give good detail in the model, while limiting the number of segments to a reasonable total (1766 segments). This model was used to predict radiation patterns in the far field at several frequencies in the H. F. region.

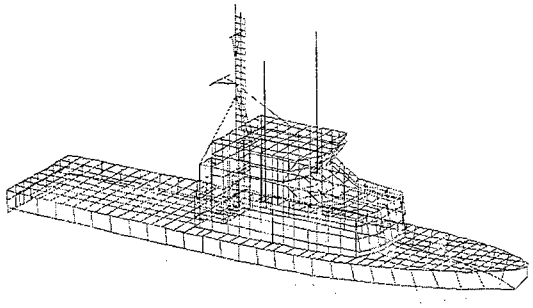

Figure 1: View of the NEC model of the coastal patrol boat containing 1766 segments with 2-ft grid spacing.

To assess the near-field effects on the inside of the wheelhouse, the grid size on the pilot house was reduced to one foot. Also, the interior deck of the wheel house was added to the model using the one-foot grid spacing. This grid density increased the total number of segments to 3349. The tighter grid spacing was selected for two reasons. First, we wanted to make certain that the windows on the bridge behaved like windows and not just part of the grid, and second, the closer grid spacing on the bridge should yield better results for the near field calculations. The cost of evaluating the fields with the higher density grid was, of course, increased computation time.

3.0 NEAR-FIELD MEASUREMENTS

Near-field measurements were gathered on the bridge of the patrol boat in June 1998. A spatial grid was established on the port side of the bridge in the vicinity of the windows. Measurements of electric field strength were recorded at approximately one-half meter separation fore and aft, and at three different distances into the bridge from the inside edge of the port bulkhead. Three vertical heights were established above the deck of the wheelhouse; 1) the bottom edge of the windows, 2) the center of the windows,

and 3) the top of the windows. This grid was used so that the measurements could be compared to calculations of electric field from the NEC program and model.

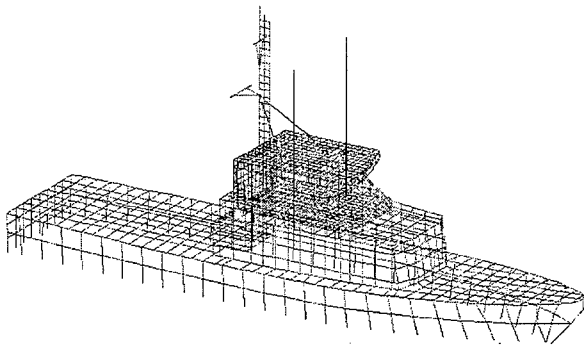

Figure 2: View of the NEC model containing 3349 segments with the one-foot grid spacing on the wheelhouse.

Near-field measurements were made using a Hewlett-Packard HP11941A close-field probe (H-field loop) and HP 8595A Spectrum Analyzer. To simplify data collection and recording, a simple data acquisition program was written to record the x, y, z coordinates, and signal strength. The coordinates were typed into the lap-top computer, and the field strength was captured from the spectrum analyzer over the Hewlett-Packard interface bus (HPIB) with a PCMCIA HPIB interface unit. The programming environment used for this data acquisition was MATLAB®. MATLAB® was selected because of the ease of manipulating and plotting the data in this environment. Data were recorded as arrays of numbers. Each array element included coordinates of the datum point and the signal strength observed at that point. The data were recorded at every point on the measurement grid at each of four frequencies; 4012 kHz, 6022 kHz, 7547 kHz and 12,560 kHz. These frequencies were selected as representative Coast Guard operating frequencies in the H. F. spectrum. We were especially interested in the radiation levels inside the bridge on the port side of the ship. This is the area of the bridge where the operators will be spending most of their time while the ship is underway. Specifically, the commanding officer's chair is just inside the wheel-house next to the H. F. whip. The navigator stands on the port side of the control console just forward of the Captain's chair, and the helmsman sits amid-ship just forward of the location of the H. F. whip. The H. F. transceiver control unit is to the left of the

Captain's chair on the side of the chart table. All interior surfaces on this ship are aluminum.

The measured signal strength levels presented in Figure 3 are based on a continuous transmitter power of 100 watts continuous carrier wave into the antenna coupler. This represents a worst case signal level from the point of view of radiation hazards. On this class of vessel in normal Coast Guard operations, all transmissions are single side-band (SSB) transmissions in the H. F. band. The duty cycle of SSB is normally something on the order of twenty-five percent of the maximum transmitter power. In Figure 3, the level representing the IEEE standard for maximum exposure limit is based on an exposure time of six minutes, and a constant signal level. Thus, the actual exposure level for personnel aboard this ship will be significantly below the levels that constitute a hazard. However, as ethical engineers, it is the opinion of the authors that there is cause for concern for the personnel on the ship, and that reasonable attempts to reduce the radiation levels would be prudent.

Observations at the other frequencies showed similar behavior as the measurement point moved around on the test grid. Higher frequencies tended to produce more points where the levels observed exceeded the existing IEEE standard exposure limits. Again, adjusting the levels for duty cycle, there is never a frequency or position on the ship where the levels represent eminent danger to personnel, but indicate that engineers should take steps to reduce potential exposure levels whenever possible.

4.0 NEAR-FIELD CALCULATIONS

To calculate the near-field strengths inside the bridge area, points matching the measurement grid were used with the NEC near-electric field commands. Computer runs were initiated for each frequency and over the grids points actually observed. The results of these computations were then compared to the measurements discussed in the previous section. Figure 4 presents the results of one of these simulations at 4.0 MHz. Additional results are pending, and will be available at the ACES conference in March 1999.

5.0 H. F. ANTENNA PLACEMENT

The H. F. antennas on this patrol boat are standard 23-foot fiberglass whip antennas fed at the bottom. The original placement of these antennas was on either side of the pilothouse. The actual whip is mounted on a pedestal approximately three inches away from the side of the pilothouse. Operationally, the H. F. antenna coupler would not tune properly in the frequency range of seven to ten megahertz. We have been asked to evaluate this problem, and also evaluate the performance of the antenna mounted on top of the forward storage locker. This work is just beginning at this writing. We will have results to present at the ACES conference in March 1999.

6.0 CONCLUSIONS

The H. F. communications system onboard the U. S. Coast Guard's new 87-foot coastal patrol boat has been evaluated. Using both computer modeling and physical measurements, radiation levels inside the bridge of the ship have been found to be safe in that the levels are below the hazard levels set forth in the existing IEEE standards. Additionally, through computer modeling, the radiation characteristics of the H. F. antennas have been evaluated. As a result of this work, the location of the H. F. transmit antenna has been moved to a more favorable location.

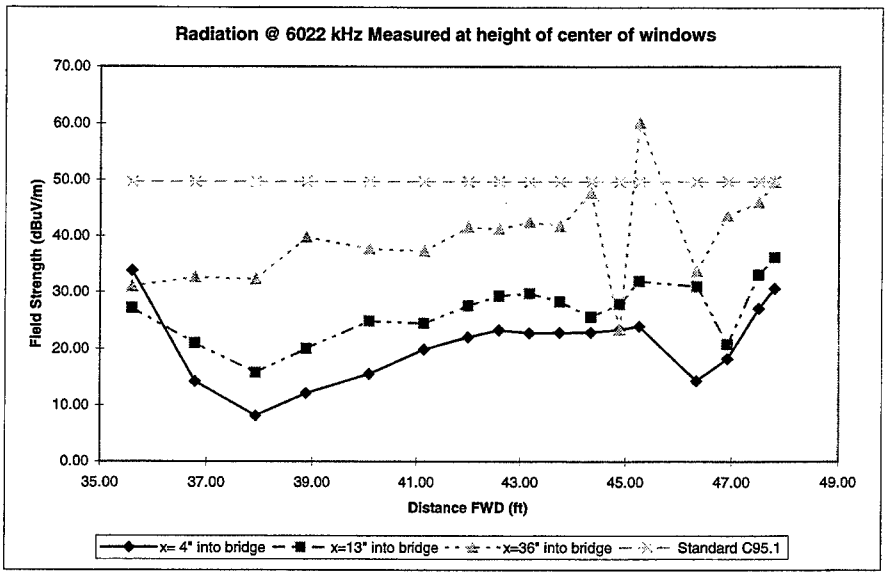

Figure 3. Graph showing near electric field strength measurements on the interior of the port side of wheel house at a height of the center of the windows. Three distances into the bridge are shown. Also included is a line showing the maximum radiation limit at a frequency of 6022 kHz according to IEEE Standard C95.1. All signal levels shown assume 100 watts of R. F. power at the antenna coupler input.

7.0 ACKNOWLEDGEMENTS

We wish to thank our sponsors for supporting this work. The USCG Research and Development Center, Groton, CT. provided the initial project idea, and supplied funding for the measurements conducted on Barracuda. The USCG Telecommunications and Information Systems Command (TISCOM), Alexandria, VA. supported the development of the computer model. Finally, the Commandant, office of acquisitions supported the work involving moving of the HF antenna.

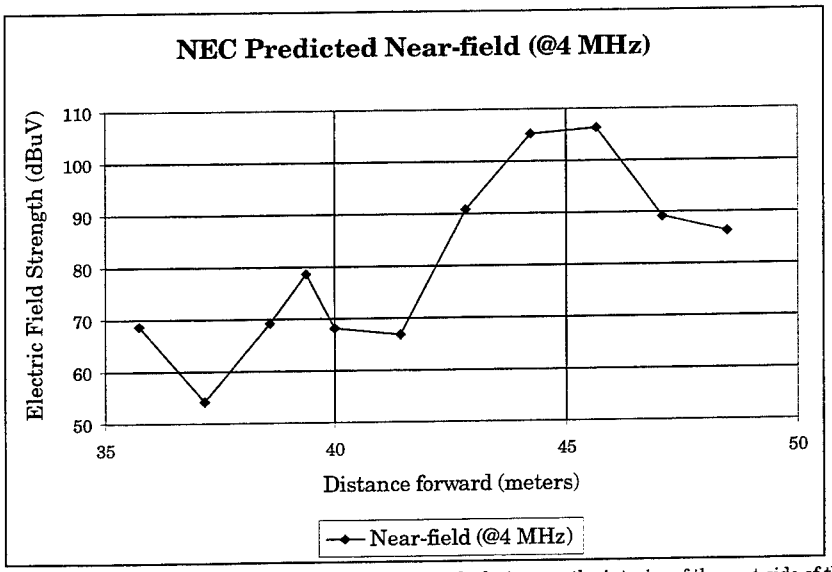

Figure 4. Graph showing the near electric field strength calculations on the interior of the port side of the wheel house at a height of the center of the windows.

REFERENCES

1. "IEEE Standard for Safety Levels with Respect to Human Exposure to Radio Frequency Electromagnetic Fields, 3 kHz to 300 GHz, IEEE C95.1-1991," published by the Institute of Electrical and Electronics Engineers, Inc., New York, NY, 1992.

2. Burke, Gerald J., "Numerical Electromagnetics Code - NEC-4 Method of Moments, Part I: User's Manual," January 1992, UCRL-MA-109338.

Principle Author may be contacted at:

Michael E. McKaughan
U. S. Coast Guard Academy
Academic Division (de)
27 Mohegan Avenue
New London, CT. 06320-8101

860.444.8538 (Voice) 860.444.8546 (FAX)

email: mmckaughan@exmail.uscga.edu

Extending a MoM/PO/UTD Hybrid Method by an Automatic Selection of the Computational Methods Based on Neural Networks

U. Jakobus, A. Buchau and F. M. Landstorfer

Institut für Hochfrequenztechnik, University of Stuttgart,
Pfaffenwaldring 47, D-70550 Stuttgart, Germany

Abstract — We present a neural network based approach which automatically assigns one of the computational methods MoM, PO or UTD to a specific region of a scattering body, so that a subsequent radiation or scattering analysis can be performed by a hybrid method combining these techniques. The automatic selection is based on geometric considerations and allows users who are not familiar with the theoretical background and limitations of the different numerical techniques to successfully apply the hybrid method to a variety of CEM problems.

1 Introduction

Highly advanced numerical methods and powerful computer codes are available today for the computation of electromagnetic fields. There is also a trend towards hybrid methods, which combine different numerical techniques in order to extend the range of applicability. However, it should be avoided that such computer codes can be used only by well trained and specialized persons. For instance, EMC engineers or antenna designers should be able to concentrate on the solution of their specific problems and should have CEM (computational electromagnetics) tools at their disposition in order to find an optimal solution or to gain physical insight. They cannot be expected to be familiar with all the details and limitations concerning the applicability of e.g. MoM (method of moments), FDTD (finite difference time domain), FEM (finite element method), UTD (uniform theory of diffraction), or PO (physical optics). A basic requirement of all CEM codes should be to give some feedback to the users and to warn them when some of the basic assumptions are violated, e.g. when the UTD is applied to an electrically small body.

In this paper we consider the computer code FEKO, which represents an implementation of a MoM/PO/UTD hybrid method (of course any of these techniques can be used alone). For unexperienced users it is a difficult task to determine the appropriate method to be used for specific regions. Therefore an automatic, neural network based selection is presented. The more general application of artificial intelligence and expert systems for CEM was already discussed in [1–3].

In Section 2 we introduce the basic idea of the hybrid method. A general representation of the geometry is described in Section 3, and Section 4 focuses on the parameter extraction and the application of a neural network. Some examples are presented in Section 5.

2 Description of the hybrid method

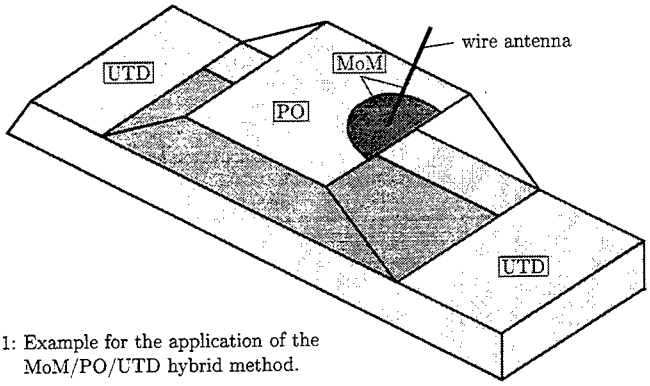

Fig. 1: Example for the application of the MoM/PO/UTD hybrid method.

The general idea of the hybrid method can be explained with the help of the symbolic representation in Fig. 1. If the radiation from the antenna on the roof of a car shall be investigated at a high frequency, one possible approach might be to model the antenna as well as a small area around the antenna with the accurate but time and memory consuming MoM. The remaining parts of the roof are taken into account by PO or the IPO variant (improved PO with correction terms, e.g. [4]) and the other parts of the car are assigned to the UTD–region. The coupling between the different methods is accurately taken into account, see e.g. [4–6] for details of the hybrid method.

The assignment of the different computational methods to the different regions requires some basic understanding of the accuracy and limitations of the methods and also their CPU–time and memory requirements. The selection, which strongly depends on the frequency under consideration, shall be automated.

3 General representation of the geometry

One basic requirement of the automated selection of an appropriate method is that the definition of the geometry by the user and the model generation are independent of the method that will be assigned only later to a particular region.

To illustrate our implementation consider the simple structure in Fig. 2 (a) consisting of two flat plates with one common edge. The user just specifies the plates through the corner points. If it turns out later that the UTD shall be used in this region, then the polygonal surfaces remain as depicted in Fig. 2 (a). The wedge, edge and corner information for treating the diffraction effects is extracted automatically.

On the other hand, the MoM and also our PO implementation require a subdivision of the structure into electrically small triangular patches. This is also done automatically (Delaunay triangulation,

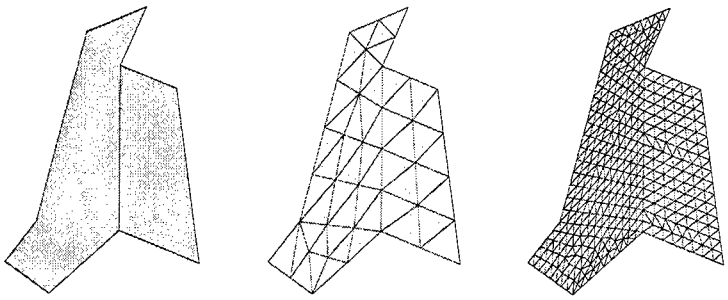

(a) Basic geometry (b) Subdivision into 51 triangular patches (c) Subdivision into 647 triangular patches

Fig. 2: Example for a simple geometry consisting of two polygonal shaped flat plates (a) with automatic subdivision into triangular patches for the MoM and PO at different frequencies (b,c).

e.g. [7,8]) without any interaction by the user and depending on the frequency more or less triangles are generated, see Fig. 2 (b,c).

4 Application of neural networks

Even though FEKO can handle dielectric bodies with either MoM or PO, the description here shall be restricted to metallic scatterers. For metallic wires the MoM is always selected, whereas metallic surfaces are subdivided into regions (no limitation in size) and a unique computational method is later assigned to each region. For instance in Fig. 1 the hood, trunk, wings etc. might represent different regions.

As illustrated in Fig. 3, for each region a set of parameters are determined:

- the surface A of the region
- minimal source distance d to the region ($d \to \infty$ for plane wave excitation)
- average radius of curvature ϱ of the region
- surface A_{proj} of the projection of the region onto a plane perpendicular to the direction of incidence
- tallness parameter $s = \frac{A_{proj}}{A_{circle}}$ where A_{circle} represents the area of the smallest circle enclosing the projection of the region

These values are normalized with respect to the wavelength (d, ϱ) or the square of the wavelength (A, A_{proj}), respectively. In order to compress the range (e.g. source distance d from 0 to ∞) and to obtain useful input values for the neural network, an additional scaling by an exponential function is performed, see labeling of the input nodes in Fig. 4.

Hence, the neural network requires 5 input nodes. We use 4 output nodes in order to represent the different computational methods available in FEKO: MoM, UTD, PO, and IPO [4] or Fock–currents [9]. The method corressponding to the highest value of the 4 output nodes is chosen. For

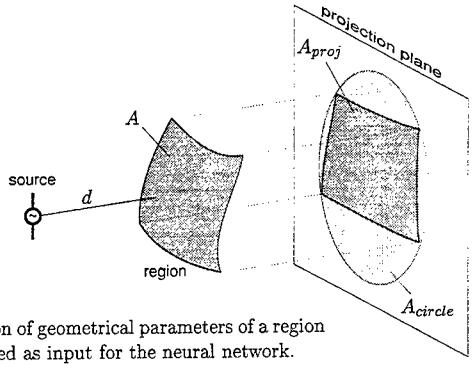

Fig. 3: Definition of geometrical parameters of a region to be used as input for the neural network.

IPO and Fock currents the same output node can be used since IPO can be applied only to flat surfaces, whereas Fock–currents are used on convex curved elements.

Investigations with SNNS (Stuttgart Neural Network Simulator [10]) have led to the non–recursive network topology as shown in Fig. 4 with 2 hidden layers and 10 nodes per layer. The nodes of adjacent layers are fully meshed. The network was trained by the standard back–propagation and the resilient back–propagation algorithms with data obtained from the analysis of numerous radiation and scattering problems. We created two different sets of weighting coefficients for:

- high accuracy, long run-times can be tolerated
- moderate accuracy (e.g. for certain EMC investigations) but emphasis on low memory requirement and CPU–time

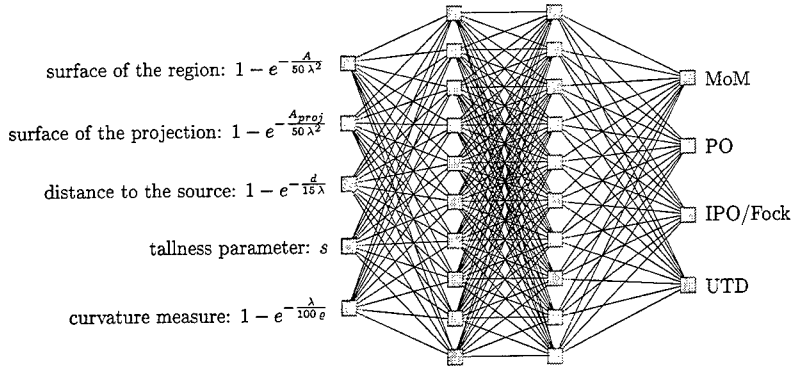

Fig. 4: Application of a neural network to the automatic selection of a computational method for a region and meaning of the input and output nodes.

5 Examples for the automatic selection of the computational method

Fig. 5: Determination of the monostatic RCS of a perfectly conducting cube with an edge length a.

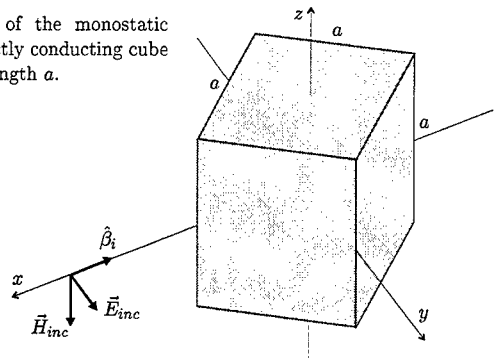

The first example is depicted in Fig. 5: The monostatic RCS of a perfectly conducting cube with an edge length a shall be determined over a wide frequency range so that $0.1 \leq \frac{a}{\lambda} \leq 7$ with the wavelength λ. The geometry is very simple and the 6 faces of the cube represent one region which is uniformly treated by either MoM, PO, IPO or UTD. It should be noted that even though the single faces are flat, the average radius of curvature ϱ of the whole region is finite.

For accurate RCS computations the neural network trained for a high accuracy should be used. It proposes the MoM up to the limit $\frac{a}{\lambda} = 2.53$ and the number of triangular patches increases continuously from 24 for $\frac{a}{\lambda} = 0.1$ up to 5816 at the limit $\frac{a}{\lambda} = 2.53$. For higher frequencies, the neural network suggests to use the IPO and the preprocessor automatically generates the

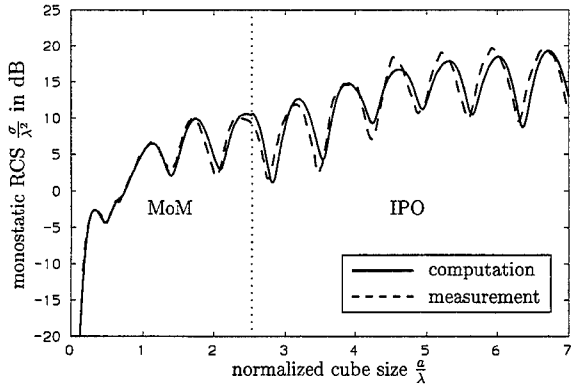

Fig. 6: Monostatic RCS σ of the cube as a function of the normalized edge length a.

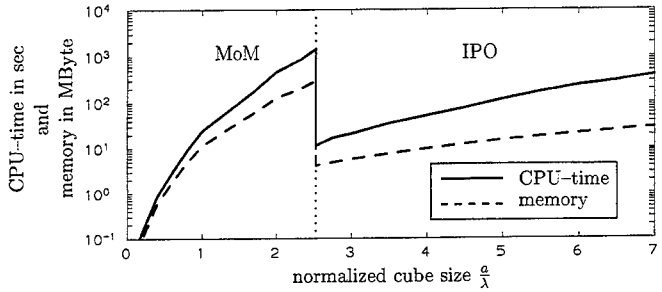

Fig. 7: Memory and CPU–time requirement for the monostatic RCS computation of the cube for (Pentium PC 266 MHz).

corresponding input file for FEKO. Even for higher frequencies the IPO remains the method being chosen, since the neural network was trained to know that we have not yet implemented the caustic corrections for the UTD required in this case for far-field computations with a plane incident wave.

In Fig. 6 we have plotted the computed RCS values and compare them to measurements from [11]. The cost in memory and CPU–time for the solution is depicted in Fig. 7.

The second example deals with a monopole antenna of height $h = 83.28\,\text{mm}$ mounted on a square plate with an edge length of $a = 1\,\text{m}$ as shown in Fig. 8. The input admittance Y of the monopole antenna as a function of the frequency f is shown in Fig. 9, where three methods are applied: MoM alone as reference solution, MoM/PO hybrid method (see Fig. 8 for regions), and the MoM/UTD hybrid method with MoM for the wire antenna and UTD for the plate.

Applying the neural network trained for high accuracy leads to an application of the MoM up to 1123 MHz, for higher frequencies the MoM/UTD combination is proposed. It is interesting to note the behavior of the neural network trained for moderate accuracy but short run–times and low memory consumption: The MoM is selected only for frequencies lower than 167 MHz

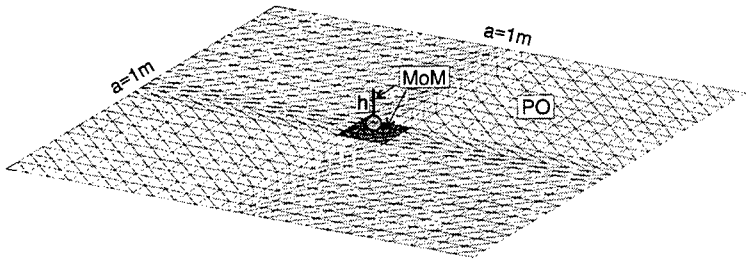

Fig. 8: Monopole antenna of the height $h = 83.28\,\text{mm}$ with a wire radius $\varrho = 0,3331\,\text{mm}$ in the center of a square metallic plate with an edge length of $a = 1\,\text{m}$. Shown is a possible arrangement for the combination of MoM and PO.

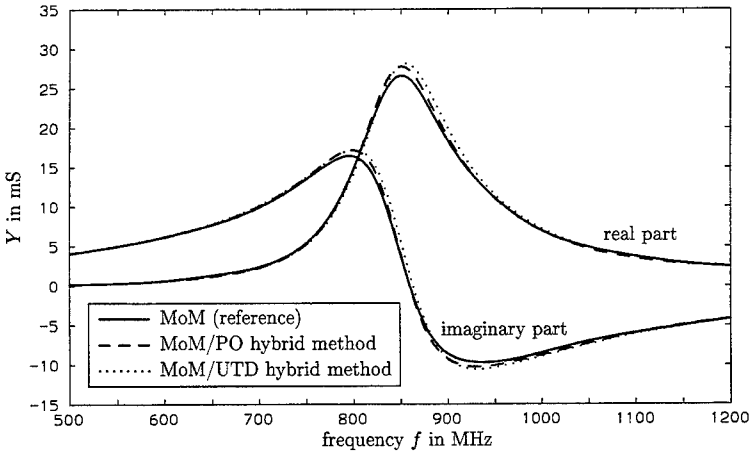

Fig. 9: Real and imaginary part of the input admittance Y of the monopole antenna on a metallic plate as a function of the frequency f.

corresponding to $\frac{a}{\lambda} = 0.56$. In the frequency range $167\,\text{MHz} < f < 313\,\text{MHz}$ ($0.56 < \frac{a}{\lambda} < 1.04$) the hybrid combination of MoM and IPO is proposed, and for higher frequencies the neural network decides to use MoM/UTD. Even though already for $\frac{a}{\lambda} = 0.56$ high frequency methods are involved, a good accuracy can be obtained as demonstrated in Fig. 10. Independent of the frequency, a solution takes less than 2 sec for a single frequency on a Pentium PC with 166 MHz.

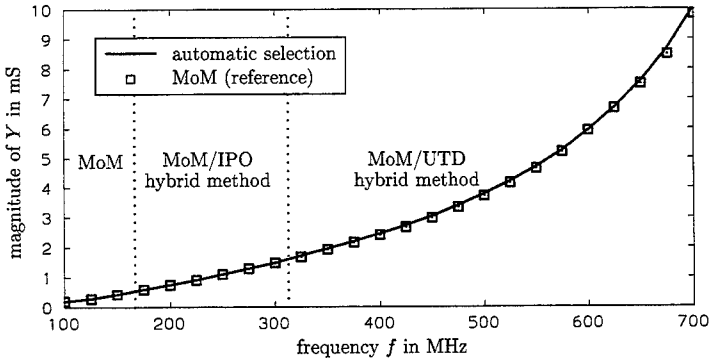

Fig. 10: Magnitude of the input admittance Y of the monopole antenna on a metallic plate as a function of the frequency f.

6 Conclusions

The application of a neural network to automatically select suitable numerical methods for the analysis of electromagnetic radiation and scattering problems has been discussed. The examples presented are based on the computer code FEKO, where MoM, PO and UTD are available. Two examples were presented which clearly show how the MoM used at lower frequencies is automatically replaced by the asymptotic methods or hybrid combinations at higher frequencies.

References

[1] A. L. S. Drozd, T. W. Blocher, and K. R. Siarkiewicz, "The intelligent computational electromagnetics expert systems (ICEMES)," *Applied Computational Electromagnetics Society Newsletter*, vol. 11, pp. 28–40, July 1996.

[2] A. L. S. Drozd, T. W. Blocher, and K. R. Siarkiewicz, "An expert system tool to aid CEM model generation," *Applied Computational Electromagnetics Society Newsletter*, vol. 12, pp. 17–23, July 1997.

[3] A. L. S. Drozd, T. W. Blocher, C. E. Carroll, and J. M. Allen, "Illustrating the application of expert systems to computational electromagnetics modeling and simulation," in *Conference Proceedings of the 14th Annual Review of Progress in Applied Computational Electromagnetics, Monterey*, vol. I, pp. 36–41, Mar. 1998.

[4] U. Jakobus and F. M. Landstorfer, "Improved PO–MM hybrid formulation for scattering from three–dimensional perfectly conducting bodies of arbitrary shape," *IEEE Transactions on Antennas and Propagation*, vol. 43, pp. 162–169, Feb. 1995.

[5] U. Jakobus and F. M. Landstorfer, "A combination of current– and ray–based techniques for the efficient analysis of electrically large scattering problems," in *Conference Proceedings of the 13th Annual Review of Progress in Applied Computational Electromagnetics, Monterey*, pp. 748–755, Mar. 1997.

[6] U. Jakobus and F. M. Landstorfer, "Current–based hybrid moment method analysis of electromagnetic radiation and scattering problems," *Applied Computational Electromagnetics Society Journal*, vol. 10, pp. 38–46, Nov. 1995. Special Issue on Advances in the Application of the Method of Moments to Electromagnetic Radiation and Scattering Problems.

[7] B. Joe, "Delaunay triangular meshes in convex polygons," *SIAM Journal on Scientific and Statistical Computing*, vol. 7, pp. 514–539, 1986.

[8] W. J. Schroeder and M. S. Shepard, "Geometry–based fully automatic mesh generation and the Delaunay triangulation," *International Journal of Numerical Methods in Engineering*, vol. 26, pp. 2503–2515, 1988.

[9] V. A. Fock, *Electromagnetic Diffraction and Propagation Problems, International Series of Monographs on Electromagnetic Waves*, vol. 1. Pergamon Press, Oxford, 1965.

[10] A. Zell and et al., "SNNS: Stuttgart neural network simulator, user manual," tech. rep., Institut für parallele und verteilte Höchstleistungssysteme, Universität Stuttgart, 1995.

[11] C. W. Trueman and S. R. Mishra, "A WWW–based data base for code validation," in *ACES 12th Annual Review of Progress in Applied Computational Electromagnetics*, vol. II, pp. 1092–1099, Mar. 1996.

Umbrella Top Loaded Antennas: Base Fed, Folded, and with a Tuned Insulated Counterpoise

John S. (Jack) Belrose, VE2CV
Radio Science Branch
Communications Research Centre
Ottawa ON Canada

Introduction

In 1982 I wrote an article [1] on umbrella top loaded antennas, based on an extensive experimental model study of base-fed antennas. However, in that article I described a method which could be used to feed an antenna with umbrella wires suspended from a grounded tower, by feeding the tower as a top-loaded folded unipole --- and this method of feed became the title of the article (editor's choice). Recently an interest in folded umbrella antennas has resurfaced [Bob Eldridge, VE7BS, private communications, August 1998]. Apparently some of VE7BS's New Zealand friends from "down under" (VK3ZL and VK6UZ) have landed on my Ham Radio article and were asking him questions about the folded version.

This paper is a result of my revisiting umbrella top-loaded antennas by computer simulation, which prompted a meticulous search of my files. This search brought to light, in my view, an interesting version of umbrella antennas. The "interesting version" of this type of antenna was devised by Carl E. Smith, now, in 1998 a silent key, which is an umbrella antenna with a tuned insulated counterpoise [2]. The subject of elevated radials is a topic that has interested me for a number of years, beginning (insofar as published papers is concerned) with my paper presented in the Amateur Radio Session of the 1996 ACES Conference [3].

The Umbrella Antenna

Electrically short tower performance can be improved by top loading, which increases the radiation resistance, and lowers the base reactance. The umbrella antenna is one method to top load a tower, without the need to install additional towers to support the top loading. This antenna is illustrated in **Fig. 1a**. The top loading consists of a number of active umbrella wires, connected to the top of the tower, and strung obliquely to ground. The important parameters for such an antenna are the height, h, of the tower; the horizontal distance, d, from the base of the tower to the extremities of the insulated guys supporting the conducting umbrella wires; and the vertical distance, s, from the top of the tower to the height where the umbrella wires are broken by an insulator.

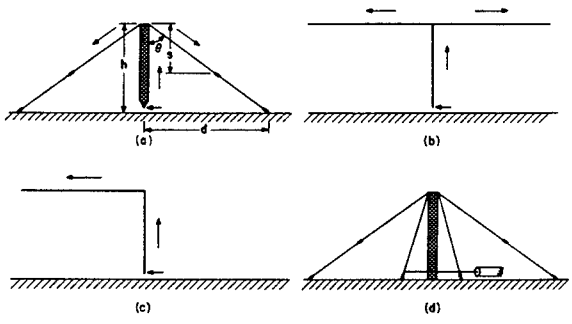

Fig. 1 Sketches illustrating phasing of currents on umbrella antenna, T- and L-type radiators. The sketch in (a) illustrates insulated base feed; that in (d) a grounded tower folded umbrella antenna.

The sketches in **Figs. 1a, 1b and 1c** illustrate the phasing of the currents on various top-loaded vertical antennas, the umbrella antenna, the T-, and the inverted L-type antennas; thus illustrating the difference between these types of radiators. In the case of the T- and inverted L-type radiators, the currents on the flat top and on the vertical part of the antenna system are not opposing, since these currents are on elements that are orthogonally oriented (in space). Also, recall, considering

the antenna and its image in the ground. that only the current on the vertical part(s) of the antenna contributes appreciably to radiation. The currents on the flat-top and on the image of the flat-top in the ground are in phase opposition, and so essentially cancel insofar as radiation is concerned. The currents on the vertical part(s) of the radiator and its image in the ground are in phase.

In the case of the umbrella antenna, however, the currents on the umbrella wires have a vertical component that is oppositely directed to the current on the tower; and therefore radiation from the top part of the tower over the distance s and from the umbrella wires partially cancel.

Thus, while the capacitive reactance of the top hat increases, and the base reactance decreases, as the length and number of umbrella wires increase; the radiation resistance, R_r, first increases, and then decreases. The radiation resistance, in accord with our experimental model study, is a maximum when s/h = 0.43.

The Folded Umbrella Antenna

The sketch in **Fig. 1D** illustrates an umbrella antenna employing a grounded tower, which is configured as a folded element. This arrangement can be designed to raise the impedance of the antenna to the value required by the feeder. The latter may then be connected directly to the antenna, if the length of the umbrella wires are adjusted for resonance, without the need for a matching unit. The tower is grounded at its base, and a cage of wires surround the tower, connected to the top of the tower, and insulated at the bottom. The feeder is connected directly to the bottom of this cage of wires, to a skirt wire that joins the ends of this cage of wires.

Nolan [4]-has used such an antenna system for MF broadcasting, but he provides no design information, other than that the height of the tower can be short (0.1 λ), and if 4-wires are used for the cage, the resonant antenna can be connected directly to the feeder. For resonance, the capacitance of the umbrella top hat must tune with the inductance of the mast and cage of wires in parallel. This will require slightly more top loading than for the base fed antenna, but how much?

The Smith Tuned Counterpoise Umbrella Antenna

Smith, in the reference cited above describes an electrically short antenna system which employs a tuned elevated electrically short radial wire ground system, see **Fig. 2**. This is an interesting antenna, not only (from my point of view) because it employs (tuned) elevated radials, but, notice the way in which he has configured the tower. The effect of the top loading can be enhanced by adding a low loss inductance at the top of the tower. This low loss inductance at the top of the tower is achieved by an insulated conductor inside the tower, and shorting it to the tower to simulate a short circuited coaxial line with an open end and inner conductor connected to the top loading hat at the top of the tower. I must say that this is rather clever --- I had previously not seen such an arrangement. Can NEC-4D (I use the EZNEC pro 4D version) model such an antenna system? We will address this below.

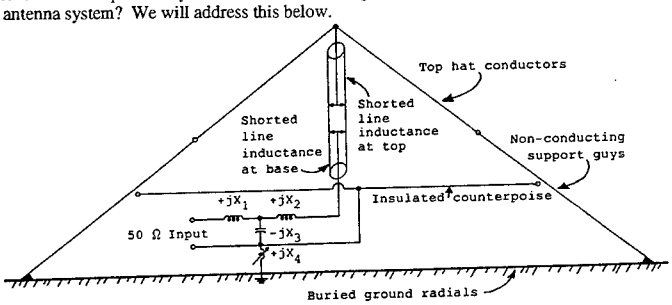

Fig. 2 Top loaded monopole with insulated counterpoise and buried radial ground system (after Smith [2]).

The current distribution on the top hat conductors can be assumed to be sinusoidal, with zero current at the outer ends and a maximum current at the top of the tower where they are joined together. At this point the top loading inductance, or open end of a short circuited coaxial line, in series can replace an appreciable portion of the sine wave, with the result that the current distribution on the tower can be essentially constant.

At the bottom of the tower more series inductance can be added by insulating a conductor up inside the tower to a shorted point.

The Smith Tuned Counterpoise Umbrella Antenna is Modelled

Smith gives some detail on a version of his umbrella top loaded antenna with a tuned elevated counterpoise in use at Kodiak, Alaska, station KVOK operating on 560 kHz. This station employs a tuned insulated counterpoise. The antenna is a vertical radiator, see **Fig. 3**, mast height 43.5 m (143 feet), 0.08 λ; with umbrella top-loading, 16 drooping radials, length 38.1 m (125 feet), 0.071 λ and s/h = 0.5; fed against 16 insulated radial wires, height 3 m, length 45.7 m (125 feet), 0.085 λ. The counterpoise is connected to the antenna system coupling unit and to ground through a counterpoise series reactance (reference **Fig. 2**) which is tuned to maximize the field strength radiated in the far field. Station KVOK employs a simple uniform tower.

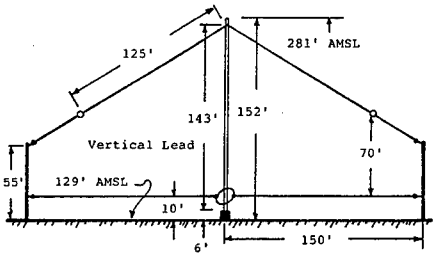

Fig. 3 Vertical plan sketch of tower top loading and counterpoise for station KVOK.

Smith describes his view with respect to minimizing ground loss. The E-field between the top hat and the counterpoise can be likened to a transmission line that is open at one end and shorted at the other. There is an E-field between the top hat and the counterpoise, and some of the E-field passes through to the ground beneath. The counterpoise potential is maintained so as to minimize the current in the lossy ground. The counterpoise series reactance ($+j X_4$ in **Fig. 2**, $+j X_C$ in our studies). His antenna employed an "abbreviated" buried radial wire ground system (but details were not given). I assume, for our model, a 6 m stake ground.

First, I have computed the antenna's self impedance. For this umbrella top loaded antenna fed against a PEC ground, $Z_a = 6.8 + j\ 145.5$ ohms. The unattenuated field strength at 1 km $E_u = 256$ mVm for a transmitter power of 1 kW. The fact that the antenna is so heavily top loaded that its base reactance is inductive was not commented on by Smith.

With the 16 elevated resonant radials over average ground, we compute $Z_a = 7.1 + j\ 130.3$ ohms; and $E_u = 255$ mV/m. The field strength E_u (for the case of real ground) is the unattenuated field strength, FS, at 1 km for a transmitter power of 1 kW, which for results given here is based on the FS at 200 metres, attenuated by 1/d to d = 1000 m.

Smith indicates that the proper method of tuning his counterpoise system is to observe the far field zone field strength while tuning the system. Indeed, **see Fig. 4**, dramatic variations in field strength should be observed as the counterpoise is tuned, which is in accord with observation. As the reactance of this counterpoise series inductance is increased, the base impedance of the antenna and the field strength change rapidly with increasing reactance, for $X_C < j\ 400$ ohms; after which the changes with increasing reactance are rather small, asymptotically approaching limiting values for a rather high reactance value. When $X_C = j\ 1000$ ohms, $Z_a = 9 + j\ 78$ ohms; and $E_u = 234$ mV/m (a coil Q-factor of 300 was assumed). Smith measured an antenna resistance of 7.2 ohms for his "tuned" antenna.

Therefore, the radiation efficiency (according to NEC-4D) for this tuned counterpoise antenna over real (average) ground $\eta = 83$ percent. This radiation efficiency estimation is based on the relation that the radiated power, P_r, varies as E_u^2. Smith's estimate for the radiation efficiency is 92-percent (based on his value for $R_r = 6.6$ ohms, and his measured antenna resistance $R_a = 7.2$ ohms).

Whatever, I concur with the conclusion of James Corum of Corum Associates, Inc. (see reference [2]), that the Smith low loss tuned counterpoise structure is a remarkable addition to the technology of electrically small antennas.

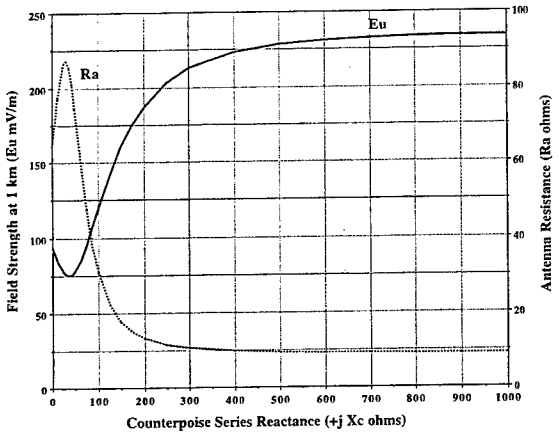

Fig. 4 Calculated change in unattenuated field strength at 1 km (E_u) and antenna system base resistance (R_a), versus counterpoise series reactance (+ j X_c).

Design Examples for 160M Antennas

In what follows I describe modelling of interest for the radio amateur, that is umbrella antennas for the 160M band. I have not tried to optimize parameters, that is reserved for a follow on study for publication in the amateur radio literature.

The Smith Tower Arrangement

First, I model a conventional base fed tower with umbrella top loading over a PEC ground. I will address later the tuned insulated counter poise. For a 15.3 m tower (diameter 243 cm), base height 1 m; with 8 umbrella wires and s/h = 0.43, d/h = 1.4 --- NEC-4D tells us that the antenna is resonate at 1.95 MHz. The base impedance Z_a = 11.1 ohms.

Next. I configure the tower as devised by Smith, see **Fig. 5**, in which the open ends of a short circuited coaxial line are employed to place a low loss inductor at the top, and at the bottom of the tower. I have arbitrarily placed the short circuits at 1/3 h and 2/3 h. The antenna system's base impedance (according to NEC-4D) Z_a (1.95 MHz) = 10.4 + j 97.2 ohms. As expected the resonant frequency of the antenna system is lowered significantly, to 1.59 MHz, and Za = 6.1 ohms. It seems that indeed NEC-4D does model this antenna, but I have no experimental data with which to compare.

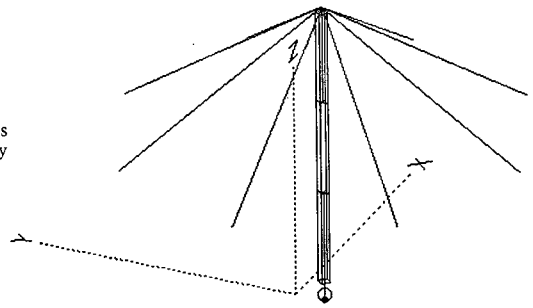

Fig. 5 Modelling umbrella antenna with low loss inductances at top and at base of the tower, by simulating short circuited coaxial line sections.

Base Fed Antenna

In my 1982 Ham Radio article I considered a design example for a 160M antenna, a frequency of 1.815 MHz. I chose s/h = 0.43 (which is the value for a maximum in the radiation resistance R_r), eight umbrella wires, and d/h = 1.4. This base-fed antenna should be resonant (according to my experimental study) when the tower height is 16.5 metres; and the radiation resistance R_r = 7 ohms.

As a result of the recent interest in umbrella antennas (referenced above), I have numerically analyzed this design example. According to NEC-4D this antenna should be resonant at 1.84 MHz (I had estimated resonance based on our experimental model studies to be 1.815 MHz); and the antenna's impedance, Z_a, (no ground loss) is 11.6 ohms.

Folded Umbrella

When I wrote the article on umbrella antennas I had done a lot of experimental modelling of such antennas, base fed. I got caught up on the idea of feeding the tower as a top-loaded folded unipole, having come across the article by Nolan. I noted that for practical use the antenna system should be made self resonant, that is the capacitance of the umbrella top-loading must tune with the inductance of the mast and the cage in parallel, and that this would require more top loading than for the base-fed antenna --- but I had no measured data. If I feed the umbrella antenna, dimensioned as above, as a folded-unipole (4-wires in the cage, distance from the tower to the ends of the cage wires 1-metre, height above ground 1 m), the resonant frequency is indeed higher, 2.122 MHz according to NEC-4D; and the input impedance equals 46.5 ohms (assuming no ground resistance loss).

Clearly more top loading or a larger antenna system (taller tower) is needed for a 160M antenna. According to NEC-4D the resonant height for the folded umbrella antenna, having parameters as above, h = 18.5 metres; and, assuming a ground loss resistance of 5-ohms the input impedance is 50 ohms.

This calculation is for the antenna parameters as given in my 1982 HR article: i.e. s/h = 0.43; d/h = 1.4, the number of top loading umbrella wires n = 8. For h = 18.5 m, f_o = 1.87 MHz.

The 2:1 50-ohm SWR bandwidth is 1.815 to 1.92 MHz: SWR increases more rapidly above resonance than below. Above resonance the antenna is inductive, and so it could be resonated by a capacitor.

Tuned Counterpoise Modelled

For the interest of the radio amateur, I have dimensioned an antenna similar to the one Smith describes for the 160M band (frequency 1.9 MHz). I have not tried to optimize parameters. Instead I have dimensioned an antenna which seems to me to be practical. Sketch it out and you will see. I have assumed that the radiator is a pipe mast 5.08 cm diameter, having a (practical) length of 10 m (0.0.063 λ); s/h = 0.5; and d/h = 2. The base of the mast is 2.5 m above the ground --- so that one can walk beneath the radial wire counterpoise system. The length of the counterpoise radial wires is 20 m (0.126 λ). That is the non-conducting support guys for the top-hat conductors connect to the 2.5 m high posts supporting the radial wires of the counterpoise. "Ground" is average ground (σ = 5 mS/m, ε = 13).

First, for reference purposes, we determine the number of umbrella wires needed to resonant this antenna, ground based, PEC ground. For n equal to 8, 16, and 24-umbrella wires, the antenna's impedance Z_a equals 3.4 - j 60.2 ohms (and E_u = 281.5 mV/m), 3.3 + j 1.6 ohms and 3.2 + j 25.2 ohms respectively.

For our example antenna we chose n = 8, see **Fig. 6**, since for the radio amateur this is practical number of umbrella wires --- hence our example antenna fed against the tuned counterpoise wires is not resonant. As the reactance of the tuning coil (+ j X_C in our study, + j X_4 in Smith's antenna system) is increased, the field strength, Eu, first decreases, then increases rapidly at first, and finally more slowly, asymptotically approaching some final value. For j X_C = j 1000 ohms, Q = 300, Eu = 221.4 mV/m, which corresponds to a radiation efficiency (assuming no loss in the antenna matching circuit) η = 62 percent --- which again in our view is rather remarkable for such an electrically short antenna. The antenna system impedance Zas = 4.5 - j 127 ohms. The space wave pattern is entirely vertically polarized (gain G = - 0.6 dBi).

This umbrella antenna, fed against 8 resonant elevated radials, length 37.55 m, height 2.5 m, would have an impedance Z_a = 3.5 - j 72 ohms, and E_u = 248.3 mV/m, η = 78 percent. But radials having a length of 37.55 m (123.2 feet) will not fit in a typical back yard.

Certainly as remarked in the discussion above, and in the discussion following Smith's paper, the antenna system devised by him has a remarkable efficiency for such a small antenna, with an abbreviated ground system.

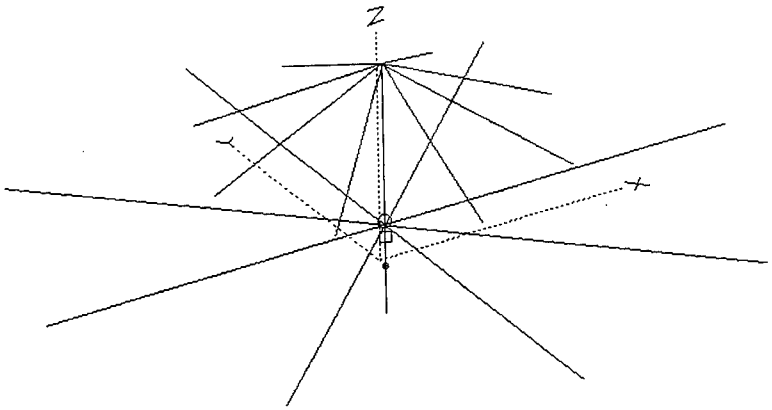

Fig. 6 Modelling a 160 M umbrella antenna with tuned elevated radials.

Concluding Remarks

The umbrella antenna with a tuned radial wire counterpoise makes a practical low loss 160M antenna, which will fit in a typical back yard. While clearly the counterpoise has to be tuned, for maximum FS, "tuning" does not resonate the antenna. As the reactance of this series reactance + jX_C is increased, the FS approaches a maximum value, and the antenna's resistance approaches the value it would have for a PEC ground (or the value it would have for the case where resonant radials were employed). But the antenna's reactance is increased over the reactance it would have over a PEC ground.

In my view, this study of an umbrella antenna fed against a tuned radial wire ground system, should be of interest to amateurs in radio desiring a practical antenna for the 160M band --- an alternative to burying a large number of radial wires.

References

1. Belrose, J.S.., "Folded Umbrella Top Loaded Vertical Antenna", Ham Radio, September 1982, pp. 12-17.

2. Smith, C.E., "Short Low Loss AM Antenna", IEEE Trans. on Broadcasting, **35**, June 1989, pp. 237-240.

3. Belrose, J.S., VE2CV, "Ground-Plane Type Antennas with Elevated Radial Systems", Conference Proceedings, 12th Annual Review of Progress in Applied Computational Electromagnetics, Naval Post Graduate School, Monterey, CA, 18-22 March 1996, pp. 2-11.

4. Nolan, S.U., "Developments in MF Radiator Systems", Sound and Vision Broadcasting, **15**, Spring 1974, pp. 1-3.

PLENARY SESSION 3

Edmund K. Miller

OBSERVATIONS FROM THE COMPUTATIONAL ELECTROMAGNETICS REVOLUTION: A PERSONAL PERSPECTIVE

E. K. Miller
3225 Calle Celestial, Santa Fe, NM 87501-9613
505-820-7371, emiller@nm-us.campus.mci.net

The tools available for, and the practice of, computational electromagnetics (CEM) have changed unimaginably since I first became involved in the field in the late 1950s. At that time the computer group at the Radiation Laboratory of the University of Michigan, which I joined as an Assistant Research Engineer, consisted of a team of female research assistants who operated electromechanical calculating machines. The mathematician group leader served as the programmer, designing both the algorithms and data-flow sheets. Each calculator operator performed designated calculations, recorded the results, and passed the data sheet to the next person in line. Although not very fast, operating at a "FLOP" rate of perhaps 2-4/minute, significant computations were done, including developing tables of various classical functions. The first Rad Lab digital computer was the IBM 704, which was programmed with patch panels, and the mainframe computer at the University on which I learned to program to complete my PhD research in 1965 was the IBM 7094.

The hardware tools available for CEM have increased in speed and storage by orders of magnitude in capability, from the 10^5 FLOP rate of the 7094 to rates now on the order of 10^12 FLOPS. Memory has similarly increased from 32k of 36-bit words of the 7094 to GBytes now. Input/output storage has changed from punched paper tape, punched cards and teletype terminals running at rates of a few Bytes/sec to magnetic and optical disks having transfer rates of 10s of MBytes/sec. Display systems that consisted of printer carriage plots and pen plotters have been replaced by color CRT monitors that seem likely themselves to be displaced by LCD displays, and color inkjet, laser and thermal-transfer printers. Finally, desktop computers have brought, what was just a short time ago mainframe power, to the direct control of the user.

Changes in the software tools used in CEM have proceeded apace. Frequency-domain integral-equation (FDIE) models made an appearance in the early to mid 1960s, followed shortly thereafter by the time-domain differential-equation (TDDE or FDTD). TDIE and FDDE models arrived towards the end of the decade. Problem sizes of the early 1960s were typically a few 10s of unknowns for FDIE models being initially limited to simple objects and shapes like wires and spheres. Problems now routinely modeled using IEs can involve 100s of thousands, and those using FDTD can have 10s of millions, of spatial unknowns. Problem complexity, including both geometrical and electrical, has advanced similarly. Recent attention has shifted towards so-called "fast" techniques whereby the reduced complexity of farther interactions is exploited to reduce the impact of frequency-scaling laws, reduced-order modeling using techniques like model-based parameter estimation, and hybrid techniques that seek to combine the best features of the individual approaches. Progress has also been made in input/output software, though this remains the weak link in most applications in terms of the overall cost of computer modeling.

This presentation will be a selective review of CEM over the past 40 years from my own experience and perspective. I'll highlight what I consider to be some of the more significant developments in both hardware and software as they have affected CEM capabilities. To conclude, I'll try to anticipate what the future might hold over the next 40 years.

SESSION 8

CONFORMAL ANTENNAS

Chairs: Doug Werner and Ping Werner

Mutual Coupling between Microstrip Antennas on a Cylindrical Surface

Kin-Lu Wong
Department of Electrical Engineering
National Sun Yat-Sen University
Kaohsiung, Taiwan 804

Abstract

Coupling characteristics of cylindrical microstrip antennas have been extensively investigated. The mutual coupling coefficients between two cylindrical microstrip antennas with rectangular, triangular, and circular patches have been analyzed theoretically and experimentally. Different theoretical approaches using full-wave analysis, cavity-model method, and generalized transmission- line model (GTLM) theory are described in this article. Comparison of the measured data with theoretical results is also given.

1. Full-wave Solution of Mutual Coupling Coefficient

The mutual coupling characteristics between two cylindrical rectangular or triangular microstrip antennas have been analyzed using a full-wave approach and a moment-method calculation [1-3]. Figs. 1(a) and 1(b) show the configurations of two cylindrical rectangular and triangular microstrip antennas, respectively. The two probe-fed microstrip antennas are first treated as a two-port network with a 2×2 port matrix $[Z^p]$ as shown in Fig. 2. The relation between the port voltages and currents are defined as

$$\begin{bmatrix} V_1^p \\ V_2^p \end{bmatrix} = \begin{bmatrix} Z_{11}^p & Z_{12}^p \\ Z_{21}^p & Z_{22}^p \end{bmatrix} \begin{bmatrix} I_1^p \\ I_2^p \end{bmatrix}, \tag{1}$$

where the superscript p denotes the port quantities. To determine the port impedance matrix, the input impedance Z_{11}^p of the excited antenna with the presence of the other antenna open-circuited and the mutual impedance Z_{12}^p between the two antennas need to be calculated. It should be noted that since the measurements of voltages and currents at microwave frequencies are difficult, a scattering matrix related to the direct measurements of incident, reflected, and transmitted waves is used to completely describe the multiport network problem. For a two-port network shown in Fig. 2, the scattering matrix [S] can be evaluated from

$$[S] = ([Z^p] - Z_c[U])([Z^p] + Z_c[U])^{-1}, \tag{2}$$

where [U] is a unit matrix of order 2×2 and Z_c is the characteristic impedance of the feeding coax (can be assumed to be 50 Ω here). As to solve Z_{11}^p and Z_{21}^p, the following formulas are applied:

$$Z_{11}^{p} = -\int_{v_{p1}} \vec{E}^{(1)} \cdot \vec{J}_{p}^{(1)} dv, \tag{3}$$

$$Z_{21}^{p} = -\int_{v_{p2}} \vec{E}^{(1)} \cdot \vec{J}_{p}^{(2)} dv, \tag{4}$$

where $\vec{E}^{(1)}$ is the total electric field inside the substrate layer due to the probe current at port 1, and v_{pi} is the volume over the probe at port i. With Z_{11}^{p} and Z_{21}^{p} determined, the mutual coupling coefficient can be calculated from Eq. (2) and given as

$$S_{12} = 2Z_{21}^{p} \cdot Z_c / [(Z_{11}^{p} + Z_c)^2 - (Z_{21}^{p})^2]. \tag{5}$$

From the above formulation, the mutual coupling characteristics have been analyzed. Typical results versus edge spacing S, the distance between edges of two patches, for the E-plane and H-plane coupling cases are presented in Figs. 3 and 4. In the study the input impedance of the isolated microstrip antenna with various cylinder radii of interest is all adjusted to be 50Ω at the TM_{01} mode excitation (rectangular patches) or the TM_{10} mode excitation (triangular patches). The obtained Z_{11}^{p} is found to vary slightly with 50Ω, and the value of Z_{21}^{p} is strongly affected by the cylinder radius and edge spacing. It is observed that for a large edge spacing, the coupling decreases more rapidly with increasing cylinder radius. Different curvature effects on the E- and H-plane mutual coupling are observed. Good agreement between experiment and theory is also seen.

2. Cavity-model Solution of Mutual Coupling Coefficient

Theoretical formulation using a cavity-model method has also been applied for the study of mutual coupling between cylindrical microstrip antennas with rectangular and circular patches [4, 5]. Expressions of the mutual impedance and mutual coupling coefficient have been derived, and typical numerical results for the E-plane and H-plane coupling cases have been reported. To adopt the cavity-model theory, the thin-substrate condition is assumed and the substrate thickness is also assumed to be much smaller than the cylinder radius and the operating wavelength. And owing to the thin-substrate assumption, the surface-wave effect on the mutual coupling can be ignored. It is also assumed that the mutual interaction does not disturb the interior field distribution inside the cavity below the microstrip patches. Based on these assumptions, the mutual impedance between the two antennas can be calculated from

$$Z_{21} = \frac{1}{I_1 I_2} \oint \vec{H}_1 \cdot \vec{M}_2 d\ell, \tag{6}$$

where I_1 and I_2 are the feed currents of the two antennas, $\vec{H}_1$ is the magnetic field set up by antenna 1 on antenna 2, and $\vec{M}_2$ is the equivalent magnetic current of antenna 2. Based on the cavity-model analysis, the mutual impedance for the E-plane and H-plane coupling cases can be derived as follows:

$$Z_{21}^{E}=\left(\frac{hE_{01}}{2\pi w_p}\right)^2\left\{R_1+\sum_{p=1}^{\infty}[R_2(p)+R_3(p)]\right\}, \tag{7}$$

where the parameters have been given in [4, 5].

With the mutual impedance obtained, the mutual coupling coefficient S_{12} for the E- and H-plane coupling cases can then be calculated from Eq. (5). And due to the assumption that the mutual interaction does not disturb the interior field distribution of the antenna, the self-impedance is here equal to the input impedance of the isolated antenna. Thus, in this case, Eq. (5) can be reduced to be

$$S_{12}=\frac{100Z_{21}}{10^4-Z_{21}^2}. \tag{8}$$

Numerical results calculated from Eq. (8) have also been analyzed. Results show that the obtained cavity-model solutions of mutual coupling coefficients agree well with the full-wave solutions. And since the computation of one cavity-model solution of S_{12} requires less time than that of the full-wave solution, this makes the cavity-model analysis useful for antenna engineers in related practical designs.

3. GTLM Solution of Mutual Coupling Coefficient

Mutual coupling between two cylindrical rectangular or circular microstrip antennas has also been studied using the GTLM theory [6, 7]. As referring to the geometry in Figs. 1(a) and 1(c) and considering the patches to be excited at their respective fundamental resonant modes, the two rectangular or circular microstrip antennas can be represented by the equivalent circuits shown in Figs. 5 and 6, respectively. In Fig. 5 the two rectangular patches are modeled as sections of transmission lines and are replaced by equivalent π networks of g_1, g_2, g_3 and g_1', g_2', g_3'. The circuit element $y_s - y_m$ is the total wall admittance at the radiating edges; y_s denotes the self-admittance and y_m denotes the mutual admittance. To solve the equivalent circuit, we decompose the circuit into three cascade connections of two-port networks. The ABCD matrix for a two-port network is used in the analysis of the cascade networks and we have [6]

$$\begin{bmatrix}V_1\\I_1\end{bmatrix}=\begin{bmatrix}A & B\\C & D\end{bmatrix}\begin{bmatrix}V_4\\-I_4\end{bmatrix}$$
$$=\begin{bmatrix}A^{(1)} & B^{(1)}\\C^{(1)} & D^{(1)}\end{bmatrix}\begin{bmatrix}A^{(2)} & B^{(2)}\\C^{(2)} & D^{(2)}\end{bmatrix}\begin{bmatrix}A^{(3)} & B^{(3)}\\C^{(3)} & D^{(3)}\end{bmatrix}\begin{bmatrix}V_4\\-I_4\end{bmatrix}. \tag{9}$$

The relation between ABCD and Z parameters can be obtained from

$$\begin{bmatrix}Z_{11} & Z_{12}\\Z_{21} & Z_{22}\end{bmatrix}=\begin{bmatrix}A/C & (AD-BC)/C\\1/C & D/C\end{bmatrix}. \tag{10}$$

With the [Z] matrix determined, the mutual coupling coefficient can be calculated from Eq. (5) with Z_c set to 50Ω. As for the equivalent circuit shown in Fig. 6 for the case of two circular patch antennas, an additional mutual admittance, y_{AB}, between the radiating edges of the two circular patches is introduced and the equivalent circuit can be simplified to be

$$\begin{bmatrix} V_1 \\ V_2 \end{bmatrix} = \begin{bmatrix} Z_{11} & Z_{12} \\ Z_{21} & Z_{22} \end{bmatrix} \begin{bmatrix} I_1 \\ I_2 \end{bmatrix}, \tag{11}$$

where I_1 and I_2 are the probe input currents, and V_1 and V_2 are the probe excitation voltages; expressions of the elements in the [Z] matrix can be found in [7]. With the [Z] matrix obtained, the mutual coupling coefficient is also readily evaluated from Eq. (5).

Typical mutual coupling coefficients versus edge spacing for the E- and H-plane coupling cases are shown in Fig. 7. From the results obtained, good agreement between the measured data and calculated GTLM solutions is observed, and the dependence of the mutual coupling on the cylinder radius is observed to be the same as that obtained using the cavity-model and full-wave solutions.

4. Conclusions

Various theoretical models such as full-wave formulation, cavity-model analysis, and GTLM theory have been successfully applied in the study of mutual coupling characteristics for two microstrip antennas mounted on a cylindrical surface. The theoretical results obtained for the mutual coupling coefficients are in good agreement with the experimental results. More calculated and measured results will be given and discussed in the presentation.

References

1. K. L. Wong, *Design of Nonplanar Microstrip Antennas and Transmission Lines*, John Wiley & Sons, Inc., New York, 1999.
2. K. L. Wong, S. M. Wang, and S. Y. Ke, "Measured input impedance and mutual coupling of rectangular microstrip antennas on a cylindrical surface," *Microwave Opt. Technol. Lett.*, vol. 11, pp. 49-50, 1996.
3. S. C. Pan and K. L. Wong, "Mutual coupling between triangular microstrip antennas on a cylindrical body," *Electron. Lett.*, vol. 33, pp. 1005-1006, 1997.
4. J. S. Chen and K. L. Wong, "Mutual coupling computation of cylindrical-rectangular microstrip antennas using cavity-model theory," *Microwave Opt. Technol. Lett.*, vol. 9, pp. 323-326, 1995.
5. J. S. Chen and K. L. Wong, "Curvature effect on the mutual coupling of circular microstrip antennas," *Microwave Opt. Technol. Lett.*, vol. 10, pp. 39-41, 1995.
6. C. Y. Huang and Y. T. Chang, "Curvature effects on the mutual coupling of cylindrical-rectangular microstrip antennas," *Electron. Lett.*, vol. 33, pp. 1108-1109, 1997.
7. C. Y. Huang and K. L. Wong, "Input impedance and mutual coupling of probe-fed cylindrical-circular microstrip patch antennas," *Microwave Opt. Technol. Lett.*, vol. 11, pp. 260-263, 1996.

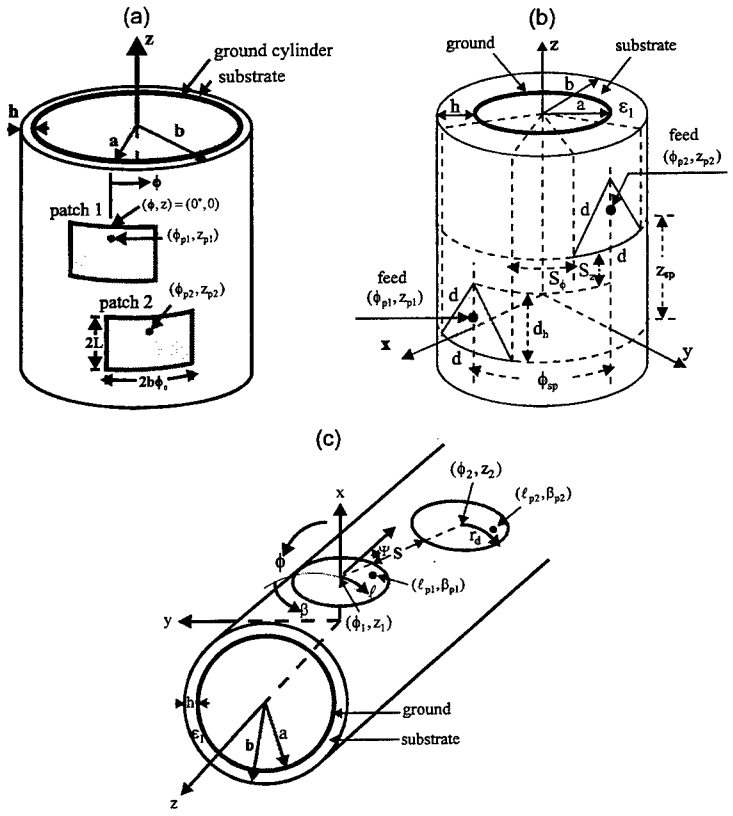

Figure 1 Configurations of two cylindrical microstrip antennas. (a) Rectangular patches. (b) Triangular patches. (c) Circular Patches.

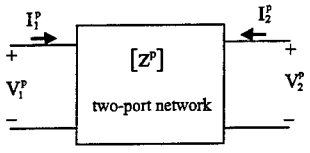

Figure 2 A two-port network representation of two coupled probe-fed microstrip antennas.

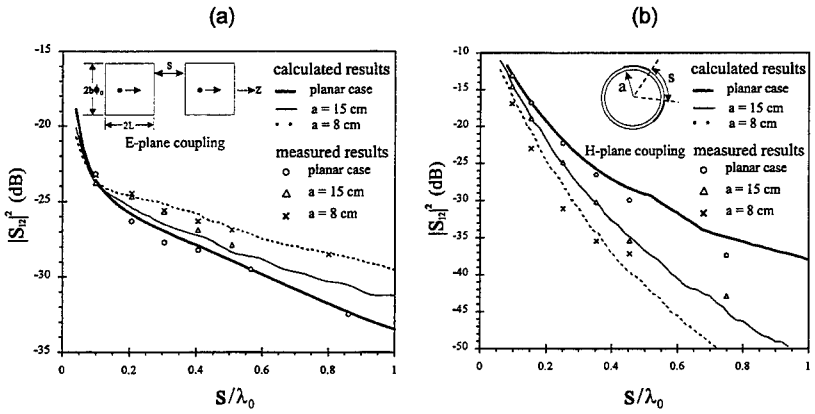

Figure 3 Calculated and measured mutual coupling coefficients for cylindrical rectangular patch antennas; h = 0.762 mm, $\varepsilon_1 = 2.98$, 2L = 6 cm, $2b\phi_0 = 4$ mm.
(a) E-plane coupling case. (b) H-plane coupling case.

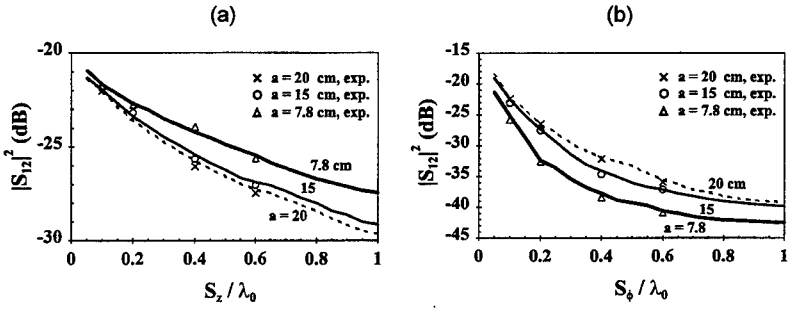

Figure 4 Calculated and measured mutual coupling coefficients for cylindrical triangular patch antennas; h = 0.762 mm, $\varepsilon_1 = 3.0$, d = 6 cm.
(a) E-plane coupling case. (b) H-plane coupling case.

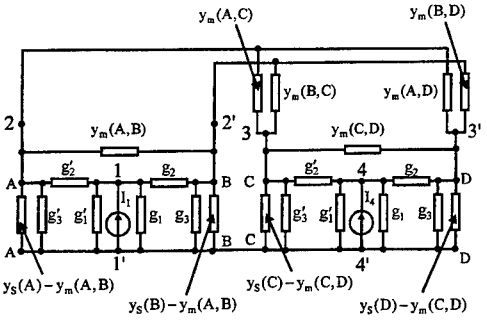

Figure 5 Equivalent circuit of two cylindrical rectangular microstrip antennas shown in Fig. 1(a).

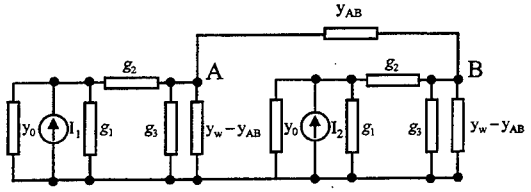

Figure 6 Equivalent circuit of two cylindrical circular microstrip antennas shown in Fig. 1(c).

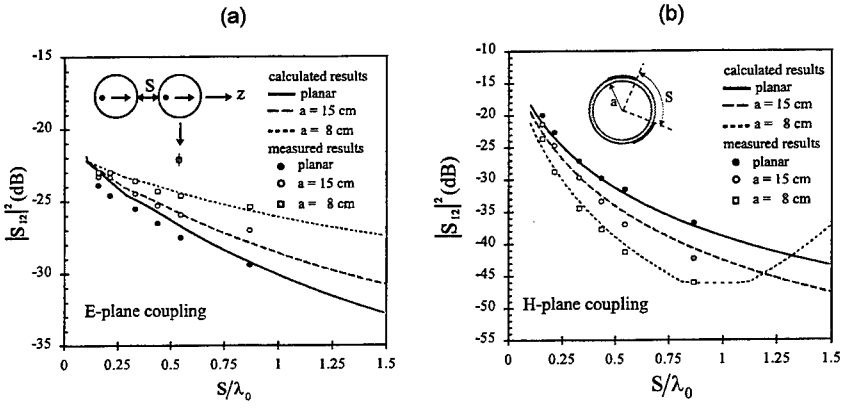

Figure 7 Calculated and measured mutual coupling coefficients for cylindrical circular patch antennas; h = 0.762 mm, $\varepsilon_1 = 3.0$, $r_d = 3.2$ cm.
(a) E-plane coupling case. (b) H-plane coupling case.

Simulating the Dielectric-loaded Quadrifilar Helix Antenna using a Brute-Force TLM Approach

O.P. Leisten, J.C. Vardaxoglou*, E. Agboraw

Navstar Systems Ltd (a division of SymmetriCom Inc), Mansard Close, Northampton NN5 5DL, UK
**Centre for Mobile Communications Research*
Dept. of Electronic and Electrical Eng., Loughborough University, LE11 3TU, UK

ABSTRACT
The performance of a dielectrically loaded quadrifilar antenna is assessed using a brute-force (Transmission Line Matrix) TLM simulation. The geometry and operation is described. The approach to casting a realistic model that is able to advance the design is discussed with a critical appraisal of the predictive accuracy. The proposed antenna falls into the category of small antennas and the simulations account for the high field concentration in the dielectric as well as the intricacies in the input impedance and feed mechanisms.

1. INTRODUCTION

The paper discusses the TLM simulation of a novel dielectric loaded quadrifilar helix antenna topology. This antenna has been the subject of considerable research using electromagnetic modelling and empirical techniques. Leisten et al [1,2] has previously published results from a study of miniaturised quadrifilar helix antennas employing ceramic dielectric materials to dielectrically foreshorten the resonant dimensions. From a computational electro-magnetics point of view this has proven to be a complex structure to simulate. The paper will demonstrate how measures to simplify the model to achieve computational efficiency have significantly reduced the predictive accuracy of the model. More realistic models that are able to advance the design is described with a critical appraisal of the predictive accuracy.

The antenna is formed as a metal circuit pattern that is printed on the surface of a cylindrical ceramic dielectric core. It offers advantages over conventional antennas with regard to the isolation of the currents on the antenna element from those on the hand-set ground-plane and near field detuning. It is targeted to be used in GPS instruments that are small enough to be used in cell phone handsets and also in Personal Communications Satellite services.

2. GEOMETRY DEFINITION

Although there are now many forms of quadrifilar antennas generically they all employ two quadrature phased bifilar helical loops which are placed at right angles to each other. The structure of the dielectric loaded quadrifilar helix antenna is shown in Figure 1.1. This antenna achieves quadrature phasing by means of using two bifilar helices which have slightly offset resonant frequencies. The elements of bifilar helix 1 are adjusted longer than resonance to produce an input impedance with a phase angle of +45° and the elements of bifilar helix 2 are adjusted shorter than resonance to produce an input impedance with a phase angle of -45°. This strategy

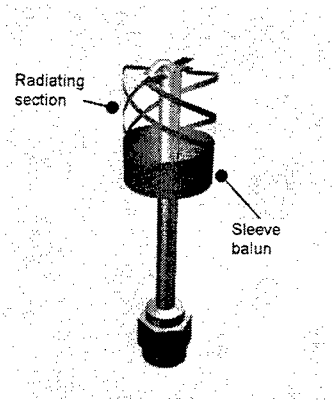

Figure 1.1: The structure of the dielectric loaded quadrifilar helix antenna

produces the 90°shift in phase between the currents in bifilar helix 1 with respect to bifilar helix 2.

In common with this configuration the structure employs balanced feed at the top and differentially phased lines to organise orthogonal current phase in ascending angle anti-clockwise around the periphery of the antenna. It incorporates a sleeve balun in the lower portion that projects a balanced signal feed to the back-fire tip of the antenna. The size of the antenna is significantly reduced with respect to its free space counterpart due to the dielectric loading that is afforded by the high permittivity ($\varepsilon_r \approx 30\text{-}90$) of the dielectric core.

The radiating section of the quadrifilar antenna can be viewed as being composed of two orthogonally disposed loops of nominal length 360°. In each loop current passes from one arm of a balanced input to flow around about a path consisting of a helical metal conductor around the rim of the balun or trap and finally in the diametrically opposite helical metal conductor to the opposite balanced member of the feed system.

3. THE ELECTROMAGNETIC MODEL

The main modelling tool that was used to model the crown-rimmed antenna was a commercial TLM electromagnetic simulator called MicroStripes™ [3]. The design methodology was to estimate dimensions by analytical means based on measured line parameters and to submit this antenna to a manual optimisation regime based on a battery of field solvers. Although MicroStripes™ can be supplied with programs which provide a means for graphical entry it was found to be more efficient to use custom Visual Basic™ programs to transcribe critical dimensions into the build language script that is interpreted by MicroStripe's geometry builder. In this way it was straightforward to submit a large number of optimisation trials to the simulator very quickly.

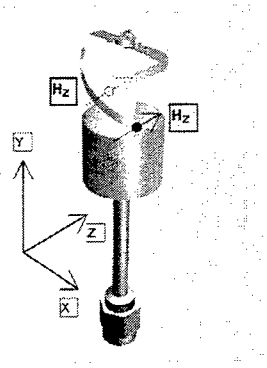

Figure 3.1: Magnetic probe measurements to indicate conditions for balanced resonance

A key advantage of a time domain simulator is that the designer does not need to have 'a priory' knowledge of the resonance frequency of the antenna. Using Fourier transformation certain indicators of resonance can be extracted as an outcome of the simulation. The method that was chosen to do this for the case of this topology can be illustrated using a simplified bifilar helix primitive model. Figure 3.1 shows how two magnetic field measurement points are defined close to conductors which demonstrate the magnetic field magnitude and phase that is associated with the currents in those conductors. For the loop mode the antenna should ideally be perfectly balanced and pass currents down one helix around the balun rim and up the diametrically opposed helix to complete the 360° loop. Therefore, at resonance the currents should be exactly equal in magnitude and opposite in phase at the probe positions that are marked in Figure 3.1. However in terms of the direction convention accorded to the H-field measurements in Figure 3.1 this state of balance is actually demonstrated by a cross-over of the H-field with frequency loci when they are both plotted on a polar plot.

The corresponding model for the quadrifilar antenna is more complicated because the antenna embodies two twisted loops, [1,2] from which four magnetic vectors, which are indicative of four currents, are obtained. The design

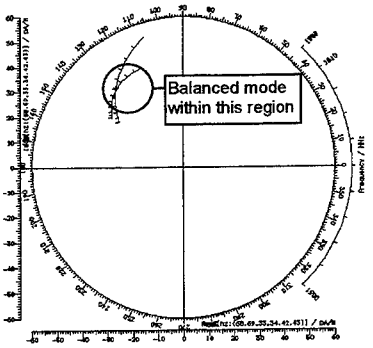

Figure 3.2: Magnetic field measurements indicating balanced resonance of twisted loop primitive

methodology was to organise the two loop pair cross-over points, each individually defined in the manner of Figures 3.1 and 3.2, into two orthogonal pairs which possess the same magnitude. This objective was visualised as a convenient optimisation goal.

4. RESOLUTION PROBLEMS WITH THE ELECTROMAGNETIC MODEL

In the course of working on the development of the dielectrically loaded quadrifilar antenna it was found that unlike the simulation of it's component twisted loop primitives [4,5], the electromagnetic modelling of the full quadrifilar antenna is a challenging task requiring a very significant computing effort. In order to attain a good gain from a small antenna (with small physical volume) it is necessary to strive for high Q-factor and conversely low operating bandwidth. The twisted loop antenna that is shown in Figure 3.1, when formed on a core of ε_r=36 material at 1.8 GHz might typically possess a 3dB fractional bandwidth of about 0.5%.

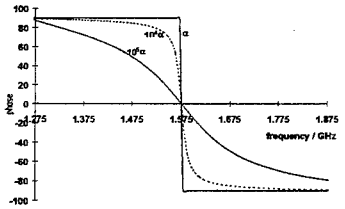

Figure 4.1: Phase (ϕ) with frequency responses of shunt connected half-wave transmission line of varying attenuation coefficients, α. (α=2×10^{-5} Nepers/m)

Another important feature of small antennas is that they have low radiation resistance. For example the radiation resistance of the twisted loop antenna can accurately be estimated from the point dipole formula because the dipole length (*dl*) is much less than the free space half wavelength of the resonant frequency. For this class of antennas the equivalent dipole is formed across the diameter of the core between the opposing centres of the helices. For the case of the 10mm diameter twisted loop antenna operating at 1.8 GHz the radiation resistance is approximately 2 Ohms.

The quadrifilar helix antenna can be conveniently considered as comprising of four shunt connected half-wave resonators. Given that each resonator is physically a low-loss helical conductor and that the radiation resistance is also small the characteristic phase shift with frequency through the resonant condition occurs over a very narrow frequency range. This principle can be illustrated by plotting the phase with frequency responses of half-wave shunt-connected transmission lines with varying values of attenuation coefficient (α). A range of responses of realistic attenuation coefficients is plotted in Figure 4.1:

As can be seen from the data of Figure 4.1 the conditions which give rise to an orthogonal phase difference between two such shunt resonators, of slightly offset resonance frequency, can only occur over a very narrow bandwidth indeed. The

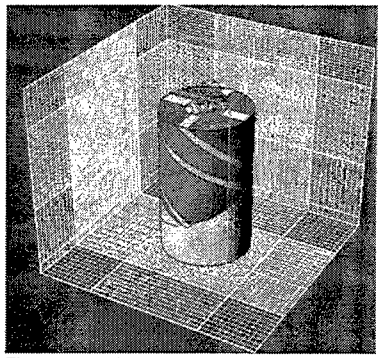

Figure 4.2: MicroStripes™ electromagnetic model of the GPS dielectric loaded quadrifilar helix antenna.

obvious corollary of this is that the antenna must have very critical dimensions in order to exploit this mode of operation. In order to predict accurately the behavior of this structure using electromagnetic simulation the resolution of the model has to be very fine indeed.
The resolution of the model is constrained by computing power and certain simulator capabilities. In this research the work was carried out on a battery of eleven Sun Sparc™ processors and the computing process was refined to balance the needs to obtain the accuracy available from a fine enough resolution meshing and the need to collect sufficient throughput of simulation results to permit manual optimisation.

An example of an electromagnetic model of a GPS antenna is presented in Figure 4.2: The model of Figure 4.2 consists of approximately 365,000 cuboid cells and employs a graded mesh

and extensive use of the MicroStripes™ 'lumped-cell' utility to optimise computational efficiency. The TLM solver runs this model in approximately 30 hours of computation time using a Sun Sparc20 machine with a processor clock speed of 200 MHz. The model has been used to computer optimise a GPS L1 (1575.42 MHz) circularly polarised antenna as is explained in the next section. However, this has not proven to be capable of supporting the strategy of using the helix current vectors as optimisation goals as these have been found to be unrealistically organised and are perhaps indicative of insufficient model resolution.

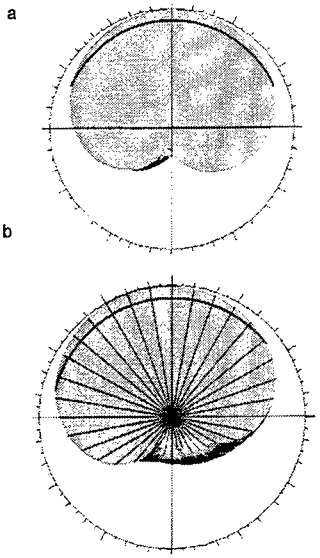

Figure 4.4: Predicted pattern for a crown-rimmed quadrifilar helix antenna.
(a) elevation
(b) orthogonal cut elevation

Use of MicroStripes™ was more sucessful as a 'proof of principle' tool to demonstrate the feasibility optimum cardiod patterns with favourable antenna parameters such as axial ratio and front-to-back ratio. Used in this way, a model cast in a certain practical meshing resolution, was optimised for pattern shape at the desired GPS L1 frequency. Figure 4.4 shows two orthogonal elevation cuts that are predicted to occur:

5. COMPLETE MODELLING OF THE FEED SYSTEM

Some improvements in the modelling of the feed to more closely match the feed used in actual measurements were implemented. Firstly, the number of cells used to model the feed were increased. This is however limited by the allowable minimum cell size. Secondly, to better predict antenna performance, it is necessary to model the feed system as physically close to the practical feed system as possible. Any approximation, further reduces the model's ability to predict performance. Previous simulation models implemented 50Ω cable dimensions, while actual measurements used a 10Ω cable, with a λ/4 transformer length to 50Ω connectors. Using 10Ω cables were more predictive of actual measurements, with the predicted frequency closer to measured results. Overall, the simulation frequencies were about 8-10% lower than measurements, as shown in Figure 5.1.

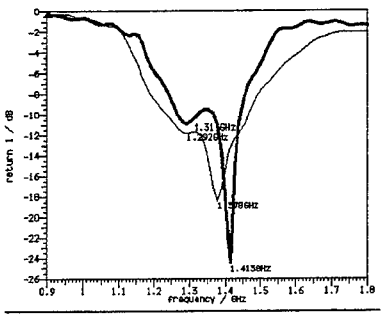

Figure 5.1: Simulation models using 50Ω ___ and 10Ω+λ/4 ___ transformer cables

6. CONCLUSIONS

The development of GPS quadrifilar helix antennas using a TLM time domain simulator has been undertaken. Traditional meshing criteria concerning the appropriate number of cells per guide wavelength to promote a desired degree of predictive accuracy break down for the quadrifilar helix antenna. This is because the resolution required to model the operation of two similar resonators which create orthogonal phase between them has to be fine enough to accurately represent the very subtle difference in physical length that is required. Basically the

resolution that has to present is being multiplied by the Q-factor of the resonators that are being modelled.

In any electromagnetic optimisation program it is vital to choose the optimisation criteria very carefully. The use of probe points to gain vector information that is indicative of field resonance is the fashion that is described here is only valid if the model is resolved sufficiently to ensure that at the micro level close to the probe point the local conditions adequately represent the conditions that are a consequence of the resonance of the global whole.

Both these conclusions argue for a significant increase in the resolution of the computer model that is required to model the component. However it is another conclusion of this work that a lower level of resolution can provide good insight into the principles of operation of the component to a degree that improves with model reality.

ACKNOWLEDGEMENTS

The authors wish to acknowledge the continued support of SymmetriCom Inc. In particular Tony Haddrell, Vice President of Technology, and Mike Duckham, Managing Director at SymmetriCom, Northampton and Tom Steipp CEO of SymmetriCom have given continuous support and commitment to this project.

REFERENCES

1. O.P.Leisten,G.Ffoulkes-Jones, 'Performance of a Miniature Dielectrically Loaded Volute Antenna' Institute of Navigation Conference, Palm Springs, 12-15 September 1995

2. O.P.Leisten, 'A Combined Right Hand Circular and Linear Polarisation Antenna For GPS and Cellular Telephone Usage' Institute of Navigation Conference, Kansas City, 17-20 September 1996

3. Microstripes, Kimberley Communications Consultants Ltd (KCC Ltd) of Nottingham, England

4. O. Leisten, J.C. Vardaxoglou, T. Schmid, B. Rosenberger, E. Agboraw, Niels Kuster, George Nicolaidis, "Miniature Dielectric-loaded Personal Telephone Antennas with Low User Exposure", Electronics Letters, August 1998, Vol. 34, No. 17, pp. 1628 - 1629

5. G. Nicolaidis, E. Agboraw, O. Leisten, J.C. Vardaxoglou "A Miniature Dielectric Loaded Antenna with Low SAR", ICT 98, Porto Carras, Greece 21-25 June, Vol. 3, 376-379.

Conformal Aperture Coupled Microstrip Patch Antennas on Cylindrical Surfaces for Radar and SDMA Applications

*D. Löffler, W. Wiesbeck

Institut für Höchstfrequenztechnik und Elektronik, Universität Karlsruhe, Kaiserstraße 12, 76128 Karlsruhe, Germany, e-mail: Dietmar.Loeffler@etec.uni-karlsruhe.de

Abstract

Modern radar sensors require efficient low profile antennas over a reasonable frequency bandwidth, which need to be flush mounted or integrated in curved surfaces. The applications reach from spaceborne and airborne radar sensors to more commercial applications for example with antennas being integrated into cars for automatic cruise control. Besides the fitting to curved structures, mostly due to aerodynamically reasons, conformal antennas offer a variety of beamforming and beamsteering capabilities which are difficult to obtain with fixed planar antennas. Cylindrical phased array antennas, for example, offer the potential either to cover 360° in azimuth by a omnidirectional pattern or to create a sharp beam in an arbitrary azimuth direction using the same array antenna. This option is particularly useful for communication applications needing an omnidirectional pattern in the acquisition phase and a high gain antenna during the communication link to enlarge the signal-to-noise ratio.
This contribution presents aperture coupled patch antennas on a cylindrical surface having more than 20% bandwidth (-10 dB) at S- and C-band for both radar and communication applications. Besides the modelling measured data for the elements, the subarray used and the array is reported. Directional patterns for the circular patch array are synthesized and measured using a beamforming network.

Introduction

New radar systems require efficient, light weight, low profile antennas over a frequency bandwidth of 10% - 20% to embed the antenna in the surface. There are different reasons requiring conformal antennas. In airborne applications the fitting to an aerodynamic body minimises drag, in commercial applications like automatic cruise control for cars and distance monitoring for parking a conformal antenna can be hidden to allow aesthetically looking

products with full electrical functionality. Conformal antennas are a solution to the geometrical problem.

Besides the capability for integration in curved surfaces conformal antennas offer more flexible radiation characteristics not known from mechanically fixed planar antennas.

The potential for both omnidirectional coverage and narrow beams at arbitrary azimuth angles is particular interesting for the next generation communication and network systems where space division multiple access (SDMA) techniques are required. The finite spectrum of frequencies will be the major limiting factor and SDMA systems are one way to overcome this problem. By sharp beam forming it is possible to use the same frequency simultaneously in different directions. Additionally either the power consumption for both base stations and handsets can be reduced during the communication link or the coverage area of the base station can be increased.

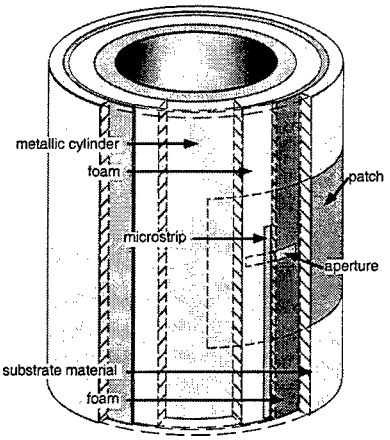

Fig. 1: 3D-view of an aperture coupled patch on a cylindrical surface

A key point in these systems is the base station antenna, which has to accept new users just applying for a link as well as to maintain communication or data links with high data rates. Base station antennas therefore need omnidirectional characteristics as well as sharp beams providing the users with a sufficient signal-to-noise ratio. These requirements can best be met by a cylindrical structure.

This contribution presents the analysis of the structure shown in fig. 1. For mounting purposes a cylinder with a metallic surface is placed in the center. The metallized surface simplifies the modelling but the presented model is not restricted to these surfaces. This cylinder is covered by 3 layers: A foam layer, e.g. ROHACELL, to keep the distance between substrate and metallic cylinder, a substrate layer, e.g. RT/duroid, for the feed line on the inner surface and the aperture on the outer surface. An outer foam layer carrying the patch completes the aperture coupled patch structure. The feeding network as well as the coupling slots may be etched on a planar substrate, which is bent afterwards around the cylinder, eventually by heating the substrate material to moderate temperatures. The patch is etched on a thin foil and placed on the outermost foam layer.

Modelling

The aperture is replaced by equivalent magnetic currents M^S, which allows the splitting of the structure in 2 parts. The microstrip line and the patch are replaced by a two dimensional electric current density J. By enforcing vanishing tangential electric fields on the patch and the microstrip line and the continuity of the magnetic field in the aperture a set of integral equations

(1) - (3) with unknown currents J^P on the patch, J^L on the microstrip and M^S in the aperture can be set up. For the equations a conventional cylindrical coordinate system with the z direction along the axis of the cylinder is used. Besides these currents the Green's functions G^{ikFQ} occur in the equations, where k represents the number of the plane containing the source Q and i represents the plane where the field F is calculated, respectively.

$$\iint_{A_P} G^{33EJ^P}\vec{J}^P d\phi\, dz + \iint_{A_S} G^{32EM^{Sa}}\vec{M}^{Sa} d\phi\, dz = \vec{0} \tag{1}$$

$$\iint_{A_L} G^{21HJ^L}\vec{J}^L d\phi\, dz = \iint_{A_P} G^{23HJ^P}\vec{J}^P d\phi\, dz - \iint_{A_S} G^{22HM^S}\vec{M}^S d\phi\, dz \tag{2}$$

$$\iint_{A_L} G^{11EJ^L}\vec{J}^L d\phi\, dz + \iint_{A_S} G^{12EM^{Si}}\vec{M}^{Si} d\phi\, dz = \vec{0} \tag{3}$$

The accurate calculation of the Green's functions is done using a transfer matrix method as described in [1]. By using this method even for large values of the radius the functions can be calculated numerically stable.

In order to save calculation time the solution of (3) is omitted. This can be done by introducing a reflection coefficient on the feeding microstrip line assuming a quasi TEM wave propagating along the line in z direction. This technique is well known for planar structures [2] and adapted here for the cylindrical case. The reflection coefficient on the line for the cylindrical case (4) looks similar to the one in the planar case [2] and includes the tangential magnetic field at the slot due to the incident magnetic field on the microstrip line h_ϕ and the magnitude of the magnetic source in the slot M_ϕ. The magnetic field h_ϕ in turn can be calculated using (5) where Z_L denotes the impedance of the microstrip line, $\tilde{G}$ the Greens function in the spectral domain and $\tilde{J}_f^L$ the Fourier transforms of the feedline current's form function in ϕ-direction.

$$R = \frac{1}{2}\iint_{A_S} M_\phi h_\phi(\phi, r = r_S) d\phi dz \tag{4}$$

$$h_\phi(\phi, r = r_S) = \frac{1}{2\pi\sqrt{Z_L}} \sum_{m=-\infty}^{\infty} \tilde{G}_{\phi z}^{21HJ^L}(k_z = -k_{za}) \tilde{J}_f^L(m) e^{-jm\phi} \tag{5}$$

Using the reflection coefficient (4) and the magnetic field of the feedline mode (5) the resulting tangential magnetic field at the inner border of the aperture $H_{\phi S}$ due to the electric current on the feedline J^L can be expressed without explicitly mentioning the current on the feedline.

With this excitation model equations (2) and (3) can be replaced by (6) resulting in a set of 2 integral equations which need to be solved simultaneously for the unknown current densities. This omits the calculation of the exact two dimensional current distribution on the feedline.

$$a_{err} H_{\phi S} = -\iint_{A_S} G^{22HM^S}\vec{M}^S d\phi\, dz + \iint_{A_P} G^{23HJ^P}\vec{J}^P d\phi\, dz \tag{6}$$

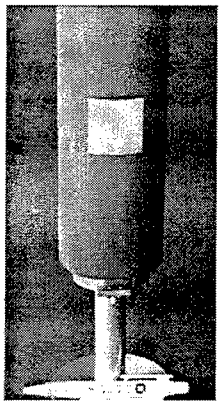

Fig. 2: Front view of the S-band element

Equations (1) and (6) are solved using a methods of moments technique with a Galerkin's scheme. Entire domain basis functions are used to model the current distribution because it is known from the analysis of planar aperture coupled patches that the current distribution on these structures can be modelled very accurately by these functions. In addition this approach needs little computation time as the number of unknown coefficients can be kept low.

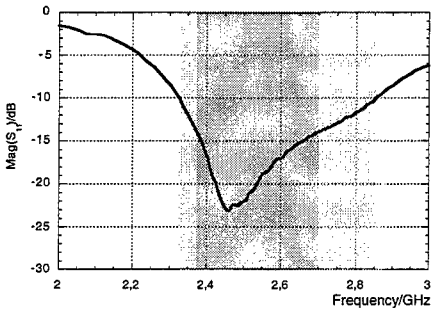

Fig. 3 Measured input reflection coefficient of the S-band element

Results

Two different antennas are designed in order to look at different values for k_0r. The S-band antenna, designed for 2.45 GHz, consists of a metal cylinder (15 mm diameter, see fig. 1) covered by 22.5 mm foam. For the feedline substrate a 0.5 mm RT/duroid was chosen, covered by 10 mm foam as substrate for the patch. The C-band antenna for 5.2 GHz is made of a metal cylinder (35 mm in diameter) covered by 14 mm foam, 0.5 mm RT/duroid and 4 mm foam for the patch.

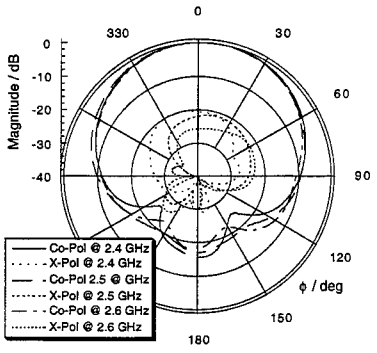

Fig. 4 Measured pattern in the azimuth plane of the S-band element

S-band element

The S-band single element is displayed in fig. 2 showing a pen for comparison. The measured input reflection coefficient for this element is plotted in fig. 3 showing a -10 dB bandwidth of 20.8% (2.32 GHz - 2.86 GHz) indicated by light grey and a -14 dB bandwidth of 12.6% (2.38 GHz - 2.70 GHz) indicated by dark grey. The pattern measured in the azimuth plane is displayed in fig. 4. A half power beamwidth of 83° and a maximum crosspolarization level of -19.5 dB is observed.

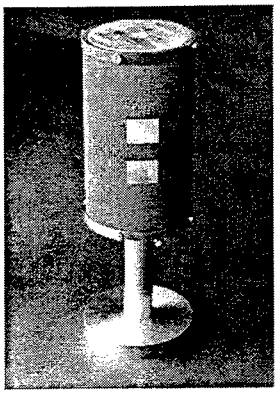

Fig. 5 Front view of the C-band subarray

C-band 1x2 subarray

The C-band 1x2 subarray is shown in fig. 5 on a cylinder which in z-direction has about the same size as the cylinder of the S-band element. The measured input reflection coefficient is plotted in fig. 6 showing a -10 dB bandwidth of 20.7% (4.82 GHz - 5.93 GHz) indicated by light grey and a -14 dB bandwidth of 12.0% (4.94 GHz - 5.57 GHz) indicated by dark grey. The pattern measured in the azimuth plane is displayed in fig. 7. The half power beamwidth of 73° at 5.0 GHz narrows to 64° at 5.4 GHz while the maximum of the crosspolarization does not change much with frequency and keeps below -30.5 dB for all measured frequencies. The measured gain of the 1x2 subarray is plotted in fig. 8 showing a minimum gain of 8.6 dBi within the -10 dB bandwidth and 9.5 dBi within the -14 dB bandwidth.

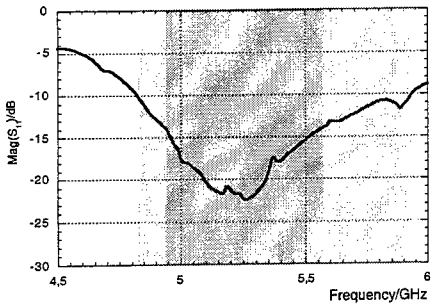

Fig. 6 Measured input reflection coefficient of the C-band 1x2 subarray

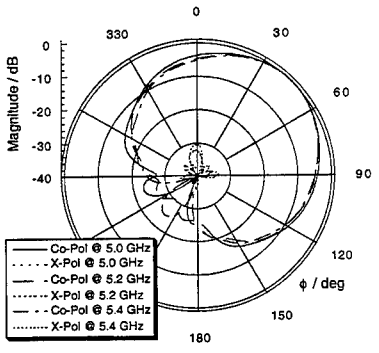

Fig. 7 Measured pattern in the azimuth plane of the C-band 1x2 subarray

C-band array

Using 8 subarrays a 8x2 array having a period of 45° is fabricated and measured using various excitations. Different beampointings for the array with respect to the element position are calculated, one between two elements, one in front of an element and one in between. Fig. 9 shows the patterns for this 3 beampositions using 8 excited elements. Neither the sidelobe level nor the half power beamwidth nor the calculated gain of 13.5 dBi gain shows a significant change with beam position. For the beam pointing towards 0° with respect to element no. 4 the measured

result is shown in fig. 10. The measured half power beamwidth varies with frequency from 38° to 39°, the sidelobelevel is below -12 dB and the crosspolarization is better than -22 dB.

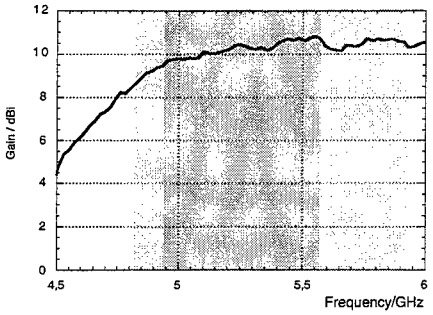

Fig. 8 Measured gain of the C-band 1x2 subarray

Conclusion

An analysis for aperture coupled patches on cylindrical surfaces using entire domain basis functions was presented. Broadband elements and arrays were fabricated in S- and C-band, respectively. The measurements show a bandwidth of more than 20% for both antennas. The measured results show the capability of the array to form a directive sector beam as well as an omnidirectional pattern necessary for SDMA base stations. As no gain variation occurs while scanning the direction the array is also recommended for 360° scanning radar sensors.

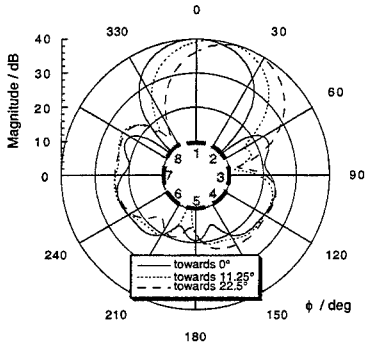

Fig. 9 Calculated scanning beam of the 8x2 array, beamposition with respect to element no. 1

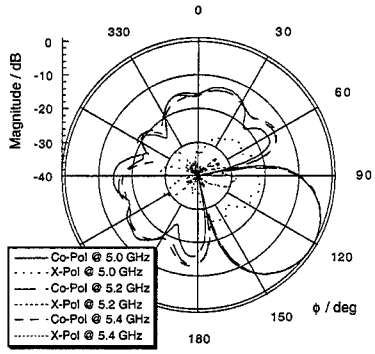

Fig. 10 Measured beam of the 8x2 array with a beamposition 0f 0° with respect to element no. 4

References

[1] A. Herschlein, G. Gottwald, W.Wiesbeck, "Patch antennas on finite and infinite cylindrical surface structures," *Proc. IEEE International Symposium on Phased Array Systems and Technology,* Boston, Massachusetts, Oct. 15-18, 1996, pp. 168-170

[2] D. M. Pozar, "A Reciprocity Method of Analysis for Printed Slot and Slot-Coupled Microstrip Antennas", *IEEE Trans. on Antennas and Propagation*, vol. 34, no. 12, pp. 1439-1446, Dec. 1986

Absorbing Boundary Conditions for Convex Object-Conformable Boundaries

Omar M. Ramahi
Compaq Computer Corporation
Omar.Ramahi@digital.com

I. Introduction

Absorbing Boundary Conditions (ABCs) are essential elements for solving open region radiation or scattering problems because they allow limiting the computational domain to a finite size. Several ABCs were developed for outer boundaries that form canonical shapes. Most practical radiation or scattering problems have geometrical shapes that do not conform to a box, circle or sphere. Hence, when using any of these shapes as outer boundaries for mesh termination, the white space around the scatterer might be unnecessarily large resulting in costly simulation in terms of both memory and run time.

To address this problem, ABCs were developed that can be applied to boundaries that conform, as close as practicable, to the radiating geometry. Several attempts were made to apply Bayliss-Turkel (BT) ABCs to non-circular outer boundaries (see [1] as a representative example of such efforts). In these works, the BT operators were *projected* onto a non-circular boundary while employing different approximations for mixed partial derivatives. Another class of flexible *mode – annihilating* ABCs were developed that were also applied to non-circular outer boundaries [2] (see also [3] and references therein). In all of these previous ABC constructions, the outer boundary had to be positioned few wavelengths from the nearest surface of the structure to obtain practical levels of accuracy [3].

In a total departure from the philosophy employed earlier, Kreigsman et al. [4] applied the BT operator directly on the surface of the scatterer, while assuming that the origin of waves is at the center of the osculating circle at each outer boundary node. The result of the application of Kreigsman et al. was not very satisfactory because it was only possible to apply second-order BT operators (higher-order operators employ radial derivatives and thus cannot be determined *apriori* on the surface of the structure). However the novelty of using local scattering centers in the work of Kreigsman et al. lead others to extend the concept of the local scattering center

to outer boundaries that are positioned at a distance from the structure's surface [3], [5],[6].

The comparative study of Lichtenberg et al. [3] showed that enforcing BT operators with local scattering centers outperforms other ABCs that use a single point of origin for all boundary points. We will refer to the N^{th} order BT operator applied with a local scattering center as BT^N_{local}. However, despite its superior performance in comparison to other operators, the BT^2_{local} does not give practical accuracy when enforced close to the scatterer. In [3], for instance, good accuracy level was possible only when the outer boundary was pushed two wavelengths away from the structure. Third- or higher-order BT operators were not implemented for application on circular or non-circular outer boundaries because of the complexity of their previous formulations.

In a recent work, BT operators were implemented in an *exact* fashion resulting in an appreciably enhanced accuracy [7]. The exactness of this recent implementation and the relative superiority of BT^2_{local} in comparison to previous techniques makes it only logical to extend the application of higher-order BT operators to non-circular outer boundaries using the concept of local scattering centers. This paper develops these operators which are implemented without any approximation other than the discretization needed to transform derivatives.

Other mesh-truncation techniques that were developed for non-circular outer boundaries in frequency domain include the class of material-based terminations. This includes impedance boundary conditions and perfectly matched layers [8]-[10]. However, these techniques witnessed analytical formulation only, and no numerical results have been made available to test their effectiveness.

II. ABCs FOR CONVEX BOUNDARIES

The development here will be demonstrated by solving the problem of plane wave scattering from a perfect electric conductor (p.e.c.) in two-dimensional space. The method of solution employed here will be the Finite Elements Method (FEM), however the discussion applies equally to the Finite Difference Method.

The governing Helmholtz equation is given by

$$\nabla^2 u + k^2 u = 0 \tag{1}$$

where k is the wave number. Equation (1) is subject to Direchlet or Neuman (or both) boundary conditions on the surface of the scattering object.

Consider the scattering object shown in Fig. 1. Using FEM, we mesh the region bounded by the p.e.c. scatterer and the object-conformable outer boundary, as shown

in Fig. 1. The Nth order BT operator specified at a circular boundary with origin at $\rho = 0$, is given by

$$B^N = \prod_{i=1}^{N} \left(\frac{\partial}{\partial \rho} + \frac{2i - 3/2}{\rho} + jk \right) \tag{2}$$

We enforce (2) on the outer boundary at each node using the osculating circle approximation. This requires determining the curvature of the osculating circle at each node (the node and two adjacent ones are sufficient to determine the curvature). Effectively, we can represent the ABC at each node as

$$B^N_{local} = \prod_{i=1}^{N} \left(\frac{\partial}{\partial n} + \kappa_{node}(2i - 3/2) + jk \right) \tag{3}$$

κ_{node} represents the curvature of the osculating circle at outer boundary nodes. For the special case of zero curvature, as in the case of planar terminal boundaries, (3) reduces to

$$B^N_{local} = \prod_{i=1}^{N} \left(\frac{\partial}{\partial n} + jk \right) \tag{4}$$

When the outer boundary is planar and coinciding with the Cartesian planes, (4) reduces to Higdon's boundary condition when it is applied in the frequency domain (after the transformation of ∂_t to jk) [11].

III. Numerical Experiment

To demonstrate the effectiveness of the proposed technique, we consider the problem of scattering by a $1.95\lambda \times 1.95\lambda$ perfectly conducting square cylinder. The most suitable outer boundary for this geometry is a square as shown in Fig. 2. The outer boundary is positioned such that the separation between it and the conductor is 0.35λ. The spacing between node layers is as before.

Figures 3(a) and 3(b) show the magnitude and phase of the electric field on the observation contour Γ (see Fig. 2) as calculated using the FEM solution. A total of 164 nodes span the observation contour. The numbering of the nodes starts at the lower left-hand corner and proceeds clockwise. So node number 20 corresponds to the middle point on the left-hand side, and node number 105 corresponds to the middle point on the righ-hand side. Results are only shown for field values on the upper half of the contour due to the symmetry of the problem. For comparison, the MoM solution is also provided for this problem. The FEM solutions were obtained using BT^2_{local} and BT^4_{local}. The agreement between BT^4_{local} and MoM solutions is very satisfactory,

especially in the observation region closest to the corner of the conducting box. In fact, it is observed from Fig. 3(a) that the maximum error in the field magnitude is kept below 1.2% over the en tire observation contour when BT^4_{local} is used.

IV. Conclusion

This paper presented the development of a new class of ABCs that can be applied on non-circular convex mesh-termination boundaries. The new ABCs are based on the exact application of BT operators using local scattering centers. This work demonstrated the application to scattering problems in two-dimensional space and in the frequency domain. However, these ABCs and their implementation are directly applicable to scattering problems in three dimensional space and to time-domain problems. These extensions will be discussed in the presentation.

V. Acknowledgement

The author is grateful to Andrew Peterson for providing the MoM code that was used for comparison in this work.

References

[1] A. Khebir, O. Ramahi and R. Mittra, "An efficient partial differential equation technique for solving the problem of scattering by objects of arbitrary shape,", *Microwave Opt. Tech. Lett.*, vol. 2, no. 7, pp. 229-233, July 1989.

[2] O. M. Ramahi, A. Khebir and R. Mittra, "Numerically derived absorbing boundary condition for the solution of open region scattering problems," *IEEE Trans. Antenn. Propagat.*, vol. 39, no. 3, pp. 350-353, March 1991.

[3] B. Lichtenberg, K. J. Webb, D. B. Meade and A. Peterson, "Comparison of two-dimensional conformal local radiation boundary conditions," *J. Electromagnetics*, vol. 16, no. 4, pp. 359-384, July-Aug., 1996.

[4] G. A. Kriegsmann, A. Taflove and K. R. Umashankar, "A new formulation of electromagnetic wave scattering using an on-surface radiation boundary condition approach," *IEEE Trans. Antenn. Propagat.*, vol. 35, no. 2, pp. 153-161, Feb. 1987.

[5] Y.-C. Ma, "A note on the radiation boundary condition for the Helmholtz equation," *IEEE Trans. Antenn. Propagat.*, vol. 39, no. 10, pp. 1526-1530, Oct. 1991.

[6] J.-M. Jin, *The Finite element Method in Electromagnetics*, John Wiley & Son s, New York, NY, 1993.

[7] O. M. Ramahi, "Exact Implementation of higher-order Bayliss-Turkel Absorbing Boundary Operators in 2D and 3D Scalar and Vector Wave Equation," submitted to The 15th Annual Review of Progress in Applied Computational Electromagnetics, March 15-20, 1999.

[8] T. B. A. Senior, J. L. Volakis and S. R. Legault, "Higher order impedance and absorbing boundary conditions," *IEEE Trans. Antenn. Propagat.*, vol. 45, no. 1, pp. 107-114, Jan. 1997.

[9] M. Kuzuoglu and R. Mittra, "Investigation of nonplanar perfectly matched absorbers for finite-element mesh truncation," *IEEE Trans. Antenn. Propagat,*, vol. 45, no. 3, pp. 474-486, March 1997.

[10] F. L. Teixeira and W. C. Chew, "Conformal Perfectly Matched Layer," in Proc. 14th Annual Review of Progress in Applied Computational Electromagnetics, Monterey, California, March 16-20, 1998.

[11] R. L. Higdon, "Absorbing boundary conditions for acoustic and elastic waves in stratified media," *J. Comp. Phys.*, vol. 101, pp. 386-418, 1992

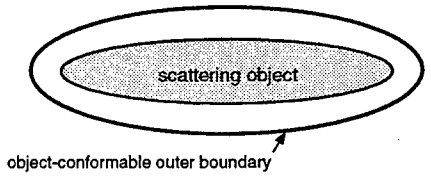

Fig. 1. Diagram illustrating an object-conformable mesh termination boundary

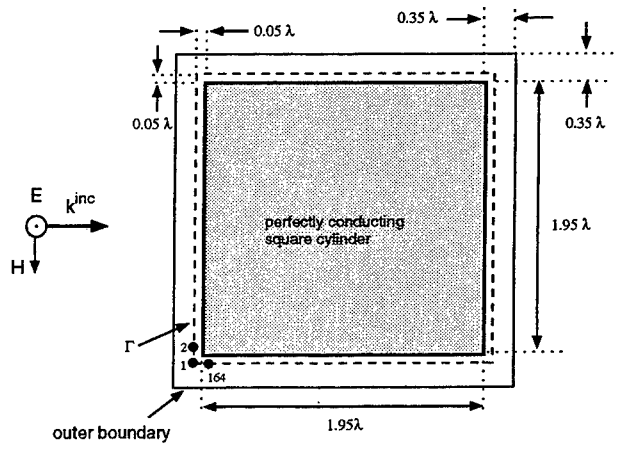

Fig. 2. Computational domain used for the problem of scattering by a perfectly conducting square cylinder.

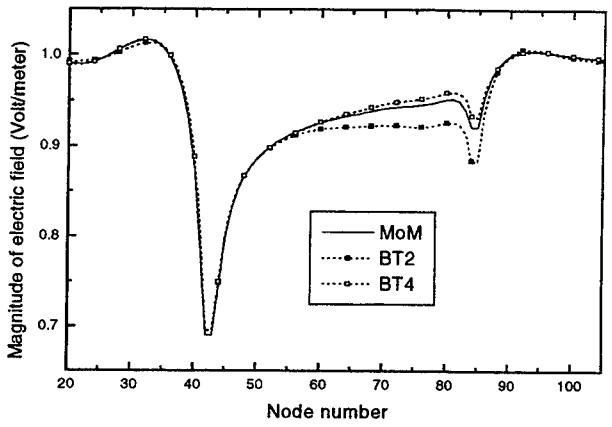

(a)

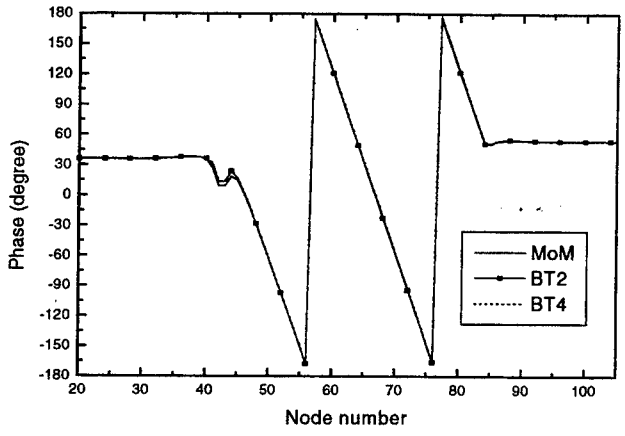

(b)

Fig. 3. Scattered electric field, H-polarization, along Γ in Fig. 2, Obtained from the MoM solution and the FEM solution using BT^{2}_{local} (BT2) and BT^{4}_{local} (BT4). (a) Magnitude. (b) Phase.

CYLINDRICAL AND CONICAL FSS

J C Vardaxoglou*, G Loukos, M Jayawardene, R Seager, J Eade

*Centre for Mobile Communications Research
Department of Electronic and Electrical Engineering
LOUGHBOROUGH UNIVERSITY
Loughborough Leicestershire LE11 3TU

Abstract

The properties of resonant frequency selective guides and horn antennas are reviewed. The importance of the array's resonance is emphasised and is an essential factor in the performance. The computational procedure for the primary propagation and radiation characteristics of these structures is discussed.

Introduction

This paper reviews the fundamental properties of resonant frequency selective guides (FSGs), [1]. These are constructed from periodic arrays that are frequency selective, and can be viewed as guiding structures at resonance and 'open' (leaky) elsewhere. Computer models have been developed to predict the propagation and mode composition of FSGs acting as a waveguides with a circular cross section. Since these are primarily open structures, the determination of the complex propagation constant was examined. This information was necessary in order to ascertain the field distributions, which in turn affect their radiation properties. The latter may be of the form of leaky or end-fire due to guided modes. The structures employ doubly periodic elements of transverse dipoles and square loops shown in Fig. 1 and Fig. 2 respectively. The radiation properties of the waveguides formed into conical antennas are discused. As well as the information given from the propagation characteristics a computer model has been developed to predict the radiation a finite model of a conical structure of dielectrically loaded dipole elements. In the computations a finite array analysis has been used and the boresight frequency response and radiation patterns can be predicted. The analysis considers a finite array of conducting elements coated with a thin arbitrary material. This may be of dielectric or ferrite material.

Propagation characteristics

The computer model produces the complex propagation constant and plots the aperture fields and field lines of the modes. The analysis is based upon the solution of the wave equation (in cylindrical co-ordinates) in conjunction with Floquet's theorem [2]. The fields have been set up as combinations of Bessel and Hankel functions. The Method of Moments (MoM) with rooftop look alike basis and testing functions has been used to determine the propagation (β) and attenuation (α) constants of a homogenous system. Once these were found the elements' currents and fields on the unit cell of the array were calculated by matrix inversion. Because of the large orders and arguments involved, necessary steps have been taken in the calculation of these functions. The propagation characteristics are obtained by a method, which chooses the appropriate Riemann surfaces. The latter is a crucial factor for bringing out surface, guided and leaky waves.

For the dipoles transverse to the length of the structure, it was found that the mode with the lower cut-off was a hybrid EH. HE types were also supported, but were highly attenuated. We have found distinct differences of the modes at different frequencies. Fig. 3 shows the real β and imaginary α propagation constants. The leakage is evident from the attenuation constant plot. It can be seen that firstly a surface wave appears, followed by a leaky (complex) wave. The monitoring of the attenuation constant and guiding modes supported at different frequencies have been extracted from the dispersion diagram by solving a homogeneous matrix system. The resonance is identified by observing the region of minimal leakage. The minima of the attenuation therefore correspond to guided waves. Square loop arrays (Fig. 4) produced minima with small attenuation constant. There is a correspondence between the transition regions (before and after the resonance) and the leaky behaviour of the structure. The effects of the periodicity and element dimensions have shown to affect the frequency and level of the leakage.

Linear dipoles exhibit weak guidance, but square loops have clearly identified guidance with small insertion loss. The dominant factor here is the resonance of the array, opening new avenues in leaky wave antennas. A study has been done on the latter in a related project. Unlike the traditional leaky wave antennas, Frequency Selective Structures have close element spacing, so there is little interference from grating lobes and scan blindness.

Radiation patterns

Fig. 5 shows a drawing of the frequency selective horn antenna as well as the geometry of the dipole and its coat. The horn is fed with a cylindrical waveguide carrying the dominant EH_{11} hybrid mode, available from the propagation results discussed above. The conventional TE_{11} of a closed waveguide has also been used. This in turn has been modelled using a superposition of point sources at each element (segment) position. The Electric Field Integral Equation (EFIE) with an arbitrary coating, of relative permeability and permitivity ε_r and μ_r respectively, takes the following form:

$$E^i(\underline{r}) = \frac{j\omega\mu_o}{4\pi}\left[\int_{-L/2}^{L/2} \mu_r I\hat{u}G(\underline{r}-\underline{r}_a)du_a - \int_{-L/2}^{L/2}(\mu_r-1)I\hat{u}G(\underline{r}-\underline{r}_b)du_b\right]$$

$$+\frac{1}{4\pi\varepsilon_o}\left[\int_{-L/2}^{L/2}\frac{1}{\varepsilon_r}\left(\frac{-1}{j\omega}\frac{dI}{du_a}\right)\nabla G(\underline{r}-\underline{r}_a)du_a + \left(1-\frac{1}{\varepsilon_r}\right)\int_{-L/2}^{L/2}\frac{1}{\varepsilon_r}\left(\frac{-1}{j\omega}\frac{dI}{du_b}\right)\nabla G(\underline{r}-\underline{r}_b)du_b\right] \quad (1)$$

I is the current flowing on the dipole of length L, G is the Green's function and E^i is the incident electric field. $\underline{r}_a$ and $\underline{r}_b$ denote vectors regarding the inner and outer radii of the cylindrical layer of the coating. The EFIE is transformed into a matrix system having segmented the elements. This system has been solved by a conjugate gradient iterative method and an elimination technique.

Varying the dielectric thickness has shifted the in band (resonance) of the antenna as well as broaden the bandwidth. This is depicted in Fig. 6, where it can be observed that the gain is also affected. The source and elements have been modelled in a finite manner by rendering the feeding aperture discrete. This approach ensures that the excitation is properly taken into account and will aid in matching the horn. The method also uses the MoM, but being finite large matrices are involved. The size of the matrix is typically 2,000 by 2,000 elements for a 10 cm long horn. The model predicted well the radiation performance on boresight, reproducing the high gain at the resonant frequency. Broadly the radiation patterns were reproduced, but there are some discrepancies of the sidelobe location and levels. This point requires further investigation. The radiated fields were calculated for the relevant mode. In addition, low crosspolarisation was achievable using tightly packed symmetrical element, such square loops and rings. Far field patterns of structures with dipoles, crossed dipole and loop-type elements with various orientations have been compared. Fig. 7 shows the boresight gain relative to the open-ended waveguide of an FSG with the same element gometry. Although the band centre is near 15 GHz, the return loss is best at slightly below that frequency. The E-plane radiation pattern at that frequency is shown in Fig. 8.

The element geometry has a noticeable influence on the gain and bandwidth of the FSG. Whereas dipole elements have narrow bandwidths, circular elements and square loops produce wider bandwidths associated with a gain increase. The bandwidth increase is related to the sensitivity of the internal

reflections to the incident angles. Horns with cross dipoles produce two bands whose separation depends on the dimension of their individual arms. The lower wave band is dominated by a surface wave.

Closing comments

Cylindrical resonant arrays of transverse dipoles and square loops have been introduced and studied. These structures exhibit attractive characteristics regarding their mode and radiation behaviour. They are also easy to construct and lightweight. The propagating modes are hybrid with symmetries in certain frequencies. Studies so far have shown that it is feasible to design a horn antenna to operate at two separate frequencies having similar beam patterns. The fruits of this effort would lead to producing multifunctional tasks with beam shaping and frequency scanning that, ultimately, would greatly enhance the performance of antennas in mobile and wireless network communication systems.

References

[1] VARDAXOGLOU, J.C., ROBINSON, A.J. and SEAGER, R.D.: 'Towards a new class of waveguiding structures and lightweight horn antennas using passive arrays', Proc. IEEE International Conference in Electromagnetics on Aerospace Applications, ICEAA, Torino, Italy, 1993, pp.343-346.

[2] VARDAXOGLOU, J.C.: 'Frequency Selective Surfaces: Analysis and Design', Research Studies Press (Wiley), Taunton, UK, 1996, ISBN 0 86380 196 X.

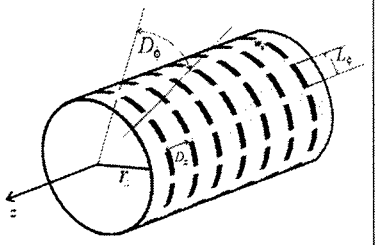

Fig. 1. A cylindrical array with transverse dipole elements.

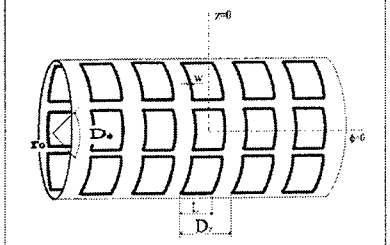

Fig. 2. FSG with square loop elements.

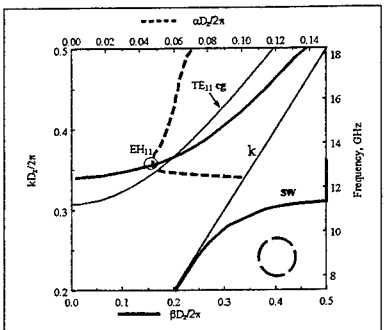

Fig. 3. Propagation curves of a singly periodic array of transverse dipoles, 4 dipoles in φ. (L= 11.75mm, D_φ= 12.33mm, D_z = 8.22mm apart, w = 0.1 D_z).

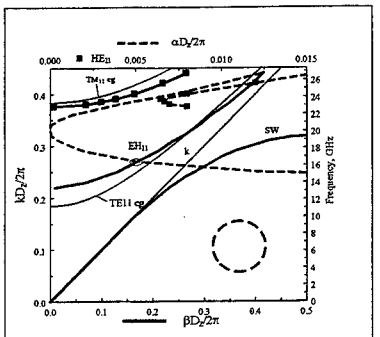

Fig. 4. Propagation and attenuation plots for an FSG with 10 square loops along φ. ($D_\varphi = D_z$ = 4932mm, $L = D_z / 1.05$ = 4.7mm, r_o =7.85mm, $w=L/7$ = 0.67mm).

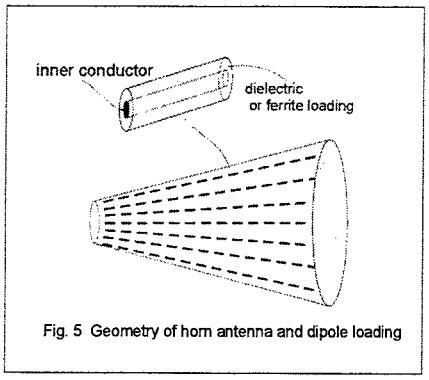

Fig. 5 Geometry of horn antenna and dipole loading

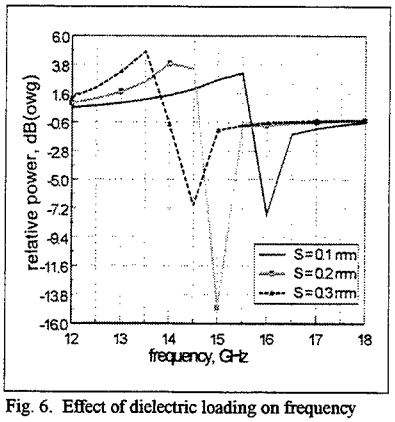

Fig. 6. Effect of dielectric loading on frequency response

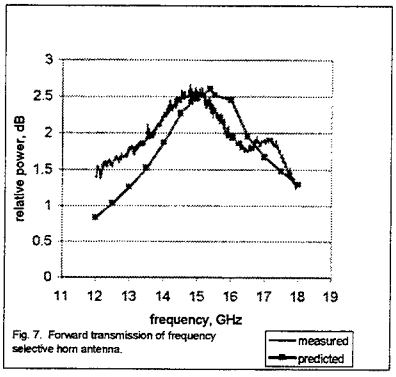

Fig. 7. Forward transmission of frequency selective horn antenna.

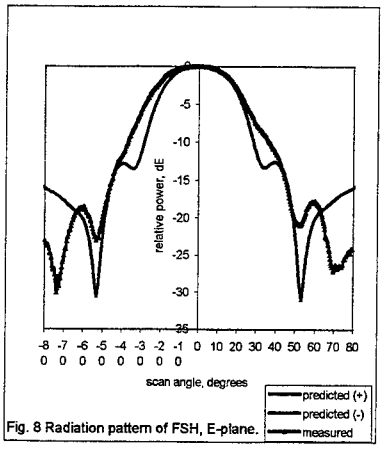

Fig. 8 Radiation pattern of FSH, E-plane.

A MATLAB CODE FOR MULTI-LAYERED FSS:S WITH GENERALLY SHAPED ELEMENTS

Anders Stjernman
Ericsson Microwave Systems AB
Core Unit Antenna Technology
SE-431 84 Mölndal
Sweden
Email: Anders.Stjernman@ericsson.com
Fax: +46 31 747 15 51
Phone: +46 31 747 21 26

Abstract

A new code has been developed which calculates the response of an infinite planar frequency selective structure with an arbitrary number of coupled layers embedded in isotropic stratified media. All layers are supposed to have the same periodicity but they can have individual element shapes and displacements. The element shape of each layer is approximated by a polygon with an arbitrary number of corner points. The media in which the structure is embedded are defined by complex permittivity and complex permeability scalars. The geometry of the problem is defined with a graphical user interface, which allows selection between defined element types including dipoles, tripoles, crosses, jerusalem crosses and anchors. Each element type can be defined either as apertures or as conductors. All types can in addition be loaded and the corners of the polygon can be smoothed. The code is based on Floquet mode expansion and convolution with the Fourier transform of the shape function of the element.

1 INTRODUCTION

Commercially available codes are generally limited either to a single simple element shape or to be defined on a grid with rectangular periodicity and poor resolution. The simply shaped elements show large sensitivity on incidence angles and polarisation and a rectangular grid has grating lobes at lower frequencies than a hexagonal grid with comparable element size. To remedy those limitation we have developed a new code which accepts general periodicity and arbitrary shaped polygons. An extensive literature search showed that the CG-FFT method [1],[2] was a promising candidate to fulfil our requirements. However previously published results was on rectangular grids and rectilinear element shapes. Our decision was therefore to modify the method for more general geometries.

2 GENERAL DESCRIPTION OF THE PROBLEM

We would like to calculate the transmitted and reflected fields when we are incident with a plane wave with given frequency, polarisation and incidence angles on an FSS structure as shown in Figure 1.

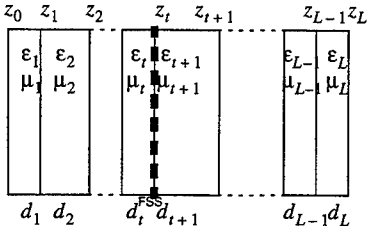

Figure 1. Single FSS-layer surrounded by dielectrics.

The FSS-layer is either a screen with perfectly conducting elements or aperture elements in a perfectly conducting screen. The elements are arranged in a doubly periodic pattern as shown in Figure 2. The periodicity is defined by the vectors $\bar{d}_1$ and $\bar{d}_2$.

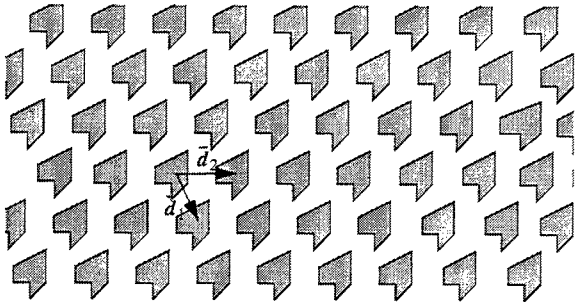

Figure 2. Periodic pattern with grating vectors

3 THE INCIDENT FIELD

We divide the electromagnetic field into an incident field and a field scattered by the periodic pattern.

The incident field which tangential components are continuous is given by

$$\begin{aligned}\overline{E}^{\text{inc}} &= \left[(E_\rho^{i,l+}\hat{\rho}^i + E_\phi^{i,l+}\hat{\phi}^i + E_z^{i,l+}\hat{z})e^{-jk_z^l z} + (E_\rho^{i,l-}\hat{\rho}^i + E_\phi^{i,l-}\hat{\phi}^i + E_z^{i,l-}\hat{z})e^{jk_z^l z}\right]e^{-j(k_x^i x + k_y^i y)} \\ \overline{H}^{\text{inc}} &= \left[(H_\rho^{i,l+}\hat{\rho}^i + H_\phi^{i,l+}\hat{\phi}^i + H_z^{i,l+}\hat{z})e^{-jk_z^l z} + (H_\rho^{i,l-}\hat{\rho}^i + H_\phi^{i,l-}\hat{\phi}^i + H_z^{i,l-}\hat{z})e^{jk_z^l z}\right]e^{-j(k_x^i x + k_y^i y)}\end{aligned} \tag{1}$$

in the interval $z_{l-1} < z < z_l$ where $z_{-1} = -\infty$, $z_0 = 0$, $z_l = \sum_{k=1}^{l} d_k$ and $z_{L+1} = \infty$.

The wave number in layer number l is given by

$$k_z^l = \sqrt{\varepsilon_l \mu_l k_0^2 - (k_x^i)^2 - (k_y^i)^2} \tag{2}$$

where $k_0 = \omega / c_0$.

Due to Maxwell's equations the longitudinal E-field is related to the transverse E-field by

$$E_z^{i,l+} = -(k_\rho^i / k_z^l) E_\rho^{i,l+} \qquad E_z^{i,l-} = (k_\rho^i / k_z^l) E_\rho^{i,l-} \tag{3}$$

and the H-field is also related to the transverse E-field by

$$\begin{aligned} H_\rho^{i,l+} &= -\frac{k_z^l}{\mu_l k_0} Y_0 E_\phi^{i,l+} & H_\rho^{i,l-} &= \frac{k_z^l}{\mu_l k_0} Y_0 E_\phi^{i,l-} \\ H_\phi^{i,l+} &= \frac{\varepsilon_l k_0}{k_z^l} Y_0 E_\rho^{i,l+} & H_\phi^{i,l-} &= -\frac{\varepsilon_l k_0}{k_z^l} Y_0 E_\rho^{i,l-} \\ H_z^{i,l+} &= \frac{k_\rho^l}{\mu_l k_0} Y_0 E_\phi^{i,l+} & H_z^{i,l-} &= -\frac{k_\rho^l}{\mu_l k_0} Y_0 E_\phi^{i,l-} \end{aligned} \tag{4}$$

hence the whole field can be described by only two field components.

4 SCATTERED FIELD AND INDUCED CURRENTS

The FSS-layer introduces a scattered field induced by the currents in the layer. These currents are confined to the conducting parts of the FSS. Assuming zero thickness and perfect conductivity the tangential components of the E field are continuous.

In general we can write the scattered field as a collection of Floquet modes

$$\bar{E}^s_{\tan} = \sum_{p,q}[(E_\rho^{p,q;l+}\hat{\rho}^{p,q} + E_\phi^{p,q;l+}\hat{\phi}^{p,q})e^{-jk_z^{p,q;l}z} + (E_\rho^{p,q;l-}\hat{\rho}^{p,q} + E_\phi^{p,q;l-}\hat{\phi}^{p,q})e^{jk_z^{p,q;l}z}]e^{-j(k_x^{p,q}x + k_y^{p,q}y)} \tag{5}$$

where $k_x^{p,q} = k_x^i + pk_{1,x} + qk_{2,x}$ and $k_y^{p,q} = k_y^i + pk_{1,y} + qk_{2,y}$. The notation $k_{1,x}$ denotes the x component of the vector $\bar{k}_1$ in the pair of vectors defined by

$$\bar{k}_1 = 2\pi\frac{\hat{z}\times\bar{d}_2}{\hat{z}\times\bar{d}_2\bullet\bar{d}_1} \tag{6}$$

and

$$\bar{k}_2 = 2\pi\frac{\hat{z}\times\bar{d}_1}{\hat{z}\times\bar{d}_1\bullet\bar{d}_2} \tag{7}$$

that spans the reciprocal grating.

Similarly the scattered H field can be written as

$$\bar{H}^s_{\tan} = \sum_{p,q}[(Y_\phi^{c,p,q;l}E_\phi^{p,q;l+}\hat{\rho}^{p,q} - Y_\rho^{c,p,q;l}E_\rho^{p,q;l+}\hat{\phi}^{p,q})e^{-jk_z^{p,q;l}z} - (Y_\phi^{c,p,q;l}E_\phi^{p,q;l-}\hat{\rho}^{p,q} - Y_\rho^{c,p,q;l}E_\rho^{p,q;l-}\hat{\phi}^{p,q})e^{jk_z^{p,q;l}z}]e^{-j(k_x^{p,q}x + k_y^{p,q}y)} \tag{8}$$

This field is also continuous except for the interface number t where the FSS-layer is present. The current in this interface is

$$\begin{aligned}\bar{J}^s &= \hat{z}\times(\bar{H}_{\tan}\big|_{l=t+1,\,z=z_t} - \bar{H}_{\tan}\big|_{l=t,\,z=z_t}) \\ &= -\sum_{p,q}(Y_\rho^{s,p,q}E_\rho^{s,p,q}\hat{\rho}^{p,q} + Y_\phi^{s,p,q}E_\phi^{s,p,q}\hat{\phi}^{p,q})e^{-j(k_x^{p,q}x + k_y^{p,q}y)}\end{aligned} \tag{9}$$

where the constants can be determined with an iterative technique.

Converting to Cartesian coordinates gives

$$\begin{bmatrix}J_x^{s;(p,q)} \\ J_y^{s;(p,q)}\end{bmatrix} = -\begin{bmatrix}\tilde{k}_x^{p,q} & -\tilde{k}_y^{p,q} \\ \tilde{k}_y^{p,q} & \tilde{k}_x^{p,q}\end{bmatrix}\begin{bmatrix}Y_\rho^{s;(p,q)} & 0 \\ 0 & Y_\phi^{s;(p,q)}\end{bmatrix}\begin{bmatrix}\tilde{k}_x^{p,q} & \tilde{k}_y^{p,q} \\ -\tilde{k}_y^{p,q} & \tilde{k}_x^{p,q}\end{bmatrix}\begin{bmatrix}E_x^{s;(p,q)} \\ E_y^{s;(p,q)}\end{bmatrix} \tag{10}$$

with $\tilde{k}_x^{p,q} = k_x^{p,q}/k_\rho^{p,q}$ and $\tilde{k}_y^{p,q} = k_y^{p,q}/k_\rho^{p,q}$.

5 INTEGRAL EQUATION

By introducing the variables s, t according to $x\hat{x} + y\hat{y} = s\bar{d}_1 + t\bar{d}_2$ we can write the scattered field in the FSS-layer as

$$\bar{E}^s = \left[\left(\sum_{p,q} E_x^{s;(p,q)} e^{-j2\pi(ps+qt)}\right)\hat{x} + \left(\sum_{p,q} E_y^{s;(p,q)} e^{-j2\pi(ps+qt)}\right)\hat{y}\right] e^{-j(k_x^i x + k_y^i y)} \tag{11}$$

where the sums can be identified by the Fourier transforms of the double discrete series $E_x^{s;(p,q)}$ and $E_y^{s;(p,q)}$ which render the continuous and periodic functions $\tilde{E}_x^s(s,t)$ and $\tilde{E}_y^s(s,t)$.

It is trivial to verify that

$$E_x^{s;(p,q)} = \int_0^1 \int_0^1 \tilde{E}_x^s(s,t) e^{j2\pi(ps+qt)} ds dt \tag{12}$$

and a similar relation holds for the y-component.

Due to the perfect conductivity the total tangential E field is zero at the conductors. This is written as

$$\begin{aligned} \xi_a \tilde{E}_x &= \tilde{E}_x \\ \xi_a \tilde{E}_y &= \tilde{E}_y \end{aligned} \tag{13}$$

where $\tilde{E}_x$ is shorthand for $\tilde{E}_x^s(s,t) + E_x^i$ where E_x^i is the complex amplitude of the x-component of the incident E field in the FSS-layer, and ξ_a is a function that is 1 in the apertures and 0 otherwise.

Another relation that must be fulfilled is that the current is 0 in apertures which can be written as

$$\begin{aligned} \xi_a \mathcal{F}(Y_{xx}\mathcal{F}^{-1}\tilde{E}_x + Y_{xy}\mathcal{F}^{-1}\tilde{E}_y) &= \xi_a(Y_{xx}^{0,0}E_x^i + Y_{xy}^{0,0}E_y^i) \\ \xi_a \mathcal{F}(Y_{xy}\mathcal{F}^{-1}\tilde{E}_x + Y_{yy}\mathcal{F}^{-1}\tilde{E}_y) &= \xi_a(Y_{xy}^{0,0}E_x^i + Y_{yy}^{0,0}E_y^i) \end{aligned} \tag{14}$$

where $\mathcal{F}$ denotes the Fourier transform defined in (11) and $\mathcal{F}^{-1}$ its inverse defined in (12).

6 TRUNCATION IN SPECTRAL DOMAIN

So far we have derived an equation with infinitely many unknowns. In order to get an approximate solution we have to truncate in the spectral domain and discretize in space domain.

Discretization in space domain by $s = m/N$ and $t = n/N$ render a periodic spectral domain with periodicity defined by $N\bar{k}_1$ and $N\bar{k}_1$, thus is it sufficient to specify the Floquet modes in a unit cell. For hexagonal gratings the usual approach is to choose a rhombic unit cell, but this choice destroys the symmetry that might exist. Thus it is preferable to choose a hexagonal one as in Figure 3.

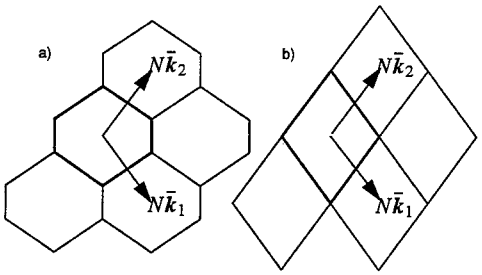

Figure 3. A hexagonal (a) and a rhombic (b) unit cell in the same lattice

A simple reordering of the selected Floquet modes makes it possible to perform the Fourier transforms with the FFT algorithm.

The discretized version of ξ_a contains only the values 0 and 1, which means that the multiplications with ξ_a represent a selection of those points that lies in the aperture. Thus the effective size of the system is reduced.

The resulting linear system is still quite large (typically 2000 unknowns with $N = 50$ and an aperture area of 40%) and the matrix multiplications are fast so the system is preferably solved with an iterative method. Our choice was the biconjugate gradient stabilized method (bicgstab [3]), since it in most cases showed a rapid convergence.

7 CODE VERIFICATION

In order to verify the code it was tested against specific cases reported in literature. As an example, our results presented in Figure 5. shows a good agreement with those by Vardaxoglou [1] presented in Figure 4. The deviations seen are due to the fact that our code uses far more Floquet modes (approx. 2500) compared to 169 used by Vardaxoglou.

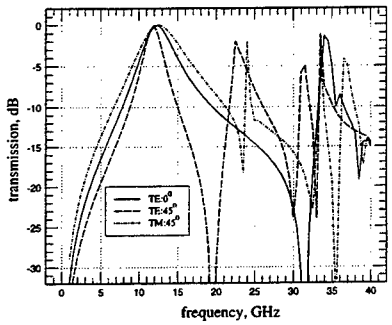

Figure 4. Results according to Vardaxoglou for a grating with aperture dipoles on a dielectric substrate.

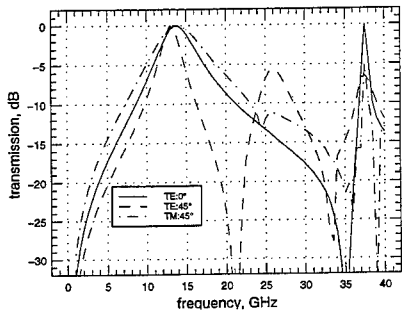

Figure 5. Results from our code for the same geometry

8 CONCLUSIONS

We have a code which accepts generally shaped elements in multiple layers. It generates results that agree well with previously reported results. Drawbacks are long execution times due to the interpreting nature of matlab. Future research will be on finding a preconditioner to increase the convergence rate and to convert the program into a compiled code on parallel machines.

9 REFERENCES

[1] J. C. Vardaxoglou, "Frequency Selective Surfaces: Analysis and Design", Research Studies Press, 1997

[2] M. F. Cátedra, "The CG-FFT Method: Application of Signal Processing Techniques to Electromagnetics", Artech House, 1995

[3] H. A. Van Der Vorst, "Bi-CGSTAB: a fast and smoothly converging variant of Bi-CG for the solution of nonsymmetric linear systems", *SIAM-Journal-on-Scientific-and-Statistical-Computing*. vol.13, no.2; March 1992; p.631-44

A RECIPROCITY APPROACH FOR CALCULATING RADIATION PATTERNS OF ARBITRARILY SHAPED PATCH ANTENNAS MOUNTED ON CIRCULARLY-CYLINDRICAL PLATFORMS

D. H. Werner, G. D. Mouyis, R. Mittra and J. S. Zmyslo
The Pennsylvania State University
Applied Research Laboratory
PO Box 30
State College, PA 16804-0030

1. INTRODUCTION

This paper presents an efficient method, based upon the reciprocity theorem, for calculating the radiation patterns of conformal patch antennas on circularly cylindrical platforms when the current distribution of the patch antenna is available from previous computations. This approach does not require the evaluation of complicated layered media Green's functions for curved geometries. It also circumvents to the need to calculate time consuming Sommerfeld integrals. Furthermore, this method is directly applicable to patch antennas of arbitrary shape.

The analysis of conformal patch antennas has evoked much interest over the past few years because of their inherent advantages for a wide range of applications [1-7]. Patch antenna implementations are highly desirable on military manned and unmanned aircraft due to their ability to aerodynamically conform to the shape of fuselages. In the commercial sector, patch antennas are increasingly being used in mobile communications systems. These and other applications are driving the requirement for highly accurate, fast and efficient techniques for evaluating conformal antenna performance characteristics.

2. THEORETICAL DEVELOPMENT

A. Domain Decomposition and Reciprocity Approach

Consider a patch antenna backed by a dielectric substrate and mounted on a circularly cylindrical, perfectly conducting body as illustrated in Figure 1. The dielectric constant and thickness of the substrate material are denoted by ε_r and h respectively. It is well understood that the current distribution on the surface of a flat cavity backed patch antenna is not appreciably altered by the introduction of a moderate degree of curvature in the structure. Hence, for many problems of practical interest, sufficient accuracy is achieved by solving for the current distribution on the surface of an equivalent flat patch rather than the original curved one – curvature, of course, adds considerable complexity to the problem. Considering a flat vice curved patch has the additional advantage in that several commercial Method of Moments (MoM) codes are available that can be used to efficiently analyze flat patch antenna configurations.

Once the current distribution $\boldsymbol{J}_s$ has been determined, we can apply the reciprocity theorem, in a manner explained below, to efficiently calculate the radiation pattern of the patch antenna on the circularly cylindrical platform operating in the receive mode. The first step in the reciprocity approach is to consider TE^z - and TM^z - polarized plane waves incident upon a dielectric-coated metallic cylinder and to solve for the total electric field $\boldsymbol{E}_t$, produced on its surface by using analytical techniques. The methodology of this procedure is illustrated in Figure 2. The final step involves carrying out the required dot product between the surface current $\boldsymbol{J}_s$ and the total electric field $\boldsymbol{E}_t$ and integrating this result over the surface of the patch.

B. General Far-Field Electric Field Expressions

Using the Hertz vectors, an electromagnetic field can be expressed in the following way [8]

$$\vec{E} = \bar{\nabla}\times\bar{\nabla}\times\vec{\Pi} - j\omega\mu\bar{\nabla}\times\vec{\Pi}^*$$
$$\vec{H} = j\omega\varepsilon\bar{\nabla}\times\vec{\Pi} + \bar{\nabla}\times\bar{\nabla}\times\vec{\Pi}^* \tag{1}$$

where $\vec{\Pi}$ is the electric Hertz vector and $\vec{\Pi}^*$ is the magnetic Hertz vector.

Beginning with the Hertz vectors and following the procedure outlined in Section A leads to the following generalized far-field expressions for the radiation pattern

$$\begin{aligned} E_\theta(r,\phi) = -j\eta_o \frac{e^{-j\beta_o r}}{4\pi r}\Bigg\{ & \frac{\beta_z}{\beta_\rho}\sum_{n=-\infty}^{\infty} n(-1)^n\left[j^{-n}J_n(\beta_\rho b) + a_n H_n^{(2)}(\beta_\rho b)\right]S_\phi(n,\theta)e^{jn\phi} \\ & -j\beta_o b\sum_{n=-\infty}^{\infty} a_n^*(-1)^n H_n^{(2)'}(\beta_\rho b)S_\phi(n,\theta)e^{jn\phi} \\ & -\beta_o b\sin\theta\sum_{n=-\infty}^{\infty}(-1)^n\left[j^{-n}J_n(\beta_\rho b) + a_n H_n^{(2)}(\beta_\rho b)\right]S_z(n,\theta)e^{jn\phi}\Bigg\}, \end{aligned} \tag{2}$$

$$\begin{aligned} E_\phi(r,\phi) = -j\eta_o \frac{e^{-j\beta_o r}}{4\pi r}\Bigg\{ & \frac{\beta_z}{\beta_\rho}\sum_{n=-\infty}^{\infty} b_n n(-1)^n H_n^{(2)}(\beta_\rho b)S_\phi(n,\theta)e^{jn\phi} \\ & -j\beta_o b\sum_{n=-\infty}^{\infty}(-1)^n\left[j^{-n}J_n'(\beta_\rho b) + b_n^* H_n^{(2)'}(\beta_\rho b)\right]S_\phi(n,\theta)e^{jn\phi} \\ & -\beta_o b\sin\theta\sum_{n=-\infty}^{\infty} b_n(-1)^n H_n^{(2)}(\beta_\rho b)S_z(n,\theta)e^{jn\phi}\Bigg\}, \end{aligned} \tag{3}$$

where the expressions that characterize a general patch current distribution are:

$$S_z(n,\theta) = \iint_{S'} J_z(\varphi',z')e^{-jn\phi'}e^{-j\beta_z z'}d\phi' dz', \quad S_\phi(n,\theta) = \iint_{S'} J_\phi(\varphi',z')e^{-jn\phi'}e^{-j\beta_z z'}d\phi' dz', \tag{4}$$

and the coefficients are given by

$$\begin{aligned} a_n &= \frac{1}{\det[\Lambda]}\{\Lambda_{22}f_1 - \Lambda_{12}f_2\}, & a_n^* &= \frac{1}{\det[\Lambda]}\{\Lambda_{11}f_2 - \Lambda_{12}f_1\}, \\ b_n &= \frac{1}{\det[\Lambda]}\{\Lambda_{22}g_1 - \Lambda_{12}g_2\}, & b_n^* &= \frac{1}{\det[\Lambda]}\{\Lambda_{11}g_2 - \Lambda_{12}g_1\}, \end{aligned} \tag{5}$$

which contain the following parameters:

$$f_1 = -j^{-n}\left\{J_n'(\beta_\rho b) - \varepsilon_r\left(\frac{\beta_\rho}{\beta_{\rho 1}}\right)\left(\frac{F_2}{F_1}\right)J_n(\beta_\rho b)\right\}, \quad f_2 = -j^{-n}\gamma_n J_n(\beta_\rho b),$$

$$g_1 = -j^{-n}\gamma_n J_n(\beta_\rho b), \qquad g_2 = -j^{-n}\left\{\left(\frac{\beta_\rho}{\beta_{\rho 1}}\right)\left(\frac{F_4}{F_3}\right)J_n(\beta_\rho b) - J_n'(\beta_\rho b)\right\},$$

$$\Lambda_{11} = H_n^{(2)'}(\beta_\rho b) - \varepsilon_r\left(\frac{\beta_\rho}{\beta_{\rho 1}}\right)\left(\frac{F_2}{F_1}\right)H_n^{(2)}(\beta_\rho b), \qquad \Lambda_{12} = \Lambda_{21} = \gamma_n H_n^{(2)}(\beta_\rho b),$$

$$\Lambda_{22} = \left(\frac{\beta_\rho}{\beta_{\rho 1}}\right)\left(\frac{F_4}{F_3}\right)H_n^{(2)}(\beta_\rho b) - H_n^{(2)'}(\beta_\rho b),$$

$$F_1 = J_n(\beta_{\rho 1} b) - \frac{J_n(\beta_{\rho 1} a)}{Y_n(\beta_{\rho 1} a)}Y_n(\beta_{\rho 1} b), \qquad F_2 = J_n'(\beta_{\rho 1} b) - \frac{J_n(\beta_{\rho 1} a)}{Y_n(\beta_{\rho 1} a)}Y_n'(\beta_{\rho 1} b),$$

$$F_3 = J_n(\beta_{\rho 1} b) - \frac{J_n'(\beta_{\rho 1} a)}{Y_n'(\beta_{\rho 1} a)}Y_n(\beta_{\rho 1} b), \qquad F_4 = J_n'(\beta_{\rho 1} b) - \frac{J_n'(\beta_{\rho 1} a)}{Y_n'(\beta_{\rho 1} a)}Y_n'(\beta_{\rho 1} b),$$

$$\gamma_n = j\frac{n\beta_z\beta_o[1-\varepsilon_r]}{\beta_\rho b\beta_{\rho 1}^2}, \qquad \left(\frac{\beta_\rho}{\beta_{\rho 1}}\right) = \sqrt{\frac{1-\cos^2\theta}{\varepsilon_r - \cos^2\theta}}.$$

The variables a and b represent the inner and outer radii of the coated cylinder, respectively, and S' denotes the area of an arbitrarily-shaped conformal patch located on the outer surface of the circular cylinder.

C. Azimuthal Plane Radiation Pattern Expressions

A special case of particular interest is the set of far-zone expressions for the radiation patterns in the azimuthal plane ($\theta = 90^0$):

$$E_\theta(r,\phi) = j\eta_0\beta_0 b\frac{e^{-j\beta_o r}}{4\pi r}\sum_{n=-\infty}^{\infty} j^n\left[J_n(\beta_o b) + c_n H_n^{(2)}(\beta_o b)\right]S_z(n,90^0)e^{jn\phi}, \tag{6}$$

$$E_\phi(r,\phi) = -\eta_0\beta_0 b\frac{e^{-j\beta_o r}}{4\pi r}\sum_{n=-\infty}^{\infty} j^n\left[J_n'(\beta_o b) + d_n^* H_n^{(2)'}(\beta_o b)\right]S_\phi(n,90^0)e^{jn\phi} \tag{7}$$

where the surface integrals involving the patch current distributions are now:

$$S_z(n,90^0) = \iint_{S'} J_z(\phi',z')e^{-jn\phi'}d\phi' dz', \qquad S_\phi(n,90^0) = \iint_{S'} J_\phi(\phi',z')e^{-jn\phi'}d\phi' dz', \tag{8}$$

and the coefficients reduced to

$$c_n = j^n a_n = \frac{J_n'(\beta_o b)F_n^1 - \sqrt{\varepsilon_r}J_n(\beta_o b)F_n^2}{\sqrt{\varepsilon_r}H_n^{(2)}(\beta_o b)F_n^2 - H_n^{(2)'}(\beta_o b)F_n^1}, \quad d_n^* = j^n b_n^* \frac{J_n(\beta_o b)F_n^4 - \sqrt{\varepsilon_r}J_n'(\beta_o b)F_n^3}{\sqrt{\varepsilon_r}H_n^{(2)'}(\beta_o b)F_n^3 - H_n^{(2)}(\beta_o b)F_n^4}, \tag{9}$$

where

$$\begin{aligned} F_n^1 &= J_n(\beta_1 b) - \frac{J_n(\beta_1 a)}{Y_n(\beta_1 a)}Y_n(\beta_1 b), & F_n^2 &= J_n'(\beta_1 b) - \frac{J_n(\beta_1 a)}{Y_n(\beta_1 a)}Y_n'(\beta_1 b), \\ F_n^3 &= J_n(\beta_1 b) - \frac{J_n'(\beta_1 a)}{Y_n'(\beta_1 a)}Y_n(\beta_1 b), & F_n^4 &= J_n'(\beta_1 b) - \frac{J_n'(\beta_1 a)}{Y_n'(\beta_1 a)}Y_n'(\beta_1 b), \end{aligned} \tag{10}$$

and

$$\beta_1 = \beta_0\sqrt{\varepsilon_r} \tag{11}$$

D. Application of Technique

To illustrate the analysis procedure we consider a half-wavelength axial patch ($L = \lambda_0/2$) with $w = \lambda_0/2$ mounted on a foam substrate ($\varepsilon_r = 1$). This type of patch configuration was originally investigated in [8], where the current was assumed to be of the form

$$J_z = \begin{cases} \hat{a}_z \dfrac{I_o}{w}\cos(\beta_o z), & -\dfrac{\lambda_o}{4} \le z \le \dfrac{\lambda_o}{4} \text{ and } -\dfrac{w}{2b} \le \dfrac{w}{2b} \\ 0, & \text{elsewhere} \end{cases} \tag{12}$$

where w is the width of the patch along the arc as illustrated in Figure 3 and the current distribution represented by (12) is as shown in Figure 4.

In this case, closed-form representations for the integrals in (8) may be found which are given by

$$S_z(n,90^0) = \frac{2I_0}{\beta_0 b}\left[\frac{\sin\left(\frac{nw}{2b}\right)}{\left(\frac{nw}{2b}\right)}\right], \qquad S_\phi(n,90^0) = 0 \tag{13}$$

Substituting the above results into (6) and (7) yields the following far-field expressions for the patch antenna:

$$E_\theta(r,\phi) = j\eta_0 I_0 \frac{e^{-j\beta_o r}}{2\pi r}\sum_{n=-\infty}^{\infty} j^n\left[J_n(\beta_o b) + c_n H_n^{(2)}(\beta_o b)\right]e^{jn\phi}\left\{\frac{\sin\left(\frac{nw}{2b}\right)}{\left(\frac{nw}{2b}\right)}\right\} \tag{14}$$

$$E_\phi(r,\phi) = 0 \tag{15}$$

Finally, (14) may be expressed in a more convenient form given by

$$E_\phi(r,\phi) = j\eta_0 I_0 \frac{e^{-j\beta_o r}}{2\pi r} \sum_{n=0}^{\infty} \varepsilon_n j^n T(n) \cos(n\phi) \left\{ \frac{\sin\left(\frac{nw}{2b}\right)}{\left(\frac{nw}{2b}\right)} \right\} \tag{16}$$

where

$$\varepsilon_n = \begin{cases} 1, & n = 0 \\ 2, & n > 0 \end{cases} \tag{17}$$

is Neuman's number and

$$T(n) = \frac{J_n(\beta_o b) H_n^{(2)}(\beta_o a) - J_n(\beta_o a) H_n^{(2)}(\beta_o b)}{H_n^{(2)}(\beta_o a)} \tag{18}$$

Equation (16) may be compared directly with (30a) from [9].

E. MoM Calculation and Technique Validation

To further demonstrate the efficiency and validity of the Reciprocity approach we next consider an example that uses a numerical method to arrive at the current distribution J_s on the surface of the patch. Although there are several commercially available method of moments codes for analysis of microstrip patch antennas, we chose to use ENSEMBLE to model the patch antenna described in the preceding section. The computed current distributions are illustrated in Figures 5 and 6. Figures 7 through 10 plot the normalized radiation patterns in the azimuthal plane produced by this patch antenna for a fixed value of h = $0.1\lambda_0$ and different radii a/λ_0 of the metallic cylinder. The plots clearly show close agreement of results thus providing a validation of the reciprocity approach presented in this paper.

ACKNOWLEDGEMENT

The authors gratefully acknowledge the computational assistance provided by Rodney A. Martin.

REFERENCES

[1] K. Luk, K. Lee, and J. Dahele, "Analysis of the Cylindrical-Rectangular Patch Antenna," *IEEE Trans. Antennas Propagat.*, Vol. 37, No. 2, pp. 143-147, Feb. 1989.

[2] T. Habashy, S. Ali, and J. Kong, "Input Impedance and Radiation Pattern of Cylindrical-Rectangular and Wraparound Microstrip Antennas," *IEEE Trans. Antennas Propagat.*, Vol. 38, No. 5, pp. 722-731, May 1990.

[3] J. Jin, J. Berrie, R. Kipp, and S. Lee, "Calculation of Radiation Patterns of Microstrip Antennas on Cylindrical Bodies of Arbitrary Cross Section," *IEEE Trans. Antennas Propagat.*, Vol. 45, No. 1, pp. 126-132, Jan. 1997.

[4] P. Slattman, P. Kildal, and A. Kishk, "Radiation from Patches on Grounded Cylindrical Substrates with Arbitrary Cross-Section," *IEEE Antennas and Propagation Society International Symposium Digest*, Vol. 3, pp. 1500-1503, July 1997.

[5] G. Vecchi, T. Bertuch, and M. Orefice, "Spectral-Domain Analysis of Printed Antennas of General Shape on Cylindrical Substrates," *IEEE Antennas and Propagation Society International Symposium Digest*, Vol. 3, pp. 1496-

1499, July 1997.
[6] D. Loffler, F. Rostan, and W. Wiesbeck, "Conformal Microstrip Patch Array for SDMA Applications," *IEEE Antennas and Propagation Society International Symposium Digest*, Vol. 3, pp. 1533-1536, July 1997.
[7] D. H. Werner, G. Mouyis, R. Mittra, "A Reciprocity Approach for Determining Radiation Patterns of Patch Antennas on Circularly Cylindrical Platforms," Proceedings of the *IEEE Antennas and Propagation Society International Symposium*, Atlanta, Georgia, pp. 1582-1585, June 1998.
[8] J. A. Stratton, *Electromagnetic Theory.* McGraw-Hill, New York, 1941.
[9] J. Ashkenazy, S. Shtrikman, and D.Treves, "Electric Surface Current Model for the Analysis of Microstrip Antennas on Cylindrical Bodies," *IEEE Trans. Antennas Propagat.*, Vol. AP-33, No. 3, pp. 295-300, March 1985.

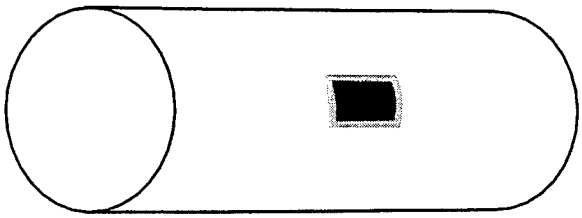

Figure 1. Conformal Patch Antenna Mounted on a Circularly-Cylindrical Platform.

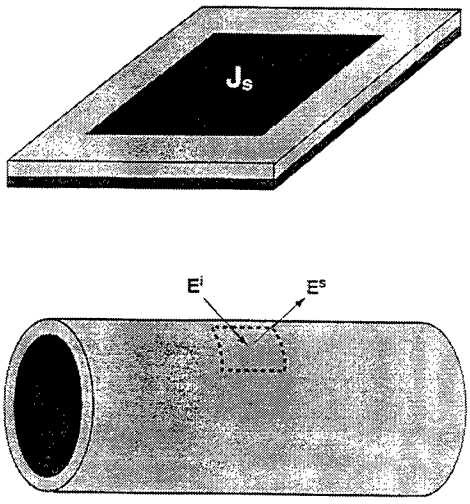

Figure 2. Application of Reciprocity Theorem.

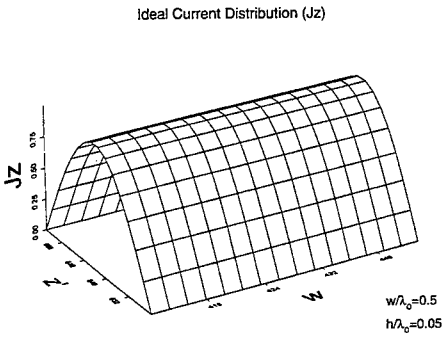

Figure 3

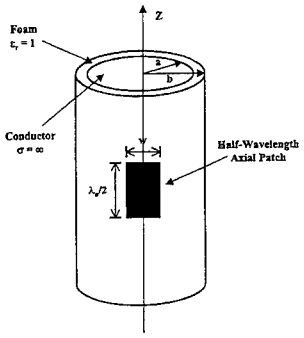

Figure 4

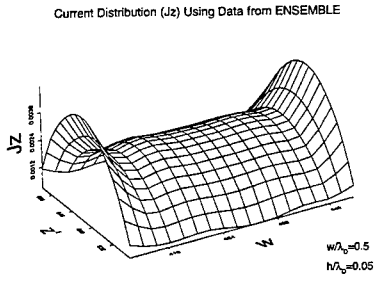

Figure 5

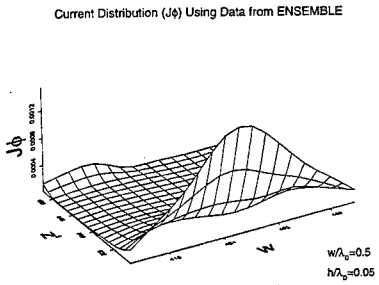

Figure 6

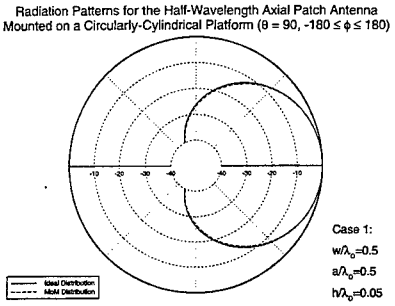

Figure 7

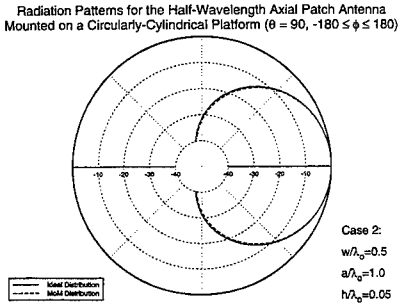

Figure 8

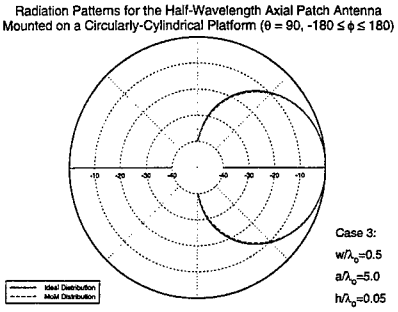

Figure 9

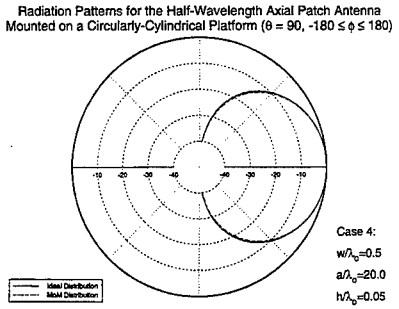

Figure 10

SESSION 9

FINITE ELEMENTS II

Chair: David B. Davidson

Hierarchal 2D and 3D Vector Finite Elements for Electromagnetic Wave Eigenvalue Problems

David B. Davidson and Riana H. Hansmann
Department of Electrical and Electronic Engineering
University of Stellenbosch, Stellenbosch 7600, South Africa
E-mail: davidson@firga.sun.ac.za.

Abstract— **This paper addresses 2D and 3D hierarchal H_0(curl) and H_1(curl) vector finite elements for high-frequency computational electromagnetics, in particular for eigenvalue problems. Some background is given on vector finite elements. H_0(curl) and H_1(curl) elements are given for both 2D and 3D. Results of waveguide eigenvalue analyses for circular, single- and dual-ridged waveguides are presented. Theoretical results for the explicit matrix entries for the 3D hierarchal H_1(curl) element are presented.**

Keywords— **Hierarchal vector finite elements; computational electromagnetics.**

I. Introduction

Vector finite elements (FE) have almost entirely displaced scalar functions for the finite element analysis of high-frequency electromagnetic fields. Because the original zero/first order elements replaced the traditional nodal-based field components with tangential fields on the element edges as the degrees of freedom, these have also been widely known as edge-based elements; for higher-order elements, there are also face- and body-based degrees of freedom. Other, historical names are Whitney/Nedelec elements.

In 1980, Nedelec published a very significant and widely-referenced paper which introduced these elements for FE computations [1]. The paper remains formidable reading; Silvester and Ferrari summarise the situation well as follows: "Since 1980, the ideas contained in Nedelec's paper have gradually filtered into the practical finite elements community, particularly amongst those concerned with electromagnetics" [2, p.295]. Amongst the earlier workers to use vector-based finite elements were Bossavit, Cendes, Crowley et al., and Lee et al.; references to these and other pioneers may be found in Webb's excellent review paper [3].

Our paper addresses both 2D and 3D vector FE analyses of eigenvalue problems, using higher-order hierarchal elements. Although 2D problems can be worked as scalar TE or TM problems, it is instructive to study the properties of vector elements in 2D, which motivated the 2D work to be presented. The eigenvalue analysis of waveguiding structures will be reported, including an analysis of single and dual-ridged waveguide; results will be presented and compared to a venerable approximate analysis. The paper concludes with theoretical results giving explicit formulas for the matrix entries for a 3D second order hierarchal element.

As will be discussed, higher-order vector elements are not unique, and the two major choices facing implementors are whether to adopt hierarchal or interpolatory elements. Savage's work indicates that the latter may be preferable from the viewpoint of matrix condition number [4], and Graglia et al. have published a systematic approach to deriving higher-order interpolatory elements, including curvilinear elements [5]. However, hierarchal elements remain very attractive for research codes using commercial mesh generators, where mesh refinement is simpler by enriching element order (p-adaptation) as opposed to h adaptation. (A discussion of error estimates and $h-p$ mesh adaptation may be found in [6], [7]).

II. Two dimensional vector finite elements

A. Hierarchal elements

The simplest basis functions are the constant tangential / linear normal (CT/LN) elements. It is by now well known in the computational electromagnetics community that vector finite elements are of mixed order; many authors use fractional order to indicate this, and such elements are often referred to as of order one-half; an alternate nomenclature is H_0(curl). (This is an extension of Nedelec's notation). There is no debate over the lowest order element: the degrees of freedom of the H_0(curl) element are the line integrals of the tangential field along each edge. (Since this is a constant times the edge length, the edge length is sometimes dropped in the literature [4]). The same is not so for higher-order elements. The reason is that the element must satisfy what have become known as the Nedelec constraints; these are contained in the definition of the linear space $\mathcal{R}^k$ [1, Definition 2]. The basis functions must satisfy these constraints [1, Definition 4]. Higher-order elements permit several choices of basis function satisfying these criteria.

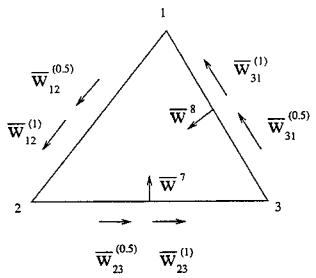

Fig. 1. Edge-based LT/QN functions and the edge directions for a triangular element. These are the directions of the basis functions on the element edges only. Reprinted, with permission, from [8] ©1998 IEEE.

When a more accurate approximation of the field variable is required, the linear tangential / quadratic normal (LT/QN) (H_1(curl)) shown in Table I may be used. This is a hierarchal element; it contains the three H_0(curl) edge-based functions, which is then "enriched" using three additional edge-based and two additional face-based functions, resulting in eight degrees of freedom. These last functions have no tangential components on any of the edges, in this way not affecting tangential continuity between elements which was established by enforcing tangential continuity for the first six basis functions. However these face functions add normal components to two of the three edges, which introduces the quadratic normal components. Note that the choice of which edge/face combination to use is arbitrary.

Order	Basis functions	
CT/LN	$\overline{w}_k = \lambda_i \nabla\lambda_j - \lambda_j \nabla\lambda_i$	$k = 1,2,3$
LT/QN	$\overline{w}_k = \begin{cases} \lambda_i \nabla\lambda_j + \lambda_j \nabla\lambda_i & k = 4,5,6 \\ (\nabla\lambda_i)\lambda_j\lambda_k & k = 7 \\ (\nabla\lambda_j)\lambda_i\lambda_k & k = 8 \end{cases}$	

TABLE I

HIERARCHAL 2D BASIS FUNCTIONS. NOTE THAT THE LT/QN ELEMENTS INCLUDE THE CT/LN FUNCTIONS.

B. FE Eigenvalue Analysis

The FE analysis of an eigenvalue problem results in the following generalised eigenmatrix equation:

$$[S][e] = k^2[T][e] \tag{1}$$

The mathematical process, and the notation, have been comprehensively described previously: a convenient summary may be found in [9]. The resulting eigenvalues for a 2D problem (with PEC boundaries) are the eigenvalues of the waveguide modes, i.e. the cut-off frequencies of each mode.

Exact TE wavenumbers	CT/LN result	LT/QN result
1.841	1.8468; 1.8468	1.8399; 1.8450
3.054	3.0641; 3.0641	3.0435; 3.0538
3.831	3.8404	3.8169
4.19	4.2093; 4.2093	4.1760; 4.1808
5.317	5.3405	5.2348; 5.2556; 5.2716
5.331	5.3470; 5.3470	5.3318

TABLE II

THE FIRST SIX TE MODES: EXACT AND CALCULATED WAVENUMBERS FOR CIRCULAR WAVEGUIDE RADIUS 1M. THE GUIDE CROSS-SECTION WAS DISCRETISED INTO 200 ELEMENTS.

B.1 Circular waveguides

A code developed by the authors was applied to calculate the cutoff frequencies of propagating modes in circular cylinders of infinite length and radius 1 m, for both the TE and TM modes. The mesh generation was done by the use of a Delaunay triangulation function available in Matlab Version 5.The accuracy of CT/LN and LT/QN is examined by comparing the values calculated with the FEM technique with the exact cutoff frequencies. From Table II it can be seen that the LT/QN solutions are indeed more accurate than the CT/LN solutions. The multiplicity of eigenvalues has also been reported by another worker [10].

B.2 Ridged Waveguide

Ridged waveguides are known to lower the cutoff frequency of the TE_{10} mode while increasing the cutoff frequencies of the higher-order modes, resulting in a larger single-mode bandwidth. This is especially useful for wideband horn feeds for microwave antennas. Possible configurations are single-ridged (Fig. 2), dual-ridged (Fig. 3) and quadruple-ridged waveguides [11, p. 457]. We show here applications of our code to dual- and single-ridged waveguides; to the best of our knowledge, this particular application is novel, albeit obvious.

B.3 Dual-ridged Waveguide

The waveguide parameters were $b/a = 0.45$, $d/b = 0.5$ and $s/a = 0.4$. The cross-section was discretised into a uniform mesh of 64 triangular elements.

No analytical solution is available for this type of waveguide, but reliable approximations are available for the cutoff frequency of the first mode [12]. These results have a maximum error between 1 and 3 percent

Pyle's TE cutoff wavelength ($\frac{\lambda_c}{a}$)	CT/LN result ($\frac{\lambda_c}{a}$)	LT/QN result ($\frac{\lambda_c}{a}$)
2.652	2.7338	2.664
-	1.0718	1.0200
-	0.8816	0.8772
-	0.8807	0.8764
-	0.6625	0.6448

TABLE III

THE TE MODES: PYLE'S APPROXIMATION FOR TE_{10} CUTOFF WAVELENGTH (NORMALISED BY a) AND FEM RESULTS FOR A DUAL-RIDGED WAVEGUIDE.

Pyle's TE cutoff wavelength ($\frac{\lambda_c}{a}$)	CT/LN result ($\frac{\lambda_c}{a}$)	LT/QN result ($\frac{\lambda_c}{a}$)
2.785	2.8318	2.7914
-	1.1983	1.1666
-	0.8806	0.8742
-	0.7991	0.8001
-	0.656	0.6433

TABLE IV

THE TE MODES: PYLE'S APPROXIMATION FOR TE_{10} CUTOFF WAVELENGTH (NORMALISED BY a) AND FEM RESULTS FOR A SINGLE-RIDGED WAVEGUIDE.

for the worst case where $s/a << 1$. The results are compared in Table III.

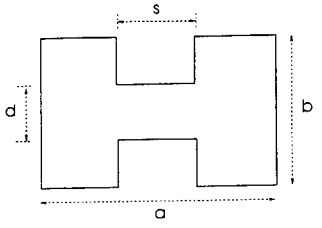

Fig. 2. Dual-ridged waveguide.

B.4 Single-ridged Waveguide

The waveguide parameters were $b/a = 0.45$, $d/b = 0.5$ and $s/a = 0.4$. The cross-section was discretised into a uniform mesh of 128 triangular elements.

Once again the result for the TE_{10} is given in [12]. The results are compared in table IV.

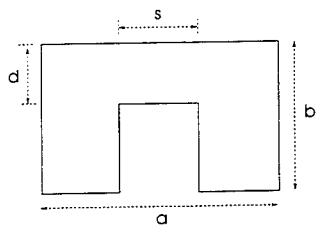

Fig. 3. Single-ridged waveguide.

III. THREE-DIMENSIONAL VECTOR FINITE ELEMENTS

Whilst defining the higher-order elements is essential, explicit forms for the contributions of the matrices derived from the variational functional are extremely useful when implementing a FE code. Lee and Mittra published very convenient expressions for H_0(curl) elements [9]; the first author recently extended this work [13]. Savage and Peterson presented a more succinct approach in [14]; they included elements up to H_2(curl) (Quadratic tangential / cubic normal) and gave explicit forms for the H_0(curl) and H_1(curl) elements. Their elements are not hierarchal, and were also not constructed along a specific interpolatory scheme. Savage went on to publish both interpolatory and hierarchal vector basis functions up to and including H_3(curl) [4], and Peterson went on to publish, with Graglia and Wilton, a full interpolatory scheme for both curl-curl and div-div elements [5]. Neither of these papers contained explicit formulas for the matrix entries. Another set of hierarchal elements has also been recently proposed [15]; we use those of [4] in the present paper.

A. *Explicit forms for 3D hierarchal H_1(curl) elements*

This paper will now present explicit forms for the H_1(curl) interpolatory elements, given in element form in [4]. Despite the significantly improved convergence rate of higher-order elements, the complexity grows so rapidly that a user-oriented, general-purpose code is arguably unlikely to routinely use more than H_1(curl) elements; the degrees of freedom grows as [1, p.323]:

$$N_k = \frac{k(k+2)(k+3)}{2} \qquad (2)$$

k here is for H_{k-1}(curl). This is summarised in Table V, where the rapid growth in degrees of freedom associated with the higher-order elements is readily apparent.

Tables VI andVII summarise the higher-order hierarchal CT/LN and LT/QN vector basis functions. This is based on [4, Table 2]. Note that what is presented are the functions for one edge, one face and the interior tetrahedron function. The overall system replicates this for each of the six edges and four faces.

Order	Degrees of freedom
H_0(curl)	6
H_1(curl)	20
H_2(curl)	45
H_3(curl)	84
H_4(curl)	140

TABLE V

HIERARCHAL VECTOR BASIS FUNCTIONS: DEGREES OF FREEDOM ASSOCIATED WITH VARIOUS ORDERS OF ELEMENT.

Order	Edge functions	Face functions	Tetra-hedron functions
H_0(curl) (CT/LN)	$\lambda_1\nabla\lambda_2 - \lambda_2\nabla\lambda_1$ $= \Omega_{12}$ $(= e1)$	—	—
H_1(curl) (LT/QN)	$\nabla[\lambda_1\lambda_2]$ $(= e2)$	$\lambda_1\Omega_{23}$ $(= f1)$ $\lambda_2\Omega_{13}$ $(= f2)$	—

TABLE VI

HIERARCHAL VECTOR BASIS FUNCTIONS: EXPLICIT FORMS. NOTE THAT THE LT/QN ELEMENTS INCLUDE THE CT/LN FUNCTIONS.

Explicit forms are required for the following integrals, once the relevant basis functions are substituted for $\vec{B}_i$ and $\vec{B}_j$ in the following:

$$E_{ij} = \int_V \nabla \times \vec{B}_i \cdot \nabla \times \vec{B}_j \tag{3}$$

and

$$F_{ij} = \int_V \vec{B}_i \cdot \vec{B}_j \tag{4}$$

(The symbols $[S]$ and $[T]$ respectively are also widely used for these matrices [2], [9]). Savage and Peterson published explicit forms for a closely related H_1(curl) element; we have extended their work and present the results here. The first six elements in Table VI are precisely as for H_0(curl) — because of course of the hierarchal nature of the elements. However, the next six edge functions and eight face functions are new.

Order	Edge functions	Face functions	Tetra-hedron functions
H_0(curl)	$6 \times 1 = 6$	—	—
H_1(curl) additional	$6 \times 1 = 6$	$4 \times 2 = 8$	—

TABLE VII

HIERARCHAL VECTOR BASIS FUNCTIONS: EXTRA UNKNOWNS ADDED PER ADDITIONAL ORDER

The face functions are as for the elements tabulated in [14]. The edge functions however are different, and the explicit forms must now be derived. Note that the $[E]$ and $[F]$ matrices consist now of several types of interaction, between the various element functions.

Consider first the curl-curl term, eqn. (3). Following the notation of [14], the interactions can be expressed as block matrices as follows:

$$E = \begin{bmatrix} E^{e1e1} & E^{e1e2} & E^{e1f1} & E^{e1f2} \\ E^{e2e1} & E^{e2e2} & E^{e2f1} & E^{e2f2} \\ E^{f1e1} & E^{f1e2} & E^{f1f1} & E^{f1f2} \\ E^{f2e1} & E^{f2e2} & E^{f2f1} & E^{f2f2} \end{bmatrix} \tag{5}$$

A similar expression pertains for $[F]$. Note here, however, that $e1$ and $e2$ are the first and second six functions of Table VI, rather than functions of the form $\lambda_{i1}\nabla\lambda_{i2}$ as originally proposed in [4].

From eqn. (3), it is clear that the elements of eqn. (5) are symmetrical, hence only the sub-matrices on and above (or below) the diagonal need be explicitly evaluated. The term E^{e1e1} is as for the CT/LN element and was evaluated in [14, eqn.10]. The additional *edge* functions of the form $\nabla(\lambda_i\lambda_j)$ ($e2$ in the above) make no contribution, since $\nabla \times \nabla\phi \equiv 0\ \forall\phi$. This is true for all terms involving the $e2$ functions. Thus the following elements are zero: $E^{e1e2} = E^{e2f1} = E^{e2f2} = 0$ (and of course the corresponding elements below the diagonal).

Now, the contribution of the face elements to $[E]$ must be established. Using some elementary vector identities, grouping like terms in the same fashion as [14, eqn.10], using [14, eqn.24] and finally the formulas for integration over tetrahedra [14, eqn.14], one obtains the following results:

$$E_{ij}^{e1e1} = 4V\ell_i\ell_j\vec{v}_{i1,i2} \cdot \vec{v}_{j1,j2} \tag{6}$$

$$E_{ij}^{e1e2} = 0 \tag{7}$$

$$E_{ij}^{e1f1} = \frac{V}{2}\ell_i\vec{v}_{i1,i2} \cdot [2\vec{v}_{j2,j3} + \vec{v}_{j1,j3} - \vec{v}_{j1,j2}] \tag{8}$$

$$E_{ij}^{e1f2} = \frac{V}{2}\ell_i\vec{v}_{i1,i2} \cdot [\vec{v}_{j2,j3} + 2\vec{v}_{j1,j3} + \vec{v}_{j1,j2}] \tag{9}$$

$$E_{ij}^{e2e2} = 0 \tag{10}$$

$$E_{ij}^{e2f1} = 0 \tag{11}$$

$$E_{ij}^{e2f2} = 0 \tag{12}$$

$$\begin{aligned} E_{ij}^{f1f1} = {} & V(4M_{i1,j1}\vec{v}_{i2,i3} \cdot \vec{v}_{j2,j3} + 2M_{i1,j2}\vec{v}_{i2,i3} \cdot \vec{v}_{j1,j3} \\ & -2M_{i1,j3}\vec{v}_{i2,i3} \cdot \vec{v}_{j1,j2} + 2M_{i2,j1}\vec{v}_{i1,i3} \cdot \vec{v}_{j2,j3} \\ & +M_{i2,j2}\vec{v}_{i1,i3} \cdot \vec{v}_{j1,j3} - M_{i2,j3}\vec{v}_{i1,i3} \cdot \vec{v}_{j1,j2} \\ & -2M_{i3,j1}\vec{v}_{i1,i2} \cdot \vec{v}_{j2,j3} - M_{i3,j2}\vec{v}_{i1,i2} \cdot \vec{v}_{j1,j3} \\ & +M_{i3,j3}\vec{v}_{i1,i2} \cdot \vec{v}_{j1,j2}) \end{aligned} \tag{13}$$

$$
\begin{aligned}
E_{ij}^{f1f2} &= V(2M_{i1,j1}\vec{v}_{i2,i3}\cdot\vec{v}_{j2,j3} + 4M_{i1,j2}\vec{v}_{i2,i3}\cdot\vec{v}_{j1,j3} \\
&\quad +2M_{i1,j3}\vec{v}_{i2,i3}\cdot\vec{v}_{j1,j2} + M_{i2,j1}\vec{v}_{i1,i3}\cdot\vec{v}_{j2,j3} \\
&\quad +2M_{i2,j2}\vec{v}_{i1,i3}\cdot\vec{v}_{j1,j3} + M_{i2,j3}\vec{v}_{i1,i3}\cdot\vec{v}_{j1,j2} \\
&\quad -M_{i3,j1}\vec{v}_{i1,i2}\cdot\vec{v}_{j2,j3} - 2M_{i3,j2}\vec{v}_{i1,i2}\cdot\vec{v}_{j1,j3} \\
&\quad -M_{i3,j3}\vec{v}_{i1,i2}\cdot\vec{v}_{j1,j2}) \qquad (14)
\end{aligned}
$$

$$
\begin{aligned}
E_{ij}^{f2f2} &= V(M_{i1,j1}\vec{v}_{i2,i3}\cdot\vec{v}_{j2,j3} + 2M_{i1,j2}\vec{v}_{i2,i3}\cdot\vec{v}_{j1,j3} \\
&\quad +M_{i1,j3}\vec{v}_{i2,i3}\cdot\vec{v}_{j1,j2} + 2M_{i2,j1}\vec{v}_{i1,i3}\cdot\vec{v}_{j2,j3} \\
&\quad +4M_{i2,j2}\vec{v}_{i1,i3}\cdot\vec{v}_{j1,j3} + 2M_{i2,j3}\vec{v}_{i1,i3}\cdot\vec{v}_{j1,j2} \\
&\quad +M_{i3,j1}\vec{v}_{i1,i2}\cdot\vec{v}_{j2,j3} + 2M_{i3,j2}\vec{v}_{i1,i2}\cdot\vec{v}_{j1,j3} \\
&\quad +M_{i3,j3}\vec{v}_{i1,i2}\cdot\vec{v}_{j1,j2}) \qquad (15)
\end{aligned}
$$

Terms such as $M_{i,j}$, $\vec{v}_{i,j}$ etc. are as given in [14].The results involving face elements only (the last three sub-matrices above) are identical to [14, eqns.(31,34 & 35)]. They have been double-checked by the present author and are correct as published. The results involving edge elements above differ from [14], in some cases subtly so.

The contribution to the div-div term, eqn. (4), is straightforward albeit tedious to derive. The result is:

$$
\begin{aligned}
F_{ij}^{e1,e1} &= V\ell_i\ell_j[\phi_{i2,j2}M_{i1,j1} - \phi_{i2,j1}M_{i1,j2} \\
&\quad -\phi_{i1,j2}M_{i2,j1} + \phi_{i1,j1}M_{i2,j2}] \qquad (16)
\end{aligned}
$$

$$
\begin{aligned}
F_{ij}^{e2/e1,e1/e2} &= V\ell_i\ell_j[\phi_{i2,j2}M_{i1,j1} \mp \phi_{i2,j1}M_{i1,j2} \\
&\quad \pm\phi_{i1,j2}M_{i2,j1} - \phi_{i1,j1}M_{i2,j2}] \qquad (17)
\end{aligned}
$$

$$
\begin{aligned}
F_{ij}^{e2,e2} &= V\ell_i\ell_j[\phi_{i2,j2}M_{i1,j1} + \phi_{i2,j1}M_{i1,j2} \\
&\quad +\phi_{i1,j2}M_{i2,j1} + \phi_{i1,j1}M_{i2,j2}] \qquad (18)
\end{aligned}
$$

$$
\begin{aligned}
F_{ij}^{e1/2,f1} &= V\ell_i(\phi_{i2,j3}N_{i1,j1,j2} \mp \phi_{i1,j3}N_{i2,j1,j2} \\
&\quad -\phi_{i2,j2}N_{i1,j1,j3} \pm \phi_{i1,j2}N_{i2,j1,j3}) \qquad (19)
\end{aligned}
$$

$$
\begin{aligned}
F_{ij}^{e1/2,f2} &= V\ell_i(\phi_{i2,j3}N_{i1,j1,j2} \mp \phi_{i1,j3}N_{i2,j1,j2} \\
&\quad -\phi_{i2,j1}N_{i1,j2,j3} \pm \phi_{i1,j1}N_{i2,j2,j3}) \qquad (20)
\end{aligned}
$$

$$
\begin{aligned}
F_{ij}^{f1,f1} &= V[\phi_{i3,j3}P_{i1,i2,j1,j2} - \phi_{i2,j3}P_{i1,i3,j1,j2} \\
&\quad -\phi_{i3,j2}P_{i1,i2,j1,j3} + \phi_{i2,j2}P_{i1,i3,j1,j3}] \qquad (21)
\end{aligned}
$$

$$
\begin{aligned}
F_{ij}^{f1,f2} &= V[\phi_{i3,j3}P_{i1,i2,j1,j2} - \phi_{i2,j3}P_{i1,i3,j1,j2} \\
&\quad -\phi_{i3,j1}P_{i1,i2,j2,j3} + \phi_{i2,j1}P_{i1,i3,j2,j3}] \qquad (22)
\end{aligned}
$$

$$
\begin{aligned}
F_{ij}^{f2,f2} &= V[\phi_{i3,j3}P_{i1,i2,j1,j2} - \phi_{i1,j3}P_{i2,i3,j1,j2} \\
&\quad -\phi_{i3,j1}P_{i1,i2,j2,j3} + \phi_{i1,j1}P_{i2,i3,j2,j3}] \qquad (23)
\end{aligned}
$$

Due to the similarity in form, the results for $e1$ and $e2$ are presented simultaneously in the above; the $\mp$ and $\pm$ in $F_{ij}^{e2/e1,e1/e2}$ (eqn. (17)) refer to $F_{ij}^{e2,e1}$ and $F_{ij}^{e1,e2}$ respectively, and similarly for the other such expressions.

The results for the face element submatrices (the last three above) are identical to [14, eqns.(41,44 & 45)]; again, these results have been checked by the present authors and are correct as given. $\phi_{i,j}$ is defined in [14, eqn.(8)].

The integration matrices $N_{i,j,k}$ and $P_{i,j,k,l}$ are as defined in [14, eqns.(46 & 47)]; these are not quite as straightforward as that of the H_1(curl) elements [14, eqn.(15)]. The reason is that the matrix entries are in turn sub-matrices, since each face i has three nodes (and hence three simplex coordinates) associated with it. As an example, the sub-matrix for faces $i = 2$ and $j = 3$, (with associated nodes $\{1,2,4\}$ and $\{1,3,4\}$ respectively, using the numbering convention of [14, Table II]) is as follows:

$$
\begin{aligned}
[P_{2,3}] &= \begin{bmatrix} P_{1,2,1,3} & P_{1,2,1,4} & P_{1,2,3,4} \\ P_{1,4,1,3} & P_{1,4,1,4} & P_{1,4,3,4} \\ P_{2,4,1,3} & P_{2,4,1,4} & P_{2,4,3,4} \end{bmatrix} \\
&= \frac{1}{840}\begin{bmatrix} 2 & 2 & 1 \\ 2 & 4 & 2 \\ 1 & 2 & 2 \end{bmatrix} \qquad (24)
\end{aligned}
$$

Such matrices can be either pre-computed, or computed on the fly by inspection.

IV. Conclusions

This paper has addressed several aspects of higher-order vector finite elements, concentrating on eigenvalue applications. Two-dimensional results have been presented for both a standard test problem (a circular waveguide), as well as a novel application to ridged waveguide. Theoretical three dimensional results have been presented, giving explicit forms for hierarchal H_1(curl) elements. This is a logical extension of previous work [14]. Such explicit forms are extremely useful when implementing a FEM code.

Progress on the implementation and application of these 3D H_1(curl) elements will be reported at the symposium. The authors already have a working 3D H_0(curl) FE code; results for cavity eigenvalue problems computed using it were presented in [13].

Acknowledgements

The work reported here was funded jointly by the (South African) FRD (via a sabbatical grant to DBD and a bursary for RHH) and by Electromagnetic Software and Systems (EMSS Pty Ltd), Stellenbosch. The work is an extension of work initiated by DBD during a sabbatical at Trinity College and CUED, Cambridge, England, during 1997. We further acknowledge various useful discussions with Dr. FJC Meyer of EMSS.

REFERENCES

[1] J. C. Nedelec, "Mixed finite element in $\Re^3$," *Numerische Mathematik*, vol. 35, pp. 315–341, 1980.

[2] P. P. Silvester and R. L. Ferrari, *Finite Elements for Electrical Engineers*. Cambridge: Cambridge University Press, 3rd ed., 1996.

[3] J. P. Webb, "Edge elements and what they can do for you," *IEEE Trans. Magn.*, vol. 29, pp. 1460–1465, March 1993.

[4] J. S. Savage, "Comparing high order vector basis functions," in *Proceedings of the 14th Annual Review of Progress in Applied Computational Electromagnetics*, pp. 742–749, March 1998. Monterey, CA.

[5] R. D. Graglia, D. R. Wilton, and A. F. Peterson, "Higher order interpolatory vector bases for computational electromagnetics," *IEEE Trans. Antennas Propagat.*, vol. 45, pp. 329–342, March 1997.

[6] F. J. C. Meyer and D. B. Davidson, "A posteriori error estimates for the two-dimensional finite element/boundary element solution of electromagnetic scattering and radiation problems," *Applied Computational Electromagnetics Society Journal*, vol. 11, pp. 40–54, July 1996.

[7] F. J. C. Meyer and D. B. Davidson, "Adaptive-mesh refinement of finite-element solutions for two-dimensional electromagnetic problems," *IEEE Antennas and Propagation Society Magazine*, vol. 37, pp. 77–83, October 1996.

[8] R. Hansmann and D. B. Davidson, "Two dimensional edge-based finite elements for guided and scattered wave problems," in *Proceedings of the 1998 SA Symposium on AP/MTT (incorporating EMC and Remote Sensing)*, September 1998. Univ. Cape Town, South Africa.

[9] J.-F. Lee and R. Mittra, "A note on the application of edge-elements for modeling three-dimensional inhomogeneously-filled cavities," *IEEE Trans. Microwave Theory Tech.*, vol. 40, pp. 1767–1773, September 1992.

[10] A. F. Peterson, "Vector finite element formulation for scattering from two-dimensional heterogeneous bodies," *IEEE Trans. Antennas Propagat.*, vol. 43, pp. 357–365, March 1994.

[11] C. A. Balanis, *Advanced Engineering Electromagnetics*. New York: John Wiley and Sons, 1989.

[12] J. R. Pyle, "The cutoff wavelength of the TE_{10} mode in ridged rectangular wavguide of any aspect ratio," *IEEE Trans. Microwave Theory and Techniques*, vol. MTT-14, pp. 175–183, April 1966.

[13] D. B. Davidson, "Comments on and extensions of 'A note on the application of edge-elements for modeling three-dimensional inhomogeneously-filled cavities'," *IEEE Trans. Microwave Theory Tech.*, vol. 46, pp. 1344–1346, September 1998.

[14] J. S. Savage and A. F. Peterson, "Higher-order vector finite elements for tetrahedral cells," *IEEE Trans. Microwave Theory Tech.*, vol. 44, pp. 874–879, June 1996.

[15] L. S. Andersen and J. L. Volakis, "Hierarchal tangential vector finite elements for tetrahedra," *IEEE Microwave Guided Wave Lett.*, vol. 8, pp. 127–129, March 1998.

Local Error Estimation for High–Frequency Problems Using Hierarchical Tangential Vector Finite Elements

Scott Savage
John Manges
Ansoft Corporation

Abstract – This paper applies the method of local error estimation to high–frequency finite element applications. Local error estimation is useful in determining the validity of a finite element solution on an element by element basis, and has previously been applied to scalar finite element analysis. Applying the method to high–frequency problems is possible due to the recent development of high–order, hierarchical, vector basis functions. This paper will provide a formulation of the local error estimation method and present numerical results which demonstrate the efficiency of the method.

I. INTRODUCTION

It is well known that high–order vector finite elements can efficiently solve high–frequency electromagnetic problems. However, field singularities, which are present in most finite element applications, can reduce the convergence rates of any order finite element analysis. Furthermore, employing singular basis functions, which is common in 2-D problems, is difficult to automate in 3-D due to the unknown rate of singularities in arbitrary problems. For these problems, traditional meshing using a wavelength criterion can be very inefficient. This paper applies the method of local error estimation to high–frequency problems. The method identifies those areas of a finite element mesh in which the solution is poor, so that some type of adaptive refinement (n–type or p–type) can be applied there.

The adaptive finite element method relies on a good refinement indicator which quantitatively ranks the elements (tetrahedra) in a mesh based on the solution accuracy. Some refinement indicators previously used in high–frequency problems include residual based indicators and local error estimation [1,2].

The technique of local error estimation is to resolve, with increased accuracy and less expense, the fields on subdomains of the original problem. Under the assumption that the solution of the local problem is significantly more accurate, the difference between the local problem solution and the original global solution is an estimate of the error in the global solution.

To obtain a more accurate local solution on a subdomain, one can either use more dense meshing, higher order basis functions, or a combination of the two. Sense hierarchical basis functions are available [5,6], the second possibility is more desirable. First, higher order basis functions offer better accuracy per degree–of–freedom. Second, a hierarchical solution avoids the need for additional mesh manipulation. This method has been successfully applied to scalar problems in quasi–statics [2,3].

II. The Local Error Problem

As a model problem, consider the determination of the fields and resonant frequencies for an enclosed cavity. The finite element solution of the weak form of the vector Helmholtz equation,

$$\iiint \nabla\times\overline{T}\cdot\nabla\times\overline{E} - k^2\overline{T}\cdot\overline{E} = \oiint \overline{T}\cdot\hat{n}\times\nabla\times\overline{E}\,, \tag{1}$$

results in a generalized Eigenvalue problem, where $\overline{E}$ and k are determined simultaneously. Since k is variationally stationary, it's solution is more accurate than $\overline{E}$. In the local error estimation, k is assumed to be exact.

The exact solution, $\overline{E}$, obeys (1). Let $\overline{E}^h$ denote the field corresponding to an approximate finite element solution. The global error function $\overline{e}$ is defined by

$$\overline{e} = \overline{E} - \overline{E}^h. \tag{2}$$

Clearly, if $\overline{e}$ is known (or can be accurately approximated), then the exact solution is known. Let $\overline{E}^l$ denote the approximate solution to the local problem for $\overline{E}$. Then,

$$\overline{e}^h = \overline{E}^l - \overline{E}^h, \tag{3}$$

is an estimate of $\overline{e}$. It then follows that

$$\left\|\overline{e}^h - \overline{e}\right\| = \left\|\overline{E}^l - \overline{E}\right\|. \tag{4}$$

In other words, the error in estimation of $\overline{e}$ by (3) is equal to the error in the local problem. So, the goal is to solve the local problem more accurately than was done in the global solution.

A deterministic local problem, defined in (1), is solved on each tetrahedron using the approximate boundary fields and k from the original global solution. In doing this, either Neumann or Dirichlet boundary conditions could be used. In this paper, the Neumann boundary condition is used as this allows full use of the degrees–of–freedom of the high–order element.

III. Hierarchical Vector Elements

Vector basis functions have proven to be the best choice in solving high–frequency finite element problems [4]. Hierarchical vector basis functions have recently been extended to high polynomial

orders [5,6]. Table 1 presents the basis functions used in this study. The basis functions are of the type first proposed by Nedelec [7]. The H_0(curl) functions are the lowest order vector functions, often referred to as edge-elements. Hierarchical functions through H_3(curl) are given. These basis functions allow the straight–forward solution of (1) on the interior of a single tetrahedron. The discretized version of (1) is

$$\left(\mathbf{S}-k^2\mathbf{T}\right)\boldsymbol{\alpha}=\mathbf{B}\boldsymbol{\beta}\,, \tag{5}$$

where $\boldsymbol{\alpha}$ is a vector of unknown coefficients, and $\boldsymbol{\beta}$ is a vector of known coefficients from the solution of the global problem, augmented by zeros for the higher–order basis functions used in the local problem. The matrices **S**, **T**, and **B** are the element matrices for the tetrahedron. Equation (5) is solved using full–matrix techniques for $\boldsymbol{\alpha}$. The approximate error field is then integrated over the tetrahedron to determine the refinement indicator,

$$r=\iiint \bar{e}^h\cdot\bar{e}^h=(\boldsymbol{\alpha}-\boldsymbol{\beta})^T\mathbf{T}(\boldsymbol{\alpha}-\boldsymbol{\beta}). \tag{6}$$

This indicator is computed for all tetrahedra to determine where adaptive meshing should be applied.

IV. Numerical Results

To demonstrate the advantage of intelligent adaptive refinement, the method of local error estimation was applied to the analysis of a resonant cavity with reentrant corners. The cavity was formed by placing a small perfectly conducting cube in the corner of another cubic cavity. The dominant mode of this cavity possesses a singularity near the corner of the small cube. The wavenumber, k, of this mode was determined to be 3.588 on a well refined mesh. Fig. 1 shows the convergence of the finite element method using H_0(curl) as more and more tetrahedra are applied to the problem. The local error estimation method using H_1(curl) on the interior is compared to uniform refinement where the goal is to keep all tetrahedra approximately the same size. As the solution approaches convergence, it is clear that intelligent mesh refinement is necessary for efficient solutions. Fig. 2 shows the same analysis where H_1(curl) functions were used globally and H_2(curl) locally. Fig. 3 uses H_2(curl) functions globally and H_3(curl) locally. In all cases, local error estimation provides more efficient meshing than uniform refinement.

One interesting trend appears with the coarse initial meshes. It appears that uniform refinement initially is more efficient than intelligent refinement. It may seem logical, then, to use uniform refinement initially, followed by refinement using local error estimation. Fig. 2 presents results from applying this technique. It appears that this approach initially provides better solutions with fewer

unknowns. However, as the mesh is further refined, the local error estimation method eventually overtakes the combined approach. Thus, it seems that using the local error estimation method from the initial mesh ultimately provides the most efficient finite element mesh.

V. Conclusion

In this paper, the method of local error estimation has been applied to high–frequency finite element solution of electromagnetic problems. This was possible due to the recent development of high order, hierarchical, tangential vector finite elements. It was demonstrated that this method can be used to improve adaptive mesh refinement over wavelength based mesh refinement. It still remains to compare this approach to other mesh refinement indicators including residual based methods.

VI. References

[1] Verfurth, *A review of A Posteriori Error Estimation and Adaptive Mesh-Refinement Techniques*, Wiley and Teubner Mathematics, 1996.

[2] Z. Cendes, D. Shenton, "Adaptive mesh refinement in the finite element computation of magnetic fields," *IEEE Trans. Mag.*, vol. 21, pp. 1811–1816, Sept. 1985.

[3] D. Shenton, Z. Cendes, "MAX – An expert system for automatic adaptive magnetics modeling," *IEEE Trans. Mag.*, vol. 22, pp. 805–807, Sept. 1986.

[4] Z. J. Cendes, "Vector finite elements for electromagnetic field computation," *IEEE Trans. Mag.*, vol. 27, pp. 3958–3966, Sept. 1991.

[5] J. P. Webb and B. Forghani, "Hierarchal scalar and vector tetrahedra," *IEEE Trans. Mag.*, vol. 29, pp. 1495–1498, Mar. 1993.

[6] J. S. Savage, "Comparing high order vector basis functions," *Proceedings of the 14th Annual Review of Progress in Applied Computational Electromagnetics*, pp. 742–749, Mar. 1998.

[7] J. C. Nedelec, "Mixed finite elements in R3," *Numer. Math.*, vol. 35, pp. 315–341, 1980.

Table 2. Hierarchical Vector Basis Functions			
Order	Edge Functions	Face Functions	Tetrahedron Functions
H_0(curl)	$\lambda_1\nabla\lambda_2 - \lambda_2\nabla\lambda_1 = \Omega_{12}$	N/A	N/A
H_1(curl) Additional	$\nabla[\lambda_1\lambda_2]$	$\lambda_1\Omega_{23}$ $\lambda_2\Omega_{13}$	N/A
H_2(curl) Additional	$\nabla[\lambda_1\lambda_2(\lambda_1 - \lambda_2)]$	$\lambda_1^2\Omega_{23}$, $\lambda_2^2\Omega_{13}$, $\lambda_3^2\Omega_{12}$ $\nabla[\lambda_1\lambda_2\lambda_3]$	$\lambda_1\lambda_2\Omega_{34}$ $\lambda_2\lambda_3\Omega_{14}$ $\lambda_3\lambda_4\Omega_{12}$
H_3(curl) Additional	$\nabla[\lambda_1\lambda_2(2\lambda_1 - \lambda_2)(\lambda_1 - 2\lambda_2)]$	$\lambda_1^3\Omega_{23}$, $\lambda_2^3\Omega_{13}$, $\lambda_3^3\Omega_{12}$, $\lambda_1^2\lambda_3\Omega_{12}$ $\nabla[\lambda_1^2\lambda_2\lambda_3]$, $\nabla[\lambda_1\lambda_2\lambda_3^2]$	$\lambda_1\lambda_2\lambda_3\Omega_{14}$, $\lambda_1\lambda_2\lambda_3\Omega_{24}$ $\lambda_1\lambda_2\lambda_4\Omega_{13}$, $\lambda_1\lambda_2\lambda_4\Omega_{23}$ $\lambda_1\lambda_3\lambda_4\Omega_{12}$, $\lambda_1\lambda_3^2\Omega_{24}$ $\lambda_2^2\lambda_3\Omega_{14}$, $\lambda_2\lambda_3^2\Omega_{14}$ $\nabla[\lambda_1\lambda_2\lambda_3\lambda_4]$

H0(curl) Basis Functions

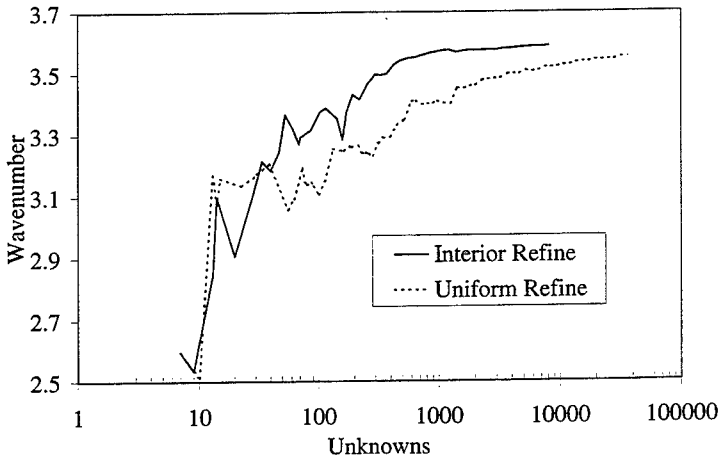

H1(curl) Basis Functions

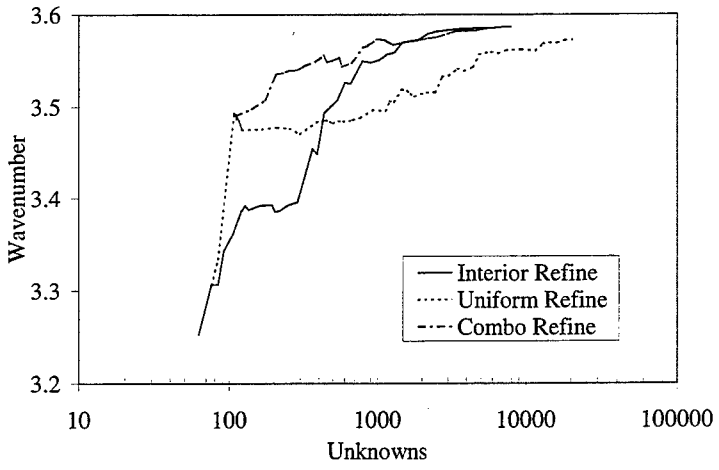

H2(curl) Basis Functions

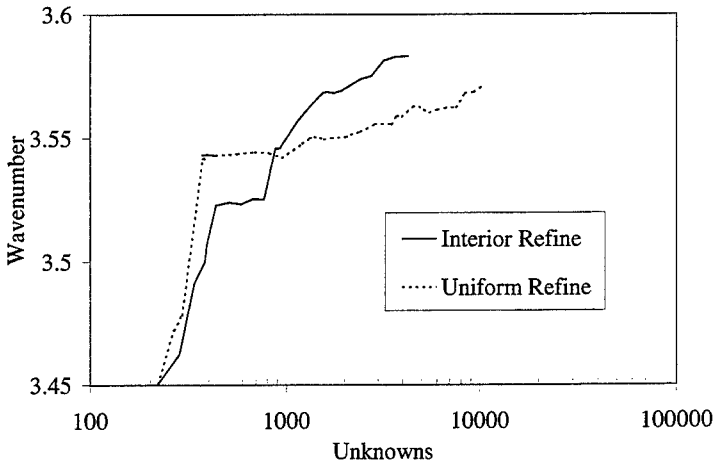

Time-Domain Simulation of Nonlinear Transmission Lines: Interface of Finite Elements to Circuit Analysis[1]

Karim N. Wassef and Andrew F. Peterson
School of Electrical and Computer Engineering
Georgia Institute of Technology
Atlanta, GA 30332

Abstract

A finite element formulation is used to compute the time-varying inductance associated with a multi-conductor transmission line with saturable magnetic materials. A time domain finite difference solution of the transmission line equations is coupled to a circuit simulator based on algebraic companion form equations. The approach is intended for the modeling of transient signals on power distribution networks.

Introduction

Several applications, including power distribution networks [1], depend on circuit analysis tools, such as Spice™, in order to model their systems. Integrating a full electromagnetic model into such simulation tools requires particular adaptation of the models' interfaces. Transmission lines form the backbone of most distribution networks, and therefore act as critical links in the simulation. Skin effect problems have been studied for simple multiconductor geometries using the transmission line matrix method exclusively [2]. In order to provide a more accurate estimation of signal propagation on transmission lines, a combination of time domain transmission line matrix and nonlinear finite element analysis is required. This allows for a more rigorous transient analysis that incorporates geometry, conductivity, and nonlinear ferromagnetic effects. The transient finite element analysis using surface impedances has been achieved via the fast Fourier transform [3]; however, since circuit simulators require time marching analysis, only a truly transient finite element solution will fit [4].

Since the algebraic, or resistive, companion form of circuit equations is commonly used, the electromagnetic model must produce a terminal interface that fits that form. The dependent relationships between the full network solver, the transmission lines matrix, and the finite element model are demonstrated.

The Transmission Line Matrix Model

Since a transmission line may be decomposed into a simple longitudinal and a complex cross-sectional geometry, it is reasonable to solve a different set of equations in each space. The

[1] This research is supported by the US Office of Naval Research under ONR Grant No. N00014-96-1-0926

voltages may be determined for the previous currents over the adjacent segments and the past node voltage.

In a nonlinear system, the inductance matrix [l] is a function of local segment currents. [l] is then also a function of position and time. For a K-segment line, K separate [l] matrices exist down the transmission line at every time step, and are updated after the new segment currents are determined.

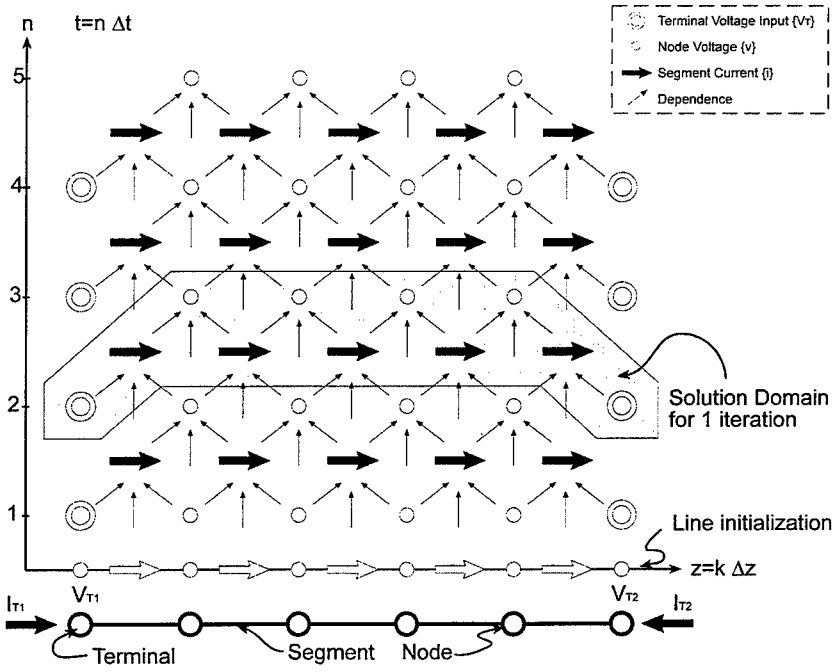

Figure 1. Solution evolution on a transmission line.

The highlighted solution domain illustrates the operations performed at each iteration. Using this approach, signals propagating in both directions on the transmission line are accounted for.

Interface to the Algebraic Companion Form

The algebraic companion form [5,6] is a system of writing circuit equations into a matrix so that the interaction of multiple local components or modules may be impressed into a global matrix whose solution is the terminal parameters (node and current) of all the modules in the system. This allows for the integration of a large number of separate functioning modules into a large network solver.

Each terminal node is assigned a voltage and current; the module has to return the expected relationship between the nodal voltage and current. For example, a module consisting of two resistive elements (Figure 2) will result in a system of equations of the form

$$\begin{Bmatrix} I_1 \\ I_2 \end{Bmatrix} = \begin{bmatrix} \frac{1}{R_{13}} & 0 \\ 0 & \frac{1}{R_{24}} \end{bmatrix} \left\{ \begin{Bmatrix} V_3 \\ V_4 \end{Bmatrix} - \begin{Bmatrix} V_1 \\ V_2 \end{Bmatrix} \right\}$$

$$\begin{Bmatrix} I_3 \\ I_4 \end{Bmatrix} = -\begin{Bmatrix} I_1 \\ I_2 \end{Bmatrix}$$

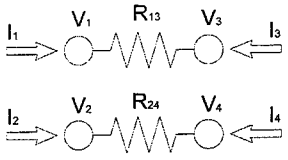

Figure 2. A module consisting of two resistive elements

The system of equations may be rewritten as

$$\begin{Bmatrix} I_1 \\ I_2 \\ I_3 \\ I_4 \end{Bmatrix} = \begin{bmatrix} -\frac{1}{R_{13}} & 0 & \frac{1}{R_{13}} & 0 \\ 0 & -\frac{1}{R_{24}} & 0 & \frac{1}{R_{24}} \\ \frac{1}{R_{13}} & 0 & -\frac{1}{R_{13}} & 0 \\ 0 & \frac{1}{R_{24}} & 0 & -\frac{1}{R_{24}} \end{bmatrix} \begin{Bmatrix} V_1 \\ V_2 \\ V_3 \\ V_4 \end{Bmatrix}$$

relating the terminal currents to voltages. The basic algebraic companion equation must fit into the mask $\{I\}_{NT} = [Y]_{NT \times NT} \{V\}_{NT} - \{B\}_{NT}$ where NT is the total number of module terminals. In the simple case of the double resistor example

transmission line matrix model is capable of simulating signal propagation down an arbitrary line given the line matrices. These are the [R], [L], [G], and [C] matrices: resistance, inductance, conductance, and capacitance respectively. These account for the interaction between all the transmission lines using the following set of equations

$$\frac{\partial}{\partial z}\{V\} = -[R]\{I\} - [L]\frac{\partial}{\partial t}\{I\}$$
$$\frac{\partial}{\partial z}\{I\} = -[G]\{V\} - [C]\frac{\partial}{\partial t}\{V\}$$

For our application, conductance may be assumed negligible compared to capacitance. Applying a basic finite difference scheme to the transmission line equations results in the following system of equations

$$\frac{v(n,k+1)-v(n,k)}{\Delta z} = -[r]i(n,k+\tfrac{1}{2}) - [l]\frac{i(n+\frac{1}{2},k+\frac{1}{2})-i(n-\frac{1}{2},k+\frac{1}{2})}{\Delta t}$$
$$\frac{i(n+\frac{1}{2},k+\frac{1}{2})-i(n+\frac{1}{2},k-\frac{1}{2})}{\Delta z} = -[c]\frac{v(n+1,k)-v(n,k)}{\Delta t}$$

where [r], [l], and [c] are the per-unit-length segment resistance, inductance and capacitance. The transmission line equations may be rewritten such that a leapfrog finite difference approach may be employed to model signal propagation in the transmission line. The first equation may be manipulated into the current update form

$$i(n+\tfrac{1}{2},k+\tfrac{1}{2}) = \left[2[l]+\Delta t[r]\right]^{-1}\left[2[l]-\Delta t[r]\right]i(n-\tfrac{1}{2},k+\tfrac{1}{2}) - \frac{2\Delta t}{\Delta z}\left[2[l]+\Delta t[r]\right]^{-1}\{v(n,k+1)-v(n,k)\}$$

Similarly, the voltage update equation is determined to be

$$v(n+1,k) = -\frac{\Delta t}{\Delta z}[c]^{-1}\{i(n+\tfrac{1}{2},k+\tfrac{1}{2})-i(n+\tfrac{1}{2},k-\tfrac{1}{2})\}+v(n,k)$$

The full transmission line is discretized into small segments based on the time interval. It is also possible to determine the time interval based on the segment length; however, since the model must fit into the larger scheme of a circuit solver, a preset time step is assumed to be inherited and fixed. In the absence of feedback loops, the segment length must be determined using the Courant limit $c\Delta t \le \Delta z$. Figure 1 illustrates the solution evolution as a function of position and time. Currents are determined over the segments at half interval steps, while voltages are available at the nodes at full time steps. The external nodes of the geometry form the terminal nodes where the input 'driving' voltage is impressed. The dependence of currents and voltages is determined by the current and voltage update equations in a leapfrog scheme. Therefore, each new segment current is dependent on the old current at that location, as well as the old node voltages of the segment. Similarly, node

$$\{Y\}=\begin{bmatrix} -\frac{1}{R_{13}} & 0 & \frac{1}{R_{13}} & 0 \\ 0 & -\frac{1}{R_{24}} & 0 & \frac{1}{R_{24}} \\ \frac{1}{R_{13}} & 0 & -\frac{1}{R_{13}} & 0 \\ 0 & \frac{1}{R_{24}} & 0 & -\frac{1}{R_{24}} \end{bmatrix} \qquad \{B\}=\begin{bmatrix} 0 \\ 0 \\ 0 \\ 0 \end{bmatrix}$$

In more complex systems involving either voltage or current lagging, the {B} vector relates to past history terms.

In order to fit the transmission line model into the algebraic companion form, a number of manipulations must be made. The network will supply the terminal node voltages and currents {V} and {I}, and expect the full system admittance [Y] and history {B}. The transmission line will keep its own internal history of nodal voltages {v}, segment currents {i} and local inductances [l].

Given the new terminal voltages, the segments' new currents may be determined. In each segment, this forcing current may then be imposed on the cross-sectional geometry via the nonlinear finite element method. A full magnetic analysis of the region (incorporating the effects of skin depth conductivity, and nonlinear ferromagnetism) will yield the new local inductance matrix {l}. New internal nodal voltages are then determined using the voltage update equation.

Since the algebraic companion forms of [Y] and {B} relate the time instantaneous terminal current and voltage, the average voltage-coincident terminal current must be determined using central differences.

$$i\left(n,k+\tfrac{1}{2}\right)=\left[\left[2[l]+\Delta t[r]\right]^{-1}\left[2[l]-\Delta t[r]\right]+[1]\right]\frac{i\left(n-\frac{1}{2},k+\frac{1}{2}\right)}{2}$$
$$-\frac{\Delta t}{\Delta z}\left[2[l]+\Delta t[r]\right]^{-1}v(n,k+1)+\frac{\Delta t}{\Delta z}\left[2[l]+\Delta t[r]\right]^{-1}v(n,k)$$

Depending on the terminal (terminal 1 or 2 corresponding to k = 1 or k = K = total number of segments), the equations may be written as functions of the terminal voltages and currents (see Fig. 1).

$$I_{T1}=+i\left(n,1+\tfrac{1}{2}\right) \qquad I_{T2}=-i\left(n,K+\tfrac{1}{2}\right)$$
$$V_{T1}=+v(n,1) \qquad V_{T2}=+v(n,K+1)$$

so that

$$I_{T1} = \frac{\Delta t}{\Delta z}\left[2[l_1] + \Delta t[r]\right]^{-1} V_{T1} + \left[\left[2[l_1] + \Delta t[r]\right]^{-1}\left[2[l_1] - \Delta t[r]\right] + [1]\right]\frac{i\left(n-\frac{1}{2},\frac{3}{2}\right)}{2} - \frac{\Delta t}{\Delta z}\left[2[l_1] + \Delta t[r]\right]^{-1} v(n,2)$$

$$I_{T2} = \frac{\Delta t}{\Delta z}\left[2[l_K] + \Delta t[r]\right]^{-1} V_{T2} - \left[\left[2[l_K] + \Delta t[r]\right]^{-1}\left[2[l_K] - \Delta t[r]\right] + [1]\right]\frac{i\left(n-\frac{1}{2},K+\frac{1}{2}\right)}{2} - \frac{\Delta t}{\Delta z}\left[2[l_K] + \Delta t[r]\right]^{-1} v(n,K)$$

which may be rewritten in the form of local terminal admittance and history terms

$$\{I_{T1}\}_{\frac{NT}{2}} = [y_{T1}]_{\frac{NT}{2}\times\frac{NT}{2}}\{V_{T1}\}_{\frac{NT}{2}} - \{b_{T1}\}_{\frac{NT}{2}}$$

$$\{I_{T2}\}_{\frac{NT}{2}} = [y_{T2}]_{\frac{NT}{2}\times\frac{NT}{2}}\{V_{T2}\}_{\frac{NT}{2}} - \{b_{T2}\}_{\frac{NT}{2}}$$

where

$$[y_{T1}] = \frac{\Delta t}{\Delta z}\left[2[l_1] + \Delta t[r]\right]^{-1}$$

$$[y_{T2}] = \frac{\Delta t}{\Delta z}\left[2[l_K] + \Delta t[r]\right]^{-1}$$

$$\{b_{T1}\} = -\left\{\left[\left[2[l_1] + \Delta t[r]\right]^{-1}\left[2[l_1] - \Delta t[r]\right] + [1]\right]\left\{\frac{i\left(n-\frac{1}{2},\frac{3}{2}\right)}{2}\right\} - \frac{\Delta t}{\Delta z}\left[2[l_1] + \Delta t[r]\right]^{-1}\left\{v(n,2)\right\}\right\}$$

$$\{b_{T2}\} = \left\{\left[\left[2[l_K] + \Delta t[r]\right]^{-1}\left[2[l_K] - \Delta t[r]\right] + [1]\right]\left\{\frac{i\left(n-\frac{1}{2},K+\frac{1}{2}\right)}{2}\right\} + \frac{\Delta t}{\Delta z}\left[2[l_K] + \Delta t[r]\right]^{-1}\left\{v(n,K)\right\}\right\}$$

The terminal parameters may then be used to determine the network interface through the algebraic companion form of the equations

$$\begin{Bmatrix} I_{T1} \\ I_{T2} \end{Bmatrix}_{NT} = \begin{bmatrix} y_{T1} & 0 \\ 0 & y_{T2} \end{bmatrix}_{NT\times NT}\begin{Bmatrix} V_{T1} \\ V_{T2} \end{Bmatrix}_{NT} - \begin{Bmatrix} b_{T1} \\ b_{T2} \end{Bmatrix}_{NT}$$

so that the full module admittance and history are

$$[Y]=\begin{bmatrix} y_{T1} & 0 \\ 0 & y_{T2} \end{bmatrix}_{NT\times NT} = \begin{bmatrix} \frac{\Delta t}{\Delta z}\left[2[l_1]+\Delta t[r]\right]^{-1} & 0 \\ 0 & \frac{\Delta t}{\Delta z}\left[2[l_K]+\Delta t[r]\right]^{-1} \end{bmatrix}$$

$$\{B\}=\begin{Bmatrix} b_{T1} \\ b_{T2} \end{Bmatrix}_{NT} = \begin{Bmatrix} -\left\{\left[\left[2[l_1]+\Delta t[r]\right]^{-1}\left[2[l_1]-\Delta t[r]\right]+[1]\right]\left\{\frac{i\left(n-\frac{1}{2},\frac{3}{2}\right)}{2}\right\}-\frac{\Delta t}{\Delta z}\left[2[l_1]+\Delta t[r]\right]^{-1}\left\{v(n,2)\right\}\right\} \\ \left\{\left[\left[2[l_K]+\Delta t[r]\right]^{-1}\left[2[l_K]-\Delta t[r]\right]+[1]\right]\left\{\frac{i\left(n-\frac{1}{2},K+\frac{1}{2}\right)}{2}\right\}+\frac{\Delta t}{\Delta z}\left[2[l_K]+\Delta t[r]\right]^{-1}\left\{v(n,K)\right\}\right\} \end{Bmatrix}$$

Once [Y] and {B} have been determined, they are returned to the network solver where all other module parameters are combined and solved for the next iteration.

The Nonlinear Finite Element Solution

A surface admittance finite element formulation for the transient modeling of skin effect and eddy current problems was presented at ACES'97 [4]. This formulation used a transient surface admittance boundary condition and employed the Prony expansion method to optimize the resulting convolution integral. This approach is adapted to model ferromagnetic materials using an iterative relaxed solution method [7,8,9,10]. Since the surface admittance boundary condition incorporates material properties, it should be readily possible to treat nonlinearity within the surface time integration. The iterative approach assumes that the magnetic permeability at the present time step is approximately the same as that in the previous one. The system of equations is solved based on this assumption, and new values of the magnetic flux density are determined in the nonlinear surface boundary elements. These new values of the element magnetic flux density result in new values of the element permeability. The calculated permeability using an associated magnetization curve is then

$$\mu_{calc} = \mu\left(B_{calc}\right)$$

A new permeability may then be determined for the next iteration using

$$\mu_{new} = \mu_{old} + \gamma\left(\mu_{calc} - \mu_{old}\right)$$

which depends on the past iteration permeability μ_{old}, the calculated permeability μ_{calc}, and the relaxation factor γ for $0 < \gamma < 1$. The literature [9,10] points to a standard value of the relaxation factor $\gamma = 0.1$. The relative change of the permeability may be determined over successive iterations as

$$\Delta\mu = \frac{\mu_{new} - \mu_{old}}{\mu_{old}}$$

A convergence criterion ε for the iteration process may then be based on the rms value of the relative changes taken over the total number of nonlinear boundary elements

$$\varepsilon = \sqrt{\frac{\sum(\Delta\mu)^2}{NLE}}$$

A maximum allowable value of $\varepsilon_{max} = 0.01$ is found acceptable in the literature [9,10]. Should this value be larger than the acceptable pre-set limit, the new value of the permeability is set and the solution is repeated.

In order to interface with the transmission line matrix formulation, an extraction of per-unit-length inductance is necessary [13]. The extraction of this matrix $[l]_{NCxNC}$ is based on the definition of inductance as a function of flux and magnetic vector potential [11,12]

$$l_{ij} = \frac{\varphi_{j0}}{\Delta z \cdot I_i} = \frac{A_j - A_0}{I_i}\bigg|_{I_1=I_2=\cdots=I_{i-1}=I_{i+1}=\cdots=I_{NC}=0}$$

where φ_{j0} is the flux between the j^{th} line and the reference conductor, and I_i is the current carried on the i^{th} line. The magnetic vector potential A_j on the surface of the j^{th} conductor is readily available from the finite element code. Due to the nonlinear nature of the problem, the converged magnetic properties of the fully excited problem are determined and then fixed. Each conductor is then excited separately in a linear regime so that one row of the segment inductance matrix may be determined. This is repeated for the number of conductors in the problem NC until the [l] matrix is filled. The remaining matrices [r] and [c] are pre-determined and assumed constant.

Complete System Interface

The individual components of the method may be assembled and summarized as follows. At each time step, the circuit simulator interfaces to the transmission line model by sending the latest terminal current and voltage updates. The transmission line, having the full data set of former currents and voltages, {i} and {v}, determines the next set of internal currents and voltages. Using the new currents, it calls the transient nonlinear finite element method to determine the segment inductance matrices [l]. Using the terminal segment inductance matrices and history, the full admittance matrix [Y] and past history vector {B} are determined and returned to the circuit simulator. The circuit simulator incorporates [Y] and {B} into its own assembly for a full system solution.

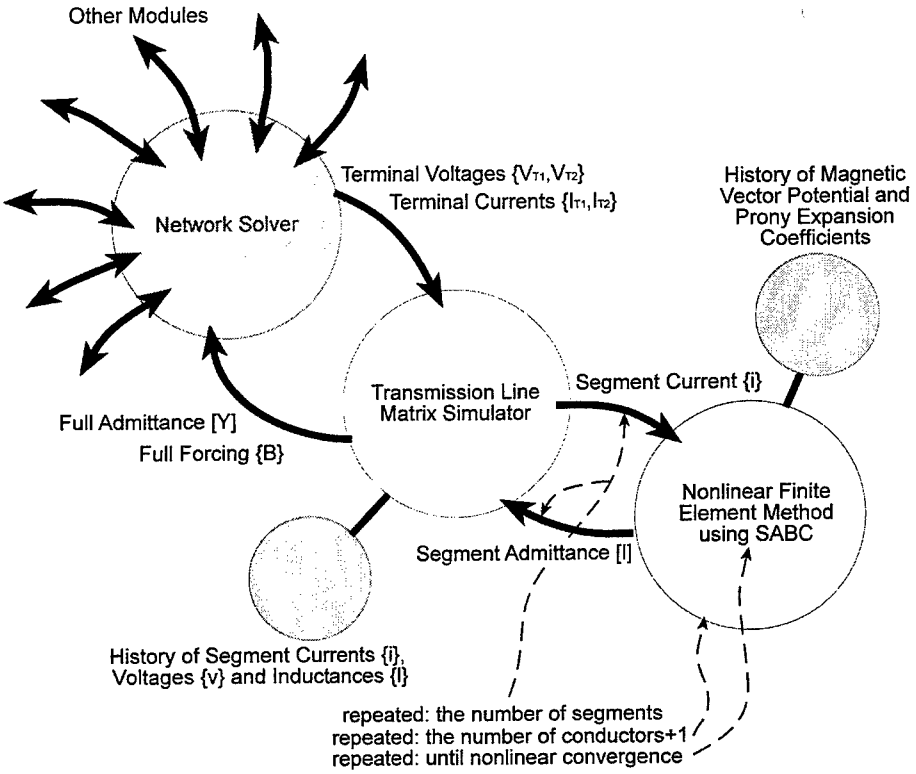

Figure 3. Complete system integration and dependence.

Conclusion

Incorporating a full magnetic simulation of transmission lines into a circuit simulator based on algebraic companion form equations is presented. Since circuit simulators and other analysis tools require time marching responses from their coupled modules, true transient analysis is applied in the transmission line formulation. This validates the need for time-marching analysis and parameter extraction using the surface admittance finite element approach.

The algebraic companion form of the transmission line and electromagnetic model is determined to produce a terminal interface that fits the network solver. This may be adapted to fit any circuit simulator and may prove beneficial in incorporating many other kinds of analysis such as those found in microelectronic packaging applications.

References

[1] A. P. S. Meliopoulos, *"Power System Grounding,"* Marcel Dekker, New York, 1988.

[2] S. Celozzi, *"On the Finite Element Time Domain Solution of the Skin Effect Equations in Multiconductor Lines,"* IEEE Trans. Magn., vol. 30, No. 5, pp. 3180-3183, September 1994.

[3] K. R. Davey, and Larry Turner, *"Transient Eddy Current Analysis for Generalized Structures Using Surface Impedances and the Fast Fourier Transform,"* IEEE Trans. Magn., vol. 26, No. 3, pp. 1164-1170, May 1990.

[4] K. N. Wassef, A. F. Peterson, *"A Surface Admittance Formulation for the Transient Modeling of Skin Effect and Eddy Current Problems,"* Conference Proceedings of the 14th Annual Review of Progress in Applied Computational Electromagnetics, Monterey, CA, March 16-20, 1998.

[5] L. O. Chua and P. M. Lin, *"Computer-Aided Analysis of Electronic Circuits: Algorithms and Computational Techniques,"* Prentice Hall, 1975.

[6] L. T. Pillage, R. A. Rohrer and C. Visweswariah, *"Electronic Circuit and System Simulation Methods,"* McGraw Hill, 1995.

[7] K. Preis, I. Bardi, O. Biro, K. R. Richter, K. Papp, H. Reisinger, *"Nonlinear Periodic Eddy Currents in Single and Multiconductor Systems,"* IEEE Transactions on Magnetics, Vol. 32, No. 3, May 1996.

[8] N. Labbe, Y. Marechal, G. Meunier, H. Ben Harara, *"2D Nonlinear Finite Element Modelling of Electromagnetic Retarders using Time-Stepping Algorithms, and the Petrov-Galerkin Method with Homogenization Techniques,"* IEEE Transactions on Magnetics, Vol. 32, No. 3, May 1996.

[9] K. R. Shao and K. D. Zhou, *"The Iterative Boundary Element Method for Nonlinear Electromagnetic Field Calculations,"* IEEE Transactions on Magnetics, Vol. 24, No. 1, Jan 1988

[10] K. S. Ismail and R. A. Marzouk, *"Iterative Hybrid Finite Element-Boundary Element Method for the Analysis of Induction Heating System with Nonlinear Charge,"* IEEE Transactions on Magnetics, Vol. 32, No. 4, July 1996.

[11] R. E. Matick, *"Transmission Lines for Digital and Communication Networks,"* IEEE Press, New York, 1969.

[12] C. R. Paul, *"Analysis of Multiconductor Transmission Lines,"* John Wiley and Sons, 1994.

[13] S. Cristina, and M. Feliziani, *"A Finite Element Technique for Multiconductor Cable Parameters Calculation,"* IEEE Trans. Magn., vol. 25, No. 4, pp. 2986-2988, July 1989.

SESSION 10

ERRORS

Chair: Edmund K. Miller

A COMPARISON OF SOLUTION ACCURACY RESULTING FROM FACTORING AND INVERTING ILL-CONDITIONED MATRICES

Edmund K. Miller
3225 Calle Celestial, Santa Fe, NM 87501-9613
505-820-7371, emiller@esa.lanl.gov

0. ABSTRACT
The residual vector R] = [Z]A] - B] where [Z] is a coefficient matrix, A] is a vector of unknowns and B] is a right-hand side vector, is often used as a measure of solution error when solving linear systems of the kind that arise in computational electromagnetics. Residual errors are of particular interest in using iterative solutions where they are instrumental in determining the next trial answer in a sequence of iterates. As demonstrated here, when a matrix is ill-conditioned, the residual may imply the solution is more accurate solution than is actually obtained.

1. MATRIX CONDITION NUMBER AND SOLUTION ACCURACY

In previous related work [Miller (1995)] a study was described that investigated the behavior of ill-conditioned matrices having the goal of numerically characterizing their information content. One numerical result from that study was that the solution accuracy (SA) is related to the coefficient accuracy (CA) and condition number (CN), all expressed in digits, approximately as $SA \leq CA - CN$. This conclusion was based on using, as one measure of SA, a comparison of [Z][Y] with [I], where [Z] is a matrix under study, [Y] is its computed inverse and [I] is the identity matrix.

CNs can generally be expected to grow with increasing matrix size, even for one as benign as having all coefficients being random numbers. For some matrices, the Hilbert matrix for example, one of those studied, the CN can grow much faster, being of order $10^{1.5N}$, for a matrix of size NxN. A large matrix CN was encountered in later work that involved model-based parameter estimation (MBPE) for adaptive sampling and estimation of a transfer function [Miller (1996)] using rational functions as fitting models (FM). For example, when using simple LU decomposition to solve even a low-order system, say one having fewer than 20 coefficients, the CN might exceed 10^6. (Note that this problem can be circumvented by using a more robust solution, such as singular-value decomposition, but that's also left for a later discussion.) An interesting aspect of these large CNs was that the match of the FM with the original data when computed using coefficients obtained from [Y]xB], with B] the right-hand-side vector, could be much less accurate than when using coefficients instead obtained from back substitution.

2. SOME NUMERICAL RESULTS

A typical result that demonstrates this behavior is shown in Fig. 1. The specific situation illustrated is the match between the original data and the FM (using a numerator polynomial of order n = 7 and denominator polynomial order of d = 6) as the sample spacing is varied. A fit of 10 digits is equivalent to a residual error of 10^{-10}. A large difference can be seen between the fit obtained using coefficients from an inverse operation compared with using those obtained from back substitution. Note that the poles in the spectrum used for this experiment are spaced one unit apart. The improvement in the inverse result as the data spacing increases towards a Nyquist-like interval of 0.5 occurs because the CN of the data matrix decreases.

Some additional computer experiments were conducted to explore this behavior, with the results of one shown in Fig. 2, where several accuracy (or, conversely, error measures) are shown as a function of matrix order for a Hilbert matrix. The quantities plotted in Fig. 2 are:

$A]_{ex} - A]_{bs}$ and $A]_{ex} - A]_{inv}$,
$[Z]A]_{bs} - B]$ and $[Z]A]_{inv} - B]$,
$[Y]_{ex} - [Y]_{comp}$,
$[Z][Y]_{comp} - [I]$

where "bs" and "inv" refer to a solution vector obtained using back substitution or inversion, and "ex" and "comp" refer to an exact analytical or computed inverse matrix, respectively. Results shown were developed using a single right-hand side having all unit entries. The various accuracy results are derived by computing an RMS difference between their respective vectors or matrices.

Although a different problem from that illustrated in Fig. 1, the residuals are qualitatively similar in exhibiting a back-substitution accuracy that is consistently higher than that from the inverse solution. Interestingly, of the six results displayed all are in substantial agreement except for the back-substitution residual. At about N = 18 and beyond, all reach a noise floor. For the former five, this implies, considering a compute precision of 24 is being used, a CN ≥ 24, which is not inconsistent with $10^{1.5 \times 18} = 10^{27}$. However, the noise floor for the back-substitution residual remains at about 13 digits, the explanation for which is not obvious. Perhaps most interesting is that $A]_{bs}$ and $A]_{inv}$ exhibit comparable accuracies in spite of the great differences displayed by their residuals. In other words, $A]_{bs}$ is not as accurate as might be inferred from its residual.

As an explanation for the declining accuracy exhibited in Fig. 2, the result of averaging some of the more-often used CNs is plotted in Fig. 3, where it can be seen that a ceiling of about the compute precision is reached. A different way to look at the CN is to plot the singular-value spectrum of a matrix as is done for the Hilbert matrix in Fig. 4. In this case, N = 30 and compute precisions ranging from 8, 16, 24, 32 and 40 are used. In each case, the dynamic range of the spectrum approximately equals the compute precision, and provides another measure of the condition number.

3. CONCLUDING COMMENTS

To return to the original problem that motivated this discussion, it's not clear why there is such a difference between the different residuals shown in Figs. 1 and 2. My particular reason for examining these results is the implication they may have when using residuals in determining the convergence of an iterative solution. It seems reasonable, if the residual error is smaller than the actual error in an iterated sequence of solution estimates, to conclude that relying on the residuals as an indicator of solution accuracy could be misleading. Of course, it must be noted that the difference between the two error measures appears to be dependent on the CN of the matrix being solved. This could be one more reason why, as problems are being modeled using more and more unknowns, the potential related increase in CN needs to be considered in developing solution strategies. Also, possibly a different measure of residual error would circumvent or reduce the effect discussed here.

4. REFERENCES

E. K. Miller (1995), "A Computational Study of the Effect of Matrix Size and Type, Condition Number, Coefficient Accuracy and Computation Precision on Matrix-Solution Accuracy," IEEE AP-S International Symposium, Marriott Hotel, Newport Beach, CA, June 18-23, pp. 1020-1023.

E. K. Miller (1996), "Using Adaptive Sampling to Minimize the Number of Samples Needed to Represent a Transfer Function," IEEE AP-S International Symposium, Hyatt Regency Hotel, Baltimore, MD, July 21-26, pp. 588-591.

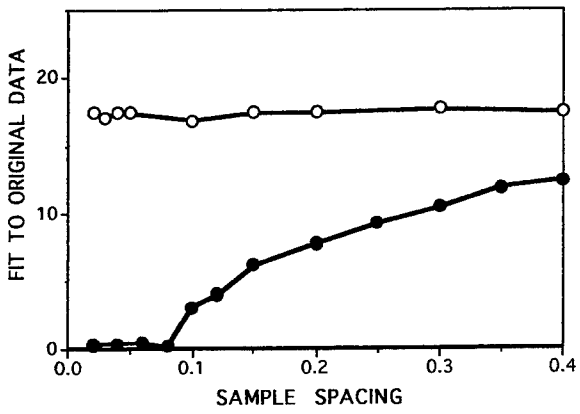

Figure 1. Fit, in digits, between the data samples used for computing the coefficients of a rational-function model and the model results as a function of normalized sample spacing, with computations done in 24-digit compute precision. Results from model whose coefficients are obtained by back substitution are shown by the open circles and those solved by multiplying the right-hand-side vector using an inverse matrix are shown by the solid circles.

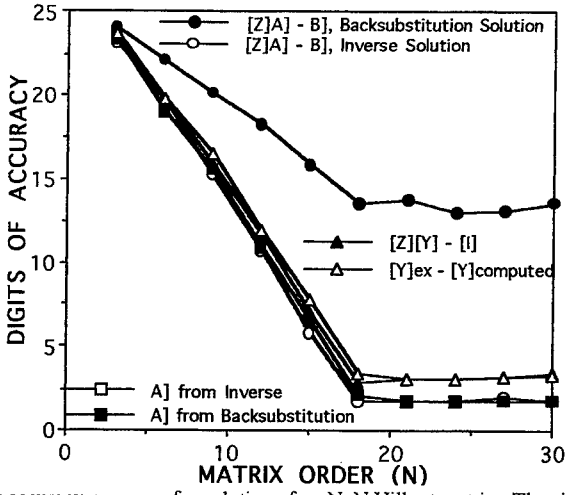

Figure 2. Various accuracy measures for solution of an NxN Hilbert matrix. The circles show results for the residuals and the squares display the solutions, both obtained for a right-hand side vector having all unit values (in both cases the open symbols represent inverse results and sold symbols the back-substitution results). The open triangles exhibit the result of comparing the computed and exact inverse matrices while the solid triangles compare the product of the original and inverse matrices with the identity matrix.

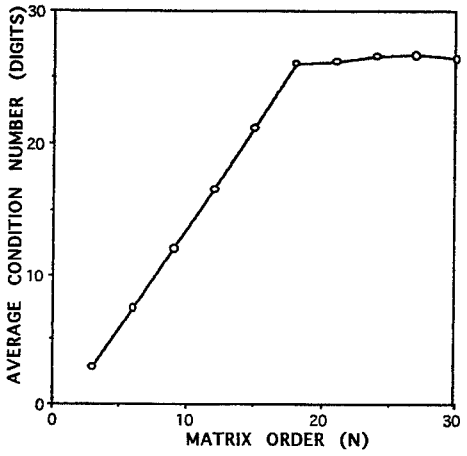

Figure 3. The average condition number of a Hilbert matrix exhibits an approximate $10^{1.5N}$ behavior as expected. It maximizes at a value of about the compute precision, which is 24 digits for this computation.

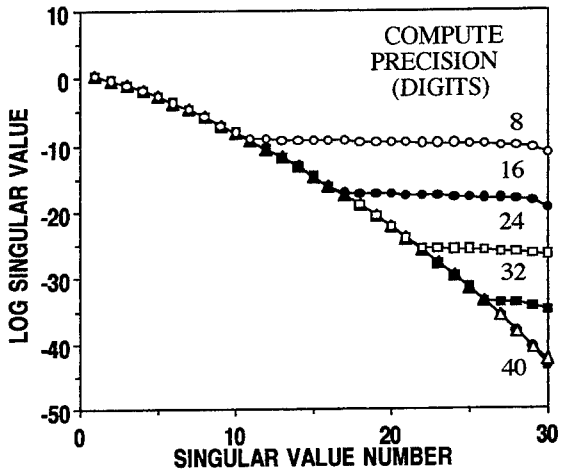

Figure 4. The normalized, singular-value spectrum for a Hilbert matrix of N = 30 with the compute precision a parameter. These results demonstrate the large condition number of a Hilbert matrix while also illustrating effect of compute precision on computations for such a problem.

BENCHMARKS FOR INTEGRAL EQUATION SOLUTIONS OF WIDEBAND SCATTERING : THE SPHERICAL CAP REFLECTOR

S. M. Booker, P. D. Smith, E. D. Vinogradova and S. S. Vinogradov
Department of Mathematics, University of Dundee, Dundee, DD1 4HN, UK

Abstract. *A new benchmark is introduced for numerical solutions of transient or wideband electromagnetic scattering problems, and is applied to a time–domain integral equation (TDIE) solution scheme. The benchmark is based on a computation of the direct backscatter of a spherical cap reflector. This structure possesses a surface, an edge and a cavity, and fully tests the ability of the TDIE to model the mechanisms involved in scattering from an arbitrary metallic obstacle. A semi–analytic solution is obtained for the direct backscatter of a spherical cap reflector using an approach based on a method of regularisation. A comparison is made of the numerical TDIE solutions with those accurately obtained by the semi–analytic regularisation method; the TDIE approach is shown to model accurately all of the scattering mechanisms observed.*

1. Introduction

One of the most fundamental problems in computational electromagnetics is that of transient or wideband scattering by an arbitrary metallic obstacle. A time–domain integral equation (TDIE) approach to this problem has many significant advantages. Arbitrary scatterers are easily modelled, since a triangular mesh may be used to discretise the obstacle surface. The Sommerfeld radiation condition is automatically enforced avoiding the need for artificially imposed boundary conditions, such as are required with finite difference schemes. The calculation is performed on a two–dimensional grid of surface quantities rather than a three–dimensional grid of fields; this allows relatively large obstacles to be modelled. Wideband scattering results can be obtained in the frequency domain without the need for repeated matrix inversion, which arises with a frequency–domain integral equation approach.

Another significant advantage of the TDIE approach is that it provides direct physical insight into the mechanisms of transient scattering. Different scattering mechanisms, such as specular and creeping wave responses, are separated in time and can be distinguished from each other, allowing their relative importance to be determined. Furthermore, since the TDIE approach is formulated in terms of the surface current and charge densities on the scatterer, physical insight can be gained into the response of the obstacle itself.

There is widespread interest in establishing the validity and accuracy of general purpose numerical electromagnetics codes. Canonical diffraction problems, such as described in [1], provide a source of accurately computable analytical solutions which therefore can be viewed as benchmarks for comparison. Unfortunately, the class of analytically soluble scattering problems is small; it is

difficult to find suitable problems to test numerical predictions of scattering from objects even of modest complexity, comprising say, edges, cavities (apertures), and dielectric or metal inclusions.

In this paper we discuss the canonical problem of transient scattering from a spherical cap reflector. This obstacle is of particular interest since it comprises a surface, an edge and a cavity, and thus tests the ability of any general purpose (time domain) numerical code to model all of the significant scattering mechanisms which might be encountered in an arbitrary metallic obstacle. The other advantage of the spherical cap reflector is that a semi–analytical solution of guaranteed accuracy may be obtained via a frequency–domain method of regularisation. The accuracy of this solution can rigorously estimated in terms of a truncation number N, and can be made arbitrarily accurate as $N \to \infty$, thus fulfilling the requirements of a benchmark.

In the next section of this paper we describe the scattering problem and how the semi–analytic solution is obtained via the method of regularisation (MoR). Section 3 describes the TDIE approach to the same problem, and the results obtained are then compared with the results of the MoR approach in section 4.

2. The method of regularisation

Our benchmark scattering problem is depicted in Figure 1 and may be described as follows. A transient or wideband electric field is incident upon the concave surface of a spherical cap reflector, along its axis of rotational symmetry. The direct backscattered electric field is determined, from which the wideband radar cross section of the spherical cap reflector may be obtained. It is this wideband spectrum which will form the basis of our comparisons.

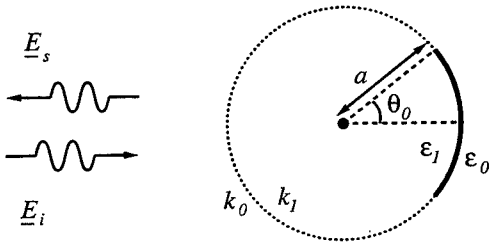

Figure 1: The dielectric sphere with spherical cap reflector.

In order to obtain a semi–analytic solution we formulate a similar, but more general, frequency–domain problem: determining the direct backscatter of a homogeneous dielectric sphere with spherical cap reflector. The sphere will be supposed to be of radius a, have dielectric constant ϵ_1, and be capped by a perfectly conducting (metallic) layer, as depicted in Figure 1. The composite structure is assumed to be surrounded by a dielectric of permittivity ϵ_0, and is illuminated by a time–harmonic incident field $\underline{E}^i$ of wavenumber k_0. Then, if the direct backscatter of the lens reflector $\underline{E}^s$ can be determined, its radar cross section (as a function of $k_0 a$) may be obtained.

Let us briefly describe the features of the method providing our benchmark solution. It is discussed more fully in [2] to which the reader is referred for further details; this reference considers the more general structure of a multi-layer dielectric sphere with a metallic cap, of which the structure depicted in Figure 1 is a particular case.

In order to calculate the time–harmonic, backscattered far-field $\underline{E}^s$ of the lens reflector the approach of [2] uses Debye potentials to describe the electric and magnetic fields. Then, due to the symmetry of the problem, the scattered fields may be represented by series expansions of spherical wave functions, with electric and magnetic Fourier coefficients to be determined.

The key to the solution method relies upon ideas contained in [3, 4, 5]. This requires a transformation of (i) the boundary conditions for the tangential electric field components on the metallic cap, and of (ii) the continuity conditions for the tangential magnetic field components on the non-metallic spherical surface, to the corresponding boundary conditions for the Debye potentials and their derivatives. The boundary conditions for the Debye potentials are not separated in the case of an unclosed (open) spherical shell, and this leads to coupling of the scattered electric and magnetic waves. This is in contradistinction to the *decoupled* system that arises in the analysis of the perfectly conducting closed sphere, leading to the well known Mie series solution.

We thus obtain two pairs of coupled dual series equations for the Fourier coefficients of the unknown electric and magnetic fields. The dual series kernels are given by the associated Legendre functions $P_n^1(\cos\theta)$. The four coupled systems of equations depend upon parameters determined by the boundary conditions on the surface of the lens..

However, the resultant system of equations is Fredholm type of the first kind. In order to provide a reliable benchmark, a transformation of this system is needed to obtain a set of equations soluble by a numerically stable and rapidly converging algorithm. The regularisation method described in [3, 4, 5] transforms this coupled system of first kind equations into four coupled systems of equations, which are Fredholm type of the second kind. These possess significant advantages for numerical stability and convergence over their counterparts of the first kind.

Whilst the resultant system has infinitely many linear equations, estimates of the rate of convergence permit the use of truncation to a finite dimensional system from which numerical results with guaranteed accuracy may be obtained. The algorithm thus employed is free from any limitations on parameters such as the permittivities ϵ_0/ϵ_1 of the dielectric regions, the angle of opening θ_0 of the spherical cap, or the relative wavenumber $k_0 a$. In particular, ϵ_0 and ϵ_1 may be assumed equal to the permittivity of free space, yielding the radar cross section of a spherical cap reflector. Further, by varying the relative wavenumber $k_0 a$ of the incident field a wideband radar cross section may be determined for the spherical cap reflector. It is this spectrum which we wish to compare with the results of the TDIE approach described in the next section.

3. Numerical solution of the scattering problem

The TDIE approach which we follow is based on a time-domain solution of the electric field integral equation (EFIE). Denote by S the surface of the spherical cap reflector which is assumed

to be surrounded by free space with permittivity ϵ and permeability μ; denote by c the speed of light. The cap is illuminated by a transient electric field $\underline{E}^i(\underline{r},t)$ which is incident upon the spherical cap along its axis of rotational symmetry. This field induces a surface current density $\underline{J}(\underline{r},t)$ and surface charge density $\rho(\underline{r},t)$ on S, which in turn give rise to a scattered electric field $\underline{E}_s(\underline{r},t)$. If the transient backscattered electric field can be determined then a wideband radar cross section can be obtained for the spherical cap reflector.

Define a vector potential in the usual manner

$$\underline{A}(\underline{r},t) \;=\; \frac{\mu}{4\pi}\int_S \frac{\underline{J}(\underline{r}',t-|\underline{r}-\underline{r}'|/c)}{|\underline{r}-\underline{r}'|}dS' \;, \tag{1}$$

and a scalar potential $\phi(\underline{r},t)$ similarly [6]. The field radiated by the scatterer, $\underline{E}^s(\underline{r},t)$, can be represented in terms of these potentials. Further, since the total electric field tangential to a perfectly conducting surface is zero, $(\underline{E}^i+\underline{E}^s)^{tan}=0$, we may derive the EFIE

$$\underline{E}^i(\underline{r},t)^{tan} \;=\; \left[\nabla\phi(\underline{r},t) \;+\; \frac{\partial \underline{A}}{\partial t}(\underline{r},t)\right]^{tan} \;. \tag{2}$$

In addition, we may deduce a continuity equation which will hold on the scatterer surface

$$\frac{\partial \rho}{\partial t}(\underline{r},t) \;+\; \nabla_S.\underline{J}(\underline{r},t) \;=\; 0 \;, \tag{3}$$

where ∇_S is the surface divergence on S. Equations (2) and (3) are sufficient to determine a solution for $\underline{J}$ and ρ, given suitable initial and boundary conditions.

In order to solve (2) and (3) numerically, using the time-domain method of moments we first discretise our problem using discrete time steps $k\Delta t, (k=0,1,\ldots)$ and setting $\rho(\underline{r},k\Delta t)=\rho^k(\underline{r})$, and similarly for other functions. Time derivatives are approximated by centred differences.

We next select spatial basis functions for $\underline{J}$ and ρ, together with a suitable testing procedure. The basis functions which we choose are those commonly exploited for numerical solutions of the EFIE, in both the time and frequency domains. They are described in more detail in [7, 8]. Define a grid on S with N_c triangular patches arranged such that the grid has N_e internal edges separating adjacent triangles. Using this grid we may define a set of spatial basis functions for the surface current, $\underline{f}_n(\underline{r})$, $1\le n\le N_e$, which are piecewise linear over the internal edges of the grid. We may also define a set of N_c spatial basis functions for the surface charge, which are piecewise constant on the triangles of the grid. See [8] for further details. The surface current may thus be approximated by

$$\underline{J}^k(\underline{r}) \;\approx\; \hat{\underline{J}}^k(\underline{r}) = \sum_{n=1}^{N_e} I_n^k \underline{f}_n(\underline{r}) \;, \tag{4}$$

where I_n^k are a set of unknown expansion coefficients. The surface charge may be similarly approximated in terms of the N_c scalar basis functions defined on the triangular grid elements.

To discretise the EFIE we apply a form of Galerkin's method. Define

$$\underline{R}_E = \left[\underline{E}_i^k(\underline{r}) \;-\; \nabla\hat{\phi}^k(\underline{r}) \;-\; \frac{\hat{\underline{A}}^{k+1}(\underline{r})-\hat{\underline{A}}^{k-1}(\underline{r})}{2\Delta t}\right]^{tan} \tag{5}$$

where $\underline{\hat{A}}^k$ may be defined in terms of the approximate surface current $\underline{\hat{J}}^k$ via equation (1) and where $\underline{\hat{\phi}}^k$ may be defined in terms of the approximate surface charge density in an analogous manner. In order to ensure that the residual error in our approximation of the EFIE is orthogonal to our chosen basis functions we apply the (Galerkin) testing procedure

$$\int_S \underline{R}_E \cdot \underline{f}_n(\underline{r})\, dS = 0\,, \quad 1 \leq n \leq N_e. \tag{6}$$

A similar approach may be used to test the continuity equation with respect to the N_c scalar basis functions. As a result a total of $N_e + N_c$ equations may be obtained in terms of the N_e unknown expansion coefficients for the surface current density, I_n^k, and the N_c unknown expansion coefficients for the surface charge density. If all of these expansion coefficients are known for the first k time steps then they may be calculated for time step $k+1$ using a time–marching algorithm, as described in [8]. Note, for example, that the unknown surface current coefficients, I_n^{k+1}, may be determined directly from equation (5). In this manner, a solution may be obtained for any given time interval.

Since the resulting equations are of the first kind they are prone to numerical instability under certain conditions. The stability of such first kind numerical schemes can be greatly improved, however, by the use of averaging techniques [9]. The method employed in our solution scheme is a three–step averaging scheme of the following form. Suppose that a solution has been obtained for the current density expansion coefficients at time step k; denote these coefficients by I_n^k. Using a simple time–marching algorithm calculate the coefficients for the next three time steps; denote these coefficients by $\tilde{I}_n^{k+1}$, $\tilde{I}_n^{k+2}$ and $\tilde{I}_n^{k+3}$. The coefficients for time step $k+1$ may now be determined by the averaging formula

$$I_n^{k+1} = \left(2I_n^k + \tilde{I}_n^{k+1} + \tilde{I}_n^{k+3}\right)/4\,.$$

4. Results

Calculations were performed using the TDIE approach described in the last section for the problem of transient electromagnetic scattering of a Gaussian waveform by the spherical cap reflector. The choice of time step and triangular grid imposed on the cap followed the standard guidelines of [7, 8]. The incident plane wave pulse (of peak amplitude 1 V/m) propagated along the axis of rotational symmetry of the reflector, as shown in Figure 1, with a polarisation perpendicular to this axis. A half–angle of $\theta_0 = 30°$ was assumed. Denote by Δ the ratio of the Gaussian pulsewidth (full width half height) to the radius of curvature of the cap, a.

Four simulations were performed with $\Delta = 1, 1/2, 1/3$ and $1/4$. In each case the direct backscattered far-field was computed and a wideband radar cross section determined via discrete Fourier transformation of the resulting time series.

The backscattered far-fields of the spherical cap reflector subject to incident fields with $\Delta = 1$ and $\Delta = 1/2$ are depicted in Figure 2, with a dash curve and a solid curve respectively. The time scale

is in units of light–metres. The late–time response of the far–field, i.e. the response for $t > 15$, has been magnified by a factor of 10^6 for clarity. The first positive peak in the backscattered far–field is that due to the specular response; however, as expected for electrically small scatterers, the early time response waveform is approximately the second derivative of the incident waveform. Thereafter late–time ringing, of smaller magnitude, can be observed due to the flow of charges back and forth on the obstacle as a result of the excitation caused by the incident field. When $\Delta = 1/2$ the pulsewidth is half that of the pulse when $\Delta = 1$. This naturally increases the high–frequency content of the incident field and leads to an increase in the specular response. Note also that the late–time response is periodic but exponentially decaying.

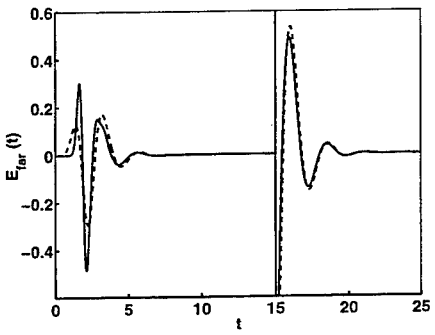

Figure 2: Backscattered far-field for $\Delta = 1$ (dash curve) and $\Delta = 1/2$ (solid curve).

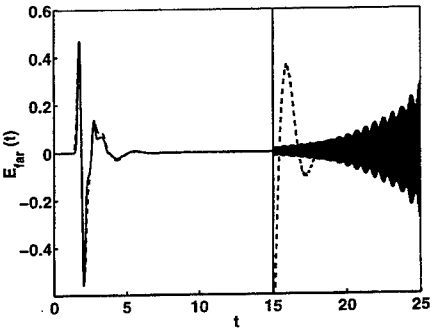

Figure 3: Backscattered far-field for $\Delta = 1/3$ (dash curve) and $\Delta = 1/4$ (solid curve).

The backscattered far-fields of the spherical cap reflector subject to incident field with $\Delta = 1/3$ and $\Delta = 1/4$ are depicted in Figure 3, with a dash curve and a solid curve respectively. The late–time response of the far–field, i.e. the response for $t > 15$, has been magnified by a factor of 10^6 for the case $\Delta = 1/3$ and by 10^3 for the case $\Delta = 1/4$. It is evident again that as the pulsewidth shortens, and the high–frequency content of the pulse increases, the specular response increases. Moreover, as expected for electrically large apertures, the early time response is now approximately proportional to the first derivative of the incident waveform; also the late–time ringing of the cap decreases in magnitude. It may also be seen that in the case $\Delta = 1/4$ the creeping wave contribution has separated itself from the late–time ringing and is quite distinctly visible. The other effect which is evident in the late–time behaviour of the far–field when $\Delta = 1/4$ is the appearance of an exponentially–growing oscillatory–type instability, as described in [9]. In order to suppress this kind of instability, recourse must be made either to a high order averaging scheme, or to a second kind numerical scheme involving some regularisation of the TDIE formulation.

In order to obtain wideband radar cross sections for the spherical cap reflector from these time–series, a discrete Fourier transform was applied to both the incident Gaussian pulse and the computed far–field response, from which the ratio of the resulting spectra was obtained. The radar cross sections are depicted in Figures 4 and 5 together with the results of the semi–analytic MoR approach, which is depicted by the dot–dash curve.

With a relatively wide pulse, $\Delta = 1$, the radar cross section agrees with the benchmark solution only for small relative wavenumbers, $k_0 a < 10$. By halving this pulsewidth, $\Delta = 1/2$, or alternatively by doubling the bandwidth of the pulse, agreement can be extended up to $k_0 a \approx 20$. Similarly with $\Delta = 1/3$, reasonable agreement can be achieved for $k_0 a < 30$. In the case when $\Delta = 1/4$, however, the radar cross section contains excessive high frequency noise, due to the late-time instability. In order to partially suppress this defect the far-field time-series was truncated. This eliminated much of the spurious high-frequency energy in the spectrum. The resulting radar cross section is depicted in Figure 5. Agreement can be seen for the expected range of relative wavenumbers, $k_0 a < 40$ but excessive high-frequency energy is still apparent in the spectrum. It is also evident, from Figures 4 and 5, that the accuracy of the numerically computed radar cross section increases as the pulsewidth of the incident field is decreased, at any particular relative wavenumber $k_0 a$.

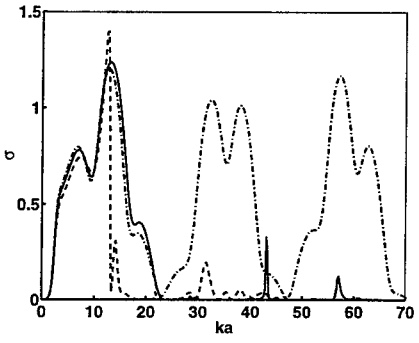

Figure 4: Radar cross section for $\Delta = 1$ (dash curve), $\Delta = 1/2$ (solid curve) and method of regularisation (dot-dash curve).

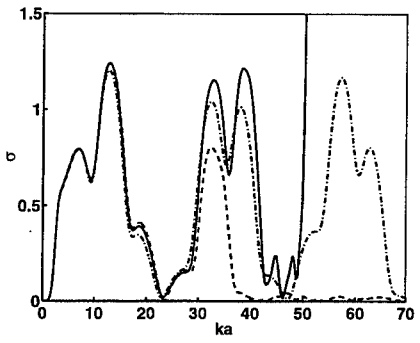

Figure 5: Radar cross section for $\Delta = 1/3$ (dash curve), $\Delta = 1/4$ (solid curve) and method of regularisation (dot-dash curve).

It is clear from these results that the TDIE scheme is modelling accurately all of the various scattering mechanisms which contribute to the response of the spherical cap reflector. This is evident from the convergence of the numerically computed radar cross section to that which has been calculated using the semi-analytic MoR approach.

5. Conclusions

The spherical cap reflector is an interesting canonical scatterer to study since it comprises a surface, an edge and a cavity. Such a structure tests the ability of general purpose numerical codes, including those based on the TDIE, to model all of the significant scattering mechanisms which might be encountered in an arbitrary metallic obstacle. This scattering problem is also particularly suitable as a benchmark, since a semi-analytical solution may be obtained via a frequency-domain method of regularisation. This method yields a second kind system of equations which can be rapidly solved to any desired degree of accuracy.

In this paper we have shown that TDIE solutions to transient scattering problems, obtained following standard discretisation guidelines, provide accurate estimates for the radar cross section resulting from the principal scattering mechanisms encountered with a spherical cap reflector. This suggests that the TDIE is well suited to the task of determining the transient or wideband scattering of an arbitrary metallic obstacle.

Of course, it is desirable to validate general purpose numerical codes against a number of benchmarks, each relating to particular physical mechanisms or the calculation of observable physical quantities. Although this paper focussed on backscatter calculations, the spherical cap reflector also provides benchmark solutions for near–field as well as far–field quantities, under any angle of illumination. In another direction, we draw attention to the validation described in [10] of wideband antenna impedance calculated by the TDIE code against benchmarks provided by known impedances of wideband (TEM) horns.

References

[1] J.J. Bowman, T.B.A. Senior & P.L.E. Uslenghi, "Electromagnetic and acoustic scattering by simple shapes" North-Holland, (1969).

[2] P.D. Smith & S.S. Vinogradov, "A rigorous treatment of electromagnetic scattering by the Luneberg lens reflector" *Proc. Electromagnetic Theory Symposium (URSI Commission B)*, 390-392, Thessaloniki, (1998).

[3] S.S. Vinogradov & V.P. Shestopalov, "Solution of a vectorial scattering problem for a sphere with a hole", *Sov. Physics Doklady*, **237 (1)**, (1977).

[4] S.S. Vinogradov, "Reflectivity of a spherical shield", *Radiophysics and Quantum Electronics*, **26 (1)**, (1983).

[5] S.S. Vinogradov & A.V. Sulima, "Investigation of the Pointing vector flux inside a partially shielded dielectric sphere", *Radiophysics and Quantum Electronics*, **32 (2)**, (1989).

[6] D.S. Jones, "Acoustic and electromagnetic waves", Oxford University Press, (1986).

[7] S.M. Rao, D.R. Wilton and A.W. Glisson, "Electromagnetic scattering by surfaces of arbitrary shape", *IEEE Trans. Antennas Propagat.*, **30**, (1982).

[8] B.P. Rynne, "Time domain scattering from arbitrary surfaces using the electric field integral equation", *J. Electromagnetic Waves & Applications*, **5 (1)**, (1991).

[9] B.P. Rynne & P.D. Smith, "Stability of time marching algorithms for the electric field integral equation", *J. Electromagnetic Waves & Applications*, **4 (12)**, (1990).

[10] S.M. Booker, P.D. Smith & A.P. Lambert. A numerical determination of transient antenna impedance via near-field integration. *J. Electromagnetic Waves & Applications* **12**, 199-223 (1998).

Propagation of Errors Through Computer Codes via Fuzzy Logic

by
R. M. Bevensee

BOMA ENTERPRISES
P.O. Box 812 Alamo, CA, 94507-0812 USA

1. Summary

We utilize the fuzzy logic concepts of *interval of confidence* at a given *level of perception* or μ – *confidence level* to study the propagation of intervals of confidence, regarded as specified error intervals, for the input data of a computer code to the error intervals of the output parameters.

We contrast the μ – *confidence level* with the conventional probability-confidence in an error interval for a variable. That probability-confidence, or p-confidence, is derived from the probability distribution for that variable. We show that a fuzzy-logic μ – *confidence* curve for a variable, when interpreted as a p-confidence curve, yields *no* information about the probability curve for that variable. Therefore the ordinary operations of addition, subtraction and multiplication of two fuzzy variables at a given level of presumption –interpreted at a p-confidence level–cannot yield the probability distribution for the resultant variable and hence its p-confidence at the same level of presumption.

We illustrate the propagation of error intervals with reference to the critical subroutines FACTR and SOLVE in the Numerical Electromagnetics NEC2 computer code. These solve the matrix equation $\mathbf{AX} = \mathbf{B}$ for $\mathbf{X}$. The fuzzy versions, FACTRFUZ and SOLVEFUZ track error intervals for each parameter calculated, based on the fuzzy arithmetic rules for sum, difference, and product of two parameters and inversion of a single parameter. The error intervals for the $\mathbf{A_{ij}}$ and $\mathbf{B_j}$ must be specified, and the fuzzy codes compute the error intervals for the $\mathbf{X_j}$.

Insertion of coding for error intervals throughout a large code is impractical, so we show how we might propagate small error intervals at the input directly through an error-insensitive portion of the code to the error-sensitive subroutine(s), then propagate the intervals through these subroutines line by line, and finally propagate the output error intervals directly through the remaining error-insensitive portion of the code to the code output.

2. Fuzzy Logic Concepts

To discuss the concepts of *interval of confidence*, which we regard as error interval, and *level of perception* or μ – *confidence* (*not a conventional confidence*) *level* consider Fig. 1, reproduced from Fig. 1.8 of [1] with some horizontal and vertical lines added. Parameter $\mu, 0 \leq \mu \leq 1$, on the vertical axis measures a *level of perception* or μ – *confidence level* for the fuzzy intervals for x, y, and z = x + y defined by the curves A, B, and C, respectively. At the μ-level of perception α the dashed horizontal line defines the fuzzy interval $[a_1{}^{(\alpha)}, a_2{}^{(\alpha)}]$ for x and corresponding intervals for y defined by curve B and z defined by curve C.

These intervals are interpreted as follows. At the α-level of presumption we presume that *all* x-values lie within $[a_1{}^{(\alpha)}, a_2{}^{(\alpha)}]$, and *all* y-values lie in the range $[b_1{}^{(\alpha)}, b_2{}^{(\alpha)}]$. Therefore, *all* z = x + y values lie in the range $[c_1{}^{(\alpha)}, c_2{}^{(\alpha)}] = [a_1{}^{(\alpha)} + b_1{}^{(\alpha)}, a_2{}^{(\alpha)} + b_2{}^{(\alpha)}]$.

The only fuzzy-logic concepts we require for our error analysis are the rules for adding, subtracting, and multiplying these error intervals, and determining the error interval for an inverted parameter from the interval for the parameter itself. We require no other information from the parameter curves such as A, B, and C of Fig. 1.

A parameter curve such as A tells us *nothing* about the probability distribution for its parameter x and *nothing* about the p-confidence that x will lie within an interval such as $[a_1{}^{(\alpha)}, a_2{}^{(\alpha)}]$. In order to gain a perspective about fuzzy logic in relation to conventional probability-confidence analysis we explain this in the next section.

3. Relationships Between Fuzzy Logic Parameters and Probability and Probability-Confidence Distributions

Curves A, B, and C in Fig. 1 all have the property that the fuzzy interval at the $\mu - confidence\ level$ decreases as μ increases. This suggests interpreting that fuzzy interval at a given value $\mu = \alpha$ as a conventional p-confidence interval, meaning the area under the probability curve for variable x, y, or z along its fuzzy interval *is* that confidence. If we do this we relate the p-confidence C_p to μ as $C_p = 1 - \mu$; when μ is zero, C_p is 1 and the variable has its maximum range of ambiguity. When $\mu = 1$, $C_p = 0$: we have no confidence that the variable will have exactly its value at the peak of its curve.

The mathematical statement of this is, for curve A in Fig. 1,

$$C_p = 1 - \mu = \int_{a_1^{(\mu)}}^{a_2^{(\mu)}} P(x)dx. \tag{1}$$

However, we cannot deduce P(x) from this relation! The reason is as follows: if we consider a small increase dC_p downward on curve A at level α, say, and the corresponding changes dx_1 (negative) at $a_1^{(\alpha)}$ and $dx_2 > 0$ at $a_2^{(\alpha)}$ we only know that $dC_p = P(x_1)(-dx_1) + P(x_2)dx_2$. This enables us to generate uniquely neither $P(x)$ on the positive-slope side of the curve nor $P(x)$ on the negative-slope side.

Without these probability curves for x and y we could not generate the p-confidence over the associated interval $[c_1^{(\alpha)}, c_2^{(\alpha)}] = [a_1^{(\alpha)} + b_1^{(\alpha)}, a_2^{(\alpha)} + b_2^{(\alpha)}]$ for z *which only coincidentally would equal* $1 - \alpha$. The conventional relation for P(z) is

$$P(z) = \int P(x)P(y = z - x)dx \qquad for\ all\ a_1^{(\alpha)} \le x \le a_2^{(\alpha)}\ and\ b_1^{(\alpha)} \le y = z - x \le b_2^{(\alpha)}, \tag{2}$$

and without $P(z)$ we could not compute the p-confidence C_p for z at this α *level* for x and y as

$$C_p = \int_{z_{min}^{(\alpha)}}^{z_{max}^{(\alpha)}} P(z)dz \tag{3}$$

Here the limits on z are determined from (2).

Fuzzy logic does not involve p-confidence levels defined this way. It only says that, at a level of presumption α, x is ambiguous *only* over the inverval $[a_1^{(\alpha)}, a_2^{(\alpha)}]$ and y is ambiguous *only* over the interval $[b_1^{(\alpha)}, b_2^{(\alpha)}]$, so an operation $A(\mathcal{O})B$, where $\mathcal{O}$ represents addition, subtraction, multiplication, or inversion, to produce C results in a fuzzy interval $[c_1^{(\alpha)}, c_2^{(\alpha)}]$ determined only by the *extremes* of the intervals for x and y.

These are the only properties of fuzzy logic we employ for the analysis of propagation of errors through computer codes.

4. Propagation of Errors Through Subroutines FACTR and SOLVE, Which Solve the Matrix Equation $AX = Y$ for X in the Numerical Electromagnetics Code NEC2

These subroutines are critical for error propagation because they involve division by a parameter which might have an error range which includes zero.

We have added coding for the appropriate error limits to FACTR and SOLVE and identified the revised subroutines by the suffix FUZ. These subroutines, FACTRFUZ and SOLVEFUZ, are appended. They employ thes fuzzy addition and subtraction rules [1]

$$A(+)B = [a_1, a_2] + [b_1, b_2] = [a_1 + b_1,\ a_2 + b_2] \tag{4}$$

$$A(-)B = [a_1 - b_2,\ a_2 - b_1]. \tag{5}$$

For multiplication the subroutines call PRODFUZ, also in Appendix A, which computes the fuzzy interval or error interval for A ($\times$) B according to one of the twelve cases summarized in Appendix A of [1].

Error intervals for the inverse $1/A[a_1, a_2] = [1/a_2, 1/a_1]$ if $0 < a_1 < a_2$ or $a_1 < a_2 < 0$ are adjusted if one of the bounds equals zero or the interval passes through zero. In the former case the bound at zero is moved toward the outer bound by 0.001 of that outerbound. In the latter case the error interval for 1/A is set to [-1.E6,+1.E6].

Comments are inserted throughout FACTRFUZ, SOLVEFUZ, and PRODFUZ for clarification.

We have not inserted these subroutines into NEC2 and specified error intervals in problems of interest for the elements of **A** (the system matrix) and computed the error intervals in the output matrix **B** of SOLVEFUZ (which is **X** in $\mathbf{AX} = \mathbf{B}$). These error intervals are specified in the matrices **AFUZ** and **DFUZ(1), DFUZ(2)** in FACTRFUZ and **AFUZ, YFUZ (1), YFUZ(2), BFUZ(1), BFUZ(2)** in SOLVEFUZ. However, this procedure would be straightforward.

5. Propagation of Small Error Intervals Through a Large Computer Code.

It might be impractical to insert fuzzy arithmetic stateements throughout a large code as we did in FACTRFUZ and SOLVEFUZ. But if we could localize the subroutines critical for rerror propagation we might proceed in an approximate way as follows.

Let the matrix $\mathbf{T_1}$ transfer the input column matrix **W** of data to the column matrix **X** which is input to these critical subroutines. Assume these subroutines act in series to transfer **X** to their output column matrix **Y**. Finally, let matrix $\mathbf{T_2}$ transfer **Y** to the code output column matrix **Z**.

These matrix operations are represented with their *row* $\times$ *column* dimensions as

$$(\mathbf{T_1})_{M\times N}\mathbf{W}_{N\times 1} = \mathbf{X}_{M\times 1}; \quad \mathbf{A}_{P\times M}\mathbf{X}_{M\times 1} = \mathbf{Y}_{P\times 1}; \quad (\mathbf{T_2})_{Q\times P}\mathbf{Y}_{P\times 1} = \mathbf{Z}_{Q\times 1} \tag{6}$$

We assume that $\mathbf{T_1}$ and $\mathbf{T_2}$ remain the same over the narrow error intervals of **W** and **Y**, respectively.

Now consider the problem of evaluating the error intervals in **X** from those in **W** without knowing (or wanting to know) the analytic form of the $(\mathbf{T_1})_{mn}$s. We must compute the error interval in $\mathbf{X}_m$ according to

$$[\mathbf{X}_m - x_m, \mathbf{X}_m + x_m] = (\mathbf{T_1})_{m1}[\mathbf{W}_1 - w_1, \mathbf{W}_1 + w_1] + (\mathbf{T_1})_{m2}[\mathbf{W}_2 - w_2, \mathbf{W}_2 + w_2]$$
$$+ \sum_{n=3}^{N}(\mathbf{T_1})_{mn}[\mathbf{W}_n - w_n, \mathbf{W}_n + w_n], \quad for\ 1 \le m \le M \tag{7}$$

We have specified the $\mathbf{X}_m, \mathbf{W}_1$, etc. to lie at the centers of their error intervals.

In the process of computing $\mathbf{T_1W} = \mathbf{X}$ for all the midrange values of the $\mathbf{X_m}$ we must know *all* values of $(\mathbf{T_1})_{mn}\mathbf{W}_n$ for each mn pair. The reason is that we must know what the magnitude and sign of each $(\mathbf{T_1})_{mn}$ will be. A term in (7) For example, represented by $t[a_1, a_2]$ will be $[ta_1, ta_2]$ if $t > 0$ but $t[a_1, a_2] = [ta_2, ta_1]$ if $t < 0$. Therefore the signs of the $(\mathbf{T_1})_{mn}$ will determine how the successive intervals are added in (7) to determine the final x_m.

In this way we evaluate all the error intervals $[\mathbf{X}_m - x_m, \mathbf{X}_m + x_m]$ for $1 \le m \le M$.

We next perform the next matrix operation in (6) to propagate the error intervals in **X** to those in **Y**, the output matrix of the error-sensitive subroutine(s). We do this by inserting line-by-line fuzzy arithmetic coding into **A** for those subroutine(s), as we did in FACTRFUZ and SOLVEFUZ.

Then we perform the last matrix operation of (6) for the error intervals through $\mathbf{T_2}$ in the same manner that we propagated the error intervals in **W** to those in **X** in (7).

8.Reference

[1] A. Kaufmann and M. M. Gupta, **Introduction to Fuzzy Arithmetic, Theory and Applications**, (paperback) Van Nostrand Reinhold, 1991.

```
      SUBROUTINE FACTRFUZ (N,A,AFUZ,IP,NDIM)
C--- A-MATRIX NOT TRANSPOSED.  Variables are Real, not Complex
C*********************
CFUZ  Changes in Subroutine FACTR of NEC2 to allow for error intervals.  Interval
CFUZ  ends are specified by the parameters denoted by suffix "FUZ".  Intervals
CFUZ  AFUZ(N,N,1), lower end, AFUZ(N,N,2), upper end, must be specified at input.
CFUZ  These are calculated at output for SOLVEFUZ, which also operates on DFUZ via
CFUZ  COMMON/SCRATM.
C*********************
      SAVE
      DIMENSION A(51,51),AFUZ(51,51,2),IP(51),ARJFUZ(2),
     .PFUZ(2),QFUZ(2),RFUZ(2)
      COMMON/SCRATM/ D(51),DFUZ(51,2)
      INTEGER R,RM1,RP1,PJ,PR
      IFLG=0
      DO 9 R=1,N
      DO 1 K=1,N
      D(K)=A(K,R)
            DFUZ(K,1)=AFUZ(K,R,1); DFUZ(K,2)=AFUZ(K,R,2)
1     CONTINUE
      RM1=R-1
      IF (RM1.LT.1) GO TO 4
      DO 3 J=1,RM1
      PJ=IP(J)
      ARJ=D(PJ)
            ARJFUZ(1)=DFUZ(PJ,1); ARJFUZ(2)=DFUZ(PJ,2)
      A(J,R)=ARJ
            AFUZ(J,R,1)=ARJFUZ(1); AFUZ(J,R,2)=ARJFUZ(2)
      D(PJ)=D(J)
            DFUZ(PJ,1)=DFUZ(J,1); DFUZ(PJ,2)=DFUZ(J,2)
      JP1=J+1
            QFUZ(1)=ARJFUZ(1); QFUZ(2)=ARJFUZ(2)
      DO 2 I=JP1,N
      D(I)=D(I)-A(I,J)*ARJ
            PFUZ(1)=AFUZ(I,J,1); PFUZ(2)=AFUZ(I,J,2)
CFUZ PRODFUZ Computes the fuzzy interval for PFUZ*QFUZ = RFUZ according to the table
CFUZ of formulas in the text.
            CALL PRODFUZ(PFUZ,QFUZ,RFUZ)
CFUZ DEFUZ next follows the subtraction formula for fuzzy intervals according to the
CFUZ formula in the text
            DFUZ(I,1)=DFUZ(I,1)-RFUZ(2)
            DFUZ(I,2)=DFUZ(I,2)-RFUZ(1)
2     CONTINUE
3     CONTINUE
4     CONTINUE
      DMAX=D(R)**2      !Just an indicator of pivot magnitude
      IP(R)=R
      RP1=R+1
      IF (RP1.GT.N) GO TO 6
      DO 5 I=RP1,N
      ELMAG=D(I)**2     !Just an indicator
      IF (ELMAG.LT.DMAX) GO TO 5
      DMAX=ELMAG
      IP(R)=I
5     CONTINUE
6     CONTINUE
      IF (DMAX.LT.1.E-10) IFLG=1          ! IFLAG
      PR=IP(R)
      A(R,R)=D(PR)
```

```
            AFUZ(R,R,1)=DFUZ(PR,1);  AFUZ(R,R,2)=DFUZ(PR,2)
      D(PR)=D(R)
            DFUZ(PR,1)=DFUZ(R,1);  DFUZ(PR,2)=DFUZ(R,2)
      IF (RP1.GT.N) GO TO 8
      ARJ=1./A(R,R)
C.....................................................
C... Involved coding for the inverse, to change the error interval if it includes
C... zero.
            X1=AFUZ(R,R,1); X2=AFUZ(R,R,2)
            IF (X1 .GT. 0.) GO TO 40  !Take +inverse
            IF (X1 .EQ. 0. .AND. X2 .GT. 0.) GO TO 42 !Increase X1
            IF (X1 .LT. 0. .AND. X2 .GT. 0.) GO TO 44 !Write and set wide bounds
            IF (X1 .LT. 0. .AND. X2 .EQ. 0.) GO TO 46 !Decrease X2
            IF (X2 .LT. 0.) GO TO 40      !Take -inverse
42          WRITE (6,102) R,R,AFUZ(R,R,1),AFUZ(R,R,2)
102         FORMAT (1X,'A(',I2,',','I2,')','has fuzz. bounds',1PE12.3,
     .     1PE12.3,'-- increase lower one to 0.001 of upper one')
            X1=0.001*X2; GO TO 40   !Take +inverse
44          WRITE (6,104) R,R,AFUZ(R,R,1),AFUZ(R,R,2)
104         FORMAT (1X,'A(',I2,',','I2,')','has fuzz. bounds',1PE12.3,
     .     1PE12.3,'-- SET BOUNDS -E6,+E6')
            ARJFUZ(1)=-1.E6; ARJFUZ(2)=+1.E6; GO TO 50
46          WRITE (6,106) R,R,AFUZ(R,R,1),AFUZ(R,R,2)
106         FORMAT (1X,'A(',I2,',','I2,')','has fuzz. bounds',1PE12.3,
     .     1PE12.3,'-- decrease upper one to 0.001 of lower one')
            X2=0.001*X1
40          ARJFUZ(1)=1./X2; ARJFUZ(2)=1./X1
50          CONTINUE
C.....................................................
      DO 7 I=RP1,N
      A(I,R)=D(I)*ARJ
            PFUZ(1)=DFUZ(I,1); PFUZ(2)=DFUZ(I,2)
            QFUZ(1)=ARJFUZ(1); QFUZ(2)=ARJFUZ(2)
            CALL PRODFUZ(PFUZ,QFUZ,RFUZ)
            AFUZ(I,R,1)=RFUZ(1); AFUZ(I,R,2)=RFUZ(2)
7     CONTINUE
8     CONTINUE
      IF (IFLG.EQ.0) GO TO 9
      WRITE (6,10) R,DMAX
      IFLG=0
9     CONTINUE
      RETURN
10    FORMAT (1H ,6HPIVOT(,I3,2H)=,E10.2)
      END
```

```
      SUBROUTINE SOLVEFUZ (N,A,AFUZ,IP,B,BFUZ,NDIM)
C--- A-MATRIX NOT TRANSPOSED.  Variables are Real, not Complex.
C*********************
CFUZ  Changes in Subroutine SOLVE of NEC2 to allow for error intervals.  This
CFUZ  subroutine acts on intervals AFUZ(N,N,1) and AFUZ(N,N,2) and YFUZ from
CFUZ  FACTRFUZ to produce intervals BCONat output.  Matrix B is X in the solution
CFUZ  of AX = B and BFUZ is the matrix of error intervals for B.
C*********************
      SAVE
      INTEGER PI
      DIMENSION A(51,51),AFUZ(51,51,2),IP(51),B(51),BFUZ(51,2),
     .PFUZ(2),QFUZ(2),RFUZ(2),SUMFUZ(2)
      COMMON/SCRATM/ Y(51),YFUZ(51,2)

      DO 3 I=1,N
      PI=IP(I)
      Y(I)=B(PI)
            YFUZ(I,1)=BFUZ(PI,1); YFUZ(I,2)=BFUZ(PI,2)
      B(PI)=B(I)
            BFUZ(PI,1)=BFUZ(I,1); BFUZ(PI,2)=BFUZ(I,2)
      IP1=I+1
      IF (IP1.GT.N) GO TO 2
      DO 1 J=IP1,N
      B(J)=B(J)-A(J,I)*Y(I)
            PFUZ(1)=AFUZ(J,I,1); PFUZ(2)=AFUZ(J,I,2)
            QFUZ(1)=YFUZ(I,1); QFUZ(2)=YFUZ(I,2)
CFUZ PRODFUZ Computes the fuzzy interval for PFUZ*QFUZ = RFUZ according to the table
CFUZ of formulas in the text.
            CALL PRODFUZ(PFUZ,QFUZ,RFUZ)
CFUZ DEFUZ next follows the subtraction formula for fuzzy intervals according to the
CFUZ formula in the test
            BFUZ(J,1)=BFUZ(J,1)-RFUZ(2)
            BFUZ(J,2)=BFUZ(J,2)-RFUZ(1)
1     CONTINUE
2     CONTINUE
3     CONTINUE
      DO 6 K=1,N
      I=N-K+1
      SUM=0.
            SUMFUZ(1)=0.; SUMFUZ(2)=0.
      IP1=I+1
      IF (IP1.GT.N) GO TO 5
      DO 4 J=IP1,N
      SUM=SUM + A(I,J)*B(J)
            PFUZ(1)=AFUZ(I,J,1); PFUZ(2)=AFUZ(I,J,2)
            QFUZ(1)=BFUZ(J,1); QFUZ(2)=BFUZ(J,2)
            CALL PRODFUZ(PFUZ,QFUZ,RFUZ)
CFUZ DEFUZ next follows the addition formula for fuzzy intervals according to the
CFUZ formula in the text
            SUMFUZ(1)=SUMFUZ(1)+RFUZ(1); SUMFUZ(2)=SUMFUZ(2)+RFUZ(2)
4     CONTINUE
5     CONTINUE
      B(I)=(Y(I)-SUM)/A(I,I)
C.....................................
C... Involved coding for the inverse, to change the error interval if it includes
C... zero.
            X1=AFUZ(I,I,1); X2=AFUZ(I,I,2)
            IF (X1 .GT. 0.) GO TO 40  !Take +inverse
            IF (X1 .EQ. 0. .AND. X2 .GT. 0.) GO TO 42 !Increase X1
```

```
            IF (X1 .LT. 0. .AND. X2 .GT. 0.) GO TO 44 !Write and set wide bounds
            IF (X1 .LT. 0. .AND. X2 .EQ. 0.) GO TO 46 !Decrease X2
            IF (X2 .LT. 0.) GO TO 40       !Take -inverse
42          WRITE (6,102) I,I,AFUZ(I,I,1),AFUZ(I,I,2)
102         FORMAT (1X,'A(',I2,',','I2,')','has fuzz. bounds',1PE12.3,
     .     1PE12.3,'-- increase lower one to 0.001 of upper one')
            X1=0.001*X2; GO TO 40    !Take +inverse
44          WRITE (6,104) I,I,AFUZ(I,I,1),AFUZ(I,I,2)
104         FORMAT (1X,'A(',I2,',','I2,')','has fuzz. bounds',1PE12.3,
     .     1PE12.3,'-- SET BOUNDS -E6,+E6')
            QFUZ(1)=-1.E6; QFUZ(2)=+1.E6; GO TO 50
46          WRITE (6,106) I,I,AFUZ(I,I,1),AFUZ(I,I,2)
106         FORMAT (1X,'A(',I2,',','I2,')','has fuzz. bounds',1PE12.3,
     .     1PE12.3,'-- decrease upper one to 0.001 of lower one')
            X2=0.001*X1
40          QFUZ(1)=1./X2; QFUZ(2)=1./X1
50          CONTINUE
C... Now get the FUZfid. bounds on (Y(I)-SUM):
            PFUZ(1)=YFUZ(I,1)-SUMFUZ(2); PFUZ(2)=YFUZ(I,2)-SUMFUZ(1)
C... Next, the final bounds on B(I):
            CALL PRODFUZ(PFUZ,QFUZ,RFUZ)
            BFUZ(I,1)=RFUZ(1); BFUZ(I,2)=RFUZ(2)
C.....................................
6     CONTINUE
      RETURN
      END
```

```
      SUBROUTINE PRODFUZ(PFUZ,QFUZ,RFUZ)
C*********************
CFUZ  This subroutine computes the error interval for PFUZ*QFUZ = RFUZ,
CFUZ  according to the twelve cases for the product in Appendix A of [1].
CFUZ  Subscript 1 denotes the lower fuzzy limit; subscript 2, the upper one.
C*********************
      SAVE
      DIMENSION PFUZ(2),QFUZ(2),RFUZ(2)
      A1=PFUZ(1); A2=PFUZ(2);  B1=QFUZ(1); B2=QFUZ(2)
      IF (0. .LT. A1) GO TO 2  !cases 1,2,3
      IF (A2 .LT. 0.) GO TO 4  !cases 7,8,9
C...  cases 4,5,6:
      IF (0. .LT. B1) GO TO 10     !case 4
      IF (B2 .LT. 0.) GO TO 12     !case 6
C...  case 5:
      X1=A1*B2; X2=A2*B1; X3=A1*B1; X4=A2*B2
      IF (X1 .LE. X2) R1=X1
      IF (X1 .GT. X2) R1=X2
      IF (X3 .LE. X4) R2=X4
      IF (X3 .GT. X4) R2=X3 ; GO TO 30
2     IF (0. .LT. B1) GO TO 14   !case 1
      IF (B2 .LT. 0.) GO TO 16  !case 3
C... case 2:
      R1=A2*B1; R2=A2*B2; GO TO 30
4     IF (0. .LT. B1) GO TO 18   !case 7
      IF (B2 .LT. 0.) GO TO 20   ! case 9
C... case 8:
      R1=A1*B2; R2=A1*B1; GO TO 30
10    R1=A1*B2; R2=A2*B2; GO TO 30
12    R1=A2*B1; R2=A1*B1; GO TO 30
14    R1=A1*B1; R2=A2*B2; GO TO 30
16    R1=A2*B1; R2=A1*B2; GO TO 30
18    R1=A1*B2; R2=A2*B1; GO TO 30
20    R1=A2*B2; R2=A1*B1
30    RFUZ(1)=R1; RFUZ(2)=R2
      RETURN
      END
```


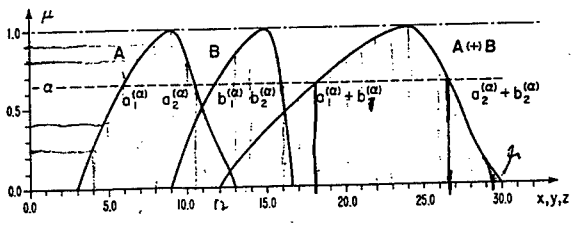

Fig. 1 Addition of Two Fuzzy Numbers, $x + y = z$ [1]

Scalable Algorithm for Solving Boundary Value Problems Arising in Electromagnetics Based on Implicit Operator Projection

Michał Rewieński, Michał Mrozowski
Department of Electronics, Telecommunications and Computer Science,
Technical University of Gdańsk,
Narutowicza 11/12, 80–952 Gdańsk, Poland
Tel: (48)(58) 347-23-24, Fax: (48)(58) 347-12-28, E-mail: mrewiens@task.gda.pl

Abstract

This paper presents a new method of solving operator boundary value problems applied to modelling electromagnetic waveguides. The algorithm is based on a concept of implicit projection of operators onto finite-dimensional domains. It is shown that this approach allows a reduction of both computation time and memory requirements necessary to solve the problem at hand. Moreover, the presented numerical tests indicate that the discussed technique may be efficiently implemented in parallel distributed memory systems providing means to deal with large-scale computational problems of electromagnetics.

1 Introduction

The necessity of solving large-scale problems, arising in electromagnetics creates a demand for more efficient new algorithms being able to deal with growing complexity of the modelled systems. One of widely investigated approaches towards solving large and complex computational problems is designing scalable algorithms suitable for use in parallel distributed memory systems. In order to use efficiently both multiple processor power and distributed memory resources of these systems in order to obtain speed-up of computations the created algorithms need to assure workload balancing across the processors and minimize the inter-processor data movement. In the case of methods of solving boundary value problems for infinite-dimensional operators, being of particular interest in computational electromagnetics, two important aspects have to be taken into account as to obtain a scalable algorithm. These include: 1) designing a method of mapping of the initial infinite-dimensional operator onto a finite-dimensional space allowing easy and efficient parallelization, 2) finding a scalable algorithm capable of solving the emerging finite-dimensional problem for an approximate discrete operator (cf. [1]).

For instance, if a class of differential operators is considered, one may easily find out that the Finite Difference (FD) projection technique allows straightforward and very efficient parallelization strategy based on static domain decomposition, as compared to Finite Element Method (FEM) which requires more sophisticated schemes in order to assure e.g. load-balancing of parallel computations.

Referring to algorithms of solving eigenproblems for finite-dimensional linear operators one has to mention the Implicitly Restarted Arnoldi Method (IRAM) [2], [3], which is a modern algorithm capable of finding eigenvalues of a finite-dimensional non-symmetric operator. The basic iteration of the method (i.e. the Arnoldi factorization) is based on an operation of creating an orthonormal basis in a Krylov space associated with a given operator. This operation may be easily parallelized and its implementation in distributed memory systems involves little inter-processor communication [4]. Consequently, the IRAM is found to be a highly efficient scalable algorithm for solving eigenproblems, capable of finding several eigenvalues from a specified part of the finite-dimensional operator spectrum, e.g. eigenvalues with the largest real part, and allowing one to reduce significantly both computational complexity as well as memory requirements of the numerical solvers. Another important feature of the discussed algorithm is that during the Arnoldi factorization the information on the input finite-dimensional matrix operator

$\underline{\underline{T}}$ is passed into the algorithm only via the matrix-vector product $\underline{\underline{T}}\underline{y}$. Consequently, the finite-dimensional linear operator does not have to be represented explicitly by a matrix of elements. This feature of IRAM together with its high performance in parallel systems are exploited in this paper to propose an efficient scalable algorithm of solving operator eigenproblems arising in electromagnetics.

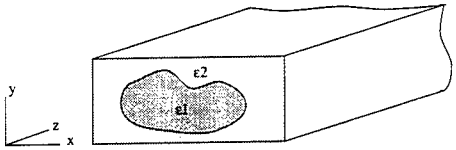

Figure 1: Schematic of a dielectric waveguide, homogeneous in the z direction and having an arbitrary electrical permittivity profile $\epsilon(x,y)$ in the $x-y$ plane.

The problem considered within this study is finding modes in a dielectric waveguide, shown in Figure 1, which is homogeneous in the z direction and has an arbitrary permittivity profile $\epsilon(x,y)$ in its cross-section ($x-y$ plane). This structure may be modelled by the following differential equation (cf. [5]):

$$\nabla_t^2 \vec{H}_t + k_0^2 \epsilon(x,y)\vec{H}_t + \frac{1}{\epsilon(x,y)}\left[\nabla_t \epsilon(x,y) \times \right.$$
$$\left. \times \left(\nabla_t \times \vec{H}_t\right)\right] = \beta^2 \vec{H}_t \qquad (1)$$

where $\nabla_t^2(\cdot) = \left(\frac{\partial}{\partial x}, \frac{\partial}{\partial y}\right)(\cdot)$, $\vec{H}_t(x,y) = (H^x(x,y), H^y(x,y))$ is the transverse magnetic field, k_0 is the wavenumber in the free space, $\epsilon(x,y)$ is the permittivity profile in the $x-y$ plane and β is a propagation constant. In mathematical terms the above problem may be viewed as an eigenproblem of the linear operator $\mathbf{T}$ (given by the left-hand side of equation (1)):

$$\mathbf{T}\vec{H}_t = \beta^2 \vec{H}_t \qquad (2)$$

with the transverse magnetic field $\vec{H}_t$ as an eigenfunction and β^2 as an eigenvalue to be found. With $\mathbf{T}$ being a second-order non-symmetric operator, problem (2) provides a challenging computational task. In the following section we shall present an method of projecting this operator onto a finite-dimensional space which allows efficient parallelization and reduction of numerical complexity of the solver based on Implicitly Restarted Arnoldi Method.

2 Cost-reducing implicit operator projection

As already mentioned, in order to make use of the Implicitly Restarted Arnoldi Method to solving boundary value problem (2) one has to apply a projection of the initial infinite-dimensional operator $\mathbf{T}$ onto a finite-dimensional space to obtain an approximate finite-dimensional operator $\underline{\underline{T}}$. An efficient cost-reducing projection method emerges if one applies the Method of Moments approach together with implicit representation of the finite-dimensional operator matrix. If a complete orthonormal set of functions $\{h_i\}_{i=1}^{\infty}$ in the domain of $\mathbf{T}$ is considered as a set of both basis and testing functions, then functions from the operator's domain may be represented in terms of the following Fourier expansions:

$$u = \sum_{i=1}^{n} (u, h_i)\, h_i \qquad (3)$$

Truncating the sequence of Fourier coefficients $\{f_i\}_{i=1}^{\infty} = \{(u,h_i)\}_{i=1}^{\infty}$ to a finite number of terms gives a finite representation of the function u:

$$\underline{u} = [(u,h_1),(u,h_2),\ldots,(u,h_n)]^T \qquad (4)$$

The method of discretization of operator $\mathbf{T}$ immediately follows from the above representation of the functions. Defining the elements of the $n \times n$ matrix $\underline{\underline{T}} = [c_{ij}]_{i,j=1}^{n}$ as:

$$c_{ij} = (\mathbf{T}h_j, h_i) \qquad (5)$$

one obtains a finite-dimensional linear operator being a mapping of operator $\mathbf{T}$. One may note that if the elements c_{ij} are computed explicitly, a dense matrix, known from the Galerkin method, is obtained. This brings a series of negative effects. Firstly, the matrix storage may involve n^2 memory locations and secondly the matrix-vector product will normally involve $O(n^2)$ operations which may cause the computation time in the methods which

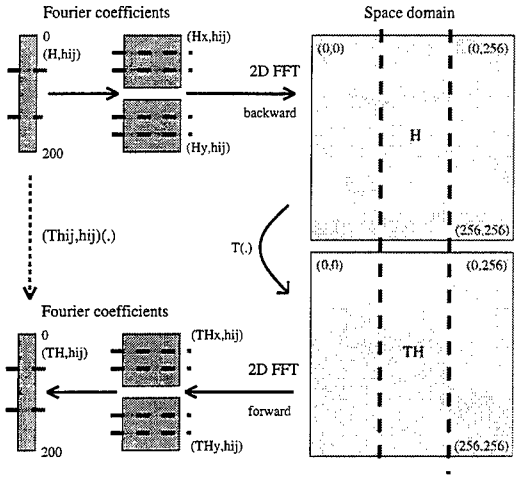

Figure 2: Schematic of parallel data distribution in matrix-vector product design for the implicitly projected operator $\mathbf{T}$ and transverse magnetic field $\vec{H}_t$ represented by 2D Fourier expansions. The dashed lines mark the block data distribution pattern across the processors.

are based on this explicit representation (e.g. Galerkin Method) to blow up for the increasing problem size n. Nevertheless a different strategy may be applied based on the following property of operator $\underline{\underline{T}}$:

$$\underline{\underline{T}}\underline{u} = \left[\sum_j (\mathbf{T}f_j h_j, h_1), \ldots, \sum_j (\mathbf{T}f_j h_j, h_n)\right] = [(\mathbf{T}\tilde{u}, h_1), \ldots, (\mathbf{T}\tilde{u}, h_n)] \tag{6}$$

where $\tilde{u} = \sum_{i=1}^{n} f_i h_i$. In view of the above, the matrix-vector product $\underline{\underline{T}}\underline{u}$ may be computed using the following scheme:

1. Step A: Find $\tilde{u} = \sum_{i=1}^{n} f_i h_i$,
2. Step B: Compute $\alpha = \mathbf{T}\tilde{u}$,
3. Step C: Compute (α, h_m), $m = 1, \ldots, n$.

As one may note, Step B will generally involve computing an approximate value of α. One of the possible methods of calculating α, applied in the presented solver, is based on sampling of function $\tilde{u}$ at N grid-points ($n \leq N$) and replacing differential operations on field components (cf. (1)) with finite difference operations on a discrete field. It is also clear from the above scheme that computation of the matrix-vector product $\underline{\underline{T}}\underline{u}$ involves in fact computation of inner products, which allows one *not* to store the elements of matrix $\underline{\underline{T}}$ explicitly. Still, although the method of computing matrix-vector product presented above is inevitably more complex than e.g. in case of a simple FD scheme, the gains from using this new approach become apparent if one considers the following situation.

If the boundary value problem (1) is considered on a rectangular region containing a cross-section of the waveguide (cf. Figure 1) then the set of appropriate trigonometric functions forms an orthonormal basis in the domain of operator $\mathbf{T}$ and may be used to represent e.g. transverse magnetic field $\vec{H}_t$. Consequently, the proposed scheme of computing matrix-vector product (illustrated in Figure 2) consists now of the following steps:

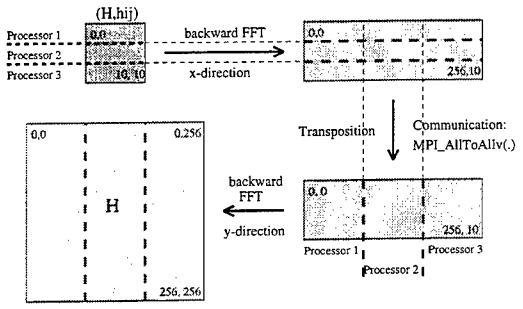

Figure 3: Idea of the parallel backward two-dimensional FFT algorithm design. Performing a parallel forward 2D FFT is analogous.

1. Using Fourier coefficients $\{f_i\}_{i=1}^n$ compute the values of the function $\tilde{u}$ at the discrete grid points from the spatial domain by performing a two-dimensional *backward* discrete FFT.
2. Calculate the values of the $\mathbf{T}\tilde{u}$ function at the grid points of the spatial domain using the previously calculated values of $\tilde{u}$.
3. Compute the inner products $(\mathbf{T}\tilde{u}, h_i)$ by performing a two-dimensional *forward* discrete FFT.

3 Parallel implementation of the matrix-vector product

The parallel implementation of the matrix-vector product based on implicit operator projection and 2D Fast Fourier Transforms applies a straightforward parallel block data decomposition shown in Figure 2. This design may be used together with IRAM algorithm as to obtain an efficient, load-balanced parallel solver. The main difficulty with computing the discussed matrix-vector product in parallel lies in performing parallel 2D FFTs. Figure 3 shows a schematic of parallel design of a backward 2D FFT. One may note that in order to compute Fast Fourier Transform in the y direction a parallel transposition of a distributed matrix has to be performed. Referring to distributed memory systems, this operation involves mainly inter-processor communication which in the proposed implementation is based on high level collective communication MPI routine `MPI_Alltoallv(.)`. The parallel design of forward 2D FFT is analogous, except that the Fourier Transform in the y direction is performed first in order to avoid costly matrix transposition while computing pairs of backward and forward Fourier transforms which takes place during calculation of the matrix-vector product.

3.1 Computational and memory cost

The numerical cost of the proposed method of computing matrix-vector product is primarily determined by the numerical complexity of Steps 1 and 3 and equals $O(K \log_2 K)$ for a single-processor execution, where K is a product of the FFT lengths in x and y directions. At this point it should be noted that the problem size N is usually considerably smaller than K, e.g. by 25 times. This is due to oversampling which should be applied in order to obtain more accurate values of inner products computed using FFT. If the discussed projection method is compared to Finite Difference discretization it is apparent that computing matrix-vector product requires significantly more operations in case of the FFT-based algorithm. Still, one should be aware that the oversampling is also needed in case of the FD discretization due to the requirements of numerical dispersion and causes an increment in the problem size N. This does not apply to the proposed implicit projection of the operator and consequently the extra time spent on calculating the matrix-vector products is then regained by spending less time on solving an eigenproblem with a reduced size. The memory requirements of computing matrix-vector product involving 2D

FFTs are also relatively small. Taking into account the memory necessary to store the samples of the function $\vec{H}_t = (H^x, H^y)$ in the spatial domain and the workspace needed to perform Fourier transforms the memory cost equals roughly $(2K + 2N + 6\sqrt{N})$ locations, which is usually significantly less as compared to the case when operator matrix $\underline{\underline{T}}$ is stored explicitly.

4 Numerical results

The parallel IRAM-based solver (IRAM-FFT) applying implicit operator projection, based on the public domain library P_ARPACK [4] and MPI implementation of the matrix-vector product has been used to find modes in dielectric waveguides described by equation (1). In the numerical tests we have computed propagation constants for an elliptical guide with the semi-axes ratio $a_x/a_y = 2/1$ and a continuous permittivity profile given by the function:

$$\epsilon(x,y) = \epsilon_0 \left[1 - \left((x/a_x)^2 + (y/a_y)^2\right)^{\alpha/2}\right] \tag{7}$$

An open structure was modelled by taking the screening walls sufficiently far away from the guide (at the distance of $10a_x$ from the centre of the waveguide). The results presented in Table 1 show a comparison of the non-dimensional normalized propagation constants Z:

$$Z = \frac{\beta^2/k_0^2 - 1}{\epsilon - 1} \tag{8}$$

computed using the IEEM [6] and the IRAM-FFT method for different profile exponents α (cf. (7)). In the tests the normalized frequency $V = k_0 \cdot 2a_x \cdot \sqrt{\epsilon - 1}$ ($\epsilon = 2.25$) equalled 3, the number of expansion functions equalled 75 in x and y directions and the respectful FFT lengths equalled 256. It is apparent that the obtained results agree almost perfectly.

Table 2 presents a comparison of the normalized propagation constants β/k_0 for a slab guide with discontinuous permittivity profile (dimensions: 21.0 × 16.0 mm; slab located symmetrically (width: 4 mm, height: 16 mm); core permittivity: $\epsilon = 2.56$; frequency: 15 GHz) computed with IRAM-FFT, Transverse Resonance Method (TRM) and the Galerkin Method (GM) with QR-based solver [8]. In the tests the number of expansion functions equalled 75 in x and y directions and the respectful FFT lengths equalled 256. The results show that the proposed algorithm may also be applied to finding fundamental and higher-order modes in guiding structures with discontinuous permittivity profiles.

α	IEEM [6], [7]	IRAM-FFT	Difference [%]
2	0.4894	0.4907	0.27
4	0.6254	0.6258	0.06
6	0.6740	0.6742	0.03
8	0.6976	0.6978	0.03
10	0.7112	0.7114	0.03

Table 1: Comparison of computed normalized propagation constants Z for an elliptical guide with $\epsilon(x,y)$ given by (8).

Apart from the tests validating the proposed method (IRAM-FFT) also parallel performance tests have been carried out in a Cray T3E scalable distributed memory system. Figures 4 and 5 show speed-ups in execution time of computing a pair of 2D FFTs and the total execution time of an iteration of the IRAM algorithm. As one may note the speed-up improves with the increasing number of expansion terms and FFT lengths and almost a perfect speed-up of computations is obtained for the available number of processors as $N = 256^2$ and $K = 1024^2$. Figure 3 also shows the performance of the parallel solver (IRAM-FD) based on IRAM and Finite Difference mapping of operator $\mathbf{T}$ with discretization grid 200 × 100. Figure 6 shows a comparison of single-processor execution times of IRAM-FD and IRAM-FFT solvers for a different number of eigenvalues to be found. In case of the IRAM-FFT algorithm the number of expansion functions used to represent the fields equalled 40 in every spatial direction ($N = 40^2$). For IRAM-FD algorithm the discretization grid equalled 200 × 100. One may note that if FFT lengths equal 128 and 256 (in every spatial direction) the IRAM-FFT method runs faster than the FD-based solver. As the FFT length increases computation of the matrix-vector product becomes more costly for the IRAM-FFT algorithm, causing an increment of the total execution time. Still, in case of this algorithm, one may note that for increasing number of eigenvalues to be found the growth in

TRM	GM	IRAM-FFT
1.2353	1.2344	1.2339
1.0833	1.0813	1.0818
1.0648	1.0648	1.0641
4.1570-01	4.1146-01	4.1412-01

Table 2: Comparison of the propagation constants β/k_0 computed for a slab guide with a discontinuous permittivity profile.

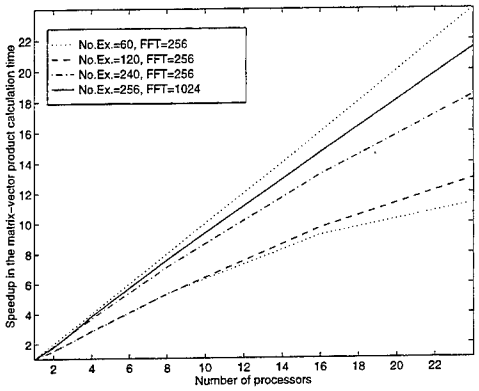

Figure 4: Speed-up in the execution time of a pair of operations: a backward 2D FFT and a forward 2D FFT as a function of the number of processors applied, for different numbers of expansion functions and FFT lengths. The tests were performed in the Cray T3E system.

execution time is slower than for IRAM-FD solver, due to quicker convergence of the Implicitly Restarted Arnoldi Method while using the implicit projection of the operator.

5 Conclusions

It has been found that the proposed method of solving boundary value problems based on Implicitly Restarted Arnoldi Method and implicit operator projection may be implemented in an efficient scalable numerical solver which can be applied to solving large-scale operator problems in parallel distributed memory systems. It has been shown that the scalability of the solver is comparable to the scalability of the solver based on the Finite Difference (FDFD) discretization. Still, due to a reduced size of the problem generated in the proposed projection technique a fast convergence of IRAM is obtained and memory requirements of the method are reduced. Referring to electromagnetic applications, the numerical tests show that the proposed method may be successfully applied to finding modes (including higher modes) in waveguides with both continuous and discontinuous permittivity profiles. Clearly, although in the paper the discussion concentrated on investigating operators arising in electromagnetics, the presented technique may be applied to solving eigenproblems in a more general class of non-symmetric infinite-dimensional operators.

6 Acknowledgments

The authors are grateful to Jacek Mielewski for providing sequential code of the Finite Difference Frequency Domain solver which has served as a basis for parallel implementation of the IRAM-FD method.

All numerical tests presented in this paper have been carried out at the facilities of the Academic Computer Centre TASK in Gdańsk and the Interdisciplinary Centre for Mathematical and Computational Modelling of the University of Warsaw. This work was supported by the Polish State Committee for Scientific Research under contract 8 T11D 01911.

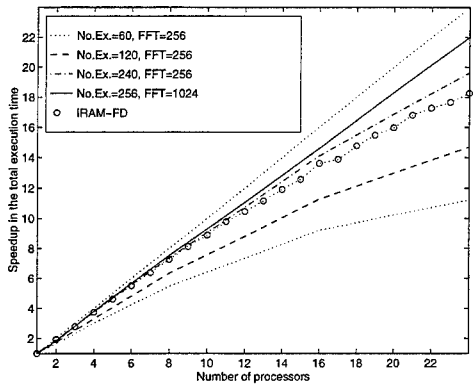

Figure 5: Speed-up in the total execution time of a single iteration of the IRAM-FFT parallel solver vs. the number of processors for different numbers of expansion functions and FFT lengths. The tests have been performed in the Cray T3E system.

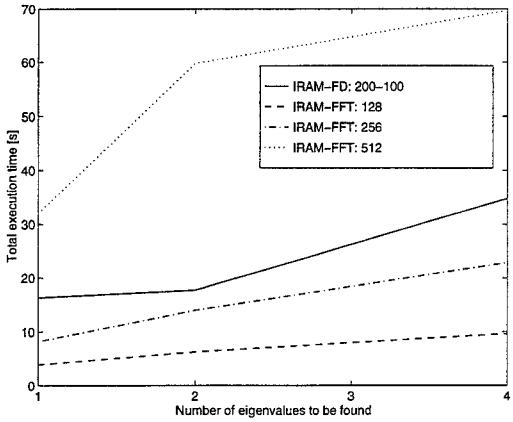

Figure 6: Comparison of single-processor execution times of IRAM-FD and IRAM-FFT solvers for different number of eigenvalues to be found and different FFT lengths applied. The tests have been performed in the Cray T3E system.

References

[1] P. Dębicki, P. Jędrzejewski, A. Kręczkowski, J. Mielewski, M. Mrozowski, K. Nyka, P. Przybyszewski, M. Rewieński, T. Rutkowski, *Coping with numerical complexity in computational electromagnetics*, Int. Microwave Symp. MIKON-98, Cracow, 1998.

[2] D. C. Sorensen, "Implicitly Restarted Arnoldi/Lanczos Methods for Large Scale Eigenvalue Calculations", *Proceedings of an ICASE/LaRC Workshop*, May 23-25 1994, Hampton, VA, D. E. Keyes, A. Sameh and V. Venkatakrishnan, eds., Kluwer, 1995.

[3] Y. Saad, *Numerical Methods for Large Eigenvalue Problems*, Manchester University Press, Manchester, UK, 1992.

[4] K. J. Maschhoff, D. .C. Sorensen, *P_ARPACK: An Efficient Portable Large Scale Eigenvalue Package for Distributed Memory Parallel Architectures*, Rice University, 1996, available at: `ftp.caam.rice.edu`.

[5] M. Mrozowski, *Guided Electromagnetic Waves, Properties and Analysis*, Research Studies Press, Taunton, Somerset, England, 1997.

[6] T. F. Jabłoński and M. J. Sowiński, "Analysis of dielectric guiding structures by the iterative eigenfunction expansion method", *IEEE Trans. Microwave Theory Tech.*, vol. MTT-37, pp. 63-70, 1989.

[7] M. Mrozowski, "IEEM FFT - A Fast and Efficient Tool for Rigorous Computations of Propagation Constants and Field Distributions in Dielectric Guides with Arbitrary Cross-Section and Permittivity Profiles", *IEEE Trans. Microwave Theory Tech.*, vol. MTT-39, pp. 323-329, 1991.

[8] G. H. Golub, C. F. van Loan, *Matrix Computations*, The John Hopkins University Press, Baltimore, 1996.

SESSION 11

TIME DOMAIN METHODS

Chairs: J. Dunn and Chris Holloway

Large Scale FD-TD—A Billion Cells

Ulf Andersson and Gunnar Ledfelt

PSCI/NADA, KTH, 100 44 Stockholm, SWEDEN

ulfa@nada.kth.se, ledfelt@nada.kth.se

Abstract

We describe an FD-TD simulation of a SAAB 2000 aircraft using more than one billion cells. This was performed on 125 nodes of an IBM SP. We also give a speed-up result for the IBM SP and discuss the possibilities for visualization of FD-TD solutions in a VR-CAVE.

1 Introduction

The Swedish center of excellence Parallel and Scientific Computing Institute (PSCI) [6] conducts a research project within its CEM program called "Large Scale FD-TD" [5]. Within this project a 3D FD-TD code, `pscyee`, has been implemented using Fortran 90.

The capabilities of the sequential version of `pscyee` includes Huygens' surfaces, PML according to Berenger as absorbing boundary condition (ABC), a generalized thin wire subcell model [4] based on the approach of Holland-Simpson and PEC surfaces. Excitation may also be performed with current/voltage sources in the thin wire model and with point sources. The first order Mur ABC is available for calculations where the accuracy demand on the ABC is not so high.

Implementation of models for frequency dispersive materials is ongoing. It has already been implemented in a 2D version of the code. `pscyee` will be used as a component in a hybrid time domain solver which will combine the FD-TD scheme with an implicit Finite-Element Time-Domain (FE-TD) scheme and an explicit Finite-Volume Time-Domain (FV-TD) scheme for unstructured meshes. This will be performed within the GEMS project which is a collaborative code development project between Swedish industry and academia involving PSCI, Ericsson Saab Avionics, Ericsson Microwave System, Saab Ericsson Space, the Swedish Institute of Applied Mathematics and the Swedish Defense Research Establishment.

2 Parallel implementation

The parallel implementation of `pscyee` uses the Message Passing Interface (MPI) standard. This was chosen to guarantee portability of the code.

Figure 1 illustrates our parallelization strategy in 1D with six cells on two nodes. When node two calculates the Ex_4-value it needs to know the value of $Hz_{3.5}$ which is stored in node one. Similarly, when node one calculates the $Hz_{3.5}$-value it needs to know the value of Ex_4 which is stored in node two. This means that during each time step two messages have to be

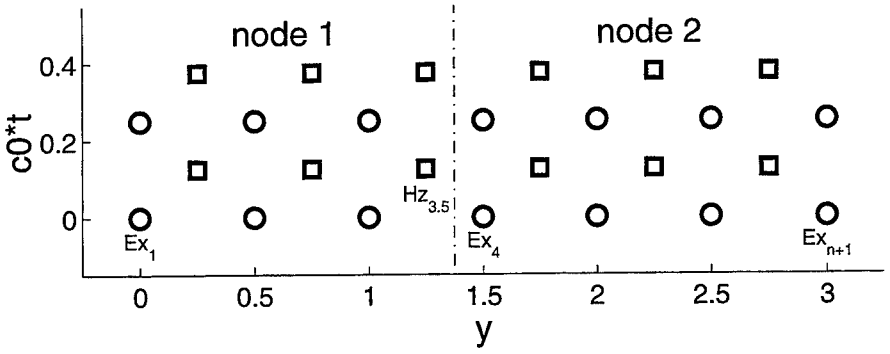

Figure 1: Illustration of our parallelization strategy. A 1D Yee grid with six cells (n=6) and $\Delta y = 0.5$ distributed on two nodes.

sent, one in each direction. In 3D two of the six electromagnetic variables must be sent across processor interfaces. We have implemented this strategy with several syntactically different MPI implementations. They are described in detail in [1].

On a parallel computer with reasonably fast communication, e.g. an IBM SP, it is possible to achieve perfect scalability. With perfect scalability we mean that when the problem size is increased linearly with the number of processors the execution time is constant. On the other hand, it is usually not possible to achieve ideal speed-up. An exception occurs when cache effects makes smaller problem sizes faster than larger ones. With speed-up we mean that the problem size is kept fixed independently of the number of processors. Figure 2 displays speed-up results for an IBM SP. A point source was used for excitation and the first order Mur scheme was used as ABC. The non blocking communication of MPI (MPI_ISEND) was used.

Portability has been demonstrated by executing the code on several different parallel computers, including an IBM SP, a Fujitsu VX, a CRAY J932 and a cluster of Digital Alpha servers. The performance was satisfactory on all these computers.

A more detailed descriptions of our parallelization strategy can be found in [2, 1]. A nice review of parallelization of FD-TD is given by Professor Gedney in Chapter 5 of [3].

3 One billion cells

For homogeneous materials we need only six floating point values per cell, the three electric and the three magnetic field components. Using 32 bit precision (four bytes) means that we need $4*6*10^9 = 22.4$ Gbyte memory for one billion cells. Clearly, only a parallel computer can supply this. We used 125 nodes with 160MHz RS/6000 processors of the IBM SP at PDC, KTH. These nodes have 256 Mbyte memory each making a total of 31.25 Gbyte. Actually, a few of them have more than 256 Mbyte, but we do not want to use it since that would destroy the load balancing.

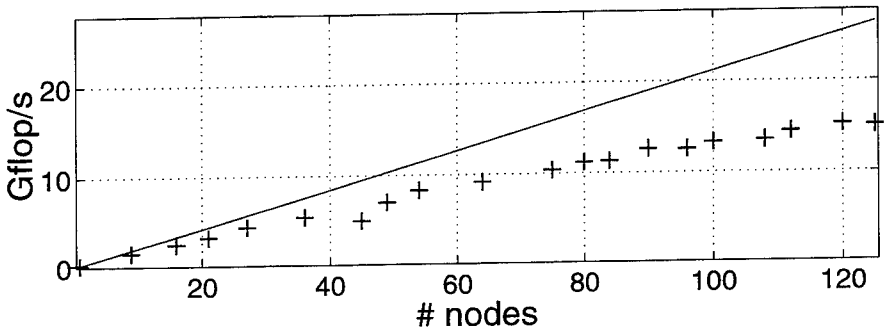

Figure 2: Speed-up of pscyee on an IBM SP with 160MHz RS/6000 processors. The problem size is $252 \times 252 \times 127$. The solid line represents ideal speed-up.

It is not possible to use all the physical memory on a node since some of the memory is used by the operating system. Using too much memory will result in swapping which must be avoided since it has a drastic effect on the performance. Tests indicated that it was safe to use up to 200 Mbyte on each node and that one usually could use up to 220 Mbyte.

The object chosen for this calculation was a SAAB 2000 aircraft. A Cartesian description of this aircraft was created from a CAD description using CADFIX. This was performed by Ericsson Saab Avionics (ESB). The file delivered from ESB only contained one half of the airplane so we had to create the entire airplane by mirroring. Hence, we got an absolutely symmetric airplane. The resolution was 2.5 cm in all three dimensions which was a factor two per space dimension smaller than the resolution previously used at ESB. We used a problem size of $1260 \times 1260 \times 635$ equaling 1 008 126 000 cells in total. The computational domain was split in $5 \times 5 \times 5$ blocks each with a size of $252 \times 252 \times 127$ cells.

The total number of **E**-fields on the surface of the SAAB 2000 was almost two millions and the number of surface quads was almost one million. The memory needed to store this information varied from node to node and was at most nine Mbytes.

The input ASCII-file containing the PEC information for one half of the SAAB 2000 contained almost one million lines. Since all nodes read this it was very inefficient to use the standard file system, `afs`, which only gave a CPU activity of 2–3% while reading the file. Instead we used the parallel file system, `pfs`, which gave a CPU activity of about 20%. A more efficient strategy would probably be to let one node read the data, analyze it and then distribute it to the other nodes.

The performance of the core of the code is almost 25 Gflop/s. This figure excludes output. When the surface currents and two cutting planes were written every 20th time step this performance dropped to about 20 Gflop/s. In this case, the time to complete one time step was about 1.8 seconds. A total of 2500 time steps were taken and the total execution time, including initializations, was 86 minutes.

The first order Mur ABC was used and excitation was performed with a point source in front of the airplane. The MPI_SENDRECV facility was used for the communication.

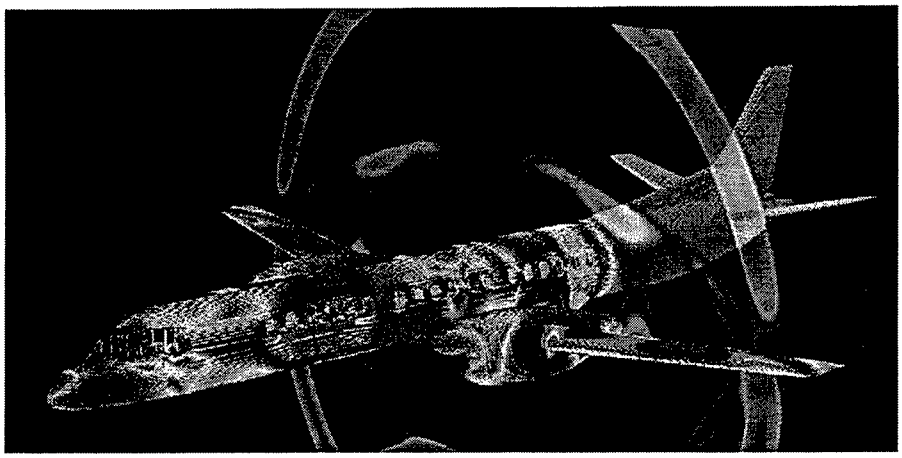

Figure 3: The surface currents after 1500 time steps on the SAAB 2000 aircraft. Also the magnitude of the **H**-field is shown on a cutting plane across the wings perpendicular to the fuselage.

4 Visualization of large FD-TD data

Running large FD-TD simulations do not only require powerful computers. It also put high demands on the post processors. For small and medium size problems you can save the whole electromagnetic field at each time step (or every n:th time step) if you have sufficiently large discs. After the simulation you can go through the data and visualize the features you are looking for and also find unexpected properties of your solution. This is not the case when you are solving large problems. Not only the disc space is limited but the I/O bandwidth is also an effective bottleneck. You have to decide a priori what field values you want to post process and save only them. Furthermore, you need a high end graphical system to visualize the multitude of polygons that constitute the objects in your simulation.

A new technique has emerged during the last few years which is believed to make the understanding of scientific computing results easier. The concept is usually called "CAVE", CAVE Automated Virtual Environment, and consist of back-projection of images onto semi transparent surfaces. If several surfaces are put together you get a room where you are surrounded by the images. By adding a tracking system where your head position is tracked, stereo images can be produced and highly realistic 3D environments are perceived. With a tracking system for a hand held device you can also interact with this virtual reality.

This technique has obvious benefits: it is easy for several people to be in the room simultaneously and therefore see images together. The users can thus interact with the virtual reality together and focus on interesting areas. Also, because users see their own hands and feet, for example, as part of the virtual world, they get a heightened sense of being inside that world.

Various CAVE-like environments exist all over the world today. Most of these have up to four

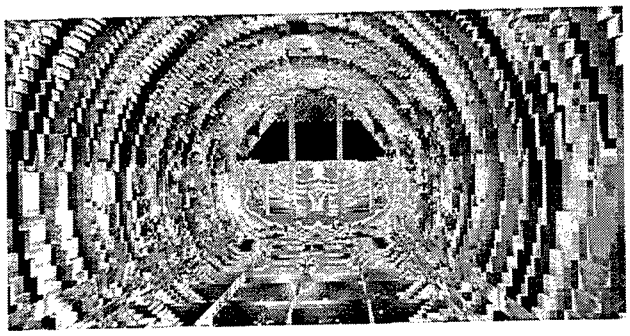

Figure 4: The interior of the SAAB 2000 aircraft. Surface currents are shown at the same time as in Figure 3.

projection surfaces; images are usually projected on three walls and the floor. Adding projection on the ceiling gives a fuller sense of being enclosed in the virtual world.

Projection on all six surfaces of a room allows users to turn around and look in all directions. Thus, their perception and experience are not limited, which is necessary for full immersion. Such a six-surface-system has recently been inaugurated at PDC, KTH and several projects on visualizing CEM solutions have been started where the users will be able to navigate, for example inside an aircraft while lightning strikes. In this case one will directly see the field penetrating the openings of the fuselage and detect "hotspots" to avoid in the context of EMC.

However, the CAVE technology does not ease the urge of effective handling of the output from FD-TD solvers. Even though the computers serving CAVE environments often are high end graphical systems you still have to limit the data saved for post processing. In Figure 3 the surface currents are displayed on each 2.5×2.5 cm^2 square constituting the surface of the FD-TD object. Approximately one million quads are put to the visual system and clearly, most of them are not visible in the picture. Furthermore, perhaps one could utilize the concept "level of details" where smaller parts in the background are combined to fewer objects and thus lower the number of polygons to be rendered. For volumetric data semitransparent 3D texture mapping can be utilized. This volume rendering technique can be used to show the field inside the aircraft.

5 Conclusions

We have demonstrated that by using a large parallel computer it is possible to do an FD-TD calculation with more than one billion cells. We showed this by using 125 nodes of an IBM SP.

The parallel implementations of PML and the subcell model for arbitrarily oriented thin wires [4] are in progress. When they are completed we plan to repeat the one billion cells calculation using these features. Excitation will be performed using the thin wire model. The parallelization approach is illustrated in Figure 5, where models for frequency dispersive materials are also included.

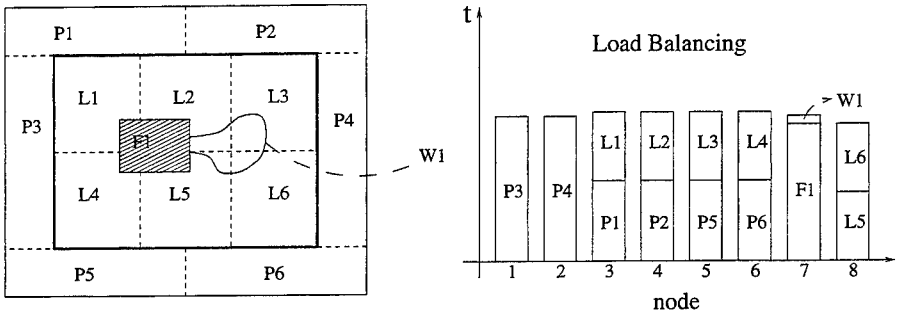

P = PML, L = Leap frog, W = Wire, F = Freq. disp. mat.

Figure 5: The load balancing for a full problem, including PML, frequency dispersive materials and an arbitrary oriented thin wire subcell model.

6 Acknowledgments

This work was supported with computing resources by the Swedish Council for Planning and Coordination of Research (FRN) and Parallelldatorcentrum (PDC), Royal Institute of Technology.

The grid for the SAAB 2000 was supplied by Ericsson Saab Avionics.

References

[1] U. Andersson. Parallelization of a 3D FD-TD code for the Maxwell equations using MPI. In B. Kågström et al., editors, *Applied Parallel Computing, PARA '98*, Lecture Notes in Computer Science, No. 1541, pages 12–19, June 1998.

[2] U. Andersson. Parallelization of a 3D FD-TD code for the Maxwell equations using MPI. In G. Kristensson, editor, *EMB 98 - Electromagnetic Computations for analysis and design of complex systems*, pages 94–101. SNRV, November 1998.

[3] T. Itoh and B. Houshmand, editors. *Time-Domain Methods for Microwave Structures.* IEEE Press, 1998.

[4] G. Ledfelt. A thin wire sub cell model for arbitrary oriented wires for the FD-TD method. In G. Kristensson, editor, *EMB 98 - Electromagnetic Computations for analysis and design of complex systems*, pages 148–155. SNRV, November 1998.

[5] Large Scale FD-TD. `http://www.nada.kth.se/~ulfa/CEM.html`.

[6] Parallel and Scientific Computing Institute (PSCI). `http://www.psci.kth.se/psci/`.

NEW HIGH ORDER TIME-STEPPING SCHEMES FOR FINITE DIFFERENCES

MARTIN AIDAM AND PETER RUSSER

LEHRSTUHL FÜR HOCHFREQUENZTECHNIK, TECHNISCHE UNIVERSITÄT MÜNCHEN
ARCISSTR. 21, D-80333 MÜNCHEN, GERMANY

ABSTRACT. To improve finite difference calculations, the use of higher order difference operators is promising. For the time-stepping, usually only the second order centred differencing is used. Since this leads only to second order accurate schemes, independent of the choice of the difference operator, we investigate classical explicit higher order multistep methods. Unfortunately, they do not satisfy completely the needs for the use with Maxwell's or telegraph equations. Therefore, we construct new explicit multistep schemes, which show stability limits comparable to centred differencing and are more adapted to our purposes. This paper discusses the construction principles of the new schemes, gives the stability limits as well as the convergence orders and error constants, and validates the approach by applying the schemes to telegraph equations using several difference operators for the approximation of the spatial derivatives.

1. INTRODUCTION

The development of higher order schemes promises algorithms with smaller errors than standard algorithms but comparable computational effort. For time domain calculations, usually centred differences are used to approximate the temporal derivatives, e.g. [4].

In [1], we also applied centred differences for the time-stepping in our algorithm using biorthogonal B-spline-wavelets. Jameson pointed out, that the use of spline-wavelets yields higher order difference operators [5]. Since we did not find a dramatic reduction in the error, as we used higher and higher order difference operators, we carried out a dispersion analysis which we extended to the use of general linear multistep methods for the time-stepping procedure [2]. From the results of [2], we were able to explain our experience made in [1]. We concluded, that the development of higher order temporal integration schemes is necessary to exploit higher order spatial differencing as much as possible.

In the subsequent sections, we show that the classical explicit multistep schemes like Adams-Bashforth or Nyström are not really satisfactory for electromagnetics since there must be no amplification or damping of travelling waves. Furthermore, based on the dispersion analysis of general linear multistep methods, we show how to construct linear multistep methods, that do not amplify or damp the waves, give their convergence order, their error constants as well as their stability limits. Numerical experiments, using our new time-stepping schemes, demonstrate their superiority over centred differencing.

2. MULTISTEP SCHEMES

If we discretize spatially a time-dependent partial differential equation, e.g. Maxwell's or telegraph equations, we are left with a system of ordinary differential equations which has to be integrated. Obviously, one could apply standard methods for solving systems of ordinary differential equations. This point of view is generally known as method of lines.

We concentrate on linear multistep methods. Their exact definition can be found e.g. in [6]. If a linear multistep method is applied to telegraph equations

$$\frac{\partial u}{\partial t} = -c\frac{\partial i}{\partial x} \tag{1a}$$

$$\frac{\partial i}{\partial t} = -c\frac{\partial u}{\partial x}, \tag{1b}$$

which are spatially discretized and the spatial derivatives are replaced by a difference operator $D = \sum_{n=-M_1}^{M_2} p_n S_x^n$ (S_x is the shift operator with respect to x, e.g.: $S_x u_{k,l} = u_{k,l+1}$), we end up in the algorithm [2]

$$\sum_{k=0}^{L} \alpha_{L,k} \begin{pmatrix} u_{m+k,l} \\ i_{m+k,l} \end{pmatrix} = \Delta t \sum_{k=0}^{L} \beta_{L,k} \begin{pmatrix} 0 & -cD \\ -cD & 0 \end{pmatrix} \begin{pmatrix} u_{m+k,l} \\ i_{m+k,l} \end{pmatrix}, \quad m,l \in \mathbb{Z}, \tag{2}$$
$$\alpha_{L,k}, \beta_{L,k} \in \mathbb{R}, \ \alpha_{L,L} \neq 0, \ |\alpha_{L,0}| + |\beta_{L,0}| \neq 0.$$

m denotes the time-step and l the point in the spatial grid. For explicit schemes, $\beta_{L,L} = 0$, and we have to know $u_{m,l}$ and $i_{m,l}$ for $m = 0, 1, \ldots, L-1$ and all l (so-called starting values) to calculate $u_{L,l}$ and $i_{L,l}$.

The dispersion relation for this reads

$$\frac{\sum_{k=0}^{L} \alpha_{L,k} e^{j\Omega k}}{\sum_{k=0}^{L} \beta_{L,k} e^{j\Omega k}} = \pm c\Delta t \sum_{n=-M_1}^{M_2} p_n e^{j\eta n}, \tag{3}$$

where Ω is the normalized frequency and η the normalized spatial frequency.

From the dispersion relation (3), one can calculate the behaviour of the numerical modes and compare them to the physical ones. Since we use multistepping, of course we have $2L$ numerical instead of 2 physical modes. Following [7], we calculate Ω_i, $i = 1, \ldots, 2L$ as function of η for all $2L$ numerical modes. Requiring that all Ω_i must not have negative imaginary parts —a negative imaginary part would mean exponential growth— allows to calculate the stability limit. The evaluation of

$$c_m = -\frac{\Delta x \, \mathrm{Re}\{\Omega_k\}}{\Delta t \, \eta} \tag{4}$$

yields the numerical phase velocity c_m and can be compared to the physical one c. Note that for this comparison to make sense, k has to be chosen correctly, i.e. we have to choose the numerical mode that converges to the physical mode and not one of the purely numerical ones.

Since the extraction of Ω_i in general can not be done analytically, the calculation of the modes, the stability limits and the phase velocities is carried out numerically.

First of all, we looked at the classical explicit multistep methods, i.e. Adams-Bashforth and Nyström type schemes. Nyström's methods, except for the case $L = 2$ (centred differencing), are unstable. To achieve imaginary parts of Ω_i greater than -10^{-14}, one has to use inacceptably small time steps (remind that these investigations have been done numerically, i.e. we have to choose zero a little bit smaller than 0!).

As stability limit, we give γ, so that in case of centred differences as approximation for the spatial derivative Δt and Δx must fulfill the inequality

$$\frac{c\,\Delta t}{\Delta x} \leqslant \gamma. \tag{5}$$

If one uses another difference operator, one has only to calculate the maximum value of the imaginary part on the right hand side of (3) for $\eta \in [-\pi, \pi]$ and divide γ by this value, e.g. for the fourth order difference operator given below one has to multiply the stability limit γ by 0.7287.

Additionally, since all modes show an imaginary part of Ω_i, we give the maximum value of the imaginary part of the mode that corresponds to the physical mode including the sign. A mode gets multiplied by the factor $\exp(-\alpha\, t/\Delta t)$. So $\alpha = 10^{-3}$ means, that after 10^3 time steps the wave is damped by e. Similarly, $\alpha = 10^{-14}$ means, that after 10^8 time steps the wave is amplified by $\exp(10^{-6})$, i.e. the amplitude error is in the order of 10^{-6}.

TABLE 1. Stability limits necessary to achieve imaginary parts $\geqslant -10^{-14}$ with Adams-Bashforth schemes. The maximum imaginary part (including sign) of the physical mode is also given.

L	1	2	3	4	5
γ	$1.421 \cdot 10^{-7}$	$4.479 \cdot 10^{-4}$	0.7236	0.4299	0.005601
α	-10^{-14}	-10^{-14}	0.135	0.0028	-10^{-14}

L	6	7	8	9	10
γ	0.01831	0.05808	0.02948	0.01496	0.007587
α	-10^{-14}	$3.8 \cdot 10^{-11}$	10^{-14}	-10^{-14}	$7 \cdot 10^{-15}$

Table 1 gives the results for the Adams-Bashforth schemes.[1]

$L = 1$ is unstable and leads to an inacceptable time step. $L = 2$ leads also to an inacceptable time step, since it is only second order accurate and centred differencing ($\gamma = 1.0$) performs much better. The cases $L = 3$ and $L = 4$ allow good time steps, but the schemes are dissipative. The cases $L \geqslant 5$ show extremely slight amplification or damping, so this would be acceptable, but the time steps are quite small.

3. Idea of Construction

The explanation for this behaviour is simple and leads directly to the construction of a new family of explicit and implicit schemes which are more adapted to the use with telegraph and Maxwell's equations.

All difference operators we normally use are antisymmetric, e.g.

- Centred differences: $D = \frac{1}{2\Delta x}(S_x - S_x^{-1})$
- 4th order differences: $D = \frac{1}{12\Delta x}(-S_x^2 + 8S_x - 8S_x^{-1} + S_x^{-2})$

this means, that the right hand side of the dispersion relation (3) is purely imaginary for all $\eta \in [-\pi, \pi]$.

We observed, that only for Nyström with $L = 2$, the left hand side is also purely imaginary for real $\Omega \in [-\pi, \pi]$. In all other cases it is not. Consequently, Ω needs to show some imaginary part, so that the term on the left hand side of (3) also becomes purely imaginary.

The idea for constructing the new schemes now comes clear. The coefficients $\alpha_{L,i}$ have to be antisymmetric

$$\alpha_{L,L-i} = -\alpha_{L,i}\,, \quad i \in \{0, \dots, L\} \tag{6}$$

and the coefficients $\beta_{L,i}$ have to be symmetric

$$\beta_{L,L-i} = \beta_{L,i}\,, \quad i \in \{0, \dots, L\}\,. \tag{7}$$

4. New Family of Schemes

Of course the choice of $\alpha_{L,i}$ and $\beta_{L,i}$ is restricted (see [6] for details).

Nevertheless choosing $\alpha_{L,L} = 1$, $\alpha_{L,0} = -1$ and $\alpha_{L,i} = 0, i = 1, \dots, L-1$ allows to construct convergent multistep schemes which are weakly stable and have the nice property to have no exponentially growing numerical modes, if the time step is chosen small enough, and no damping.

[1] Since the calculations have been carried out numerically, we only give the first digits.

If L is odd, it is not possible to construct an explicit scheme where the $\beta_{L,i}$ are symmetric (if one wants to have the highest convergence order possible). Consequently, these schemes exhibit exponentially growing modes. Therefore we do not give their coefficients nor their characteristics.

Table 2 gives the coefficients, and table 3 the convergence orders, the error constants [6] and the stability limits for the new schemes. The stability limits given have been verified in our experiments, i.e. increasing them by only 1% leads to rapid exponential growth.

TABLE 2. Coefficients of the explicit schemes.

Length L	Coefficients $\beta_{L,L}, \ldots, \beta_{L,0}$
2	$0, 2, 0$
4	$0, \frac{8}{3}, -\frac{4}{3}, \frac{8}{3}, 0$
6	$0, \frac{33}{10}, -\frac{21}{5}, \frac{39}{5}, -\frac{21}{5}, \frac{33}{10}, 0$
8	$0, \frac{736}{189}, -\frac{848}{105}, \frac{1952}{105}, -\frac{19672}{945}, \frac{1952}{105}, -\frac{848}{105}, \frac{736}{189}, 0$
10	$0, \frac{20225}{4536}, -\frac{4175}{324}, \frac{41675}{1143}, -\frac{137675}{2268}, \frac{169555}{2268}, -\frac{137675}{2268}, \frac{41675}{1143}, -\frac{4175}{324}, \frac{20225}{4536}, 0$

TABLE 3. Characteristics of the explicit schemes.

Length L	Convergence Order	Error Constant	Stability Limit γ
2	2	$\frac{1}{6}$	1.0
4	4	$\frac{7}{90}$	0.4330
6	6	$\frac{41}{840}$	0.1143
8	8	$\frac{989}{28350}$	0.02949
10	10	$\frac{16067}{598752}$	0.007587

We compare these new schemes with the Adams-Bashforth cases. The case $L = 2$ gives centred differencing. $L = 4$ gives a slightly greater stability limit than Adams-Bashforth, but shows of course no damping. $L = 6$ increases the possible time step by a factor of 6 and also shows no damping. $L = 8$ and $L = 10$ seem to have no advantages, since the stability limits are the same and the Adams-Bashforth's schemes have practically no imaginary part.

A disadvantage of the new schemes is, that they have greater memory requirements than Adams-Bashforth's schemes.

To illustrate the dispersion behaviour of the new schemes, the error of the phase velocity in the maximum norm $||c_m| - c|$ (remind that c_m can be positive or negative, depending in the sign of the right hand side of (3)) is given in the plots in Fig. 1. The plots show the errors for all five integration schemes given in this paper for four different difference operators. All calculations have been carried out at the stability limits given.

Top left, we used the fourth order difference operator given above. If centred differencing ($L = 2$) is used, only second order convergence can be achieved; if one uses a more accurate integration scheme, the

FIGURE 1. Phase velocity errors of the new schemes for several higher order (spatial) difference operators.

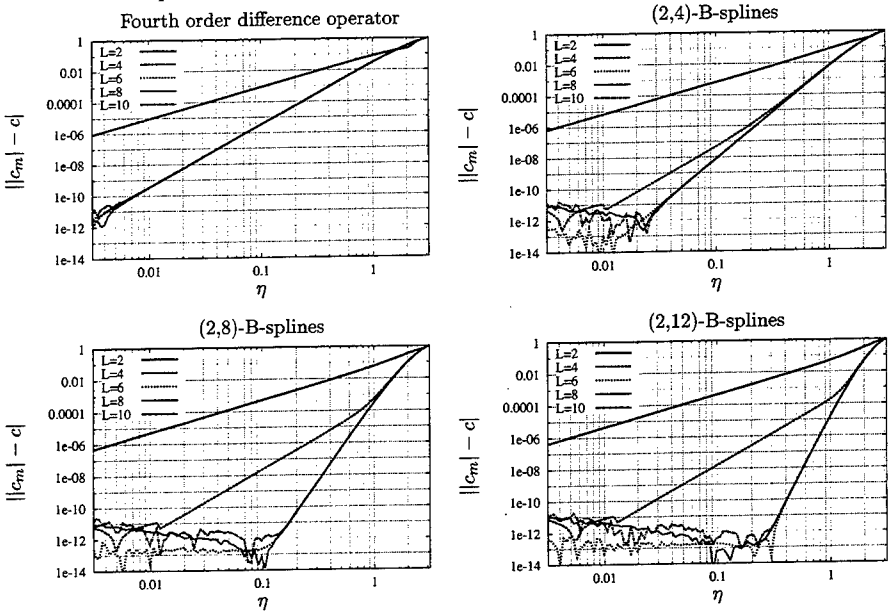

fourth order convergence of the difference operator can be obtained. Note that increasing the order of the integration scheme to more than four does not improve the convergence behaviour any further.

The other three plots show the phase velocity errors for the difference schemes obtained by applying a Petrov-Galerkin procedure using the primal scaling functions of the biortogonal B-spline-wavelets [3] as expansion functions and the dual scaling functions as test functions [1]. We give results for (2,4)-, (2,8)-, and (2,12)-B-splines. The resulting difference operators seem to be of convergence orders 6, 10 , and 14 (taken from the behaviour of the error of the phase velocity). As expected, the integration scheme $L = 2$ leads to second order convergence, $L = 4$ to fourth order. The other three integrators can't be distinguished. We believe that their error constants are so small, that we can't observe the reduction in the convergence order, due to the integration schemes, using double precision arithmetic. From this we conclude that $L = 8$ and $L = 10$ should not result in smaller errors than $L = 6$, if we use single or double precision arithmetic.

5. NUMERICAL VALIDATION

For numerical validation of the new integration schemes, we apply them to telegraph equations (1) with $c = 1$. As boundary conditions we have to choose something that does not disturb the homogeneous scheme for infinite spatial extension. Possible choices are periodic boundary conditions and ideal electric or magnetic walls using the mirror principle. Our test line is defined on the interval $[0, 1]$. For this problem, the analytic solution is known. For $t_n = 2n, n \in \mathbb{N}$, voltage and current must equal the initial

FIGURE 2. $l_{2,\Delta x}$-errors in dependence on the discretization.

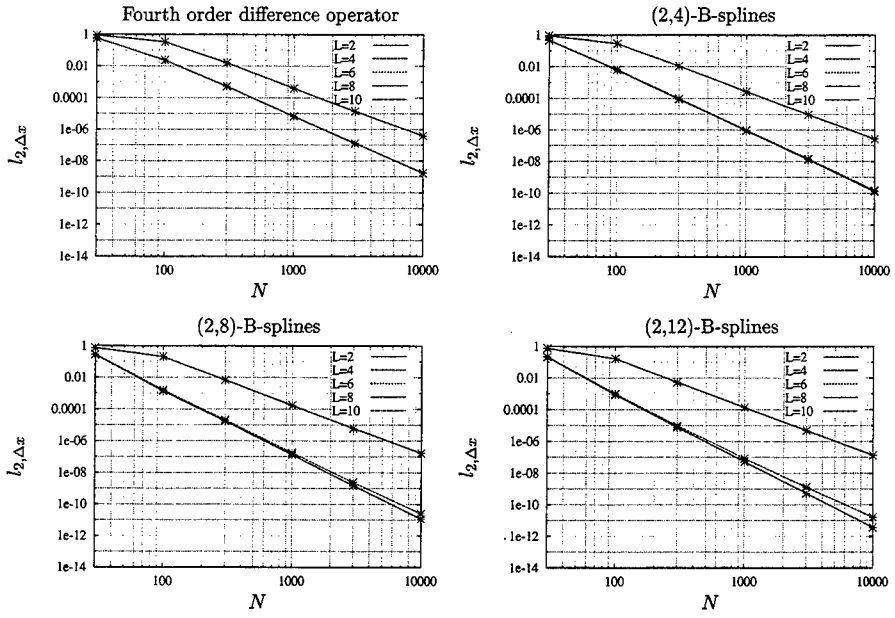

condition for all three possible boundary conditions. As initial condition, we set

$$u_0 = \begin{cases} 10^8(x-0.4)^4(x-0.6)^4 & \text{if} \quad 0.4 \leqslant x \leqslant 0.6 \\ 0 & \text{else} \end{cases} \tag{8a}$$

$$i_0 = 0 \tag{8b}$$

As starting values for the multistep schemes, we use the analytic solution to avoid additional errors.

Fig. 2 gives the $l_{2,\Delta x}$-errors [7] for the fourth order, (2,4)-, (2,8), and (2,12)-B-spline difference operators for all five integration schemes.

For centred differencing ($L = 2$), we have a convergence order around 3. From the dispersion analysis, we would expect only second order. The reason for this faster convergence is not clear.

As can be seen, increasing the order of the integrator decreases dramatically the error. But the convergence order is limited by something around fourth order. The reason for this lies in the regularity of our initial condition. Its Fourier transform decreases as $1/\omega^4$. This means even though we have excellent schemes, if we don't excite them smoothly enough, we get a worse convergence behaviour.

If we choose u_0 to be smoother (seven times continuously differentiable)

$$u_0 = \begin{cases} 10^{16}(x-0.4)^8(x-0.6)^8 & \text{if} \quad 0.4 \leqslant x \leqslant 0.6 \\ 0 & \text{else} \end{cases} \tag{9}$$

we can achieve higher convergence orders, since its Fourier transform now decreases as $1/\omega^8$; see fig. 3.

FIGURE 3. Error behaviour for the smoother initial conditions.

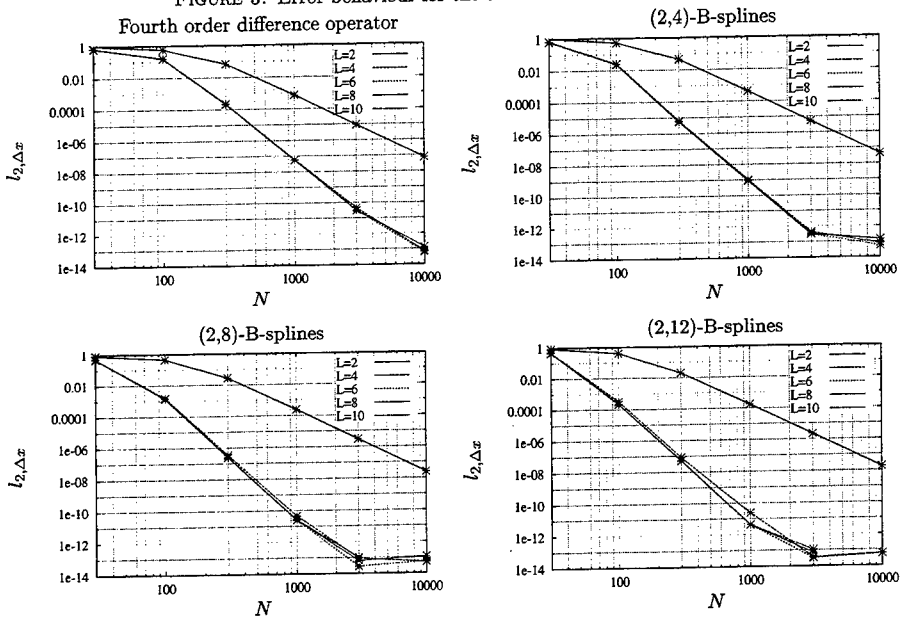

Again, the reason for the 'too fast' convergence of the cases $L = 2$ and $L = 4$ is not clear. The others behave like predicted from the dispersion analysis and the regularity of the initial value. One can see also very nicely the influence of the round-off errors, which limit the achievable accuracy to something around a hundred times the relative accuracy of double precision.

6. CONCLUSION

We investigated explicit higher order multistep methods for their usefulness with telegraph and Maxwell's equations. We found Nyström's methods except for the centred differencing case $L = 2$ to be useless. Adams-Bashforth's methods might be of use, if one accepts a (by the time step) tunable growth or damping. Of course, this complicates the choice of the time step.

To overcome these limitations, we constructed a new class of multistep schemes, which doesn't show any amplification or damping of the physical modes. This new family includes centred differencing as special case. Especially the cases $L = 4$ and $L = 6$ are interesting, since they behave better than the Adams-Bashforth pendants. The higher order cases show no significant improvement with respect to the Adams-Bashforth cases, since the practical stability limits seem to be comparable but the new family has greater memory requirements.

Furthermore, we showed that our approach leads to extremely small errors with moderate computational effort for the simple telegraph equations.

The application of multistep methods can be easily extended to Maxwell's equations. For a linear, homogeneous, isotropic, lossless and frequency-independent medium and a cubic, non-graded mesh, we

are left with the algorithm

$$\sum_{k=0}^{L} \alpha_{L,k} \begin{pmatrix} E^x_{m+k,l,i,j} \\ E^y_{m+k,l,i,j} \\ E^z_{m+k,l,i,j} \\ H^x_{m+k,l,i,j} \\ H^y_{m+k,l,i,j} \\ H^z_{m+k,l,i,j} \end{pmatrix} = \Delta t \sum_{k=0}^{L} \beta_{L,k} \begin{pmatrix} 0 & 0 & 0 & 0 & -\frac{1}{\varepsilon}D_z & \frac{1}{\varepsilon}D_y \\ 0 & 0 & 0 & \frac{1}{\varepsilon}D_z & 0 & -\frac{1}{\varepsilon}D_x \\ 0 & 0 & 0 & -\frac{1}{\varepsilon}D_y & \frac{1}{\varepsilon}D_x & 0 \\ 0 & \frac{1}{\mu}D_z & -\frac{1}{\mu}D_y & 0 & 0 & 0 \\ -\frac{1}{\mu}D_z & 0 & \frac{1}{\mu}D_x & 0 & 0 & 0 \\ \frac{1}{\mu}D_y & -\frac{1}{\mu}D_x & 0 & 0 & 0 & 0 \end{pmatrix} \begin{pmatrix} E^x_{m+k,l,i,j} \\ E^y_{m+k,l,i,j} \\ E^z_{m+k,l,i,j} \\ H^x_{m+k,l,i,j} \\ H^y_{m+k,l,i,j} \\ H^z_{m+k,l,i,j} \end{pmatrix}$$

Again, m denotes the time-step and l, i, j the point in the three-dimensional spatial grid. The first partial derivatives $\partial/\partial x, \partial/\partial y, \partial/\partial z$ are approximated by the difference operators

$$D_x = \sum_{n=-M_{1x}}^{M_{2x}} p_n S_x^n, \quad D_y = \sum_{n=-M_{1y}}^{M_{2y}} q_n S_y^n, \quad D_z = \sum_{n=-M_{1z}}^{M_{2z}} r_n S_z^n$$

S_x, S_y, S_z are the shift operators with respect to the x, y, z-axis. ε is the dielectric constant and μ the magnetic constant for the medium.

The dispersion relation is given by

$$\frac{\sum_{k=0}^{L} \alpha_{L,k} e^{j\Omega k}}{\sum_{k=0}^{L} \beta_{L,k} e^{j\Omega k}} = \pm c\Delta t \sqrt{\left(\sum_{n=-M_{1x}}^{M_{2x}} p_n e^{j\eta_x n}\right)^2 + \left(\sum_{n=-M_{1y}}^{M_{2y}} q_n e^{j\eta_y n}\right)^2 + \left(\sum_{n=-M_{1z}}^{M_{2z}} r_n e^{j\eta_z n}\right)^2}$$

The implementation of algorithms of this type is on its way, and hopefully, we are able to present results soon.

Acknowledgement

We would like to thank Siemens AG for making this work possible by generously granting an Ernst-von-Siemens scholarship.

References

1. M. Aidam and P. Russer, *Application of biorthogonal B-spline-wavelets to Telegrapher's equations*, 14th Annual Review of Progress in Applied Computational Electromagnetics, Monterey, 16.–20.3.1998, March 1998, pp. 983–990.
2. ———, *Comparison of finite difference and wavelet-galerkin methods for the solution of telegraph equations*, 28th European Microwave Conference, Amsterdam, Holland, 6.–8.10.1998, vol. II, October 1998, pp. 712–717.
3. A. Cohen, I. Daubechies, and J.-C. Feauveau, *Biorthogonal bases of compactly supported wavelets*, Comm. Pure Appl. Math. **45** (1992), 485–560.
4. G. Haussmann and M. Piket-May, *FD-TD M24 dispersion and stability in three dimensions*, 13th Annual Review of Progress in Applied Computational Electromagnetics, Monterey, 17.–21.3.1997, March 1997, pp. 82–89.
5. L. Jameson, *On the spline-based wavelet differentiation matrix*, Tech. Report ICASE 93-80, Institute for Computer Applications in Science and Engineering, NASA Langley Research Center, Hampton, 1993.
6. K. Strehmel and R. Weiner, *Numerik gewöhnlicher Differentialgleichungen*, Teubner, Stuttgart, 1995.
7. J.W. Thomas, *Numerical partial differential equations: Finite difference methods*, Springer-Verlag, New York, 1995.

E-mail: aidam@hft.ei.tum.de, russer@hft.ei.tum.de

The Mismatch of Perfectly Matched Layers (PML) in Cylindrical and Spherical Coordinate System

Li Zhao* and Andreas C. Cangellaris**

(*) ANSYS Inc.
Southpointe, 275 Technology Drive
Canonsburg, PA 15317
(**) Center for Computational Electromagnetics
Department of Electrical and Computer Engineering
University of Illinois at Urbana-Champaign
1406 West Green Street, Urbana, IL 61801

Abstract. In this paper, the generalized theory for perfectly matched layers (GT-PML) that was presented as a systematic development of the unsplit-field formulation of perfectly matched layers in Cartesian coordinates, is extended to investigate the absorbing properties of perfectly matched layers in cylindrical and spherical coordinates. Several differences are identified between PML in Cartesian coordinates and PML in cylindrical or spherical coordinates. It is concluded that no PML can be constructed in cylindrical and spherical coordinates as it has been done in Cartesian coordinates. The theory presented in this paper is also validated by FDTD simulation on the cylindrical grid.

1. Introduction

With the advent of Berenger's theory of perfectly matched layers (PML) [1] and its subsequent variations [2]-[4], numerical reflections from the grid truncation boundary in finite-difference time-domain (FDTD) and finite element (FE) solutions of unbounded electromagnetic problems can be kept at levels low enough to facilitate numerical solutions of high accuracy. The most successful implementations of PMLs using either Berenger's original split-field formulation or the unsplit-field formulation, has been demonstrated in Cartesian coordinates. More recently, several investigators have proposed the ways for the extension of the original PML theory to cylindrical and spherical coordinate using the mapping technique in modified Maxwell's system and the split-field components [5]-[8].

In this paper, a systematic derivation of the anisotropic absorbing medium in orthogonal curvilinear coordinates is presented, based on the Maxwellian physical system, to construct PML in orthogonal coordinates in addition to Cartesian coordinates. The development begins with the conjecture that, as in the original formulation of the generalized theory of PML (GT-PML) in Cartesian coordinate [4], the perfectly matched layers can be presented by the anisotropic permittivity and permeability tensors $\bar{\epsilon} = \epsilon[\mathbf{\Lambda}]$ and $\bar{\mu} = \mu[\mathbf{\Lambda}]$ with diagonal elements λ_i. This conjecture is motivated by the tensor that describes the anisotropic matched absorbers in Cartesian coordinates [4]. It is shown that this form of the permittivity and permeability tensors can be translated to a modified definition of the ∇ operator in orthogonal curvilinear coordinates, with the generalized variables

$v_i (i = 1, 2, 3)$, in order to investigate the reflection properties of propagating wave at the interface between the absorbing layer and the computational domain, and construct the reflectionless absorbers. Finally, such a mathematical framework of the generalized theory of perfectly matched layers leads to that either cylindrical or spherical PMLs do not behave exactly like the ones developed for Cartesian grids, and a reflectionless interface can not be affected. This result is validated through a numerical experiment on cylindrical grids.

2. Maxwell's Equation in Orthogonal Curvilinear Coordinates

With the assumption of a time dependence of the form $e^{j\omega t}$, Maxwell's equations in anisotropic medium have the form

$$\nabla \times \mathbf{E} = -j\omega\mu[\mathbf{\Lambda}]\cdot\mathbf{H} \tag{1a}$$

$$\nabla \times \mathbf{H} = j\omega\epsilon[\mathbf{\Lambda}]\cdot\mathbf{E} \tag{1b}$$

$$\nabla\cdot(\epsilon[\mathbf{\Lambda}]\cdot\mathbf{E}) = 0 \tag{1c}$$

$$\nabla\cdot(\mu[\mathbf{\Lambda}]\cdot\mathbf{H}) = 0 \tag{1d}$$

where the tensor $[\mathbf{\Lambda}] = \mathrm{diag}\{\lambda_1, \lambda_2, \lambda_3\}$ is determined in orthogonal curvilinear coordinate $\{u_1, u_2, u_3\}$, and the elements of the diagonal matrix are complex, dimensionless and constants. For example, the component of Maxwell's first equation and the divergence equation for the electric field have the form

$$-j\omega\mu\lambda_i H_i = \frac{1}{h_j h_k}\{\frac{\partial}{\partial u_j}(h_k E_k) - \frac{\partial}{\partial u_k}(h_j E_j)\} \tag{2a}$$

$$\frac{1}{h_1 h_2 h_3}\sum_{i=1}^{3}\frac{\partial}{\partial u_i}(\epsilon\lambda_i h_j h_k E_i) = 0 \tag{2b}$$

To determine the elements of the tensor of PML, we introduce the scaling of physical electromagnetic field

$$\mathbf{E} = [\mathbf{Q}]\hat{\mathbf{E}}, \qquad \mathbf{H} = [\mathbf{Q}]\hat{\mathbf{H}} \tag{3}$$

where the matrix $[\mathbf{Q}] = diag\{q_1, q_2, q_3\}$ is a coordinate-independent constant matrix. The component forms of Maxwell's curl equations with the scaling components of electromagnetic field are cast by

$$-j\omega\mu\hat{H}_1 = \frac{1}{h_2 h_3}\{\frac{1}{\lambda_1 q_1}\frac{\partial}{\partial u_2}(h_3 q_3 \hat{E}_3) - \frac{1}{\lambda_1 q_1}\frac{\partial}{\partial u_3}(h_2 q_2 \hat{E}_2)\} \tag{4a}$$

$$-j\omega\mu\hat{H}_2 = \frac{1}{h_3 h_1}\{\frac{1}{\lambda_2 q_2}\frac{\partial}{\partial u_3}(h_1 q_1 \hat{E}_1) - \frac{1}{\lambda_2 q_2}\frac{\partial}{\partial u_1}(h_3 q_3 \hat{E}_3)\} \tag{4b}$$

$$-j\omega\mu\hat{H}_3 = \frac{1}{h_1 h_2}\{\frac{1}{\lambda_3 q_3}\frac{\partial}{\partial u_1}(h_2 q_2 \hat{E}_2) - \frac{1}{\lambda_3 q_3}\frac{\partial}{\partial u_2}(h_1 q_1 \hat{E}_1)\} \tag{4c}$$

Also, the divergence equation for the electric field becomes

$$\frac{\epsilon}{h_1 h_2 h_3} \sum_{i=1}^{3} \frac{1}{\lambda_j \lambda_k q_j q_k} \frac{\partial}{\partial u_i}(h_j h_k \hat{E}_i) = 0 \tag{5}$$

Comparing the coefficients of the derivative items in (4) suggests the following expressions for the determination of the scaling constants q_i in terms of the elements of tensor matrix $[\Lambda]$

$$\left(\frac{q_1}{q_2}\right)^2 = \frac{\lambda_2}{\lambda_1}, \qquad \left(\frac{q_2}{q_3}\right)^2 = \frac{\lambda_3}{\lambda_2}, \qquad \left(\frac{q_3}{q_1}\right)^2 = \frac{\lambda_1}{\lambda_3} \tag{6}$$

Defining the constants

$$\frac{1}{s_i} = \frac{q_k}{\lambda_j q_j} \tag{7}$$

the relations of (6) yield

$$s_i = \sqrt{\lambda_j \lambda_k} \tag{8}$$

Next, after introducing the variable change $v_i = s_i u_i$, Maxwell's equations with scaling fields may be written in orthogonal curvilinear coordinate (v_1, v_2, v_3) as follows

$$\nabla_a \times \hat{\mathbf{E}} = -j\omega\mu\hat{\mathbf{H}} \tag{9a}$$

$$\nabla_a \times \hat{\mathbf{H}} = j\omega\epsilon\hat{\mathbf{E}} \tag{9b}$$

$$\nabla_a \cdot \left(\epsilon\hat{\mathbf{E}}\right) = 0 \tag{9c}$$

$$\nabla_a \cdot \left(\mu\hat{\mathbf{H}}\right) = 0 \tag{9d}$$

where

$$\nabla_a \times \hat{\mathbf{F}} = \frac{1}{h_1 h_2 h_3} \sum_{i=1}^{3} \{\frac{\partial}{\partial v_j}(h_k \hat{F}_k) - \frac{\partial}{\partial v_k}(h_j \hat{F}_j)\} h_i \mathbf{e}_i \tag{10a}$$

$$\nabla_a \cdot \hat{\mathbf{F}} = \frac{1}{h_1 h_2 h_3} \sum_{i=1}^{3} \frac{\partial}{\partial v_i}(h_j h_k \hat{F}_i) = 0 \tag{10b}$$

Equation (9)-(10) may be used for the construction of the anisotropic PMLs in various orthogonal coordinate systems, although the generalized variables may be adjusted in terms of the scale factor h_i of the special coordinates system.

3. PML in Cartesian Coordinates

For a plane wave in Cartesian coordinate system ($h_1 = h_2 = h_3 = 1$), the general solution of (11) is the familiar expression

$$\hat{\mathbf{E}} = \hat{\mathbf{E}}_0 e^{-j\mathbf{k}\cdot\mathbf{v}} \tag{12a}$$

$$\omega\mu\hat{\mathbf{H}} = -\mathbf{k} \times \hat{\mathbf{E}} \tag{12b}$$

where $\mathbf{k} = k_x\mathbf{e}_x + k_y\mathbf{e}_y + k_z\mathbf{e}_z$, $\mathbf{e}_x, \mathbf{e}_y, \mathbf{e}_z$ are the unit vectors, and $\mathbf{v} = v_x\mathbf{e}_x + v_y\mathbf{e}_y + v_z\mathbf{e}_x = s_x x\mathbf{e}_x + s_y y\mathbf{e}_y + s_z z\mathbf{e}_z$. The apparent wavenumbers along x, y, z direction satisfy the dispersion equation

$$k_x^2 + k_y^2 + k_z^2 = k^2 = \omega^2\epsilon\mu \tag{13}$$

where $k_x = ksin\theta cos\phi$, $k_y = ksin\theta sin\phi$, $k_z = kcs\theta$, and $k = \omega\sqrt{\mu\epsilon}$. Without loss of generality, the planar interface between the computational domain and anisotropic medium is taken to coincide with the $z = 0$ plane. The medium 1 ($z < 0$) is filled with a homogeneous medium with tensors $\epsilon_1[\Lambda_1]$, $\mu_1[\Lambda_1]$, where $[\Lambda_1] = diag\{\lambda_{1x}, \lambda_{1y}, \lambda_{1z}\}$, and corresponding s_{1x}, s_{1y} and s_{1z} values given by (8). The medium 2 ($z > 0$) is filled with a homogeneous medium with tensors $\epsilon_2[\Lambda_2]$, $\mu_2[\Lambda_2]$, where $[\Lambda_2] = diag\{\lambda_{2x}, \lambda_{2y}, \lambda_{2z}\}$, and corresponding s_{2x}, s_{2y} and s_{2z} values given by (8). A plane wave propagating from medium 1 to ward medium 2 is assumed to be obliquely incident on the interface. Its polarization is assumed to be arbitrary, and the standard decomposition of the field in its transverse electric to z (TE_z) and transverse magnetic to z (TM_z) parts is used for the purposes of investigating the reflection properties of the interface. Following the procedure in [4], it can be shown that the interface is reflectionless provided that $\epsilon_1 = \epsilon_2$, $\mu_1 = \mu_2$, $s_{1x} = s_{2x}$, $s_{1y} = s_{2y}$, and $s_{2z} = 1 + s''/j\omega$. On the basis of those results, the elements of the tensor for medium 2 are constructed in such a manner that the propagating wave is attenuated in the medium. The details for such a construction are given in [4].

4. PML in Cylindrical Coordinates

As we mentioned in the Introduction, the cylindrical PMLs have been proposed by several groups [5]-[8]. However, in contrast to the case of cartesian coordinates, the numerical performance of cylindrical PMLs is not well documented. We approach the development of PMLs in cylindrical coordinates in a manner that is different from the ones used in the aforementioned references.

We define the anisotropic tensor $[\Lambda] = diag\{\lambda_\rho, \lambda_\phi, \lambda_z\}$, and introduce a set of scaled fields through the relations in (3), where $[Q] = diag\{q_\rho, q_\phi, q_z\}$. With the scale factor of cylindrical coordinates, $h_\rho = 1$, $h_\phi = \rho$ and $h_z = 1$, we seek the relationship between the scaling coefficients and the elements of the anisotropic tensor that allow the Maxwellian system of (1) to be cast in a generalized variable form that is consistent with cylindrical coordinates. The development is straightforward and leads to the following results:
a) Relationship between q's and λ's:

$$\left(\frac{q_\rho}{q_\phi}\right)^2 = \frac{\lambda_\phi}{\lambda_\rho}, \quad \left(\frac{q_\phi}{q_z}\right)^2 = \frac{\lambda_z}{\lambda_\phi}, \quad \left(\frac{q_z}{q_\rho}\right)^2 = \frac{\lambda_\rho}{\lambda_z}, \tag{14}$$

b) Generalized coordinate variables:

$$\bar{\rho} = \sqrt{\lambda_\phi\lambda_z}\rho = s'_\rho\rho, \quad \bar{\phi} = \sqrt{\frac{\lambda_\rho}{\lambda_\phi}}\phi = s'_\phi\phi, \quad \bar{z} = \sqrt{\lambda_\rho\lambda_\phi}z = s'_z z \tag{15}$$

In terms of the generalized variables defined the above, Faraday's law and Gauss' law, (9)-(10), for the electric field assume the form

$$\frac{1}{\bar{\rho}}\frac{\partial \hat{E}_z}{\partial \bar{\phi}} - \frac{\partial \hat{E}_\phi}{\partial \bar{z}} = -j\omega\mu\hat{H}_\rho \tag{16a}$$

$$\frac{\partial \hat{E}_\rho}{\partial \bar{z}} - \frac{\partial \hat{E}_z}{\partial \bar{\rho}} = -j\omega\mu\hat{H}_\phi \tag{16b}$$

$$\frac{1}{\bar{\rho}}\frac{\partial}{\partial \bar{\rho}}(\bar{\rho}\hat{E}_\phi) - \frac{1}{\bar{\rho}}\frac{\partial \hat{E}_\rho}{\partial \bar{\phi}} = -j\omega\mu\hat{H}_z \tag{16c}$$

$$\frac{1}{\bar{\rho}}\frac{\partial}{\partial \bar{\rho}}(\bar{\rho}\hat{E}_\rho) + \frac{1}{\bar{\rho}}\frac{\partial \hat{E}_\phi}{\partial \bar{\phi}} + \frac{\partial \hat{E}_z}{\partial \bar{z}} = 0 \tag{16d}$$

The remaining two Maxwell's equations are obtained easily from (16) using duality.

The reflection properties of a cylindrical interface between a homogeneous medium and a PML can be affected by considering separately the TE_z and the TM_z cases. In view of (16), the general solution for the z components of the scaled electric field, $\hat{E}_z$, and the scaled magnetic field, $\hat{H}_z$, for the TM_z and TE_z case, respectively, are of the form

$$\hat{E}_z = \sum_\rho \sum_n A_{\rho,n} H_n^{(1,2)}(k_\rho \bar{\rho}) cos(n\bar{\phi}) e^{-jk_z \bar{z}} \tag{17a}$$

$$\hat{H}_z = \sum_\rho \sum_n B_{\rho,n} H_n^{(1,2)}(k_\rho \bar{\rho}) sin(n\bar{\phi}) e^{-jk_z \bar{z}} \tag{17b}$$

where $H_n^{(1)}$, $H_n^{(2)}$ are the nth-order Hankel functions of the first and second kind, respectively, while $k_\rho^2 + k_z^2 = k^2$.

For a truncation boundary along an interface perpendicular to the z axis, it is apparent from (17a,b) that continuity of the tangential fields along the interface, requires continuity of the tangential generalized coordinates along the interface. Hence, $s'_\rho = s'_\phi = 1$. In addition, in order to effect attenuation inside PML, the scaling coefficient along z must be chosen as $s'_z = w = 1 + w''/j\omega$. From (16) it is immediately clear that these conditions are easily satisfied for the following choice of the tensor $[\Lambda]$ inside the PML

$$[\Lambda] = diag\{w, w, \frac{1}{w}\} \tag{18}$$

For a PML perpendicular to the ρ-direction, continuity of the tangential components of the scaled fields along the interface requires continuity of the generalized coordinates, $\bar{\phi}$, $\bar{z}$, which implies $s'_\phi = s'_z = 1$. In addition, the choice $s'_\rho = w$ must be made in order to effect attenuation inside the PML. In view of (16), these choices lead to the following form for the anisotropic tensor inside the PML

$$[\Lambda] = diag\{1, 1, w^2\} \tag{19}$$

and the scaling factors become, $q_\rho = q_\phi = 1$, $q_z = 1/w$.

The last result implies that even though the scaled z components of the fields will be continuous at the interface, the corresponding physical components will not be continuous unless $w = 1$. In other words, unless w is allowed to increase from a value of 1 at the interface in a continuous fashion inside the PML, a reflectionless interface cannot be affected. However, such a continuous, gradual growth of w can not be obtained because of the discrete implementation of PML. Clearly, this is in direct contrast with the result in cartesian coordinates where PMLs could be constructed with any complex constant value of $w = 1 + w''/j\omega$ other than 1.

In order to confirm this theoretical result for cylindrical PML, an unsplit-field FDTD implementation was attempted on a two-dimensional cylindrical grid to validate the possibility that PML can be realized The grid was constructed with increments along the ρ and ϕ of $\Delta\rho = 1.5cm$ and $\Delta\phi = 4^o$, respectively. A z-directed infinite line source at point $(50\Delta\rho, 45\Delta\phi)$ inside a $(70\Delta\rho \times 90\Delta\phi)$-cell domain, Ω_N, was excited by the smooth compact pulse of [9]. The computational domain was truncated with a 16-cell PML backed by a cylindrical perfectly conducting boundary. The benchmark FDTD solution with zero truncation boundary reflection was obtained by simulating the radiation by the aforementioned line source in a much larger domain Ω_L, of outer radius $\rho = 400\Delta\rho$, terminated by a perfectly conducting circular boundary. The time-step for the FDTD simulation was $1.57ps$. Fig. 1 depicts the global error over the domain Ω_N. Despite the rather long, 16-cell PML, the global error increases slowly with time, indicating the presence of reflection from the cylindrical PML.

5. PML in Spherical Coordinates

Following the above procedure, We define the anisotropic tensor $[\Lambda] = diag\{\lambda_\rho, \lambda_\theta, \lambda_\phi\}$ as well a scaling matrix of fields $[Q] = diag\{q_\rho, q_\theta, q_\phi\}$. With the scale factor of cylindrical coordinates, $h_\rho = 1$, $h_\theta = \rho$ and $h_\phi = \rho sin\theta$, the relationship between the scaling coefficients and the elements of the anisotropic tensor is determined and the derivation leads to the following results:

a) Relationship between q's and λ's:

$$\left(\frac{q_\rho}{q_\theta}\right)^2 = \frac{\lambda_\theta}{\lambda_\rho}, \quad \left(\frac{q_\theta}{q_\phi}\right)^2 = \frac{\lambda_\phi}{\lambda_\theta}, \quad \left(\frac{q_\phi}{q_\rho}\right)^2 = \frac{\lambda_\rho}{\lambda_\phi}, \tag{20}$$

b) Generalized coordinate variables:

$$\bar{\rho} = \sqrt{\lambda_\theta \lambda_\phi}\rho = s'_\rho \rho, \quad \bar{\theta} = \sqrt{\frac{\lambda_\rho}{\lambda_\theta}}\theta = s'_\theta \theta, \quad \bar{\phi} = \sqrt{\frac{\lambda_\rho}{\lambda_\phi}}\phi = s'_\phi \phi \tag{21}$$

Also, for a PML perpendicular to the ρ-direction, the continuity of the tangential components of the fields along the interface requires $s'_\theta = s'_\phi = 1$. In addition, s'_ρ should be a complex constant to effect attenuation inside the PML. These choices lead to the following form for the anisotropic tensor inside the PML

$$[\Lambda] = diag\{w, w, w\} \tag{22}$$

and the scaling factors become, $q_\rho = q_\theta = q_\phi = 1$.

In terms of the generalized variables defined the above, Faraday's law and Gauss' law, (9)-(10), for the electric field have the form

$$\frac{1}{\bar{\rho}}\left(\frac{\partial \hat{E}_\phi}{\partial \theta} + \hat{E}_\phi cot\theta - \frac{\partial \hat{E}_\theta}{\partial \phi}\right) = -j\omega\mu\hat{H}_\rho \tag{23a}$$

$$\left(\frac{1}{\bar{\rho}sin\theta}\frac{\partial \hat{E}_\rho}{\partial \phi} - \frac{\partial \hat{E}_\phi}{\partial \bar{\rho}} - \frac{\hat{E}_\phi}{\bar{\rho}}\right) = -j\omega\mu\hat{H}_\theta \tag{23b}$$

$$\frac{1}{\bar{\rho}}\frac{\partial}{\partial \bar{\rho}}(\bar{\rho}\hat{E}_\theta) - \frac{1}{\bar{\rho}}\frac{\partial \hat{E}_\rho}{\partial \theta} = -j\omega\mu\hat{H}_\phi \tag{23c}$$

$$\frac{1}{\bar{\rho}^2 sin\theta}\left[\frac{\partial}{\partial \bar{\rho}}(\bar{\rho}^2 sin\theta\hat{E}_\rho) + \frac{\partial}{\partial \theta}(\bar{\rho}sin\theta\hat{E}_\theta) + \frac{\partial}{\partial \phi}(\bar{\rho}\hat{E}_\phi)\right] = 0 \tag{23d}$$

Clearly, such a medium is the same as the usual isotropic lossy medium. Although some PML requirements are satisfied, it is impossible to realize the reflectionless PML in this kind of lossy medium, since the factor s'_ρ in the expression of fields leads to the reflection of propagating wave at the interface.

6. Conclusions

In conclusion, the generalized theory of the Perfectly Matched Layers has been used to investigate the feasibility of constructing perfectly matched layers in orthogonal curvilinear coordinates. The performance of perfectly matched layers in both cylindrical and spherical coordinates were examined using the mathematical framework of the generalized theory of perfectly matched layers. It was found that cylindrical and spherical perfectly matched layers do not behave exactly like the ones developed for cartesian grids. More specifically, a reflectionless interface cannot be affected in such two coordinate systems unless the perfectly matched layer properties are introduced in a smooth continuous fashion, so that a smooth transition is achieved from the properties of the media inside the computational domain to those of an absorbing layer. This result was validated through a numerical experiment in cylindrical coordinates.

References

[1] J.P. Berenger, "A perfectly matched layer for the absorption of electro-magnetic waves," *J. Computational Physics*, vol. 114, pp. 185–200, 1994.

[2] W.C. Chew and W.H. Weedon, "A 3-D perfectly matched medium from modified Maxwell's equations with stretched coordinates," *Microwave Opt. Technol. Lett.*, vol. 7, no. 13, pp. 599–604, Sept. 1994.

[3] Z.S. Sacks, D.M. Kingsland, R. Lee and J.F. Lee, "A perfectly matched anisotropic absorber for use as an absorbing boundary condition," *IEEE Trans. Antennas Propagat.*, vol. 43, pp. 1460–1463, Dec. 1995.

[4] L. Zhao and A.C. Cangellaris, "GT-PML: Generalized theory of perfectly matched layers and its application to the reflectionless truncation of finite-difference time-domain grids," *IEEE Trans. Microwave Theory Tech.*, vol. 44, no. 12, pp. 2555–2563, Dec. 1996.

[5] J. Maloney, M. Kesler, and G. Smith, "Generalization of PML to cylindrical geometries," *Proc. 13th Annual Rev. of Progress in Applied Computational Electromagnetics*, pp. 900-908, Monterey, CA, March 1997.

[6] W.C. Chew, J.M. Jin, and E. Michielssen, "Complex coordinate system as a generalized absorbing boundary condition," *Microwave Opt. Tech. Lett.*, vol. 15, no. 6, pp. 363-369, 1997.

[7] F.L. Teixeira and W.C. Chew, "Systematic derivation of anisotropic PML absorbing media in cylindrical and spherical coordinates," *IEEE Microwave Guided Wave Lett.*, vol. 7, no. 11, pp. 371-374, Nov. 1997.

[8] P. Collino and P. Monk, "The perfectly matched layer in curvilinear coordinates," *SIAM J. Scientific Computing*, (to appear), 1998.

[9] T.G. Moore, J.G. Blaschak, A Taflove and G.A. Kriegsmann, "Theory and application of radiation boundary operators," *IEEE Trans. Antennas Propagat.*, vol. 36, pp. 1797–1812, Dec. 1988.

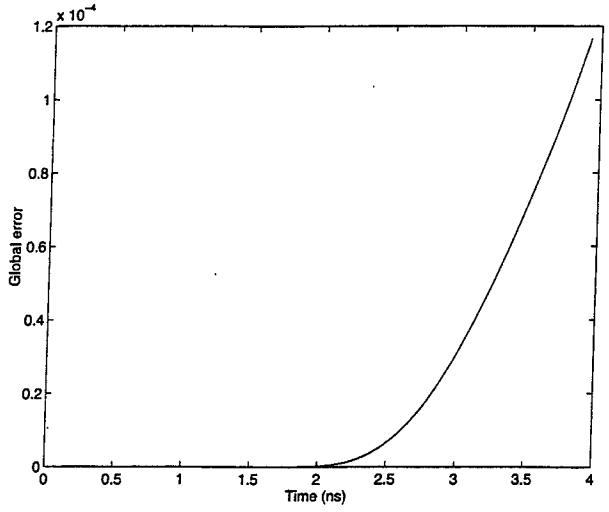

Fig. 1. The global error for the two-dimensional TE_z simulation of the transient radiation of a z-directed line source in a cylindrical domain truncated by a 16-cell cylindrical PML.

The Effect of the Binding Material Permittivity on the Input Impedance of CTHAs

Khaled M ElSherbini
Franz A. Pertl
Robert P.M. Craven
James E. Smith

Center for Industrial Research Applications
Mechanical and Aerospace Engineering
West Virginia University
Morgantown, WV 26506-6106

Abstract

This study discusses the effect of the binding material permittivity on the input impedance of contrawound toroidal helical antennas (CTHAs). Using the finite difference time domain method (fdtd), two types of CTHAs are studied, the core CTHA and the printed circuit board CTHA (PCB-CTHA). The results are compared to a general theoretical analysis of the effect of permittivity on input impedance. The study shows that the effect of permittivity on the input impedance for core CTHAs follows very closely the predicted effect, while the effect on PCB-CTHAs is slightly different from the predicted effect. The difference can be attributed to discontinuities in the fringe fields as evidenced by the ideal behavior observed when covering the CTHA in a block of the binder material.

Introduction

The Contrawound Toroidal Helical Antenna (CTHA) is a patented antenna developed at the Center for Industrial Research Applications (CIRA) of West Virginia University. The antenna essentially consists of two toroidal windings of wire, with opposite pitch, supported by a binding material. The binding material, in addition to holding the antenna together, also plays a significant role in the characteristics of the antenna, namely affecting its input impedance and gain. The parameter of interest is the permittivity of the binding material. In this paper, the theoretically predicted effect is compared to the simulation results for two main types of CTHAs, the toroidal core CTHA and the printed circuit board CTHA (PCB-CTHA).

The core CTHA, shown in Figure 1, consists of two helical windings of wire supported upon a central core. The binding material of the core CTHA is a full block of material. Figure 1 shows three instances of the core CTHA. The first, for clarity, is just the wire windings with no support material. The second shows the CTHA with full core material, and the third is for a core CTHA with a hollow center. All analysis will be conducted on the full block core CTHA.

The PCB-CTHA, on the other hand, as is clear from its name, has the two wire windings in the shape of traces upon a printed circuit board (PCB) and holes filled with conducting material drilled through the PCB. Figure 2 shows two instances of the PCB-CTHA; the first shows the traces alone with no binding material, while the second shows the complete PCB-CTHA.

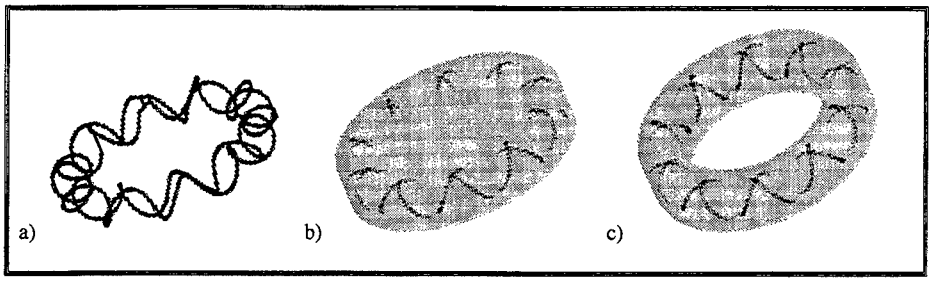

Figure 1 The core CTHA: a) wire only, b) full core, c) hollow core

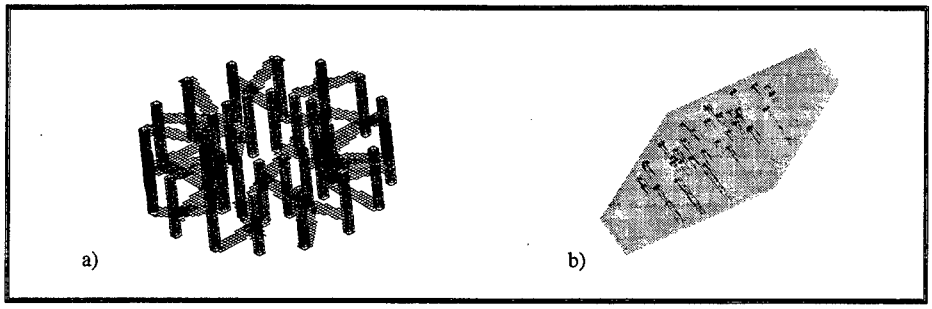

Figure 2 The PCB-CTHA: a) wire only, b) complete CTHA

Resonance and Dielectric

A small antenna such as the CTHA can often be viewed as a lumped circuit. Resonance occurs when the reactive components of the impedance cancel at the particular resonance frequency. For simplicity, the CTHA can be considered as a lumped RLC circuit. For lumped parallel and series RLC circuits, this frequency is given by Equation 1,

$$2 \cdot \pi \cdot f_{res} = 1/\sqrt{L \cdot C}, \qquad (1)$$

where L is the circuit inductance and C is the circuit capacitance. Since the dielectric constant primarily affects electric field storage, it will change the capacitance of the circuit.

The influence of the dielectric on the capacitance can be seen if one considers Equation 2, which gives the capacitance of a perfect (no fringe fields) parallel plate capacitor:

$$C = \frac{A}{d \cdot \varepsilon} \qquad (2)$$

where A is the plate area, d is the seperation distance between the plates, and ε is the dielectric constant.

If Equation 2 is substituted into Equation 1, then the relationship of the resonance frequency to the dielectric becomes apparent. The resonance frequency is related to the dielectric constant via an inverse square; if two constants, a and b, are allowed to account for the fringe fields of a particular CTHA geometry, a similar relation can be expressed as in Equation 3:

$$f_{res_dielectric} \approx \left(\frac{a}{\sqrt{\varepsilon}} + b\right) \cdot f_{res} . \tag{3}$$

From Equation 3, the effect of the dielectric can thus be defined as follows

$$eff = \frac{f_{res_dielectric}}{f_{res}} \approx \left(\frac{a}{\sqrt{\varepsilon}} + b\right) . \tag{4}$$

Numerical Analysis

The numerical code used for this analysis was REMCOM's XFDTD 4.03. This code uses the finite difference time domain method for electromagnetic calculations. The method is a transient marching-in-time approach, in which time is divided into small discrete steps, and the electric and magnetic fields on a fine grid are calculated at each time step. For more details on this method refer to [1].

Core CTHA

A typical core CTHA was modeled using XFDTD. The parameters for this CTHA are shown in Table 1. The relative permittivity ε_r of the model was then varied between 1 and 5 in steps of 0.4. In addition to the cases of ε_r=2 and ε_r=4, 13 simulations were conducted. The first four resonant frequencies for all these simulations were then found and grouped. The effect of the permittivity was then calculated as shown in Equation 4. Table 2 shows the effect of the permittivity on the first four resonance frequencies, the average effect for each permittivity value, and the ideal effect for the case of a=1 and b=0 in Equation 3.

Table 1 Parameters of the core CTHA

Parameters of the core CTHA			
Major Radius	26.67 mm	Feed Type	6
Minor Radius	4.70 mm	Feed Position	Polar
Wire Radius	0.35 mm	Wire Material	PFC
Wraps	10	Cell Size	0.55 mm

Table 2 The effect of permittivity on the first four resonance frequencies for the core CTHA

	ε_r=1.0	ε_r=1.4	ε_r=1.8	ε_r=2.0	ε_r=2.2	ε_r=2.6	ε_r=3.0	ε_r=3.4	ε_r=3.8	ε_r=4.0	ε_r=4.2	ε_r=4.6	ε_r=5.0
Res #	F_{air} (GHz)	eff	eff	eff	eff	eff	eff	eff	eff	eff	eff	eff	eff
1	0.323	0.851	0.752	0.718	0.685	0.627	0.596	0.566	0.530	0.509	0.500	0.476	0.450
2	0.620	0.853	0.757	0.721	0.688	0.636	0.593	0.558	0.529	0.511	0.498	0.477	0.458
3	0.965	0.853	0.760	0.722	0.688	0.636	0.595	0.557	0.527	0.513	0.503	0.480	0.460
4	1.253	0.853	0.757	0.720	0.688	0.635	0.593	0.558	0.529	0.513	0.501	0.479	0.460
Ave	-	0.853	0.757	0.720	0.687	0.634	0.594	0.560	0.529	0.512	0.500	0.478	0.457
theory	-	0.845	0.745	0.707	0.674	0.620	0.577	0.542	0.513	0.500	0.488	0.466	0.447

Using regression, the *a* and *b* factors of Equation 3 were then found for all five sets of data (the four resonant frequencies and the average). The factors for the sixth set of data, the no fringe fields case, are 1 and 0 by definition. Table 3 shows the *a* and *b* factors for all six equations. These six equations were then plotted in Figure 3.

Table 3 Factors obtained from the six sets of data for the core CTHA

	a	b
res1	0.981	0.022
res2	0.983	0.022
res3	0.980	0.025
res4	0.979	0.025
ave	0.981	0.024
theory	1.000	0.000

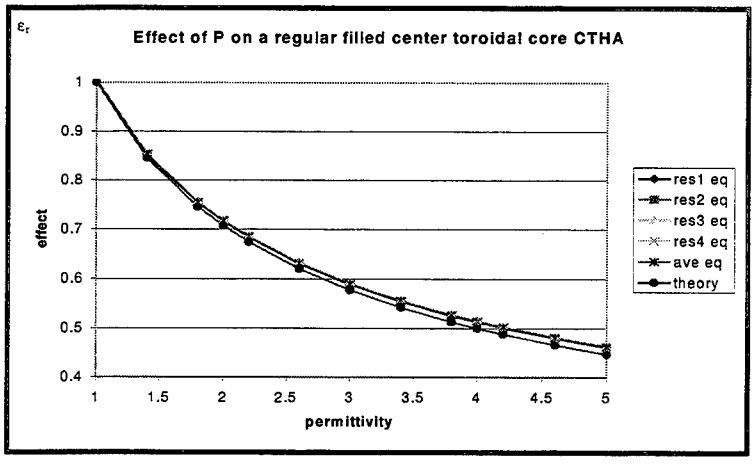

Figure 3 Effect of ε_r on the input impedance of the core CTHA

PCB-CTHA

Table 4 shows the parameters of the first PCB-CTHA modeled for this study. The same procedure described above was followed. Table 5 shows the effect of ε_r on the first 5 resonant frequencies, and Table 6 shows the factors obtained from the seven sets of data. Figure 4 plots the seven equations together.

Table 4 Parameters of the PCB-CTHA

Parameters of the PCB-CTHA			
Length, Width	30.30 mm	Feed Type	6
Height	3.23 mm	Feed Position	Top plane
Wraps	8	Wire Material	PFC

Table 5 The effect of permittivity on the first five resonance frequencies for the PCB-CTHA

	ε_r=1	ε_r=1.5	ε_r=2	ε_r=2.5	ε_r=3	ε_r=3.5	ε_r=4	ε_r=5
Res #	F_{air} (GHz)	eff	eff	eff	eff	eff	eff	eff
1	0.760	0.841	0.740	0.668	0.617	0.574	0.536	0.481
2	1.391	0.841	0.740	0.668	0.615	0.573	0.538	0.484
3	2.327	0.842	0.744	0.675	0.620	0.576	0.542	0.485
4	2.903	0.843	0.742	0.672	0.618	0.575	0.540	0.488
5	3.979	0.845	0.749	0.678	0.623	0.581	0.546	0.488
Ave		0.842	0.743	0.672	0.619	0.576	0.541	0.485
theory	1	0.816	0.707	0.632	0.577	0.535	0.500	0.447

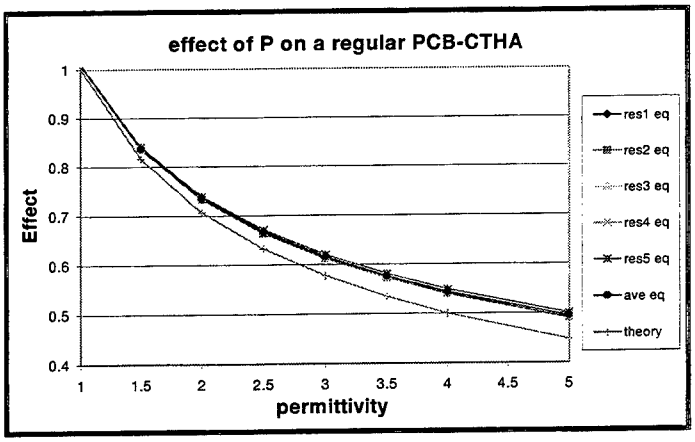

Figure 4 The effect of ε_r on the input impedance of the PCB-CTHA

Table 6 The factors obtained from the seven sets of data for the PCB-CTHA

	a	b
res1	0.937	0.072
res2	0.935	0.073
res3	0.929	0.079
res4	0.929	0.079
res5	0.923	0.087
Ave	0.931	0.078
theory	1	0

Other PCB-CTHAs

Table 6 and Figure 4 above show that the resulting equation for the effect of ε_r on the previous PCB-CTHA is fairly far from the ideal case, where *a* and *b* have an average of 0.931 and 0.078 respectively. To check on this result, three other PCB-CTHAs were modeled, and the same previous analysis was conducted on them. As shown in Table 7, the average factors obtained for these three other PCB-CTHAs gave the similar results as those of the previous case. Figure 5 plots the average for all four PCB-CTHAs and the ideal case together.

Table 7 The average factors a and b for four PCB-CTHAs

	a	b
Geo2	0.932	0.077
Geo3	0.962	0.051
Geo4	0.937	0.063
theory	1	0

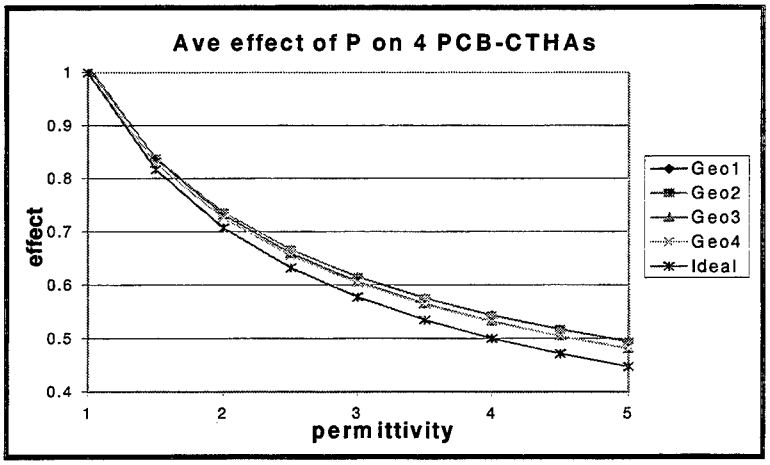

Figure 5 The average effect of ε_r on 4 PCB-CTHAs compared to the ideal effect

Covered PCB-CTHA

The difference obtained for the 4 PCB-CTHAs was suspected to be caused by the fringe fields of this CTHA geometry. To verify that, the first PCB-CTHA modeled above was remodeled, but this time the whole CTHA was covered in a thick layer of dielectric material. In this case, most of the fringe fields for the CTHA will fall within the binding material. Table 8 shows the factors obtained from the first five resonant frequencies of this CTHA, in addition to the average and ideal factors, while Figure 6 plots these 7 equations together.

It is clear that for this geometry the effect of ε_r on the resonant frequencies was almost identical to that predicted by the perfect case of Equation 3.

Table 8 The factors obtained from the seven sets of data for the covered PCB-CTHA

	a	b
res1	0.990	0.008
res2	0.995	0.005
res3	1.002	0.000
res4	0.995	0.005
res5	1.003	0.000
Ave	0.997	0.003
theory	1	0

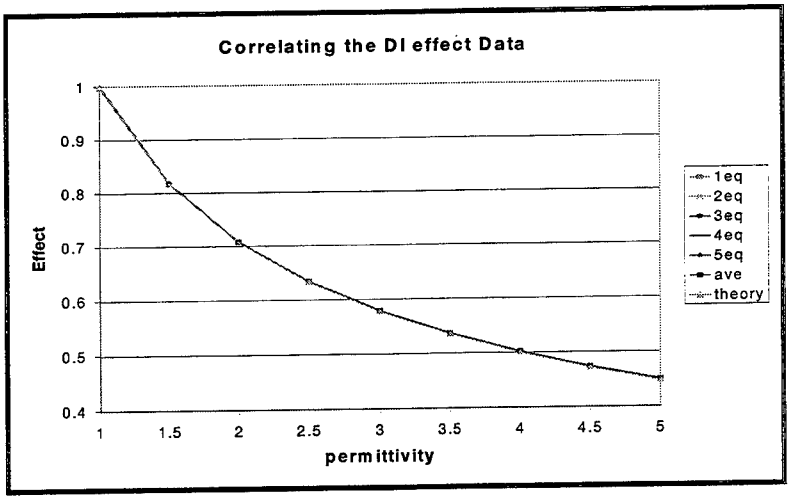

Figure 6 The effect of ε_r on the input impedance of the covered PCB-CTHA

Conclusion

Theory suggests a relationship between resonant frequency and the relative permittivity of a binder material for a CTHA. Modeling verifies this relationship for toroidal core CTHAs and is closely, but not exactly, followed for PCB-CTHAs. The theory that this deviance may be attributed to fringe fields traversing the air/dielectric boundary is supported by the exact match of theory and simulation when a PCB-CTHA is covered by the dielectric (i.e. no air/dielectric boundary within the near field).

The average factors *a* and *b* of Equation 3 for the core CTHA and the covered PCB-CTHA highly agree with the perfect case of equation 3. In both cases *a* was approximately 1 while *b* was approximately 0. On the other hand, all the regular PCB-CTHAs modeled showed a slight shift from the ideal case. For all 4 PCB-CTHAs modeled, *a* was approximately 0.93 while *b* was approximately 0.07.

These results provide a precise tool for predicting the input impedance and resonant frequencies for CTHAs with only the knowledge of the input impedance at one known value of ε_r required. It must be noted that it is assumed that ε_r is constant with respect to frequency and that the dielectric is a simple isotropic material. This study also shows that the fringe fields of the PCB-CTHA have a clear effect on its input impedance, contrary to the core CTHA, where this effect is negligible.

References

1. Kunz, K.S., and Luebbers, R.J. *Finite Difference Time Domain Method For Electromagnetics*, CRC Press, Boca Raton, FL, 1993.
2. Cheng, D.K., *Field and Wave Electromagnetics*, Addison Wesley, Reading, MA, 1992.
3. Johnson, R.C. *Antenna Engineering Handbook*, McGraw Hill, New York, NY, 1993.

Nomenclature

ε	absolute permittivity
ε_r	relative permittivity
a, b	regression coefficients
C	capacitance
CTHA	Contrawound Toroidal Helical Antenna
eff	effect of the dielectric on the resonance frequency
f_{res}	resonance frequency
$f_{res_dielectric}$	resonance frequency for a specific dielectric
L	inductance
PCB-CTHA	Printed Circuit Board CTHA

Numerical Dispersion in Haar-Wavelet Based MRTD Scheme — Comparison between Analytical and Numerical Results

Masafumi Fujii and Wolfgang J.R. Hoefer
Department of Electrical and Computer Engineering
University of Victoria
PO BOX 3055, Victoria, B.C. CANADA V8W 3P6
email: fujii@ece.uvic.ca, FAX:(250)721-5310, phone:(250)721-6511

Abstract

The numerical dispersion relation of a 2-D time-domain Haar wavelet modeling technique has been examined by simple but precise numerical experiments, and the results were compared with analytical results. It was found that, under the presence of boundary conditions, the numerical dispersion is not in agreement with those obtained with analytical formulae; it is better than that of the FDTD method when the discretization is coarse, and it asymptotically converges to that of FDTD as the discretization becomes finer.

I. Introduction

Space-discrete analysis techniques intrinsically have a numerical dispersion error due to the finite-interval sampling of the continuous space. For those techniques, analysis of the numerical dispersion relation is important because it provides a clear insight into the accuracy and the efficiency of the numerical technique.

For the Haar-wavelet based multiresolution time-domain (Haar-MRTD) technique [1], [2], the analytical formula for the numerical dispersion has been reported in [3]. However, it has not been verified by precise numerical experiments. Moreover, since the Haar-MRTD technique employs boundary conditions that enforce the basis functions coupled at the boundaries, it is predicted that the numerical dispersion behaves differently form the analytical formulae under the presence of the boundary conditions.

In this paper, we investigate the numerical dispersion relation of the Haar-MRTD technique by means of numerical experiments and compare the results with the analytical formulae available in the literature.

For the numerical experiments, rectangular waveguide cavity resonators with various aspect ratios were used to realize oblique angle propagation of plane waves. This allows us to obtain dispersion relations for various angles of propagation. The boundaries were all perfect electric conductor (PEC) conditions; this avoids the unknown dispersion error of absorbing boundary conditions. For a waveguide with a fixed aspect ratio, TE_{11} mode oscillation was excited and the resonant frequency was extracted from the time response by Fourier transformation. The error of the resonant frequency was plotted as a function of the normalized wavenumber.

II. Time Iterative Difference Equations

Discretization of Maxwell's curl equations for the TE case involves the E_y, H_x and H_z components. Using Haar scaling and wavelet functions yields time stepping update equations of the following form [2]

$$
\begin{aligned}
{}^{z}_{h}I_{h0} &= {}^{z}_{\bar{h}}I_{h0} + {}^{z}C^{m}_{ik}\left({}^{y}_{0}V_{10} - {}^{y}_{0}V_{00}\right) && (1)\\
{}^{x}_{h}I_{0h} &= {}^{x}_{\bar{h}}I_{0h} + {}^{x}C^{m}_{ik}\left(-{}^{y}_{0}V_{01} + {}^{y}_{0}V_{00}\right) && (2)\\
{}^{y}_{1}V_{00} &= {}^{y}C^{0}_{ik}\,{}^{y}_{0}V_{00} + {}^{y}C^{e}_{ik}\left\{{}^{x}_{h}I_{0h} - {}^{x}_{\bar{h}}I_{0\bar{h}} - \left({}^{z}_{h}I_{h0} - {}^{z}_{\bar{h}}I_{\bar{h}0}\right) - {}^{y}_{h}\hat{I}_{00}\right\} && (3)
\end{aligned}
$$

where the notations for voltage ${}^{y}_{n}V_{ik}$, currents ${}^{x}_{n}I_{ik}$, ${}^{z}_{n}I_{ik}$ and current source ${}^{y}_{n}\hat{I}_{ik}$ are defined as ${}^{y}_{0}V_{10} \equiv {}^{y}_{n}V^{\xi\zeta}_{i+1,k}$, ${}^{z}_{\bar{h}}I_{0h} \equiv {}_{n-1/2}{}^{z}I^{\xi\zeta}_{i,k+1/2}$, ${}^{y}_{h}I_{00} \equiv {}_{n+1/2}{}^{y}I^{\xi\zeta}_{i,k}$, and so on, for the wavelet and scaling functions $\xi, \zeta = \phi, \psi$, and for the time and space indices n, i and k, respectively. The coefficients are given by

$$
\begin{aligned}
{}^{x}C^{m}_{ik} &= -\frac{\Delta t}{\mu_{ik}} \cdot \left[\frac{\Delta x}{\Delta z}\right]_{ik} && (4)\\
{}^{z}C^{m}_{ik} &= -\frac{\Delta t}{\mu_{ik}} \cdot \left[\frac{\Delta z}{\Delta x}\right]_{ik} && (5)\\
{}^{y}C^{0}_{ik} &= \frac{2\epsilon_{ik} - \sigma_{ik}\Delta t}{2\epsilon_{ik} + \sigma_{ik}\Delta t} && (6)\\
{}^{y}C^{e}_{ik} &= \frac{2\Delta t}{2\epsilon_{ik} + \sigma_{ik}\Delta t} \cdot \left[\frac{1}{\Delta x\,\Delta z}\right]_{ik}. && (7)
\end{aligned}
$$

The equations (1)–(3) are computed independently for the individual basis functions $\xi\zeta = \phi\phi$, $\phi\psi$, $\psi\phi$ and $\psi\psi$.

III. Numerical Dispersion Relation

Numerical techniques that involve discrete finite difference grids inherently have a numerical dispersion error. It is caused by the finite dimension of the grid and cannot be ignored when the wavelength is comparable to the unit cell size. An analytical dispersion relation is derived by substituting a time-harmonic trial solution in the finite difference form of Maxwell equations [4]. The dispersion error is a function of the number of cells per wavelength, the angle of propagation and the Courant stability factor defined by

$$
s = c\,\Delta t/\Delta l \qquad (8)
$$

where c is the speed of light, Δt the time step and Δl the spatial grid interval.

A. Analytical formula

The analytical dispersion relation for the conventional FDTD algorithm in the case of two space dimensions is [4]

$$
\left\{\frac{1}{c\,\Delta t}\sin\left(\frac{\omega\Delta t}{2}\right)\right\}^2 = \left\{\frac{1}{\Delta x}\sin\left(\frac{k_x\Delta x}{2}\right)\right\}^2 + \left\{\frac{1}{\Delta z}\sin\left(\frac{k_z\Delta z}{2}\right)\right\}^2 \qquad (9)
$$

while the dispersion relation for the Haar-MRTD technique is given in [3] as

$$\left\{\frac{1}{c\,\Delta t}\sin\left(\frac{\omega\Delta t}{2}\right)\right\}^2 = \left\{\frac{2}{\Delta x}\sin\left(\frac{k_x\Delta x}{4}\right)\right\}^2 + \left\{\frac{2}{\Delta z}\sin\left(\frac{k_z\Delta z}{4}\right)\right\}^2 . \tag{10}$$

These analytical dispersion relations are shown in Fig.1 for two stability factors $s = 0.9/\sqrt{2}$ and $0.4/\sqrt{2}$ and two directions of propagation $\alpha = 45°$ and $90°$ (identical to $0°$). The grids were square $\Delta x = \Delta z = \Delta l$. The dispersion relation for the Haar-MRTD technique is in general superior to that of the conventional FDTD method. The dispersion relation for a plane wave $\omega = c\,k$ leads to the ideal dispersion relation for a certain number of Δt and Δl as

$$\Omega = \chi\, s\ , \tag{11}$$

where Ω $(= \omega\,\Delta t)$ and χ $(= k\,\Delta l)$ denote the normalized angular frequency and the normalized wavenumber, respectively, and s the stability factor (8).

B. Numerical Experiments

The numerical dispersion relation was tested by analyzing the TE_{11} mode resonance in rectangular cavities.

The resonant frequency of the TE_{11} mode in a rectangular cavity of width a and length b shown in Fig. 2 is given by

$$f_r = c_0\sqrt{\left(\frac{1}{2a}\right)^2 + \left(\frac{1}{2b}\right)^2} \tag{12}$$

and the wavenumber

$$k = \sqrt{k_x^2 + k_z^2} = \sqrt{\left(\frac{\pi}{a}\right)^2 + \left(\frac{\pi}{b}\right)^2} . \tag{13}$$

In the cavity with TE_{11} mode oscillation, the field can be considered as the superposition of plane waves propagating at the angle of

$$\theta = \arctan\frac{b}{a} \tag{14}$$

with respect to the main coordinate axis. Therefore, by testing resonances in various aspect ratios of rectangular cavities, one can experimentally obtain the numerical dispersion relation as a function of the angle of propagation. The testing procedures were as follows: (i) fix the propagation constant k by (13), and the angle of propagation θ by (14), then (ii) perform numerical analysis and obtain resonant frequency f_r from the time response by Fourier transformation, and finally, (iii) plot the frequency error $(\Omega - \chi s)/(\chi s)$ $(\Omega = 2\pi f_r \Delta t)$ as a function of the normalized wavenumber χ $(= k\Delta l)$.

The angle of propagation of $45°$ $(a = 1, b = 1)$, $63°$ $(a = 1, b = 2)$, $78°$ $(a = 1, b = 5)$ and $84°$ $(a = 1, b = 10)$ were investigated and compared to the analytical solution of the dispersion equations in Fig. 3. Because of the location of the PEC boundaries that are shifted by quarter cell size from the grid lines, the angles of propagation cannot be exactly identical for the different discretizations; they have a tolerance of approximately 1%, but the computational results are not sensitive to this tolerance.

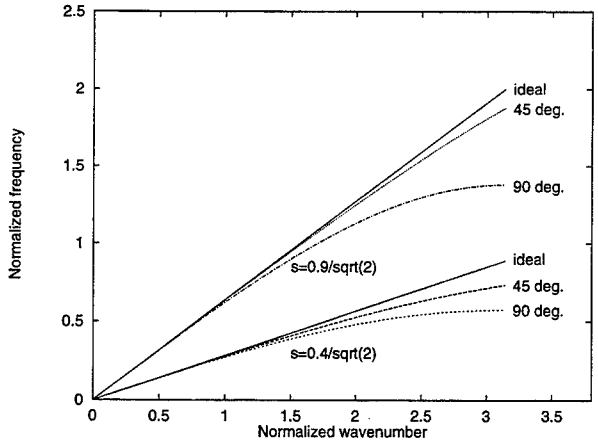

(a) FDTD

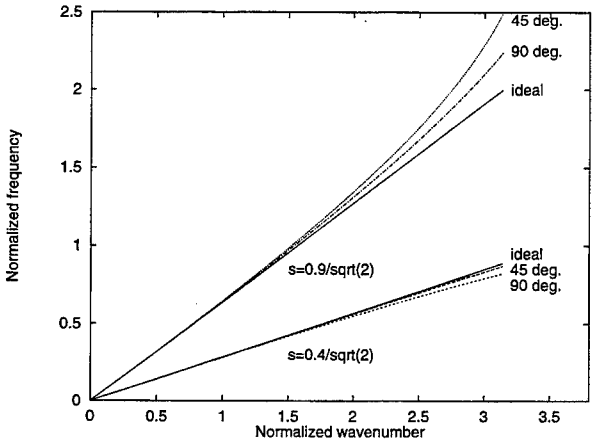

(b) Haar-MRTD

Fig. 1. Analytical dispersion relations for (a) 2-D FDTD [4], and (b) Haar-MRTD techniques [3]. Normalized angular frequency $\Omega = \omega\Delta t$ is plotted as a function of normalized wavenumber $\chi = k\Delta l$.

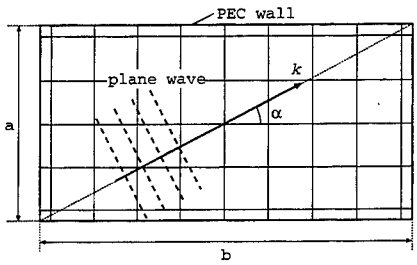

Fig. 2. A top view of the rectangular cavity resonator for the numerical experiments. α denotes the angle of propagation, and k the propagation constant of the plane wave. Thin lines represent Yee's grid lines, PEC walls are located at a quarter cell size away from the grid lines.

It is shown in these figures that, in the limit of infinitely small grids, the experimentally obtained dispersion curves agree with those of the analytical dispersion relation of the FDTD method, while for coarser grids, the Haar-MRTD technique is less dispersive than the conventional FDTD.

It should be mentioned here that the analytical dispersion relation of (10) shown in Fig.1 is not in agreement with the dispersion relations obtained experimentally (shown in Fig.3). The dispersion of the Haar-MRTD technique should obviously follow that of FDTD in the limit of fine grids when the normalized wavenumber tends to zero. As the grids become coarser, the influence of the boundary conditions on the experimental results becomes apparent. For coarse grids (largest normalized-wavenumber in the plots), the dispersion relation changes abruptly because the opposite sides of the PEC boundaries approach and cause mutual interaction.

IV. Conclusions

The numerical dispersion relation of the time-domain Haar-wavelet modeling technique was investigated with simple but precise numerical experiments. The dispersion relation that was obtained by numerically analyzing the TE_{11} mode in rectangular cavities suggests results that are similar to those obtained with FDTD method; the numerical dispersion of the Haar-MRTD technique is better than that of the conventional FDTD method when coarser grids are incorporated, and it asymptotically converges to that of FDTD as the discretization becomes finer.

References

[1] K.Goverdhanam, L.P.B.Katehi, and A.Cangellaris, "Application of multiresolution based FDTD multigrid", *1997 IEEE MTT-S Int. Microwave Symposium Digest*, pp. 333–336.

[2] M.Fujii and W.J.R.Hoefer, "Formulation of a Haar-wavelet-based multi-resolution analysis similar to the 3-D FDTD method", *1998 IEEE MTT-S Int. Microwave Symposium Digest*, 1998.

[3] K.Goverdhanam, E.Tentzeris, M.Krumpholz, and L.P.B.Katehi, "An FDTD multigrid based on multiresolution analysis", *Proc. IEEE Antennas and Propagation Society Int. Symposium 1996*, pp. 352–355.

[4] A.Taflove, *Computational Electrodynamics The Finite-Difference Time-Domain Method*, Artech House Publishers, 1995.

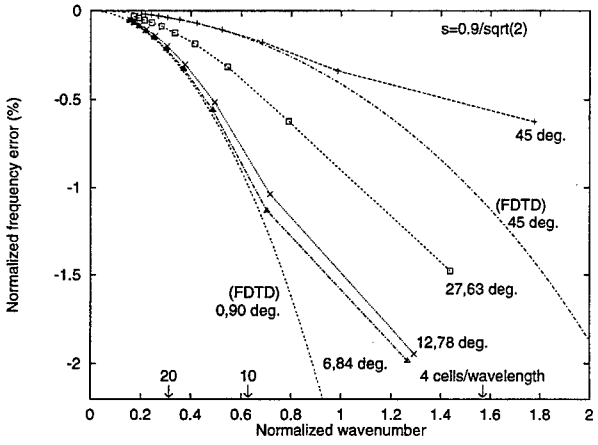

(a) stability factor $s = 0.9/\sqrt{2}$

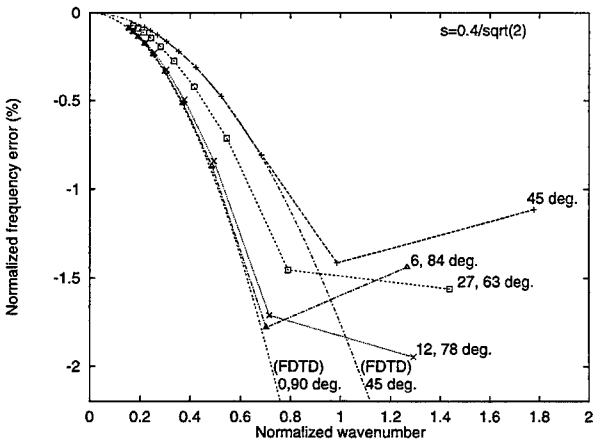

(b) $s = 0.4/\sqrt{2}$

Fig. 3. Experimentally obtained numerical dispersion relations for 2-D Haar-MRTD modeling. Normalized frequency error $(\Omega - \chi s)/(\chi s)$ is plotted as a function of normalized wavenumber $\chi = k\,\Delta l$.

Comparison between Discontinuous Galerkin method and a Finite Volume Time-Domain method in solving Maxwell equations, in heteregeneous media

M. REMAKI †- L. FEZOUI ‡
†INRIA Sophia-Antipolis, BP 93, 06 902 Sophia-Antipolis Cedex (France),
mremaki@sophia.inria.fr, tel: (33).4.92.38.76.12, fax: (33).4.92.38.77.40
‡INRIA Sophia-Antipolis, BP 93, 06 902 Sophia-Antipolis Cedex (France),
fezoui@sophia.inria.fr, tel: (33).4.92.38.79.15 fax: (33).4.92.38.77.40

Abstract:

The aim of this study is to develop and compare a Finite Element method called the Discontinuous Galerkin method and a Finite Volume method, solving Maxwell equations in heterogeneous media. The comparisons are based on the CPU time, and the quality of the solutions. The first advantage of these two methods is their flexibility in treating complicated geometries. The second advantage is their ability to capture the discontinuities of the electromagnetic fields through different media, without producing spurious oscillations. We describe in this paper the above mentioned methods and give numerical comparisons.

1 Introduction:

These both methods are well suited for handling complex geometries, therefore we use unstructured meshes that conform to these geometries. Moreover, they make use of the volume integral form of the Maxwell equations, which provides a very natural way to verify the transmission conditions at the material interfaces. Owing to these properties, we can treat difficult problems, such computing a scattered wave across complex objects.
The Maxwell equations are given by :

$$\begin{cases} \dfrac{\partial \mathbf{B}}{\partial t} + rot(\mathbf{E}) = 0 \\ \dfrac{\partial \mathbf{D}}{\partial t} - rot(\mathbf{H}) = -\mathbf{J} \\ div(\mathbf{D}) = \rho \\ div(\mathbf{B}) = 0 \end{cases} \tag{1}$$

where $\mathbf{E}$ and $\mathbf{H}$ are the electric and magnetic fields respectively, and $\mathbf{D}$ and $\mathbf{B}$ are the electric and magnetic inductions respectively . $\mathbf{J}$ is the current density and ρ is the charge density. The electric permittivity $\varepsilon = \varepsilon(x, y, z)$, and the magnetic permeability $\mu = \mu(x, y, z)$ are piecewise constant functions. In the linear and isotropic case, we have the following relationships :

$$\mathbf{B} = \mu \mathbf{H}$$
$$\mathbf{D} = \varepsilon \mathbf{E}$$

We need the conservative form of the system (1) to construct the numerical schemes, it is given by :

$$\frac{\partial \mathbf{Q}}{\partial t} + div\mathbf{F}(\mathbf{Q}) = -\mathbf{J} \tag{2}$$

with $\mathbf{Q} = {}^t(\mathbf{B}, \mathbf{D})$, and $\mathbb{F} = (\mathbf{F_1}, \mathbf{F_1}, \mathbf{F_3})$, with

$$\mathbf{F_1}(\mathbf{Q}) = \begin{Bmatrix} 0 \\ -D_z/\varepsilon \\ D_y/\varepsilon \\ 0 \\ B_z/\mu \\ -B_y/\mu \end{Bmatrix}, \quad \mathbf{F_2}(\mathbf{Q}) = \begin{Bmatrix} D_z/\varepsilon \\ 0 \\ -D_x/\varepsilon \\ -B_z/\mu \\ 0 \\ B_x/\mu \end{Bmatrix}, \quad \mathbf{F_3}(\mathbf{Q}) = \begin{Bmatrix} -D_y/\varepsilon \\ D_x/\varepsilon \\ 0 \\ B_y/\mu \\ -B_x/\mu \\ 0 \end{Bmatrix},$$

Because of the truncated scattered wave domain, we consider an artificial boundary which requires that any outgoing wave disappear without reflection. Thus, we consider two types of boundary conditions:
1-The metallic boundary condition given by $\vec{n} \wedge \mathbf{E} = 0$.
2- The Silver-Müller absorbing condition on the artificial boundary given by:
$\vec{n} \wedge \mathbf{E} = -\sqrt{\mu/\varepsilon}.\vec{n} \wedge (\vec{n} \wedge \mathbf{H})$

2 Development of the numerical schemes:

2.1 Finite Volume Scheme:

The approach consists in integrating the conservative form (2) over "control volumes". We consider a conforming unstructured mesh made up of triangles T_i with centroids G_i. We use as control volumes, the triangles (figure 1). One of the advantages is that the triangles are the most appropriate cells to define the interfaces between different media, and to take into account the current sheets, especially in the heterogeneous materials case ([3], [4]).

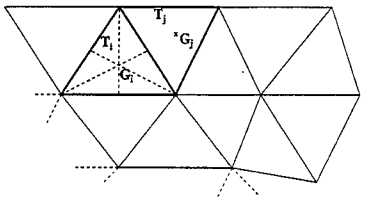

Figure 1: Control volume

Using a Green's formula and an approximation of the interface integrals, yields the following result:

$$|T_i|(\mathbf{Q})_i + \sum_{j=1}^{3} \Phi_{ij} + \text{boundary terms} = -\mathbf{J}_i, \tag{3}$$

$$\Phi_{ij} = \Phi(Q_i, Q_j) \simeq \int_{\partial T_i \cap \partial T_j} \mathbb{F}.n_{ij}$$

where Φ_{ij} is an approximation of the integral over the interfaces, depending on both values Q_i and Q_j. The first value is the approximate solution into the interior of the element, and the second one is the approximate solution outside the element. n_{ij} is the outward unit normal to $\partial Ti \cap \partial T_j$. To obtain a high order space scheme, we use the MUSCL [5] technique: we replace the arguments of the flux function Φ_{ij} by linear reconstruction functions L_{ij} given by the following equation :

$$\mathbf{L}_{ij} = \mathbf{Q}_i + (1 - 2\beta)\frac{(\mathbf{Q}_j - \mathbf{Q}_i)}{2} + 2\beta\bar{\nabla}\mathbf{Q}_{T_i}.\mathbf{S}_{ij}, \quad \beta \in [0, 1]$$

$\mathbf{S_{ij}}$ is the distance between the mass center G_i of T_i and the mid-point of the edge $\partial T_i \cap \partial T_j$. We have to evaluate the discrete gradient $\bar{\nabla}\mathbf{Q}_{T_i}$ on each element T_i.

Finite Volume Gradient

We approach the gradient by the following formula :

$$\vec{\nabla}\mathbf{Q}_{T_i} = \frac{1}{|T_i|}\sum_{j=1}^{3}\int_{\partial T_i \cap \partial T_j} \mathbf{Q} n_{ij} \simeq \sum_{j=1}^{3}\frac{\mathbf{Q}_i + \mathbf{Q}_j}{2}\eta_{ij}, \qquad \eta_{ij} = \int_{\partial T_i \cap \partial T_j} n_{ij}$$

Treatment of the metallic boundary condition

In order to compute a value of a numerical flux at the metallic boundary, we use a local exact resolution of the system taking into account the condition $\vec{n} \wedge \mathbf{E} = 0$.

Time scheme

In order to obtain a third order accurate scheme in time, we use a Runge-Kutta scheme with three steps.
We present here as an example, the computed result for the magnetic field of an heterogeneous circular dielectric cylinder scatterer (figure 2).

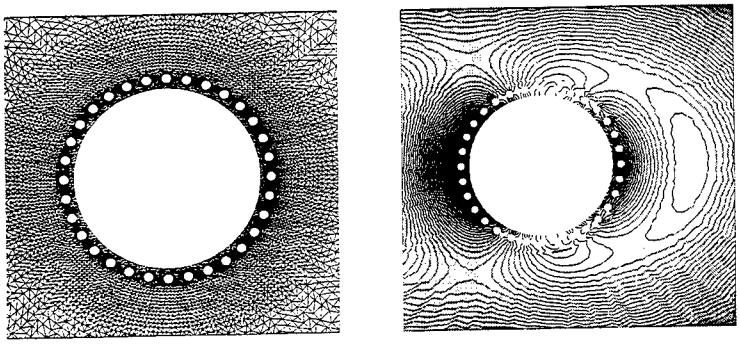

Figure 2: A zoom of the mesh of the cylinder at left and the scattered magnetic wave across a dielectrical material at right.

2.2 Finite Element scheme (Discontinuous Galerkin method):

In this section, we extend the Discontinuous Galerkin method [1] to solve the Maxwell equations, in heterogeneous media. This method is based on the choice of a local basis functions and quadrature rules. Note that the functions are discontinuous in the space of discretization. We propose to construct a second order scheme, therefore we use polynomials of degree 1 as basis functions [2]. In order to verify the transmission conditions between different media, we use a Godunov scheme to compute the numerical flux. Let the solution domain Ω be divided into a set of triangles T_i. The solution in each element T_i will be possibly discontinuous across element boundaries.
We first define the space of discretization V_h^1 by:

$$V_h^1 = \{v \in V / v|_{T_i} \in P^1, i = 1, ...M\}$$

where

$$V = L^2(\Omega \times [0, \infty])$$

P^1 is the set of polynomials of degree 1. To construct the approximate solution $\mathbf{Q_h} \in \mathbf{V_h^1}$,
we use the weak solution defined as follows :

$$\frac{d}{dt}\int_{T_i} \mathbf{Q}(X,t)\varphi_k(X)dT_i + \sum_{j\in N(i)} \int_{\partial Ti \cap \partial T_j} \mathbf{IF}(\mathbf{Q}(X,t)).n_{ij}\varphi_k(X)d\sigma$$

$$- \int_{T_i} \mathbf{IF}(\mathbf{Q}(X,t))\nabla\varphi_k(X)dT_i = -\int_{T_i} \mathbf{j}(X,t)\varphi_k(X)dT_i$$

N(i) denotes the number of neighbours of the triangle T_i, n_{ij} the outward unit normal to the edge $\partial Ti \cap \partial T_j$, and $\varphi_k, k = 1, ..3$ are the basis functions. each φ_k takes the value 1 at the mid-point m_k of the k-th edge, and 0 at the others mid-points of the triangle's edges.
We first approach $\mathbf{IF}(\mathbf{Q}(X,t)).n_{ij}$ by a numerical flux, and then we replace each integral by a Gauss quadrature rule in order to obtain a second order in space scheme. After inverting the mass matrix, which is diagonal since the basis functions are orthogonal, we get the **ODE** :

$$\frac{d}{dt}\mathbf{Q}_h = L_h(\mathbf{Q}_h, \mathbf{Q}_h^b)$$

We use for the time discretization, a Runge-Kutta scheme with two steps given by :

$$\begin{cases} \mathbf{Q}_h^0 = \mathbf{Q}^n \ , \\ \mathbf{Q}_h^l = \sum_{e=0}^{l-1} \alpha_{le}\mathbf{Q}_h^e + \beta_{le}\Delta t L_h(\mathbf{Q}_h^e, \mathbf{Q}_h^b(t + d_e\Delta t)) \quad l = 1, 2 \ , \\ \mathbf{Q}_h^{n+1} = \mathbf{Q}_h^2 \ . \end{cases}$$

$\mathbf{Q}_h^b$ is the boundary condition, The parameters are given by :

$\alpha_{10} = 1$	$\alpha_{20} = \frac{1}{2}$	$\alpha_{21} = \frac{1}{2}$
$\beta_{10} = 0$	$\beta_{20} = 0$	$\beta_{21} = \frac{1}{2}$
$d_0 = 0$	$d_1 = 1$	

Table 1: parameters of the Runge-Kutta scheme

We give here some numerical results obtained with the Discontinuous Galerkin method. The figure (3) is a scattered electric wave across an heterogeneous cylinder section, and the figure (4) is the electric field produced by a sheet of current over the cross section of a rectangular waveguide.

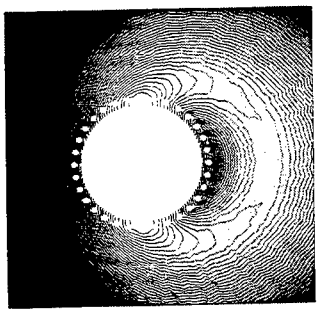

Figure 3: Scattered electric wave across a dielectrical material.

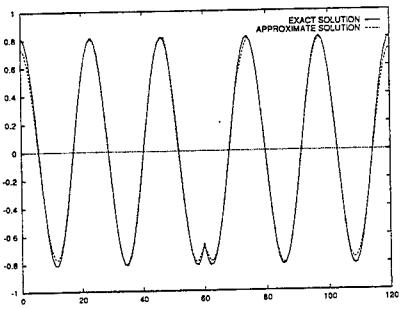

Figure 4: Electric wave in a rectangular waveguide

We recall that the aim of this study is to compare the two methods. We present in this section two numerical tests. The first test consists in computing the evolution of a mode of resonance in a cavity, and we give the time of computation for the two methods (table 2). We also give the comparison of the energies (figure 6). We use two different meshes for the two methods in order to have the same number of degrees of freedom. It gives the same resolution for ten wavelengths (figure 5). The numerical experiments are run on a **DEC** machine (Alpha $400-233$ MHZ, 5 Specfp 95) .

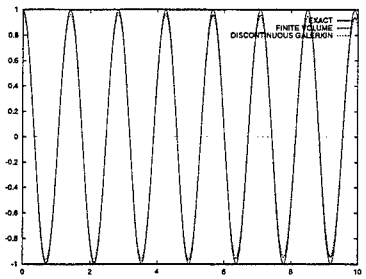

Figure 5: Time evolution of the resonance mode (electric field)

method	Finite Volume	Discontinuous Galerkin
CFL	0.7	0.2
time/iteration (s)	1	2.98
global time(s)	70	220

Table 2: Time of computation (CPU).

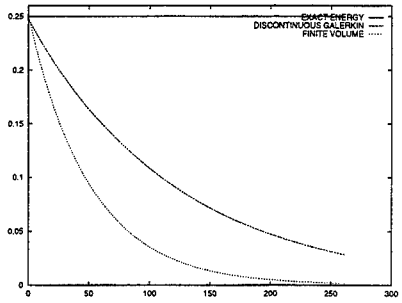

Figure 6: A comparison of energy

(Figure 6) shows that the Discontinuous Galerkin method diffuse less than the Finite Volume one, however they both tend to zero.
The second test consists in a qualitative analysis in an heterogeneous case. It represents a propagation of a pulse into a material composed of vacuum at right of $x = 0$ and a glass at the left (figure 7). We notice that both methods give a good approximate solution.

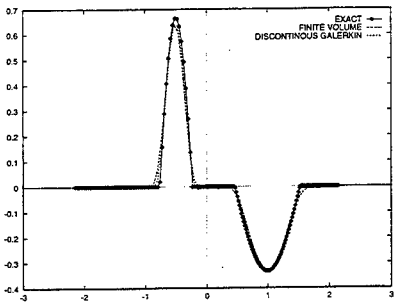

Figure 7: Pulse propagation into an heterogeneous medium

3 Conclusion

We have presented in this paper two methods for solving the Maxwell system, with discontinuous coefficients. We can notice that the use of the triangles as integration volumes facilitates the treatment of problems with complex geometries. We can also remark, that the transmission conditions are verified in the heterogeneous case, by both methods. Numerical results are shown, and we deduce that the Finite Volume method gives better CPU performance than the Discontinuous Galerkin one, to obtain the same quality results.

References

[1] *The Runge-Kutta Discontinous Galerkin Method for Conservation laws V*, Multidimensional systems. J.Comp.Phys, 141, 199 – 224, 1998.

[2] B.Cockburn, C.W.Shu, *The Runge-Kutta local projection P^1-discontinuous-Galerkin finite element method for scalar conservation laws*, IMA Preprint Series 388, University of Minnesota, 1988.

[3] M.Remaki, L.Fézoui, F.Poupaud, *Un nouveau schéma de type volumes finis appliqué aux équations de Maxwell en milieu hétérogène*, rapport de recherche INRIA no 3351, january 1998.

[4] M.Remaki, L.Fézoui, *Une méthode de Galerkin Discontinu pour la résolution des équations de Maxwell en milieu hétérogène*, rapport de recherche INRIA no 3501, september 1998.

[5] VAN LEER B., *Towards the ultimate conservative difference schemes V: a second order sequel to Godunov's method*, J. Comp. Phy., Vol 32, 1979.

A controllability method for the calculation of the time periodic solutions of the Vlasov-Maxwell system

Mihai BOSTAN
INRIA 2004 route des Lucioles, BP 93, 06902 Sophia-Antipolis Cedex (France),
mbostan@sophia.inria.fr, tel: (33)04.92.38.76.04, fax: (33)04.92.38.77.40

Introduction

The master system of equations of collision-less plasma physics is the Vlasov-Maxwell system. The main result in this field has been obtained in 1989 by R.J.DiPerna and P.L.Lions [2]. They prove existence of global weak solutions for the Cauchy problem with arbitrary data. The situation is much better for the Vlasov-Poisson system. This system is obtained for the first one by neglecting the magnetic field. However for applications like vacuum diodes, tube discharges, cold plasma, solar wind, satellite ionization, thrusters, etc... boundary conditions have to be taken into account. Periodic regimes are particularly important. One strong motivation to study such solutions is the great difficulty to compute it numerically. In this paper we introduce the Limit Absorption Method (LAM) which has been developed by the authors in [1] to obtain numerical periodic solutions of PDE. The principle of this method was proved on a reduced 1D model. We apply then this methodology to the electro-magnetic scattering problems and also to the transport of charged particles in electro-magnetic field.

1 A reduced 1D model

In this section we study the convergence to the periodic regimes for the solutions of an ODE with a periodic source term. The main tool consist of a new controllability method, the *Limit Absorption Method* (LAM). Consider the model ODE :

$$\frac{dx}{dt} + \varepsilon \cdot x(t) = f(t)\ ,\ t > 0 \tag{1}$$

with the initial data $x(0) = x_0$, where f is a T periodic function in time. It is easy to see that the exact solution of this problem is given by :

$$x(t) = x_0 \cdot e^{-\varepsilon t} + \int_0^t f(s) \cdot e^{-\varepsilon(t-s)} ds. \tag{2}$$

Thus the condition of periodicity $x(0) = x(T)$ implies :

$$x_0 = \frac{\int_0^T f(s) \cdot e^{-\varepsilon(T-s)} ds}{1 - e^{-\varepsilon T}}. \tag{3}$$

and therefore, the periodic solution is given by the formula :

$$x_\infty(t) = \frac{\int_0^T f(s) \cdot e^{-\varepsilon(T-s)} ds}{1 - e^{-\varepsilon T}} \cdot e^{-\varepsilon t} + \int_0^t f(s) \cdot e^{-\varepsilon(t-s)} ds. \tag{4}$$

Now it is clear to see that if (3) is not satisfied, reaching a η-approximation of the periodic regime x_∞ requires a time :

$$t^* \approx O(\frac{1}{\varepsilon} \log(\frac{1}{\eta})). \tag{5}$$

For small values of the parameter ε, this time become very long, which implies an important amount of calculus. In order to accelerate the convergence to the periodic states, an absorption term $\lambda \cdot x(t)$ was introduced :

$$\lambda \cdot x(t) + \frac{dx}{dt} + \varepsilon \cdot x(t) = f(t)\ ,\ t > 0. \tag{6}$$

This time, we get a η-convergence time :

$$t^* \approx O(\frac{1}{\varepsilon + \lambda} \log(\frac{1}{\eta})) < O(\frac{1}{\lambda} \log(\frac{1}{\eta})). \tag{7}$$

In contrast to (5), the time given by (7) is independent in respect to the parameter ε. However, the solution obtained from the modified equation (6) doesn't verify (1). The idea consist of replacing the absorption parameter $\lambda > 0$ by a sequence $(\lambda_n)_{n\geq 0}$ which converges to 0. We have proved the following proposition:

Proposition 1 *Let $(\lambda_n)_{n\geq 0}$ be a sequence of positive real numbers which verifies:*

$$\begin{array}{ll} (i) & \lim_{n\to\infty} \lambda_n = 0, \\ (ii) & \Sigma_{n\geq 0} \lambda_n < \infty, \end{array} \tag{8}$$

and x_∞ be the periodic solution (4) of the problem (1). Then the equation:

$$\lambda(t) \cdot x(t) + \frac{dx}{dt} + \varepsilon \cdot x(t) = f(t)\ ,\ t > 0, \tag{9}$$

with the initial condition:

$$x(0) = x_0,$$

where $f \in L^\infty$ is a T periodic function and $\lambda(t) = \lambda_n$, $t \in [nT, (n+1)T[$, $n \geq 0$ has a unique solution which converges to the periodic state :

$$\lim_{n\to\infty} \| x(nT + \cdot) - x_\infty(\cdot) \|_{L^\infty(0,T)} = 0. \tag{10}$$

We want to apply *Proposition 1* for a particular choice of $(\lambda_n)_{n\geq 0}$. We have the following proposition:

Proposition 2 *With the same notations as in Proposition 1, we assume that $f \in L^\infty$ is a periodic function which verifies:*

$$\int_0^T f(s)ds = 0,$$

and that the sequence $(\lambda_n)_{n\geq 0}$ is given by:

$$\begin{array}{rcl} \lambda_0 & = & 1, \\ \lambda_{n+1} & = & \lambda_n, \ \ if\ \ |x_{n+1} - x_n| > \eta,\ n \geq 0, \\ \lambda_{n+1} & = & \lambda_n e^{-T}, \ \ if\ \ |x_{n+1} - x_n| \leq \eta,\ n \geq 0. \end{array} \tag{11}$$

Then, the convergence time to a η-approximation of the periodic state is given by:

$$t^* \approx O(\frac{1}{\sqrt{\eta}} \cdot \log(\frac{1}{\eta})). \tag{12}$$

Remark 1 *The time evolution of the parameter λ can be given also by an ODE :*

$$\frac{d\lambda}{dt} + \lambda(t) \cdot \chi_{[-\eta,\eta]}(x_n - x_{n-1}) = 0,\ t \in [nT, (n+1)T[, \tag{13}$$

where $\chi_{[-\eta,\eta]}$ is the characteristic function of $[-\eta, \eta]$ and we get the same result as in Proposition 2.

Generally, the resolution of the problem (1) is performed using the system :

$$\lambda(t) \cdot x(t) + \frac{dx}{dt} + \varepsilon \cdot x(t) = f(t),\ t > 0,$$
$$\frac{d\lambda}{dt} + \chi_{[-\eta,\eta]}(\mathcal{C}(x))\lambda(t) = 0,\ t > 0, \tag{14}$$

with the initial conditions :

$$x(0) = x_0,$$
$$\lambda(0) = \lambda_0,$$

where $\mathcal{C}$ denotes a criterion of periodicity. This method is called the *Limit Absorption Method* (LAM). It is easy to see that if $\lambda_0 = 0$, then $\lambda(t) = 0, \forall t > 0$ and therefore the solution of (14) is exactly the solution of (1). This method is called the *Classical Method* (CM).
We consider a periodic term source $f(t) = \cos(\omega t)$. The periodic state of (1) is given by :

$$x_\infty(t) = (\varepsilon cos(\omega t) + \omega sin(\omega t))/(\varepsilon^2 + \omega^2),\ t > 0. \tag{15}$$

We compare the numerical solutions obtained for $\varepsilon = 0.01$ and $\varepsilon = 0.0001$, using the two methods. In the first

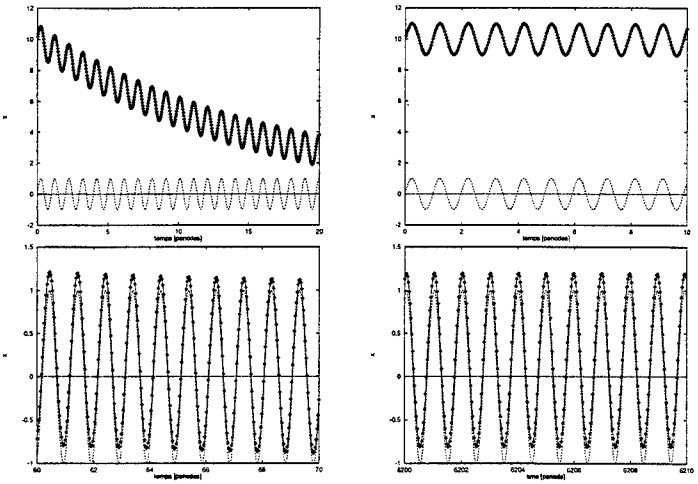

Figure 1: *Convergence to the periodic states by the Classical Method*
(left : $\varepsilon = 0.01$ / right : $\varepsilon = 0.0001$)

case ($\varepsilon = 0.01$) a good approximation of the periodic state is obtained after 70 periods using the (CM) and after 7 periods using the (LAM). In the second case ($\varepsilon = 0.0001$), a very long time is required to approximate the periodic regime using the (CM) (about 6000 periods), whereas, using the (LAM), a good approximation is obtained only after 7 periods.

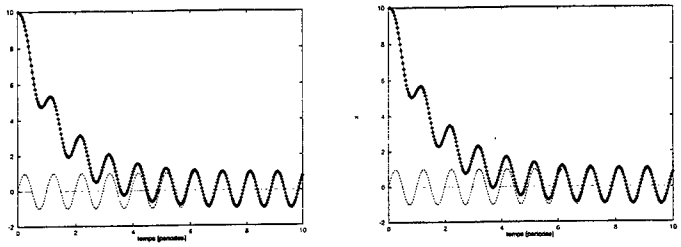

Figure 2: *Convergence to the periodic states by the LAM*
(left : $\varepsilon = 0.01$ / right : $\varepsilon = 0.0001$)

2 Application of the LAM to the Maxwell system

We are concerned now with the resolution of the scattering problems for harmonic planar waves by two dimensional purely reflecting non-convex obstacles. Numerical results obtained by the two methods introduced above are compared. Using the methodology of the previous section, the Maxwell equations write :

$$\begin{cases} \lambda(t)\vec{H} + \mu_0 \dfrac{\partial \vec{H}}{\partial t} + rot(\vec{E}) = 0, \\ \\ \lambda(t)\vec{E} + \varepsilon_0 \dfrac{\partial \vec{E}}{\partial t} - rot(\vec{H}) = 0, \end{cases} \tag{16}$$

where (E, H) denotes the electro-magnetic field, ε_0 and μ_0 are respectively the permittivity and the permeability of the vacuum and Ω is the computational domain. Boundary conditions are imposed on $\Gamma = \Gamma_{met} \cup \Gamma_\infty$ where Γ_{met}, Γ_∞ are respectively the metallic and artificial boundaries. The time evolution of the absorption parameter $\lambda(t)$ is given by the control equation:

$$\frac{d\lambda}{dt} + \chi_{[-\eta,\eta]}(\mathcal{C}(H,E)) \cdot \lambda(t) = 0, \; t > 0, \tag{17}$$

where $\mathcal{C}$ represents a criterion of periodicity. Since the Maxwell system is conservative and hyperbolic, we choose the numerical approximation based on finite-volume upwind schemes [6, 3].
We present now the criterion of periodicity. Suppose that the solution is an harmonic wave :

$$Q(t,x) = Q_0(x)cos(\omega t + \varphi).$$

Then, we have :

$$\frac{d^2Q}{dt^2} + \omega^2 Q = 0.$$

Performing integration with respect to t and x, we get :

$$\int_\Omega \left(\frac{dQ}{dt}\right)^2 + \omega^2 Q^2 dx = constant,$$

which leads to the following criterion of periodicity :

$$\mathcal{C}^1 = \frac{\left| \int_\Omega \{ \left(\frac{dQ}{dt}\right)^2 (ndt) + \omega^2 Q^2(ndt) - \left(\frac{dQ}{dt}\right)^2 ((n-1)dt) - \omega^2 Q^2((n-1)dt) \} dx \right|}{\int_\Omega \{ \left(\frac{dQ}{dt}\right)^2 ((n-1)dt) + \omega^2 Q^2((n-1)dt) \} dx}.$$

If the solution is not an harmonic wave, the following more general criterion can be used :

$$\mathcal{C}^2(Q(nT)) = \frac{\left|\int_\Omega \{Q^2(nT,x) - Q^2((n-1)T,x)\}dx\right|}{\int_\Omega Q^2((n-1)T,x)dx},\ n \geq 1,$$

$$\mathcal{C}^3(Q(nT)) = \frac{\int_\Omega |Q(nT,x) - Q((n-1)T,x)|^2\, dx}{\int_\Omega Q^2((n-1)T,x)dx},\ n \geq 1.$$

The numerical experiment concerns a perfectly conducting circular cavity with an open crack, and we consider the transverse magnetic (TM) problem on a domain $\Omega =]0, 11m[\times]0, 11m[$:

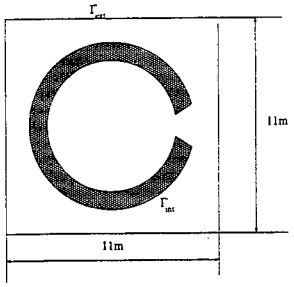

Figure 3: *Circular Cavity*

The incident field is given by the formulas :

$$H_x = -\frac{k_y}{|k|}cos(\omega(t - \frac{k_x x + k_y y}{c|k|})),\ H_y = +\frac{k_x}{|k|}cos(\omega(t - \frac{k_x x + k_y y}{c|k|})),\ E_z = cos(\omega(t - \frac{k_x x + k_y y}{c|k|})),$$

with $|k| = \omega/c = \pi\sqrt{2}$, $k_x = -|k|$, $k_y = 0$. The mesh used is finite-element type and nonstructured (triangles). The number of points per wavelength ($\lambda = \sqrt{2}$) is approximately 15. Figures (4) shows the component H_x of

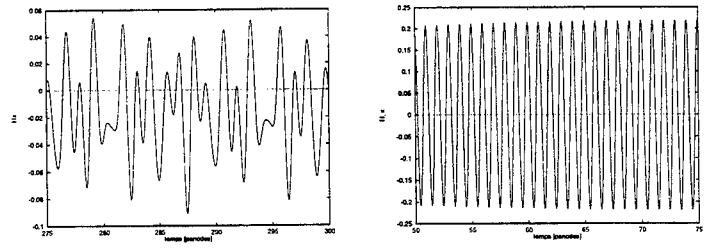

Figure 4: *H_x component of the magnetic field*
(left : Classical Method / right : LAM)

the magnetic field. The solution calculated by the (CM) ($\lambda = 0$) doesn't converge even after 300 periods, whereas, using the (LAM), good solutions are obtained after 50 periods. Figure (5) shows the convergences to zero of the criterion of periodicity and the time evolution of the absorption parameter $\lambda(t)$, which tends also to zero.

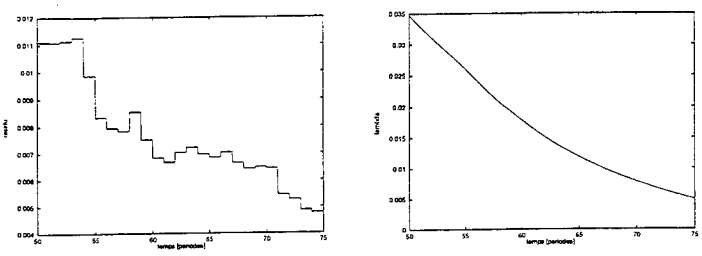

Figure 5: *Criterion of periodicity using the LAM/ Evolution of parameter* $\lambda(t)$

3 Application of the *LAM* to the transport of charged particles

The motion of a fluid of charged particles placed in an electro-magnetic field can be described in terms of particle distribution function by the Vlasov equation :

$$\partial_t f + v \cdot \nabla_x f + \frac{q}{m}(E + v \wedge (\mu_0 H)) \cdot \nabla_v f = 0. \tag{18}$$

The electro-magnetic field (E, H) verifies the Maxwell equations. Using the (LAM), these equations write :

$$\begin{cases} \mu_0 \dfrac{\partial \vec{H}}{\partial t} + rot(\vec{E}) = -\lambda(t)\vec{H}, \\ \varepsilon_0 \dfrac{\partial \vec{E}}{\partial t} - rot(\vec{H}) = -\lambda(t)\vec{E} - \vec{j}, \end{cases} \tag{19}$$

where the current density is given by:

$$\vec{j}(t,x) = \int_v \vec{v} f(t,x,v) dv. \tag{20}$$

The Vlasov equation is numerically solved by means of a deterministic particle method [5]. For the numerical resolution of the Maxwell equations, we use the same scheme as in the previous section.
In the following we consider the transverse electric mode on a domain $\Omega =]0, 1m[\times]0, 1m[$. Two kinds of charged particles are injected on the right side of the box:

$$g_e(t,x,v) = \begin{cases} -(2 + cos(\omega t)) \cdot \delta(v-3), & x = 0, v_x > 0, \\ 0, & \text{otherwise,} \end{cases}$$

and :

$$g_i(t,x,v) = \begin{cases} +(2 + sin(\omega t)) \cdot \delta(v-3). & x = 0, v_x > 0. \\ 0, & \text{otherwise.} \end{cases}$$

where $\omega = 2\pi\nu = \frac{\pi\sqrt{2}}{\sqrt{\varepsilon_0 \mu_0}}$ (resonant frequency of the box). Figure (6), (7) shows the electro-magnetic energy of the solutions and the H_z component of the electro-magnetic field calculated by the two methods. The good behavior of the solution calculated by the (LAM) can be seen, whereas the (CM) seems to be non adequate for the computation of the periodic solutions.

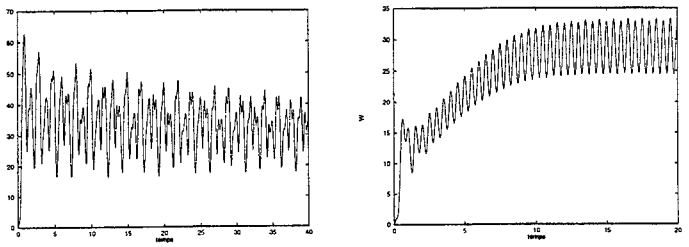

Figure 6: *Electro-magnetic energy*

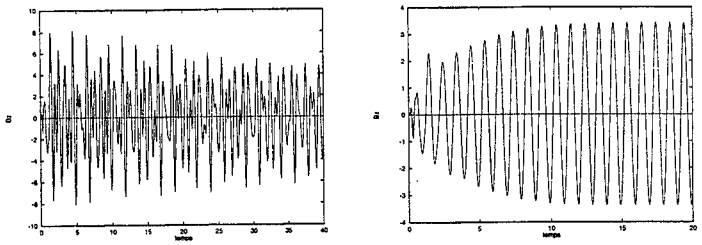

Figure 7: *Component H_z of the electro-magnetic field (left : CM / right : LAM)*

4 Conclusion

We have presented a controllability method for the calculation of time-periodic solutions. The key point consist of an absorption parameter $\lambda(t)$. In a reduced 1D model we have shown that using this method allows us to spare time without loss of accuracy. This methodology was applied to the resolution of scattering problems for electro-magnetic waves and to the transport of charged particles in electro-magnetic field.

References

[1] M. Bostan and F. Poupaud, *Controllability methods for the calculation of periodic solutions of the Vlasov-Maxwell system with boundary conditions*, Manuscrit, Rapport de Recherche INRIA.

[2] R. J. Diperna et P. L. Lions, *Global weak solutions of Vlasov-Maxwell system*, Comm. Pure Appl. Math. XVII(1989), pp. 729-757.

[3] J.P. Cioni, L. Fezoui et D. Issautier *High-order upwind schemes for solving time-domain Maxwell equation.* La Recherche Aérospatiale, no 5, 1994, pp. 319-328.

[4] J.P. Cioni, L. Fezoui et H. Steve *Approximation des équations de Maxwell par des schémas décentrés en éléments finis* Rapport INRIA, no 1601, (1992).

[5] S. Mas-Gallic *A deterministic particle method for the linearized Boltzmann equation*, Transp. Theory Stat. Phy. vol. 16, pp. 855-887, (1987).

[6] B. Van Leer, *Flux vector splitting for the Euler equations*, Lecture Notes in Physics, vol. 170, pp. 405-512 (1982).

Time-Domain Equivalent Edge Currents

A. Altıntaş[1], S. Lindenmeier and P. Russer
Institut für Hochfrequenztechnik, Technische Universität München, Arcisstr.21, D-80333, Munich, Germany

Introduction

The use of high frequency (HF) techniques in the frequency-domain scattering can hardly be overemphasized. The results obtained by Geometrical Theory of Diffraction (GTD) and its uniform versions have widely been used in predicting the time-domain responses of targets through inverse Fourier transformation [1, 2, 3].

The direct application of high frequency techniques in the time domain (TD) has been discussed and proposed in [4], however only recently, this interest has resurfaced [5, 6, 7]. The advantages are several: efficient and faster computation than inverse Fourier transformation of frequency domain solution, more suitable solutions when the pulse width is narrow compared with the geometrical dimensions of the scattering object, feasibility to implement a hybrid solution by combination with various numerical time domain methods such as FDTD and TLM.

Obviously, these HF-based time-domain solutions are not accurate when the input pulse has strong low frequency components. The other difficulty in applying GTD (and its uniform versions) in the TD is that, GTD requires a convolution of the input field with the so called "time-domain diffraction coefficients". Some suggestions have already been made to make this convolution more efficient [7]. However, equivalent edge currents (EEC) which are widely employed in the frequency-domain do not appear to be exploited directly in the time-domain. In addition to all the advantages in the frequency-domain, EEC approach in the time-domain does not require any formal convolution integral with the incident field. So, in this paper the time-domain EEC (TD-EEC) have been derived, and employed for the scattering from perfectly conducting planar geometries.

Derivation of time-domain equivalent edge currents

In the physical optics (PO), the surface currents are approximated through geometrical optics; namely they are twice the tangential component of the incident magnetic field on the illuminated side, and zero on the shadowed side. The far-zone field is then found from the radiation integral of these currents as:

$$\overline{E}^{PO} = \frac{Z_o}{4\pi r c}\hat{s} \times \hat{s} \times \iint_{S(illuminated)} 2\hat{n} \times \frac{\partial \overline{h}^{inc}(\tau - \overline{r}' \cdot \hat{s}'/c)}{\partial t} ds' \qquad (1)$$

[1]On leave from Bilkent University, Dept. Elect. Eng, Bilkent 06533 Ankara, Turkey

where $\tau = (t - \frac{r}{c} + \frac{\overline{r'} \cdot \hat{s}}{c})$, Z_o is the free space impedance, c is the velocity of light in vacuum, $\hat{s}'$ and $\hat{s}$ are the unit vectors for the incident and radiation direction respectively, and finally $\hat{n}$ is the unit normal to the surface. It is noted that the PO surface current is retarded by the observation distance and additional path at any source point $\overline{r}'$. This approach has been applied and discussed in [5] mainly for the radiation from reflector antennas. For planar perfectly conducting scatterers and for far field observation, the PO surface integration in (1) can be reduced to a contour integration via Stokes' theorem. The resulting expression is given as:

$$\overline{e}^s = \frac{Z_o}{\pi r} \hat{s} \times \hat{s} \times \oint_C \hat{n} \times \overline{h}^{inc} \frac{(\hat{s}' - \hat{s}) \cdot (\overline{\overline{I}} - \hat{a}_z \hat{a}_z)}{\mid (\hat{s}' - \hat{s}) \cdot (\overline{\overline{I}} - \hat{a}_z \hat{a}_z) \mid} \cdot \hat{l} dl \tag{2}$$

where the scatterer is assumed to lie on the xy-plane, $\hat{a}_z$ is the unit vector in z-direction and $\overline{\overline{I}}$ is the unit dyad. By comparing this expression with the radiation integral of equivalent electric and magnetic line sources on the edge contour given by

$$\overline{e}^s(t, r) = \frac{Z_o}{4\pi r c} \hat{s} \times \hat{s} \times \frac{\partial}{\partial t} \oint_C I(\tau) \hat{l} dl + \frac{1}{4\pi r c} \hat{s} \times \frac{\partial}{\partial t} \oint_C M(\tau) \hat{l} dl \tag{3}$$

one obtains

$$I(\tau) = \int_{-\infty}^{\tau} [Z_o^{-1} D_e^I \overline{e}^{inc}(t') \cdot \hat{l} + D_h^I \vec{h}^{inc}(t') \cdot \hat{l}] c \, dt' \tag{4}$$

and

$$M(\tau) = \int_{-\infty}^{\tau} [Z_o D_h^M \vec{h}^{inc}(t') \cdot \hat{l}] c \, dt' \tag{5}$$

where D_e^I, D_h^I and D_h^M are the angle dependent coefficients. It is noted that the scattered field is given in terms of an edge contour integration and requires no convolution integral. Also, since the consequtive time derivative and integrations cancel, it is directly related to the incident field rather than its derivative. The coefficients D_e^I, D_h^I, and D_h^M are exactly the same as the ones in the frequency domain EEC [8], and they contain a PO part and a fringe part. The PO part is given by the following coeficients[9]

$$D_e^{I,PO} = -2 \frac{\sin \phi' (\sin \beta \cos \phi + \sin \beta' \cos \phi')}{[(\cos \beta - \cos \beta')^2 + (\sin \beta \cos \phi + \sin \beta' \cos \phi')^2] \sin \beta'} \tag{6}$$

$$D_h^{I,PO} = 2 \frac{(cot \beta \cos \phi + cot \beta' \cos \phi')(\sin \beta \cos \phi + \sin \beta' \cos \phi')}{[(\cos \beta - \cos \beta')^2 + (\sin \beta \cos \phi + \sin \beta' \cos \phi')^2]} \tag{7}$$

$$D_h^{M,PO} = 2 \frac{\sin \phi (\sin \beta \cos \phi + \sin \beta' \cos \phi')}{[(\cos \beta - \cos \beta')^2 + (\sin \beta \cos \phi + \sin \beta' \cos \phi')^2] \sin \beta} \tag{8}$$

where the angles β', β, ϕ', and ϕ are the diffraction angles as shown in Figure 1. $\beta'(\beta)$ is the angle between the edge tangent and the incident (scattering) direction. $\phi'(\phi)$ is measured on the normal plane from the plate surface to the projection of the incident (scattering) direction. These coefficients when substituted into the contour integration in (3) exactly recover the PO surface integration. Using the developments in the frequency domain [10], one can improve the equivalent current formulation over PO by adding the non-uniform or fringe current contribution. The coefficients for this contribution are:

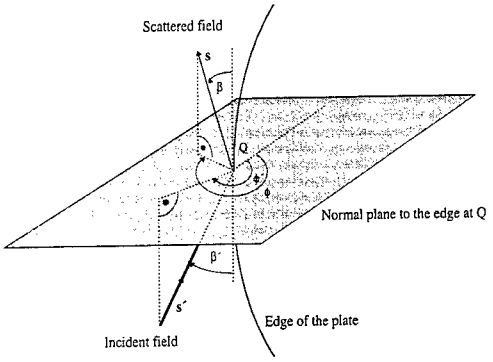

Figure 1: Definition of the diffraction angles for an edged geometry.

$$D_e^{I,f} = -4\frac{\sin(\phi'/2)(\gamma - \sin\beta'\cos(\phi'/2))}{\sin\beta'[\sin\beta'(\sin\beta\cos\phi + \sin\beta'\cos\phi') + \cos\beta'(\cos\beta - \cos\beta')]} \tag{9}$$

$$D_h^{I,f} = -2\frac{\sin\beta'[cot\beta\cos\phi + cot\beta'\cos\phi' + \cos(\phi'/2)\gamma^{-1}\zeta]}{\sin\beta'(\sin\beta\cos\phi + \sin\beta'\cos\phi') + \cos\beta'(\cos\beta - \cos\beta')} \tag{10}$$

$$D_h^{M,f} = -2\frac{\sin\beta'\sin\phi[1 - \sin\beta'\cos(\phi'/2)\gamma^{-1}]}{\sin\beta[\sin\beta'(\sin\beta\cos\phi + \sin\beta'\cos\phi') + \cos\beta'(\cos\beta - \cos\beta')]} \tag{11}$$

where

$$\gamma = [(\sin\beta'(\sin\beta' - \sin\beta\cos\phi) - \cos\beta'(\cos\beta - \cos\beta'))/2]^{\frac{1}{2}} \tag{12}$$

and

$$\zeta = cot\beta'[\sin\beta\cos\phi + cot\beta'(\cos\beta - \cos\beta')] - \sin\beta' cot\beta\cos\phi. \tag{13}$$

The substitution of the sum of these coefficients in (6-8) and (9-11) into (3) should yield the first order diffraction from the planar scatterer.

Results

A TLM calculation of a gaussian pulse-excited dipole in the presence of a metallic enclosure (see Figure 2) has been given in [11]. The metallic box has a height of 10 cm, a width of 34 cm, and a depth of 10cm. The dipole is directly in front of the box with a separation of 55 cm. The orientation of the dipole is vertical and the scattered fields in the vertical direction are considered. There are also two small apertures on the front wall of the box which cause some interior resonances to occur. Backscattering and resonances of the metallic enclosure which is

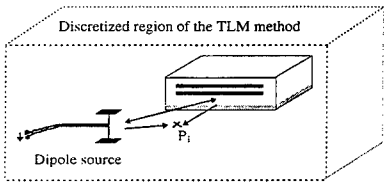

Figure 2: A short dipole antenna interfering with metallic enclosure.

interfered by the antenna at point P_1 in distance of 5 cm from the aperture is computed using TLM with a metallic wall thickness of 5 mm. The same geometry is also analyzed using PO, in which case apertures on the front wall are neglected so the surface currents are assumed to flow on the perfectly conducting front wall. The results are shown in Figure 3 and the comparison is generally good up to about 3 nanoseconds. After this time, higher order diffraction and interior resonances take place which are ignored in the PO. Since the observation point P_1 is quite near to the enclosure, the radiation contribution due to divergence of the PO surface current is also included in the calculations, which improved the calculations slightly.

The second geometry studied is a square plate for which a space-time integral equation solution is given in the literature [12]. The incident field is a plane wave of gaussian shape given by

$$e^{inc}(t) = \frac{1}{\sqrt{\pi}\sigma} e^{-(t/\sigma)^2} \tag{14}$$

where σ is taken as $1.11c^{-1}$ (not specified in [12]).

The axial backscatter (normal incidence) plots using TD-EEC of (3) are calculated and compared with the space-time integral equation approach in Figure 4. The second positive pulse in the solution of [12] is due to "waves traveling across the plate face and returning to the observer". This higher order effect is not included in the TD-EEC analysis.

Note that in this geometry, a direct application of GTD is not possible due to caustic problem. It should be mentioned that another reason for the poor comparison in Figure 4 is because of the strong low frequency component of the input pulse. (In the previous example, the incident field coming from the dipole was proportional to the second derivative of a gaussian (such as in (14)), so the low frequencies were suppressed).

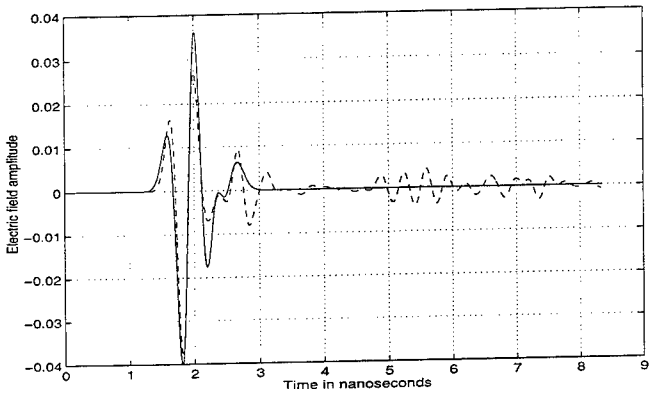

Figure 3: Comparison of the field for the metallic box. Solid line: PO, dashed line:TLM

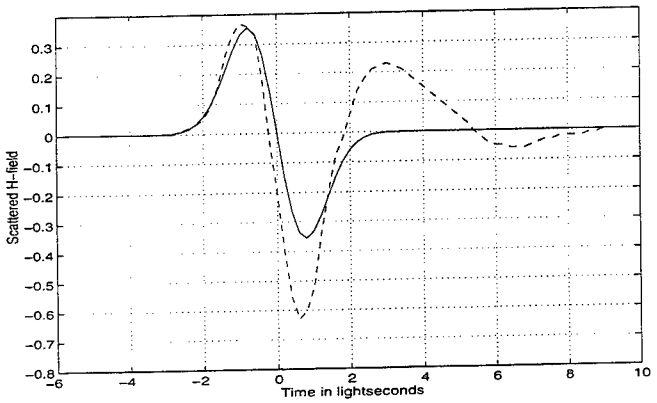

Figure 4: Gaussian pulse response of a square plate of size 1m. The solid line is the TD-EEC, and the dashed lines are space-time integral equation calculations.

Conclusions

Time domain equivalent edge currents are derived. Their limitations and theoretical advantages over the other high-frequency-based time-domain approaches are discussed. The applications for the planar perfectly conducting scatterers are presented.

References

[1] A. Dominek, "Transient Scattering Analysis for a Circular Disk", *IEEE Trans. AP*, vol.39, no.6, June 1991, pp.815-819.

[2] H. Shirai, "Deemphasizing Low Frequency Defects in GTD Analysis of Pulsed Signal Scattering by a Perfectly Conducting Flat Strip", *IEEE Trans. AP*, vol.34, no.10, Oct. 1986, pp.1261-1266.

[3] W.D. Burnside, B. Dewitt, and B.Z. Hollman, "Analysis of TD Scattering by a Flat Plate", *IEEE Trans. AP*, vol.33, no.8, August 1985, pp. 917-922.

[4] E.M. Kennaugh, and D.L. Moffatt, "Transient and Impulse Response Approximations",*Proc. IEEE*, vol.56, no.8, August 1965, pp.893-901.

[5] E. Sun, and W.V.T. Rusch, "Time-Domain Physical-Optics", *IEEE Trans. AP*, vol.42, no.1, Jan.1994, pp.9-15.

[6] T. Veruttipong, "Time-Domain Version of the Uniform GTD", *IEEE Trans. AP*, vol.38, no.11, Nov. 1990, pp.1757-1764.

[7] P. Rousseau, and P.H. Pathak, "Time-Domain Uniform GTD for a Curved Wedge", *IEEE Trans. AP*, vol.43, no.12, Dec. 1995, pp.1375-1382.

[8] O. Breinbjerg, "EEC Analysis of Electromagnetic Scattering by Plane Structures", Ph.D. Thesis, Technical University of Denmark, Dept. Electromagnetics Systems, March 1991.

[9] T. Oguzer, A. Altıntaş, and O.M. Büyükdura, "On the Elimination of Infinities in the PO Component of Equivalent Edge Currents", *Wave Motion*, vol.18, no.1, Jan.1993, pp.1-10.

[10] A. Michaeli, "Elimination of Infinities in Equivalent Edge Currents, Part I: Fringe Current Components", *IEEE Trans. AP*, vol.34, no.7, July 1986, pp.912-918.

[11] S. Lindenmeier, L. Pierantoni, and P. Russer, "Adapted Radiating Boundaries for Efficient Time-Domain Simulation of Electromagnetic Interferences", *1998 IEEE-MTT-S Int. Mic. Symp.*, Baltimore, Maryland, USA, June 1998, pp.465-468.

[12] C.L. Bennett, and G.F. Ross, "Time-Domain Electromagnetics and Its Applications", *Proc. IEEE*, vol.66, no.3, March 1978, pp. 299-318.

A NUMERICAL STUDY ON THE ACCURACY OF TLM-SCN FORMULATIONS FOR THE SOLUTION OF INITIAL VALUE PROBLEMS

JÜRGEN REBEL, MARTIN AIDAM AND PETER RUSSER

INSTITUT FÜR HOCHFREQUENZTECHNIK,TECHNISCHE UNIVERSITÄT MÜNCHEN
ARCISSTR. 21, D-80333 MUNICH, GERMANY

ABSTRACT. In this paper, we investigate different mappings between the discretized electromagnetic fields and the state variables of the three-dimensional TLM-SCN scheme. The different mappings are studied with respect to their suitability to the solution of a numerical initial value problem (IVP). The convergence rate of the relative error between a benchmark solution and the solution obtained by simulations with coarser discretizations is studied. It is shown, that both the TLM-SCN method without stubs for modelling homogeneous media and the TLM-SCN method with stubs for modelling inhomogeneous media, converge with second order accuracy, if the initial value (IV) is properly applied. In the case of TLM-SCN without stubs, it emerges that imposing the initial condition at the boundary of the TLM cell and also sampling the fields at the boundary, yields a much smaller error constant. This result shows, that the accuracy of the TLM scheme is not only dependent upon the dispersion of the SCN mesh, but also influenced by the mapping between discretized fields and TLM state variables. However, imposing the initial condition at the boundaries of the TLM cells in a TLM-SCN network with stubs results in the excitation of spurious modes. The reason for this is that the initial states of the stubs are not properly set.

1. INTRODUCTION

In previous work, the dispersion and coarseness error and the performance of absorbing boundary conditions of the SCN - TLM method were studied [9, 10]. The influence of the mapping between the discretized electromagnetic fields and the TLM state variables on the error of the numerical solution was not subject of these studies. In this paper, we investigate the influence of the mapping between the discretized electromagnetic fields and the TLM state variables on the convergence of various TLM schemes.

The original formulation of the symmetrical condensed node based on network analogies was given by Johns [6]. The initial field is imposed on the TLM network at the node and the discretized electromagnetic fields are sampled at the node as a function of the incident TLM state variables. Later, this formulation was extended to include losses [11].

In the literature, various other mappings between the sampled electromagnetic field quantities and the TLM state variables were introduced. In a Method of Moments based derivation of the SCN, the initial field is imposed on the TLM network and the fields are sampled at the boundaries of a TLM cell [7]. By this definition, an isomorphic mapping between the 24 discretized electromagnetic fields and the 24 state variables at the boundary (taking both incident and reflected states into account) of a TLM cell is possible. Essentially the same mapping (apart from a normalization to power waves) between discretized field and TLM states was used in a derivation of the SCN based on Finite Integration [1]. The finite difference interpretation of the SCN given by [2] can be interpreted as imposing the IV at the boundary and sampling the fields at the centre of a cell. Here, the mapping between the discretized field and the TLM states at the boundary is the same as in [7], although a different notation is used. At the node, Johns' original mapping between the incident state variables and the discretized field is used. For the SCN with stubs, a finite difference interpretation following [5], and an interpretation of a discrete propagator integral [4] exist.

In this paper we investigate the different methods of imposing the initial field on the TLM-SCN network and the different ways of sampling the electromagnetic field with respect to their convergence following [4, 6, 7, 11]. In the next section, the different mappings are shown.

2. Comparison of various mappings

Using the notation presented in [12], the discretized electromagnetic fields and the TLM state variables at the boundary of a TLM cell are related by

$$\begin{pmatrix} \boldsymbol{a}_{k;l,m,n} \\ \boldsymbol{b}_{k;l,m,n} \end{pmatrix} = \begin{pmatrix} \boldsymbol{I} & Z\boldsymbol{I} \\ \boldsymbol{I} & -Z\boldsymbol{I} \end{pmatrix} \begin{pmatrix} \boldsymbol{E}_{k;l,m,n} \\ \boldsymbol{H}_{k;l,m,n} \end{pmatrix}, \qquad \begin{pmatrix} \boldsymbol{E}_{k;l,m,n} \\ \boldsymbol{H}_{k;l,m,n} \end{pmatrix} = \frac{1}{2} \begin{pmatrix} \boldsymbol{I} & \boldsymbol{I} \\ Z^{-1}\boldsymbol{I} & -Z^{-1}\boldsymbol{I} \end{pmatrix} \begin{pmatrix} \boldsymbol{a}_{k;l,m,n} \\ \boldsymbol{a}_{k;l,m,n} \end{pmatrix}, \tag{1}$$

with

$$\boldsymbol{E}_{k;l,m,n} = \begin{bmatrix} {}_kE^y_{l-\frac{1}{2},m,n} \\ {}_kE^y_{l+\frac{1}{2},m,n} \\ {}_kE^z_{l-\frac{1}{2},m,n} \\ {}_kE^z_{l+\frac{1}{2},m,n} \\ {}_kE^z_{l,m-\frac{1}{2},n} \\ {}_kE^z_{l,m+\frac{1}{2},n} \\ {}_kE^x_{l,m-\frac{1}{2},n} \\ {}_kE^x_{l,m+\frac{1}{2},n} \\ {}_kE^x_{l,m,n-\frac{1}{2}} \\ {}_kE^x_{l,m,n+\frac{1}{2}} \\ {}_kE^y_{l,m,n-\frac{1}{2}} \\ {}_kE^y_{l,m,n+\frac{1}{2}} \end{bmatrix}, \qquad \boldsymbol{H}_{k;l,m,n} = \begin{bmatrix} {}_kH^z_{l-\frac{1}{2},m,n} \\ -{}_kH^z_{l+\frac{1}{2},m,n} \\ -{}_kH^y_{l-\frac{1}{2},m,n} \\ {}_kH^y_{l+\frac{1}{2},m,n} \\ {}_kH^x_{l,m-\frac{1}{2},n} \\ -{}_kH^x_{l,m+\frac{1}{2},n} \\ -{}_kH^z_{l,m-\frac{1}{2},n} \\ {}_kH^z_{l,m+\frac{1}{2},n} \\ {}_kH^y_{l,m,n-\frac{1}{2}} \\ -{}_kH^y_{l,m,n+\frac{1}{2}} \\ -{}_kH^x_{l,m,n-\frac{1}{2}} \\ {}_kH^x_{l,m,n+\frac{1}{2}} \end{bmatrix}, \tag{2}$$

where $\boldsymbol{a}$ denotes incident TLM pulses, $\boldsymbol{b}$ reflected TLM pulses, and k, l, m, n are temporal and spatial indices of the respective TLM cell. $\boldsymbol{I}$ denotes the 12 by 12 unity matrix. Z is the impedance of free space.

At the node, we have to distinguish the mappings of the various authors. For Johns' formulation of the SCN without stubs, the relation between electromagnetic fields and TLM state variables at the node reads with $\boldsymbol{f} = [E^x, E^y, E^z, ZH^x, ZH^y, ZH^z]^T$

$$\boldsymbol{a}_{k;l,m,n} = \boldsymbol{Q}\, \boldsymbol{f}_{k;l,m,n}, \qquad \boldsymbol{f}_{k;l,m,n} = \boldsymbol{P}\, \boldsymbol{a}_{k;l,m,n}. \tag{3}$$

$\boldsymbol{Q}$ and $\boldsymbol{P}$ are given by

$$\boldsymbol{P} = \boldsymbol{Q}^T = \frac{1}{2} \begin{pmatrix} 0 & 0 & 0 & 0 & 0 & 0 & 1 & 1 & 1 & 1 & 0 & 0 \\ 1 & 1 & 0 & 0 & 0 & 0 & 0 & 0 & 0 & 0 & 1 & 1 \\ 0 & 0 & 1 & 1 & 1 & 1 & 0 & 0 & 0 & 0 & 0 & 0 \\ 0 & 0 & 0 & 0 & 1 & -1 & 0 & 0 & 0 & 0 & -1 & 1 \\ 0 & 0 & -1 & 1 & 0 & 0 & 0 & 0 & 1 & -1 & 0 & 0 \\ 1 & -1 & 0 & 0 & 0 & 0 & -1 & 1 & 0 & 0 & 0 & 0 \end{pmatrix}, \tag{4}$$

If the SCN has stubs, the mapping is as follows, where in the case of the SCN following [6] without losses, $G_x, G_y, G_z, R_x, R_y, R_z = 0$:

$$\boldsymbol{P} = \begin{pmatrix} 0 & b_y & 0 & 0 & 0 & d_z \\ 0 & b_y & 0 & 0 & 0 & -d_z \\ 0 & 0 & b_z & 0 & -d_y & 0 \\ 0 & 0 & b_z & 0 & d_y & 0 \\ 0 & 0 & b_z & d_x & 0 & 0 \\ 0 & 0 & b_z & -d_x & 0 & 0 \\ b_x & 0 & 0 & 0 & 0 & -d_z \\ b_x & 0 & 0 & 0 & 0 & d_z \\ b_x & 0 & 0 & 0 & d_y & 0 \\ b_x & 0 & 0 & 0 & -d_y & 0 \\ 0 & b_y & 0 & -d_x & 0 & 0 \\ 0 & b_y & 0 & d_x & 0 & 0 \\ b_x Y_x & 0 & 0 & 0 & 0 & 0 \\ 0 & b_y Y_y & 0 & 0 & 0 & 0 \\ 0 & 0 & b_z Y_z & 0 & 0 & 0 \\ 0 & 0 & 0 & -d_x & 0 & 0 \\ 0 & 0 & 0 & 0 & -d_y & 0 \\ 0 & 0 & 0 & 0 & 0 & -d_z \end{pmatrix}^T, \quad \boldsymbol{Q} = \frac{1}{2} \begin{pmatrix} 0 & v & 0 & 0 & 0 & -w \\ 0 & v & 0 & 0 & 0 & w \\ 0 & 0 & w & 0 & v & 0 \\ 0 & 0 & w & 0 & -v & 0 \\ 0 & 0 & w & -u & 0 & 0 \\ 0 & 0 & w & u & 0 & 0 \\ u & 0 & 0 & 0 & 0 & w \\ u & 0 & 0 & 0 & 0 & -w \\ u & 0 & 0 & 0 & -v & 0 \\ u & 0 & 0 & 0 & v & 0 \\ 0 & v & 0 & u & 0 & 0 \\ 0 & v & 0 & -u & 0 & 0 \\ ua_x & 0 & 0 & 0 & 0 & 0 \\ 0 & va_y & 0 & 0 & 0 & 0 \\ 0 & 0 & wa_z & 0 & 0 & 0 \\ 0 & 0 & 0 & -uc_x & 0 & 0 \\ 0 & 0 & 0 & 0 & -vc_y & 0 \\ 0 & 0 & 0 & 0 & 0 & -wc_z \end{pmatrix}, \tag{5}$$

with the coefficients

$$\begin{aligned} b_x &= \frac{2}{u(G_x + Y_x + 4)}, & d_x &= \frac{2}{u(R_x + Z_x + 4)}, & a_x &= \frac{Y_x + G_x}{Y_x}, & c_x &= (Z_x + R_x), \\ b_y &= \frac{2}{v(G_y + Y_y + 4)}, & d_y &= \frac{2}{v(R_y + Z_y + 4)}, & a_y &= \frac{Y_y + G_y}{Y_y}, & c_y &= (Z_y + R_y), \\ b_z &= \frac{2}{w(G_z + Y_z + 4)}, & d_z &= \frac{2}{w(R_z + Z_z + 4)}, & a_z &= \frac{Y_z + G_z}{Y_z}, & c_z &= (Z_z + R_z). \end{aligned} \tag{6}$$

If TLM is interpreted in terms of a discrete propagator integral as in [4], the stubs are treated as internal degrees of freedom and consequently not mapped. It should be stressed, that it was assumed in [4], that when the TLM scheme is started, there must be *no* initial field present. At the cell boundary, the mapping between the discretized electromagnetic fields and the TLM state variables is given by (1). The fields at the node are taken as the averages of the fields at the boundaries, i.e.

$$\boldsymbol{f}_{k;l,m,n} = \boldsymbol{P}_t(\boldsymbol{E}_{k;l,m,n} + \boldsymbol{H}_{k;l,m,n}), \tag{7}$$

where $\boldsymbol{P}_t$ is given by

$$\boldsymbol{P}_t = \frac{1}{4} \begin{pmatrix} 0 & 0 & 0 & 0 & 0 & 0 & 1 & 1 & 1 & 1 & 0 & 0 \\ 1 & 1 & 0 & 0 & 0 & 0 & 0 & 0 & 0 & 0 & 1 & 1 \\ 0 & 0 & 1 & 1 & 1 & 1 & 0 & 0 & 0 & 0 & 0 & 0 \\ 0 & 0 & 0 & 0 & 1 & -1 & 0 & 0 & 0 & 0 & -1 & 1 \\ 0 & 0 & -1 & 1 & 0 & 0 & 0 & 0 & 1 & -1 & 0 & 0 \\ 1 & -1 & 0 & 0 & 0 & 0 & -1 & 1 & 0 & 0 & 0 & 0 \end{pmatrix}. \tag{8}$$

3. Numerical analysis of convergence

To compare the convergence of various TLM schemes, the propagation of a linearly polarized Gaussian pulsed plane wave in an axial direction of the TLM mesh was analyzed numerically. Fig. 1 shows the investigated structure. For a plane wave, linearly polarized in z-direction, propagating in x-direction, a linear row with a single TLM cell in the transverse directions is representative. The ports of the TLM cells are short-circuited in z-direction and open in y-direction. Cubic TLM cells were considered. The

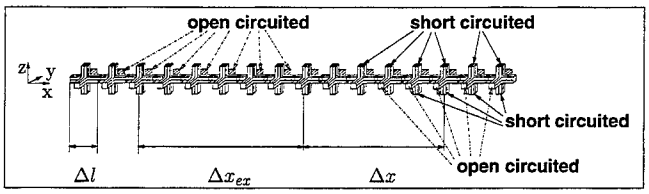

FIGURE 1. TLM model of parallel-plate waveguide.

no.	Δl_{no} $[\mu m]$	N_{no}	M_{no}
1	1.0	70	6
2	0.5	140	12
3	0.25	280	24
4	0.125	560	48
5	0.015625	4480	384

TABLE 1. Parameters of different discretization levels.

size of a TLM cell is Δl. The initial field is distributed across the distance Δx_{ex}. The distance between initial field and observation point is denoted Δx.

The numerical IVP was solved with various discretisations. The respective simulation parameters can be found in Table 1. Fig. 2 shows schematically the TLM models for two subsequent discretization steps. The upper sketch refers to the case where the fields are sampled at the node, and the sketch at the bottom refers to the case where the fields are sampled only at the boundaries of a TLM cell.

The initial field distribution, given by the discretized truncated Gaussian pulse

$$E^z_{k=1}(x) = \begin{cases} E_0 e^{-\pi\left(\frac{x-x_0}{\sqrt{2}\sigma}\right)^2} & \text{for} \quad \frac{N_{no}}{2}\Delta l_{no} \le x - x_0 \le (\frac{N_{no}}{2}+1)\Delta l_{no} \\ 0 & \text{elsewhere} \end{cases} \tag{9}$$

is distributed across the distance $\Delta x_{ex} = N_{no}\Delta l_{no}$. The region, where the initial field is given, is symbolized by the shaded cells in Fig. 2. The pulse is centred around $\Delta x_0 = (N_{no}/2+1)\Delta l_{no}$, i.e. around a node in the one case or a boundary between two cells in the other case (see the dashed line in Fig. 2). The width of the pulse is $\sqrt{2}\sigma = N_{no}\Delta l_{no}/p$, where p was chosen $3\sqrt{2}$.

The overall length of the structure was chosen such, that in connection with the duration of the simulation no reflections from the terminating walls in the positive and negative x-direction occured at the observation point.

In the case with stubs, a medium with $\varepsilon_r = 2$, and $\mu_r = 1$ was assumed. In the case of a lossy medium, the electric conductivity was chosen isotropically $\sigma_e = 30Sm^{-1}$.

If one reduces Δt, Δl, the deviation between the numerical solution for finite Δt, Δl and the exact solution decreases by the order of accuracy of the method [13]. In this experiment, the exact solution was given by a benchmark solution, obtained from a simulation with very small cell size (no. 5 of Table 1).

The relative error between reference and simulated solution is given by

$$\eta = \sqrt{\frac{\sum_k \left(|u_k|^2 + |\nabla_t\, u_k|^2\right)}{\left(|E^z_{k,\text{bench}}|^2 + |\nabla_t\, E^z_{k,\text{bench}}|^2\right)}} \qquad \text{with} \qquad u_k = E^z_{k,\text{bench}} - E^z_k. \tag{10}$$

∇_t denotes the backward difference between two neighbouring elements devided by the time step of the respective discretization level, to approximate the temporal partial derivative. The relative error is

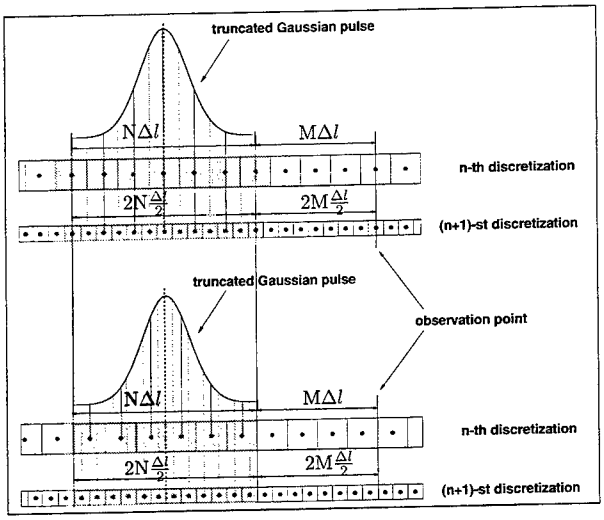

FIGURE 2. TLM models for two subsequent discretization steps.

calculated using the norm of an adequate discrete Sobolev Space, where the approximations of the first partial derivatives are also considered [14].

Table 2 indicates the different investigated mappings between the discretized electromagnetic fields and the TLM state variables.

Table 2: Location of excitation and field sampling of different TLM - SCN interpretations.

no.	Excitation	Sampling	Stubs	lossy	Author
A	node	node	no	-	[6]
B	boundary	boundary	no	-	[7]
C	node	node	yes	no	[6]
D	node	node	yes	yes	[11]
E	boundary	boundary	yes	no	[4]

4. RESULTS

4.1. **TLM without stubs.** Fig. 3 shows the relative error η for TLM without stubs (case A and B, Table 2). In case A, when the initial field is mapped to the TLM-SCN network at the node and the fields are also sampled at the node, one can recognize a second order convergence for coarser discretizations.

However, this result shows, that the mapping between the discretized fields and the TLM states has an influence on the accuracy of the TLM solution, as the SCN mesh without stubs exhibits no dispersion in axial direction!

Though, the second order convergence corroborates the results of other work, where an overall second order convergence was predicted with the aid of the dispersion relation of the TLM mesh [8–10].

In case B, when the initial data are imposed on the TLM-SCN network at the boundary and the fields are also sampled at the boundary, a much smaller relative - error η is observed. As the TLM-SCN scheme

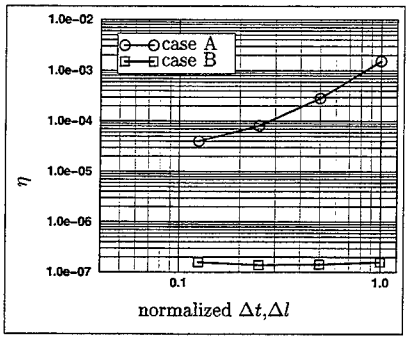

FIGURE 3. The relative - error of the E^z field of SCN-TLM without stubs for various discretizations.

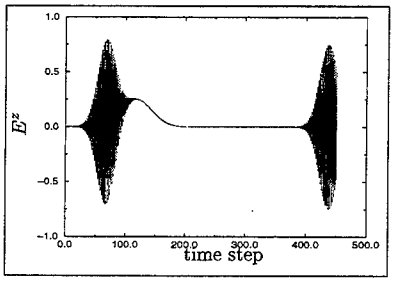

FIGURE 4. Excitation of spurious modes, when applying an IV at $k = 1$ at the cell boundary and field sampling at the cell boundary (case E of Table 2).

without stubs has no dispersion in the axial directions, we only see the numerical round-off error (we worked with single precision arithmetic), as expected.

4.2. **TLM with stubs.** First, we want to have a look what happens when we impose the initial field at the boundaries of the TLM cells with stubs. If we map the fields at the boundary (Case E, Table 2), we observe the excitation of spurious modes (see Fig. 4). This is due to a wrong initialization of the stubs.

However, it was stressed in [4], that the initial electric and magnetic fields have to be zero, when the TLM scheme is started. If this condition is neglected, one will inevitably excite spurious modes. The excitation of spurious modes when imposing an initial field at the boundary was also observed by others [3].

Besides, sampling the fields at the node when imposing the initial field at the boundary [4], averages out most of the spurious modes (see Fig. 5), which is a bit surprising.

No spurious modes where observed, when imposing the IV on the TLM-SCN network in the manner proposed by Johns. This is due to also exciting the stubs correctly and not treating them as internal degrees of freedom as in [4].

As it makes no sense to study the convergence when spurious modes are excited, we have only compared the convergence rates of case C and D of Table 2, i.e. with and without ohmic losses. The results are compiled in Fig. 6.

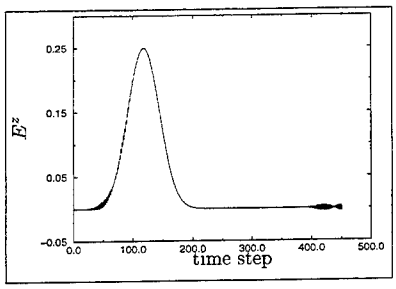

FIGURE 5. Excitation with spatial field distribution at $k = 1$ at the cell boundary. Field sampling at the node averages out most of the spurious modes (case E of Table 2).

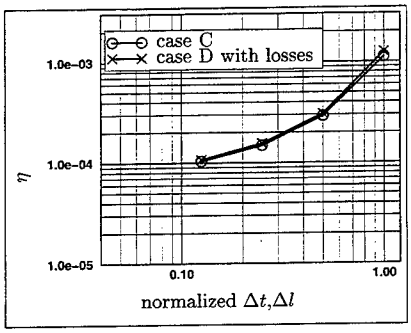

FIGURE 6. The relative - error of the E^z field of SCN-TLM with stubs for various discretizations when exciting at the node (cases C and D of Table 2).

For TLM with stubs following Johns' and Naylor et al.'s interpretation (case C and D), the error decreases with second order for coarser discretization levels, as predicted by [5]. However, we can recognize a flattening of the error curve towards smaller cell sizes.

5. CONCLUSION

We have investigated the accuracy of different mappings between the discretized electromagnetic fields and the TLM state variables when solving a discrete IVP with the TLM-SCN algorithm. It emerged, that the mapping between discretized electric and magnetic field components and TLM state variables influences the accuracy of the TLM solution as well as the dispersion behaviour of the TLM-SCN mesh.

Considering a TLM-SCN mesh without stubs, imposing the initial values at the boundary of the TLM cells and also sampling the fields at the boundary, yields an error of the order of numerical round-off errors for the axial - directions, as expected by inspecting the dispersion relations of the SCN mesh without stubs.

Imposing the initial field distribution at the node and sampling the fields at the node, we observed a second order convergence in axial direction and not a dispersion free propagation, which indicates the influence of the mapping between discretized fields and TLM state variables on the accuracy of the numerical solution.

In the case of a TLM-SCN mesh with stubs, we observed second order convergence in axial direction, when the fields are sampled at the node and the initial values are imposed at the node, as in Johns' original formulation. The observed flattening of the error curve towards finer discretizations is subject to further studies.

Imposing the initial field on a TLM-SCN network with stubs only at the boundary results in the excitation of spurious modes. This is due to a wrong initialization of the stub states. Therefore we can apply this mapping only in cases where we have initial values zero, i.e. all electric and magnetic field components are initially zero (this was stressed in [4]). The excitation of the TLM network has then to be imposed in the sense of an initial-boundary value problem, where one specifies the electric and magnetic field components at the boundaries of some arbitrary TLM cells as a *smooth* function of time.

This means, that if we have initially a field free space, we can choose freely between imposing the initial values at the node or at the boundary, without decreasing the convergence order.

If one has an initial field distribution unequal zero, one has to use the mapping between the discretized field distribution and the TLM states as proposed by Johns or Naylor et al. in case of modelling a lossy medium.

6. Acknowledgment

The authors would like to thank Siemens AG for generously granting Ernst-von-Siemens scholarships.

E-mail: rebel@hft.ei.tum.de, aidam@hft.ei.tum.de, russer@hft.ei.tum.de

References

1. M. Aidam and P. Russer, *Derivation of the Transmission Line Matrix Method by Finite Integration*, AEÜ Int. J. Electron. Commun. **51** (1997), no. 1, 35–39.
2. Z. Chen, M.M. Ney, and W.J.R. Hoefer, *A New Finite-Difference Time-Domain Formulation and its Equivalence with the TLM Symmetrical Condensed Node*, IEEE Trans. Microwave Theory Tech. **39** (1991), no. 12, 2160–2169.
3. R. Gehring, *Analyse von Streifenleitungen nach der Transmission-Line-Matrix Methode (TLM)*, private communication, Spinner GmbH, 80335 München (1998).
4. S. Hein, *Consistent finite-difference modelling of Maxwell's equations with lossy symmetrical condensed node*, Int. J. Num. Modelling **6** (1993), 207–220.
5. H. Jin and R. Vahldieck, *Direct Derivations of TLM Symmetrical Condensed Node and Hybrid Symmetrical Condensed Node from Maxwell's Equations Using Centered Differencing and Averaging*, IEEE Trans. Microwave Theory Tech. **42** (1994), no. 12, 2554–2561.
6. P.B. Johns, *A Symmetrical Condensed Node for the TLM Method*, IEEE Trans. Microwave Theory Tech. **35** (1987), no. 4, 370–377.
7. M. Krumpholz and P. Russer, *A Field Theoretical Derivation of TLM*, IEEE Trans. Microwave Theory Tech. **42** (1994), no. 9, 1660–1668.
8. ———, *On the dispersion of TLM and FDTD*, IEEE Trans. Microwave Theory Tech. **44** (1994), no. 7, 1275–1279.
9. L. De Menezes, C. Eswarappa, and W.J.R. Hoefer, *A Comparative Study of Dispersion Errors and Performance of Absorbing Boundary Conditions in SCN-TLM and FDTD*, 13th Annual Review of Progress in Applied Computational Electromagnetics Digest (1997).
10. L. De Menezes and W.J.R. Hoefer, *Accuracy of TLM Solutions of Maxwell's Equations*, IEEE Trans. Microwave Theory Tech. **44** (1996), no. 12, 2512–2517.
11. P. Naylor and R.A. Desai, *New three dimensional Symmetrical Condensed Lossy Node for Solution of Electromagnetic Wave Problems by TLM*, Electron. Lett. **26** (1990), no. 7, 492–495.
12. P. Russer and M. Krumpholz, *The Hilbert space formulation of the TLM method*, Int. J. Num. Modelling **6** (1993), no. 1, 29–45.
13. J.W. Thomas, *Numerical Partial Differential Equations*, Springer, New York, 1995.
14. E. Zeidler, *Nonlinear Functional Analysis and its Applications II/B*, Springer, 1985.

SESSION 12

BIOELECTROMAGNETICS

Chairs: Cynthia Furse and Susan Hagness

Computational estimate of the frequency response of metallic implants in biological tissues exposed to RF fields.

Author: A.H.J. Fleming*, V. Anderson** and J. Rowley**
*Monash University, Clayton, Victoria, Australia, 3168
**Telstra Research Laboratories, Clayton, Victoria, Australia, 3168

Introduction

Radiofrequency (RF) exposure of metallic objects can induce differential heating of neighbouring biological tissues. Conductors may be located external to the body or within the body's tissues.[1] Fig 1a shows a sternum implant following open-heart surgery and Fig. 1b an implant resulting from a fracture [Joyner et al. 1988] [Fleming et al. 1992]. When an implant is illuminated by a RF field the absorbed power of the incident field may be preferentially redistributed at particular points adjacent to the implant. In such cases, the resonant response of the implant requires determination. This report examines the electric field and RF currents associated with a rod-type wire implant embedded in muscle.

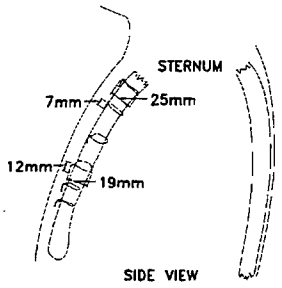

Fig. 1a: Sternum implant

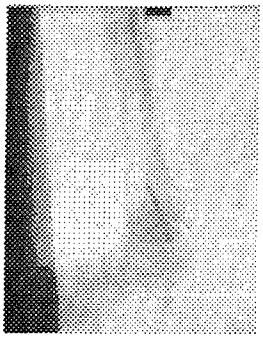

Fig. 1b: Ankle implant

A common belief is that electric fields and derived quantities such as specific absorption rate (SAR) are resonant when the implant length is a half-wavelength in tissue, ie $\lambda_T/2$. However, in this report it is found that electric fields and other derived quantities are resonant at lengths shorter than $\lambda_T/2$. This occurs because currents on implants are influenced by the highly conductive nature of the surrounding tissues [King and Harrison 1969]. Apart from its

[1] Conductors surgically positioned within the body are termed implants as distinct from electrodes, to indicate that their shape and material are not designed for any short-term electrical effect, but can be used as a biologically inert agent within the body, eg as a brace during recalcification of bone fractures, in place for extended periods up to ten years or more. In this report, we use the term wire implant to indicate the origin of the study.

theoretical interest, this finding has relevance for effective hyperthermia design [Iskander and Tumeh, 1989] and in the assessment of RF heating effects around metallic implants.

King and Harrison [1969] studied rod antennas in dissipative media from a theoretical viewpoint. They derived analytic expressions for currents and near fields of wires of various lengths. Also, King and Iizuka [1963] obtained the currents on, and fields near, quarter- and half-wave dipoles in a series of saline solutions. Examination of input admittance as a function of the electrical length of the rod antenna reveals that as the conductivity increases, resonance occurs (periodically) at less than $\lambda_T/2$ [King and Harrison 1969].

Fleming and Joyner used a thin-wire antenna code AMPC to study wire-type structures immersed in an infinite conducting medium [1989]. AMPC was validated using the analytical solutions and experimental results obtained by King and Harrison [1969] and King and Iizuka [1963]. MMP a general purpose semi-analytic electromagnetic code based on the multiple multipole method [Hafner and Bombolt 1993] is also suitable for examining the fields and currents associated with thin wire structures. In the following, these two codes have been used to determine the induced current and total electric fields near the tip of a particular test rod-type wire implant. This leads to the concept of a 'region of influence'. The effect of implant tip shape on localised SAR enhancement is also investigated.

Method

A 30 mm rod of 2 mm radius was selected as the wire implant test case. Both codes, AMPC and MMP, were used to produce volume-averaged estimates of the squared magnitude of the total electric field (incident and scattered), $|E|^2$, over a 1 cm³ volume of tissue adjacent to the implant tip although different methods were used in determining this average (see Fig. 2),. AMPC used a spherical averaging region centred on the tip, while MMP used a cubic averaging volume that abutted the tip corresponding to a 1 gram cube of tissue [ANSI 1990]. The square of the electric field is directly proportional to the rate of absorption of RF energy, the SAR. A 1 V/m incident field was incident on the rod.

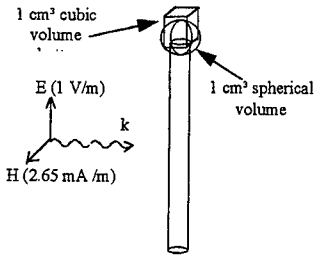

Fig. 2 Rod implant 30 mm long – total electric field magnitude squared was averaged over 1 cm³ volume of tissue next to tip. AMPC used a spherical averaging volume centred on the tip, while MMP used a Cartesian volume abutting the tip.

Estimates of the currents on the rod and the electric fields at the implant tips were sought at 1, 27.12, 40.68, 80, 200, 433, 600, 915, 2450, 5800, 10000 MHz. These frequencies include those commonly used within the bioeffects community [NCRP 1981]. Additional frequencies at 80 (whole-body resonance), 200 and 600 MHz were also included so that uniform coverage was obtained in the range 1 - 10,000 MHz. For the test case, the 30 mm wire implant was modelled to be immersed in muscle (high water content) tissue. Tissue dielectric properties were based on dielectric data obtained from the NRCP report [1981] (AMPC), and the Hurt polynomials [Durney et al. 1986] (MMP). While slightly different tissue dielectric parameters were used by the two codes, the same characteristic results for the currents and the fields are expected.

The wires were modelled using segment lengths that were, at most, $\lambda_T/10$ for the tissue in which the implant was assumed. There are differences in the way in which the two codes segmented the model of the rod. Like NEC, AMPC uses a thin-wire kernel [Burke and Poggio 1981], and as such models the tip region as a 'ring of current'. MMP on the other hand, is more versatile, capable of modelling the implant as a filamentary wire similar to AMPC, or as an explicit cylinder while modelling the tip as flat or pointy. The results shown here represent part of the validation for a much more extensive research effort to obtain RF energy absorption estimates for a range of different length implants at various locations in the body, eg, knee.

Results

Figure 3 shows the AMPC calculated current magnitude along the 30 mm wire implant versus frequency. It is seen that maximum current occurs at approximately 433 MHz, $\lambda_T/3$. Fig. 4 shows the AMPC calculated volume averaged squared magnitude of the total electric field near the implant tip at the peak frequency 433 MHz as a function of volume surrounding the tip. This result shows that surrounding the tip there is a 'region of influence', in this case around 70 cm^3., a cube of around 4.1 mm, or a sphere of radius 2.6 mm Outside this region, no significant effects occur due to the wire. Fig. 5 shows the MMP calculated variation in the enhancement of the 1 gram averaged SAR versus frequency due to different wire implant tips. As for the induced current, peak SAR occurs at $\sim\lambda_T/3$.

Discussion

The RF induced currents on conducting objects in dissipative media are dependent on the type of medium in which the interaction takes place with resonance occurring at a lower frequency than in free-space. We propose that this is because currents in highly dissipative media tend to be concentrated near the wire centre and are attenuated at points near the tips away from the centre. This is a direct consequence of the dissipative medium acting on the wire current as it forms along the wire length away from the peak at the wire centre. This parallels the findings of King and Harrison who studied currents on wire antennas (radiators) and the electric fields near them [1969]. Thus for the wire implant examined in this study, it is resonant at a physical length of approximately $\lambda_T/3$. It is interesting to note the effect of the shape of the implant tip on the localised SAR peak, with the pointed tip showing the least enhancement. The difference between the pointed and flat tip is probably due to greater attenuation between the field at the tip and the nodes of the averaging volume. Also the SAR enhancement is not very

significant for this implant at lengths longer than $\lambda_T/2$ using either the pointed or flat tips. Further investigations are needed to understand the reason for the difference between the pointed and flat tips relative to the AMPC type tip.

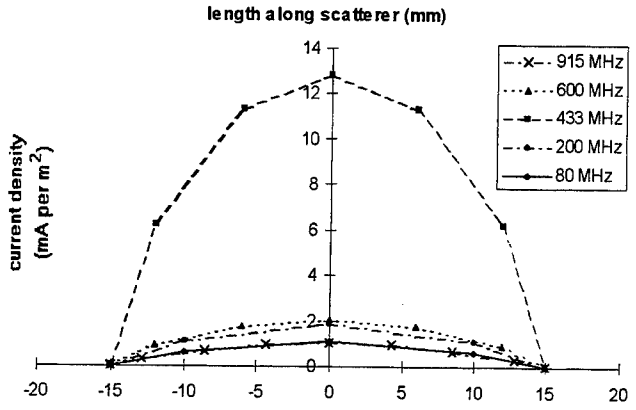

Fig. 3 AMPC calculated current along the 30 mm long wire implant for various frequencies of the incident EM field. The magnitude of the incident E-field is 1 V/m and its polarization relative to the implant is shown in Fig. 2.

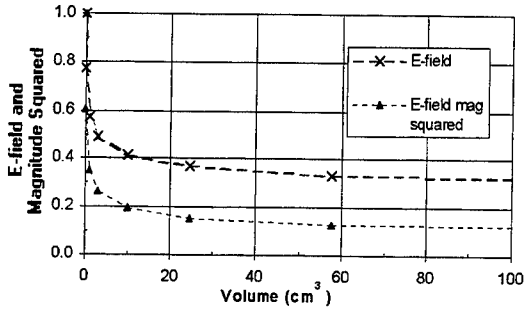

Fig. 4 Volume-averaged total electric field magnitude and its square near the tip of 30 mm long wire implant at 433 MHz calculated by AMPC using a spherical averaging volume. The field is normalised wrt the peak value at the tip. The incident EM field is shown in Fig. 2.

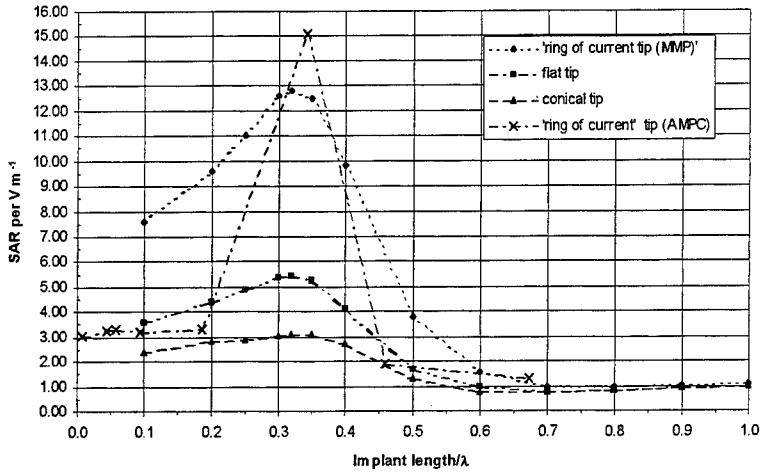

Fig. 5: 1 gram averaged SAR for implant in muscle for various tip shapes. SAR is calculated relative to an incident E_field of 1 V m-1 at the implant site in the absence of the wire. Implant length = 30 mm, diameter = 4 mm. MMP used a cubed averaging volume, and AMPC a spherical averaging volume (see Fig. 2).

Conclusions

In this report, two computational electromagnetics codes were used to analyse the currents on, and fields near, the tips of a wire implant. Two codes, the thin wire code AMPC, and the more versatile electromagnetics code MMP which can model either volume, surface, and/or filamentary segments, were used to analyse a 30 mm long, 2 mm radius wire implant. Resonance of the currents and fields was found to occur at about $\lambda_T/3$ (433 MHz). This lowering of the resonant frequency of wire sactterers is in agreement with theoretical predictions for wire antennas in a highly dissipative medium [King and Harrison 1969]. Also the localised mass averaged SAR enhancement is less due to a pointed tip relative to a flat tip as a result of the attenuation of the surrounding medium.

References

American National Standards Institute (ANSI), *American national standard safety levels with respect to human exposure to radio-frequency electromagnetic fields, 3 kHz to 300 GHz*, ANSI, New York, 1991.

Burke, G.J. and Poggio, A.J., *Numerical Electromagnetics Code (NEC)-method of moments*, Naval Ocean System Centre, Office of Naval Research Contract N00014-71-C-0187, 1981.

Durney, C.H., Massoudi, H. and Iskander, M.F., *Radiofrequency radiation dosimetry handbook*, 4th edn., Brooks Air Force Base, TX, USAF School of Aerospace Medicine, SAM-TR-85-73, 1986.

Fleming A.H.J. and K.H. Joyner, "Moment method analysis of radiation and scattering by thin wires in an infinite conducting medium", Special Issue ACES Journal on electromagnetic code validation, pp. 51-74, 1989.

Fleming A.H.J, V. Lubinas and K.H. Joyner, "Calculation of electric fields in tissue near metallic implants", 1992 Asia-Pacific Microwave Conference, Adelaide, 11-14 August, 1992.

Hafner, C. and Bombolt, L., The 3D electrodynamic wave simulator, West Sussex: John Wiley and Sons Ltd, 1993.

Iskander M.F. and A.M. Tumeh, "Design optimization of interstitial antennas", IEEE Trans. BME-36, pp. 238-246, 1989.

Joyner, K.H., Hocking, B., Fleming, A.H.J. and Macfarlane, I.P., "Metallic implants and exposure to radio-frequency radiation", Seventh International Congress of the International Radiation Protection Association, Sydney, April 10-17, 1988.

King, R.W.P. and Harrison Jr., C.W., *Antennas and waves - a modern approach*, M.I.T. Press, Massachusetts, 1969.

King, R.W.P. and Iizuka, K., "The complete electromagnetic field of a half-wave dipole in a dissipative medium", Trans. IEEE AP-11, pp. 275-285, 1963.

National Council on Radiation Protection (NCRP) (U.S.), *Radiofrequency electromagnetic fields: properties, quantities and units, biophysical interaction, and measurement*, NCRP Report No. 67, NCRP, Washington, 1981.

Taylor H.C. and R.W.M. Lau, "Evaluation of clinical hyperthermia treatment using time domain finite difference modelling technique", ACES Journal, vol. 7, no. 2, pp. 85-96, 1992.

Towards computational methods for studying cellular effects due to EM fields.

Author: A.H.J. Fleming

Monash University, Clayton, Australia, 3168

1. Introduction

In this paper, it is suggested that computations based on multi-particle methods be developed to model cellular effects due to static and time-varying electromagnetic (EM) exposures. Plasma physicists have for some time successfully modelled complex electromagnetic interactions by using multi-particle methods [Dawson 1983]. Electric (E-) and magnetic (B-) fields can originate from complex biological processes in which case they are often called biogenic fields, or due to solar, lunar, and planetary origin, and also due to modern technological advances. In biological tissues there are a variety of charged and inducibly dipolar particles such as electrolytes and complex proteins that can respond to electric and magnetic stimuli. Computational methods can be an important tool for the biologist, capable of providing comparison with results from 'wet studies', or as a 'what if' tool to investigate hypotheses. Experimental methods can be costly and difficult to set up for cellular investigations, and in this situation, computational methods can yield useful information prior to experimentation. Computational methods can also be used where it is suspected that weak effects are present and where epidemiological inference is flawed without large population bases upon which to draw. This paper points to several important situations where computational techniques might be used to assist the study of cellular effects due to a variety of EM fields.

Bioeffects due to static and time-varying EM fields depend upon the biological microstructure and may thus require to be studied using microdosimetric techniques [Tenforde 1992]. It is no surprise that there are effects due to biological microstructure that are not measurable using macroscopic methods. Fig. 1 shows a schematic of a human cell. New methods of electron microscopy are being developed and used to uncover previously unrevealed cell structure of exquisite complexity. Penman [1995] discussed how these new images are demanding a rethink of our previous ideas of cytoskeleton, nuclear matrix, mitosis, and the relation of membranes to cytostructure. Powerful new fluorescent markers are also being used to determine cellular concentrations of ions [Grynkiewicz et al. 1985] [Wolke et al. 1994]. Motions of cell components are also being revealed using these methods [Sowers and Hackenbrock 1981] [White et al. 1990]. In line with these advances, mathematical models of biological and cellular interactions with electric and magnetic fields based on simple geometries, eg cells and tissues represented by isolated layered spheres and ellipsoids, also need reworking.

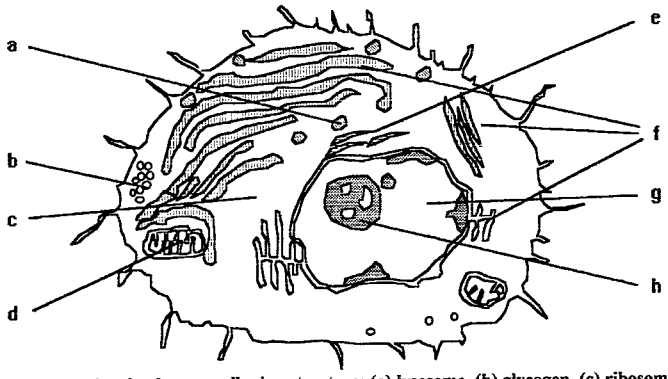

Fig. 1 Schematic showing human cell microstructure: (a) lysosome, (b) glycogen, (c) ribosomes, (d) mitochondrion, (e) golgi apparatus, (f) endoplasmic reticulum, (g) nucleus, (h) nucleolus

2. Towards development of methods of computational cell biology

Life in the industrialized world gives modern man devices and opportunities that were unimaginable a century ago. However, we are now bathed in a variety of E- and B-fields that are often much higher than the field levels that existed before modern times. The local geomagnetic flux density is around 1 x 10^{-4} T (1 Gauss) depending upon position on the globe. Some medical devices, eg. MRI, involve exposure to fields above 1 T. Environmental E-field levels vary between 150 V m^{-1} in fair weather, to 10 kV m^{-1} for brief periods during thunderstorms. Power transmission lines may cause long term exposures exceeding 10 kV m^{-1}. Little wonder that reports of cellular bioeffects due to weak exposure levels attract concern among the public and the scientific community. While such reports have not been widely accepted amongst the bioeffects community, they have caused a flurry of research into cellular and other microbiological effects.

In a recent review of E- and B-field bioeffects, Carpenter and Ayrapetyan [1994] detailed the need for research into the influence upon biological cells of both static and time-varying fields. Matters of concern and also opportunity in the areas of biohazards, biomedicine, and other bioelectromagnetic areas such as developmental and plant cell biology, need resolution. Glimpses of the possibilities exist, such as the use of pulsed magnetic fields (PMFs) in bone refracture therapy [Bassett 1989], high intensity PMFs as a prophylactic against the often fatal damage caused by ischaemic attacks (blockage of arteries) [Grant et al. 1994], and to mitigate against pain [Ellis 1994]. While there are no known mechanisms for a wide range of experimental B-field observations [WHO 1987], understanding of E-field effects is emerging.

Over the last decade, the body of knowledge of the influence of endogenous and exogenous E-fields upon cells has been expanding rapidly. While weak effects remain the subject of debate, a range of medium to strong effects is now at least partially understood. The range of effects observed on single cells due to E-fields includes electrophoresis, the translation of whole cells in the direction of the applied field, dielectrophoresus, the movement of cells in a dielectric medium associated with time-varying fields, electrorotation, the rotation (alignment) of cells in polarized fields, membrane electrophoresis, the diffusion of components within the plasma membrane, and electrodeformation, the distortion of the shape of the cell due to membrane stresses.

In many of these E-field effects, a quantitative understanding has emerged and theory can be tested against computation and observation. However no complete picture has emerged of the way in which E-fields operate to affect cell function. While 'snap-shots' of theories exist, numerical methods based on three-dimensional cell structure might provide a more meaningful 'moving picture' of these effects. A model which can calculate in the primary unit of cell effect, namely any changes in charged particle flux flowing in and around cells, and then obtain any flux dependent effects, would be most instructive. As distinct from one-dimensional (circuit analysis type) calculations which offer only an 'on-off' answer, there may be subtle effects revealed by detailed three-dimensional numerical analysis of a process involving many different interacting particles that evolves over time. Simple three-dimensional models of cells of this kind have begun to emerge. Sala and Hernández-Cruz [1990] examined the intracellular calcium inside a spherical model of a neuron due to buffers and tracers. No complete model that includes the membrane is available; certainly nothing to assist study of E-field effects.

3. Exposure of Cells to Electric Fields.

There are several interrelated research areas concerned with electrical exposure of cells. In this section, we survey three reported non-destructive bioeffects with an eye towards the eventual implementation of a computational approach towards cell biology. There is a natural progression through the three, from direct electrical contact, through medium to strong non-contact E-field exposure, to weak E-field exposure. Only the first is accepted without question since it can be tested theoretically against a number of observed effects. Mechanisms underlying the other two are unclear at present. Not until there is validated understanding will these bioeffects be accepted also as resulting from E-field exposure without

question by the bioeffects community. This is perhaps where numerical calculations can be most useful, as an aid to theoretical understanding.

It is worth pointing out that strong bioeffects tend to be able to be modelled using lumped circuit analysis techniques. As the bioeffect becomes more subtle, circuit concepts become less adequate as the particle diffusion becomes more disperse. Methods less filamentary, and more suited to volumetric analysis are needed, such as finite difference and finite element methods by which the overall inhomogeneous problem domain is subdivided into a series of smaller homogeneous entities, and where time is similarly subdivided into small time increments.

3.1 Direct Contact Effects: Membrane Voltage Patch Clamp.

Some cells act together to form physiological systems such as the heart, nerve fibres, muscles, and neuromuscular junctions. When the membrane of these cells are electrically 'fired', ions are released across the membrane. This occurs when a certain membrane potential has been reached. Commonly the cells are then able to propagate an ionic signal to their neighbours which are physically adjacent and a macroscopic effect follows. Electrophysiology is the study of such cellular systems that oscillate between resting and active states and are controlled by voltages applied across their membranes.

The study of membrane biophysics owes much to the pioneering work of Hodgkin and Huxley beginning in the early 1950's [Plonsey and Barr 1988]. Using voltage patch clamp electrodes, they investigated membrane ionic currents and their dependence on transmembrane potential. Starting with a resting membrane, in dynamic equilibrium, they increased the transmembrane potential until the cell became active deriving equations relating the time-varying ionic currents and the membrane potentials. Their work has lead to a deepening quantitative understanding of transmembrane dynamics [Chay and Keizer 1983] [Chay and Rinzel 1985]. The stochastic gating mechanism of individual ion channels is now understood so that this near molecular analysis ties in with effects at the cellular level [Plonsey and Barr 1988]. This direct contact effect has in turn lead to more recent experiments trying to elucidate the corresponding transmembrane ion dynamics when cells are exposed to external E-fields [Ehrenberg et al. 1987].

3.2 Biogenic E-field Effects[1].

Growth and development of cells is thought to be partly controlled by bioelectric fields. While the strong effects of electrophysiology are theoretically and experimentally indisputable, the weaker effects of biogenic E-fields are yet to be fully understood although recent efforts are progressing our understanding. Some effects may well depend upon the flow of ionic currents near cells [Jaffe 1979] and upon protein diffusion within plasma membranes [Poo 1981].

In a recent study, spherical *Mougeotia* protoplasts, originally cylindrical, were exposed to E-fields of 20 V m^{-1} [White et al. 1990]. Over some hours, the protoplast walls regenerated re-establishing the original shape. How regrowth occurs is unclear; but one possibility concerns electrophoresis of membrane proteins [Poo 1981].

Effects of exposure to static E-fields of 1000 V m^{-1} upon cytoskeleton were noted in experiments designed to observe and quantify galvanotaxis of fibroblasts [Hui 1994]. Changes in intracellular calcium flux were measured using aequorin, a calcium chemiluminescent indicator protein, and fluo-3, a calcium-sensitive fluorescent dye. Motility of the fibroblasts was measured, fluorescent micrographs showing

[1]There is a rich history of research into bioelectric fields and cells going going back at least to the discovery of the cell as a fundamental unit of biology by Schwann and Schleiden in 1847 [Lund 1947]. It is worth noting that since Mesmer in the 1770's to our own time, those who attempt to claim biological effects due to magnetism, ('animal magnetism'), have often been denounced as quacks and frauds, in total contrast with the popular success of experiments by Galvanni and Volta to demonstrate 'animal electricity' [Frankel 1986].

changes in actin-containing stress fibre patterns of the cytoskeleton that span across the cell body and are attached via proteins to the inner plasma membrane.

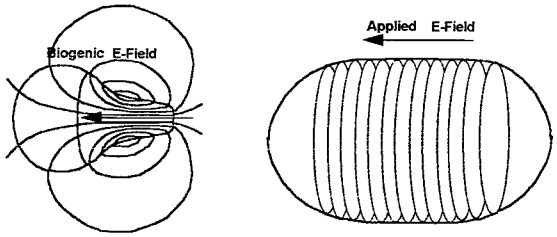

(a) (b)

Fig. 2 Development and growth in cells: (a) Asymmetric growth tip of seaweed *Fucus* embryo (b) Symmetric regrowth of *Mougeotia* protoplast. Symmetry is defined wrt left-right shape.

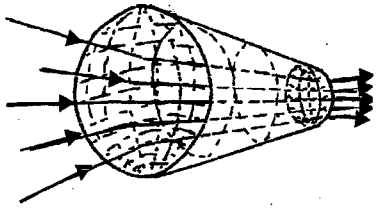

Fig. 3. Ionic currents flowing through *Mougeotia* protoplast. Proteins imbedded within the membrane adapt their positions by diffusion across the surface when exposed to electric fields (electrophoresis). These proteins presumably act as ion channels enabling currents to flow into and through the cell interior. Cylindrical growth is intrinsically symmetric, hence proteins presumably move to either end depending upon polarity to enable current flow.

3.3 Weak E-field Exposure Effects.

Over the past two decades, a number of reports have emerged of weak extremely low frequency (ELF) and ELF modulated radiofrequency (RF) exposures inducing measurable ionic changes in cells. Windowed effects at power densities less than 1 mW cm^{-2} across both ELF and RF frequencies have been reported [Adey 1980] [Adey and Sheppard 1987] [Bawin et al. 1989]. In the earliest experiments, chick brain hemispheres in saline solution inside a test tube of about 1.4 cm diameter were exposed to ELF and ELF modulated RF fields in air (see Fig. 4a). Extracellular tissue fields at ELF are estimated to be 10^{-6} V m^{-1} (see Fig. 4b), and the corresponding RF levels are around 10 V m^{-1}.

These experiments reportedly result in frequency dependent changes in intra and extracellular calcium ion (efflux/influx) concentration levels both at ELF and modulated ELF frequencies [Bawin et al. 1975] [Bawin and Adey 1976] [Liboff et al. 1987]. The original observations in which in-vitro specimens were exposed in air remain unsubstantiated as replication experiments have sometimes failed to support the primary findings [Schwartz et al. 1990] [Wood et al. 1993] raising suggestions that there is no actual effect, only experimental artefact; perhaps some other parameter apart from ELF exposure, eg temperature, is involved. Since the observations are not understood mechanistically, there is question within the bioeffects community about the validity of these effects at weak exposure levels. Further controversy exists as the

modulated effects, if valid, appear at levels below those set down by national and international RF exposure standards [IRPA 1988] [SAA 1990] [ANSI 1991], while the ELF effects occur at much weaker levels. In all this, it is not at all clear that any actual frequency dependence constitutes a health hazard, apart from being an interesting bioeffect. Public concern nevertheless demands further studies that will hopefully lead to a clear understanding.

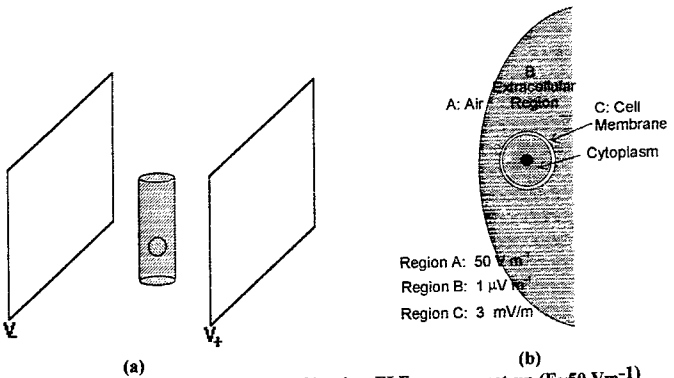

Fig. 4 (a) Schematic of in-vitro ELF exposure set-up ($E \approx 50\ V m^{-1}$)

(b) Fields inside extracellular medium and cell membrane due to 50 V m^{-1} E-field in air

4. Conclusion

At this point in time, there is a need for computational methods to be developed to provide tools to assist the theory and understanding of microbiological processes, and then to provide substantiation or otherwise for any cellular bioeffects.

Multi-particle methods seem appropriate as collective behaviour of charged particles, eg. ions and proteins, and polarizable particles, in particular cells, can be important in biology. Simple multi-cell methods using continuum (finite difference) equations, along with a simple but specialized grid incorporating (finite) periodic boundary conditions might permit feasible computations. Using appropriate special purpose but relatively simple multi-particle methods, cellular effects may be studied.

(1) By treating cellular tissues as suspended cells in an extracellular fluid, much as Maxwell did, but using numerical techniques based on multi-particle methods, it may be possible to develop working dielectric models that reflect fields in tissues that behave as expected and as measured [Foster and Schwan 1986] [Pethig 1988]. Such models would involve ions diffusing within the extracellular and intracellular media, and proteins diffusing within the plasma membrane, and would involve ion transport across the membrane surfaces. By allowing both the extracellular fluid and the charged particles on and within the cells, and the cells themselves, the freedom to move as a function of time, models of fluids may also be modelled and tested against measured data. Polarization of individual cells, and cell-cell effects, such as dipolar rotation and alignment, can be studied, and theory tested and improved.

(2) Biological processes such as growth and development of cells where biogenic E-fields processes are thought to be involved could be modelled. The time-evolutionary way in which biogenic fields are established in multi-cell tissues might be studied.

(3) Effects of chemical agents might be modelled as volumes of electrolytic fluids in which concentration gradients cause flows of ionic currents. Similarly, application of externally applied ELF or RF exposures, or development of biogenic E-fields would involve flows of the charged and dipolar particles.

(4) Bioeffects due to ELF or RF exposures might be studied using a two-tiered approach involving two levels of models, one overall macroscopic model and one or more microscopic model. The E- and B-field exposures in the microscopic studies could be estimated using macroscopic calculations; realistic models (eg using MRI scans) of the whole biological entity can give detailed exposure levels within different macroscopic tissues. Knowledge of the level of exposure within each microscopic model would come from this overall model. Thus, the overall problem might be solved using a two-tiered numerical approach, a macroscopic calculation combined with ensuing microscopic calculations to determine cellular effects. Use of finite periodic boundary conditions could allow the macroscopic fields to be incorporated as a variable far-field in the microscopic model. This would allow the inhomogeneity of the macroscopic fields to take effect at the cellular level within the microscopic models.

5. Acknowledgments

The author would like to thank Prof. Joe Monaghan and Dr Rosemary White for their kind help including some useful discussion sessions, and his daughter Ms Jane Fleming for her assistance with the illustrations.

6. References

Adey W.R., "Frequency and power windowing in tissue interactions with weak electromagnetic fields", Special issue on biological effects and medical applications of electromagnetic energy, Ed. O. Gandhi, IEEE Proc., vol. 68, no. 1, pp. 119-125, 1980.

Adey W.R. and A.R. Sheppard, " Cell surface ionic phenomena in transmembrane signalling to intracellular enzyme systems", in *Mechanistic approaches to interactions of electric and electromagnetic fields with living systems*, eds M. Blank and E. Findl, Plenum Press, New York, pp. 365-388, 1987.

American National Standards Institute (ANSI), *American national standard safety levels with respect to human exposure to radio-frequency electromagnetic fields, 3 kHz to 300 GHz*, ANSI, New York, 1991.

Bassett C.A.L., "Fundamental and practical aspects of therapeutic uses of pulsed electromagnetic fields (PEMFs)", Critical reviews in biomedical engineering, vol. 17, no. 5, pp. 451-527, 1989.

Bawin S.M., L.K. Kaczmarek and W.R. Adey, "Effects of modulated VHF fields on the central nervous system", Ann. NY Acad. Sci., vol. 247, pp. 74-91, 1975.

Bawin S.M. and W.R. Adey, "Sensitivity of calcium binding in cerbral tissue to weak environmental electric fields oscillating at low frequency", Proc. Nat. Acad. Sci. USA, vol. 73, pp. 1999-2003, 1976.

Bawin S.M., L.S. Kinney, D.E. House, and W.T. Joines, "Multiple power-density windows and their possible origin", Bioelectromagnetics, vol. 10, pp. 115-128, 1989.

Carpenter D O and S. Ayrapetyan (eds), *Biological effects of electric and magnetic fields*, Academic Press, San Diego, 1994.

Chay T.R. and J. Keizer, " Minimal model for membrane oscillations in the pancreatic β-cell", Biophys. J., vol. 42, pp. 181-190, 1983.

Chay T.R. and J. Rinzel, " Bursting, beating and chaos in an excitable membrane model", Biophys. J., vol. 47, pp. 357-366, 1985.

Dawson J.M., "Particle simulation of plasmas", Reviews of Modern Physics, vol. 55, no. 2, pp. 403-447, 1983.

Ehrenberg B., D.L. Farkas, E.N. Fluhler, Z. Lojewskz and L.M. Loew, " Membrane potential induced by external electric field pulses can be followed with a potentiometric dye", Biophys. Soc., vol. 51, pp. 833-837, 1987.

Ellis W. V., "Pain control using high-intensity pulsed magnetic stimulation", Bioelectromagnetics, vol.14, pp. 553-556, 1994.

Foster K.R. and H.P. Schwan, "Dielectric properties of tissue", in *Handbook of biological effects of electromagnetic fields*, eds C. Polk and E. Postow, CRC Press, Florida, pp. 27-96, 1986.

Frankel R.B., "Biological effects of static magnetic fields", in *CRC handbook of biological effects of electromagnetic fields*, eds C. Polk and E. Postow, CRC Press, Florida, pp.169-196, 1986.

Grant G., R. Cadossi and G. Steinberg, "Protection against focal cerebral ischemia following exposure to a pulsed electromagnetic field", Bioelectromagnetics, vol.15, pp. 205-216, 1994.

Grynkiewicz G., M. Poenie and R.Y. Tsien, "A new generation of Ca^{2+} indicators with greatly improved flourescence properties", J. Biol. Chem., vol. 260, pp. 3440-3450, 1985.

Hui S.W., "Electric field-induced calcium flux and changes in cell shape, motility, and cytoskeleton", in *Biological effects of electric and magnetic fields*, eds D.O. Carpenter and S. Ayrapetyan, Academic Press, San Diego, 1994.

International Non-Ionizing Radiation Committee of the International Radiation Protection Association (IRPA), "Guideline on limits of exposure to radio-frequency electromagnetic fields in the frequency range from 100kHz to 300 GHz", Health Physics, vol. 54, no. 1, pp. 115- 123, 1988.

Jaffe L.F., "Control of development by ionic currents", in *Membrane transduction mechanisms*, eds. R.A. Cone and J.E. Dowling, Raven, New York, pp. 199-231, 1979.

Lund E.J., *Bioelectric fields and growth*, University of Texas Press, Austin, 1947.

Penman S., "Rethinking cell structure", Proc. Natl. Acad. Sci. USA, vol. 92, pp. 5251-5257, 1995.

Pethig R., "Electrical properties of biological tissue", *Modern bioelectricity*, Marcel Dekker, New York, pp. 125-179, 1988.

Plonsey R. and R.C. Barr, *Bioelectricity - a quantitative approach*, Plenum Press, New York, 1988.

Poo M., "In situ electrophoresus of membrane components", Ann. Rev. Biophys. Bioeng., vol. 10, pp. 245-276, 1981.

Sala F. and A. Hernández-Cruz, " Calcium diffusion modelling in a spherical neuron", Biophys. J., vol. 57, pp. 313-324, 1990.

Schwartz J.L, D.E. House and G.A.R. Mealing, "Exposure of frog hearts to CW or amplitude-modulated VHF fields: selective efflux of calcium ions at 16 Hz", Bioelectromagnetics, vol. 11, pp. 349-358, 1990.

Sowers A.E. and C.R. Hackenbrock, "Rate of lateral diffusion of intramembrane particles: measurement by electrophoretic displacement and rerandomization", Proc. Natnl. Acad. Sci. USA, vol. 78, pp. 6246-6250, 1981.

Standards Association of Australia (SAA), *Radio-frequency radiation Part 1: maximum exposure levels - 100 kHz to 300 GHz*, North Sydney, Standards House, AS2772.1, 1990.

Tenforde T.S., "Microscopic dosimetry of extremely-low-frequency electric and magnetic fields", Bioelectromagnetics, suppl. issue no. 1, pp. 61-66, 1992.

White R.G., G.J. Hyde and R.L. Overall, "Microtubule arrays in regenerating Mougeotia protoplasts may be oriented by electric fields", Protoplasma, vol. 158, pp. 73-85, 1990.

Wolke S., U. Neibig, R. Elsner, F. Gollnick and R. Meyer, "A setup for measurement of intracellular calcium during high frequency application", Sixteenth Annual Meeting Bioelectromagnetics Society, Copenhagen, June 12-17, 1994.

Wood A.W., V. Lubinas, K.H. Joyner and B.A. Hocking, "Calcium efflux from toad heart: a replication study", in *Electricity and magnetism in biology and medicine*, ed. M. Blank, San Fransisco Press, San Fransisco, pp. 484-484, 1993.

World Health Organization (WHO), "Health criteria document 69: Magnetic fields", World Healtth Organization, Geneva, 1987.

Comparison of Computer Simulated and Measured SAR Values in the Head of a Human Phantom next to Mobile Phone

FJC Meyer* and U Jakobus+
* EM Software & Systems (EMSS), Stellenbosch, South Africa: E-mail: fjcmeyer@emss.co.za
+ Institut für Hochfrequenztechnik, Univ. Stuttgart, Germany: E-mail: jakobus@ihf.uni-stuttgart.de

Abstract

The Specific Absorption Rate (SAR) in the head of a mobile phone operator is investigated using both numerical and experimental dosimetry[1]. A box and a sphere phantom (test phantoms) as well as a female phantom are used, with a dipole antenna and a mobile phone as RF sources. The Method of Moments (surface equivalence principle) is employed for the simulations with geometrically accurate numerical models representing the human phantom and antennas. For the measurements, fibre-glass phantom casings are filled with liquid based equivalent biological material. Near field and SAR results obtained from measurements and simulations are compared.

1 Introduction

The popularization of mobile phone communication through the cellular phone industry in the past few years has, among other things, increased awareness of the possible health risk involved in using a mobile phone. In the past five years various international research groups and institutions have been involved in research activities related to the possible hazardous effect of mobile phones on human operators. The nature of the problem is such that the activities can be sub-divided into three main fields of research: 1) Dosimetry research: This field of research can generally be described as the calculation, deduction or measurement of the electromagnetic fields penetrating into the head of a human operator or the power dissipation associated with the penetrating fields; 2) Biological research: This involves studies performed on biological tissues or animals when exposed to non-ionizing radiation at cellular phone frequencies; 3) Epidemiological research: Epidemiological studies involve the statistical evaluation of the association between disease (or illness) and exposure to electromagnetic fields at mobile phone frequencies.

An excellent summary of *biological* and *epidemiological* research and results can be found in reference [1]. The work presented in this paper falls under the dosimetry research category. The energy absorption in the head of a mobile operator is investigated using both experimental (measurements) and numerical dosimetry. The investigation is limited to dosimetry involving homogeneous phantoms (equivalent muscle tissue only) in free-space. SAR results for inhomogeneous phantoms (muscle, brain and bone tissue) in free-space as well as in a motor vehicle can be found in reference [2].

Section 2 of this paper describes the establishment of the measurement setups as well as the general preparations for performing *experimental* dosimetry. Equivalent biological materials were prepared using recipes found in the literature and the properties of the materials (permitivity and conductivity) were measured for validation purposes. Fibre-glass based phantoms were filled with equivalent tissues which were prepared in a liquid based (gel-like) form. A box and a sphere phantom were used as test phantoms with a dipole antenna with balun as RF source. Field measurements were performed inside the equivalent tissue material in the test phantoms. From this the SAR (Specific Absorption Rate) can be extracted. A female phantom filled with muscle tissue was used, with a dipole antenna and a mobile phone (with extended and short antenna arms) as RF sources.

Section 3 presents the technical aspects of *numerical* dosimetry and considers some results obtained as well as a technical interpretation thereof. Geometrically accurate numerical models of the female phantom as well as the

[1]The word dosimetry has been derived from the dosimetric concept (where the 'dose' is defined as the energy per unit mass) used by international regulating bodies for protection from non-ionizing radiation.

dipole and mobile phone were developed and used with the MoM simulations. Method of Moments (MoM) results for the test phantoms as well as the female phantom are compared to measurements.

The emphasis of this paper is on the *comparison* between measured and calculated field values (and related SAR values) inside the phantoms. The methodology employed with measurements and numerical simulations will also be considered. Due to the sensitive nature of the topic, the absolute SAR values obtained will not be presented here.

2 Experimental Dosimetry

2.1 Phantom development

Three types of equivalent biological tissue materials were prepared namely muscle, brain and bone tissue (see reference [2]). The work presented in this paper concerns measurements and simulations using only muscle tissue (homogeneous phantoms).

A coaxial measurement system in conjunction with a Baker-Jarvis extraction algorithm [3] was used to measure the electrical properties of all the synthetic tissue equivalents. The measured material parameters of the equivalent biological tissue are given in table 1. These values compare reasonably well with those published in the literature [4] (a 5-10% difference for muscle and brain tissue). The only exception is the conductivity of the equivalent bone tissue (see reference [2] for more detail).

Table 1: Material parameters of simulated human tissue at 900MHz.

Tissue Type	Measured		From Literature	
	ϵ_r	σ [S/m]	ϵ_r	σ [S/m]
Muscle	51.75	1.25	54.7	1.38
Brain	38.25	1.10	41.2	1.22
Bone	7.89	0.072	7.4	0.16

Fibre-glass phantom casings were manufactured and used as containers of the equivalent tissue (prepared in liquid form) when measurements were performed. The rectangular shaped box phantom (31cm x 23cm x 10cm) and the spherical phantom (r=9.4cm) are test phantoms used for preparation (setting up the measurement procedures) and validation purposes. The third and fourth casings are fibre-glass shells of a female (see figure 2) and a male human being. The female and male phantoms were constructed using a mannikin. These human phantoms were filled with equivalent muscle tissue material when measurements were performed. Only the results for the box, sphere and female phantoms will be considered in this paper.

2.2 Measurements at the US Setup

An experimental dosimetry setup in the Anechoic chamber at the Department of Electrical and Electronic engineering, University of Stellenbosch (the US setup) has been established. A network analyzer was used to perform measurements on a two-port system.

The probe used is an electrically small dipole antenna. The probe consists of a Marchand balun with two semirigid coaxial waveguides extruding one-and-a-quarter wavelengths out of the balun. This ensures a balanced dipole probe with reasonable matching properties. The probe movement is controlled by the automated x-y positioning system, and a semi-automated third axis (z-axis) positioning arm.

As the first "test" source antenna, another dipole was used (see figure 1), also fed with a Marchand balun. This antenna is resonant at 900MHz. A mobile phone, with extended and short antenna arm, was converted so that it could be used as a source antenna for the human phantom measurements. A thin 50-ohm semi-rigid cable was guided inside the phone from the feed-point of the antenna to a suitable area for a connector to be attached. S_{11} (with antennas in position next to phantom head), radiation patterns and gain of the dipole and the mobile phone were measured. S_{11} together with the internal losses, determines the actual power transmitted by the antennas.

In the measurement setup, the transmitting antenna is connected to port 1 of the network analyser and the probe to port 2. The measured data obtained from the network analyser is S_{21}. Using S_{21} and the measured antenna characteristics, the electric field components at the measurement position can be computed [2] for a specified input power. A SAR value can then be extracted from this vector E-field using the following equation [1]:

$$SAR = \frac{1}{2}\frac{\sigma|E|^2}{\rho} \tag{1}$$

with σ the conductivity (in S/m) and ρ the density (in kg/m^3) of the equivalent biological material. Both σ (see table 1) and ρ (1.30 g/cm^3) were measured for the equivalent muscle tissue.

Measurements were performed using the sphere, box and female phantoms at the US Setup. For the box phantom the dipole antenna was positioned with dipole arms 3.5cm below the box with the dipole feed point (voltage gap) aligned with the centre of the box. The dipole arms were parallel to the longest sides (31cm sides) of the box. The probe penetrated into the box from the top. Measured results along a line across the box, 1cm from the bottom, are presented in figure 4.

A 3cm long, 3mm wide slot was cut out of the sphere phantom. This slot was used to fill the sphere with muscle tissue. The dipole antenna was positioned 1cm from the bottom of the sphere. The dipole probe penetrated into the sphere through the slot (mentioned above) cut out of the "top" of the sphere. This allows for movement of the probe in the vertical direction only. Measured results along a line starting at the bottom of the sphere and extending along a centre-line to the top of the sphere are shown in figure 5.

Figure 2 shows the female phantom measurement at the US setup. In order to measure both polarizations of the electric field, all measurements were repeated with the dipole probe aligned in both the x- and z-directions. Figures 6 and 7 show the SAR values along a line penetrating vertically into the head of the female phantom. The dipole and mobile phone with extended antenna were used for these measurements.

2.3 The EMSS Setup

An experimental dosimetry setup has been established at the offices of EM Software & Systems. The differences between the US-Setup and the EMSS-Setup lie mainly in the methodology of probing the electric field inside the phantoms. Figure 3 shows a diagram of the EMSS measurements setup.

At the EMSS setup a signal generator (900 MHz) is connected to a 13 Watt amplifier. The output of the amplifier is connected to the RF source antennas (dipole or mobile phones). A diode-based probe has been designed and manufactured for this project. The 900MHz electric field at the probe tip is converted to a DC-signal by the diode. The voltage at the end of the DC-lines is a function of the electric field at the probe tip. A low pass filter reduces any unwanted signals received along the data acquisition lines which might be picked up by the diode and converted to a DC-signal. (The detail workings of such a probe is discussed in references [5]).

The probe developed is polarized and yields only one of the three spatial components of the electric field. A second component can be measured by rotating the probe by 90 degrees and repeating the measurement. The third component cannot be measured with the current probe. The probe positioning at the EMSS facility is controlled by a three-axis positioning system — two PC controlled and one manual controlled to within 2mm positioning accuracy.

For probe calibration, temperature measurements were performed in the box phantom filled with muscle tissue (see figure 4). A thermocouple was used as temperature probe with the same data acquisition electronics used for the diode-based electric field probe. More detail on probe calibration can be found in references [1, pp.36] and [2].

SAR values can be obtained from the electric field measurements at the EMSS setup using equation 1. Measurements were performed at the EMSS setup using the box and homogeneous female phantoms. The sensitivity of the probe (or lack thereof) and the DC-voltage noise level (caused by various devices in the system) were the two main reasons causing unreliable measured results in regions of low SAR values. It was thus not possible to perform accurate measurements in the sphere phantom.

3 Numerical Dosimetry

The method of moments (MoM) [6] as implemented in the computer code FEKO [7] is the numerical technique used for the simulations. The Finite Element Method and Finite Different Time Domain are two other techniques

suitable for SAR calculations. Technical information on the MoM, FEM and FDTD techniques as SAR prediction tools can be found in reference [1].

3.1 MoM implementation in FEKO

With the MoM implementation in FEKO metallic surfaces are subdivided into triangular patches and the treatment is similar to reference [8], with some minor modifications. Metallic wires and the connection of wires with surfaces are also supported. These features were used for modelling the dipole and mobile phone antennas.

Several possibilities exist in order to consider dielectric bodies within the framework of the MoM: Application of the volume or the surface equivalence principles. Both techniques are available in FEKO, but for this paper the surface equivalence principle was chosen because of the requirement of a 3-D discretization for the volume equivalence principle, the memory requirement is too high at the frequency range under consideration. The surface equivalence principle, on the other hand, requires only a 2-D discretization of the scatterer's surface, but limits the application of the MoM to partly homogeneous bodies. This is acceptable for the current application to homogeneous phantoms filled with muscle tissue.

Similar to metallic structures, the surface of the dielectric body is also represented by triangular patches (see figure 4) and the unknown equivalent surface current densities of electric and magnetic type are expressed by the superposition of basis functions:

$$\vec{J} = \sum_{n=1}^{N} \alpha_n \vec{f}_n \qquad \vec{M} = \sum_{n=1}^{N} \beta_n \vec{g}_n \ . \tag{2}$$

The same rooftop basis functions $\vec{f}_n$ used for metallic surfaces are also applied to model the equivalent electric current density $\vec{J}$. Depending on the kind of integral equation (EFIE, MFIE, CFIE, PMCHW, Müller, see e.g. [9, 10] for more details) the simple selection $\vec{g}_n = \vec{f}_n$ leads to singular matrices of the system of linear equations. An alternative for $\vec{g}_n$ was proposed in [11]. However, for the computation of peak SAR values right at the surface of the dielectric body, it turned out that these basis functions lead to some oscillating behavior in the scattered electric near-field very close to the dielectric/air interface. Alternative basis functions $\vec{g}_n = \hat{n} \times \vec{f}_n$ proposed in [12, 13] are therefore used in this paper in conjunction with the EFIE (Galerkin method).

3.2 Models of the source antennas

The dipole antenna was modelled as two metallic arms with a voltage gap. The inclusion of the balun casing in the MoM model was essential. The voltage gap source model described above ensures a balanced dipole feed. It was thus **not** necessary to include the balun network into the models, only the geometry of the balun casing.

The mobile phone antenna was modelled using two flat metallic boxes, representing the cellphone base and battery, and a metallic rod representing the extended or short antenna arms. A voltage gap feed segment (connected on the one end to the cellphone base and on the other end to the extended arm) was used. The mobile phone models developed for the MoM simulations are reasonably accurate when radiation patterns are compared. However, there is certainly room for improvement.

3.3 Phantom models

The MoM sphere and box phantoms were created using FEKO's sphere and quadrangular element geometric control cards. The surface equivalence principle is used (see section 3.1 above) with the appropriate material parameters (ϵ_r and σ) for the enclosed dielectric region. The MoM requires only a surface mesh which was discretised as fine as 0.1 λ_r maximum triangular element side length (with λ_r the wavelength inside the dielectric region). The dipole antenna was used with the sphere and box phantoms which allowed for the utilization of symmetry in the FEKO models.

Accurate numerical models of the female phantom was created from CAT scans of the phantoms and a *CAT-scan-to-Polygon-shaped* conversion program developed for this project. The coordinates of the polygons representing the various cross-sections of the head (at different levels) were used as nodal points on a surface mesh consisting of triangles. The triangles were written to a STL (Stereolithography) format for inclusion in FEKO.

The female phantom model for the MoM is shown in figure 7. This model consists of 2294 triangular elements (6882 unknowns) on the surface of the phantom head. This is very close to the largest dielectric body (consisting of muscle tissue) which can be solved at 900MHz with the available computer hardware[2].

3.4 Computer simulated results

In this section we will consider the results obtained with the numerical phantom models described above. The results will be compared to measurements at the two experimental dosimetry setups. Note that all SAR results have been normalized such that the maximum value on each figure is equal to 1 [W/g]. The comparison between measurements and simulations is thus presented without presenting the absolute SAR values.

Results obtained with the box phantom are compared to measurements in figure 4. There is good agreement in general. The MoM seems to slightly over-predict SAR values when compared to both sets of measurements. The shape of the SAR predictions from the temperature measurements is clearly not as smooth as would be expected. The temperature measurement at the centre point of the line was used for calibrating the diode-based probe.

With the sphere phantom simulations convergence test results showed that the MoM models were discretised fine enough using $\lambda_r/5$ maximum triangle edge length on the surface of the sphere. The agreement between measured and MoM simulated results is excellent (see figure 5). The position as well as the depth of the nulls is almost identical.

For the numerical simulations involving the homogeneous female phantoms, material parameters for equivalent muscle tissue ($\epsilon_r = 51.75$ and $\sigma = 1.25$ — see table 1) were used. Figure 6 shows SAR results on a vertical line starting close to the antenna and penetrating into the phantom head. This is for a homogeneous female phantom with dipole antenna.

The MoM results (complete head) agree well with the measurements at the US Setup except close to the side of the head furthest from the antenna. A spatial shift is observed in the null. The reason for this is that the complete female phantom head is used with the simulations while the female phantom is **not** completely filled with equivalent muscle tissue when measurements are performed (see figure 2). The null seems to arise from an out of phase reflection originating at the material discontinuity where the muscle tissue ends, and the air starts again. The null would certainly be expected to shift if the position of the material discontinuity shifts. The MoM *partial head* result on the same figure shows how the null moves close to the measured null when a partial female phantom head is simulated.

Figure 7 shows SAR results on a vertical line penetrating into the phantom head of a homogeneous female phantom with mobile phone antenna (extended). The MoM results are for a partial phantom head. The MoM results compare well with the measured results of the US Setup. The EMSS results compare well with the US Setup measurements and the simulations in the region close to the antenna. No EMSS measurements were performed deeper into the phantom head due to the relatively high noise level of the diode based probe at the EMSS setup. The discontinuity in the EMSS measurements at approximately 2.5cm into the head is where the SAR values are below the current noise level.

4 SAR distribution in the phantom head

The numerical simulations can be used to calculate the SAR values on a 3D grid inside the phantom head. This allows one to compare the SAR distribution in the phantom head for different RF source antennas. (This would also be possible for measurements if a 3D grid of measured data is available.) Figures 8 to 10 show some of the SAR distribution results in the head of the human phantoms using different source antennas. It is clear from these and other results not presented that the distributions differ for the different source antennas. The SAR is certainly distributed more smoothly along the inside of the head with the extended mobile phone antenna than with the short antenna.

[2] A 512M RAM, 200MHz, dual processor, Pentium Pro PC

5 Conclusions

Two experimental dosimetry setups have been established. At the US setup measurements were performed inside a completely shielded anechoic chamber using a small dipole probe and a network analyser. The probe penetrated into equivalent biological tissue contained in a fibre-glass phantom head (muscle tissue).

At the partially shielded EMSS setup temperature measurements were performed inside equivalent muscle tissue to calibrate a diode-based E-field probe. This field probe, with data acquisition electronics and software, was then used to perform electric field measurements inside a female phantom filled with muscle tissue. From these electric field measurements, SAR values could be obtained.

Computer models of the human phantoms were created using CAT scans and geometrical coordinate extraction software. Models of the mobile phone antennas were also created. Numerical simulations were performed using the Method of Moments. From these results it is possible to extract various parameters including the SAR values inside the phantoms.

SAR results were compared with each other to investigate the validity of the techniques employed. It was not possible to investigate all the different scenarios in which a mobile phone can be used by an operator. The three antennas (dipole, mobile phone with extended arm and with short arm) were each positioned in only one typical operational position next to the phantom head.

It should be noted that the hand of a user could absorb a significant percentage of the power transmitted from a mobile phone. The hand could also alter the effectiveness of the phones resulting in changes in the SAR levels as well as the SAR distribution in the head. No hand was included in any of the measurements or simulations and this is an important improvement which could be considered for future work.

There is some room for improvement of the measurement equipment as well as the computer models but the agreement between simulations and measurements are in general very good. A reliable and accurate experimental and numerical dosimetry capability has been establish that could serve as a basis from which to address more challenging dosimetry problems, e.g. low SAR antenna design.

References

[1] N. Kuster, Q.Balzano, and J. Lin, *Mobile Communication Safety.* Chapman & Hall, 1997.

[2] F. J. C. Meyer, "Cellular phone / human phantom interaction: Final technical report," Tech. Rep. P02-MN04-97, EM Software & Systems, May 1998.

[3] M. Bingle and D. Pansegrouw, "A coaxial system for measuring the complex permittivity of fluids and gels from 1-12 Ghz," tech. rep., Department of Electrical and Electronic Engineering, University of Stellenbosch, May 1997.

[4] G. Hartsgrove, A. Kraszewski, and A. Surowiec, "Simulated biological materials for electromagnetic radiation absorption studies," *Bioelectromagnetics*, vol. 8, pp. 29–36, 1987.

[5] T. Schmid and N. Kuster, "Novel e-field probe for close-near field scanning," *IEEE Trans. Veh. Technol.*, 1996.

[6] J. Wang, *Generalized Moment Methods in Electromagnetics.* Wiley, 1991.

[7] U. Jakobus, *FEKO User's Manual.* EM Software & Systems, South Africa, April 1997.

[8] S. M. Rao, D. R. Wilton, and A. W. Glisson, "Electromagnetic scattering by surfaces of arbitrary shape," *IEEE Transactions on Antennas and Propagation*, vol. 30, pp. 409–418, May 1982.

[9] A. A. Kishk and L. Shafai, "Numerical solution of scattering from coated bodies of revolution using different integral equation formulations," *IEE Proceedings H: Microwaves, Antennas and Propagation*, vol. 133, pp. 227–232, June 1986.

[10] J. R. Mautz and R. F. Harrington, "Boundary formulations for aperture coupling problems," *Archiv für Elektronik und Übertragungstechnik*, vol. 34, no. 9, pp. 377–384, 1980.

[11] U. Jakobus and F. M. Landstorfer, "Novel basis function for the equivalent magnetic current in the method of moments solution of dielectric scattering problems," *Electronics Letters*, vol. 29, pp. 1272–1273, July 1993.

[12] S. M. Rao, T. K. Sarkar, P. Midya, and A. R. Djordevic, "Electromagnetic radiation and scattering from finite conducting and dielectric structures: Surface/surface formulation," *IEEE Transactions on Antennas and Propagation*, vol. 39, pp. 1034–1037, July 1991.

[13] T. K. Sarkar, S. M. Rao, and A. R. Djordjević, "Electromagnetic scattering and radiation from finite microstrip structures," *IEEE Transactions on Microwave Theory and Techniques*, vol. 38, pp. 1568–1575, Nov. 1990.

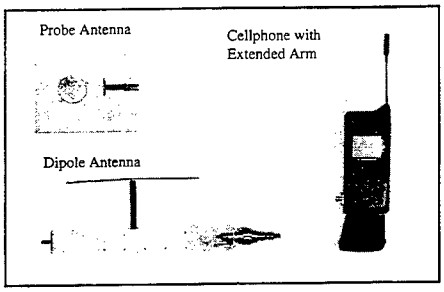

Figure 1: Dipole probe and RF source antennas.

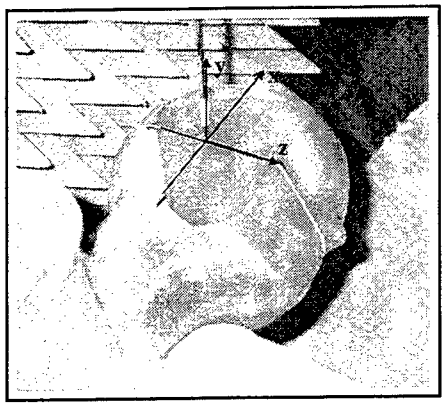

Figure 2: Coordinate system used with female phantom measurements at US Setup.

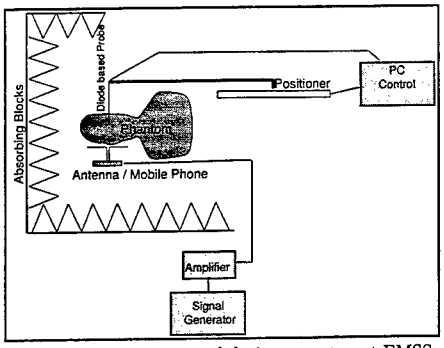

Figure 3: The experimental dosimetry setup at EMSS.

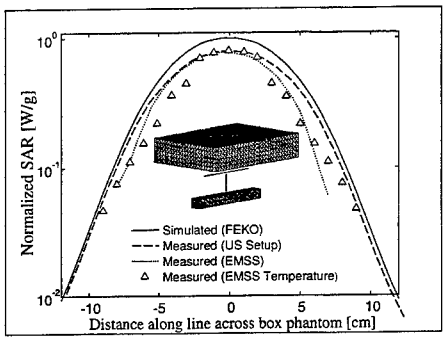

Figure 4: Measured and computer simulated SAR results along a line in the Box phantom.

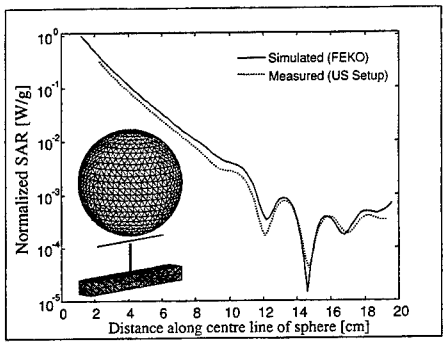

Figure 5: Measured and computer simulated SAR results along a vertical line from the bottom of the sphere phantom upwards.

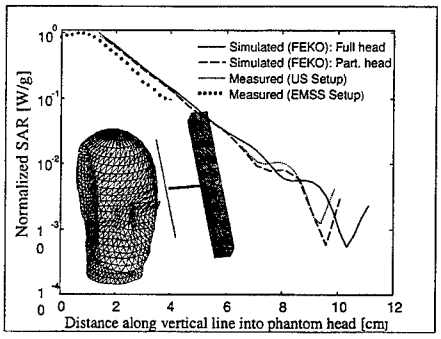

Figure 6: Comparison of MoM simulations and US Setup measurements on a vertical line penetrating into the head of a homogeneous female phantom.

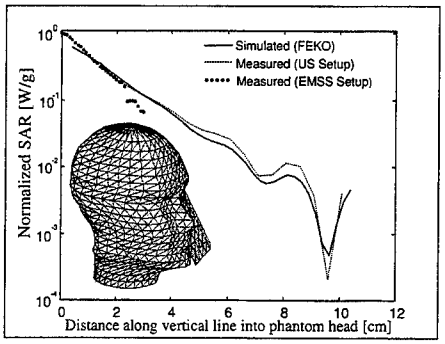

Figure 7: Comparison of MoM simulations and US Setup measurements using a mobile phone antenna with extended arm.

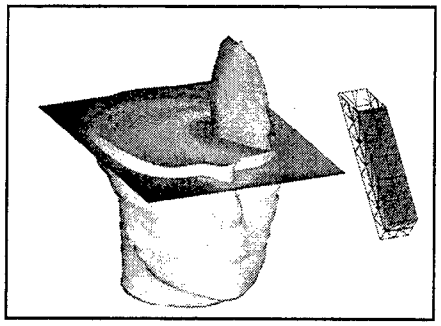

Figure 8: SAR distribution: female phantom, dipole antenna.

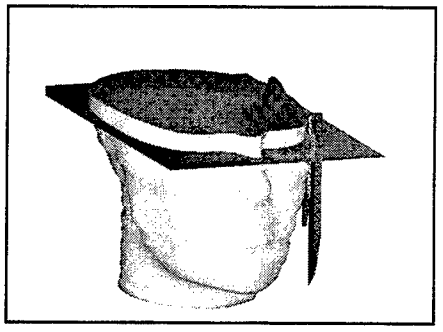

Figure 9: SAR distribution: female phantom, extended mobile phone antenna.

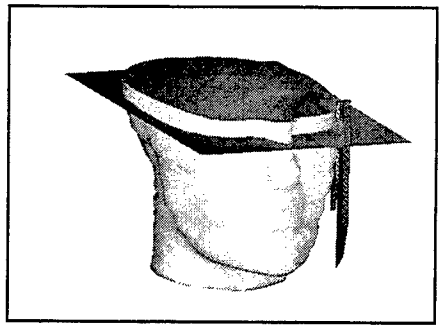

Figure 10: SAR distribution: female phantom, short mobile phone antenna.

Validation of the FDTD Near Fields of a Portable Radio Handset and Simple Head

C. W. Trueman
S.J. Kubina
Electromagnetic Compatibility Laboratory,
Concordia University,
Montreal

D. Cule
W.R. Lauber
Communications Research Centre,
Ottawa

Abstract-This paper examines the near field of a portable radio handset at 850 MHz operating near a model of the human head. The handset and head are solved by the finite-difference time-domain method. For the handset in isolation, the near field computed with FDTD is compared with that computed with the Numerical Electromagnetics Code, with excellent agreement. The near field was measured using a three-axis probe positioned with a planar scanner system in an anechoic chamber. The FDTD computation is compared with the measured near field and very good agreement is shown. Introducing a box or sphere model of the head changes the field of the handset. The measured near field of the handset and box head, and of the handset and sphere head are shown to be in good agreement with the FDTD computation.

Introduction

Fig. 1 shows a portable radio "handset"[1] comprised of an aluminum box 5.35 by 1.74 by 16.77 cm, with an antenna 8.82 cm in length, located 0.87 cm from three adjacent edges of the case. The antenna is a quarter-wave monopole operating at 850 MHz. In this paper we investigate the vertical component of the near field of the handset in an *xz* plane located at *y*=-21.8 mm in Fig. 1, where the base of the antenna is at the origin. The objective is to validate computations of the near field done with the finite-difference time-domain(FDTD) method[1,2].

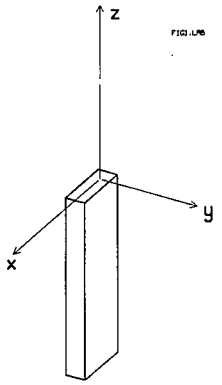

Fig. 1 The portable radio handset in the *xyz* coordinate system.

Near Field of the Handset Alone

Using a cell size of 2.205 cm, the handset case is very close to 24 by 8 by 76 cells, and the antenna is 40 cell edges in length. The perfectly-matched layer(PML) absorbing boundary[2] is used, 6 cells in thickness with a surface reflection coefficient of 0.001 and parabolic evolution of the conductivity. The handset is embedded in a cell space 96 by 88 by 188 cells with the base of the antenna on cell edge 41, 41, 113. The surfaces of the handset and the tip of the antenna are separated from the first layer of the PML by 30 cells of free space or "whitespace". In all cases in this paper the FDTD computation is

run for 4096 time steps with a sinusoidal generator at 850 MHz at the base of the monopole. The FDTD code is used to compute a set of "conical cut" radiation patterns[1] that cover the surface of the radiation sphere. The radiated power is computed from the patterns as

$$P_{rad} = \frac{1}{2\eta}\int_{\theta=0}^{\pi}\int_{\phi=0}^{2\pi}(E_\theta^2 + E_\phi^2)\sin\theta d\phi d\theta$$

and the fields presented in this paper are scaled to correspond to a radiated power of 600 mW.

An initial validation of the FDTD computation was obtained by comparing the near field of the handset computed with FDTD with that found using a wire-grid model of the handset[1] solved with the Numerical Electromagnetics Code(NEC)[3]. Fig. 2 shows the vertical component E_z of the near field of the handset in an xz plane in Fig. 1 at y=-21.8 mm. The field is shown in decibels with 1 volt per meter as the 0 dB reference. The black contours were computed with FDTD. The region of space around the edges of the map corresponding to the PML layers were removed from the FDTD data. In Fig. 2, the FDTD-computed contours are superimposed on the near field computed with the wire-grid model of the handset, shown in gray. There is excellent agreement between the two computations. The near field is large surrounding the tip of the antenna, the top of the case and the base of the case. At the surface of the case the E_z component of the field would be zero. At our xz plane, 13.1 mm from the case surface, the near field falls to values below 24 dB over the center of the case. The frequency-domain, moment-method based NEC computation obtains almost the identical near fields to the time-domain FDTD method.

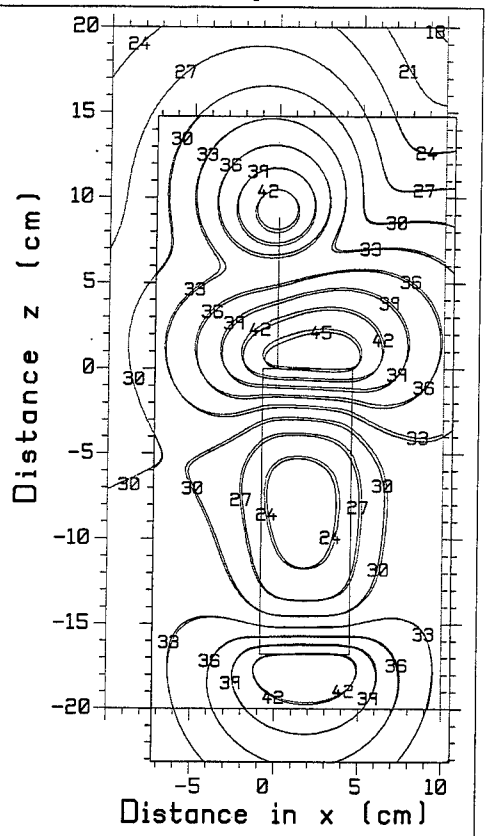

Fig. 2 Comparison of E_z computed with FDTD (black) and computed with NEC(gray), at 21.8 mm from the antenna.

Measurement of the Near Field

The near field of the handset was measured[4] in an anechoic chamber 2.5 m in height and 3.74 m in width and depth. The ceiling and walls were lined with 12 inch thick absorber. The probe was moved over the measurement plane using an Orbit Advanced Technologies planar scanner. The scanner was covered with 12 inch absorber as much as possible. The positioning mechanism was covered with three-inch absorber.

A "DASY-2" three-axis probe[5] uses three small, orthogonal dipoles to measure the magnitude of each of the three components of the near field. The dipoles are terminated with Schottky diodes, which are connected with high-resistance lines to a battery-operated data acquisition unit at the base of the probe. The signals are then sent via a fiber-optic cable to a computer plug-in card. We note that the probe does not measure E_x, E_y, and E_z at exactly the same point. Components E_x and E_z are measured at slightly offset points in the same xz plane; whereas E_y is measured in an xz plane 1.1 millimeters further from the tip of the probe.

The 850 MHz oscillator in the handset is powered by a rechargeable battery, with a life of about 2 hours, sufficient to measure a plane of the size presented in Figs. 3, 4 and 5. The oscillator output declines over the course of a measurement. The change in field strength over time was monitored and recorded, and the measured data presented in this paper has been compensated to account for declining battery power.

Fig. 3 compares the FDTD-computed(black) and measured(gray) contours for the handset alone at y=-21.8 mm. The measured fields must be scaled to correspond in level to the computation. This was done by computing the RMS

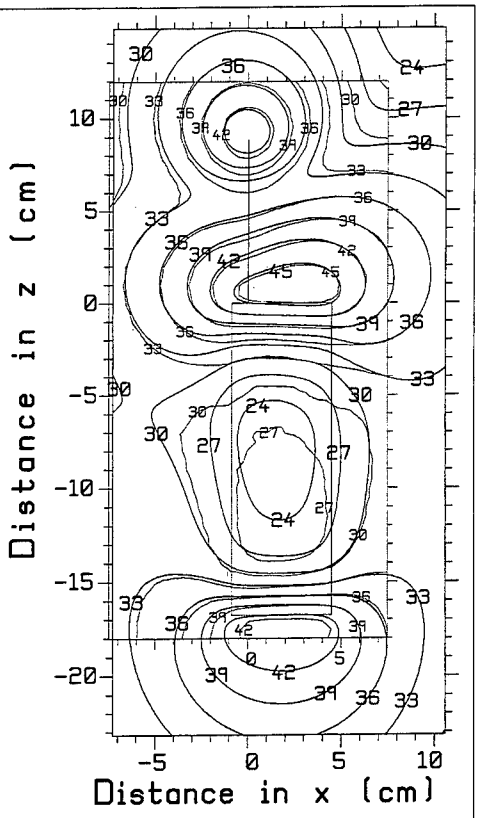

Fig. 3 Comparison of E_z computed with FDTD (black) and the measured field(gray), at 21.8 mm from the antenna.

field strength along a "tie line",

$$E_{RMS} = \sqrt{\frac{1}{L}\int E^2 dz}$$

where L is the length of the tie line. The tie line was chosen as the left-hand edge of the computed contour map in Fig. 3, at x=-7.277 cm, from z=-18.01 cm to z=11.95 cm. If E_c is the RMS field along the tie line in the computation, and E_m the RMS field in the measurement, then the measured data is scaled by E_c/E_m. Tie-line normalization aligns the measured and computed contours to approximately the same level at the left edge of the contour map. If the maps are in good agreement, the remaining contours will then align well.

In Fig. 3 the computed contours(black) align very well with the measured contours(gray) around the tip of the antenna and the top of the handset case. At the base of the case the 42 dB contour is smaller in the measurement than in the computation. Over the surface of the case there is a large computed contour at 24 dB; whereas the measured contour over the case is 27 dB. The measured field is about 3 dB stronger over the case. The contours to the left of the antenna and handset case align quite well, particularly near the top of the handset case. In the top right-hand corner of the contour map, we note that the measured contours tend to lie somewhat further from the antenna than do the computed contours.

The Handset and the Box Head

The "box head" is a plexiglas box 17.07 by 13.89 by 21.06 cm, with a wall thickness of 0.51 cm. The box is filled with "brain liquid", a sugar, salt and water mixture having the electrical parameters of brain matter[6]. The relative permittivity and conductivity of the brain liquid were measured to be 40.42 and 1.064 S/m, respectively, and these values were used in the computations. With the base of the antenna in Fig. 1 at the origin, the box head is located in the +y halfspace with one corner at x=-6.73, y=1.81 and z=-16.77 cm. The bottom of the handset is at the same height as the bottom of the box head. Using 2.205 mm cells, the box is modeled in FDTD with 78 by 63 by 95 cells, and the plexiglas wall is two cells thick. The 2.205 mm cell size corresponds to one-tenth wavelength in the brain liquid at 2125 MHz. To find the coefficients for updating the electric field on each cell edge, the FDTD code averages the permittivity and conductivity of the four adjacent cells. The FDTD cell space was terminated with a PML as described above. A bigger cell space was used for the box head problem, 149 by 147 by 188 cells, which puts the base of the antenna on cell edge 67, 41, 113. The FDTD model was run for 4096 time steps, more than adequate to reach the sinusoidal steady state.

Fig. 4 shows the computed(black) field contours for the vertical component of the near field at y=-21.8 mm. This xz plane is on the opposite side of the handset from the box head. Comparing Figs. 3 and 4 shows a 42 dB contour surrounding the tip of the antenna for both the handset alone and the handset and box head. The tip is well above the top of the box head. However, the contour for the handset alone near the top of the handset is at 45 dB, but only 42 dB for the handset and box head. Similarly, the contour at the bottom of the handset is 42 dB for the handset alone but only 39 dB for the handset and box head. The computed field over the surface of the handset falls to values less than 18 dB in Fig. 4, much less than the field of 24 dB for the handset alone in Fig. 3.

Fig. 4 compares the computed(black) and measured(gray) contours for the vertical component of the field. The measurement was scaled to match the level of the computation along a

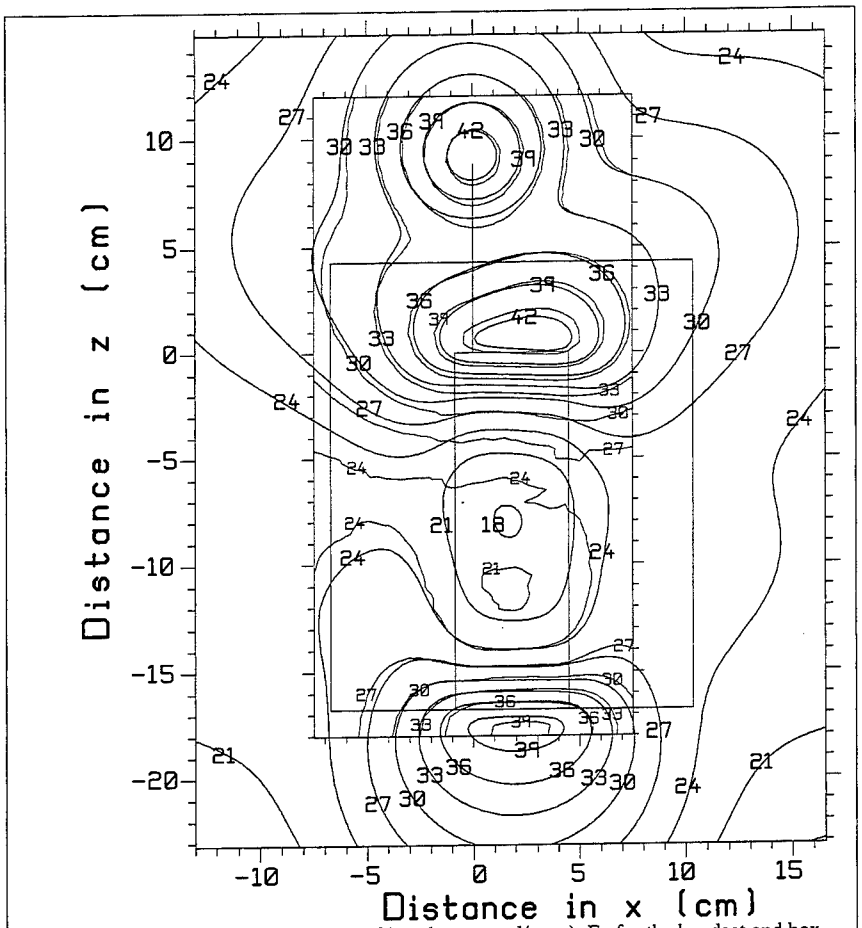

Fig. 4 Comparison of the computed(black) and measured(gray) E_z for the handset and box head, at 21.8 mm from the antenna.

tie line along the left edge of the measured contour map, at x=-7.494 cm, from z=-18.01 to z=11.95 cm. The measurement and computation agree very well near the tip of the antenna. At the top of the handset case, the computed 42 dB contour is somewhat smaller in the computation than in the measurement. Conversely at the base of the handset the computed 39 dB contour is larger than the measured 39 dB contour. Over the surfaces of the handset case, the measured field falls to values below 21 dB, considerably smaller than the smallest measured contour of 27 dB for the handset alone. We note that the computed field falls to below 18 dB, about 3 dB less than the measured

field. Also the location of the smallest fields in the measurement is more towards the bottom of the case than in the computation.

Handset and Sphere Head

The "sphere head" is 20.68 cm in diameter with a wall thickness of 3.65 mm. The box head and the sphere head have nearly the same volume. With the base of the antenna at the origin, the center of the sphere is at x=1.81, y=12.15 and z=-6.43 cm. This puts the lowest point on the sphere at the same height as the bottom of the handset case. The sphere's curved surface was

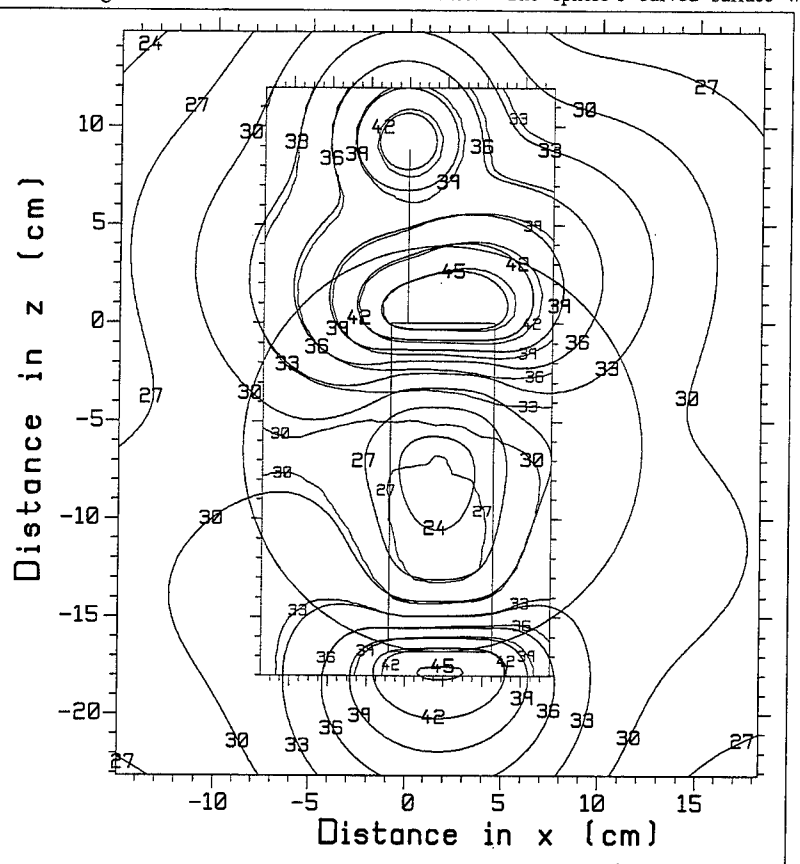

Fig. 5 Comparison of the computed(black) and measured(gray) E_z for the handset and sphere head, at 21.8 mm from the antenna.

approximated with a "staircase" of 2.205 mm cells. The 3.65 mm plexiglas wall thickness is about 1.65 cells thick; it was approximated as either one cell or two cells thick, being the difference

between the staircase modeling the outer sphere and the inner sphere defining the plexiglas wall. The sphere is 94 cells or 20.73 cm in diameter, a reasonable approximation of the true 20.68 cm diameter. The FDTD code uses coefficients for updating the electric field on each cell edge which average the permittivity and conductivity of the four adjacent cells. This tends to smooth the staircased surface of the sphere. The FDTD cell space was terminated with a PML as described above. The sphere head required a larger cell space than the box head, 166 by 178 by 188 cells, with the base of the antenna on cell edge 76, 41, 113.

Fig. 5 shows the vertical component of the near field of the sphere in an xz plane at y=-21.8 mm. Comparing the near field of the handset and box head, Fig.4, and the handset and sphere head, Fig. 5, we see that the field around the tip of the antenna is about the same at 42 dB. At the top of the handset case the field of the handset and sphere head shows a large 45 dB contour, considerably stronger than that of the handset and box head. Again at the base of the handset case, the handset and sphere head field exceeds 45 dB, whereas the handset and box head field has a small 39 dB contour. Indeed, the fields of the handset and sphere head are much more like the fields of the handset alone in Fig. 3. The square shape of the box head keeps the box close to the handset case at the top and bottom of the handset case. The round surface of the sphere is close to the handset near the center of the case, but curves away from the handset at the top of the case and particularly at the bottom of the case.

Comparing the handset and sphere head fields of Fig. 5 with the handset fields of Fig. 3, the 45 dB contour around the top of the case is larger with the sphere head than for the handset alone. The handset and sphere head shows fields higher than 45 dB near the bottom of the case, whereas for the handset alone there is no 45 dB contour.

Fig. 5 compares the FDTD-computed field(black contours) with the measured field(gray contours). The measured data was scaled to the level of the computed data along the left edge of the contour map, as for the box head. The computation and measurement agree very well. The 42 and 39 dB contours at the tip of the antenna almost coincide. The 45 dB contour at the top of the handset case is almost the same. At the bottom of the case the 39 and 42 dB contours correspond well. However, the computation shows a small region with fields in excess of 45 dB, not seen in the measurement. Over the surface of the handset case the computed fields fall below 24 dB, but the measured fields never fall as low as this.

Conclusion

This paper has presented a validation of FDTD computations of the vertical component of the near field of a portable radio handset in a plane close to the case of the handset. The field computed with FDTD was compared with a moment-method computation of the near field with excellent agreement. The near field of the handset was measured and shown to be in very good agreement with the computed near field. The field of the handset and box and sphere models of the head were measured, and very good agreement with the FDTD computation was shown. The fields are strong near the tip of the antenna, and near the top and bottom of the handset case. The computed fields in these regions agree very well with the measured fields particularly for the handset alone and for the handset and sphere head.

The agreement is slightly less good for the handset and box head. We note that the box head cell model uses 4 cells between the handset surface and the box surface, or 8.82 mm. However, the actual separation is 9.4 mm, almost half a cell further away. This modeling error could be reduced

by more sophisticated material averaging in the FDTD code, or by discarding the Yee FDTD algorithm in favor of scheme able to resolve the geometry more precisely.

This paper compared the fields of the handset, handset and box head, and handset and sphere head on the basis of equal *radiated* power. The box head near field in Fig. 4 is more different from the field of the handset in isolation, Fig. 3, than is the field of the handset and sphere head in Fig. 5. The box head reduces the field strength near the top and the bottom of the handset by 3 dB, but changes the field near the tip of the antenna very little. The sphere head curves away from the handset, and so the handset and sphere head fields are comparable to those of the handset alone near the top and bottom of the box.

A real head is neither a sphere nor a box. It is more like a sphere at the top of the head, and perhaps more box-like at the jaw and neck. Nor is the handset held vertically in normal operation. If held in a natural position, our rather large handset is close to the head at the top of the handset, above and behind the ear. There the fields are likely to be like those of the handset and box head. But the bottom of the handset juts out beyond the jaw, and so the fields are likely to be close to those of the handset and sphere. Measurements are planned for the handset and a realistic five-tissue phantom of the head, with the handset positioned realistically relative to the head.

References

[1] C.W. Trueman and S.J. Kubina, "A Research Study on Electromagnetic (EM) Fields Produced by Portable Transceivers", Final Report in Contract Number U68000-7-0726/001/ST, Technical Note No. TN-EMC-94-01, Dept. of Electrical and Computer Engineering, Concordia University, March 31, 1998.

[2] "Advances in Computational Electrodynamics – The Finite-Difference Time-Domain Method", A. Taflove, editor, Artech House, 1998.

[3] G.J. Burke, A.J. Poggio, J.C. Logan and J.W. Rockway, "NEC - Numerical Electromagnetics Code for Antennas and Scattering", 1979 IEEE International Symposium on Antennas and Propagation Digest, IEEE Publication No. 79CH1456-3AP, Seattle, Washington, June, 1979.

[4] D. Cule and J. Bertrand, "Measurements of the Electromagnetic Near-Fields Produced by a Portable Radio Transmitter", CRC Technical Memorandum VPRB-02-98, August, 1998.

[5] T. Schmid, O. Egger and N. Kuster, "Automated E-Field Scanning System for Dosimetric Assessments", IEEE Trans. On Microwave Theory and Techniques, Vol. MTT-44, No. 1, pp. 105-113, January, 1996.

[6] G. Hartsgrove, A. Kraszewski and A. Surowiec, "Simulated Biological Materials for Electromagnetic Radiation Absorption Studies", *Bioelectromagnetics*, Vol. 8, pp. 29-36, 1987.

FDTD for Bioelectromagnetics: Modeling MICS Implants in the Human Body

Eduardo Villaseca
Medtronic Inc.
Minneapolis, MN 55432

Medtronic Inc. is developing a communication system for implanted medical devices. For MICS (Medical Implant Communications System) to be successful, it is important to be able to predict the electromagnetic performance of such an implant.

Preliminary models used a mathematical technique called the Method of Moments to model the performance of an implanted device, but the Method of Moments could not predict effects around the entire body.

These initial models were very important in establishing the practicality of MICS, but they need refinement and expansion before they can provide the type and quality of information needed as MICS development proceeds. In particular, we need to be able to see the variation of gain with location around the body, to ensure that MICS will operate reliably, and to evaluate the absorption rate of power into the body while MICS is operating, to ensure that MICS will operate safely.

FDTD Modeling

For this more advanced, improved modeling, we have adopted the Finite Difference Time Domain, or FDTD, modeling. FDTD was originally developed by [Yee[1]]and has been described extensively in the literature. The method is a direct solution of the differential form of Faraday's and Ampere's laws. These differential equations are converted into difference equations using the central difference approximations. The field components are interleaved on each unit cell, so that the E and H components are half a cell apart, which is referred to as "leap-frog" scheme. In addition to being leap-frogged in space, they are also leap-frogged in time. The E field is assumed to be at time $n\Delta t$, and the H field is assumed to be at time $(n+1/2)\Delta t$.

FDTD has become the preferred method for bioelectromagnetic calculations at radio frequencies. It is efficient for modeling large-scale heterogeneous penetrable objects — like the human body. FDTD allows the use of many dielectric constants, allowing definition of different types of tissue and organs within the body. The Method of Moments, in contrast, is computationally extremely expensive to use with more than two dielectric constants, severely limiting our ability to define different tissue types. The Method of Moments also makes unreasonably large demands on computer memory and time when modeling internal fields in electrically large lossy dielectric bodies, such as the human body, which FDTD can handle more economically and simply. However, the Method of Moments works excellently with wires and metal patches, which made it the preferred choice for the preliminary MICS analysis.

[1] Yee, K.S., Numerical solution of initial boundary value problems involving Maxwell's equations in isotropic media, *IEEE Trans. Ant. Prop.*,14(3), 302, 1966

FDTD has numerous other advantages for more advanced modeling. It is very accurate and fairly easy to use. It operates with a regular, orthogonal grid, with the wave frequencies of the modeling dependent on the dimensions of the grid. In the case of MICS modeling, a 5 mm grid of six million cells allowed creation of a model effective up to 1 gigahertz. Newly available high performance absorbing boundary conditions allow good computations throughout the body without the distortions that occurred in earlier models as a result of reflections from the outer radiation boundaries of the model.

The Visible Human Model

MICS modeling started with a human body model obtained from REMCOM, Inc. This model was created from "frozen man" slices from the Visible Human Project, obtained via the Internet and meshed using custom software.

The bioelectromagnetic human body model is a digitized version of a real human body. A donated cadaver was frozen and sliced in 5 mm slices. Each slice was identified for parameters such as muscle, fat, and bone. The results were digitized to create a total numerical model, using a 5 mm cell, for a total of about six million cells. Twelve different types of tissue were identified. Constitutive parameters were assigned based on the original data, and checked and corrected using interactive editing.

Figure 1 shows a demonstration cross section of the human body model.

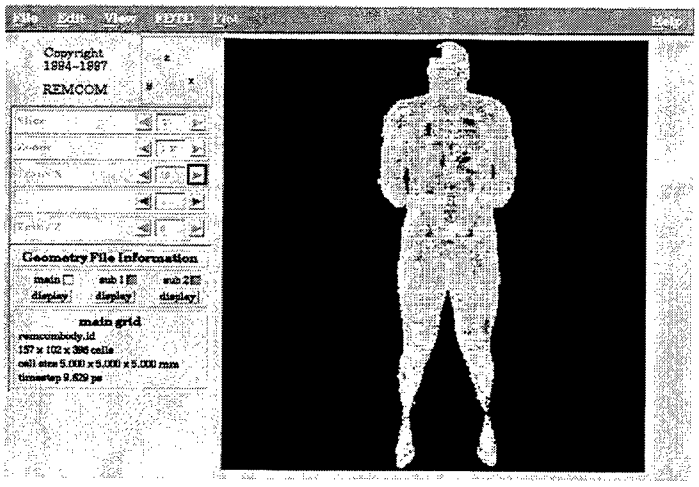

Figure 1. Sample bioelectromagnetic human body cross-section model.

MICS Implant

The MICS implant placed in the chest is shown in Figure 2.

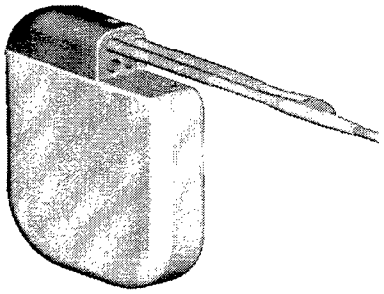

Figure 2. MICS implant with coaxial antenna.

Figure 3 shows the electromagnetic field distribution in the chest area of the body with the MICS implant in place in the upper right quadrant, modeled at UHF.

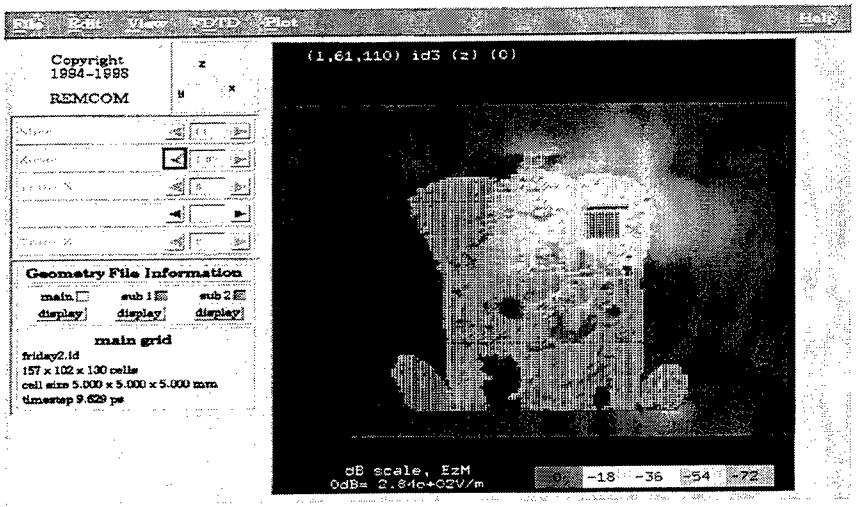

Figure 3. The MICS is visible in the upper left quadrant of the chest in this section.

Figure 4 shows the coverage around the implant, in terms of the azimuth. An azimuth of 90° is directly in front of the body, 0° and 180° are to the sides, and 270° is directly behind the body.

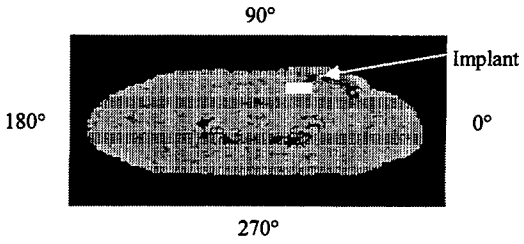

Figure 4. Azimuth coverage of measurements around the MICS implant.

Variation in Gain Around the Human Body Model

Figure 5 shows the results of measuring the implant antenna gain around the body according to the azimuth coverage in Figure 4. The variation of gain with azimuth is clearly visible. The gain varies with the length of the travel path around the body to the receiver; overall, the combination of horizontal and vertical polarization yields a gain that can vary from about –25 to about –40 dBi.

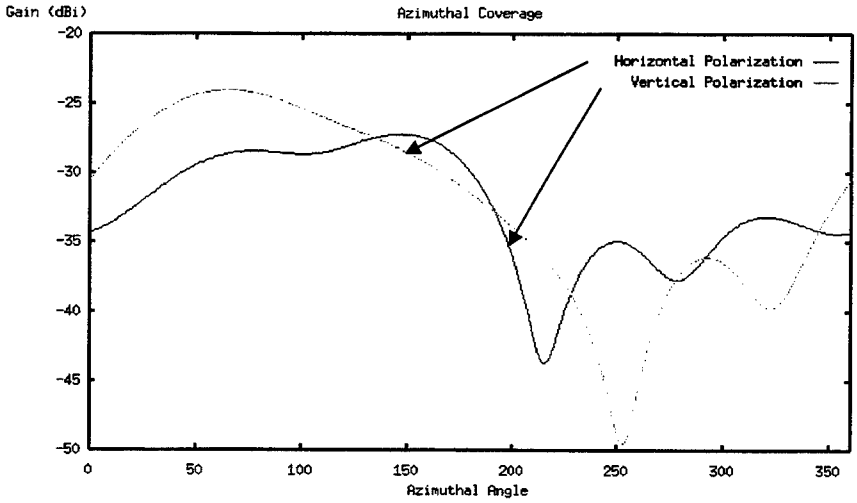

Figure 5. Implant antenna gain as a function of azimuthal angle around the body section shown in Figure 4.

Specific Absorption Rate Modeling

In addition to evaluating MICS performance by modeling the variations in antenna gain around the body, the human body model can be used to evaluate the safety of the MICS implant by examining the Specific Absorption Rate (SAR) in the body. In general, the FDTD method calculates the time-domain vector E and H fields at every location inside and outside of the body. These can be converted to frequency domain fields (magnitude and phase at given frequencies). From them, values commonly of interest in bioelectromagnetic simulations can be calculated, including specific absorption rate, current density, total power absorbed, temperature rise, etc.

SAR is an important measure of the amount of power the implant is putting into the human body per kilogram of tissue. For near-field applications, such as a medical implant with telemetry transmitter, it is important to determine if the device complies with the ANSI/IEEE safety guidelines[ANSI] and newly-mandated FCC guidelines. These guidelines state that an exposure can be considered to be acceptable if it can be shown that it produces SAR's "below 0.08W/kg, as average over the whole body, and spatial peak SAR values not exceeding 1.6 W/kg, as averaged over 1 g of tissue (defined as a tissue volume in the shape of a cube)"[ANSI].

SAR for the MICS implant was evaluated for the Medical Implant Communication System operating at 0 dBm, or power input of 1 milliwatt into the body. The SAR at a given location is given by the following formula

$$SAR = \frac{\sigma_x}{\rho_x}|E_x|^2 + \frac{\sigma_y}{\rho_y}|E_y|^2 + \frac{\sigma_z}{\rho_z}|E_z|^2$$

where σ is the electrical conductivity and ρ is the mass density at the location of interest.

Three different values must be evaluated to ensure that the implant meets safety standards:

- the maximum SAR considering total power applied to total weight
- the maximum SAR considering the same amount of power applied to 1 gram of tissue
- the maximum SAR considering the same amount of power applied to 10 grams of tissue.

Figure 6 summarized these values and showed the location of the maximum in each case.

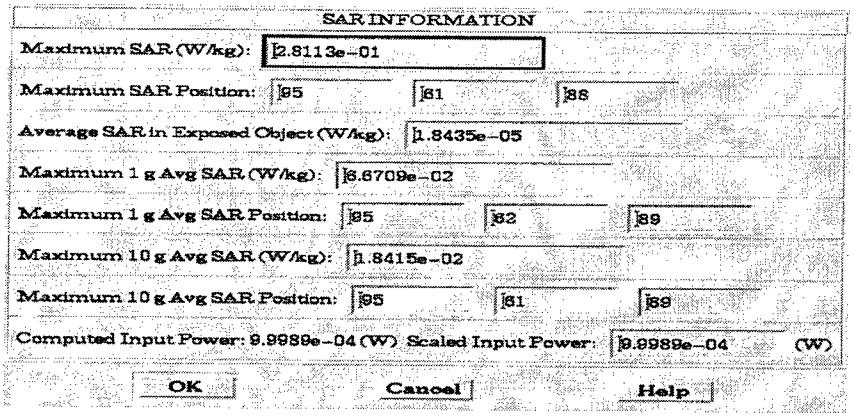

Figure 6.Summary of SAR Information

Figures 7 and 8 illustrate the SAR distribution and maximum for the 1 g average and 10 g average cases respectively.

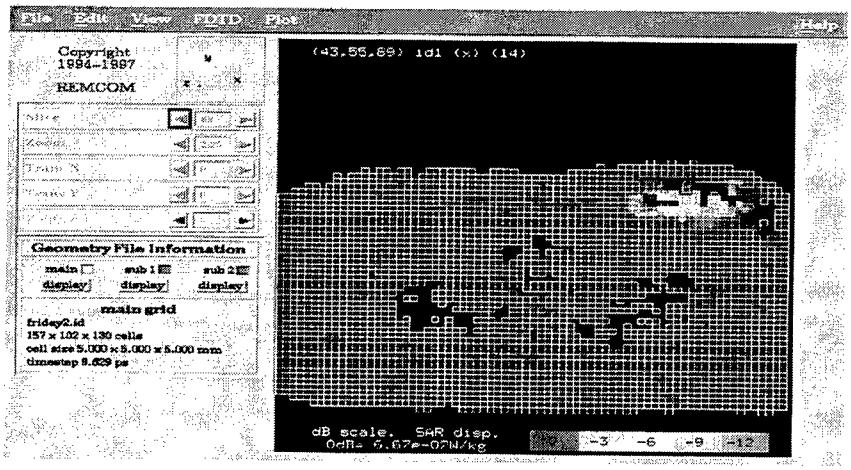

Figure 7. 1 g Average SAR (W/kg). The maximum SAR occurs in the location of the connector terminal to the implant.

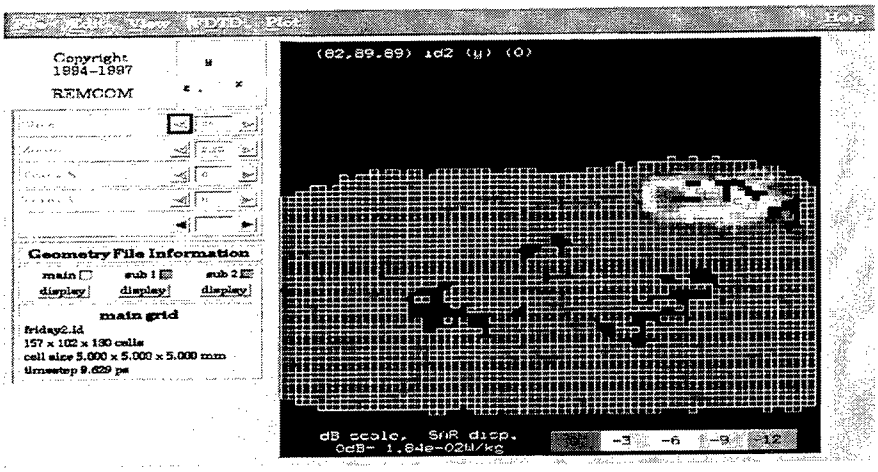

Figure 8. 10 g Average SAR (W/kg). As in Figure 7, the maximum SAR is the location of the connector terminal to the implant

Implant Safety Conclusions

Figures 6 – 8 illustrate the important SAR conclusions:

- The SAR average over the whole body is 1.8e-05 W/kg. This is 36 dB below the ANSI safety standard of 0.08 W/kg.
- The maximum 10 g average SAR is 1.9e-02 W/kg. This is 23 dB below the ANSI safety standard of 4 W/kg.
- The maximum 1 g average SAR is 6.7e-02 W/kg. This is 14 dB below the ANSI safety standard of 1.6 W/kg.

Summary of FDTD Modeling Conclusions

FDTD modeling has been used for the first time with the bioelectromagnetic human body model to obtain implant performance..

The results of modeling implant antenna gain show a variation of gain with location around the body that must be accounted for to ensure that MICS will operate reliably.

Analysis of SAR over the total body, over 1 g of tissue, and over 10 g of tissue reveal an absorption rate of power into the body well within the standard guidelines for safety, demonstrating the ability of MICS to operate safely within the human body.

Numerical Studies of an Ultrawideband Microwave Radar Technology for the Detection of Nonpalpable Breast Tumors

Susan C. Hagness
Department of Electrical and Computer Engineering, University of Wisconsin, Madison, WI 53706

Allen Taflove
Department of Electrical and Computer Engineering, Northwestern University, Evanston, IL 60208

Jack E. Bridges
Interstitial, Inc., Park Ridge, IL 60068

Abstract

We are investigating a new ultrawideband microwave radar technology to detect and image early-stage malignant breast tumors that are often invisible to X-rays. In this paper, we present the methodology and results of two- and three-dimensional finite-difference time-domain simulations. The discussion concentrates on the investigation of signal-to-clutter ratios and dynamic range requirements of the microwave system. Our FDTD studies have demonstrated that the sensitivity and dynamic range of an optimized antenna array in conjunction with existing microwave equipment should be adequate to detect noncalcified tumors less than 5 mm in diameter located at depths of up to about 5 cm in the breast.

I. Introduction

X-ray mammography is currently the most effective screening modality for detecting nonpalpable breast tumors. However, X-ray mammography has limited sensitivity and specificity in 1) assessing dense glandular tissue and tissue close to the chest wall or underarm and 2) imaging very early-stage tumors that do not yet exhibit microcalcifications. According to the National Cancer Institute, screening mammograms miss up to 25% of all breast cancers. A related concern is the high rate of false positives that result in unnecessary biopsies. Since these problems remain unresolved, complementary modalities based on imaging other physical tissue properties are needed to further improve detection capabilities.

We have recently proposed a novel pulsed microwave confocal system for the detection of early-stage breast cancer [1, 2, 3, 4]. Our system has the potential to detect very small non-calcified cancers, including those in radiographically dense breasts and in regions near the chest wall or underarm. Furthermore, this noninvasive approach avoids exposure to ionizing radiation and does not require breast compression. The microwave exposure is well within the safety limits set by ANSI/IEEE [5]. The safety, comfort, ease-of-use, and low-cost features should permit frequent screening. Augmenting X-ray mammography in this manner could help to reduce the number of false negatives and false positives.

The physical basis of this technology is the differential microwave backscatter response from tissues based on their water content, a tissue-radiation interaction mechanism that is distinct from density-based attenuation of X-rays. As shown in Table 1, the differing water content of normal and malignant breast tissues results in an order-of-magnitude dielectric-property contrast at microwave frequencies [6, 7, 8]. Thus a malignant tumor has a significantly larger radar cross section than that of normal, fatty breast tissue. Normal breast tissue dielectric heterogeneity is observed on a distance scale of about 0.5 cm and is bounded in a $\pm 10\%$ range about the nominal values given in Table 1.

tissue type	ϵ_r	σ (S/m)
normal fatty breast	9.0	0.4
tumor	50.0	7.0
skin [6]	36.0	4.0
vein [6]	50.0	7.0
mammary glands (15% higher than fat)	10.45	0.46
mammary glands (50% higher than fat)	13.5	0.6

Table 1: Dielectric parameters of breast tissue at 6 GHz.

Our pulsed microwave confocal system is based on ultrawideband radar technology and confocal optical microscopy. The microwave sensor is comprised of an electronically scanned antenna array. Each ultrawideband antenna element located at a particular position on the surface of the breast is excited and the backscattered waveform is collected. This is repeated in sequence for the other elements in the array. The low attenuation in normal breast tissue (less than 4 dB/cm up to 10 GHz) permits constructive addition of the wideband backscattered returns. Therefore, as a post-processing step, the set of backscattered waveforms are variably time-shifted to achieve coherent addition for a desired virtual focal point within the breast. Backscatter from off-focus scatterers in the heterogeneous breast add incoherently and are thereby suppressed. We note that our approach has no relation to matrix schemes using microwave or impedance measurements, microwave backscatter methods based on broad illumination of the breast, or techniques involving passive thermography or active tomography. Three wide-ranging U.S. patents for our technology were awarded recently, and several additional patents are pending.

Two key performance specifications for the microwave sensor are the signal-to-clutter (S/C) ratio, defined as the ratio of the peak backscatter return from a tumor to the peak backscatter return from clutter, and the system dynamic range, defined as the ratio of the peak pulse power of the source to the system noise floor due to reverberations and thermal noise. We have developed two- and three-dimensional finite-difference time-domain (FDTD) [9, 10] models of the microwave sensor to analyze S/C ratios and the dynamic range requirements, and to assess the overall feasibility of the proposed system for detecting early-stage breast cancer.

II. FDTD Simulations of the Coherent-Addition Antenna Array: Signal-to-Clutter Ratios

Fig. 1a illustrates the FDTD model of a microwave sensor comprised of a 17-element monopole array spanning 8 cm. The monopoles are spaced at 0.5-cm intervals along the surface of a 1-mm-thick skin layer. A 0.5-cm-diameter circular tumor is embedded in a slab of normal fatty breast tissue at a depth of 3.0 cm directly below the center of the monopole array. To simulate the heterogeneity of the normal breast tissue [7, 8], $\pm 10\%$ random fluctuations of ϵ_r and σ were assigned to the breast tissue half-space in a checkerboard pattern of 5-mm square blocks.

The modeling procedure involves simulating an impulsive excitation of each monopole element, one at a time, then recording the backscattered pulse response observed at the excited element. The pulse excited by the transmitting antenna is a differentiated Gaussian with the following time dependence:

$$V(t) = V_0(t - t_0)e^{-[(t-t_0)/\tau]^2} \quad \text{volts} \tag{1}$$

where $\tau = 0.04$ ns, and $t_0 = 4\tau$. This pulse has a temporal width of 110 ps (FWHM), an amplitude spectral width of 9.0 GHz (FWHM), and zero dc content. We chose a different pulse shape here from that

reported in our previous publications to verify that our proposed detection system is robust relative to the precise shape of the exciting pulse. As a post-processing operation on the FDTD-calculated backscatter data, the 17 individual waveforms are time-shifted to achieve a coherent sum of the backscattered response for the desired focal point. Varying the distribution of these time shifts across the array creates the synthetic focal point. For each investigation, simulations are performed with and without the tumor present. The latter case establishes the background clutter. Fig. 2a depicts the received power waveform upon coherently summing the 17 backscatter responses. The solid curve represents the composite received signal from the 0.5-cm-diameter. The dotted curve represents the composite clutter signal received without the tumor present. The tumor response is clearly visible.

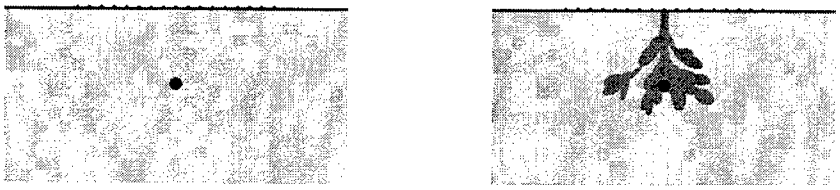

a) b)

Figure 1: a) 2-D FDTD computational model of the 17-element sensor placed at the surface of the breast. Here, the breast model includes skin, heterogeneous normal breast tissue, and a 0.5-cm diameter tumor located at a depth of 3.0 cm. b) Computational model with mammary ducts and lobules added.

To accurately quantify the S/C ratio, it is convenient to subtract the exponential decay from the two curves in Fig. 2a.[1] Fig. 2b shows the results after performing the subtraction and normalizing the curves. Upon forming the ratio of the peak backscattered pulse amplitude with the tumor present to the peak amplitude without the tumor present, the S/C ratio is found to be greater than 30 dB. (In our prior publications, the S/C ratios were estimated without subtracting the exponential decay and as a result represent an underestimate of the actual ratios.) Fig. 3 graphs the calculated S/C ratio as a function of tumor diameter for a tumor fixed in position at the in-breast synthetic focus. These results show that tumors having diameters as small as 1 mm yield responses that are well above the background clutter, illustrating the potential for high sensitivity with our proposed detection method. As reported in [4], we also tested the performance of the system under the condition wherein the heterogeneous normal breast tissue is assumed to have a Debye dispersion. The frequency-dependent parameters were incorporated into the FDTD algorithm using the auxiliary differential equation method [11]. We observe essentially no degradation of the S/C ratio relative to the corresponding nondispersive modeling results.

Fig. 1b illustrates the geometry that results from surrounding the 0.5-cm-diameter tumor with a cluster of mammary lobes and ducts. Here, the simulated gland cluster is modeled in the FDTD grid by positioning a group of ellipses having higher ϵ_r and σ than normal breast tissue. Since we have not found measured data on the dielectric properties of mammary glands, we have performed sensitivity tests of our assumed values of ϵ_r and σ for these structures. For example, Figs. 4a and 4b graph the post-processed backscattered signals for mammary glands having 15% and 50% higher ϵ_r and σ than normal breast tissue, respectively. In comparing Figs. 4a and 4b with Fig. 2a, it is clear that the tumor

[1] A third simulation is performed for the geometry of Fig. 1a without the tumor and without the normal breast tissue heterogeneity. The composite received signal for this homogeneous case consists solely of the exponential decay in the time window from 0.5 ns to 1.4 ns. It is this signal that is used to subtract off the exponential-decay baseline of Fig. 2a.

response is only slightly degraded. We note that these results are obtained using the same distribution of time delays across the antenna array used in the previous model of Fig. 1a. Optimizing the time delays should mitigate the minor level of degradation observed. Apparently, the modeled cluster of lobes and ducts generates a backscattered return that propagates incoherently to the multiple observation locations. Similar to the modeled random heterogeneity of the fatty breast tissue, this clutter signal is suppressed upon coherent addition in favor of the tumor's signature.

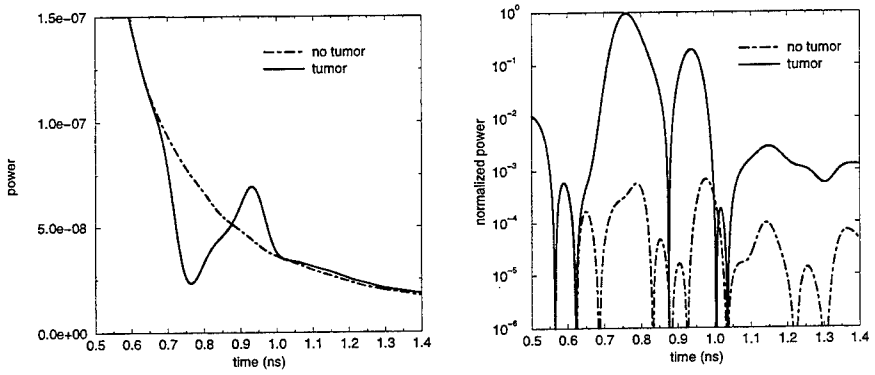

Figure 2: a) FDTD-computed time-domain waveforms resulting from time-shifting and summing backscattered responses for the system shown in Fig. 1a. b) Waveforms after subtracting off the exponential decay from both curves of Fig. 2a.

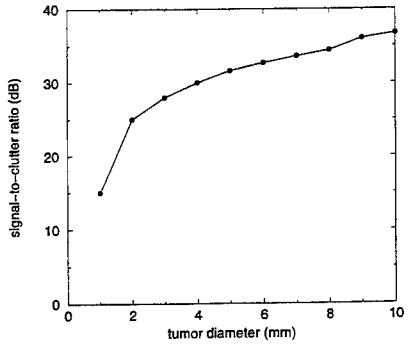

Figure 3: S/C ratio for the backscattered response of the tumor located at the in-breast synthetic focus, shown in Fig. 1a, as a function of the tumor diameter.

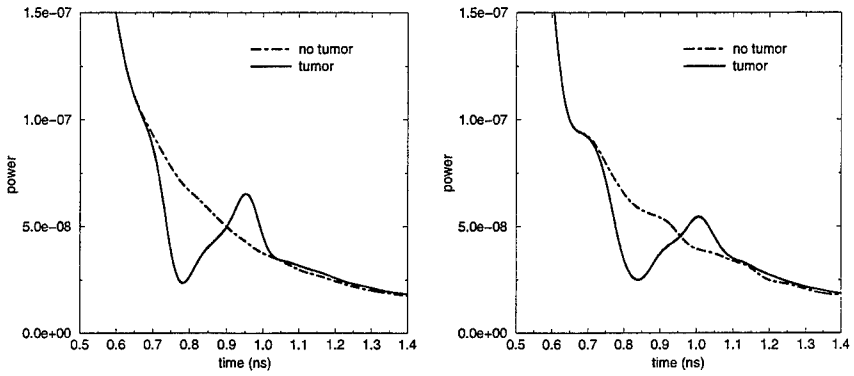

Figure 4: FDTD-computed time-domain waveforms for the tissue geometry of Fig. 1b. The mammary ducts and lobules are assigned values of ϵ_r and σ that are (a) 15% or (b) 50% higher than the nominal values used for the heterogeneous surrounding breast tissue.

III. FDTD Simulations of an Antenna-Array Element: Dynamic Range Requirements

We have conducted 3-D FDTD simulations to design a wideband bowtie antenna for use as an element in the pulsed microwave confocal array [12, 13]. The bowtie antenna has a flare length of 4 cm and a flare angle of 53°. As reported in [12, 13], the antenna is resistively loaded in order to suppress the reflections from the ends of the bowtie. The antenna is embedded within a large block of lossy dielectric material that matches the dielectric parameters of normal breast tissue. In the FDTD models, the bowtie antenna element is located at the surface of the breast. The breast model is comprised of a 1-mm-thick layer of skin and a homogeneous half-space of normal breast tissue. The slanted edges of the bowtie antenna are approximated using staircasing with a sub-mm spatial grid resolution. The zero-dc ultrawideband excitation is implemented as a 1-V, 50-Ω resistive voltage source at the antenna feed point [14]. The FDTD grid is terminated with a perfectly matched layer absorbing boundary condition [15]. The resistive loading together with the lossy nature of the biological tissue and the bandpass nature of the excitation drops the antenna reverberation to -125 dB relative to the exciting pulse.

Using the resistively loaded bowtie antenna, we have performed benchmark simulations to estimate the dynamic range requirements of the microwave system for detecting a compact breast tumor located directly below the antenna feed point. The dynamic range should be large enough to permit detection of a tumor of specified size and depth. The depth of a typical normal, non-lactating human breast is on the order of 5 cm (for example, see [16]). This suggests that a flattened breast of a patient in supine position would span less than 5 cm between the skin surface and the rib cage. Further, almost 50% of all breast tumors occur in the quadrant near the underarm where the breast is less than about 2.5 cm deep [17]. Accordingly, we have based our computational models of the confocal microwave system on detecting tumors to depths of up to 5 cm with a typical depth of 3 - 4 cm.

To determine the dynamic range required to detect a tumor of a specific diameter and depth, the peak-to-peak amplitude of the backscattered response of the tumor is compared with the peak-to-peak amplitude of the exciting pulse. In each simulation, we record the FDTD-computed magnetic field

tumor depth	tumor diameter	tumor response
3.0 cm	5.28 mm	-83 dB
	3.52 mm	-88 dB
	1.76 mm	-96 dB
4.0 cm	5.28 mm	-92 dB
	3.52 mm	-97 dB
	1.76 mm	-106 dB
5.0 cm	5.28 mm	-101 dB
	3.52 mm	-106 dB
	1.76 mm	-115 dB

Table 2: Normalized backscatter data as a function of the tumor diameter and depth.

circulating the voltage source at the feed point, since this field is proportional to the induced current. The simulation is performed for tumor diameters of 5.28 mm, 3.52 mm, and 1.76 mm at depths of 3.0 cm, 4.0 cm, and 5.0 cm. The backscatter response levels are tabulated in Table 2. The peak power in the backscatter return drops approximately 9 dB per cm increase in the depth of the tumor.

The backscatter response for the "worst case" tumor studied here (diameter of 1.76 mm, depth of 5.0 cm) is seen to be -115 dB relative to the source power. We note that the -125 dB reverberation due to reflections from the ends of the resistively loaded bowtie antenna, reported in [13], is sufficiently low enough to permit backscattered returns from this tumor to be sensed. Furthermore, we have observed a dynamic range in the order of 120 dB for the Hewlett-Packard HP8720D vector network analyzer when properly configured and programmed with processing times adequate for preclinical testing. This can be improved to 135 dB with minor modifications. Thus, given the discussion above, our optimized resistively loaded bowtie antenna in combination with commercial vector network analyzers yield more than adequate dynamic range for our tumor-detection system.

V. Summary and Conclusions

This paper presented the methodology and results of FDTD simulations of an UWB microwave sensor array to detect and image early-stage malignant breast tumors. Our 2-D FDTD studies of the S/C ratio demonstrate the robustness of the coherent-addition process relative to the dielectric properties and complexity of the breast. We conducted 3-D FDTD simulations to study the co-polarized backscattered response of small idealized spherical tumors (diameters less than or equal to 5 mm) located at depths up to 5.0 cm within the homogeneous breast. The results reported here and in [4, 13] indicate that a system realized with existing microwave equipment has sufficient sensitivity and dynamic range to detect small tumors less than 5 mm in diameter located within 5 cm of the skin surface. Using these simulations as a design tool, we are constructing a sensor system for pre-clinical experimentation.

VI. Acknowledgments

This work was supported in part by the Small Business Innovative Research Grant 1-R43-CA67598-D1A2 from the National Institutes of Health and internal funding from Interstitial, Inc. Computing resources were provided by Cray Research, Inc. We gratefully acknowledge technical guidance from Prof. Alan Sahakian of Northwestern University, Dr. Melvin Griem of the University of Chicago, Dr. John Aarsvold of the Atlanta VA Medical Center, and Dr. Frederick Kelcz of the University of Wisconsin-Madison.

VII. References

[1] S. C. Hagness, A. Taflove, and J. E. Bridges, "FDTD analysis of a pulsed microwave confocal system for breast cancer detection," in *Proc. Int. Conf. IEEE Engineering in Medicine and Biology Soc.*, Chicago, IL, Oct. 1997, pp. 2506–2508.

[2] S. C. Hagness, A. Taflove, and J. E. Bridges, "FDTD modeling of a coherent-addition antenna array for early-stage detection of breast cancer," in *IEEE Antennas and Propagat. Soc. Int. Symposium Digest*, Atlanta, GA, June 1998, vol. 2, pp. 1220–1223.

[3] M. Popović, S. C. Hagness, A. Taflove, and J. E. Bridges, "2-D study of fixed-focus elliptical reflector system for breast cancer detection: Frequency window for optimum operation," in *IEEE Antennas and Propagat. Soc. Int. Symposium Digest*, Atlanta, GA, June 1998, vol. 4, pp. 1992–1995.

[4] S. C. Hagness, A. Taflove, and J. E. Bridges, "Two-dimensional FDTD analysis of a pulsed microwave confocal system for breast cancer detection: Fixed-focus and antenna-array sensors," *IEEE Trans. Biomed. Eng.*, vol. 45, no. 12, pp. 1470–1479, Dec. 1998.

[5] ANSI/IEEE C95.1-1992, *American National Standard - Safety Levels with Respect to Human Exposure to Radio Frequency Electromagnetic Fields, 3 kHz to 300 GHz*, IEEE Press, New York, 1992.

[6] C. Gabriel, S. Gabriel, and E. Corthout, "The dielectric properties of biological tissues: I. Literature survey," *Phys. Med. Biol.*, vol. 41, no. 11, pp. 2231–2249, Nov. 1996.

[7] W. T. Joines, Y. Z. Dhenxing, and R. L. Jirtle, "The measured electrical properties of normal and malignant human tissues from 50 to 900 MHz," *Med. Phys.*, vol. 21, pp. 547–550, Apr. 1994.

[8] S. S. Chaudhary, R. K. Mishra, A. Swarup, and J. M. Thomas, "Dielectric properties of normal and malignant human breast tissues at radiowave and microwave frequencies," *Indian J. Biochem. and Biophys.*, vol. 21, pp. 76–79, Feb. 1984.

[9] K. S. Kunz and R. J. Luebbers, *The Finite Difference Time Domain Method for Electromagnetics*, CRC Press, Boca Raton, FL, 1993.

[10] A. Taflove, *Computational Electrodynamics: The Finite-Difference Time-Domain Method*, Artech House, Boston, MA, 1995.

[11] R. M. Joseph, S. C. Hagness, and A. Taflove, "Direct time integration of Maxwell's equations in linear dispersive media with absorption for scattering and propagation of femtosecond electromagnetic pulses," *Optics Lett.*, vol. 16, no. 18, pp. 1412–1414, 1991.

[12] S. C. Hagness, A. Taflove, and J. E. Bridges, "Wideband ultralow reverberation antenna for biological sensing," *Electron. Lett.*, vol. 33, no. 19, pp. 1594–1595, 1997.

[13] S. C. Hagness, A. Taflove, and J. E. Bridges, "Three-dimensional FDTD analysis of a pulsed microwave confocal system for breast cancer detection: Design of an antenna-array element," *IEEE Trans. Antennas Propagat.*, in press.

[14] M. Piket-May, A. Taflove, and J. Baron, "FD-TD modeling of digital signal propagation in 3-D circuits with passive and active loads," *IEEE Trans. Microwave Theory Tech.*, vol. 42, no. 8, pp. 1514–1523, Aug. 1994.

[15] J.-P. Berenger, "A perfectly matched layer for the absorption of electromagnetic waves," *J. Comput. Phys.*, vol. 114, no. 1, pp. 185–200, 1994.

[16] X. Wu, G. T. Barnes, and D. M. Tucker, "Spectral dependence of glandular tissue dose in screen-film mammography," *Radiology*, vol. 179, no. 1, pp. 143–148, Apr. 1991.

[17] W. H. Parsons, *Cancer of the Breast*, Charles Thomas, Springfield, IL, 1959.

Numerical Dosimetry for Human Occupational Exposure to Realistic 60-Hz Magnetic Fields

Trevor W. Dawson, K. Caputa and Maria A. Stuchly
Dept. Elec. & Comp. Eng., University of Victoria
PO Box 3055 Stn CSC Victoria BC Canada V8W 3P6

Abstract

Human exposure to occupational non-uniform 60-Hz magnetic fields produced by realistic three-phase conductor systems is evaluated numerically. Two specific scenarios are considered. The first involves a seated worker performing cable maintenance in an underground vault with conductors carrying 500 A (rms) per phase. The second involves a standing worker near iso-phase buses of a 700 MW generator, with conductors carrying 20 kA (rms) per phase. The modeling is based on a scalar potential finite difference (SPFD) method, applied to a high-resolution (3.6 mm) voxel conductivity model of the human body. Good correspondence between various external field measures and the associated induced field measures in various organs is observed The lower currents in the vault conductors produce correspondingly low induced current densities, with tissue average values typically below 0.2 mA m^{-2}. Conversely, the generator bus currents result in 1.5-mT fields at a distance of 1.2 m. The resulting organ-average induced current densities are in the 2–8 mA m^{-2} range, with maximum values above 10 mA m^{-2}. A comparison with uniform field exposures indicates that induced fields in organs can be reasonably well-estimated from the accurately computed exposure fields averaged over the organs and the organ dosimetric data for uniform magnetic fields. The nonuniform field exposures generally result in lower induced fields than those for uniform fields of the same intensity.

1 Introduction

While the issue of health effects of 60-Hz magnetic fields remains unresolved [*NIEHS*, 1998], there are established biological interactions for fields strong enough to induce tissue current densities of the order of 10 mA m^{-2} [*ICNIRP*, 1998]. This level is used as a benchmark in safety guidelines [*ICNIRP*, 1998]. Human exposure to relatively high magnetic flux densities most often occurs in occupational settings. Numerical modeling involving realistic conductivity representations of the human body can provide a useful tool for investigating the connection between the external field and the induced internal fields. Earlier modeling of worker live-line exposures has considered mostly high-voltage transmission lines [*Stuchly and Zhao*, 1996; *Dawson et al.*, 1998]. In all cases, the current-carrying conductors have been represented as infinite straight-line sources. Such models clearly are not appropriate for modeling representative exposures to complicated conductor systems such as in power generating plants or substations. The present work extends the source modeling to multi-phase conductor systems composed of rectilinear elements, including finite line segments, as well as half- and full-lines (to model current systems closed "at infinity"). This expanded source treatment is used in conjunction with realistic high-resolution conductivity models of the human body in representative postures. Two scenarios are considered. The first scenario pertains to a seated worker performing maintenance of secondary cables and bus bars in an underground vault in a substation. This is a three-phase current configuration with 500-A (rms) per phase. The source model involves a total of 9finite segments and half-lines. The second scenario involves an upright worker inspecting the isophase buses of a 700 MW generator. There are three conductor systems carrying 20 kA per phase, with the currents summing to zero at the star point. The source model involves 11 elements, either finite segments or half-lines.

This research has three objectives. The first is a realistic evaluation of the electric fields and current densities induced in various organs of the human body by nonuniform magnetic fields in representative electric utility work locations. The second objective is a comparison of the resulting nonuniform dosimetry to recently published data

for uniform field exposures, e.g. [*Dawson and Stuchly,* 1998; *Dawson et al.*, 1997]. The third objective is to consider induced field levels in light of various quantitative measures of the source magnetic field. The latter are simpler to compute. Therefore, it would be useful to have "rule-of-thumb" estimates of the true induced fields obtained from local measures of the non-uniform source field combined with dosimetric data for uniform field exposures

2 Methods

2.1 Body Models

All computations involve heterogeneous models of the human body comprising cubic voxels with 3.6-mm edges. The present models are derived from the basic upright configuration used in earlier uniform field calculations [*Dawson et al.*, 1997; *Dawson and Stuchly,* 1998]. The limbs of the original model have been numerically articulated to obtain the required postures. Care has been taken to maintain electrical continuity of bone, muscle, blood vessels and skin. The models have some 80 tissues identified, with each voxel is assigned a recently measured conductivity value corresponding to its dominant tissue type. The model resolution is sufficiently high to resolve all major body components, as well as some of the smaller organs and tissues.

2.2 Exposure Scenarios

The two scenarios are illustrated in Figures 1 . Panels (a) and (b) show the arrangement of the body model and the 9 current-carrying elements in the vault maintenance scenario. All conductors are spaced 5.08 cm on-centre, with one cable pair and bus-bar for each conductor (and phase). The lower and upper horizontal cables are respectively 1.05 m and 2.1 m above the floor. The bus-bars are 0.52 m apart. Each phase carries 500 A (rms). The workers midplane is approximately 0.3 m to the right of the nearest bus-bar. Inspection of the isophase buses of a 700-MW generator are shown in panel (c) of Fig. 1. Two overhead horizontal segments within the neutral box meet at the star point, and 3 angled segments run to the generator (which is itself not modeled). Three vertical segments run from generator to lead-box, and thence three half-lines run to a remote transformer. There are a total of 11 conductors, carrying 20 kA (rms) per phase. The lower and upper horizontal conductors are respectively 1.2 m and 3 m above the ground. The conductors are 0.9 m apart. The worker is approximately 1.2 m from the closest (vertical right) conductor in the lead box.

It is assumed that any protective suit is completely permeable to the 60-Hz source magnetic field. Any conductors other than the the human body and the primary magnetic field sources described above are neglected. All source conductors are assumed to be infinitely thin in the transverse dimension. These simplifying assumptions introduce negligible errors in modeling of the actual exposure situations.

2.3 Computational Method

The numerical modeling is based on a representation which reflects the quasistatic approximation (Dawson et al., 1997), namely

$$\boldsymbol{E}^i(\boldsymbol{r}) = -j\omega \left\{ \boldsymbol{A}_0(\boldsymbol{r}) + \nabla\psi(\boldsymbol{r}) \right\}. \tag{1}$$

for the internal electric field, $\boldsymbol{E}^i(\boldsymbol{r})$. Here $\psi(\boldsymbol{r})$ is a scalar potential, $\omega = 2\pi f$ denotes the radian frequency, and f (=60 Hz) is the frequency used in the modeling. The associated period is $T = 1/f$. The applied magnetic field is described by a vector potential, with , $\boldsymbol{B}_0^e(\boldsymbol{r}) = \nabla \times \boldsymbol{A}_0(\boldsymbol{r})$. A common time-factor $e^{+j\omega t}$ is suppressed throughout. With $\sigma(\boldsymbol{r})$ denoting the body conductivity distribution, the scalar potential must satisfy the differential equation

$$\nabla\cdot\left[\sigma(\boldsymbol{r})\,\nabla\psi(\boldsymbol{r})\right] = -\nabla\cdot\left[\sigma(\boldsymbol{r})\,\boldsymbol{A}_0(\boldsymbol{r})\right] \tag{2}$$

subject to the boundary condition of tangential current flow at the surface. These equations are valid for low frequencies in the absence of any external applied electric field.

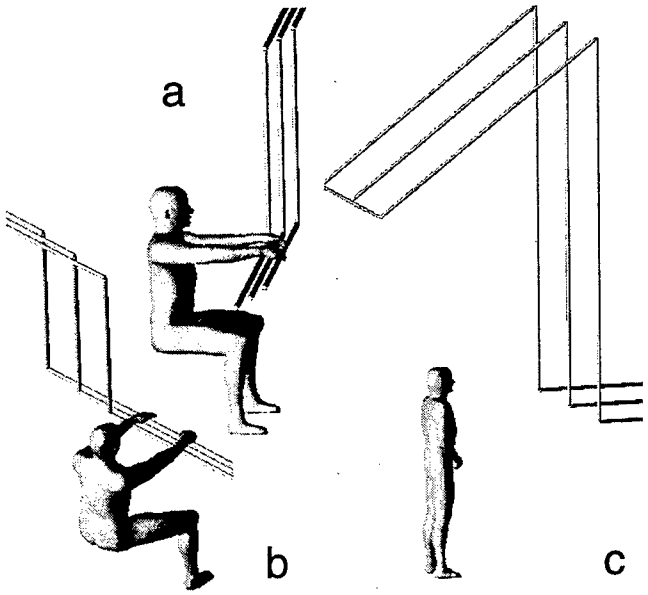

Figure 1: Two views (a, b) of the underground vault maintenance scenario, and one (c) of the generator inspection scenario.

In polar coordinates (ρ, φ, z) and using the Biot-Savart law [7], a current i_0 flowing along the z-axis from $z = \alpha$ to $z = \beta$ may be interpreted as contributing a partial magnetic field

$$\boldsymbol{H}_0(\boldsymbol{r}; \alpha, \beta) = K_0 \left\{ \frac{\beta - z}{\rho R_\beta} - \frac{\alpha - z}{\rho R_\alpha} \right\} \hat{\boldsymbol{\varphi}}, \quad \text{where} \quad K_0 \equiv \left(\frac{i_0}{4\pi} \right) \quad \text{and} \quad R_\gamma \equiv \sqrt{\rho^2 + (z - \gamma)^2}. \tag{3}$$

This partial field is non-physical since it is not divergence-free, but must form part of a larger closed current system. It has well-defined half-line limits $\boldsymbol{H}_0(\boldsymbol{r}; -\infty, \beta)$ and $\boldsymbol{H}_0(\boldsymbol{r}; \alpha, +\infty)$, as well as the elementary full-line limit $\boldsymbol{H}_0(\boldsymbol{r}; -\infty, +\infty) = 2K_0 \hat{\boldsymbol{\varphi}}/\rho$.

It may be verified that suitable half-line vector potentials are

$$\boldsymbol{A}_0(\boldsymbol{r}; \alpha, +\infty) = -\hat{\boldsymbol{z}}\, K_0 \ln \left[R_\alpha - (z - \alpha) \right]. \quad \text{and} \quad \boldsymbol{A}_0(\boldsymbol{r}; -\infty, \beta) = -\hat{\boldsymbol{z}}\, K_0 \ln \left[R_\beta + (z - \beta) \right]. \tag{4}$$

Suitable vector potentials for the whole or finite segments $[\alpha, \beta]$ of the z-axis are then given by

$$\boldsymbol{A}_0(\boldsymbol{r}; -\infty, +\infty) = \boldsymbol{A}_0(\boldsymbol{r}; -\infty, \gamma) + \boldsymbol{A}_0(\boldsymbol{r}; \gamma, +\infty) = -\hat{\boldsymbol{z}} K_0 \ln \left(\rho^2 \right). \tag{5}$$

and

$$\boldsymbol{A}_0(\boldsymbol{r}; \alpha, \beta) = \boldsymbol{A}_0(\boldsymbol{r}; \alpha, +\infty) - \boldsymbol{A}_0(\boldsymbol{r}; \beta, +\infty) = \boldsymbol{A}_0(\boldsymbol{r}; -\infty, \beta) - \boldsymbol{A}_0(\boldsymbol{r}; -\infty, \alpha) \tag{6}$$

Magnetic field and vector potential expressions for arbitrarily oriented elements are easily derived from the above using translation and rotation of the coordinates.

To account for the three-phase source current, each field quantity is represented the complex spatial vector form $\boldsymbol{C}(\boldsymbol{r}) = \boldsymbol{c}_r(\boldsymbol{r}) + j\boldsymbol{c}_i(\boldsymbol{r})$, having an associated real field,

$$\boldsymbol{c}(\boldsymbol{r},t) = \Re\left\{\boldsymbol{C}(\boldsymbol{r})\, e^{j\omega t}\right\} = \boldsymbol{c}_r(\boldsymbol{r})\cos(\omega t) - \boldsymbol{c}_i(\boldsymbol{r})\sin(\omega t), \tag{7}$$

which is the quantity of physical interest. It can be shown that the temporal minimum, maximum and root-mean-square (over one period) field amplitudes at the point $\boldsymbol{r}$ are

$$c_<(\boldsymbol{r}) \equiv \min_{0\le t\le T} ||\boldsymbol{c}(\boldsymbol{r},t)|| = \sqrt{\left[p_c(\boldsymbol{r}) - q_c(\boldsymbol{r})\right]/2}, \qquad c_>(\boldsymbol{r}) \equiv \max_{0\le t\le T} ||\boldsymbol{c}(\boldsymbol{r},t)|| = \sqrt{\left[p_c(\boldsymbol{r}) + q_c(\boldsymbol{r})\right]/2}, \tag{8}$$

and

$$c_\mu(\boldsymbol{r}) \equiv \sqrt{\frac{1}{T}\int_0^T ||\boldsymbol{c}(\boldsymbol{r},t)||^2\, dt} = \sqrt{\frac{p_c(\boldsymbol{r})}{2}}, \quad \text{where} \quad p_c(\boldsymbol{r}) \equiv ||\boldsymbol{C}(\boldsymbol{r})||^2 \quad \text{and} \quad q_c(\boldsymbol{r}) = |\boldsymbol{C}(\boldsymbol{r})\cdot\boldsymbol{C}(\boldsymbol{r})|. \tag{9}$$

The numerical solution of the boundary value problem is described elsewhere (Dawson et al., 1997). The only substantial differences between the earlier uniform field calculations and the present ones are the choice of applied magnetic vector potential to model the nonuniform fields, and the allowance for multiphase sources. Since the boundary value problem has real coefficients, the excitation due to the in-phase and quadrature components of the source can be computed separately. The resulting solutions can then be combined at the post-processing stage to yield the complex induced field.

3 Results and Discussion

The evaluation of a given configuration requires computation of approximately 1.7×10^6 electric field and associated current density vectors, distributed over approximately 80 elementary tissues. The temporal behaviour at a single point can be characterized by the minimum, maximum and root-mean-square values over one period. To describe the spatial behaviour, the elementary tissues are aggregated into composite tissue groups (e.g. organs) as appropriate. Scalar spatial dosimetric data of either a local (minimum and maximum) or a global (average, root-mean square) nature can then be computed for each tissue group. The two global measures for a spatial vector field $c_*(\boldsymbol{r})$ are defined analytically as

$$\text{Avg}\left\{c_*(\boldsymbol{r})\right\} = \frac{1}{V}\int_V ||c_*(\boldsymbol{r})||\, dV, \quad \text{and} \quad \text{Rms}\left\{c_*(\boldsymbol{r})\right\} = \sqrt{\frac{1}{V}\int_V ||c_*(\boldsymbol{r})||^2\, dV}. \tag{10}$$

The integrations are taken over the full volume of the particular organ under consideration, and are approximated by discrete sums over the appropriate voxel data.

3.1 External field measures

Table 1 shows the four whole-body volumetric measures of the external field based on temporal rms values. The

Table 1: Whole-body external field measures (mT)

	Min.	Max.	Avg.	Rms.
Vault	0.01	3:67	0.05	0.15
Generator	0.71	2.47	1.50	1.55

table indicates that the vault scenario exposes the body to the highest peak fields, due to the close proximity of the hands to the conductors. However, conductors in the generator scenario expose the worker to significantly higher whole-body fields, as indicated by the average and spatial rms values. Also, this latter scenario has a much higher whole-body minimum source field. The significant discrepancy of the spatial average and rms measures for the vault scenario is indicative of a high degree of field nonuniformity, largely due to the close proximity of the body to the conductors. The source field is more uniform over the body in the generator scenario, as indicated by the similar spatial average and rms measures.

3.2 Induced Field Dosimetry

Table 2 summarizes the spatial maximum, average and rms induced electric field (columns 2-4) and current density

Table 2: Selected tissue dosimetry for the vault maintenance scenario.

	$\|\|\boldsymbol{E}\|\|$ (mV m^{-1})			$\|\|\boldsymbol{J}\|\|$ (mA m^{-2})			$\|\|\boldsymbol{B}\|\|$ (mT)		
	Max	Avg	Rms	Max	Avg	Rms	Min	Max	Rms
blood	1.66	0.25	0.31	1.16	0.17	0.21	0.013	0.708	0.053
marrow	9.95	0.41	0.63	0.50	0.02	0.03	0.011	1.125	0.100
brain	3.99	0.57	0.65	0.40	0.05	0.06	0.039	0.065	0.050
csf	1.45	0.33	0.40	2.90	0.66	0.80	0.039	0.065	0.049
heart	2.22	0.64	0.72	0.22	0.06	0.07	0.032	0.044	0.038
kidneys	1.44	0.37	0.42	0.14	0.04	0.04	0.020	0.030	0.025
lungs	2.07	0.46	0.54	0.17	0.04	0.04	0.023	0.048	0.035
muscle	11.09	0.41	0.56	3.88	0.14	0.20	0.010	2.630	0.111
prostate	0.58	0.23	0.25	0.23	0.09	0.10	0.016	0.018	0.017
spleen	1.20	0.45	0.49	0.12	0.05	0.05	0.028	0.037	0.032
testes	0.83	0.29	0.33	0.33	0.12	0.13	0.017	0.020	0.018
whole body	25.03	0.55	0.93	3.88	0.09	0.15	0.010	3.665	0.147

(columns 5-7) dosimetry in selected organs for the vault scenario, based on the temporal rms fields (9a). Associated spatial minimum, maximum and rms values of the source magnetic field are also shown in columns 8 through 10.

The dosimetric data are largely consistent with the external field measures; namely, tissues that are close to the current-carrying conductors (bone and muscle, whole body) have high maximum induced electric field. These also have disparate values of the spatial average and rms measures, indicative of a high degree of source nonuniformity. Other organs have more similar average and rms spatial measures. The electric fields measures are generally in the 0.2–0.5 mV m^{-1} range. Induced current densities are generally below 1 mA m^{-2}, except for a few maximum values associated with tissues close to the conductors or having high conductivity values. However, all average and rms values are less than 0.2 mA m^{-2}, with the exception of cerebrospinal fluid (csf). Thus, this particular occupational exposure, when accurately modeled, is associated with induced current densities that are well below the 10 mA m^{-2} threshold stipulated in a recent guideline [*ICNIRP*, 1998].

Table 3 presents analogous data for the generator scenario. The dosimetric data are again generally consistent

Table 3: Selected tissue dosimetry for the generator inspection scenario.

	$\|\|\boldsymbol{E}\|\|$ (mV m^{-1})			$\|\|\boldsymbol{J}\|\|$ (mA m^{-2})			$\|\|\boldsymbol{B}\|\|$ (mT)		
	Max	Avg	Rms	Max	Avg	Rms	Min	Max	Rms
blood	100.0	12.7	15.0	70.04	8.89	10.50	0.78	2.43	1.67
marrow	149.6	19.9	26.1	7.48	0.99	1.30	0.74	2.10	1.40
brain	155.7	24.6	27.7	15.57	2.08	2.43	2.03	2.44	2.23
csf	55.6	13.7	16.2	111.20	27.35	32.44	2.03	2.44	2.22
heart	76.8	22.2	25.3	7.68	2.22	2.53	1.77	1.95	1.86
kidneys	120.1	30.4	34.0	12.01	3.04	3.40	1.49	1.71	1.61
lungs	136.2	29.8	33.9	10.89	2.38	2.71	1.56	2.00	1.81
muscle	183.2	19.8	24.4	64.12	6.93	8.54	0.71	2.41	1.47
prostate	48.6	17.4	18.5	19.44	6.96	7.41	1.35	1.41	1.38
spleen	120.9	56.7	58.5	12.09	5.67	5.85	1.66	1.86	1.75
testes	67.4	18.1	20.6	26.97	7.22	8.24	1.35	1.48	1.40
whole body	523.2	26.3	33.7	111.20	4.56	6.59	0.71	2.47	1.55

with the exposure field measures. There are smaller differences between the average and rms fields, indicative of a more uniform external field over the body in comparison with the vault scenario. On the other hand, the relatively higher source field levels produce higher induced quantities.

In many organs the average electric fields are of the order of 20 mV m^{-1}. Only in a few cases do the spatial average or rms induced current densities exceed 10 mA m^{-2}. The limit of 10 mA m^{-2} is exceeded by the maximum values in several tissues. It may be noted than the maximum values are overestimated by perhaps 10–25% due to the staircasing inherent in the human body voxel model. On the other hand, this scenario assumes a 1.2-m body/conductor separation; significantly higher fields will be induced at closer separations.

3.3 Comparison with Uniform Field Exposure

Table 4 presents normalized values of the spatial average ($\hat{E}_\mu$) and maximum ($\hat{E}_>$) induced electric fields in selected

Table 4: Selected tissue dosimetry, normalized to the whole-body average applied magnetic field, for the vault maintenance and generator inspection scenarios, and for a uniform field exposure.

	Vault			Generator			Uniform		
	$\hat{B}_\mu$	$\hat{E}_\mu$	$\hat{E}_>$	$\hat{B}_\mu$	$\hat{E}_\mu$	$\hat{E}_>$	$\hat{B}_\mu$	$\hat{E}_\mu$	$\hat{E}_>$
		(V/m/T)			(V/m/T)			(V/m/T)	
blood	0.7	4.9	32.8	1.1	8.4	66.5	1.0	8.2	81.8
marrow	0.8	8.0	196.5	0.9	13.2	99.4	1.0	16.1	152.3
brain	1.0	11.3	78.9	1.5	16.4	103.5	1.0	11.7	72.8
csf	1.0	6.5	28.7	1.5	9.1	36.9	1.0	7.5	38.7
heart	0.7	12.7	43.9	1.2	14.8	51.0	1.0	19.2	68.3
kidneys	0.5	7.3	28.4	1.1	20.2	79.8	1.0	25.2	72.0
lungs	0.7	9.0	41.0	1.2	19.8	90.5	1.0	20.8	85.6
muscle	0.9	8.1	219.0	1.0	13.2	121.8	1.0	14.9	144.8
prostate	0.3	4.6	11.5	0.9	11.6	32.3	1.0	17.0	53.6
spleen	0.6	8.9	23.7	1.2	37.7	80.3	1.0	41.2	91.2
testes	0.4	5.7	16.3	0.9	12.0	44.8	1.0	14.8	73.5
whole body	1.0	10.8	494.3	1.0	17.5	347.7	1.0	18.9	368.8

tissues for the present vault and generator scenarios, as well as for corresponding values taken from earlier uniform-field exposure [*Dawson and Stuchly*, 1998]. The data are normalized by the external magnetic field whole-body averages (Table 1), and so have units of V m^{-1} T^{-1}. The column headed $\hat{B}_\mu$ indicates the associated normalized values of the organ-average source magnetic field; these data are therefore dimensionless and represent fractions of the whole body average.

The following observations can be made based on these data: (i) The average induced electric fields in all organs, except for the brain and csf in the generator scenario, are lower than those for the comparable uniform field exposure, and (ii) The rms magnetic field within the brain in the generator scenario (2.23 mT, Table 3) is 50% higher than the whole-body value (1.55 mT), and is associated with an average induced electric field of 16.4 V m^{-1} T^{-1}. This value may be compared with an average electric field of 17.6 mV m^{-1} that would be produced by a uniform 1.5-mT magnetic field (Table 4).

These results have a useful practical application. For nonuniform magnetic field exposures, the expected average induced fields in a given organ may be estimated using the associated organ-average value of the non-uniform magnetic field in conjunction with the previously-computed fields induced by a uniform magnetic field of the same strength.

The true values induced in organs obtained from full non-uniform source computation are not likely to exceed the estimated values. Exceptional cases may be associated with a part of a large organ being in a much stronger field than the average.

4 Conclusions

Human exposure to nonuniform magnetic fields from spatially complex conductor configurations has been modeled using a scalar potential finite difference (SPFD) computer code with proper modifications. Dosimetric data in terms of various spatial measures of the induced electric fields and current densities in a high-resolution model of the human body have been computed for two realistic exposure scenarios.

The vault maintenance scenario is associated with induced current densities that are well below a 10 mA m^{-2} threshold. For the generator scenario, on the other hand, spatial average, rms or maximum values in several organs exceed this threshold.

A comparison of the full non-uniform source dosimetric data with equivalent uniform magnetic exposure values shows that the average induced fields and currents in organs are generally smaller for the non-uniform exposures. For organs that are exposed to fields significantly stronger than the whole-body average value, the average field within the volume of the organ should be considered. Higher maximum values of the induced fields occur in tissues that are in magnetic fields much stronger than the rest of the body, e.g. in tissues of the hands close to conductors. Overall, these comparisons suggest the possibility of using the dosimetry data for uniform magnetic fields together with accurate spatial maps of the non-uniform exposure field within the body volume for reasonably reliable estimation of the organ and tissue induced electric fields and currents under non-uniform field conditions.

Acknowledgment

This research was supported by EPRI Contract No. WO 2966-14.

References

[1] National Institute of Environmental Health Sciences. Assessment of health effects from exposure to power-line frequency electric and magnetic fields. Working Group Report NIH 98-3981, National Institute of Health, Research Triangle Park, NC, USA, August 1998.

[2] International Commission on Non-Ionizing Radiation Protection. Guidelines for limiting exposure to time-varying electric, magnetic and electromagnetic fields (up to 300 GHz). *Health Physics*, **74**(4):494–522, April 1998.

[3] M. A. Stuchly and S. Zhao. Magnetic field-induced currents in the human body in proximity of power lines. *IEEE Trans. on Power Delivery*, **11**:102–108, 1996.

[4] T. W. Dawson, K. Caputa, and M. A. Stuchly. High-resolution numerical magnetic field dosimetry for live-line workers. Paper presented at the IEEE Conference on Electromagnetic Field Computation (CEFC'98), June 1-3, 1998, Tucson, Arizona., 1998.

[5] T. W. Dawson and M. A. Stuchly. High resolution organ dosimetry for human exposure to low frequency magnetic fields. *IEEE Trans. Magn.*, 34(3):708–718, May 1998.

[6] T. W. Dawson, K. Caputa, and M. A. Stuchly. A comparison of 60-Hz uniform magnetic and electric induction in the human body. *Phys. Med. Biol.*, **42**(12):2319–2329, 1997.

[7] J. A. Stratton. *Electromagnetic Theory.* McGraw-Hill Book Company, New York, 1941.

Characterization of Near Electromagnetic Fields From Hand-held Radio Antennas

Malcolm J. Packer
Harris Corporation, RF Communications Division
1680 University Avenue, Rochester, NY 14610

Abstract

This paper presents characterization of near field distributions radiated from hand-held communication devices calculated with the Numerical Electromagnetic Code[1]. A wire-grid model of a hand-held cellular telephone was developed and validated with extensive measurements. This wire-grid model was then used to examine four antenna types and the differences in electromagnetic radiation exposure based on electric field intensity in the projected location of the head and hand. The four candidate antennas are the quarter-wave monopole, half-wave dipole, inverted-F antenna, and a half-loop antenna.

The results indicate that all candidate antennas had localized areas where the IEEE Maximum Permissible Exposure (MPE) standard for total body immersion are exceeded. Of the four antennas examined, the half-wave dipole had minimum exceeded area in the projected head space. The half-wave dipole also excites less currents on the hand-held shell, allowing the hand to grasp the hand-held with minimum absorption. Therefore, the maximum useable power is radiated from a half-wave dipole antenna due to minimum power absorbed by the head or hand.

I. Introduction

Hand-held communication devices have been at the research forefront with their wide spread use and concern of possible health risk from electromagnetic absorption. An early paper points out that the human body has different specific absorption rates (SAR) along its surface with the highest levels around the head and the neck[2]. This work was extended by research into SAR as a function of hand-held proximity to the head[3] and head shape[4]. Electromagnetic energy radiated by a hand-held radio integral antenna is a function of antenna and radio shape, excitation point, antenna attachment, and scatterers and absorbers in the near field. This paper focuses on near field electromagnetic intensity as a function the antenna type, location, and size. Four antennas are analyzed for use with mobile cellular telephone systems.

The typical antenna used with a hand-held cellular radio is an integral monopole. Hand-held radios are usually supported by a hand when in use. The integral monopole creates currents on the hand-held shell, the counterpoise. The grasping hand has a profound effect on the radio's communication efficiency due to impeding and altering surface current's direction and magnitude. In fact, the interaction of the head, hand, and body have several effects that require investigation: 1) radiation efficiency, 2) radiation pattern distortion, 3) compliance with standards, and 4) specific absorption rate.

This paper examines alternative antenna types from the view point of electromagnetic radiation in the projected head space. The first goal is to construct a wire-grid numerical model and validate with empirical data, and then use the numerical model to determine the ideal antenna type and mounting location. Four simple antennas were compared: quarter-wave monopole, half-wave dipole, inverted-F,

and a half-loop. This paper determines the electromagnetic field strengths close to these simple antenna structures and compares the values to the IEEE RF safety standard[5].

II. Maximum Permissible Exposure

According to the IEEE RF safety standard, safety to personnel from electromagnetic fields and contact with conductive objects exposed to such fields is a function of body resistance and capacitance to ground[5]. The work performed was confined to measurements and numerical modeling of the electromagnetic fields associated with small wireless systems and it did not address thresholds on health hazards. More specifically, we were attempting to determine by empirical and numerical models of simple antennas whether the set standards[5] were exceeded

The current IEEE standard provides the Maximum Permissible Exposure (MPE) in terms of rms electric (E) and magnetic (H) field strengths, power density (S), and induced currents (I) in the human body. The MPE to electric fields, magnetic fields and power density shown in Figure 1 are for the equivalent vertical cross-sectional area of the human body. Two sets of curves are displayed: controlled (people aware of potential exposure) and uncontrolled (people unaware of potential exposure). These MPE field levels are set to limit the maximum surface current over the body to 100 mA through each foot to ground. Over a six minute time frame, this results in about 144 J/kg in an average 68 kg person. This is equivalent to a specific absorption ratio (SAR) of about 0.4 W/kg averaged over the entire body mass or spatial peak of 8 W/kg averaged over 1 gram of tissue, cubic in shape.

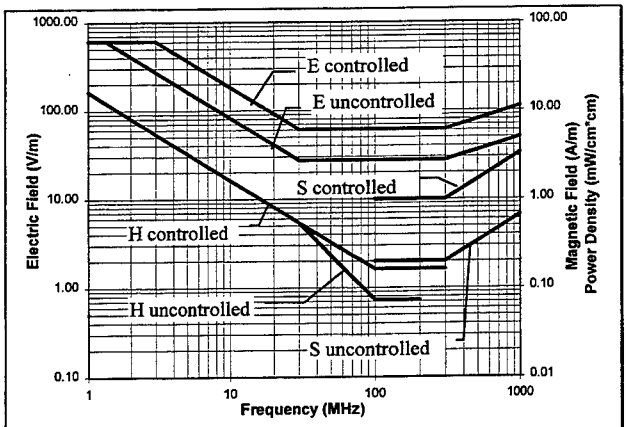

Figure 1. Maximum Permissible Exposure Standard for RMS Electromagnetic Field Strengths and Power Density from 1 to 1000 MHz

The power density is calculated from the electric and magnetic radiated fields. In the far field, several wavelengths from the antenna, the ratio of the electric field to magnetic field is equal to the intrinsic impedance of free space, $120\pi\ \Omega$. In the near field, this relationship is not true, and it is difficult to calculate the MPE from an individual electric or magnetic field, therefore both must be measured separately. The power density in watts per square meter is equal to the electric field in volts per meter multiplied by the magnetic field in amps per meter. However, the IEEE standard allows freedom above 300 MHz and requires only one field to be measured, generally the electric, and then the free-space equivalent power densities (S)can be computed, equation 1.

$S(E) = E^2/120\pi$ and $S(H) = H^2 * 120\pi$ for frequencies > 300 MHz (1)

These MPE power densities are for the equivalent vertical cross-sectional area of the human body. Permitted exposure levels apply to all parts of the body except the extremities. Arms, hands, legs, and feet contain no vital organs and provide more surface area that enhances cooling. For this reason, extremities can be exposed to up 20 W/kg averaged over any 10 gram cube of tissue. There is an exclusion in the IEEE safety standard for low-powered devices. The MPE may be exceeded if the radiated power is less than 7*450/*f*(MHz) (controlled) or 1.4*450/*f*(MHz) (uncontrolled) watts. However, this exclusion does not apply if the antenna is within 2.5 cm from the body.

III. Model Development and Validation

The Numerical Electromagnetic Code Version 4[1] (NEC-4) is a well-known implementation of the moment method[6] algorithm. NEC-4 is considered the best method of moments electromagnetic modeling tool, having achieved this status through constant improvement and extensive validation by many independent users. NEC-4 computes the current distribution on a segmented wire-grid or surface patch model of the antenna and platform structures. The wire-grid models were created using an interactive graphical user interface, EAM:NEC[7]. The current distribution in each wire-grid segment is then used to compute near electric and magnetic field strengths.

A numerical model was developed for a plastic coated hand-held cellular radio with integral monopole antenna. Figure 2 displays the wire-grid model that was used to compute the electromagnetic fields. The wire-grid model contains 117 wire segments to model the aluminum back plane, LCD/speaker enclosure, antenna, and battery. The model was segmented so that there are approximately 15 segments per wavelength at 850 MHz. The model is situated such that the 11.0 cm monopole is aligned with the z-axis in the Cartesian coordinate system. For validation purposes, the near electric field was calculated every 10 cm from -1.0 to 1.0 m in the x- and y-axis and from 1.0 to 2.0 m in z-axis creating two orthogonal planar views that bisect at the hand-held.

For accurate comparison to the model, the cellular phone was situated in a large open area free of metallic obstacles at a height of 150 cm. The hand-held's vertical dimension was 15 cm and the antenna was 11 cm long. Measurements were performed in linear paths on the axis away from the radio centered on the antenna at 110, 130, 150, 160, and 170 cm high. The electric field strength was measured using a small 3-axis probe[8]. The probe was connected to the readout by a length of fiber optic cable to minimize measurement interaction. The readout provided the summation of all three vector components, therefore minimizing fluctuations due to probe orientation.

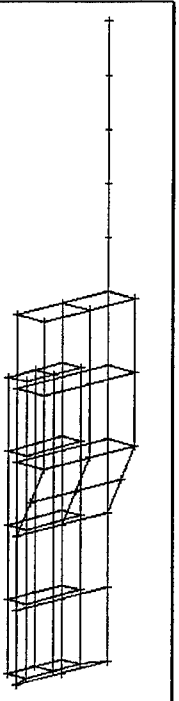

Figure 2. Wire-grid Model of a Typical Wireless Cellular Radio

Data was collected at 10 cm increments at one transmitting frequency on a single channel between 825 and 850 MHz. This measurement increment, although coarse for detailed analysis, was ideally suited for validation of the numerical model. Figure 3 displays the empirical and numerical data for heights of 150, 160, and 170 cm above the ground. The power used in the model was adjusted until on average the peak gradients aligned with the measurements. The cellular phone output is rated at 240 to 950 milliwatts, with 600 nominal. Adjusting the power used in the numerical model to 240 milliwatts provided excellent agreements in terms of attenuation versus distance. empirical

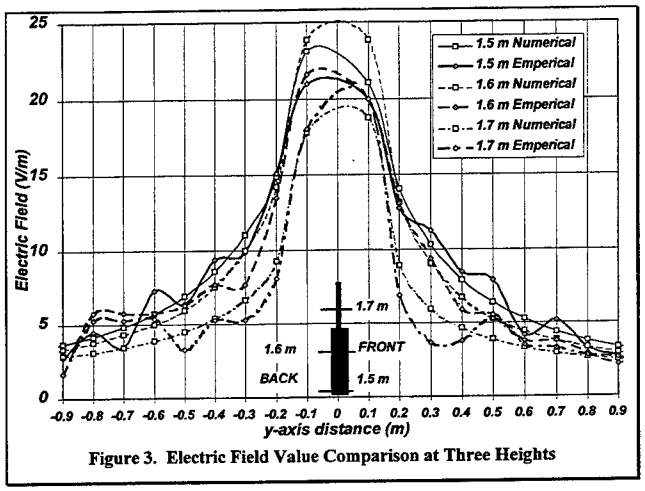

Figure 3. Electric Field Value Comparison at Three Heights

Figure 4 displays the empirical data in a different format, orthogonal planar views of electric field strengths as amplitude contours. The left hand side is the y-z plane slicing through the hand-held from back-to-front. The right hand side is the x-z plane slicing through from left-to-right. The largest electric field occurs near the radio between a height of 150 and 165 cm. The measurement resolution was 10 cm. Closer to the radio and antenna the values had a steep gradient similar to 10 cm to 40 cm. At this reduced power level it is estimated that the peak electric field reaches 100 V/m.

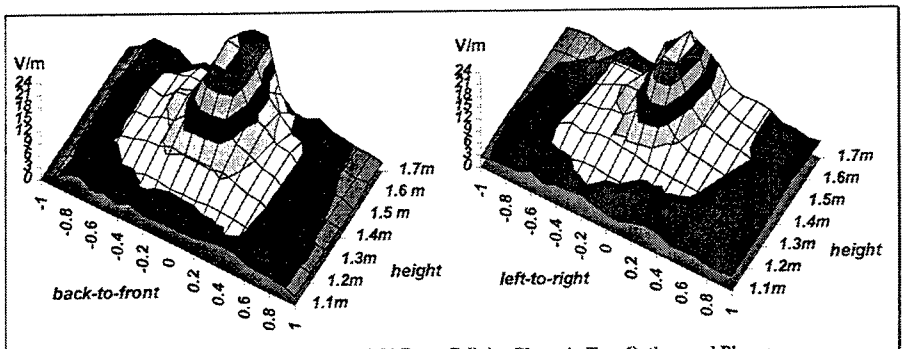

Figure 4. Measured Electric Field From Cellular Phone in Two Orthogonal Planes

The same measurements were performed with a subject's hand around the phone and the left ear against the hand-held. Figure 5 displays the orthogonal planar views. It was impossible to measure the fields within the subject. Therefore, the fields are displayed as zero. If we look at the contour area edges where the field drops below 3 V/m (dark to light gray), the contour overall size is reduced when the subject is present. The body interacts with the test object's radiated power and absorbs power resulting in reduced electric field values. The exact amount of absorbed power by the body, head, and hand is difficult to measure without complete 2π steradians of measurements, or measuring the surface current induced onto the body.

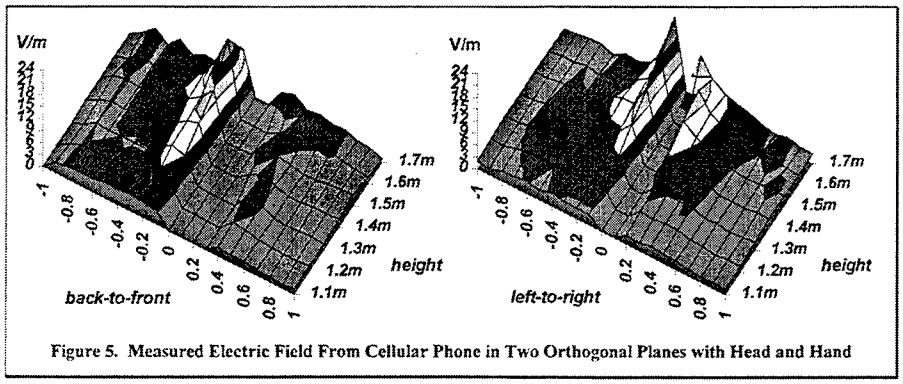

Figure 5. Measured Electric Field From Cellular Phone in Two Orthogonal Planes with Head and Hand

Comparison to the safety standard must be performed without the test subject present. Once the subject is present, the subject absorbs power resulting in lower values.

Papers to date[2,3,4,9] have analyzed the effect internal to the head and not the root cause. With a validated wire-grid model, the next section will investigate different antennas and their near electric field, in an effort to reduce the head and hand exposure.

IV. Antenna Comparisons

Four alternative antennas were analyzed for their applicability to hand-held usage from the perspective of electromagnetic radiation in the projected head space: quarter-wave monopole, half-wave dipole, inverted-F, and half-loop. Each antenna was numerically constructed on the validated wire-grid model. Then the numerical models were used to determine the electromagnetic near field generated by the hand-held/antenna structures and these predicted values were compared with the IEEE RF safety standard. To analyze near the projected head area, the near fields were predicted in a centimeter grid that covered a planar area that encircled the hand-held radio and antenna.

The near electric field around a quarter-wave monopole is shown in Figure 6. The hand-held shell and antenna are drawn as white rectangles in the correct location. The white oval outline represents the projected head space. The power level is now adjusted to the nominal value of 600 milliwatts at the antenna port. Electromagnetic field peaks occur in three locations: the antenna tip, antenna/hand-held interface, and the hand-held shell's base. When the head is placed near the hand-held, it is exposed to localized electromagnetic fields that exceed the IEEE standard for total body exposure of 100 V/m (45

V/m) controlled (uncontrolled). Within this plane, the projected head space encircles 32 sq. cm that exceed 100 V/m. Approximately 45%[9] of the radiated power is absorbed by the head, resulting in a SAR of 2.93 W/Kg[9]. The head area exposed includes skin, muscle, bone, and gray matter. When only a fraction of the body is exposed, localized SAR can reach 8 W/kg averaged over one gram of body mass (1.6 W/kg uncontrolled). This equates to approximately 275 V/m (125 V/m) for controlled (uncontrolled) localized electric field levels.

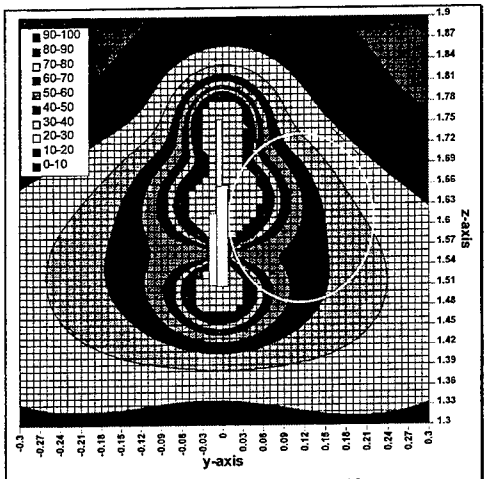

Figure 6 The Near Electric Field About a Monopole on a Hand-held Radio

An undesirable feature seen in Figure 6, is the amount of electric field radiating directly from the hand-held shell. The electric field lowest level is above 50 V/m. When a hand grasps the hand-held shell, surface currents flow over the hand and power is absorbed. For the monopole, approximately 10%[9] of the radiated power is absorbed by the grasping hand.

The shape of the electric field contours in Figure 6 implies that radiation pattern directivity is downwards towards the ground. Thus, the ground will absorb power, an undesirable characteristic for the radiation pattern. It is desirable to reduce these percentages by finding an antenna configuration that does not produce peak electromagnetic fields within the white oval outline and minimizes currents on the hand-held's shell.

For a half-wave center fed dipole antenna, Figure 7, the electric field peaks at the dipole ends, although these peaks exceed the MPE standard. However, isolation of the antenna from the hand-held shell has significantly reduced the size of the exceeded area at the shell's base. This antenna's detachment has also reduced the electric field along the hand-held shell to 15 V/m. This can allow the hand the grasp to radio with less power absorption.

In this planar cut, only 5 sq. cm are within the projected head area, appreciably less than the 32 sq. cm from the monopole. The shape of the electric field contours implies that directivity is slightly upwards, a desirable

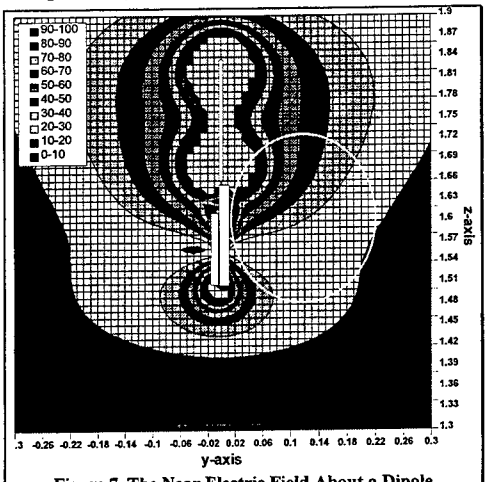

Figure 7 The Near Electric Field About a Dipole Above the Hand-held

characteristic for a broad-beamed radiation pattern.

The inverted-F antenna is a monopole bent at 90° with an inductive shorting stub to balance the increase capacitance. Figure 8 displays the antenna configuration with the near electric field contours. There are two large areas that exceed the MPE standard. The driven element is now on the head side of the hand-held shell. This is realized by a large area within the projected head space, 28 sq. cm, within which the MPE standard is exceeded. The lowest level of electric field generated from the hand-held shell is 50 V/m, the same as the monopole. Grasping this hand-held will significantly reduce the EIRP, as discussed earlier. The electric field contour shape implies that the radiation pattern is upwards towards zenith. These results indicated that the inverted-F antenna is not suitable for this application, at least not in the analyzed configuration.

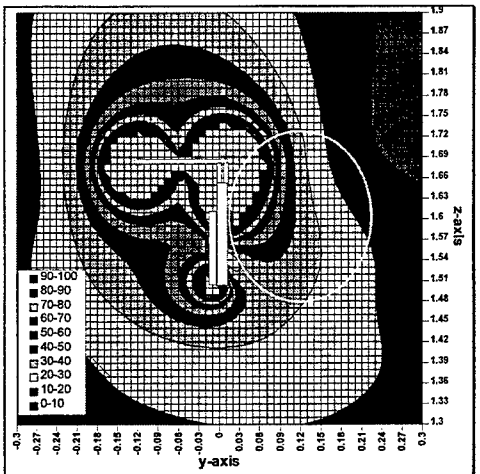

Figure 8 The Near Electric Field About an Inverted-F on the Hand-held

The last antenna analyzed is a half-loop antenna, the antenna is driven at the top attachment and shorted to the bottom of the hand-held. Figure 9, displays one large circular area that exceeds the MPE standard. The half-loop is attached to the hand-held's shell, therefore it incorporates the hand-held conductive shell as part of a loop. Current flows through both sections and radiates as a full loop.

There is a large area that exceeds the MPE standard within the projected head space, 36 sq. cm. The exceeded area is centralized in the projected head space, therefore the SAR region is around the cheek and eyes, but not gray matter. Grasping the shell with a hand places the hand directly at the peak electric field value. The electric field contour shapes imply that the radiated power is toward the horizon. In summary, this version of a half-loop has the largest area of exceeded electric field within the projected head space and has the highest exposure to the hand.

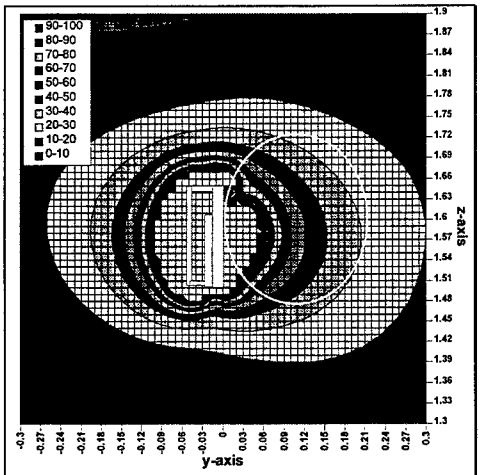

Figure 9 The Near Electric Field About a Half-Loop on the Hand-held

V. Conclusions

A number of factors are used to select antenna types and mounting configurations for any communication radio. This paper focused on minimizing electromagnetic exposure of the user. To perform a numerical antenna type comparison, a wire-grid model of a hand-held cellular telephone was developed and validated with extensive measurements. Four candidate antenna types were combined with the validated wire-grid model and examined to determine potential radiation intensities in the projected location of the head and grasping hand.

The goal was to select an antenna type and mounting configuration that minimizes the electromagnetic exposure of the user. Two key points were found, first, minimization of the RF currents on the shell reduces power absorbed in the grasping hand as well as undesirable perturbation of the antenna radiation patterns. Second, understanding that near field radiation intensity occurs at the antenna ends and not at the antenna feed emphasizes that antenna position is critical to minimizing near-field intensity within the projected head space.

The data indicates that all the antennas have localized areas where the IEEE MPE standard for total body immersion for both controlled and uncontrolled use is exceeded. Of the four candidate antennas, the half-wave dipole provided the lowest electric field intensity within the projected head space. It also had the minimum current on the hand-held shell, resulting in less absorption by the hand. Therefore, maximum useable power radiated and minimum electromagnetic exposure from the hand-held occurs with a half-wave dipole due to minimum power absorption by the head and hand.

VI. References

[1] G. J. Burke, "Numerical Electromagnetics Code - NEC-4, Method of Moments," Part I: User's Manual, Lawrence Livermore National Laboratory, Jan. 1992.

[2] M.A. Stuchly, R. J. Spiegel, S.S. Stuchly, and A. Kraszewski, "Exposure of Man in the Near-Field of a Resonant Dipole: Comparison Between Theory and Measurements," *IEEE Trans on MTT*, vol. MTT-34, no. 1, January 1986.

[3] M. Okoniewski, M.A. Stuchly, "A study of the Handset Antenna and the Human Body Interaction," *IEEE Trans on MTT*, vol. MTT-44, no. 10, October 1996.

[4] V. Hombach, K. Meier, M. Burkhardt, E. Kuhn, and N. Kuster, "The dependence of EM Energy Absorption Upon Human Head Modeling at 900 MHz," *IEEE Trans on MTT*, vol. MTT-44, no. 10, October 1996.

[5] IEEE Standard for Safety Levels with Respect to Human Exposure to Radio Frequency Electromagnetic Fields, 3 kHz to 300 GHz, IEEE C95.1-1991.

[6] R.F. Harrington, *Field Computation by Moment Methods*, Krieger Publishing Company, 1968.

[7] M.J. Packer, "Graphical Shell for Numerical Electromagnetic Code," *Applied Computational Electromagnetic Society Symposium*, March 1993.

[8] Holaday Industries, Inc., HI-4433 Series Broadband Isotropic Field Probes.

[9] O.P. Gandhi, G.Lazzi, C.F.Furse, "Electromagnetic Absorption in the Human Head and Neck for Mobile Telephones at 835 and 1900 MHz," *IEEE Trans on MTT*, vol. MTT-44, no. 10, October 1996.

Application of Multigrid Method for Quick Simulation of SAR and Temperature Distribution During Hyperthermia Treatment of Cervical Malignancies.

Michał P. Dębicki*, Michał Mrozowski*and Piotr Dębicki*

Abstract

The paper presents the application of the adaptive multigrid technique to the solution of SAR and temperature distribution in a patient undergoing hyperthermia treatment. A modified brachytherapy applicator is used as a hyperthermia source in order to use a single device for both treatments. Voltage of frequency 500 kHz is applied to the applicator's electrodes and thus quasi–static approximation is possible. The $\bar{E}$–field distributions for basic excitation modes are obtained by a solution of Laplace equation using adaptive multilevel finite element code. Then the solution for an arbitrary excitation is obtained by summation of basic modes with adjusted amplitudes and phases. The temperature distribution is obtained using the same multigrid approach. The short evaluation time of the modeling enables the on-line simulation during treatment.

1 Introduction

In recent years multigrid techniques have emerged as an efficient tool for the solution of linear equation system resulting from some discretization scheme such as finite element (FE) or finite difference (FD) methods [1, 2]. Their effectiveness can be even further improved by application of adaptive grid refinement of the computational domain [3]. These methods are especially valuable for the high resolution meshes, when the standard iterative schemes result in long solution times due to poor convergence. In this paper we present an application of the adaptive multigrid approach to the solution of quasi–static boundary value problem and then re-apply obtained results in order to obtain the temperature distribution. Our research stems from the need for fast treatment planning in the hyperthermia of cervical malignancies.

The aim of a hyperthermia treatment is to raise the temperature of a treated region to values from the range of 43°C to 48°C in order to slowly destroy tumor cells. The hyperthermia is, in most cases, performed synergetically with radiotherapy as a means to enhance the response of cells and to increase the possibility of an effective treatment [4, 5]. The method, most commonly used for the treatment of cervical malignancies, is brachytherapy (BT). This is a kind of radiation therapy in which radioactive materials are placed in direct contact with the tissue being treated. This type of therapy is applicable for those tumours, which might be directly accessed with interstitial or intracavitary brachytherapy applicators. The BT for the cervical malignancies is usually carried out by means of a commonly used and commercially available cervical Fletcher–Suit (FS) applicator for afterloading devices (Fig. 1). This applicator consists of three subunits designed to accept radioactive Cs-137 pellets. When the applicator is assembled and placed in the desired treatment position the Cs-137 sources are moved into their planned place according to the treatment plan. The source placement and their removal is accomplished with the use of compressed air. The irradiation lasts for about 10 hours.

The purpose of this study was to adapt the brachytherapy applicator as a hyperthermia device (in order to perform both HT and BT treatments imediately one after another and to reduce the trauma associated with positioning the applicator within a patient's body) and to investigate the possibility of an effective treatment by software simulations, which then can be used as a core of a hyperthermia treatment planning system. The idea is to complete the modeling and treatment planning while the patient is being subjected to BT. Such an approach requires:

*Technical University of Gdańsk, Department of Electronics, Telecommunications and Informatics,
ul. Narutowicza 11/12, 80–952, Gdańsk, tel. (+ 48 58) 347 2324, fax. (+ 48 58) 347 12 28, e-mail: patryk@eti.pg.gda.pl

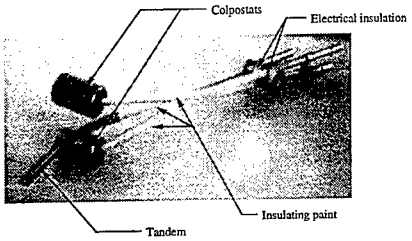

Figure 1: *Modified selectron compatible Fletcher-Suit cervical applicator. The colpostats are both 2 cm in diameter and 3 cm in length. The tandem is 0.6 cm in diameter and curved by 30 degrees. The tubes supporting the colpostats and the proximal part of the tandem are covered by insulating paint (white) in order to prevent health tissues from undesired heating. Each of the subunits are electrically insulated. The relative position of the colpostats and tandem depends on a patient. A thin metal foil, working as a ground electrode is additionally placed around a patient*

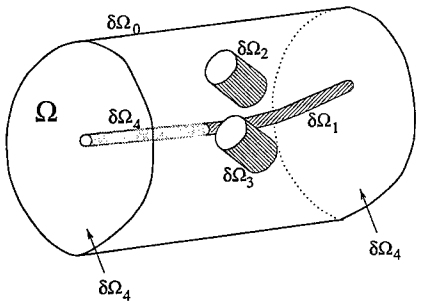

Figure 2: *The description of the domain. Boundary $\delta\Omega_0$ represent a thin metal foil around a patient's lower abdomen. Boundaries $\delta\Omega_1$ to $\delta\Omega_3$ represent applicator's electrodes where voltage is applied and $\delta\Omega_4$ represent Neumann boundary conditions*

- modification of the FS applicator to work as a hyperthermia applicator,
- a fast solver to carry out computations for each patient based on the X-ray pictures of a FS applicator positioned inside patient body.

Some minor changes, which enabled the use of the FS applicator as hyperthermia source are presented in Fig. 1. These include: (a) an electrical separation of the three subunits in order to function as three separate electrodes (b) an electrical insulation of these parts of the applicator, where heating is not desirable.

2 Problem Definition

The temperature increase during hyperthermia system is accomplished by dissipating electric current flowing between the modified Fletcher-Suit applicator placed in the treatment position and a large external electrode surrounding the patient's lower abdomen. Schematic configuration is presented in Fig. 2. The 500 kHz voltage is applied to three of the applicator's electrodes (boundaries $\delta\Omega_1$ to $\delta\Omega_3$), while external electrode is always grounded

(boundary $\delta\Omega_0$). Since low frequency field is used we may apply the quasi–static approach and find the electric field inside the tissue by solving the following boundary value problem:

$$\begin{cases} \nabla \cdot (\sigma \nabla V) = 0 & \text{in } \Omega \\ V = 0 & \text{on } \delta\Omega_0 \\ V = V_n & \text{on } \delta\Omega_n, \quad n = 1,2,3 \\ \frac{\partial V}{\partial n} = 0 & \text{on } \delta\Omega_4 \end{cases} \tag{1}$$

where σ represents the conductivity and V the electric potential. Solving (1) for V we obtain the electric field distribution, from the relation:

$$\vec{E} = -\nabla V \tag{2}$$

Power absorbed by the tissues is proportional to the tissue conductivity and a square of the electric field amplitude:

$$P = \frac{1}{2}\sigma |\vec{E}|^2 \quad \left[\frac{W}{m^3}\right] \tag{3}$$

This quantity further divided by tissue mass density ρ represents the specific absorption rate (SAR):

$$SAR = \frac{P}{\rho} \quad \left[\frac{W}{kg}\right] \tag{4}$$

which expresses the amount of power absorbed by mass volume of tissue and thus is the main cause of temperature elevation.

The applicator's construction (see Figs 1 and 2) implies that three independent modes of excitation exist – 001 (left electrode is excited, while others are grounded), 010 (central electrode is excited, while others are grounded) and 100 (right electrode is excited, while others are grounded). The outer electrode is always grounded. Knowing the solution for three basic modes it is possible to find $\vec{E}$ – field distribution for arbitrary excitation using a superposition of the three basic mode solutions $\vec{E}_i$:

$$\vec{E}_{tot} = \sum_i^3 A_i \vec{E}_i e^{-j\theta_i} \tag{5}$$

where A_i is is the amplitude and θ_i is the phase–shift of the i–th applicator's electrode.

In order to obtain the temperature distribution, the Pennes bio-heat transfer equation [6] for a stationary case has to be solved:

$$-\nabla \cdot (k \nabla T) + c_b W (T - T_b) = P \tag{6}$$

where k is a thermal conductivity, c_t is tissue specific heat, W is a volumetric perfusion rate in $[kg\, m^{-3}\, s^{-1}]$, T_b is blood temperature and P is the power density obtained from (3).

Boundary conditions (BC) for the modeling of temperature distribution are specified for the domain shown in Fig. 2. Assuming the constant basic body temperature the boundary $\delta\Omega_0$ is specified as Dirichlet BC with $T = 37°C$. The remaining boundaries are assumed to have the temperature of adjacent tissue and thus the boundary condition is set as the Neumann type (material, the applicator is made of, is characterized by small thermal conductivity). For the case of air cooling of the electrodes, another boundary condition of the Cauchy type have to be specified on cooled surfaces ($\delta\Omega_1$ to $\delta\Omega_3$):

$$k \frac{\partial T}{\partial n} = -\alpha (T - T_{air}) \tag{7}$$

where α is a heat transfer coefficient and T_{air} is a temperature of cooling air.

3 Adaptive Multigrid Approach

As the computation domain is large comparing to applicator dimensions and the configuration is complex (see Fig. 1), it was essential to use a fast numerical technique to solve (1) and then (6). Note that the simulation

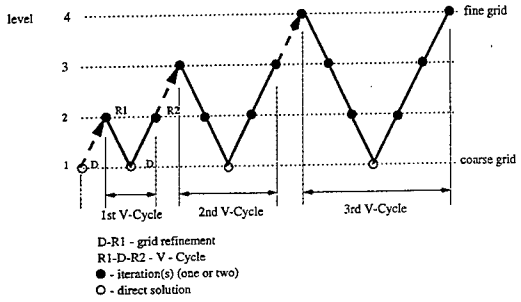

Figure 3: *Schematic representation of Full multigrid V-cycle.*

starts after the X-ray pictures are taken and has to be completed before BT treatment is finished. To this end, a multigrid method (MG) based on finite elements (FE) method was employed. The FE discretization scheme enables the use of irregular tetrahedral mesh, which may be well fitted to conform to the complicated shape of the electrodes. After the FE discretization, we obtain a set of linear equations, which may be written in a matrix form as:

$$\mathbf{A}u = f \tag{8}$$

where $\mathbf{A}$ is a sparse and banded matrix, f is a vector representing voltage on the electrodes and u is the vector of unknowns.

The equation (8) is usually solved in standard approaches by some iterative schemes. Unfortunately these methods may suffer from poor convergence, especially for high resolution meshes.

These problems are obviated in multigrid methods [2, 3], where the initial guess for the first iteration step is found by a direct solution of (8) on a very coarse grid. Then the mesh is alternately refined and restricted (coarsened) after just one or two iteration(s) on every grid size. The restriction is performed in order to eliminate slowly converging components of the solution (smooth error modes which are difficult to eliminate become more oscillatory on a coarser grid and thus are more successfully eliminated). Every time the result obtained on a coarser grid serves as an initial guess for a finer grid. As a result the convergence is much faster than in a regular relaxation scheme. The solution of the problem involving N unknowns is found at a cost of $\mathcal{O}(\mathcal{N})$ operations [2] for a typical multigrid algorithm, called the full multigrid V-Cycle (FMV) (Fig. 3). If used with adaptive grid refinement strategy, the algorithm has an additional useful feature. The adaptive techniques are the methods, which perform a local mesh adaptation according to the error estimator, which indicates where the domain refinement would be computationally most profitable. It may be especially effective for the FMV cycle, as the algorithm starts on a coarse grid, which can then be effectively refined using an adaptive technique. Such an approach reduces the memory requirements and shortens the evaluation time. This is explained by the fact that the adaptively refined grid has much fewer nodes for the same level of the solution error then the one refined uniformly.

4 Implementation

The KASKADE system [7, 8] was used as a core for the computer implementation of the adaptive multigrid scheme. The system accepts the initial triangulation of the problem together with its BC as an input. The automatic triangulation is performed using the QMG [9] mesh generator with the input data obtained from the two X-ray pictures of the patient with the positioned FS applicator. Then the finite element discretization is performed and the resulting set of equations can be solved using one of the implemented methods. These include a direct LU-decomposition of the system matrix $\mathbf{A}$ (Harwell-MA28 sparse matrix solver) or iterative procedures. Relaxations routines operate on a residual equation of the original system and use different kind of preconditioning in order to improve the convergence of the system. More specifically, it is possible to choose a single or multilevel

Table 1: *Comparison of total number of iterations, solution time and memory allocation for adaptive finite elements and multigrid schemes.*

Total problem size: 105445 (initial 3962)	Memory [MB]	Number of iterations	Total time [s]
Nested iteration – no preconditioning	222.6	772	74.45
Nested iteration – single level preconditioning	222.6	111	19.05
Full multigrid (multilevel preconditioning)	241.1	56	15.94

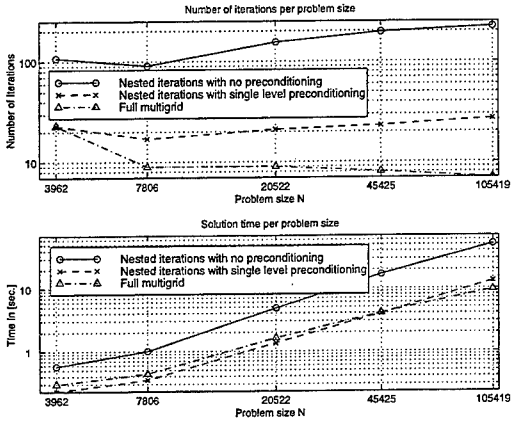

Figure 4: *Number of iterations (top) and solution times (bottom) per problem size (for selected refinement levels). Each refinement level uses the solution of its preceding level as an initial guess and is referred to as a nested iteration scheme. It can be seen, that the number of iterations significantly increases if no preconditioning is applied (except for the first level with arbitrary initial guess). The use of a single level preconditioning significantly improves the situation resulting in almost constant number of iterations per problem size. The application of a multigrid preconditioner results in the decrease of the number of iterations, for the subsequent refinements. The solution time per one iteration is longer for multigrid algorithm, but one needs to keep in mind that, unlike in other methods, the number of iterations decreases with each refinement step.*

preconditioners. The former ones are a typical routines of Jacobi, SSOR or ILU preconditioning, which do not change the resolution of the system matrix. The letter ones compute the coarse grid matrices via a Galerkin procedure or by simply storing the system matrices for selected refinement steps. Since adaptive mechanism gives different final meshes for each of 3 excitations, additional mesh processing is needed in order to use the superposition principle (5). Thus additional procedures were added to the KASKADE system. These procedures perform grid interpolation, which transforms the three basic solutions to a single grid. Once the solutions for $\vec{E}$–field are summed up with prescribed amplitudes and phases, further calculations are performed giving the power (3) or SAR (4) distribution. Such an approach gives the flexibility in obtaining an arbitrary solution for different amplitudes and phases of the excitation and also for switching between two distinct modes (i.e. the solution when

Table 2: *Overall solution time. CPU: R10000, 195MHz.*

Grid generation		**315 s. (5:15 min.)**
$\vec{E}$ – field distribution for a basic mode	Grid refinement	88.6 s.
	Solution	12.2 s.
	Error estimation	100.8 s.
	Mesh interpolation	57.3 s.
	Total	**314.7 s. (5:15 min.)**
Total (3 basic modes)		**944.1 s. (15:44 min.)**
Field summation and calculation of SAR		0.2 s.
Temperature distribution	Grid refinement	6.3 s.
	Solution	5.2 s.
	Error estimation	45.5 s.
	Total	**70.6 s. (1:11 min.)**
Total		**1329.9 s. (22:01 min.)**

two different modes are interlaced with some time interval). Obtained results for the power distribution are then again interpolated onto initial grid of the thermal problem solution (6), which is again solved using the KASKADE system.

5 Numerical tests

The results of selected numerical tests are presented in Table 1 and in Figure 4. It can be inferred that, comparing to nested iteration scheme, the full multigrid algorithm significantly improves the convergence for the problem at hand with the decreasing number of iterations with each refinement step at the cost of some additional memory. Nevertheless, the solution time is only improved for the last refinement step for the largest problem size, as multigrid preconditioning has higher numerical cost than the single-level one. This however is profitable for large number of refinement steps, when the number of iteration for multigrid scheme is much lower.

6 Results

Times required for modeling the SAR and temperature distribution are presented in Table 2. The modeling was performed on SGI Onyx 2 computer with R10000 CPU, 195 MHz and 2.5 GB of RAM. Initial grid was 19120 nodes and 86528 tetrahedrals. The author's intention is to use a different grid generator in the future in order to obtain coarser initial grid and thus to improve the effectiveness of multigrid scheme. The final grid resulted in 126211 points and 704221 tetrahedrals. Then the mesh was interpolated on a regular grid with 336336 nodes.

The total modeling procedure takes 22 minutes. The most time is spent in a solution of basic modes and grid generation. Nevertheless, those are calculated only once and the adjustment of amplitudes and phases are found in less than a second. Thus, the most important treatment parameters can be easily adjusted in order to obtain desired pattern of power deposition. Once the excitations have been found, the simulation of temperature distribution can be performed within a minute.

Using the AVS* system for the presentation of the results, different visualization methods are possible. Figure 5 presents ISO–level surfaces of the SAR distribution, while Figure 6 shows examples of temperature distribution

*Advanced Visual Systems Inc.

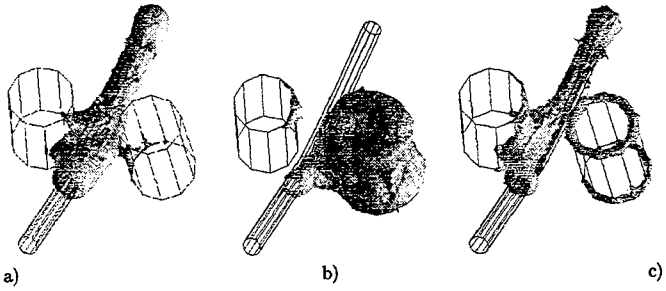

a) b) c)

Figure 5: *ISO-surfaces of 50% level of SAR; a) mode 010 b) mode 100 c) mode 110 – combination of the two previous ones.*

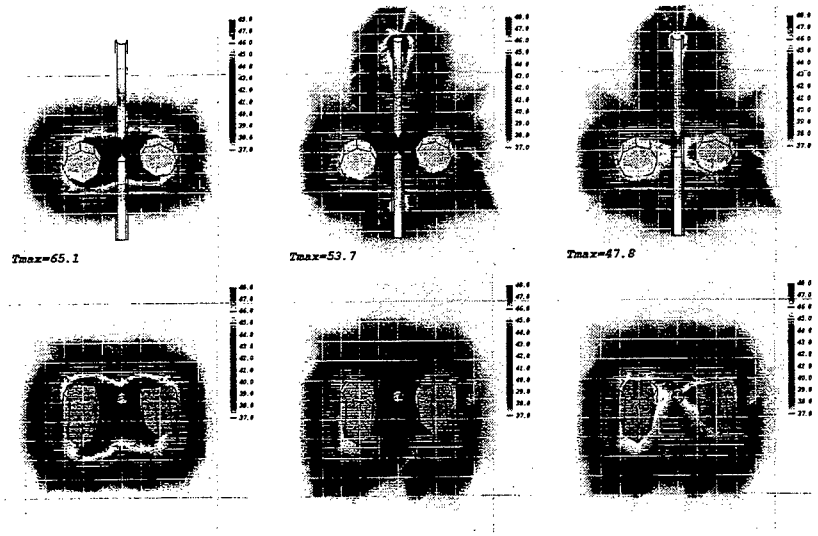

a) $|V| = 65, 0, 70$
$\phi = 0, 0, 180$

b) $|V| = 85, 85, 85$
$\phi = 0, 0, 0$

c) $0.35 \cdot a) + 0.65 \cdot b)$

Figure 6: *Example of solutions obtained for different amplitudes and phases applied to the electrodes of the applicator. Case c) is obtained by switching between mode a) and b) with proportion of 35 to 65 percent.*

for selected cross-sections of the domain and for different excitation modes.

7 Conclusions

A fast numerical method was applied to determination of SAR and temperature distribution. This approach enables the on-line simulations during hyperthermia treatment.

8 Acknowledgments

Computations reported in this paper were performed using the facilities in at the Academic Computer Center in Gdańsk (CI TASK). The research was supported by the Polish State Committee for Scientific Research under contract 8 T11E 02015.

References

[1] Briggs W. L. *A multigrid tutorial.* SIAM, Philadeplphia, 1987.

[2] Wessling P. *An Introduction to Multigrid methods.* John Wiley & Sons, New York, 1992.

[3] McCormick S. F. *Multilevel Adaptive Methods for Partial Differential Equations.* SIAM, New York, USA, 1992.

[4] Overgaard J. Simultaneous and sequential hyperthermia and radiation treatment of an experimental tumor and its surrounding tissue in vivo. *International Journal of Radiation Oncology, Biology and Physics*, (6):1507–1517, 1980.

[5] Overgaard J. Hyperthermia as an adjuvant to radiotherapy. *Sthralentherapie and Onkologie*, 8949(163):453–457, 1987. Review of the randomized multicenter studies of the European Society Hyperthermic Oncology.

[6] Pennes H. H. Analysis of tissue and arterial blood temperatures in the resting human forearm. *J. Appl. Phys.*, (1):93–122, 1948.

[7] Beck R., Erdmann B., and Reiner R. Kaskade 3.0, an object-oriented adaptive finite element code. Technical Report TR 95-4, ZIB Konrad-Zuse-Zentrum für Informationstechik, Berlin, Germany, 1995.

[8] Beck R., Erdmann B., and Reiner R. An object oriented adaptive finite element code: Design issues na applications in hyperthermia treatment planninig. In Arge E., Bruaset A. M., and Langtangen H. P., editors, *Modern Software Tools for Scientific Computing*, pages 105–124. Birkhäuser, Boston–Basel–Berlin, 1997.

[9] Vavasis S. A. *QMG 1.1 Mesh Generation.* Cornell University, USA, http://www.cs.cornell.edu/home/vavasis/qmg1.1/meshgen.html, 1996.

AUTHORS INDEX

Agboraw, E. 479
Aidam, Martin 578, 628
Allard, R.J. 286
Altintas, A. 622
Andersen, Lars S. 250
Anderson, V. 638
Andersson, Ulf 572
Archambeault, Bruce 137
Baharav, Zachi 387
Bakr, M.H. 326
Bandler, J.W. 326
Barbisch, Brian J. 348
Bardati, Fernando 32
Beggs, John H. 45
Belrose, John 442, 463
Best, Steven R. 420
Bevensee, R.M. 171, 555
Bindiganavale, Sunil 232
Booker, S.M. 547
Bostan, Mihai 615
Breakall, James K. 436
Bridges, Jack E. 675
Briley, W. Roger 45
Brown, A.D. 302
Buchau, A. 455
Burke, Gerald J. 404
Cangellaris, Andreas 316, 586
Caputa, K. 682
Chen, Jiang-Bin James 24
Chew, Weng Cho 198, 294
Chung, You Chung 359
Cohen, Nathan 101
Collins, Peter J. 191
Cooper, Brett 93, 184
Craven, Robert P.M. 594
Cule, D. 660
Davidson, David B. 518
Dawson, Trevor W. 143, 682
Debicki , Michal P. 697
Debicki, Piotr 697
Demkowicz, L. 205
Dietz, D. 4
Dunn, John M. 412
Eade, J. 496
Eibert, Thomas F. 250
Elsherbeni, Atef Z. 130
ELSherbeni, Khaled M. 594
Erdemli, Y.E. 302
Fang, Da-Gang 218
Feng, Ningning 218
Fenton, Mun-Won 436
Fezoui, L. 608
Fichtner, W. 16
Fisher, S.E. 371
Fleming, A.H.J. 638, 644
Fujii, Masafumi 602
Georgieva, N. 326
Golik, Wojciech L. 156
Guidry, Rene D. 226
Greenwood, Andrew 258
Hagness, Susan C. 675
Hansmann, Riana H. 518
Haupt, Randy 359
Haviland, R.P. 54
Hill, Kueichien C. 178
Hoefer, Wolfgang J.R. 602
Hom, Kam 184
Huang, Chun-Wen Paul 24
Iskander, Magdy 212
Ismail, M.A. 326
Jakobus, U. 455, 652
Jayawardene, M. 496
Jin, Jian-ming 218, 258
Jones, Eric A. 342
Joines, William T. 342
Kempel, Leo C. 242
Kesler, Oren B. 86
Kim, Jacob J. 86
Korner, T.O. 16
Kubina, S.J. 660
Landstorfer, F.M. 455
Lauber, W.R. 660
Ledfelt, Gunnar 572
Leisten, O.P. 479
Li, Zhifang 250
Liang, Changhong
Lindenmeier, S. 622
Ling, Feng 218
Ling, Hao 272
Liou, Lee L. 38
Loffler, D. 484
Loukos, G. 496
Lu, Yilong 150, 365
Ma, Yan-Chow 232
MacGillivray, J.T. 4
MacMillan, Hugh 412
Marrocco, Gaetano 32
McKaughan, Michael E. 449
Melton, David 449
Meyer, F.J.C. 652
Michielssen, E. 371
Miller, E.K. 278, 470
Mittra, R. 69, 334, 428, 508, 542
Mohammed, Osama A. 394
Mosallaei, H. 379
Mouyis, G.D. 508
Mrozowski, Michal 563, 697
Nott, Nott 107
Packer, Malcolm 689
Perez, Reinaldo 122
Pertl, Franz A. 594
Peterson, Andrew F. 530
Piket-May, Melinda 12
Rachowicz, W. 205
Radhakrishnan, K. 294
Rahmat-Samii, Y. 379
Ramahi, Omar M. 163, 266, 490
Rebel, Jurgen N. 628
Remaki, Malika 608
Remis, R.F. 308
Rewienski, Michal 563
Rowley, J. 638
Rumsey, Ian 12
Russer, Peter 578, 622, 628
Sancer, Maurice 232
Savage, Scott 524
Seager, R. 496
Seals, Kelly 449
Sertel, Kubilay 250
Shaeffer, John 93, 184
Skinner, J. Paul 191
Slepnev, Y. 116
Smith, Charles E. 24
Smith, James E. 594
Smith, P.D. 547
Speciale, Ross A. 72
Stamm, James 436
Steich, David J. 404
Stjernman, Anders 500
Stuchly, Maria A. 682
Su, Tao 272
Swanson, Jr., D.G. 326
Taflove, Allen 675
Theis, Sidney W. 86
Trott, Keith D. 226
Trueman, C.W. 660
van den Berg, P.M. 308
Vardapetyan, L. 205
Vardaxoglou, J.C. 479, 496
Veremey, N.V. 69
Villaseca, Eduardo H. 668
Vinogradova. E.D. 547
Vinogradov, S.S. 547
Volakis, John L. 250, 302
Von. Hagen, J. 428
Wang, Yuanxaun 272, 472
Warnick, K. 198
Wassef, Karim N. 530
Weile, D.S. 371
Werner, D.H. 69, 286, 334, 348, 428
Werner, D.H. 508
Werner, P.L. 69, 334
Wiesbeck, W. 484
Wood, JR., William D. 178
Woody, W. 371
Wu, Kuang 86
Xiao, Ying 150
Yakura, S.J. 4
Yeo, Beng-Kiong 365
Yousif, Hashim 130
Zhao, Li 316, 586
Zmyslo, J.S. 508